

Lecture Notes in Mechanical Engineering

Andrey A. Radionov

Oleg A. Kravchenko

Victor I. Guzeev

Yurij V. Rozhdestvenskiy *Editors*

Proceedings of the 5th International Conference on Industrial Engineering (ICIE 2019)

Volume I

 Springer

Lecture Notes in Mechanical Engineering

Lecture Notes in Mechanical Engineering (LNME) publishes the latest developments in Mechanical Engineering - quickly, informally and with high quality. Original research reported in proceedings and post-proceedings represents the core of LNME. Volumes published in LNME embrace all aspects, subfields and new challenges of mechanical engineering. Topics in the series include:

- Engineering Design
- Machinery and Machine Elements
- Mechanical Structures and Stress Analysis
- Automotive Engineering
- Engine Technology
- Aerospace Technology and Astronautics
- Nanotechnology and Microengineering
- Control, Robotics, Mechatronics
- MEMS
- Theoretical and Applied Mechanics
- Dynamical Systems, Control
- Fluid Mechanics
- Engineering Thermodynamics, Heat and Mass Transfer
- Manufacturing
- Precision Engineering, Instrumentation, Measurement
- Materials Engineering
- Tribology and Surface Technology

To submit a proposal or request further information, please contact the Springer Editor in your country:

China: Li Shen at li.shen@springer.com

India: Dr. Akash Chakraborty at akash.chakraborty@springernature.com

Rest of Asia, Australia, New Zealand: Swati Meherishi at swati.meherishi@springer.com

All other countries: Dr. Leontina Di Cecco at Leontina.dicecco@springer.com

To submit a proposal for a monograph, please check our Springer Tracts in Mechanical Engineering at <http://www.springer.com/series/11693> or contact Leontina.dicecco@springer.com

Indexed by SCOPUS. The books of the series are submitted for indexing to Web of Science.

More information about this series at <http://www.springer.com/series/11236>

Andrey A. Radionov · Oleg A. Kravchenko ·
Victor I. Guzeev · Yuriy V. Rozhdestvenskiy
Editors

Proceedings of the 5th International Conference on Industrial Engineering (ICIE 2019)

Volume I

 Springer

المنارة للاستشارات

Editors

Andrey A. Radionov
South Ural State University
Chelyabinsk, Russia

Victor I. Guzeev
South Ural State University
Chelyabinsk, Russia

Oleg A. Kravchenko
Platov South-Russian State
Polytechnic University
Novocherkassk, Russia

Yurij V. Rozhdestvenskiy
South Ural State University
Chelyabinsk, Russia

ISSN 2195-4356

ISSN 2195-4364 (electronic)

Lecture Notes in Mechanical Engineering

ISBN 978-3-030-22040-2

ISBN 978-3-030-22041-9 (eBook)

<https://doi.org/10.1007/978-3-030-22041-9>

© Springer Nature Switzerland AG 2020

This work is subject to copyright. All rights are reserved by the Publisher, whether the whole or part of the material is concerned, specifically the rights of translation, reprinting, reuse of illustrations, recitation, broadcasting, reproduction on microfilms or in any other physical way, and transmission or information storage and retrieval, electronic adaptation, computer software, or by similar or dissimilar methodology now known or hereafter developed.

The use of general descriptive names, registered names, trademarks, service marks, etc. in this publication does not imply, even in the absence of a specific statement, that such names are exempt from the relevant protective laws and regulations and therefore free for general use.

The publisher, the authors and the editors are safe to assume that the advice and information in this book are believed to be true and accurate at the date of publication. Neither the publisher nor the authors or the editors give a warranty, expressed or implied, with respect to the material contained herein or for any errors or omissions that may have been made. The publisher remains neutral with regard to jurisdictional claims in published maps and institutional affiliations.

This Springer imprint is published by the registered company Springer Nature Switzerland AG
The registered company address is: Gewerbestrasse 11, 6330 Cham, Switzerland

Preface

The International Conference on Industrial Engineering took place on March 25–29, 2019, in Sochi, Russian Federation. The conference was organized by four universities—South Ural State University (National Research University), Moscow Polytechnic University, Platov South Russian State Polytechnic University, and Volgograd State Technical University.

The conference was carried out under financial support of the South Ural State University (National Research University).

The conference was really large-scaled and international. The International Program Committee has selected more than 500 reports. The conferees represented 63 Russian cities from the western and central parts to the Far East regions. International participants represented such countries as China, Germany, Kazakhstan, Kyrgyzstan, Portugal, Saudi Arabia, Tajikistan, Ukraine, USA, and Uzbekistan.

The conference participants submitted papers reflecting recent advances in the field of industrial engineering, in Russian and English. The conference was organized in 13 sections, including Part I “Mechanical Engineering” (machinery and mechanism design; dynamics of machines and working processes; friction, wear, and lubrication in machines; design and manufacturing engineering of industrial facilities; transport and technological machines; mechanical treatment of materials; industrial hydraulic systems; green manufacturing) and Part II “Materials Engineering and Technologies for Production and Processing” (polymers, composites and ceramics; steels and alloys, metallurgical and metalworking technologies; chemical and hydrometallurgical technologies; surface engineering and coatings; processing and controlling technologies).

The International Program Committee selected 294 papers from Part I of the conference technical sections for publication in book series “Lecture Notes in Mechanical Engineering.”

The Organizing Committee would like to express our sincere appreciation to everybody who has contributed to the conference. Heartfelt thanks are due to authors, reviewers, participants, and to all the team of organizers for their support and enthusiasm which granted success to the conference.

Chelyabinsk, Russia

Andrey A. Radionov

Contents

Gear Transmission with Conic Axoid on Parallel Axes	1
S. Shevchenko, A. Mukhovaty and O. Krol	
Mathematical Model of Mechanism for Sealing Hardly Deformable Materials	11
E. I. Kromsky, S. V. Kondakov and M. A. Asfandiarov	
Promising Machine for Compacting Road-Building Materials	21
E. I. Kromsky, S. V. Kondakov and K. Z. Tilloev	
Assessing Effectiveness of Technical Measures for Improving Working Conditions of Wheeled Vehicle Operators	29
V. Shkrabak, A. Kalugin and Y. Averyanov	
Definition of Rational Modes of Use of Marginal Dug-Out Wells	41
V. Kushnir, O. Benyukh and S. Kim	
Hose Regulating Device with Swirling	49
A. V. Fominykh, I. R. Chinyaev and A. A. Ezdina	
Theoretical and Experimental Evaluation of Diesel Engine Derating Effect on Its Life Time	55
A. Malozemov, V. Dooun and D. Kozminykh	
Failure Model for Gear Couplings Under the Criterion of Working Surface Endurance	65
M. G. Slobodianskii, Alexey V. Antsupov and S. V. Lukinskih	
Analytical Model of Wear-Out Failures in Spur Gears of External Gearing	75
Alexander V. Antsupov, M. G. Slobodianskii and V. P. Antsupov	
Development of Analytical Methodology for Detail Durability Test While Arranging Metallurgical Machines	83
Alexey V. Antsupov, Alexander V. Antsupov and V. P. Antsupov	

Application of Kantorovich-Vlasov Method for Shaped Plate Bending Problem	91
S. V. Konev, A. S. Fainshtein and I. E. Teftelev	
Comparative Analysis of Stress–Strain Condition of Cylindrical Gears Arc Teeth and Spurs	101
K. Syzrantseva, V. Syzrantsev and D. Babichev	
Thermomechanical Fatigue Analysis of Diesel Engine Piston: Finite Element Simulation and Lifetime Prediction Technique	109
S. M. Sivachev and L. L. Myagkov	
Quantitative Assessment of Thermal Properties of the Metal-Cutting Machine Design	119
B. M. Dmitriev	
Estimation Method of Slip Ring Mechanical Strength in Current Collectors in Static Setting	129
I. V. Kudryavtsev, O. I. Rabetskaya and A. E. Mityaev	
Ensuring Operational Life and Reliability of Contact Rings in Plastic State	137
I. V. Kudryavtsev, E. S. Novikov and V. G. Demin	
Deformation and Stability of Cylindrical Shells Under Irregular Radial Loading	145
S. V. Makhnovich, D. A. Permyakov and Yu. M. Khishchenko	
Evaluation of Possible Limits of Forcing of High-Capacity Air-Cooled Engines	159
A. V. Vasilyev, A. M. Lartsev and E. A. Fedyanov	
Torsional Rigidity of Elastic Rods of Polygonal Cross Section	167
A. V. Korobko, Yu. E. Lygina and S. Yu. Savin	
Strength Calculation of the Frame of Tourist Solar-Powered Vehicle in the Conditions of Static Loading	175
A. A. Polivanov and V. S. Galuschak	
Durability of Centrifugal Pump Impeller Blades Exposed to Corrosive–Erosive Wear	181
V. A. Pukhliy and S. T. Miroshnichenko	
Theoretical Calculation of Compressed Media Leaks in Working Bodies of Single-Rotor Screw Compressor with Circumferential Tooth Shape	191
A. F. Minikayev, V. A. Pronin and D. V. Zhignovskaya	

Contact Strength Calculation of Straight Bevel Precessional Gears with Small Shaft Angle	197
V. Syzrantsev and A. Pazyak	
Research of Direction of Rope-Hydraulic Quarry Excavator Creation	205
S. A. Khoroshavin, V. S. Shestakov and V. I. Saitov	
Formation of Quality Indicators System at Design of Mechanical Engineering Products	213
E. A. Ivakhnenko, L. M. Chervyakov and O. Yu. Erenkov	
Mini-Converter for Processing of Poor-Quality Charge and Metal-Containing Waste	223
S. Eronko, S. Gorbatyuk and M. Tkachev	
Cabled Feeder for Underground Drilling Machines	231
A. M. Busygin	
Solving Problem of Curved Surface Approximation by Layers with Constant and Variable Sections During Forming by Additive Methods	239
A. N. Grechukhin, V. V. Kuts and M. S. Razumov	
Assessment of Natural Oscillation Frequencies of Rotor for Development of Hard-Bearing Balancing Machine	249
S. O. Gaponenko, A. E. Kondratiev and I. R. Tazeev	
Equipment with Disc Cutters for Destruction and Removal of Strength Snow and Ice Formations on Road Surface	259
A. V. Lysyannikov, Yu. N. Bezborodov and V. G. Shram	
Improvement of Equipment for Knocking Out Castings from Molds	269
V. G. Nekrutov, A. V. Irshin and B. A. Reshetnikov	
Theoretical Study of Sifting Heap on Finger Chaffer Sieve	277
A. V. Butovchenko, E. E. Petrov and A. A. Doroshenko	
Modeling Polymeric Centrifugal-Pump Impeller Blades	287
V. A. Pukhliy, S. T. Miroshnichenko and V. V. Sokolov	
Vibration Isolating and Impact Protecting Systems with Quasi-Zero Stiffness Providing Wide Operating Area	299
A. Zotov and A. Valeev	
Locating of Oscillating Defect in Rotary Equipment via Remote Strain Gauge Analysis	309
A. Valeev and A. Tokarev	

Results of Studying Cleaning of Exhaust Gases of Preheater-Equipped KamAZ-740 Diesel Engine	319
A. A. Melbert and A. V. Mashensky	
Features of Rotor Friction Losses Balancing in Centrifugal Electric-Driven Pumps for Spacecrafts	329
A. Bobkov	
Deformation of Prismatic Samples of U-Shaped Grooves and Their Stress–Strain State	337
E. V. Zenkov and D. A. Elovenko	
Analysis of Gears’ Engagement Parameter in Period of Steady Wear	349
M. Akopyan, S. Reznikov and O. Kuznetsova	
Kinostatics of Rotationally Reciprocating Stirred Tank Planetary Actuator	359
A. A. Prikhodko	
Automation of Heat Exchanger Shell Holes Machining Operation	367
A. Yu. Gorelova, M. G. Kristal and V. A. Martynenko	
Arching Design of Device for Cooling Cutting Zone of Milling Machine Based on Graph Model of Physical Working Principle	377
A. A. Yakovlev, V. S. Sorokin and S. G. Postupaeva	
Processing of Renewable Wood Biomass into Thermally Modified Pellets with Increased Combustion Value	387
R. G. Safin, D. B. Prosvirnikov and T. O. Stepanova	
Influence Estimate of Spectral Model of Combustion Product Radiation on Results of DKVR-10/13 Steam Boiler Furnace Simulating	399
D. A. Akhmedzaynov, A. E. Kishalov and V. D. Lipatov	
Automated Control of Truck Drive Axle Performance Characteristics	411
A. Yu. Barykin, M. M. Mukhametdinov and R. Kh. Takhaviev	
Simulation of Transforming Magnetic Systems Based on Permanent Magnets to Control Microparticles	419
N. N. Merzlova, A. V. Pashkovskiy and D. V. Boldyrev	
Use in Cycle of Biogas Plant Boiler for Waste Disposal	431
S. A. Naumov, V. Y. Sokolov and A. V. Sadchikov	
Simulation of Rectification Process Taking into Account Longitudinal Diffusion on Equations of Working Lines	441
A. B. Golovanchikov, V. N. Karev and N. A. Prokhorenko	

Investigation of Process of Cutting Fruit and Vegetable Raw Materials into Slices Using Rotary Chopper	451
N. Lebed, N. Antonova and G. Rusakova	
Investigation of Kinematics of 3D Printer Print Head Moving Systems	461
A. R. Avdeev, A. A. Shvets and I. S. Torubarov	
Development of Algorithm for Creating Parametric 3D Models, Controlled by Mathcad Calculations, to Study Parameters of Enclosed Gears Housing	473
E. Petrakova and V. Sumatokhin	
Automated Method for Modular Selection of Components for Multi-bearing Unit of Internal Combustion Engine Assembling	485
V. A. Saninsky, V. V. Korzin and A. V. Petrukhin	
Improving Synthesis Accuracy of Topology Elements in Laser Pattern Generators with Circular Scanning Mode	497
A. V. Kiryanov and V. P. Kiryanov	
Estimation of Heat Losses in Fuel Combustion by Analysis of Gas Pressure in the Cylinder of Diesel	507
E. A. Lazarev, V. E. Lazarev and M. A. Matculevich	
Determination of Parameters and Characteristics of Injection in Fuel System of Accumulating Type at Cold Start of the Diesel Engine	515
V. V. Shishkov and E. A. Lazarev	
Influence of Main Design Parameters of Motion Conversion Mechanism of Crankless Reciprocating Machine (Engine) on Torque Value on Output Shaft	523
B. A. Sharoglazov and V. V. Klementev	
Research of Dynamic Characteristics of Bearing Structures at Takeaway of Ventilation Equipment on the Workshop Roof	533
G. Voronkova, N. Borisova and A. Borisov	
Features of Pulsating Flows Thermomechanics in Exhaust System of Piston Engine with Turbocharging	541
L. V. Plotnikov, Yu M. Brodov and N. I. Grigor'ev	
Improvement of Environmental Characteristics of Diesel Locomotive Engine with Turbocharging by Changing Valve Timing (Based on Miller Cycle)	549
L. V. Plotnikov, S. Bernasconi and P. Jacoby	

Calculated Analysis of Efficiency of Fresh Charge Heating in Diesel Engine Under Cold-Start Conditions	559
A. E. Popov, Z. V. Almetova and V. D. Shepelev	
Theoretical Studies of Automobile Smooth Running on High-Safety Wheels	567
V. V. Mazur	
Computer Simulation of Numerical Description of Closed Curve Using Fourier Coefficients	575
S. Ibrayev, Zh. Bidakhmet and Ay. Rakhmatulina	
Simulation of Fuel Ignition Chemical Kinetics in Diesel Engine at Cold Start with Modelica Language	585
A. Malozemov, A. Savinovskikh and G. Malozemov	
Dynamic Pattern of Safe Operation Indicators for Heavy-Duty Machines	595
Yu. A. Izvekov, V. V. Dubrovsky and A. L. Anisimov	
Influence of Spherical Body Diameter on Impact Interaction Dynamics	603
V. Lapshin, V. Yashenko and A. Eliseev	
Indicative and Efficient Parameters of the Engine Operating Cycle When Using Fuels with Various Octane Numbers	611
V. E. Lazarev, M. A. Matculevich and E. A. Lazarev	
Interaction of Elastic Wheel with Bumps of Rectangular Shape	621
A. Startcev, S. Romanov and O. Vagina	
Opportunities for Using Spline Method to Calculate Orthotropic Plate Under Bending Conditions	631
V. S. Zhernakov, V. P. Pavlov and V. M. Kudoyarova	
Experiments to Find the Rolling Resistance of Non-pneumatic Tires Car Wheels	641
V. V. Mazur	
Peculiarities of Motion of Pendulum on Mechanical System Engine Rotating Shaft	649
A. I. Artyunin, S. V. Barsukov and O. Yu. Sumenkov	
Reducing Dynamic Loads in Hoisting Mechanism of Excavator Based on Feedbacks on Elastic Torque	659
N. K. Kuznetsov, I. A. Iov and E. S. Dolgih	
Determination of Magnetization Efficiency of Wheel-Rail Contact Zone	669
D. Ya. Antipin, V. O. Korchagin and M. A. Maslov	

Forecasting of Life Service of Hopper Car Body Load-Bearing Structure on Basis of Mathematical Modeling Methods	677
D. Ya. Antipin, V. V. Kobishanov and A. S. Mitakov	
Evaluation of Heat Mechanical Loading of Piston of Gasoline Engine 4CH8,2/7,56 When It Is Forced at Average Effective Pressure	687
G. V. Lomakin and V. M. Myslyayev	
Losses Analysis in Gas Turbine Engines Flow Parts	697
I. A. Krivosheev, N. B. Simonov and K. E. Rozhkov	
Transfer Functions for Shearing Stress in Nonstationary Fluid Friction	707
V. Sokolov	
On Splitting of Bending Frequency Spectrum of Geometrically Imperfect Shells	717
S. V. Seregin	
Mathematical Model of Spindle Unit Bearing Assembly	725
E. S. Gasparov and L. B. Gasparova	
Evaluation of Contact Stresses in Railway Wheel When Rolling Through Rail Joint	733
E. S. Evtukh and G. A. Neklyudova	
Determination of Eigenforms and Frequencies of Transverse Vibrations of a Rod of Variable Cross Section in the Field of Centrifugal Forces	743
A. P. Levashov and O. Yu. Medvedev	
Problem of Calculation of Reliability of Hierarchical Complex Technical Systems	753
P. A. Kulakov, D. D. Galyautdinov and V. G. Afanasenko	
Developing Methods for Calculating Gas-Dynamic Parameters in Launch Canister During the Missile Launch	765
R. A. Peshkov and A. V. Erpalov	
The Detection of Electrode Breakage in Electric Discharge Process by Methods of Vibroacoustic Diagnostics	775
M. Kozochkin, A. Porvatov and D. Allenov	
Method of Estimation of Pressure Forces from Power Plant in Microtunneling	783
E. Y. Kulikova and I. I. Shornikov	
Diesel Work Cycle at Start	791
V. V. Shishkov	

Dynamic Analysis of Lifting Cranes	801
N. N. Panasenکو and A. V. Sinelschikov	
Vibration Isolation Properties of Vehicle Suspension at Optimal Instantaneous Damping Control in Oscillation Cycle	819
K. V. Chernyshov, A. V. Pozdeev and I. M. Ryabov	
Monitoring Engine Toxicity Parameters and Selective Control of Its System Operation	829
A. V. Gritsenko, Z. V. Almetova and V. V. Rudnev	
Finding Stable Region of Torsional Vibrations of Agro-Industrial Rotary Cultivators	839
S. A. Partko, L. M. Groshev and A. N. Sirotenko	
Improvement of Fuel Injection and Atomization Processes in Transport Diesel Engine	845
V. A. Markov, S. N. Devyanin and V. G. Kamaltdinov	
Finding New Component in Displacement of Normal Supporting Surface Reaction to Car Wheels	855
T. A. Golubeva and E. V. Balakina	
Numerical Research of Combustible Mixture Inert Components Influence on Compression-Ignition Engines Combustion Process	865
V. G. Kamaltdinov, V. A. Markov and K. S. Leonov	
Results of Bench Tests of Pneumatic Suspension with Air-Hydraulic Damping	875
V. V. Novikov, A. V. Pozdeev and D. A. Chumakov	
Investigation of Stress-Strain State of Ball Mill Trunnion	883
Ju. A. Bondarenko, S. I. Khanin and O. V. Bestuzheva	
Influence of Stiffness of Rear Leaf Spring on Van Vibration Loading	895
Yu. A. Polyakov	
Hydroelastic Oscillations of Three-Layered Channel Wall Resting on Elastic Foundation	903
D. V. Kondratov, V. S. Popov and A. A. Popova	
Use of Vibration Isolation Systems with Negative Stiffness on the Basis of Special Shaped Guides to Reduce Pump Piping Vibration	913
A. Tokarev, A. Valeev and A. Zotov	
Effect of Two Cracks in a Rotor on Stiffness Using the Theory of Fracture Mechanics	921
Salam Ahmed Abed, Mohammad Reza Bahrami and Jassim Farij Thijel	

How Asymmetric Initial Imperfections in Shape Affect Free Oscillations of Thin Shells	931
S. V. Seregin	
Test Bench for Analyzing Adaptability of Foil Gas-Dynamic Bearings to External Changes	941
A. V. Gorin, R. N. Poliakov and A. V. Sytin	
Automatic System of Low-Pressure Gas Recycling at Liquid Removal from Wells and Gas Collectors	951
M. Yu. Prakhova, A. N. Krasnov and E. A. Khoroshavina	
Improvement of Procedure for Determining Antioxidant Additive (Ionol) in Insulating Oils	963
M. Lyutikova and S. Korobeynikov	
Resource-Saving Multifunctional Apparatus for Autonomous Energy and Water Supply Systems	973
I. V. Dolotovskij and N. V. Dolotovskaya	
Slag Cut-off During Steel Casting	983
Yu. I. Eremenko and D. A. Poleshchenko	
Arresting Longitudinal Cracks in Steel Pipelines: Computational Analysis Technique	993
Baraa M. H. Albaghdadi and A. O. Cherniavsky	
Improvement of Operational Characteristics of Aggregates by Nanostructuring Surfaces of Tribounits	1003
M. Yu. Karelina, T. Yu. Cherepnina and N. Yu. Bugakova	
Advantages of Using Wheel Rolling Radius for Calculating Friction Characteristics in Wheel-to-Road Contact Patch	1015
E. V. Balakina, E. Y. Lipatov and D. S. Sarbayev	
Lubrication Conditions and Development of Pre-failure State of Crankshaft Bearings	1023
A. T. Kulakov, E. P. Barylukova and I. P. Talipova	
Investigations of Antifriction Films Formation in Dioctyl Sebacate Medium with Cholesteryl Esters	1035
M. V. Boiko, A. P. Sychev and I. V. Kolesnikov	
Dependence of Automatic Installation of Tool Carrier Process on Orientation Errors and Their Effect on Performance Characteristics of Spindle-Tool Subsystem	1043
O. Yu. Kazakova and L. B. Gasparova	

Automated Calculation and Control of Body Wear in Friction Pair	1053
V. A. Saninsky, V. V. Korzin and M. A. Kononovich	
Method for Modelling of Circulation of Lubricating Fluid in Models of Machine-Building Products	1063
A. S. Gorobtsov, E. G. Gromov and N. V. Chigirinskaya	
Influence of Physicochemical Processes on Reliability of Node of Sliding Current Collector of Electric Machines	1073
S. A. Izotov, A. I. Izotov and A. A. Fominyh	
Bench-Scale Tests Aimed at Finding Rate and Acceleration of Wear Determining Service Life of Thrust Bearing in Submersible Electric Motor	1089
V. A. Butorin, I. B. Tsarev and R. T. Guseynov	
Macromechanism Destruction of Structurally and Crystallographically Textured Titanium Billets	1097
M. A. Skotnikova, G. V. Ivanova and A. A. Strelnikova	
Study on Factors Having Influence Upon Efficiency of AC Motor Chain Drive Using Newly Developed Method and Procedure for Identification of Its Friction Losses	1107
V. Belogusev, A. Egorov and I. Polyaniin	
Discrete Contact in Toothed Gearing	1117
Alexander Vladimirovich Titenok and Igor Alexandrovich Titenok	
Contact Movement in Mating Conical Joints Within Resting Friction	1127
V. Feropontov, N. Perfileva and A. Maksimenko	
Forming Laminar Flow of Engine Oil Under Conditions of High-Speed Sliding Friction	1137
V. I. Kubich, E. A. Zadorozhnaya and O. G. Cherneta	
Study of Dependence of Kinematic Viscosity and Thermal-Oxidative Stability of Motor Oils	1155
V. G. Shram, Yu. N. Bezborodov and A. V. Lysyannikov	
Complex Method for Evaluating Lubricating Properties of Technological Tools and Stresses When Drawing Products from Sheet Steel	1163
G. I. Shulga, A. O. Kolesnichenko and I. Y. Lebedinsky	
Monitoring Technical Status of Engine Bearings by Pressure Parameters in Central Oil Line	1175
A. V. Gritsenko, V. D. Shepelev and A. G. Karpenko	

Evaluation of Thermal Condition of Turbocharger Rotor Bearing	1183
E. Zadorozhnaya, V. Hudyakov and I. Dolgushin	
Ensuring Tightness of Sealing Joints at the Design Stage	1195
P. Ogar, A. Kozhevnikov and V. Kushnarev	
Modeling Introduction of Rigid Sphere into Layered Elastic Body	1205
P. Ogar, A. Kozhevnikov and V. Kushnarev	
Influence of Oxidation Products on Anti-wear Properties of Lubricants	1215
B. I. Kovalsky, N. N. Lysyannikova and E. G. Kravcova	
Experimental Modeling of Wearing the Friction Surfaces of “Piston-Cylinder” Tribounit	1225
A. Doikin and K. Gavrilov	
Investigation of Influence of Steel SH 15 on Oxidation and Anti-wear Properties of Mineral Oil	1233
E. G. Kravtsova, B. I. Kowalsky and N. N. Lysyannikova	
Theoretical Research of Kinematic Pair “Shaft-Sleeve” of Friction Bearing of Gas-Compressor Unit at Variable Speeds of Shaft Rotation	1241
Y. P. Serdobintsev, M. P. Kukhtik and A. M. Makarov	
Design Engineering and Manufacturing of Technology of Bearings for Heavy-Duty Friction Units	1251
R. V. Yudin, D. A. Parinov and I. N. Medvedev	
Surface Films Formation on Steel During Friction of Polymer Composites Containing Microcapsules with Lubricant	1259
A. V. Sidashov and M. V. Boiko	
Fabrication and Triboengineering Properties of Aluminum Composite Ceramic Coatings	1269
A. N. Bolotov, V. V. Novikov and O. O. Novikova	
Formation and Properties of Multilayer Composite Solid Lubricant Coating	1279
I. N. Shcherbakov, A. A. Korotkiy and E. V. Egelskaya	
Modeling Wear of Tool’s Front Surface During Turning	1287
S. A. Kurguzov and M. V. Nalimova	

Evaluation of Lubricants Use with Ultrafine Copper-Containing Additives in Sliding Bearings with Reversible Friction	1295
S. G. Dokshanin, V. S. Tynchenko and V. V. Bukhtoyarov	
Numerical Modelling of Fluid-Film Bearing Lubricated with Magnetorheological Fluid	1303
A. Babin, A. Fetisov and V. Tyurin	

Gear Transmission with Conic Axoid on Parallel Axes



S. Shevchenko, A. Mukhovaty and O. Krol

Abstract The article presents the results of a study for gear transmission on parallel axes with gear axoids and wheels in the form of truncated cones (CGA). The tangential gear teeth and CGA wheels in the longitudinal direction coincide with the conical helical lines lying on the truncated cones, which are the axes of the CGA. In this case, the angle of these cones is invariant with respect to the transfer value of the CGA, which allows them to vary widely. The length of the CGA teeth is determined, the growth of which will lead to a decrease in bending and contact stresses in the teeth of the CGA. As a result, there will be an increase in the load capacity of the CGA in comparison with a cylindrical gear transmission with chevron teeth (CGCh) with the same dimensions according to the basic criteria for the performance of this type of transmission—bending and contact fatigue strength. For the practical calculation of the CGA, an enlarged scheme of the algorithm for calculating the CGA is proposed, with reference to the current calculation procedure for the CGCh. The design features of the CGA are noted.

Keywords Conical line · Cylindrical gear · Chevron teeth · Tangential teeth · Axoids

1 Introduction

The technical level of the technological and transport equipment largely predetermines the technical and economic indicators of the mechanical drives contained in them. This explains the relevance of research aimed at improving existing types of

S. Shevchenko · A. Mukhovaty
Volodymyr Dahl Lugansk National University, 20-a Kvartal Molodezhny,
Lugansk 91034, Ukraine

O. Krol (✉)
Volodymyr Dahl East Ukrainian National University, 59-a Central Pr,
Severodonetsk 93400, Ukraine
e-mail: krolos@snu.edu.ua

engagement gearing and creating their fundamentally new modifications which are introduced in the paper.

1.1 Formulation of the Problem

Improving the technical level of gearing engagement is associated with a set of problems optimizing the design parameters of mechanisms [1–4], upgrading devices already used [5–8], modifying working surface shapes [9–12] and researching tribological factors in the contact zone [13–16]. This article presents the research material connected with using the conical surfaces as axoids for pinions and wheels with parallel axes of rotation proposed by the authors [17].

The task is to perform a comparison of some classical cylindrical gear geometric characteristics for involute gearing with chevron teeth (hereinafter referred to as CGCh) and its analog [17]—gear on parallel axes. The axoids of the considered gear are treated as cones with tangential teeth (hereinafter referred to as CGA). It is required to achieve the possibility of increasing the length of the gear teeth and wheel in gearbox transmission without changing the gear engagement width, which will give an advantage in terms of the load capacity of the gearbox in comparison with the CGCh transmission with other things being equal. There is a need to prove the possibility of increasing the load capacity of the CGA gearing by the main criterion—the contact endurance of the teeth, as compared with the existing type of gear on parallel axes—chevron gearing with the same overall dimensions and other conditions being equal.

2 Theoretical Part

1. Since the CGCh consists of two helical gears (hemi-chevron) with opposite teeth at the same angle of inclination, to calculate the length of the CGCh teeth we use the parametric equation of the helical teeth surface for the involute engagement [18].

$$\begin{cases} x = r_{O1} \cdot \cos v + u \cdot \cos \beta_O \cdot \sin v; \\ y = r_{O1} \cdot \sin v - u \cdot \cos \beta_O \cdot \cos v; \\ z = P \cdot v - u \cdot \sin \beta_O. \end{cases} \quad (1)$$

here, v —an independent variable that varies within $[v_1; v_2]$; u, r_{O1}, β_O, P —constants; the coordinate z passes along the axis of gears rotation. The limits of variable v change are of the obvious condition: $z = [0; b_{W\Sigma}]$, where

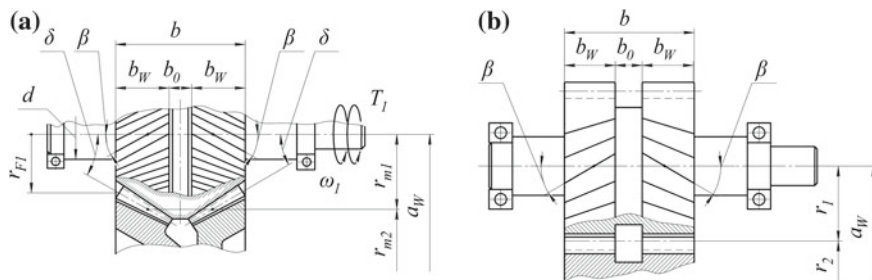


Fig. 1 a Gear of CGCh; **b** gear of CGA

$b_{W\Sigma} = 2 \cdot b_W$ —the width of the CGCh engagement gearing, equal to the width of the two hemi-chevrons b_W , Fig. 1a. As a result,

$$v = [v_1; v_2] = \left[u \cdot \frac{\sin \beta_O}{P}; \frac{u \cdot \sin \beta_O + b_{W\Sigma}}{P} \right], \quad (2)$$

where $\beta_O = \arctg(r_1/r_{O1} \cdot \tg \beta)$ —the angle of the teeth on the base cylinder pinion CGCh; $r_1 = 0,5 \cdot m_n \cdot z_1 / \cos \beta$ and $r_{O1} = r_1 \cdot \cos \alpha_t$ —the radii of the pitch and base pinion cylinders, respectively; $\alpha_t = \arctg(\tg \alpha_n / \cos \beta)$ —face angle of the teeth profile on the pitch cylinder of the pinion, ($\alpha_n = 20^\circ$); β —slope angle of the teeth on the pitch cylinder pinion; $P = r_1 \cdot \tg(\pi/2 - \beta)$ —helix teeth parameter.

The parameter u that determines the position of a point on the pitch circle of the tooth surface (1) is found from the condition:

$$\sqrt{x^2 + y^2} = r_1.$$

After substituting the coordinates $[x, y]$ from the system of equations (1), we get

$$u = \frac{m_n \cdot z_1}{2} \cdot \frac{\sin \alpha_t}{\cos \beta \cdot \cos \beta_O}, \quad (3)$$

where $\alpha_t = \arctg(\tg \alpha_n / \tg \beta)$ —the angle of the tooth profile on the pitch cylinder in the face section.

The joint consideration of dependencies (1) and (3) allows to determine the coordinates of the tooth longitudinal line on the hemi-chevron of the CGCh transmission (Fig. 1a), which is a helical cylindrical line. Its length L is

$$L = \int_{v_1}^{v_2} \sqrt{\dot{x}_v^2 + \dot{y}_v^2 + \dot{z}_v^2} \cdot dv, \quad (4)$$

where $\dot{x}_v = dx/dv$; $\dot{y}_v = dy/dv$; $\dot{z}_v = dz/dv$.

$$\begin{cases} \dot{x}_v = u \cdot \cos \beta_O \cdot \cos v - r_{O1} \cdot \sin v; \\ \dot{y}_v = u \cdot \cos \beta_O \cdot \sin v + r_{O1} \cdot \cos v; \\ \dot{z}_v = P. \end{cases} \quad (5)$$

After integrating the function (4) with the substitution of derivatives (5) and the limits of integration (2) into it, we obtain

$$L = \frac{b_W}{P} \cdot \sqrt{u^2 \cdot \cos^2 \beta_O + r_{O1}^2 + P^2}. \quad (6)$$

For practical calculations, a simpler version of the dependency is proposed for calculating the length of the CGCh tooth (Fig. 1a):

$$L' = b_{W\Sigma} / \cos \beta \quad (7)$$

Calculations show that numerical values L and L' differ by a fraction of a percent.

2. Considering the limited volume of the article and the more cumbersome structure of analytical dependencies for the CGA surface of the teeth, we will calculate their length L_K for the CGA pinion based on the following assumptions (Fig. 1b). The longitudinal direction of the tangential tooth on each hemi-chevron of the bevel gear is determined by the conical helix:

$$\begin{cases} x = a \cdot v \cdot \cos v; \\ y = a \cdot v \cdot \sin v; \\ z = b \cdot v. \end{cases} \quad (8)$$

Therefore, the length of the tangential tooth can be considered as the length of the conical helix (8) on a truncated cone with dimensions:

$r_{F1} = r_{m1} - 0,5 \cdot b_W \cdot \operatorname{tg} \delta$ —radius of the smaller base of the cone, ($r_{m1} = r_1$);
 b_W —the height of the truncated cone between its bases (coordinate z), equal to the width of one CGA hemi-chevron;
 β —the angle between the tangent to the helix and generating line a cone;
 δ —the angle between the generatrix of the cone and the axis z .

These parameters are given.

In the environment KOMPAS-3D, three-dimensional models of cylindrical gear transmission with chevron teeth (Fig. 2a) and gear transmission on parallel axes with gear axoids and wheels in the form of truncated cones on parallel axes (Fig. 2b) are developed. In this case, the “shafts and mechanical transmission” application included in the KOMPAS-3D [19–22].

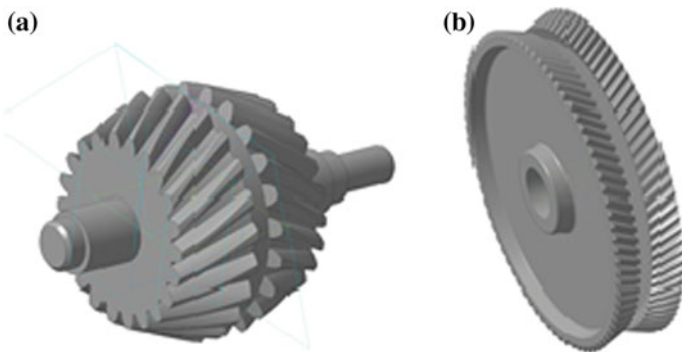


Fig. 2 a 3D model gear of CGCh; b 3D model gear of CGA

When determining a helical cylindrical line, the following parameters are determined:

b_W —the height of the truncated cone between its bases (coordinate z), equal to the width of one CGA hemi-chevron; β —the angle between the tangent to the helix and generating line a cone; δ —the angle between the generatrix of the cone and the axis z .

These parameters are given.

In contrast to bevel gears with intersecting axes of links in CGA gearing (Fig. 1b), the angles of the pitch cones of the pinion (δ_1) and the wheel (δ_2) are the same that is $\delta_1 = \delta_2 = \delta$, and their numerical values are set independently of the gear ratio, but with one restriction:

$$\delta \leq \arctg \left(\frac{r_{m1} - 3,5 \cdot \sqrt[3]{T_1}}{0,5 \cdot b_W} \right), \quad (9)$$

where T_1 —the torque on the pinion shaft, N m; r_{m1} —the average pitch radius of the toothed hemi-chevron of the CGCh pinion, mm; (the size r_{m2} in Fig. 1b denotes the average pitch radius of the toothed hemi-chevron of the CGA wheel); b_W —in mm.

3 Experimental Part

The specified limitation for the angle β is aimed at preventing possible flanking of the pinion teeth on a smaller base of the cone with a radius r_{F1} (Fig. 1b) into the shaft body with a diameter d_B , that is, for the realization of a constructive condition $r_{F1} \geq d_B/2$. We illustrate the constraint (9) as applied to the CGA, whose parameters are given in the numerical calculation of the function (13) given below in the article. Determine the values of the parameters included in the formula (9)

$$r_{m1} = m_{tm} \cdot z_1 / 2 = 39.9 \text{ mm},$$

where $m_{tm} = m_n / \cos \beta = 4 / \cos 17.82^\circ = 4.2$ —the average face module CGA;

$$T_1 = \frac{T_2}{u \cdot \eta} = \frac{3097.8}{5.26 \cdot 0.97} = 607.1 \text{ N m},$$

where $u = \frac{z_2}{z_1} = \frac{100}{19} = 5.26$ and $\eta = 0.97$, respectively, the gear ratio and the coefficient of performance for the CGA.

After substituting these parameters in condition (9), we obtain the restrictive value of the angle δ :

$$\delta_{\max} = \arctg \left(\frac{39.9 - 3.5 \cdot \sqrt[3]{607.1}}{0.5 \cdot 4.2} \right) \approx 26^\circ.$$

Thus, for the CGA with the specified parameters, the pitch angle of the axoid cones of the pinion and wheels should be assigned with the restriction:

$$\delta \leq \delta_{\max} = 26^\circ.$$

The length of the conical helix (8) is determined from the following dependence [20]:

Conical helix length:

$$L_K = \int_{v_1}^{v_2} \sqrt{\dot{x}_v^2 + \dot{y}_v^2 + \dot{z}_v^2} \cdot dv = \int_{v_1}^{v_2} \sqrt{a^2 \cdot (v^2 + 1) + b^2} \cdot dv, \quad (10)$$

where

$$\begin{aligned} \dot{x}_v &= dx/dv = a \cdot (\cos v - v \cdot \sin v); \\ \dot{y}_v &= dy/dv = a \cdot (\sin v + v \cdot \cos v); \\ \dot{z}_v &= dz/dv = b. \end{aligned}$$

The limits of integration of the function (10) are determined by the parameters of the pinion axoid, that is, the truncated cone on which the conical helix (8) is located:

$$\begin{aligned} v_1 &= \frac{\operatorname{tg} \beta}{\sin \delta}; \\ v_2 &= v_1 \cdot \left(1 + \frac{b_W}{r_{F1}} \cdot \operatorname{tg} \delta \right) = \frac{\operatorname{tg} \beta}{\sin \delta} \cdot \left(1 + \frac{b_W}{r_{F1}} \cdot \operatorname{tg} \delta \right). \end{aligned} \quad (11)$$

Constant values:

$$a = r_{F1} \cdot \sin \delta / \text{tg } \beta; \quad b = a / \text{tg } \delta = r_{F1} \cdot \cos \delta / \text{tg } \beta. \tag{12}$$

As a result,

$$L_K = 2 \cdot (L_{K2} - L_{K1})|_{v_1}^2, \tag{13}$$

where

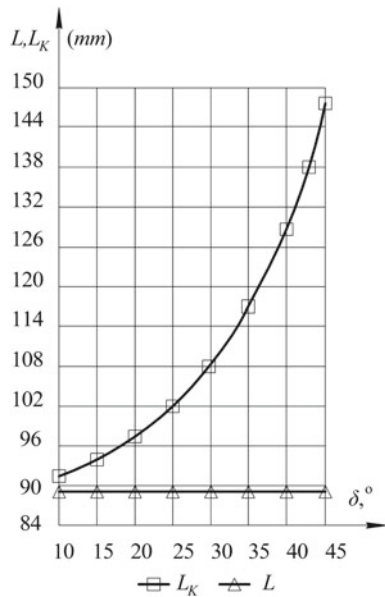
$$L_{K1,2} = \frac{v_{1,2}}{2} \cdot \sqrt{a^2 \cdot (v_{1,2}^2 + 1) + b^2} + \frac{a^2 + b^2}{2 \cdot a} \cdot \ln \left[\sqrt{a^2 \cdot (v_{1,2}^2 + 1) + b^2} + v_{1,2} \cdot a \right]. \tag{14}$$

The factor “2” in the formula (13) takes into account the fact that the pinion in the CGA transmission consists of two hemi-chevrons, that is, of two truncated cones, each of which has parameters $[r_{F1}, b_W, \beta, \delta]$.

The calculations of function (13) show a nonlinear dependence $L_K = L_K(\delta)$. In Fig. 3 shows the graph of this function, built on the dependencies (8)–(13) for transmission with the parameters:

$$a_W = 250 \text{ mm}; \quad m_n = 4 \text{ mm}; \quad z_1/z_2 = 19/100; \quad \beta = 17.82^\circ; \\ b_W = 42.5 \text{ mm}.$$

Fig. 3 Lengths of teeth in CGCh (L) and CGA (L_K)



For comparison, Fig. 3 shows a graph of the CGCh teeth length with the same engagement parameters as in the transmission of the CGA. An increase in the length of CGA teeth in comparison with CGCh with their identical overall dimensions will lead to an increase in the load capacity of CGA for bending and contact endurance of the teeth.

The increase in the teeth length of the CGA compared with the CGCh is from 5.3% at $\delta = 15^\circ$ up to 65% at $\delta = 45^\circ$. For a preliminary assessment of the reduction of contact stresses in the teeth during the transition from the CGCh transmission to the CGA transmission, we use the Hertz dependence for the linear contact of two surfaces [19]. With other things being equal, contact stresses in CGA and CGCh are connected by the relation:

$$\sigma_{H(K)}/\sigma_H = \sqrt{L/L_{(K)}}.$$

For the specified gains L_K , we get

$$\sigma_{H(K)}/\sigma_H = \begin{cases} 0.97 & \text{for } \delta = 15^\circ; \\ 0.8 & \text{for } \delta = 45^\circ. \end{cases}$$

That is the reduction of contact stresses in the CGA as compared with the CGCh is from 3 to 20%. It is obvious that for a more significant reduction, it is advisable to take large values of the axoids angle, but taking into account the restrictive condition (9).

3. Pinion 1 CGA transmission performed together with the shaft. Wheel CGA is an assembly unit consisting of two wheels—2 and 3, each of which has tangential teeth. Conical semi-chevrons mounted on the centers and bolted to them. In order to exclude vibrations when the transmission is in operation, the semi-chevrons should be centered in three directions:

- radial—due to the interference fit of rims on the centers;
- axial—with the help of a shim gasket;
- circumferential—by means of annular grooves in which fastening bolts are placed (in Fig. 2, only the teeth rims of the hemi-chevrons are depicted, and the centers on which they are mounted with the help of bolts, annular grooves and shim gasket are not shown).

Wheels 2 and 3, bolted 4 and centered in three directions:

- radial—by fit on the bead diameter D_6H_7/m_6 ;
- axial—using the shim 5;
- circumferential—through the annular grooves in which the bolts 4 are placed.

4. The following calculation algorithm is recommended for the design of the CGA transmission.

- 4.1. The allowable stresses, as well as the design calculation, in which the axial distance a_w and the main engagement parameters $m_n, b_w, \beta, z_1, z_2$ of the condition of the teeth contact endurance are performed according to the existing design of cylindrical helical transmission [23] (here, m_n —the average normal engagement modulus used in the calculations of modern bevel gears).
- 4.2. The angle of the pitch cones of the pinion and the wheel $\delta \approx 30^\circ \dots 60^\circ$ is assigned, taking into account the obtained limitation—formula (9). To accept the numerical value of the angle, the average face module $m_{tm} = m_{nm} \cos \beta$ is preliminarily calculated, along which the average pitch diameters of the pinion and wheel are $r_{m1} = m_{tm} \cdot z_1/2; r_{m2} = m_{tm} \cdot z_2/2$ (wherein $r_{m1} + r_{m2} = r_1 + r_2 = a_w$).
- 4.3. Tests for contact points (σ_H) and bending (σ_{F1}, σ_{F2}) stresses are carried out using the existing method of calculating cylindrical helical gears [23, 24] with one difference—calculations σ_{F1} and σ_{F2} are carried out using tooth shape factors Y_{F1} and Y_{F2} according to the graph [23] or table depending on biequivalent numbers of CGA pinion teeth and wheel teeth: $z_{vni} = z_i / (\cos^3 \beta \cdot \cos \delta)$, ($i = 1, 2$) as in bevel gears. This is due to the fact that the pitch surfaces of the CGA transmission links are cones, which is different from the CGCh transmission where axoids are cylinders.

4 Conclusion

1. An analytical base for designing CGA bevel transmission on parallel axes with tangential pinion teeth and wheel teeth has been developed.
2. A comparative assessment of the CGA transmission with its analog—a cylindrical transmission with chevron teeth CGCh with the same dimensions is made. The result of an increase in the teeth length of the CGA is an increase in the transmission capacity according to the main criterion for the performance of closed gears—the contact endurance of the teeth.
3. An enlarged scheme of the algorithm for the practical calculation of the CGA transmission with reference to the current method of calculating the CGCh is proposed.

References

1. Kosarev OI (2011) Reducing the vibration in helical transmissions. J Probl Mashinostr Nadezhn Mash 1:19–27
2. Shevchenko SV, Stoyanov AA (1993) Some properties of gears with slope-arched teeth. J Des Prod Transp Veh 22:64–69
3. Niemann G, Winter G (1985) Maschinenelemente, Band 2. Springer, Berlin

4. Shevchenko S, Mukhovaty A, Krol O (2017) Gear clutch with modified tooth profiles. *J Procedia Eng* 206:979–984. <https://doi.org/10.1016/j.proeng.2017.10.581>
5. Mayor VP (1983) Study of the loading and contact endurance of cylindrical gears with arched teeth. Dissertation, University of Kurgan
6. Malakhov AG (1983) Investigation of the bending endurance of cylindrical gears with arched teeth. Dissertation, University of Kurgan
7. Dusev II (1977) Synthesis of gearing with controlled contact. *J Issues Designing Studying Mech Mach Automat*, 3–14
8. Kosarev OI, Bednyi IA, Mamonova MG (2011) Reducing the vibration of a chevron gear. *J Vestn Mech Eng* 11:19–23
9. Wagaj P, Kahraman A (2002) Influence of tooth profile modification on helical gear durability. *J Trans ASME Mech Des* 124:501–510
10. Kahraman A, Bajpai P, Anderson N (2005) Influence of the deviation of the profile of the helical gear. *J Trans ASME Mech Des* 127:656–663
11. Kravchuk AA (1975) Theoretical and experimental study of a cylindrical transmission with arc teeth. Dissertation, University of Khabarovsk
12. Shevchenko S, Mukhovaty A, Krol O (2016) Geometric aspects of modifications of tapered roller bearings. *J Procedia Eng* 150:1107–1112. <https://doi.org/10.1016/j.proeng.2016.07.221>
13. Holmes MJA, Evans HP, Snide RW (2005) Analysis of mixed lubrication effects in simulated gear tooth contacts. *J Trans ASME Tribol* 127:61–69
14. Ren N, Zhu W, Chen W et al (2009) Three-dimensional, deterministic model for rough surface, line contact. ehl problems. *J Trans ASME Tribol* 131:1–9
15. Drozdov YuN, Nazhestkin BP, Smirnov NI (1990) Development of methods for calculating the wear of gears. *J Bull Mech Eng* 11:15–17
16. Pirro DM, Wesso AA (2001) *Lubrication fundamentals*. Marcel Dekker, Marsel
17. Shevchenko SV, Krol OS, Khmelnytsky AV (2017) Bevel gear. Ukraine Patent 120217, 20, 25 Oct 2017
18. Litvin FL (1968) *Theory of gearing*. Science, Moscow
19. Krol O, Sokolov V (2018) Modelling of spindle nodes for machining centers. *J Phys Conf Ser* 1084:1–7. <https://doi.org/10.1088/1742-6596/1084/1/012007>
20. Krol O, Sokolov V (2018) Development of models and research into tooling for machining centers. *J Eastern-Eur J Enterprise Technol* 3(1(93)):12–22. <https://doi.org/10.15587/1729-4061.2018.131778>
21. Sokolov V, Rasskazova Y (2016) Automation of control processes of technological equipment with rotary hydraulic drive. *J Eastern-Eur J Enterprise Technol* 2(2(80)):44–50. <https://doi.org/10.15587/1729-4061.2016.637111>
22. Sokolov V, Krol O (2019) Determination of transfer functions for electrohydraulic servo drive of technological equipment. *Advances in design, simulation and manufacturing*. DSMIE 2018. *Lecture Notes in Mechanical Engineering*. Springer, Cham, pp 364–373. https://doi.org/10.1007/978-3-319-93587-4_38
23. Reshetov DN, Gusenkov AP, Drozdov YN (1995) *Mechanical Engineering, Encyclopedia*. V. IV-1. In: Reshetov DN (ed) *Machine parts, structural strength, friction, wear, lubrication*. Mechanical Engineering, Moscow
24. Korn G, Korn T (1970) *Handbook of mathematics*. Science, Moscow

Mathematical Model of Mechanism for Sealing Hardly Deformable Materials



E. I. Kromsky, S. V. Kondakov and M. A. Asfandiarov

Abstract A schematic diagram of the shock-vibration for compacting materials (including hard-to-deform) and the principle of its action based on the lever of Archimedes, which is part of a four-link mechanism, is considered. The article shows the expression for calculating the gain mechanism of the compression mechanism. In the course of work, a mathematical model of the mechanism is described; formulas for the kinematic and force calculation of all links of the mechanism are derived. With the help of the derived mathematical model, it is possible to select the most optimal options for the sizes of links according to the force or dimensional characteristics. The necessary conditions for a successful operation of the new mechanism are described. Its 3D model and general view of the pilot plant, which was designed and installed at SUSU at the Wheeled and Tracked Vehicles department, are shown. According to the tests carried out on it, the technological capabilities and advantages of this mechanism were confirmed in comparison with the vibration compaction technology adopted on modern wheeled or crawler concrete pavers, namely concrete control samples obtained on a molding machine with a shock-vibration mechanism showed an increase in strength of 1.3–1.5 times in comparison with the strength of the samples obtained by a traditional sealing technology.

Keywords Road-building machines · Sealing of especially rigid mixtures · Archimedes' shoulder · Molding unit · Four-link mechanism

1 Introduction

In the Russian Federation, as in the rest of the world, hard-surface construction machines use vibratory mechanisms to compact road-building materials. This mechanization of compaction allows to obtain the required quality of the road

E. I. Kromsky · S. V. Kondakov · M. A. Asfandiarov (✉)
South Ural State University, 76, Lenin Avenue, Chelyabinsk 454080, Russia
e-mail: loko315@mail.ru

© Springer Nature Switzerland AG 2020
A. A. Radionov et al. (eds.), *Proceedings of the 5th International Conference on Industrial Engineering (ICIE 2019)*, Lecture Notes in Mechanical Engineering,
https://doi.org/10.1007/978-3-030-22041-9_2

surface only with high quality compacted mixture. But even so, the process of laying cement concrete mixtures requires the use of strict regulations on the recipe of the original mixture [1–3].

2 Vibration Technology

In the construction of road construction machines are used submersible and surface vibrators. At the same time, the concrete mix must have a cone draft $OK = 0 \dots 4$ cm and water/cement ratio $0.45 \dots 0.5$. If you take the consumption of cement 400 kg/m^3 , then for the specified W/C water consumption will be $W = 180 \dots 200$ L; theoretically, 100 L is required for cement hydration. In accordance with the technological regulations, in 1 m^3 of the concrete mix there is an excess amount of chemically unbound water in a volume of about 80–100 L. With a smaller amount of free water (hard concrete mixtures) in the structure, channels are formed after passing immersion vibrators, which is unacceptable. The presence of a large amount of free water in the concrete mixture leads to a decrease in the physico-mechanical and operational properties of concrete: strength (Fig. 1), frost resistance, abrasion and durability [1, 4–9].

3 Archimedes Lever

Authors developed a method and device for compacting difficultly deformable (hard) concrete mixtures based on Archimedes lever, and four-stage mechanism later will be called as new mechanism [10–12].

A significant advantage of the Archimedes lever is to obtain a pressure plot for the hyperbolic function, compaction occurs gradually from the minimum compression force to the maximum (see Fig. 2), that is, the compression force Q acting on the elementary particle embedded under the working plate is determined by the formula [10, 11, 13]:

$$Q = P \cdot \frac{l}{a} \quad (1)$$

Fig. 1 Graph of the strength of concrete depending on the W/C ratio

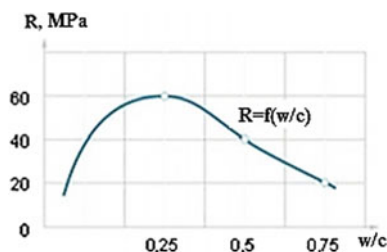
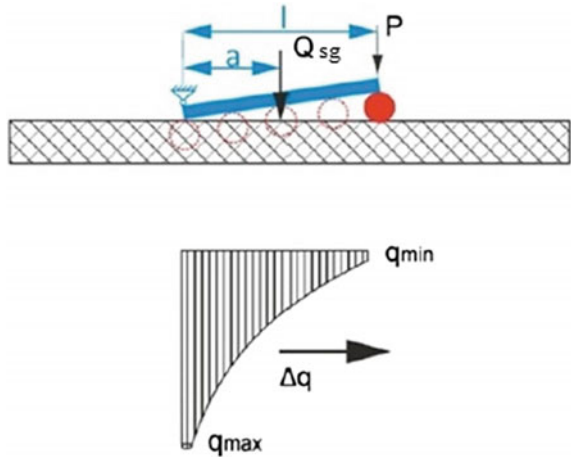


Fig. 2 Diagram of the sealing mechanism in the form of a lever of Archimedes. Plot of pressure



4 Four-Link Mechanism

The new mechanism contains a supercharger plate 1, a bracket 2, a smoothing Sect. 3 of the supercharger plate, a crank with a radius r and a pendulum rod.

The plates of the supercharger 1 contain a bracket 2 at one end and a smoothing Sect. 3 at the other end.

The plate of the supercharger is connected with a crank of radius r , rotating with an angular velocity ω , and with a pendulum suspension of radius R . The working surface of the plate of the supercharger 1 is made in the form of a broken line consisting of several sections (a, b, c). Plot (a) has a zero bias ($i = 0$), plot (b) has a bias $ib > 0$, and plot (c) has even greater bias $ic > ib$. The slope of the bracket 2—negative with respect to the working surface of the plate of the supercharger 1 (sections a, b, c)—is made for drawing material from the hopper to the pressing zone [12, 14, 15] (Fig. 3).

A significant advantage of the new mechanism is a two-step increase in the driving force P (Fig. 4), that is, the compressive force Q acting on the elementary particle introduced under the working plate is determined by the formula:

$$Q = P \cdot k_1 \cdot k_2 \tag{2}$$

where P is the force developed by the drive, k_1 и k_2 are the gain factors [14].

5 Mathematical Model

When creating a mathematical model of the four-link mechanism with the Archimedes lever, the initial data were taken [16, 17]:



Fig. 3 Schematic diagram of the new mechanism

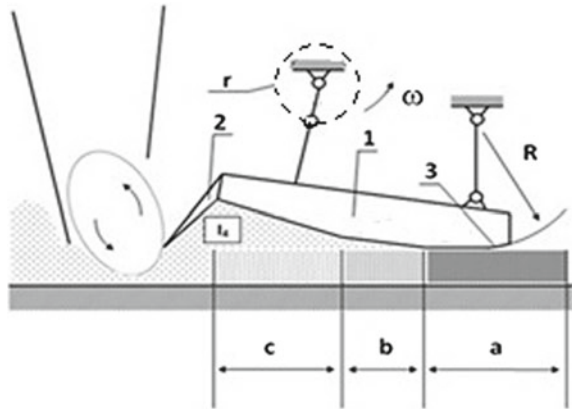
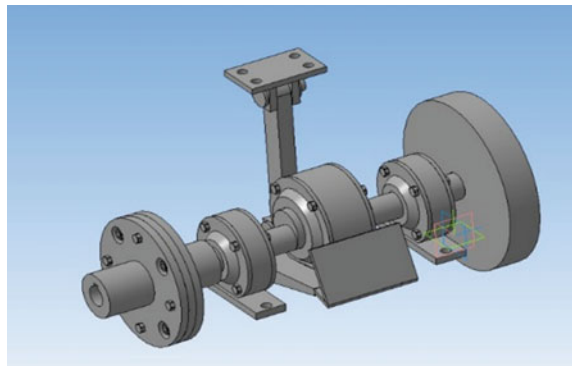


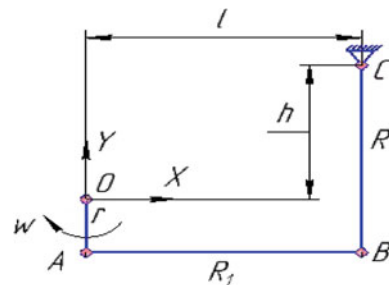
Fig. 4 3D model of the experimental mechanism



l ; h —the distance from the point of attachment of the crank to the point of attachment of the pendulum along the X and Y axes, respectively; r —crank radius; R —pendulum radius; and φ —crank angle (Fig. 5).

The movement of the crank radius r occurs in a circle with a center at the point O ; taking its point as the origin, we get the equation:

Fig. 5 Sketch of the four-link mechanism



$$x_A^2 + y_A^2 = r^2 \quad (3)$$

The coordinates of point A, knowing the angle of rotation of the crank, at any time are found through the equations:

$$\begin{cases} x_A = r \cdot \cos \varphi \\ y_A = r \cdot \sin \varphi \end{cases} \quad (4)$$

The coordinates of point B are found as the solution of the system of equations:

$$\begin{cases} (x_B - x_A)^2 + (y_B - y_A)^2 = R_1^2 \\ (x_B - x_C)^2 + (y_B - y_C)^2 = R^2 \end{cases} \quad (5)$$

In Eq. (8), the coordinates of point A from (7) are known, based on the sketch of the coordinates of point C:

$$x_C = l; y_C = h; R_1 = l \quad (6)$$

From formulas (4), (5) and (6), we get:

$$\begin{cases} (x_B - r \cdot \cos \varphi)^2 + (y_B - r \cdot \sin \varphi)^2 = l^2 \\ (x_B - l)^2 + (y_B - h)^2 = R^2 \end{cases} \quad (7)$$

Solving the system of Equation (8), we find the unknown coordinates [7, 17, 19]. Knowing the coordinates of the links of the mechanism in any position of the crank, we find the angles α —between the crank and the plate; β —between the plate and the pendulum; and γ —between the plate and the horizon:

$$\alpha = \arctan \left| \left(\frac{\frac{y_A - y_O}{x_A - x_O} - \frac{y_B - y_A}{x_B - x_A}}{1 + \frac{y_A - y_O}{x_A - x_O} \cdot \frac{y_B - y_A}{x_B - x_A}} \right) \right| \quad (8)$$

$$\beta = \arctan \left| \left(\frac{\frac{y_B - y_A}{x_B - x_A} - \frac{y_C - y_B}{x_C - x_B}}{1 + \frac{y_B - y_A}{x_B - x_A} \cdot \frac{y_C - y_B}{x_C - x_B}} \right) \right| \quad (9)$$

$$\gamma = \arctan \left| \left(\frac{y_B - y_A}{x_B - x_A} \right) \right| \quad (10)$$

6 Kinematic and Force Calculation

According to the obtained mathematical model of the mechanism, we solve the problem of velocities, accelerations and forces, and the initial data are:

1 link—crank; 2 link—plate; 3 link—pendulum;

$w_1 = \text{const}$ —crank speed; $G_1; G_2; G_3$ —weight of links 1, 2 and 3;
 $I_1; I_2; I_3$ —moments of inertia of link 1, 2 and 3; Q —force required to seal.

$$\left\{ \begin{array}{l} A \in 1; \vec{V}_A \perp OA; V_A = w_1 \cdot r \\ B \in 3; \vec{V}_B \perp BC; V_B = w_3 \cdot R \\ B \in 2; \vec{V}_B = \vec{V}_A + \vec{V}_{BA} \\ \vec{V}_{BA} \perp BA; V_{BA} = w_2 \cdot R_1 \\ w_2 = \frac{V_{BA}}{R_1}; w_3 = \frac{V_B}{R} \end{array} \right. \quad (11)$$

Formulas for solving the problem of accelerations:

$$\left\{ \begin{array}{l} A \in 1; \vec{a}_A = \vec{a}_A^n + \vec{a}_A^\tau; \\ \vec{a}_A^n \parallel OA; a_A^n = w_1^2 \cdot r; a_A^\tau = 0; \\ B \in 3; \vec{a}_B = \vec{a}_B^n + \vec{a}_B^\tau; \\ \vec{a}_B^n \parallel BC; a_B^n = w_3^2 \cdot R; \\ \vec{a}_B^\tau \perp BC; a_B^\tau = \varepsilon_3 \cdot R; \\ B \in 2; \vec{a}_B = \vec{a}_A + \vec{a}_{BA}^n + \vec{a}_{BA}^\tau; \\ \vec{a}_{BA}^n \parallel BA; a_{BA}^n = w_2^2 \cdot R_1; \vec{a}_{BA}^\tau \perp BA; a_{BA}^\tau = \varepsilon_2 \cdot R_1; \\ \varepsilon_2 = \frac{a_{BA}^\tau}{R_1}; \varepsilon_3 = \frac{a_B^\tau}{R}. \end{array} \right. \quad (12)$$

The task of forces consists of three parts:

- (1) We determine the inertial force factors of the mechanism for each of the links. The inertial factors are the inertial forces of the links and the moments of inertia forces [18]:

$$\vec{P}_{ini} = -m_i \cdot \vec{a}_i; P_{ini} = \frac{G_i \cdot a_i}{g} \quad (13)$$

$$\vec{M}_{ini} = -I_i \cdot \vec{\varepsilon}_i; M_{ini} = I_i \cdot \varepsilon_i \quad (14)$$

where a_i —acceleration in the center of gravity i link; ε_i —angular acceleration of i link; g —acceleration of gravity.

- (2) Force calculation group Assur II₁.

The reaction in the joint C and A is presented as the vector sum of the normal reaction force and the tangent. Then we get:

$$\begin{cases} \sum \tilde{M}_{BC} = \vec{R}_C^r \cdot R + \tilde{M}_{in3} + \vec{G}_3 \cdot h_{G_3} + \vec{P}_{in3} \cdot h_{P_{in3}} = 0 \\ \sum \tilde{M}_{BC} = \vec{R}_A^r \cdot R_1 + \tilde{M}_{in2} + \vec{G}_2 \cdot h_{G_2} + \vec{P}_{in2} \cdot h_{P_{in2}} + \vec{Q} \cdot h_Q = 0 \\ \sum \vec{P} = \vec{R}_C^n + \vec{R}_C^r + \vec{G}_3 + \vec{P}_{in3} + \vec{Q} + \vec{P}_{in2} + \vec{G}_2 + \vec{R}_A^r + \vec{R}_A^n = 0 \\ \sum \vec{P}_3 = \vec{R}_B + \vec{G}_3 + \vec{P} + \vec{R}_C^n + \vec{R}_C^r = 0 \end{cases} \quad (15)$$

Solving this system of equations, we find the reaction in the hinge A , B and C [7].

(3) Force calculation mechanism class I.

The reaction in the joint O is represented as the vector sum of the normal reaction force and the tangent. Then we get:

$$\begin{cases} \vec{R}_A = \vec{R}_A^r + \vec{R}_A^n; R_A = \sqrt{(R_A^r)^2 + (R_A^n)^2} \\ \sum \tilde{M}_O = \vec{R}_A \cdot h_{R_A} + \tilde{M}_{yp} = 0 \\ \sum \vec{P} = \vec{R}_A + \vec{G}_1 + \vec{R}_O = 0 \end{cases} \quad (16)$$

The required engine power calculated by the formula [16, 18, 19]:

$$N = M_{ur} \cdot w_1 \quad (17)$$

The peculiarity of the four-link mechanism is the change of speeds, accelerations, forces and moments according to the position of the mechanism. This causes oscillations, drops and increases in the required power; therefore, it is necessary to provide a flywheel in this mechanism. We replace the real mechanism with an equivalent dynamic model consisting of one link with the reduced moment of inertia and the moment of resistance forces, which are:

$$I_{pr} = I_1 + \frac{G_2}{g} \cdot \left(\frac{V_2}{w_1}\right)^2 + I_2 \cdot \left(\frac{w_2}{w_1}\right)^2 + \frac{G_3}{g} \cdot \left(\frac{V_3}{w_1}\right)^2 + I_3 \cdot \left(\frac{w_3}{w_1}\right)^2 \quad (18)$$

$$M_{pr} = G_2 \cdot \frac{V_2 \cdot \cos(\vec{G}_2; \vec{V}_2)}{w_1} + Q \cdot \frac{V_2 \cdot \cos(\vec{Q}; \vec{V}_2)}{w_1} + G_3 \cdot \frac{V_3 \cdot \cos(\vec{G}_3; \vec{V}_3)}{w_1} \quad (19)$$

where V_2 и V_3 —speeds in the center of gravity of 2 and 3 links, respectively.

According to formulas (18) and (19), we calculate the moments of inertia and moments of resistance forces for 12 crank positions per cycle. Based on the obtained values, we construct diagrams of moments of inertia, moments of forces, work and energies. Combining the diagram of moments of inertia and energy, we obtain the graph of energy and mass, according to which we subsequently select the flywheel [17].



Fig. 6 General view of the prototype of the molding unit

7 Experiment

At present, an experimental molding installation has been created (Fig. 6), using the mechanism of the lever of Archimedes. Tests of a prototype of an experimental molding installation, carried out at the Department of Wheel and Tracked Machines of SUSU, confirmed the technological capabilities and advantages of the new mechanism in comparison with the vibration compaction technology adopted by modern concrete pavers, namely control samples of concrete showed an increase in strength of 1.3–1.5 times in comparison with the strength of the samples obtained by the traditional sealing technology; when they were cut, no visible pores were found, which indicates the effectiveness of mechanism.

8 Conclusion

1. A mathematical model of the four-link mechanism was created; formulas for calculating the trajectory of motion, kinematic and force characteristics were derived.
2. For the successful operation of the device, we must comply with the following conditions: The maximum angle of inclination of the platform plate to the horizon γ should not exceed 20° so that the material does not slip from the throat of the platform into the hopper; for maximum compression force in the lower position of the platform, the crank should look down and prevent vibrations and the occurrence of peak loads on the crankshaft; it is advisable to install a flywheel.

3. The device based on the four-link mechanism provides: obtaining directional shear deformations in the compression material; reduction of external loads due to their two-step amplification; drawing material from the hopper; transportation of the material to the pressing zone of a specially designed bracket; and grouting the surface.
4. An experimental facility was created to test the mechanism's performance, which made it possible to increase the strength of concrete by 1.3 ... 1.5 times.

References

1. Novikov AN (1979) Machines for the construction of cement concrete pavements, 2nd edn. High School, Moscow, 256 p
2. Tsupikov SG (2005) Handbook of the road master. Construction, operation and repair of highways. Infra-Engineering, Moscow, 928 p
3. Kondakov SV, Kromsky EI, Asfandiyarov MA (2018) Substantiation of the parameters of the shock-vibration mechanism for compacting a concrete mix for a caterpillar-type concrete paver. In: All-Russian scientific-practical conference. OU VO "South Ural Institute of Management and Economics", Chelyabinsk, 182 p
4. Zubkin VE, Konovalov VM (2007) RK mini 01. Popular Concr Stud 1(15):73
5. Zubkin VE, Konovalov VM, Korolev NE (2002) Zone injection of loose media, or how to cost from ordinary land very cheap, strong, warm and fire-resistant houses through the "Russian swing": Practical Guide. Izd-vo "RUSAKI", Moscow, 144 p
6. Snip (1990) 3.06.03-85 Highways. Moscow, 42 p
7. Bazhenov YM (1979) Technology of concrete. Textbook for high schools. Moscow, 415 p
8. Kromsky EI, Bazanov AA, Nemykin AA (2018) Concrete paver. RU Patent 176735, Bll. No. 01
9. Kromsky EI, Bondar VN, Svirid AV (2010) A device for obtaining articles from composite materials. RU Patent 93320, 12 p
10. Vasiliev AP, Yakovlev YM, Koganson MS (1998) Reconstruction of highways. Textbook. MADI, Moscow, 78 p
11. Artobolevsky II (1988) Theory of mechanisms and machines: Proceedings for universities, 4th edn. Science. Ch. Ed. Phys.-Math. lit., Moscow, 640 p
12. Kromsky EI, Akhmetshin NI, Yarov BA (2014) Pressing of composite materials using shear deformations, Publishing House SUSU, Chelyabinsk, 10 p
13. Kromsky EI, Kondakov SV, Asfandiyarov MA (2018) Future development of construction equipment for cement-concrete road pavement, Publishing House SUSU, Chelyabinsk, 30 p
14. GOST 12.2.100-97 (1998) Machines and equipment for the production of clay and silicate bricks, ceramic and asbestos-cement articles. General safety requirements. IPK Publishing House of Standards, Moscow, 11 p
15. Timofeev YL (2002) Technology of vibratory compaction of concrete in the construction of monolithic structures. Textbook for technical universities. Rostov-na-Donu, 47 p
16. Afanasyev AA (1987) Technology of pulsed compaction of concrete mixtures. Stroizdat, Moscow, 186 p
17. Pozhbelko VI, Vinitsky PG, Akhmetshin NI (2003) Theory of Mechanisms and Machines. Tutorial, part 1. Chelyabinsk, 108 p
18. Boehm BU (1985) Engineering design of software. Translation from English under the editorship of prof. AA Krasilova. Radio and Communication, Moscow, 512 p
19. Timofeev GA (2010) Theory of mechanisms and machines. Course of Lectures. Moscow, 351 p

Promising Machine for Compacting Road-Building Materials



E. I. Kromsky, S. V. Kondakov and K. Z. Tilloev

Abstract The choice of the design type of sealing machines depends on many factors: the type of compacted material (soil, crushed stone, gravel, slag, rock coarse soils, asphalt concrete, concrete); the state of the soil (optimal humidity, waterlogged, watering, bulk, subsidence); the thickness of the compacted layers (layer-by-layer compaction thin layers, compaction immediately to the entire thickness of the filling to the design mark); and the working conditions of the machine (cramped working conditions, a wide range of works). The article presents the design of the aggregate for deep soil compaction, developed by the specialists of the Institute of Hydrodynamics “Siberian branch of the Russian Academy of Sciences” (SB RAS). Based on the assessment of the advantages and disadvantages of this unit, a new technical solution based on a cone-shaped roller is proposed, which provides more favorable conditions for the removal of air from the mass of the compacted material. A mathematical model of a cone rollout using the method of decomposition of the periodic function into a Fourier series is presented. The design of a physical model of a cone-shaped roller in the form of a single roller and a self-centering working body with several rollers is considered.

Keywords Excavation · Material compaction · Compaction device · Deep tamping · Conical rolling · Precessing shaft

1 Introduction

Bulk road-building materials and subsidence soils before the construction of structures on them are subject to artificial compaction.

The sealing machine is distinguished by the following main methods of compaction: compacted (working body—packer roller moves over the surface of the sealing material); compaction—impact effect is achieved by the periodic strikes of

E. I. Kromsky · S. V. Kondakov · K. Z. Tilloev (✉)
South Ural State University, 76, Lenin Avenue, Chelyabinsk 454080, Russia
e-mail: kudratullo.tilloev@bk.ru

the working plate via the sealing material; and vibration impact (material misleading short successive pulses). The relative disadvantage of road machines for compaction of road-building materials is a small height of the deposited soil layers of 0.3–0.8 m. Higher earth structures (embankments, dams, etc.) have to be made multilayered, which leads to heterogeneity of soil compaction and, as a consequence, to subsequent deformations from external loads [1–11].

For large volumes of excavation (height of the embankment and their length), it requires more modern technology of compaction.

2 New Machine Design for Soil Compaction

Specialists of the Institute of Hydrodynamics “Siberian branch of the Russian Academy of Sciences” (SB RAS) and its design and technological branch developed and used the unit for deep soil compaction (Fig. 1), which pushes the soil in a horizontal direction, forming a conical pit. The resulting pits are filled with more durable materials (recommended crushed stone, sand, etc.), which are additionally compacted by road rollers (vibro-rollers). As a result of the use of the unit for deep soil compaction and the conducted research, the soil density increases by 20–30% and its bearing capacity increases 2–3 times [12].

The economic effect of the use of the new unit in the construction of a 9-story residential building is 810.4 thousand rubles [12].

The relative disadvantage of the unit for deep soil compaction is a large contact surface of the working body with the soil. The contact surface of the working body



Fig. 1 Unit for deep soil compaction

with the diameter of the base of the conical shell, embedded in the ground, equal to 0.9 m, and the height of the cone 3 m reaches 6 m², which requires a large amount of power to extend the soil in the horizontal direction when working hydro-pneumatic hammer. The cone shell of the working body of the unit seals the space around the side surface of the cone, so the air moves inside the soil mass when the shell is introduced. This technology is “air-proof.”

Employees of the South Ural State University (SUSU) offer to improve the technique of deep compaction by rolling the pit working body in the form of a conical roller [13].

The main advantage of the proposed method is to reduce the area of contact of the working body with the ground several times, because the length of the arc $\overset{\frown}{AB}$ is many times smaller than the circumference of the working body of the unit for depths of compaction of the soil (Fig. 2).

During the operation of the new working body, conditions are created for continuous air output from the soil mass due to the presence of gaps between the working body and the surface of the pit. This technology is called “air-purging.”

The working body of the new device is a cone 2 with an angle φ at the top (point O) $\varphi < \frac{\pi}{2}$. The leading link of the conical working body is the crankshaft (precessing shaft) 1, which is connected to the rotation drive (drive in Fig. 2 conditionally not shown). The sections of the crankshaft are angled α to each other and intersect at the point (O) coinciding with the top of the cone 2. When the crankshaft 1 is rotated and the axial load is affected Q , the cone 2 is pressed into the soil mass, making a run-in inside the produced pit 3.

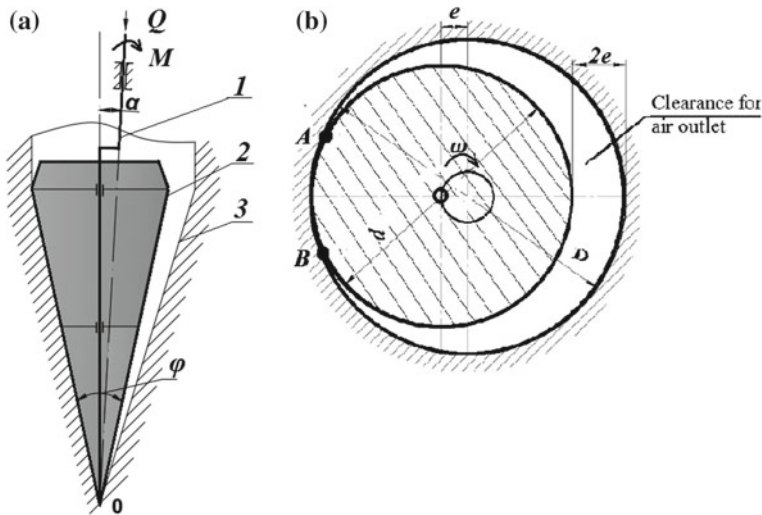


Fig. 2 Scheme of the conical rolling of the pit, **a** side view **b** top view. 1—Precessing shaft, 2—working body, 3—pit

3 Mathematical Model

The main working body of machines for cone rolling of road-building materials is rollers with variable diameter in height. When rolling the roller, it acts on the sealing surface in a narrow zone, in the center of which the compressive force F is the maximum, and at the edges of this zone, it decreases to zero. The graph of the force change under the roller in the first approximation has the form of a half sine wave (Fig. 3) [14–16].

When moving, the roller is periodically rolled through the same place with a frequency f (and with an angular frequency $\omega = 2\pi f$). The dependence of the change in force on time in this case is presented in Fig. 4.

In this figure, the law of force $f(t)$ change has the form of pulses duration τ with a maximum denotation F and a period $T = \frac{2\pi}{\omega}$ (Fig. 4).

The analytical function $f(t)$ can be written as follows:

$$f(t) = \begin{cases} F \cos \frac{\pi}{\tau} \left(t + \frac{2\pi}{\omega} \right), & -\frac{2\pi}{\omega} < t < \frac{2\pi}{\omega} + \frac{\tau}{2} \\ F \cos \frac{\pi}{\tau} t, & -\frac{\tau}{2} < t < \frac{\tau}{2} \\ F \cos \frac{\pi}{\tau} \left(t - \frac{2\pi}{\omega} \right), & \frac{2\pi}{\omega} - \frac{\tau}{2} < t < \frac{2\pi}{\omega} \end{cases} \quad (1)$$

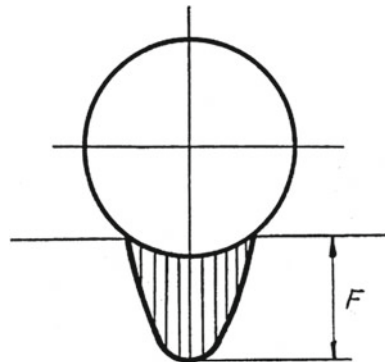
We decompose the function $f(t)$ into a Fourier series:

$$f(t) = \sum_{k=0}^{\infty} a_k \cos k\omega t, \quad (2)$$

were

$$a_k = \frac{\omega}{2\pi} \int_{-\frac{2\pi}{\omega}}^{\frac{2\pi}{\omega}} f(t) \cos k\omega t dt \quad (3)$$

Fig. 3 Scheme of soil compaction with a smooth metal roller



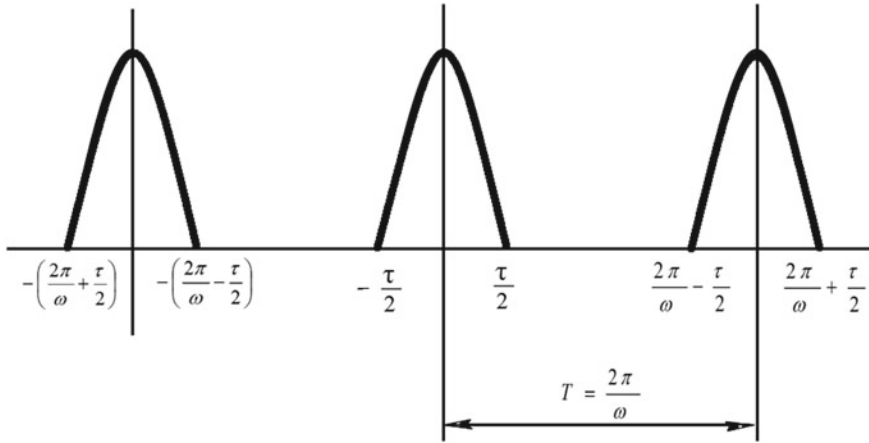


Fig. 4 Graph of the force change depending on the time when the roller is rolled

We present the integral in formula (3) as a sum of integrals:

$$a_k = \frac{\omega}{2\pi} \left[\int_{-\frac{2\pi}{\omega} + \frac{\tau}{2}}^{-\frac{2\pi}{\omega} - \frac{\tau}{2}} f(t) \cos k\omega t \, dt + \int_{-\frac{\tau}{2}}^{\frac{\tau}{2}} f(t) \cos k\omega t \, dt + \int_{\frac{2\pi}{\omega} - \frac{\tau}{2}}^{\frac{2\pi}{\omega} + \frac{\tau}{2}} f(t) \cos k\omega t \, dt \right] \quad (4)$$

Here, it is taken $f(t) = 0$ into account that in the intervals between pulses. Substituting the representation $f(t)$ by formulas (1) in (4) and performing the appropriate calculations, we obtain an expression to calculate the coefficients a_k :

$$a_k = \frac{4F\tau\omega}{\pi} \quad (5)$$

$$a_{ki} = \frac{2F\omega}{\tau} \left[1 + (-1)^k \right] \frac{\cos \frac{k\omega\tau}{2}}{\left(\frac{\pi}{\tau}\right)^2 - (k\omega)^2}, \quad k_i = 1, 2, 3, \dots \quad (6)$$

Thus, if the roller is rolled periodically at the same place with frequency $f = \frac{\omega}{2\pi}$ when rolling, it is equivalent to the fact that a constant force (5) and the sum of harmonic forces with amplitudes (6) acts on “this place.”

Therefore, periodic rolling of the roller has the advantage that, firstly, affects a small area the material to be rolled and, secondly, acts on this material by means of a multi-frequency vibration, which is known to reduce external and internal friction in the material [17–19].



4 The Design of the Cone Roller

The design of the new working body can be made in the form of one conical roller (Fig. 2) or in the form of several rollers (Fig. 5), which greatly simplifies the dynamic balancing of the mechanical system.

New working bodies can be installed on excavators instead of buckets (Fig. 6) or on drilling machines.

Running a conical roller is equivalent to the static load in the form of compressive force and vibration impact on the compacted soil.

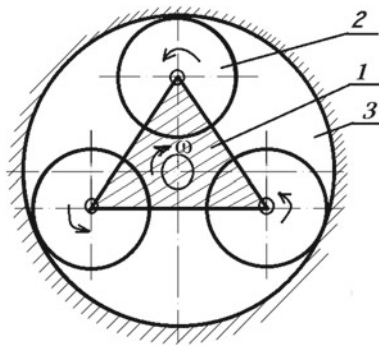


Fig. 5 The scheme is rolling out of the pit with three card. 1—Leading link, 2—rink, 3—pit



Fig. 6 Conical roller on the basis of a hydraulic crawler excavator. 1—Working body, 2—hydraulic motor, 3—traverse

As the experience of Novosibirsk researchers [12] shows, the effective zone of soil compaction in the horizontal direction is about two radii of the introduced working body in the form of a cone, so the inter-center distance between adjacent pits can be equal to two diameters of the base of the conical working body.

Earlier it was shown that the power of the drive of the roll is determined by the dependence [20]:

$$N = M \cdot \omega = M \frac{n\pi}{30}$$

where M —the required torque, ω —angular velocity, n —the number of revolutions of the crankshaft (drove) per minute.

$$M = 0.266 \cdot Q \cdot 1.55 \sqrt{1 - \frac{\sigma^2}{E} \tan \frac{\alpha}{2}}$$

where Q —the external force applied to the vertical axis of the carrier, E —the modulus of elasticity of the compacted material, σ —Poisson's ratio, α —the angle of the axis of the precessing shaft.

5 Conclusions

1. The design of a new working body of the excavator is proposed, and different from the known unit for deep compaction of soil (Novosibirsk) is much smaller contact surface and creates conditions for continuous air output from the soil massif.
2. The pit cutter has the advantage that, firstly, it acts on a small area of the rolled material and, secondly, acts on this material by means of a multi-frequency vibration, which reduces the external and internal friction in the material.
3. The working body in the form of a conical roller can be installed on road-building machines, for example, on the basis of commercially available hydraulic excavators or drilling machines of lower mass and lower power.

References

1. Balovnev VI, Kustarev GV, et al (2001) Road-building machines and complexes. Moscow-Omsk
2. Volkov AP, Krikun VJ, Totolin PE et al (1992) Machines for earthworks. Mechanical Engineering, Moscow
3. Kustarev GV, Danilov RG, Balovnev VI (2012) Road rollers. The device of the bases of calculation. MADI, Moscow

4. Balovnev VI, Ivanchenko SN, Danilov RG (2016) Road rollers: development, design, calculation. TOGU, Khabarovsk
5. Charhuta NY, Vasilev YM (1975) Strength, stability and compaction of the soil subgrade of roads. Transport, Moscow
6. Charuta NY, Kapustin MI, Semenov VP, Eventov YM (1976) Road machine. Theory, design and calculation. Mechanical Engineering, Moscow
7. Minaev OP (2014) Bases and methods of soil compaction bases for the construction of buildings and structures. St. Petersburg
8. Barats NI (2008) Soil mechanics. SibADI, Omsk
9. Balovnev VI, Glagolev SN, Danilov RG et al (2011) Loading and unloading and sealing machines. BSTU, Belgorod
10. Lutsky SY, Sakun BA (2015) Intensive technology procne-tion of weak bases subgrade. Transport construction 8:18–22
11. Krivorotov AP, Lubyagin AV (2006) The effectiveness of the compaction of soft ground by rolling the wells. Sibstrin Novosibirsk 5:59–65
12. Mironov VS, Fadeev PY, Fadeev VY, Mandrik MS (2015) Technology and equipment for deep soil compacting. Constr Road Mach 8:2–4
13. Kromsky EI, Kayupov DR, Gladchenko AS (2016) The device for rolling pits. RU Patent 161212, 10 April 2016
14. Blekhman II (1998) What can vibration? About “vibration mechanics” and vibration technology. Nauka, Moscow
15. Forssblad L (1981) Vibratory soil and rock fill compaction. Dynapac Maskin AB, Stockholm, Sweden
16. Forssblad L (1980) Compaction meter on vibrating rollers for improved compaction control. Proc Int Conf on Compaction, Paris, Fr 2:541–546
17. Boldyrev GG (2008) Methods for determining the mechanical properties of soils. Status. Monograph, PGUAS Penza
18. Baidya DK, Murali Krishna G (2001) Investigation of resonant frequency and amplitude of vibrating footing resting on a layered soil system. Geotech Test J 24(4):409–417
19. Dumn DJ (2007) Solid mechanics. Dynamics. Tutorial—damped vibrations. Handbook
20. Kromsky EI, Kondakov SV, Tilloev KZ (2018) Cone ratcatcher for crawler excavator. Bull SUSU. Series “Mechanical Engineering” 1:34–39. <https://doi.org/10.14529/engine140104>

Assessing Effectiveness of Technical Measures for Improving Working Conditions of Wheeled Vehicle Operators



V. Shkrabak, A. Kalugin and Y. Averyanov

Abstract The chapter considers the issue of assessing the effectiveness of technical measures aimed at improving the working conditions of wheeled vehicle operators. A problem is caused by a contradiction between the need to assess the effectiveness of technical measures, on the one hand, and the lack of an objective methodology for their assessment which would take into account the operator working conditions, on the other hand. The paper proposes a solution to the existing problem, which is based on an original method for comparative assessment of the effectiveness of technical measures that contribute to the improvement of working conditions for wheeled vehicle operators. The methodology for assessing the effectiveness of technical measures is based on the justified assumption that technical devices do not equally influence the safety level and conditions of wheeled vehicle operators. The proposed methodology was approved based on comparative testing of the existing and newly developed technical devices of wheeled vehicles. We assessed the effectiveness of the proposed technical devices and compared it with that of their analogs. The implementation of the proposed methodology for assessing the effectiveness of technical measures for the improvement of working conditions of wheeled vehicle operators will improve their safety in the operational process.

Keywords Wheeled vehicles • Operator working conditions • Safety • Comparison testing • Assessment methodology

V. Shkrabak
Saint Petersburg State Agrarian University, 2 St. Petersburg Highway,
St. Petersburg 196605, Russia

A. Kalugin (✉)
South Urals Chamber of Commerce and Industry, 56 Soni Krivoy Str.,
Chelyabinsk 454080, Russia
e-mail: starfruitworks@gmail.com

Y. Averyanov
South Ural State University, 76 Lenin Avenue, Chelyabinsk 454080, Russia

1 Introduction

Basic technological and transport operations involve the use of wheeled vehicles. The effectiveness of using wheeled vehicles largely depends on their safety conditions. It is possible to increase the operating safety of wheeled vehicles by taking technical measures aimed at improving operator working conditions. The effectiveness of technical measures for improving the working conditions of wheeled vehicle operators is assessed with various techniques [1–3]. It is well known that technical measures for improving the operating safety of wheeled vehicles have varying impacts on operator working conditions [2, 4–9]. Thus, if a new technical measure is introduced without being first compared and assessed, it may be of little significance in terms of its contribution to the improvement of working conditions. Therefore, it is important not only to introduce measures for improving the operating safety of wheeled vehicles but also to assess its significance in terms of its impact on operator working conditions [1–3]. It is noteworthy that Korean scientists [10] have established a clear correlation between what they call “safety ethics” and the number of accidents. The level of the latter in our country fails to compensate for the lack of technical solutions that would protect employees.

This situation results in a contradiction between the need to assess the effectiveness of technical measures, on the one hand, and the lack of an objective methodology for their assessment which would take into account operator working conditions, on the other hand. This contradiction calls for the justification of a methodology to assess the effectiveness of technical measures on improving the working conditions of wheeled vehicle operators. This problem can be solved by developing a methodology for and conducting a comparative assessment of the effectiveness of technical measures which contribute to the improvement of the working conditions of wheeled vehicle operators. The development of a methodology for assessing the effectiveness of technical measures should be based on the justified assumption that technical devices do not equally influence the safety level and conditions of wheeled vehicle operators. To approve the methodology for assessing the effectiveness of technical measures, existing and newly developed technical devices of wheeled vehicles should best tested and compared.

2 Methodology for Assessing the Effectiveness of Technical Measures for the Improvement of Working Conditions

The effectiveness of technical measures for improving the working conditions for wheeled vehicle operators can be assessed by an index which takes into account their aggregate significance. The proposed index (1), unlike the well-known integral indices [1, 4, 11–13], not only sums up the degree of influence that the factors of the operational environment have, but also calculates the aggregate significance of the

technical measures introduced to each wheeled unit based on the scale of working conditions class (WCC). The significance of the introduced measure K is understood as its predictable ability to reduce the working conditions class or its degree of hazard:

$$M_{is} = \sum_{i=1}^n K_i \quad (1)$$

where M_{is} (measures of industrial safety) is the index of effectiveness of technical measures, points; K_i is the significance of the introduced technical measure; and n is the number of introduced technical measures, units.

Formula (1) shows that if the significance of the introduced technical measures is summed up, it is possible to obtain the value of the M_{is} index, which allows us to make conclusions on their effectiveness. It is reasonable not only to aim toward increasing the number of introduced measures but also toward increasing their significance, that is, to introduce the technical measures that would reduce the WCC as much as possible. This will make it possible to reach maximum effectiveness with fewer technical measures.

The basis for determining the significance of the introduced technical measures using the M_{is} index is the known WCC index, which takes into account all the features of working conditions, including workplace safety and the condition of the operational environment [11, 15, 16]. The significance of technical measures can be determined as follows, for example: If the proposed technical measure reduces the WCC by one, the significance of the K_i measure can be assessed as one point, and if it reduces WCC by two, the significance of K_i is assessed as two points, etc.

However, the situation can be just the opposite, when the introduced technical measure for some reason fails to improve working conditions, worsening them instead. For example, air-heat curtains were installed in an operational workplace to reduce the maximum permissible concentration of dust. For some workers, it improved the working conditions, while for other workers, who were closest to the curtains, it worsened them because it increased the rate of respiratory diseases [14, 16, 17]. In such cases, the significance of a measure can take on negative values, and the effectiveness of its introduction tends to zero.

Let us consider the possible effectiveness states of technical measures:

- A technical measure is effective, and therefore, the WCC becomes lower, and its significance is higher, for example: If the WCC is reduced by 1 unit, then $K_i = 1$, etc;
- A technical measure fails to change working conditions, so the working conditions class remains the same, and its significance is equal to zero, for example: If $WCC = \text{const}$, then $K_i = 0$;
- A technical measure is ineffective, so the working conditions class becomes higher, and its significance can take negative values, for example: If the WCC increases by 1 unit, then $K_i = -1$; if by 2 units, then $K_i = -2$, and so on.

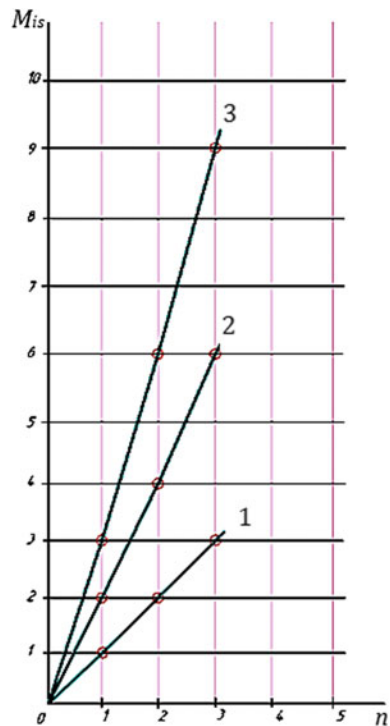
Taking into account the possible effectiveness states of technical measures and expression (1), the set of conditions for determining the effectiveness index of technical measures for improving the operating safety of wheeled vehicles is a scale of the WCC based on changes in the number and significance of measures.

For example, if each of the two technical measures reduces the WCC by one, then their total effectiveness index $M_{is} = 2$, and if another measure reduces the WCC by three units, $M_{is} = 3$, respectively. That is, in this case, one technical measure will be more effective than two joint technical measures.

The theoretical dependence of the effectiveness index of positive technical measures (Fig. 1) shows that if three measures are introduced (provided that each measure reduces the WCC by one unit), $M_{is} = 3$; and if three measures are introduced (provided that each measure reduces the WCC by three units), $M_{is} = 9$. This means that if the same number of measures is introduced, most effective will be the measures which have greater significance.

To assess the effectiveness of the set of proposed technical measures according to the methodology described in [14], it is necessary to determine the working conditions class and the value of the M_{is} index based upon it for the workplace before and after introducing one or more technical measures to a wheeled vehicle. In this case, the significance of each technical measure can be assessed, for example, in comparison with a machine that is not equipped with additional means

Fig. 1 Illustration of the theoretical dependence of the effectiveness index of technical measures with respect to M_{is} on their number n , which takes into account the significance of K_i : 1—when introducing measures that reduce the WCC by one unit; 2—when introducing measures that reduce the WCC by two units; and 3—when introducing measures that reduce the WCC by three units



of improving safety and working conditions or means that have comparatively low effectiveness (analogs). It also helps determine which of the proposed technical measures or combination thereof is most effective for improving the working conditions for wheeled vehicle operators. To compare the assessment results of the working conditions of wheeled vehicle operators, we use the criteria for hygienic assessment of the working environment and the labor process factors when calculating the M_{is} index [18].

3 Results of Comparative Testing for Assessing the Effectiveness of Technical Measures

Let us consider the assessment of effectiveness of introducing technical measures for the improvement of the working conditions of wheeled vehicle operators by examining the automatic differential lock of a vehicle, automatic adhesive weight transfer, vehicle engine preheater, and cabin floor heater.

4 Assessment of the Effectiveness of an Automatic Differential Lock

Comparative testing of the automatic differential lock of a vehicle and the semi-automatic differential lock of the ZIL-4331 drive axle (for example, a model manufactured and installed by the company LLC “Nash Profil,” Novosibirsk, with node serial number № 433112400010) was assessed with the proposed M_{ot} index. Preliminary experiments showed [14] that the use of the automatic differential lock (Fig. 2) (patent No. 122460 of the Russian Federation, 2011) makes it possible to significantly (from 18 to 32%) reduce skidding of the ZIL-4331 truck on surfaces of small bearing strength. Skidding is reduced due to an increase in the traction of the drive wheels on the road surface, which improves the stability of rectilinear motion, reduces braking distance and risk of accidents.

In this regard, skidding is reduced by the proposed differential locking device, which leads to an improvement in working conditions and safety in general.

Comparative assessment of the introduction of the two locking options allowed us to conclude that the degree of hazard of the working conditions class, determined using the integral assessment method, is reduced by one unit (from $WCC = 3.3$ to $WCC = 3.2$) for a semi-automatic differential lock and by two units (from $WCC = 3.3$ to $WCC = 3.1$) for the proposed automatic device. The positive effect is a result of reducing the influence of severity factors in the operator working process: the total body burden (involving the muscles of hands, body, and legs) and the number of perceived signals per unit of time (paragraphs 5.10.3 of Manual P2.2.2006-05, Table 17 ... 19) [18–20]. Detailed measurements of limb activity

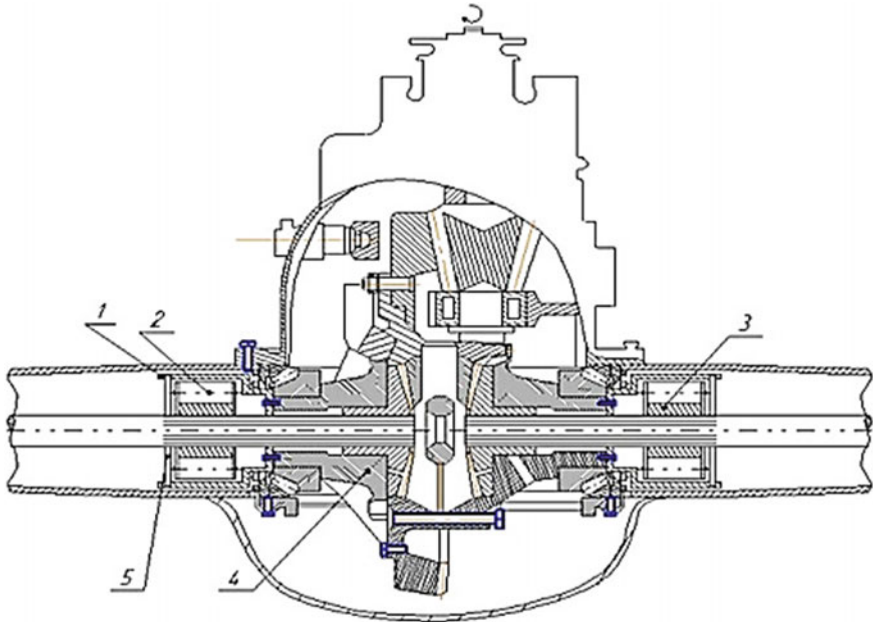


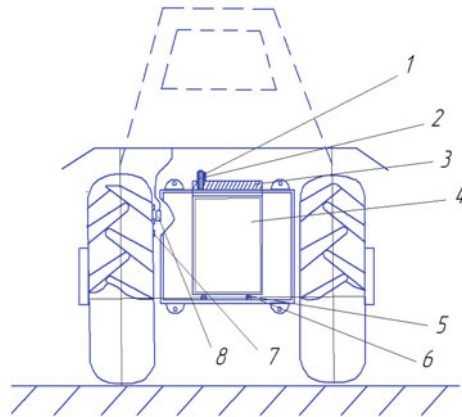
Fig. 2 Schematic of an automatic differential lock: 1—outer race; 2—spacer with rollers and springs; 3—sprocket; 4—differential cage; and 5—locking wheel

have been taken by both Russian and foreign [7] scientists, for example, when studying hand biomechanics. In this case, when a semi-automatic differential lock is used, the effectiveness index of safety measures M_{is} , calculated in accordance with the system (2), will be equal to two ($M_{is} = 2$), and when an automatic differential lock is used, it will be equal to three ($M_{is} = 3$), respectively. This is explained by the fact that in the first case, operators must spend time assessing the moment when the mechanism is switched on and brought into operation, while in the second case, these actions are not required.

5 Assessment of the Effectiveness of Automatic Adhesive Weight Transfer

In order to reduce skidding, the adhesive weight of a tractor is often increased by various means: filling the tires with water, installing metal loads (disks) on the drive wheels, installing loads on special platforms in the front and rear sections of the tractor [14], as well as by using an automatic adhesive weight transfer device (Fig. 3), patent No. 110357 of the Russian Federation, 2011.

Fig. 3 Schematic diagram of a tractor equipped with an automatic adhesive weight transfer device: 1—gear rack of the hydraulic cylinder; 2—drive gear of the transmission mechanism; 3—gear rack of the detachable tank; 4—detachable tank with liquid; 5—rubberized rollers; 6—frame with brackets for mounting on the tractor; 7—crown; and 8—inductive sensor



Comparative testing of tractors with loads installed on special platforms in the front and rear sections and the proposed automatic adhesive weight transfer aimed at assessing the working conditions showed that in the first case, the degree of hazard is reduced from $WCC = 3.3$ to $WCC = 3.2$ and in the second, is reduced by two units from $WCC = 3.3$ to $WCC = 3.1$, respectively.

In the first case, a slight decrease is associated with both a decrease in the skidding process and an increase in labor-intensive loading and unloading, which can also lead to injuries. Thus, the effectiveness index of safety measures M_{is} , calculated in accordance with the system (2.2), will be equal to one ($M_{is} = 1$).

In the second case, when an automatic adhesive weight transfer device is used, labor-intensive loading and unloading are not required, and the calculated M_{is} index is equal to three ($M_{is} = 3$).

6 Assessment of the Effectiveness of the Preheater of the Vehicle Internal Combustion Engine (ICE)

Vehicle operators start the ICE by the means made available, such as a crank. Starting the car engine with a crank is unsafe and can be ineffective at rather low temperatures ($-25\text{ }^{\circ}\text{C}$ and below), which makes the driver remain in unfavorable working conditions for an extended period of time (up to one hour). At present, many agricultural enterprises use individual and group torch preheaters. These make it possible to reduce the ICE start-up time, but starting the engine, this way often results in the ignition of mobile equipment and injuries [2, 13, 14].

The proposed preheater (patent for invention No. 2451207 RU, 2012) of the vehicle ICE (Fig. 4) eliminates the above disadvantages.

In addition, the gas infrared preheater allows for the ICE of the wheeled vehicle (UAZ-2206) to be started up more quickly, which reduces the time the driver

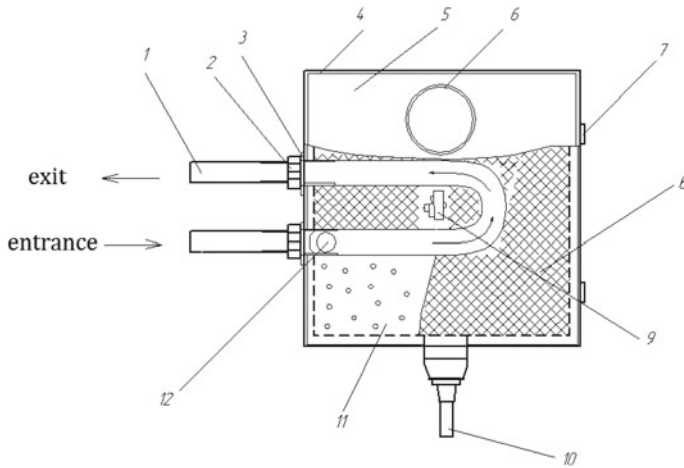


Fig. 4 Schematic diagram of the gas infrared ICE preheater: 1—shaped branch pipe; 2—nut; 3—sealing washer; 4—heater housing; 5—heater cover; 6—hot air branch pipe; 7—hinge of the heater cover; 8—grid of the infrared burner; 9—piezo-ignition button; 10—gas reducer connection; and 11—ceramic heating element

spends in low temperatures up to 11 ... 20 min; moreover, it almost completely eliminates injury and fire hazard compared to a torch preheater.

Comparative testing of tractors equipped with a torch preheater and a gas infrared ICE preheater aimed at assessing operator working conditions showed that the degree of hazard in the first case is reduced by one unit (from WCC = 3.4 to WCC = 3.3), and in the second—by three units (with WCC = 3.4 to WCC = 3.1), respectively. The effectiveness of the gas infrared ICE preheater is due to a reduction in workers' occupational diseases thanks to the reduced influence or elimination of the harmful factors of the working environment: WCC with respect to the index of air temperature (Table 9 ... 11 of Manual P2.2.2006-05) [14].

Thus, in the first case (the use of a torch heater), the index of effectiveness of safety measures M_{is} calculated according to the system (2) will be equal to one ($M_{is} = 1$), and in the second case (when using the proposed device based on an infrared emitter), the calculated index M_{is} will be equal to three ($M_{is} = 3$).

7 Assessment of the Effectiveness of the Cabin Floor Heater of the Vehicle

The effectiveness of the proposed electric floor for heating the soles of operators' feet (Fig. 5) was confirmed by the experimental results [14].

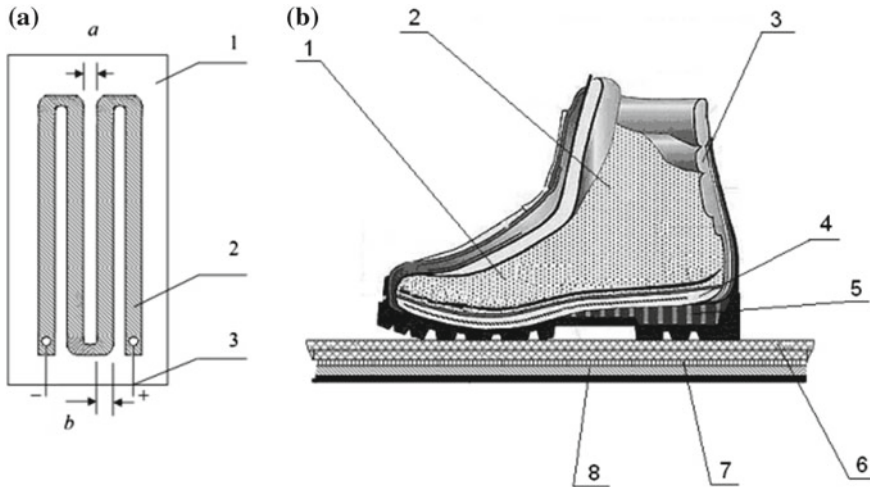


Fig. 5 a Schematic of the radiant electric film heater device: 1—two-layer sheet made of polyethylene terephthalate film; 2—resistive elements; 3—current-conducting wires; a—distance between the branches of the resistive elements; b—the width of the resistive element tape; **b** position of the operator’s foot on the surface of the floor covering: 1—foot; 2—sock (cotton); 3—leather shoe material; 4—insole; 5—footwear sole; 6—layer of rug rubber; 7—heating element; and 8—cabin floor

With the help of the automatic temperature regulator, the device sets the temperature of the cabin floor surface within the selected range (18 ... 22 °C) in the steady state, which meets the requirements of the regulatory documents (Table P17.2 of the Manual P2.2.2006-05).

The degree of hazard of the working conditions class when introducing the flooring in the ZIL-4331 car cabin is reduced by two units: from WCC = 3.2 to WCC = 2, which is categorized as acceptable working conditions. The improvement of working conditions is also confirmed by the increase in the proposed index of assessment M_{ot} , calculated before and after the introduction of the measure to the ZIL-4331. When considering the index of the effectiveness of measures M_{ot} for a regular vehicle, its value (according to the criteria of the cooling and heating microclimate in the workplace), calculated according to system (1), will be equal to one ($M_{is} = 1$).

By introducing electric heating floor, the calculated M_{is} value will be equal to two ($M_{is} = 2$).

The value of M_{ot} index is doubled when the proposed device is introduced, which confirms its effectiveness for improving operator working conditions.

After assessing the effectiveness of introducing the proposed technical devices [14], we compiled a summary table which shows their impact on operator working conditions (Table 1).

Table 1 Results of comparative testing of technical measures for improving operator working conditions

Technical measure	The results of assessing the effectiveness of technical safety measures according to the M_{is} index before and after their introduction	
	Before introduction	After introduction
Automatic differential lock of a vehicle	1	3
Automatic adhesive weight transfer	1	2
Engine preheater	1	3
Cabin floor heater of the vehicle	1	2

8 Conclusion

The results of the comparative testing allow us to conclude that the proposed methodology for assessing the effectiveness of technical measures can be used to select the most effective technical solutions for improving the working conditions of wheeled vehicle operators.

References

1. Bogdanov AV (2010) Increase of safety and improvement of assessment of working conditions of mobile wheel car operators in agrarian industrial production. Dissertation, St. Petersburg-Pushkin
2. Gorshkov YuG, Kalugin AA, Bogdanov AV (2011) Assessment of organizational and technical measures for improving the safety of mobile wheeled vehicle operators. *J Labor Prot Saf Agric* 2:43–45
3. Mohammadfam I, Kamalinia M, Momeni B, Golmohammadi R, Hamidi Y, Soltanian A (2017) Evaluation of the quality of occupational health and safety management systems based on key performance indicators in certified organizations. *J Saf Health Work* 8(2):156–161. <https://doi.org/10.1016/j.shaw.2016.09.001>
4. Anishchenko EB, Trankovskaya LV (2014) Hygienic aspects of the working conditions assessment and state of health of the workers of the railway departmental security forces. *Gig Sanit*, pp 48–50, PMID: 25051740
5. Cacciabue PC, Cojazzi G (1994) A human factors method-ology for safety assessment based on the DYLAM approach. *J Reliab Eng Syst Saf* 45(1–2):127–138. [https://doi.org/10.1016/0951-8320\(94\)90081-7](https://doi.org/10.1016/0951-8320(94)90081-7)
6. Dame Carol Black (2012) Work, health and wellbeing. *J Saf Health Work* 3(4):241–242. <https://doi.org/10.5491/SHAW.2012.3.4.241>
7. Kyung-Sun Lee, Myung-Chul Jung (2015) Ergonomic evaluation of biomechanical hand function. *J Saf Health Work* 6(1):9–17. <https://doi.org/10.1016/j.shaw.2014.09.002>
8. Meng L, Wolff MB, Mattick KA, DeJoy DM, Wilson MG, LeeM Smith (2017) Strategies for worksite health interventions to employees with elevated risk of chronic diseases. *J Saf Health Work* 8(2):117–129. <https://doi.org/10.1016/j.shaw.2016.11.004>
9. Carder M, Hussey L, Money A, Gittins M, McNamee R, Stocks SJ, Sen D, Agius RM (2017) The health and occupation research network: an evolving surveillance system. *J Saf Health Work* 8(3):231–236. <https://doi.org/10.1016/j.shaw.2016.12.003>

10. Ya Kim, Park Ju, Park M (2016) Creating a culture of prevention in occupational safety and health practice. *J Saf Health Work* 7(2):89–96. <https://doi.org/10.1016/j.shaw.2016.02.002>
11. Averyanov YI (2006) Improving the safety of the process of harvesting grain crops on the basis of improving the system “Operator-Machine-Environment”. Dissertation, University of St. Petersburg
12. Andros VA (1973) Theoretical studies of the effect of hazards on human operator. *Znanie, Moscow*, p 64
13. Borisova EV (2013) Material and technical provision and efficiency of agricultural production (on the materials of the Russian Federation). Dissertation, Moscow
14. Gorshkov YG, Zolotykh SV, Starunova IN, Kalugin AA (2016) Increase in effectiveness and safety of motion of wheeled machines under agricultural conditions: monograph. Printing house “City-Print”, FE Myakotin IV, Chelyabinsk, 484 p
15. Andros VA (1970) Substantiation of the initial assumptions for the analysis of the causes of industrial injuries. In: *Proceedings of VIM*, vol 46, Moscow
16. Gavrichenko AI, Vasiliev GP (1999) Working conditions and incidence of rural machine operators. *J Eng Equip Village* 7:21–22
17. Gavrichenko AI (1998) Labor protection at the present stage. In: *State and scientific problems of health hazard and workers’ industrial injuries in the Russian agroindustrial complex: Sat. sci. tr. Eagle: VNIOT*, 1998, pp 11–16
18. Guideline R 2.2.2006-05 Guide on hygienic assessment of factors of working environment and work load. Criteria and classification of working conditions
19. Kalugin AA, Gorshkov YG, Starunova IN (2013) Expert appraisal is a tool for managing professional risk indices in the Russian agrarian industrial complex. *J Nauka* 3:74–81
20. Zio E, Baraldi P, Librizzi M, Podofilini L, Dang VN (2009) A fuzzy set-based approach for modeling dependence among human errors. *J Fuzzy Sets Syst* 160(13):1947–1964

Definition of Rational Modes of Use of Marginal Dug-Out Wells



V. Kushnir, O. Benyukh and S. Kim

Abstract One of the factors limiting the development of cattle-breeding in conditions of semi-desert grasslands is the lack of subsaline water resources. In most cases, surface freshwater lenses, opened with relatively dug-out wells, do not give a large production rates. Therefore, the rational use of the well, aimed at obtaining the maximum possible (or required) amount of water, is important, provided that all the requirements ensuring project life and water source safety and reliable operation are met. The main factors influencing the water yield of the well, its condition and service life, are the features of the pumping equipment and operating modes, that is, the modes of pumping water from the well. The task of increasing the water-yield coefficient of a marginal water source can be solved by using water-elevating equipment with optimal parameters and regimes corresponding to the water yield of the water source. The intermittent cycle of joint operation of a water source and a water elevator, expressed in the periodic pumping of water, increases the economic efficiency of the system of mechanized water supply and although it somewhat reduces the coefficient of use of water sources, it provides the needs of objects in water.

Keywords Water sources · Water layer · Water supply · Shallow pit

1 Introduction

The effective operation of the mechanized water supply system, along with other factors, is influenced by the optimal operation of dug-out wells with low production rates. Such a regime can be established in the event that the technical parameters of the water-lifting device, the flow rate, the depth, thickness of the water layer, and the volume of the catchment area of the well are known. The most complex

V. Kushnir · O. Benyukh (✉) · S. Kim
A. Baitursynov Kostanay State University, 47, Baitursynov St.,
Kostanay 110000, Kazakhstan
e-mail: beolan@mail.ru

relationship parameter of the wells has its current production rate, which depends, first of all, on the maximum flow rate and the static water level in the well.

The concept of the “marginal water source” does not have a clear definition and quantification. Comparing the flow rate of the well with the water demand (or, in some cases with supply of equipment) can be roughly established that the values of relative flow rate less than a certain value, the water source will be called “marginal” in relation to an object with a specific water consumption [1–10].

The yield of dug-out wells mainly depends on the capacity of the aquifer, the nature of the aquifer rocks, construction of wells, etc. In most cases, these parameters for specific water sources are unknown. Therefore, it is necessary to seek a new approach to the determination of the current production rate of wells and their operation modes together with the water elevator. To increase the production rate of the well without reconstruction is usually not possible. However, with the available maximum flow rate, optimum use of the well provide the possibility of extraction for a certain period of time, the largest amount of water [11–20].

2 Common Part

To “marginal” wells for a given consumer, we will refer such water sources, which relative clock output (maximum) is equal or less than 1.4 weight hourly object needs in water— B_h . Consequently, we are talking about the relative rate of debility, which we will estimate by the coefficient of K_{dh} .

$$K_{dt} = q_m/B_h \leq 1.4 \quad (1)$$

If K_{dh} is more than 1.4, the well is not a marginal for the given consumer.

Under real conditions, actual fluid loss of the well depends on the mode of use of equipment, construction volume, and water receiving portion terrestrial reservoir tank, wherein the water supply is formed. In those cases when wind-pump or solar water-elevators are used on pastures, the alternation of working and non-working construction periods and the change in their actual production in time have a great influence on the return of water to the well.

As already mentioned, one often encounters a large unevenness of water consumption during the day (B_c), estimated by the coefficient of unevenness (K_n), so the relative rate of productivity index is more indicative if it is determined by the daily characteristics

$$K_d = 24q_m/B_cK_n \quad (2)$$

Therefore, in semi-desert pastures, in most cases, dug-out wells are built water tanks W_m in the water intake part of the well.

We take the supply of a water-elevating construction constant, and also $Q/q_m = K = \text{const}$ for a given well. When considering modes of collaboration and source water elevator, the attention should be paid to three boundary cases.

I mode means that $Q = q_m$. In this case, the water-elevating construction can operate in two modes: the water is evacuated, the level of which is at such a distance from the earth's surface, that the thickness of the water layer in the water source provides q_m and the system works together in a steady state, the thickness of the water layer in the well is not changed, since $Q = q_m$; the water-elevating construction starts to work at W_m , that is, when the water level in the well is the highest, therefore, there is no water inflow into the well. In this case, in the beginning, the accumulated water is pumped out; the inflow of water into the well gradually increases as the pump is pumped out. This leads to the fact that the output time at the steady-pumping mode is greater than in the other two modes. In this mode, continuous use of water-lifting equipment is possible. However, due to the fact that most of the wells on the pastures have a negligible amount of water inflow, the operation of the water source on a regulated supply is necessary. Therefore, there is often a doubt about the advisability of using such regimes, since this will lead to incomplete use of the supply of a water elevator, over-expenditure of energy resources, and inefficient use of labor.

II mode—the water flow rate is maximum and q_m is greater than the supply of the construction. In this case, the construction cannot operate at the maximum production rate of the well. Consequently, the water source will receive less water than q_m . The system “water elevator—well” always works on the so-called regulated inflow, that is $q_i = Q$. This leads, on the one hand, to the need for longer use of pumping equipment, and on the other hand, to underutilization of the potential of the well. Thus, this regime should be attributed to irrational. Such modes are most acceptable only in conditions of using wind turbines operating with variable feeds depending on the wind speed.

III mode—the rated flow of the water elevator is greater than the maximum current flow rate of the water source $Q > q_m$. In this case, the water-elevating construction is constantly operating in a mode where the water level in the well provides the maximum inflow. In this case, it is possible to quickly pump out the accumulated reserve of water in the well, sending it into the tank. Then, the work goes on in a steady state, determined by the level below which the pumping equipment no longer raises the water, that is, it pumps out everything that is guaranteed by the inflow of water into the water source. For this regime, it is necessary to find the optimal emptying of the well, which, on the one hand, allows obtaining maximum water loss, and on the other, does not lead to spoilage of the well itself and water-lifting equipment.

Proceeding from the joint operation of the equipment and the source, it is necessary to establish such regimes that, along with technical capabilities, would give the greatest use to the yield of low-yield shafts and thereby provide water to consumers. In marginal dug-out wells, the widening of the water intake part significantly increases their water yield. Water accumulates in it during the day and rises as necessary. To quickly collect the necessary water supply in the well,

the pumping is done with constructions with a large feed. Therefore, the supply of the construction is always greater than the current production rate of the well.

Coefficient of use of the well:

$$K_{isp} = B_c K_{ner} / 24q_m \quad (3)$$

which characterizes the level of use of the maximum possible return of the water source.

When considering the residual volume of water in the well W_0 , which the water elevator cannot lift, K_{isp} can be defined as follows:

$$K_{isp} = B_c K_{ner} / 24(q_m - W_0) \quad (4)$$

Daily water consumption. Its volume depends mainly on the rate of water consumption by animals per day and the number of livestock at the water pipe station and is determined by the formula [13]:

$$B_c = bn/1000 + x/1000 \text{ (m}^3\text{)} \quad (5)$$

b —the rate of water consumption per day, l; n —livestock at the water pipe point; and x —water consumption for household needs at the water pipe point, l.

Substituting the value B_c from the Eq. (5), we obtain

$$K_{isp} = (bn + x)K_{ner} / (24q_m - W_0) \cdot 1000 \quad (6)$$

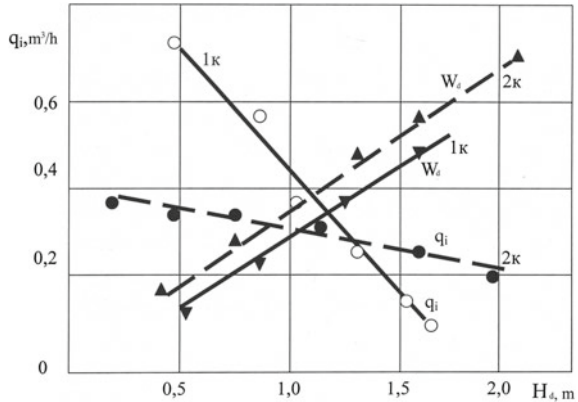
In the steady-state operation mode ($Q = q_m$), the maximum amount of water (theoretical) that can be lifted from the well is $Vb_{theo} = 24q_m$. It corresponds to $K_{isp} \approx 1$.

In actual conditions, K_{isp} is always less than 1, since it is difficult to ensure the operation of the equipment during the day in strict accordance with the production rate. It is not always necessary to use all possible water loss of the well, and sometimes, due to the limited capacity of the ground reservoir, it is impossible to store all the amount of water that can be extracted from the well, but cannot be consumed by the facility during the current day. In addition, the design of the water lift is such that and in some cases, it is impossible to pump the water to the required level, and therefore the average flow rate is less than the maximum.

In terms of the reduced specific costs, in most cases it is inappropriate to pump out water with a small supply of the construction for most of the day. It is more profitable to pump out water in the modes of increased feed as the well is filled.

To establish the level of reliability and validity of the proposed methods, an experimental study of the flow rate of dug-out wells has been carried out so that, on the basis of a comparison of the results of calculations and experiments, it is possible to establish coincidences and possibilities for recommending these methods for determining production rates.

Fig. 1 Change in production and filling of the water intake part of the well



Production rate of the well is considered to be the amount of water pumped per time unit in steady dynamic level (when the amount of water in the well is equal to the feed). However, in marginal dug-out wells with an insignificant static water level, the determination of the flow rate by this method is difficult.

Of the existing methods, the most suitable for determining the flow rate of dug-out wells is the measurement of water inflow using a level recorder [21]. It was carried out in the wells FF “Krysin B.”

The values of water inflow into the well, according to the recorder’s records, served as initial data in calculating the amount of water that entered the well in the time that has elapsed since the next pumping. The inflow of water in the first well decreases significantly with an increase in H_d , and slowly in the second well (Fig. 1).

This is probably due to the fact that the pressure of the aquifer and the filtration of water in the well are not the same. If the initial inflow of water in the well is significant (for example, the first well), then to satisfy the consumers at the water pipe point, the missing water can be raised, continuing the operation of the water elevator at the current production rate of the well or re-pumping after accumulating the required volume of water. However, all this depends on the CMB on a particular watering points.

It was determined the rational mode of water and dug-out wells FF “Krysin B.” It was found that it is advantageous to exploit the system “water elevator—well” with breaks (mode 3). Figures 2 and 3 give comparative data (actual and calculated) for $q_i = f(t)$, $W_{gi} = f(t)$ and $H_{gi} = f(t)$. It can be seen that the curves for all ranges of the argument t give an error not exceeding 10%, which is acceptable for practical calculations.

Thus, the rational operating mode of the CMB for the pasture zones of the republic can be selected through experimental data and analytical calculations.



Fig. 2 Comparison of calculated and experimental data on $q_i = f(t)$ and $W_{gi} = f(t)$: ————experimental; ————calculated

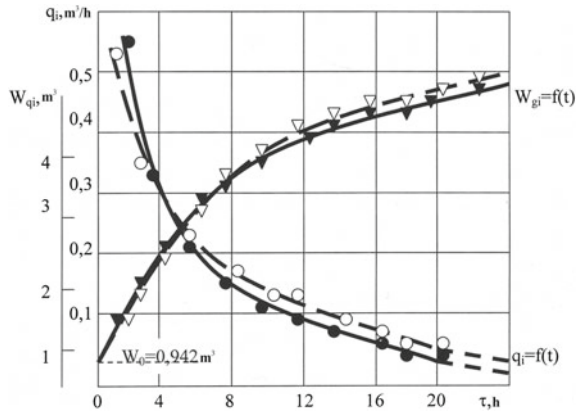
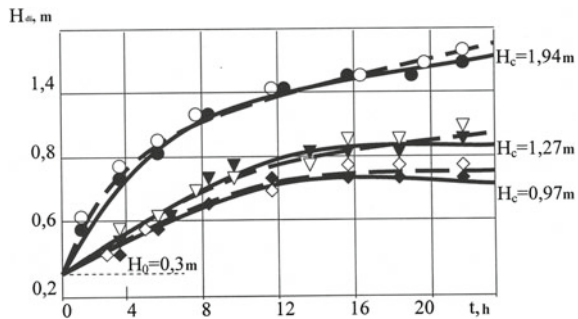


Fig. 3 Comparison of calculated and experimental data on dynamic water level in the well: ————experimental; ————calculated



3 Conclusion

Based on the developed classification of factors affecting the parameters of the elements of the system of mechanized water supply, the principles were established and zoning of the pasture area was applied in relation to the tasks of developing mechanized water supply systems. It is shown that the main factors that should be taken into account in the construction of rational systems of mechanized water supply are daily water consumption at the site, types and characteristics of the water source, energy resources in the area of the location of the facility, the mutual location of water points, their distance from the cultural zone, and road conditions that provide a link between them. Marginal water sources, significant water salinity in them, the difficulties of power supply for mechanized water supply systems, as well as heavy operating conditions, require an appropriate approach to the formation of mechanized water supply systems, the construction of water elevators and other equipment, the operation system of all elements that differ significantly from the methods used in mechanized water supply systems at other objects of agriculture.

The concept of “marginal water source” and the coefficient of its use are defined. Under marginal water source is recommended to understand the relationship of the well and flow rate of water consumption for the final time interval smaller than a certain value. It is recommended to consider the water source as marginal for the given consumer, if the ratio is less than 1.4. As a result of static processing of available data, it is established that 83.7% of the total number of water sources in pastures of Northern Kazakhstan is marginal.

The task of increasing the water-yield coefficient of a marginal water source can be solved by using water-elevating equipment with optimal parameters and regimes corresponding to the water yield of the water source. It is shown that the intermittent cycle of joint operation of a water source and a water elevator, expressed in the periodic pumping of water, increases the economic efficiency of the system of mechanized water supply and although it somewhat reduces the coefficient of use of water sources, it provides the needs of objects in water.

Most pasture zones have favorable wind conditions for the use of low-power wind turbines, which is confirmed by research in production conditions. The most suitable operating parameters for pasture conditions at $2.5 \leq v \leq 4$ m/s are aggregates with a belt-type water lift, and for $v \leq 4$ m/s—high-speed installations with a belt-type water lift, a screw and high-speed electric pump.

References

1. Zhukovsky NE (1949) *Gidrodinamika* (Hydrodynamics). Gos. Publishing House technical and theoretical of literature, Moscow, 760 p
2. Leibenzon LS (1924) *Teoriya shnuruvkh nasosov* (The theory of the cord pumps). Oil shale and economy, Moscow
3. Schoenberg SP (1915) *Gidrodinamika vyazkoy zhidkosti i gidravlicheskaya mashina treniya* (Hydrodynamics of a viscous fluid and hydraulic friction machine). Kiev
4. Baranov VN, Zakharov VE (1977) *Elektrogidravlicheskiye i vibratsionnyye mekhanizmy* (Electro-hydraulic and vibration mechanisms). Mechanical Engineering, Moscow, 326 p
5. Gumarov GS (1995) *Uluchshen rabochiy protsess i obosnovan parametr lentchnogo vodopod'yemnika dlya poyeniya zhitovnykh na pastbishchnykh usloviyakh* (Improved workflow and justification parameter tape water lift for watering animals pasture conditions). Dissertation, SSU, Saratov
6. Isaev VA, Kulagin PI, Danilov VN (1975) *Vypolneniye lenty vodopod'yemnika. Mekhanizatsiya raboty v zhitovnovodstve* (Performance of tape of water lift. Mechanization of work in animal husbandry). SSU, Saratov
7. Isaev VA, Danilov VN, Kulpin PI (1975) *Eksperimental'noye issledovaniye na proskal'zyvaniye lenty vodopod'yemnika. Mekhanizatsiya raboty v zhitovnovodstvo* (Experimental Study on slippage tape of water lift. Mechanization of work in animal husbandry). SSU, Saratov
8. Kaplan PM (1959) *Mekhanizatsiya vody na pastbishchnykh ugod'yakh v Kazakhstane* (Mechanization of water on pasture transhumance in Kazakhstan). Alma-Ata, 36 p
9. Koba VG, Braginets NV, Murusidze DN, Nekrashevich VF (1999) *Tekhnologiya mekhanizatsii i zhitovnovodstva* (Mechanization and livestock production technology). Kolos, Moscow, 525

10. Kulpin PI (1973) Issledovaniye malogabaritnogo lentochnogo vodopod"yemnika dlya pastbishchnykh shakhtnykh kolodtsev. (Study of small-sized tape water lift for grazing mine wells). Abstract of a thesis of Candidate of engineering, Alma-Ata, 43 p
11. Mashkov VN (1978) Vybor ratsional'nogo varianta mekhanizatsii vodopod"yema v pustynnykh lugakh Sredney Azii (Choice of a rational variant of mechanization of water lifting in the desert grasslands of Central Asia). Proc Central Asian Res Inst Irrig 125:51–67
12. Kaplan RM, Yakovlev AA (1986) Mekhanizatsiya vody na pastbishchakh (Mechanization of water in pastures). Kynar, Alma-Ata
13. Kushnir VG (2012) Issledovaniye vody nizkopotochnoy skvazhiny (Investigation of water of low-flow well). "3i" 3:57–60
14. Kaplan RM, Yakovlev AA (1986) Mekhanizatsiya vody na pastbishchakh (Mechanization of water in the pastures). Kaynar, Alma-Ata, 47 p
15. Kaplan RM (1965) Optimal'nyye parametry vodopod"yemnika shakhtnogo kar'yera (The optimal parameters of water lift-mine pit). Bulletin agr. Science of Kazakh SSR, Kaynar, Alma-Atapp., 16 p
16. Hellenov OB, Ostanin VS (1966) Orosheniye i mekhanizatsiya vody v pustynnykh lugakh Turkmenskoy SSR (Irrigation and mechanization of water in the desert grasslands of the Turkmen SSR), Ashgabat, 23 p
17. Karambirov N A (1978) Sel'skokhozyaystvennoye vodosnabzheniye (Agricultural water supply). Kolos, Moscow, 35 p
18. Kunin VN (1959) Mestnyye pustynnyye vody i problemy ikh ispol'zovaniya (Local desert waters and issues of their use). Publishing House of the USSR Academy of Sciences, Moscow
19. Sokolov BI (1958) Poliv pastbishch pustyn' (Watering pastures of deserts). State Publishing House of the Uzbek SSR, Tashkent
20. Shefter YI, Hellenov OB (1981) Obosnovaniye ratsional'nogo ispol'zovaniya nizkodokhodnykh skvazhin (Substantiation of rational use of low-yield wells). Hydraulic engineering and melioration, no. 10, Moscow
21. Hellenov OB (1974) Opredeleniye debita shakhtnykh skvazhin na pustynnykh pastbishchakh (Determination of the flow rate of mine wells on desert pastures). Problemy osvoenia pustyn, no. 1, Tashkent

Hose Regulating Device with Swirling



A. V. Fominykh, I. R. Chinyaev and A. A. Ezdina

Abstract The rods of the proposed regulating device (RD) by the means of the drive are tilted relative to its axis and pinch the hose from which the spiral channels are formed. The direct channels of the throttling device in the hose are formed by rods curved in the plane passing through the RD axis. Theoretical studies of the RD with input and output nozzles are performed in the software Solid Works 2017. Experimental studies were performed in the turbulent self-similarity zone. The RD resistance coefficient and the coefficients of friction losses along the length in the input and output nozzles are determined. To visualize the vortex motion of the liquid, air and cut flower petals were fed into the pipe. In the vertical and horizontal arrangements of the RD, the flow of bubbles was located at the pipe axis. In the horizontal arrangement of the RD, the flow of bubbles fluctuated near the axis of the pipe but did not touch its walls. The resistance coefficient of the RD with the direct channels is 6.03, and the area of the middle narrow section is 494 mm². The resistance coefficient of the RD with the twisted channels made up of is 0.70, and the area of the middle narrow section is 475 mm². The coefficient of the RD resistance with the direct channels is greater than that of the device with the twisted channels.

Keywords Fluid · Regulating device · Swirling · Resistance coefficient

A. V. Fominykh (✉) · I. R. Chinyaev · A. A. Ezdina
Federal State Budgetary Educational Institution of Higher Education, Kurgan State
Agricultural Academy by T.S. Maltsev, (Kurgan SAA), Kurgan Region, Ketovsky District,
Village Lesnikovo 641300, Russia
e-mail: prof_fav@mail.ru

© Springer Nature Switzerland AG 2020
A. A. Radionov et al. (eds.), *Proceedings of the 5th International Conference on
Industrial Engineering (ICIE 2019)*, Lecture Notes in Mechanical Engineering,
https://doi.org/10.1007/978-3-030-22041-9_6

1 Introduction

The main works on screw and spiral motion of liquid are the works of the Austrian inventor Victor Schaubberger [1–3]. In such a pipe, the bearing capacity and efficiency of the flow increase due to the reduction of friction and the prevention of sedimentation. The twist in the waterlines reduces the loss of pressure significantly.

2 Timeliness

One of the ways to improve the efficiency of hydraulic systems in agriculture is the use of swirling [4–6]. The demand for regulating pipeline valves is growing, and its production is increasing [7–10]. The majority of scientific researches devoted to the process of fluid flow regulation are aimed at improving the accuracy of the flow regulation and increasing the service life of the equipment [11–16]. Pipes made of polymeric materials are increasingly used. It is advisable to use the regulating devices made of the same materials including hose. The motion of the fluid in the hose of the regulatory unit (RU) with swirling of liquid is not sufficiently studied [17–21]. You must select the software to calculate the swirling.

3 Setting

We have obtained a patent for a useful model No. 166585 “Regulatory device” with swirling and solved the problem of determining its hydraulic characteristics [22–25].

4 Theoretical

Through the drive 1, the sleeve 2 rotates around an axis (RD) and the ends of the rods 3 shift with it, see Fig. 1.

The rods pinch the hose from which the spiral channels 4 are formed. In this case, the sleeve 5 moves only along the axis of the switchgear. RD has four rods, so four identical channels are formed. In the control mode, the confuser and the diffuser of the switchgear are mirror-symmetric about the average cross section.

Theoretical studies of the regulating device with the inlet and outlet nozzles in the software Solid Works 2017, see Fig. 2, are performed.

It can be seen from the figure that before the RD water, particles move along straight trajectories parallel to the axis of the nozzle, but after RD they move on spiral paths. In order to determine the capabilities of the Solid Works 2017 software for the study of swirling, calculations were made with different lengths of inlet and outlet

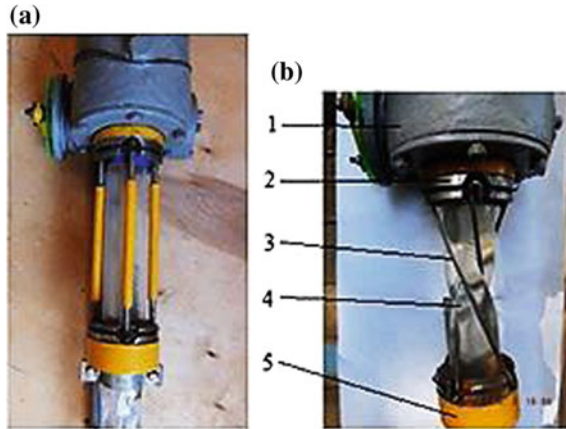


Fig. 1 a Regulating device with a rods diameter of 12 mm; b regulating device with a rods diameter of 4 mm; 1—drive; 2—rotary sleeve; 3—rods; 4—channels; 5—sleeve

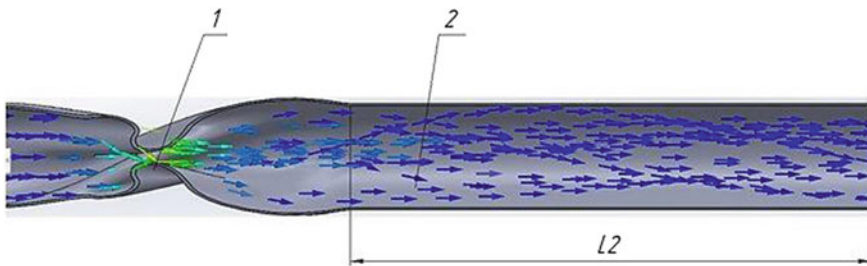


Fig. 2 Results of the calculation of the regulating device with inlet and outlet nozzles in the software Solid Works 2017; inlet nozzle is not shown; 1—regulating device; 2—outlet nozzle; L2—the length of the outlet nozzle

nozzles of the same diameter 50 mm with zero roughness and constant pressure drop of 100 kPa (10 m water column). Analyzing the results of calculations, it can be concluded that to determine the total coefficient of the reactor resistance with the input and output nozzles it is necessary to use the following equation:

$$\zeta_y = \frac{2 \cdot g \cdot \Delta h}{V_i^2} \tag{1}$$

where Δh —is the pressure differential between the RD inlet and outlet nozzles with the steam pipes, m; V_i —water velocity in the pipe, m/s.

According to the calculation results with different lengths of nozzles, we determined the coefficients of friction loss along the length of the inlet and outlet nozzles according to the formula:

$$\lambda_2 = \frac{\Delta\zeta_2 \cdot D_1}{\Delta L_2} \quad (2)$$

where $\Delta\zeta_2$ is the difference of the resistance coefficients determined by the formula (1) for different lengths of the outlet nozzle;

ΔL_2 is the difference in length of the outlet nozzle, m;

D_1 is the diameter of the nozzle, $D_1 = D_2$, m.

5 Experimental

In accordance with [26, 27], the hydraulic characteristics of the RD plant are determined in the accredited laboratory of LLC NPF MKT-ASDM [3, 4]. Conducting experimental studies from a tank with a volume of 46 m³ water enters the centrifugal pump, which supplies water through a screen filter to the pipeline [28–30]. The water through the pipeline enters the control valve. Changing the position of the regulating element set the pressure P1 to the tested RI. After passing through the RD water through the pipeline enters the second control valve, which sets the pressure P2. The information from pressure sensors is transmitted and recorded in the “Ecograph-T” ADC. For fixing the flow water rate Q on the return pipeline of the «Hydro-circle» stand, an electromagnetic flowmeter ERSV-550F is installed. After passing through the flow meter, the water through the pipeline returns to the tank.

The tests were carried out with vertical and horizontal arrangements of the RD with a diameter of 50 mm. To visualize the vortex motion, the air and chopped flower petals were fed into the tube. With a vertical location of the RD water, flow rates were selected at which the bubbles slightly moved along the axis of the RD channels and in the pipe after the switchgear. Flower petals have a density close to the density of water and, therefore, move along trajectories close to the trajectories of water particles.

The straight channels are formed by rods bent in a plane passing through the axis of the RD.

6 Determination

The theoretical studies were carried out in the range of Reynolds numbers from 67714 to 80485. According to the results of calculations in Solid Works 2017 software, the resistance RD coefficient without nozzles was 58.8 with an average narrow section area 234 mm². The coefficient of friction loss along the length in the outlet pipe was obtained by 15.5% more than in the inlet pipe.

The experimental studies were performed in the range of Reynolds numbers from 16800 to 29755. With the vertical and horizontal arrangements of the RD, the flow of bubbles was located at the axis of the pipe. With a horizontal RD location, the flow of bubbles fluctuated around the axis of the pipe but did not touch its walls. The resistance coefficient of the RD with straight channels was 6.03 with an average narrow section area 494 mm². The resistance coefficient of the RD with twisted channels was 0.70 with an average narrow cross-sectional area 475 mm².

7 Conclusion

The advantages of a hose RD with swirling in the open position the RD hose are full bore and have a minimum coefficient of the resistance; fluid comes into contact with the hose only; the zone of collapse of cavitation bubbles is removed from the RD walls, good RD washability and disinfection of the switchgear.

The resistance coefficient of the RD with the straight channels is greater than that of the RD with the twisted channels.

The Solid Works 2017 software does not reflect the effect of reducing the loss of fluid movement when the flow is swirled.

References

1. Schauburger V (2007) Energy of water. Yauza, Eksmo, Moscow, p 320
2. Pipe of Viktor Schauburger (2009) Available via DIALOG. <http://khd2.narod.ru/shau/pipe.htm>. Accessed 25 Mar 2009
3. The pipeline according to Schauburger (2005) Available via DIALOG. <http://www.evgars.com/tr.htm>. Accessed 5 Sept 2005
4. Fominykh AV, Fomina SV, Strekalovskikh NS (2017) Installation of increasing of the liquid feed additives concentration. Vestnik of Kurgan KSAA 3:75–80
5. Fominykh AV, Fomina SV, Strekalovskikh NS (2018) The installation for determining the characteristics of a water-jet pump. In: Sukhanova SF (ed) Ways to implement the Federal Scientific and Technical Program for the Development of Agriculture for 2017–2025, Lesnikovo, pp 1105–1109
6. Fominykh AV, Chinyaev IR, Poshivalov YA, Sukhov SA (2014) Flow control at the water intake in the system of the first water rise. Vestnik of ChSAA 70:136–140
7. Ionaitis RR (2014) Concept and examples of renewal and modernization of pipe fittings and reinforcing security. In: Pipeline valves, and equipment, 4th edn, p 81
8. Ionaitis RR (2003) Passive elements of systems important to safety of nuclear installations. Bauman, Moscow, p 96
9. Blagov EE, Ivnitkiy BY (1974) Throttle-control valves in the energy sector. Energy, Moscow, p 264
10. Rednikov SN, Nigert KV (2016) Automation of the working process of a magnetorheologic restrict device. Vestnik of SUSU 14:23–32
11. Eismont VP (2012) Regulators. Publishing house OOO “Deaton”, St. Petersburg, p 326
12. Blagov EE (2007) Prediction of flow regimes fluid in a hydraulic constriction devices. Armaturostroenie 4:45–52

13. Spiridonov EK, Bitiutskikh EK (2015) Characteristics and calculation of cavitation jet mixer. *Chem Pet Eng* 4:6–9
14. Spiridonov EK (2015) Characteristics and calculation of cavitation mixers. In proceedings of the international scientific and technical conference of FGBOU VPO “South Ural state University”, pp 14–16
15. Spiridonov EK, Ismagilov AR (2014) Universal method of analysis and design of liquid-gas jet pumps. *Hydraulic machines, hydro pneumatic automation. Current state and prospects of development: collection of scientific papers of the 8th all-Russian scientific-technical conference with international participation*. Publishing house of Polytechnic University, Saint Petersburg, pp 101–103
16. Nigert KV, Rednikov SN (2016) Technologies for controlling flow characteristics by changing the rheological properties of working media. *Vestnik of SUSU* 16:52–60
17. Gurevich DF (2008) Calculation and design of pipeline valves. Moscow, p 480
18. Idelchik IE (1992) Handbook of hydraulic resistance. *Mashinostroenie*, Moscow
19. Altshul AD (1982) Hydraulic resistance. *Nedra*, Moscow, p 224
20. Chernoshtan VI, Blagov EE (2012) Experimental determination of the critical flow criterion. *Armaturostroenie* 4:50–57
21. Natural science educational portal (2010) Available via DIALOG. <http://WWW.en.edu.zu>
22. Fominykh AV, Ponomareva OA, Ezdina AA (2018) Modeling of the regulating device with swirling. *Polzunovsky Vestnik* 1:106–110
23. Fominykh AV, Ovchinnikov DN, Ezdina AA (2018) Hose control device for hydraulic systems in agriculture. *Feeding of farm animals and fodder production* 6:55–61
24. Fominykh AV, Ponomareva OA, Ezdina AA (2018) Methods of calculating the diffuser of the regulating device with the twisting of the flow. In: Sukhanova SF (ed) In the composite book: Priority directions of energy development in the agro-industrial complex Collection of articles on the materials of the II All-Russian (national) scientific-practical conference, pp 237–242
25. Ezdina, AA, Ponomareva OA, Fominykh, AV (2017) A regulating device using twisting of a flow of a conducted medium. In the collection: Scientific support for the implementation of state programs in the agro-industrial complex and rural areas, pp 393–396
26. GOST R 55508-2013 (2013) Pipeline fittings. The method of experimental determination of the hydraulic and cavitation characteristics
27. Standard CKBA (2006) CJSC NPF “Central design Bureau of valve industry”. Pipeline fittings. The method of experimental determination of the hydraulic and cavitation characteristics
28. Fominykh AV, Chinyayev IR, Poshivalov YA, Ilinykh YA (2016) Determination of the hydraulic and cavitation characteristics of the cell valve. *Vestnik of Kurgan SAA* 1:71–75
29. Chinyayev IR, Fominykh AV, Poshivalov EA, Ilinykh EA (2016) The experience of using GOST R 55508-2013 in determining the hydraulic and cavitation characteristics of a cell shut-off and control valve. In Territory “NEFTEGAZ”, pp 96–100
30. Poshivalov EA, Chinyayev IR, Shanaurin AL, Fominykh AV (2016) Analysis of methods for experimental determination of cavitation characteristics of pipeline valves. *Pipeline Valves* 4:42–45

Theoretical and Experimental Evaluation of Diesel Engine Derating Effect on Its Life Time



A. Malozemov, V. Dooun and D. Kozminykh

Abstract The mathematical model for predicting diesel lifetime has been developed. Equations that can be used to determine a relative rate of engine details damage accumulation depending on design, adjustment parameters and load from the objects of application are proposed. These equations take into account inertial loads due to engine speed change, gas pressure in the combustion chamber, heat change and engine parts wearing. Equation for determining the rate of damages accumulation caused by heat changes is proposed. Numerical and experimental studies were carried out, which made it possible to predict a change in the diesel engine lifetime due to a change in its operation modes during adaptation for an industrial tractor. The study results can be used to create diesel engines derated modifications and to develop similar methods for predicting internal combustion engines, which differ in power and objects of application, life time. The calculation methodology, developed on basis of the proposed mathematical model, is used in Chelyabinsk Tractor Plant and South Ural State University at the development of industrial tractor diesel engine modifications.

Keywords Diesel engine · Derating · Endurance · Mathematical model · Experiment

1 Introduction

At present, on the basis of forced transport diesel engines, its modifications designed to work as part of civil engineering (industrial tractors, engineering and road-building machines based on them, power plants, etc.) are being developed [1, 2]. Forced diesel engines do not fully meet the requirements for civil engineering. For example, to use a diesel engine as part of an industrial tractor, it is

A. Malozemov (✉) · V. Dooun · D. Kozminykh
South Ural State University, 76, Lenin Avenue, Chelyabinsk 454080, Russia
e-mail: malozemov@gmail.com

© Springer Nature Switzerland AG 2020
A. A. Radionov et al. (eds.), *Proceedings of the 5th International Conference on Industrial Engineering (ICIE 2019)*, Lecture Notes in Mechanical Engineering,
https://doi.org/10.1007/978-3-030-22041-9_7

necessary to reduce specific fuel consumption by up to 8%, oil—1.5–5 times and to increase resource by 4–8 times. At the same time, designers have a reserve for reducing the nominal power (derating) by 2–5 times.

2 Problem

One of the main problems encountered in development of diesel engines derated modifications is need to ensure significantly higher reliability. This problem is usually solved by derating engine at maximum power and speed. Level of derating should be determined by numerical calculation and confirmed by test results. The currently existing methods for calculating reliability parameters are based on statistical and semi-empirical mathematical models of wear, the disadvantage of which is that it is impossible to use for design derated engine modifications. In addition, according to statistics, due to wear 18–65% failures happen, at the same time 35–70% of failures occur due to breakdowns, cracks, fractures and ruptures. Therefore, when forecasting resource indicators, it is necessary to consider accumulation of mechanical and thermal damage together with wear [3–6].

3 Mathematical Model

Analyses of the works available on this topic showed that the following principles should be put on the basis of mathematical model for predicting engine life time:

- it is assumed that lifetime indicators of the base engine, operating modes of the base and derated engines are known, and reliability parameters distribution law of the base and derated engines are same (i.e., you can operate with center of the parameters distribution and not take into account variation of parameters);
- engine lifetime before parametric (gradual) failure is determined by the speed of wear process, functional (sudden) failure—by the speed of damages accumulation process, which, in turn, is determined by the total effect of inertial forces, gas forces, thermal loads and variable speed (acceleration);
- problem of lifetime prediction can be solved using a mathematical model based on physical models of wear and damage accumulation and statistical data on typical loading modes of the base and derated engines as parts of objects of application, principles of damages linear summation and superposition (independent influence of various forces) [7, 8].

In the most general form, relationship between the load (tension, amplitude, range) S and the number of cycles H on different modes is described by the Weller equation [9]:

$$S_i^m \cdot N_i = \text{const} \quad (1)$$

here m —exponent depending on properties of the material and actual load; i —mode number.

Total damages accumulation from the j -factor per time unit over spectrum of operating modes is determined taking into account frequency f_i of i -mode occurrence:

$$C_j = \sum_1^i (N_i \cdot S_i^m \cdot f_i) \quad (2)$$

Relative speed of derated engine damage accumulation from the j -factor (relative to the base one):

$$K_j = \frac{C_j}{C_j'} \quad (3)$$

here symbol ' refers to the base engine.

Rate of damages accumulation from inertial loads, which are proportional to the square of engine speed, after simple transformations of Eq. (2) can be represented as:

$$C_n = \sum_1^i (n_i^{2m+1} \cdot f_i) \quad (4)$$

here n_i —engine speed at i -mode.

Rate of damages accumulation from gas forces, which amplitude is determined by the maximum combustion pressure P_z :

$$C_{Pz} = \sum_1^i (P_{zi}^m \cdot n_i \cdot f_i) \quad (5)$$

Evaluation of the thermal stress influence on diesel engine lifetime indicators is conveniently made according to the Kostin criterion [10, 11]:

$$q = k \cdot \left(\frac{G_m}{F_n} \right)^a \cdot \frac{1}{(A \cdot n \cdot S_\Sigma \cdot \rho_a)^b} \quad (6)$$

here G_m —fuel consumption; F_n —piston area; S_Σ —maximum piston stroke; ρ_a —air density at the cylinder inlet; $A = CR/(CR - 1)$, where CR is compression ratio; a and b —exponents, depended on surface type; k —proportionality coefficient.

The parameters for estimating thermal stress level can be applied only to engines that are very similar in design and working process, such as basic and derated diesel

engines. In our case, we use the parameter q not to compare different diesel engines thermal stress levels, but to compare different quasi-stationary modes of the same diesel engine, i.e., we estimate the level of forcing by thermal stress for different modes in a dimensionless form, taking each specific mode of operation in a quasi-stationary form.

In this case, for i -mode, change in the thermal stress criterion relative to nominal mode:

$$K_{Ti} = \frac{q_i}{q_{\text{nom}}} = \frac{K \cdot \left(\frac{G_{mi}}{F_n}\right)^a \frac{1}{(A \cdot S_{\Sigma} \cdot \rho_{\theta i})^b \cdot n_i^b}}{K \cdot \left(\frac{G_{m \text{ nom}}}{F_n}\right)^a \frac{1}{(A \cdot S_{\Sigma} \cdot \rho_{\theta \text{ nom}})^b \cdot n_{\text{nom}}^b}} \quad (7)$$

After transformation:

$$K_{Ti} = \left(\frac{G_{mi}}{G_{m \text{ nom}}}\right)^a \cdot \left(\frac{n_{\text{nom}} \cdot \rho_{\theta \text{ nom}}}{n_i \cdot \rho_{\theta i}}\right)^b \quad (8)$$

Air intake density [12]:

$$\rho_a = \frac{P_c \cdot 10^6}{R_a \cdot T_c} \quad (9)$$

here P_c —air pressure after compressor; T_c —air temperature after compressor; R_a —gas constant for air.

Intake air temperature for a diesel engine without supercharging is equal to ambient air temperature, with supercharging [13]:

$$T_c = T_0 \cdot \left(\frac{P_c}{P_0}\right)^{\frac{n_c-1}{n_c}} \quad (10)$$

here P_0 —ambient air pressure; T_0 —ambient air temperature; n_c —polytropic coefficient.

Using the Eqs. (6)–(10), we obtain the formula for determining rate of damages accumulation caused by heat changes at i -mode:

$$C_{Ti} = \left(\frac{G_{mi}}{G_{mi \text{ nom}}}\right)^a \cdot \left(\frac{n_{\text{nom}}}{n_i} \cdot \left(\frac{P_{c \text{ nom}}}{P_{ci}}\right)^{0.61}\right)^b \quad (11)$$

here the symbol “nom” refers to the mode selected as nominal.

In this case, rate of damages accumulation from heat changes:

$$C_T = \sum_1^i (C_{Ti}^m \cdot f_i \cdot n_i) \quad (12)$$

Rate of damages accumulation from variable speed (accelerations— ε):

$$C_\varepsilon = \sum_1^i (|\varepsilon|^m \cdot f_i \cdot n_i) \quad (13)$$

Relative total rate of derated engine damages accumulation K_Σ , leading to functional failure, is determined in accordance with hypothesis of linear damages summation and the principle of superposition:

$$\frac{1}{K_\Sigma} = \sum_1^j \left(\frac{1}{K_j} - 1 \right) \quad (14)$$

Engine wear rate can be estimated using known dependencies, for example, offered by Grigoriev, Ponomarev, Zhdanovsky, Nikolaenko, Gurvich [14–16] or according to the method described below.

Engine wear is caused by frictional forces, which are proportional to the mechanical pressure loss P_f , defined by the Chen-Flynn equation [17, 18]:

$$P_f = K_1 + K_2 \cdot P_z + K_3 \cdot c_p + K_p \cdot c_p^2 \quad (15)$$

here c_p —average piston speed; K_1 – K_4 —constants.

Conditional wear rate:

$$C_w = \sum_1^i (P_f \cdot f_i \cdot n_i) \quad (16)$$

The proposed mathematical model of diesel engine lifetime prediction has the following advantages (differences) as compared to the existing ones:

- the model can be used at diesel engine design experimental data that is absent;
- the model includes submodel of fatigue and thermal damages accumulation, which makes it possible to determine engine lifetime not only up to parametric but also up to functional failure;
- the model includes expressions for determining effect of thermal changes on damages accumulation rate;
- the model takes into account rate of wear, duration of gas and inertial forces actions and their amplitudes;
- rate of the engine basic parameters change is determined depending on the rate of wear.

4 Numerical and Experimental Works

Two modifications of the 12CHN15/18 and 12CH15/18 diesel engines, used as part of the transport machines and industrial tractors, were chosen as base and derated engines, respectively. Analysis of the features and statistical processing of observational data for different machines operating modes made it possible to identify the frequency distribution of factors occurrence that affect engine lifetime indicators and their amplitude (Figs. 1 and 2).

Using the histograms of factors distribution and the developed mathematical model (Eqs. 1–5, 12–14), lifetime change of derated engine relative to base engine was calculated. Estimated value of the tractor engine lifetime exceeds one, which obtained from results of long-term and operational tests and recorded in technical

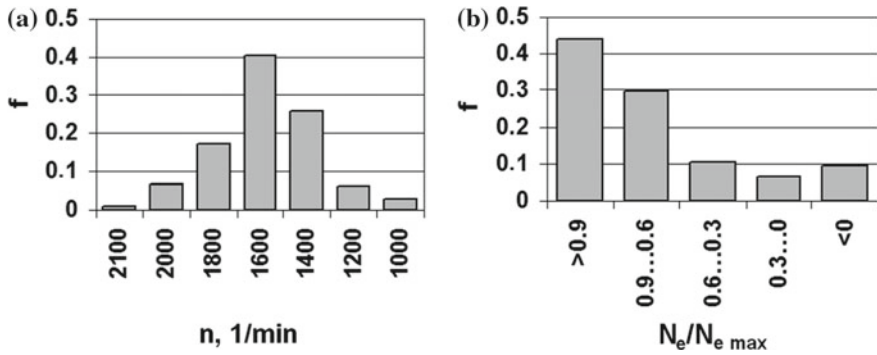


Fig. 1 Histograms of the operation modes distribution over time: **a** base engine speed and **b** base engine load (N_e)

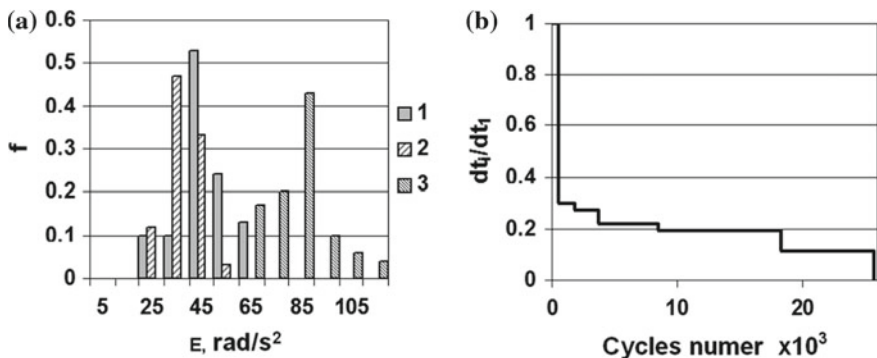


Fig. 2 **a** Distribution of the maximum engine crankshaft angular accelerations when tractor is operating in bulldozing mode: 1—acceleration; 2—braking; 3—accelerations amplitude (acceleration-braking) and **b** ordered diagram of the tractor engine heat changes for 1000 h (dt_i/dt_1 —ratio of the i -th heat amplitude to maximum value)

specifications, by 26% that confirms adequacy of the proposed mathematical model. Numerical experiment was carried out to assess effect of diesel engine derating in terms of engine speed and power (expressed through gas forces amplitude) on lifetime relative change [18].

Dependence of the derated engine damages accumulation relative speed due to the inertial forces influence can be approximated by power function:

$$K_n = 3.17 \cdot \left(\frac{n}{n'}\right)^{8.6} \quad (17)$$

due to gas forces:

$$K_{P_z} = 1.21 \cdot \left(\frac{n}{n'}\right) \cdot \left(\frac{P_z}{P'_z}\right)^6 \quad (18)$$

due to heat change:

$$K_T = 7.48 \cdot \left(\frac{n}{n'}\right)^{1.13} \cdot \left(\frac{P_z}{P'_z}\right)^{10.6} \quad (19)$$

For practically significant ranges $1 \leq \frac{n}{n'} \leq 0.6$ and $1 \leq \frac{P_z}{P'_z} \leq 0.7$, the dependence of the total relative damages accumulation rate was obtained:

$$\frac{1}{K_\Sigma} = -0.98 + 0.91 \cdot \left(\frac{P_z}{P'_z}\right)^{-8.05} + 0.77 \cdot \left(\frac{n}{n'}\right)^{-6.62} \quad (20)$$

Dependence of the derated diesel engine relative wear rate due to friction forces can be represented by the equation without taking into account minor parameter P_z :

$$K_w = 1.83 \cdot \left(\frac{n}{n'}\right)^{1.85} \quad (21)$$

Relative rate of nominal parameters change: maximum power, brake-specific fuel consumption (BFSC) and brake-specific oil consumption (BOSC) can be represented by expressions:

$$K_{N_e} = 0.90 \cdot K_w \quad (22)$$

$$K_{BFSC} = 0.71 \cdot K_w \quad (23)$$

$$K_{BOSC} = 0.90 \cdot K_w \quad (24)$$

It was determined that due to more frequent cyclical loading and higher amplitude of influenced factors (especially gas forces and accelerations), lifetime of basic industrial tractor diesel engine 12CH15/18, without design and adjusting

changes, will decrease by approximately 30%. According to the study results, recommendations were formulated on choice of permissible gas forces in combustion chamber and nominal speed values for industrial tractor engines 12CH15/18 and 12CHN15/18 [19, 20].

5 Conclusion

In the course of this study, method for predicting diesel engines lifetime was developed, which will reduce time and material cost for design and ensure durability. The data on diesel engines 12CH15/18 and 12CHN15/18 and their derated modifications operating modes for industrial tractor, which can be used in solving problems of lifetime prediction, is systematized. Recommendations for determining required level of engine derating to ensure required durability are formulated. Results of the study can be used to create diesel engines derated modifications, to develop similar methods for predicting internal combustion engines, that differ in power and objects of application, lifetime at design and modification stages. Developed, on basis of the proposed mathematical model, numerical calculation methodology is used in Chelyabinsk Tractor Plant at development of industrial tractor diesel engine modifications; South Ural State University—at conducting research to fine-tune derated diesel engines lifetime indicators.

References

1. Hofbauer P (2005) Opposed piston opposed cylinder (OPOC) engine for military ground vehicles. SAE Technical Paper 2005-01-1548
2. Podgayetskiy VM, Smirnova TN (2011) Otechestvennyye i zarubezhnyye transportnyye dizeli dvoynogo naznacheniya (Domestic and foreign double purpose transport diesel engines). *Dvigatel* 2(74):39–42
3. Breitkopf GE, Speer TM, Edmunds TM et al (1984) Engine cyclic durability by analysis and testing. In: Papers presented at the propulsion and energetic panel 63-rd specialists meeting, Lisse, 30 May–1 June 1984
4. Sreenath AK, Venkatesh S (1970) Experimental studies on the wear of engine components. *Wear* 169:45–56
5. Gurvich IB (1967) Dolgovechnost avtomobilnykh dvigateley (Durability of automobile engines). Mashinostroyeniye, Moscow
6. Bolotin VV (1984) Prognozirovaniye resursa mashin i konstruksiy (Forecasting the resource of machines and structures). Mashinostroyeniye, Moscow
7. Bertado R (1970) Design of large diesels for operations reliability. In: Proceeding Institute of Mechanical Engineering, pp 5–9
8. Khevilend R (1966) Inzhenernaya nadezhnost i raschot na dolgovechnost (Engineering reliability and design for durability). Energiya, Leningrad
9. Gusyatinikov VA (1982) Vliyaniye faktorov ekspluatatsionnogo rezhima na traktorny dvigatel (Influence of operating mode factors on a tractor engine). In: Sbornik nauchnykh trudov CHIMESH, pp 80–84

10. Kostin AK, Larionov VV, Mikhaylov LI (1979) Teplonapryazhennost dvigateley vnutrennego sgoraniya: Spravochnoye posobiye (Thermal stress of internal combustion engines: a reference guide). Mashinostroyeniye, Moscow
11. Kostin AK (1962) Parametr dlya sravnitel'noy otsenki teplonapryazhennosti dizeley (Parameter for a comparative assessment of diesel engine thermal stress). Trudy LPI 221:166–179
12. Heywood JB (1988) Solutions manual to accompany internal combustion engine fundamentals. McGraw-Hill, New-York
13. Taylor CF (1977) The internal-combustion engine in theory and practice. Vol. I: Thermodynamics, fluid flow, performance. The M.I.T. Press, Cambridge
14. Grigoryev MA, Ponomarev NN (1976) Iznos i dolgovechnost avtomobil'nykh dvigateley (Wear and durability of automobile engines). Mashinostroyeniye, Moscow
15. Zhdanovskiy NS, Nikolayenko AV (1981) Nadezhnost i dolgovechnost avtotraktornykh dvigateley (Reliability and durability of automotive engines). Kolos, Leningrad
16. Gurvich IB, Syrkin IB (1984) Ekspluatatsionnaya nadezhnost avtomobilnykh dvigateley (Operational reliability of automobile engines). Transport, Moscow
17. Chen SK, Flynn PF (1965) Development of single cylinder compression ignition research engine. SAE Paper 650733:750–770
18. Taylor CM (1993) Engine tribology. Elsevier, Amsterdam
19. Malozemov AA, Shikin AS (2009) Raschetno-eksperimental'naya otsenka vliyaniya urovnya deforsirovaniya na resurs dizelya tipa V-2 (Numerical and experimental assessment of the derating level impact on diesel engine B-2 life time). Vestnik YUUrGU 24:89–96
20. Shikin AS (2007) Problemy i zadachi razrabotki dvigateley dvoynogo naznacheniya (Problems and objectives of the dual-purpose engines development). Nauchnyy vestnik CHVVAKIU 19:138–143

Failure Model for Gear Couplings Under the Criterion of Working Surface Endurance



M. G. Slobodianskii, Alexey V. Antsupov and S. V. Lukinskih

Abstract Although it is shown that in some cases the gear couplings durability is significantly less than the turnaround time of a metallurgical unit according to the criterion of teeth contact endurance. As a rule, this leads to unplanned downtime of metallurgical machines and to additional time and financial costs. In order to solve this problem, there is a need for a preliminary assessment of the couplings life before putting them into commercial operation. For this purpose, the article proposes a mathematical model of gear couplings failures according to the fatigue strength criterion. The model is based on the mathematical formalization of the basic concepts of the reliability theory for machine parts, the basic equation for the kinetic concept of structural damage of materials, and the thermodynamic strength condition of solids. In order to implement the created model, the algorithm and the program “The durability” have been developed, which allows evaluating their average design resource under the specified operating conditions. Using the calculation program, theoretical durability studies of the plate feeder coupling were carried out under the operating conditions of the sintering plant. The resource was estimated for two options for calculating contact stresses: using classical methods of the elasticity theory and considering the finite element method of computer-aided design systems. In the first variant, the prediction error was 24%, in the second—9.7%. This indicates a sufficiently high level of the mathematical model reliability and the correct use of the calculation algorithm at the design stage of machines.

Keywords Toothed clutch · Drive · Prediction · Longevity · Resources · Model

M. G. Slobodianskii (✉) · A. V. Antsupov
Nosov Magnitogorsk State Technical University, 38, Lenin Street,
Magnitogorsk 455000, Russia
e-mail: m.slobodianskii@gmail.com

S. V. Lukinskih
Ural Federal University Named After the First President of Russia B.N. Yeltsin,
19, Mira Street, Ekaterinburg 620000, Russia

1 Purpose and Objectives of Research

The number of the least efficient elements of metallurgical units includes gear couplings [1], the failure of which leads to unplanned production downtime. The moment of their failure is impossible to prevent at the stage of conducting periodic technical inspections since the design of the coupling does not provide for checking its technical condition without complete disassembly.

In this case, the design calculation of the expected life of the gear coupling will allow checking its compliance with the established overhaul period.

As practice shows, the failure of gear couplings occurs due to the chipping of the surface layer of the teeth, which is caused by high contact stress σ_H .

Currently, the performance of the gear coupling is determined by the static strength condition:

$$\sigma_H \leq [\sigma_H], \quad (1)$$

where σ_H is the maximum stress on the teeth surface [2, 3] or the maximum contact stress [4]; $[\sigma_H]$ is permissible contact stress, depending on the type of heat treatment of the teeth.

At the same time, it is believed that if condition (1) is fulfilled, the coupling will be in working condition for an arbitrarily long time.

In order to determine the maximum contact stress σ_H , in works [2, 3] (where σ_H is indicated by the symbol p , i.e., $\sigma_H = p$), the well-known dependence is used

$$\sigma_H = \frac{T \cdot k_h \cdot k_{nr}}{b_m \cdot d_m^2}, \quad (2)$$

where T is the torque transmitted by the coupling; d_m is the diameter of the pitch circle of the ring gear; k_h is tooth height ratio; k_{nr} is coefficient of uneven specific load.

The work [4] proposes for calculating the maximum contact stress σ_H (where σ_H is indicated by the symbol $\sigma_{H\gamma}$), the dependency that takes into account a number of design features:

$$\sigma_H = K_{H\gamma} \cdot \sigma_{H_0}, \quad (3)$$

where $K_{H\gamma}$ is the coefficient taking into account the uneven distribution of stress along the length of the contact line defined as a function of the geometric and contact deformation of the tooth [4]; σ_{H_0} is contact stress without taking into account the concentration of contact stress due to misalignment between the axes of the coupling halves; σ_{HP} is allowable contact stress [4].

The value σ_{H_0} is determined by one of two equations:
for the flat form of the tooth profile

$$\sigma_{H_0} = K_p \cdot P_0 / (b \cdot m \cdot K_h), \quad (4)$$

for modified tooth profile

$$\sigma_{H_0} = 0.418 \cdot \sqrt{K_p \cdot P_0 \cdot E / (b \cdot R_b)}. \quad (5)$$

In these equations, the equally designated parameters are determined according to the appropriate shape of the tooth according to the dependencies [4]:

K_p is the coefficient taking into account the uneven distribution of the load between the teeth in connection with the step errors of the gear rims of the coupling halves [4];

P_0 is average load acting on a pair of teeth [4];

E is the elasticity modulus of the teeth materials;

b is the width of the ring gear;

R_b is the given radius of the tooth barrel [4];

m is teeth module

To date, the application of the finite element method in computer-aided design systems (Autodesk Inventor, Solid Works, Ansys, Abaqus, Nastran IN-CAD, and others) has become topical for estimating the stress state of loaded parts' volumes. In this case, this method allows calculating the stress state in the contact volumes of the teeth, taking into account all the design features, including σ_H under the condition (1).

Thus, if the contact stress σ_H calculated by conditions (2)–(5) or by the finite element method satisfies condition (1), and then the coupling is assumed to be in a working state for an arbitrarily long time. This is contrary to the practice of exploitation.

However, the question of analytical prediction of the gear couplings resource by the criterion of contact endurance of teeth is not considered in the literature. This problem, in our opinion, can be solved on the basis of modern achievements of the physical theory of machine parts reliability [5–8] and the kinetic concept of processes interpretation of the solid destruction [9–13].

In this regard, the purpose of these studies is to develop an analytical model of gear couplings failure on the criterion of teeth contact fatigue without using parameters that require additional experimental studies.

2 Gear Coupling Failure Model Under the Criterion of Teeth Surface Endurance

Based on the main principles of the predicting theory for the reliability of machine parts [5, 7, 8, 11], we take the density u_{et} parameter of the structure of the most intense contact volumes of tooth material (where it occurs σ_H) as a parameter of the condition of a gear coupling. If we assume stationary conditions for loading the teeth, then due to fatigue chipping, the failure of the gear coupling will occur under the condition u_{et} that the critical value u_{e^*} is reached [5, 7, 8, 11]:

$$u_{et} = u_{e0} + \dot{u}_e \cdot t = u_{e^*}, \quad (6)$$

where u_{e0} is the initial (at the time moment $t = t_0$) density of the hidden energy u_{et} of defects in the teeth material structure, determined as a function of Vickers hardness [10, 14–17].

Solving Eq. (6) relatively $t = t_{pr}$, we determine the value of the average expected life of the gear coupling by the criterion of the teeth contact endurance:

$$t = \frac{u_{e^*} - u_{e0}}{\dot{u}_e}. \quad (7)$$

The average damage rate of the contact volumes structure of tooth materials can be determined according to [6, 7, 10] by the equation:

$$\dot{u}_e = \frac{k_{str} \cdot k \cdot T_f \cdot U(\sigma_0, T_f)}{h} \cdot \left(\exp\left(-\frac{\overline{U}(\sigma_i, T_f) \cdot V_{at}}{k \cdot T_f}\right) - \exp\left(-\frac{\overline{U}(\sigma_i, T_f) \cdot V_{at}}{k \cdot T_f}\right) \right), \quad (8)$$

where

$k_{str} = 2 \cdot (u_{e^*} - u_{e0}) / (3 \cdot u_{e^*} - u_{e0})$ is the Le Chatelier coefficient, taking into account the material structure resistance to its damage [15]; k , h , V_{at} are Boltzmann constant, Planck constant, the atomic volume of the part material;

$\sigma_0 = (\sigma_1 + \sigma_2 + \sigma_3) / 3$ is average hydrostatic stress [18–20];

$\sigma_1 = -0.18 \cdot \sigma_H$, $\sigma_2 = -0.288 \cdot \sigma_H$, $\sigma_3 = -0.78 \cdot \sigma_H$ are the principal stress determined as a maximum stresses function arising in the body [18–20];

$\sigma_i = \sqrt{((\sigma_1 - \sigma_2)^2 + (\sigma_2 - \sigma_3)^2 + (\sigma_1 - \sigma_3)^2)} / 2$ is normal stress intensity [18–20];

$T_f = T_0 + (T_* - T_0) / (44 \cdot v_0)$ is average heating temperature over the entire volume of the surface layer [15];

$T_* = T_0 \cdot (3 \cdot \sigma_T)^2 / ((3 \cdot \sigma_T)^2 - \sigma_H^2)$ is heating temperature of local volumes [15];

σ_T is yield strength of the teeth material;

σ_H is maximum contact stress;

$U(\sigma_0, T_f) = U(p_{T,0}) - \Delta U_T(T_f) - A_V(T_f)$ is the height of the symmetric energy barrier [14, 15];

$U(p_{T0})$ is the initial activation energy of the structural destruction, taking into account the thermal pressure at T_0 and $\sigma_H = 0$ determined by the method from the following works [14, 15];

$\Delta U_T = 1,5 \cdot \alpha_0 \cdot K \cdot T_f$ is the change in the activation energy from the self-heating temperature of local volumes from $T = 0$ °C to $T = T_f$ °C [11, 14];

$A_V = M_r^2 \cdot \phi_\sigma^2 \cdot \sigma_0^2 / (2 \cdot K)$ is specific energy of change per volume unit of a real crystal under conditions of equivalent static stretching [14, 15];

$M_r^2 = (\sigma_T \cdot (65 + 0.46 \cdot HV)) / \sigma_r^2$ is equivalence ratio of cyclic and static stress states [14, 15];

$\vec{U}(\sigma_i, T_f) = U(\sigma_0, T_f) - 0.5 \cdot A_f$ is activation energy of the defects nucleation process (in the direction σ_H) [14, 15];

$\overleftarrow{U}(\sigma_i, T_f) = U(\sigma_0, T_f) + 0.5 \cdot A_f$ is activation energy of the defects destruction process (in the opposite σ_H direction) [14, 15];

$A_f = M_r^2 \cdot \phi_\sigma^2 \cdot \sigma_i^2 / (6 \cdot G)$ is the specific energy of shaping a volume unit of a real crystal under conditions of equivalent static stretching [14, 15];

G is shear modulus of the teeth;

α_0 is linear thermal expansion coefficient of the teeth material.

K is bulk elasticity modulus;

HV is Vickers hardness of the teeth friction surfaces;

σ_r is the endurance limit of the teeth material;

$\phi_\sigma = k_\sigma \cdot \nu_0^{0.5}$ is overstress coefficient on interatomic bonds [14, 15];

$\nu_0 = T_0/870$ is the coefficient of distribution non-uniformity of the internal energy density over a deformable volume [15];

k_σ is complex structural parameter of the material [15].

The system of Eqs. (6)–(8) and dependencies for the calculation of their parameters is a mathematical model of the design failures formation of gear couplings according to the criterion of teeth contact endurance. On the basis of the proposed model, the algorithm and the program “Durability of gear couplings” have been developed, which allows evaluating their average design resource t_p under the specified operating conditions.

3 Theoretical Results Verification

In order to verify the developed model, it is necessary to compare the estimated coupling life t of 1-1600-50-1U2 GOST R 50895-96 of plate feeder of the sintering plant of PAO “MISW” with its assigned resource, which is $t_p = 25920$ h (see the

table) according to the technological instruction. The calculated resource for the transmission of torque $M_{kr} = 1500 \text{ N m}$ and the stationary temperature of the gearing $T_0 = 60 \text{ }^\circ\text{C}$ will be determined by the algorithm of the program for implementing the mathematical model (6)–(8) for the contact stress values σ_H calculated by two options:

- according to Eqs. (3)–(4);
- using the finite element method in the Nastran IN-CAD software package.

The results of theoretical research are presented in Figs. 1, 2 and in the table. Figure 1 demonstrates a general view of the coupling (Fig. 1a) and the stresses distribution in the volumes of the sleeve teeth material (Fig. 1b). The maximum

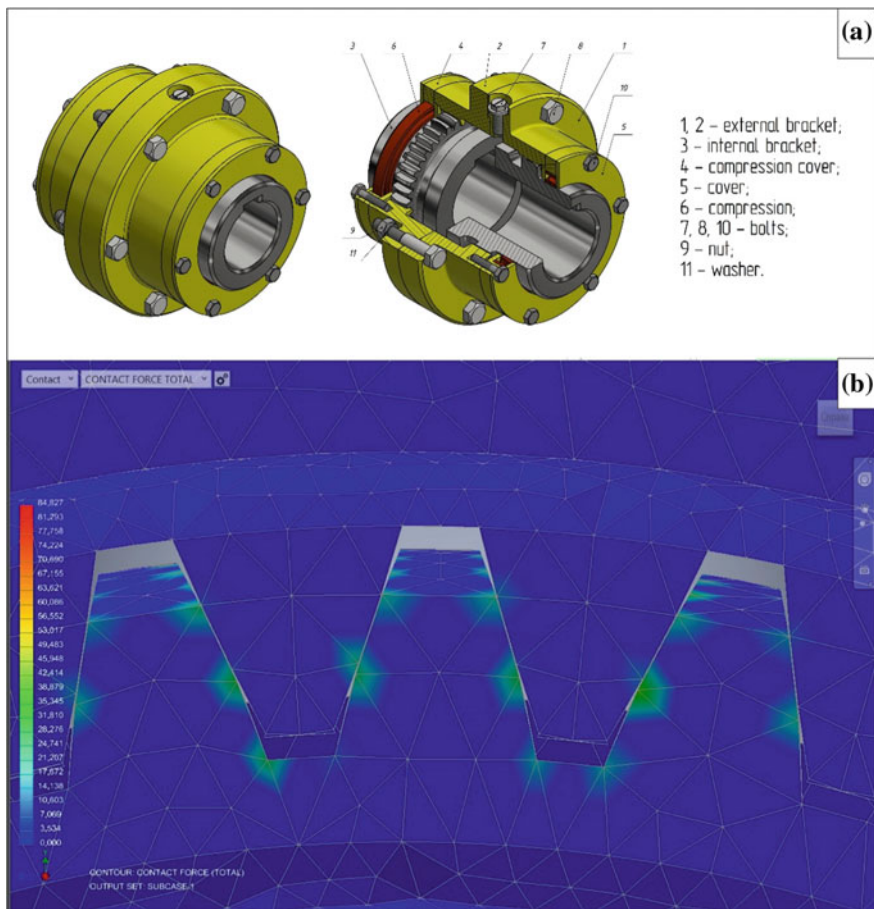


Fig. 1 a Three-dimensional model of a gear coupling and b the results of modeling contact stress

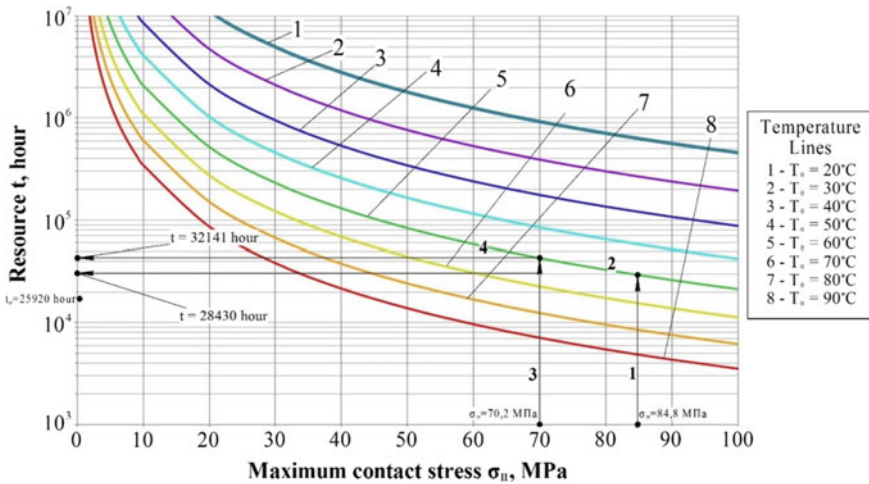


Fig. 2 Temperature and power parameters effect on the magnitude of the gear coupling resource

contact stresses $\sigma_H = 84.827$ MPa on the side surface of the teeth calculated using the Nastran IN-CAD software package are listed in the table (the first row, the second column). The calculated resource for the stress according to the algorithm of the computer program “Durability of gear couplings” is also presented in the table (the first row, the third column). The graphical interpretation of this calculation is presented in the nomogram of Fig. 2 in the direction of arrows 1–2.

The magnitude of the contact stress determined by E.L. Ayrapetov dependence (4) and the corresponding resource are listed in Table 1 (the second row, the second and the third column, respectively). The graphical interpretation of this calculation is presented in the nomogram of Fig. 2 in the direction of arrows 3–4.

The fourth and fifth columns of the table show the assigned resource value and the performed calculations errors.

The analysis of the presented data showed that the calculations error for the two options is 9.7% and 24%, respectively. This indicates, in our opinion, the acceptable reliability of the calculation results and the mathematical model adequacy.

Table 1 Comparative analysis of the various approaches application to the contact stress assessment in the surface layer of gear coupling teeth when predicting their resource

Methods for assessing contact stresses in the surface layer of teeth	Maximum contact stress σ_H (MPa)	Designed life t (h)	Assigned coupling life t_p (h)	Calculation error δ_t (%)
Nastran In-CAD	84.827	28.430	25.920	9.7
Technique of Airapetova E. L. [4]	70.207	32.141	25.920	24

4 Conclusions

1. On the basis of modern achievements of the theory of reliability, physics and damage and destruction mechanics of machine parts, a model of gear couplings failures was formulated according to the criterion of tooth materials contact endurance. During its development, the main technological parameters of loading, geometrical dimensions, and physic mechanical properties of the teeth material are taken into account.
2. The results of theoretical studies of the coupling 1-1600-50-1U2 GOST R 50895-96 durability of plate feeder in the operating conditions of the sintering plant of PAO “MISW” showed that:
 - for calculating contact stress, it is possible to use both traditional dependences of the elasticity theory and finite element methods of computer-aided design systems.
 - the resource forecasting error does not exceed 25%, which indicates an acceptable reliability of the calculation results.
3. The model can be used in order to search for effective solutions to improve the gear couplings durability by changing operating conditions, design, and selection of materials.

References

1. GOST 21354-87 Gear couplings. Technical conditions. Standards publishing house
2. Kuzmin A, Chernin I, Kozintsov B (1986) Calculations of machine parts. Higher School, Moscow
3. Ivanov M, Finogenov V (2008) Machine parts. Higher School, Moscow
4. Airapetov E, Aparkhov V, Nakhatakyan F et al (1991) The method for calculating the strength of gear couplings. USSR State Standard. VNIINMASH, Moscow
5. Pronikov A (2002) Parametric reliability of machines. Publishing House of Bauman Moscow State Technical University, Moscow
6. Antsupov AV, Antsupov AV, Antsupov VP (2017) Analytical method for project resource estimation of metallurgical machinery parts. *Izvestiya Vysshikh Uchebnykh Zavedenij. Chernaya Metallurgiya*, pp 62–66. <https://doi.org/10.17073/0368-0797-2017-1-30-35>
7. Antsupov V, Antsupov A, Antsupov A, Jr, Slobodiansky M (2012) Prediction of the reliability of parts and assemblies of metallurgical equipment during their design and operation. Magnitogorsk publishing house. Nosov state tech. un., Magnitogorsk
8. Antsupov A Jr, Slobodiansky M, Antsupov V et al (2018) Assessment of the life of parts and components of metallurgical machines at the stage of their design and operation. Publishing House. Nosov Magnitogorsk state tech. un. Magnitogorsk
9. Regel V, Slutsker A, Tomashevsky E (1974) The kinetic nature of the strength of solids. The publishing house “Science”, Moscow
10. Fedorov V (1985) Kinetics of damaging and breakdown of solid bodies. Publishing center “Fan” UzSSR, Tashkent

11. Antsupov A Jr, Antsupov A, Antsupov V (2015) Theory and Practice of Assurance of Machine Element Reliability according to Criteria of Material Kinetic Strength and Wear Resistance. Nosov Magnitogorsk State Technical University Publ., Magnitogorsk
12. Zhurkov S (1957) The problem of the strength of solids. Bull Acad Sci 11:78–82
13. Zhurkov S, Nurzullaev B (1953) The time dependence of the strength under different loading conditions. ZhTF 10:1677–1689
14. Antsupov A, Antsupov V, Antsupov A (2016) Estimation and assurance of machine component design lifetime. Proc Eng 150:726–733. <https://doi.org/10.1016/j.proeng.2016.07.094>
15. Fedorov V (2014) Fundamentals of ergodynamics and synergetics of deformable bodies. Publishing house FGBOU VPO “KSTU”, Kaliningrad
16. Fedorov V (1979) Thermodynamic aspects of strength and fracture of solids. Publishing House “Fan” UzSSR, Tashkent
17. Fedorov S (2003) The basics of triboergodynamics and the physic chemical background of the compatibility theory. KSTU, Kaliningrad
18. Belyaev N (1976) Resistance of materials. “Science”, Moscow
19. Tselikov A, Polukhin P, Grebenik V et al (1988) Machines and units of metallurgical plants. Metallurgy, Moscow
20. Garber E (2004) Cold rolling mills: (theory, equipment, technology). OAO Chernetinformatsiya, Cherepovets

Analytical Model of Wear-Out Failures in Spur Gears of External Gearing



Alexander V. Antsupov, M. G. Slobodianskii and V. P. Antsupov

Abstract The paper presents the failures of spur gears by the wear resistance criterion of abraded surfaces as one of the main reduction reasons of technical and economic indicators of mechanical equipment. High wear rates of gears lead to an increase in the share of unplanned downtime of metallurgical machines and an increase in labor intensity of repair operations. Therefore, in order to solve the problem of increasing the gear's wear resistance and durability and to search for appropriate structural and technological solutions in this work, an analytical model of the forming process of their gradual wear failures has been built. The model is based on a basic relationship for estimating the rate of wear-out conjugation elements, obtained as a result of the joint-equation solution of molecular mechanical and structural energy friction theory. The equation for predicting the technical resource of gears is obtained from the condition of getting critical energy density of defects in the structure of the material in the wear products. Based on the solution of this equation system, taking into account the dependencies describing the initial and boundary conditions of the interaction of gearing elements, the algorithm calculating their average expected resource is formulated. It can be used to analyze the effectiveness of various structural and technological methods of increasing the durability of gears and selecting the most appropriate ones. A distinctive feature of the proposed model implementation is the fact that it does not require experimental characteristics of similar linear wear rates, coefficients, or wear factors.

Keywords Spur gear · Durability · Model · Criterion · Prediction · Lifetime · Life · Failure

A. V. Antsupov

Ural Federal University Named After the First President of Russia B.N. Yeltsin,
19, Mira Street, 620000 Ekaterinburg, Russia

M. G. Slobodianskii (✉) · V. P. Antsupov

Nosov Magnitogorsk State Technical University, Lenin Street, 38,
455000 Magnitogorsk City, Chelyabinsk Region, Russia
e-mail: slobodianskii@gmail.com

© Springer Nature Switzerland AG 2020

A. A. Radionov et al. (eds.), *Proceedings of the 5th International Conference on Industrial Engineering (ICIE 2019)*, Lecture Notes in Mechanical Engineering,
https://doi.org/10.1007/978-3-030-22041-9_9

1 Introduction

One of the most common causes of downtime in metallurgical aggregates is the failure of spur gears (SG). In some cases, the failure occurs not only because of chipping or breakage of the teeth but due to the limiting wear. If the methods of the design assessment of the SG performance by the criterion of gearing and bending strength are widely known [1–5], then the prediction of their durability by the wear resistance criterion causes a number of difficulties.

The researchers describe experimental and analytical approaches in order to predict the gear's durability by the criterion of their wear resistance [6–8], which is based on the main dependence that has the following form:

$$t_{1,2} = \frac{[\delta]}{2.25 \cdot I_{h1,2} \cdot \sqrt{q_n \cdot \frac{\rho_{pr}}{E_{pr}} \cdot \left(1 - \frac{1}{u_{1,2}} \cdot \frac{\rho_2}{\rho_1}\right) \cdot n_{1,2} \cdot n_3}}, \quad (1)$$

where

- $[\delta] = 0.3 \cdot m$ is the allowable value of the gear or wheel wear;
 m module gearing;
 $I_{h1,2}$ respective rate of gear and wheel wear;
 q_n linear load on the contact line length;
 ρ_{pr} the given curvature radius at the characteristic point of profiles contact;
 E_{pr} the material elasticity modulus of the gear pair;
 ρ_1, ρ_2 are the curvature radii of the gear and wheel tooth profile at a characteristic point;
 $u_{1,2}$ gear ratio from link 1 to link 2;
 n_1, n_2 rotational speed of the gears and wheels, respectively;
 n_3 the number of gears pairs with the considered gear.

In order to estimate the amount of wear rate of gearing elements, the authors of the work [6] proposed to use Drozdov dependence [7, 8] in the form of the dimensionless complex product:

$$I_h = k \cdot \left(\frac{\sigma_H}{HB}\right)^{m_1} \cdot \left(\frac{\chi}{h_{sm}}\right)^{m_2} \cdot \left(\frac{R \cdot T}{Q}\right)^{m_3} \cdot \left(\frac{v_{100}}{v_T}\right)^{m_4}, \quad (2)$$

where

k is the coefficient taking into account the physical-mechanical properties of the gearing;

$\frac{\sigma_H}{HB}$ is a dimensionless complex characterizing the stress state of the gearing and the actual touch area;

$\frac{\lambda}{h_{sm}}$ is a complex that takes into account the lubricant layer thickness and the working surface roughness of the teeth;

$\chi = \sqrt{R_{a1}^2 + R_{a2}^2} = R_a$ is the given parameter of surface roughness;

R_{a1}, R_{a2} is arithmetic mean of roughness deviations;

h_{sm} is the lubricating layer thickness;

$\frac{R \cdot T}{Q}$ is a complex characterizing the boundary lubricant properties of adsorption nature;

R is universal gas constant;

T is surface temperature;

Q is the lubricant adsorption heat;

$\frac{\nu_{100}}{\nu_T}$ is a complex characterizing the oil viscosity properties;

ν_{100} and ν_T is, respectively, the oil kinematic viscosity at 100 °C and at the lubricant operating temperature.

However, the coefficients $k, m_1, m_2, m_3,$ and m_4 determination requires additional experimental studies, which leads to a significant increase in time and financial costs for the gear's design development. Since analytical solutions from literature data are not known, therefore, the development of gear wear failures models is an urgent problem without additional experimental research.

To our opinion, while solving this problem, it is advisable to use modern achievements of the physical theory of machine parts reliability [9–11] and the energy-mechanical concept of solid wear [12–14], which is based on the main principles of the molecular mechanical [15] and structural energy [16] friction theories.

2 Module for Wear-Out Failure of Spur Gear Drives

In accordance with the basic principles of the reliability prediction theory for friction units [10, 14, 16], we take the value of the average current linear wear of the gear $x_{t(sh)}$ and $x_{t(k)}$ wheel in the most loaded points of the teeth as the gear condition parameter. We will assume that the tribocoupling operates in normal operating conditions under steady-state frictional fatigue wear.

The parameters related to the gear will be denoted with index 1, and to the wheel with index 2.

The conditions for the gear and wheel transition to the limiting state can be written as [14, 15] by the teeth criterion of wear resistance:

$$x_{t(1,2)} = I_{h(1,2)} \cdot L_{1,2} = I_{h(1,2)} \cdot V_{sk(1,2)} \cdot t = x_{t(1,2)pr}, \quad (3)$$

where

$I_{h(1,2)}$ is the linear wear rate of the gear and wheel teeth in the most loaded zones (the teeth flanks [6, 7]);

$L_{1,2}$ is the path of friction, committed by the most worn-out points of a gear or wheel tooth over time t ;

$V_{sk(1,2)}$ is sliding speed of points located in the area of the gear or wheel tooth flank, respectively;

$x_{t(1,2)pr}$ is the limit value of the teeth linear wear.

Solving the equality (3) relatively $t = t_{pr}$, we obtain the dependencies for calculating the expected average life of gears and wheels according to the wear resistance criterion of their teeth:

$$t_{1,2} = \frac{x_{t(1,2)pr}}{I_{h(1,2)} \cdot V_{sk(1,2)}}. \quad (4)$$

The minimum value will determine the very gearing resource.

In order to calculate the wear rate, we use the basic dependence of the energy-mechanical damage theory of stationary tribocoupling of the form [14–16]:

$$I_{h(1,2)} = \frac{\alpha_{1,2}^* \cdot v_{1,2} \cdot P_{sr(1,2)} \cdot f_{mech(1,2)}}{\Delta u_{e(1,2)}^*}, \quad (5)$$

The parameters included in expression (5) are defined as follows.

The overlap coefficients $\alpha_{1,2}^*$ are determined by the ratio of the teeth contact area to their friction area [15].

The mechanical component of the friction coefficient included in the condition (5) is determined by the method from the given works [15, 16].

The conversion factors for external energy $v_{1,2}$ (of friction forces work) in the change in the internal energy of the gear and wheel surface layer are determined by B. V. Protasov method [17]:

$$v_1 = \frac{\varepsilon}{\varepsilon + 1} \text{ and } v_2 = 1 - v_1, \quad (6)$$

where

$\varepsilon = \frac{\theta_1^2 \cdot R_{a(1)}^{\frac{1}{2}}}{\theta_2^2 \cdot R_{a(2)}^{\frac{1}{2}}}$ is the distribution coefficient of energy between the gear and the wheel; $\theta_{1,2} = \frac{1 - \mu_{1,2}^2}{E_{1,2}}$ are elastic permanent of gear and wheel materials; $\mu_{1,2}$ is Poisson's ratio of gear and wheel materials; $E_{1,2}$ is elasticity modulus of gear and wheel materials.

The average pressure in the condition (5) on the contact of the gear tooth plank or of the wheel tooth plank is determined according to [18]:

$$p_{sr1,2} = \frac{\pi}{4} \cdot \sqrt{\frac{F_n \cdot E_{pr}}{2 \cdot \pi \cdot (1 - \mu_{1,2}^2) \cdot l_p \cdot \rho_{pr(1,2)}}}, \quad (7)$$

where $F_n = \frac{F_t}{\cos \alpha \cdot \cos \beta}$ the normal force in the contact is determined by the standard method [18]; $E_{pr} = \frac{2 \cdot E_1 \cdot E_2}{E_1 + E_2}$ is the given elasticity modulus; l_p is the gear and wheel face width; $\rho_{pr(1,2)}$ the given curvature radii of the examined contacts are, respectively, determined by the standard method [18]; β is the angle of the teeth inclination; α is the action angle; F_t is the action circumferential force.

The critical power requirement of the materials of the gear and wheel surface layer (see condition (5)) is determined by the method in work [13]:

$$\Delta u_{e(1,2)}^* = \Delta H_{S(1,2)} - (u_{T(1,2)} - u_{e0(1,2)}), \quad (8)$$

where $\Delta H_{S(1,2)}$ is the melting enthalpy of gear and wheel materials; $u_{T(1,2)} = \rho_{1,2} \cdot c_{1,2} \cdot T_0$ is the enthalpy of the gear elements material at the temperature of the steady friction regime; T_0 is gear temperature; $c_{1,2}$ is specific heat capacity of the gear material; $\rho_{1,2}$ is the density of the gear and wheel teeth material; $u_{e0(1,2)} = \frac{(0.071 \cdot HV_{1,2})^{2.4}}{6 \cdot G_{1,2} \cdot (6.47 \times 10^{-6} \cdot HV_{1,2} + 0.12 \times 10^{-2})^2}$ is the defect energy density in the material structure of the gear and wheel surface layer in the initial state; $HV_{1,2}$ is Vickers hardness of gear and wheel.

The sliding speed in the considered contact of the gear and wheel tooth included in the condition (4) is determined by the method of work [18]:

$$V_{sk(1)} = v_{FH(1,2)} - v_{Fa(2,1)} \text{ and } V_{sk(2)} = -(v_{FH(1,2)} - v_{Fa(2,1)}), \quad (9)$$

where

$v_{FH(1,2)} = \omega_{1,2} \cdot \rho_{H1,2}$ is the speed of the common point of contact along the profiles of the gear and wheel teeth, respectively, on the curvature radius of the active tooth profile, the lower point of action [18];

$v_{Fa(1,2)} = \omega_{1,2} \cdot \rho_{a1,2}$ is the speed of a point along the gear and wheel tooth profiles, respectively, on the curvature radius of the tooth profile at the upper boundary point of single contact [18];

$\rho_{a1,2}$ is curvature radius of the tooth profile at the upper boundary point of gear and wheel single contact, respectively [18];

$\omega_{1,2}$ is the angular rotation velocity of the gears and wheels.

The set Eqs. (4)–(9) represents the design failure model of a spur gear drive by the wear resistance criterion of gear and wheel teeth. On the basis of the model, an

algorithm and the program “Durability of spur gear drives” have been developed, allowing estimating the expected life of transmission elements $t_{1,2}$ at the design stage under given force conditions.

3 Conclusion

The analytical model has been developed for the formation of gradual wear failures of spur gear drives. The described model does not require additional laboratory or industrial tests to determine traditional physical quantities: the intensity or rate of materials wear.

Thereupon, the algorithm and the program for predicting the durability of spur gear drives are built. The algorithm and the program can be used to solve the following tasks:

- calculating the expected life of transmission elements at the stage of design development or operation ahead of time;
- conducting theoretical studies in order to assess the effectiveness to improve the wear resistance and durability of gear and the choice of the most appropriate options in different ways.

References

1. GOST 21354-87 Transmission toothed cylindrical involute external gearing. Calculation of strength
2. ISO 6336-2:2006 Calculation of load capacity of spur and helical gears. Part 2: Calculation of surface durability (pitting)
3. ISO 6336-3:2006 Calculation of load capacity of spur and helical gears. Part 3: Calculation of tooth bending strength
4. Klebanov B, Barlam D, Nystrom F (2008) Machine elements: life and design. CRC Press, New York
5. Budynas R, Nisbett K (2015) Shigley’s mechanical engineering design, tenth edition. McGraw-Hill Education
6. Timofeev G, Krasavin S, Silchenko P et al (2017) Calculation of durability of gear mechanisms of electromechanical drives. News of higher educational institutions. Eng. Ind 9:12–21
7. Drozdov Yu, Frolov K (1982) Theoretical-invariant method for calculating the intensity of surface destruction of solids under friction. Surface Phys Chem Mech 5:138–146
8. Drozdov Yu, Yugin E, Belov A (2010) Applied tribology (friction, wear, lubrication). Eco-Press, Moscow
9. Pronikov A (2002) Parametric reliability of machines. Publishing House of Bauman Moscow State Technical University, Moscow
10. Antsupov A, Antsupov A, Antsupov V (2017) Analytical method for project resource estimation of metallurgical machinery parts. Izvestiya Vysshikh Uchebnykh Zavedenij. Chernaya Metallurgiya, pp 62–66. <https://doi.org/10.17073/0368-0797-2017-1-30-35>

11. Antsupov A, Antsupov V, Antsupov A (2016) Estimation and assurance of machine component design lifetime. Proc Eng 150:726–733. <https://doi.org/10.1016/j.proeng.2016.07.094>
12. Fleischer G, Gröger H (1972) Methode zur Bestimmung des Verschleißes auf der Grundlage der Energiehypothese. Bericht im Rahmen der wiss. technischen Zusammenarbeit auf dem Gebiet Reibung, Schmierung und Verschleiß zwischen dem IMASCH, Moskau und den Forschungsinstitutionen der DDR. TH Magdeburg, pp 285–296
13. Fedorov V (2014) Fundamentals of ergodynamics and synergetics of deformable bodies. Publishing house FGBOU VPO KSTU, Kaliningrad
14. Antsupov A Jr, Slobodiansky M, Antsupov V et al (2018) Assessment of the life of parts and components of metallurgical machines at the stage of their design and operation. Publishing House. Nosov Magnitogorsk state tech. un. Magnitogorsk
15. Kragelsky I, Dobychin M, Komalov V (1977) Fundamentals of calculations for friction and wear. Mashinostroenie, Moscow
16. Antsupov A, Antsupov V, Slobodianskii M et al (2016) Energy-mechanical concept of the durability prediction of friction units on the wear resistance criterion of elements. J Friction Wear 37(5):494–499. <https://doi.org/10.3103/S1068366616050032>
17. Protasov B (1979) Energy relations in tribocoupling and prediction of its durability. Saratov University, Saratov
18. GOST 16532-70 Transmission spur involute external gearing. Geometry calculation

Development of Analytical Methodology for Detail Durability Test While Arranging Metallurgical Machines



Alexey V. Antsupov, Alexander V. Antsupov and V. P. Antsupov

Abstract The article deals with the solution of the actual problem of forecasting the technical resource of the most loaded machine parts at the design stage when performing the layout of individual components and mechanisms. This operation is called a control test of parts for durability according to various criteria of their working capacity, and it is intended for comparing the calculated expected resources of elements with the technical specification requirements, which indicates the minimum service life of the machine or individual mechanisms. For this purpose, the article developed a forming process model for gradual failures of the investigated parts according to various strength criteria. It is based on a universal kinetic dependence for calculating the damage rate to the structure of materials under conditions of static and cyclic elements loading over the entire range of stresses and temperatures. The theoretical dependence for estimating their expected resource is derived from the thermodynamic strength condition describing the equality moment of the defect energy density in the most loaded volumes of the critical value. The reliability of theoretical developments is confirmed by comparing the calculated and experimental values of the life of specimens from steel 45 in the annealed condition, subjected to a symmetric loading-tension cycle. The comparison results demonstrated that the prediction error of the average resource does not exceed 35%, which confirms the correctness of the calculated dependencies.

Keywords Reliability · Durability · Criterion · Kinetic strength · Hidden energy density · Resource

A. V. Antsupov · V. P. Antsupov
Nosov Magnitogorsk State Technical University, 38, Lenin Street,
455000 Magnitogorsk City, Chelyabinsk Region, Russia

A. V. Antsupov (✉)
Ural Federal University Named After the First President of Russia
B.N. Yeltsin, 19, Mira Street, 620000 Ekaterinburg, Russia
e-mail: antsupov.alexander@gmail.com

1 Introduction

At the stage of designing machines in the layout of the main elements in the process of comparative analysis of various design options for the least durable (resource) parts, they perform a control check of their reliability [1]. Such operations are necessary to check the compliance of the expected service life of the machine with the requirements of the technical task. The basis for determining the design indicators of product durability is the calculation of the expected resource of the least reliable machine elements according to various criteria for the material strength [1–11]. In the works [12, 13], when predicting the reliability of the studied parts under the given operating conditions, it was proposed to use mathematical models of failures, based on a kinetic approach to describing the process of material damage and the thermodynamic condition for the solid destruction [14, 15].

Below the paper gives one of the options for creating methods for calculating the expected life of machine parts based on building models of their gradual failures according to the material strength criteria under static or stationary cyclic loading.

2 Development of the Failure Model and Project Evaluation Methods for the Expected Resource of the Investigated Parts According to Different Strength Criteria

According to the thermodynamic concept, the current density of the latent energy u_{et} of structural defects of the material local volumes, in which the maximum static σ or cyclic stresses σ_{\max} act at the operating temperature T [14–16], is taken as the technical state parameter of the studied elements.

In this case, in order to calculate the average resource t_* of various designs of the least durable parts, it is proposed to use the basic dependence of the theory predicting the technical object reliability of the form [14, 15, 17, 18]:

$$t_* = \frac{u_{e*} - u_{e0}}{\dot{u}_e}, \quad (1)$$

where u_{e*} , u_{e0} are the critical and initial (at the moment of time $t = t_0$) values of the latent energy density u_{et} of the structural defects of the investigated part material [15, 16];

$$u_{e*} = \Delta H_{\text{TB}} - c(T) \cdot \rho(T) \cdot T \quad (2)$$

$$u_{e0} = (0.071 \cdot \text{HV}_0)^{2,4} \cdot k_\sigma^2 / (6 \cdot G) \quad (3)$$

ΔH_{TB} enthalpy of material fusion in the solid state;
 $c(T), \rho(T)$ the material heat capacity and density;
 G shear modulus of the part material;
 HV_0 Vickers hardness average value;
 k_σ complex structural parameter [15]:

$$k_\sigma = (6.47 \times 10^{-6} \cdot HV_0 + 0.12 \times 10^{-2})^{-1} \quad (4)$$

\dot{u}_e the average rate of structural damage of local volumes of the studied parts materials.

In order to estimate the value \bar{u}_e , the kinetic damage equation was derived in the following works [16, 19]:

$$\dot{u}_e = j_{rez} \cdot k_{str} \cdot U(\sigma_0, T), \quad (5)$$

where

$j_{rez} = \vec{j} - \bar{j}$ is the resulting specific rate of defects accumulation without taking into account the medium resistance according to Le Chatelier [16, 19]:

\vec{j} —the average specific rate of elementary acts of defect birth:

$$\vec{j} = \frac{k \cdot T}{h} \cdot \exp\left(-\frac{\vec{U}(\sigma_p^{ekv}, T) \cdot V_{at}}{k \cdot T}\right), \quad (6)$$

\bar{j} —the average specific rate of elementary acts of defect destruction:

$$\bar{j} = \frac{k \cdot T}{h} \cdot \exp\left(-\frac{\bar{U}(\sigma_p^{ekv}, T) \cdot V_{at}}{k \cdot T}\right), \quad (7)$$

$k_{str} = 2 \cdot (u_{e*} - u_{e0}) / (3 \cdot u_{e*} - u_{e0})$ is Le Chatelier coefficient, taking into account the resistance of the material structure to its damage [16];

k, h, V_{at} are the Boltzmann constant, the Planck constant, the atomic volume of the part material;

$\vec{U}(\sigma_p^{ekv}, T)$ is activation energy of the nucleation process of defects (in the direction σ_p^{ekv}) [15, 16]:

$$\vec{U}(\sigma_p^{ekv}, T) = U(\sigma_0, T) - 0,5 \cdot A_f^{ekv}, \quad (8)$$

$\bar{U}(\sigma_p^{ekv}, T)$ is activation energy of the defect destruction process (in the opposite σ_p^{ekv} direction):

$$\bar{U}(\sigma_p^{ekv}, T) = U(\sigma_0, T) + 0,5 \cdot A_f^{ekv}, \quad (9)$$

$U(\sigma_0, T)$ is the height of the symmetric energy barrier [15, 16]:

$$U(\sigma_0, T) = U(p_{T,0}) - \Delta U_T - A_V^{ekv}, \quad (10)$$

$\Delta U_T = 1.5 \cdot \alpha_0 \cdot K(T) \cdot T$ is change in the activation energy from the temperature of self-heating of local volumes from $T = 0^\circ\text{C}$ to $T = T_f^\circ\text{C}$;

$U(p_{T,0})$ is the initial activation energy of the structure destruction with regard to thermal pressure at T_0 and $\sigma_p^{ekv} = 0$: [15, 16]

$$U(p_{T,0}) = \frac{-2.415 \times 10^{-28} \cdot T_0^3 + 5.955 \times 10^{-25} \cdot T_0^2 + 0.0121 \times 10^{-28} \cdot T_0 + 12.286 \times 10^{-20}}{V_{at}}, \quad (11)$$

$A_V^{ekv} = M_r^2 \cdot A_V(T)$ is specific energy of change per volume unit of a real crystal under conditions of equivalent static stretching at $\sigma_p^{ekv} = \sigma$ or $\sigma_p^{ekv} = \phi_\sigma \cdot M_r \cdot \sigma_{\max}$; $A_f^{ekv} = M_r^2 \cdot A_f(T)$ is specific energy of forming a volume unit of a real crystal under conditions of equivalent static stretching;

$A_V(T) = \varphi_\sigma^2 \cdot A'_V(T)$ is specific energy of change per volume unit of a real crystal [15, 16];

$A_f(T) = \varphi_\sigma^2 \cdot A'_f(T)$ is specific energy of forming a volume unit of a real crystal [15, 16];

M_r^2 is equivalence rate of cyclic and static stress states [15, 16]:

$$M_r^2 = \frac{\sigma_T(T) \times (65 + 0.46 \times HV(T))}{\sigma_r^2(T)}, \quad (12)$$

$A'_V(T) = \sigma_0^2 / (2 \cdot K(T))$ is specific energy of change per volume unit of an ideal crystal [15, 16];

$A'_f(T) = \sigma_i^2 / (6 \cdot G(T))$ is the specific energy of forming a volume unit of an ideal crystal;

$\varphi_\sigma = k_\sigma \cdot \nu_0^{0.5}$ is overvoltage factor on interatomic bonds;

$\mu(T)$, $E(T)$ are Poisson's ratio and elasticity modulus as a function of temperature:

$$\mu(T) = \mu \cdot e^{-0.0005 \cdot T} \quad E(T) = E \cdot e^{-0.0007 \cdot T}, \quad (13)$$

$G(T)$ shear modulus;

$K(T)$ bulk modulus of elasticity;

$\sigma_T(T)$ yield strength as a function of temperature;

$\sigma_r(T)$ endurance limit;

T_* heating temperature of local volumes [15]:

$$T_* = \frac{T_0 \cdot (3 \cdot \sigma_T)^2}{(3 \cdot \sigma_T)^2 - \sigma_{\max}^2}, \quad (14)$$

$\nu_0 = T_0 / 870$ is the distribution non-uniformity coefficient of the internal energy density over a deformable volume [15];

$T_f = T_0 + (T_* - T_0) / (44 \cdot \nu_0)$ is average heating temperature over the entire volume of the surface layer [15];

$\sigma_0 = (\sigma_1 + \sigma_2 + \sigma_3) / 3$ is average hydrostatic voltage [20];

σ_i is normal stress intensity:

$$\sigma_i = \sqrt{\frac{(\sigma_1 - \sigma_2)^2 + (\sigma_2 - \sigma_3)^2 + (\sigma_1 - \sigma_3)^2}{2}}, \quad (15)$$

$\sigma_1, \sigma_2, \sigma_3$ are the principal stresses determined as a function of the maximum stresses arising in the body;

E is the elasticity modulus of the ring materials;

μ is Poisson’s ratio of materials;

HB is Brinell friction surface hardness;

HV is Vickers hardness of friction surfaces.

σ_T is yield strength of materials;

σ_B is strength of materials;

α_0 is coefficient of linear thermal expansion of the material.

Substituting the expression (2) with (2.a)–(2.n) into the condition (1), we obtain the theoretical dependence for estimating the project resource:

$$t_n = \frac{u_{e^*} - u_{e0}}{\left(\frac{k \cdot T}{h} \cdot \left(\exp\left(-\frac{\bar{U}(\sigma_p^{max}, T) \cdot V_{am}}{k \cdot T} \right) - \exp\left(-\frac{\bar{U}(\sigma_p^{min}, T) \cdot V_{am}}{k \cdot T} \right) \right) \right) \cdot k_{comp} \cdot U(\sigma_0, T)} \tag{16}$$

The system of Eqs. (16), (2)–(4), (6)–(15) is a mathematical model of the process of forming gradual design failures of metallurgical machine parts according to the strength criteria for any kind of static and cyclic loadings. The sequence of solving this equation system for the initial and boundary conditions of each investigated part is an analytical method for calculating their expected resource using the selected strength criterion. Theoretical studies using these techniques allow choosing the most effective options for the studied parts and to ensure the required durability level of the machine, indicated in the technical task, at its design stage.

In order to assess the accuracy of the calculations, the authors present the verification results of the proposed theoretical developments.

3 Theoretical Development Verification

Based on the mathematical model (16), (2)–(4), (6)–(15), a predicting method was developed for the expected life of samples subjected to a symmetric stretching-compression cycle in the experiment by Fedorov [14]. Reliability is verified by

Table 1 Comparison of experimental and calculated data

№	Cycle amplitude σ (MPa)	Damageability speed \bar{v}_e^p J/(mm ³ s)	Average resource		Calculation error δ_t (%)
			Experiment (s)	Calculation t_* (s)	
1	225	0.000294	20,400	19,198	5.89
2	231	0.000353	10,640	7078	33.47
3	239	0.000733	7040	5730	18.60
4	248	0.001567	4720	4340	8.05
5	253	0.003613	2240	1640	26.77

comparing (see Table 1) the calculated average values of the life of the samples with the corresponding experimental values.

Values of damage rate and average resource were obtained by conducting experimental research of the damage process and fatigue failure of samples from annealed steel 45 (o) with a symmetric stretching-compression cycle under various loading conditions described in the work [14].

The results given in the table show the correctness of the calculated dependences since the errors of comparing the values of the average life of the samples do not exceed 35%.

References

1. Shashkin V, Karzov G (1992) Reliability in machine-building. Engineering, Saint-Petersburg
2. Kapur K, Lamberson L (1980) Reliability and system design. World, Moscow
3. Haywood R (1969) Engineering design taking into account material fatigue. Machine-building, Moscow
4. Khazov B, Didusev B (1986) Reference book for calculation of machine reliability at design stage. Machine-building, Moscow
5. Frolov K, Klyuev V et al (2003) Machine-building: encyclopedia in 40 vol. Vol. IV-3. Machine reliability. Machine-building, Moscow
6. Kogaev V, Makhutov N, Gusenkov A (1985) Stress and fatigue calculation for machine and structure components. Machine-building, Moscow
7. Kogaev V, Drozdov Y (1991) Strength and wear resistance of machine components: a study guide for machine-building faculties of universities. Higher education, Moscow
8. Reshetov D, Ivanov A, Fadeev V (1988) Machine reliability: a study guide. Higher education, Moscow
9. American Society for Testing Metals Handbook, Properties and Selection vol 1, 8th edn (1969)
10. Bombas-Smith J (1973) Mechanical survival: the use of reliability data. McGraw-Hill, New York
11. Lipson C, Sheth N, Disney R (1967) Reliability prediction—mechanical stress/strength interference, Rome Air Development Center, Technical Report No. RADCR-TR-66-710, March 1967
12. Antsupov A Jr, Antsupov A, Antsupov V (2015) Theory and practice of assurance of machine element reliability according to criteria of material kinetic strength and wear resistance. Nosov Magnitogorsk State Technical University Publ., Magnitogorsk
13. Antsupov A Jr, Antsupov A, Antsupov V (2013) Assurance of reliability of machine friction nodes at design stage. Nosov Magnitogorsk State Technical University Publ., Magnitogorsk
14. Fedorov V (1985) Kinetics of damaging and breakdown of solid bodies. Publishing center “Fan” UzSSR, Tashkent
15. Fedorov V (2014) Fundamentals of ergodynamics and synergetics of deformable bodies. Publishing center of FSBEI HPE “KSTU”, Kaliningrad
16. Antsupov AV (Jr), Antsupov AV, Antsupov VP (2016) Estimation and assurance of machine component design lifetime. Procedia Eng 150:726–733. <https://doi.org/10.1016/j.proeng.2016.07.094>
17. Pronikov A (2002) Parametric reliability of machines. Publishing center of Bauman MSTU, Moscow
18. Ibatullin I (2008) The kinetics of damage and fatigue fracture surface layers. Samara. state. tehn. University Press, Samara

19. Antsupov AV, Antsupov AV, Antsupov VP (2017) Analytical method for project resource estimation of metallurgical machinery parts. Izvestiya Vysshikh Uchebnykh Zavedenij. Chernaya Metallurgiya, pp 62–66. <https://doi.org/10.17073/0368-0797-2017-1-30-35>
20. Belyaev N (1976) Resistance of materials. “Science”, Moscow

Application of Kantorovich-Vlasov Method for Shaped Plate Bending Problem



S. V. Konev, A. S. Fainshtein and I. E. Teftelev

Abstract The flexure function $W(x, y)$ of a ribbed rectangular plate is determined by the Kantorovich-Vlasov method on the basis of the sum of series $\sum_{i=1}^n W_i(y)X_i(x)$ with functions $X_i(x)$ satisfying specified kinematic boundary conditions, while functions $W_i(y)$ are determined as the solutions of differential equations of the fourth order. The problem is complicated by the absence of the target selection of functions $X_i(x)$ required to attain the desired accuracy. A special beam function $X_1(x)$ defined by the initial parameters method was proposed to be used in the first term of series. This function is defined at a single beam with the boundary conditions equal to those of a ribbed plate with respect to the selected coordinate. This allows one to reasonably increase in the accuracy of the specified variation method when one series term is used. The practical calculations of a real object—shaped sheet as per Russian GOST—conducted using the proposed function are provided. Flexure tables were obtained for the shaped sheets provided in the specified standard. The analysis of resulting flexures shows that the use of the sheet profile with more reinforcement ribs is more cost effective as the sheet flexure decreases faster than the sheet weight increases. For example, if one rib is added to S-15-1000-06 profile sheet, sheet flexure in the initial range of 8–12 ribs decreases by no less than 8% with the sheet weight increase by 5%.

Keywords Plate · Reinforcement ribs · Flexure · Kantorovich-Vlasov method · Beam function · Unit stiffness · Shaped sheet

S. V. Konev · A. S. Fainshtein (✉)
Magnitogorsk State Technical University Named After G.I.Nosov,
38, Lenin Pr, 455000 Magnitogorsk, Russia
e-mail: swetlana@mgn.ru

I. E. Teftelev
Magnitogorsk Hardware-Metallurgical Plant—United Joint Stock Company
“MMK-Metiz”, 5, Metiznikov St. Magnitogorsk, 455002 Magnitogorsk, Russia

1 Introduction and Problem Statement

Bending of plates with uniform thickness is widely studied using direct variation methods. However, it is difficult to use variation methods when modelling plates with ribbed stiffeners. For example, when modelling a stepped thickness plate, its potential bending energy must be determined using the Rayleigh-Ritz method [1, 2]. On the other hand, when calculating flexures of this plate using the Bubnov-Galerkin method, the selection of orthogonal approximating functions that meet static and kinematic boundary conditions represents a challenge [3, 4].

The authors of the article [5] use the Kantorovich-Vlasov method to model rectangular ribbed plates. With this method, the plate flexure is defined based on the sum of series $\sum_{i=1}^n W_i(y)X_i(x)$ where one of the functions, $X_i(x)$ is defined and the second one, $W_i(y)$ is found in the process of solving the problem. When addressing the problem, the authors initially transform the absolute q term of Eq. (1) of plate flexures (virtually, the external load applied to the plate)

$$D\nabla^2\nabla^2w(x,y) = q \quad (1)$$

into

$$\begin{aligned} \bar{q}(x,y) = q(x,y) - \sum_{i=1}^n EI_x W^{IV}(y)X(a_i)\delta(x-a_i) - \sum_{i=1}^n \frac{GA}{k_i} W^{II}(y)X(a_i)\delta(x-a_i) \\ - \sum_{i=1}^n EI_\omega W^{IV}(y)X^I(a_i)\delta^I(x-a_i) - \sum_{i=1}^n GI_k W^{II}(y)X^I(a_i)\delta^I(x-a_i) \end{aligned} \quad (2)$$

where Eq. (2) takes into account geometrical I_x, A, I_ω and mechanical E, G parameters of ribbed stiffeners. The ribbed stiffener arrangement is taken into account either by Dirac δ -function or by Heaviside functions. This is followed by the application of the Kantorovich-Vlasov method procedure with the use of a random set of defined beam $X_i(x)$ functions that meet kinematic conditions of the problem. The resulting problem with accuracy is addressed in the article [6].

However, artificial variation of the Eq. (1) parameters followed by solving this equation with the use of multiple beam functions seems overly conceptualized and more complex when compared to using a single beam function that is specifically defined based on the initial parameter method [7].

The goal of this article is the use of the specially chosen beam function in the Kantorovich-Vlasov method when modelling a plate with ribbed stiffeners. This allows to reasonably limit the number of terms of series $\sum_{i=1}^n W_i(y)X_i(x)$ and to simplify mathematical treatment of the resulting differential equations of fourth order.

2 Selecting the Beam Function for a Ribbed Plate

We examine the bending of a rectangular shaped (ribbed) sheet with $a \times b$ dimensions, which is freely placed on top of four cross-bars (Fig. 1, hinge supports represented by the dotted line). The sheet is elastically deformed like a thin stiff plate. We assume that the uniformly distributed load (e.g. snow load) q is applied to the plate.

To address the set problem, we consider the sum of series $\sum_{i=1}^n W_i(y)X_i(x)$ and choose the $X_1(x)$ function in the first product of the series based on the logic of plate deformation. We take a ribless strip beam (Fig. 2) with the same boundary loading conditions as those for the plate under consideration in the direction perpendicular to the ribs, along the X -axis shown in Fig. 1. For this strip beam, the moment of flexure at the support is zero ($M_A = 0$) and the displacements can be expressed as follows:

$$W(x) = \frac{q(2lx^3 - x^4 - l^3x)}{24EI} \tag{3}$$

We adjust the flexure equation taking into account the presence of ribs. For this purpose, we form a flexure equation for a beam with variable stepped section. It is known that the general solution of differential equation for a curved beam axis can be presented as follows [11]:

$$w = w_0 + \theta_0x - \sum \int_0^x \int_0^x \frac{M_y(x)}{EI_y(x)} dx dx \tag{4}$$

Fig. 1 Shaped sheet [8–10]

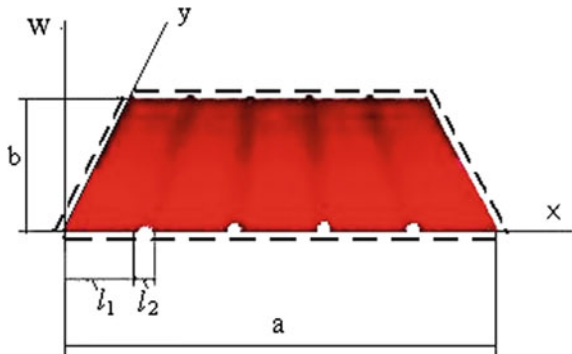
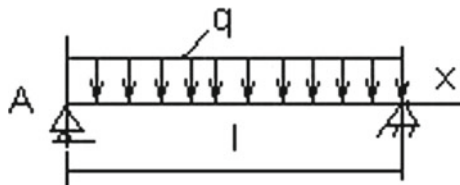


Fig. 2 Ribless strip beam



We use the I_y^0 symbol to denote the inertia moment for particular section, for example, in the first area, where $0 < x < l_1$. We enter the symbol as follows:

$$k(x) = \frac{I_y}{I_y^0} \tag{5}$$

Hence, the Eq. (4) can be presented as follows:

$$w = w_0 + \theta_0 x - \sum \int_0^x \int_0^x \frac{M_y(x)}{EkI_y^0(x)} dx dx \tag{6}$$

and the initial beam with variable stiffness is corrected to the beam with invariable stiffness $EI_y^0(x)$.

To maintain the equivalence of the computational pattern, the external forces applied to the ribbed stiffener and the internal forces existing in the sections along the ribbed stiffener borders (on the ribbed stiffener side) are k -times reduced. The flexure of the area with the ribbed stiffener is calculated based on the effect of the assumed external and internal forces calculated as the sum of internal forces exerted from the smooth side of the beam and from the side of the ribbed stiffener. Point moments $\Delta m = M_x^0[k(x) - 1]$ and forces $\Delta P = Q_x^0[k(x) - 1]$ existing at the ribbed stiffener border points are added to the loading diagram of the stepped beam (Fig. 3).

Further solution to the problem of determining beam flexures implies the application of the initial parameter method to a beam with modified stiffness $EI_y^0(x)$.

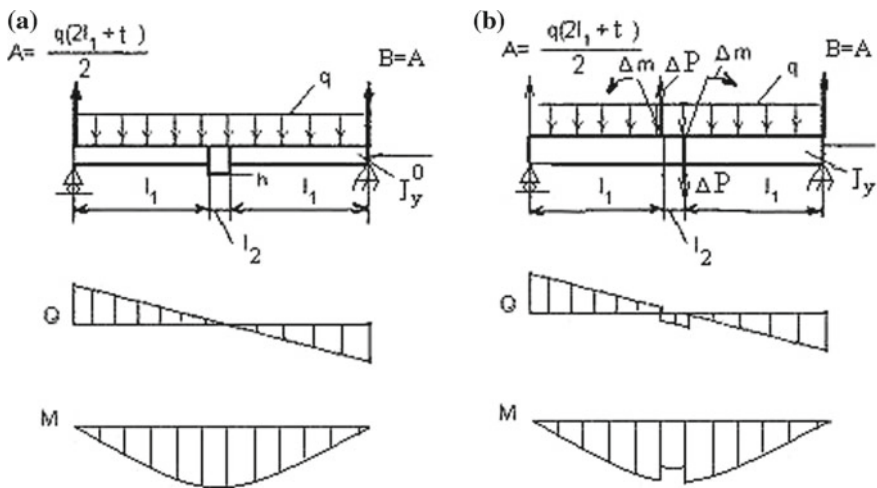


Fig. 3 Equivalent strip beam with hinge-supported edges: **a** with a ribbed stiffener, **b** with modified stiffness



For the beam with hinge-supported edges as illustrated in Fig. 3, the equation of flexures calculated based on the initial parameter method, as applied to the Mathcad environment [12, 13], can be written as follows:

$$X(x) = \frac{1}{EI_y^0(x)} \left[\theta_0 x + \frac{qax^3}{12} - \frac{qx^4}{24} + A1(x) + A2(x) \right], \tag{7}$$

where $A1(x)$ and $A2(x)$ refer to the equation components taking into account the effect of point forces ΔP and moments Δm on the beam flexure, which are taken into consideration when the coordinate of the point under examination exceeds the coordinate of the applied load.

Beam function (7) meets the specified boundary conditions when $x = 0$ and $x = a$: $w = 0, \frac{d^2 w}{dx^2} = 0$.

3 Implementation of the Obtained Method When Modelling Sheet Elements of Civil Structures

We apply the obtained function to real object modelling. The typical diagram of the $X(x)$ function for a single beam with corrugated (ribbed) profile parameters is shown in Fig. 4. This figure illustrates the $X(x)$ function of a ribbed beam whose profile in the X-axis direction matches with the S15-1000-0.6 profile described in GOST 24045-94 (Fig. 5). In the figure, the ribbed beam flexure function is compared with the flexure function of a ribless beam with the same thickness.

Due to the significant difference in flexural resistance of beam sections, the graph of the $X(x)$ of the beam flexure is presented in Fig. 4 and is noticeably curved in the rib area while the extent of the ribbed beam flexure is reduced by more than 30% when compared to the flexure of the ribless beam.

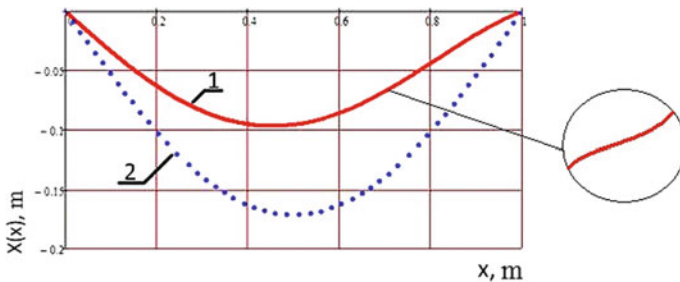


Fig. 4 Beam function graphs. 1—flexure of a ribbed beam whose ribs are the same as those of the S15-1000-0.7 profile, 2—flexure of a ribless beam whose thickness is the same as that of the S15-1000-0.7 profile sheet



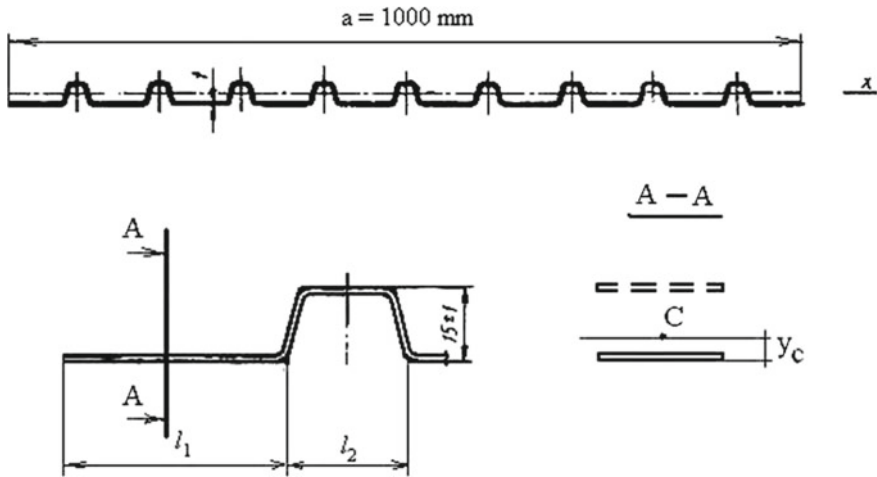


Fig. 5 Ribbed beam as per GOST 24045-94 and defining the conditional centre of gravity y_c in the A-A section of the beam

The inertia moment coefficient of various cross sections of a beam with long ribs (corrugations) $k(x) = \frac{l_2}{l_1}$ (please refer to formula 5) used in the flexure $X(x)$ calculations was determined as described below. Figure 5 shows that the coordinate of the centre of gravity y_c in the A-A cross section of the beam must be defined based on the beam layers located both within and beyond the cross section. Such condition requires to consider the ratio between the lengths of ribbed and ribless beam areas.

For example, the S15-1000-06 profile shown in Fig. 5 can have—using one of the alternative numbers of produced ribs—a 80 mm long ribless area and a 20 mm long ribbed area. In this case, the ratio of lengths between ribless and ribbed areas is 8:2.

Hence, we calculate the inertia moments for sections of ribbed and ribless areas to obtain the coefficient $k(x) = \frac{l_2}{l_1}$ which, for different profiles shown in Fig. 5, is 100–170.

We apply the obtained $X(x)$ function in dimensionless form in the system of functional equations of the Kantorovich-Vlasov method and obtain the following for the term of series:

$$AW^{IV}(y) + 2\lambda^2 BW''(y) + \lambda^4 CW(y) = q(y), \tag{8}$$

where $\lambda = a/b$ refers to the ratio between the sides of the deformed plate; A, B, C refer to the coefficients defined by the following equations:



$$A = \int_0^a X^2(x)dx, \quad B = \int_0^a X''(x)X(x)dx, \quad C = \int_0^a X^{IV}(x)X(x)dx.$$

Absolute term of equation $q(y) = \int_0^a X(x)dx$.

Bending stiffness of the plate $D = \frac{EH^3}{12(1-\mu^2)}$ is taken into account at the end of the calculation.

In order to solve the differential Eq. (8), we derive a characteristic equation [14–17] and find its roots by using the method described in [2], for example. Once the equation roots are found, we calculate the flexures of a ribbed plate based on the

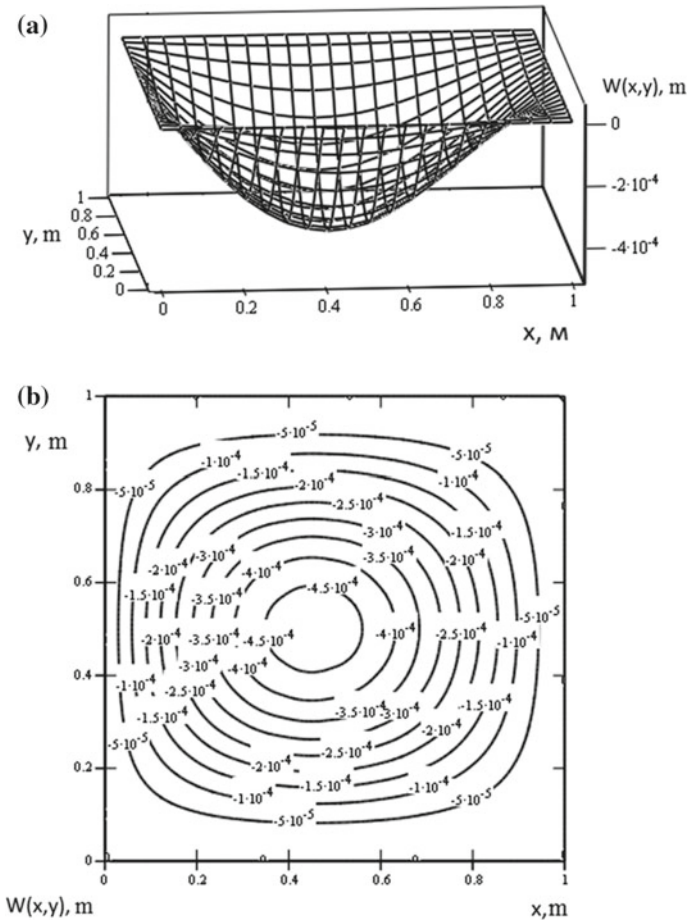


Fig. 6 Shaped sheet flexure: **a** deformed sheet surface; **b** level curves of a deformed sheet surface

Table 1 Flexure of shaped sheets as per Russian GOST 24045-94

Profile type	k-coefficient	Plate bending stiffness D (MPa m ³)	Sheet flexure $W(a/2, b/2)$ (10 ⁻³ m)
S10-1000-0.6	159	107	1.35×10^{-8}
S10-1000-0.7	164	107	2.048×10^{-8}
S10-1000-0.6	120	107	2.047×10^{-8}
S10-1000-0.7	124	107	2.047×10^{-8}
S10-1000-0.6	115	195	1.123×10^{-8}
S10-1000-0.7	119	195	1.123×10^{-8}

Table 2 Maximum flexures of a shaped S15-1000-06 sheet with $a = 1$ m and $b = 1$ m, subjected to uniform load $q = 1000$ Pa, with a different number of ribs

Number of ribs	6	7	8	9	10	11	12
Sheet flexure. (10 ⁻³ m)	-2.274	-1.931	-1.760	-1.547	-1.407	-1.310	-1.201

equation $W(x, y) = W_1(y)X_1(x)$, where $W_1(y)$ and $X_1(x)$ represent functions of the first term of the series.

The surface of the obtained plate flexures is shown in Fig. 6. The graph of the modelled surface shows that there is no deformation at its supporting points around the periphery of the plate and the curved frame indicates the presence of deformation at other points (Fig. 6a). The oval level curves (Fig. 6b) refer to the equal plate flexures.

Flexures of shaped sheets S10-...S18-1000-0.6...0.7 as per GOST 24045-94 are shown in Table 1.

Given the possibility to calculate flexures of a ribbed sheet, we can optimize its physical dimensions such as the number of ribs (within a reasonable range). Table 2 shows the calculated data of flexures for a S15-1000-06 sheet based on a different number of ribs.

Based on the table, when the number of ribs is increased from 8 to 9, for example, the flexure is reduced by 12% and the sheet mass per additional rib is increased by approximately 5%, according to Fig. 5. The increase in the number of ribs from 11 to 12 reduces the degree of flexure by 8.3% with the same 5% increase in the sheet mass. Thus, the relative decrease in flexure resulting from the addition of ribs is greater than the relative increase in the sheet mass.

The identified relationships are essential for designing and manufacturing shaped sheets.

4 Conclusions

1. The authors have developed a method for calculating flexures of rectangular plates with ribbed stiffeners, using static beam functions for a beam with invariable stiffness, which are equivalent to stepped beam functions.
2. Practical tables of flexures of shaped sheets as per Russian GOST 24045-2010 were compiled.
3. It is established that the use of a sheet profile with an increased number of ribbed stiffeners is more cost effective since the sheet flexure is reduced faster than the sheet mass is increased. By adding one rib to the initial number of 8–12 ribs of a S-15-1000-06 profile sheet, the sheet flexure is decreased by minimum 8% with 5% increase in the sheet mass.

Acknowledgements The authors wish to thank Vladimir F. Mikhaylets for his helpful discussions and consultations.

References

1. Gots AN (2013) Numerical methods of calculation in power plant engineering. Study guide. Part 2. Publishing House of the Vladimir State University, Vladimir
2. Introduction to Elasticity/Rayleigh-Ritz method (2018) https://en.wikiversity.org/wiki/Introduction_to_Elasticity/Rayleigh-Ritz_method
3. Ivanov VN (2004) Variational principles and problem-solving techniques related to the elasticity theory. RUDN Publishing House, Moscow, Study guide
4. Mama BO, Nwoji CU, Onah HN et al (2017) Bubnov-Galerkin method for the elastic stress analysis of rectangular plates under uniaxial parabolic distributed edge loads—Dept of Civil Engineering, University of Nigeria, Nsukka, Enugu State, Nigeria. <https://doi.org/10.21817/ijet/2017/v9i6/170906060>
5. Suryaninov NG, Kozolup GN (2009) Kantorovich-Vlasov method applied in the ribbed plate bending problem. Proc Odessa Polytech Univ 1(33)–2(34):205–209
6. Orobey VF, Purich VN (2013) Accuracy of the variation Kantorovich-Vlasov method. Proc Odessa Polytech Univ 2(41):19–24
7. Aleksandrov AV, Potapov VD, Derzhavin BP (2003) Strength of materials. Textbook for institutions of higher education. Vysshaya Shkola, Moscow
8. GOST RF 24045-2016. Bent steel sheet profiles with stair landings and railings for construction. Specifications (2018). Standartinform, Moscow
9. BS EN 506 (2008) Roofing products of metal sheet. Specification for self-supporting products of copper or zinc sheet
10. BS EN 14782 (2006) Self-supporting metal sheet for roofing, external cladding and internal lining—Product specification and requirements
11. Belyaev NM (2014) Strength of materials. Study guide. Alyans, Moscow
12. Makarov EG (2007) Engineering calculations in Mathcad-14. Piter Publishing House, St.-Petersburg

13. Kiryanov DV (2007) Mathcad-14. BHV-Peterburg, St.-Petersburg
14. Zwillinger D (1997) Handbook of differential equations. Academic Press, Boston
15. Polyanin AD, Zaitsev VF (2003) Handbook of exact solutions for ordinary differential equations. Chapman & Hall/CRC Press, Boca Raton
16. Arnold VI (1992) Ordinary differential equations. Springer, Berlin
17. Petrovskii IG (1973) Ordinary differential equations. Dover Publications, New York

Comparative Analysis of Stress–Strain Condition of Cylindrical Gears Arc Teeth and Spurs



K. Syzrantseva, V. Syzrantsev and D. Babichev

Abstract The paper deals with a comparative analysis of the stress–strain condition (SSC) of cylindrical gear arc teeth and spurs at different angles of shafts misalignment. The calculation of the teeth SSC was performed using the finite element method under their loading with distributed load on the top edge of the tooth. The laws of load distribution on the top edge of the tooth were established as a result of solving the problems of loading arc and spur gears for different angles of misalignment. The results of the research showed that compared to spur gears, arc tooth gears are exposed to 27% (6' misalignment) less overall displacements and have 18% (6' misalignment) greater bending strength and durability in actual service conditions. It allows making a conclusion about the expediency of application of arc teeth cylindrical gears in high-loaded transmissions (for example, in the high-loaded transmissions of electric locomotives EP-100 and EP-200).

Keywords Cylindrical gear arc teeth · Stress–strain condition · ANSYS · Bending strength · Misalignment angle

1 Introduction

One of the ways to increase the load-bearing capacity and service life of cylindrical gears, operating in conditions of non-rigid housings and a wide range of variable external loads, is a transition from spur to arc tooth gears [1–4]. To obtain the required durability of transmissions, the gears must be subjected to thermal hardening, after which finishing of the teeth is necessary. Despite the fact that by now a number of methods of manufacturing arc teeth gears have been known [5–8], not all of them allow implementing sizing of gears with high hardness of teeth surfaces. The method proposed in the paper [9] appeared to be very promising in this regard. Since the process of forming arc teeth according to the method [9] is fundamentally

K. Syzrantseva (✉) · V. Syzrantsev · D. Babichev
Tyumen Industrial University, 38, Volodarskiy Street, Tyumen 625000, Russia
e-mail: kv.syzr@gmail.com

different from the known ones [10–14], in papers [15–17] tooth surface geometries have been studied, the features of contact in meshing arc teeth have been obtained, arc teeth gear contact loading and contact endurance have been determined under conditions when the external load and teeth relative position errors in meshing are random variables with distribution laws, either known or established by the methods of nonparametric statistics [4, 16, 18] for a given sample. The results obtained allow determining an optimal arc teeth surface geometry, which provides maximum contact endurance of gears [19, 20] in specified operating conditions.

2 The Theoretical Part

It is known that for hardened gears, an important criterion of performance is bending strength of teeth, estimated by the values of maximum normal stresses in the root of the tooth dedendum on its tension side, occurring as a result of loading by a distributed load applied to the top of the tooth. There are two ways of determining the nature of the stress distribution: either in the course of experimental studies or by computational methods. The first way is associated with significant material and time costs. Under the current economic conditions, these costs practically exclude any possibility of obtaining the required information in the open range of new geometry arc teeth gear parameters variation. The consequence of the above is that the determination of stress distribution in the root of arc teeth experimentally is carried out only in exceptional cases and practically on single samples [9].

With the development of computer technology, currently, software packages that implement numerical methods of elasticity theory, in particular, finite element and boundary element methods (FEM and BEM) are widely used to study the stress–strain condition (SSC) of machine parts [21–25]. The results of the calculations allow not only estimating the nature of stress distribution in the root of the teeth, but also determining reasonable transmission parameters according to the adopted strength criteria when changing the mutual position of teeth in meshing (variation of meshing phase, taking into account the angle of the shafts misalignment).

The use of thermo-strengthened gears provides for the required durability of gears with high strength. We have started to design arc cylindrical gears as a result of the urgency of increasing the bearing capacity and durability of high-loaded arc gears of locomotives EP100 and EP200. In previous papers [15, 26], the following tasks have been solved: methods for calculation of transmission geometrical parameters and determination of load in the contact have been given, calculated relationships to determine the durability have been obtained, a comparative estimation of contact endurance of spur and arc teeth gears has been given, and all above has been implemented in appropriate software.

3 Computer Simulation

As is known, one of the most common parts in mechanical engineering is gears, the cause of failure of which are tooth root high bending stresses which occur in the process of gear operation [18, 22]. To calculate the stress–strain condition (SSC) of cylindrical spur and arc teeth gears, we use the ANSYS software package, which implements the finite element method to solve physical problems described by differential equation systems.

SSC calculations using the arc tooth finite element method are performed for the case of loading from the concave surface. Since the most dangerous case of tooth operation is loading its top, the teeth SSC calculations are performed when they are loaded at the top edge normally to the side surface. The distribution law of the load applied to the tooth top edge is a fundamentally important feature of loading the contact in meshing, and is established as a result of solving the problem of contact loading of gears in [15].

The boundary conditions of the studied teeth were described as follows: the displacements on the lower surface of the tooth were set equal to zero (rigid restraint); the load was applied along the line at the top of the tooth normally to the surface. The finite element models and computational schemes for spur and arc teeth are shown in Fig. 1a, b, respectively. They show the distribution of the applied load in a spur and an arc tooth with the gear axes misalignment of $6'$.

We compare the SSC of spur and arc teeth cylindrical gears along the length of the teeth at different angles of misalignment. The distributed load determined by the method [15] for a spur corresponded to misalignment angles of $0'$, $2'$, $4'$, and $6'$ (Fig. 2a), and for an arc tooth— $0'$, $2'$, $4'$, $6'$, and $8'$ (Fig. 2b). Spurs are not considered at a misalignment angle of $8'$, since the stresses occurring at the root of a tooth exceed the maximum permissible ones, which lead to destruction.

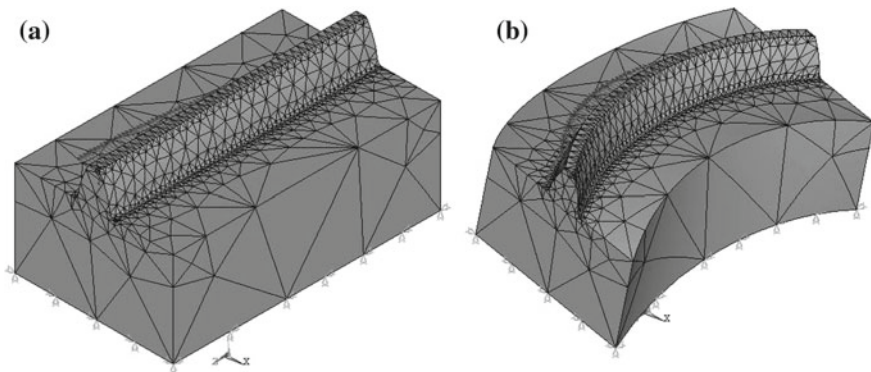


Fig. 1 Computational scheme and distribution of loading forces for a spur gear (a) and for an arc tooth gear (b) at $6'$ misalignment

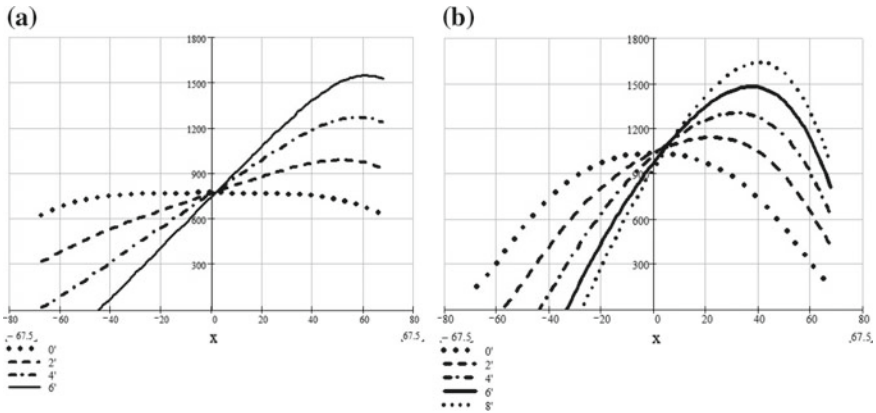


Fig. 2 Load distributed at the top of spur (a) and arc tooth (b) at different misalignment

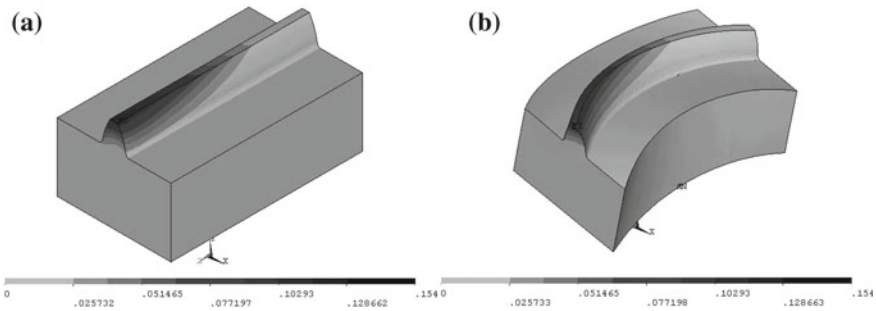


Fig. 3 Overall displacement field at the misalignment angle of 6' in spur (a) and arc tooth (b)

The overall displacement fields in teeth for the misalignment angle of 6' are shown in Fig. 3. For evidence, the distribution patterns are drawn in one scale. The distribution diagrams of the overall displacements along the load application line at the above misalignment angles are shown in Fig. 4.

It is easy to notice that in a spur during a misalignment, the contact pad comes to the tooth end, which, after a sufficiently a large number of loading cycles, will inevitably lead to a fracture of the tooth edge. In an arc tooth, the maximum of overall displacements is only shifted to the tooth end; such localization is less dangerous for the tooth bending strength.

Figure 4 shows that when gears operate without misalignments the spur (curve 0' in Fig. 8) has less overall displacements than that of the arc tooth (curve 0' in Fig. 4b). The situation changes with an increase in a misalignment angle. As can be seen from the figures, the maximum displacements in blocks are 0.156715 mm for a spur, and 0, 114506 mm for an arc tooth, which is 27% less than that of the spur.

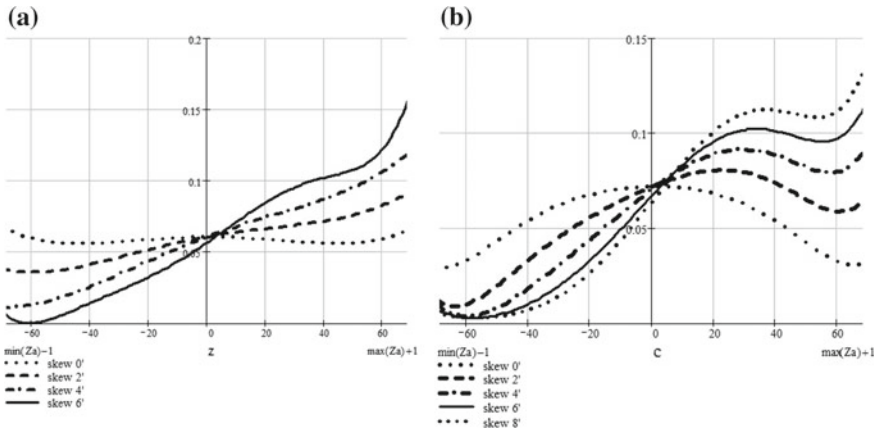


Fig. 4 Diagrams of overall displacements distribution along the line of load application for spur (a) and arc tooth (b)

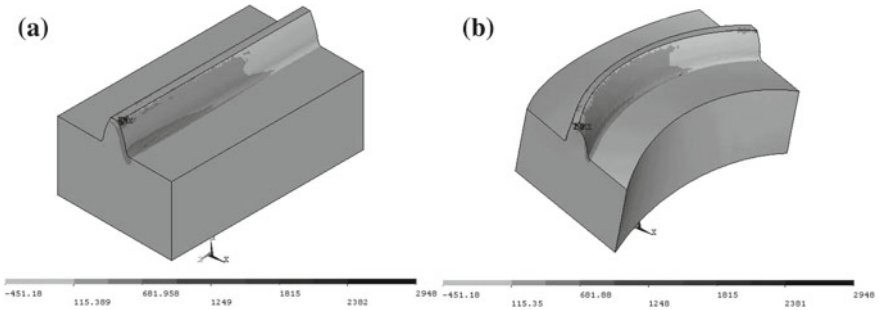


Fig. 5 Stress σ_1 distribution at misalignment angle of $6'$ in spur (a) and arc tooth (b)

The most important for a tooth SSC analysis is the distribution of the principal stress σ_1 in its root. The bending strength and bending endurance of the tooth under study depend on the value of this stress. The distribution fields of the principal stresses σ_1 of spurs and arc teeth, for the misalignment angle of $6'$ are shown in Fig. 5 (for evidence the stress fields are drawn in one scale), and the diagrams for all the misalignment angles are shown in Fig. 6. The maximum stress values in both cases are observed in the tooth root near its end due to the influence of the edge effect. The comparative analysis of principal stresses σ_1 for different misalignment angles by the maximum values is given in Table 1.

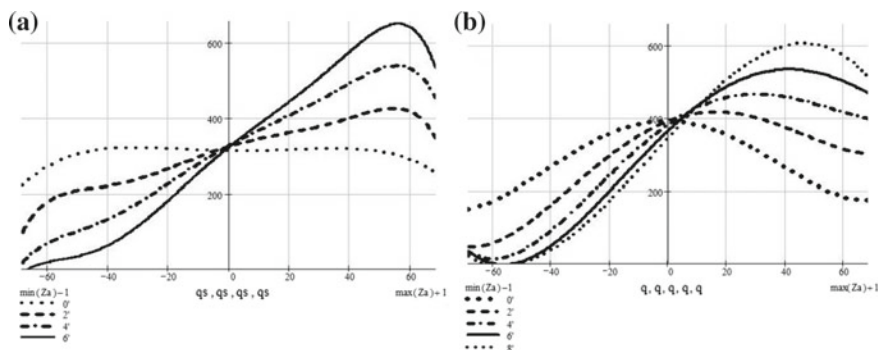


Fig. 6 Diagrams of stress σ_1 distribution in the spur (a) and arc tooth (b) root

Table 1 Comparative analysis of stresses σ_1 in the teeth root

Misalignment angle	Spur (MPa)	Arc tooth (MPa)	%
0'	322.644	391.426	-21.318
2'	427.714	417.22	2.453
4'	540.119	466.602	13.611
6'	652.412	533.949	18.158
8'	Loss of bending strength	605.7	-

4 Conclusions

The comparative analysis showed that under the condition of shaft parallelism, spur gears are characterized by a higher load capacity. However, in high-loaded transmissions, it is almost impossible to actualize this condition, and the load capacity of the both transmissions is almost identical at misalignment angle of 2'. The finite element analysis of the teeth SSC has confirmed the undeniable advantages of arc teeth cylindrical gears at misalignment.

The results of the researches show the expediency of use of cylindrical arc teeth gears in high-loaded transmissions of locomotives EP-100 and EP-200. Compared to spur gears, arc tooth gears are exposed to 27% (6' misalignment) less overall displacements and have 18% (6' misalignment) greater bending strength and durability in actual service conditions.

Acknowledgements This work was performed within the governmental assignment from the Ministry of Education and Science of the Russian Federation for the period of 2017–2019 in Tyumen Industrial University (project N9.6355.2017/BCh).



References

1. Tseng RT, Tsay CB (2004) Contact characteristics of cylindrical gears with curvilinear shaped teeth. *Mech Mach Theory* 39(9):905–919. <https://doi.org/10.1016/j.mechmachtheory.2004.04.006>
2. Chang Q, Hou L, Li B, Jia1 B (2015) Modal Analysis of cylindrical gears with arcuate tooth trace. *Periodica Polytech Mech Eng* 59(1):23–29. <https://doi.org/10.3311/ppme.7540>
3. Ma Z, Wang X (2002) Research on a highly durable and heavy duty gearing. *J Xi'an Jiaotong Univ* 36(3):282–286
4. Su JZ, Fang ZD, Cao XM (2010) Tooth contact analysis of face gear drive with curvilinear shaped tooth by format cutting. *J Aerosp Power* 25(6):1427–1431
5. Tseng JT, Tsay CB (2005) Mathematical model and surface deviation of cylindrical gears with curvilinear shaped teeth cut by hob cutter. *J Mech Des Trans ASME* 127(5):982–987
6. Dai Y, Yukinori A, Jiang D (2006) Hobbing mechanism of cylindrical gear with arcuate tooth traces and experimental investigation. *China Mech Eng* 17(7):706–709
7. Fang ZD, Cao XM, Shen YB (2010) Tooth surface design and manufacture for arcuate tooth trace face-gear. *J Aerosp Power* 25(1):224–227
8. Cai XW, Fang ZD, Su JZ (2012) Study on meshing characteristics of face gear drive with arcuate tooth based of manufacture on NC machine (2012). *J Aeros Power* 27(1):198–203
9. Belyaev AI, Siritsyn AI, Siritsyn DA (1997) Wear and fatigue resistance of arched gear teeth in flexure. *Russ Eng Res* 17(1):6–9
10. Litvin FL, Fuentes A, Zanzi C, Pontiggia M (2002) Design, generation, and stress analysis of two versions of geometry of face-gear drives. *Mech Mach Theory* 37(10):1179–1211. [https://doi.org/10.1016/S0094-114X\(02\)00050-2](https://doi.org/10.1016/S0094-114X(02)00050-2)
11. Song A, Yi H, Tang W, Ni Z, Li L (2006) Involute arc cylindrical gear and its mesh characteristics. *China Mech Eng* 17(18):1888–1892
12. Song AP, Wu WW, Gao S, Gao WJ (2010) The ideal geometry parameters of arch cylindrical gear and its process method. *J Shanghai Jiaotong Univ* 44(12):1735–1740
13. Jiang YQ, Hou L, Zhao Y (2014) The equation of the contact line of the involute curvilinear-tooth cylindrical gear pump for the agricultural tractor. *Open Mech Eng J* 8:879–884. <https://doi.org/10.2174/1874155X01408010879>
14. Wei Y, Ma D, Wu Y, Luo L, Bai Q, Hou L (2017) Study on the tooth surface and curvature characteristics of cylindrical gear with variable hyperbolic arc-tooth-trace. *Adv Eng Sci* 49(6):196–203. <https://doi.org/10.15961/j.jsuese.201700372>
15. Syzrantsev V, Syzrantseva K, Varshavsky M (2001) Contact load and endurance of cylindrical gearing with arch-shaped teeth. In: *Proceedings of the international conference on mechanical transmissions*. Chongqing, China, p 425
16. Syzrantseva KV (2009) Predicting the failure of gear transmissions by nonparametric statistics. *Russ Eng Res* 29(2):1206–1208. <https://doi.org/10.3103/S1068798X09120028>
17. Syzrantseva K, Syzrantsev V (2017) Estimation of Novikov gearing loading capacity on a base of Integral Strain Gauges application. *Procedia Eng* 206:1081–1086
18. Syzrantseva KV (2009) Development of a method to calculate the strength reliability of tooth gears based on the fatigue resistance when the teeth bend. *J Mach Manuf Reliab* 38(6):552–556. <https://doi.org/10.3103/S1052618809060065.10>
19. Wang SJ, Hou L, Dong L, Xiao HJ (2012) Modeling and strength analysis of cylindrical gears with curvilinear shape teeth for manufacture. *J Sichuan Univ (Eng Sci Ed)* 44(2):210–215
20. Sun Z, Hou L, Wang J, Li W, Chang Q (2016) Contact strength analysis of circular-arc-tooth-trace cylindrical gear. *J Braz Soc Mech Sci Eng* 38(3):999–1005
21. Chen YC, Gu ML (2010) Contact stress of modified curvilinear gears. *AIP Conf Proc* 1285:546–560. <https://doi.org/10.1063/1.3510577>
22. Jia F, Hou L, Wei Y, Li B, You Y (2015) Modelling and bending strength analysis of cylindrical gears with arcuate tooth trace. *Aust J Mech Eng* 13(2):77–86. <https://doi.org/10.7158/M13-068.2015.13.2>

23. Syzrantseva K (2016) Load on multipair contact zones of operating parts of screw pumps and motors: a computer analysis. *Procedia Engineering* 150:768–774
24. Syzrantseva K, Syzrantsev V (2016) Reliability estimation of machine parts with complicated geometry on a base of methods of nonparametric statistics. *J Eng Appl Sci* 11(2):204–209. <https://doi.org/10.3923/jeasci.2016.204.209>
25. Syzrantseva K, Dvoynikov M (2016) Computer analysis of durability and leakproofness of multi-lateral junction of wells. *IOP Conf Series Mater Sci Eng* 142
26. Syzrantsev V, Syzrantseva K, Varshavsky M (1999) Contact load in cylindrical gearings. In: *Proceedings of 5th international conference “Akademika dubnica-99”*, Dubnica nad Vahom, Slovakia, pp 167–171

Thermomechanical Fatigue Analysis of Diesel Engine Piston: Finite Element Simulation and Lifetime Prediction Technique



S. M. Sivachev and L. L. Myagkov

Abstract Nowadays, piston aluminum–silicon alloys are widely used for high-powered engines due to their low specific gravity, high thermal conductivity, and good castability. However, under the conditions of increase of thermomechanical loads caused by the rise in the specific power output of diesel engines, and the operating temperatures of pistons go up to 0.8–0.9 of the melting temperature resulting in a significant reduction of the Al–Si alloy high-temperature strength. In this regard, to provide a required lifetime of pistons, it is necessary to more precisely simulate their thermal and stress-strain state, taking into account two-frequency loading and inelastic deformation. In this paper, a review of existing methods for the piston life estimation is carried out; a calculation method of the piston transient temperature and strain fields for engine start-stop cycles and one operating cycle at a nominal power mode is developed. The material constants in plasticity and creep models for the Al–12Si–Cu–Ni–Mg alloy are determined. On the basis of the obtained stabilized elastoplastic hysteresis loop, the piston low-cycle fatigue is estimated using the energy criterion. According to experimental data, the piston life is corrected taking into account high-frequency load.

Keywords Diesel engine · Piston · Two-frequency loading · Plasticity · Creep · Low-cycle fatigue

1 Introduction

1.1 Background

The aluminum–silicon alloys of the Al–Si–Cu–Ni–Mg system containing up to 12 different elements have high wear resistance, high thermal conductivity, low ther-

S. M. Sivachev (✉) · L. L. Myagkov
Bauman Moscow State Technical University, 5/1 ul. Baumanskaya 2-ya,
Moscow 105005, Russia
e-mail: stassivachev@yandex.ru

mal expansion coefficient, low specific weight, good casting properties, and high mechanical characteristics [1–3]. The rise in specific power output of high-powered diesel engines leads to increase in mechanical and thermal loads on the combustion chamber components: the cylinder pressure can reach 200 bar, and the maximum piston temperatures represent a homologous temperatures (the ratio to the melting temperature in K) range 0.8–0.9 [3–5].

The high homologous temperatures on the piston bowl rim cause a significant decrease in piston thermal strength. Therefore, it is necessary to more precisely predict the piston operating life. The development of lifetime prediction techniques is possible using the mathematical modeling of stress-strain state of pistons, which takes into account two-frequency loads and inelastic effects of the material.

The heat-stressed components of combustion chamber (in particular, piston and cylinder head) work under two-frequency thermomechanical loading: low-frequency cycles correspond to changes in engine operating modes, and high-frequency cycles represent each operating cycle (two rotation of crankshaft for four-stroke engine). Moreover, high temperatures at the piston bowl edge lead to the appearance of plastic and creep deformations.

Belov [6] used the damage linear summation rule to account high- and low-frequency loads:

$$d_n + d_i^f + d_i^c + d_i = 1 \quad (1)$$

where d_n and d_i denote the damages obtained on the nominal and idle modes, d_i^f and d_i^c are the fatigue and creep-induced damages obtained on the transient modes, respectively.

The damages obtained on the nominal and idle modes are defined as the ratio of the number of applied cycles to the number of cycles to failure. The fatigue and creep damages are calculated using the strain-based criterion:

$$d_i^f = N / \left(\frac{\varepsilon_f(T)}{2\Delta\varepsilon_p} \right)^2; \quad d_i^c = \frac{\Delta\varepsilon_p N}{\varepsilon_f(T)} \quad (2)$$

where N is the number of applied cycles, $\varepsilon_f(T)$ is the true fracture ductility, $\Delta\varepsilon_p$ is the elastoplastic hysteresis loop width, $\Delta\varepsilon_p$ is the one-sided translation of the elastoplastic hysteresis loop in one cycle.

Ivanchenko [7] proposed other relation:

$$A = \frac{n}{N_f} + \frac{n^*}{N_f^*} \quad (3)$$

where A is the total damage, N_f is the allowable number of cycles corresponding to the stress amplitude resulting from the high- and low-frequency loads, N_f^* is the allowable number of cycles corresponding to the stress amplitude resulting from the

thermal high-frequency load, n and n^* are the number of low- and high-frequency cycles to fatigue crack initiation, respectively.

Saltykov with colleagues [8] in considering the two-frequency loading spectrum of diesel engine piston crown proposed to determine the ratio of the durability of structure with two-frequency loading to the lifetime under one-frequency loading with amplitude equal to the sum of the two-frequency loading components amplitudes:

$$\frac{N_f}{N_h} = \frac{\sigma_a^t}{\sigma_a^l \sqrt{1 + \left(\frac{f_h}{f_l}\right) \left(\frac{\sigma_a^t}{\sigma_a^l}\right)^2}} \quad (4)$$

where N_f is the longevity under a two-frequency loading as determined by the number of cycles of the low-frequency component, N_h is the longevity under a one-frequency loading, which corresponds to a stress amplitude equal to the sum of the amplitudes of the two-frequency load components, σ_a^l is the low-frequency stress amplitude, σ_a^t is the total amplitude of the high- and low-frequency components, f_h, f_l are the loading frequencies.

It should be noted that this approach is applicable in the case of elastic deformation.

The recent studies on the durability of materials for heat-stressed parts operating under two-frequency loading show that damage linear summation rule (Palmgren-Miner rule) is not confirmed [9]. This is because the crack propagation mechanisms under one- and two-frequency loadings are different [10]. Thus, it should be used the low-cycle fatigue curves representing relation between the number of low-frequency cycles of thermomechanical load and the amplitude of superimposed high-frequency mechanical load.

1.2 Current Work

For this research, the following tasks have been formulated:

- Develop a method based on the commercial software ANSYS for calculating transient temperature and strain fields of the piston resulting from high- and low-frequency loads;
- Determine material constants in plasticity and creep models for the working temperature range of piston;
- Investigate the elastoviscoplastic deformation of the piston combustion bowl edge;
- Evaluate the piston fatigue lifetime.

2 FEM Computational Analysis

2.1 Object of Study

The piston of the v-type 8-cylinder YaMZ-6586 diesel engine with a rated power of 309 kW is chosen as the object of this study. The main technical characteristics of the engine are shown in Table 1.

The solid model of piston was built in the design software SolidWorks. To increase the stress concentration, the combustion bowl rim was made sharp without fillet radius.

2.2 Calculation Methodology

The developed method consists of performing a series of piston thermal and stress-strain state calculations (see Fig. 1). The transient temperature field for engine start-stop cycle is used for modeling of low-cycle thermal stress. The high-cycle thermomechanical stress is calculated using transient temperature field for one operating cycle and mechanical load (gas pressure and inertia).

Table 1 Technical characteristics of YaMZ-6586 diesel engine

Bore (mm)	130
Stroke (mm)	140
Rated power (kW)	309
Nominal rotational speed (min ⁻¹)	1900
Specific effective fuel consumption (g kW ⁻¹ h ⁻¹)	195

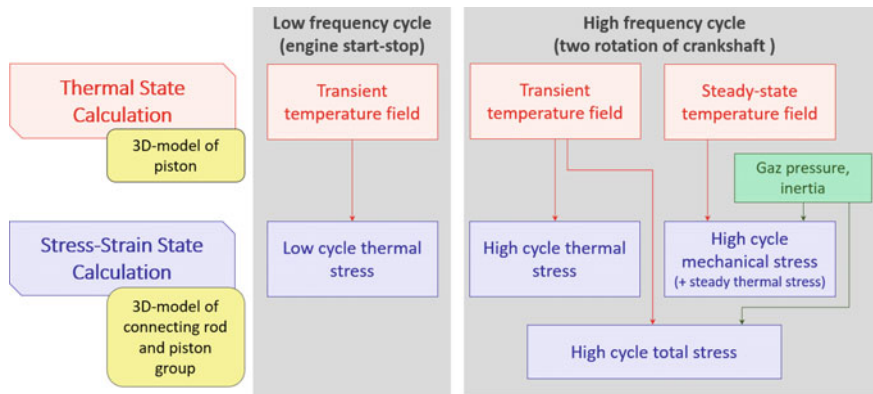


Fig. 1 Scheme of thermal and stress-strain state calculation methodology

2.3 Determination of Plasticity and Creep Models Coefficients

Presently, it is necessary to use mathematical models which describe nonlinear hardening of material [11]. The curves of cyclic deformation of piston aluminum–silicon alloys show that silumin is characterized by kinematic hardening [12]. This means that the yield surface size does not change and the surface translates in the load direction. In the present work, the model proposed by Chaboche [13] is used. According to this model, the translation of the center of yield surface $\Delta\alpha$ is calculated by the following relation:

$$\Delta\alpha = \frac{2}{3} C \Delta\varepsilon_p - \gamma\alpha\Delta\hat{\varepsilon}_p \quad (5)$$

where α is the back stress, C is the hardening modulus, $\Delta\varepsilon_p$ is the plastic strain increment, γ is the rate of hardening modulus decrease, and $\Delta\hat{\varepsilon}_p$ is the equivalent plastic strain increment.

The coefficients C and γ were evaluated according to the stress-strain curves using the least-squares method.

The mathematical description of creep phenomena is based on the constitutive equations obtained from experiments. The Norton's law shows the relation between minimum creep strain rate $\dot{\varepsilon}_{\min}^c$, applied stress σ , and temperature T [14]:

$$\dot{\varepsilon}_{\min}^c = A\sigma^n \exp\left(-\frac{Q}{RT}\right) \quad (6)$$

where A , n are the material constants, Q is the creep activation energy, and R is the universal gas constant.

The experiments were done for specimens of Al–12Si–3.5Cu–2Ni–0.8Mg alloy in temperature range of 250–300 °C and stress range of 80–140 MPa show that this alloy is characterized by dislocation type creep [15]. The material constants were determined by this data.

2.4 Calculation of Boundary Conditions

The engine cycle at nominal power mode was calculated using the engine simulation software Diesel-RK. The thermal boundary conditions for piston surfaces were determined through ICE program. These computer tools are developed at the Bauman University. To obtain the high-cycle temperature variation for one operating cycle, the local values of heat transfer coefficient as a function of crank angle were calculated according to relation from [16]. To calculate the mechanical loading, the gas pressure and piston acceleration were applied to finite element model. The piston acceleration was calculated by the equation [17]:

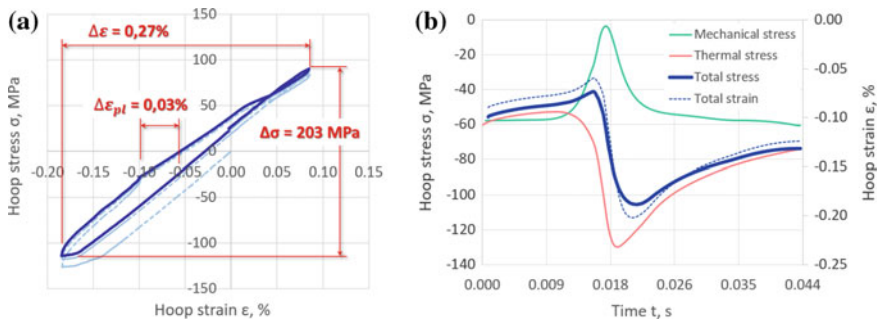


Fig. 2 Stress-strain state of piston bowl edge pin-axle. **a** Stabilized elastoplastic hysteresis loop corresponding to three start-stop cycles and **b** High-frequency variations of stresses and strains during one operating engine cycle

$$j = R\omega^2(\cos \alpha + \lambda \cos 2\alpha) \quad (7)$$

where j is the piston acceleration of the first- and second-order, R is the crank radius, ω is the angular velocity of crankshaft rotation, α is the current value of crank angle, and λ is the ratio of crank radius to connecting rod length.

2.5 Results

After calculating three start-stop cycles, the stabilized elastoplastic hysteresis loop for the bowl edge in the piston pin plane was obtained which is shown in Fig. 2a. The simulation of operating cycle allowed to obtain the stress variations as a result of high-frequency thermomechanical loads (see Fig. 2b).

3 Calculation of Piston Fatigue Lifetime

The low-cycle fatigue criteria are divided into phenomenological, cumulative damage, and crack growth models [18]. The classical phenomenological fatigue criterion represents the relation between a criterion function and the number of cycles to failure N_f [19]:

$$\max_{x \in \Omega} [\Phi(\varepsilon, \varepsilon_{pl}, \sigma, \dots)] = aN_f^b \quad (8)$$

where a , b are two material parameters, ε is the strain tensor, ε_{pl} is the plastic strain tensor, and σ is the stress tensor.

As per the energy criterion proposed by Skelton [20], the left side of “Eq. 8” is the inelastic energy determined by stabilized hysteresis loops:

$$\Delta W_p = W_f' (2N_f)^\beta \quad (9)$$

where W_f' , β are the material constants, ΔW_p is the plastic energy dissipated per cycle.

The experimental studies suggest that the hysteresis energy approach is a better choice to evaluate the thermomechanical damage as it includes both stress and strain effects [21].

The number of start-stop cycles to failure (288,000 cycles) was obtained using the constants for Al–Si–Cu–Ni–Mg alloy from [2].

The decrease of piston lifetime due to superimposition high-frequency load on low-frequency loading was done according to experimental curves from [9]. These curves are the relations between the number of macrocycles of thermomechanical loading (with the low-frequency strain amplitude of 0.275% and the maximum cycle temperature of 300 °C) and the amplitude of applied high-frequency mechanical strain. Since the strain amplitude during the engine operating cycle is 0.07% (see Fig. 2b), the durability of sharp bowl edge will decrease by 80% to 57,600 cycles.

4 Conclusions

The transient temperature and strain fields of the piston corresponding to high- and low-frequency thermomechanical loading were obtained. The piston low-cycle fatigue life was evaluated using energy criteria and it is equal to 288,000 cycles. It was found that superimposed high-frequency load decreases durability of sharp combustion bowl edge to 57,600 cycles.

References

1. Liu J, Zhang Q, Zuo Z et al (2013) Microstructure evolution of Al–12Si–CuNiMg alloy under high temperature low cycle fatigue. *Mater Sci Eng, A* 574:186–190. <https://doi.org/10.1016/j.msea.2013.03.027>
2. Zhang Q, Zuo Z, Liu J (2013) High-temperature low-cycle fatigue behavior of a cast Al–12Si–CuNiMg alloy. *Fatigue Fract Eng Mater Struct* 36(7):623–630. <https://doi.org/10.1111/ffe.12029>
3. Morgenstern R, Kenningley S (2013) Transient microstructural thermomechanical fatigue and deformation characteristics under superimposed mechanical and thermal loading, in AlSi based automotive diesel pistons. In: Sadler BA (ed) *Light metals*. The Minerals, Metals & Materials Series, Springer, Cham, pp 397–403

4. KS Mono-Block Steel Pistons for Commercial Truck Applications (2018) Kolbenschmidt Pierburg Group. http://www.kspg.com/fileadmin/media/kspg/Broschueren/Produktbroschueren/KS_Kolbenschmidt/Kolben_Nkw/ko_pistonsteel_truck_e.pdf. Accessed 20 Sept 2018
5. Kenningley S, Morgenstern R (2012) Thermal and mechanical loading in the combustion bowl region of light vehicle diesel AlSiCuNiMg pistons; reviewed with emphasis on advanced finite element analysis and instrumented engine testing techniques. SAE Technical Paper 2012-01-1330. <https://doi.org/10.4271/2012-01-1330>
6. Belov VP (1986) Raschetno-eksperimental'naya otsenka termostoykosti porshney forsirovannykh avtomobil'nykh i traktornykh dvigateley (Computational and experimental estimation of thermal stability of high-powered automobile and tractor engines pistons). Dissertation, BMSTU
7. Ivanchenko AB (1995) Metodika otsenki termoustalostnoy prochnosti porshney forsirovannykh dizeley (Estimation method of thermal fatigue strength of high-powered diesel engines pistons). Dissertation, BMSTU
8. Saltykov MA, Chainov ND, Vasin ES (1991) Otsenka prochnosti golovok porshney vysokoforsirovannykh teplovoznnykh dizeley pri dvukhchastotnom nagruzhenii (Strength estimation of piston crowns of high-powered diesel engines under two-frequency loading). Vestnik MGTU. Ser. Mashinostroenie, Moskva
9. Beck T, Henne I, Löhle D (2008) Lifetime of cast AlSi6Cu4 under superimposed thermal-mechanical fatigue and high-cycle fatigue loading. Mater Sci Eng, A 483–484:382–386. <https://doi.org/10.1016/j.msea.2006.09.139>
10. Beck T, Löhle D, Luft J et al (2007) Damage mechanisms of cast Al-Si-Mg alloys under superimposed thermal-mechanical fatigue and high-cycle fatigue loading. Mater Sci Eng, A 468–470:184–192. <https://doi.org/10.1016/j.msea.2006.05.177>
11. Trampert S, Pischinger T (2008) Thermomechanical fatigue life prediction of cylinder heads in combustion engines. J Eng Gas Turbines Power 130:1–10. <https://doi.org/10.1115/1.2771251>
12. Mao J, Engler-Pinto C, Su X et al (2014) Cyclic behavior of an Al–Si–Cu alloy under thermo-mechanical loading. SAE Int J Mater Manf 7(3):1–8. <https://doi.org/10.4271/2014-01-1012>
13. Chaboche JL (1989) Constitutive equations for cyclic plasticity and cyclic viscoplasticity. Int J Plast 5:247–302. [https://doi.org/10.1016/0749-6419\(89\)90015-6](https://doi.org/10.1016/0749-6419(89)90015-6)
14. Manson SS, Halford GR (2009) Fatigue and durability of metals at high temperatures. ASM Int, Materials Park
15. Zuo L, Ye B, Feng J et al (2018) Microstructure, tensile properties and creep behavior of Al-12Si-3.5Cu-2Ni-0.8Mg alloy produced by different casting technologies. J Mater Sci Technol 34:1222–1228. <https://doi.org/10.1016/j.jmst.2017.06.011>
16. Stankevich IV (1984) Opredeleniye teplonapryazhennosti kryshek tsilindrov dizeley s uchetom nelineynosti zadachi teploprovodnosti (Determination of thermal stresses of diesel engines cylinder heads taking into account nonlinearity of heat conduction problem). Dissertation, BMSTU
17. Chainov ND, Ivaschenko NA, Krasnokutsky AN, Myagkov LL (2008) Konstruirovaniye dvigateley vnutrennego sgoraniya (Design of internal combustion engines). Mashinostroenie, Moskva
18. Gomez T, Awarke A, Pischinger S (2010) A new low cycle fatigue criterion for isothermal and out-of-phase thermomechanical loading. Int J Fatigue 32:769–779. <https://doi.org/10.1016/j.ijfatigue.2009.11.003>

19. Amiable S, Chapuliot S, Constantinescu A et al (2006) A computational lifetime prediction of a thermal shock experiment. Part II: discussion on difference fatigue criteria. *Fatigue Fract Eng Mater Struct* 29:219–227. <https://doi.org/10.1111/j.1460-2695.2006.0983.x>
20. Skelton RP (1991) Energy criteria for high temperature low cycle fatigue. *Mater Sci Technol* 7:427–440. <https://doi.org/10.1179/mst.1991.7.5.427>
21. Wang M, Pang JC, Zhang MX et al (2018) Thermo-mechanical fatigue behavior and life prediction of the Al-Si piston alloy. *Mater Sci Eng, A* 715:62–72. <https://doi.org/10.1016/j.msea.2017.12.099>

Quantitative Assessment of Thermal Properties of the Metal-Cutting Machine Design



B. M. Dmitriev

Abstract As machine manufacturing develops, the requirements for productivity and accuracy of parts produced on machines become more and more stringent, which, in turn, increases heat generation and adversely affects these parameters. This results in a contradiction between the requirement for machine manufacturing development and machine tool industry capabilities. Basically, it proves impossible to eliminate the contradiction; however, it is possible to reduce the level of confrontation through the creation of a rational design. During design and operation of the machine tool, there is a regular need to evaluate the thermal state of the machine tool. The existing knowledge system uses a qualitative evaluation of the machine thermal state, i.e., “better/worse.” The method has neither a start point nor the measurement unit and, as a consequence, forms a rough estimate of the condition. If there is a need to provide a required level of thermal design state when debugging a test sample at the stage of design development, a method is required that ensures design quantification. This research paper describes a method for evaluating the thermal properties of a structure in quantitative terms. A method based on the developed package of measures consisting of a unit of measurement, standard of this unit, scale of quantitative values, etc. The scope of application of this method is governed by the tasks to conduct a quantitative assessment of thermal properties throughout the life cycle of the machine tool design.

Keywords Machine tool • Thermal scale • Thermal unit • Standard unit • Thermal test • Property value • Operation

B. M. Dmitriev (✉)

Bauman Moscow State Technical University, 5, 2-nd Baumanskaya str.,
Moscow 105005, Russia
e-mail: dmitriev@bmstu.ru

© Springer Nature Switzerland AG 2020

A. A. Radionov et al. (eds.), *Proceedings of the 5th International Conference on Industrial Engineering (ICIE 2019)*, Lecture Notes in Mechanical Engineering,
https://doi.org/10.1007/978-3-030-22041-9_14

119

1 Introduction

It is a characteristic feature of the current trend in machine-building industry that requirements for the quality of products made become more stringent as output of these products is growing [1]. The basis of engineering products is formed by metal-cutting machines. The machine bearing system (MBS) performs simultaneously two basic functions [2]. It is the ability of the structure to support the conditions and the ability of the process to shape the opposition against thermal *vozdeystviyna*. The design ability ensures the accuracy and performance of parts made [3]. MBS forms thermal properties. It is based on the fact that thermal resistance forces of the structure act against the action of external heat. This property in the design is concealed from an external observer [4]. The property of the cutting process is the ability to perform mechanical work and thus to ensure the performance of the process accompanied by the formation of heat. While the machine is performing mechanical work, it improves performance and generates more heat [5]. Gain in heat entering the structure reduces the accuracy of the machine tool [6] and its components [7]. This results in a contradiction between the industrial requirement and machine tool industry capabilities. The physical basis of the contradiction is formed by effects of the heat on MBS [8]. Due to the fact that both basic properties are inseparable during the production of parts, this is an ongoing problem throughout the life cycle of the machine tool [9]. A study into the ways to solve this problem indicates that the most appropriate way is to create a rational design of the machine tool [10]. The thermal property of the structure is achieved at the design stage through the use of various measures. Used in the design of various refrigeration devices, use thermo-constant premises to accommodate precision machines. In other cases, when a pilot sample of the machine is debugged or following restoration of working condition, the ability is evaluated in qualitative terms “better/worse,” “more/less.” This assessment has a wide uncertainty of results. This approach is not useful. There is a need to evaluate different design options. There are costs of time for carrying out an assessment. There are costs of material resources. An evaluation method based on quantitative assessment is required in order to obtain an evaluation with the required level of differences in the thermal state [11]. If it is necessary to maintain the calculated thermal state within the established limits, a quantitative method for assessing the state is required. For this purpose, the assessment should be based on the use of the unit of measurement of the property, the scale of the thermal quality of the structure, methods and means of assessing the thermal condition of the machine.

1.1 *The Purpose and Objectives of the Study*

The aim of the work was to develop a set of measures according to the methodology designed to assess the thermal condition of the machine in quantitative terms. The

development of the method involves a number of issues. This is the task of forming a unit of measurement, the development of a standard unit of measurement of the thermal state, the formation of the scale of thermal properties, the creation of a method, and a means of measuring properties.

The ability of the structure to produce resistance against thermal effects is concealed from the external observer inside the structure. To assess the level of the internal state of the structure, compensation of the error by an indirect method of measuring this property is necessary [12].

1.2 Assessment of the Internal State of the Structure

The essence of the method is that the structure is exposed to a thermal effect of a known value and the reaction of the structure to this effect is measured [13]. The ratio of these two values determines the quantitative value of the internal structure property. Thermal properties of the structure are expressed in the following way:

$$\chi_i = \text{structure's response/thermal effects}$$

where i —the current coordinate of the machine geometric accuracy.

Response of the structure is evaluated by changes in the position of the spindle axis relative to the workpiece. These are three linear coordinates (δ_i) and two angular coordinates (α_i). These parameters determine the accuracy of the parts produced. The parameters are lumped, with dimensions expressed in micrometers and are evaluated through direct measurement.

1.3 Parameter Determining the Thermal State of the Structure

The quantitative value of parameters that specify the thermal state of the structure in the existing knowledge system (EKS) is estimated using such parameters as the design temperature (T -deg C0) or the spindle rotation speed (n). Both parameters are distributed both in space and time. When these parameters are used for calculation of the thermal property, it is necessary to know the temperature at one point equals to the distributed parameter. To that end, the field should be curtailed down to a specific value. The procedure is methodologically possible for both temperature and spindle rotation speed [14]. However, curtailing results in data loss. This influences the estimation error. In an effort to overcome the difficulties arisen, it was proposed to use another thermodynamic parameter. This is power consumption (W) at the machine tool input [15]. This lumped parameter is evaluated through direct measurement (kWh). The process of changes in the geometric accuracy of the machine tool during operation is a mechanical motion under the

influence of heat. The study into the mechanical motion parameters provides for availability of a reference system. The reference system consists of a coordinate system, line and angle measurement tools (5 pc). A time meter is required for the parameters to be synchronized. The course of examination involves changes in the ambient temperature which modifies the structure's thermal state. For these changes to be considered, the ambient temperature is measured. The package of measuring tools forms the information and measuring system. All tools included in the measuring system are standard tools. They have methods of measurement and verification tools. The structure of the design thermal properties (κ_i) on the i -coordinate is the ratio of the values and can be calculated by the formula as follows: $\kappa_1 = \delta/n$; $\kappa_2 = \delta/W$ $\kappa_3 = T/n$ $\kappa_4 = T/W$ $\kappa_5 = \delta/T$ where δ (parameter of spindle position relative to workpiece) and T (distributed design temperature). An investigation of these expressions has revealed that measurement of the thermal property is the most acceptable way in practical terms, ratio 2 ($\kappa_2 = \delta/W$). The peculiar feature of this expression is that it uses lumped parameters. Moreover, the expression shows the cost of one μm of machine tool thermal accuracy (RUB/ μm).

1.4 Unit of Measurement of Thermal Properties of the Machine

For the value of the investigated property to be determined, measurements should be carried out. To measure a physical magnitude means compare it with another identical physical magnitude taken as being equal to 1. A unit of physical magnitude is its value taken as a basis to compare with physical magnitudes of the same kind in cases where quantitative evaluation of such magnitudes is made. The sizes of physical magnitude units are reproduced, stored and transmitted with the help of standards. It is necessary to have a standard unit of the thermal property measurement to be able to proceed to the evaluation of the thermal property in quantitative terms. Such standard is not included in EKS. There is a need to develop such standard. The positions for the creation of the standard in the solids' linear expansion coefficient were used as equivalent to develop a standard of the machine's thermal property. Similarly, when estimating the linear expansion coefficient, a metal rod with the predefined properties was used. A system for the evaluation of the machine's thermal properties was used as a measurement system. Experimental evaluation of the unit of measurement requires specific experimental conditions. In particular, the significant criterion is a selection of the thermal action reproduction mode. To eliminate the effect of non-equilibrium transition from the initial state to the heat equilibrium condition, the thermal action rate should be less than the relaxation rate of the sample rod material. Ambient conditions should be taken into consideration. This system state is taken under normal conditions as equal to zero. The unit of measurement will be the value of the rod thermal property calculated as the ratio between the rod thermal elongation value at the time of its

heat equilibrium and the power supplied for this elongation. The experiment results in two reference points. One point is a start point. The second point is evaluation of the properties in the heat equilibrium state of the system. This magnitude acquires the status of a thermal property unit. The thermal equilibrium condition in the heated state was evaluated by a linear displacement sensor. Power consumption was measured by a wattmeter. The impact of ambient temperature was evaluated. A time meter was used to synchronize the process parameters. Following the evaluation, the value $1.02 \cdot 10^3 \mu\text{m}/\text{kW} \cdot \text{h}$ or $1.00 \text{ mm}/\text{kWh}$ was obtained. This magnitude defines the unit of property measurement. Due to the fact that this value is high enough to assess the machine's thermal properties, it is necessary to include the fractional values. These are the microunits of the machine's thermal properties (mUTP). The value of this measurement unit part is 1 mUTP or $1.0 \pm 0.1 (\mu\text{m}/\text{kWh})$.

1.5 The Formation of Scale Thermal Properties

Nano-units of the machine's thermal properties (nUTP) are used for smaller values of this magnitude. In this case, the scale is presented in two concepts: One of them is the scale of measurements as a set of values to display the quantitative properties of the measurement object and the other is a scale as part of the indicating measuring device. To make a distinction between these concepts, we will refer to it as a "scale" in the first case and as a "scale of tools" in the second case. A scale is required to size this property in order to measure the thermal property of a structure in specific units of measurement. The structure of the hotel offers to distinguish 5 types of measurement scales: scale names, order, differences (intervals), relations and absolute scale. As the analysis showed, the ratio scale is the most appropriate "scale of tools" for assessing the thermal properties of the structure. A characteristic feature of the ratio scale is that it consists of the same ranges and has a unit of measurement and the selected starting zero point. Due to these properties, the scale does not impose any restrictions on the mathematical body used in the processing of measurement results. The scale has uniform ranges within the reference points of the entire scale. The scale of relations is the most perfect, the most informative. It defines all the mathematical operations: addition, subtraction, multiplication and division. It follows that the values of any size on the scale of relations can be added to each other, subtracted, multiplied and divided. Therefore, by applying a "tool scale" it is possible to determine how much or how many times one thermal dimension of one machine is larger or smaller than the other. The scale can be compressed or stretched by scaling. Due to the fact that the thermal motion of the structure can manifest itself in both positive and negative directions, depending on the selected starting position, the scale of the initial value continues in both directions. The scale of the measuring device is necessary to determine the value of this property and to measure the thermal properties of the structure in specific units, with a fixed starting point, a uniform division of the scale ranges. And when

developing the scale of the measuring device, the distances between the reference points are divided into homogeneous parts from 0 to 1 properties. The scale, an integral part of the measuring device, which receives data from the main linear angle, power, ambient temperature sensors and these processes are synchronized by the time meter. The value of the thermal property of the structure is fixed on the scale of the device after conversion. The list of design works for the metal-cutting machine includes the required level of resistance to thermal effects with a quantitative assessment of this value [16]. The result of the design is the creation of a structure with a certain level of thermal resistance, which is compared either by calculation or by testing the prototype of the machine [17]. The obtained value is compared with the required level using the proposed method. One is the scale of measurements as a set of values to display quantitative properties of the measurement object.

1.6 Instrument Scale Assessment of the Thermal Properties of the Machine

And the scale as part of the indicating measuring device. In order to distinguish between these concepts, we will indicate it as “scale” in the first case and as “instrument scale” in the second case. A scale is required to determine the size of this property in order to measure the thermal property of the structure in specific units of measurement. The property structure proposes to distinguish between 5 types of measurement scales: scale of names, procedure, differences (ranges) and ratios. As shown by the analysis, the ratio scale is the most appropriate scale in order to evaluate the structure’s thermal properties. A characteristic feature of the ratio scale is that it consists of the same ranges and has a unit of measurement and the selected starting zero point. Due to these properties, the scale does not impose any restrictions on the body of mathematics used in the processing of measurement results. The scale has equidimensional ranges within the reference points of the entire scale. The scale may be compressed or stretched using scaling. Due to the fact that the thermal motion of the structure is able to manifest itself in both positive and negative directions, depending on the selected starting position, the scale from the initial value is continued in both directions. An instrument scale is required to determine the size of this property and to measure the thermal property of the structure in specific units of measurement, with a fixed start point, a uniform division of the scale ranges. And when developing the instrument scale, distances between the reference points are divided into uniform parts from 0 to 1 of the property. The scale is an integral part of the device which receives data from the primary linear-angle transducers, power, ambient temperature, and these processes are synchronized by a time meter. The value of the structure’s thermal property is fixed on the instrument scale following conversion. The statement of design works for a metal-cutting machine shall include the required level of resistance to thermal

effects, with a quantification of this value [16]. The design results in the creation of a structure having a specific level of thermal resistance that is compared either by calculation or by testing a machine prototype [17]. The value obtained is compared with the required level by means of the proposed method. If the resulting value is less than the required value, then the structure will be calculated which is suitable based on this parameter and vice versa.

2 Discussion of Work Results

Thermophysical properties of coordinate boring machine 2Y450 were evaluated in order to check the proposed suggestions. The works consisted of two parts. The first phase was formed by the scale for assessment of the thermal state of the structure of the cutting machine. To do this, instead of the standard unit of measurement, the results of the study from the sample were used. This value determines the unit of the ability of the structure to withstand thermal stress. It is high enough to evaluate the properties of the machine. Therefore, you must use fractional parts of the property unit. The second stage included the study of the quantitative characteristics of the thermal properties of the machine relative to this value. Jig boring machine 2U450 was used for the examination. The procedure for the consideration of the thermal properties of the machine takes into account several specific facts. Note that the total power is measured at the machine input. However, it is spent on the thermal motion of the structure in degrees of freedom. Each of them consumes part of the incoming energy. For this purpose, one of the general principles of physics is used: the Boltzmann principle, the principle of equal distribution of energy between degrees of freedom. This principle is as follows: if the system has several degrees of freedom, its energy will be distributed between them approximately in equal parts [18]. The degree of freedom means some way the system can use energy by performing mechanical movement. Each degree of freedom in this case accounts for one-fifth of the power measured at the input of the machine. The property of the machine structure in three main coordinate directions is investigated. As a result, the following results were obtained. The value of thermal properties of resistance to thermal stress on the OX-axis was 12 mUTP, on the OY-axis—76 mUTP, on the OZ-axis—65 mUTP (in this case, the size of mUTP (mm/kWh). The thermal resistance of the structure along the OX-axis allowed the structure to move by 12 μm , along the OY-axis by 76 μm , along the OZ-axis by 65 μm . The force along the OY-axis is 6.3 times less than the resistance to thermal stress along the OX-axis. The force in the OZ-axis is 5.3 times less than in the OX-axis. The developed system for assessing the thermal condition of the structure can be used for operating equipment, during the debugging of the machine design, in the design. The presence of a unit of measurement of the thermal state of the machine creates conditions for a more accurate study of the design when the design is put into production.

Quantitative assessment of thermal properties of the structure requires a lot of needs in the machine tool industry [19, 20]. However, the most significant need is

that for the study of the thermal state of the structure is required to have a quantitative assessment of the thermal state of the machine. Such a mechanism allows a more accurate study of the physical processes that form the thermal properties of the structure [20]. High accuracy is achieved by the fact that it is possible not only to compare by assessing the difference in properties but also to estimate how many times one design is better/worse than the other. The results of this work allowed to form the conditions that determine the order of creation of the unit of measurement of the calculated thermal property of the machine [21]. In turn, the unit of measurement of thermal properties of MBS for resistance to thermal effects formed the basis for the construction of the ratio scale. According to the scale, the size of the thermal states of machine structures is formed as differences in size and their ratios. For the use of this position, the special scheme providing construction of a standard of a thermal condition of a design is developed. These properties of the method form a set of interrelated positions. This suite makes an integral part of the feedback system in order to ensure the structure's thermal quality by forming its information channel. Field of application—assessment of the thermal condition of the structure at various stages of the design life cycle from design to evaluation of repair results [22, 23]. The required level of procedural error can be achieved both by improving the standard and by using the measurement tools.

3 Conclusions

1. In practical terms, the scale makes it possible to assess the current thermal level of the structure in situations arising both during the operation and the testing of machine tools;
2. Development of a unit of measurement of a physical property enables a more in-depth study into the thermal state of the machine design in terms of both the machine accuracy and the other related issues (changes in structural rigidity under the influence of heat);
3. The unit of measurement of thermal properties forms a mechanism that makes it possible to compare different structure states during both the analysis of design options and the operation. Evaluation is possible in quantitative terms at both the levels “how much more/less” and “how many times more/less.”

Acknowledgements The author would like to express his gratitude to Professor N. N. Zubkov for his efforts to edit this article and introduce some useful comments.

References

1. Kinkel S, Lay G (2006) Technologietrends in der Produktion: Praxis der Anlagenmodernisierung in der deutschen Metall- und Elektroindustrie. Mitteilungen aus der Produktionsinnovationserhebung
2. Grossmann K (2014) Thermo-energetic design of machine tools: a systemic approach to solve the conflict between power efficiency. Accuracy and productivity demonstrated at the example of machining production. Springer, Cham
3. Zubkov NN, Ovchinnikov AI (2016) Vasil'ev S.G. Tool-workpiece interaction in deformational cutting. *Russ Eng Res* 36(3):209–212
4. Yagopolskiy AG, Vinikov DA (2017) Sravnitelnyy analiz i obobshcheniye sposobov korrektsii temperaturnykh deformatsiy v metallorezhushchikh stankakh (Comparative analysis and synthesis of methods for the correction of temperature deformations in machine tools). *Izvestiya Vuzov. Mashinostroyeniye* 68291:16–18
5. Kuznetsov AP (2017) Evolution of methods of assessing the accuracy of metal-cutting machines. *Russ Eng Res* 37(3):171–179
6. Yash R, Bhojar PD Kamble (2013) Finite element analysis on temperature distribution in turning process using deform-3D. *Int J Res Eng Technol*
7. Mekid S (2009) Introduction to precision machine design and error assessment. CRC Press
8. Schneider D, Lauer M, Voigt I, Drossel W (2016) Development and examination of switchable heat pipes. *Appl Therm Eng* 99:857–865. <https://doi.org/10.1016/j.applthermaleng.2016.01.086>
9. Putz C, Richter J, Regel (2018) Industrial consideration of thermal issues in machine tools. German Academic Society for Production Engineering (WGP)
10. Mayr J, Jedrzejewski J, Uhlmann E, Donmez MA, Knapp W, Hartig F, Wendt K, Moriwaki T, Shore P, Schmitt R, Brecher C (2012) Thermal issues in machine tools. *Wu rz, K. Wegener. CIRP Ann—Manuf Technol* 61:771–793
11. Dmitriyev BM (2017) Sposob ispytaniya metallorezhushchego stanka po parametram tochnosti pri deystvii termicheskikh protsessov (Method of testing metal cutting machine for accuracy parameters during thermal processes). *Tekhnologiya Mashinostroyeniya* 4:15–19
12. Clough DA, Fletcher S, Longstaff AP, Willoughby P (2012) Thermal analysis for condition monitoring of machine tool spindles. *J Phys Conf Ser* 364. <http://eprints.hud.ac.uk/14160>
13. Fletcher S, Longstaff AP, Myers A (2007) Measurement methods for efficient thermal assessment and error-compensation. In: *Proceedings of the topical meeting: thermal effects in precision systems*, Maastricht
14. International standard ISO 230-3 Second edition 2007-08-15 Test code for machine tools. Part 3: Determination of thermal effects Code d'essai des machines-outils—Partie 3: Évaluation des effets thermiques
15. Dmitriev BM (2018) Assessing the thermal rigidity of a metal-cutting machine. *Russ Eng Res* 38(2):94–97. <https://doi.org/10.3103/S1068798X18020065>
16. Kinkel S (2005) Anforderungen an die Fertigungstechnik von morgen: Wie verändern sich Variantenzahlen, Losgrößen, Materialeinsatz, Genauigkeitsanforderungen und Produktlebenszyklen tatsächlich Mitteilungen aus der Produktionsinnovationserhebung
17. Ramesh R (2000) Error compensation in machine tools—a review: Part II: thermal errors. *Int J Mach Tools Manuf* 40(9):1257–1284
18. Lipson H (1968) *The great experiment in physics*. Oliver & Boyd, Edinburgh
19. Dolgova IV, Kavtarev AR, Ryabykh GR (2016). Importnoye stankostroyeniye kak oriyentir dlya razvitiya otechestvennoy otrasli (Import machine tool industry as a guideline for the development of the domestic industry), vol 6. *Gumanitarnyy vestnik (MGTU im. N.E. Bauman): elektronnyy zhurnal*, p 8. <http://hmbul.ru/catalog/ecoleg/econom/367.html> <https://doi.org/10.18698/2306-8477-2016-6-367>
20. Dornfeld D, Lee D-E (2008) *Precision manufacturing*. Springer Science + Business Media, LC, p 775

21. Perri GM, Bräunig M, Gironimo GD, Tarallo A, Wittstock V, Putz M (2016) Numerical modeling and analysis of the influence of an aircooling system on a milling machine in virtual environment. *Int J Adv Manuf Technol* 86(5–8):1853–1864. <https://doi.org/10.1007/s00170-015-8322-5>
22. Popov IA, Shchelchikov AV, Gortyshov YuF, Zubkov NN (2017) Heat transfer enhancement and critical heat fluxes in boiling of microfinned surfaces. *High Temp* 55(4):524–534. <https://doi.org/10.1134/S0018151X17030208>
23. Shouchen T, Utenkov VM, Molchanov AA (2017) Optimizatsiya komponovok stankov osnovno rascheta epyury davleniya na napravlyayushchikh (Optimization of the layout of machine tools based on the calculation of the pressure profile on the guides). *Izvestiya Vuzov. Mashinostroyeniye* 9(6901)(9):6–8

Estimation Method of Slip Ring Mechanical Strength in Current Collectors in Static Setting



I. V. Kudryavtsev, O. I. Rabetskaya and A. E. Mityaev

Abstract A performance capacity of ring-shaped current collectors is crucially important for power supply systems of various application mechanisms. As a rule, increasing the downforce acting on contact surfaces helps to improve electrical performance values of slip ring contacts and, above all, contact resistance. However, this could lead to the structural failure of the slip ring material and the current collector breakdown. This paper presents a method of analytical estimation of the slip ring stress state in a static setting that would ensure the slip ring mechanical strength. Bending stresses resulting from the slip ring compression and contact stresses at points of ring conjunction with the outer and inner current-collecting rings are considered in the estimation. The estimation results have revealed that bending stresses caused by compression of the slip ring have the most adverse effect on it. The estimation techniques developed for slip rings may be also used both to assess their mechanical strength within existing current collectors and to design new types of current-collecting devices. Comparative evaluations were conducted using the ANSYS application system following the finite element method for verification of the developed techniques, which demonstrated a good level of the repeatability of results.

Keywords Ring-shaped · Current collector · Slip ring · Stress · Strain · Mechanical strength

1 Introduction

Current collectors, which have low material intensity of use and good tool life and allow for transmission of considerable electrical power under conditions of an unlimited device shaft rotation, are commonly used for electrical power transmission to rotating elements of mechanism structures and machines. Spacer slip rings

I. V. Kudryavtsev (✉) · O. I. Rabetskaya · A. E. Mityaev
Siberian Federal University, 79, Svobodny pr., Krasnoyarsk 660041, Russia
e-mail: ikudryavcev@sfu-kras.ru

that actually collect current and transmit electrical power between rotating and static current-collecting rings are the essential components of a current collector.

As the machinery becomes more advanced, it requires higher power transfer which leads to increasing energy load on the current-carrying components of ring-shaped current collectors, thus making their reliability improvement a priority. However, weight and space restrictions applied to today's current collectors create a need to miniaturize the components of current-conducting devices, which reduces their mechanical strength characteristics. A review of the related literature [1–13] leads to a conclusion that this focus area requires further consideration while the existing studies are based only on the empirical data.

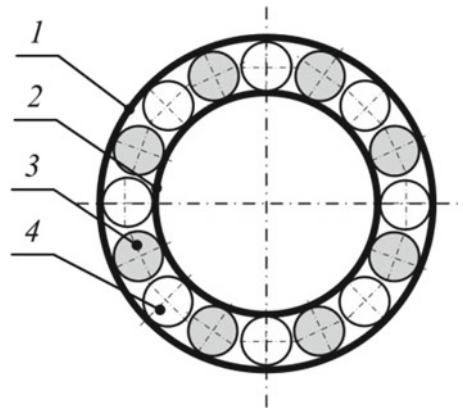
The authors of this work seek to develop a method of analytical estimation that could be used to calculate static load strength of slip rings during design and engineering process, which would ensure normal operation of manufactured current collectors. To verify the technique, numerous calculations were performed using the ANSYS software finite element method.

2 Research Objective and Analytical Mode

A current collector design (Fig. 1) includes an inner moving ring 1, an outer static ring 2, which are separated by slip rings 3 divided by insulators 4. To ensure electrical contact and power transmission between the outer and inner rings, their surfaces are pressed into the slip rings on both sides.

We will discuss low-speed rotation of the current-collecting rings, at which the inertial force can be neglected and the estimations could be performed in the elastic static setting [14, 15]. This type of approach is valid, for example, for rotating structures of spacecraft solar panels, the rotation speed of which is one cycle per day. The largest size of slip ring section (width b or thickness t) is considerably

Fig. 1 Current collector design: 1—outer current-collecting ring, 2—inner current-collecting ring, 3—slip ring, 4—spool insulator



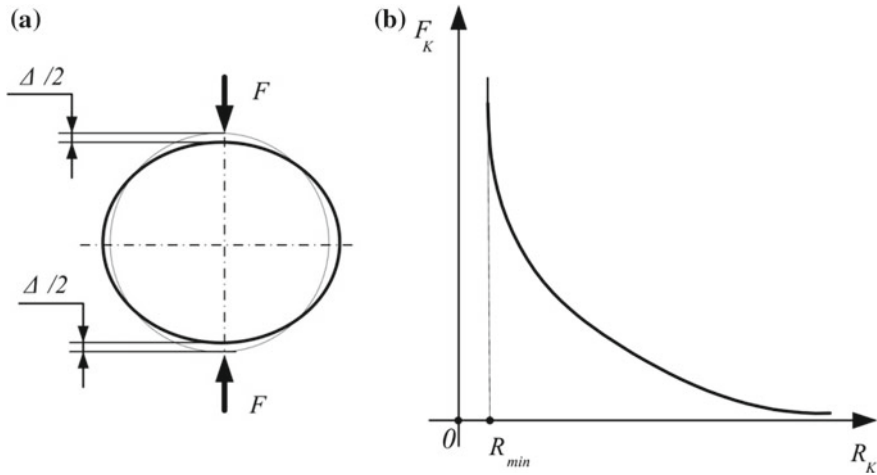


Fig. 2 Slip ring loading: **a** distorting load and equivalent strength load; **b** dependence of transition resistance R_K on compression force F_K

smaller than its circumference L . Due to this factor, a rod theory could be used as the analytical model [16].

To ensure a reliable electrical contact between the inner and outer current-collecting rings of the ring-shaped current collector, prior to its installation a slip ring is compressed on both sides by a distorting load of Δ magnitude, which will be replaced by the equivalent strength load represented by two cross forces in the analytical model (Fig. 2a).

An increasing compression force acting on the slip ring reduces transient contact resistance to a certain minimal constant value (Fig. 2b). For contact elements with recently removed insulation, according to the empirical equation [17], dependence of the transition resistance on pressure takes a nonlinear form as follows:

$$R_K = \frac{k}{(0,1F_K)^m} \cdot 10^{-6} \tag{1}$$

where m and k are empirical coefficients.

Apart from enhancing contact quality [18–20], an excessive increase in compression force acting on the slip ring may cause its structural failure that is why it is necessary to develop techniques for assessment of the ring performance capability. We will develop a method of analytical estimation of the slip ring stress state in a static setting that would ensure the slip ring mechanical strength. Device symmetry (Fig. 1) provides for equal loading conditions of all slip rings; therefore, the stress state of only one ring will be discussed.



3 Solution Technique

When the slip ring is compressed, its overall stress state could be broken down into two phases:

- (1) occurrence of slip ring bending stresses,
- (2) occurrence of contact stresses in the points of slip ring conjunction with the outer and inner current-collecting rings.

Each type of loading will be further considered individually.

3.1 Bending Stresses of the Slip Ring

According to [21], a relation between the applied force F and its corresponding ring strain by a Δ magnitude (Fig. 2a) in this case will be written as follows:

$$F = \Delta \cdot \frac{EJ}{r^3(2/\pi - \pi/4)} \quad (2)$$

where J is the inertia moment of the ring as follows:

$$J = bt^3/12 \quad (3)$$

Δ is the ring deformation caused by compression; E is the elasticity module of the material; b , t and r are, respectively, width, thickness and radius of the ring.

When a slip ring is compressed, its cross sections will be influenced by the following forces: axial compression force N , cross force Q and bending moment M , which, according to [21], maybe calculated using equations:

$$N = -\frac{F}{2} \sin \varphi; \quad Q = -\frac{F}{2} \cos \varphi; \quad M = Fr \left(\frac{1}{\pi} - \frac{1}{2} \sin \phi \right) \quad (4)$$

Diagrams of inner acting forces and bending moment are given in Fig. 3.

Action of inner forces and moments will create direct and shear stresses, the current and maximum magnitude of which could be defined using the following dependences [21]:

$$\sigma_{N_{\max}} = -\frac{F}{2 \cdot bt}, \quad \tau_{Q_{\max}} = -\frac{3 \cdot F}{4 \cdot bt}, \quad \sigma_{M_{\max}} = \frac{6Fr}{\pi \cdot bt^2} \quad (5)$$

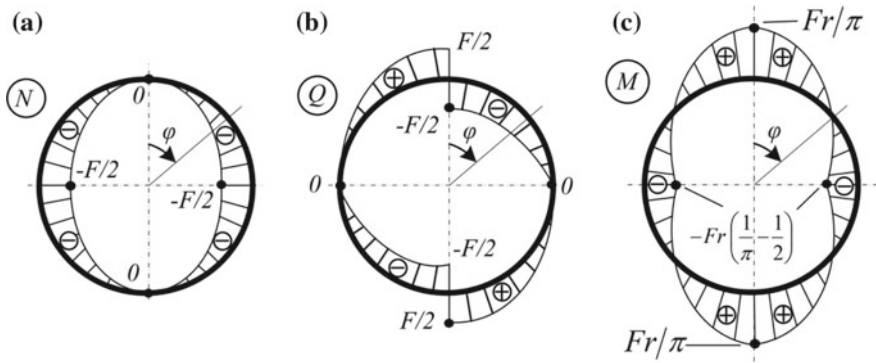


Fig. 3 Diagrams of inner forces and bending moment acting in a slip ring: **a** axial force *N*; **b** cross force *Q*; **c** bending moment *M*

3.2 Contact Stresses in the Slip Rings

The slip ring 3 is compressed by the outer 1 and inner 2 rings of the current collector in points *A* and *B* (Fig. 4), where direct contact stresses will occur. Direct contact stresses σ_K are defined using Hertz formula [22, 23] as follows:

$$\sigma_K = 0,418 \sqrt{\frac{F \cdot E}{b \cdot R}} \tag{6}$$

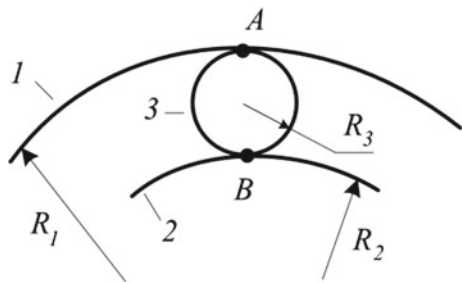
where *R* is a relative radius of curvature.

Equation (6) is valid for both contact points (*A* and *B*) and only differs by dependence for the relative radius of curvature as follows:

$$R_A = \frac{R_1 \cdot R_3}{R_1 - R_3}, R_B = \frac{R_2 \cdot R_3}{R_2 + R_3} \tag{7}$$

where R_1 , R_2 and R_3 are, respectively, internal, external and current-collecting ring radiuses.

Fig. 4 Slip ring interface circuit: 1—outer current-collecting ring; 2—inner current-collecting ring; 3—slip ring



Dependences (6, 7) demonstrate that the highest contact stresses will act at point *B* (Fig. 4).

4 Estimation Results and Verification

To verify the developed technique, a comparative evaluation of the stress state of the current collector current-conducting ring was performed using the proposed analytical method and finite element method. The simulation was carried out in the ANSYS software environment. The evaluation results revealed a good level of repeatability: for all types of the considered stresses, the disarrangement was 2.1–4.5% suggesting the proposed method of analytical estimation is valid.

The evaluation results analysis indicated that direct stresses in the slip ring of the considered current collector caused by bending moment action are many times greater than stresses caused by any other force. Stresses from axial ($\sigma_{N_{\max}}$) and cross forces ($\tau_{Q_{\max}}$) are approximately 50 times smaller, and contact (σ_K) stresses are approximately four times smaller than bending stresses ($\sigma_{M_{\max}}$).

5 Conclusion

The authors have proposed a method of analytical estimation of the stress state of slip rings, which could be used to define static load strength allowing to perform checking calculations for existing current collectors and to provide grounds for design and engineering decisions made while producing new types of current collectors, in order to ensure normal operation of these devices.

The obtained results may be used when developing new methods of mechanical strength estimation of current-collecting rings in a dynamic setting at high rotation speed and with regard to occurring flywheel and fatigue effects.

Acknowledgements The reported study was funded by Russian Foundation for Basic Research, Government of Krasnoyarsk Territory, Krasnoyarsk Regional Fund of Science, to the research project: “Development of methods of modeling and analytical calculation of a static and quasistatic state of extended thin-walled not axisymmetric designs of wave guides of antenna-feeder systems”.

References

1. Kosurina TA (2012) Actual problems of improvement of electric power supply systems of spacecrafts. *Kosmonavtika i raketostroenie* 3(68):66–69
2. Grishin AA, Smirnov NA, Haritonov AI (2014) Analysis of constructions of current-collecting devices. *Vestnik SibGAU* 5(57):146–153

3. Grishin AA (2017) Losses on current-collecting devices by transfer of electrical energy from solar batteries on the spacecraft. *Trudy MAI* 97:6–7
4. Holmberg K (2006) Tribological contact analysis of a rigid ball sliding on a hard coated surface. Part I: modelling stresses and strains. *Surf Coat Tech* 200:3793–3809
5. Taeva IS (1987) Fundamentals of the theory of electric devices. Vysshaya shkola, Moscow
6. Gerasimova VG (1981) Electric reference book. Energoizdat, Moscow
7. Demkin NB (1981) Quality of a surface and contact of details. Mashinostroenie, Moscow
8. Komarov AA (2001) Electric contacts. SamIIT, Moscow
9. Holm R (1958) Electric contacts. Springer, Berlin
10. Boychenko VI (1978) Contact connections of conductor line. *Energiya*, Leningrad
11. Merl V (1962) Elektricheskie kontakty. Gosenergoizdat, Moscow-Leningrad
12. Bredihin AN (1980) Electric contact connections. *Energiya*, Moscow
13. Domkin NB (1970) Engagement of rough surfaces. Nauka, Moscow
14. Troschenko VT (1978) Strength of metals at variable loadings. *Nauk. dumka*, Kiev
15. Golovin SA, Pushkar A, Levin DM (1987) The elastic and damping properties of structural metal materials. Metallurgiya, Moscow
16. Feodos'ev VI (1999) Strength of materials. MGTU, Moscow
17. Shlykov YP (1977) Contact and thermal resistance. *Energiya*, Moscow
18. Kim EI, Omel'chenko VG, Harin SN (1977) Mathematical models of processes in electric contacts. Nauka, Alma-Ata
19. Zalesskiy AM (1967) Thermal calculations of electric contacts. *Energiya*, Leningrad
20. Usov VV (1963) Metallurgical science of electric contacts. Gosenergoizdat, Moscow
21. Birger IA, Shorr BF, Iosilevich GB (1993) Calculation on strength of details of machines. Mashinostroenie, Moscow
22. Landau LD, Livshits EM (1987) Elastic theory. Nauka, Moscow
23. Johnson KL (2001) Contact mechanics. Cambridge University Press, London

Ensuring Operational Life and Reliability of Contact Rings in Plastic State



I. V. Kudryavtsev, E. S. Novikov and V. G. Demin

Abstract Reliability of collector rings throughout their service role plays a key role in the performance of power supply systems of various equipment and largely depends on strength and reliability of all of their components, particularly contact rings. One of the most important features of collector rings is their contact resistance. It is usually decreased by using non-ferrous and precious metals and a simultaneous increase of tracking force. However, this approach leads to a sharp increase of stresses within the contact rings. These stresses may even reach or exceed the yield limit of the material and cause its eventual destruction. Nonetheless, performance of contact rings outside the yield limit is possible with using the low-cyclic fatigue area of the fatigue curve. This paper proposes the respective methods of analytical calculation of contact rings' fatigue and probability of their no-failure performance in plastic state.

Keywords Collector ring · Contract ring · Strength · Plasticity · Low-cyclic · Fatigue · Durability · Probability · Failure

1 Introduction

Collector rings are used to transfer electric power from rotating parts to fixed base of various equipment, for instance, in rotating solar panels, rotating platforms, towers, etc. [1–5].

Ensuring necessary reliability of collector rings during their service life largely depends on performance conditions of all of their components, particularly contact rings. The most important features of the collector rings are their electrical characteristics, namely their resistance. The most effective method to increase conductivity consists in using non-ferrous and precious metals (copper, silver, gold, etc.) to manufacture collector rings, as these metals possess decent electrical

I. V. Kudryavtsev (✉) · E. S. Novikov · V. G. Demin
Siberian Federal University, 79, Svobodny pr., Krasnoyarsk 660041, Russia
e-mail: ikudryavcev@sfu-kras.ru

characteristics, as well as in increasing the tracking force to obtain minimal contact resistance [3–13]. However, these materials are very malleable and have low yield limits; therefore, this approach leads to quick increase of stresses within the contact ring, which may exceed the yield limit of materials even at relatively low tracking forces.

The situation may be even worse for important objects such as space satellites, which should work in the orbit in a totally autonomous mode for 10–12 years or more.

Still, if the required number of load cycles of contact rings is relatively small, then the plastic loading of their material is possible by using the low-fatigue area of the fatigue curve. This paper proposes the respective methods of analytical calculation. Their accuracy is ensured through using well-known provisions of fatigue theory and reliability theory when analyzing mechanical systems.

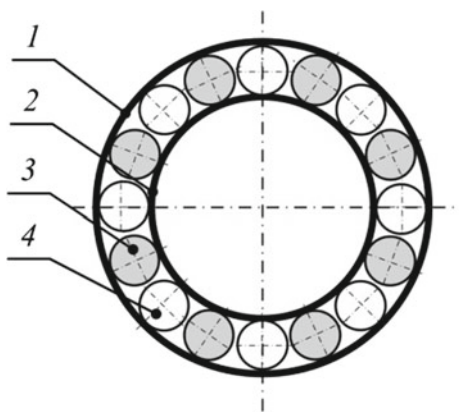
2 Problem Statement

The function of the collector ring (Fig. 1) is to transfer electric power using pressed contact rings (4) located between the external (1) and internal (2) rings. Since, we analyze a rather large compression of contact rings, Fig. 1 shows them in a very compressed state. Isolators 3 act as separators and ensure even distribution of contact rings on circumference.

In order to ensure electric contact between internal and external rings of the collector ring, contact ring is subject to compression at a set strain load, Δ which we will replace in our calculation by the equivalent force F (Fig. 2a).

As the compression force F of contact ring increases, contact resistance decreases to a minimal value R_{\min} (Fig. 2b) and does not decrease further even as the force increases more and more. The dependence of contact resistance on

Fig. 1 Design of connector ring: 1—external connector ring; 2—internal connector ring; 3—isolating roll; 4—contact ring



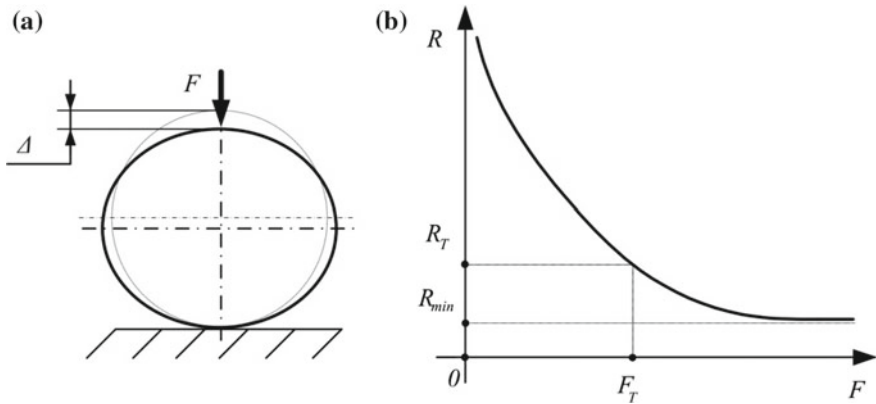


Fig. 2 Loading of contact ring: **a** strain load and equivalent force F ; **b** dependence of contact resistance R on compression force F

compression force is non-linear and is calculated according to the following empirical formula [14–17]:

$$R_K \sim k \cdot F^{-m} \tag{1}$$

where m and k are reference constants obtained empirically.

When using metals such as copper, silver, gold, etc., yield limit of the contact ring material may be reached at the compression force value FT , at which contact resistance R_T is significantly lower than the minimal value of R_{min} . Further increase of the contact ring’s compression force may lead to exceeding its strength limits; therefore, one has to develop methods to evaluate its performance in a plastic state.

Suppose the rotation rate of collector rings is as negligible as it is possible, therefore we can neglect inertial effect. Let us use a static problem [18, 19] in the elastic range. This is true, for instance, for collector rings of solar panels of space modules, the rotation rate of which is about 10–4 rpm. Cross section of contact rings is rectangular in shape (width b and thickness t), and their dimensions are substantially smaller than their circumference, which makes it possible to use the rod theory for our calculations [20]. Due to symmetrical design (Fig. 1), loading conditions of all contact rings are the same, and it is enough to analyze the strain of only one ring.

In order to describe the behavior of non-ferrous and precious metals used to manufacture contact rings under loading, we take the model of ideal elastoplastic material. In this case, evaluation of material state boils down to check whether maximum normal compression values have reached its yield limit.



3 Problem Solution

When compressing a contact ring, within it a range of force factors and their respective stresses appears. Preliminary studies [21] have shown that contact rings work in the conditions of cross flexure caused by force F , and the most important in their compressed state is flexural stresses.

3.1 Maximum Flexural Stresses of Contact Rings

Normal stresses $\sigma_{M_{\max}}$ caused by flexure of contact rings due to compression force F (Fig. 2a) are determined [22, 23] according to the following equation:

$$\sigma_{M_{\max}} = \frac{M(\varphi)}{W_z} = \frac{Fr}{\pi \cdot W_z} \quad (2)$$

where M is the flexure moment as a function of contact ring position; F is the compression force equivalent to deformation at a value Δ and is determined according to the formula:

$$F = \Delta \cdot \frac{2EJS}{r^3 S(\pi/4 + 1/4 - 2/\pi) + rJ(\pi/4 + 1/4)} \quad (3)$$

$J = bt^3/12$ is the moment of inertia of ring's cross section; $W_z = bt^2/6$ is the resistance moment of ring's cross section; Δ is the ring deformation; E is the Young modulus; r is the average ring radius; and $S = b \cdot t$ is the ring's cross-sectional area.

In order for the contact ring material to transfer into the plastic state (according to the accepted design model), the following condition should be met:

$$\sigma_{M_{\max}} \geq \sigma_T \quad (4)$$

Obtained dependencies (2–6) help to determine contact ring deformation value at which the material would turn into the plastic state.

3.2 Fatigue Strength of Contact Rings

During its performance, a contact ring continuously rolls over the surfaces of external and internal collector rings, and each of its points is subject to fluctuating stresses $\sigma_{M_{\max}} = f(\varphi)$, which change cyclically over time from zero to material's yield limit (Fig. 3).

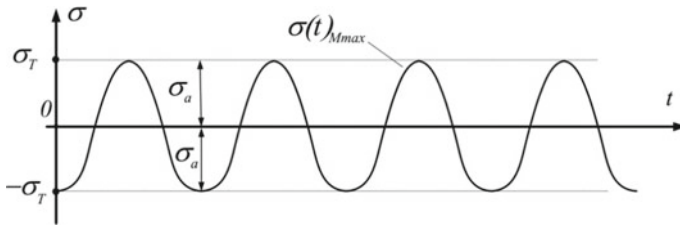
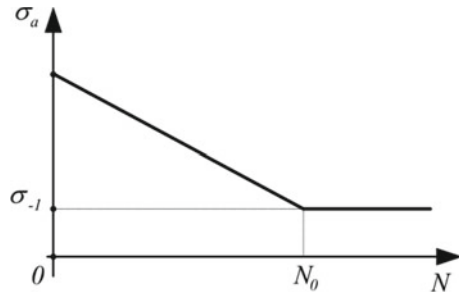


Fig. 3 Symmetrical loading cycle of contact ring

Fig. 4 An example of fatigue curve



When subject to cyclical loading, the material strength is calculated based on the fatigue curve [23], which determines the dependence of material yield limit from the number of loading cycles of the contact ring (Fig. 4). In order to ensure performance of contact ring material in the conditions of yield, one has to analyze the number of loading cycles significantly smaller than the yield limit (107). This condition is met in slow-speed devices; for instance, collectors in ЭКСПИЕСС (EXPRESS) space modules. Their contact rings are subject to about 7×10^4 loading cycles throughout their entire service life.

A slope on the left of the fatigue curve corresponds to low-cycle fatigue at which the number of loading cycles is significantly lower than the value corresponding to low-cycle fatigue limit ($N \ll 107$), and tolerable stresses would be substantially larger than the durability limit, reaching the material’s yield limit.

The equation for the fatigue curve’s slope on logarithmic scale is as follows:

$$\sigma_a + K \lg N = \sigma_{-1}(N) + K \lg N_0 \tag{5}$$

where σ_{-1} is the material’s durability limit for set a number of loading cycles N ; σ_a is the amplitude of fluctuating stresses and the respective number of loading cycles N (if $N = 1$, then $\sigma_a = \sigma_B$); σ_B is the strength limit of contact ring material; and K is the factor determining the inclination of straight fatigue line on logarithmic scale based on physical and mechanical properties of the material used to manufacture parts under analysis and their dimensions.



Now, it is possible to calculate durability limit for the set number of loading cycles according to the inverse dependence:

$$\sigma_{-1}(N) = \sigma_B + K(\lg N - \lg N_0) \quad (6)$$

At low-cycle fatigue ($N \ll N_0$), there is a specific range of loading cycles where $\sigma_{-1}(N) = \sigma_T$, therefore, the contact ring material will perform in the conditions of plastic loading.

3.3 Contact Ring Reliability

Reliability of contact rings in plastic state will be determined according to the no-failure possibility. The condition for destruction is when maximum stresses within the contact ring exceeds the durability limit of the material used to manufacture this ring [24]:

$$\sigma_{\max} = \sigma_{M_{\max}} > \sigma_{-1}(N) \quad (7)$$

Let us introduce the non-destruction function:

$$\Delta\sigma = \sigma_{-1}(N) - \sigma_{\max} \quad (8)$$

Suppose σ_{\max} and $\sigma_{-1}(N)$ are random variables and assume that their values are distributed normally. The following statistical parameters are known for their distribution: mean values $\bar{\sigma}_{\max}$, $\bar{\sigma}_{-1}$, and SD $S_{\Delta\sigma}$. Then, the likelihood of destruction corresponds to the likelihood of the following condition being met:

$$P_{\text{failure}} = P(\Delta\sigma) = P(\Delta\sigma < 0) = F(0) \quad (9)$$

and the no-failure probability is

$$P_{\text{no-failure}} = 1 - P_{\text{failure}} \quad (10)$$

Here, $P(\Delta\sigma)$ is the distribution function of the random variable $\Delta\sigma$:

$$P(\Delta\sigma) = \frac{1}{2} + \Phi\left(\frac{\Delta\sigma - \Delta\bar{\sigma}}{S_{\Delta\sigma}}\right) \quad (11)$$

where $\Phi(x)$ is Laplace's function. Specify

$$v_{\Delta\sigma} = \frac{S_{\Delta\sigma}}{\Delta\bar{\sigma}} = \frac{\sqrt{S_{\sigma_{-1}}^2 + S_{\sigma_{\max}}^2}}{\bar{\sigma}_{-1} - \bar{\sigma}_{\max}} \quad (12)$$

By approximating the Laplace function [25], the equation to determine the likelihood of destruction will be as follows:

$$P_{\text{failure}} = \frac{v_{\Delta\sigma}}{\sqrt{2\pi}} \cdot e^{\left(\frac{-\frac{1}{2v_{\Delta\sigma}^2}}{v_{\Delta\sigma}^2}\right)} \cdot (1 - v_{\Delta\sigma}^2 + 3v_{\Delta\sigma}^4 - v_{\Delta\sigma}^6 + \dots) \quad (13)$$

After introducing these values into (17) and by limiting terms of series to the 6th power inclusive, we will obtain accurate values of destruction and no-failure performance likelihood for contact rings.

4 Conclusion

This paper has proposed methods to analyze and calculate fatigue strength and reliability of contact rings of collector rings (in a stressed state) which work in conditions of plasticity and helps to ensure their reliability, as well as to determined the likelihood of their no-failure performance within the specified service life. These methods could be used to justify design and technological solutions made when designing a new or verifying current collector rings.

Acknowledgements The reported study was funded by Russian Foundation for Basic Research, Government of Krasnoyarsk Territory, Krasnoyarsk Regional Fund of Science, to the research project: “Development of methods of modeling and analytical calculation of a static and quasistatic state of extended thin-walled not axisymmetric designs of wave guides of antenna-feeder systems”.

References

1. Kosurina TA (2012) Actual problems of improvement of electric power supply systems of spacecrafts. *Kosmonavtika i raketostroenie* 3(68):66–69
2. Grishin AA, Smirnov NA, Haritonov AI (2014) Analysis of constructions of current-collecting devices. *Vestnik SibGAU* 5(57):146–153
3. Grishin AA (2017) Losses on current-collecting devices by transfer of electrical energy from solar batteries on the spacecraft. *Trudy MAI* 97:6–7
4. Holmberg K (2006) Tribological contact analysis of a rigid ball sliding on a hard coated surface. Part I: modelling stresses and strains. *Surf Coat Tech* 200:3793–3809
5. Taeva IS (1987) Fundamentals of the theory of electric devices. *Vysshaya shkola*, Moscow
6. Gerasimova VG (1981) Electric reference book. *Energoizdat*, Moscow
7. Demkin NB (1981) Quality of a surface and contact of details. *Mashinostroenie*, Moscow
8. Komarov AA (2001) Electric contacts. *SamIIT*, Moscow
9. Holm R (1958) *Elektric contacts*. Springer, Berlin
10. Boychenko VI (1978) Contact connections of conductor line. *Energiya*, Leningrad
11. Merl V (1962) *Elektricheskie kontakty*. Gosenergoizdat, Moscow-Leningrad
12. Bredihin AN (1980) Electric contact connections. *Energiya*, Moscow
13. Domkin NB (1970) Engagement of rough surfaces. *Nauka*, Moscow

14. Shlykov YP (1977) Contact and thermal resistance. Energiya, Moscow
15. Kim EI, Omel'chenko VG, Harin SN (1977) Mathematical models of processes in electric contacts. Nauka, Alma-Ata
16. Zalesskiy AM (1967) Thermal calculations of electric contacts. Energiya, Leningrad
17. Usov VV (1963) Metallurgical science of electric contacts. Gosenergoizdat, Moscow
18. Troschenko VT (1978) Strength of metals at variable loadings. Nauk. dumka, Kiev
19. Golovin SA, Pushkar A, Levin DM (1987) The elastic and damping properties of structural metal materials. Metallurgiya, Moscow
20. Feodos'ev VI (1999) Strength of materials. MGTU, Moscow
21. Grishin AA, Kudryavtsev IV (2018) Strength of contact rings of current-collecting devices of spacecrafts. Kosmonavtika i raketostroenie 3(102):81–91
22. Birger IA, Shorr BF, Iosilevich GB (1993) Calculation on strength of details of machines. Mashinostroenie, Moscow
23. Terent'ev VF, Korableva SA (2015) Fatigue of metals. Nauka, Moscow
24. Pechinkin AV (2004) Probability theory. MGTU, Moscow
25. Ventcel' ES (2001) Probability theory. Vysshaya shkola, Moscow

Deformation and Stability of Cylindrical Shells Under Irregular Radial Loading



S. V. Makhnovich, D. A. Permyakov and Yu. M. Khishchenko

Abstract The article considers a non-axisymmetric deformation and stability of a compressed aircraft shell. Particular attention is paid to modeling contact interaction of shells with transverse shock-absorbing belts. To analyze shell deformations, we used the iteration method, taking into account a nonlinear change in the reaction of the shock-absorbing belt when there are structure displacements. The shell stability equations were discretized by the Bubnov–Galerkin method using Fourier series. The developed model was used to study the deformation mode of constructively and technologically orthotropic shells exposed to local loads of shock-absorbing belts. The simulation models were verified with the results of testing model and actual shells.

Keywords Orthotropic shell · Irregular loading · Bearing pressures · Asymmetric deformation · Shell stability · Comparison with an experiment

1 Introduction

The article discusses a design model of the deformations of a cylindrical body of the aircraft shells under the launch load. In addition to the traditional loads—the axial compression N and the external pressure p —the body is exposed in this case to the reaction forces of the transverse shock-absorbing belts z_R and the guiding devices [1]. The effect of these reactions on the body shell is non-axisymmetric and is of a contact nature. This circumstance represents the main difficulty in modeling shell deformation and, in particular, its loss of stability.

The solution of contact problems within the theory of shells was discussed in [2–5]. When the contact area is of a relatively small width, the contact is considered only along the generatrix or the meridian. The contact problem becomes one-dimensional and is usually solved by the method of integral equations. Stated

S. V. Makhnovich (✉) · D. A. Permyakov · Yu. M. Khishchenko
South Ural State University, 76, Lenin Av., 454080 Chelyabinsk, Russia
e-mail: makhnovichsv@susu.ru

like this, the problems of contact action of rigid supports along the circular arcs of a semi-infinite shell have been solved. The problems of contact interaction of cylindrical shells with the elastic foundation were considered in [6]. Narrow supports with contact areas, acceptably set equal to a line segment, and also the interaction over the two-dimensional contact area were also considered. The solution is made with the method of trigonometric series. The importance of choosing the elastic foundation model is emphasized. Usually, the simplest linear Winkler model with one or two coefficients of subgrade reaction is used. The coefficients are determined from approximate elastic body models or experimentally. It has been noted that the stiffness parameters of the foundation greatly affect the distribution of contact forces. The main disadvantage of such models is complexity of the problem solution, especially when the stiffness property of the elastic foundation is distinctly nonlinear. This circumstance, as well as the asymmetry of the effect, significantly complicates the analysis of the deformational stability of the shell. The solution to the stability problem of a cylindrical shell subjected to non-axisymmetric pressure was first considered by Mushtari [7]. However, numerical results were obtained later [8]. This study, unlike the classical formulation of [7], determines the subcritical state of the shell basing on the equations of the linear moment theory. The characteristic features of stability loss by cylindrical shells under non-axisymmetric cosine and locally uniform pressure were studied in [9, 10]. The qualitative changes detected in the deformation and stability of shells under such loads proved to be so diverse that the research is still under way. Important results were obtained in [11–14].

A review of the obtained results shows that although the pressure is local, the Euler method makes it possible to obtain critical load values sufficiently accurate for practical purposes in many cases. In this case, the solution is much simpler than the solutions obtained by methods involving geometric nonlinear equations of shell theory. It is also noteworthy that in known studies, the function of the transverse load distribution along the shell surface is assumed to be unchanged during loading. Studies of deformation and stability of shells subjected to contact loads that vary nonlinearly during loading are at the initial stage, despite their practical importance.

The paper considers a computational model of deformation of an orthotropic shell subjected to loading, which involves transverse contact effects. Its reliability is confirmed by comparing it with experiments and known solutions to the problem that considers transverse loading without taking into account the contact characteristics.

2 Shell Deformation Before Stability Loss

An orthotropic cylindrical shell with the radius R , thickness h , and length L , is loaded with axisymmetric axial and radial loads, as well as with nonuniform pressure $q_z = q_0 z_1(\xi, \theta)$ along a part of the side surface, where $\xi = x/R$ and $\theta = y/R$ are the longitudinal and the circumferential relative coordinates in Fig. 1.

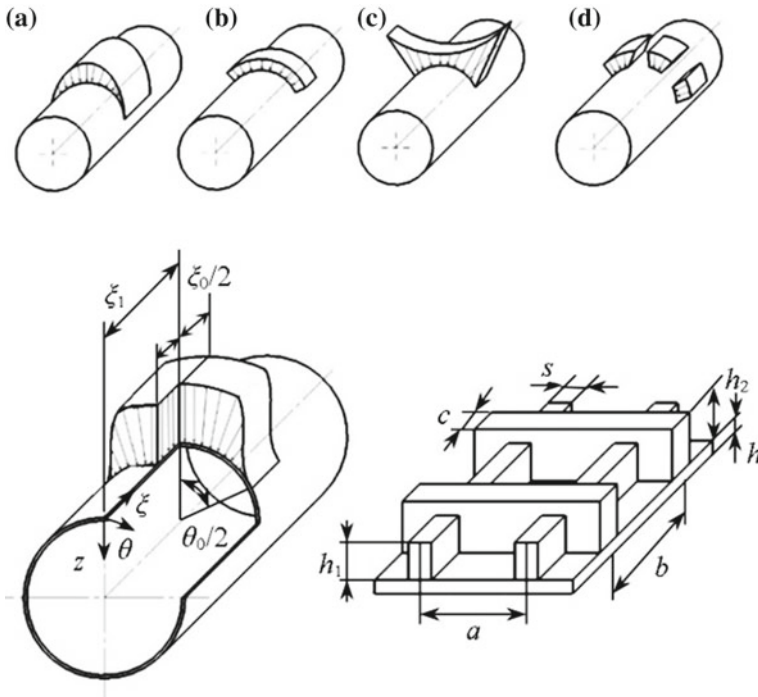


Fig. 1 Design diagram of a shell and types of local loads: **a** cosine type, **b** locally uniform, **c** parabolically distributed, and **d** pressure on several areas

The composite material stack in the shell sheeting is generally orthotropic, and the axes of elastic symmetry are parallel to the coordinate axes.

Stiffening ribs are unidirectionally reinforced and located along the lines of the main shell curvatures. The mechanical characteristics of each sheeting layer of the shell and ribs are determined as those of unidirectionally reinforced material [15]. The stiffness matrix components for the multilayer stack are determined on the assumption of skidless combined action of the layers [16] using the Kirchhoff–Love hypotheses to define the shell deformation. Equations of elastic equilibrium of the shell in the cylindrical coordinate system ξ, θ, z are written in the matrix form:

$$\mathbf{LW} = \mathbf{Z}_H R^2, \tag{1}$$

where $\mathbf{W} = \{u_0, v_0, w\}^T$ is the column vector of shell displacements before it loses stability along the axes ξ, θ, z ; $\mathbf{Z}_H = \{q_x, q_y, q_z\}^T$ is the external load vector; $\mathbf{L} = \{L_{ij}\}$, ($i, j = 1, 2, 3$) is the matrix of differential operators:

$$\begin{aligned}
L_{11} &= C_{11} \frac{d^2}{d\xi^2} + C_{66} \frac{d^2}{d\theta^2}; & L_{12} &= (C_{12} + C_{66}) \frac{d^2}{d\xi d\theta}; & L_{21} &= L_{12}; & L_{22} &= C_{66} \frac{d^2}{d\xi^2} + C_{22} \frac{d^2}{d\theta^2}; \\
L_{13} &= C_{12} \frac{d}{d\xi} + \frac{1}{R^2} \left(D_{11} \frac{d^3}{d\xi^3} - D_{66} \frac{d^3}{d\xi d\theta^2} \right); & L_{23} &= -C_{22} \frac{d}{d\theta} + \frac{1}{R^2} (D_{12} + 3D_{66}) \frac{d^3}{d\xi^2 d\theta}; \\
L_{31} &= L_{13}; & L_{32} &= L_{23}; \\
L_{33} &= C_{22} + \frac{1}{R^2} \left[D_{11} \frac{d^4}{d\xi^4} + 2(D_{12} + 2D_{66}) \frac{d^4}{d\xi^2 d\theta^2} + D_{22} \left(\frac{d^4}{d\theta^4} + 2 \frac{d^2}{d\theta^2} + 1 \right) \right].
\end{aligned}$$

The components of the stiffness matrix C_{ij} and D_{ij} have the following form:

$$\begin{aligned}
C_{11} &= C_{11}^0 + \frac{E_{1p}sh_1}{a}; & C_{22} &= C_{22}^0 + \frac{E_{2p}ch_2}{b}; & C_{12} &= C_{12}^0; \\
C_{66} &= C_{66}^0; & D_{11} &= D_{11}^0 + \frac{E_{1p}sh_1}{4a} (h_1 + h)^2 + \frac{E_{1p}sh_1^3}{12a}; & & (2) \\
D_{22} &= D_{22}^0 + \frac{E_{2p}ch_2}{4a} (h_2 + h)^2 + \frac{E_{2p}ch_2^3}{12b}; & D_{12} &= D_{12}^0; & D_{66} &= D_{66}^0;
\end{aligned}$$

where according to [16], the multi-layer shell sheeting has the form:

$$\begin{aligned}
C_{ij}^0 &= 2 \left[B_{ij}^{k+1} h_{k+1} + \sum_{n=1}^k B_{ij}^n (h_n - h_{n+1}) \right]; \\
D_{ij}^0 &= 2 \left[B_{ij}^{k+1} h_{k+1}^3 + \sum_{n=1}^k B_{ij}^n (h_n^3 - h_{n+1}^3) \right]; \quad i, j = 1, 2
\end{aligned}$$

E_{1p} and E_{2p} are the reduced elastic moduli of the longitudinal and circumferential ribs, respectively. The elasticity coefficients B_{ij}^k for the k th elementary layer with the thickness h_k are obtained by solving the system of six equations of the generalized Hooke's law when the layers are symmetrically arranged with respect to the middle surface of the shell sheeting.

Given the hinged bearing of the shell ends, $v_0 = 0$; $w_0 = 0$; $N_{11}^0 = 0$; $M_{11}^0 = 0$; ($\xi = 0, L/R$) the solution of Eq. (1) can be found in the following form:

$$\begin{aligned}
u_0 &= \sum_{m=0}^{\infty} \sum_{n=0}^{\infty} u_{mn} \cos \bar{m} \xi \cos n\theta; & v_0 &= \sum_{m=1}^{\infty} \sum_{n=1}^{\infty} v_{mn} \sin \bar{m} \xi \sin n\theta; \\
w_0 &= \sum_{m=1}^{\infty} \sum_{n=0}^{\infty} w_{mn} \sin \bar{m} \xi \cos n\theta,
\end{aligned} \quad (3)$$

where $\bar{m} = \frac{m\pi R}{L}$; $m = 1, 2, 3 \dots$; $n = 0, 1, 2 \dots$; $w_{mn} = \frac{q_0 R^2}{C_{11}} \frac{\Delta_{33}}{A} q_{mn}$;
 $u_{mn} = \frac{q_0 R^2}{C_{11}} \frac{\Delta_{31}}{A} q_{mn}$; $v_{mn} = \frac{q_0 R^2}{C_{11}} \frac{\Delta_{32}}{A} q_{mn}$;

$$\begin{aligned}
A_{31} &= a_{13}a_{22} - a_{12}a_{23}; \quad A_{32} = a_{13}a_{21} - a_{11}a_{23}; \quad A_{33} = a_{11}a_{22} - a_{12}^2; \\
A &= a_{13}A_{22} - a_{23}A_{23} + a_{33}A_{33}; \quad a_{11} = -(\bar{m}^2 + \delta_3 n^2); \\
a_{12} &= (\delta_2 + \delta_3)\bar{m}n; \quad a_{13} = -\delta_2\bar{m} - \bar{m}(\omega_1\bar{m}^2 - \omega_4 n^2); \quad a_{21} = a_{12}; \\
a_{22} &= -(\delta_3\bar{m}^2 + \delta_1 n^2); \quad a_{23} = n[\delta_1 + (\omega_3 + 3\omega_4)\bar{m}^2]; \\
a_{33} &= \delta_1 + \omega_1\bar{m}^4 + 2(\omega_3 + 2\omega_4)\bar{m}^2 n^2 + \omega_2(n^2 - 1)^2; \quad a_{31} = -a_{13}; \\
a_{32} &= -a_{23}; \quad \delta_1 = \frac{C_{22}}{C_{11}}; \quad \delta_2 = \frac{C_{12}}{C_{11}}; \quad \delta_3 = \frac{C_{66}}{C_{11}}; \\
\omega_1 &= \frac{D_{11}}{C_{11}R^2}; \quad \omega_2 = \frac{D_{22}}{C_{11}R^2}; \quad \omega_3 = \frac{D_{12}}{C_{11}R^2}; \quad \omega_4 = \frac{D_{66}}{C_{11}R^2}; \\
q_{mn} &= \frac{2\delta_n R}{\pi L} \iint_{S_0} z_1(\xi, \theta) \sin \bar{m}\xi \cos n\theta d\xi d\theta;
\end{aligned} \tag{4}$$

q_{mn} are the coefficients of expansion into the Fourier series of the external load with the intensity q_z , distributed within the region S_0 of the lateral shell surface according to the law $z_1(\xi, \theta)$; $\delta_n = 1$ with $n = 0$; $\delta_n = 2$ with $n \geq 1$.

Subcritical displacements (3) from Cauchy's equations and Hooke's law correspond to the internal forces and moments in the shell:

$$\begin{aligned}
N_{11}^0 &= \frac{C_{11}}{R} \sum_{m=1}^{\infty} \sum_{n=0}^{\infty} [\delta_2 n v_{mn} - \bar{m} u_{mn} - (\delta_2 + \bar{m}^2 \omega_1) w_{mn}] (sc)_{mn}; \\
M_{22}^0 &= C_{11} \sum_{m=1}^{\infty} \sum_{n=0}^{\infty} [\omega_3 \bar{m}^2 - \omega_2 (1 - n^2)] w_{mn} (sc)_{mn}; \\
N_{22}^0 &= \frac{C_{11}}{R} \sum_{m=1}^{\infty} \sum_{n=0}^{\infty} \{ \delta_1 n v_{mn} - \delta_2 \bar{m} u_{mn} - [\delta_1 + (1 - n^2) \omega_2] w_{mn} \} (sc)_{mn}; \\
M_{12}^0 &= -2C_{11} \sum_{m=1}^{\infty} \sum_{n=0}^{\infty} \omega_4 (\bar{m} v_{mn} + \bar{m} n w_{mn}) (cs)_{mn}; \\
N_{12}^0 &= \frac{C_{11}}{R} \sum_{m=0}^{\infty} \sum_{n=1}^{\infty} [(\delta_3 + 2\omega_4) \bar{m} v_{mn} - \delta_3 n u_{mn} - 2\omega_2 \bar{m} n w_{mn}] (cs)_{mn}; \quad (sc)_{mn} = \sin \bar{m}\xi \cos n\theta; \\
M_{11}^0 &= C_{11} \sum_{m=1}^{\infty} \sum_{n=0}^{\infty} [\omega_1 \bar{m} u_{mn} - \omega_3 n v_{mn} + (\omega_1 \bar{m}^2 + \omega_3 n^2) w_{mn}] (cs)_{mn}; \quad (cs)_{mn} = \cos \bar{m}\xi \sin n\theta.
\end{aligned} \tag{5}$$

3 Peculiarities of Contact Interaction Between the Shock-Absorbing Belt and the Shell

When solving the problem of shell deformation, it is quite difficult to take into account the contact interaction between the shock-absorbing belts and its surface. The reaction of a shock-absorbing belt is formed by the individual contraction

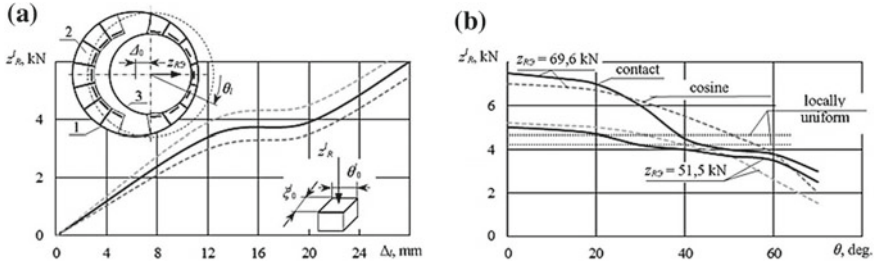


Fig. 2 Load-bearing characteristic of shock absorbers (a) and distribution of contact load in the transverse section of the shell (b); 1—belt ring; 2—shock absorbers; 3—shell

forces of shock-absorbing elements, arranged along the circle of the belt ring in a certain order as shown in Fig. 2a. The geometric axes of the aircraft body and the belt ring fixed, for example, on the tube, coincide if there are no external disturbances. When the aircraft is displaced in the tube, in the launch process, the distribution of reactions along the lateral surface of the body shell is determined by solving the contact problem. According to the operating conditions, the stiffness characteristic of shock absorbers is essentially nonlinear, see Fig. 2a. Its part is almost parallel to the axis of displacements. This significantly affects the redistribution of contact pressure over the shell surface during loading. To solve the nonlinear contact problem, we proposed an algorithm which represents a combination of a stepping procedure for loading and an iterative procedure for determining the contact zone and the magnitude of contact pressure.

Due to the small size of the contact strip in comparison with that of the shell, the distribution of the contact load within its area is assumed to be uniform. The tangential forces caused by Coulomb sliding friction are assumed to be proportional to the normal strip pressure. Then, the radial q_R^l and the tangential τ_R^l components of the surface load on the shell from each contacting shock absorber are written as follows:

$$\tau_R^l = f q_R^l; \quad q_R^l = \begin{cases} 0, & \text{when } |\xi - \xi_l| > \frac{\xi_0^l}{2}, \quad |\theta - \theta_l| > \frac{\theta_0^l}{2} \text{ or when } (\Delta_0^l + w_l) \leq 0; \\ \frac{z_R^l(\Delta_l)}{\xi_0^l \theta_0^l R^2}, & \text{when } |\xi - \xi_l| \leq \frac{\xi_0^l}{2}, \quad |\theta - \theta_l| \leq \frac{\theta_0^l}{2} \text{ and } (\Delta_0^l + w_l) > 0. \end{cases} \quad (6)$$

here $\xi_1 = L_1/R$ and θ_1 are the dimensionless axial and circumferential coordinates of the shock absorber strips; $\xi_0^l = l_0/R$ and θ_0^l are the relative strip dimensions; $\Delta_0^l = \Delta_0 \cos \theta_l$ is the shock absorber contraction, when the belt ring is displaced against the shell as a rigid whole by Δ_0 ; w_l is the radial deflection of the shell under the shock absorber center (which is positive in the direction of the inner normal to the shell surface); $\Delta_l = \Delta_0^l + w_l$ is the complete shock absorber contraction; z_R^l is the force of the shock absorber reaction, which depends on the contraction Δ_l , and is determined



by the experimental characteristic in Fig. 2a; f is the sliding friction coefficient, which is considered independent of the sliding speed.

The total overall reaction acting on the shell in the transverse direction is:

$$z_R = \sum_{l=1}^{l_c} z_R^l(\Delta_l) \cos \theta_l = \sum_{l=1}^{l_c} q_R^l \xi_0^l \theta_0^l R^2 \cos \theta_l, \quad (7)$$

where l_c is the number of shock absorbers contacting with the shell when $\Delta_l > 0$.

Equilibrium Eq. (1) for the shell, which takes into account the contact load, can be written in the matrix form as follows:

$$LW = [Z_H - L_c Q_c(\Delta_0 + W)]R^2; \quad (8)$$

$Q_c = (\tau_{Rx}, \tau_{Ry}, q_R)$ is the vector of contact loads on the shell, which depends nonlinearly on the shell displacements and the level of external action $z_{R\mathcal{D}}$ on the belt; L_c is the operator that characterizes this dependence.

The algorithm for solving the problem has the following sequence:

- (a) Let the external load vector Z_H and the level of external action on the shock-absorbing belt $z_{R\mathcal{D}}$ (its total overall reaction) be given. In the initial estimate, Eq. (8) is solved with the cosine distribution of the transverse load without taking into account its contact nature:

$$W_0 = L^{-1}Z_H R^2;$$

- (b) After that, let us determine the belt displacement at the first step Δ_{01} , the test contact zone l_{c1} and the contact reaction on each shock absorber (z_R^l) for the given total reaction $z_{R\mathcal{D}}$, assuming that the shell is absolutely stiff. To this end, with the initial displacement of the belt Δ_{01} , we determine the contractions of the shock absorbers $\Delta_{01}^l = \Delta_{01} \cos \theta_l$. Checking contact conditions (6) for each one and using the stiff characteristic (Fig. 2a), we find the acting forces (z_R^l)₁, the number of shock absorbers contacting the shell l_{c1} and the overall reaction z_{R1} according to formula (7). This procedure is repeated if there is a gradual increase in belt displacement with a step $\delta\Delta_0 \approx 0,05 \Delta_0$ until the value $(z_R)_{k+1}$ exceeds $z_{R\mathcal{D}}$ at a certain step $(k + 1)$. Then, the values Δ_l , z_R^l and l_c are improved, for example, by the method of bisecting the step $\delta\Delta_0$;
- (c) To determine the displacement vector from Eq. (8) and to adjust the contact load, taking into account these displacements, an iterative process is formed:

$$W_1 = L^{-1}[Z_H - L_c Q_c(\Delta_0^1 + W_0)], \quad W_{i+1} = L^{-1}[Z_H - L_c Q_c(\Delta_0^i + W_i)]. \quad (9)$$

Each iteration (9) involves checking of all possible contact zones according to conditions (6) and determination of the contact reaction of the shock absorbers z_R^l in these zones by the stiffness characteristic, see Fig. 2a. Iterations are stopped by the condition:

$$\frac{|W_{i+1} - W_i|}{|W_i|} < \varepsilon, \varepsilon \text{—the given accuracy of calculations;}$$

- (d) Since the reaction of the shock-absorbing belt depends nonlinearly on the system displacements, its value z_{R1} , calculated taking into account the shell deformations at the first calculation step, will differ from the given $z_{R\mathcal{D}}$. Having determined the discrepancy $\delta_{z1} = z_{R\mathcal{D}} - z_{R1}$, we can judge by its magnitude and sign, to what extent the shell is “overloaded” or “underloaded” by the first step load. Taking into account the calculated discrepancy, we find the next step load $z_{R1} = z_{R\mathcal{D}} + \delta_{z1}$, and, repeating the calculations from (b), we obtain new values of the components of the displacement vector W_2 and the reaction z_{R2} . The calculations are repeated until the discrepancy of the overall contact reaction at a certain step becomes less than the accepted accuracy of the load calculation.

Under real conditions, the tangential components of the contact interaction τ_R are much smaller than the radial component q_R and can be neglected. In this case, the coefficients of expansion into the Fourier series of the contact load (6) are:

$$q_R = \sum_{m=1}^{\infty} \sum_{n=0}^{\infty} q_{mn} \sin \bar{m}\xi \cos n\theta, \left(\bar{m} = \frac{m\pi R}{L} \right),$$

have the following form:

$$q_{m0} = \frac{\theta_0^l}{2} A(\bar{m}) \sum_{l=1}^{l_c} q_R^l; \quad q_{mn} = \frac{2}{n} \sin \left(n \frac{\theta_0^l}{2} \right) A(\bar{m}) \sum_{l=1}^{l_c} q_R^l \cos n\theta_l;$$

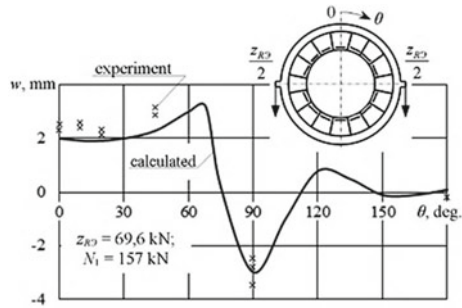
$$A(\bar{m}) = \frac{4}{\pi^2 m} \sin \bar{m}\xi_1 \sin \bar{m} \frac{\xi_0^l}{2},$$

where l_c is the number of strips (shock absorbers) contacting with the shell at this iteration step.

The program exit from the summation cycles for calculating the series of contact loads, as well as for all displacements and stresses of the shell (w , u , v , σ_1 , and σ_2), is made when the given accuracy (usually 0.01) is reached after the sum of ten terms of the series remainder has been compared with the value of the accumulated sum.

To confirm the reliability of the assumed model, we tested a wafer shell with a longitudinally transverse set of ribs with rectangular cross section. The elasticity modulus of the alloy is $E = 4.5 \times 10^4$ MPa; $\nu = 0.3$. The geometrical parameters of the shell and ribs: $R/h = 575$; $L/R = 1.4$; $\psi = 1 + h_p/h = 6.5$; $h_1 = h_2 = h_p$; $\varphi_1 = 2\pi s/a = 0.396$; $\varphi_2 = 2\pi c/b = 0.476$. The lower end frame of the shell is rigidly attached to the test platform plate. The axial compressive force N_1 was transmitted to the upper frame through the rigid cover. The transverse load $z_{R\mathcal{D}}$ was imposed in the middle of the shell ($L_1 = 836$ mm) by transverse displacement of the belt ring. The shock-absorbing elements are uniformly attached to the ring with a

Fig. 3 Radial deflection of the shell cross section under the middle of the shock-absorbing belt



pitch of 9°. The dimensions of the shock absorber strips are $\xi_0 R \times \theta_0 R = 110 \times 125$ mm. The displacements of the shell and the belt ring were measured by sensors with an error of 6%.

Figure 2 shows the field of the load-bearing spread of the shock absorbers (a) and the circumferential distribution of the calculated contact forces on the shell (b). For comparison, the dashed line and the dotted line show the cosine and the uniform distribution of forces on the shock absorbers with the same resultant reaction of the belt z_{R0} . The distribution of the contact load in the shell section according to the cosine law, which is usually adopted in the calculations [17], is acceptable only at low loading levels.

The experimental values of the shell displacement in its middle section (under the belt middle) are compared with the calculated values in Fig. 3.

The coincidence of the calculated deflection w in the shell cross section in Fig. 3 with the test results confirms the adequacy of the assumed computational model.

4 Solving the Shell Stability Equations

To estimate the stability of the elastically deformed state of the shell, we use the system of neutral equilibrium equations [18]:

$$\frac{C_{11} d^4 F}{\Omega_0 d\xi^4} + \left(\frac{1}{C_{66}} - 2 \frac{C_{12}}{\Omega_0} \right) \frac{d^4 F}{d\xi^2 d\theta^2} + \frac{C_{22} d^4 F}{\Omega_0 d\theta^4} + R \frac{d^2 w}{d\xi^2} + L(w_0, w) = 0;$$

$$\frac{1}{R^2} \left[D_{11} \frac{d^4 w}{d\xi^4} + 2(D_{12} + 2D_{66}) \frac{d^4 w}{d\xi^2 d\theta^2} + D_{22} \left(\frac{d^4}{d\theta^4} + 2 \frac{d^2}{d\theta^2} + 1 \right) w \right] - \frac{1}{R} \frac{d^2 F}{d\xi^2} - \frac{1}{R^2} L(w_0, F) - Q = 0. \tag{10}$$

here $\Omega_0 = C_{11} C_{22} - C_{12}^2$; $L(x_0, x) = \frac{d^2 x_0}{d\xi^2} \frac{d^2 x}{d\theta^2} + \frac{d^2 x_0}{d\theta^2} \frac{d^2 x}{d\xi^2} - 2 \frac{d^2 x_0}{d\xi d\theta} \frac{d^2 x}{d\xi d\theta}$, when $(x_0, x) \rightarrow (w_0, w) \vee (w_0, F)$; $Q = N_{11}^0 \frac{d^2 w}{d\xi^2} + N_{22}^0 \left(\frac{d^2 w}{d\theta^2} + w \right) + 2N_{12}^0 \frac{d^2 w}{d\xi d\theta}$; w_0 ; N_{11}^0 ; N_{22}^0 и N_{12}^0 are the deflection and the internal forces in the elastically subcritical state of the shell;



w and F are the deflection functions and internal forces of the shell at the moment of stability loss. The efforts are expressed by the following correlations:

$$N_{11} = \frac{1}{R^2} \frac{d^2 F}{d\theta^2}; N_{22} = \frac{1}{R^2} \frac{d^2 F}{d\xi^2}; N_{12} = -\frac{1}{R^2} \frac{d^2 F}{d\xi d\theta}.$$

Assuming that the shell is hinged at the moment of stability loss, we determine the solution for the system of Eq. (10) as follows:

$$w = \sum_{i=1}^{\infty} \sum_{j=0}^{\infty} w_{ij} \sin(\tau\xi) \cos(j\theta); F = \sum_{i=1}^{\infty} \sum_{j=0}^{\infty} F_{ij} \sin(\tau\xi) \cos(j\theta), \left(\tau = \frac{i\pi R}{L} \right). \quad (11)$$

$i = 1, 2, 3, \dots, j = 0, 1, 2, \dots$ – wavelength constants.

Solving Eq. (10) by the Bubnov–Galerkin method and eliminating the unknowns $F_{i,j}$, we obtain a system of homogeneous algebraic equations with respect to w_{ij} :

$$\begin{aligned} A_{k,p} w_{k,p} + \sum_{i=1}^{\infty} w_{i,p} \left[\bar{Q} \beta_{i,p}^0 + \bar{Q}^2 (\gamma_{i,p}^0 + \gamma_{i,p}) \right] + \sum_{i=1}^{\infty} \sum_{n=1}^{\infty} [w_{i,p+n} (\bar{Q} \beta_{i,p+n} + \bar{Q}^2 \gamma_{i,p+n}) \\ + w_{i,p-n} (\bar{Q} \beta_{i,p-n} + \bar{Q}^2 \gamma_{i,p-n})] + w_{i,p+2n} \bar{Q}^2 \gamma_{i,p+2n} + w_{i,p-2n} \bar{Q}^2 \gamma_{i,p-2n} = 0; k = 1, 2, 3, \dots; p = 0, 1, 2, \dots \end{aligned} \quad (12)$$

here

$$\begin{aligned} A_{k,p} &= S_4(\bar{k}, p) + \frac{\bar{k}^4}{S(\bar{k}, p)}; \bar{k} = \frac{k\pi R}{L}; \bar{Q} = \frac{q_0 R}{\pi C_{11}}; \beta_{i,p}^0 = b_1 p^2 \sum_{m=1}^{\infty} f_{m,0} q_{m,0} \bar{m}^2 d_1 f_0; \\ \beta_{i,p\pm n}^0 &= b_2 \sum_{m=1}^{\infty} f_{mn} q_{mn} \Phi(\pm n) f_1(\pm n); \gamma_{i,p}^0 = b_3 p^2 \sum_{m=1}^{\infty} f_{m0} q_{m0} \bar{m}^2 d_1 (2\Psi_0 + \Psi_{p+n} + \Psi_{p-n}); \\ \gamma_{i,p} &= b_4 \sum_{m=1}^{\infty} \sum_{n=1}^{\infty} f_{mn} q_{mn} [\Phi(-0)\Psi_{p+n} + \Phi(+0)\Psi_{p-n}]; \gamma_{i,p\pm n} = b_5 \sum_{m=1}^{\infty} f_{mn} q_{mn} \Phi(\pm n) \Psi_0; \\ \gamma_{i,p\pm 2n} &= b_6 \sum_{m=1}^{\infty} f_{mn} q_{mn} \Phi(\pm 2n) \Psi_{p\pm n}; \end{aligned}$$

where

$$\begin{aligned}
 f_0 &= \frac{\bar{k}^2}{S(\bar{k}, p)} - \frac{1}{p^2 \bar{m}^2 \Delta_{33}^0} [p^2 S_2(\bar{m}, 0) + \tau^2 S_1(\bar{m}, 0)] + \frac{\tau^2}{S(\tau, p)}; \\
 f_1(\pm n) &= \frac{\bar{k}^2}{S(\bar{k}, p)} - \frac{f_2(\pm n)}{\Phi(\pm n) \Delta_{33}} + \frac{\tau^2}{S(\tau, p \pm n)}; \\
 f_2(\pm n) &= [(p \pm n)^2 S_2(\bar{m}, n) + \tau^2 S_1(\bar{m}, n)] d_1 \mp 2\tau(p \pm n) S_3(\bar{m}, n) d_2; \\
 \Phi(\pm x) &= [(p \pm x) \bar{m}^2 + n^2 \tau^2] d_1 \pm 2\bar{m} n \tau(p \pm x) d_2, \text{ with the values } x = 0, n, 2n; \\
 \Psi_0 &= p^2 \sum_{i=1}^{\infty} \sum_{m=1}^{\infty} \frac{m^2}{S(\tau, p)} f_{m0} q_{m0} d_1; \Psi_{p \pm n} = \sum_{i=1}^{\infty} \sum_{m=1}^{\infty} \sum_{n=1}^{\infty} \frac{\Phi(\pm n)}{S(\tau, p)} f_{mn} q_{mn}; f_{m0} = \frac{\Delta_{33}^0}{\Delta^0}; f_{mn} = \frac{\Delta_{33}}{\Delta}; \\
 d_1 &= [(-1)^{k+m+i} - 1] [(k-m-i)^{-1} + (k+m+i)^{-1} - (k-m+i)^{-1} - (k+m-i)^{-1}]; \\
 d_2 &= [(-1)^{k+m+i} - 1] [(k-m-i)^{-1} + (k+m+i)^{-1} + (k-m+i)^{-1} + (k+m-i)^{-1}]; \\
 S(x_1, x_2) &= \frac{1}{\delta_1 - \delta_2^2} \left[x_1^4 + \left(\frac{\delta_1 - \delta_2^2}{\delta_3} - 2\delta_2 \right) x_1^2 x_2^2 + \delta_1 x_2^4 \right], \\
 \text{when } (x_1, x_2) &= (\bar{k}, p) \vee (\tau, p) \vee (\tau, p \pm n); \\
 S_1(\bar{m}, n) &= \delta_2(\bar{m} \Delta_{32} - \Delta_{33}) - \bar{m} \Delta_{31} - \omega_1 \bar{m}^2 \Delta_{33}; \\
 S_2(\bar{m}, n) &= \delta_1(n \Delta_{32} - \Delta_{33}) - \delta_2 \bar{m} \Delta_{31} - \omega(1 - n^2) \Delta_{33}; \\
 S_3(\bar{m}, n) &= \delta_3(\bar{m} \Delta_{32} - n \Delta_{33}) + \omega_4(2\bar{m} n \Delta_{33} - n \Delta_{31} - \bar{m} \Delta_{32}); \\
 S_4(\bar{k}, p) &= \omega_1 \bar{k}^4 + 2(\omega_3 + 2\omega_4) \bar{k}^2 p^2 + \omega_2 (p^2 - 1)^2; \\
 b_1 &= 0, 5; b_2 = 0, 25; b_3 = b_5 = 0, 125; b_4 = b_6 = 0, 0625.
 \end{aligned} \tag{13}$$

Δ , Δ_{31} , Δ_{32} , and Δ_{33} are the determinant and the minors, composed of coefficients (4).

Thus, the problem was reduced to finding the minimum value of the inherent parameter \bar{Q} of the homogeneous system of algebraic Eq. (12).

The condition for a non-trivial solution of system (12) is fulfillment of the equality:

$$\det[\lambda^2 \mathbf{A}^{(k,p)} + \lambda \mathbf{B}^{(k,p)} + \mathbf{C}^{(k,p)}] = 0, \tag{14}$$

where $\lambda = 1/\bar{Q}$; $\mathbf{A}^{(k,p)} = \{A_{k,p}\}$ is the diagonal matrix, and $\mathbf{B}^{(k,p)} = \{\gamma_{ij}\}$ and $\mathbf{C}^{(k,p)} = \{\gamma_{ij}^*\}$ are the matrices composed of coefficients (13) of system (12). The critical parameter \bar{Q}^* of the load is determined as the reciprocal of the largest root λ^* of characteristic Eq. (14). The eigenvector $\{w_{ij}\}$ corresponding to this value determines the supercritical configuration of the middle shell surface.

Numerical solution of Eq. (12) considered the finite order matrices, which increased until the value λ^* stabilized within the given accuracy. At each such step,

λ^* and the corresponding eigenvector $\{w_{ij}\}$ were determined by the power iteration method and verified by a change in the sign of determinant (14).

The algorithm for improving the critical value of the load, taking into account its contact nature, is analogous to the one given above when solving deformation Eq. (8). In this case, the load value $z_{R\mathcal{D}}$ is not given but is determined as the critical value $z_{R\ cr}$ from the solution of stability problem (12).

5 Comparison of Critical Loads with Known Theoretical and Experimental Data

To confirm the adequacy of the designed model, we compared it with the published experimental and theoretical data. Such data is relatively little. The authors point to the technical complexity of simulating non-axisymmetric loads in structural tests.

Solutions by the method of finite differences of the geometrically nonlinear problem, as well as the stability problem of the nonlinear subcritical state of the shell for the particular case of locally uniform loading—band loading—are given in [9, 10]. Let us compare these solutions with our results of the calculation of critical loads, taking into account the momental subcritical state of the shell according to the linear theory (12). This comparison is especially interesting because solutions were obtained by various methods and can be compared with known experimental data [10, 21].

Figure 4 shows the change of the critical asymmetric pressure q^* and the relative parameter of the critical pressure $k_0 = q^*/q_0^*$ depending on the angular size of the

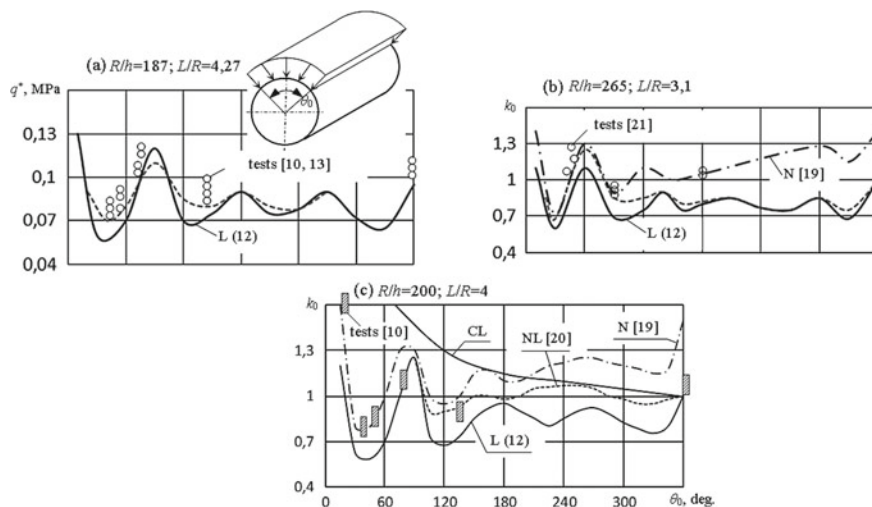


Fig. 4 Comparison of obtained solution (12) with the known experimental [10, 21] and theoretical [19, 20] data

loading site θ_0 . Here, q_0^* is the critical value of the axisymmetric lateral pressure. The CL curves were obtained by calculating the critical loads within the classical Eulerian approach, the L curves—in linear subcritical state (12), the NL curves—in nonlinear subcritical state [20], and N are the limiting loads from the solution of geometrically nonlinear problem [19]. Theoretical calculations are compared with the experimental data from [10, 13, 21]. The comparison shows that the critical load values determined from the solution of linearized Eq. (12) in the linear subcritical state are below the limiting values (NL and N) and reflect all the qualitative features of the dependence of these loads on the shell dimensions and the width of the loading site. This solution is also quite acceptable for computational practice, since it represents a lower estimate of the known experimental data and is much simpler than the nonlinear one. Moreover, design calculations can use a simplified solution of linearized Eq. (10) without taking into account the subcritical deflection in the equation of deformation compatibility. Then the problem becomes linear with respect to the critical load as an inherent parameter of the system matrix. Figure 4 shows the loads of this simplified solution as dashed lines.

6 Conclusion

When body shells are transversely loaded with a shock-absorbing belt, the distribution of contact forces along the shock absorbers depends on the level of external action and the ratio of the stiffness parameters of the shell and the belt. In the known computational models, the distribution of belt pressure on the shell in its transverse section was cosine. The actual distribution of the belt contact reaction is intermediate between the cosine and the uniform distribution.

When evaluating the deformation of body shells subjected to the shock-absorbing belt reaction, it should be taken into account that at the operational loading levels, the maximum displacements and stresses on the shell are outside its contact area with the shock absorbers.

A good agreement between the calculation and the experiment confirms reliability of the obtained results and the proposed algorithm of successive approximations, taking into account the nonlinear dependence of the shock-absorbing belt reaction on the structure displacements.

The stability problem of the deformed state of a cylindrical shell has been modeled for the first time, taking into account the specifics of its interaction with the nonlinear elastic foundation on a part of the lateral surface.

References

1. Konyukhov SN, Logachev PP (1997) Mortar launch of intercontinental ballistic missiles. NAS, NSA of Ukraine, Institute of Technical Mechanics, State Design Office “Yuzhnoye”, Dnepropetrovsk, p 211
2. Darevsky VM (1966) Contact problems in the theory of shells. In the book: Proceedings of the Sixth All-Union Congress. Conference on the theory of shells and plates. Baku, 1965. Nauka, Moscow, pp 927–934
3. Johnson K (1989) The mechanics of contact interaction. Mir, Moscow, p 510
4. Galin LA (1984) Contact problems of the theory of elasticity and viscoelasticity. Nauka, Moscow, p 232
5. Emelyanov IG, Kuznetsov VYu (2000) Solution of contact problems for cylindrical shell constructions with allowance for tangential forces. Issues of machine building and machine reliability 1:59–64
6. Mossakovsky VI, Gudramovich VS, Makeev EM (1978) Contact problems of the theory of shells and rods. Mechanical Engineering, Moscow, p 247
7. Mushtari HM (1954) On the stability of a cylindrical shell under the action of nonuniform loads, vol I. In: Proceedings of the Physicotechnical Institute. Kazan, pp 77–103
8. Almroth BV (1962) Buckling of a cylindrical shell subjected to nonuniform external pressure. Trans ASME Ser E 29(4):675–682
9. Andreev LV, Obodan NI (1966) Experimental study of the stability of a cylindrical shell under the action of an nonuniform pressure. In: Proceedings of the Sixth All-Union Congress. Conference on the theory of shells and plates. Moscow, pp 74–76
10. Andreev LV, Mossakovsky VI, Obodan NI (1970) On the stability of a cylindrical shell under arbitrary external pressure. In: Proceedings of the 7th All-Union Congress. Conference on the theory of shells and plates. Moscow, pp 629–633
11. Kabanov VV, Kurtsevich GI, Mikhailov VD (1978) The limiting state and stability of a cylindrical shell under non-uniform non-axisymmetric external pressure, vol 4. In: Proceedings of AS USSR, Mechanics of a solid body, pp 129–134
12. Kabanov VV, Zhelezov LP (1981) Study of nonlinear deformation and stability of cylindrical shells under nonaxisymmetric pressure by the finite element method. Appl Mech 17(5):71–76
13. Andreev LV, Obodan NI, Lebedev AG (1988) Stability of shells for nonaxisymmetric deformation. Nauka, Moscow, p 208
14. Kolomoets AA, Modin AS (2014) Stability of the equilibrium states of a cylindrical shell under the action of nonuniform external pressure, vol 1. Issues of Institutions of Higher Education. Building. Moscow, pp 13–17
15. Malmeyer AK, Tamuzh VP, Teters GA (1980) Resistance of polymeric and composite materials. Zinatne, Riga, p 572
16. Ambaturmyan SA (1974) The general theory of anisotropic shells. Nauka, Moscow, p 448
17. Lizin VT, Pyatkin VA (1994) Designing of thin-walled structures. Mechanical Engineering, Moscow, p 382
18. Grigolyuk EI, Kabanov VV (1978) Stability of shells. Nauka, Moscow, p 360
19. Kabanov VV, Mikhailov VD (1979) The limiting state of a cylindrical shell under inhomogeneous external pressure, vol 2. In: Proceedings of Institutions of Higher Education. Aviation equipment pp 27–31
20. Kabanov VV, Mikhailov VD (1982) Algorithm for studying nonlinear deformation and stability of a cylindrical shell under nonaxisymmetric loading. Calculation of structural elements of aircraft. Mechanical Engineering, Moscow, p 55–64
21. Kudinov AN (1974) Results of experiments on the stability of shells with uneven external pressure, vol 4. In: Proceedings of the Institute of Applied Mathematics and Mechanics, pp 150–154

Evaluation of Possible Limits of Forcing of High-Capacity Air-Cooled Engines



A. V. Vasilyev, A. M. Lartsev and E. A. Fedyanov

Abstract Currently, concern in the development of the Far North and the Arctic has sharply increased. High-power air-cooled diesel engines can be widely used in such severe conditions. In this regard, the problem of determining the possible limits of forcing air-cooled diesel engines becomes relevant again. The solution of the problem was performed by calculation and experimental determination of possible limits of forcing air-cooled diesel engines according to the chosen criterion that defines the forcing limit. As a result, the acceptable levels of forcing air-cooled diesel engines supercharged at different excess air ratios, and the degree of cooling of supercharged air were determined. Based on the analysis of the calculation results, it is concluded that supercharged air-cooled diesel engines are particularly critical to the ratio of the boost pressure to the back pressure at the outlet. It is shown that with an increase in this ratio, the maximum and average temperatures of the injector firing face decrease linearly. The estimation of the possible limits of increasing the diameter of the air-cooled diesel cylinder with different levels of forcing on the average effective pressure is performed.

Keywords Air cooling · Engine boost · Boost level · Cylinder head

1 Introduction

The main design feature that complicates forcing multi-cylinder air-cooled engines is the absence of a monolithic cylinder block [1]. Mentioned design feature complicates forcing, but is not a factor determining the maximum permissible level of power increase. A factor that fundamentally limits the achievable level of forcing air-cooled engines is the thermal stress of the cylinder-piston group and cylinder head parts [2–9].

A. V. Vasilyev · A. M. Lartsev (✉) · E. A. Fedyanov
Volograd State Technical University, 28, Lenin Pr., 400131 Volograd, Russia
e-mail: lartsev.am@yandex.ru

With the increase in the dimension of air-cooled diesel engines, the task of increasing their power becomes especially difficult [10–12]. With the increase in the dimension, the combustion chamber volume and, consequently, the amount of the combustion air-fuel mixture grow approximately in proportion to the cube of the cylinder's diameter. At the same time, the area of the air-cooled surfaces increases in proportion to the square of the diameter. Taking into account the above mentioned, while maintaining the proportion of heat transferred to the walls of the combustion chamber, the density of the heat flux from the outer surfaces should increase significantly with the diameter of the cylinder. In practice, this is possible only by increasing the temperature on the cooled surfaces and, as a consequence, the average temperature of the engine parts. It can be argued [13–15] that for air-cooled engines, there is a limit to increase the dimension above which it is impossible to provide an acceptable temperature regime of the cylinder-piston group and cylinder head parts at a given level of forcing.

Among the formerly and commercially produced air-cooled diesel engines in the present time, the greatest dimension had B-400 diesel [16, 17] manufactured at the Volgograd engine plant. This diesel engine also had the highest level of forcing among air-cooled diesel engines designed for traction vehicles. All this suggests that the assessment of the possible limits of forcing of air-cooled diesel engines is advisable to consider the example of this diesel.

2 The Limits of Supercharge Forcing of Air-Cooled Diesel Engines

The solution of the problem of evaluating the possible limits of forcing air-cooled diesel engines started with the analysis of the thermal state of the cylinder, piston and cylinder head on the example of B-400 diesel engine [18–20].

The evaluation of the thermal state of the cylinder at different levels of forcing was performed using the finite element method in ANSYS environment. Figure 1 shows a field of temperatures of B-400 diesel engine cylinder at the limit level of forcing.

Evaluation of the thermal state of the piston was carried out by thermometry of the edge of the combustion chamber. Even at the maximum level of forcing, the temperature of the combustion chamber edge did not exceed the permissible temperature for the material used: 600–610K. This became possible due to the placement around the combustion chamber of specially designed oil gallery and the dosed flow rate of the oil circulating through it.

Evaluation of the thermal state of the cylinder head is performed by multipoint thermometry of the injector firing face, which showed a significant increase in temperatures when forcing the diesel engine, and at the limit levels—exceeding the permissible values.

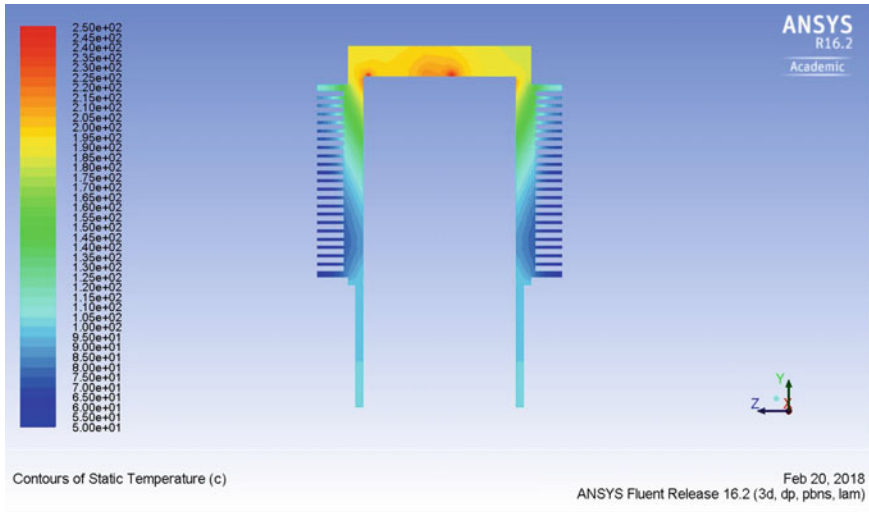


Fig. 1 Temperature field of B-400 diesel engine cylinder under $N_e = 404$ kW mode, $n = 1700$ rpm

Analysis of the temperature fields of the cylinder, piston and cylinder head at different levels of forcing showed that the maximum temperature gradient of the head is almost three times higher than the maximum temperature gradients of the cylinder or piston.

On the basis of calculations and results of tests of B-400 diesel engine, it was established that at a sufficient margin of rigidity, durability of a skeleton and bearing capacity of a crankshaft, the factor limiting admissible level of forcing is the thermal condition of the cylinder head. As a criterion for determining the limit of forcing of air-cooled diesel engine, we have chosen the maximum temperature of injector firing face (T_{max}).

The evaluation of possible limits of supercharge forcing of air-cooled diesel engines at different levels of cooling supercharge air and various adjustments on the excess air ratios was carried out by means of calculation and experimental method of estimation of the thermal condition of the cylinder head [21] on the example of B-400 diesel engine.

Figure 2 shows the dependence of the possible condition for limiting the maximum temperature of the cylinder head (T_{max}) of N_e nominal power values on the cooling depth of the supercharge air (ΔT) at different adjustments to the excess air ratio α . Parameters of turbochargers were changed in order to increase airflow.

Calculations were made to reduce the excess air ratio by increasing the cyclic supply without changing the parameters of the turbocharger. Figure 3 shows the dependence of the maximum temperature of the cylinder head on the rated power with detailed differentiation of the excess air ratio.

As it is well known, a significant impact on the performance of the engine has the ratio of the supercharge pressure p_s to the back pressure on the release p_b ,

Fig. 2 Engine power limit according to the thermal condition of the cylinder head

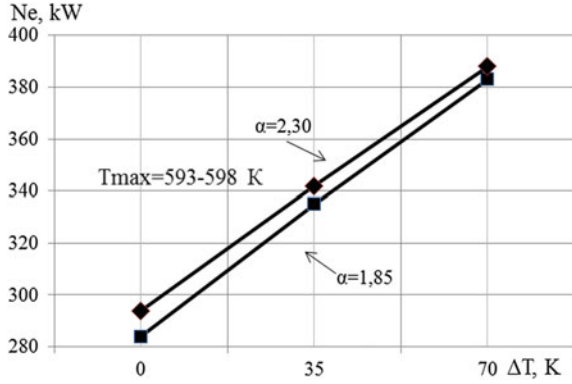


Fig. 3 Dependence of the thermal state of the cylinder head on the effective power at different

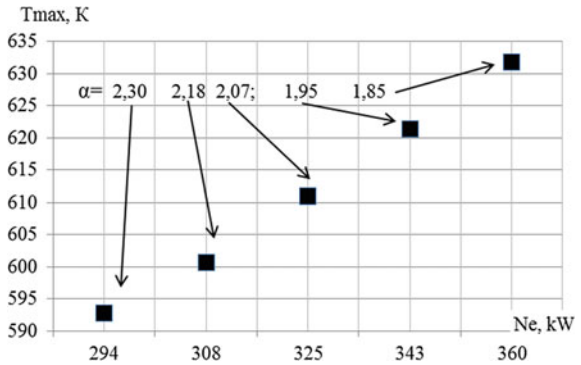
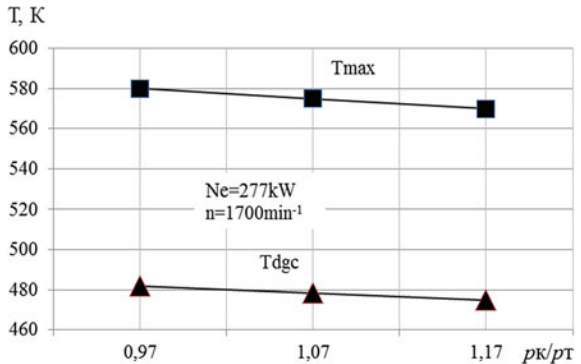


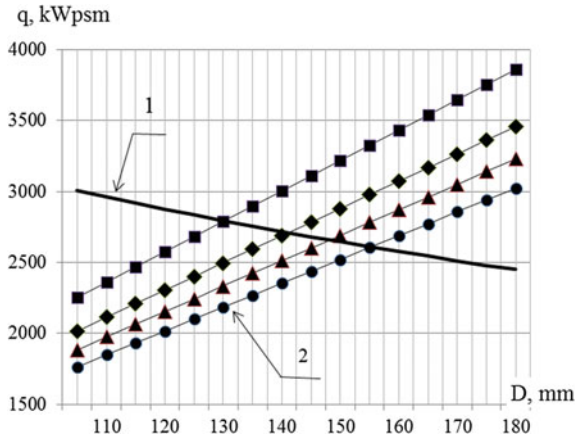
Fig. 4 Dependence of the thermal state of the cylinder head on p_s/p_b



determined by the parameters of the turbocharger. The increase in the specified ratio makes it possible to reduce the coefficient γ_r of the residual gases and to increase the delivery ratio η_v , and to reduce heat intensity. Figure 4 shows the dependence of the maximum (T_{max}) and mean temperature of the injector firing face (T_{ff}) from the ratio p_s/p_b at constant power of the diesel engine.



Fig. 5 Maximum permissible diameters of cylinders of air-cooled engines at different levels of forcing: 1—limiting by the thermal limit of the head; 2—the actual thermal flux: black circle— $p_e = 0.96$ MPa, black up-pointing triangle— $p_e = 1.03$ MPa, black rhomb— $p_e = 1.11$ MPa, black square— $p_e = 1.26$ MPa. ($\Delta T = 35K, T_{max} = 623K$)



With the increase in the displacement volume of the air-cooled engine, the task of maintaining its permissible thermal state becomes more complicated. This is especially critical for diesel engines with their characteristic irregularity of temperature field in the combustion chamber and larger, compared with gasoline engines, combustion process duration as a whole.

In this regard, the evaluation of possible values of the diameters of air-cooled diesel cylinders, at which it is possible to provide the necessary cooling of the cylinder head, is based on the maximum permissible density of the heat flux q in the head face. Figure 5 shows how the maximum possible cylinder diameter due to cooling conditions changes depending on the level of forcing (p_e —mean effective pressure).

3 Conclusion

Based on the analysis of the calculation results, it is concluded that from the standpoint of the thermal state air-cooled diesel engines at supercharging, the value of the ratio p_s/p_b is especially critical.

Showed results of numerical experiments allow us to select the parameters of supercharge air coolers, supercharging units and the values of excess air ratios that ensure the permissible thermal state of the air-cooled engine at a given level of forcing.

References

1. Pospelov D (1971) Dvigateli vnutrennego sgoraniya s vozdushnym ohlazhdeniem. Teoriya i raschet (Air-cooled internal combustion engines. Theory and calculation). Mechanical Engineering, Moscow



2. Vasilyev A, Lartsev A, Fedyanov E (2017) Ocenka teplovogo sostojanija golovki cilindra dvigatelja vozdušnogo ohlazhdenija pri ego forsirovanii (Assessment of thermal condition of cylinder head of the air-cooling engine when forcing it). *Gruzovik* 11:24–27
3. Arnol'd L (1979) Tehniceskaja termodinamika i teploperedacha (Technical thermodynamics and heat transfer). Higher education, Moscow
4. D'jachenko N et al (1969) Teploobmen v dvigateljah i teponaprjazhennost' ih detalej (Heat exchange in engines and heat stress of their parts). Mechanical Engineering, Moscow
5. Shelkov S et al (1983) Optimizacija konstrukcii teponaprjazhennyh detalej dizelej (Design optimization of heat-stressed diesel parts). Mechanical Engineering, Moscow
6. Lartsev A (2015) Osobennosti forsirovanija nadduvom dizelej vozdušnogo ohlazhdenija bol'shoj razmernosti (Features of boost supercharged diesel engines air cooling large dimension). Volgograd
7. Lartsev A (2014) Povyšenie termociklicheskoj stoykosti golovki cilindra dvigatelya vozdušnogo ohlazhdenija (Increase of thermocyclic resistance of the cylinder head of the air-cooling engine). Volgograd
8. Lartsev A (2014) Vliyanie perehodnyh processov na temperaturnoe pole golovki cilindra dvigatelya vozdušnogo ohlagdenija (Effect of transients on the temperature field of the cylinder head of an air-cooled engine). Volgograd
9. Lartsev A (2015) Ecsperimentalnoe issledovanie vliyanija regulirovochnih parametrov na economiccheskie i ecologiceskies pocazateli tractornogo dizelya vozdušnogo ohlagdenija (Experimental study of the influence of regulatory parameters on the economic and environmental performance of air-cooled tractor diesel). *Spravochnic. Inženerniy gurnal* 2015 (8):37–42
10. Kosugi T, Seino T (1985) Valve motion simulation method for high-speed internal combustion engines. SAE Technical Paper Series No. 850179, pp 1–10
11. Lartsev A (2012) Perspektivy sovershenstvovaniya dizeley vozdušnogo ohlazhdenija bolshoy moshnosti (Prospects of improvement of diesel engines of air cooling of big power). Volgograd
12. Lartsev A (2013) Vliyanie parametrov turbocompressora na pocazateli dizeley vozdušnogo ohlagdenija (Influence of turbocharger parameters on the performance of air-cooled diesels). Volgograd
13. Lartsev A (2013) Vliyanie tipa turbocompressora na osnovnye pocazateli dvigatelya vozdušnogo ohlagdenija bolshoy moshnosti pri ego forsirovanii (The influence of the turbocharger type on the main indicators of the engine of air cooling of high power when forcing it). Volgograd
14. Lartsev A (2014) Ocenka effektivnyh pokazatelej dvigatelja vozdušnogo ohlazhdenija V-400 pri ego forsirovanii (Evaluation of the effective performance of the air cooling engine V-400 when forcing it). *Dvigatelsestroenie* 1:26–29
15. Lartsev A (2013) Osobennosti proizvodstva dvigatelej vozdušnogo ohlazhdenija bol'shoj moshnosti (Features of production of air cooling engines of high power). *Dvigatelsestroenie* 254(4):9–13
16. Men'shenin G (2006) Povyšenie tehničeskogo urovnja i nadezhnosti dizel'nyh dvigatelej vozdušnogo ohlazhdenija 8ChVN15/16 s uchetom rezul'tatov jekspluatacii (Improving the technical level and reliability of air-cooled diesel engines 8CHVN15/ 16 taking into account the results of operation). Volgograd
17. Men'shenin G (1986) Dizel' 8DVT-330. Tehniceskoe opisanie i instrukcija po jekspluatacii (Diesel 8DWT-330. Technical description and operating instructions). Mechanical Engineering, Moscow
18. Nomura T, Matsushita K, Fujii Y, Fujiwara H (2014) Development of temperature estimation method of whole engine considering heat balance under vehicle running conditions. *SAE Int J Engines* 8(1):120–134
19. Krstic B, Rasuo B, Trifkovic D, Radisavljevic I, Rajic Z, Dinulovic M (2013) An investigation of the repetitive failure in an aircraft engine cylinder head. *Eng Fail Anal* 34:335–349

20. Mărdărescu V, Ispas N, Năstăsoiu M Considerations about designing of an air cooled cylinder head for a direct injection small diesel engine. INMATEH—Agri Eng 42(1):137–144
21. Vasilyev A, Lartsev A, Fedyanov E (2016) Metod ocenki izmenenija teplovogo sostojanija golovki cilindra dvigatelja vozdušnogo ohlazhdenija pri ego forsirovanii (Method of estimation of change of thermal condition of the cylinder head of the engine of air cooling at its forcing). Izvestiya MG TU “MAMI” 30(4):15–19

Torsional Rigidity of Elastic Rods of Polygonal Cross Section



A. V. Korobko, Yu. E. Lygina and S. Yu. Savin

Abstract This article compares the known handbook- and paper-cited reduced geometric rigidities of regular polygon-shaped cross sections in the free torsion of bars against the values of the same parameter obtained by means of integral geometric cross-sectional arguments (the form factor and the conformal radii ratio). In the first case, the construction approximating function returns an approximation to the known values with an up to 1% error; the second-case error is up to 0.5%. The dependencies shown herein can be used to evaluate the torsional rigidity of the cross sections of bar-shaped elements employed in various mechanical systems, robotics, and equipment exposed to elastic deformation.

Keywords Torsion of elastic bars · Regular polygon-shaped cross sections · Reduced geometric rigidity of cross sections · Form factor · Conformal radii ratio

1 Introduction

The torsion of prismatic bars is one of the major problems in the theory of elasticity [1–9]. Torsional strain of structures is not uncommon in civil and mechanical engineering. When computing the torsion of bars, the first step is to find the geometric torsional rigidity I_k of the bars, and then to use it for stress–strain analysis. The theory of elasticity knows very few accurate solutions to this problem, in particular for the case of elliptic/rectangular bar cross section. In other cases, engineers use various (and rather labor-intensive) approximate analytical and numerical methods [2–17].

A. V. Korobko · Yu. E. Lygina
Orel State University Named After I.S. Turgenev, 95, Komsomolskaya str.,
Orel 302026, Russia

S. Yu. Savin (✉)
Southwest State University, 94, 50 Let Oktyabrya str., Kursk 305040, Russia
e-mail: suwin@yandex.ru

In recent decades, geometric methods such as the isoperimetric method (ISPM) [10] and form-factor interpolation method (FFIM) [11, 14, 16, 19] have found application in this area. These methods are based on the isoperimetric properties of the geometric torsional cross-sectional rigidity and integral geometric properties such as the form factor K_f and the ratio of the conformal radii (inner-to-outer \dot{r}/\bar{r}) [13, 15, 17, 18]. Studies have shown the geometric properties K_f and \dot{r}/\bar{r} to be analogous to the geometric rigidity I_k of cross sections. It has been found that the geometric rigidity of regular polygon-shaped cross section forms part of the bottom boundary for the entire set of values I_k for bars whose cross section has an arbitrary convex shape.

Some problems of the $I_k - K_f$ interrelation have already been covered in scientific papers [1, 10, 11], although the interrelation of I_k and \dot{r}/\bar{r} has not. It is only the papers [13, 15, 17, 18, 20] that apply the argument \dot{r}/\bar{r} to the problems of transversal bending, free oscillations, and stability of elastic plates with a convex contour. The goal of publishing this paper is to show civil engineers the novel application of interpolation methods to the problems of free torsion of prismatic bars.

2 Methods Representing the Geometric Rigidity of Regular Polygon-Shaped Cross Sections as a Function of Their Form Factor and Conformal Radii Ratio

Stress–strain analysis of bars subjected to torsion gives rise to the problem of finding the geometric torsional rigidity I_k .

Paper [13] presents the geometric torsional rigidity I_k of an arbitrary cross section as follows:

$$I_K = \max 4 \left(\iint_A f dA \right)^2 / \iint_A (f_x^2 + f_y^2) dA. \quad (1)$$

here $f(x, y)$ is a smooth function (stress function, or Prandtl function) that equals zero at the contour, such that $0 \leq f \leq 1$; the integral in the denominator is the Dirichlet integral.

Let us use a modified Rayleigh–Ritz method and transform the expression (1) by substituting the dual-parameter stress function $f(x, y)$ with a single-parameter function $g(\rho)$, the contour lines of which are similar to the cross-sectional contour:

$$f(x, y) = g[t/r(\phi)] = g(\rho), \quad (2)$$

where $\rho = t/r(\phi)$ is a dimensionless polar coordinate; t and ϕ are polar coordinates; $r(\phi)$ is the cross-sectional contour equation. Substitute the function (2) in the expression (1) and make necessary transformations for the numerator and for the denominator separately.

$$\iint_A f(x, y) dA = \int_0^{2\pi} \int_0^r g^2(\rho) t dt d\phi = \int_0^{2\pi} r^2 d\phi \int_0^1 g(\rho) \frac{t dt}{r r} = 2A \int_0^1 g(\rho) \rho d\rho. \quad (3)$$

The resultant expression is

$$4 \left(\iint_A f dA \right)^2 = 16A^2 \cdot \left(\int_0^1 g(\rho) \rho d\rho \right)^2. \quad (4)$$

The Dirichlet integral can be written in polar coordinates:

$$\iint_A (f_x^2 + f_y^2) dA = \int_0^{2\pi} \int_0^r \left(f_t^2 + \frac{1}{t^2} f_\phi^2 \right) t dt d\phi. \quad (5)$$

Find the derivative of the function $f(t, \phi)$:

$$\begin{aligned} f_t &= \left[g\left(\frac{t}{r}\right) \right]' = g'\left(\frac{t}{r}\right) \frac{1}{r} = g'(\rho) \frac{1}{r}; f_\phi = \left\{ g\left[\frac{t}{r(\phi)}\right] \right\}' = -g' \left[\frac{t}{r(\phi)} \right] \frac{r'(\phi)t}{r^2(\phi)} \\ &= -g'(\rho) \frac{r't}{r^2}. \end{aligned} \quad (6)$$

Substitute the derivatives in the Dirichlet integral:

$$\begin{aligned} \int_0^{2\pi} \int_0^r \left(f_t^2 + \frac{1}{t^2} f_\phi^2 \right) t dt d\phi &= \int_0^{2\pi} \int_0^r \left(g'^2(\rho) \frac{1}{r^2} + \frac{1}{t^2} g'^2(\rho) \frac{r'^2 t^2}{r^4} \right) t dt d\phi \\ &= \int_0^{2\pi} \left(1 + \frac{r'^2}{r^2} \right) d\phi \int_0^r g'^2(\rho) \frac{t dt}{r r} = K_f \int_0^1 g'^2(\rho) \rho d\rho. \end{aligned} \quad (7)$$

here K_f is the form factor of an arbitrary simply connected two-dimensional convex-shaped area, which form factor equals a contour integral:

$$K_f = \min \oint_L ds/h,$$

where L is the contour of the area; ds is an elementary part of the contour; h is a normal drawn from a point inside a contour to a contour point as shown in Fig. 1. The form factor is a quantitative characteristic of the areal shape. A lesser K_f means the area is closer to being “regular”; thus, a circle has the smallest form factor of any regular polygon. For more information on this integral parameter, its

isoperimetric properties and application to the theory of elasticity problems, see the monograph [11].

The resultant expression is

$$\iint_A (f_x^2 + f_y^2) dA = K_f \int_0^1 g'^2(\rho) \rho d\rho. \quad (8)$$

Substitute the expressions (4) and (8) in (1) to get:

$$I_k \geq \frac{16A^2}{K_f} \left(\int_0^1 g \rho d\rho \right)^2 / \int_0^1 g'^2(\rho) \rho d\rho. \quad (9)$$

The sign of inequality in the expression (9) is due to using the approximate variational Rayleigh-Ritz method. The accuracy of the right-side numerical value in this inequality is quantitatively dependent on the chosen Prandtl function. This side can be linked to the form factor via the proportionality constant K_I . In this case

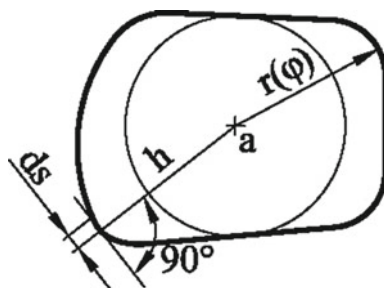
$$I_k \geq K_I A^2 / K_f. \quad (10)$$

In this expression, the proportionality constant K_I depends on the cross-sectional shape (triangle, rectangle, trapezoid, etc.) or on the type of geometric transformation. In other words, this constant is variable (a function). This is why it is correct to use the following inequality [13] instead of the expression (10):

$$I_k \geq K_I A^2 / K_f^n, \quad \text{or} \quad I_k \geq A^2 (K_I + B / K_f), \quad \text{or} \quad I_k \geq A^2 (K_I + B \times f(K_f)), \quad (11)$$

which has two unknown variables. If a set of cross sections has a common continuous or discrete geometric transformation, for which the problem above has known solutions for at least to areal shapes (the “basic” solutions), then the unknown variables of the expression (11) can be found.

Fig. 1 Arbitrary simply connected flat convex-shaped area



For convenience, use the reduced geometric torsional rigidity of the cross section $i_k = I_k/A^2$:

$$i_k \geq K_I/K_f^n, \quad \text{or} \quad i_k \geq K_I + B/K_f, \quad \text{or} \quad i_k \geq K_I + B \times f(K_f). \quad (12)$$

Since the form factor has isoperimetric properties, the reduced geometric torsional rigidity i_k will have the same properties.

The expression (9) shows that for an arbitrary cross section, the geometric torsional rigidity I_k depends only on K_f , which is why the form factor can be considered geometrically analogous to i_k . Thus, the isoperimetric properties of the form factor are related to the geometric rigidity of cross sections.

Let us present the geometric torsional rigidity of polygonal cross sections as a function of form factor and conformal radii ratio.

Handbooks and scientific papers [1, 9] present the geometric rigidity of cross sections I_k as a regular polygon, see Table 1, row 2. Row 3 gives the reduced geometric rigidities $i_k = I_k/A^2$ (A is the cross-sectional area), row 4 gives the form factors for these cross sections, row 5 gives their corresponding conformal radii ratios (Fig. 2).

For regular polygons, the conformal radii ratio \dot{r}/\bar{r} (inner to outer) can be found by the formula [10]:



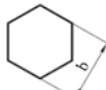

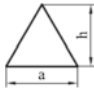
$$\frac{\dot{r}}{\bar{r}} = \frac{\Gamma(1 - 1/n)}{2^{1-2/n}\Gamma(1/2)\Gamma(1/2 - 1/n)} \bigg/ \frac{\Gamma(1 + 1/n)}{2^{1+2/n}\Gamma(1/2)\Gamma(1/2 + 1/n)}, \quad (13)$$

where n is the number of edges of an n -angular polygon; $\Gamma(x)$ is a gamma function. A. A. Chernyaev's thesis [11] presents an approximating function constructed on the basis of computed conformal radii ratios:

$$\dot{r}/\bar{r} = f + bn^{-1} + cn^{-2} + dn^{-3} + en^{-4}, \quad (14)$$

where $f = 0.99997$; $b = 0.013472$; $c = -0.33812$; $d = -1.9499$; $e = -9.7087$. The error returned by this function does not exceed 0.01%.

Table 1 Known values of geometric rigidity for some regular polygons; corresponding form factors and conformal radii ratios

No.	Circle	Octagon	Hexagon	Square	Equilateral triangle
1					
2	$I_k = 0.5\pi R^4$	$I_k = 0.115b^4$	$I_k = 0.108b^4$	$I_k = 0.140a^4$	$I_k = ah^3/30$
3	$i_k = 1/(2\pi)$	$i_k = 0.1568$	$i_k = 0.1533$	$i_k = 0.1406$	$i_k = 0.1155$
4	$K_f = 2\pi$	$K_f = 6.6274$	$K_f = 6.9282$	$K_f = 8$	$K_f = 10.392$
5	$\dot{r}/\bar{r} = 1$	$\dot{r}/\bar{r} = 0.9903$	$\dot{r}/\bar{r} = 0.9762$	$\dot{r}/\bar{r} = 0.9139$	$\dot{r}/\bar{r} = 0.7748$

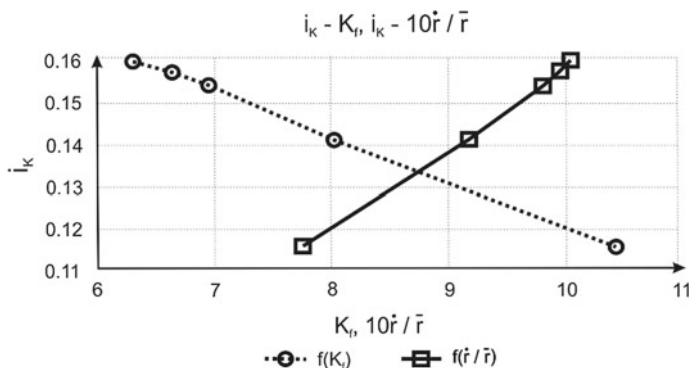


Fig. 2 $i_k - K_f$ and $i_k - \dot{r}/\bar{r}$ dependences for polygonal cross section

3 Results and Discussion

The input data from Table 1 has been used to construct the approximating functions i_k of K_f and i_k of \dot{r}/\bar{r} :

$$i_k = \frac{1}{4.913 + 0.0346K_f^2}; \tag{15}$$

$$i_k = 0.0498 + 0.1094(\dot{r}/\bar{r})^2. \tag{16}$$

Table 2 provides an analysis of these functions.

Column 5 presents solutions found by the formula (4), column 8 presents solutions by the formula (5). In the first case, the error is within 1%; in the second case, within 0.5%. Thus, using the conformal radii ratio as the argument halves the error of approximate dependencies.

Table 2 Analysis of the geometrical torsion rigidity for regular polygon-shaped cross sections

Area's form	i_k by [9]	K_f	$1/K_f$	i_k by (4)	$\Delta, \%$	\dot{r}/\bar{r}	i_k by (5)	$\Delta, \%$
1	2	3	4	5	6	7	8	9
Circle	0.1592	6.2832	0.1592	0.1592	0	1	0.1592	0
<i>Sections in the form of regular polygons</i>								
Octagon	0.1568	6.6274	0.1509	0.1554	0.89	0.9903	0.1571	0.19
Hexagon	0.1533	6.9282	0.1443	0.1521	0.78	0.9762	0.1540	0.46
Square	0.1406	8	0.1250	0.1403	0.21	0.9139	0.1412	0.42
Triangle	0.1155	10.392	0.0962	0.1156	0.09	0.7748	0.1155	0

4 Conclusion

The paper shows that the reduced geometric rigidity of regular polygon-shaped cross sections in the free torsion of a bar is functionally linked to the integral geometric arguments characterizing the cross-sectional shape: the form factor K_f and the conformal radii ratio \dot{r}/\bar{r} .

The known solutions given in handbooks and papers on the matter are presented as a function of the integral geometric characteristics of cross sections: the form factor and the conformal radii ratio. The approximating function i_k of K_f has returned results that deviate from the known solutions within 1%, while the approximating function i_k of \dot{r}/\bar{r} errs within 0.5%.

Therefore, the formula (5) is recommended for higher valuations of the reduced geometric cross-sectional rigidity of elastic bars.

References

1. Arutyunyan NH, Abramyan VL (1963) Torsion of elastic solids. Physmathgiz Publishing, Moscow
2. Jawed MK, Novelia A, O'Reilly OM (2018) Material frames and measures of twists. Springer Briefs in Applied Sciences and Technology 47–57. Print ISBN 978-3-319-76964-6
3. Lembo M (2018) Exact equilibrium solutions for nonlinear spatial deformations of nanorods with application to buckling under terminal force and couple. Int J Solids Struct 135:274–288. <https://doi.org/10.1016/j.ijsolstr.2017.11.026>
4. Rajesh Kumar P, Parthasarathy NS (2018) Stiffness of a single layered cable assembly over a sheave with internal friction. Int J Mech Eng Technol 9:156–168
5. Hu J, Gao H, Meng Y, Zhang Z, Gao L (2018) Effects of free-end torsion on the microstructure evolution and fatigue properties in an extruded AZ31 rod. Mater Sci Eng, A 726:215–222. <https://doi.org/10.1016/j.msea.2018.04.078>
6. Grazioso S, Di Gironimo G, Siciliano B (2018) Analytic solutions for the static equilibrium configurations of externally loaded cantilever soft robotic arms. In: 1st IEEE international conference on soft robotics, RoboSoft 2018, Livorno, Italy. pp 140–145. <https://doi.org/10.1109/robosoft.2018.8404910>
7. Morassi A (1999) Torsion of thin tubes with multicellular cross-section. J Mech 34(2): 115–132
8. Morassi A, Freddi L, Paroni R (2004) Thin-walled beams: the case of the rectangular cross-section. J Elast 76:45–66
9. Wang CY (1998) Torsion of tubes of arbitrary shape. J Solids Struct 35(7–8):719–731
10. Polya G (1948) Torsional rigidity, principal frequency, electrostatic capacity and symmetrization. Q Appl Math I:267–277
11. Korobko VI (1997) Isoperimetric method of structural mechanics: theoretical basis of isoperimetric method. ASV, Moscow
12. Korobko AV (1999) Geometrical modeling of area form in two-dimensional problems on elasticity theory. ASV, Moscow
13. Korobko VI, Korobko AV, Chernyaev AA (2016) Isoperimetric properties of the torsion rigidity of convex section. Proc Eng 150:1648–1656. <https://doi.org/10.1016/j.proeng.2016.07.146>

14. Korobko AV, Savin S Yu, Ivlev IA (2017) Stability analysis of orthotropic rectangular plates compressed all over the contour. *J Appl Eng Sci* 15(3):332–338. <https://doi.org/10.5937/jaes15-14603>
15. Korobko VI, Korobko AV, Chernyaev AA, Savin SY (2015) Determination of maximum deflection at cross bending parallelogram plates using conformal radius ratio interpolation technique. *J Serb Soc Comp Mech* 9(2):36–45. <https://doi.org/10.5937/jsscm1501036k>
16. Korobko VI, Korobko AV, Savin SY, Chernyaev AA (2016) Solving the transverse bending problem of thin elastic orthotropic plates with form factor interpolation method. *J Serb Soc Comp Mech* 10(2):9–17. <https://doi.org/10.5937/jsscm1602009k>
17. Korobko AV, Chernyaev AA, Korobko VI (2017) Determination of basic dynamic vibration frequency at trapezoid plates using conformal radius ratio interpolation technique. *Proc Eng* 206:25–30. <https://doi.org/10.1016/j.proeng.2017.10.432>
18. Chernyaev AA (2017) Improving the accuracy of geometric interpolation for determining fundamental frequency of parallelogram plates vibration. *Proc Eng* 206:31–34. <https://doi.org/10.1016/j.proeng.2017.10.433>
19. Korobko VI, Savin SY, Ivlev IA (2017) Stability analysis of orthotropic plates by the form factor interpolation method. *Proc Eng* 206:924–928. <https://doi.org/10.1016/j.proeng.2017.10.573>
20. Korobko AV, Balikhina YE (2017) The definition of the geometric torsional rigidity for sections in the shape of the figure intermediate between a circle and a regular polygon. *Build Reconstr* 5(63):21–26. [http://oreluniver.ru/public/file/archive/Stroitel'stvo_i_rekonstruktsiya_5\(73\)-2017.pdf](http://oreluniver.ru/public/file/archive/Stroitel'stvo_i_rekonstruktsiya_5(73)-2017.pdf)

Strength Calculation of the Frame of Tourist Solar-Powered Vehicle in the Conditions of Static Loading



A. A. Polivanov and V. S. Galuschak

Abstract The paper summarizes the strength calculations made for the frame of the Tourist solar-powered vehicle. The peculiarities of the frame manufacture and its main characteristics were considered. Strength calculations were carried out in ANSYS, as it is a versatile software package that offers considerable functionality for core calculations. For the material model, the researchers picked a bilinear plasticity model with kinematic hardening; the plasticity condition was a von Mises criterion. The frame was rigidly fixed to the front wheel and rear suspension mounting points. A static load of 50–250 kg was set to the seat mounting points. According to these results, maximum static load is 172.5, as exceeding it will cause irreversible deformations. Static load capable of causing destabilization and destruction of the frame equals 228 kg. The obtained results mean it is recommendable to reinforce the lower frame in the seat mounting points in order to reduce the frame deflection. This requires either additional reinforcements or altering the frame configuration whatsoever. Further, research is required to find the most optimal solution.

Keywords The electric bike · Solar electric mobile · Renewable energy · Engineering vehicles

1 Introduction

The paper summarizes the strength calculations made for the frame of the Tourist solar-powered vehicle [1, 2]. This is a single-occupancy Tourist electric bike running on a solar-charged battery. When not propelled by the rider's efforts, the Tourist can run infinitely in sunlight or up to 35 km without it [1, 2]. Such vehicles in various designs are the future of personal transportation.

A. A. Polivanov (✉) · V. S. Galuschak
Kamishin Technological Institute (Branch) The Volgograd State
Technical University, 6A, Lenin St., Kamyschin 403874, Russia
e-mail: polivanov@kti.ru

The Tourist solar-powered vehicle is made by the staff and students of the Kamyshin Technological Institute (branch) of VSTU (Kamyshin, Volgograd region, Russian Federation).

In the previous paper [3], the authors formulated the tasks that need to be performed to form the technical appearance of the Tourist solar-powered vehicle. Features of the formation of the technical appearance of vehicles are discussed in detail in [4]. One of the first tasks to be considered is to determine the strength characteristics of the Tourist solar-powered vehicle frame and prepare recommendations for its optimal design.

The main task of this paper is determination the strength characteristics of the Tourist solar-powered vehicle frame and prepare recommendations for its optimal design.

2 Research Goals

The research presented herein was to produce strength calculations for the Tourist solar-powered vehicle subjected to static load; expected findings would be the recommendations for the design of series-produced models.

3 The Description of Calculation Method

Strength calculations were carried out in ANSYS, as it is a versatile software package that offers considerable functionality for core calculations. ANSYS is a common choice for vehicle strength calculations, see e.g. [5–8].

Generally, the structure of a frame depends on the vehicle the frame is to be used in. The on-road behavior of a vehicle depends on the profile and structure of its frame components. The mechanical properties of the frame material are of importance, too. Frames may differ in stiffness and strength, even if made of the same material but differing in geometry; likewise, similar designs will have different properties, if different materials are used. In-frame joining method (welding, bolting, or hinge, etc.) is of paramount significance.

The Tourist prototype frame was designed and made empirically without preliminary strength calculations; that said, the geometry and material solutions were based on the designers' gut feeling. This design method was widely used before, and fully justified itself, due to the lack of specialized software systems for strength calculations. The manufacturers of the most diverse mechanisms carry out a whole range of field and virtual tests today (includes strength calculations), before launching it on the market. The quantitative characteristics of the Tourist frame carrying capacity are not currently known, because the field strength tests were not carried out. With no field strength tests, quantifying the carrying capacity of the frame seemed impossible. Therefore, finding that capacity was crucial. This was to be done by the authors hereof.

To make the mainframe of the prototype, the designers used a square-section 20×20 mm metal profile; the lower part was made of 20×40 mm rectangular profiles (GOST 30245-2003, St3 steel, 2 mm thick). The designers chose that kind of steel due to its availability, low cost, and ease of machining. Joints were mostly welded, occasionally bolted. Regardless of this, all the frame joints were assumed permanent when constructing a geometric model. Whether this material is actually suitable for making solar-powered vehicle frames is a question yet to be answered.

Thus, the Tourist frame is a solid non-dismountable element, except the front drive wheel mounting point, the rear-wheel suspension, and the steering handles. A transparent fairing made of 3 mm thick polycarbonate sheets is screwed to the frame top to make the entire structure stiffer. The fairing top carries three solar cells. In these calculations, the fairing effects on the frame strength were largely neglected.

Let us now proceed to the frame strength calculations. To that end, we had to measure all the frame sections take to make a frame model. Figure 1 shows the ANSYS model we made.

The model consisted of 132 nodes and 180 node-to-node edges, for which we chose Beam189. The roof joints were reinforced with four stiffeners represented by Solid285. In the actual design, these stiffeners were made of 3 mm thick St3 steel sheets and welded to the frame. Solid285 was also used to make the front-wheel mount.

This figure does not show the elements of the suspension and steering.

The material has the following characteristics:

- modulus of normal elasticity: 200 GPa;
- Poisson's ratio: 0.3;
- yield strength: 240 MPa;
- tensile strength: 370 MPa;
- relative elongation at break: 30%.

The design weight is always less than the actual weight, as it is difficult to calculate the weight of metal in welds in and bolted joints. For the material model, the researchers picked a bilinear plasticity model with kinematic hardening; the plasticity condition was a von Mises criterion.

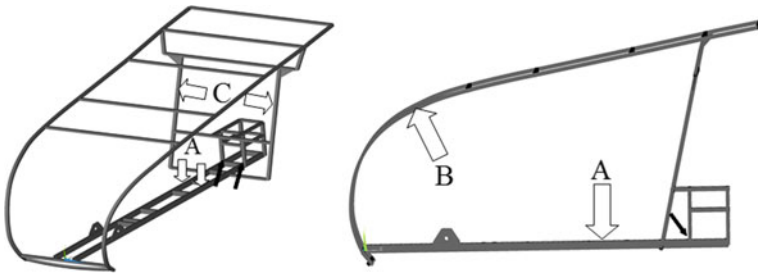


Fig. 1 The appearance of a geometric model built using ANSYS

In these calculations, the frame was rigidly fixed to the front wheel and rear suspension mounting points. A static load of 50–250 kg was set to the seat mounting points. Such loads match well this solar-powered vehicle model, as they correspond to the possible weight of the pilot plus payload while also reflecting the dynamic loads in long-distance travels.

The calculation was aimed at obtaining critical loads that might cause irreversible plastic deformation in the frame. In addition, it was necessary to find element-specific deformations as a function of load; these values could be used to estimate the stiffness of the frame in general.

4 Experimental Results

When running the calculations, the research team identified the frame sites of most significant bending deformation. These are the lower section near the seat mounting point (A in Fig. 1), the roof arc curvature points (B), and the vertical frame section behind the seat (C). Light arrows show the frame deflection directions. Elsewhere, deflections are less significant. Dark arrows signify the points of primary irreversible deformation. These are the points where the lower frame is attached to the rear-wheel suspension nodes.

Figure 2 shows the maximum frame deflection in the seat mounting points as a function of load. An asterisk, “*,” stands for loads, exceeding which causes plastic deformation in the deflection point. According to these results, maximum static load is 172.5, as exceeding it will cause irreversible deformations. Actual load in use is expected to be below this value; to find it, one must simulate the frame dynamically in the context of all possible mechanical impacts.

Static load capable of causing destabilization and destruction of the frame equals 228 kg, see “#” in the figure. Frame destruction onset points are the same points, where primary irreversible deformations occur.

Figure 3 shows the roof arc deflection as a function of load. This parameter is non-ignorable, as the roof carries the solar cells, the most expensive component of this vehicle. Considerable deflection in the frame roof arcs might cause the destruction of solar cells even if the metal deformation is reversible. Asterisks also signify the loads, at which the roof arc material could demonstrate plastic deformation.

Figure 3 shows that upon reaching a static load of 172.5 kg, the roof arc deflection is less than 1 mm, which this type of fairing or solar cells can endure well. However, these calculations ignore the strength of the fairing, which can make the entire structure stiffer and reduce the deflection. This might reduce the necessary number of frame reinforcements, making it cheaper and more lightweight. Such approaches find use in the automotive industry, where both the front window and the rear window belong to the body frame, enabling the use of less stiff sheet steel to make door pillars or roof. In that case, one must consider the strength of the glass itself. Paper [9] presents a method for using ANSYS to calculate the strength of the

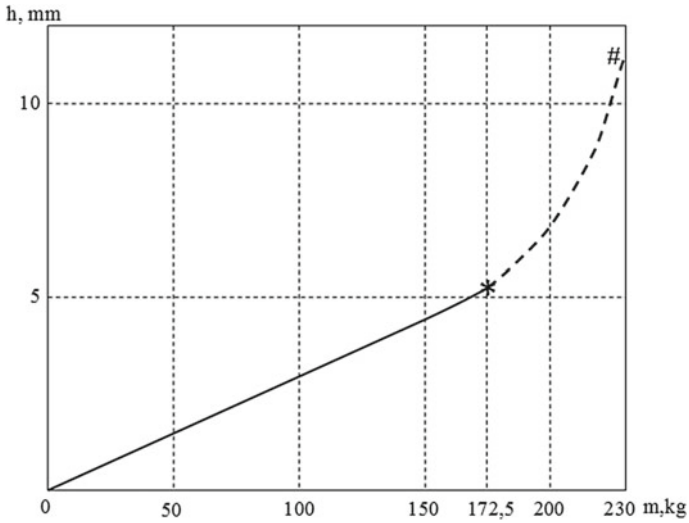


Fig. 2 The dependence of the maximum buckling of the frame at the points of the seat attachment on the load magnitude

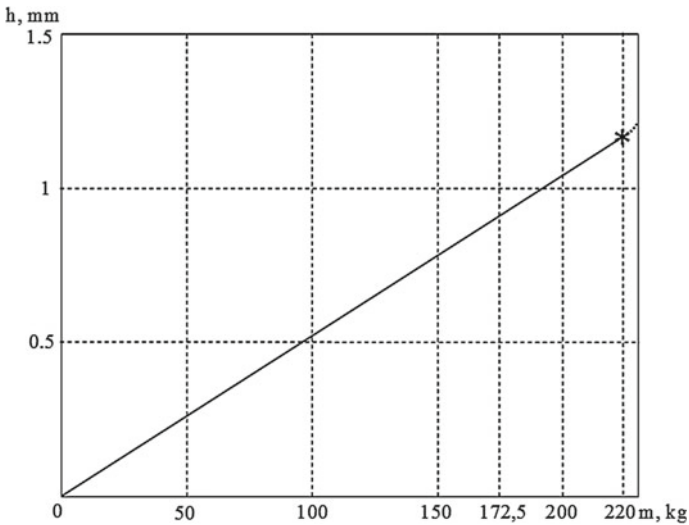


Fig. 3 The dependence of the deflection of the arcs that form the roof, depending on the load

windshield in a VAZ-2172 Priora car. Calculating the strength of the Tourist fairing can be approached similarly.

However, the upper frame may reach such stress-strained condition, in which the roof arc deflection will become supercritical, entailing a brittle fracture in the fairing (for example, if it is made of polymethylmethacrylate, less durable material than

polycarbonate). This will inevitably lead to the rupture and destruction of the solar panel. Further, research is required to find the parameters of such a condition, as well as to define when and where it might occur.

Besides, further efforts to design the solar-powered vehicle must take into account that significant cyclic deformations might damage or even destroy the painting, causing the product to have worse appearance, or even to corrode. This is why the frame painting type and application method must be selected in the light of maximum permissible deflections in the frame.

5 Conclusions

The findings hereof mean it is recommendable to reinforce the lower frame in the seat mounting points in order to reduce the frame deflection. This requires either additional reinforcements or altering the frame configuration whatsoever. Further research is required to find the most optimal solution.

References

1. Galuschak VS, Soshinov AG, Karpenko OI (2009) Solar bicycle. RUS Patent 82640, 10 May 2009
2. (2018) The solar-electric-mobile. <http://solncekat.ru/>. Accessed 20 Nov 2018
3. Polivanov AA, Galuschak VS (2017) Fundamentals of conceptual positions in the design of the solar-electric-mobile "Tourist". *Successes Mod Sci* 4(4):61–63
4. Kalimulin MR (2012) Analysis of the process of formation of the technical appearance of especially lightweight high-mobility wheeled vehicles for mountainous operating conditions. *Electron Sci Tech J "Sci Educ"* 11:121–138
5. Kovenya AS, Pronkevich SA, Chernyshev DA (2011) Modeling of the stress-strain state of the city bus carcass in the ANSYS environment. *Automot Ind* 3:16–19
6. Markova EV, Chechuga OV (2016) Using the ANSYS program for analyzing the performance of structures. *News of Tula State University. Tech Sci* 8–2:206–209
7. Kosenko EE (2014) Simulation of the stress state of an element of the frame structure of a car in the CE complex ANSYS. *Bull Donetsk Acad Road Transp* 4:79–84
8. Molchanov AI, Molchanova EA (2012) Solving engineering problems using ANSYS, vol 1. *Bulletin of the Khakass State University. N.F. Katanova*, pp 114–120
9. Pereverzev AS, Semenikhin BA, Kuznetsova LP (2016) Using the ANSYS software package to study the strength characteristics of a car windshield, vol 2, issue no 19. In: *Proceedings of the South-West State University. Series: Engineering and technology*, pp 108–114

Durability of Centrifugal Pump Impeller Blades Exposed to Corrosive–Erosive Wear



V. A. Pukhliy and S. T. Miroshnichenko

Abstract The researchers have developed a theory of the corrosive–erosive wear applicable to the plates and shells of centrifugal or axial pump impellers; the theory takes into consideration the stress state and the stationary temperature field. Omitting the intermediate calculations, we present a system of differential equations in Marguerre-type partial derivatives on a normal deflection w and a stress function of the eighth order, which describe the stress state of a variable-thickness blade in the context of temperature effects. In this research, the blade thickness change function is set as cubic splines. Analytical solution of the equation system with the boundary conditions is based on using the Dorodnitsyn’s integral ratios method. Pursuant to the method, write the original equation system as a divergent system. Limited to binomial approximation and also choosing power polynomials and their derivatives as weights, apply the integral ratios method to the original system of equations to obtain a system of ordinary differential equations (8n order) with variable coefficients. The boundary value problem is solved by the modified method of successive approximations, developed by Prof. V. A. Pukhliy and published by him in the academic press.

Keywords Durability · Centrifugal pumps · Impeller blades · Corrosive–erosive wear

1 Introduction

In some industries, particularly in chemistry, nuclear power, etc., centrifugal pumps are exposed to aggressive environments that makes the impeller blades and plates susceptible to corrosion. Besides the aggressive environment, blades and plates are exposed to particulate matter, resulting in their erosion. How the stress–strain state affects the corrosion and erosion rate is also of importance. For instance, 1% strain

V. A. Pukhliy (✉) · S. T. Miroshnichenko
Sevastopol State University, 31, Street Universitetskaya, Sevastopol 299053, Russia
e-mail: pu1611@rambler.ru

increases the rate at which silica iron corrodes in a 0.01% sulfurous acid solution by 53% compared to non-strained metal.

Corrosive cracking of stressed metals has been studied earlier. This phenomenon occurs when reaching certain critical (threshold) stress values, which depend on the effective stress and on the potential energy. Less than critical stress does affect the general corrosion while not resulting in cracking.

Centrifugal pump blades exposed to corrosive wear are usually made as thin-walled plates or shells. The durability of centrifugal pump blades is a problem of durability concerning plates and shells whose thickness varies over time while being exposed to aggressive environments that have certain parameters (chemical activity, temperature, flow rate, etc.) and to a stress–strain state.

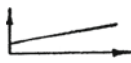


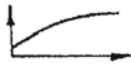
One of the pioneer works in this focus area was a paper by Kornishin [1] that dwelled upon the simultaneous solution of corrosion equation (corrosion rate as a linear function of stress) and equations describing the stress–strain state of a variable-thickness shell. The system of simultaneous equations describing the shell behavior in a corrosive environment was then solved in finite differences following a time-stepped two-layer explicit scheme.

Today, there are multiple semi-empirical models to approximate the corrosive wear in the context of the stress state. Table 1 presents a number of models used in computation [2].

Table 1 uses the following notation: h is the wear layer depth; t is time; σ and ε are stress and strain; T is the temperature; k , α , β and γ are constants; $\varphi(t)$ are some functions.

Centrifugal pump impeller blades and the elements of pipelines transporting fluids with particulate matter are exposed to erosive wear due to being impacted by

Table 1 Corrosive wear models

Corrosive wear equation	Stress and corrosion rate correlation law	
$\frac{dh}{dt} = \phi(t)(1 + k\sigma)$	$\frac{dh}{dt}$	
$\frac{dh}{dt} = \phi(t)e^{\alpha\sigma/RT}$	$\frac{dh}{dt}$	
$\frac{dh}{dt} = \alpha + \beta(\sigma - \sigma_0)\varepsilon$	$\frac{dh}{dt}$	
$\frac{dh}{dt} = \alpha - \beta e^{-\gamma\sigma}$	$\frac{dh}{dt}$	

such particulate matter. Blade surface wear intensity and nature greatly depend on the particle size and density as well as on the centrifugal pump operating parameters. When modeling the erosive wear of a blade mathematically, one needs to obtain experimental correlations between metal wear intensity and impact parameters such as the particle speed and the angle of attack. These matters were discussed in a number of papers by Pukhliy and Mikhailov [3] with respect to centrifugal superchargers.

2 Statement of Problem

Figure 1 shows the diagram of a centrifugal pump.

Consider the durability of centrifugal pump impeller blades that are essentially trapezoidal shells of variable stiffness, see Fig. 2. The blade is exposed to corrosive and erosive wear simultaneously.

The rate at which the thickness changes in this point of the blade is assumed to follow a functional dependency:

$$\frac{dh}{dt} = F(t, T, \sigma) \quad (1)$$

with the initial condition:

$$h(x, y, 0) = h_0(x, y), \quad (2)$$

where x and y are the blade median surface coordinates; T is the temperature; σ is a function to correlate the thickness change rate to the surface point stress state. The function F must be found experimentally.

Fig. 1 Centrifugal pump diagram: 1 is the confuser; 2 is the impeller; 3 is the diffuser

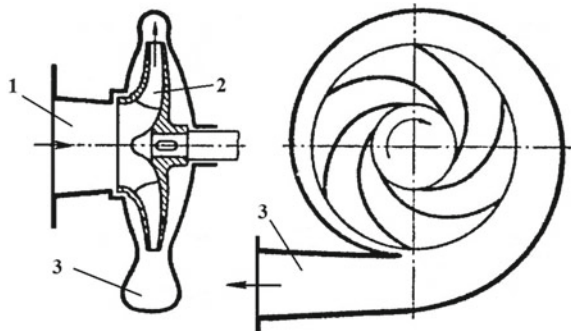
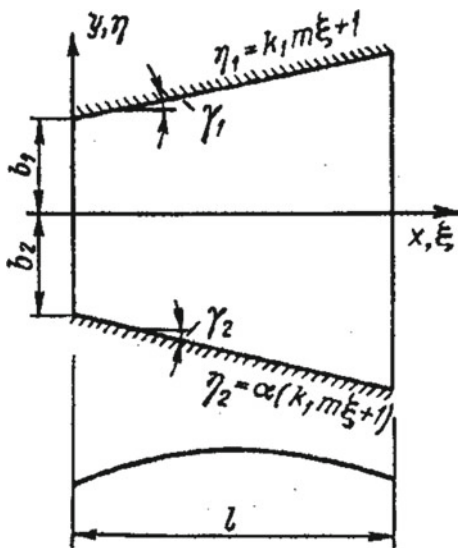


Fig. 2 Centrifugal pump blade geometry and coordinate system



Assume that the rate of change of erosive–corrosive wear is a linear function of stress intensity. Then, rewrite the Eq. (1) as follows:

$$\frac{dh}{dt} = \phi(t)(1 + k\sigma_{ij}). \quad (3)$$

Equations of the variable-thickness shell theory must be concatenated to Eq. (3).

Omitting the intermediate calculations, let us present a system of differential equations in Marguerre-type partial derivatives [4] on a normal deflection w and a stress function F of the eighth order, which describe the stress state of a variable-thickness blade in the context of temperature effects:

$$\begin{aligned} D\nabla^4 w + 2\frac{\partial D}{\partial x}\frac{\partial}{\partial x}\nabla^2 w + 2\frac{\partial D}{\partial y}\frac{\partial}{\partial y}\nabla^2 w + \nabla^2 D\nabla^2 w - (1-\nu)L(D, W) - h\nabla_k^2 F \\ = q - \nabla^2 M_T; \\ \frac{1}{B}\nabla^4 F + 2\frac{\partial}{\partial x}\left(\frac{1}{B}\right)\frac{\partial}{\partial x}\nabla^2 F + 2\frac{\partial}{\partial y}\left(\frac{1}{B}\right)\frac{\partial}{\partial y}\nabla^2 F + \nabla^2\left(\frac{1}{B}\right)\nabla^2 F - (1+\nu)L\left(F, \frac{1}{B}\right) + \frac{(1-\nu^2)}{h}\nabla_k^2 w \\ = -(1-\nu)\frac{1}{h}\nabla^2\left(\frac{N_T}{B}\right) \end{aligned} \quad (4)$$

here, $T = T(x, y, z)$ is a temperature field, standard form; α is the linear expansion coefficient of the blade material. ∇^2 and ∇^4 are the harmonic and bi-harmonic operators; ∇_k^2 is the meta-harmonic operator: $\nabla_k^2 = k_{11}\frac{\partial^2}{\partial x^2} + k_{22}\frac{\partial^2}{\partial y^2}$; $L(D, w)$ and $L\left(F, \frac{1}{B}\right)$ are the linear differential operators of the second order.

Power factors resulting from temperature effects are written as follows:

$$N_T = \frac{\alpha E}{1 - \nu} \int_{-h/2}^{h/2} T(x, y, z) dz; \quad (5)$$

$$M_T = \frac{\alpha E}{1 - \nu} \int_{-h/2}^{h/2} T(x, y, z) z dz.$$

Let us introduce a dimensionless coordinate system:

$$\xi = x/l; \eta = y/b_1; m = l/b_1 \quad (6)$$

as well as dimensionless unknown functions

$$\bar{w} = w/h_0; \bar{F} = \frac{F}{E^* h_0^2}. \quad (7)$$

here, h_0 is the characteristic blade thickness; E^* is the elastic modulus of the blade material at $T = 20^\circ\text{C}$.

Boundary conditions at the blade edges adjacent to plates $\eta_1 = k_1 m \xi + 1$ and $\eta_2 = \alpha(k_1 m \xi + 1)$ are as follows:

$$\bar{w} = \bar{w}_{,n} = \bar{F} = \bar{F}_{,n} = 0. \quad (8)$$

Boundary conditions for the input and output edges of the blade match those of the free edge. In this case,

$$N_\xi = N_{\xi\eta} = M_\xi = 0; Q_\xi - \frac{\partial M_{\xi\eta}}{\partial \eta} = 0. \quad (9)$$

It is important to set the blade thickness change function $h = h(x, y)$, which applies to corrosion- or erosion-induced changes.

This function can be set in different ways, i.e., by means of interpolation polynomials or rational fractions. However, both methods are suboptimal in terms of approximation for functions of not too great a smoothness. The main disadvantage is that their behavior in the neighborhood of a point determines their behavior in general. Preliminary calculations based on Lagrange interpolation polynomials and using blade profile approximation by least squares show that such approaches are impractical.

In this research, the blade thickness change function is set as cubic splines [5].

In this case, the blade thickness can be written as 2D spline interpolations as follows:

$$h(\xi_i, \eta_j) = h_0 \sum_{\alpha=0}^3 \sum_{\beta=0}^3 A_{\alpha\beta}^{(ij)} (\xi - \xi_i)^\alpha (\eta - \eta_j)^\beta (i = 0, 1, \dots, n; j = 0, 1, \dots, m). \quad (10)$$

For every element of the blade surface, this function

$$[\xi_i, \xi_{i+1}; \eta_j, \eta_{j+1}]$$

is a bicubic polynomial, continuous and has continuous partial derivatives up to and inclusive of $\frac{\partial^4 h(\xi, \eta)}{\partial \xi^2 \partial \eta^2}$, i.e., $h(\xi, \eta) \in C^{2,2}$.

Rewrite the system (4) in a dimensionless form:

$$\left. \begin{aligned} L_{11}(\bar{w}) + L_{12}(\bar{F}) &= L_1; \\ L_{21}(\bar{w}) + L_{22}(\bar{F}) &= L_2, \end{aligned} \right\} \quad (11)$$

where $L_{ik}(i, k = 1, 2)$ are dimensionless differential operators of the shell theory, belonging to the surface curvature lines; $L_m (m = 1, 2)$ are the components of the set superficial and thermal load.

3 Solving the 2D Boundary Value Problem

Analytical solution of the equation system (11) with the boundary conditions (8) is based on using Dorodnitsyn's integral ratios method.

Pursuant to the method, write the original equation system (11) as a divergent system:

$$\frac{\partial \bar{X}}{\partial \xi} + \frac{\partial \bar{Y}}{\partial \eta} + \bar{L} = 0, \quad (12)$$

where

$$\begin{aligned} \bar{X} &= \{X_i\} = \{\bar{w}, z_1, z_2, z_3, \bar{F}, z_4, z_5, z_6\}; \\ \bar{Y} &= B_0 \bar{X} + B_1 \frac{\partial \bar{X}}{\partial \eta} + B_2 \frac{\partial^2 \bar{X}}{\partial \eta^2} + B_3 \frac{\partial^3 \bar{X}}{\partial \eta^3}; \bar{L} = B \bar{X} + \bar{b}. \end{aligned}$$

z_1, \dots, z_6 stands for:

$$\begin{aligned} z_1 &= \bar{w}_{,1}; z_2 = \bar{w}_{,11}; z_3 = \bar{w}_{,111}; \\ z_4 &= \bar{F}_{,1}; z_5 = \bar{F}_{,11}; z_6 = \bar{F}_{,111}. \end{aligned}$$

In Eq. (12), $B_r = \{b_{mn,s}\}$ and $B = \{b_{mn}\}$ ($s = 0, 1, 2, 3; m, n = 1, 2, \dots, 8$) are conversion matrices.

Pursuant to Dorodnitsyn’s method [6], find a solution to the system of Eq. (12) as a decomposition:

$$X_i(\xi, \eta) = \begin{cases} \sum_{j=1}^n X_{ij}(\xi)P_j(\xi, \eta) & (i = 3, 6, 7, 8) \\ \sum_{j=1}^n X_{ij}(\xi)P_{j,2}(\xi, \eta) & (i = 1, 2) \\ \sum_{j=1}^n X_{ij}(\xi)P_{j,22}(\xi, \eta) & (i = 4, 5) \end{cases} \quad (13)$$

Choose Jacobi orthogonal polynomial systems [7, 8] and their derivatives as approximating and weight functions:

$$P_j(\xi, \eta) = P_1(\xi, \eta) \sum_{j=1}^n \left[\eta - \frac{(1 + \alpha)r}{2} \right]^{j-1};$$

$$P_1(\xi, \eta) = \eta^4 - 2(1 + \alpha)r\eta^3 + (1 + 4\alpha + \alpha^2)r^2\eta^2 - 2\alpha(1 + \alpha)r^3\eta + \alpha^2r^4.$$

here, $r = 1 + k_1m\xi$ is the equation of the blade slope.

Note that the polynomials $P_j(\xi, \eta)$ are orthogonal in the segment $[\eta_1, \eta_2]$ and form a system of linearly independent functions, thus meeting the boundary conditions of the slanting edges of the blade (8).

Notably, their derivatives $P_{j,2}(\xi, \eta)$ and $P_{j,22}(\xi, \eta)$ are also orthogonal.

Limited to binomial approximation and also choosing power polynomials $P_j(\xi, \eta)$ and their derivatives as weights, apply the integral ratios method to the original system of Eq. (12) to obtain a system of ordinary differential equations (8n order) with variable coefficients:

$$\frac{dX_m}{d\xi} = \sum_{v=1}^s B_{v,m}X_v + f_m, \quad m = 1, 2, \dots, s. \quad (14)$$

Note that math offers no exact solution of such equations in general, except some special cases like the Bessel equation.

The boundary value problem is solved by the modified method of successive approximations, developed by Prof. V. A. Pukhliy and published by him in academic press [9, 10].

The method was further extended to apply to initial-boundary value problems [11, 12], which used C. Lanczos’s telescoping of power series to accelerate the convergence of the solution [13]. To that end, they used the option to write any power series in terms of misaligned Chebyshev polynomials [7, 8]. Such an approach was first presented in V. A. Pukhliy’s papers [14, 15].

4 Modified Method of Successive Approximations

Pursuant to the method, let us write the variable coefficients $B_{v,m}$ and the constant terms f_m in terms of shifted Chebyshev polynomials:

$$f_m = \sum_{r=0}^q f_{m,r} (d_r \cdot r!)^{-1} \sum_{k=0}^r a_k T_k^*(\xi), B_{v,m} = \sum_{r=0}^q b_{v,m,r} d_r^{-1} \sum_{k=0}^r a_k T_k^*(\xi) \quad (15)$$

here, q is the degree of the interpolation polynomial; a_k are the coefficients of decomposing ξ^r in series by Chebyshev polynomials $T_k^*(\xi)$. In the expressions (15), $d_r = 1$ for $r = 0$ and $d_r = 2^{2r-1}$ for any other r .

General solution of the equation system (14) is written as follows [8, 9]:

$$X_m = \sum_{\mu=1}^s C_\mu \left[d_0^{-1} a_0 T_0^*(\xi) \delta + \sum_{n=1}^{\infty} X_{m,\mu,n} \right] + \sum_{j=0}^q t_{m,j,0} [d_{j+1} (j+1)!]^{-1} \sum_{k=0}^{j+1} a_k T_k^*(\xi) + \sum_{n=2}^{\infty} X_{m,n} \quad (16)$$

where $t_{m,j,0} = f_{m,r}$ at $j = r$; μ is the number of the basic function; C_μ are integration constants. In the solution (16), $\delta = 1$ if $m = \mu$ and $\delta = 0$ for the remaining μ .

First approximation $X_{m,\mu,1}$ is obtained by substitution of the zero approximation:

$$d_0^{-1} a_0 T_0^*(\xi) \delta \text{ in the right side of the system } \frac{dX_m}{d\xi} = \sum_{v=1}^s B_{v,m} X_v.$$

The next approximations are done by the formulae:

$$\begin{aligned} X_{m,\mu,n} &= \sum_{j=1}^{\beta} t_{m,\mu,n,j} [d_{n+j-1} (n+j-1)!]^{-1} \sum_{k=0}^{n+j-1} a_k T_k^*(\xi); \\ X_{m,n} &= \sum_{j=1}^{\beta} t_{m,n,j} [d_{n+j-1} (n+j-1)!]^{-1} \sum_{k=0}^{n+j-1} a_k T_k^*(\xi), \end{aligned} \quad (17)$$

where $\beta = n(q+3) - 2$.

The systems of basic functions (17) are uniformly converging series, whereby the coefficients $t_{m,\mu,n,j}$ and $t_{m,n,j}$ are found from the coefficients of the previous approximation by recurrent formulae:

$$\begin{aligned} t_{m,\mu,n,j} &= \sum_{v=1}^s \sum_{r=0}^q b_{v,m,r} t_{v,\mu,n-1,j-r} (n+j-1)^{-1} \prod_{\gamma=0}^r (n+j-1-\gamma), \\ t_{m,n,j} &= \sum_{v=1}^s \sum_{r=0}^q b_{v,m,r} t_{v,n-1,j-r} (n+j)^{-1} \times \prod_{\gamma=0}^r (n+j-\gamma). \end{aligned}$$

The constants C_μ , being part of the general solution (16), are found from the boundary conditions of the input and output edges of the blade (9).

Thus, the problem is reduced to the simultaneous solution of the Eq. (3), and the system of Eq. (11) provided the initial conditions (2) and the boundary conditions (8) and (9). At each of the time step, obtain numerical values of thickness from Eq. (3), which are further used to construct the spline function (10). Then, solve the equation system (11), which produces the values σ_{ij} .

The criterion to stop the stepwise process is the condition:

$$\sigma_{ij} \leq [\sigma_T], \quad (18)$$

where σ_T is the yield point of the material.

The duration of an element of a radial turbomachine impeller is obtained by summation of the time steps.

5 Conclusions

The researchers have developed a theory of the corrosive–erosive wear of centrifugal and axial pump impeller elements (plates and shells) that takes into consideration the stress state and the stationary temperature field.

Multiple rate-affecting factors such as the particle angle of attack, the particle speed and size, physicochemical characteristics, temperature and humidity are taken into account in a generalized manner by composing a differential equation of the impeller element thickness change rate.

The limit state criterion of the turbomachine impeller elements consists in reaching the material yield point σ_T .

There have been developed an algorithm for analytical solution of the erosive–corrosive wear problem for turbomachine impeller elements; the algorithm combines integral ratios and a modified method of successive approximations in shifted Chebyshev polynomials.

Acknowledgements Research has been funded by RFBR and the City of Sevastopol under Research Project No. 18-48-920,002.

References

1. Kornishin MS, Karpunin VG, Kleshchyov SI (1975) Computation of plates and shells in an overall corrosion context. In: Proceedings of the X All-Soviet conference of shell and plate theory, Tbilisi, pp 17–24
2. Ovchinnikov NG, Sabitov KA (1986) Comparative study into the extrapolatory capacities of some corrosive-wear models, exemplified by computing a cylindrical shell. Univ Bull Constr Archit 1:42–45

3. Mikhailov IA, Pukhly VA (1981) Method and algorithm to compute the erosive wear of impeller blades in radial dust-air superchargers. In: Abstracts of the VI All-Soviet research and engineering conference on compressor construction, Leningrad, p 1981
4. Marguerre K (1939) Zur theorie der gekrümmten Platte großer Formänderung. Jahrbuch 1939 der deutschen Luftfahrtforschung. Bd I, pp 413–418
5. Ahlberg J, Nielson E, Walsh J (1972) The theory of splines and their applications. Mir, Moscow, p 318
6. Dorodnitsyn AA (1960) One method to solve equations of laminar boundary layer. J Appl Math Technol Phys 3:111–118
7. Courant R, Hilbert D (1953) Methods of mathematical physics, vol I. Gostekhizdat, Moscow
8. Luke VL (1975) Mathematical functions and their approximations. Academic Press. Inc., New York, p 608
9. Pukhliy VV (1978) Method for analytical solution of 2D boundary-value problems for elliptic-equation systems. J Comput Math Math Phys 18(5):1275–1282
10. Pukhliy VA (1979) One approach to solve boundary-value problems of mathematical physics. Differ Eqn 15(11):2039–2043
11. Pukhliy VA (2015) Solving initial-boundary value problems of mathematical physics by modified method of successive approximations. Rev Appl Industriam Math 22(4):493–495
12. Pukhliy VA (2016) Accelerating the convergence of solutions when using modified method of successive approximations. Rev Appl Industriam Math 23(4):17–20
13. Lanczos C (1961) Practical methods of applied analysis. Fizmatgiz, Moscow, p 524
14. Pukhliy VA (1983) Analytical method to solve boundary-value shell theory problems. In: Proceedings of the XIII All-Soviet conference on plates and shells theory. Part IV. TPU Publishing, Tallinn, p 101–107
15. Pukhliy VA (1986) Cylindrical three-layer panel oblique-angled in plane: modified method of successive approximations to solve its bending problem. Appl Mech 22(10):62–67

Theoretical Calculation of Compressed Media Leaks in Working Bodies of Single-Rotor Screw Compressor with Circumferential Tooth Shape



A. F. Minikayev, V. A. Pronin and D. V. Zhignovskaya

Abstract In this paper, the problem of leakage of the medium being compressed in the working part of a single-rotor screw compressor (SSC) with a circumferential tooth shape is considered. The initial system of differential equations of hydro-gas dynamics in relative motion in a rotating system of cylindrical coordinates associated with a cutter tooth of a circumferential profile is shown. It was established that when considering the task, the system of differential equations of hydro-gas dynamics should relate to the thermal and caloric equations of the state of a continuous medium, the dependencies characterizing its viscosity and thermal conductivity, as well as boundary and initial conditions. Reasonably, the simplification of the obtained dependences is possible when evaluating the order of all their members, considering the specificity of the working medium flow in narrow gaps, which takes place in the engagement of the working bodies of a single-rotor screw compressor.

Keywords Single-rotor screw compressor · Hydrodynamic equations · A cutter tooth of a circumferential profile · Leakage of a compressed medium

1 Introduction

The current state of the economy is such that a fundamental restructuring of the entire economic mechanism is put in the forefront, the purpose of which is to bring industry to a qualitatively new level, and this is possible only if there are products of world quality.

Scientific and technical creativity should be directed not only at the improvement of the existing equipment and technology but also at the creation of fundamentally new highly efficient developments. Without this, it is impossible to conquer and

A. F. Minikayev (✉) · V. A. Pronin · D. V. Zhignovskaya
St. Petersburg National Research University of Information Technologies,
Mechanics and Optics, 49, Kronverksky Pr., 197101 St. Petersburg, Russia
e-mail: Minikayev@corp.ifmo.ru

hold leading positions, both in the scientific and technical, and in the economic and foreign policy spheres.

The development of scientific and technological progress leads to the expansion of the areas of application of artificial cold and pneumatic devices in various fields of human activity, and, consequently, to an increasing need for high-performance compressors.

The widespread use of compressed media in various industries requires significant energy consumption for their production. Therefore, increasing the energy efficiency of the compressor, considering the latest achievements of science and technology, is important for the country's economy. The energy efficiency of such machines depends on various factors.

To date, the problem of leakage of the compressed medium in the working part of a single-rotor screw compressor (SSC) with a circumferential tooth shape is very relevant. When solving the task, it is necessary to consider the specificity of the construction of the circumferential shape of the teeth of the cutters, which engage with the central screw [1–5]. Consequently, it is necessary to consider the original system of differential equations of hydro-gas dynamics in relative motion in a rotating system of cylindrical coordinates [6, 7], associated with a cutter tooth of a circumferential profile.

2 Materials and Methods

We assume that the system of cylindrical coordinates r, φ, z rotates together with the considered cutter tooth while the OZ axis is parallel to the axis of the $O'Z'$ cutter and passes through the center of the circle, which describes the tooth contour in the axial plane (Fig. 1). The distance between the center of the tooth contour and the axis of rotation of the cutter O_1O is equal to r_1 .

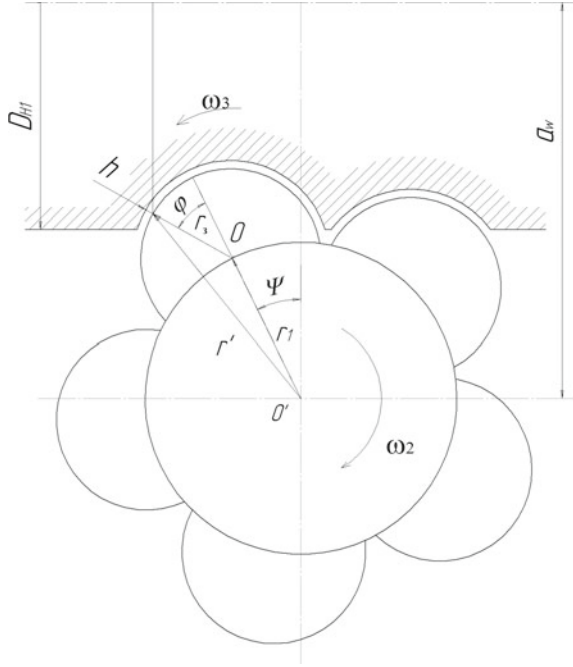
In the case of non-stationary motion of a compressible medium, the continuity equation in a cylindrical coordinate system [8] is:

$$\frac{\partial \rho}{\partial t} + \frac{\partial(\rho w_r)}{\partial r} + \frac{1}{r} \cdot \frac{\partial(\rho w_\varphi)}{\partial \varphi} + \frac{\partial(\rho w_z)}{\partial z} + \frac{\rho w_r}{r} = 0 \quad (1)$$

where ρ —the density of the working environment; t —time; w_r, w_φ, w_z —radial, circumferential, and axial components of the relative flow velocity with respect to the cutter tooth.

Differential equations of motion of a continuous medium in the considered coordinate system should contain bulk inertia forces, which are described by the equation:

Fig. 1 Engagement of the working bodies of a single-screw screw compressor in the axial plane



$$\vec{F} = \omega_2^2 \vec{r}' - r \vec{\omega}_3 \cdot \vec{w} \tag{2}$$

where \vec{r}' —radius vector drawn from the axis of rotation of the cutter to the point in question; $\vec{\omega}_3$ —vector of the angular velocity of the screw relative to the cutter; \vec{w} —relative velocity of continuum. Then, the components of bulk inertia forces considering Fig. 1 can be written in the form of a system of equations:

$$\begin{cases} F \approx \omega_3^2(r_3 + r_1 \cos \phi) + 2\omega_3 w_\phi \\ F_\phi \approx -\omega_3^2 r_1 \sin \phi - 2\omega_3 w_r \\ F_z = 0 \end{cases} \tag{3}$$

The differential equations of laminar motion [9] can be represented in the form:

$$\frac{dw_r}{dt} - \frac{w_\phi^2}{r} = -\frac{1}{\rho} \cdot \frac{\partial p}{\partial r} + \omega_3^2(r + r_1 \cos \phi) + 2\omega_3 w_\phi + \varphi_r; \tag{4}$$

$$\frac{dw_\phi}{dt} + \frac{w_r w_\phi}{r} = -\frac{1}{\rho r} \cdot \frac{\partial p}{\partial \phi} - \omega_3^2 r_1 \sin \phi - 2\omega_3 w_r + \varphi_\phi; \tag{5}$$

$$\frac{dw_z}{dt} = -\frac{1}{\rho} \cdot \frac{\partial p}{\partial z} + \varphi_z; \tag{6}$$



here p —pressure; $\varphi_r, \varphi_\phi, \varphi_z$ —are the terms of the equations characterizing the effect of the viscosity of the medium and are related to the tangential stresses in the flow $\tau_{rr}, \tau_{r\phi}, \tau_{rz}, \tau_{\phi\phi}, \tau_{\phi z}$ and τ_{zz} by the relations:

$$\varphi_r = \frac{1}{\rho} \left[\frac{\partial \tau_{rr}}{\partial r} + \frac{\partial \tau_{r\phi}}{r \partial \phi} + \frac{\partial \tau_{rz}}{\partial z} + \frac{\tau_{rr} - \tau_{\phi\phi}}{r} - \frac{2}{3} \cdot \frac{\partial}{r \partial r} \cdot (\mu \cdot \text{div} \vec{w}) \right] \quad (7)$$

$$\varphi_\phi = \frac{1}{\rho} \left[\frac{\partial \tau_{r\phi}}{\partial r} + \frac{\partial \tau_{\phi\phi}}{r \partial \phi} + \frac{\partial \tau_{\phi z}}{\partial z} + 2 \frac{\tau_{r\phi}}{r} - \frac{2}{3} \cdot \frac{\partial}{r \partial \phi} \cdot (\mu \cdot \text{div} \vec{w}) \right] \quad (8)$$

$$\varphi_z = \frac{1}{\rho} \left[\frac{\partial \tau_{rz}}{\partial r} + \frac{\partial \tau_{\phi z}}{r \partial \phi} + \frac{\partial \tau_{zz}}{\partial z} + \frac{\tau_{rz}}{r} - \frac{2}{3} \cdot \frac{\partial}{\partial z} \cdot (\mu \cdot \text{div} \vec{w}) \right] \quad (9)$$

in which μ —dynamic viscosity, and $\text{div} \vec{w}$ —the divergence of the relative flow velocity, which can be determined from the equation:

$$\text{div} \vec{w} = \frac{1}{r} \cdot \frac{\partial}{\partial r} (r w_r) + \frac{1}{r} \cdot \frac{\partial w_\phi}{\partial \phi} + \frac{\partial w_z}{\partial z} \quad (10)$$

3 Results

Tangential stresses are related to the components of the strain rate tensor: $\dot{S}_{rr}, \dot{S}_{r\phi}, \dot{S}_{rz}, \dot{S}_{\phi\phi}, \dot{S}_{\phi z}, \dot{S}_{zz}$ the following dependencies [10–14]:

$$\tau_{rr} = 2\mu \dot{S}_{rr}, \tau_{rz} = 2\mu \dot{S}_{rz}, \tau_{\phi z} = 2\mu \dot{S}_{\phi z}$$

$$\tau_{r\phi} = 2\mu \dot{S}_{r\phi}, \tau_{\phi\phi} = 2\mu \dot{S}_{\phi\phi}, \tau_{zz} = 2\mu \dot{S}_{zz}$$

It should be noted that the following expressions are valid for the components of the strain rate tensor:

$$\begin{cases} \dot{S}_{rr} = \frac{\partial w_r}{\partial r} \\ \dot{S}_{r\phi} = \frac{1}{2} \left(\frac{\partial w_\phi}{\partial r} - \frac{w_\phi}{r} + \frac{\partial w_r}{r \partial \phi} \right) \\ \dot{S}_{rz} = \frac{1}{2} \left(\frac{\partial w_z}{\partial r} + \frac{\partial w_r}{\partial z} \right) \\ \dot{S}_{\phi\phi} = \frac{\partial w_\phi}{r \partial \phi} + \frac{w_r}{r} \\ \dot{S}_{\phi z} = \frac{1}{2} \left(\frac{\partial w_z}{r \partial \phi} + \frac{\partial w_\phi}{\partial z} \right) \\ \dot{S}_{zz} = \frac{\partial w_z}{\partial z} \end{cases} \quad (11)$$

The energy balance equation [15, 16] we write in the form:

$$\rho \frac{di}{dt} = \frac{dp}{dt} + N_{\partial uc} + \text{div}(\lambda \cdot \text{grad}T) \quad (12)$$

In the above equation, i —specific enthalpy of the moving continuous medium; T —temperature; λ —thermal conductivity coefficient; $N_{\partial uc}$ —power of friction forces dissipated into heat and related to the components of the strain rate tensor by the equation:

$$N_{\text{dis}} = 4\mu \left(\dot{S}_{r\phi}^2 + \dot{S}_{\phi z}^2 + \dot{S}_{rz}^2 \right) + \frac{2}{3}\mu \left[(\dot{S}_{rr} - \dot{S}_{\phi\phi})^2 + (\dot{S}_{\phi\phi} - \dot{S}_{zz})^2 + (\dot{S}_{zz} - \dot{S}_{rr})^2 \right] \quad (13)$$

The last member of Eq. (12), which characterizes the thermal conductivity, can be represented as:

$$\text{div}(\lambda \cdot \text{grad}T) = \frac{\partial}{\partial r} \left(\lambda \frac{\partial T}{\partial r} \right) + \frac{1}{r} \cdot \frac{\partial}{\partial \phi} \left(\lambda \frac{\partial T}{r \partial \phi} \right) + \frac{\partial}{\partial z} \left(\lambda \frac{\partial T}{\partial z} \right) + \frac{\lambda}{r} \cdot \frac{\partial T}{\partial r} \quad (14)$$

In this case, in Eqs. (4)–(6) and (12) operator $\frac{d}{dt}$ can be written as:

$$\frac{d}{dt} = \frac{\partial}{\partial t} + w_r \frac{\partial}{\partial r} + \frac{w_\phi}{r} \cdot \frac{\partial}{\partial \phi} + w_z \frac{\partial}{\partial z} \quad (15)$$

If we use the continuity Eq. (1) and the equations of motion (4)–(6), then we can write the energy balance equation as:

$$\begin{aligned} \frac{\partial}{\partial t} (\rho i^* - p) + \frac{1}{r} \cdot \frac{\partial}{\partial r} (r_\phi w_r i^*) + \frac{1}{r} \cdot \frac{\partial}{\partial \phi} (\rho w_\phi i^*) + \frac{\partial}{\partial z} (\rho w_z i^*) \\ = \rho w_r \varphi_r + \rho w_\phi \varphi_\phi + \rho w_z \varphi_z + \rho \omega_3 [w_r (r + r_1 \cos \phi) - w_\phi z \sin \phi] + N_{\partial uc} + \text{div}(\lambda \cdot \text{grad}T); \end{aligned} \quad (16)$$

where $i^* = i + \frac{1}{2} (w_r^2 + w_\theta^2 + w_z^2)$.

4 Conclusions

When considering the task, it is necessary to connect the thermal and caloric equations of the state of a continuous medium, the dependences characterizing its viscosity and thermal conductivity, as well as the boundary and initial conditions to the system of differential equations of hydro-gas dynamics.

Simplification of the dependences is possible when evaluating the order of all their members, considering the specificity of the flow of the working medium in

narrow gaps that occur in the engagement of the working bodies of a single-rotor screw compressor [8, 17–21]. The calculations show that if we use the continuity equation and the equations of motion, then we can obtain the energy balance equation.

Acknowledgements The authors would like to thank the IEEE member Yerezhap Darkhan and for the financial support of ITMO University.

References

1. Pronin VA (1998) Screw single-rotor compressors for refrigeration and pneumatics. Dissertation, St. Petersburg State Academy of Cold and Food Technologies
2. Pronin VA, Zhelyabov VL, Kovalenko VV (1986) To the question of determining the geometric parameters of the cracks in the working part of a single-rotor screw compressor. *Intensification Prod Use Artif Cold Abstr All-Union Sci Tech Conf* 236:15–19
3. Pronin VA, Socks AN (1996) Features of the design of the working bodies of screw single-rotor compressors with a circumferential tooth profile. *Compressors Pneumatics* 112:60–63
4. Pronin VA, Den GN, Novikov II (1992) Single-rotor screw machine. USSR Patent 181,392,4 Nov 1992
5. Pronin VA, Kovalenko VV, Isaev YuA (1989) Cutter single rotor screw machine. USSR Patent 147,969,2 Sept 1989
6. Vimmr JA, Fryc OA (2006) Numerical simulation of leakage flow between moving rotor and housing of screw compressor engineering simulation, vol 521. Gliwice, pp 461–468
7. Reddy CG (2007) CFD studies on flow through screw compressor. Institute of Technology, Rourkela
8. Den GN, Pronin VA, Voevodsky AA (1990) To the calculation of leakage through the gaps between the semi-circular cutter tooth and the screw of a single-rotor oil-filled screw compressor. *Res Improv Des Refrigerating Machi* 214:52–59
9. Zucker R, Biblarz O (2002) *Fundamentals of gas dynamics*. Wiley, USA
10. Rathakrishnan E (2010) *Applied gas dynamics*. Wiley
11. Bose TK (2014) *High temperature gas dynamics*. Springer Science & Business
12. Balachandran P (2006) *Fundamentals of compressible fluid dynamics*. PHI Learning Pvt Ltd
13. Liepmann HW, Roshko A (2013) *Elements of gas dynamics*. Courier Corporation
14. Amosov PE (1966) Influence of the physical properties of gases on the speed of rotation of screw compressor machines. *Compressor Refrigeration Eng*
15. Ginsburg IP (1953) Outflow of a viscous gas from a moving gap. *Bull Leningrad State Univ*
16. Hirschfelder JO, Curtiss CF, Bird RB (1964) *The molecular theory of gases and liquids*. Wiley-Interscience
17. Pronin VA, Verboloz AL (2012) Estimation of the effect of the mobility of the walls of the cracks on the leakage of the medium being compressed in a single-screw screw compressor (SSC). *Bull IAC* 210:13–17
18. Chen N (2011) *Aerothermodynamics of turbomachinery—analysis and design*. Wiley
19. Seppo A (2011) *Principles of turbomachinery*. Wiley, Korpela
20. Murty VD (2018) *Turbomachinery: concepts, applications, and design*. CRC Press
21. Pronin VA, Prilutsky AA, Dolgovskaya OV, Podbolotova TE (2015) Investigation of the performance of the scrubber in absorbing carbon dioxide. *Sci J NRU ITMO Seri Process Devices Food Prod* 247:132–140

Contact Strength Calculation of Straight Bevel Precessional Gears with Small Shaft Angle



V. Syzrantsev and A. Pazyak

Abstract Straight bevel precessional gears with a small shaft angle are a principally new type of bevel gears. It has a lot of great characteristics such as high efficiency due to multi-pair tooth meshing—high torque. A straight bevel precessional gear with a small shaft angle mainly has a wide range of gear ratios (100 and more) and small starting torque compared to worm and spiroid gearboxes. Furthermore, the straight bevel precessional gear with a small shaft angle can better adapt to the oil and gas industry because transmission provides a high loading capacity which is necessary in the Far North and Arctic climates. According to the Hertz contact theory, this paper described the final formula for contact strength of straight bevel precessional gears with a small shaft angle. The contrast analysis of contact strength between the straight bevel precessional gear with a small shaft angle and cylindrical gear and worm gear was investigated by computer simulation. The results reveal that the straight bevel precessional gear with a small shaft angle has a high loading capacity and contact strength in tooth meshing. The results of this paper can be used for the design and production of these types of gearboxes.

Keywords Precessional gearbox · Straight precessional bevel gear with a small shaft angle · Contact strength · Loading capacity

1 Introduction

The oil and gas branch is currently one of the most important industries. Reliable production and transportation of oil and gas are associated with the creation of an appropriate infrastructure, including an extensive network of technological and trunk pipelines with a large number of various shut-off and control valves. Valve control is performed using drives and gearboxes; their diversity is determined by the conditions of valve operation and its functional purpose. Reliability and safety

V. Syzrantsev · A. Pazyak (✉)
Industrial University of Tyumen, 38, Volodarskiy Street, 625000 Tyumen, Russia
e-mail: a.a.pazyak@gmail.com

© Springer Nature Switzerland AG 2020
A. A. Radionov et al. (eds.), *Proceedings of the 5th International Conference on Industrial Engineering (ICIE 2019)*, Lecture Notes in Mechanical Engineering,
https://doi.org/10.1007/978-3-030-22041-9_23

of valves in operating conditions, their competitiveness in the Russian and world markets are largely determined by the properties of the drive mechanisms.

In various pipeline systems, quarter ball valves with manual gear drives are widely used. Today, most of the modern stop valve gear drives which are used in the oil and gas industry are based on the use of worm [1–4] or spiroid [5–15] gears. Despite their successful layout schemes, excellent weight-dimension characteristics, and kinematic specifications, these types of gear drives have some disadvantages such as low efficiency and high starting torque (up to 10 times higher than the nominal torque) which can lead to the impossibility of shutting the pipeline and the use of high-power electric drives. In conditions of implementing remote control valve systems, it can lead to failure of electric motors due to the impossibility of their operation when the presence of “stickings” of ball valves and worm or spiroid gears in the Far North.

One of the ways to improve manual drives of the oil and gas equipment ensuring its performance is to use drives based on precessional bevel gears with a small shaft angle [16–22]. They realize multi-pair teeth engagement and higher transmitted torque compared to worm-type gears and a much smaller starting torque (Fig. 1).

It is shown that in a bevel gear with a small shaft angle in each fixed phase of engagement, the contact between the surfaces of the gear and pinion teeth is carried out along the line while gears geometrically conjugate. According to the methods for determining the contact load, this gearing is close to the helical gear.

At the same time, in comparison with the cylindrical gearing, the contact ratio in which is usually in the region of 1.4 ... 1.7, in a straight bevel precessional gear with a small shaft angle, the number of teeth pairs involved in the mesh can reach 3–5, which requires determining the total length of contact lines at a fixed engagement phase.

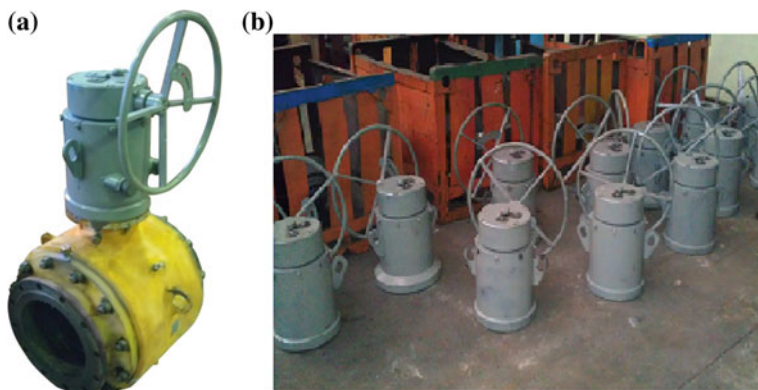


Fig. 1 a, b Ball valve gearboxes DN 300 based on a bevel precessional gear with a small shaft angle

Another task necessary for calculating the contact stresses in the engagement is to determine the main reduced curvatures included in the calculated dependencies (Hertz formulas) and showing the features of the engagement geometry.

2 Methods for Determining the Total Length of the Contact Lines

Mathematical models of the pinion generating process and geometry of gearing for these gears have already been discussed in the previous articles [19–26]. However, up to now, methods for determining the loading capacity of the gearboxes containing straight bevel precessional gears with a small shaft angle have not been developed.

The algorithm for solving the problem is to consider two limit cases of the contact lines location on the gear tooth surface.

As a result, we can determine the minimum length of contact lines in the studied straight bevel precessional gears with a small shaft angle which is necessary to calculate its load capacity (contact strength).

$$L_{\Sigma} = \min(L_{\Sigma}^{(a)}, L_{\Sigma}^{(d)}) \quad (1)$$

Contact lines location on the gear tooth surface (gear parameters are presented in the article [19]) for the considered case is shown in Fig. 3. In the studied straight bevel precessional gears with a small shaft angle, we determined that four tooth pairs are simultaneously in gearing meshing. As a result of the realization of the algorithm, the lengths of the contact lines are obtained and their total length (Fig. 2) is determined as: $L_{\Sigma}^{(a)} = 51,251$ mm. Similar calculations for contact lines (Fig. 3) made it possible to calculate the total length of the contact lines for this case: $L_{\Sigma}^{(d)} = 61.331$ mm. In addition, another case of contacting the teeth in the gear when the contact line passes through the calculated point of the tooth is considered $L_{\Sigma} = 55.014$ mm.

3 Methods for Calculating the Contact Strength of Straight Bevel Precessional Gears with a Small Shaft Angle

The experience of operating bevel gears in drives of various machines shows that the main criterion for the performance of these gears is contact strength. The contact strength of orthogonal bevel gears has been studied in numerous papers by various authors [23–31]. The results of these studies were the methods for calculating the

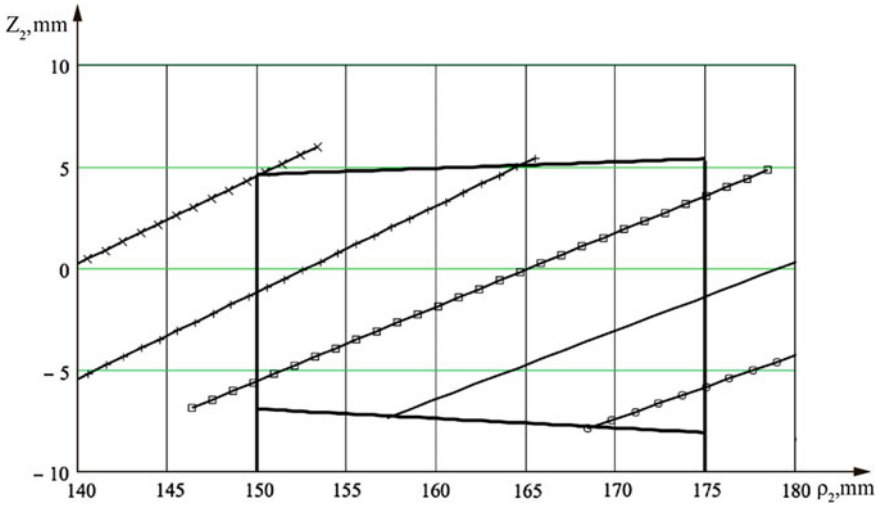


Fig. 2 Contact lines location on the gear tooth surface in the first case

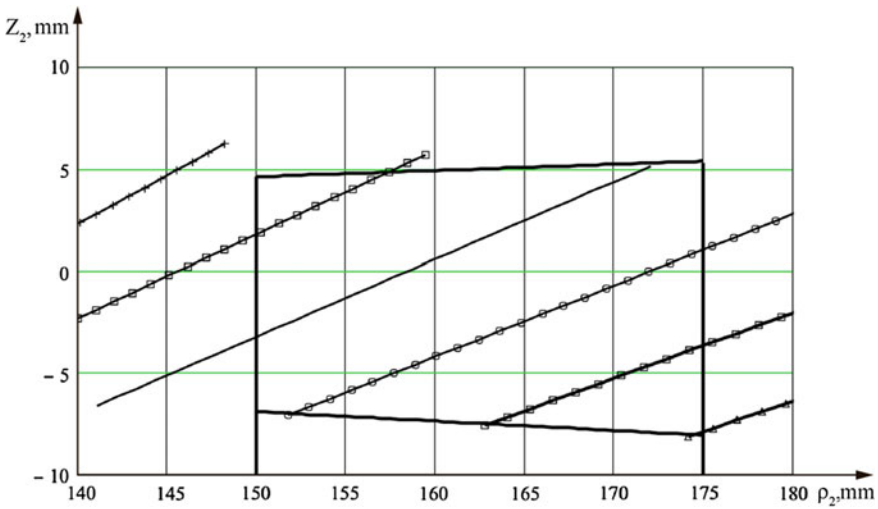


Fig. 3 Contact lines location on the gear tooth surface in the second case

stresses arising at the contact of the teeth, based both on the well-known analytical solutions of the contact problem [23–25], and on the realization of numerical methods of estimating the stress–strain condition of the teeth [26–31].

To develop methods for determining the contact strength of gears with a linear contact of tooth surfaces, the formula for maximum normal contact stresses [25, 32],

obtained in the theory of elasticity for the case of contact of two cylinders of unlimited length, is used as a result:

$$\sigma_H = \frac{1}{\sqrt{2 \cdot \pi \cdot (1 - \mu^2)}} \sqrt{\frac{g \cdot E_{np}}{\rho_{np}}} \quad (2)$$

where g —specific (linear) normal load at the contact of cylinders; μ —Poisson's ratio of cylinder materials; E_{np} —modulus of elasticity $E_{np} = \frac{E_1 E_2}{E_1 + E_2}$; E_1, E_2 —Poisson's ratio of cylinder materials; ρ_{np} —reduced curvature radius, with external contact of cylinders which have radii of curvature $\rho_1, \rho_2, \rho_{np} = \rho_1 \cdot \rho_2 / (\rho_1 + \rho_2)$.

For steel gears $\mu = 0,3$; $E_1 = E_2 = 2,15 \times 10^5$ MPa. As a result, formula (2) takes the form:

$$\sigma_H = 137,05 \sqrt{\frac{g}{\rho_{np}}} \quad (3)$$

Let the torque acts on the gear shaft of the studied straight bevel precessional gears with a small shaft angle. Knowing the current gear radius r_2 , and bearing in mind that the normal force, which arises in the engagement of pinions and gears teeth, makes an angle α_n to the initial surface (plane) of the gear tooth, and we determine the value of the total normal load P_Σ in the gear:

$$P_\Sigma = T_2 / (r_2 \cdot \cos \alpha_n) \quad (4)$$

Using the results of subsection 2 of this article, this load is distributed between all pairs of the contacting teeth on the working (contact) lines, the total length of which is equal to L_Σ . In this case, the linear load in formula (3) can be calculated from the dependencies:

$$g = P_\Sigma / L_\Sigma = T_2 / (r_2 \cdot L_\Sigma \cdot \cos \alpha_n) \quad (5)$$

To determine the value ρ_{np} , we use the results obtained in [19]. There, it was found that the main reduced curvature (in the profile direction) is determined by the relation in the case of linear contact of the teeth in the engagement: $\rho_{np} = 1/K_1$. Based on the article [19], it follows that curvature K_1 (6) changes smoothly both along the contact lines ($\approx 8\%$) and moving from one contact teeth pair to another ($\approx 20\%$).

$$K_1 = \frac{f_u \sin \theta_{f2} \cos \alpha_n \cdot w_{\phi y} + f_h \cos \theta_{f2} \cdot w_{\phi y} + f_u \sin \alpha_n \cdot w_{\phi x}}{r_2 (\cos \Sigma - i) (f_u \sin \theta_{f2} \cos \alpha_n + f_h \cos \theta_{f2}) + f_\phi \cos \theta_{f2} \sin \alpha_n} \quad (6)$$

where $w_{\phi x} = (\cos \Sigma - 1/i) \cos \alpha_n$; $w_{\phi y} = (\cos \Sigma - 1/i) \sin \theta_{f2} \sin \alpha_n - \cos \theta_{f2} \sin \alpha_n$
 $\sin \Sigma$; $f_u = \cos \alpha_n [i^{-1} \cdot \cos \theta_{f2} + \cos (\theta_{f2} + \Sigma)]$; $f_h = -\sin \theta_{f2} (1/i - \cos \Sigma) - \cos \theta_{f2} \cdot \sin \Sigma$
 $f_\phi = i^{-1} \cdot \sin \alpha_n \cdot \sin \Sigma \cdot (d \cdot \sin \theta_{f2} - r_2 \cos \theta_{f2})$.

To determine the value, we use the results obtained in [19] which referred to the study of the geometry of straight bevel precessional gears with a small shaft angle.

Substituting the dependencies (5) and (6) into formula (3), we define the expression for calculating the value of the maximum normal contact stresses in the test gear:

$$\sigma_H = 137,05 \sqrt{\frac{T_2 \cdot K_1}{r_2 \cdot L_\Sigma \cdot \cos \alpha_n}} \quad (7)$$

In the case when the value σ_H is set as allowed by the material $\sigma_H = [\sigma_H]$, formula (7) with known geometric parameters is followed by the formula for determining the maximum torque $T_{2\max}$:

$$T_{2\max} = \frac{r_2 \cdot L_\Sigma \cdot \cos \alpha_n}{K_1} \left[\frac{[\sigma_H]}{137,05} \right]^2 \quad (8)$$

The dependence (7) to calculate the value of the maximum stress in the teeth contact of straight bevel precessional gears with a small shaft angle was obtained without extensive experimental research of the loading capacity. So, it is only the first approximation in developing methods for calculating its contact strength for several reasons. When calculating formula (7), a geometrically ideal gear was considered, the errors of gear production, as well as the errors in the relative position of the gear and pinion, were not taken into account. Lots of geometrical features such as geometry of the gear teeth, the diagonal arrangement of the contact lines in the engagement and the multi-tooth contact lead to some kinds of deformations and significantly impact the load distribution irregularity both along the length of the contact lines as well as between the pairs of teeth involved in the required torque [17, 18, 23, 33]. When developing methods for determining the contact strength of gears, in order to take into account the dynamic load, as well as the load distribution irregularity over the length of the contact lines due to errors of gear production and transmission errors of the mating gears, two coefficients K_{HV} and $K_{H\beta}$ are introduced into formulas (2, 8). Since values of the coefficient $K_{H\beta}$ for the straight bevel precessional gear with a small shaft angle have not been obtained yet, it is recommended to take on the basic recommendations for bevel gears. This straight bevel precessional gear with a small shaft angle is supposed to be used in manual pipeline drives for the oil and gas industry, so this coefficient can be taken equal to one: $K_{H\beta} = 1$.

Taking into account the geometry of straight bevel precessional gears with a small shaft angle and the teeth contact features, a MathCad program was developed to determine the value of contact stresses according to formula (7). According to the results of this program, calculations for straight bevel precessional gears with a small shaft angle were performed, which showed that with $K_{HV} = 1$, $K_{H\beta} = 1$, contact stress and loading capacity (torque) are equal to $\sigma_H = 322.743$ MPa, $T_2 = 18,000$ N*m.

4 Main Results

An original ball valve gearbox containing straight bevel precessional gears with a small shaft angle is considered. The new scientific results of the article are: methods for determining the total length of the contact lines; an algorithm to determine the value of contact stresses and loading capacity (transmitted torque) taking into account the geometry of straight bevel precessional gears with a small shaft angle and the teeth contact features.

References

1. Nabiev RM (2010) Chervyachnyy reduktor elektroprivoda—perezhitok proshlogo ili aktual'naya klassika (Screw gear motor is a relic of the past or current classical) *Territoria neftegaz* (Oil and gas territory) 6:100–102
2. Litvin FL, Yukishima K, Hayasaka K et al (2007) Geometry and investigation of Klingenberg-type worm gear drive. *J Mech Des Trans ASME* 129(1):17–22
3. Gurevich DF (2008) Raschet i konstruirovaniye truboprovodnoy armatury. *Promyshlennaya truboprovodnaya armatura. Konstruirovaniye truboprovodnoy armatury* (Calculation and design of pipeline valves. Industrial pipeline valves. Construction of pipeline valves). LKI Publishing
4. Gavrilenko VA (1962) *Zubchatyye peredachi v mashinostroyenii* (Gears in mechanical engineering). Mashgiz Publishing
5. Goldfarb VI (2011) *Spiroidnyye reduktory truboprovodnoy armatury* (Spiroid gearboxes for pipeline valves). Veche Publishing, Moscow
6. Litvin FL, Fuentes A, Zanzi C et al (2002) Face gear drive with spur involute pinion: geometry, generation by a worm, stress. *Anal Comput Methods Appl Mech Eng* 191:2785–2813
7. Goldfarb VI, Trubachev ES (2004) Manufacturing synthesis of spiroid gearing. In: Huang T (ed) *Proceeding of the 2004 the eleventh world congress in mechanism and machine science, Tianjin, China, 1 April 2004 through 4 April 2004 Code 63248*, pp 901–904
8. Goldfarb VI, Trubachev ES, Savelieva TV (2005) Unification of the hobs in spiroid gears. In: *VDI Berichte, Issue 1904 II*, VDI Verlag GMBH, pp 1755–1759
9. Goldfarb VI, Reshetnikov SM, Trubachev ES et al (2015) Slip bearing and lubricants in low-speed heavy-duty spiroid gears. *Russ Eng Res* 35(8):584–588
10. Trubachev E (2016) Several issues of tooth generating process by two-parametric families of generating lines. *Mech Mach Sci* 34:97–116
11. Saari OE (1954) Speed-reduction gearing. US Patent 2,696,125 7 Dec 1954
12. Nelson WD (1961) Spiroid gearing. *Mach Des* 3:136–144
13. Nelson WD (1961) Spiroid gearing. *Mach Des* 4:93–100
14. Nelson WD (1961) Spiroid gearing. *Mach Des* 5:165–171
15. Bohle F (1955) Spiroid gear. *Machinery* 62(2):155–161
16. Syzrantsev V, Kotlikova V (2000) Mathematical and program provision of design of bevel gearing with small shaft angle. In: *Proceedings of the international conference on gearing, transmissions, and mechanical systems, Nottingham Trent University, UK, 3–6 July 2000*
17. Syzrantsev V, Denisov J, Wiebe V, Pazyak A (2015) The design and production of drives based on pan precess gear for oil and gas machinery. In: *ASME 2015 international design engineering technical conferences and computers and information in engineering conference*, vol 10, Boston, USA, 2–5 August 2015. <https://doi.org/10.1115/detc2015-47096>

18. Syzrantsev V, Syzrantseva K, Pazyak A (2015) Method of loading capacity calculation of bevel precessional gear for pipeline valve drives. 10(8):243–246
19. Syzrantsev V, Syzrantseva K, Pazyak A, Milanovic M (2017) Research on geometrical characteristics of straight bevel gears with a small shaft angle with a non-generated gear and generated pinion. FME Trans 45(4):661–669. <https://doi.org/10.5937/fmet1704661S>
20. Syzrantsev VN, Pazyak AA (2017) Precessional gears for drives of stop valves of oil and gas pipelines and gearboxes of pumps to produce heavy crude oil. Geo Assets Eng, Bulletin of the Tomsk Polytechnic University, 328(2):15–27
21. Syzrantsev VN, Pazyak AA (2017) Calculating loading capacity of bevel gears with a small shaft angle with a non-generated gear and a generated pinion for drives of stop valves. Bulletin of the Tomsk Polytechnic University, Geo Assets Engineering 328(3):64–74
22. Denisov JG, Syzrantsev VN, Vibe VP (2014) Soosnyy reduktor [Coaxial gearbox]. RF Patent 2,529,943 10 Oct 2014
23. Airapetov EL (1990) Static loading of multi-pair toothed transmissions. Soviet Eng Res 5(12): 4–7
24. Airapetov EL (1985) Calculation of contact stresses in gear transmissions with localized tooth contact. Soviet Eng Res 101:8–17
25. Airapetov EL (1985) Contact loads in gear engagement. Soviet Eng Res 210:3–5
26. Medvedev VI, Sheveleva GI (1993) Method of contact and bending stresses determination in gear-wheels. Problemy Prochnosti i Nadezhnos'ti Mashin 6:35–40
27. Medvedev VI, Sheveleva GI (1996) Synthesis of bevel gear on the base of quasilinear contact theory. Problemy Prochnosti i Nadezhnos'ti Mashin 2:25–32
28. Sheveleva GI (1984) Chislennyy metod resheniya kontaktnoy zadachi priszhatii uprugikht el (Numerical method for solving the contact problem in the compression of elastic bodies). Mashinovedeniye (Machine Science) 4:92–98
29. Sheveleva GI (1988) Analiz osobennostey raspredeleniya davleniy pri reshenii kontaktnoy zadachi teorii uprugosti (Analysis of the pressure distribution characteristics for solving the contact problem of elasticity theory) Izvestiya vuzov. Mashinostroyeniye (News of universities. Engineering) 11:14–17
30. Sheveleva GI (1999) Teoriya formoobrazovaniya i kontakta dvizhushchikhya tel (Theory of formation and contact of moving bodies). Stankin Publishing, Moscow
31. Shchekin BM (1990) Investigation of the stress-strain state of bevel gear transmissions. Soviet Eng Res 1012:20–23
32. Ginzburg EG (1980) Zubchatyye peredachi (Gears). Mashinostroyeniye Publishing, Leningrad
33. Chernaya LA (1993) Modelirovaniye kontakta vint-rolik v roliko-vintovoy planetarnoy peredache (Simulation of a screw-roller contact in a roller-screw planetary gear) Izvestiya vuzov. Mashinostroyeniye (News of universities. Engineering) 2:17–19

Research of Direction of Rope-Hydraulic Quarry Excavator Creation



S. A. Khoroshavin, V. S. Shestakov and V. I. Saitov

Abstract The relevance of the paper is due to the need to improve the efficiency of mining excavators. The traditional scheme of a hydraulic excavator straight shovel is considered. Studies have shown that it is possible to increase the performance of an excavator by reducing the weight of working equipment and increasing the bucket capacity while retaining all the advantages of hydraulic excavators and without changing the initial weight of the entire machine, to reduce the weight of the developed scheme of working equipment with a cable-hydraulic drive. The transfer of hydraulic cylinders to the rotary platform of the excavator and the transfer from them of efforts through the cable system provided an exception to the bending moments on the boom and stick, which allows reducing the cross section of these elements and, accordingly, their mass. To expand the scope of hydraulic excavators, studies have been conducted on the creation of a control algorithm for the main mechanisms. Objective: To study the possibility of using a combined cable-hydraulic drive for mining excavators. Research methodology: mathematical modeling of the workflow. Results: A mathematical model, algorithm and program in algorithmic language have been developed for a career shovel with working equipment “direct shovel,” which allows determining the required graphs of the control law of the main drives for shaping the displacement speeds of the hydraulic cylinders ensuring the movement of the bucket along the desired trajectory.

Keywords Career excavator · Rope-hydraulic · Working equipment · Hydraulic cylinder · Drive · Speed · Model · Algorithm

S. A. Khoroshavin (✉)

Ural Federal University Named After the First President of Russia B. N. Yeltsin, 19, Mira Street, 620002 Ekaterinburg, Russia
e-mail: horoshavin.s3@gmail.com

V. S. Shestakov · V. I. Saitov

Ural State Mining University, 30, Kuibyshev Street, 620144 Ekaterinburg, Russia

© Springer Nature Switzerland AG 2020

A. A. Radionov et al. (eds.), *Proceedings of the 5th International Conference on Industrial Engineering (ICIE 2019)*, Lecture Notes in Mechanical Engineering,

https://doi.org/10.1007/978-3-030-22041-9_24

1 Introduction

Now on quarry, two types of quarry excavators are used: rope and hydraulic. Hydraulic excavators compared to are have about half the weight cable excavators with at equal load capacity of the buckets, develop big in 1.5 times of effort of digging, provide a possibility of selective extraction of mineral, smaller expenses of energy when digging by the turn of a ladle [1–4]. Shortcomings of hydraulic excavators: in comparison with rope, it has the smaller linear sizes of the working equipment and the smaller sizes of the work area connected with it on height. The impossibility of application of an arrow and handle for hydraulic excavators of the big sizes is explained by the fact that the arrow and a handle work for a bend and compression, therefore their section should be done big, increase in length will lead to significant growth of mass of the working equipment and excavator in general. In some conditions, it is required to provide the movement of a ladle on the set trajectory, for this purpose, it is necessary to set certain values of speeds of mechanisms of lifting and a pressure. In work, the model of determination of speeds for control system is presented.

2 Purpose and Tasks of Work

The purpose of the conducted researches is identification of a possibility of increase in the sizes of the working equipment when maintaining advantages of hydraulic excavators.

3 Solution of Research Problems

For increase in the linear sizes of the traditional scheme of the working equipment of the hydraulic excavator “direct shovel,” we developed the original scheme in which hydraulic cylinders provide transfer pressure head efforts through a pressure head beam [5]. The mechanism of lifting can be traditional with the winch or also with a hydraulic cylinder and a polyspast system. The second option in comparison with the winch provides decrease in weight and also reduction of dynamic efforts when latching a ladle in the course of digging as the lag effect of hydraulic cylinders considerable is less and in a hydraulic actuator protection against emergencies is more simply provided. In the offered option, the arrow, a handle, the balance weight, and a pressure head beam are unloaded from the bending moments, work only for compression therefore working the equipment, despite the increased sizes, provide decrease in weight in comparison with hydraulic excavators and in comparison with traditional rope at which the arrow is affected by efforts from the pressure head mechanism. The ladle can be fixed rigidly on a handle or to make

rotary for digging by the turn of a ladle with installation of the corresponding hydraulic cylinder. The scheme with a rotary ladle will demand increase in section of a handle as it will be in addition loaded with effort of a hydraulic cylinder of turn of a ladle, but will provide completely all advantages of hydraulic excavators. The handle can serve as the case of a hydraulic cylinder.

The necessity of decrease in mass of the working equipment is caused by the fact that the working equipment essentially influences productivity and cost of the excavator [6–20]. Decrease in mass of the equipment much reduces the mass of the excavator and the moment of inertia of its rotary part. A reserve of decrease in mass of elements of the working equipment (arrows, handles, a ladle, etc.) in the choice of optimum sections of these elements, in the rational scheme of the drive [8]. Selection of sections of elements of the working equipment and the subsequent calculation of weight are carried out on working efforts which depend on efforts of digging and coordinates which change in the work area. We developed a mathematical model for calculation of coordinates.

In Fig. 1 is shown the scheme for a conclusion of mathematical model of calculation of coordinates, speeds, and efforts.

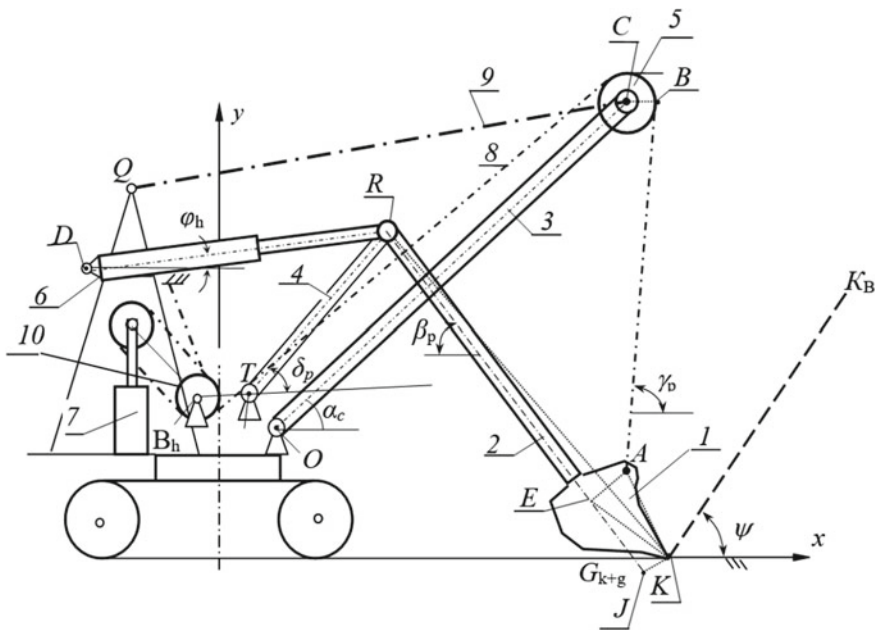


Fig. 1 Scheme for calculation: 1—a ladle, 2—a handle, 3—an arrow; 4—balancer, 5—head blocks, 6—pressure hydraulic cylinder, 7—lifting hydraulic cylinder, 8—lifting ropes, 9—boom suspension; 10—deflecting unit of hoisting ropes; O, A, B, C, D, K, T, R—points of the design scheme; E, J—projections of points A, K on the handle axis; B is the vanishing point of lifting cables from the head units; F_n, F_H —lifting force and pressure, $KK\theta$ —face slaughter; Ψ —slope of the working area



Basic data for determination of the required speeds of the movement of rods are the linear and angular sizes of all elements of the working equipment, coordinate of hinges of fastening of an arrow of O , balance weight T , points of fastening of a pendant to a superstructure of Q , the hinge of a pressure head beam on a superstructure of D , and also coordinates of a trajectory of movement of a ladle and the required speed of movement of a ladle on a trajectory of V_k .

At a task of a trajectory of digging by a segment with beginning coordinates (x_{tr}, y_{tr}, h) and a corner of Ψ , the current position of tooth of a ladle will be determined by formulas of numerical integration

$$x_{K(i+1)} = x_{K(i)} + \Delta L \cdot \cos \psi \quad (1)$$

$$y_{K(i+1)} = y_{K(i)} + \Delta L \cdot \sin \psi \quad (2)$$

$x_{K(i+1)}, y_{K(i+1)}, x_{K(i)}, y_{K(i)}$ —coordinates of the subsequent and previous point of i of a piece of the set trajectory, for the first piece of a trajectory of $x_{K(i)} = x_{tr,h,K(i)} = y_{tr,h}$; ΔL —length of i of a piece of the set trajectory.

Length of i of a piece of the set trajectory is defined by numerical integration of the required speed of the movement of a ladle

$$\Delta L = V_k \cdot \Delta t, \quad (3)$$

Δt —integration step on time.

Coordinates of points of the settlement scheme are determined by the expressions given below. Designations in formulas for the linear size of basic data include letters at the edges of a piece, and for the calculated parameter include letter L , and also the indication of points. For the angular sizes, the sign \angle with the indication of final points and vertexes of angle is used. For designation of a corner at its counting from a horizontal, the letter is used x . Coordinates of a point are designated by symbols x and y with the indication of a point.

The mathematical model of calculation of coordinates includes the following expressions:

$$x_C = x_O + OC \cdot \cos \alpha_C \quad (4)$$

$$y_C = y_O + OC \cdot \sin \alpha_C \quad (5)$$

$$L_{KT} = \sqrt{(x_K - x_T)^2 + (y_K - y_T)^2} \quad (6)$$

$$\angle_{TKx} = \arctg \frac{y_T - y_K}{x_K - x_T} \quad (7)$$

$$\angle_{TKR} = \arccos \frac{L_{KT}^2 + RK^2 - TR^2}{2 \cdot L_{TK} \cdot RK} \quad (8)$$

$$\angle_{KTR} = \arccos \frac{L_{KT}^2 + TR^2 - RK^2}{2 \cdot L_{KT} \cdot TR} \quad (9)$$

$$\angle_{RTx} = \angle_{KTR} - \angle_{TKx} \quad (10)$$

$$\angle_{RKx} = \angle_{TKx} + \angle_{TKR} \quad (11)$$

$$\beta_p = \angle_{RKx} + \angle_{RKJ} \quad (12)$$

$$\angle_{ARE} = \arctg \frac{AE}{RE} \quad (13)$$

$$\angle_{RAx} = \angle_{RJx} - \angle_{ARE} \quad (14)$$

$$L_{RA} = \sqrt{RE^2 + AE^2} \quad (15)$$

$$x_R = x_K - RK \cdot \cos \angle_{RKx} \quad (16)$$

$$y_R = y_K + RK \cdot \sin \angle_{RKx} \quad (17)$$

$$x_A = x_R - L_{RA} \cdot \cos \angle_{RAx} \quad (18)$$

$$y_A = y_R - L_{RA} \cdot \sin \angle_{RAx} \quad (19)$$

$$x_E = x_R + RE \cdot \cos \angle_{RJx} \quad (20)$$

$$y_E = y_R - RE \cdot \sin \angle_{RJx} \quad (21)$$

$$L_{AC} = \sqrt{(x_C - x_A)^2 + (y_C - y_A)^2} \quad (22)$$

$$L_{\Pi} = \sqrt{L_{AC}^2 + CB^2} \quad (23)$$

$$\angle_{CAB} = \arcsin \frac{CB}{L_{AC}} \quad (24)$$

$$\angle_{CAx} = \arctg \frac{y_C - y_A}{x_C - x_A} \quad (25)$$

$$\gamma_P = \pi - \angle_{BAx} \quad (26)$$

$$x_B = x_A + L_A \cdot \cos \gamma_P \quad (27)$$

$$y_B = y_A + L_A \cdot \sin \gamma_P \quad (28)$$

$$L_H = \sqrt{(x_R - x_D)^2 + (y_R - y_D)^2} \tag{29}$$

The required speeds of promotion of a rod of a hydraulic cylinder of DR , lifting ropes of AB for movement of tooth of a ladle of K on the set trajectory of KK_B are defined by numerical differentiation:

$$V_{H(i)} = [L_{H(i+1)} - L_{H(i)}] / \Delta t \tag{30}$$

$V_{H(i)}$, $V_{P(i)}$ —current values of speed of a pressure and lifting, respectively; $L_{P(i+1)}$, $L_{P(i)}$, $L_{H(i+1)}$, $L_{H(i)}$ —the distances between points of AB and DR defined through an integration step Δt .

The algorithm of determination of the required speeds includes a cycle in which on the given expressions, the current coordinates of a ladle on the set trajectory, coordinates of points of the working equipment, and distances between points pay off. Results of calculation are moved in the table. For check in the form of the scheme of the working equipment, according to the table the schedule of change of speeds is issued. It is simple to organize calculation at working off of all area, and for this purpose, it will be required two more cycles for the shift of an initial trajectory on width of a working area and on depth. On an algorithm, the program in algorithmic language is made and calculations of two options are executed. In Fig. 2a results for a trajectory at an angle 60° are given in Fig. 2b—for a horizontal trajectory.

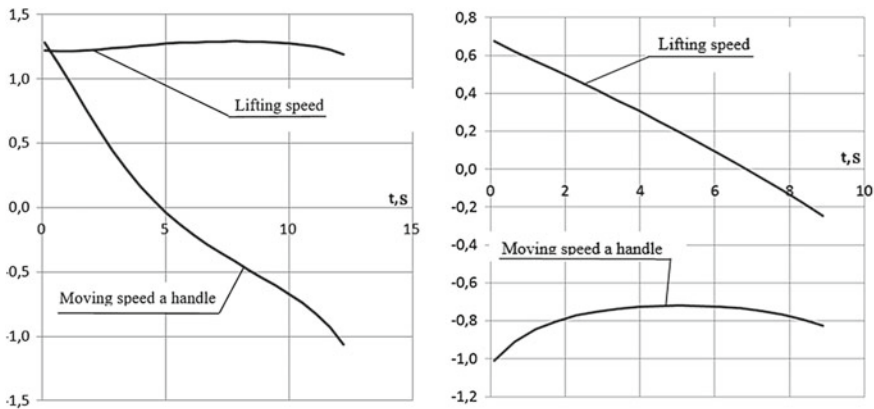


Fig. 2 Graphs change speeds: **a** lifting and moving when the shovel moves along a trajectory at an angle of 60; **b** lifting and moving when moving the shovel is along a horizontal path

4 Conclusions

1. Researches showed that with a length of arrow of 14 m promotion of a pressure head beam within 4 m, therefore, it is possible to implement a pressure mechanism driven by a hydraulic cylinder. Change of length of lifting ropes happens within 10 m; the lifting mechanism with the drive from a hydraulic cylinder will require a polispast system.
2. The made mathematical model allows to define:
 - The work area of the excavator with by the linear sizes of the working equipment;
 - The speed of movement of the pressure beams and lifting ropes to ensure the movement of the bucket along a predetermined path;
3. Values of speeds depend on parameters of the required trajectory of the movement of a ladle and parameters of the working equipment of the excavator; therefore, in a control system, the presented model and the block of definition of the initial point working off the whole working area.

References

1. Poderni RYu, Boules P (2015) Comparative analysis of hydraulic and mechanical excavators with a straight shovel. *Min Mag* 1:55–61
2. Pobegailo PA (2014) Powerful single-bucket hydraulic excavators: selection of basic geometric parameters of working equipment in the early stages of design. LENAND, Moscow
3. Lagunova YuA, Komissarov AP, Shestakov VS (2017) Design of mining excavators. Innovative Mechanical Engineering, Moscow
4. Poderni RYu, Peter B (2015) Efficiency of the use of powerful hydraulic excavators is the result of increasing their reliability. *Mining* 1:46
5. Komissarov AP, Shestakov VS, Khoroshavin SA (2012) Working equipment of a career excavator. RU Patent for utility model 122670 U1 MPK E02F 3/42, 10 Dec 2012
6. Ivanov IYu, Komissarov AP, Teliman IV, Lukashuk OA (2017) Analysis of lever-hydraulic mechanisms of working equipment of hydraulic excavators. *Technol Equip Min Oil Gas Ind* 1:51–54
7. Krikun VY, Manasyan VG (2001) Calculation of the main parameters of hydraulic excavators with working equipment backhoe. *ASV*
8. Zykov PA (2014) A technique for the optimal choice of a single-bucket hydraulic excavator model for the given mining-geological and technical conditions. *Min Equip Electromech* 1:37–42
9. Babenkov PYu, Shestakov VS (2018) Modeling of the working process of a hydraulic excavator. *Min Equip Electromech* 1:10–14
10. Shestakov VS, Khoroshavin SA (2011) Optimization of the working equipment of hydraulic excavators. *Min Equip Electromech* 5:50–53
11. Sushkov SI, Makeev VN, Pleshkov DD (2012) Analysis of design features of lifting mechanisms of hydraulic excavators. *Const Road Mach* 6:13–15
12. Karasev GN, Pavlov VP (2011) Road construction machinery. System design, modeling, optimization. SFU, Krasnoyarsk

13. Gruening GT, Kunze G, Katterfeld A (2010) Simulating the working process construction machines. In: Bulk Solids Europe. Glasgow
14. Frimpong S, Li Y (2005) Virtual prototype simulation of hydraulic shovel kinematics for spatial characterization in surface mining operation. *Inter J Surf Min Reclam Environ* 4: 238–250
15. Komissarov AP, Lagunova YuA, Lukashuk OA (2018) Determination of functions of controlling drives of main executive mechanisms of mining excavators. In: IOP conference series: material science and engineering, p 052024
16. Pobegailo PA (2017) Powerful single-bucket hydraulic excavators: working equipment design methodology. ARGUS, Moscow
17. Pobegailo PA, Rakov DL (2014) Tasks of structural sintez at the stage of choosing the appearance of technical systems. *Technol Equip Min Oil Gas Ind* 1:294–297
18. Abdrakhmanov AA, Safin GG (2016) On coefficients affecting the efficiency of operation and management of a mining excavator. *Mod Res Innov* 3:153–156
19. Pevzner LD (2012) Automated control system for heavy dragline and quarry excavator. *Min Inf Anal Bull Sci Tech J* 1:294–300
20. Kragel AA, Bessonov IV, Sharin EB, Kopysov NA, Karyakin AL (2012) The modernized career excavator EKG-12A. *Min J* 7:77–80

Formation of Quality Indicators System at Design of Mechanical Engineering Products



E. A. Ivakhnenko, L. M. Chervyakov and O. Yu. Erenkov

Abstract The choice justification of the engineering products concept is carried out on the basis of their quality indicators comparison for various designs including the consumers requirements and expectations, as well as the products of competitors. The various studies main focus is made on the development and application of multi-criteria methods for finding optimal and rational solutions. This paper is devoted to justifying the choice of indicators by which further comparison of alternative options will be made, that is, to the criteria system formation itself. The basis of the quality indicators system formation for engineering products is the relationships setting between their properties, the life cycle stages, and strategies for the implementation of these stages. A method for substantiating the quality indicators system choice which can be used in the qualimetric differential and complex assessment of the of product quality level is presented. The practical implementation of the methodology for designing a gear pump range with the foundations of the quality indicators selection is considered. The enterprise strategic development plan was developed at the preparation of new products release using the developed methodology.

Keywords Conceptual design · Quality indicators · Mechanical engineering

1 Introduction

The concept of mechanical engineering products is defined at the earliest design stages. The concept is a certain way of understanding how requirements and expectations of consumers and other interested parties will be realized in this product. The main tool used for the translation of the requirements and expectations

E. A. Ivakhnenko (✉) · L. M. Chervyakov
Southwest State University, 94, 50 Let Oktyabrya, 305040 Kursk, Russia
e-mail: evgeniy.ivakhnenko@gmail.com

O. Yu. Erenkov
Pacific National University, 136, Tikhookeanskaya Street, 680035 Khabarovsk, Russia

of consumers and other interested parties is quality function expansion. The improvement of this tool is considered in this work. The consideration of products properties manifestation at of their life cycle stages with an accepted strategy of these stages realization is the base of such improvement.

1.1 Relevance

The product quality is generally founded on decisions which made at a conceptual design stage. At the same time, the product quality is reflected in life cycle processes documentation and is realized in its design [1, 2]. Reasonable adoption of these decisions is possible only in case of the installed system of product quality indicators presence. Thus, formation of the quality indicators system should be referred to an important stage of mechanical engineering products conceptual design.

1.2 The Question Scientific Importance with the Short Review of Literature

The area of researches in this work belongs to the qualimetry considering quantitative assessment methods of various nature objects quality including mechanical engineering products [3–5]. The group of the GOST standards of the four series with the general name the Product Quality Indicator System (PQIS) was created in the USSR. However, the name of each standard of this series has the expression “Product indicators,” for example [6]. Such names of this standards series reflect the obvious fact that the system approach was not used at determining indicators of products quality. In the theoretical and applied qualimetry, this approach is implemented by means of drawing up and the analysis of an object properties tree and indicators tree used for values determination of relative and absolute measures of properties.

Also it is necessary to consider the situation of objects quality estimation in the qualimetry. Such objects include stages of life cycle, a possibility of modernization, moral and physical wear, interaction with groups of people, the place in type and size classification, impact on the environment and others [3–5].

The considered approach development is executed in the works [7, 8]. The approach to improvement the conceptual design process is offered in the work [7]. This approach is based on integration of the standards ISO 9000 and 14,000, development of the quality function expansion method, the quality indicators choice, and definition of technical characteristics optimization problem. The two alternative strategy concepts with use of the known concepts system focused on creation of information models are offered in the work [8]. The conditions for

formation of the quality indicators system were defined and the processes characterizing the realization strategy of life cycle various stages are considered also [8].

The quality of a product is generally characterized by the following properties [9]: functionality, reliability, ergonomics, esthetics, profitability, safety, environmental friendliness, and technological effectiveness.

The leading world companies are using the design for environment (DfE) methodology of ecologically focused design to improve the machine quality and to decrease their influence on the environment [10–13]. The methodology base is transition from products design to design of products life cycle.

Within this methodology, the decrease in impact on the environment is an integral part of a product development along with other directions at design such as ensuring product profitability and consumer requirements.

These directions can be considered as a part of the design general function which named Design for X (DfX), i.e. design taking into account X , where X represents various requirements which treat, except already mentioned requirements, convenience of assembly, maintainability, etc. [14–18].

The consumption of energy of different types, primary and secondary materials, components and modules at all processes of products life cycle is considered for assessment of impact on the ecosphere. Also, a possibility of reuse of both the product and the materials which are its part, components and modules and waste, emissions and dumpings are undertaken in attention.

1.3 Problem Definition

The task of this work is to develop the justification technique for choice of quality indicators system and its application at conceptual design of gear pumps scale.

2 Theoretical Part

The main properties of products [9] we will present in the form of great number (vector) $X = \{x_i, i = 1, \dots, n\}$, where n is amount of the considered properties, $n = 8$ here; x_1 is functionality; x_2 is reliability; x_3 is ergonomics; x_4 is esthetics; x_5 is profitability; x_6 is safety; x_7 is environmental friendliness; and x_8 is technological effectiveness. These properties are compound and are characterized by the corresponding vector sets of simple properties, for example, $x_2 = \{x_{21}$ is non-failure operation; x_{22} is durability; x_{23} is maintainability; and x_{24} is storage ability}. The life cycle stages of mechanical engineering products, we will present in vector form $Y = \{y_j, j = 1, \dots, m\}$, where m is quantity of the considered stages, $m = 6$ here; y_1 is design; y_2 is production; y_3 are tests; y_4 is realization and delivery; y_5 is operation, repair and maintenance; and y_6 is the order of product after its operation

completion. The allocated stages can also unite or decompose on the processes and subprocesses.

Let's enter the binary relation of compliance as Cartesian product of sets of $XY \subseteq X \times Y$. This relation can present in the form matrixes $XY(n \times m)$, which each element $xy_{i,j} = 1$, if j property is shown on i —stage, and $xy_{i,j} = 0$ otherwise.

For establishment of the properties importance of and of life cycle stages, we use expert estimates:

$$\alpha^{\text{ext}} \{ \alpha_i^{\text{ext}}, i = 1, \dots, n \} u \alpha^{\text{int}} \{ \alpha_i^{\text{int}}, i = 1, \dots, n \} \\ \beta^{\text{ext}} \{ \beta_j^{\text{ext}}, j = 1, \dots, m \} u \beta^{\text{int}} \{ \beta_j^{\text{int}}, j = 1, \dots, m \}, \quad (1)$$

where α^{ext} and α^{int} —a vector of expert estimates of external and internal interested parties of the importance of properties of products; β^{ext} and β^{int} —a vector of expert estimates of external and internal interested parties of the importance of stages of life cycle.

Let's enter a matrix of the importance of manifestation of properties of products of mechanical engineering at stages of their life cycle:

$$Z = XY(\gamma^{\text{ext}}(\alpha^{\text{ext}})^t \beta^{\text{ext}} + \gamma^{\text{int}}(\alpha^{\text{int}})^t \beta^{\text{int}}), \quad (2)$$

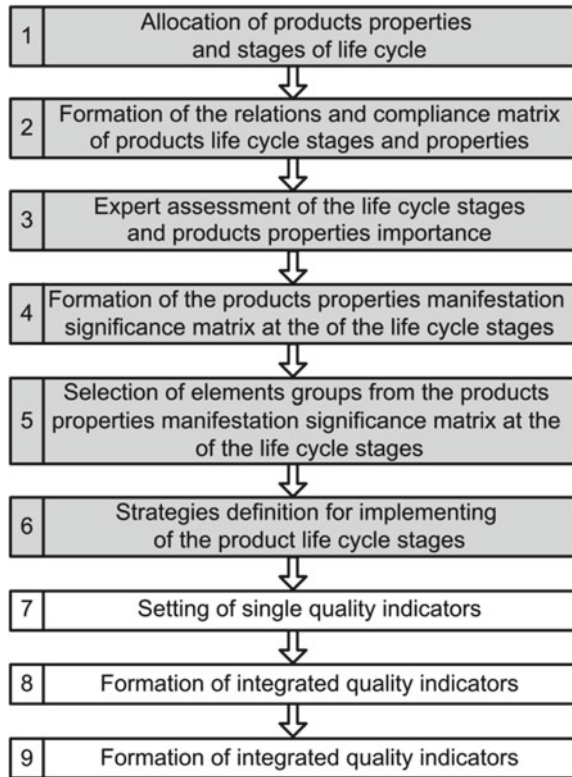
where γ^{ext} and γ^{int} —weight coefficients of the opinions importance of external and internal interested parties, respectively; \otimes —operator of step-by-step multiplication of matrixes; t —a transposing symbol.

To allocate the single quality indicators, included in the system of indicators directly or as a part of complex indicators, it is offered to divide Z matrix elements into three groups: the 1st group (obligatory inclusion in a system); the 2nd group (desirable inclusion in a system); and 3rd group (optional inclusion in a system). The established properties manifestation importance of mechanical engineering products at life cycle various stages is a necessary condition for definition of the corresponding indicators and their inclusion in the quality indicators system. The sufficient conditions for corresponding indicators definition and their inclusion in the quality indicators system have to install during analysis of the accepted strategy of life cycle stages realization.

For example, the product can be restored or nonrestorable that will define existence or lack of repair at refusal in use and therefore, using of quality various indicators is the probability of no-failure operation or coefficient of technical use.

On the basis of the established conditions, the justification technique for choice of the quality indicators system is created and presented in Fig. 1. The sequence entering blocks 1–9 can be considered as a component of the algorithm of qualimetric complex assessment of quality products level and the sequence entering blocks 1–7 can be considered as a component of the algorithm of qualimetric differential assessment of quality products level.

Fig. 1 Methodology for the quality indicators choice justifying (blocks 1–6)



The allocation of properties and products life cycle stages is carried out in block 1. At the same time, it can be used the product listed properties only and its life cycle stages or the new stages (installation, balancing and commissioning, etc.) and properties (patent purity, a compliance to the standard, etc.) depending on a concrete type of the product can be added.

The formation of the relations and compliance matrix of products life cycle stages and properties is carried out in block 2, and the example of the matrix is given in [8].

The expert assessment of the life cycle stages and products properties importance is performed in block 3. This assessment is made by poll of outer and internal interested parties, i.e. determination of vectors values α^{ext} , α^{int} , β^{ext} , β^{int} and weight coefficients of the importance of γ^{ext} , γ^{int} .

The formation of the products properties manifestation significance matrix at the life cycle stages using expression (2) is performed in block 4 and its basis is the matrix of relationships and the results of significance expert assessment.

The selection of elements groups from the products properties manifestation significance matrix at the life cycle stages is performed in block 5.



The block 6 corresponds to the strategies definition for implementing of the product life cycle stages examples of which are discussed in [8].

The following steps 7–9 correspond to the definition of unit, complex, and integral indicators of product quality.

3 The Practical Significance, the Implementation Proposals and Results, and the Results of Experimental Studies

The practical implementation of the methodology for justifying the choice of quality indicators system and the extended method of the quality function deploying was carried out with the participation of specialists from one of the machine-building enterprises in the design of the gear pumps range. The nomenclature of the main quality indicators and the main parameters of these pumps are given, respectively, in GOST 4.118-84 [6] and GOST 19027–89 [19]. In [19], the following technical characteristics are regulated: supply, l/s (m^3/h); pump pressure, MPa (kgf/cm^2); rated speed, s^{-1} (rpm); pump efficiency, %; and pump weight, kg.

In GOST 4.118–84 “SPKP. Pumping equipment. The nomenclature of the main indicators” the following quality indicators are included:

1. Destination indicators (classification)—feed, m^3/s ; pressure, Pa; rotational speed, s^{-1} ;
2. Indicators of technical and energy efficiency—efficiency, %; allowable cavitation reserve, m;
3. Constructive and technological indicators—mass, kg; or specific gravity, kg/MJ;
4. Reliability indicators—the established trouble-free operating time, h; the established resource (before capital repairs or before write-off), h, or the assigned resource (before capital repairs or before write-off), h.

The next expert assessments of the product properties and the life cycle stages significance were determined: $\alpha^{\text{ext}} = \{4; 4; 0; 0; 4; 3; 3; 2\}$; $\alpha^{\text{int}} = \{4; 4; 0; 0; 4; 3; 3; 4\}$; $\beta^{\text{ext}} = \{1; 2; 1; 3; 4; 4\}$; $\beta^{\text{int}} = \{3; 4; 3; 3; 4; 4\}$, where $\gamma^{\text{ext}} = \gamma^{\text{int}} = 1$. The gear pump properties stages significance matrix at the life cycle stages is presented in Table 1.

The value of the concordance coefficient of expert’s opinions was: for external stakeholders $W_{\text{ext}} = 0.895$; for internal stakeholders $W_{\text{int}} = 0.927$.

Imagine some of the proposed quality indicators for the various stages of the pumps life cycle. All known strategies for the of the manufacturing stage implementation (including the adopted transition strategy to lean manufacturing) include the following processes: production of blanks, machining (roughing, semi-finishing, finishing and finishing), control of geometric parameters, and parameters of material properties, transportation and assembly.

Table 1 Gear pump properties stages significance matrix at the life cycle stages

Design	Production	Test	Implementation and delivery	Operation, repair, and maintenance	Order	
0	0	16	0	32	(32)	Functionality
0	(24)	16	(24)	32	(32)	Reliability
0	0	0	0	0	0	Ergonomic
0	0	0	0	0	0	esthetics
(16)	(24)	(16)	(24)	32	(32)	Efficiency
0	(18)	(12)	(18)	(24)	(24)	Security
(12)	(18)	(12)	(18)	24	(24)	Environmental friendliness
(14)	(20)	(14)	(18)	(24)	(24)	Manufacturability

Note Matrix elements in brackets are not included in GOST 4.118

To characterize the reliability in the pumps manufacturing process, the single quality indicator was proposed $k_{pov} = N_{pov}/N_{tr}$, where k_{pov} is the persistence factor, which is the ratio of the number of damaged parts and sets during transportation between workplaces N_{pov} and the total number of transported units and details N_{tr} .

The labor inputs (man-hours) $T_{tr.zagot}$, $T_{tr.obr}$, $T_{tr.contr}$, and $T_{tr.sb}$ are comprehensive indicators of such properties as cost-effectiveness and manufacturability of processes for obtaining blanks, machining, control of geometric parameters and parameters of materials properties of and assemblies.

For the complex characteristics of such properties as cost-effectiveness, environmental friendliness, and manufacturability the utilization factor was adopted for materials $k_{im} = M_{got}/M_{zag}$, where M_{got} is the materials mass in the finished product, kg; M_{zag} —the blanks material mass, kg.

The adopted strategy for the implementation of the all pumps full-scale tests includes the processes: installation on the test bench, the fluid pumping, the parameters measuring, and dismantling from the bench.

To characterize the manufacturability of these stage operations, the following individual quality indicators were selected:

$T_{mont.isp}$ and $T_{demon\cdot isp}$ —time for the pump installation and disassembly on the test bench, respectively, min;

T_{isp} —duration of the pump test program, min.

The tests labor intensity indicator $T_{tr.isp}$ (person hour) was proposed for comprehensive description the efficiency and adaptability of the liquid pumping working process during tests.

The known strategies for the implementation phase include the following processes: preservation, packaging in tare, loading, transportation, unloading, unpacking, and installation.



To characterize the reliability of this stage the single quality indicator $P_{vr.transp} = N_{povpr}/N_{dost}$ was proposed, where $P_{vpr.transp}$ is the product damage probability upon delivery to the consumer; N_{povpr} —the number of damaged products upon delivery, units; N_{dost} —the total number of products delivered to consumers, units.

The environmental friendliness and safety at this stage are associated with the container destruction probability when performing the above operations. The complex indicators F_{st} and F_{din} were proposed for their characteristics and the indicators are the values of static and dynamic loads, respectively, which lead to the destruction of the container.

The following indicators of average duration, min per product, are proposed to evaluate the characteristics of the operation processability of at this stage: conservation— T_{cons} ; packaging in the container— T_{upak} ; loading— T_{pogr} ; unloading— T_{rasgr} ; unpacking from the container— T_{raspak} ; and installation— T_{mont} .

For the stage of the product disposal after its operation completion, the new strategy was adopted. The strategy is based on the reuse of the components and materials included in the product. This strategy is associated with the used product return to the manufacturer (take-back) while the consumer receives a discount on the new product purchase or material compensation. This strategy includes the following main processes: disassembly, sorting, and recycling.

In order to characterize the products environmental friendliness, the single indicator was proposed as the level of processability (utilization rate of recyclable materials) $U_{perer} = M_{perer}/M$, where M_{perer} —the mass of recyclable materials from which the pump parts are made, kg; M is the mass of the pump, kg.

To characterize the functionality, reliability, cost-effectiveness, and environmental friendliness, the complex indicator was introduced as reuse level $M_{povtr.isp}/M$, where $M_{povtr.isp}$ is the mass of pump parts that can be reused after disassembly and quality and parameters control.

Thus, the system of gear pumps quality indicators includes not only the indicators included in GOST 4.118-84 but also the indicators obtained using the developed methodology for the quality indicators system choice justifying.

The practical implementation of the expanded method of the quality function deploying was carried out simultaneously with formation of the quality indicators system with the participation of the machine-building enterprise specialists.

There was proposed to use the technology of non-abrasive ultrasonic finishing of the surfaces of bearings and gears [20] to improve wear resistance and efficiency, as well as to reduce the noise level. The proposal is based on the results analysis of the gear pumps quality function deployment.

This technology of friction pairs forming eliminates the use of abrasive materials and in some cases, grinding machines. At the same time the number of technological operations is reduced and such lengthy and energy-intensive operations as cementation, nitrating or hardening by high-frequency currents are eliminated.

The formed quality indicators system as well as the requirements and expectations of interested parties transformed into the product and components technical characteristics allowed us to offer the following measures:

- the introduction of the integrated design-technological computer-aided design system;
- the use of the block-modular construction principle which ensured the unity of the pumps entire range designs;
- the standard technological processes development for the manufacture and testing of the pumps range at the capacity from 0.111 to 3.889 m³/h;
- the automated multi-position test bench creation equipped with automatic safety devices to eliminate the possibility of products damage during testing;
- the introduction of surface non-abrasive ultrasound finishing;
- the reduction of overall volumes in comparison with NMSH type pumps at least 10% and the development of special containers to ensure the reliability of products during transportation;
- the pumps mass reducing by 20–29% due to the execution of the flow part from an aluminum alloy;
- the hydraulic compensators using which reduce the discharge pressure on the covers and the mechanical seal to eliminate any leakage.

The proposed measures were the basis for the enterprise strategic development plan when expanding the of products range and preparing for the new products release.

4 Conclusion

The developed methodology application allowed to justify the quality indicators system choice in preparation for the design and new products manufacture as range of gear pumps. The practice of joint use the methodology for the quality indicator system choice justifying and the quality function deploying expanded method showed that they complement each other since the method of the quality function deploying is more focused on the product itself and the methodology is on its life cycle processes in accordance with adopted strategies for their implementation.

References

1. Taura T, Yoshikawa H (1994) Managing function concepts in the design process. In: Management of design: engineering and management perspectives. https://doi.org/10.1007/978-94-011-1390-8_10
2. Zadnik Z, Karakasic M, Kljajin M et al (2009) Function and functionality in the conceptual design process. *Strojniski Vestnik J Mech Eng* 55(7–8):455–471
3. Azgaldov GG, Kostin AV (2011) Applied qualimetry: its origins, errors and misconceptions. *Benchmark Inter J* 18(3):428–444
4. Azgaldov GG, Kostin AV, Sadovov VV (2012) *Kvalimetriyadyavsekh (Qualimetry for all)*. Informznanie, Moscow

5. Azgaldov GG, Kostin AV, Padilla Omiste AE (2015) The ABC of qualimetry: the toolkit for measuring immeasurable. Ridero, Yekaterinburg
6. GOST (State Standard) 4.118–84 (1984) Product reliability index system. Pumping equipment. Basic index nomenclature. USSR State Committee on Standards, Moscow
7. Ivakhnenko EA, Oleinik AV, Chervyakov LM (2017) Improvement of the design process of an engineering product concept. News of the Tula state university. Tech Sci 8(1):313–323
8. Ivakhnenko EA, Zotov IV, Chervyakov LM (2018) Substantiation choice engineering produce quality indices at adopted strategies of stage realization of their life cycle. https://doi.org/10.30987/article_5bf3cb4d183e11.06361598
9. Oleinik AV (2005) Creation of competitive mechanical engineering products: the environmental aspect. Publishing House of Kursk State Technical University, Kursk
10. Allenby BR (1991) Design for environment: a tool whose time has come. SSA J 12(9):5–9
11. Telenko C, Seepersad CC, Webber ME (2008) A compilation of design for environment principles and guidelines. In: Proceedings of the ASME international design engineering technical conferences and computers and information in engineering conference, New York, pp 3–6
12. Oehlberg L, Bayley C, Hartman C et al (2012) Mapping the life cycle analysis and sustainability impact of design for environment principles. In: Dornfeld D, Linke B (eds) Leveraging technology for a sustainable world, Berlin, Heidelberg
13. Kampf C, Seiler TB, Beger AL (2017) Life cycle assessment sustainable engineering context near net shape grown components: striving towards a sustainable way of future production. <https://doi.org/10.1186/s12302-017-0125-x>
14. Owen CL (1993) Design for integrity. Institute of Design Communications Center, Illinois Institute of Technology, Chicago
15. Boothroyd G, Dewhurst P, Knight P (2002) Product design for manufacture and assembly, 2nd edn. Marcel Dekker, New York
16. Chiu M-C, Okudan GE (2010) Evolution of design for X tools applicable to design stages: a literature review. <https://doi.org/10.1115/detc2010-29091>
17. Dombrowski U, Schmidt S, Schmidtchen K (2014) Analysis and integration of design for X approaches in lean design as basis for a lifecycle optimized product design. <https://doi.org/10.1016/j.procir.2014.06.023>
18. Baptista AJ, Peixoto D, Ferreira AD et al (2018) Lean design-for-X methodology: integrating modular design, structural optimization and ecodesign in a machine tool case study. <https://doi.org/10.1016/j.procir.2017.12.003>
19. GOST (State Standard) 19027–89 (1989) Gear pumps. Basic parameters. Standards Publishing, Moscow
20. Abrasive-free ultrasonic finishing processing (BUFO), ultrasonic pulse hardening-finishing processing (2018) LLC Ultrasonic technique—INLAB, Saint-Petersburg. <http://www.utinlab.ru/articles/bezabrazivnaya-ultrazvukovaya-finishnaya-obrabotka-bufo-ultrazvukovaya-impulsnaya-uprochnyayushe-chistovaya-obrabotka>. Accessed 10 Oct 2018

Mini-Converter for Processing of Poor-Quality Charge and Metal-Containing Waste



S. Eronko, S. Gorbatyuk and M. Tkachev

Abstract The authors considered the requirements that should be met by a steel melting unit for the production of cast iron from waste containing harmful impurities. Further, the paper demonstrated the efficiency of using an oxygen converter with a rotating body as a prototype for this purpose. As a result of a comparative analysis of the known smelting systems, a converter with two axes of rotation was used as a prototype for the implementation of the Kalda process, allowing to produce high-quality steel from highly phosphorous cast irons with increased consumption (40–50%) of metal-containing waste. The proposed oxygen mini-converter is advisable to use in combination with a blast furnace with a volume of 110–130 m³ or an oxygen cupola with a capacity of 15 tons per hour under the operating conditions of the foundry of a machine-building plant to produce steel used in the production of castings or forgings. The practical use of the proposed technical solutions will allow steel to be smelted from low-quality cupola iron with partial or full replacement of deficient scrap with metal-containing waste in the conditions of foundries of small engineering and repair plants. At the same time, along with the direct economic benefit obtained, the task of reducing the accumulation in the dumps of industrial metal-containing wastes that adversely affect the environment is being solved.

Keywords Steel melting unit · Converter · Tuyere · Purge · Poor-quality charge · Metal-containing waste · Cast iron · Harmful impurities

S. Eronko · M. Tkachev
National Technical University of Donetsk, 58, Artyom Street, 83000 Donetsk,
Ukraine

S. Gorbatyuk (✉)
National University of Science and Technology MISiS, 4, Leninsky Prospect,
119049 Moscow, Russia
e-mail: sgor02@mail.ru

1 Introduction

In recent years, the problems associated with an increase in the share of depreciation scrap with a high content of undesirable impurities and the accumulation in the dumps of metal-containing industrial by-products that are harmful to the environment have been exacerbated. In the developed countries, the volume of metallurgical slag processing has already exceeded 93%, and the disposal of industrial wastes makes it possible to produce useful products worth more than \$70 billion a year [1].

In the economic conditions of states of the former Soviet Union, the achievement of such indicators on their territory requires the creation of special technological complexes designed to produce ferrous and non-ferrous metals by processing low-quality raw materials, including substandard scrap, metallurgical, and coal sludge. At the same time, the use of such complexes is economically feasible in micro-plants.

The prospect of such metallurgical plants is due to significantly smaller investments required when they are launched, as well as the possibility of a more flexible solution to the issue of supplying small volumes of metal products to medium and small engineering companies specializing in the production or repair of both primary and secondary process equipment for a number of industries of the domestic economy. Besides, to ensure the rhythmic work of the micro-plant, there is no need to resort to the services of railway transport, since the logistics and cargo volumes of such plant with lower costs can be provided by road transport [2].

In world practice, the positive applications of various technologies for producing cast iron in plants with annual production of several tens of thousands of tons have been already known. So the company ThyssenKrupp Steel has developed an oxygen cupola which allows smelting iron from the waste with a capacity of up to 15 tons per hour.

In 2016, metallurgical company Companhia Siderurgica do Cuchi (Angola) put into operation the first stage of the plant for the production of high-quality cast iron with an annual output of more than 90 thousand tons [3].

At the company “Energocapital,” Makeevka, Donetsk region, new technology was introduced in production, intended for the production of cast iron from pellets from coal and metal sludge [4] in the blast furnace with a volume of 128 m³.

2 The Goal of the Research

Analysis of trends in the development of small-scale metallurgy in the world and the offer of technical solutions that allow steel to be smelted from the low-quality cupola iron in the conditions of foundries of small engineering and repair plants for the production of castings and forgings.

3 Materials and Results of the Research

Issues related to the development of technologies aimed at minimizing environmental pollution [5–11] that are becoming increasingly relevant. Successful use of small-sized oxygen furnaces and blast furnaces for producing cast iron and commercial iron from metallurgical wastes suggests that it is advisable to find ways to use small-sized melting units that can process the liquid iron and the metal-containing wastes with high content of harmful impurities in steel of acceptable quality, except from the installation process chain for its refining.

Naturally, the processing of low-quality charge and metal-containing waste implies the existence of technological processes that differ from the traditional ones by a number of indicators, and melting units that meet the complex of requirements [12–14]:

- ensuring the maximum possible intensity of mixing of the melt bath and an increase in the contact surface of media in the different phase states;
- the possibility of a regulated supply of refining additives in both lumpy and finely dispersed form;
- a high degree of beneficial use of energy carriers to provide the necessary heat balance in the working space;
- preventing of aggressive final slag into the casting ladle in the course of steel production.

At the departments of “Mechanical equipment of ferrous metallurgy plants named after professor V. Ya. Sedush” of the Donetsk National Technical University and “Engineering of Technological Equipment” of the National Research Technological University “MISiS” over the past 5 years, work is being done to improve the metallurgical equipment [15–19], including the creation of an oxygen mini-converter that meets all of the above requirements.

As a result of a comparative analysis of the advantages and disadvantages of the known melting systems as a prototype, when choosing the design scheme of the developed unit, the converter with two axes of rotation was used to implement the Kalda process, allowing produce high-quality steel from highly phosphorous cast iron at an increased flow rate (40–50%) of scrap metal [20]. Related to the need to eliminate several significant shortcomings had been identified in this type of converter and which had been the main reason for the termination of its industrial use in Europe, Japan, and America, the design of the modernized melting unit incorporated new technical solutions protected by patents of Ukraine and the Russian Federation [21, 22]. First of all, it should be noted the modified kinematic scheme of the mechanism of rotation of the converter housing relative to its longitudinal axis. As is well known, at the Kalda converter, the drive of this mechanism was installed directly on the rotary system of the melting unit, which not only complicated its repair and maintenance, but also increased the mass of the moving part, and this entailed the need to increase the drive power of the case turning mechanism relative to axles of basic pins.

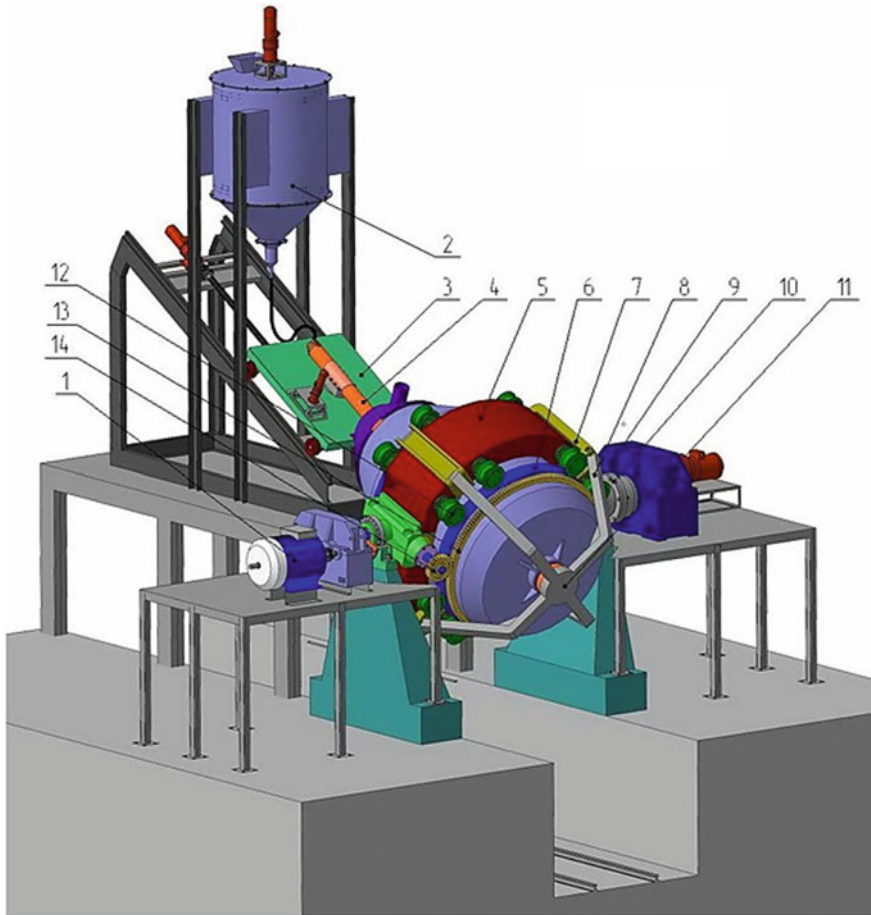


Fig. 1 3D model of 10 ton Kalda converter (evacuation system of gases and dust is not shown)

In the proposed design of the converter, the general view of which is shown in Fig. 1, the upgraded drive 1 of the case rotation mechanism was installed, the delivery system for powdered lime from container 2 to oxygen tuyere 4 installed on movable carriage 3 was upgraded.

Fixing the converter housing relative to the support ring 5 is carried out by sixteen rollers 12, each of which has two flanges. The rollers are installed in pairs on the lower- and upper-end surfaces of the support ring 5, equipped with four rigidly fixed plates 7, which are connected to curved section beams 8 that hold the bearing 11 pins of the converter bottom part.

On the outer cylindrical surface of the converter case, two tires 6 are mounted, which cooperate with the support rollers 12. In the lower part of the converter case there is a toothed rim 13 that meshes with the gear 14.

In order to improve the conditions of rapid melting of scrap, increase the degree of dephosphorization while reducing the consumption of burnt lime, the converter was equipped with a melt mixing system with an inert gas, allowing perform bottom blowing during rotation of the unit casing without the use of expensive automation tools [23–25].

When the converter is rotated, there is a continuous change in the areas of the lining located in the high-temperature zone, which is formed during the combustion of CO gas. At the same time, the particles of powdered materials blown into the oxygen jet through a tuyere nozzle moving along a given complex trajectory. Thus, getting under the metal and slag levels, the overheated lining gives them heat, and the reagents directly enter into the chemical interaction with melt.

In the developed mini-converter, a system of gas-dynamic cutoff of the slag melt is provided. It makes possible to prevent the aggressive final slag from entering the bottling ladle, which can cause of increased waste of deoxidizers and alloying additives. Besides, the use of gas-dynamic cutoff of the final process slag eliminates the supply of lime to thicken it.

The proposed oxygen mini-converter is advisable to use in combination with a blast furnace with volume of 110–130 m³ or the oxygen cupola with capacity of 15 tons per hour under the operating conditions of the foundry of machine-building plant to produce steel used in the production of castings or forgings according to the flowchart shown in Fig. 2.

Because in the converter with a rotating body relative to a longitudinal axis inclined to the horizontal plane, complete combustion of carbon to CO₂ is ensured with a threefold excess of the amount of heat produced during the course of this chemical reaction in comparison with other types of oxygen converters, increase from 25 to 50% and, accordingly, reduce the consumption of liquid iron from 75 to 50%.

Rotation of the converter with the possibility of additional intensification of heat and mass transfer due to the bottom blowing with an inert gas, blowing fine reagents in the oxygen jet through the lance making movement inside the unit along a complex trajectory, as well as the gas-dynamic cutoff of the final process slag at the metal release into the pouring ladle allows providing the most flexible and effective management of the kinetics, sequencing, and rate of chemical reactions in the aggregate bath. This allows recycling the mixture of any composition, so the increased costs of refractories due to their accelerated wear caused by intense mixing of the metal bath and the formation of a large amount of aggressive final slag overlap with a relatively low price for recycled solid metal-containing waste and the low-quality liquid cast iron with high content of harmful impurities. As a result, you can get a liquid steel of acceptable quality with the lowest cost.

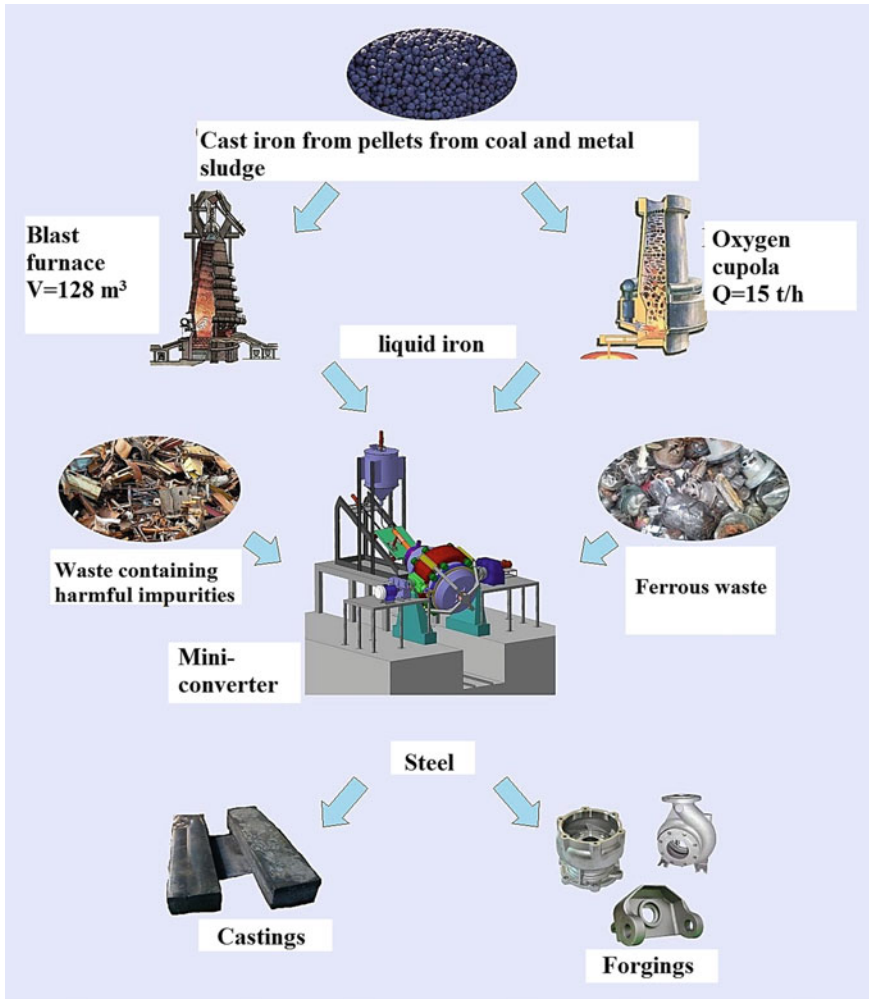


Fig. 2 Production scheme for forgings and castings using the mini-converter

4 Conclusions

1. Based on the results of the analysis of the state and trends in the development of small-scale metallurgy in the world, the feasibility has been substantiated and, ensuring the processing of the low-quality charge and the industrial metal-containing waste with a high content of harmful impurities, the design concept of oxygen mini-converter has been developed.

2. The practical use of the proposed technical solutions will allow smelting steel from the low-quality cupola iron in the conditions of foundries of small engineering and repair factories for the production of castings and forgings. At the same time, along with the obtained direct economic benefit, the task of reducing the accumulation in the dumps of the industrial metal-containing wastes that adversely affect the environment is being solved.

References

1. Viner R (2011) *Metal Scrap* 2:9
2. Smirnov AN, Safonov VM, Dorokhova LV (2005) *Metallurgical mini-plants*. Nord-Press, Donetsk, p 465
3. Ovchinnikov AM (2016) *Iron and steel industry*. Bull Inst Chermetinformatsia 2:96–100
4. Artiukh V, Mazur V, Adamtsevich A (2017) Priority influence of horizontal forces at rolling on operation of main sheet rolling equipment. MATEC web of conferences, vol 106, p 040011. <https://doi.org/10.1051/mateconf/201710604001>
5. Artiukh V, Mazur V, Prakash R (2016) Increasing hot rolling mass of steel sheet products. *Solid State Phenom* 871:3–8. <https://doi.org/10.4028/scientific.net/MSF.871.3>
6. Keropyan AM, Kantovich LI, Voronin BV et al (2017) Influence of uneven distribution of coupling mass on locomotive wheel pairs, its tractive power, straight and curved sections of industrial rail tracks. *IOP Conf Ser Earth Environ Sci* 87(6):062005
7. Keropyan AM, Gerasimova AA (2017) Connection of the temperature in the contact area of the wheel-rail system with the railway slope of industrial railway transport. *Izvestiya Vysshikh Uchebnykh Zavedenij Chernaya Metallurgiya* 60(5):355–363
8. Bardovskiy AD, Gorbatyuk SM, Keropyan AM, Bibikov PY (2018) Assessing parameters of the accelerator disk of a centrifugal mill taking into account features of particle motion on the disk surface. *J Friction Wear* 39(4):326–329
9. Zarapin AYU, Shur AI, Chichenev NA (1999) Improving the installation for rolling an aluminum strip coated with corrosion-resistant steel. *Steel Transl* 29:69–71
10. Zarapin AYU, Levitsky IA, Mokretsov AS, Chichenev NA (1999) Modeling of rolling of three-layer strips with resistance of heating. *Steel* 7:61–64
11. Zarapin AYU, Stanishevsky SE, Chichenev NA (1999) Continuous line for the production of strips with a gas-thermal coating of nickel alloys. *Tyazheloe Mashinostroenie* 6:21–25
12. Zarapin AYU, Chichenev NA (1999) Designing lines for the production of composite materials based on the object-oriented approach. *Heavy Eng* 6:16–20
13. Kobelev OA, Tsepin MA, Skripalenko MM, Popov VA (2009) Features of technological layout of manufacture of unique mono-block large-dimension plates. *Adv Mater Res* 59:71–75. <https://doi.org/10.4028/3-908454-01-8.71>
14. Pimenov GA, Kostyukov GA, Ryabov PS et al (1991) Making of large-sized solid-forged blanks. *Tyazheloe Mashinostroenie* 9:21–24
15. Eron'ko SP, Gorbatyuk SM, Oshovskaya EV, Starodubtsev BI (2017) Development of the automatic system of gas-dynamic cut-off of slag for the converter with rotating vessel shell. *Izvestiya Vysshikh Uchebnykh Zavedenij. Chernaya Metallurgiya* 60(11):863–869
16. Sivak BA, Grachev VG, Parshin VM et al (2009) Magnetohydrodynamic processes in the electromagnetic mixing of liquid phase in the ingot on continuous bar—and bloom-casting machines. *Steel Transl* 39(9):774–782
17. Grachev VG, Sivak BA, Kuz'mina LI, Zarubin SV (2002) Physico-mathematical modeling of the electromagnetic stirring process of a liquid metal in the crystallizer of graded continuous billet casting machines. *Tyazheloe Mashinostroenie* 5:2–6

18. Gorbatyuk SM, Gerasimova AA, Belkina NN (2016) Applying thermal coatings to the narrow walls of the continuous-casting molds. *Mater Sci Forum* 870:564–567
19. Gerasimova AA, Radyuk AG, Titlyanov AE (2015) Creation of a diffusional aluminum layer on the narrow walls of continuous-casting molds. *Steel Transl* 45(3):185–187
20. Dragobetskii V, Shapoval A, Naumova E (2018) The technology of production of a copper—aluminum—copper composite to produce current lead buses of the high—voltage plants. In: *Proceedings of the international conference on modern electrical and energy systems MEES 2017*, pp 400–403
21. Boichenko BM, Okhotsky VB, Kharlashin PS (2006) *The BOF steel production: theory, technology, steel quality, unit design, materials recycling and environment*. RVA Dnepro-VAL, Dnepropetrovsk
22. Eron'ko SP et al (2012) Oxygen converter. UA Patent for utility model 71568, IPS C 21C 5/28
23. Eron'ko SP et al (2017) Oxygen converter for processing iron and scrap metal with a high content of harmful impurities. RU Patent 2623934, IPS C21C 5/42, C21C 5/28
24. Eron'ko SP, Oshovskaya EV, Yushchenko MV, Starodubtsev BI (2014) Screw systems for supplying slag-forming mixture to the molds of continuous-casting machines. *Steel Transl* 44(9):640–645
25. Sedush VY, Sidorov VA, Eron'ko SP, Oshovskaya EV (2003) Optimal methods of maintaining of serviceability of mechanical equipment. *Stal* 7:77–79

Cabled Feeder for Underground Drilling Machines



A. M. Busygin

Abstract The feeding system (feeder) of a drilling machine is designed to feed the drilling assembly with the drilling head to the bottom and make the drilling assembly generate axial force acting upon the bottom and operate the drilling assembly. Feeders can use pneumatic, hydraulic, or electric engines alongside with pneumatic and hydraulic cylinders. Feeder mechanisms also can be of various types: screw drives, rack-and-pinion drives, or chain-and-cable drives. The feeder is a part of a drilling machine; when designing an underground drill, design simplicity, reliable functionality, and cost-effective manufacture are the basic criteria of selecting the feeder type. The article considers four feeder types: a screw feeder, a rack-and-pinion feeder, a piston-and-cable feeder and a chain feeder. It presents kinematic diagrams and describe the operation of each feeder, and covering their respective pros and cons. The paper also covers existing types of feeders used in drilling machines: fixed-chain feeders, chain-and-piston feeders, piston feeders with manual interception and two parallel cylinders, automatic-interception feeders with two parallel cylinders, etc. The paper also presents a novel cable feeder designed by the author hereof; the feeder meets the criteria, against which new feeder types must be tested. Find herein the kinematic diagram and a detailed operation summary of this feeder.

Keywords Feeding system • Drilling machine • Cable mechanism

1 Introduction

Advancements in mining, which is a fundamental industry in Russia's economy, are the key to the economic growth of this country. Whether it is open-pit or underground mining, drilling is the fundamental process. Drilling machines can use

A. M. Busygin (✉)

National University of Science and Technology "MISIS", 24, 2 Glavnaya Ul., Moscow Region, Zheleznodorozhny 143983, Russia
e-mail: Busy9@rambler.ru

© Springer Nature Switzerland AG 2020

A. A. Radionov et al. (eds.), *Proceedings of the 5th International Conference on Industrial Engineering (ICIE 2019)*, Lecture Notes in Mechanical Engineering,
https://doi.org/10.1007/978-3-030-22041-9_27

231

two types of methods to break the rock: mechanical or physical methods. Physical rock breaking includes thermal, explosive, hydraulic, electro-hydraulic, and ultrasound drilling, which affects the rock through a liquid or a gaseous medium. Despite creating and implementing novel physical or combined methods, mechanical breaking remains crucial. In case of blasting, most time is spent to drill. This is why state-of-the-art technology and equipment [1–16] requires novel, improved-performance drills to considerably cut the time consumption of drilling operations. In particular, the drilling machines include a separate group: underground drilling machines, where the feeder is a crucial component.

A feeding system of a drilling machine, hereinafter referred to as a feeder, is intended for feeding the drilling assembly to a bottom with a drilling head (of a rotary or percussive and rotary action), providing a necessary axial effort towards the bottom from the drilling assembly as well as for the conduct of installation and disassembly operations involving the drilling assembly during drilling or when dismantling the bottom after a pit has been drilled. Feeders can be driven by pneumatic, hydraulic, or electric engines alongside with pneumatic and hydraulic cylinders. Feeder mechanisms also can be of various types: screw drives, rack-and-pinion drives, or chain-and-cable drives.

The feeder is an important part of a drilling machine; when designing an underground drill, design simplicity, reliable functionality, usability, cost-effective manufacture, and operation are the basic criteria of selecting the feeder type.

The paper further presents the kinematic diagram of a cable feeder to be used in underground drilling machines; the author believes this feeder meets all of the above criteria, especially the design simplicity and cost-effective manufacture criteria; it has not been used to far.

2 Principal Part

When writing this paper, the author overviewed a bulk of papers in this research area [17–29], dating from mid-twentieth century to this day.

The most detailed classification of feeders for underground drilling machines is presented in Chernilov's *Feeding Devices of Drilling Machines for Underground Works* [30, 31]. To compare the author's feeder design against the existing drilling feeders, let us analyze several feeders, their kinematic diagrams, and operating principles.

Figure 1 presents the most common type: the screw feeder.

The sled 4, which carries the drilling head, can perform translational motion as the nut 5 acts on the sled 4. The nut 5 is moved by the screw 3, which rotates in its fixed supports. The engine 1 causes the screw 3 to rotate via the reduction drive 2. Sled 4 rotation direction depends on that of the engine 1. The axial force generated by this device depends on the power of the engine 1, the gear ratio of the reduction drive 2, as well as on the geometry of the screw pair (the screw pitch and diameter). This diagram offers sufficient rigidity. However, the force couple generated by the

Fig. 1 Kinematic diagram of a screw feeder

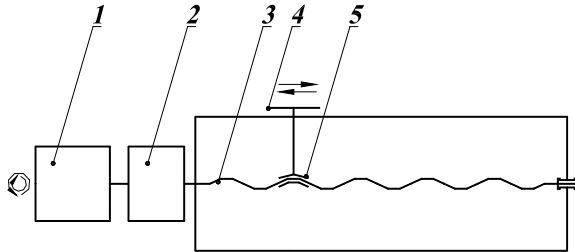
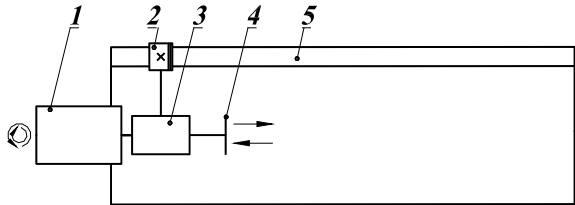


Fig. 2 Kinematic diagram of a rack-and-pinion feeder



screw 3 and drilling bottom forces does induce extra loads on the screw-feeder elements, which adversely affects its operation. The cost of making the screw 3, as well as its weight, is nothing to be ignored.

Figure 2 presents the diagram of a rack-and-pinion feeder.

Connected by the reduction drive 3, the engine 1 causes the pinion 2 to rotate; the latter engages the fixed toothed rack 5. Rolling around the toothed rack 5, the rotating pinion 2 causes the sled 4 and the drilling head it carries to start translational motion; it also moves the drive, which comprises the engine 1 and the reduction drive 3. The engine 1 is a bidirectional one, enabling sled 4 to change the direction of its motion. The axial force generated by this device depends on the power of the engine 1, the gear ratio of the reduction drive 3, as well as on the geometry of the pinion 2. One of the disadvantages of this feeder is the high cost of making a gear set (a rack and a pinion).

Figure 3 shows the kinematic diagram of a piston-and-cable feeder.

This feeder operates as follows. Compressed air is fed into the cylinder 5 chamber through the channel a, actuating the piston 4, the piston rod of which is the cable 2 that goes around the pulley wheels 3, 6 and is connected to the sled 1. Feeding compressed air to the channel b causes the sled 1 to reverse their direction. The cable 2 has a special sealing device. One pro of this feeder is its simple design. The con is the bulkiness of the cylinder, which depends on the sled 1 travel; expensive-to-make cylinders are not an advantage either 7.

Figure 4 shows the diagram of a movable-chain feeder. The drive sprocket 3 is driven by the engine 1 via the reducing gear 2. The chain 5 connects the sprockets 3 and 6 and moves alongside, the sled 4 as the drive sprocket rotates and causing the drilling head to travel. The disadvantage here is that the chain may overstretch in operation.

Fig. 3 Kinematic diagram of a piston-and-cable feeder

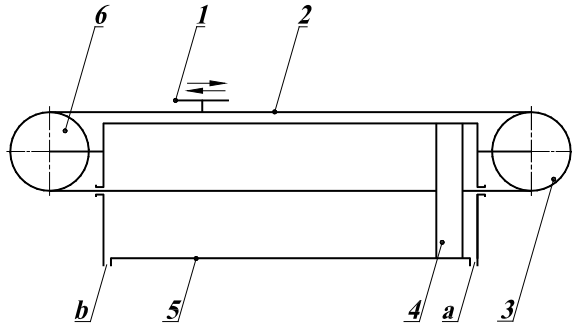
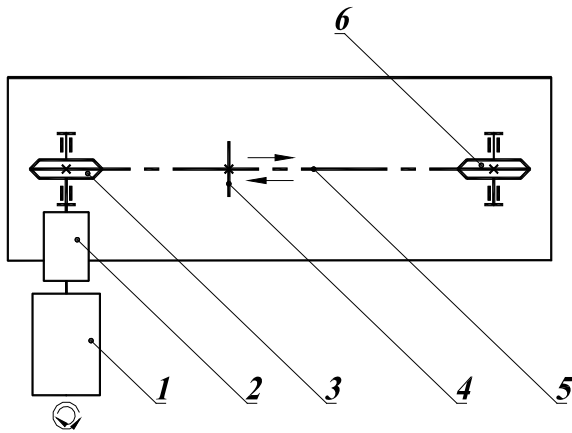


Fig. 4 Kinematic diagram of a movable-chain feeder



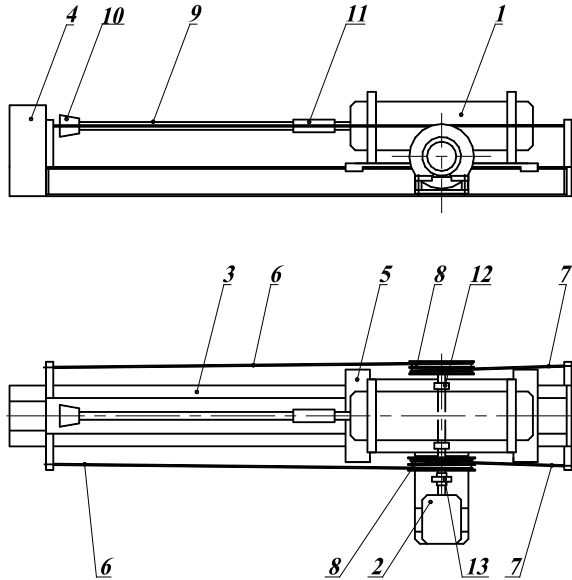
There are also other feeder types, which will not be covered in detail here due to space considerations: movable-chain feeders, chain-and-piston feeders, piston feeders with manual interception and two parallel cylinders, automatic-interception feeders with two parallel cylinders, long-stroke piston feeders, double-stroke feeders, piston feeders with twin cylinders, piston-and-chain feeders, and piston-and-rack feeders.

3 Conclusion

Now let us describe the author-presented feeder for underground drilling machines. Figure 4 presents the diagram of a cable feeder for underground drilling machines.

The feeder comprises the drilling head 1 of a rotary or percussive and rotary type, which is fastened to the sled 5 that can move along the frame 3, thus moving the drilling assembly (the drill rod 9, the coupling 11, the drill column 10) towards the bottom when drilling, building-up the drilling assembly, or disassembling the assembly after a pit has been drilled.

Fig. 5 Diagram of a cable feeder for underground drilling machines



Sled 5 direction depends on the engine 2 direction.

The drilling assembly is lowered towards the bottom by reeling the two cables 6 onto the spools 8, which are carried by the single shaft resting upon the two bearing supports 12. The single shaft of the spools 8 is connected to the engine 2 by the coupling 13. The cables 6 are reeled onto the spools 8 by the engine 2 rotating clockwise; see front view in Fig. 5. The drilling head 1 and the sled 5 can be placed back to the original position by reeling the cables 7 onto the spools 8 as the engine 2 rotates counterclockwise. When the cables 6 are reeled onto the spools 8, the cables 7 are unreeled, and vice-versa.

The grip 4 is intended for holding the drilling assembly when installing or uninstalling it.

This paper will be of use for engineers designing drilling machines for the mining industry.

References

1. Keropyan AM, Gerasimova AA (2017) Connection of the temperature in contact area of the wheel-rail system with the railway slope of industrial railway transport. *Izvestiya Vysshikh Uchebnykh Zavedenij Chernaya Metallurgiya* 60(5):355–363. <https://doi.org/10.17073/0368-0797-2017-5-355-363>
2. Gerasimova AA, Keropyan AM, Girya AM (2018) Study of the wheel-rail system of open-pit locomotives in traction mode. *J Mach Manuf Reliab* 47(1):35–38. <https://doi.org/10.3103/S1052618818010065>

3. Keropyan AM, Gerasimova A, Goloshapov K (2017) Influence of the track gradient on the contact temperature at the wheel-rail zone for open-pit locomotives. MATEC web of conferences, 129. <https://doi.org/10.1051/mateconf/201712906009>
4. Bardovsky A, Gerasimova A, Aydunbekov A (2018) The principles of the milling equipment improvement. MATEC Web Conf 224:01019. <https://doi.org/10.1051/mateconf/201822401019>
5. Gorbatyuk S, Kondratenko V, Sedykh L Tool stability analysis for deep hole drilling. MATEC web conference, vol 224. P 01035. <https://doi.org/10.1051/mateconf/201822401035>
6. Gerasimova A, Gorbatyuk S, Devyatiarova V (2018) Application of gas-thermal coatings on low-alloyed steel surfaces. Solid State Phenom (SSP) 284:1284–1290. [10.4028/www.scientific.net/SSP.284.1284](https://doi.org/10.4028/www.scientific.net/SSP.284.1284)
7. Gerasimova AA, Radyuk AG, Titlyanov AE (2015) Creation of a diffusional aluminum layer on the narrow walls of continuous-casting molds. Steel Transl 45(3):185–187. <https://doi.org/10.3103/S0967091215030079>
8. Mazhirin EA, Chichenev NA, Zadorozhnyi VD (2008) Modernizing the track units of the 2800 thick-sheet mill at OAO Ural'skaya Stal. Steel Transl 38(12):1048–1050. <https://doi.org/10.3103/S0967091208120255>
9. Nikolaev VA, Rusakov AD, Chichenev NA (1996) Forecasting a multiroll mills rolls hardness. Stal' 9:58–60
10. Zarapin AYu, Levitsky IA, Mokretsov AS, Chichenev NA (1999) Modeling of rolling of three-layer strips with resistance of heating. Steel 7:61–64
11. Zarapin AYu, Stanishevsky SE, Chichenev NA (1999) Continuous line for the production of strips with a gas-thermal coating of nickel alloys. Tyazheloe Mashinostroenie 6:21–25
12. Zarapin AYu, Chichenev NA (1999) Designing lines for the production of composite materials based on the object-oriented approach. Heavy Eng 6:16–20
13. Gorbatyuk SM, Morozova IG, Naumova MG (2017) Reindustrialization principles in the heat treatment of die steels. Steel Transl 47(5):308–312. <https://doi.org/10.3103/S0967091217050047>
14. Gorbatyuk SM, Morozova IG, Naumova MG (2017) Development of the working model of production reindustrialization of die steel heat treatment. Izvestiya Vysshikh Uchebnykh Zavedenij Chernaya Metallurgiya 60(5):410–415. <https://doi.org/10.17073/0368-0797-2017-5-410-415>
15. Naumova M, Basyrov I, Aliev K (2018) Reengineering of the ore preparation production process in the context of almayk MMC. JSC MATEC Web Conf 224:01030. <https://doi.org/10.1051/mateconf/201822401030>
16. Naumova MG, Morozova IG, Zarapin AY, Borisov PV (2018) Copper alloy marking by altering its surface topology using laser heat treatment. Metallurgist 62(5–6):464–469. <https://doi.org/10.1007/s11015-018-0682-2>
17. Tarasov Y, Radyuk A, Gorbatyuk S (2018) Research of heat stresses in components of blast furnace tuyere. MATEC Web Conf 224:02029. <https://doi.org/10.1051/mateconf/201822402029>
18. Alimov OD, Dvornikov AT (1976) Drilling machines. Mashinostroyeniye, Moscow, p 295
19. Medvedev IF (1975) Drilling modes and drilling machine selection. Nedra, Moscow, p 224
20. Vodyanik GM, Ryl'yevev EV (1979) New drilling machines of rotative action. Tekhnika, Kiev
21. Ivanov KI, Latyshev VA, Andreyev VD (1987) Technics of drilling at developing mineral deposits. 3rd edn. Nedra, Moscow, p 131
22. Kantovich LI, Naumkin VM, Razumov MV, Grebennikov VN (2016) Drilling machine NKR-100 M. Practical course, 2nd edn. p 83
23. Kvanigidze VS, Kozovoi GI, Chakvetadze FA, Antonov YuA, Koretskiy VB (2017) Drilling machines at quarries. In: Structures, operation, calculation, p 291
24. Lemeshko MA, Volkov RYu (2015) Rotating drilling analysis. Young Sci 21:179–185
25. Lemeshko MA, Volkov RYu (2014) Method of adaptive process of rock cutting. In: Topical problems of humanities and natural sciences. pp 46–50

26. Regotunov AS, Antonov VA (2015) Experimental research of rock percussive drilling modes. *News HEIs Min J* 8:61–69
27. Yao N, Zhang J, Jin X, Huang H (2014) Status and development of directional drilling technology in coal mine. *Procedia Eng* 73:289–298
28. Li H, Hu Y, Wu Y, He Z, Qin W, Amp M (2015) Research on the high precision measurement technique for the underground drilling depth. *Geotech Investig Surv* 43:80–86
29. Shigina AA, Shigin AO, Stupina AA, Kurchin GS, Kirsanov AK (2016) Model of rock drilling process in terms of roller cone bit remaining life. *Inter J Appl Eng Res* 11(19):9792–9799
30. Kurchin GS, Vokhmin SA, Kirsanov AK, Shigin AO, Shigina AA (2015) Calculation methodology of blasting and explosion operations' parameters for construction of horizontal and inclined excavations. *Inter J Appl Eng Res* 10(15):35897–35906
31. Chernilov EG (1970) Feeding devices of drilling machines for underground works. Institute of Mining of the Siberian Department of the Academy of Sciences, USSR, Novosibirsk, p 131

Solving Problem of Curved Surface Approximation by Layers with Constant and Variable Sections During Forming by Additive Methods



A. N. Grechukhin, V. V. Kuts and M. S. Razumov

Abstract The paper considers the accuracy of the formation of engineering products' surface layers using additive methods. It was determined that in case of additive forming, the accuracy characteristics of the surface layer differ significantly from the accuracy characteristics of the surface layers obtained using traditional methods. This is due to the high values of the error of forming (approximation) in additive methods. To improve the accuracy characteristics of products' complex surfaces obtained using additive methods, it was proposed to ensure the dynamic spatial orientation of the final element of the additive equipment forming system. To control the spatial orientation of the forming system final element, it was proposed to use mechatronic 5 and 6 coordinate devices. The related area for solving the issues of improving the accuracy of additive forming methods was indicated. This area includes parallel control of the spatial orientation and section dimensions of a single layer, which, at certain values, will form the required value of approximation error at the specified performance. In this regard, the solutions of the problem of the parts' curved surface approximation by layers with constant and variable sections were proposed. The results of geometric and computer simulation are given. A comparative assessment of the results of solving the above problems is provided. The proposed method will allow reducing the error in forming the products obtained with the help of additive methods.

Keywords Additive technologies · Layer-by-layer synthesis · Forming · Error

A. N. Grechukhin (✉) · V. V. Kuts · M. S. Razumov
Southwest State University, 94, 50 Let Oktyabrya, Kursk, Russia
e-mail: agrechunin@mail.ru

© Springer Nature Switzerland AG 2020
A. A. Radionov et al. (eds.), *Proceedings of the 5th International Conference on Industrial Engineering (ICIE 2019)*, Lecture Notes in Mechanical Engineering,
https://doi.org/10.1007/978-3-030-22041-9_28

239

1 Introduction

Recently, additive technologies have been actively developing; not only the range of products obtained using additive methods is expanding, but also devices based on industrial robots, which can expand the application range of additive devices and improve the quality of the formed surfaces, are increasingly used [1–20].

The papers [2, 3] consider the accuracy of additive methods for forming, propose the method for improving the accuracy characteristics of complex surfaces of products obtained using additive methods, which is to ensure the dynamic spatial orientation of the final element of the additive equipment forming system, propose the mechanisms for ensuring spatial orientation, which are based on the use of mechatronic systems. It was shown that the use of dynamic spatial orientation reduces the value of the approximation error and improves the accuracy of the formed surfaces.

However, studies show that the related area for the development of accuracy of the additive forming methods can be parallel control of the spatial orientation and section dimensions of a single layer, which, at certain values, will form the required value of approximation error at the specified performance. The problems of approximating the curved sections of a part by portions of the single layer, logically following from the purpose indicated above, require an integrated solution based on theoretical and empirical studies.

In the context of the geometric theory for forming surfaces, this problem can be solved in several stages.

2 The Solution to the Problem of a Single Layer with Constant Section Orientation When Approximating the Part Section

The problem will meet the condition that the single layer corresponds to the shape of an ellipse with the width and height parameters $a = \text{const}$, $b = \text{const}$. Under this condition, the problem of approximation is reduced to solving a system of equations for the unknown parameters t_{0i} , t_{i-1} , t_i [21] (Fig. 1).

$$\begin{cases} \overline{i_0} \cdot \overline{A_{i-1}(t_{0(i-1)}) \cdot r_{i-1}(t_{i-1})} = \overline{i_0} \cdot \overline{A_i(t_{0i}) \cdot r_i(t_i)}; \\ \overline{j_0} \cdot \overline{A_{i-1}(t_{0(i-1)}) \cdot r_{i-1}(t_{i-1})} = \overline{j_0} \cdot \overline{A_i(t_{0i}) \cdot r_i(t_i)}; \\ \frac{\overline{A_{i-1}(t_{0(i-1)}) \cdot r_{i(i-1)}(t_{i-1}) \cdot A_i(t_{0i}) \cdot r_{ii}(t_i)}}{|\overline{A_{i-1}(t_{0(i-1)}) \cdot r_{i(i-1)}(t_{i-1})}| \cdot |\overline{A_i(t_{0i}) \cdot r_{ii}(t_i)}|} = -1, \end{cases} \quad (1)$$

where

A_{i-1} , A_i installation matrix for the coordinate system of the $i - 1$ and i deposited layers, respectively;

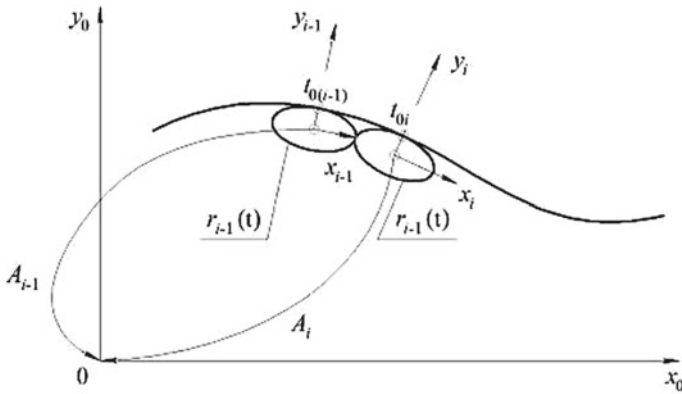


Fig. 1 Scheme of the part section approximation at constant parameters of the single-layer section

- $t_{0(i-1)}, t_{0i}$ part section parameters defining the installation point of the $i - 1$ and i layers;
- t_{i-1}, t_i parameters of the $i - 1$ and i layers corresponding to their tangency point;
- $\bar{r}_{i-1}(t_{i-1}), \bar{r}_i(t_i)$ tangency points of the $i - 1$ and i layers;
- $\bar{r}_{i(i-1)}(t_{i-1}), \bar{r}_{ii}(t_i)$ derivative of the $i - 1$ and i layers for the parameter t .

The matrix $A_i(t_i)$ is calculated according to the following dependency:

$$A_i(t_i) = A_{0i}(t_i) \cdot A_{ki}^{-1}(t_{ki}) \tag{2}$$

where

$A_{0i}(t_i)$ is the matrix for the transition from the cutting plane coordinate system at the part section point to the part coordinate system;

$A_{ki}(t_{ki})$ is the matrix for the transition from the cutting plane coordinate system at the i th point of the deposited layer, defined by the parameter t_{ki} .

In turn, the matrix $A_{0i}(t_i)$ can be determined on the basis of the method described in [4–22] using the specified vectors that determine the position and direction of the axes of the cutting plane, namely:

$$\begin{bmatrix} -\bar{i}_0 \cdot \bar{r}_{0ii}(t_{0i}) & -\bar{j}_0 \cdot \bar{r}_{0ii}(t_{0i}) & 0 & 0 \end{bmatrix}^T \\ \begin{bmatrix} \bar{i}_0 \cdot \bar{r}_{0ii}(t_{0i}) & \bar{j}_0 \cdot \bar{r}_{0ii}(t_{0i}) & 0 & 0 \end{bmatrix}^T \times \begin{bmatrix} 0 & 0 & -1 & 0 \end{bmatrix}^T; \tag{3} \\ \begin{bmatrix} \bar{i}_0 \cdot \bar{r}_{0i}(t_{0i}) & \bar{j}_0 \cdot \bar{r}_{0i}(t_{0i}) & 0 & 0 \end{bmatrix}^T.$$



The matrix $A_{ki}(t_{ki})$ is calculated similarly according to the given vectors:

$$\begin{aligned} & [\bar{i}_i \cdot \bar{r}_{ii}(t_i) \quad -\bar{j}_i \cdot \bar{r}_{ii}(t_i) \quad 0 \quad 0]^T; \\ & [\bar{i}_i \cdot \bar{r}_{ii}(t_i) \quad \bar{j}_i \cdot \bar{r}_{ii}(t_i) \quad 0 \quad 0]^T \times [0 \quad 0 \quad -1 \quad 0]^T; \\ & [\bar{i}_i \cdot \bar{r}_i(t_i) \quad \bar{j}_i \cdot \bar{r}_i(t_i) \quad 0 \quad 0]^T. \end{aligned} \tag{4}$$

Figure 2 shows the results of geometric simulation of approximation of the curved surface area of the RK-section shaft with the following parameters: the number of faces $N = 3$, circumscribed-circle radius $R = 12$ mm, eccentricity $e = 1.2$ mm, by single layers with width $a = 0.631$ mm, height $b = 0.5$ mm.

3 Solution to the Problem of Calculating the Maximum Value of Approximation Error

The value of approximation error is defined as a function:

$$A_i(t_{0i}, t_{i-1}, t_i, a_{i-1}, b_{i-1}, a_i, b_i) = \left| \overline{A_i(t_{0i}, a_i, b_i) \cdot r_i(t_i, a_i, b_i)} \right| - \left| \overline{r_0(t_{\Delta})} \right| \tag{5}$$

where $r_0(t_{\Delta})$ is a vector defining a point at the part section with the parameters t_{Δ} towards the vector (Fig. 3).

The parameter t_{Δ} is determined by solving the equation:

$$\frac{\overline{A_i(t_{0i}, a_i, b_i) \cdot r_i(t_i, a_i, b_i)} \cdot \overline{r_0(t_{\Delta})}}{\left| \overline{A_i(t_{0i}, a_i, b_i) \cdot r_i(t_i, a_i, b_i)} \right| \cdot \left| \overline{r_0(t_{\Delta})} \right|} = 1 \tag{6}$$

Figure 4 shows the results of calculating the error of approximation of the curved surface by sections of the single layer with constant dimensions.

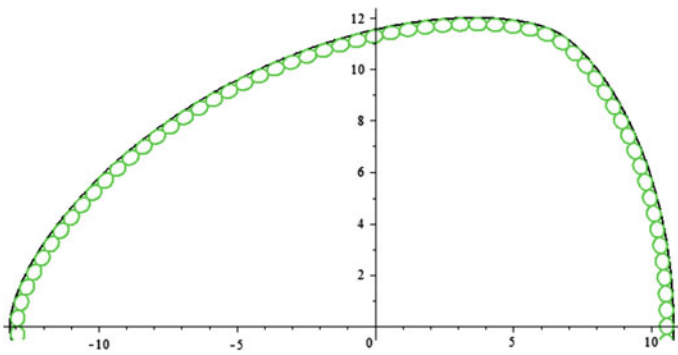


Fig. 2 Simulation of approximation of the RK-section shaft curved surface by cross sections of the single layer with constant parameters

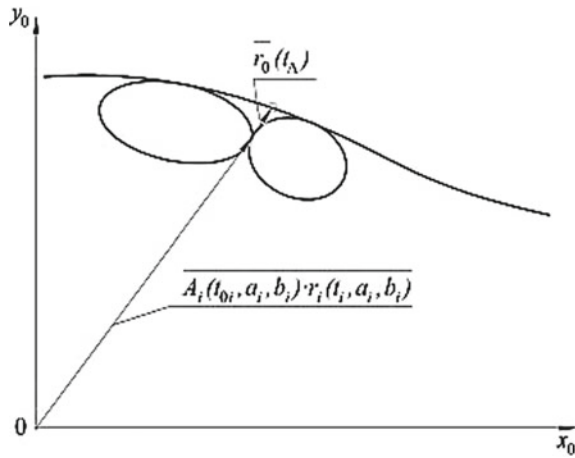


Fig. 3 Graphical representation of the function

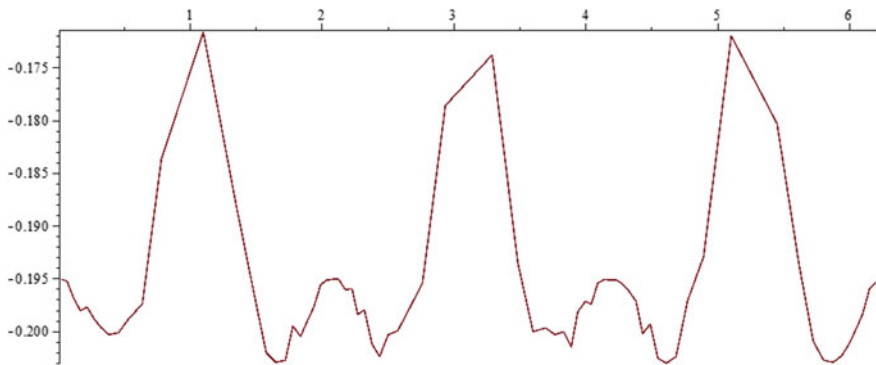


Fig. 4 Graph of changes in the error in the approximation of the RK-section shaft surface by the single layer with constant parameters

Analysis of the graph presented above shows that the error in the approximation of the RK-section shaft section by the single layer with constant dimensions varies in the range of 35 μm .

4 Solution to the Problem of Approximating the Part Section by Layers with Variable Section

To stabilize and narrow the range of the approximation error values, approximation by layers with variable sections is performed (with a variable dimension—the width a and height b of the cross section). The following conditions correspond to this



problem: $a_i \neq \text{const}$, $b_i \neq \text{const}$, $a_{i-1} \neq \text{const}$, $b_{i-1} \neq \text{const}$ and $\Delta_i \approx \Delta_{\text{req}}$. In this case, the problem of approximation can be solved in two stages [22]:

1. Providing orientation of the initial two layers, respectively, which is reduced to solving the system of equations:

$$\left\{ \begin{array}{l} \overline{i_0} \cdot \overline{A_{i-1}(t_{0(i-1)}, a_{i-1}, b_{i-1}) \cdot r_{i-1}(t_{i-1}, a_{i-1}, b_{i-1})} = \overline{i_0} \cdot \overline{A_i(t_{0i}, a_i, b_i) \cdot r_i(t_i, a_i, b_i)}; \\ \overline{j_0} \cdot \overline{A_{i-1}(t_{0(i-1)}, a_{i-1}, b_{i-1}) \cdot r_{i-1}(t_{i-1}, a_{i-1}, b_{i-1})} = \overline{j_0} \cdot \overline{A_i(t_{0i}, a_i, b_i) \cdot r_i(t_i, a_i, b_i)}; \\ \frac{\overline{A_{i-1}(t_{0(i-1)}) \cdot r_{i(i-1)}(t_{i-1}) \cdot A_i(t_{0i}) \cdot r_{ii}(t_i)}}{|\overline{A_{i-1}(t_{0(i-1)}) \cdot r_{i(i-1)}(t_{i-1})}| \cdot |\overline{A_i(t_{0i}) \cdot r_{ii}(t_i)}|} = -1; \\ \Delta_i(t_{0i}, t_{i-1}, t_i, a_{i-1}, b_{i-1}, a_i, b_i) = \Delta_{\text{req}}; \\ a_{i-1} = a_i; \\ b_{i-1} = b_i; \\ b_i = f(a_i), \end{array} \right. \quad (7)$$

where $\Delta_i(t_{0i}; t_{i-1}; t_i; a_{i-1}; b_{i-1}; a_i; b_i)$ is the function of calculating the error value of the section formed by the $i - 1$ and i layers; $f(a_i)$ is the function that determines the largest value of the parameter b_i at a given value of the parameter a_i of the deposited layer section.

2. Providing the orientation of the subsequent layers, respectively, at $i > 2$, when the geometric parameters of the previous layer $a_{i-1} = \text{const}$, $b_{i-1} = \text{const}$ and $a_i \neq \text{const}$, $b_i \neq \text{const}$, it is necessary to solve the system of equations:

$$\left\{ \begin{array}{l} \overline{i_0} \cdot \overline{A_{i-1}(t_{0(i-1)}, a_{i-1}, b_{i-1}) \cdot r_{i-1}(t_{i-1}, a_{i-1}, b_{i-1})} = \overline{i_0} \cdot \overline{A_i(t_{0i}, a_i, b_i) \cdot r_i(t_i, a_i, b_i)}; \\ \overline{j_0} \cdot \overline{A_{j-1}(t_{0(j-1)}, a_{j-1}, b_{j-1}) \cdot r_{j-1}(t_{j-1}, a_{j-1}, b_{j-1})} = \overline{j_0} \cdot \overline{A_j(t_{0j}, a_j, b_j) \cdot r_j(t_j, a_j, b_j)}; \\ \frac{\overline{A_{i-1}(t_{0(i-1)}) \cdot r_{i(i-1)}(t_{i-1}) \cdot A_i(t_{0i}) \cdot r_{ii}(t_i)}}{|\overline{A_{i-1}(t_{0(i-1)}) \cdot r_{i(i-1)}(t_{i-1})}| \cdot |\overline{A_i(t_{0i}) \cdot r_{ii}(t_i)}|} = -1; \\ \Delta_i(t_{0i}, t_{i-1}, t_i, a_{i-1}, b_{i-1}, a_i, b_i) = \Delta_{\text{req}}; \\ b_i = f(a_i). \end{array} \right. \quad (8)$$

In order to construct the $b = f(a)$ function, experimental studies on the influence of the build-up modes were carried out: T —the temperature of the material, h —the thickness of the material layer, V —the speed of the extruder movement by the value a —length, b —width of the single deposit layer.

According to the experiment schedule, samples of single layers were deposited using FDM printing. Variable parameters are single-layer thickness h , mm; extruder heating temperature t , °C; extruder speed V , mm/sec; microscopic sections were made, which were tested using an instrumental microscope MMI-2. The coordinates of the points on the curves that form the cross section of the single layer were

recorded; approximation of these points was performed by the ellipse equation—it was this cross-sectional form of the single layer that was observed in the samples; the parameters of width a and height b of the single layer were determined according to the difference of coordinates of the characteristic points on the surface of the single-layer cross section.

For a mathematical description of the deposited single-layer geometrical characteristics, the experimental results were processed, functions were obtained that reflect the influence of the elements of additive forming modes on the width a and height b of the single deposited layer:

$$a(h, T, v) = h(3.56h + 8.536) - t(0.043h - 0.02) + v(0.0002t - 0.04) - 3.87; \tag{9}$$

$$b(h, T, v) = h(4,267 - 5.595h) - t(0.0006h - 0.028) + v(0.000312t - 0.065) - 31.45. \tag{10}$$

Then, the desired function $b = f(a)$ will be considered as:

$$f(a) = \begin{cases} b(h, T, v) \rightarrow \max; \\ a(h, T, v) = a; \\ h_{\min} \leq h \leq h_{\max}; \\ T_{\min} \leq T \leq T_{\max}; \\ v_{\min} \leq v \leq v_{\max}. \end{cases} \tag{11}$$

As a result of the implementation of this model, the following results were obtained when the curved surface was approximated by portions of the single layer with variable dimensions (Fig. 5).

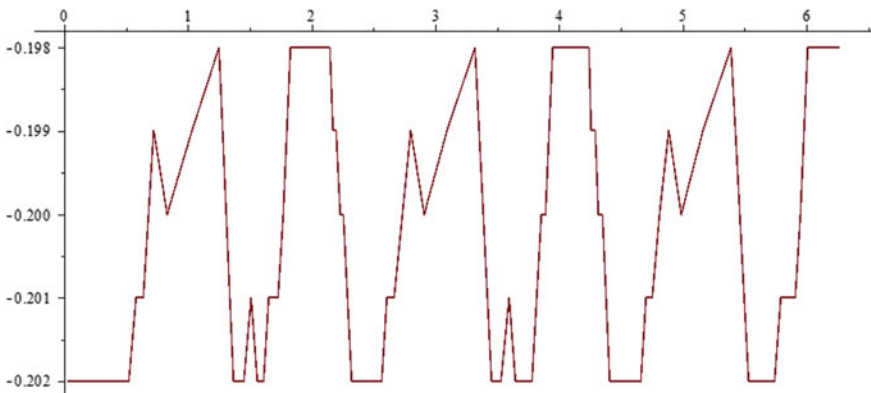


Fig. 5 Graph of changes in the error in the approximation of the RK-section shaft surface by the single layer with variable cross-sectional parameters

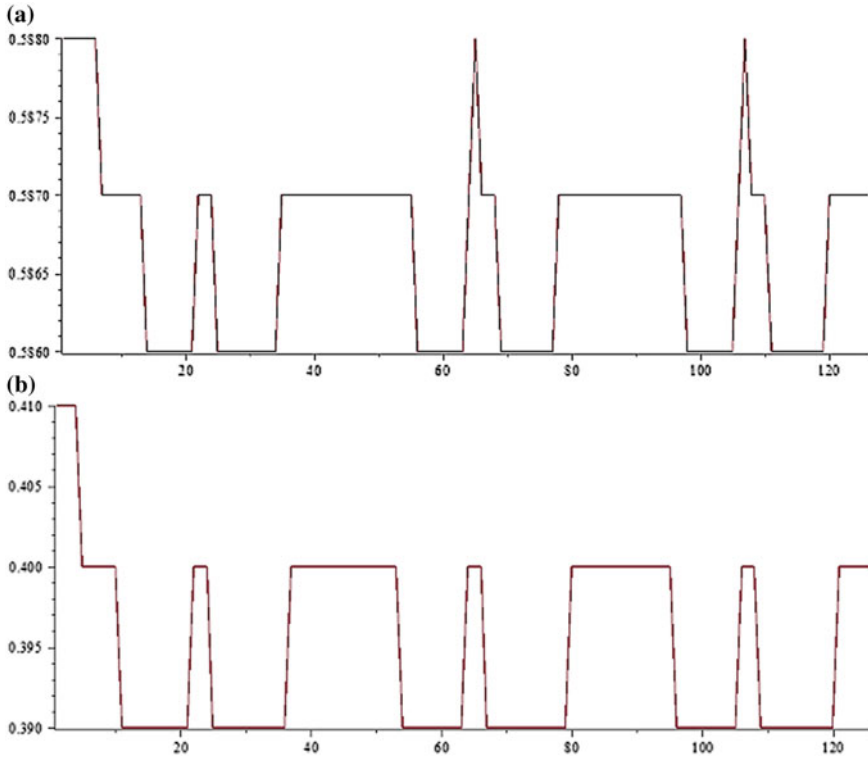


Fig. 6 Graph of changes in the parameters of the cross section of the single layer: *a*—width, *b*—height

The graph (see Fig. 5) shows that the section error varies within $4\ \mu\text{m}$.

The results of the variation of the width and height parameters of the cross section of the single layer are presented in Fig. 6.

5 Conclusion

The studies show that the implementation of the spatial orientation of the final element of the forming system in combination with the control over the cross-sectional parameters of the single layer in the case of additive forming of the surfaces makes it possible to significantly stabilize the approximation error in the sections of the RK-section shaft with variable curvature.

Acknowledgements The study was supported by the grant of the President of the Russian Federation for young scientists MK-6406.2018.8

References

1. Burns M (1993) Automated fabrication: improving productivity in manufacturing. PTR Prentice Hall, Englewood Cliffs, NJ, p 369
2. Saprykin AA (2006) Increasing the productivity of the process of selective laser sintering in the manufacture of prototypes. Thesis of candidate of technical Sciences. Tomsk Polytechnic University, Yurga, p 153
3. Pronikov A, Averyanov OI, Apollo Yu S (1994) Designing of metal-cutting machines and machine tools (Handbook-textbook vol 3), MSTU them NE Bauman: Mechanical Engineering, Moscow, p 444
4. Kuts VV, Razumov MS, Grechukhin AN, Bychkova NA (2016) Improving the quality of additive methods for forming the surfaces of odd-shaped parts with the application of parallel kinematics mechanisms. *Int J Appl Eng Res* 11:11832–11835
5. Chervyakov LM, Bychkova NA, Yeliseyeva NV et al (2016) Transfer of additive technologies: the industry of the Kursk region. ZAO University Book, Kursk, p 168
6. Grechukhin AN, Kuts VV, Razumov MS (2018) Control of spatial orientation of the nodes of the robot in the process of forming additive products. *Bulletin of Voronezh state technical University*, pp 122–129
7. Grechukhin AN, Kuts VV, Razumov MS (2018) Ways to reduce the error of additive methods of forming. *MATEC Web Conf.* <https://doi.org/10.1051/mateconf/201822601002>
8. Grechukhin AN, Kuts VV, Razumov MS (2018) Management of space orientation of the end effector of generation of geometry system five axis manufacturing machinery for additive generation of geometry. *MATEC Web Conf.* <https://doi.org/10.1051/mateconf/201822601004>
9. Hur J, Lee K (1998) The development of a CAD environment to determine the preferred build-up direction for layered manufacturing. *Manuf Technol* 14:247–254
10. Kim JY, Lee K, Park JC (1994) Determination of optimal part orientation in stereolithographic rapid prototyping technical report. Department of mechanical design and production engineering, Seoul National University, Seoul, pp 356–366
11. Lan PT, Chou S, Chent Y, Gemmill LD (1997) Determining fabrication orientations for rapid prototyping with stereolithography apparatus. *Comput Aided Des* 29:53–62
12. Massod SH, Rattanawong W, Iovenitti P (2003) A generic algorithm for part orientation system for complex parts in rapid prototyping. *J Mater Process Technol* 139:110–116
13. Masood SH, Rattanawong W (2002) A generic part orientation system based on volumetric error in rapid prototyping. *Int J Adv Manuf Technol* 19:209–216
14. Egorov IN (2010) Position-force control of robotic and mechatronic devices. Vladimir State University, Vladimir, p 243
15. Lashnev SI, Borisov AN, Emelyanov SG (1997) Geometric theory of surface formation by cutting tools Kursk State Tech. Un-t, Kursk, p 391
16. Emelyanov SG (2001) Development of the theory methods and means of surface formation by assembled metal-cutting tools on the basis of system modeling of their design process. Thesis of doctor of technical sciences, Moscow, p 407
17. Kuts VV (2012) Methodology of pre-project studies of specialized metal-cutting systems. Thesis of doctor of technical sciences, Kursk, p 366
18. Kuts VV, Ponomarev VV (2017) Construction of a model for the formation of long shafts with a RK profile of a prefabricated disk milling cutter. *Fundamental and applied problems of technology*, pp 110–115
19. Grechishnikov VA, Kuts VV, Razumov MS et al (2017) Determination of the error in the shape of a part shaping by a planetary mechanism using the methods of geometric cutting theory. *STIN* 4:24–26
20. Grechishnikov VA, Romanov VB, Pivkin PM (2017) Errors in shaping by a planetary mechanism. *Russ Eng Res* 37(9):824–826

21. Grechukhin AN, Kuts VV, Razumov MS (2018) Experimental determination of the cross-section parameters of a single layer in the additive forming products. News Tula State Univ Tech Sci 10:264–270
22. Grechukhin AN, Razumov MS, Kudelina DV et al (2018) Development of information-analytical system for technological requests monitoring, taking into account regional specifics. In: International conference on actual issues of mechanical engineering, vol 157, pp 198–202

Assessment of Natural Oscillation Frequencies of Rotor for Development of Hard-Bearing Balancing Machine



S. O. Gaponenko, A. E. Kondratiev and I. R. Tazeev

Abstract An imbalance appears during the manufacture, operation, and maintenance of power equipment. The rotor imbalance arises due to the unbalanced masses of the rotor which leads to the emergence of variable loads on the supports and bending of the rotor. The dynamic balancing of the rotor on the balancing machine is the way to avoid the negative effects of centrifugal forces. The balancing machines in resonant and soft-bearing modes are usually used on modern production. However, the soft-bearing method of balancing has a number of shortcomings, which can be solved by using the hard-bearing method. In particular, by using the hard-bearing method, it is possible to balance products with large initial imbalances and to increase the accuracy of balancing. The Autodesk Inventor CAD software was used for modeling of the balancing machine and the rotor. The modal analysis was conducted by using the block method of Lanczos on the basis of the ANSYS. The main assumption during the modal analysis process was that the form of free fluctuations is calculated in relative units and does not allow one to determine absolute shifts. The application of soft-bearing balancing method needs to be added in other ways, taking into account high requirements of the power equipment. A model of a hard-bearing balancing machine was designed for balancing rotors and rotating elements of power equipment. The natural oscillation frequencies of the 3D models of the balancing machine bed and the rotor of the gas turbine engine 16M were calculated to determine the informative frequency range that the rotor should be hard-bearing balanced.

Keywords Hard-bearing balancing machine · Vibration · Natural oscillation frequencies · Unbalance · Rotor · Frequency range · Autodesk Inventor CAD · ANSYS

S. O. Gaponenko (✉) · A. E. Kondratiev · I. R. Tazeev
Kazan State Power Engineering University (KSPEU), 51, Krasnoselskaya Str.,
Kazan 420066, Russia
e-mail: sogaponenko@yandex.ru

© Springer Nature Switzerland AG 2020
A. A. Radionov et al. (eds.), *Proceedings of the 5th International Conference on Industrial Engineering (ICIE 2019)*, Lecture Notes in Mechanical Engineering,
https://doi.org/10.1007/978-3-030-22041-9_29

249

1 Introduction

The modern heat power equipment contains many the rotating elements and knots. It is possible to carry rotors of turbines, electric motors, reels, and also impeller of fans and driving wheels of centrifugal pumps, fans, and compressors to them. In the course of their production and further use, there are unbalanced internal forces and an imbalance.

Balancing of rotors is a process which is intended for the unbalanced rotating parts of the machines. The reason of emergence of uncompensated centrifugal forces and the moments is the deviation of an axis of rotation of a rotor from the main central axis of inertia. In this case, the vibration of all equipment is possible during the rotation of rotor that has negative effect on service life of bearings, the base and the pedestals [1–8].

Vibration is a mechanical oscillation of a body or the whole mechanical system. Activators of vibration of a body are the forces applied to an object from the outside or arising into it. Vibration of a specific object is defined completely by the excitement force, its direction, and frequency. These forces depend on a condition of the machine, and knowledge of their characteristics and laws of interaction allow diagnosing defects. The reasons of defects can serve inaccuracies during installation, adjustment, and repair work. The timely detection of hidden defects allows avoiding equipment failures, which entail large material costs [2–10].

The most widespread sensors for measurement of vibrations are piezoelectric.

Piezoelectric sensors are intended for measurement of mechanical parameters (effort, pressure, accelerations, weight, angular speeds, the moments, deformations, etc.), development of thermal devices (thermal sensors, sensors of a consumption, vacuum, measuring instruments of electric parameters, sensors of thermal streams), and also for control of structures and concentration of gases, humidity, and micromasses. These devices in many cases surpass the sensors executed on other physical principles in the resolution and accuracy [3–17].

On the one hand, structure of control and measuring piezoelectric converters is influenced by necessary electro-acoustic parameters. On the other hand, the general geometric, mechanical, chemical, and temperature requirements for the system in which they are used have a great influence. In many cases, these requirements contradict each other that it is necessary to look for some compromised constructive solution [4, 11].

Balancing is performed on balancing machines. The balancing machine is the measuring device defining the place and degree of static or dynamic imbalance of the rotating details of machines and the equipment [5].

Questions of reliability of operation of the heat power equipment of thermal and nuclear power plants became especially relevant now, after implementation of reforming of power industry, access of the generation companies into the wholesale market of the electric power and power. The analysis and management of reliability of such power objects became one of the most important at planning and maintenance [6, 13].

One of priority factors to ensure durable and reliable work and long service life of the equipment is application of effective non-destructive testing methods which

have to be a component of technical diagnostics of various equipment. In order to diagnose the mechanical state of the equipment, it is necessary to know how a particular unit will behave, and also indicate in the structure of the product, in which place(s) the specific damage is determined. First of all, it is necessary to expect failure of unit with high-power-intensive details [16].

2 Research Methods

Development of the balancing machine for balancing of rotors.

3D model of the balancing machine was designed to simplify the development of the balancing equipment and to carry out further tests. The Autodesk Inventor software product was chosen from a large number of the existing computer-aided engineering systems (CAD). The main advantages of this program are a convenient interface and compatibility of 2D drawings with 3D design.

There are two main types of balancing machines, hard-bearing and soft-bearing. The horizontal hard-bearing balancing machine is considered in this work.

Advantages of balancing machines in hard-bearing mode:

- structural rigidity which excludes a possibility of damage of the machine during maintenance;
- only supporting rollers and belts, which are easily replaceable, are exposed of wear;
- a possibility of balancing of products with huge initial imbalances [7].

3D model of the hard-bearing balancing machine is illustrated in Fig. 1.

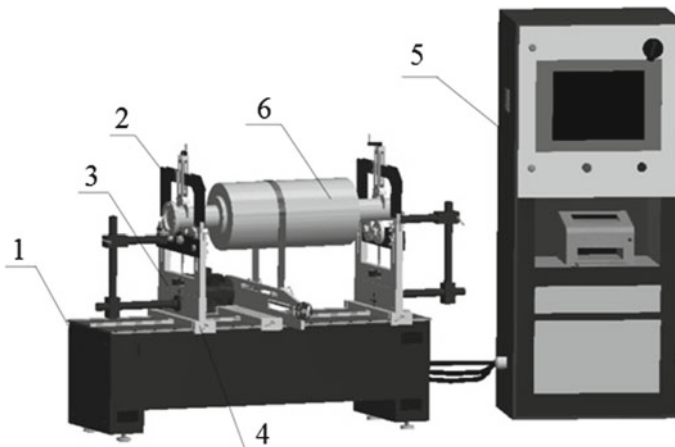


Fig. 1 3D model of balancing machine: 1—bed; 2—pedestal; 3—basis pedestal; 4—pedestal plate; 5—control unit, 6—rotor

The hard-bearing balancing machine contains bed 1 and two pedestals 2 which are regulated on height. The pedestal includes the basis pedestal 3 and pedestal plate 4. Pedestals can move relatively to each other by the rail which is established on the bed. Each pedestal is equipped with the piezoelectric sensor of force.

The maintenance of the machine is controlled by the control unit 5 which is connected with force sensors from each pedestal and the driving electric motor. The electric motor sets in motion a balancing rotor 6. The imbalance leads to deformation of the sensitive elements located on the basis of pedestals. Piezoelectric sensors of force transform these vibrations to an electric signal [18, 19].

The gas turbine engine GTE-16M is considered as the object of balancing of the rotor. The rotor of a turbo compressor represents a shaft with is a disk of the turbine on the one end (Fig. 2a), on the other end—an impeller of the compressor (Fig. 2b). The rotor rotates on the rolling bearings which are installed in the compressor case [12].

Further work consisted of research of the considered rotor by application of the modal analysis in the program ANSYS [18]. The modal analysis is the basis of any dynamic analysis, allowing estimating dynamic behavior of an object. It serves for determination of natural frequencies and forms of natural fluctuations [15].

Calculation of natural frequencies of a rotor of GTE-16M was carried out in the following sequence:

- The rotor geometry is imported to the ANSYS WB environment from a CAD of Autodesk Inventor 2017 (Fig. 3a);
- Properties of materials are set:
 - density: 7850 kg/m^3 ;
 - Young's modulus: $2e+11 \text{ N/m}^2$;
 - Poisson's ratio: 0.3;
- Contact conditions are established: the fixed fastening on sides of model along an axis of rotation of a rotor and cylindrical fastening in places of a support of a

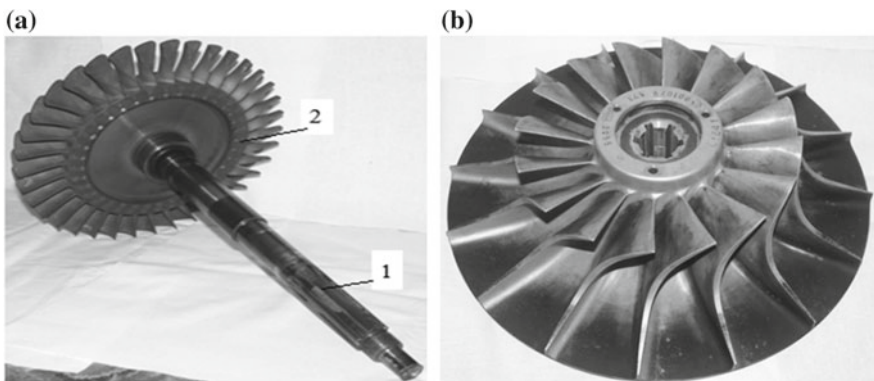


Fig. 2 a Rotor shaft of a turbo compressor with disk 1—shaft; 2—disk with blades; b compressor impeller

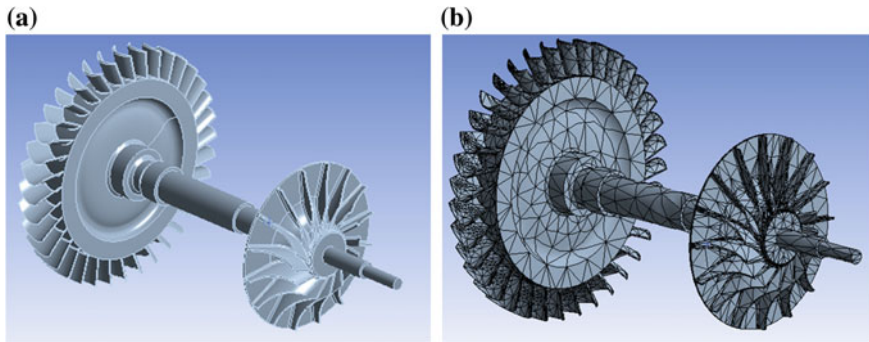


Fig. 3 a Imported model and b finite elements mesh of a model of GTE-16M rotor

shaft of a rotor. Due to the modal analysis is linear, inclusion of contacts in this calculation can be neglected.

- The mesh of finite elements is created (Fig. 3b). Selecting:
 - mesh type: mesh on solid body;
 - mesh quality: high;
 - nodes: 44015;
 - elements: 23219.

As a result of the conducted research, 24 first forms of fluctuations of the counted rotor are defined. In the analysis of results of modal calculation, it is necessary to consider that the form of free fluctuations is calculated in relative units and does not allow determining absolute shifts.

Table 1 shows the results of the calculation of the natural frequencies of the rotor of the GTE-16M; the first 24 forms of fluctuations of the studied rotor were determined.

Table 1 Forms of fluctuations of the studied rotor

Fluctuation form number	Frequency, Hz	Fluctuation form number	Frequency, Hz	Fluctuation form number	Frequency, Hz
1	269,67	9	159,47	17	319,08
2	394,52	10	1597	18	322,72
3	395,1	11	194,74	19	355,09
4	428,13	12	246,35	20	356,46
5	703,52	13	247,54	21	402,23
6	704,88	14	293,16	22	414,75
7	130,96	15	2936	23	426,32
8	131,31	16	308,65	24	426,78

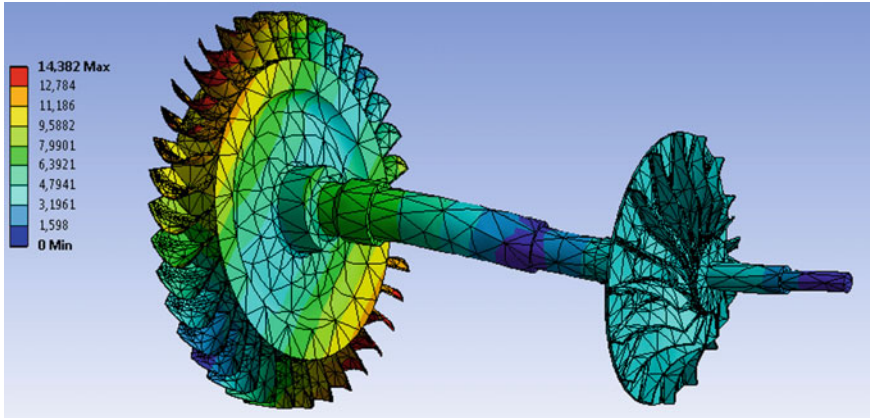


Fig. 4 Results of the modal analysis

The form of fluctuation of the first mode of a balancing rotor with a frequency of 269,67 Hz is shown on Fig. 4.

It is necessary to determine natural frequencies of the bed of the balancing machine to subtract these frequencies from frequency mode of the researched rotor [9, 14].

2.1 Calculation of Natural Frequencies of the Base of the Balancing Machine

For calculation of natural frequencies and mode of natural fluctuations of the bed of the machine, the bed model is imported to the ANSYS WB (Fig. 5a).

The bed is manufactured of polymeric granite, and this material has the following properties:

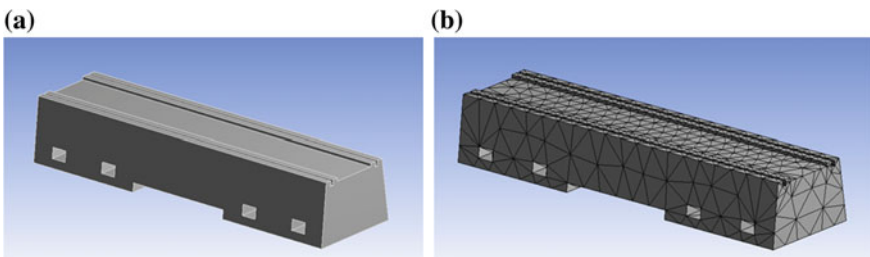


Fig. 5 **a** Geometrical model of bed in ANSYS WB and **b** finite elements mesh on a bed model

Table 2 Forms of fluctuations of the researched bed of the balancing machine

Fluctuation form number	Frequency, Hz	Fluctuation form number	Frequency, Hz	Fluctuation form number	Frequency, Hz
1	101,55	9	228,81	17	314,45
2	108,34	10	2290	18	322,98
3	133,97	11	240,42	19	323,11
4	141,96	12	262,07	20	3311
5	160,36	13	267,83	21	338,99
6	176,92	14	300,38	22	343,25
7	192,78	15	303,06	23	351,58
8	201,95	16	3112	24	356,78

- density: 4680 kg/m³;
- Young’s modulus: 5.5e+10 N/m²;
- Poisson’s ratio: 0.25.

Figure 5b shows the finite element mesh, during the development of which in the ANSYS WB program the following parameters were selected:

- mesh type: mesh on solid body;
- mesh quality: high;
- nodes: 9817;
- elements: 5471.

As a result of the conducted research, 24 first forms of fluctuations of the counted bed are defined.

Table 2 shows the first 24 forms of fluctuations of the researched bed of the balancing machine.

The form of fluctuation of the first mode of the bed of the machine with a frequency of 101,55 Hz is illustrated on Fig. 6.

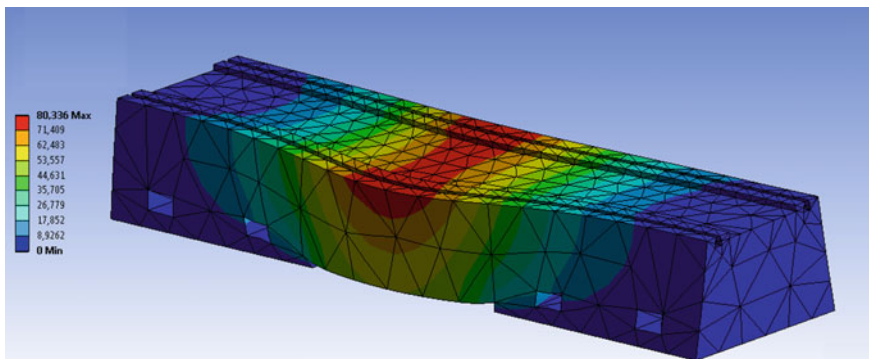


Fig. 6 Results of the modal analysis

3 Results of a Research

As a result of the calculation, the range of own frequencies of fluctuations of the bed of the balancing machine is determined.

It is visible that frequencies of the first 6 modes of own fluctuations of a rotor lie below own frequencies of fluctuations of the bed of the machine while comparing Tables 1 and 2. This is informative frequency range which is necessary to carry out hard-bearing balancing of a rotor.

4 Discussion and Conclusions

The informative range of frequencies which allows carrying out balancing of rotors in the hard-bearing maintenance mode was received, as a result of the carried-out modal analyses of a rotor and the bed of the balancing machine. The hard-bearing balancing machine is more effective because balancing without calibration launching is carried out on this machine, and high precision of balancing is reaching and possibility of balancing of any types of rotors appropriate to overall dimensions of the machine.

References

1. Tazeyev IR (2017) Features of the construction of 3D-model of the balancing equipment. In: Materials of the XII international youth scientific conference on natural sciences and technical subjects. Volga state university of technology, Part 2, Yoshkar-Ola, p 192
2. Gaponenko SO, Kondratiev AE (2017) Device for calibration of piezoelectric sensors. *Procedia Eng* 206:146–150
3. Gaponenko SO, Kondratiev AE, Kostyleva EE, Zagretdinov AR (2016) Device for calibration of piezoelectric sensors. In: Proceedings of the higher educational institutions. Energy Sect Probl 7–8:79–86
4. Gaponenko SO (2016) Installation for calibration of the device of low-frequency vibroacoustic control. In: International scientific and technical conference innovative machine-building technologies, the equipment and materials—2016 (ISTC “IMTEV-2016”), pp 288–292
5. Pashkov EN (2013) Definition of time of automatic balancing of a rotor at the established speed. *Min InfAl Anal Bull (Sci Tech J)* 4(1):476–482
6. Diouf P, Herbert W (2014) Understanding rotor balance for electric motors. In: Pulp and paper industry technical conference, conference record of 2014 annual. IEEE, pp 7–17
7. Qin R et al (2017) Study on the frequency compensation of the dynamic unbalance signal extraction for general hard bearing dynamic balancing machine. *Appl Mech Mater* 870:173–178 (Trans Tech Publications)
8. Ziyakaev GR, Pashkov EN, Urnish VV (2013) Influence of friction on the accuracy of automatic balancing of rotors. In *World Sci Discov* 10.1(46):104–117
9. Doroshev Yu S, Nestrugin SV (2016) Practical balancing of rotors of electrical machines in own support. *Electr Saf* 4:3–8

10. Mamontov AV (2002) Methods of vibration diagnostics of unbalanced rotors for decrease in vibration and noise of the production equipment. *Radio Electron Inform Sci Tech J* 3:68–70
11. Sharapov V, Sotula J (2012) Piezoelectric transducers. New design technologies. *J Electron Sci Technol Bus* 5:096–102
12. Rezinskikh VF, Lukyanenko VA, Sargsyan VA (2013) Technique of nondestructive control of rotors of average and low pressure of turbines of thermal power plant without removal of mounted disks at repair of the equipment. *Power Plants* 8:44–50
13. Smirnov AN (2014) Analysis of damageability of rotors of steam turbines (review). *Vestn Kuzbass State Tech Univ* 2:102
14. Homenko AP, Yeliseyev SV (2012) Dynamic balancing of the rotating shaft as a form of dynamic clearing of fluctuations of mechanical systems. *Mod Technol Syst Anal Model* 3:35
15. Kochkin SV, Malev BA (2007) Method of measurement of an imbalance of rigid rotors in the mode of the spherical circulating movement. *Univ Proc Volga RegN Tech Sci* 3:105–115
16. Kravchenko VM (2009) Technical diagnosing of the mechanical equipment: the textbook for students of higher education institutions. OOO YUgo-Vostok, Ltd., Donetsk, p 458
17. Sidorov VA, Sotnikov AL, Sushko AE, Cyba SA (2009) Technique of assessment of economic efficiency of balancing of rotors under production conditions. *Vibration of mashines: measurement, decrease, protection. Univ Proc Volga RegN Tech Sci*, 38–43
18. Xu ZH, Cui ZQ, Zhang T (2012) Modal analysis of 6300 diesel engine crankshaft based on ANSYS. *MeikuangJixie (Coal Mine Mach)* 33(2):102–103
19. Smirnov VA (2015) Vibration measurement bases. http://www.vibration.ru/osn_vibracii.shtml/. Accessed 20 Jan 2015

Equipment with Disc Cutters for Destruction and Removal of Strength Snow and Ice Formations on Road Surface



A. V. Lysyannikov, Yu. N. Bezborodov and V. G. Shram

Abstract The chapter presents an analysis of the current state and development of snow removal equipment structures equipped with disc cutters for the destruction of strength snow–ice formations on the road surface. For the maintenance of roads in the winter, the most common snow removal equipment is motor grader. The blade of the motor grader provides effective removal from the road surface only the new-fallen loose snow and slightly compacted snow (up to 0.6 m thick). To remove strength and ice formations on the road surface, a combination of several units of specialized snow removal equipment (mechanical, chemical, friction method) is used, which increases economic costs. The urgency is the use of snow removal equipment in the construction of disc cutters. Disc cutters have shown their effectiveness in the working bodies of rotary excavators, rippers, drilling, disc-cutting and earth-cutting machines for the destruction of frozen soils. The construction of snow removal equipment uses cutting disc tools of various shapes and sizes in order to reduce the energy consumption of the process of destruction of snow and ice coating. The developed construction of the of snow removal equipment with disc cutters and blade is presented. The proposed technical solution will improve the energy efficiency and productivity of the snow removal process without increasing the power of the base machine.

Keywords Snow and ice formations · Disc cutter · Design snow removal equipment · Energy efficiency · Installation angle · Road surface · Destruction

1 Introduction

The winter period of the year (from 20 in the southern regions and up to 260 days in the northern regions of the Russian Federation) is the most difficult for road operation and traffic management. Road surface conditions and traffic conditions in

A. V. Lysyannikov (✉) · Yu. N. Bezborodov · V. G. Shram
Siberian Federal University, 79, Svobodny Pros., Krasnoyarsk 660041, Russia
e-mail: alysyannikov@sfu-kras.ru

winter are influenced by negative air temperatures, wind, snowfall, Blizzard, ice and limited meteorological visibility, as well as a combination of these factors. Winter maintenance of road surfaces should ensure uninterrupted and safe movement of vehicles with high speeds and loads that meet the established requirements in the rules of maintenance of roads [1–3].

The thickness of snow and ice formations on the road surface should not exceed 100–120 mm under the conditions of evenness. It is important to note that although the evenness of the snow and ice formations varies slightly with a small thickness of the layer, snow on roads of categories I–III should still be removed from the coating to ensure the required coupling qualities. On roads of IV–V categories, the thickness of snow–ice formations should not be more than 60 mm provided constant profiling and full clearing of snow on sites of rises and descents, and only in exceptional cases on separate sites can be allowed to 200 mm [1–4].

For the maintenance of roads in the winter, the most common snow removal equipment is grader. The blade of the grader provides effective removal of only fresh and slightly compacted snow (up to 0.6 m thick). For removal of strength snow–ice formations, the blade of the grader is ineffective, the main flaw at destruction of snow–ice formations by means of creation in it of deformations of shift at the movement of the grader, are: the instability of the regime cleaning of surfaces of road, at small thicknesses snow and ice formations on the road surface; inefficient loading scheme massif snow and ice formations on the road surface deformation, i.e. shear stresses arising from the movement of the knife, as when driving exposure is exposed simultaneously, a large area of the snow and ice formations located in front of the blade grader, the impact is not localized, spread over a large area and reduces the intensity of loading snow and ice formations, his cleavage [2, 3]. The disadvantage of the device, which is a grader blade tip, is the inability to track the profile of the surface of the road surface (recesses and protrusions), i.e. with this solution, damage to the coatings and associated structures (manholes, curbs, curbs, etc.) are inevitable. It is more effective to remove solid snow and ice formations from the road surface which is the use of a combination of several units of specialized snow removal equipment (mechanical, chemical, friction method), which increases financial costs.

Actual is the development of designs of snow removal equipment providing effective destruction and removal of snow and ice formations, reducing the probability of damage to road surfaces and related structures.

2 The Main Part

The patent information analysis showed that there is the use of disc cutters in the designs of snow removal equipment, which have shown their effectiveness in the working bodies of rotary excavators, rippers, drilling, disc-cutting and earthmoving machine for the destruction of frozen soils in order to reduce the energy intensity of the process of destruction of snow and ice formations. Figure 1 shows a device for removing snow and ice formations from the road surface [5].

The device is moved by the vehicle over the surface of the snow and ice formations. Due to the resulting friction forces at the points of contact of the disc cutters 3 and the array development, they begin to rotate passively, thereby reducing the fracture force. Due to the own weight of the device, the orientation of the axes 3 with respect to each other at an angle α , in snow and ice formations arise normal N and tangential T forces (on mechanical impact occurs on the snow and ice formations), leading to the destruction. To increase the intensity of destruction, the impact is carried out by periodically creating normal and tangential forces in the run-up with frequencies equal to the natural frequencies of the device's vertical and horizontal vibrations, respectively. The angle α and the own frequencies at which the destruction snow and ice formations will be most effective are determined experimentally by visual observation of the process of removing snow and ice formations with road surface [5]. A similar scheme for the installation of disc cutters and their axes and the process of impact is used in the structures [6, 7]. The mouldboard blade 7 moves fragment formations outside of the roadway in the area.

The technical result is to increase the efficiency of removal from the road surface snow and ice formation by installing the disc axes at different angles to the direction of movement. In the construction of the machine for splitting ice from pavements [8], one-sided tapered disc cutters are used, installed in a row, and are wedges. In order to combine the functions of several snowploughs, a scraper conveyor was installed and a blade to move the chipped fragments to the side. The main disadvantage is the complexity, large dimensions of the structure and the number of mechanisms.

Figure 2 shows the working body of the ice-cutting machine [9] which is mounted on the blade circle. The design uses discs with double-sided sharpening, located wedge. The destruction of the snow and ice formations by the central disc is carried out according to a blocked scheme, the others according to a semi-blocked scheme.

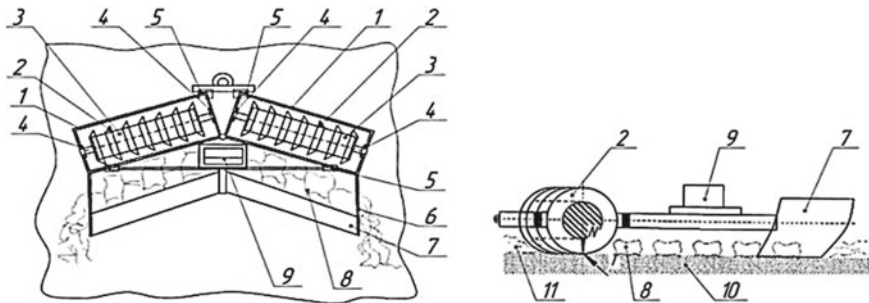


Fig. 1 Device for removal from the road surface of the snow and ice formations: 1—frame; 2—disc cutters; 3—axis; 4—bearings; 5—devices by which the frame can be installed at an angle α to each other in a horizontal plane; 6—stops; 7—mouldboard blade; 8—fragments snow and ice formations; 9—vibrators; 10—road surface; and 11—snow and ice formations

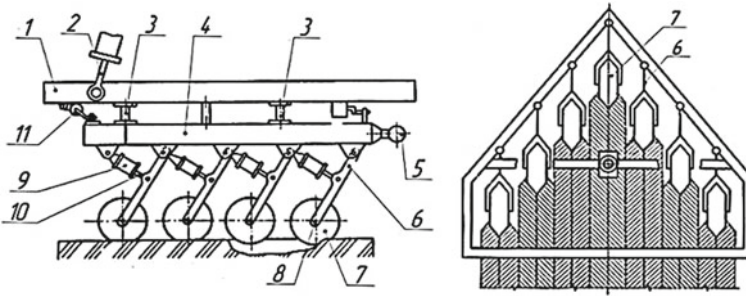


Fig. 2 Working body of the ice-cutting machine: 1, 4—frame; 2, 11—hydraulic cylinder; 3, 5—ball joint; 6 levers; 7—disc cutters; 8—axis; 9—telescopic hydraulic cylinder; and 10—stocks

The working body is moved by the motor grader in the direction of motion, with one front or two subsequent disc cutters 7 at each moment of time striking (due to the operation of the hydraulic cleaver), and the rest are moved along the run-up surface without rotation on the axis 8. If a disc cutter 7, a snow and ice formations, is cut through the entire thickness and it begins to move along the surface of the road surface, the torque increases and the disc starts to rotate around the axis 8. When rolling a disc 7 on any obstacle, it rises overcoming the pressure created by the hydro-accumulator. The main disadvantage is that in the design, there are driving discs with double-sided sharpening, constructively designed to be located only at right angles to the destructible array, what provides frontal cutting—more energy—intensive than tangential. Cutting discs move along the surface without turning on the axis, which requires a considerable amount of energy, compared to cutting with passive-rotating discs, and contributes to the uneven accelerated wear of the cutting edges.

Figure 3 shows the design of the ice breaker with disc cutters which are affected by vibration [10]. Disc cutters 2 are installed with intervals not exceeding $1/3$ of their diameter on horizontal axes 1 ($110\text{--}160^\circ$ angled to each other) which destroy the main part of the snow ice formations on the road surface, and the remaining is cut off cutting prongs 8 mounted on the blade 7 (located at an angle to each other, $10\text{--}30^\circ$ less than the angle between the axes 1) and shifted to the side. Changing the angle between the axes 1 allows you to change the force impact on the developed array. Vibrators 5 allow to increase the efficiency of destruction of snow ice formations due to the intensification of the process [10].

The disadvantage of the working body is: the inability to adjust the depth of cut, which may lead to the contact of the pointed edges of the disc cutters with the road surface and their partial destruction, the step of installing two extreme discs in the centre of the working body is twice the pitch of the other discs, resulting in the middle part the array being developed will not be destroyed.

The main mechanism of the ice breakers are sets of rotating serrated cutting discs mounted on horizontal axes [11]. Disks cut and tear snow-ice formations from the road surface. Sets of rotating serrated cutting discs and auger are driven by

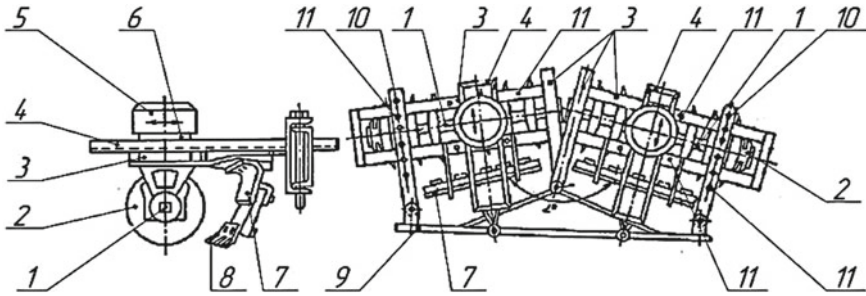


Fig. 3 Ice breakers machine with disc cutters: 1—horizontal axis; 2—disc cutters; 3—bracket; 4—frame; 5—vibrator; 6—weights; 7—blade; 8—cutting prongs; 9—additional frames; 10—holes for changing the angle between the axes; and 11—fixing holes

mechanical transmission from a motor grader motor. The design provides a spring device that allows sets of cutting discs to roll through obstacles without damage. With a auger and a blade, the destroyed snow-ice formations remove away from the road.

The main disadvantages are as follows: when a motor grader is moving, a moment occurs when the disc cutters are installed across the direction of movement, resulting in increased energy consumption, the likelihood of damage to the equipment, as well as design complexity, a large number of discs and large dimensions [11].

Figure 4 shows the device for the destruction of the snow and ice formations runway on the road surface [12]. The device is towed by the base machine. The design is used disc cutters with double-sided sharpening. The cutters are installed in three separate sections, rotate passively due to the friction that occurs between the cutters and the array under development. The sections are spring-loaded, which ensures that the pavement profile is copied. Disc cutters are equipped with carbide

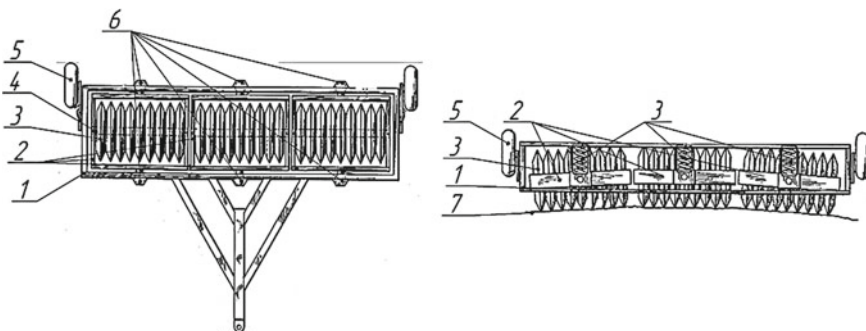


Fig. 4 Device for the destruction of the snow and ice formations on the road surface: 1—frame; 2—separate sections of discs; 3—cutting discs; 4—axis; 5—castor; 6—springs; and 7—road surface

metal inserts. To improve the efficiency of destruction of the developed array, the device can be additionally loaded with a load [12].

The main disadvantage is that the design uses cutting discs with double-sided sharpening. Since there is a sufficiently large distance between sections than between disc cutters, there will be an unbroken array.

Device for the destruction of the snow and ice formations on the road surface [13] is mounted on the base unit. The hydraulic cylinders lower the device into the working position, the base unit is moved forward and the disc cutters under the pressure of the hydraulic cylinders are embedded in the snow–ice formations, resulting in chipping. The discs are mounted on two axes in a staggered arrangement, in order to increase the efficiency of cleaving the array under development [13]. The main disadvantages are: a small width of the treated surface, half of the total number of disc incisors destroys the snow–ice formations in a blocked scheme, which increases energy intensity.

A device for removing snow–ice formations from pavements is shown in Fig. 5 [14].

The device is mounted on the base unit and moves in the direction of movement of the machine and rotates around an axis due to a forced drive. The cutting tip of chipping disc incisors, 3, 4, 5, 6 and 7, cantilever located at different levels along with the height of the rotor 2 and with different distances from its centre, rotate the rotor and move the machine to cut into the snow and ice formations along the cutting lines and destroy it. The cutting edge of each subsequent shearing tapered disc cutter is offset along the height of the rotor 2 with a decrease in the diameter of the cutting edge rolling along the lines of depth of cut. Moreover, these tapered discs form cutting lines both below and above the upper surface of the rotor disc, parallel to the surface to be machined, providing a semi-blocked cutting. For all chipping tapered disc, the cutting angle is reduced to the recommended rational values from 30° to 35° , and the larger base of the shearing tapered disc is located at a rational rear angle to the cutting lines. Due to the fact that chipping tapered disc

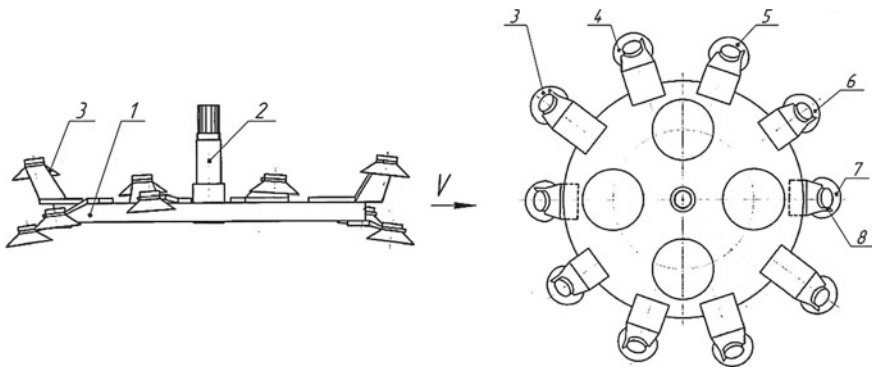


Fig. 5 Device for removing snow–ice formations from pavements: 1—disc; 2—rotor; 3–7—shearing tapered disc cutters; and 8—teeth

with cutting edges are arranged along cutting lines, have the ability to rotate around their axis, providing a semi-blocked cutting pattern with rational cutting angles, depth and thickness of chips, much less energy is required to destroy and remove snow-ice formations from the face [14]. The disadvantage is the need for an additional drive device.

In a device for cleaning pavements from ice and compacted snow [15, 16], disc cutters are mounted at an angle to the treated surface on a frame rotating in its plane. Such arrangement of the discs causes the introduction of the front disc cutter in the snow-ice formations with a force directed down and to the side, the opposite of the movement of the device. The rear disk cuts the broken edge of the ice, partially using the force directed in the direction opposite to the movement and arising from the movement of the front disk. As a result, energy consumption for ice chipping is reduced. Reducing energy intensity is carried out by redistributing the load between the front and rear discs, due to their installation [15, 16].

In the construction of ice-cutting equipment [17], there is a parallelogram suspension on the levers of which disc cutters are installed. Under the action of centrifugal and reactive forces, the incisors interact alternately with the medium. The design provides for adjustment of the pressing force of the incisors [17]. The disadvantage of the structures [16, 17] is the high-energy intensity of the process of destruction of the snow-ice formations since the cutting elements work according to the blocked scheme.

Figure 6 shows the design of the working body for removing the snow-ice formations from the road surface [18].

The working device is installed on the surface being cleaned with a capture angle β of no more than 43° between the longitudinal axis of the working body and the intended direction of its movement V . The working body is moved by the base unit in the V direction, and the cutting discs 3, with the angle of inclination α of the lower base of the disc to the surface of the snow and ice formations, are not more than 10° , crashing into the snow and ice formations, destroy it. The products of destruction move to the elastic mouldboard blade 5 and with its help move to the side [18].

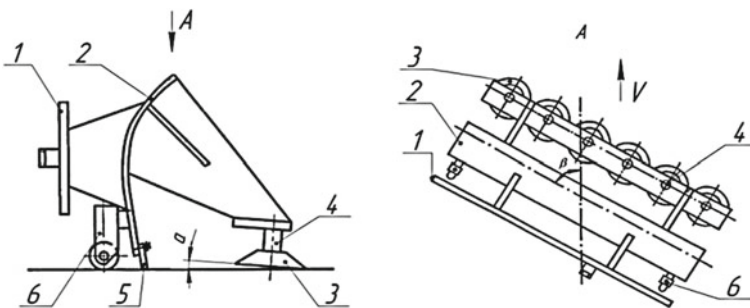


Fig. 6 Working body to remove the snow-ice formations from the road surface: 1—base plate; 2—blade; 3—cutting disc; 4—axis; 5—elastic mouldboard blade; and 6—castor

In the design of the working body to remove the snow and ice formations from the surface of roads and airfields [19], there are two blades installed at an angle of 60–70° to each other in order to overlap the working areas of adjacent discs and ensure the interaction of discs with an array according to a semi-blocked scheme. Disc cutters are installed along the mouldboard blade with the possibility of passive rotation on axes. When moving the base unit, the cutting disc cutters, cutting at an acute cutting angle (not more than 10°) into the snow and ice formations, destroy it, the products of destruction move to the knives, which give them directional movement to the longitudinal axis of movement of the base machine and shift it to the bucket conveyor and loaded into the vehicle body. The technical solution allows simultaneous chipping and loading of the snow and ice formations into the vehicle [19].

Figure 7 shows mounted disc ice-cutting equipment providing destruction of snow–ice formations up to 40 mm thick, working speed 2–10 km/h [20, 21]. The working tool of the equipment is a freely rotating tapered disc (diameters of 457 and 559 mm) with a pointed cutting edge.

Patent information search showed disc cutters which are installed vertically and horizontal to the destroyed array, and in some designs, they rotate around an axis due to a forced drive, but they are all installed on the axes and passively rotate due to the generated force. Disc cutters with one-sided sharpening are more energy efficient. The disadvantage of the vertical installation of discs is a small contact area when they interact with snow and ice formations is cut through narrow paths, as a result of which the quality of cleaning is not ensured. The most effective is the horizontal installation of disc cutters. The object of the invention is to simplify the design and to increase the efficiency of the destruction of snow and ice formations.

Figure 8 shows the design of the developed equipment for splitting ice consisting of a blade and 5 passively rotating discs cutters with cuts along the perimeter, for more rotation when meeting with dense snow–ice formations, resulting in reduced energy intensity.

The working body moves with the base unit in the direction of motion, the cutting discs 1 freely rotate on the axes and they can fit snugly to the road surface, as a result of which they are honed. The maximum angle of inclination of the lower base of the disc to the surface of the snow and ice formations (α) is not more than 10°.

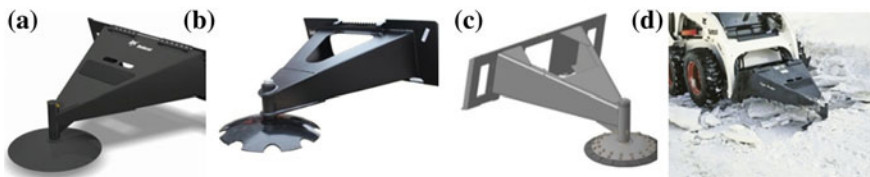


Fig. 7 Mounted disc ice-cutting equipment: **a** Bobcat scraper (disc working member); **b** Bobcat scraper (disc tool with cut-outs); **c** the scraper (disc working body with replaceable cutters); and **d** equipment mounted on Bobcat

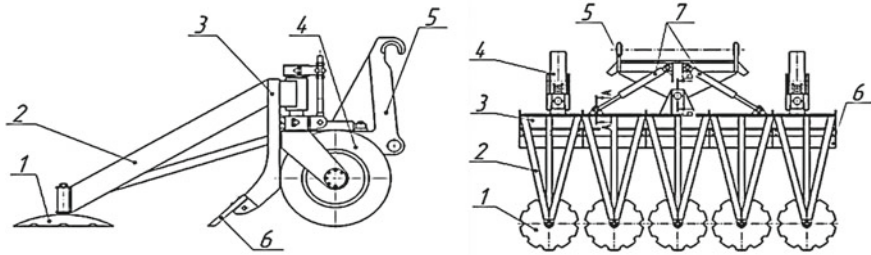


Fig. 8 Ice-cutting working body: 1—disc cutter with notches; 2—frame; 3—blade; 4—castor; 5—mount; and 6—mouldboard blade

A change in the specified angle α of installation of the cutting disc 1 by an amount greater than 10° will entail an increase in the cutting angle determined by the sum of the angle α of installation of the disc and the angle of sharpening its working edge. This will lead to a significant increase in the level of effort and energy intensity of the cutting process as a whole, which will increase as the cutting disc penetrates into the massif under development. Since at the same time, the side surfaces of the discs will begin to interact with the destructible medium over a large area, providing a shift of the products of destruction. Due to the installation of hydraulic cylinders 7, it is possible to change the angle of installation of the working body, and therefore, the scheme of interaction with the destroyed array. The optimal installation is the installation of the working body so that the working areas of the adjacent cutting discs 1 mutually overlap at a working width that provides sufficiently high performance, which contributes to improving the quality of destruction of the array under development and reducing energy intensity. In case of failure to ensure mutual overlapping of the working areas of the cutting discs, and in the intervals between the discs there will be areas of the non-destroyed array. In addition, each cutting disc will interact with a solid, closed from all sides array (blocked cutting scheme), which will significantly increase the cutting force and process power consumption compared to cutting when working areas overlap, when each cutting disc (except the frontmost one) interacts with an array partially destroyed by the adjacent previous disc (semi-blocked cutting scheme).

3 Conclusion

The proposed solution will simplify the design of the snow removal equipment; combine the functions of two units of snow removal equipment (auto grader, cleaver); reduce the energy intensity of the cleaning process; and increase the efficiency of destruction of compacted snow-ice formations without increasing the power of the base machine, due to the use of disc cutters with cut-outs around the perimeter.

References

1. Molev UI (2007) Ensuring road safety of road transport in winter. Dissertation, Vladimir
2. Zhelukevich RB (2013) Theory and practice of creating working bodies of construction and road machines with disc cutters. Dissertation, Siberian State Automobile and Highway University
3. Lysyannikov AV (2013) Methods and means of monitoring the load parameters of the working bodies of the dump type of snowplows. Dissertation, Tomsk Polytechnic University
4. Vasiliev AP (2004) Repair and maintenance of roads. T. 2: Road builder reference encyclopedia, Moscow, p 1279
5. Kozin VM (2010) The way removal from the surface of airfield and solid pavement of ice and snow formation. RU Patent 2,390,602, 27 May 2010
6. Kozin VM, Litovchenko AK, Makeeva VS (2009) A device for removing ice and snow from the surface of solid pavements. RU Patent 2,416,690, 20 April 2009
7. Schneider AI, Karpekin PA, Stankevich VA (1970) Working body to remove the snow-ice runway from the surface of roads, airfields and similar structures. SU Patent 2,840,05, 10 Nov 1970
8. Sobkovich FI (1939) Ice splitting machine from bridges. SU Patent 5,560,9, 01 Jan 1939
9. Sivkova ON, Belokrylov VG, Sivkova EV et al (1986) Working body of an ice cutting machine. SU Patent 1,404,572, 17 July 1986
10. Shabanov VP, Konyukhov LV, Ochakov NV (1986) The working body of the snowblower. SU Patent 1,219,707, 23 March 1986
11. Upine VM (1960) Attachment equipment for cleaning the pavement of ice and compacted snow. SU Patent 1,265,11, 10 Nov 1960
12. Mark Y (1963) Machine for disintegrating ice and packed snow on roadways. US Patent 3,094,315, 18 June 1963
13. Rypkema M (1943) Highway ice crusher and loosener. US Patent 2,319,520, 18 May 1943
14. Zhelukevich RB, Kaiser Yu F, Lysyannikov AV et al (2018) A device for removing snow and icy overruns from pavements. RU Patent 2,649,342, 02 Apr 2018
15. Pogorelsky SV (1992) A device for removing pavements from ice and compacted snow. SU Patent 1,761,856, 15 Sep 1992
16. Pogorelsky SV (1997) Devices for splitting, crushing or shifting ice or dense snow. RU Patent 2,100,524, 27 Dec 1997
17. Ivannikov PA, Kirillov FF (1998) A device for removing roads from snow ice formations. RU Patent 2,134,323, 08 Nov 1999
18. Zhelukevich RB, Bezborodov Yu N (2010) Working body to remove the snow ice formations from the surface of roads and airfields. RU Patent 2,396,389, 10 Aug 2010
19. Zhelukevich RB, Lysyannikov AV, Kaiser Yu F et al (2011) Working body to remove the snow ice formations from the surface of roads and airfields. RU Patent 1,111,49, 12 Nov 2011
20. Bobcat machinery. Scraper (ice cleaver) Bobcat. <http://bobcatspec.ru/>. Accessed 12 Nov 2018
21. Miromaks. Disc ice cleaver on mini loader. <http://mmaks.ru/product/diskovyy-skalyvatel-lda-na-mini-pogruzchik>. Accessed 12 Nov 2018

Improvement of Equipment for Knocking Out Castings from Molds



V. G. Nekrutov, A. V. Irshin and B. A. Reshetnikov

Abstract The process of knocking out castings is considered, consisting of removing hardened and chilled to certain temperature castings from the mold, which in this case is destroyed. Shaking out of castings is carried out at various knockout installations, while the main type of equipment for knocking out castings from molds is mechanical knockout grates. In order to improve the efficiency of the knockout process, the design of the foundry knockout grate has been improved. It is proposed to use a coaxial two-rotor vibration exciter of increased power as the vibration drive of the foundry knockout grate. This allows to separately adjust the frequency and amplitude of the oscillations as well as increase the range of regulation of these parameters. It was also revealed that when using this exciter, the load on the supports decreases in comparison with the unbalanced load. The computer and experimental studies of the developed vibration drive have been carried out, and the dependencies of the oscillation parameters on the tuning modes have been determined. The design of a foundry knockout grate with two-rotor coaxial vibro-exciters has been developed.

Keywords Vibrating machines · Foundry knockout grate · Rotor coaxial vibration exciter · Vibration parameters

V. G. Nekrutov (✉)

South Ural State University, 67, Krupskaya St., Ust-Katav 456040, Russia

e-mail: nekrutovvg@susu.ru

A. V. Irshin

South Ural State University, 44-11, Lenin St., Ust-Katav 456000, Russia

B. A. Reshetnikov

South Ural State University, 9-77, Medik St., Zlatoust 456228, Russia

© Springer Nature Switzerland AG 2020

A. A. Radionov et al. (eds.), *Proceedings of the 5th International Conference on Industrial Engineering (ICIE 2019)*, Lecture Notes in Mechanical Engineering,

https://doi.org/10.1007/978-3-030-22041-9_31

1 Introduction

Currently, in the foundry process, the process of knocking out foundry molds using knockout grills continues to be relevant. The most common foundry knockout lattices of the following designs: eccentric, inertial and inertial-shock [1]. The essence of the process of knocking out forms on vibration gratings for foundry production is as follows: on the knockout grid, which performs vibratory movements, set the mold assembly or individual flasks. In connection with the fact that the vertical component of the lattice acceleration exceeds the acceleration of free fall, there are detachments of the flask from the grate and its subsequent drops, which end with impacts on the lattice. It is these strokes that lead to the knockout of the cast from the flask, and the mixture collapses and spills out under the grate.

The main drawbacks of existing structures include significant shock loads (in some cases leading to the destruction of castings), dynamic loads on the structure and foundation of the knockout device, energy consumption and low productivity. At the same time, the main problem remains the possibility of regulating and controlling the parameters and nature of the oscillations, as well as their quantitative and qualitative characteristics.

The relevance of this problem related to controlling various characteristics of the oscillatory process can be traced in the works of the following authors Blekhman I. I., Poduraev V. N., Frolov K. V., and also in the works of other authors [2–4].

In connection with the foregoing, the aim of the work is to improve the technology and equipment for knocking out castings from casting molds by means of a coaxial two-rotor exciter used as a vibration shaker.

2 Main Part

It is known that vibration machines are used to intensify various technological processes [3, 4]. To create vibration, vibration exciters are used (devices for exciting mechanical vibrations). These devices allow you to specify the shape of the trajectory, the law of speed and acceleration of the working element, which depend on the geometric dimensions of the links of the machine and on the nature of the disturbance of vibrations and on the dynamic parameters of the processes occurring in the rotor nodes of the machine [3].

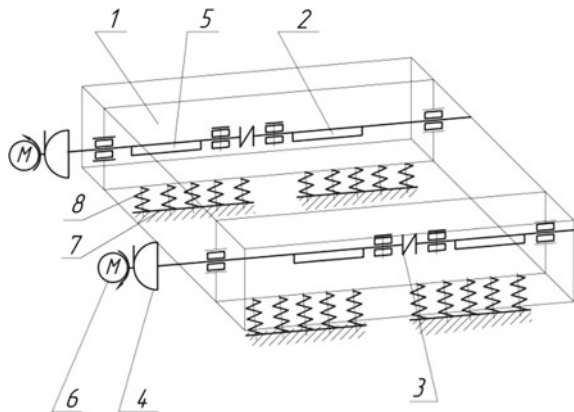
In the existing designs of foundry knockout grates (see Figs. 1 and 2), the possibility of flexible regulation by vibration parameters is limited, since unbalanced exciters are used, which consist of one or two unbalanced masses. This limits the functionality of the knockout gratings and requires additional design adjustments when knocking molds of different strength and weight.

In the South Ural State University, rotor inertial vibro-exciters [5, 6] have been developed, which allow to regulate the parameters of oscillations. This is achieved due to the fact that the parameters of the oscillations, namely the frequency and



Fig. 1 Foundry knockout grates

Fig. 2 Kinematic diagram of the foundry grate before modernization (1 grate housing, 2, 5 vibrator, 3, 4 coupling, 6 drive, 7 frame, 8 spring)



amplitude, depend (apart from the geometric dimensions of the structural elements) on the dynamic parameters of the system. In the course of investigations of this class of exciters, their main disadvantages were revealed: increased loads on the supports and low power of the oscillations created.

In order to eliminate these drawbacks, a model of an improved coaxial rotor inertial exciter of high power was developed, in which the oscillation excitation method consists in the fact that the rotating body 1 (rotor) and counter body 2 of a similar shape (Fig. 3) are mated to the calibrated force P_{ax} , so that the contact region has a closed form with rotational symmetry.

In the process of oscillation excitation, both rotors begin to rotate at a velocity ω_{rt} around the axis of the rotational symmetry of the contact region. The main indicators of this process are the frequency and amplitude of the oscillations controlled by the following ratios (1, 2):

$$\omega = \frac{P_{ax}}{2lm\omega_{rt}} + \sqrt{\frac{P_{ax}^2}{4l^2m^2\omega_{rt}^2} + \frac{j}{m}}, \tag{1}$$

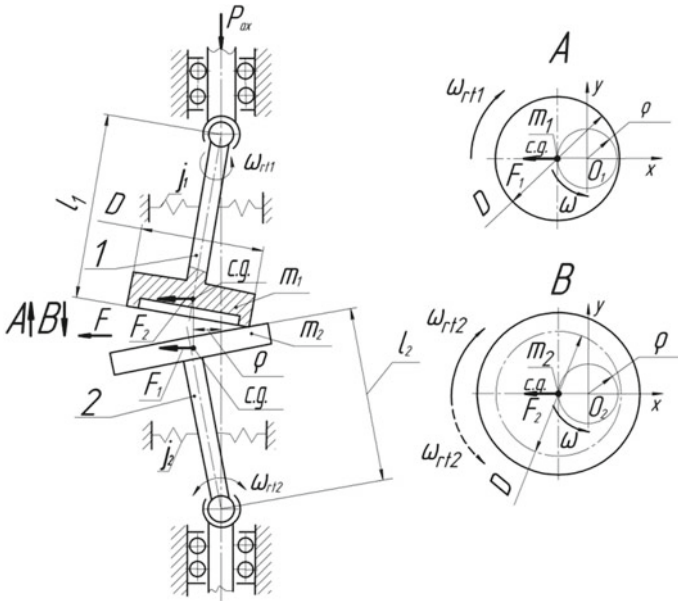


Fig. 3 Diagram of a two-rotor coaxial vibro-exciter. (ω —oscillation frequency of rotors; ω_{r11} , ω_{r12} —rotor speed; ρ —amplitude of oscillation; m_1 , m_2 —given rotor masses; D —diameter of the rotor in the zone of its interface with the counter body; l_1 , l_2 —rotor fallout; F_1 , F_2 —forcing forces; j_1 , j_2 —stiffness of rotors; C.G.—center of gravity)

$$\rho = \frac{D\omega_{rt}}{2\omega} \tag{2}$$

where $l = l_1 + l_2$; $m = m_1 + m_2$; $j = j_1 + j_2$; $\omega_{rt} = \omega_{r11} \pm \omega_{r12}$, $\rho = \rho_1 = \rho_2$.

Alignment of vibration frequencies of rotors at different speeds of their rotation is achieved due to their non-holonomic coupling at the point of their contact. As a result, a dynamic effect of their merging into one unbalanced mass is created [7–9]. This generates the total driving force F , the amplitude value of which is equal to (3)

$$F = F_1 + F_2 = m\rho\omega^2, \tag{3}$$

resulting in a more favorable distribution of loads in the active rotor assemblies of the inertial vibro-exciter of increased power shown in Fig. 4.

In order to recreate the oscillatory process, an experimental setup with coaxial arrangement of the rotors was designed and manufactured. The installation scheme is shown in Fig. 5, the general view in Fig. 6.

During the experiments, the value of the axial force of the clamping of the rotors, as well as the frequencies and their mutual direction of rotation, was changed. In this case, the oscillograms of the movements of the two rotors were recorded in order to confirm or disprove the effect of synchronization of the oscillations of the rotors. The obtained results confirmed theoretical assumptions.

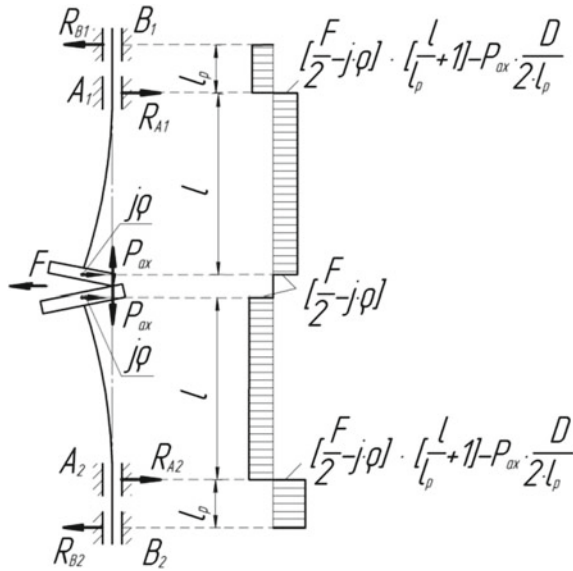


Fig. 4 Diagram of load distribution in a two-rotor coaxial vibration exciter

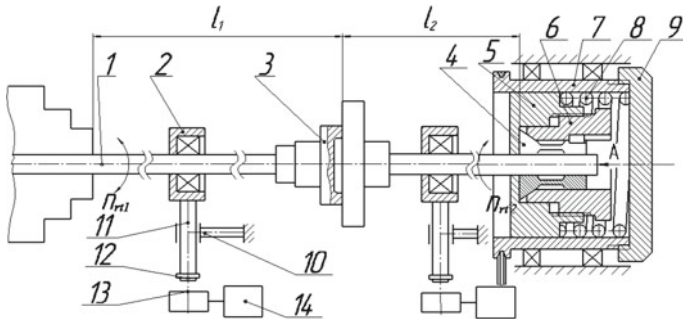


Fig. 5 Diagram of installation with coaxial arrangement of rotors. (1 rotor shaft, 2 rolling support, 3 rotor plate, 4 collets, 5 counter body, 6 stop, 7 rotating body, 8 spring, 9 screw cover, 10 support sleeve, 11 rod, 12 permanent magnet, 13 hall sensor, 14 oscilloscope)

Computer studies were carried out on the developed model of a vibration drive in order to estimate the expected control efficiency of the vibration parameters and compared with the experimental data. Dependency of the oscillation parameters: frequency ω and amplitude ρ , in the system under consideration from the adjustment modes: The axial force P_{ax} and the rotational speed n_{r2} of the counter body are shown in Fig. 7.

In the course of the research, it was found that when using a two-rotor coaxial exciter of increased power, separate regulation of the frequency and amplitude of

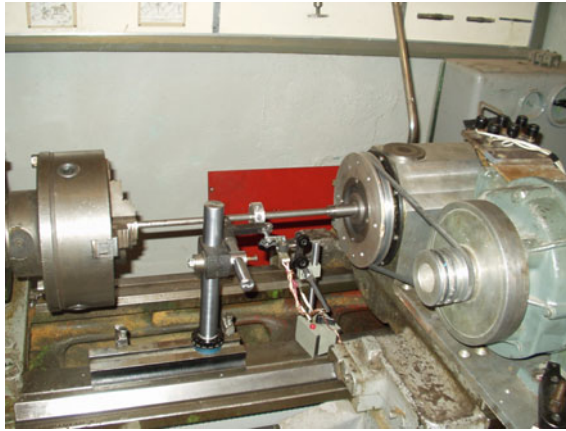


Fig. 6 General view of the installation

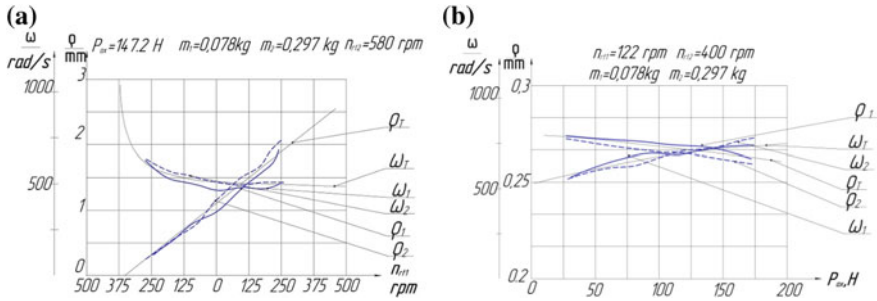


Fig. 7 Dependency of frequency and amplitude of oscillations on: **a** rotor speed; **b** axial force

oscillations is possible, while the range of regulation of these parameters has increased, and the maximum load on the supports has decreased in comparison with unbalanced exciters.

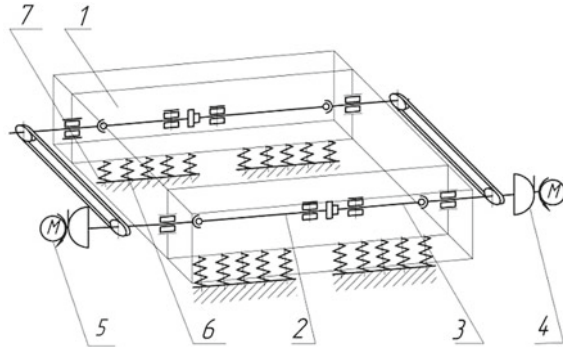
3 Conclusion

In this regard, the wide universality of rotor vibro-excitors with large technological capabilities has been proved, which make it possible to use them as oscillation sources for various vibrating machines [10–12], including the foundry knockout grid for knocking castings from castings of various strengths and mass without additional constructive adjustment.

In the course of the work, the design of a foundry grating with two-rotor coaxial vibration exciters, presented in Fig. 6, was developed. Its production tests were



Fig. 8 Foundry knockout grate after modernization (1 grate housing, 2, 3 rotor, 4 coupling, 5 drive, 6 frame, 7 spring)



carried out, which confirmed its effectiveness. The foundry knockout grate after the modernization is shown in Fig. 8.

Improved foundry gratings with two-rotor coaxial vibration exciters installed on them have the following advantages: the load on the support nodes is reduced by 20%, thereby increasing the durability of the structure; there was the possibility of separately adjusting the oscillation frequency in the range 0–3000 Hz and the amplitude of the oscillations in the range 0–30 mm. These advantages make it possible to knock out molds from mixtures of various strengths and weights without additional constructive adjustment of the foundry knockout grate and hence will increase the efficiency of its operation.

References

1. Trukhov AP, Sorokin Yu A, Ershov M Yu et al (2005) Technology of foundry: sand casting: textbook. Publishing Center "Academy", Moscow, p 528
2. Frolov KV (1984) Methods of improving machines and modern problems of engineering science. Mechanical Engineering, Moscow, p 224
3. Blekhman II (1994) Vibration mechanics. Science. Firm Publishers "Phys-Math Lit", Moscow, p 394
4. Igusa T, Xu K (1994) Vibration control using multiple tuned mass dampers. J Sound Vibration 175(4):491–503
5. Lakirev SG, Khilkevich Ya M, Sergeev SV (1991) Method of excitation of circular oscillations and a device for its implementation. RF Patent 1664412, Bul. No. 27
6. Sergeev SV, Reshetnikov BA, Zakirov RG, Sergeev Yu S (2011) Method of excitation of oscillations. RF Patent 2410166, IPC B06B 1/16, 2009119832/28, Bul. No. 3
7. Sergeev SV, Reshetnikov BA, Zakirov RG (2007) Vibratory rotary drives of machines: monograph. SUSU, Chelyabinsk, p 242
8. Nagaev RF, Guzev VV (1990) Self-synchronization of inertial vibro-exciters. Mechanical Engineering, Leningrad, p 178
9. Kelzon AS (1992) Control of oscillations of rotors. Polytechnic, St. Petersburg, p 119
10. Sergeyev SV (2004) Increase in the efficiency of vibration processes in the machining of various materials: monograph. SUSU, Chelyabinsk, p 262

11. Sergeev SV, Nekrutov VG (2011) Intensification of the process of mixing low-viscosity food products. *Food Ind* 2:54–56
12. Sergeev SV, Nekrutov VG (2012) Vibromechanical methods in the preparation and regeneration of lubricant and coolant fluids. *Russ Eng Res* 32(11–12):754–757

Theoretical Study of Sifting Heap on Finger Chaffer Sieve



A. V. Butovchenko, E. E. Petrov and A. A. Doroshenko

Abstract The basic way of harvesting grain crops is combining where the main role belongs to the combine harvester. One of the most important combine harvester cleaning systems is air and screen cleaning. Despite carried out researches, the world practice has not made essential changes in the classical scheme of air-sieve cleaning. Considering the design of traditional and non-traditional cleanings, it is necessary to note that improving the quality of grain separation, in modern manufacturers, is achieved mainly by increasing the area of cleanings, which leads to an increase in metal consumption. It is possible to raise the efficiency of the separation process technology in air-sieve cleaning, due to its better organization on the finger chaffer on the sieve. The significant disadvantages of the currently used finger chaffer are the low quality of the separation process technology, owing to its low organization, as well as the complexity of the design. This leads to the need for carrying out research and the creating of a finger chaffer, which increases the efficiency of the separation process technology. The article shows a theoretical justification of the design parameters of the finger chaffer, providing a better organization of the heap separation. The design of the original finger chaffer is justified. The results of a theoretical study of the dynamics process of moving components of a heap during sieving on the original finger chaffer are presented. The numerical values of the design parameters of the original chaffer are determined.

Keywords Separation process · Finger chaffer · Quality · D'Alembert's principle

A. V. Butovchenko (✉) · E. E. Petrov · A. A. Doroshenko
Don State Technical University, 1, Gagarin Sq., Rostov on Don 344000, Russia
e-mail: Butovchenkoav@yandex.ru

© Springer Nature Switzerland AG 2020
A. A. Radionov et al. (eds.), *Proceedings of the 5th International Conference on Industrial Engineering (ICIE 2019)*, Lecture Notes in Mechanical Engineering,
https://doi.org/10.1007/978-3-030-22041-9_32

277

1 Introduction

The separation process on the grating of the finger chaffer on the sieve is a complex phenomenon, depending on many simultaneous factors. It is possible to increase the efficiency of heap separation on the finger chaffer by changing the design of its work elements. Thus, the aim of the work is the theoretical substantiation of the design parameters of the finger chaffer, providing a better organization of the heap separation.

2 Main Body

Preliminary studies have shown that it is possible to improve the quality of the functioning of the finger chaffer, through effective organization of separation on it, which can be achieved through its more advanced design. The experience in this direction allowed us to develop a finger chaffer [1], and the scheme is illustrated in Fig. 1.

The finger chaffer is a set of working elements 1 lying in one surface (plane), the upper parts are made in the form of crests (combs) 2, and the lower ones are in the form of notches (cut) with slope, 3 forming gutter, at the bottom of each of which there are cracks 4.

At the theoretical study of the dynamic process of moving the components of the heap during sieving, it is necessary to consider the system: technological material (heap)—device (finger chaffer) effects, components of the grain component of the heap (free grain and non-threshed ears)—as free solid bodies, having mass and dimensions. It is known [2–8] that the finger chaffer, like other devices of the combine cleaning system, performs harmonic oscillations and its kinematics in the same along the whole length. The body movement on the slope, we will consider with respect to the fixed inertial reference system, with the Cartesian coordinate system XOY , presented in Fig. 2.

As a reference point, choose a point at the intersection of the following planes: a cross-section of a finger chaffer drawn along the axial section of the crest (ridge)

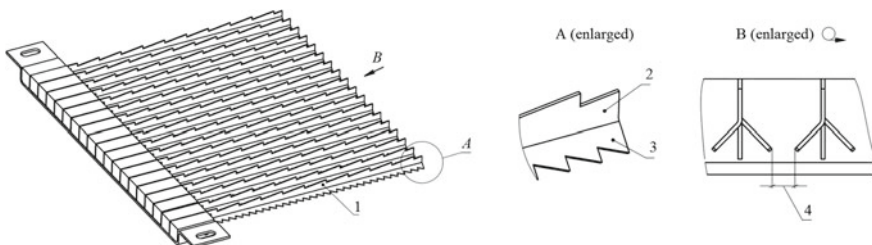
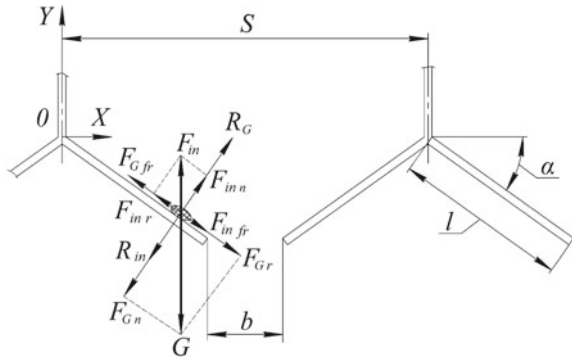


Fig. 1 Scheme of finger chaffer design

Fig. 2 Scheme of forces acting on the body moving along the slope of the finger chaffer (decoding positions in the text)



and passing along the line of intersection of the crests (ridges) and slopes, in the lowest position of the finger grid, during its cycle of movement in the longitudinal vertical plane. The X -axis is located at the intersection of the plane of the cross-section of the finger grid and the plane drawn along the line of intersection of the ridges and slopes and the right direction.

The Y -axis is located at the intersection of the plane of the cross-section of the finger grid and the plane drawn along the axial section of the crest and is directed upwards. Gravity, inertia, friction and normal reaction from the side of the slope to the grain act on the solid body located on the slope of the finger chaffer. Consider in detail the listed forces, the scheme of which is shown in Fig. 2.

The gravity of the body (see Fig. 2) in N is determined by the formula:

$$\vec{G} = m \cdot \vec{g}, \tag{1}$$

where m —body weight in kg; \vec{g} —Gravity acceleration in $kg\ m/sec^2$.

Gravity force decomposes into two components: normal force and force along the slope. The values of these components are determined by the formulas:

$$F_{Gr} = G \cdot \sin \alpha = m \cdot g \cdot \sin \alpha; \tag{2}$$

$$F_{Gn} = G \cdot \cos \alpha = m \cdot g \cdot \cos \alpha, \tag{3}$$

where α —is the angle between the slope and the axis OX .

The inertial force of the body from oscillations in the longitudinal plane of the finger chaffer, parallel to the crest, is determined by the formula:

$$F_{inv} = m \cdot \omega^2 \cdot R \cdot \cos(\omega \cdot t), \tag{4}$$

where ω —frequency cyclic of oscillations in rad/sec; R —radius of crank in m; t —time in sec.



The inertial force expands into two components: normal force and force along the slope. The values of these components are determined by the formulas:

$$F_{\text{in}r} = F_{\text{inv}} \cdot \sin \alpha = m \cdot \omega^2 \cdot R \cdot \cos(\omega \cdot t) \cdot \sin \alpha; \quad (5)$$

$$F_{\text{in}n} = F_{\text{inv}} \cdot \cos \alpha = m \cdot \omega^2 \cdot R \cdot \cos(\omega \cdot t) \cdot \cos \alpha. \quad (6)$$

The frictional force of a body sliding on the slope surface will have two components, the gravity force and the inertial force:

$$F_{\text{fr}} = F_{G\text{fr}} + F_{\text{infr}}, \quad (7)$$

which are determined by the formulas:

$$F_{G\text{fr}} = \mu_{b-s} \cdot F_{Gn} = \mu_{b-s} \cdot G \cdot \cos \alpha = \mu_{b-s} \cdot m \cdot g \cdot \cos \alpha; \quad (8)$$

$$F_{\text{infr}} = \mu_{b-s} \cdot F_{\text{in}n} = \mu_{b-s} \cdot F_{\text{inv}} \cdot \cos \alpha = \mu_{b-s} \cdot m \cdot \omega^2 \cdot R \cdot \cos(\omega \cdot t) \cdot \cos \alpha, \quad (9)$$

where μ_{b-s} —is the body friction coefficient (free grain or unthreshed) on steel.

The normal reaction from the slope to the body, module, is equal to the normal component of gravity and inertial forces, but opposite to them in direction. After determining the reactions of forces system and reactions acting on the body on the slope of the finger chaffer, it is necessary to determine the law of its movement under the influence of the considered forces. The kinetostatic method is used for solving problems of dynamics, which is based on the D'Alembert's principle, according to which, at each moment of time, the active and reactive forces acting on the body, together with the inertial force of a point, make a balanced system of forces:

$$\vec{F} + \vec{N} + \vec{\Phi} = 0, \quad (10)$$

where \vec{F} —is the resultant vector of all active forces; \vec{N} —is the resultant vector of all reactive forces; $\vec{\Phi}$ —is the vector of inertial force,

$$\vec{\Phi} = -m \cdot \vec{a}. \quad (11)$$

Then the equation of the second basic law of dynamics for the body in a vector form, in general, will be as follows:

$$m \cdot \vec{a} = \sum \vec{F}_i, \quad (12)$$

where m —is the body mass in kg; \vec{a} —is the body acceleration in m/sec^2 ; \vec{F}_i —is the forces acting on the body in N .

And in our case:

$$m \cdot \vec{a} = \sum \vec{F}_i = \vec{F}_{Gr} + \vec{F}_{Gn} + \vec{F}_{Gfr} + \vec{R}_G + \vec{F}_{inr} + \vec{F}_{inn} + \vec{F}_{infr} + \vec{R}_{in}, \quad (13)$$

where m —is the body mass in kg; \vec{a} —is the vector of the body acceleration in m/sec^2 ; \vec{F}_{Gr} —is the vector of the rolling component of the body gravity in N ; \vec{F}_{Gn} —is the vector of the normal component of body gravity in N ; \vec{F}_{Gfr} —is the vector of friction force of a body sliding along the surface of a slope from the normal component of gravity in N ; \vec{R}_G —is the vector of reaction from the side of a slope on the body from the normal component of gravity in N ; \vec{F}_{inr} —is the vector of the rolling component of the body inertial force in N ; \vec{F}_{inn} —is the vector of the normal component of the body inertial force in N ; \vec{F}_{infr} —is the vector of the friction force of the body sliding along the surface of the slope from the normal component of the inertial force in N ; \vec{R}_{in} —is the vector of reaction from the side of a slope on the body from the normal component of the inertial force in N .

In general, the system of equations of the second basic law of dynamics for a body in projections on an axis of the coordinate system, adopted by us, has the following form:

$$\begin{cases} m \cdot a_x = \sum F_{xi}; \\ m \cdot a_y = \sum F_{yi}; \end{cases} \quad (14)$$

where a_x, a_y —are the projections of the acceleration of the body on the corresponding coordinate axis; F_{xi}, F_{yi} —are the projection of the i -force on the corresponding coordinate axis.

And in our case:

$$\begin{cases} m \cdot a_x = F_{xGr} - F_{xGn} - F_{xGfr} + R_{xG} - F_{xinr} + F_{xinn} + F_{xinfr} - R_{xin}; \\ m \cdot a_y = -F_{yGr} - F_{yGn} + F_{yGfr} + R_{yG} + F_{yinr} + F_{yinn} - F_{yinfr} - R_{yin}; \end{cases} \quad (15)$$

Substituting instead of F_i of their values and converting, we get:

$$\begin{cases} m \cdot a_x = -\mu_{b-s} \cdot m \cdot g \cdot \cos^2 \alpha + m \cdot g \cdot \cos \alpha \cdot \sin \alpha \\ \quad + \mu_{b-s} \cdot m \cdot \omega^2 \cdot R \cdot \cos(\omega \cdot t) \cdot \cos^2 \alpha - m \cdot \omega^2 \cdot R \cdot \cos(\omega \cdot t) \cdot \cos \alpha \cdot \sin \alpha; \\ m \cdot a_y = -m \cdot g + \mu_{b-s} \cdot m \cdot g \cdot \cos \alpha \cdot \sin \alpha + m \cdot g \cdot \cos^2 \alpha + m \cdot \omega^2 \cdot R \cdot \cos(\omega \cdot t) \\ \quad - \mu_{b-s} \cdot m \cdot \omega^2 \cdot R \cdot \cos(\omega \cdot t) \cdot \cos \alpha \cdot \sin \alpha - m \cdot \omega^2 \cdot R \cdot \cos(\omega \cdot t) \cdot \cos^2 \alpha. \end{cases} \quad (16)$$

In general, the system of differential equations in projections on the axis, the adopted coordinate system, has the following form:

$$\begin{cases} m\ddot{x} = \sum \vec{F}_{ix}; \\ m\ddot{y} = \sum \vec{F}_{iy}, \end{cases} \quad (17)$$

where \ddot{x}, \ddot{y} —are the projections of the second derivative displacements on the axis.
And in our case:

$$\begin{cases} m \cdot \ddot{x} = -\mu_{b-s} \cdot m \cdot g \cdot \cos^2 \alpha + m \cdot g \cdot \cos \alpha \cdot \sin \alpha + \mu_{b-s} \cdot m \cdot \omega^2 \cdot R \cdot \cos(\omega \cdot t) \cdot \cos^2 \alpha \\ \quad - m \cdot \omega^2 \cdot R \cdot \cos(\omega \cdot t) \cdot \cos \alpha \cdot \sin \alpha; \\ m \cdot \ddot{y} = -m \cdot g + \mu_{b-s} \cdot m \cdot g \cdot \cos \alpha \cdot \sin \alpha + m \cdot g \cdot \cos^2 \alpha + m \cdot \omega^2 \cdot R \cdot \cos(\omega \cdot t) \\ \quad - \mu_{b-s} \cdot m \cdot \omega^2 \cdot R \cdot \cos(\omega \cdot t) \cdot \cos \alpha \cdot \sin \alpha - m \cdot \omega^2 \cdot R \cdot \cos(\omega \cdot t) \cdot \cos^2 \alpha. \end{cases} \quad (18)$$

We accept the initial conditions:

$$\begin{cases} t_0 = 0; \\ x_0 = 0, y_0 = 0; \\ \dot{x}_0 = 0, \dot{y}_0 = 0, \end{cases} \quad (19)$$

where t_0 —is considered the initial moment of time; x_0 —is the initial coordinate of the body on the X -axis; y_0 —is the initial coordinate of the body on the Y -axis; \dot{x}_0 —is the speed of movement body along the X -axis at the time; \dot{y}_0 —is the body velocity along the Y -axis at the time.

By adding initial conditions, we obtain the Cauchy problem. Consider the first equation of system (18):

$$\begin{aligned} m \cdot \ddot{x} = & -\mu_{b-s} \cdot m \cdot g \cdot \cos^2 \alpha + m \cdot g \cdot \cos \alpha \cdot \sin \alpha \\ & + \mu_{b-s} \cdot m \cdot \omega^2 \cdot R \cdot \cos^2 \alpha \cdot \cos(\omega \cdot t) \\ & - m \cdot \omega^2 \cdot R \cdot \cos \alpha \cdot \sin \alpha \cdot \cos(\omega \cdot t). \end{aligned} \quad (20)$$

After performing the transformation, we obtain:

$$\begin{aligned} \frac{dx}{dt} = & -\mu_{b-s} \cdot g \cdot \cos^2 \alpha \cdot t + g \cdot \cos \alpha \cdot \sin \alpha \cdot t + \mu_{b-s} \cdot \omega \cdot R \cdot \cos^2 \alpha \cdot \sin(\omega \cdot t) \\ & - \omega \cdot R \cdot \cos \alpha \cdot \sin \alpha \cdot \sin(\omega \cdot t) + C_1. \end{aligned} \quad (21)$$

Substituting the initial conditions (19) into Eq. (21), we get:

$$\left. \frac{dx}{dt} \right|_{t=0} = \dot{x}_0 = C_1 = 0. \quad (22)$$

By integrating expression (22) and substituting the initial conditions (19), we obtain:

$$x_0 = -\mu_{b-s} \cdot R \cdot \cos^2 \alpha + R \cdot \cos \alpha \cdot \sin \alpha + C_2 = 0, \quad (23)$$

where

$$C_2 = \mu_{b-s} \cdot R \cdot \cos^2 \alpha - R \cdot \cos \alpha \cdot \sin \alpha. \quad (24)$$

We obtain the final equation for moving the body along the X -axis:

$$\begin{aligned} x = & -\mu_{b-s} \cdot g \cdot \cos^2 \alpha \cdot \frac{t^2}{2} + g \cdot \cos \alpha \cdot \sin \alpha \cdot \frac{t^2}{2} - \mu_{b-s} \cdot R \cdot \cos^2 \alpha \cdot \cos(\omega \cdot t) \\ & + R \cdot \cos \alpha \cdot \sin \alpha \cdot \cos(\omega \cdot t) + \mu_{b-s} \cdot R \cdot \cos^2 \alpha - R \cdot \cos \alpha \cdot \sin \alpha. \end{aligned} \quad (25)$$

Consider the second equation of system (18):

$$\begin{aligned} m \cdot \ddot{y} = & -m \cdot g + \mu_{b-s} \cdot m \cdot g \cdot \cos \alpha \cdot \sin \alpha + m \cdot g \cdot \cos^2 \alpha + m \cdot \omega^2 \cdot R \cdot \cos(\omega \cdot t) \\ & - \mu_{b-s} \cdot m \cdot \omega^2 \cdot R \cdot \cos \alpha \cdot \sin \alpha \cdot \cos(\omega \cdot t) - m \cdot \omega^2 \cdot R \cdot \cos^2 \alpha \cdot \cos(\omega \cdot t). \end{aligned} \quad (26)$$

Performing the transformation, we get:

$$\begin{aligned} \frac{dy}{dt} = & -g \cdot t + \mu_{b-s} \cdot g \cdot \cos \alpha \cdot \sin \alpha \cdot t + g \cdot \cos^2 \alpha \cdot t + \omega \cdot R \cdot \sin(\omega \cdot t) \\ & - \mu_{b-s} \cdot \omega \cdot R \cdot \cos \alpha \cdot \sin \alpha \cdot \sin(\omega \cdot t) - \omega \cdot R \cdot \cos^2 \alpha \cdot \sin(\omega \cdot t) + C_1. \end{aligned} \quad (27)$$

Substituting the initial conditions (19) in Eq. (27), we obtain:

$$\left. \frac{dy}{dt} \right|_{t=0} = \dot{y}_0 = C_1 = 0. \quad (28)$$

By integrating the expression (28) and substituting the initial conditions (19), we get

$$y_0 = -R + \mu_{b-s} \cdot R \cdot \cos \alpha \cdot \sin \alpha + R \cdot \cos^2 \alpha + C_2 = 0, \quad (29)$$

where

$$C_2 = R - \mu_{b-s} \cdot R \cdot \cos \alpha \cdot \sin \alpha - R \cdot \cos^2 \alpha. \quad (30)$$

We obtain the final equation for moving a body along the Y -axis:

$$\begin{aligned}
 y = & -g \cdot \frac{t^2}{2} + \mu_{b-s} \cdot g \cdot \cos \alpha \cdot \sin \alpha \cdot \frac{t^2}{2} + g \cdot \cos^2 \alpha \cdot \frac{t^2}{2} - R \cdot \cos(\omega \cdot t) \\
 & + \mu_{b-s} \cdot R \cdot \cos \alpha \cdot \sin \alpha \cdot \cos(\omega \cdot t) \\
 & + R \cdot \cos^2 \alpha \cdot \cos(\omega \cdot t) + R - \mu_{b-s} \cdot R \cdot \cos \alpha \cdot \sin \alpha - R \cdot \cos^2 \alpha.
 \end{aligned}
 \tag{31}$$

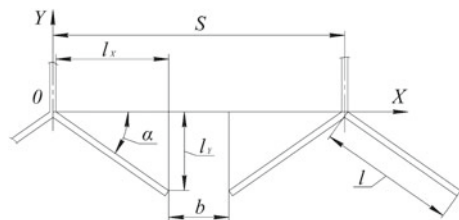
By combining Eqs. (25) and (31), we obtain the system of equations that determine the trajectory of the body movement along the slope of the finger chaffer:

$$\begin{aligned}
 x = & -\mu_{b-s} \cdot g \cdot \cos^2 \alpha \cdot \frac{t^2}{2} + g \cdot \cos \alpha \cdot \sin \alpha \cdot \frac{t^2}{2} - \mu_{b-s} \cdot R \cdot \cos^2 \alpha \cdot \cos(\omega \cdot t) \\
 & + R \cdot \cos \alpha \cdot \sin \alpha \cdot \cos(\omega \cdot t) + \mu_{b-s} \cdot R \cdot \cos^2 \alpha - R \cdot \cos \alpha \cdot \sin \alpha; \\
 y = & -g \cdot \frac{t^2}{2} + \mu_{b-s} \cdot g \cdot \cos \alpha \cdot \sin \alpha \cdot \frac{t^2}{2} + g \cdot \cos^2 \alpha \cdot \frac{t^2}{2} - R \cdot \cos(\omega \cdot t) \\
 & + \mu_{b-s} \cdot R \cdot \cos \alpha \cdot \sin \alpha \cdot \cos(\omega \cdot t) \\
 & + R \cdot \cos^2 \alpha \cdot \cos(\omega \cdot t) + R - \mu_{b-s} \cdot R \cdot \cos \alpha \cdot \sin \alpha - R \cdot \cos^2 \alpha.
 \end{aligned}
 \tag{32}$$

Knowing the trajectory of the body on the surface of the slope, we determine the numerical values of the design parameters of the finger chaffer, and the scheme is shown in Fig. 3.

Analysis of the study [9] and the structures of existing finger chaffers allowed, in the course of theoretical studies, to take the installation step of working elements S equal to 20 mm. The width of the gap b should ensure the passage of free grain through it and exclude the passage of non-threshed ears. The passage or non-passage of the heap components through the gap regulates their width and thickness. The analysis of the sources [10, 11] showed that the width of free grains is 1.6–4.0 mm and thickness is 1.5–3.8 mm. The width of the non-threshed ear is 3.5–11.4 mm, and the thickness is 3.5–10.9 mm. Based on the above, in the process of theoretical studies, the width of the gap b was assumed to be 4.0 mm. According to the scheme presented in Fig. 3, the length of the slope projection on the X -axis:

Fig. 3 Scheme of the finger chaffer, in determining its design parameters (decoding positions in the text)



$$l_X = \frac{S - b}{2} = \frac{20 - 4}{2} = 8 \text{ mm.} \quad (33)$$

This is the maximum x value depending on (32). In order for the body, during separation, to move along the slope to the gap, the following condition must be met:

$$F_{Gr} + F_{inr} - F_{Gfr} - F_{infr} > 0. \quad (34)$$

Substituting into inequality (34), expressions (2), (5), (8) and (9), we get:

$$m \cdot g \cdot \sin \alpha + m \cdot \omega^2 \cdot R \cdot \cos(\omega \cdot t) \cdot \sin \alpha - \mu_{b-s} \cdot m \cdot g \cdot \cos \alpha - \mu_{b-s} \cdot m \cdot \omega^2 \cdot R \cdot \cos(\omega \cdot t) \cdot \cos \alpha > 0. \quad (35)$$

After performing the transformation, we obtain:

$$(\sin \alpha - \mu_{b-s} \cdot \cos \alpha) \cdot (g + \omega^2 \cdot R \cdot \cos(\omega \cdot t)) > 0. \quad (36)$$

Inequality (36) can be solved numerically. To do this, substitute the source data: $\mu_{b-s} = 0.7$ (the maximum coefficient of friction is accepted); $R = 18$ mm; $\omega = 26.4$ rad/sec; $t = 2\pi/\omega = 0.237$ s, and we obtain the solution of the inequality for one cycle of oscillation of the finger chaffer. As a result of a series of calculations, it was established that condition (36) is observed at an angle $\alpha > 35^\circ$. This is the minimum angle of inclination of the slope to the horizontal plane of the finger chaffer, providing the beginning of the body movement along the slope down to the gap. Then the maximum value of the projection of the slope on the Y -axis:

$$l_Y = l_X \cdot \text{tg} \alpha = 8 \cdot \text{tg} 35 = 5.6 \text{ mm.} \quad (37)$$

This is the maximum value of y depending on (32).

3 Conclusion

The obtained analytical dependencies in the study result give an idea of the main regularities of the process and allow you to describe the trajectory of movement of the components of the heap on the finger chaffer and identify the main factors (installation step of the working elements S , slit (gap) width b and the angle of installation of the slopes to the horizontal plane of the finger chaffer α , providing movement of free grain and non-threshed ears), which can have a significant impact on the quality of functioning of the finger chaffer and determine their numerical values ($S = 20$ mm; $b = 4$ mm; $\alpha = 35^\circ$).

References

1. Petrov EE, Butovchenko AV, Shapoval BG (2018) Pal'tsevaya reshetka stryasnoi doski (Finger chaffer sieve). RF Patent 178,042, 21 Mar 2018
2. Ermol'ev YI, Chistyakov AD, Androsov AA (2006) Osnovy proektirovaniya sel'skohozyajstvennyh mashin (Basic design of agricultural machinery). Grif i K, Tula
3. Martynenko DS (2015) Improving the efficiency of the combine harvester cleaning system by using the recuperative drive of sieves and transport Board. Dissertation, Northern Trans-Ural State Agricultural University
4. Ridnyj SD (2002) Improvement of technology and means of mechanization of harvesting of alfalfa testes. Dissertation, Stavropol Research Institute of Agriculture
5. Sorochenko SF, Ryazanov AV (2012) Rezul'taty laboratornykh issledovaniy adaptera sistemy ochistki zernouborochnogo kombaina dlya raboty na sklonakh (Results of laboratory researches of the adapter of system of cleaning of the combine harvester for work on slopes). Bull Polzunov 1:282–285
6. Sorochenko SF (2016) Matematicheskaya model' dvizheniya zernovogo vorokha po reshetu adaptera ochistki zernouborochnogo kombaina (Mathematical model of grain heap movement on the sieve of the grain combine cleaning adapter). Bull PASTU 12:131–138
7. Sorochenko SF (2017) Matematicheskaya model' dvizheniya zernovogo vorokha po reshetu 3D-ochistki zernouborochnogo kombaina (Mathematical model of grain heap movement on the sieve of 3D-cleaning of a combine harvester). Sci Life 12:134–140
8. Sorochenko SF (2018) Mekhaniko-tehnologicheskie osnovy sozdaniya sistemy ochistki zernouborochnogo kombaina dlya raboty na sklonakh (Mechanical-technological bases of creation of system of cleaning of the grain combine to work on slopes). Dissertation, Polzunov Altai State Technical University
9. Marchenko AT (1994) Sovershenstvovanie tekhnologii uborki lyucerny na semena s obrabotkoj voroha na stacionare (Improving the technology of harvesting alfalfa seeds with the treatment of heap in the Stationary). Dissertation, Kuban State Agrarian University
10. Ermol'ev YI, Butovchenko AV (2010) Proektirovanie tekhnologicheskikh processov i vozdušno-reshyotnyh i reshyotnyh zernoochistitel'nyh mashin (Design of technological processes and air-sieve and sieve grain cleaning machines). Don State Technical University, Rostov on Don
11. Petrov EE, Butovchenko AV, Shapoval BG (2018) Obosnovanie sostava i svoystv vorokha, postupayushchego so stryasnoi doski na pal'tsevuyu reshetku, pri modelirovanii protsessa separatsii v laboratornykh usloviyakh (Substantiation of the composition and properties of the heap coming from the stress Board to the finger chaffer when modeling the separation process in the laboratory). State Prospect Dev Agric Mach 11:20–22

Modeling Polymeric Centrifugal-Pump Impeller Blades



V. A. Pukhliy, S. T. Miroshnichenko and V. V. Sokolov

Abstract The paper describes a mathematical model and an algorithm to compute the stress–strain state of polymeric centrifugal-pump impeller blades. We explore the stress–strain state of a centrifugal-pump trapezoidal anisotropic blade constrained on both sides that are adjacent to plates (median-plane displacement is possible) while not constrained on the two other sides where the blade is exposed to the inertial forces of the blade eigen-weight. Differential equations of bending of a cylindrical anisotropic shell are obtained with respect to the deflection function and the stress function in the field of centrifugal inertia forces. To solve the boundary value problem described by the system of equations in partial derivatives and in boundary conditions, use the Dorodnitsyn’s method of integral ratios. Pursuant to the method, write the original equation system as a divergent system. Further apply the method of integral ratios to the original system of equations in partial derivatives to obtain a system of ordinary differential equations (order $8n$) with variable coefficients, which are generally non-Euler. The boundary value problem is solved by the modified method of successive approximations, developed by Prof. V. A. Pukhliy and published by him in academic press. A numerical implementation has been programmed according to the analytical solution above. Computations were run for an orthotropic material of a blade where the principal elastic symmetry axes are turned by an angle φ against the blade axes x, y . The finding of the analysis is that it is necessary to take into account the anisotropy that occurs due to the main axes of the elastic orthotropic material not matching the computed axes of the blade.

Keywords Centrifugal pumps · Polymeric blades · Strength computations · Modified method of successive approximations

V. A. Pukhliy (✉) · S. T. Miroshnichenko · V. V. Sokolov
Sevastopol State University, 31, Street Universitetskaya, Sevastopol 299053, Russia
e-mail: pu1611@rambler.ru

© Springer Nature Switzerland AG 2020
A. A. Radionov et al. (eds.), *Proceedings of the 5th International Conference on Industrial Engineering (ICIE 2019)*, Lecture Notes in Mechanical Engineering,
https://doi.org/10.1007/978-3-030-22041-9_33

287

1 Introduction

Rapid development of chemistry, nuclear power, etc. requires a lot of different pump types. Unlike water pumps, chemical pumps as well as pumps used in primary nuclear reactor circuits are difficult to make since the same head and throughput values require making the pump of different materials depending on the chemical properties of the fluid to be pumped. Using polymers also requires detailed data on the stress–strain state of centrifugal-pump parts.

Today, there are numerous approaches to finding the stress–strain state of machine and mechanism parts; the approaches are based on the plate and shell theory. Generally, these methods have been created to apply to isotropic materials. Meanwhile, polymeric materials that feature orthotropic elastic properties have found wide application in modern mechanical engineering, especially in turbomachines. It is important to take into account the anisotropy that occurs due to the principal axes of the elastic material not matching the computed axes of the blade. As a result, when designing machine elements and mechanism, appropriate orientation of the material becomes crucial, as it enables more rational use of its properties. Materials of generally anisotropic elastic properties are widespread as well. It is therefore apparent how important it is to design machine and mechanism parts made of anisotropic materials.

The paper presents a computation of the stress–strain state of anisotropic trapezoidal blades used in centrifugal pumps, see Fig. 1.

Linear theory of shallow anisotropic shells is used to describe the blade behavior [1]. The initial system of equations in partial derivatives on the stress function $F(x, y)$ and normal displacement $W(x, y)$, Marguerre-type [2] is reduced to a system of ordinary differential equations by means of Dorodnitsyn's method of integral ratios [3]. This equation system has variable coefficients and is solved analytically by the modified method of successive approximations [6, 7].

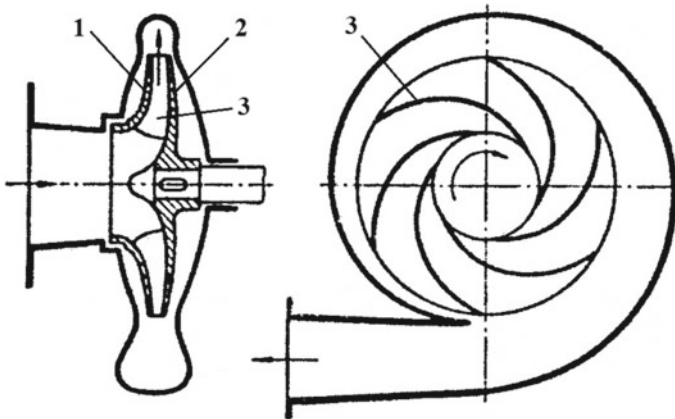


Fig. 1 Centrifugal-pump impeller diagram: 1 is the front plate; 2 is the main plate; 3 is the blade

1.1 Statement of Problem and Goal

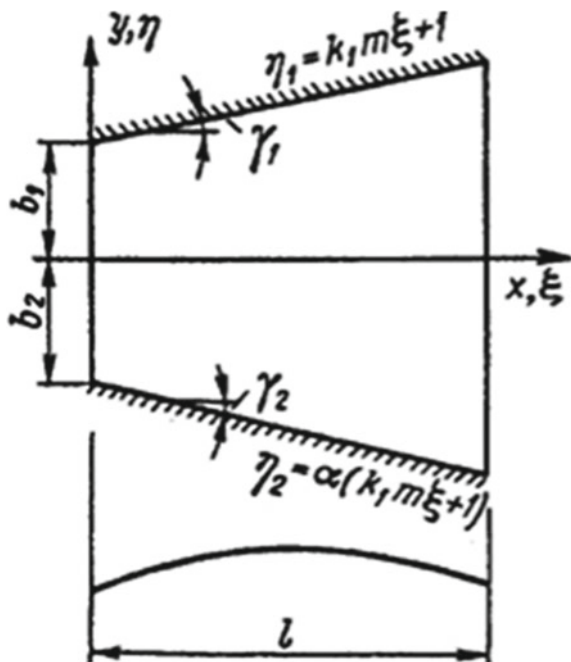
The goal of this study is to mathematically model and algorithmize the strength computation of centrifugal-pump impeller blades made of anisotropic materials.

1.2 Statement of Problem

Let us explore the stress-p-strain state of a centrifugal-pump trapezoidal anisotropic blade constrained on both sides that are adjacent to plates (median-plane displacement is possible) while not constrained on the two other sides (see Fig. 2) where the blade is exposed to the inertial forces of the blade eigen-weight.

For analysis, use the thin anisotropic shell bending theory [1] based on the following assumptions: (1) adopt the straight-normal hypothesis; (2) at each point, the material has a single plane of elastic symmetry that is parallel to the median surface of the shell.

Fig. 2 Centrifugal-pump blade geometry and coordinate system



Based on these assumptions, rewrite Hooke's generalized law equations as follows:

$$\left. \begin{aligned} \varepsilon_x &= a_{11}\sigma_x + a_{12}\sigma_y + a_{16}\tau_{xy}; \\ \varepsilon_y &= a_{12}\sigma_x + a_{22}\sigma_y + a_{26}\tau_{xy}; \\ \varepsilon_{xy} &= a_{16}\sigma_x + a_{26}\sigma_y + a_{66}\tau_{xy}, \end{aligned} \right\} \quad (1)$$

where a_{ik} are elastic constants.

Differential equations of cylindrical anisotropic shell bending in relation to the deflection function $W(x, y)$ and the stress function $F(x, y)$ in the field of centrifugal inertia forces are written as follows:

$$\left. \begin{aligned} L_1(D_{ik})W + \frac{1}{R} \cdot \frac{\partial^2 F}{\partial y^2} &= q - p_x \frac{\partial W}{\partial x}; \\ L_2(A_{ik})F - \frac{1}{R} \cdot \frac{\partial^2 W}{\partial y^2} &= -\frac{\partial^2 U}{\partial x^2}. \end{aligned} \right\} \quad (2)$$

where q and p_x are the normal and the tangential components of the centrifugal load; U is the tangential-load potential. Note that Eq. (2) coincide with the well-known Marguerre equations for isotropic shells in form [2].

The differential operators $L_1(D_{ik})$ and $L_2(A_{ik})$ are written as:

$$\left. \begin{aligned} L_1(D_{ik}) &= D_{11} \frac{\partial^4}{\partial x^4} + 4D_{16} \frac{\partial^4}{\partial x^3 \partial y} + 2(D_{12} + 2D_{66}) \frac{\partial^4}{\partial x^2 \partial y^2} + 4D_{26} \frac{\partial^4}{\partial x \partial y^3} + D_{22} \frac{\partial^4}{\partial y^4}; \\ L_2(A_{ik}) &= A_{22} \frac{\partial^4}{\partial x^4} - 2A_{26} \frac{\partial^4}{\partial x^3 \partial y} + 2(A_{12} + A_{66}) \frac{\partial^4}{\partial x^2 \partial y^2} - 2A_{16} \frac{\partial^4}{\partial x \partial y^3} + A_{11} \frac{\partial^4}{\partial y^4}, \end{aligned} \right\} \quad (3)$$

where D_{11} , D_{22} are the bending stiffness values in the principal directions; D_{16} , D_{12} , D_{26} are side stiffness values; D_{66} is the torsion stiffness.

Let us express the coefficients A_{ik} in terms of stiffness:

$$\left. \begin{aligned} A_{11} &= (C_{22}C_{66} - C_{26}^2)\Omega_1^{-1}; \\ A_{22} &= (C_{11}C_{66} - C_{16}^2)\Omega_1^{-1}; \\ A_{12} &= (C_{16}C_{26} - C_{12}C_{26})\Omega_1^{-1}; \\ A_{66} &= (C_{11}C_{22} - C_{12}^2)\Omega_1^{-1}; \end{aligned} \right\} \left. \begin{aligned} A_{16} &= (C_{12}C_{26} - C_{16}C_{22})\Omega_1^{-1}; \\ A_{26} &= (C_{12}C_{16} - C_{26}C_{11})\Omega_1^{-1}; \\ \Omega_1 &= (C_{11}C_{22} - C_{12}^2)C_{66} \\ &\quad + 2C_{12}C_{16}C_{26} - C_{11}C_{26}^2 - C_{22}C_{16}^2. \end{aligned} \right\} \quad (4)$$

Shell stiffness C_{ik} and D_{ik} are linked to the elastic constants by the following ratios:

$$C_{ik} = hB_{ik}; \quad D_{ik} = \frac{h^3}{12}B_{ik}, \quad (5)$$

where

$$\left. \begin{aligned}
 B_{11} &= (a_{22}a_{66} - a_{26}^2)\Omega^{-1}; \\
 B_{22} &= (a_{11}a_{66} - a_{16}^2)\Omega^{-1}; \\
 B_{12} &= (a_{16}a_{26} - a_{12}a_{66})\Omega^{-1}; \\
 B_{66} &= (a_{11}a_{22} - a_{12}^2)\Omega^{-1}; \\
 B_{16} &= (a_{12}a_{26} - a_{22}a_6)\Omega^{-1}; \\
 B_{26} &= (a_{12}a_{16} - a_{11}a_{26})\Omega^{-1}; \\
 \Omega &= (a_{11}a_{22} - a_{12}^2)a_{66} + 2a_{12}a_{16}a_{26} - a_{11}a_{26}^2 - a_{22}a_{16}^2.
 \end{aligned} \right\} \tag{6}$$

For an orthotropic material, in which the principal elastic symmetry axes are rotated against the axes x and y by an angle ϕ , we have [1]:

$$\left. \begin{aligned}
 a_{11} &= \frac{\cos^4 \phi}{E_1} + \left(\frac{1}{G} - \frac{2\nu_1}{E_1}\right) \sin^2 \phi \cos^2 \phi; \\
 a_{22} &= \frac{\sin^4 \phi}{E_1} + \left(\frac{1}{G} - \frac{2\nu_2}{E_2}\right) \sin^2 \phi \cos^2 \phi; \\
 a_{12} &= \left(\frac{1+\nu_1}{E_1} + \frac{1+\nu_2}{E_2} - \frac{1}{G}\right) \frac{1}{4} \sin^2 2\phi - \frac{\nu_1}{E_1}; \\
 a_{66} &= \left(\frac{1+\nu_1}{E_1} + \frac{1+\nu_2}{E_2} - \frac{1}{G}\right) \sin^2 2\phi + \frac{1}{G}; \\
 a_{16} &= \left[\frac{\sin^2 \phi}{E_2} - \frac{\cos^2 \phi}{E_1} + \frac{1}{2} \left(\frac{1}{G} - \frac{2\nu_1}{E_1}\right) \cos 2\phi\right] \sin 2\phi; \\
 a_{26} &= \left[\frac{\cos^2 \phi}{E_2} - \frac{\sin^2 \phi}{E_1} - \frac{1}{2} \left(\frac{1}{G} - \frac{2\nu_2}{E_2}\right) \cos 2\phi\right] \sin 2\phi.
 \end{aligned} \right\} \tag{7}$$

Introduce dimensionless coordinates $\xi = \frac{x}{l}$ and $\eta = \frac{y}{b_1}$, then rewrite Eq. (2) as follows:

$$\left. \begin{aligned}
 \nabla_m^4 \bar{W} + \frac{m^2 p^2}{RD_{11}A_{22}} \frac{\partial^2 \bar{F}}{\partial \eta^2} &= 1 - \frac{\nu_1^3}{D_{11}} \frac{\partial \bar{W}}{\partial \xi}; \\
 \nabla_m^4 \bar{F} - \frac{m^2 l^2}{pR} \frac{\partial^2 \bar{W}}{\partial \eta^2} &= -\frac{l^2}{p^2} \frac{\partial^2 U}{\partial \xi^2}.
 \end{aligned} \right\} \tag{8}$$

Here, the differential operators $\nabla_m^4 \bar{W}$ and $\nabla_m^4 \bar{F}$ are written as:

$$\begin{aligned}
 \nabla_m^4 \bar{W} &= \frac{\partial^4 \bar{W}}{\partial \xi^4} + 4d_1 m \frac{\partial^4 \bar{W}}{\partial \xi^3 \partial \eta} + 2d_2 m^2 \frac{\partial^4 \bar{W}}{\partial \xi^2 \partial \eta^2} + 4d_3 m^3 \frac{\partial^4 \bar{W}}{\partial \xi \partial \eta^3} + d_4 m^4 \frac{\partial^4 \bar{W}}{\partial \eta^4}; \\
 \nabla_m^4 \bar{F} &= \frac{\partial^4 \bar{F}}{\partial \xi^4} + 2b_1 m \frac{\partial^4 \bar{F}}{\partial \xi^3 \partial \eta} + 2b_2 m^2 \frac{\partial^4 \bar{F}}{\partial \xi^2 \partial \eta^2} + 2b_3 m^3 \frac{\partial^4 \bar{F}}{\partial \xi \partial \eta^3} + b_4 m^4 \frac{\partial^4 \bar{F}}{\partial \eta^4},
 \end{aligned} \tag{9}$$



where

$$\begin{aligned} d_1 &= \frac{D_{16}}{D_{11}}; & d_2 &= \frac{D_{12} + 2D_{66}}{D_{11}}; & d_3 &= \frac{D_{26}}{D_{11}}; \\ d_4 &= \frac{D_{22}}{D_{11}}; & b_1 &= -\frac{A_{26}}{A_{22}}; & b_2 &= \frac{A_{12} + A_{66}}{A_{22}}; \\ b_3 &= -\frac{A_{16}}{A_{23}}; & b_4 &= \frac{A_{11}}{A_{22}} \end{aligned}$$

There are dimensionless stiffness parameters of the blade: $m = l/b_1$ is the geometric parameter of the blade; $\bar{W} = \frac{w}{p}$ and $\bar{F} = FA_{22}/p^2$ are the dimensionless values of the deflection and stress functions; and $p = ql^4/D_{11}$ is the load parameter.

The edges adjacent to the plates ($\eta_1 = k_1 m \xi + 1$ and $\eta_2 = \alpha \eta_1$) are stiffened, not constrained (i.e., edge displacement in the blade plane is possible). Here, $k_1 = tg\gamma_1$; $k_2 = tg\gamma_2$; and $\alpha = -\frac{k_2}{k_1} = -\frac{b_2}{b_1}$ are the geometric parameters of the blade.

Let us write the boundary conditions for the deflection function $\bar{W}(\xi, \eta)$ and the stress function $\bar{F}(\xi, \eta)$ for these edges as follows:

$$\begin{aligned} \bar{W} &= \frac{\partial \bar{W}}{\partial \eta} = 0; \\ \bar{F} &= \frac{\partial \bar{F}}{\partial \eta} = 0 \end{aligned} \tag{10}$$

For the input and output edges of the blade $\xi = 0$ and $\xi = 1$, the boundary conditions are written as follows:

$$\begin{aligned} \frac{\partial^2 \bar{W}}{\partial \xi^2} + (d_2 - 2d_3)m^2 \frac{\partial^2 \bar{W}}{\partial \eta^2} + d_1 m \frac{\partial^2 \bar{W}}{\partial \xi \partial \eta} &= 0; \\ \frac{\partial^3 \bar{W}}{\partial \xi^3} + 4d_1 m \frac{\partial^3 \bar{W}}{\partial \xi^2 \partial \eta} + (d_2 + 2d_5)m^2 \frac{\partial^3 \bar{W}}{\partial \xi \partial \eta^2} + 2d_3 m^3 \frac{\partial^3 \bar{W}}{\partial \eta^3} &= 0 \\ \frac{\partial^2 \bar{F}}{\partial \eta^2} &= -\frac{l^2 A_{22}}{m^2 p^2} U; \\ \frac{\partial^2 \bar{F}}{\partial \xi \partial \eta} &= 0 \end{aligned} \tag{11}$$

1.3 Two-Dimensional Boundary Value Problem and Its Solution

To solve the boundary value problem described by the system of equations in partial derivatives (8) and in boundary conditions (10) and (11), use Dorodnitsyn's method of integral ratios [3].

Pursuant to the method, write the original equation system (8) as a divergent system:

$$\frac{\partial \bar{X}}{\partial \xi} + \frac{\partial \bar{Y}}{\partial \eta} + \bar{L} = 0; \tag{12}$$

$$\bar{X} = \{X_i\} = \{\bar{u}, \bar{v}, \bar{w}, z_1, z_2, z_3, z_4, z_5\}$$

$$\bar{Y} = B_0 \bar{X} + B_1 \frac{\partial \bar{X}}{\partial \eta} + B_2 \frac{\partial^2 \bar{X}}{\partial \eta^2} + B_3 \frac{\partial^3 \bar{X}}{\partial \eta^3};$$

$$\bar{L} = B \bar{X} + \bar{b}.$$

Here, $B_r = \{b'_{mn}\}$ and $B = \{b_{mn}\}$ ($r = 0, 1, 2, 3; m, n = 1, 2, \dots, 8$) are elements of the transformation matrices.

Pursuant to the method of integral ratios, find a solution to the system of Eq. (12) as decomposition:

$$X_i(\xi, \eta) = \begin{cases} \sum_{j=1}^n X_{ij}(\xi) P_j(\xi, \eta) & (i = 3, 6, 7, 8) \\ \sum_{j=1}^n X_{ij}(\xi) P_{j,2}(\xi, \eta) & (i = 1, 2) \\ \sum_{j=1}^n X_{ij}(\xi) P_{j,22}(\xi, \eta) & (i = 4, 5) \end{cases} \tag{13}$$

Jacobi orthogonal-polynomial systems [4, 5] are used herein as approximating functions:

$$P_j(\xi, \eta) = P_1(\xi, \eta) \sum_{j=1}^n \left[\eta - \frac{(1 + \alpha)r}{2} \right]^{j-1}; \tag{14}$$

$$P_1(\xi, \eta) = \eta^4 - 2(1 + \alpha)r\eta^3 + (1 + 4\alpha + \alpha^2)r^2\eta^2 - 2\alpha(1 + \alpha)r^3\eta + \alpha^2r^4.$$

Here, $r = 1 + k_1 m \xi$ is the equation of the blade slope.

Note that the polynomials $P_j(\xi, \eta)$ in the segment $[r, \alpha r]$ meet the orthogonality conditions:

$$(P_i, P_k) = \int_r^{\alpha r} P_i P_k d\eta = 0 \quad \text{at } i \neq k. \tag{15}$$

They make a system of linearly dependent functions and meet the boundary conditions (10).



The constructed polynomials have another important property: Their first and second derivatives are also orthogonal. For proof, consider:

$$\cos(P_i, P_j) = \frac{(P_i, P_j)}{\|P_i\| \|P_j\|}. \quad (16)$$

Here, the polynomials P_i and P_j are analyzed as generalized vectors in a Hilbert space L_2 [4].

At specific values for polynomials (4), we obtain:

$$\cos(P_1, P_2) = 0; \quad \cos(P_{1,2}, P_{2,2}) = 0; \quad \cos(P_{1,22}, P_{2,22}) = 0,$$

which corresponds to 90° angles.

Also choose the polynomials $P_j(\xi, \eta)$ and their first derivatives as the weight functions:

$$P_j(\xi, \eta) = \begin{cases} P_j(\xi, \eta) & (i = 3, 6, 7, 8), \\ P_{j,2}(\xi, \eta) & (i = 1, 2, 4, 5). \end{cases} \quad (17)$$

Further apply the method of integral ratios to the original system of equations in partial derivatives (12) to obtain a system of ordinary differential equations, order $8n$, with variable coefficients, which are generally non-Euler.

1.4 Integrating the System of Differential Equations with Variable Coefficients

The obtained system of ordinary differential equations of an $8n$ -order problem with variable coefficients can be written in a Cauchy normal form:

$$\frac{dX_m}{d\xi} = \sum_{v=1}^s B_{v,m} X_v + f_m, \quad (m = 1, \dots, s). \quad (18)$$

Note that math offers no exact solution of such equations in general, except some special cases like the Bessel equation.

The boundary value problem is solved by the modified method of successive approximations, developed by Prof. V. A. Pukhliy and published by him in academic press [6, 7].

The method was further extended to apply to initial-boundary value problems [8, 9], which used the C. Lanczos's telescoping of power series to accelerate the convergence of the solution [10]. To that end, they used the option to write any power series in terms of misaligned Chebyshev polynomials [5, 10]. Such an approach was first presented in V. A. Pukhliy's papers [11, 12].

Pursuant to the method, let us write the variable coefficients $B_{v,m}$ and the constant terms f_m in terms of shifted Chebyshev polynomials:

$$f_m = \sum_{r=0}^q f_{m,r} (d_r \cdot r!)^{-1} \sum_{k=0}^r a_k T_k^*(\xi), \quad B_{v,m} = \sum_{r=0}^q b_{v,m,r} d_r^{-1} \sum_{k=0}^r a_k T_k^*(\xi). \quad (19)$$

Here, q is the degree of the interpolation polynomial; a_k are the coefficients of decomposing ξ^r in series by Chebyshev polynomials $T_k^*(\xi)$. In the expressions (19), $d_r = 1$ for $r = 0$ and $d_r = 2^{2r-1}$ for any other r .

General solution of the equation system (18) is written as [8, 9]:

$$X_m = \sum_{\mu=1}^s C_\mu \left[d_0^{-1} a_0 T_0^*(\xi) \delta + \sum_{n=1}^{\infty} X_{m,\mu,n} \right] + \sum_{j=0}^q t_{m,j,0} [d_{j+1} (j+1)!]^{-1} \sum_{k=0}^{j+1} a_k T_k^*(\xi) + \sum_{n=2}^{\infty} X_{m,n} \quad (20)$$

where $t_{m,j,0} = f_{m,r}$ at $j = r$; μ is the number of the basic function; C_μ are integration constants. In the solution (20), $\delta = 1$ if $m = \mu$ and $\delta = 0$ for the remaining μ .

First approximation $X_{m,\mu,1}$ is obtained by substitution of the zero approximation: $d_0^{-1} a_0 T_0^*(\xi) \delta$ in the right side of the system $\frac{dX_m}{d\xi} = \sum_{v=1}^s B_{v,m} X_v$.

The next approximations are done by the formulae:

$$X_{m,\mu,n} = \sum_{j=1}^{\beta} t_{m,\mu,n,j} [d_{n+j-1} (n+j-1)!]^{-1} \sum_{k=0}^{n+j-1} a_k T_k^*(\xi); \quad (21)$$

$$X_{m,n} = \sum_{j=1}^{\beta} t_{m,n,j} [d_{n+j-1} (n+j-1)!]^{-1} \sum_{k=0}^{n+j-1} a_k T_k^*(\xi),$$

where $\beta = n (q + 3) - 2$.

The systems of basic functions (21) are uniformly converging series, whereby the coefficients $t_{m,\mu,n,j}$ and $t_{m,n,j}$ are found from the coefficients of the previous approximation by recurrent formulae:

$$t_{m,\mu,n,j} = \sum_{v=1}^s \sum_{r=0}^q b_{v,m,r} t_{v,\mu,n-1,j-r} (n+j-1)^{-1} \prod_{\gamma=0}^r (n+j-1-\gamma),$$

$$t_{m,n,j} = \sum_{v=1}^s \sum_{r=0}^q b_{v,m,r} t_{v,n-1,j-r} (n+j)^{-1} \prod_{\gamma=0}^r (n+j-\gamma).$$

The constants C_μ , being part of the general solution (20), are found from the boundary conditions of the input and output edges of the blade (11).

Calculation Example. A numerical implementation has been programmed according to the analytical solution above. Computations were run for an orthotropic material of a blade where the principal elastic symmetry axes are turned by an angle φ against the blade axes ξ, η .

Here are the initial impeller data: $R_2 = 400$ mm; $R_1 = 276$ mm; $n = 1600$ rpm; $\beta_1 = 0.6$ rad; $\beta_2 = 0.87$ rad; for the blade: $l = b_1 = 200$ mm; $h = 5$ mm; $R_s = 500$ mm; $\gamma_1 = 0.3$ rad; $\gamma_2 = 0$. The impeller is made of KACT-B fiberglass that has the following physical and mechanical properties: $E_1 = 21.5 \times 10^4$ kG/cm²; $E_2 = 12.3 \times 10^4$ kG/cm²; $G = 2.1 \times 10^4$ kG/cm²; $\nu_1 = 0.19$; $\nu_2 = 0.11$.

Figure 3 presents the results of computing the dimensionless stresses $\bar{\sigma}_\eta$ in three blade sections: the input edge, the median part and the output edge. The values $\bar{\sigma}_\eta$ are found as the total of membrane and bending stresses:

$$\bar{\sigma}_\eta = \frac{hp}{D_{11}A_{22}} \cdot \frac{\partial^2 \bar{F}}{\partial \xi^2} - 6 \left[d_4 m^2 \frac{\partial^2 \bar{W}}{\partial \eta^2} + (d_2 - 2d_5) \frac{\partial \bar{W}}{\partial \xi^2} 2d_3 m \frac{\partial^2 \bar{W}}{\partial \xi \partial \eta} \right]$$

As can be seen, the most stressed part of the blade is its output edge.

We also studied how deflection and power factors were affected by the anisotropy resultant from the principal elasticity axes of the orthotropic material mismatching the computed axes of the blade. Figure 4 shows the dimensionless maximum principal stress \bar{S} in the blade center as a function of the parameter φ . As can be seen in the figure, the correlation between maximum principal stresses and this parameter is significant. It is therefore important to take into account the anisotropy that occurs due to the principal axes of the elastic orthotropic material not matching the computed axes of the blade.

Fig. 3 Distribution of dimensionless stresses $\bar{\sigma}_\eta$ on the orthotropic blade of a radial supercharger

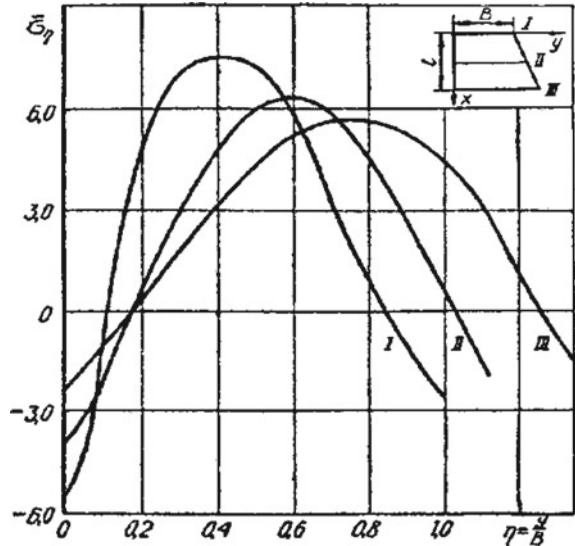
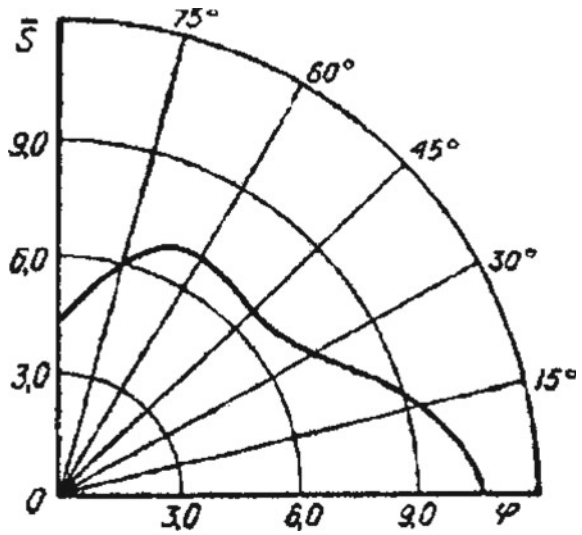


Fig. 4 Changes in the maximum principal stresses $\bar{\sigma}$ in the center of a trapezoidal blade as a function of the parameter φ



2 Conclusion

- There have been developed a mathematical model and an algorithm to compute the stress–strain state of polymeric centrifugal-pump impeller blades.
- Solution of the boundary value problem for elliptic equations is based on using a modified method of successive approximations devised by Prof. V. A. Pukhliy and published by him in Academic Press.
- The finding of the analysis is that it is necessary to take into account the anisotropy that occurs due to the main axes of the elastic orthotropic material not matching the computed axes of the blade.

Acknowledgements Research has been funded by RFBR and the City of Sevastopol under Research Project No. 18-48-920002.

References

1. Hambarzumyan SA (1974) General theory of anisotropic shells. Nauka, Moscow, p 446
2. Marguerre K (1939) Zur Theorie der gekrümmten Platte großer Formänderung.—Jahrbuch 1939 der deutschen Luftfahrtforschung 1:413–418
3. Dorodnitsyn AA (1960) One method to solve equations of laminar boundary layer. J Appl Math Technol Phys 3:111–118
4. Courant R, Hilbert D (1953) Methods of mathematical physics, vol I. Gostekhizdat, Moscow
5. Luke VL (1975) Mathematical functions and their approximations. Academic Press Inc., New York, p 608

6. Pukhliy VV (1978) Method for analytical solution of 2D boundary-value problems for elliptic-equation systems. *J Comput Math Math Phys* 18(5):1275–1282
7. Pukhliy VA (1979) One approach to solve boundary-value problems of mathematical physics. *Differ EquS* 15(11):2039–2043
8. Pukhliy VA (2015) Solving initial-boundary value problems of mathematical physics by modified method of successive approximations. *Differ EReview Appl Ind Math* 22(4): 493–495
9. Pukhliy VA (2016) Accelerating the convergence of solutions when using modified method of successive approximations. *Rev Appl Ind Math* 23(4):17–20
10. Lanczos C (1961) Practical methods of applied analysis. Fizmatgiz, Moscow, p 524
11. Pukhliy VA (1983) Analytical method to solve boundary-value shell theory problems. In: Proceedings of the XIII all-Sovient conference on plates and Shells theory. Part IV. TPU Publ, Tallinn, pp 101–107
12. Pukhliy VA (1986) Cylindrical three-layer panel oblique-angled in plane: modified method of successive approximations to solve its bending problem. *Appl Mech* 22(10):62–67

Vibration Isolating and Impact Protecting Systems with Quasi-Zero Stiffness Providing Wide Operating Area



A. Zotov and A. Valeev

Abstract This study presents systems with quasi-zero stiffness. The interest in these systems has been constantly increasing recently. In most of the systems with quasi-zero stiffness, the force characteristic with quasi-zero stiffness is obtained due to the combination of systems with negative and systems with positive stiffness. Generally, the length of the working sections of such systems is small and less than few centimeters. The well-known systems with quasi-zero stiffness are observed, main advantages and disadvantages are discussed, and a new classification is presented. Also, this study demonstrated how to upgrade a pneumatic spring into a system with quasi-zero stiffness for increasing their vibration isolating and impact protection properties. For modifying force characteristics of standard pneumatic spring, it is offered to use a pack of Belleville springs. The advantage of such a pneumatic spring with quasi-zero stiffness is the absence of the necessity of its major modifications. Analytical calculations are made for proving such an idea.

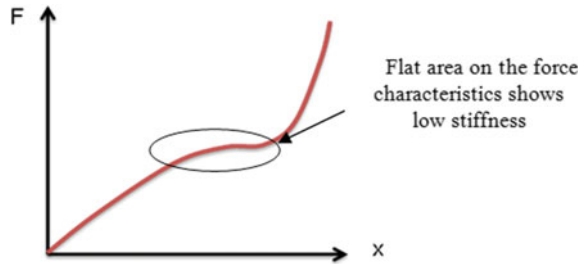
Keywords Quasi-zero stiffness · Vibration

1 Introduction

Modern world is characterized by great amount of various high power machines. They produce noise and vibration, which harmfully influence on objects around them: other machines, buildings, and humans. This problem can be solved via vibration isolation. Usually, vibration isolator is just an elastic element like rubber or metal spring. From mechanical point of view, usual vibration isolators have linear force characteristic. Disadvantage of these isolators is well-known: it is difficult to obtain low natural frequency, i.e., high vibration isolating properties. Another way to design vibration isolators is to use nonlinear force characteristics. In

A. Zotov (✉) · A. Valeev
Ufa State Petroleum Technological University, 1, Kosmonavtov Street,
Ufa 450062, Russian Federation
e-mail: a-zot2@yandex.ru

Fig. 1 Force characteristic of mechanical system with quasi-zero stiffness



the case of almost horizontal nonlinear force characteristics at one point (i.e., vibration isolator has almost zero stiffness), it is said that vibration isolator has quasi-zero stiffness. Such mechanical system is called “system with quasi-zero stiffness.” Sometimes they are also called as “systems with low stiffness” or “systems with high-static-low-dynamic stiffness” [1, 2].

The principle sketch of force characteristic of system with quasi-zero stiffness is presented in Fig. 1.

Vibration isolators with quasi-zero stiffness are characterized by high-static load and low-dynamic stiffness. These properties allow isolating wide range of vibration with high efficiency. But disadvantage of these vibration isolators is complexity in designing and manufacturing.

Note stiffness of elastic element with linear force characteristics can be reduced via parallel connection of elements with negative stiffness. Such an element can be also named as stiffness compensator, stiffness corrector, or bistable element. These elements usually have more than one stable state.

Despite a big number of various systems and prototypes with quasi-zero stiffness, it is suggested by authors that vibration isolators with quasi-zero stiffness (or generally systems with quasi-zero stiffness) can be divided into four types.

2 Classification of Systems with Quasi-Zero Stiffness

The first type obtains one or few supporting elastic elements and parallels to it stiffness compensator.

The main idea here is the following: supporting elastic element has positive stiffness, and stiffness compensator has negative stiffness. Parallel connection leads to addition of values of stiffness, and at a certain condition, overall stiffness becomes zero.

General view of such a system is presented in Fig. 2. On the left side of Fig. 2, system without a load is shown; on the right side, the system at working point is presented.

Such a system was suggested by Alabuzhev. Supporting elastic element usually is a metal spring. Rarely, it is presented by a pneumatic spring. Compensator can be

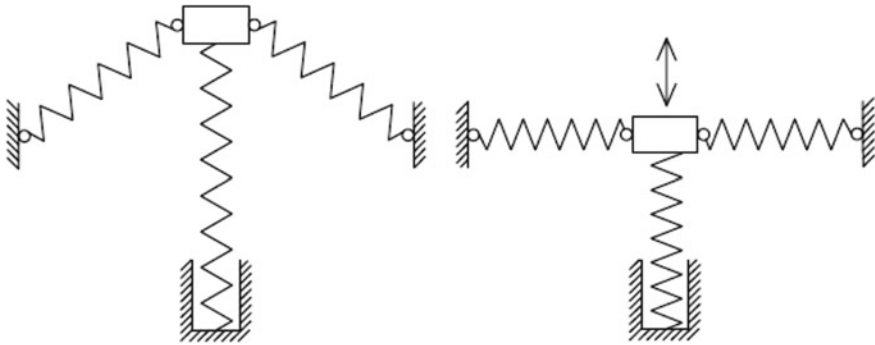


Fig. 2 General view of systems with quasi-zero of the first type: supporting elastic elements with stiffness compensator

various: inclined spring in the case of Alabuzhev system [1, 2], bistable plate in the case of system offered by Carrella [3–5], “scissor-like” system [6], beams or Belleville spring in pre-buckling condition.

The second type has main element that simultaneously has properties of supporting elastic element and stiffness compensator, i.e., nonlinear force characteristics are created by only one element (Fig. 3). It obtains element with complex structure that has pre-buckling condition at a certain point.

Construction of a dome type is described in [7]. Also, this type is suitable for designing so-called metamaterial with quasi-zero stiffness [8, 9]. Another way to provide quasi-zero stiffness is to use honeycomb structure [10–12].

Advantage of such type is compactness, but it usually suffers from relaxation or creep effects. Due to these problems, the whole system may become unset.

The third type has elastic elements that move along a guide with special shape. This shape provides the defined force characteristics. Advantage of this type is possibility to get various force characteristics, particularly with very wide zone with quasi-zero stiffness. Disadvantages of such a system are complexity and high friction. An example of such a system is presented in Fig. 4. There is a cam of special shape that provides quasi-zero stiffness. Such a system, like in Fig. 4, was suggested by Alabuzhev [1].

The fourth type presents a huge number of active and semi-active systems with quasi-zero stiffness. Usually, there are supporting elastic elements and different active elements that create force opposite to the direction of movement at vibration (Fig. 5). The most evident way is to use electromagnet as a stiffness compensator.

Fig. 3 General view of systems with quasi-zero of the second type: one element providing properties of supporting element and stiffness compensator

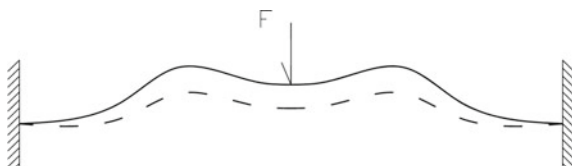


Fig. 4 General view of systems with quasi-zero of the third type: one element moves along a guide

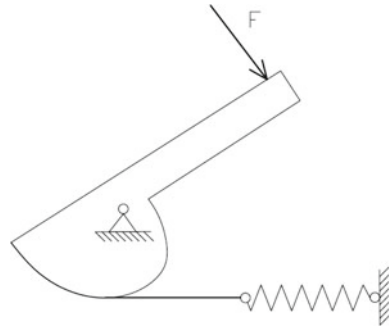
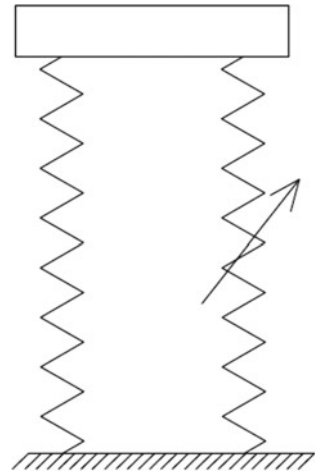


Fig. 5 General view of systems with quasi-zero of the fourth type: active and semi-active systems



Seat suspensions with semi-active devices are proposed by Choi et al. [13, 14]. Electromagnetic linear actuators are used by Gan et al. [15]. Electric servomotor with a ball screw mechanism as the active seat suspension actuator is used by Kawana and Shimogo [16]. Electromagnetic systems are presented by Robertson et al. [17]. Systems with quasi-zero stiffness controlled by rotor drive are presented by Ning et al. [18]. Also, a vibration isolator with high-static-low-dynamic stiffness is made by Zheng et al. [19]. It is implemented by connecting a negative stiffness magnetic spring in parallel with membranes springs to cancel its positive stiffness. The isolator consists of two coaxial ring magnets that are axially magnetized and their magnetization directions are the same. Quasi-zero stiffness can be also obtained with the help of off-road seat suspension system using intelligent active force control [20]. Note active systems with quasi-zero stiffness are usually rather expensive.

Each type of systems with quasi-zero stiffness has advantages and disadvantages that are shown in Table 1, so it is hard to conclude what type is better.

Table 1 Comparison of various types of systems with quasi-zero stiffness

Property	Type 1	Type 2	Type 3	Type 4
General description	Supporting elastic element + stiffness compensator	One supporting element in pre-buckling condition	Elastic elements move along guides with special shape	Active and semi-active systems: (e.g., supporting elastic element + electromagnetic stiffness compensator)
Dimensions	Big	Small	Usually big	Usually big
Width of zone with quasi-zero stiffness	Small	Small	Big	Tiny
Potential for wide broad manufacturing	Medium	Big	Low	Depend on design
Potential vibration isolating coefficient relative to other systems with quasi-zero stiffness	High	Medium	Low	High
Disadvantages	Usually need stabilizers/ guides	Relaxation, and creep effects	High friction	Active system with power consumption; expensive

Note all author's comments are subjective and may not correspond to some designs of other researches

3 Developing of Systems with Quasi-Zero Stiffness Based on Pneumatic Spring with a Help of Belleville Springs

In various industries, pneumatic spring is used. Sometimes, they are used as vibration isolators or shock absorbers. From practical point of view, it is possible to upgrade them into systems with quasi-zero stiffness for increasing their vibration isolating/absorbing properties. So, further a pneumatic spring with stiffness compensator presented by Belleville springs is shown.

According to this idea, Belleville springs are installed into pneumatic spring (Fig. 6). Outer diameter of Belleville springs is a bit less than inner diameter of the pneumatic spring. Usually, Belleville springs have low maximum compression, but application of a number of them allows removing this disadvantage.

Connection of pneumatic and Belleville springs is parallel, so total restoring force of the upgraded pneumatic spring equals to sum of restoring forces of the pneumatic spring (F_p) and Belleville springs (F_B):

$$F = F_p + F_B.$$

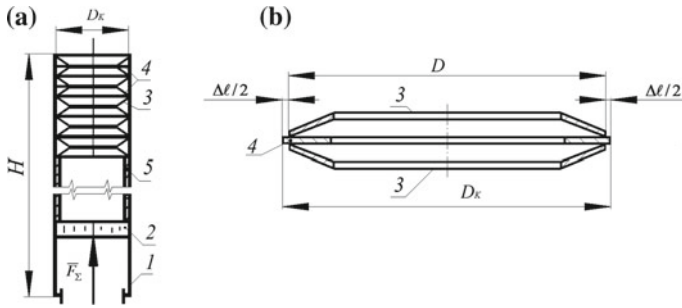


Fig. 6 Proposed pneumatic spring with Belleville springs: 1—cylinder; 2—piston; 3—Belleville springs; 4—shim; and 5—sleeve

Restoring force of the pneumatic spring equals

$$F = p_0 \cdot S_0 \cdot H^n / (H - x)^n$$

Here, the following descriptions are used: p_0 —initial pressure in the pneumatic spring; S_0 —square of the piston; H —length of the piston; x —displacement of the piston (Fig. 7); n —polytropic index. Polytropic index can be $n = 1.15$ – 1.35 for various gases.

Restoring force of Belleville spring according to [21] equals

$$F_B = 8 \cdot \pi \cdot E \cdot s \cdot x \frac{\left\{ (f - x) \cdot (f - (x)/2) \cdot \left[\frac{(D+d)}{2 \cdot (D-d)} - \frac{1}{\ln(D/d)} \right] + s^2 \cdot \ln\left(\frac{D}{d}\right) / 12 \right\}}{(D - d)^2}$$

Here, the following descriptions are used: E —Young’s modulus of material of the Belleville spring; s —thickness of the cone; f —the height of the Belleville spring; D —outer diameter of the Belleville spring; d —inner diameter of the Belleville spring.

Fig. 7 Description of the pneumatic spring

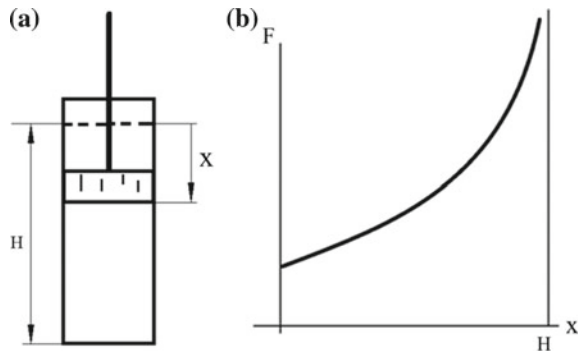
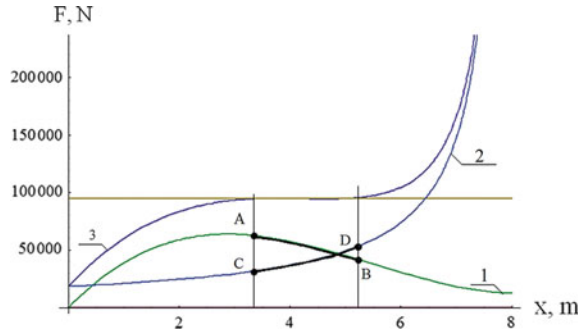


Fig. 8 Total force characteristic of the upgraded pneumatic spring without taking into account volume change inside it: 1—force characteristic of Belleville springs package; 2—force characteristic of pneumatic spring; and 3—total force characteristic



Total restoring force equals:

$$F = \frac{p_0 \cdot \left(\frac{\pi \cdot D^2}{4}\right) \cdot H^n}{(H - x)^n} + 8\pi E s \left(\frac{x}{N}\right) \frac{\left\{ \left(f - \frac{x}{N}\right) \cdot \left(f - \left(\frac{x}{N}\right)/2\right) \cdot \left[\frac{(D+d)}{2 \cdot (D-d)} - \frac{1}{\ln(D/d)}\right] + s^2 \cdot \ln\left(\frac{D}{d}\right)/12 \right\}}{(D - d)^2}$$

Figure 6 shows the dependencies obtained without taking into account the change in volume of the pneumatic spring due to Belleville springs and sleeves. If the sections AB and CD (Fig. 8) are added, an area with quasi-zero stiffness is obtained. The force characteristic is obtained due to the following parameters: $D = 0.056$ m; $d = 0.047$ m; $s = 0.002$; $H = 8$ m; $f = 0.005$ m; $N = 1100$; $p_0 = 7.5$ MPa.

Actually, Belleville springs reduce volume inside the pneumatic spring and change its force characteristics. Volume of one Belleville springs can be estimated as

$$V_* = s \cdot \frac{\pi(D^2 - d^2)}{4} + \delta \cdot \frac{\pi(D^2 - d^2)}{4}$$

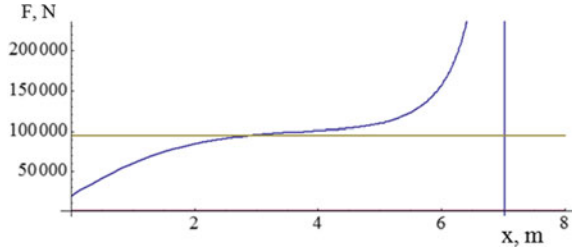
Here, δ —thickness of sleeve.

Restoring force of the pneumatic spring with taking into account volume change inside it equals:

$$F = S_0 \cdot p_0 \cdot \frac{(S_0 \cdot H - N \cdot V_*)^n}{((H - x) \cdot S_0 - N \cdot V_*)^n}$$



Fig. 9 Total force characteristic of the upgraded pneumatic spring with taking into account volume change inside it



Hence, total restoring force of the upgraded pneumatic spring with taking into account volume change inside it equals:

$$F = \frac{p_0 \cdot \left(\frac{\pi \cdot D^2}{4}\right) \cdot \left(H \cdot \left(\frac{\pi \cdot D^2}{4}\right) - N \cdot V_*\right)^n}{\left(\left(H - x\right) \cdot \left(\frac{\pi \cdot D^2}{4}\right) - N \cdot V_*\right)^n} + \frac{8\pi E s}{N} \frac{x \left\{ \left(f - \frac{x}{N}\right) \cdot \left(f - \left(\frac{x}{N}\right) / 2\right) \cdot \left[\frac{(D+d)}{2 \cdot (D-d)} - \frac{1}{\ln(D/d)}\right] + s^2 \cdot \ln\left(\frac{D}{d}\right) / 12 \right\}}{(D-d)^2}$$

So, the force characteristic of upgraded pneumatic spring looks like at Fig. 9.

As we can see from Figs. 8 and 9, taking into account volume change due to Belleville springs only slightly modifies force characteristic. Note that stiffness is slightly increased.

4 Conclusions

As a conclusion, it should be noted that obtaining quasi-zero stiffness for pneumatic springs can be easily provided via Belleville springs. It requires no significant modification of pneumatic springs. Moreover, it does not change its dimensions or technology of application. So, vibration isolators and shock absorbers with quasi-zero stiffness can be obtained via the discussed method.

Acknowledgments The reported study was funded by The Ministry of Education and Science of the Russian Federation according to the research project MK-2965.2018.8.

References

1. Alabuzhev PA, Gritchin L, Kim L, Migirenko G, Chon V, Stepanov P (1989) Vibration protecting and measuring systems with quasi-zero stiffness. Hemisphere Publishing, New York
2. Carrella A (2008) Passive vibration isolators with high-static-low-dynamic-stiffness. Ph.D. thesis, University of Southampton, UK



3. Carrella A, Friswell MI (2008) A passive vibration isolator incorporating a composite bistable plate. In: Proceedings of 6th European nonlinear dynamics conference, Saint Petersburg (Russia), 30 June-4 July 2008
4. Carrella A, Brennan M, Waters TP (2007) Static analysis for a passive vibration isolator with quasi-zero stiffness characteristic. *J Sound Vib* 301(3-5):678-689
5. Carrella A, Brennan M, Waters TP (2007) Optimization of a quasi-zero-stiffness isolator. *J Mech Sci Technol* 21:946-949
6. Sun X, Xu J, Jing X, Cheng L (2014) Beneficial performance of a quasi-zero-stiffness vibration isolator with time-delayed active control. *Int J Mech Sci* 82:32-40
7. Valeev AR, Zotov AN, Kharisov S (2015) Designing of compact low frequency vibration isolator with quasi-zero stiffness. *J Low Freq Noise, Vib Act Control* 34(4):459-474 (Multi-Science Publishing Company Ltd.)
8. Valeev AR (2017) Numerical and experimental analysis of metamaterials with quasi-zero effect for vibration isolation. *AIP Conf Proc* 1859:020061
9. Valeev AR (2017) Vibration isolating metamaterial with arc-structure. *IOP conference proceedings* 225:012142
10. Correa DM, Seepersad CC, Haberman MR (2015) Mechanical design of negative stiffness honeycomb materials. *Integr Mater Manuf Innov* 4:10
11. Correa DM, Klatt TD, Cortes SA, Haberman MR, Kovar D, Seepersad CC (2015) Negative stiffness honeycombs for recoverable shock isolation. *Rapid Prototyp J*
12. Wang Z, Zhang Q, Zhang K, Hu G (2016) Tunable digital metamaterial for broadband vibration isolation at low frequency. *Adv Mater*
13. Choi SB, Han YM (2007) Vibration control of electrorheological seat suspension with human-body model using sliding mode control. *J Sound Vib* 303:391-404
14. Choi SB, Nam MH, Lee BK (2000) Vibration control of a MR seat damper for commercial vehicles. *J Intell Mater Syst Struct* 11:936-944
15. Gan Z, Hillis AJ, Darling J (2015) Adaptive control of an active seat for occupant vibration reduction. *J Sound Vib* 349:39-55
16. Kawana M, Shimogo T (1998) Active suspension of truck seat. *Shock Vib* 5:35-41
17. Robertson W, Wood R, Cazzolato B, Zander A (2006) Zero-stiffness magnetic springs for active vibration isolation. In: Proceedings of the 6th international symposium on active noise and vibration control, Cairns (Australia), 9-12 July 2007
18. Ning D, Sun S, Zhang J, Du H, Li W, Wang X (2016) An active seat suspension design for vibration control of heavy-duty vehicles. *J Low Freq Noise Vib Act Control* 4(35):264-278
19. Zheng Y, Zhang X, Luo Y, Yan B, Ma C (2016) Design and experiment of a high-static-low-dynamic stiffness isolator using a negative stiffness magnetic spring. *J Sound Vib* 360:31-52
20. Gohari M, Tahmasebi M (2014) Active off-road seat suspension system using intelligent active force control. *J Low Freq Noise Vib Act Control* 34(4):475-490
21. Andreeva LE (1981) Elastic elements of devices. *Mashinostroenie, Moscow*

Locating of Oscillating Defect in Rotary Equipment via Remote Strain Gauge Analysis



A. Valeev and A. Tokarev

Abstract The study is devoted to improve the reliability of diagnosing the technical condition of rotary equipment. Nowadays different methods of diagnostics of equipment are used, but the currently applied methods do not allow enough reliable determining defects, because the methods of non-destructive testing use indirect and expert methods of their identification. Moreover, methods usually are focused on some type of defect or a certain part of equipment, so they do not allow identifying any defect. In this study, it is proposed to use an approach to determine the position of the defect according to strain gauges located on the supports of the unit. Information about the location of the defect, together with information about the frequency and intensity of the defect oscillations, allows identifying this defect with high reliability. The fundamentals of the calculation scheme and mathematical model, which allow determining the vertical and horizontal coordinates of the defect by analyzing the dynamic reactions on the supports and phase delays, are presented.

Keywords Diagnostics · Strain gauge · Tensometry · Mathematical modeling · Rotary equipment

1 Introduction

Many industries apply powerful energy-intensive machines that need constant high reliable maintenance. Failure of critical equipment due to not detection a defect can lead to an emergency, as well as additional costs for repairs, costs of downtime, etc.

Exploitation of machines with defects leads to their non-optimal work and causes loads in them. It increases operating temperatures, noise levels, and rates of wear. It all leads to:

A. Valeev (✉) · A. Tokarev
Ufa State Petroleum Technological University, 1, Kosmonavtov Street,
Ufa 450062, Russia
e-mail: anv-v@yandex.ru

- increased energy consumption;
- reduced operational efficiency;
- shortened component life (premature failure) [1].

Reliable and efficient operation of machines and equipment needs careful diagnostics of their technical condition. Careful and forehanded diagnostic reduces the cost of repair and maintenance and also increase durability and reliability of equipment [2].

The idea of any diagnostics is the fact that defect changes some operating parameters of equipment and machines, so some quantitative and qualitative characteristics can be measured. Knowledge of statistical material on the relationship between the characteristics of diagnostic parameters and the state of the object for each type of equipment allows to create different diagnostic methods.

So of these diagnostic methods are better and more reliable, some of them are less. In this study, the method of remote tensometric analysis of dynamic loads on equipment support is presented.

2 Defect Detection and Identifying for Rotary Equipment

The following list includes the main condition monitoring methods applied for rotary equipment [3]:

- vibration analysis;
- overall vibration level control;
- lubricant analysis;
- acoustic emission (airborne ultrasound);
- infrared thermography;
- ultrasound testing;
- motor condition monitoring and motor current signature analysis;
- model-based voltage and current systems;
- parametric diagnostics.

Parametric diagnostics of rotary equipment is a control of such parameters as temperature, pressure, power, energy characteristics, efficiency, etc. Deviation of the current parameters or tendency of their change can be controlled. This method is used both at the initial stage of the unit operation, in order to reveal defects of the factory character, installation and repair, and during the period of operation for timely detection and assessment of the reasons for the degradation of the operating parameters of equipment [2].

Based on operating experience, this method allows indirectly identifying some defects, but a detailed analysis of defects cannot be made. At the same time, if the parametric diagnostics of equipment contribute to the achievement of more economical operating parameters, then the vibration one first of all solves the problem

of increasing the reliability of equipment, making it possible to identify specific defects on the basis of frequency analysis.

Vibration analysis of equipment is based on comparing the values of vibration at a given time with the maximum allowable values and estimating the rate of change of vibration in two operating time intervals. Current vibration values are processed using statistical analysis methods. As a controlled parameter of vibration, the root-mean-square value of vibration velocity is established. Vibration diagnostics solve the problem of identifying the causes of an increased level of vibration of the aggregates and the detection of hidden structural defects. This is the main method of monitoring the technical state of the machines [4].

Depending on the tasks vibration diagnostics can be of the first, second, and third levels:

The first level is the assessment of the state of the unit as a whole, the correlation of the state of the unit (by vibration level) to one of the predetermined states: “good,” “satisfactory,” “acceptable,” and “unacceptable.” Diagnosing at this level is to compare the measured vibration levels with the vibration levels set by standards and technical documentation. In this case, the root-mean-square value of the vibration velocity is compared with the threshold values for various types of machines, depending on their power and technical condition zones; that is, they can only be used for the purposes of vibration protection for critical defects.

The second level is the assessment of the state of equipment is based on the results of frequency analysis and allows indirectly detection defects.

The third level is prediction of the technical condition of equipment, determination of the residual resource, and planning of the next service time.

Regulatory levels of vibration intensity of oil main pumps are presented in the regulatory documentation [5]. Control points are strictly defined (bearing units, housing, and support). Norms for electric motors are presented [6–8]. Other norms can be seen in [9–13].

To identify the causes of vibration of equipment a spectral method of analyzing vibration signals is mainly used, that is based on the primary Fourier transform. The advantage of the analysis in frequency bands with a relatively constant width is the possibility of representing a wide frequency range on a single graph with a rather narrow resolution at low frequencies. The resolution in the high-frequency region decreases at increasing of frequency [14].

Also, this transformation has certain disadvantages: due to the loss of information about the time factor, the idea of the dynamics of changes in the spectral composition of the signal is distorted, which does not allow for a comprehensive analysis of the vibration signal. In some cases, this leads to the impossibility of unambiguously identifying defects leading to frequency and amplitude modulation of the vibration signal, such as violation of the bearing lubrication conditions, bending deformation of the impeller, and there are difficulties in identifying hidden defects and separating the main faults that have similar diagnostic signs. The spectrum of the vibration signal, in addition, inevitably includes the frequencies of

various noises, noise, and resonance phenomena; it is possible to contribute to the overall spectrum of other sources of vibration. Under the influence of noise, induced oscillations and other polyharmonic processes, useful signals can easily get lost at those frequencies at which defects manifest themselves most clearly. Therefore, the risk of missing a defect is large enough.

The other diagnostic method is lubricant analysis. It is known that tribodiagnostics of friction pairs is ahead of the effectiveness of vibration diagnostics and thermography. Lubricant analysis provides reliable information on the technical condition of bearings, seals, lubrication status, additive performance, presence of ferromagnetic (metal) and non-ferromagnetic inclusions, watering, viscosity parameters, and lubricant quality. However, due to non-full range of diagnosable defects, this method can be used as the main one [15].

Methods of diagnostics of an electric motor by electric parameters and electromagnetic fields allow to fully analyze the state of the electric motor and some general parameters of the whole unit (e.g., imbalance). However, the other part of equipment can be analyzed [16].

Thus, at the moment there is no method that allows to sufficiently reliably and objectively to identify defects in rotary equipment. Existing methods use an indirect definition of defects based on equipment operating experience. In particular, therefore, they are very poorly fed automation [17]. Also at the moment there are no methods allowing to determine the position of the defect in space, identify the defect, and find out the degree of its danger not on the basis of experimental or empirical data, but on the basis of accurate and fundamental analysis [18, 19].

3 The Concept of Using Remote Strain Gauging for Detecting and Determining the Location of Defects of Rotary Equipment

The authors are investigating the method that allows to reliably identify a defect of rotary equipment via remote strain-gauge signal analysis. The method is based on the following. Strain gauges are located under the supports of the rotary equipment (Fig. 1). Strain gauges with amplifiers and microcontroller allow determining dynamic reactions to the supports in real time. If it is not possible to install them, strain gauges can be glued on the supports or equipment frame. It slightly increases error but such an installation is valid. Note, the application of strain gauges is rather convenient [20].

The thesis is used that the equipment is made of steel, therefore, equipment may be considered as an absolutely rigid body. Hence, the dynamic force from oscillating defects and parts is completely and without loss transfers to equipment supports and strain gauges. So, a very important advantage of this method is very accurate initial data for diagnosis.

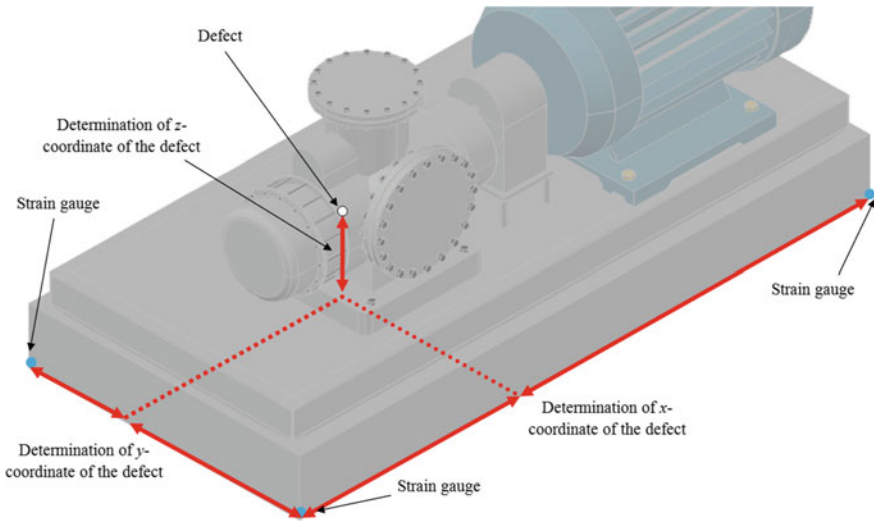


Fig. 1 General scheme for determining the location of a defect

Next, an analysis of reaction forces on supports is made, which allows to obtain a spectrum of dynamic forces and a spectrum of phases of reaction changes. Based on the developed spatial mathematical model, it is possible to obtain the exact position of the sources of oscillation, in other words, to determine the coordinate of the defect in space, both the location in the horizontal plane (in two horizontal coordinates) and the vertical coordinate. Information about the location of the defect, its frequency and vibration intensity allows to fully and accurately identify the defect and determine the degree of its danger.

Below the basics of mathematical model for determining the location via measurement of dynamic loads on supports are presented.

4 Mathematical Modeling of the Concept of Using Remote Strain Gauging for Detecting and Determining the Location of Defects of Rotary Equipment

Consider the design scheme presented in Fig. 2. According to it, the equipment with a source of oscillations is located on supports and is presented in a projection on the vertical plane.

The center of mass is located at the point O. The defect is located at the point D and creates a disturbing force F , the vector of which rotates counterclockwise, with a frequency ω . Geometric parameters are shown in Fig. 2.



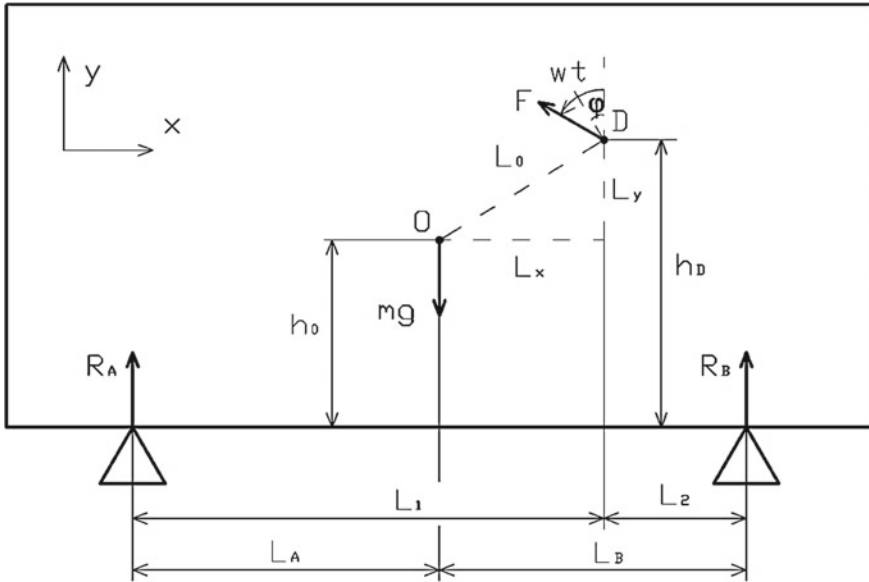


Fig. 2 Calculation scheme for determining the dynamics of equipment on supports under the action of a defect

Having considered the general equation of the movement of equipment in the plane of impact of a defect in the projections on the vertical axis y and the equation of moments relative to the center of mass of the equipment (point O), we can come to the following pair of equations describing the dynamic components of the reaction of supports $\Delta R_A(t)$ and $\Delta R_B(t)$ from time t :

$$M\ddot{y}_0(t) = \Delta R_A(t) + \Delta R_B(t) + F \cos(\omega t) \quad (1)$$

$$I\ddot{\phi}_0(t) = \Delta R_B(t) \cdot L_B - \Delta R_A(t) \cdot L_A + F \cdot L_0 \cos(\omega t - \phi) \quad (2)$$

Then it is necessary to analyze the amplitude values of the dynamic reactions of the supports. It is accepted that the equipment is connected to the supports rigidly. Equations based on the averaged values are the following.

$$0 = \Delta R_A(t) + \Delta R_B(t) + F \cos(\omega t) \quad (3)$$

$$0 = \Delta R_B(t) \cdot L_B - \Delta R_A(t) \cdot L_A + F \cdot L_0 \cos(\omega t - \phi) \quad (4)$$

The transformations allow obtaining the horizontal coordinates of the defect in the presented calculation scheme determined by the distance L_1 :

$$L_1 = \frac{\Delta R_B}{\Delta R_A + \Delta R_B} L \quad (5)$$

Then the dynamics of the equipment for estimation the vertical coordinate will be analyzed.

The displacement of the supports is denoted by y_A and y_B , and the stiffness of the supports, respectively, k_A and k_B . In this case, the dynamic reactions of the supports equals to:

$$\Delta R_A(t) = -k_A y_A \quad (6)$$

$$\Delta R_B(t) = -k_B y_B \quad (7)$$

When the supports are shifted, in other words, when y_A and y_B change, the vertical position of the center of mass changes. The elevation of the center of mass is defined as:

$$y_0 = \frac{y_A L_B + y_B L_A}{L_A + L_B} \quad (8)$$

Rotation of equipment relative to a point due to swinging on supports is defined as

$$\phi_0 = \frac{y_B - y_A}{L_A + L_B} \quad (9)$$

In this regard, the equations of motion of equipment on supports equal

$$M \frac{\ddot{y}_A L_B + \ddot{y}_B L_A}{L_A + L_B} = -k_A y_A - k_B y_B + F \cos(\omega t) \quad (10)$$

$$I \frac{\ddot{y}_B - \ddot{y}_A}{L_A + L_B} = -k_B y_B \cdot L_B + k_A y_A \cdot L_A + F \cdot L_0 \cos(\omega t - \phi) \quad (11)$$

So, it leads to

$$y_A = \sqrt{a_1^2 + a_2^2} \cos(\omega t - \alpha) \quad (12)$$

$$y_B = \sqrt{b_1^2 + b_2^2} \cos(\omega t - \beta) \quad (13)$$

where

$$a_1 = F \frac{k_B L_B (L_A + L_B) - I \omega^2 - L_0 (k_B (L_A + L_B) - L_B M \omega^2) \cos \phi}{k_A k_B (L_A + L_B)^2 - (k_A + k_B) (I + L_A L_B M) \omega^2 + I M \omega^4} \quad (14)$$

$$a_2 = -F \frac{L_0 (k_B (L_A + L_B) - L_B M \omega^2) \sin \phi}{k_A k_B (L_A + L_B)^2 - (k_A + k_B) (I + L_A L_B M) \omega^2 + I M \omega^4} \quad (15)$$

$$b_1 = F \frac{k_A L_A (L_A + L_B) - I \omega^2 - L_0 (k_A (L_A + L_B) - L_A M \omega^2) \cos \phi}{k_A k_B (L_A + L_B)^2 - (k_A + k_B) (I + L_A L_B M) \omega^2 + I M \omega^4} \quad (16)$$

$$b_2 = -F \frac{L_0 (k_A (L_A + L_B) - L_A M \omega^2) \sin \phi}{k_A k_B (L_A + L_B)^2 - (k_A + k_B) (I + L_A L_B M) \omega^2 + I M \omega^4} \quad (17)$$

The oscillation phase is defined as

$$tg \alpha = \frac{a_2}{a_1} \quad (18)$$

$$tg \beta = \frac{b_2}{b_1} \quad (19)$$

The tangent of the phase difference of oscillations ψ equals to

$$tg \psi = tg(\beta - \alpha) = \frac{tg \beta - tg \alpha}{1 + tg \alpha \cdot tg \beta} = \frac{a_1 b_2 - a_2 b_1}{a_1 b_1 + a_2 b_2} \quad (20)$$

Thus, a general equation is obtained for determining the phase difference of dynamic reactions of the supports.

In case the equipment is fixed rigidly, then the stiffness of the supports is many times greater than the corresponding values associated with the inertia of the equipment, in other words by the mass and moment of inertia, i.e., $M \rightarrow 0$ and $I \rightarrow 0$. Also accept the symmetrical arrangement of equipment ($L_A = 0.5L$ and $L_B = 0.5L$). Then expressing the vertical coordinate of the defect h_D relative to the phase difference of the oscillations, we get

$$h_D = h_0 + \frac{L}{2} \left(-ctg \psi \pm \sqrt{ctg^2 \psi + 1 - \left(\frac{2\Delta R_B}{\Delta R_A + \Delta R_B} - 1 \right)^2} \right) \quad (21)$$

where ψ is the phase difference of oscillations between the dynamic reactions of the supports. When $\psi = 0$, the height is defined as $h_D = h_0$.

5 Conclusion

This study proposes a new method for diagnosing of equipment via remote strain-gauge analysis. The distinctive feature of which is the determination of the location of the defect source of oscillations in space. This allows accurately to identify the location of the defect. And in combination with information on the frequency of oscillations and their intensity, the defect can be reliably identified.

On the basis of this study out, a spatial model for identifying defects and distributing potentially dangerous elements of rotary equipment based on tensor-metric analysis and a method of preventive maintenance will be developed in the future.

This method will improve the reliability of technical diagnostics of the oil pumping unit, improve the ability to implement the diagnostic system according to the actual condition, and ultimately increase the reliability and durability of the equipment and reduce the costs of its operation and repair.

Acknowledgements The reported study was funded by The Ministry of Education and Science of the Russian Federation according to the research project MK-2965.2018.8.

References

1. Lisin YuV, YaM Fridlyand, Aralov OV (2015) Povyshenie nadezhnosti oborudovaniya magistral'nyh nefteprovodov (Raising the hope of equipment for trunk pipelines). Standarty i kachestvo 8:36–40
2. Gumerov AG, Gumerov RS, Akberdin AM (2001) Eksploatatsiya oborudovaniya nefte-perekachivayushchih stancij (Operation of oil pumping station equipment). Nedra
3. Barkov AV, Barkova NA, Azovcev YuA (2004) Monitoring i diagnostika rotornykh mashin po vibracii (Monitoring and diagnostics of rotary machines by vibration). SPbGMTU
4. Sullivan GP, Pugh R, Melendez AP, Hunt WD (2004) Operations & maintenance. Best practices (release 2.0) a guide to achieving operational efficiency. U.S. Department of Energy, pp 55–57
5. RD-75.200.00-KTN-119-16 Main pipeline transport of oil and petroleum products. Maintenance and repair of mechano-technological equipment and facilities of the PS. PJSC Transneft, Moscow, 2016
6. RD 29.020.00-KTH-185-08 Regulations on the system of maintenance and repair of electrical equipment of trunk pipelines for pressure up to 10 MPa
7. Heno H, Capolino GA, Fernandez-Cabanas M (2014) Trends in fault diagnosis for electrical machines: a review of diagnostic techniques. IEEE Ind Electron Mag 8(2):31–42
8. Choi S (2012) Electric machines: modeling, condition monitoring, and fault diagnosis. CRC Press
9. GOST R 55265.7-2012 (ISO 10816-7: 2009) Vibration. Monitoring the state of machines by measuring vibration on non-rotating parts. Part 7. Industrial dynamic pumps
10. ISO 17359 Condition monitoring and diagnostics of machines—general guidelines
11. ISO 13373-1 Condition monitoring and diagnostics of machines—vibration condition monitoring—Part 1: General procedures
12. ISO 13373-2 Condition monitoring and diagnostics of machines—vibration condition monitoring—Part 2: Processing, presentation and analysis of vibration data

13. ISO 5348 Mechanical vibration and shock—mechanical mounting of accelerometers
14. Muszynska A (1994) Vibrational diagnostics of rotating machinery malfunctions. *Int J Rotating Mach* 1:237–266
15. ASTM D6595-00 Standard test method for determination of wear metals and contaminants in used lubricating oils or used hydraulic fluids by rotating disc electrode atomic emission spectrometry
16. Petukhov V (2005) Diagnostics of the state of electric motors. The method of spectral analysis of current consumption. *News Electr Eng* 1 (31)
17. Valeev A, Zotov A, Tokarev A (2017) The monitoring system of an actual technical condition for pumping units with frequency analysis. *Procedia Eng* 176:137–143
18. Filippetti F, Bellini A, Capolino GA (2013) Condition monitoring and diagnosis of rotor faults in induction machines: state of art and future perspectives. In: *Proceeding of the conference: electrical machines design control and diagnosis*
19. Ishibashi T, Han B, Kawai T (2017) Rotating machinery library for diagnosis. In: *Proceedings of the 12 th international Modelica conference, 15–17 May, Prague, Czech Republic*
20. Hoffman KJ, Blass B (2012) An introduction to stress analysis and transducer design using strain gauges

Results of Studying Cleaning of Exhaust Gases of Preheater-Equipped KamAZ-740 Diesel Engine



A. A. Melbert and A. V. Mashensky

Abstract The study aims to address the important environmental problem of reducing the harmful emissions of the exhaust gases produced by preheater-equipped diesel engines when operated in winter. It analyzes the cleaning of prestart-heater exhaust gases in the catalytic converter during the heating of catalyst bricks as the KamAZ-740 diesel engine is being prepared to start. Redirecting the preheater exhaust gases to the catalytic converter cleans them from the products of incomplete combustion and nitrogen oxides while using their heat for the preheating of catalyst bricks. The paper presents the results of studying the composition of exhaust gases produced by the PZhD-30 preheaters used in KamAZ-740 diesel engines. The composition of exhaust gases is found to be the function of the air-excess factor, while the efficiency of preheater exhaust-gas cleaning is determined as a function of the catalyst-brick temperature. It is found out that increasing the air-excess factor from $\alpha_{\text{mn}} = 1.20$ to $\alpha_{\text{mn}} = 1.60$ increases the nitrogen-oxide emissions in exhaust gases 1.64 times while reducing the emissions of incomplete-combustion products: 1.39 times less hydrocarbon emissions, 1.50 times less carbon monoxide emissions, and 1.60 times less particulate-matter emissions. The results of studying the quality of cleaning the preheater exhaust gases in catalyst bricks produced by self-propagating high-temperature synthesis (SHS) show that heating them reduces nitrogen-oxide emissions at 713 K, hydrocarbon emissions at 593 K, and carbon monoxide emissions at 713 K.

Keywords Environment · Harmful · Emissions · Diesel engine · Preheater · Converter · Catalytic

A. A. Melbert (✉) · A. V. Mashensky
Polzunov Altai State Technical University, 46, Lenin Avenue, Altai Krai,
Barnaul 656038, Russia
e-mail: aamelbert@mail.ru

© Springer Nature Switzerland AG 2020
A. A. Radionov et al. (eds.), *Proceedings of the 5th International Conference on Industrial Engineering (ICIE 2019)*, Lecture Notes in Mechanical Engineering,
https://doi.org/10.1007/978-3-030-22041-9_36

319

1 Introduction

The annual growth in the number of internal combustion engines (ICE) is considerably outpacing the improvement in their environmental performance.

Diesel-engine operations entail considerable environmental pollution. Diesel-engine exhaust gases affect humans and animals, vegetation and flora, buildings and structures, as well as cultural monuments [1].

Reducing the atmospheric pollution attributable to diesel engines to normative values is projected to increase the newborns' life expectancy by 3–5 years, and reduce the general morbidity and mortality by 4.5%, which includes a 20–50% reduction in bronchitis morbidity, a 25% reduction in emphysema morbidity, and a 10% reduction in cardiovascular morbidity [1, 2].

Specific emissions of diesel engines running at full load reach 1.5–12.0 g/(kW·h) of carbon monoxide (CO); 0.4–2.5 g/(kW·h) of sulfur oxides (SO_x); 0.06–0.2 g/(kW·h) of aldehydes; a total of 1.5–8.0 g/(kW·h) of hydrocarbons (C_xH_y); 1·10⁻⁶–2·10⁻⁶ g/(kW·h) of benzo-pyrene; 10–30 g/(kW·h) of (NO_x); 0.25–2.0 g/(kW·h) of particulate matter, including soot [1–3].

Rule 83-02 of the UNECE stipulates control values of catalytic converter efficiency and specifies them for particular components of exhaust gases: 78% for CO, 79.5% for C_xH_y total, 88.5% for NO_x total, and 86% for C_xH_y+NO_x total. For the urban (heated) cycle, the regulated catalytic-converter efficiency values are as follows: 98% for CO; 88% for C_xH_y; 81% for NO_x [2–4].

During pre-starting, the catalytic-converter bricks have to be heated up from the ambient temperature to the operating temperature for efficient gas cleaning [3–6].

For preheater-equipped diesel engines operated at negative ambient temperatures and parked outdoors, preheating time and harmful preheater emissions are two relevant problems [3, 6–10].

For most converters, the lowest operating temperature is in the range of 420–520 K. Such catalytic-converter temperatures cannot be reached without long preheating by exhaust gases, especially if the diesel engine is operated at negative temperatures. At starting, idling, or low-loads, an unheated converter is inefficient [1, 2, 10, 11].

Placing a catalytic converter next to the engine is a common approach, since it reduces the time to heat the converter at cold start. However, such placement does increase the exhaust-gas pulsation, which may reduce the gas cleaning effectiveness by as much as 30% [6, 7, 11].

Meanwhile, Boysen has designed an exhaust-gas cleaning system for the BMW NG-R6 family, which implies near-engine placement of catalytic converters and using a set of short interconnecting pipes of various shape. Komatsy Ltd, Japan, has created and patented in the US a diesel engine with fast cold-start heating [12]. There is a system for heating three-way catalytic converters and nitrogen-oxide absorbers placed consecutively in the exhaust system. Toyota, Japan, has created a device for ICEs running on lean air-fuel mixture and containing the starting catalytic NO_x absorber and the primary one placed consecutively [2, 13]. Volkswagen,

Germany, has proposed faster cold-start converter heating by letting the exhaust gases through the inner pipe only to reduce heat loss. General Motors Corporation, USA, has created an electronic system that speeds up the catalytic converter heating after starting an ICE; the system is efficient at $-20\text{ }^{\circ}\text{C}$ or higher [14–20].

The relevance of this study consists in addressing the important environmental problem of reducing the exhaust-carried harmful emissions produced by diesel engines when operated in winter.

2 Scientific Significance

Atmospheric air used as the oxidizer in preheaters contains the following basic components (the figures are volumetric fractions): 0.7808 nitrogen, 0.2095 oxygen, 0.0093 argon, 0.0003 carbon dioxide, 0.0000246 sundry gases, and substance vapors [3, 5].

As diesel fuel burns in the preheater combustion chamber, the released exhaust gases contain the following components (the figures are volumetric fractions): 0.76–0.78; 0.02–0.09 oxygen; 0.005–0.04 water vapor [3, 6, 7]. Known and published sources do not provide any more details on the composition of diesel-engine preheater exhaust gases.

In order to find and account for the contribution of diesel-engine preheater emissions to environmental pollution, the research team has studied the exhaust gases produced by a stationary test stand equipped per GOST.

3 Materials and Methods

The composition of PZhD-30 preheater exhaust gases was measured at different combustion-chamber air-excess factor values while running the engine in winter-time at the ambient temperature $T_0 = 248\text{--}249\text{ K}$, the pressure $P_0 = 762\text{ mmHg}$, the humidity $W_0 = 82\%$, and the wind speed $V_B = 10\text{ m/s}$.

The additional features were as follows:

- Pump unit (air compressor and fluid pump) motor rotation speed was controlled by a rheostat.
- The air flow was measured by a double diaphragm and a differential manometer.

The multistage catalytic converter with bricks produced by self-propagating high-temperature synthesis (SHS, see Table 1) was intended to clean the exhaust gases of diesel engines consuming up to $950\text{ m}^3/\text{h}$ [2, 7, 8].

The experiment was usually carried out over 24 h to make observations under different atmospheric conditions. After running a series of experiments, the diesel

Table 1 Characteristics of porous permeable SHS catalytic bricks for converters

Charge composition, wt%	
SHS bricks charge components	Content, wt%
18 XHBA, 18 XHMA alloyed-steel scale	47.5
Chromium oxide	17.9
ПХ-1 chromium per TU 882-76	6.9
ПНХ-ОТ-1 nickelper ГОСТ 9722-79	12.4
АСД-1 aluminum per ТУ 485-22-87	15.2
Iridium	0.1
Rhodium	0
Copper	0
Exhaust-gas cleaning efficiency at $P_e/P_{enom} = 100\%$, $T_{og} = 833\text{ K}$, $T_{kat} = 833\text{ K}$, %	
Exhaust components	Reduction in content, %
Nitrogen oxides, NO_x (total)	52
Carbon monoxide, CO	86
Hydrocarbons, C_xH_y (total)	67
Particulate matter	85
<i>Characteristics of catalyst bricks</i>	
Average pore size, cross-section, μm	150
Compressive strength, MPa	12.2
Pore tortuosity ξ_1	1.39
Corrosion resistance by change of mass, %	10
Material porosity Φ , %	40
Specific weight of the porous material ρ_{kb} , kg/m^3	–

unit was poured with cold tosol from the reserve tank to quickly stabilize its temperature.

Preheating took 25 min. Over that time, the sump oil temperature rose to 308 K, the coolant temperature at the unit outlet rose to 353 K.

The catalytic-converter brick temperature rose to 523 K at an hourly fuel consumption of 4.5 kg/h and $\alpha_{pp} = 1.20$.

Exhaust-gas composition was analyzed per GOST 10448-80, GOST R 41.24-2003, and GOST R 51249-99.

4 Results and Discussion

Table 2 presents the results of experimental studies to find the content of harmful components in the exhaust gases produced by a PZhD-30 preheater operated as part of a KamAZ-740 diesel engine.

As can be seen in Table 2, increasing the air-excess factor from $\alpha_{pp} = 1.20$ to $\alpha_{pp} = 1.60$ increases the nitrogen-oxide emissions in exhaust gases 1.64 times while

Table 2 Content of harmful substances in the exhaust gases of a KamAZ-740 PZhD-30 preheater, $T_{og} = 833$ K

Harmful components of exhaust gases (regulated)	Air-excess factor, α_{pp}				
	1.2	1.3	1.4	1.5	1.6
Nitrogen oxides– NO_x , g/m^3	1.499	1.643	1.848	2.054	2.464
Hydrocarbons (total)– C_xH_y , g/m^3 , $\times 10^{-3}$	4.78	4.21	3.86	3.57	3.43
Carbon monoxide–CO, g/m^3	0.413	0.375	0.337	0.313	0.275
Particulate matter–PM, g/m^3	0.24	0.20	0.18	0.16	0.15

reducing the emissions of incomplete-combustion products: 1.39 times less hydrocarbon emissions, 1.50 times less carbon monoxide emissions, and 1.60 times less particulate-matter emissions.

At the same time, diesel engines stored at subzero temperatures outside garages sometimes need to use preheaters for post-start heating. In this case, one has to deal with diesel-engine emissions and preheater emissions simultaneously.

Using catalytic converters in the exhaust systems to clean gases from both the engine and the preheater simultaneously is a problem that has not been detailed so far in published papers; it therefore requires a deeper analysis.

In the present case, there is no need to analyze the situation for compliance with EURO standards, as the diesel engines does not run simultaneously with the preheater when using the 13-mode test cycle.

It is, however, imperative to analyze the cleaning of prestart-heater exhaust gases in the catalytic converter during the heating of catalyst bricks as the diesel engine is being prepared to start.

Redirecting the preheater exhaust gases to the catalytic converter cleans them from the products of incomplete combustion and nitrogen oxides while using their heat for the preheating of catalyst bricks, thus effectively addressing two issues at the same time.

Table 3 presents data on the quality of preheater exhaust-gas cleaning in catalyst bricks.

As can be seen in Table 3, heating the catalyst bricks has a considerable effect on the reduction of nitrogen-oxide emissions, which manifests at 713 K or above; hydrocarbon emissions are reduced at 593 K or above, while carbon monoxide

Table 3 Efficiency of cleaning preheater exhaust gases in catalyst bricks at $\alpha_{pp} = 1.3$

Preheater exhaust gas components	Emissions at $T_{og} = 833$ K, no CC, g/m^3	Component-specific emissions if there is a CC in place, g/m^3 at different catalyst-brick temperatures						
		250 K	273 K	298 K	377 K	593 K	713 K	833 K
NO_x	1.643	1.643	1.643	1.643	1.620	1.610	0.94	0.44
C_xH_y	4.210	4.210	4.210	4.100	4.00	3.30	1.98	0.33
CO	0.375	0.375	0.375	0.375	0.375	0.320	0.290	0.15
PM	0.20	0.06	0.06	0.06	0.06	0.04	0.02	0.02

emissions drop at 713 K or above. Particulate-matter emissions are reduced at the soot ignition temperature or above.

We have, therefore, found the composition of exhaust gases to be the function of the air-excess factor, while the efficiency of preheater exhaust-gas cleaning is determined as a function of the catalyst-brick temperature.

Figure 1 presents the levels of harmful emissions carried with preheater exhaust gases as a function of fuel consumption.

Notably, the characteristics of harmful emissions have been recorded at the same air intake of 87.32 m³/h. Increasing the fuel injection from 4.86 to 6.49 kg/h results in a 1.64 × reduction in nitrogen-oxide emissions. Emissions of incomplete-combustion products do increase: particulate-matter emissions become 1.6 times larger while those of carbon monoxide become 1.5 times larger and those of hydrocarbons become 1.39 times larger.

It is found out that at an air-fuel ratio of $\alpha_{\text{III}} = 1.18$, the rising gas temperature at the start heats the catalytic-converter bricks to 880 K. The efficiency of cleaning δ_{NO} , δ_{CH} , δ_{CO} , and δ_{PM} begins to manifest at about 300 K and increases significantly while heating to 880 K. Increasing the gas flow by means of increased air-fuel ratio results in less efficient gas cleaning in terms of all primary components (carbon monoxide, nitrogen oxides, hydrocarbons, and particulate matter).

Figure 2 shows the dynamics of efficiency of cleaning PZhD-30 exhaust gases in a catalytic converter which uses porous bricks produced by self-propagating high-temperature synthesis (SHS). As can be seen in the graph, intensive-cleaning temperature is component-specific. Thus, hydrocarbons are cleaned at 630–340 K or above, while carbon monoxide is cleaned at 530–540 K or above; particulate matter is filtered to 50% at up to 735 K, then to 89% by catalytic burning at higher temperatures. Nitrogen oxides are cleaned at 425 K or above, with the cleaning being intensified while increasing the temperature to 635 K and stabilizing at $\delta_{\text{NOx}} = 73\text{--}89$ at 880 K.

5 Conclusions and Recommendations

1. When preheating a diesel engine, a preheater emits a considerable amount of harmful substances carried with the exhaust gases; the amount depends on the air-excess factor. Increasing the latter from $\alpha_{\text{pp}} = 1.2$ to $\alpha_{\text{pp}} = 1.6$ results in 1.64 times greater emission of nitrogen oxides; 1.39 lesser emission of hydrocarbons; 1.56 times lesser emission of carbon monoxide; 1.6 times lesser emission of particulate matter.
2. Increasing the fuel injection from 4.86 to 6.49 kg/h reduces the nitrogen-oxide emissions 1.64 times. Emissions of incomplete-combustion products do increase: particulate-matter emissions become 1.6 times larger while those of

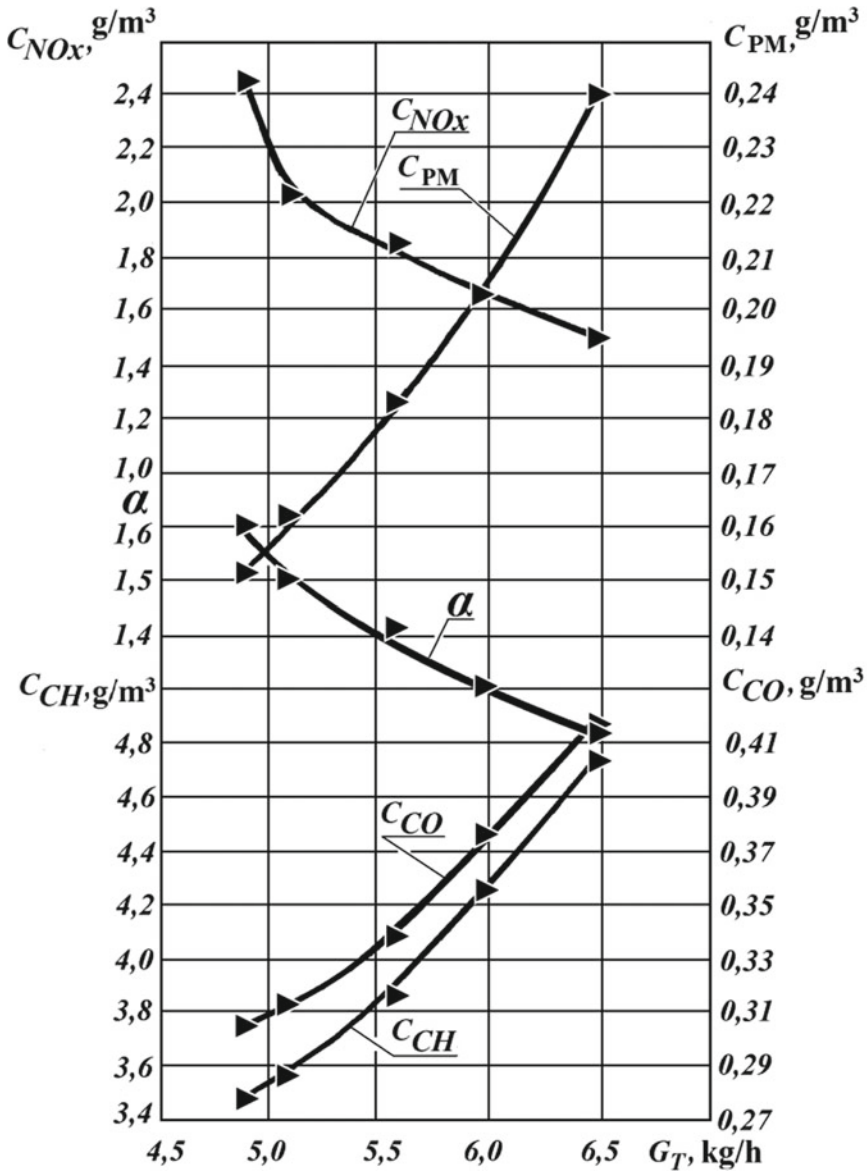


Fig. 1 Harmful emissions in PZhD-30 preheater exhaust gases as a function of fuel consumption

carbon monoxide become 1.5 times larger and those of hydrocarbons become 1.39 times larger.

3. The efficiency of cleaning the preheater exhaust gases in the catalytic converter depends on the catalyst-brick temperature.



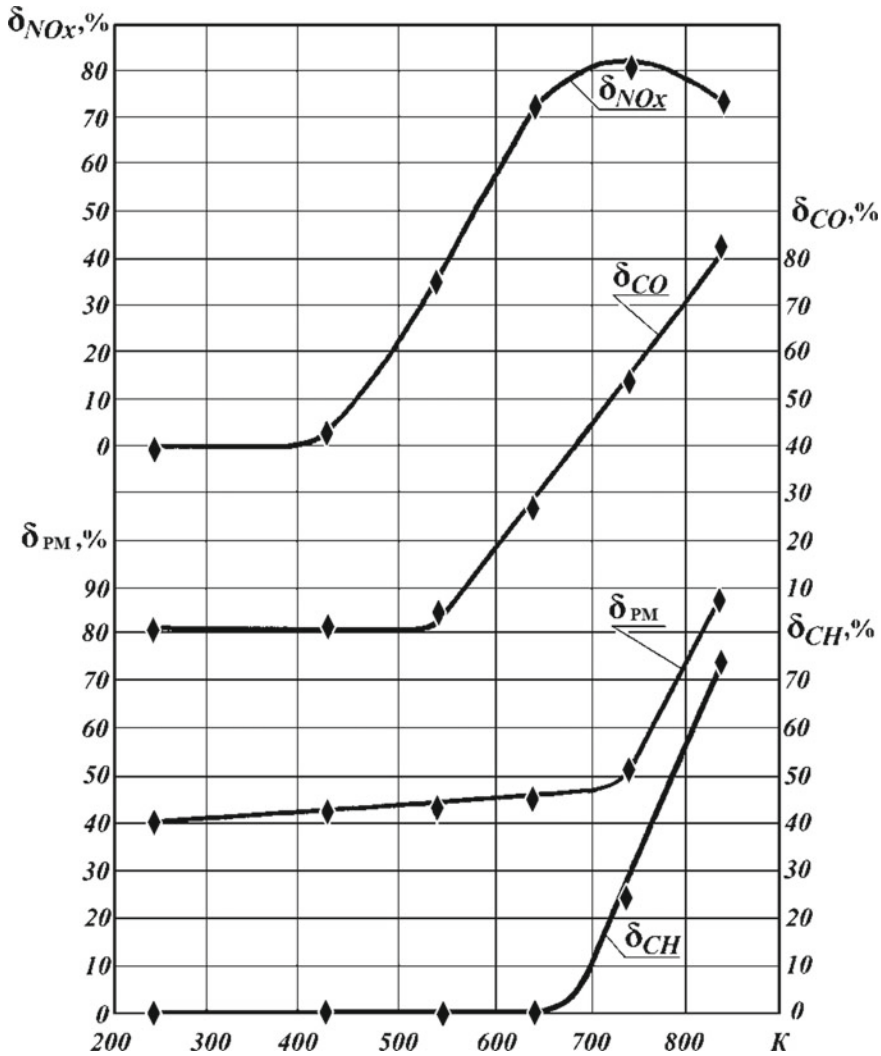


Fig. 2 Effects of heating the catalytic-converter bricks on the efficiency of cleaning the PZhD-30 exhaust gases

- It is relevant to cover the preheating time and to take into account the atmospheric pollutions attributable to preheating when analyzing the environmental damage as a part of the regulated-substance emissions analysis. The situation becomes worse when running a preheater as well as during the post-start heating of diesel engines.

- To ensure efficient cleaning of exhaust gases in the catalytic converter, we recommend adjusting the preheater by $\alpha_{pp} = 1.18-1.2$.

References

- Melbert AA (2003) *Povysheniye ekologicheskoy bezopasnosti porshnevnykh dvigateley* (Cleaner Piston Engines). Nauka, Novosibirsk, p 170
- Novosyolov AL, Melbert AA, Zhuykova AA (2007) *Snizheniye vrednykh vybrosov dizeley* (Reducing the Harmful Emissions of Diesel Engines). Nauka, Novosibirsk, p 139
- Kukis VS, Sultanov FT (2006) *Umensheniye vybrosa tverdykh chastits s otrabotavshimi gazami DVS zaschet povysheniya effektivnosti raboty kataliticheskogo neytralizatora* (Reducing the Particulate Emissions in ICE Exhaust Gases by Optimizing the Catalytic Converter). *Bulletin of Tula State University* 10:126–131
- Krokhta GM (2017) *Osobennosti ekspluatatsii traktorov v usloviyakh nizkikh temperature* (Low-temperature tractor operations). Monograph. Zolotoy Kolos, a NSAU Research Center, 376 p
- Belousov IS, Krokhta GM, Fedyunin PI (2005) *Pusk traktornykh dizeley* (Starting a tractor diesel engine). Novosibirsk State Agrarian University, Institute of Engineering, Novosibirsk, p 146
- Kuperschmidt VL (2001) *Sredstva obespecheniya puska dvigateley v kholodnykh usloviyakh* (Tools for Starting an Engine in Cold). *Tractors and Agricultural Machinery* (Traktory i selkhoz mashiny) 1:18–20
- Maksimeyko YuG, Novosyolov AA, Melbert AA (2011) *Zavisimost sostava otrabotavshikh gazov dizelya 8412/12 ot temperature okruzhayushchey sredy* (Correlation of Ambient Temperatures and 8412/12 Diesel Engine Exhaust Gas Composition). *Sci Probl Transp Sib Far East* (Nauchnyye problem transporta Sibiri i DalnegoVostoka) 2:198–200
- Maksimeyko YuG, Melbert AA, Bekbayev BF, Grabovskaya NN (2008) *Ochistka otrabotavshikh gazov predpuskovogo podogrevatelya PZhD-30 v period predpuskovoy podgotovki dizelya 8412/12* (Cleaning the PZhD-30 Preheater Exhaust Gases While Prestarting a 8412/12 Diesel Engine), *Power Plant Improvement Problems* (Problemy sovershenstvovaniya energeticheskikh ustanovok). AltSTU Publ., Barnaul, p 73–77
- Tashchkinov GA (1977) *Rabota dizelnykh dvigateley pri nizkikh temperaturakh* (Low-Temperature Diesel-Engine Operations). Irkutsk, 86 p
- Golovatenco AG (2004) *Povysheniye ekologichnosti i economichnosti avtotraktornykh dvigateley* (Improving the environmental and efficiency of automotive engines). *Traktory i selkhoz mashiny* 9:16–17
- Rakopoulos CD, Dimaratos AM, Giakoumis EG (2011) *Investigation of turbocharged diesel engine operation. Exhaust emission, and hot conditions*. In: *Proceedings of the Institution of Mechanical Engineers, Part D/C.D, J Automob Eng vol 9*
- Shirahata J, Tomiyasu K, Ito K (2005) *Exhaust-gas purifying catalyst: application 1561509 EPO, IPC7B 01 J 35/00, B 01 D 53/94. Cataler Corp., Paris (FR). 04293173.3, 10 Aug, 2005, Prior. Jan 29, 2004, No. 2004021873 (Japan)*
- Development of closed loop secondary air control three-way catalyst system (1980), *SAE Techn Par Sgr* (800395):1–9
- General motors corp. Rozario Frederick J (2005) *Catalytic converter early light off using cylinder deactivation*. USA Patent. 6922986, IPC7 F 01 N 3/00. No. 10/017441, 2 Aug, 2005
- Jacob E, Lammernann R, Pappenheimen A (2005) *Ein Abgasnach-behandlungs system fur Euro 4. Rothe Dieter (MAN Nutzfahrzeug e Gruppe, Nürnberg). MTZ: Motortechn* 6:444–446,448–451

16. Jakobs R, Westbrooke K (1990) Aspects of influencing oil consumption in diesel engines for low emissions. SAE Tehn Pap Ser 900587:1–18
17. Borman FN (1982) The effects of air pollution on the New England landscape. *Ambio* 11 (6):338–346
18. Diez R, Bühler F (2006) Modular aufgebautes Abgasreinigungssystem eines Reihensechsylinder-Ottomotors. (Friedrich Boysen GmbH und Co. KG, Altensteig). *MTZ: Motortechn* 67(2):92–95
19. Rohefing H, Peters M, Koning A (2005). Nebenreaktion am Abgas-Katalysator. *MTZ: Motortechn-Z*.4 989-50-N6- pp 269–272
20. Volkswagen AG, Herding G (2005) Verfahren zum Aufheizen eines Katalysatorsystems. Patent 10338935.0, MPK⁷ F 01 N 9/00, F 01 N 3/30. (Reinhardt & Pohlmann Partnerschaft, 60316 Frankfurt), 21 Apr 2005

Features of Rotor Friction Losses Balancing in Centrifugal Electric-Driven Pumps for Spacecrafts



A. Bobkov

Abstract Centrifugal electric-driven pumps with the capacity less than 300 W provide circulation of heat transfer fluid within closed loops of a spacecraft thermal regulation system. Taking into account the geometrical arrangement feature of the rotor pump and drive sections of electric-driven pumps, which implies that radial dimensions of these parts are comparable, it is concluded that analyzing rotor friction losses, two types of losses shall be considered separately: friction against butt-end surfaces and friction against cylindrical surfaces of the rotor. In this case, the first type prevails in the rotor pump section, and the second type is primary for the rotor drive section. Calculations show that the rotor pump section makes the largest contribution to rotor friction losses. The main reason is large size butt-end surfaces of the pump section impeller. The paper represents potential friction reduction in the rotor pump section due to increase in the number of electric-driven pump stages and decrease in diameter of each stage impeller.

Keywords Spacecraft · Electric-driven pump · Rotor · Friction · Butt-end surface · Cylindrical surface

1 Introduction

Centrifugal electric-driven pumps (CEDPs) with capacity less than 300 W provide circulation of a heat transfer fluid within closed loops of a spacecraft thermal regulation system (TRS) [1–7]. CEDP consumes the significant part of spacecraft power. For example, capacity of more than 30 CEDPs of MIR orbital station was approximately 1 kW [8]. Reduction of CEDP power consumption, due to decrease of losses related to friction between the heat transfer medium and CEDP rotor, is the relevant problem of spaceborne devices improvement [4].

A. Bobkov (✉)

Komsomolsk-na-Amure State University, 27, Lenin Prospect,
Komsomolsk-na-Amure 681013, Russia
e-mail: bobkov@knastu.ru

© Springer Nature Switzerland AG 2020

A. A. Radionov et al. (eds.), *Proceedings of the 5th International Conference on Industrial Engineering (ICIE 2019)*, Lecture Notes in Mechanical Engineering,
https://doi.org/10.1007/978-3-030-22041-9_37

329

2 Relevance

Drives for spacecraft CEDP are non-contact DC motors with the shaft (3–10) speed of 10^3 RPM.

Total power losses $(N)_{\Sigma}$ in the electric drive of CEDP are comprised of the following components [9]:

$$N_{\Sigma} = N_{asl} + N_{fc} + N_{cwl} + N_{al} \quad (1)$$

where N_{asl} —anchor steel losses due to hysteresis and eddy currents; N_{fc} —friction losses; N_{cwl} —copper windings losses; N_{al} —additional losses under load.

Stator and rotor of spacecraft CEDP drives are separated by a shielding sleeve, enabling rotor immersion into the heat transfer fluid, that leads to losses in a rotor due to heat transfer fluid friction N_{fc} , which are included into the total friction loss N_{fl} :

$$N_{fl} = N_{flb} + N_{fc} \quad (2)$$

where N_{flb} —friction losses in bearings.

Rotor friction losses N_{fc} occur in two parts of a rotor shown in Fig. 1 as a Drive Section I and a Rotor Drive Section II according to their functional features.

Spacecraft CEDPs are small-size boosters with comparable dimensions of the rotor pump section and the rotor drive section which do not exceed 50×10^{-3} m [3, 5]. According to the functional purpose, the rotor can be provisionally subdivided into 11 parts $F1$ – $F11$ shown in Fig. 2.

Rotor friction losses N_{fc} depend on a revolving surface type and consist of 2 components [10–15]:

- Losses due to friction on rotor butt-end surfaces
- Losses due to friction on rotor cylindrical surfaces

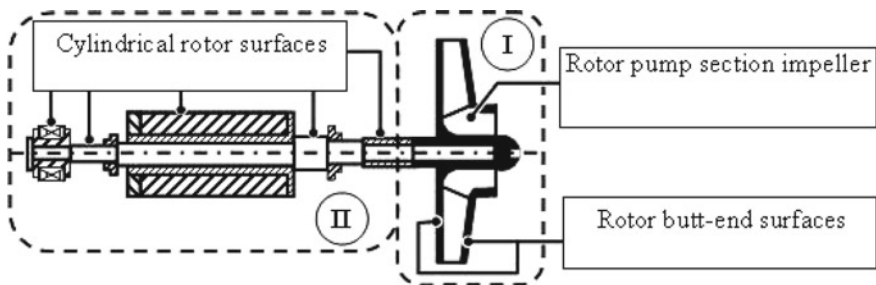


Fig. 1 Electric-driven pump rotor subdivided into parts as per functionally: I—rotor pump section; II—rotor driving section

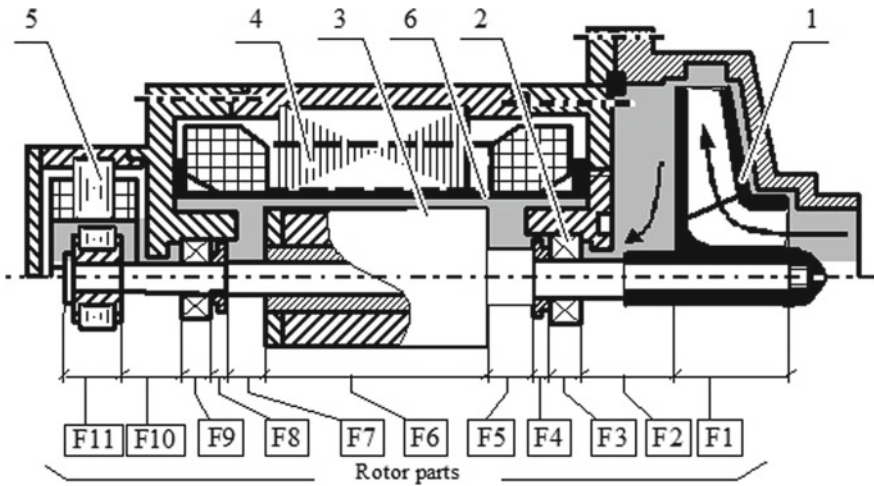


Fig. 2 CEDP rotor: 1 impeller, 2 rolling bearing, 3 drive shaft, 4 stator, 5 proximity switch, and 6 shielding sleeve

In CEDP, the first type of losses prevails in the pump section consisting of parts *F1* and *F2*, and the second type is primary the rotor drive section, consisting of parts *F4–F8*, *F10*, *F11*.

3 Methods

For CEDP rotor design optimization, it is required to evaluate friction-based power losses separately for pump N_{fc}^p and drive sections N_{fc}^{ds} of the rotor.

As an example, let us study the balance of friction losses in CEDP which is equipped with a motor DB-9 [16] and has the following parameters:

- Pressure head $H = 60 \text{ J/kg}$
- Heat transfer fluid flow $Q = 140 \times 10^{-6} \text{ m}^3/\text{s}$
- Rotor speed $n = 6000 \text{ RPM}$

Capacity N_{fc}^p means losses in the rotor pump section $N_{fc}^p = (N_{fc})_1$, and capacity N_{fc}^{ds} allows evaluating total losses at other 10 sections $N_{fc}^{ds} = \sum_{i=2}^{11} (N_{fc})_i$, where $(N_{fc})_i$ —friction losses at *i*th rotor part. Total losses will be:

$$N_{fc} = N_{fc}^p + N_{fc}^{ds} \tag{3}$$

Friction losses capacity for each rotor part $(N_{fc})_i$ can be determined as per the formula [9]:



$$(N_{fc})_i = 10^{-3} k_i \cdot \rho \cdot n^3 d_{ri}^4 (d_{ri} + 5 \cdot L_{ri}) \quad (4)$$

where k_i —friction coefficient depending on the Reynolds number Re_i at the area of rotor i th part; ρ —heat transfer fluid density; n —rotor speed; d_{ri} —diameter of rotor i th part; L_{ri} —length of rotor i th part.

The Reynolds number is calculated as per the formula:

$$Re_i = \frac{\Delta \sqrt{4v^2 + u_{ri}^2}}{\nu} \quad (5)$$

where Δ —radial clearance; v —fluid speed in the clearance between rotor and casing; u_{ri} —peripheral speed of rotor i th part; ν —fluid kinematic viscosity coefficient.

Setting the values $\Delta = 0.3 \times 10^{-3}$ m; $v = 0.7 \times 10^{-6}$ m²/s; $\rho = 691$ kg/m³; and $\nu = 15 \times 10^{-6}$ m²/s, one gets specific gravity of losses N_{fc}^p in rotor pump section I, which includes the largest diameter part—CEDP impeller, which is $N_{fc}^p/N_{fc} = 0.844$. Thus, friction losses of rotor pump section I comprises the largest part of rotor friction losses N_{fc} .

Dependency (4) comprising proportionality $(N_{fc})_i \sim d_{ri}^5$ indicates reasonability of reducing rotor diameter, particularly the diameter of rotor pump section I impeller.

One of the design methods to decrease impeller diameter d_r is to implement CEDP multistage principle [17]. Parametric result of multistaging is specific velocity increase at each stage n_s , which is calculated as per the formula [18]:

$$n_s = 3.65 \cdot n \cdot \frac{\sqrt{Q}}{H^{0.75}}, \quad (5)$$

where n —speed rate, RPM; Q —working fluid volume flow, m³/s; H —pump head, m.

4 Results

Let us consider the possibility of reduction N_{fc}^p/N_{fc} by increasing the number of stages up to 2 and 3 sets that typical for CEDP TRS head coefficient value $\bar{H} = 0.587$ [3] will be constant.

Impeller diameter change d_{imp} is evaluated by means of a relative diameter $\bar{d}_{imp} = d_{imp1}/dN$, where d_{imp1} —impeller diameter in a single-stage CEDP; dN —impeller diameter in CEDP, with N stages.

Passing from two-stage variant to one-stage one, the relative diameter $\bar{d}_{imp} = 0.72$, and in three-stage variant of CEDP $\bar{d}_{imp} = 0.59$. Stage-specific velocity increase from $n_s = 67$ to $n_s = 112$ and $n_s = 152$, respectively. Such changes in CEDP parameters are acceptable in terms of a process and positive in terms of power consumption.

The diagram of change in the relative value of friction losses in the rotor pump section N_{fc}^p/N_{fc} due to increase of the number of stages is shown in Fig. 3. The value N_{fc}^p/N_{fc} goes down to 0.677 in two-stage variant of CEDP and down to 0.549 in three-stage variant of CEDP, respectively, by 20 and 35% in comparison with the initial level $N_{fc}^p/N_{fc} = 0.844$.

The diagram of friction losses changes N_{fc} converted to CEDP power output $N_{out} = \rho \cdot \dot{V} \cdot H$ is shown in Fig. 4. The number of stages which increases accompanied by the reduction of impeller radial dimensions allows to significantly reduce the specified type of losses: by 2.9 times for the three-stage variant that verges to the level of full-size industrial CEDPs.

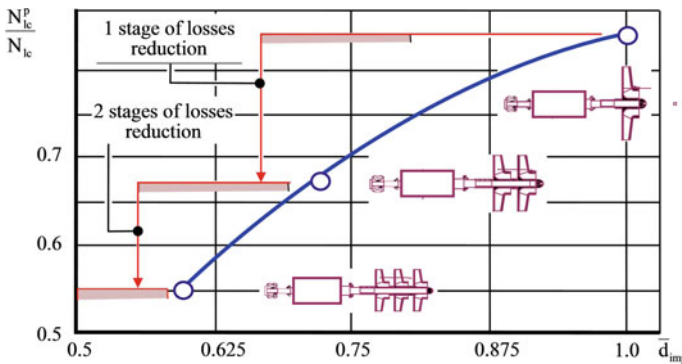


Fig. 3 Level of friction losses reduction in the rotor pump section due to increase in the number of CEDP stages

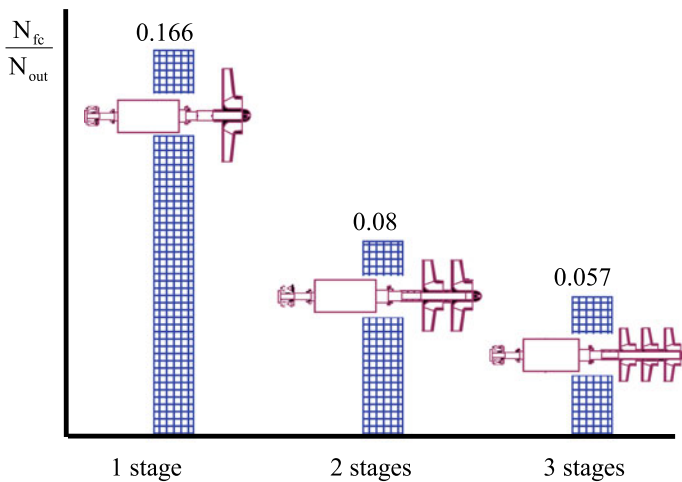


Fig. 4 Relative friction losses reduction in the context of the number of CEDP stages increase

The considered method of rotor friction losses reduction is also acceptable for other impeller-based devices of low power, for example, for aerospace compressors and fans, which have comparable radial dimensions of drive and pressure rotor sections [19, 20].

References

1. John Col., Keese E, Spacecraft thermal control Systems. <http://ocw.mit.edu/courses/aeronautics-and-astronautics/16-851-satellite-engineering-fall-2003/lecture-notes/123thermalcontro.pdf>. Accessed 21 Jan 2017
2. NASA Astronauts went to space for the third time to repair the pump. <https://ria.ru/science/20100816/265764991.html>. Accessed 21 Nov 2016
3. Borovin GK, Petrov AI, Protopopov AA, Isaev NY (2016) Dinamika rotorov maloraskhodnykh tsentrobezhnykh nasosov s gidrostaticheskimi podshipnikami i privodom ot elektrodvigatelye postoyannogo toka (Dynamics of rotors of low flow centrifugal pumps with hydrostatic bearings and driven by direct current electric motors). https://doi.org/10.20948/prepr_2016_142
4. Kuzmin VN, Mikhaylov EM, Stoma SA (1996) Elektronasosnyye agregaty kosmicheskikh apparatov s gidroporami rotora (Electric power units of space vehicles with rotor hydro bearings), vol 5. Elektrotehnika, Moscow
5. Kraev MV, Lukin VA, Ovsyannikov BV (1985) Maloraskhodnyye nasosy aviatsionnykh i kosmicheskikh sistem (Low-flowrate pumps of aviation and space systems). Mashinostroyeniye, Moscow
6. Yudina ZA, Maslovskaya AM, Usmanov DB (2016) Modifikatsiya elektronasosnogo agregata kosmicheskogo apparata (Modification of the electric pump unit of space apparatus). Aktual'nyye problemy aviatsii i kosmonavtiki 1(12):139–141
7. Laser DJ, Santiago JGA (2004) Review of micropumps. J Micromech Microeng 14(6):35–64
8. Weinberg DM, Vereshchagin VP, Miroshnik OM (2001) Unikal'nyye elektromekhanicheskiye bortovyye sistemy orbital'noy kosmicheskoy stantsii "Mir" (Unique electromechanical on-board systems of the Mir space station). Nauka, Moscow
9. Burenin VB, Gaevik DV, Dronov VP (1977) Konstruktsiya i ekspluatatsiya tsentrobezhnykh germetichnykh nasosov (Design and operation of centrifugal hermetic pumps). Mashinostroyeniye, Moscow
10. Baibikov AS, Karakhian VK (1982) Gidrodinamika vspomogatel'nykh traktov lopatnykh mashin (Hydrodynamics of auxiliary tracts of vane machines). Mashinostroyeniye, Moscow
11. Klimova KG, Zagayko SA (2018) Matematicheskaya model' rascheta poter' moshchnosti na treniye podshipnikov skol'zheniya (Mathematical model of calculation of the losses of friction for the friction of slide bearings) vol 2/19, Molodezhnyy vestnik Ufimskogo gosudarstvennogo aviatsionnogo tekhnicheskogo universiteta, Ufa
12. Martsinkovskiy VA (1970) Gidrodinamika i prochnost' tsentrobezhnykh nasosov (Hydrodynamics and Strength of Centrifugal Pumps). Mashinostroyeniye, Moscow
13. Ovsyannikov BV, Borovsky BI (1986) Teoriya i raschot agregatov pitaniya zhidkostnykh raketnykh dvigateley (Theory and calculation of power units of liquid rocket engines). Mashinostroyeniye, Moscow
14. Vysokooborotnyye lopatochnyye nasosy (High-speed vane-type pumps) (1975). In: Ovsyannikov BV, Chebaevskiy VF (eds) Mashinostroyeniye, Moscow
15. Verbitska OA (1957) Raspredeleniye davleniy v bokovykh pazukhakh tsentrobezhnykh nasosov s uchetom utehek (Pressure distribution in lateral sinuses of centrifugal pumps taking into account leakages). VINITI, Moscow

16. Bobkov AV (2003) Tsentrobezhnyye nasosy sistem termoregulirovaniya kosmicheskikh apparatov (Spacecraft thermal regulation systems centrifugal pumps). Dalnauka, Vladivostok
17. Laboratory course of hydraulics, pumps and hydraulic transmissions (1974). In: Rudnev SS, Podviz LG (eds) Mashinostroenie, Moscow
18. Borovsky BI (1989) Energeticheskiye parametry i kharakteristiki vysokooborotnykh lopastnykh nasosov (Energy parameters and characteristics of high-speed vane-type pumps). Mashinostroenie, Moscow
19. Pamrin (1973) Aerodynamics of small-sized compressors and fans. papers of American society for mechanical engineers. Power Mach Plants 3:125–132
20. Barenboym AB (1974) Malorashodnyye freonovyye turbokompressory (Low cost freon turbochargers). Mashinostroenie, Moscow

Deformation of Prismatic Samples of U-Shaped Grooves and Their Stress–Strain State



E. V. Zenkov and D. A. Elovenko

Abstract The analysis of regularities of the change in the stress–strain state (SSS) in prismatic laboratory samples with stress concentrators of the U-shaped grooves is presented. On the basis of numerical simulation of deformation by the finite element method, the dependence of stiffness coefficient of the stress state P and concentration of the equivalent stress K_σ from its basic dimensionless design parameters are determined. The regularities account for a reasonable choice of the geometric parameters of the samples for experimental studies of resistance to static and fatigue deformation in various materials and structural units of various shapes made of them. The calculated estimation of the SSS is carried out by solving the contact problem of deformable body mechanics using the MSC solver NASTRAN and bilinear Coulomb friction model. Analysis of the results of computational experiments showed that when the values of the relative angle of the support surface do not exceed 20° , the account of forces of friction changes as the values of maximum contact pressure on the contact surfaces and the maximum value of the stress intensity in the working area of the considered samples are not more than 5%.

Keywords Stress–strain state · Prismatic laboratory sample · Stiffness coefficient of the stress state · Variant computational experiments · Biaxial tension

1 Introduction

A large number of industrial parts with stress concentrators, including choke points of the capacitive equipment, suspension elements of vehicles, compressors, turbine disks, aircraft skin, and pipeline parts, are used in machines and units in power engineering, petrochemical sector, and transport. Under operating conditions, engineering structures are usually subjected to a complex of repeated (cyclic) loads. Their stress–strain state is characterized by stress concentration located near the

E. V. Zenkov (✉) · D. A. Elovenko
Irkutsk National Research Technical University, 83, Lermontov Str., Irkutsk 664074, Russia
e-mail: jovanny1@yandex.ru

structural heterogeneities (holes, protrusions, grooves, etc.). As a rule, the stress–strain state that occurs near such concentrators is two-dimensional or three-dimensional. It determines the service life of the structure under cyclic loading [1].

The type of stress–strain state at the certain point of the on-load structure (the observation point) is characterized by the value of its stiffness coefficient P equal to the ratio of the first invariant of the stress tensor to the second one [2]

$$P = \frac{\sigma_1 + \sigma_2 + \sigma_3}{\sigma_i}, \quad (1)$$

where σ_1 , σ_2 , and σ_3 stand for the main stresses occurring at the observation point, and σ_i stands for equivalent stress defined by the equation

$$\sigma_i = \frac{1}{\sqrt{2}} \sqrt{(\sigma_1 - \sigma_2)^2 + (\sigma_1 - \sigma_3)^2 + (\sigma_2 - \sigma_3)^2}. \quad (2)$$

It is observed [3, 4] that an increase in stiffness coefficient of the stress–strain state in a certain zone of the structure may lead to the displacement of the deformation center towards this zone, even when the maximum stress level for the whole structure is not achieved. It is critical to note that such a displacement can occur in the case of the cyclic loading of the structure [3] as well as in the case of its quasi-static deformation [4]. This phenomenon must be considered when designing not only the structure as a whole but also its localized stiffening which reduces the stress level in the places of structural heterogeneity.

The problem encountered in the previous experimental studies of resistance to static and fatigue deformation deals with the difficulty of creating biaxial stress–strain state characterized by the ranging ratio of positive components of principal stresses ($1 < P < 2$) in the laboratory sample, as such type of the stress–strain state is the most critical for defect nucleation and growth.

When information is received on the strength of the material under current conditions of biaxial stress–strain often used samples of tubular shape, their tests are tested on complex test machines with several power drives [5–7]. Cross-shaped [8–10] and rectangular [11] samples are widely used to study the behavior of growth of fatigue cracks in the fields of tensile and compressive stresses. Loading of samples is carried out by power drives simultaneously in several directions.

The solution of the presented problem becomes possible with the development of mathematical modeling methods and modern technologies of engineering analysis [12, 13].

To solve the problem of contact mechanics of the deformed body and analyze the strengths of the deformable systems, the finite element method (FEM) is employed. FEM permits applying various design solutions for simulation true stress–strain state in the structural units, thus increasing the accuracy and reliability of calculations for engineering structures.

In this paper, we analyze particular aspects of deformation of prismatic samples [5] for static and fatigue mechanical testing which should simplify the solution to the problem in question.

2 Construction and Conditions for Deformation of the Prismatic Samples

The prismatic sample [5] *I* is supported by the L-shaped projections 2 and bevels 3 at the ends of the protrusions (Fig. 1). For simplicity, we will assume that the directions “up,” “down,” “vertically,” and “horizontally” correspond to Fig. 1. On the side of the inner part of the prismatic sample, the projection 2 is conjugated with radius transition 9. The L-shaped projection 2 has a rectilinear vertical bar 10 adjacent to the prismatic body *I* in the cross section and is connected to the horizontal bar 11 by a hollow chamfer 6. During the mechanical testing, the prismatic sample is supported by its end parts on the surface of the end supports 5 over the area S_1 (see Fig. 1). In the central part of the prismatic sample, a transverse

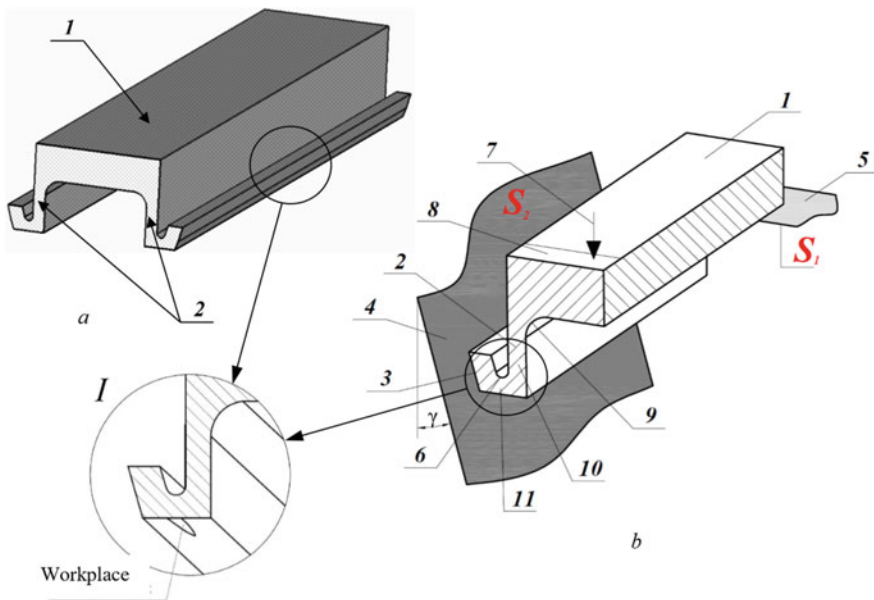


Fig. 1 Prismatic sample (a) and its design features (b) (the view of the quarter of the sample) 1 prismatic body, 2 L-shaped projections, 3 support bevels, 4 inclined support surface of prismatic support S_1 , 5 bearing surface of the end surface S_2 , 6 hollow chamfer, 7 test force, 8 loading surface, 9 internal radial transition, 10 vertical bar of the L-shaped projection, 11 horizontal bar of the L-shaped projection, γ —angle of the slope of support surface S_1 , *I*—area of the working zone of the sample

(in Fig. 1—vertical) test force 7 is applied to its loading surface 8. Under the influence of the force, the prismatic support bevels 3 slide along the inclined support surface of the lateral support 4. In this case, a contact interaction perpendicular to the surface of the support bevel 3 is applied to the protrusions of the sample on the side of the bevels 3. The working zone of the sample is the lower surface of the L-shaped projection 2 (horizontal bar *II*) in its middle part, adjacent to its transverse plane of symmetry where a biaxial bending occurs.

In the study, the values of the coefficients K_σ and P were taken as the characteristics of the stress–strain state of structures when evaluating deformation features and using numerical simulation for prismatic samples. The value of P was determined by Eq. (1), while the value of K_σ (the coefficient of equivalent stress concentration) was defined by the formula:

$$K_\sigma = \frac{\sigma_i^{\max}}{\sigma_i^{\text{nom}}}, \quad (3)$$

where σ_i^{\max} —equivalent stresses in the working zone of the sample (Fig. 2a); σ_i^{nom} —nominal equivalent stresses (intensity of stresses in the working zone of the corresponding sample similar to a loaded prismatic sample without concentrators on its laterals by length, height, and width) (Fig. 2b).

It is assumed that the stress–strain state of the laboratory sample is identified by numerical simulation, and the corresponding values of K_σ and P are known prior to the deformation of the sample upon conducting mechanical tests. Coefficients K_σ and P are chosen as similarity criteria for the laboratory sample and the structural unit as they are physically significant invariants of the stress fields appearing in the simulated structural unit and determining its strength under static or cyclic loading conditions [9].

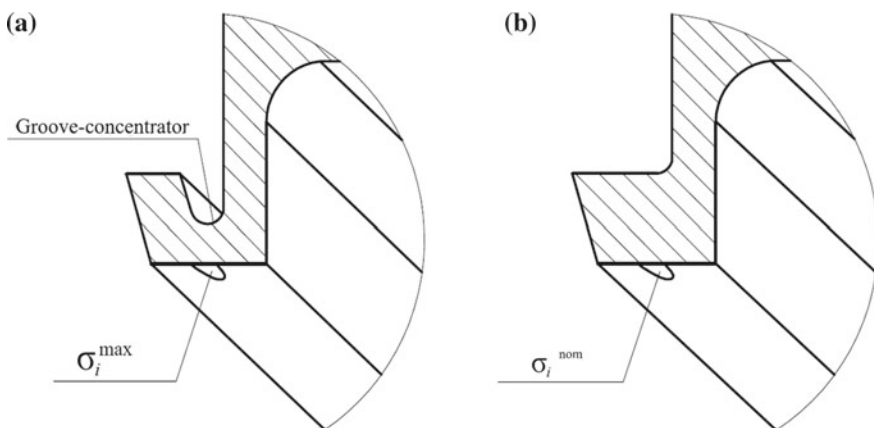


Fig. 2 Scheme for the determining stress concentration K_σ in the prismatic sample

3 Choice of Variable Parameters for Prismatic Samples

The task set at this stage of research is to examine the features of elastic deformation of prismatic samples on the basis of variant computational experiments. This allows us to assess the strength of the structural unit by selecting the values of the geometric parameters of the prismatic samples, thus ensuring the same values of the coefficients K_{σ} and P in the critical zone of the unit and in the corresponding sample.

The prismatic sample is characterized by a number of geometric parameters: the height of the main prism of the sample H_1 , the height of the vertical bar of the L-shaped projections H_2 , the radii of the hollow chamfer r , and the angles of inclination of the support surfaces γ (Fig. 3). The parameters were chosen based on conditions of simulating the value of P in accordance with the equation $1 < P < 2$. Ranges of variation of the dimensionless geometric parameters of prismatic samples are also examined (Fig. 3)

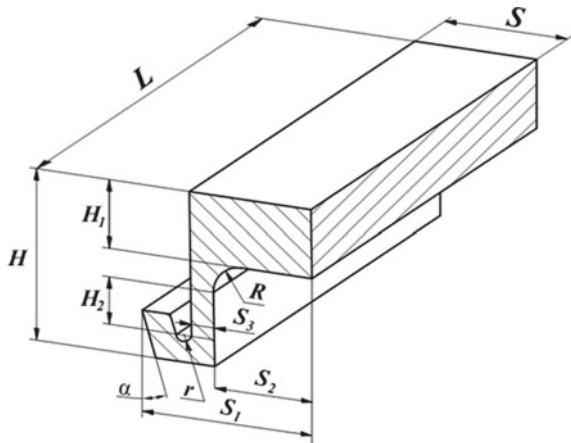
$$h_1 = \frac{H_1}{S} \in [0.25 : 0.4]; \quad h_2 = \frac{H_2}{S} \in [0 : 0.28]; \quad \rho = \frac{r}{S} \in [0.03 : 0.06]; \quad \gamma \in [10^\circ, 15^\circ] \quad (4)$$

where h_1 —relative thickness of the prismatic body; h_2 —relative height of the vertical bar of the L-shaped projection; ρ —relative radius of the hollow chamfer—concentrator; γ —a relative angle of the inclination of support surface; S —total sample thickness; H_1 —the height of prismatic part of the sample; H_2 —the height of vertical bar of the L-shaped projection; r —radius of the hollow chamfer.

Conservative values chosen in the process of the variant studies included:

- sample length $L = 220$ mm;
- sample width $S = 44$ mm;

Fig. 3 Geometric parameters of the prismatic sample (the view of the quarter of the sample)



- radius transition $R = 5$ mm;
- the width of the lateral projections $S_1 = 62$ mm;
- internal groove $S_2 = 36$ mm;
- thickness of the vertical bar $S_3 = 4$ mm.

Variable parameters (4) assist in the formation of biaxial stress. The parameters h_1 and h_2 determine the degree of influence of the longitudinal bending stresses σ_1 , ρ , and γ —transverse bending stresses σ_2 .

To ensure that the prismatic sample is operational, certain restrictions on angles deviating from the vertical bar on the support surfaces are required (angles γ in Figs. 1 and 3). Angles γ are considered adequate under the condition when the forces of the contact interaction lie outside the corresponding friction cone in the contact zone during the process of contact interaction [10]. When the values of the frictional coefficient between the contacting surfaces are small, this condition is satisfied for sufficiently small values of γ . To determine the influence of the angle γ and frictional contact forces on the stress–strain state in the working zone of the sample, an estimate of the SSS was calculated using the FEM. The contact interaction problem was resolved with the help of the MSC NASTRAN solver using the bilinear Coulomb friction model [11].

Figure 4a shows the change in the contact stress p determined by the ratio of the stresses to the applied test load F . Figure 4b shows the change in the contact stresses calculated as the ratio of the stress σ_i appearing in the working zone, to the load F when frictional forces are absent on the inclined contact surface ($\mu = 0$), and when friction forces are ($\mu = 0.2$).

Analysis of the results of numerical experiments (Fig. 4) showed that when the values of the angle γ do not exceed 20° , the accounted friction forces change the

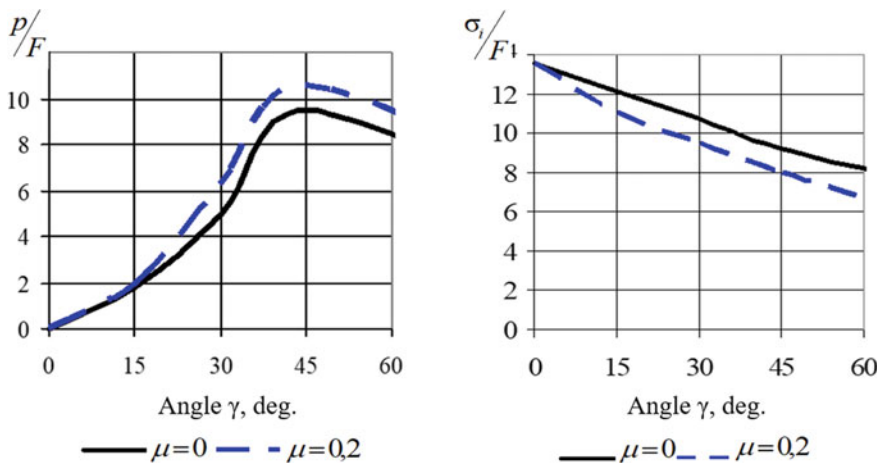


Fig. 4 Dependence of contact stresses p on the inclined support surfaces (left curves) and intensity stresses σ_i (right curves) in the working zone of the prismatic sample

value of maximum bearing pressure on the contact surfaces as well as the maximum value of stress intensity in the working zone of the samples for no more than 5%.

Analysis of the results of numerical experiments (Fig. 4) showed that for values of the angle γ not exceeding 20° , the account of the forces of friction gives a change values of maximum contact pressures on contact surfaces and maximum value of stress intensity not more than 5%.

4 Development of Mathematical Models of Prismatic Samples Deformation

In order to minimize the error and provide the necessary conditions for a biaxial stretching in the prismatic sample and its loading scheme in accordance with Fig. 1, detailed design of all components is performed. Development of deformation models is carried out with the help of numerical finite element modeling coupled with solving the problem of contact mechanics of the deformed body.

In the computational study of the stress–strain state of the samples, their material was assumed to be homogeneous, isotropic, and free of prestressing. Three-dimensional equations of the theory of elasticity with respect to the displacement vector \mathbf{u} were solved:

$$Lu = (\lambda + \mu) \text{grad div } u + \mu \Delta u = 0. \quad (5)$$

Equation (5) is applied to the area occupied by the material of the sample where the bounded surface is $S = S_\sigma + S_{u\sigma}$ under the boundary conditions

$$(v \cdot T)|_{S_\sigma} = F(M), M \in S_\sigma; \quad (u \cdot v)|_{S_{u\sigma}} = 0, (v \cdot T \cdot \tau)|_{S_{u\sigma}} = 0, M \in S_{u\sigma}. \quad (6)$$

Due to the symmetry of the sample and its loading scheme, a quarter of the sample was examined as the boundary conditions for the kinematic fixation were specified in the Cartesian coordinate system (Fig. 5). The boundary conditions for the contact interaction were implemented using the MSC Patran software. Monolithic end supports were designed in order to create tensile longitudinal stresses σ_1 caused by the longitudinal bending of the prismatic sample; prismatic support with a longitudinal groove was constructed with a view to initiate transverse tensile stresses σ_2 caused by the sliding of the support bevels of the L-shaped projections of the sample along the inclined support surface (Fig. 5).

To carry out the testing of the samples, a test force created by the pusher of the testing machine is applied to the loading surface (Fig. 5). When designing the finite element models, a gradual transition from large finite elements to smaller ones, especially near the contact surfaces, was necessitated.

In the deformation model, four pairs (a quarter is taking into account) of the contact surfaces are used (see Fig. 5). The surfaces can be divided into two types in accordance with their designation:

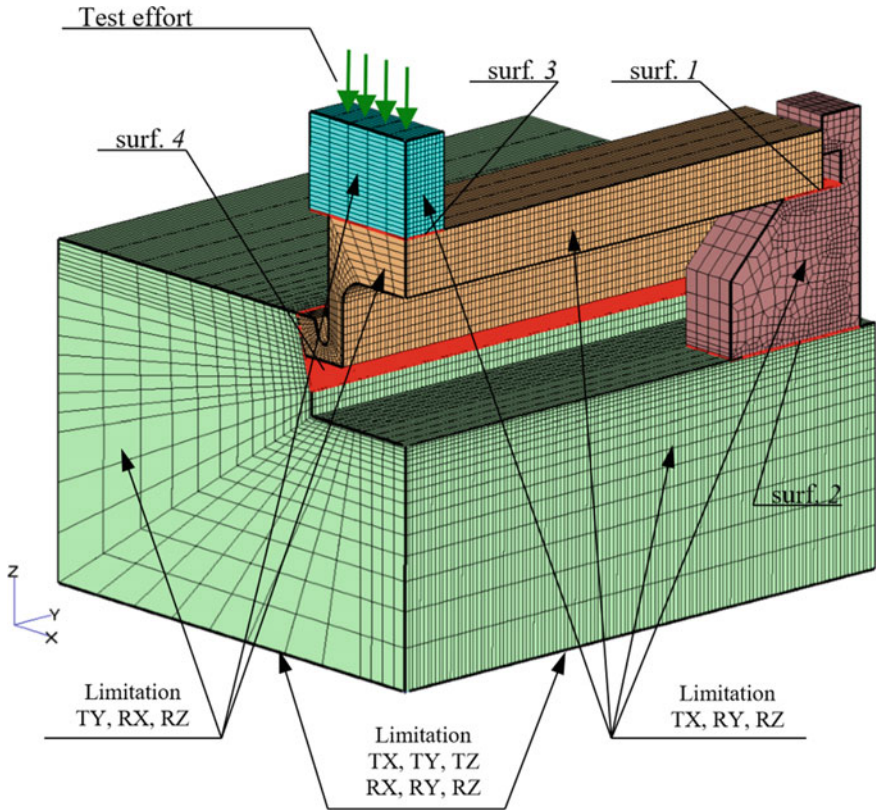


Fig. 5 FEM of prismatic sample for variant researches (the view of the quarter of the sample)

1. Contact of the support surfaces which are perpendicular to the test force and define the longitudinal bending of the prismatic sample. These include the following surfaces (Fig. 5):
 - between the end bearing surfaces of the sample and the corresponding support surfaces of the terminal supports (surf. 1);
 - between the bearing surfaces of the terminal support and the surface of the groove of the prismatic support (surf. 2);
 - between loading side of the sample and the push machine testing (surf. 3).
On these surfaces, the interface circuit is implemented in the form of a contact without friction while lagging of the contacting surfaces remains possible.
2. The contact surfaces that determine the transverse bending of the prismatic sample and are positioned at an angle to the action of the test force—between the inclined support surfaces of the sample and the inclined support surfaces of the prismatic support (surf. 4 in Fig. 5).

In the computational model, the boundary conditions for the kinematic fixation were applied to the base of the prismatic support as restriction of displacements and rotations in the direction of the x , y , and z axes (Fig. 5). To determine the dependences of P and K_σ , the loading of the samples is carried out by the unit pressure.

In a numerical experiment, hardened spring steel 50rV4 (GS-50CrV4) served as the material for the prismatic samples, where elastic modulus $E = 218,000$ MPa, Poisson’s ratio $\mu = 0.3$, and mass density $\rho = 7.85E-9$ tons/mm³. Steel 30ChGSA (14331 for Czech Republic) served as the material of the remaining elements of the composite model (prismatic and terminal supports) and the pusher, where elastic modulus $E = 215,000$ MPa, Poisson’s ratio $\mu = 0.3$, and mass density $\rho = 7.89E-9$ tons/mm³.

5 Results of Numerical Experiments

In the process of numerical simulation, about 80 design variants of prismatic type samples were made, in accordance with Fig. 3. Selected intermediate values of the geometric parameters h_1 , h_2 , ρ , and γ were combined according to the “each with each” scheme. The relative computational error in the numerical determination of the values of the components in the principal and equivalent stresses in the working zone did not exceed 5% [8]. The processing of the results of the finite element modeling is presented in Figs. 6 and 7.

Figure 6 demonstrates the dependence of the coefficients P and K_σ from the height of the vertical bar of the L -shaped projection h_2 and hollow chamfer radius ρ for fixed parameters of the angle of thrust bevel $\gamma = \gamma_{\min} = 10^\circ$ and the thickness of the prismatic body $h_1 = h_1^{\max} = 0.4$. Figure 7 shows the dependence of the coefficients P and K_σ from the height of the vertical bar of the L -shaped projection h_2 and hollow chamfer radius ρ for fixed parameters of the angle of thrust bevel

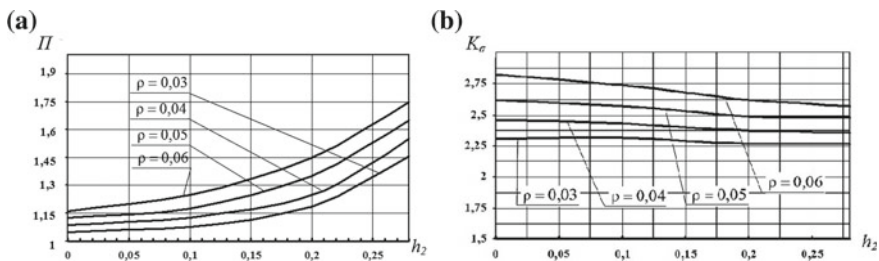


Fig. 6 Dependence of coefficient P (a) and concentration of equivalent stresses K_σ (b) from the height of the vertical bar of L -shaped projection h_2 for $\gamma = 10^\circ$, $h_1 = 0.4$



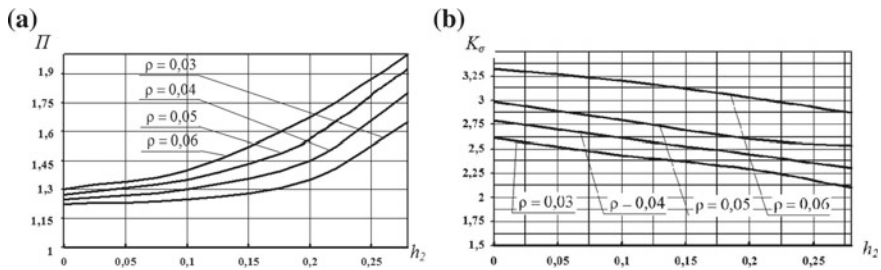


Fig. 7 Dependence of coefficient P (a) and concentration of equivalent stresses K_{σ} (b) from the height of the vertical bar of the L -shaped projection h_2 for $\gamma = 15^\circ$, $h_1 = 0.2$

$\gamma = \gamma_{\min} = 15^\circ$ and the thickness of the prismatic body $h_1 = h_1^{\max} = 0.25$. Both figures illustrate that an increase in the height of the vertical bar of the L -shaped projection h_2 and hollow chamfer radius ρ leads to an increase in P (Figs. 6a and 7a). In this case, these parameters have the same effect on the creation of the biaxial stretching in the working zone up to the maximum possible $P = 2$. The influence of these parameters on the stress intensity level K_{σ} in the working zone varies (Figs. 6b and 7b): the coefficient K_{σ} decreases monotonically with an increase in h_2 while the increase in ρ leads to an increase in K_{σ} , where $2.1 < K_{\sigma} < 3.3$.

Upon the analysis of the results presented in Figs. 6 and 7, it can be concluded that to increase P in the working zone of prismatic samples, the thickness of the prismatic body h_1 should be as small as possible ($1 < P < 2$). A decrease in the parameter h_1 not only leads to a pronounced increase in P but also to a significant increase in the concentration of equivalent stresses in the working zone of the sample. It can also be noted that the value of P is significantly influenced by the angle of the inclined support surfaces γ . Figures 6a and 7a demonstrate that in the case of an increase from $\gamma = \gamma_{\min} = 10^\circ$ to $\gamma = \gamma_{\max} = 15^\circ$, the value of P tends to increase, and any value in the range $1 < P < 2$ can be assigned to it.

The results of variant studies of design characteristics of stress–strain state for prismatic samples are provided for fixed thicknesses of the prismatic body $h_1 = 0.4$ (Fig. 6) and $h_1 = 0.25$ (Fig. 7). Regularities amply illustrated in Figs. 6 and 7 are informative and sufficient when choosing the necessary sizes of prismatic samples to simulate the required values of P . The dependency analysis proved that for any stress–strain state of the constructive unit which operates under conditions of biaxial stretching when the value of P is known, it is always possible to choose a prismatic sample modeling the view of this stress–strain state with the same value of P . Presented data cover the entire range of biaxial stretching ($1 < P < 2$) with the possibility of regulation the equivalent stresses level ($2.1 < K_{\sigma} < 3.3$).

6 Conclusions

It is established that for the proposed prismatic sample, the variation of its geometric parameters allows modeling various types of biaxial stretching up to a stress–strain state characterized by the maximum possible value of the coefficient P ($P_{\max} = 2$). This allows us to apply the proposed samples in assessing the strength of structural units of various shapes.

Increase in the height of the vertical bar of the L -shaped projection h_2 and hollow chamfer radius ρ leads to an increase in stiffness of the stress–strain state (coeff. P). Stress intensity level K_σ causes different dependencies: as h_2 goes up, K_σ decreases monotonically while an increase in ρ leads to an increase in K_σ . Such a phenomenon allows for any stress–strain state of a structural unit in the critical area with a known value of P operating under biaxial tension conditions to select an appropriate prismatic type model simulating the form of this stress–strain state with the same value of P .

References

1. Kogaev VP, Makhutov NA, Gusenkov AP (1985) Calculations of machine parts and structures for strength and durability: directory. Mechanical Engineering, Moscow
2. Smirnov-Alyayev GA (1968) Mechanical basis of plastic of metal processing. Engineering methods. Mechanical Engineering, Leningrad
3. Tsvik LB, Pimshtein PG, Borsuk EG (1978) Experimental study of the stress–strain state of a multilayer cylinder with a monolithic insert. Strength Mater 10(4):448–452. <https://doi.org/10.1007/BF01523798>
4. Tsvik LB, Shcheglov BA, Fedotova SI (1993) Strengthening of holes and static strength of axisymmetric chimney unit. Probl Mach Build Mach Reliab 1:58–65
5. Shtayura ST (2015) Influence of stiffness of the stressed state under biaxial loading of tubular specimens on the strength characteristics of 20 steel in hydrogen. Mater Sci 51(2):254–260. <https://doi.org/10.1007/s11003-015-9837-5>
6. Ivanyts'kyi YL et al (2012) Fracture strength of steels under biaxial loading in hydrogen. Mater Sci 48(3):274–280
7. Carraro PA, Maragoni L, Quaresimin M (2012) Influence of the stress ratio on the multiaxial fatigue behaviour of glass/epoxy tubes. In: Proceeding of 15th European conference on composite materials Venice, Italy, 24–28 June 2012
8. Zhao X et al (2014) Novel design of cruciform specimens for planar biaxial testing of soft materials. Exp Mech 54(3):343–356
9. Aistov IP, Vansovich KA (2017) Estimation of the growth of non through cracks in the high-pressure cylinder of a long-stroke compressor. Chem Pet Eng 52(9–10):614–619
10. Vansovich KA, Aistov IP, Yadrov VI (2016) The fatigue surface cracks growth model taking into account plastic deformations for a cylinder of a low-speed long-stroke compressor. Procedia Eng 152:240–246
11. Kannusamy R, Ramesh K (2014) Analytical prediction of fatigue crack growth behavior under biaxial loadings. J Press Vessel Technol 136(2):021204
12. Zhang J et al (2008) Elastic–plastic finite element analysis of the effect of compressive loading on crack tip parameters and its impact on fatigue crack propagation rate. Eng Fract Mech 75(18):5217–5228

13. Slazansky M et al (2016) Analysis of accuracy of biaxial tests based on their computational simulations: accuracy of biaxial tests. *Strain* 52(5):424–435
14. Zenkov EV, Tsvik LB, Pikhlov AA, Zapolsky DV (2014) Prismatic sample to evaluate of material strength. RU Patent 2516599, MPK G01N3/08./–2012140619/28
15. Zenkov EV, Tsvik LB, Pikhlov AA (2011) Discrete modeling of the stress–strain state of plane-cylindrical samples with stress concentrators in the form of grooves. *Proc ISTU* 7: 23–31
16. Birger IA, Shorr BF, Ioselevich GB (1979) *The machine parts calculation of the strength*. Mechanical Engineering, Moscow
17. Kuznetsov AM, Livshits VI, Tatarinov VG et al (1999) *Vessels and high pressure pipelines: directory*. 2nd edn., Augmented, Irkutsk
18. Zenkov EV (2018) Update of the equations of the limit state of the structural material with the realization of their deformation. *J Phys Conf Ser* 944:012128
19. Targ SM (1980) *Short course of theoretical mechanics*. High School, Moscow
20. Galin LA (1980) *Contact problems of the theory of elasticity and viscoelasticity*. The Science, Moscow

Analysis of Gears' Engagement Parameter in Period of Steady Wear



M. Akopyan, S. Reznikov and O. Kuznetsova

Abstract The paper is devoted to the study of behavior gears' wear parameters after burn-in period, to obtain reliable data about behavior of gear drive, to simplify development of new gears by reducing the number of test cycles, due to the given measurement and calculation data. The article provides a brief description of the automated device for study of gears, on which the measurements of parameters of gear engagement were held. The software, which is specially developed for processing of results of measurements of the device in the automatic mode, carried out necessary calculations with displaying all necessary parameters for a research of impact of wear in transmission. During the experiment, gears with various quantity of teeth were tested, and couples of interaction were chosen so that to capture the big range of the transfer relations. The results of measurements and calculations are presented in graphical form, which allows demonstrating the dynamics of their changes. Due to the large amount of statistical data, at the end of the paper conclusions were drawn about the applicability of the results obtained, using the developed measurement methods, as data for the calculation of gears and gearing.

Keywords Wear · Gear · Gearing · Steady wear · Transmission

1 Introduction

Teething is one of the most widespread types of transfer of mechanical energy. Researches of optimization ways of gears interaction are very important for the industry and are important components of mechanics evolution.

M. Akopyan (✉)

OOO "NPP Advent", 227/1, Nab. Obvodnogo Kanala, 190020

Saint-Peterburg, Russia

e-mail: akopyan.miso@yandex.ru

S. Reznikov · O. Kuznetsova

Saint Petersburg National Research University of Information Technologies,

Mechanics and Optics, 49, Kronverkskiy Prospekt, St. Petersburg 197101, Russia

© Springer Nature Switzerland AG 2020

A. A. Radionov et al. (eds.), *Proceedings of the 5th International Conference on Industrial Engineering (ICIE 2019)*, Lecture Notes in Mechanical Engineering,

https://doi.org/10.1007/978-3-030-22041-9_39

349

Numerous works are devoted to a pilot study of process gears' wear out [1–6]. At the domestic enterprises, the set of machines and stands is used to test details, methods, and control devices of cogwheels [7, 8]. However, the lack of uniformity in the conditions of experiments held and the difference in methods of results processing in many cases brings to loss of important information and significantly reduces efficiency of experimental studies [9].

Optimization of gears' engagement is inseparably linked with a research of their interaction among themselves. For simplification of such researches, the device for gears tests was developed, the description of which is provided in this work [10]. Due to a special technique of carrying out tests and computer processing of the received results, the output data of researches are such indicators of gearing as efficiency, backlash, kinematic error, etc.

Operation of any gear wheel as part of the mechanism begins with a period of running-in, having an uneven nature of changes of parameters of wear and reliability [11]. The detailed research of period of running-in with the use of mathematical modeling of process of interaction of gears is conducted [12]. Accuracy of the applied mathematical model is investigated [13].

The period of running-in is followed by the period of the established gearing which is one of the most important periods of functioning of gearings [14]. The period of the established wear is characterized by the constant speed of wear for the chosen interaction conditions. This period is the longest, which leads to its importance in the design and testing of gears.

The research of indicators dynamics of wear out and reliability in the period of the established gearing will allow to predict a resource and reliability at different stages of an operating time of gears. Considering the difficulty of monitoring the state of gearing under actual operating conditions, due to their use in closed and hard-to-reach mechanical units, knowledge of the reliability parameters will allow to avoid unforeseen failure of the unit, and conduct timely maintenance.

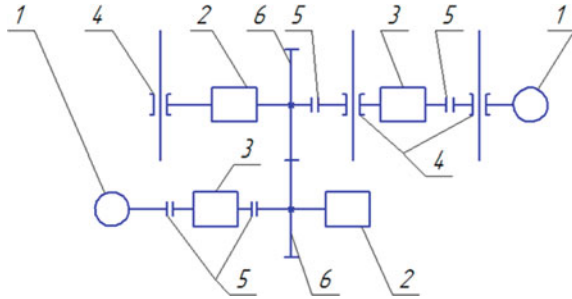
Researches of indicators of gears in the period of the established wear out are directed to receiving the reliable data allowing to formulate recommendations for calculation of gears with similar environment.

2 Description of the Device and Samples

The device for gears study, used for research, has the ability to transfer the measured data to a computer, where a special software package is processing the data. The kinematic scheme of the installation is shown in Fig. 1 [10].

Due to the existence of sensors of angular movement, the software of a computer calculates such indicators of teething as a kinematic and cyclic error, changes of the transfer relation, the backlash, etc. The majority of the indicators calculated by the software package will be used for a research of the period of the established wear.

Fig. 1 Kinematic scheme of the installation: 1—engines; 2—angular displacement sensors (speed sensors); 3—torque sensors; 4—linear guides; 5—compensation couplings; 6—studied gear



The research was conducted with the use of gears which parameters are specified in Table 1.

The parameters of the gears are selected in such a way that the gear ratios are obtained 1; 1:3; 1:6; 2; 3; 3:5; 4:0, and engagement module 1 mm.

3 Description of Methods for Processing the Measurement Results

Theoretical gear, in which there are no errors in manufacturing, installation, etc., reproduces the linear function of the angle of rotation:

$$\varphi_2 = \frac{\varphi_1}{i_{12}} \tag{1}$$

where φ_2 —angle of the wheel rotation, φ_1 —angle of the gear rotation, i_{12} —gear ratio [14–17].

Hereinafter, if it is necessary to note that the parameter refers to the gear, it is supplied with an index $i = 1$, to the wheel— $i = 2$.

In real transmission, the dependence (1) is violated due to the presence of errors and elastic deformations of the transmission elements arising under the action of the transmitted load [18–20].

Table 1 Parameters of gears

Number of teeth of a gear wheel	Number of teeth of a wheel							
18	18	23	29	36	45	54	63	72
20	20	26	32	40	50	60	70	80
22	22	29	35	44	55	66	77	88
25	25	32	40	50	62	75	88	100
30	30	39	48	60	75	90	105	120

Kinematic error $\delta\varphi_2$ in angular values is determined:

$$\delta\varphi_2 = \varphi_{2r} - \varphi_{1r}, \quad (2)$$

where φ_{2r} —valid wheel rotation angle, φ_{1r} —valid gear rotation angle.

The difference of kinematic errors of the transmission at forward and reverse motion is its backlash:

$$j = \delta\varphi_{2rev} - \delta\varphi_{1dir}, \quad (3)$$

where $\delta\varphi_{2rev}$ —kinematic error at reverse motion, $\delta\varphi_{1dir}$ —kinematic error at direct motion.

The period of the function $\delta\varphi_{2r} = f(\varphi_2)$ equals:

$$T = \frac{2\pi z_1}{x}, \quad (4)$$

where x —general multiplier of number of teeth of gear (z_1) and wheel (z_2).

If z_1 and z_2 have no general multipliers, then:

$$T = 2\pi z_1, \quad (5)$$

The kinematic error of transmission is the sum of the harmonic components with a frequency k over a period T , having $k > 1$ and always being an integer. The main component can be found by harmonic analysis. The dominant influence on the kinematic error of the transmission has harmonic components with a repetition frequency of k_1, k_2 and k_z for the period T , where k_1 —the number of revolutions of the gear z_1 ; k_2 —the number of revolutions of the wheel z_2 ; k_z —the number of entrances of the teeth in engagement. Moreover, $z_1 k_1 = z_2 k_2$.

Cyclic error is a component of the wheel kinematic error. This error is determined by the constancy of the gear ratio within the wheel rotation per tooth and is characterized by the waviness of the side surfaces of the wheel teeth. Cyclic errors of gears affect the quality of the profile and the uniformity of the circumferential pitch and, hence, the accumulated error of this parameter. In high-speed gears, cyclic error causes excessive noise, vibration, and mechanism failure [18, 19, 21].

The cyclic error of the transmission is understood to be twice the amplitude of the harmonic component of the kinematic error of the gear or wheel, respectively.

The cyclic error of the tooth frequency in the transmission $f_{z\text{zor}}$ is called the cyclic error with a repetition frequency equal to the frequency of the teeth entering in engagement [18, 19, 22].

Measurement data are received on a computer with special software that automatically processes the results and calculates the required parameters. During the experiment, the software was configured to display the results graphically.

4 Description of Research Results

The period of steady wear in most cases is a major part of the total operating time of the gear. To analyze the change of parameters of the engagement in this period, we should consider the graphs given in Figs. 2 and 3 (where f_{zzor} —the cyclic frequency error, j —the backlash, n —the gear operating speed, Δi_{21} —the gear ratio fluctuation, z_1 —the number of gear teeth, z_2 —the number of wheel teeth).

The transition from the period of running into sustainable wear significantly affects the nature of the changes in the reduced functions. At the beginning of the running-in period, there is a rapid increase in cyclical error and deviation of the gear ratio, as well as a slight decrease in the overlap coefficient. The end of the formation of the stable shape of the tooth profiles and the onset of the steady wear period is characterized by the stabilization of all the specified parameters and the constant rate of increase of the backlash.

Analysis of the results of the experiment allows us to conclude that the steady-state values of the cyclic error, deviations of the gear ratio, and the rate of increase in the dead stroke are the main parameters characterizing the process of wear of the gear transmission in the steady state. Analysis of the results of the experiment allows us to conclude that the steady-state values of cyclic error, deviations of the gear ratio, and the rate of increase in the backlash are the main parameters characterizing the process of wear of the gear in the steady state.

Fig. 2 Changes of a cyclic error and backlash

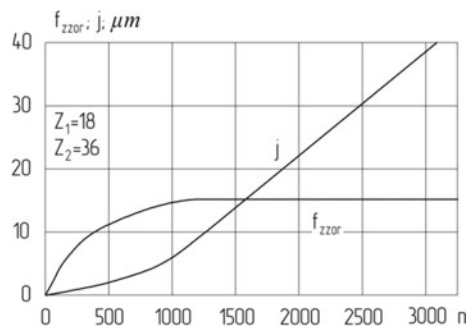
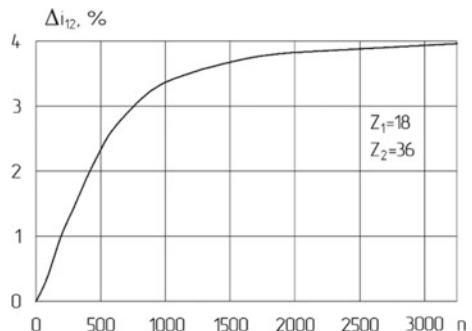


Fig. 3 Changes in gear ratio fluctuations



Due to the almost uniform wear of the teeth in the steady state, the rate of increase in the backlash that actually characterizes the wear rate of the gearing as a whole.

For most of the considered gears, the wear out in steady state is accompanied by a gradual decrease in cyclic error. Therefore, we will take the maximum value of cyclic error, which usually corresponds to the end of the period of running-in, as established.

Let us consider the dependence of the main parameters characterizing the engagement in the period of steady wear, on the gear ratio at various numbers of gear teeth. To compare changes in the transmission parameters, the obtained values of the backlash and cyclic error were converted from angular values to linear ones. Figure 4 shows the graphs of changes in the rate of increase in the backlash.

Figure 4 shows that with an increase of gear ratio and number of gear teeth, the rate of increase in backlash, and consequently, wear rate of the gearing decreases. The greatest dependence of these quantities on the gear ratio (u) is observed at $1 < u < 1.5$. In this interval, for all values of the number of gear teeth (z_1), they are almost halved. At $1.5 < u < 2.2$, the rate of increase in backlash strongly depends on the number of gear teeth. A change in z_1 from 18 to 30 is accompanied by its decrease of 1.5–2 times. When $u > 2.5$, these dependences are weakly expressed.

Graphs of changes in cyclic error and fluctuations in the gear ratio are shown in Figs. 5 and 6. The gear ratio and the position function are inextricably linked to each other (they are similar). For all transmissions, the cyclic error is within 10–25 μm , and the deviation of the gear ratio is within 2–7%. When changing the gear ratio from 1.0 to 1.4, these values quickly increase and reach maximum values at $1.4 < u < 1.7$. When $1.7 < u < 2$, they decrease rapidly. With a further increase in the gear ratio, the change in cyclic error and fluctuations in the gear ratio are determined by the number of gear teeth. For $z_1 = 30$, a gradual decrease in the indicated values occurs. For smaller z_1 , their increase is observed.

Fig. 4 Changes in the rate of increase of backlash

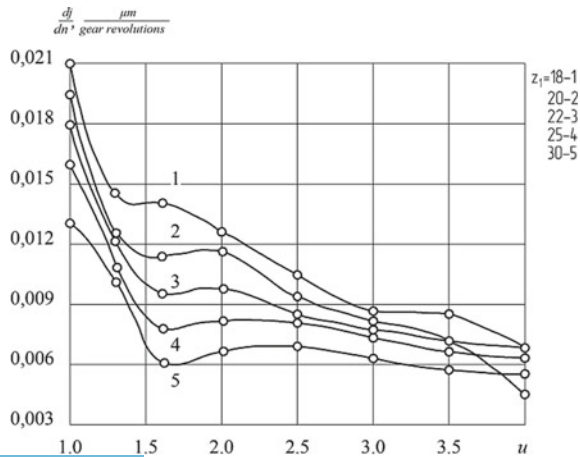


Fig. 5 Cyclic error variations

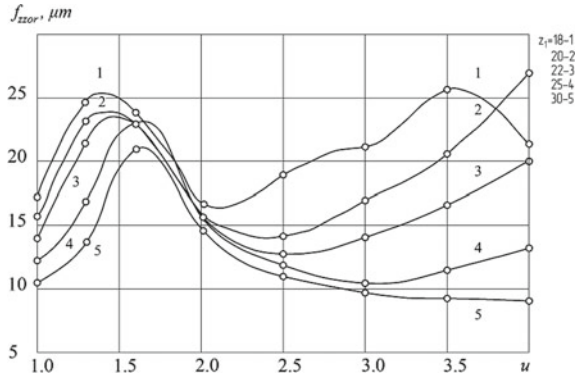
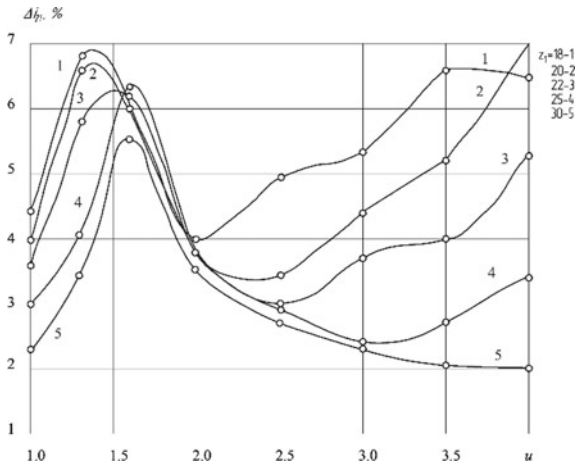


Fig. 6 Oscillation of the gear ratio



Wear out at constant loads cannot lead to disconnection of contact of the contacting teeth. Therefore, despite the fact that the geometrical overlap ratio of the wearing gear is equal to one, the elastic overlap coefficient varies slightly. For most broadcasts, it remained within 1.40–1.45.

5 Conclusion

The conducted research suggests the universality of installation for gear testing. Due to the constructive solutions applied in the device, mounting of gears, possible combinations on the transfer relations and obtaining measurement data were simplified to the maximum and required the minimum expenses of time. The software used in a complex with device displays the most detailed picture of the coupling

gears, and the high accuracy of the device as a whole allows unambiguous conclusions from the obtained data to be made.

The diagrams provided in Figs. 4, 5, and 6 can be recommended for calculation of transmissions, which work conditions approach the conditions put when carrying out an experiment (small rotational speeds and lack of abrasive particles in a zone of contact of teeth).

Using these graphs, it is possible to:

- make a selection of the number of teeth and a breakdown of the gear ratio of the gears, which provides after running-in the minimum speed of increase in backlash or minimum cyclic error and deviation of the gear ratio;
- determine the characteristics of the accuracy of the transmission, established during its operation.

References

1. Ajrapetov EHL (2000) The state and prospects of development of methods for calculating the load and strength gears gearing. Metodicheskie materialy, IzGTY, Moscow
2. Baranov AV, Vagner VA, Tarasevich SV, Baranova YuA, Ponomareva AN (2010) The problem of assessing the wear of the interfaces of gears of transport vehicles and power equipment. Polzunovskij Vestn 1:99–105
3. Onishchenko VP, Goldobin VA (2007) Predicting the health of gears, taking into account the interaction of the shape of worn teeth and contact characteristics. Visnik Skhidnoukraïns'kogo universitetu imeni Volodimira Dalya 9(115):165–171
4. Onishchenko VP (1998) Predicting the shape of tooth profiles of gears as a result of their wear. Progressivnye tekhnologii i sistemy mashinostroeniya. Mezhdunarodnyj sb. nauchnyh trudov 5:155–163
5. Bakhanovich AG (2010) Analysis of the stressed state of teeth of drive toothed belts of standard structures. Mekhanika mashin, mekhanizmov i materialov 1(10):21–28
6. Varsimashvili RSh, Kahiani MR, Varsimashvili ZR (2013) New gears with variable gear ratio. Progressivni tekhnologii i sistemi mashinobuduvannya 1(45):77–84
7. Reshetov DN (1979) Machines and stands for testing components. Mashinostroenie, Moscow
8. Markov AL (1977) Measuring gears. Tolerances. Methods and means of control. Mashinostroenie, Leningrad
9. Tishchenko OF, Valedanskij AS (1977) Interchangeability, standardization and technical measurements. Mashinostroenie, Moscow
10. Reznikov SS, Akopyan MG, Belozubov AV (2017) Automated equipment for testing of gears. ZHurnal Vestnik MGTU Stankin 1(40):39–42
11. Kraskovskij EYa, Druzhinin YuA, Filatova EM (2001) Calculation and design of the mechanisms of devices and computing systems: Tutorial. Vyssh shk, Moscow
12. Akopyan MG (2018) The research in field of gears wearing by using the evolutionary model of gears interaction. Izvestie Vuzov. Priborostroenie 61(2):123–128
13. Akopyan MG, Reznikov SS, Fedotova VN (2017) Comparison of the results of wear gears in the simulation and real tests. Nauchno-tekhnicheskie vedomosti SPBGPU 23(1):184–189
14. Palej MA, Romanov AB, Braginskij VA (2001) Tolerances and landings. Handbook: in 2 parts. Politekhnik, SPb
15. Dunaev PF, Lelikov OP (2004) Designing units and parts of machines. Tutorial. Izdatel'skij centr Akademiya, Moscow

16. Anur'ev VI (2006) Handbook designer-mechanical engineer: In 3 volumes. Volume 1, 2, 3. Izdatel'stvo Mashinostroenie-1, Moscow
17. SHul'c VV (1990) Form of normal wear of machine parts and tools. Mashinostroenie, Moscow
18. Sushkov OD (2009) Metrology, standardization and quality management. KGMTU, Kerch', Tutorial
19. Vinogradov AN et al (1980) Handbook controller machine factory. Tolerances, fit, linear measurements. Mashinostroenie, Moscow
20. GOST 1643-81 Basic standards of interchangeability. Transmission gear cylindrical. Tolerances
21. Kosilova AG, Meshcheryakov RK (1985) Handbook technologist-mechanical engineer. In two volumes. Vol.2. Mashinostroenie, Moscow
22. Istomin SN, SHuvalov SA, Popov PK, Borisov SG, Firsav AF (1987) Kinematic accuracy of instrumental wave gears. Mashinostroenie, Moscow

Kinetostatics of Rotationally Reciprocating Stirred Tank Planetary Actuator



A. A. Prikhodko

Abstract Mechanical stirrers are widely used in chemical, petrochemical, food, construction and many other industries. Currently, a large number of stirred tank actuators with various types of the impeller motion have been developed, and at the moment the most promising constructions are rotationally reciprocating stirred tanks, since they make it possible to ensure high intensity of heat and mass transfer processes in the reactor, to eliminate stagnant zones and to increase the velocity gradient of the stirred liquid. As an actuator, the author proposes to use a planetary gear with elliptical gearwheels, which allows to convert the rotational motion of the motor shaft into a rotationally reciprocating motion of the impeller. For the design and manufacture of stirred tank, it is necessary to investigate its kinetostatics. In the article, the force analysis of the planetary actuator of the mixing device was carried out, as a result of which the design schemes were obtained and expressions were found for determining reactions in kinematic pairs. This will allow further calculations of the elements of kinematic pairs and links for strength, as well as determining the efficiency of the actuator.

Keywords Rotationally reciprocating stirred tank · Planetary gear · Elliptical gearwheels · Kinetostatics · D'Alembert's principle

1 Introduction

Reactors with mixing devices are used in various industries: chemical, oil refining, food, construction and others [1]. They allow to intensify many processes associated with heat and mass transfer. Such processes include widespread chemical technology operations: heating or cooling, dissolution, crystallization, extraction, absorption, electrolysis and heterogeneous chemical reactions, which in most cases occur in a liquid medium [2].

A. A. Prikhodko (✉)

Kuban State Technological University, 2, Moskovskaya Str, 350072 Krasnodar, Russia
e-mail: sannic92@gmail.com

© Springer Nature Switzerland AG 2020

A. A. Radionov et al. (eds.), *Proceedings of the 5th International Conference on Industrial Engineering (ICIE 2019)*, Lecture Notes in Mechanical Engineering,

https://doi.org/10.1007/978-3-030-22041-9_40

359

Currently, classic rotational stirred tanks are mainly used. They are the simplest and most reliable, and a lot of experience has been gained in their design, calculation, mathematical modeling and experimental research. However, in steady state mode of such devices, operation speeds of the impeller and the processed liquid are aligned, and this leads to a decrease in the intensity of mixing.

To eliminate this drawback, there are developed mixing device drives that allow different types of impeller motion:

- plane-parallel (planetary mixers) [3, 4];
- complex spatial [5];
- reciprocating [6, 7];
- rotational with intra-cycle change of angular velocity [8–10];
- reciprocating rotational [11–15].

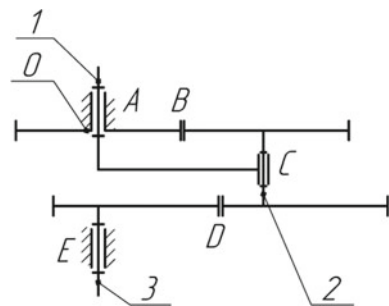
Many studies conducted by various authors show that the use of devices with non-stationary modes of impeller motion contributes to the intensification of heat and mass transfer in the reactor. The most promising for further practical applications are rotationally reciprocating stirred tanks, since they provide a high velocity gradient of the mixed medium, and the use of standard seals allows for integration into existing technological equipment, which can significantly reduce the cost of introducing new machines into the industry.

In [16], there was carried out a structural synthesis and kinematic analysis of a planetary converter of the rotational motion into the rotationally reciprocating motion (Fig. 1).

As a result of structural synthesis, there was obtained a planetary mechanism, which consists of three 1-DOF (A, C, E) and two 2-DOF kinematic pairs (B, D); one three-vertex (link 2) and two two-vertex links (links 1, 3); three connections to the rack 0 ($S = 3$). If we connect the input shaft of the considered actuator with the engine, fix the working element on the output shaft and place it in the reactor, we will get a rotationally reciprocating stirred tank.

When designing the proposed mixing device, it is necessary to carry out a force analysis, which will allow determining the reactions in kinematic pairs and then

Fig. 1 Structural scheme of the mechanism



calculating the parts of the future machine for durability. In the study of kinetostatics, we assume that we know [16–19]: active forces, moments of forces, masses and moments of inertia of links, as well as kinematic parameters (positions, speeds and accelerations).

2 Kinetostatics of Link 3

Force analysis is carried out, starting from the output link 3. In accordance with the D’Alembert principle, we apply external forces and moments acting on the link, as well as forces and moments of inertia forces (Fig. 2).

The following forces act on link 3: the reaction \vec{R}_{30} in the kinematic pair E , the direction of which is unknown; the reaction \vec{R}_{32} in the kinematic pair D , which is directed at an angle α to the tangent O_1O_2 ; normal \vec{F}_{in3}^n and tangential \vec{F}_{in3}^τ inertia forces; the moment of liquid resistance \vec{M}_r and the moment of inertial forces \vec{M}_{in3} . The gravity forces are directed perpendicular to the plane of the figure, so they are not projected on the x - and y -axes. Denote the rotation angles of the carrier and the output shaft φ_1 and φ_3 , respectively. The line O_1O_2 makes an angle γ with the axis Ox_2 . Since O_1O_2 is tangent to the ellipse at point D , then to determine the angle γ , we write the equation of the tangent in the plane Ox_2y_2 [20, 21]:

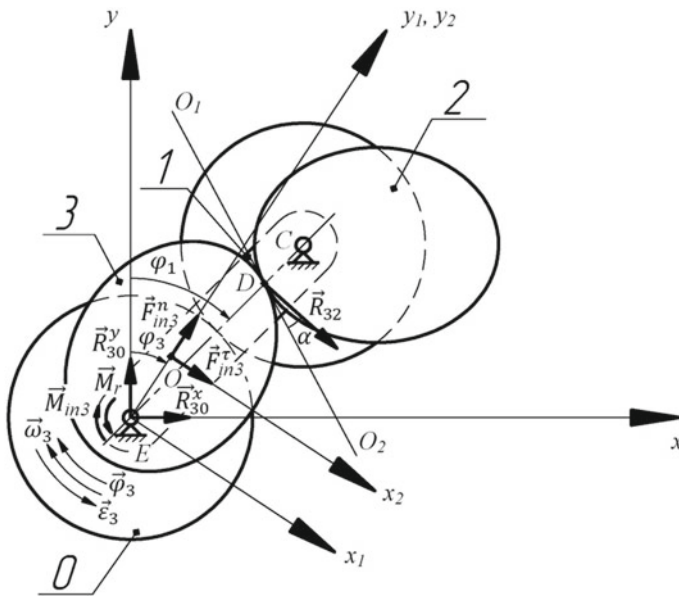


Fig. 2 Design scheme of the link 3

$$\frac{x_0 \cdot x}{a^2} + \frac{y_0 \cdot y}{b^2} = 1 \quad (1)$$

where $x_0 = DE \cdot \sin(\varphi_1 - \varphi_3)$ and $y_0 = DE \cdot \cos(\varphi_1 - \varphi_3) - OE$ are the coordinates of point D in the plane Ox_2y_2 , a and b are the semiaxes of the ellipse, and $OE = c$ is the focal distance of the ellipse. The distance DE is known from [16].

Transforming (1), we obtain an expression for finding γ :

$$\gamma = \text{arctg} \left(-\frac{x_0}{y_0} \cdot \frac{b^2}{a^2} \right)$$

Since all the forces acting on the mechanism links lie in the same plane, the condition of kinetostatic balance is represented as a system of three equations—the sum of the projections of all forces on the x - and y -axes and the sum of moments relative to point E :

$$R_{30}^x + F_{in3}^x \cdot \cos(-\varphi_3) + F_{in3}^y \cdot \cos(\pi/2 - \varphi_3) + R_{32} \cdot \cos(\gamma + \alpha - \varphi_3) = 0; \quad (2)$$

$$R_{30}^y + F_{in3}^y \cdot \sin(-\varphi_3) + F_{in3}^x \cdot \sin(\pi/2 - \varphi_3) - R_{32} \cdot \sin(\gamma + \alpha - \varphi_3) = 0; \quad (3)$$

$$M_c - M_{in3} - F_{in3}^x \cdot c - R_{32}^x \cdot DE \cdot \sin \varphi_1 - R_{32}^y \cdot DE \cdot \cos \varphi_1 = 0. \quad (4)$$

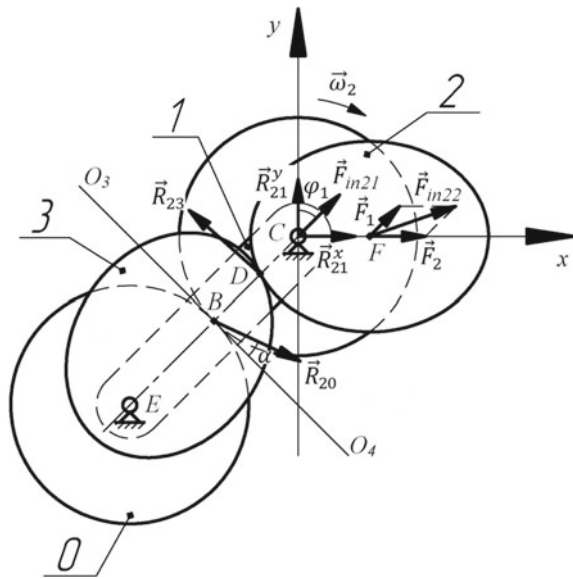
Considering that $R_{32}^x = R_{32} \cdot \cos(\gamma + \alpha - \varphi_3)$ and $R_{32}^y = R_{32} \cdot \sin(\gamma + \alpha - \varphi_3)$, we find the reaction R_{32} from Eq. (4). Then, we find R_{30}^x and R_{30}^y from (2) to (3).

3 Kinetostatics of Link 2

Let us consider balance of the link 2 (Fig. 3). The link performs planar motion, the instantaneous velocity center of which is point B . Dynamic analysis of the machine shows [17, 18] that the angular velocity of the input link is not a constant value due to the change in load on the impeller. However, speed fluctuations do not have a large effect on the forces acting on the machine links. Therefore, for convenience of calculations, we assume that $\omega_1 = \text{const}$ and $\omega_2 = \text{const}$.

The following forces act on link 2: the reaction \vec{R}_{21} in the kinematic pair C , the direction of which is not known; the reaction \vec{R}_{23} in the kinematic pair D , which is directed opposite to the found reaction \vec{R}_{32} ; the reaction \vec{R}_{20} in the kinematic pair B , which is directed at an angle α to the tangent O_3O_4 ; as well as inertial forces that are applied to the center of mass of the link. For convenience of solving the problem, we consider link 2 as the sum of two bodies: body 2.1 (cylindrical gear and satellite shaft), whose inertia force \vec{F}_{in21} is applied to point C and body 2.2 (elliptical gear), which inertia force \vec{F}_{in22} is applied to point F .

Fig. 3 Design scheme of the link 2



Let us find the accelerations of points C and F . Since $\varepsilon_1 = 0$, then $a_C = a_C^n = \omega_1^2 \cdot CE$. Taking the point C as a pole, we get $\vec{a}_F = \vec{a}_C + \vec{a}_{FC}$, where $a_{FC} = a_{FC}^n = \omega_2^2 \cdot CF$ is the acceleration of point F relative to the pole C .

The desired inertia forces \vec{F}_{in21} and \vec{F}_{in22} are determined as follows:

$$\vec{F}_{in21} = m_{21} \cdot \vec{a}_C;$$

$$\vec{F}_{in22} = m_{22} \cdot \vec{a}_F = m_{22} \cdot \vec{a}_C + m_{22} \cdot \vec{a}_{FC}.$$

We introduce the notations $\vec{F}_1 = m_{22} \cdot \vec{a}_C$ and $\vec{F}_2 = m_{22} \cdot \vec{a}_{FC}$ (Fig. 3) and write the balance condition in the form of a system of three equations—the sum of the projections of all forces on the x - and y -axes and the sum of moments relative to point C :

$$R_{21}^x + (F_{in21} + F_1) \sin \varphi_1 + F_2 \sin 2\varphi_1 - R_{23} \cos(\gamma + \alpha - \varphi_3) + R_{20} \cos(\alpha - \varphi_1) = 0;$$

(5)

$$R_{21}^y + (F_{in21} + F_1) \cos \varphi_1 + F_2 \cos 2\varphi_1 + R_{23} \sin(\gamma + \alpha - \varphi_3) + R_{20} \sin(\alpha - \varphi_1) = 0;$$

(6)



$$\begin{aligned}
 & - (F_1 \sin \varphi_1 + F_2 \sin 2\varphi_1) \cdot CF \cos 2\varphi_1 - (F_1 \cos \varphi_1 + F_2 \cos 2\varphi_1) \cdot CF \sin 2\varphi_1 \\
 & - R_{20}^x \cdot BC \sin(\pi + \varphi_1) - R_{20}^y \cdot BC \cos(\pi + \varphi_1) - R_{23}^x \cdot DC \sin(\pi + \varphi_1) \\
 & - R_{23}^y \cdot DC \cos(\pi + \varphi_1) = 0.
 \end{aligned} \tag{7}$$

Considering that $R_{20}^x = R_{20} \cos(\alpha - \varphi_1)$, $R_{20}^y = R_{20} \sin(\alpha - \varphi_1)$ and $\vec{R}_{23} = -\vec{R}_{32}$, we find the reaction R_{20} from Eq. (7). Then, we find the reactions R_{21}^x and R_{21}^y from (5) to (6).

4 Kinetostatics of Link 1

Consider the kinetostatic balance of link 1 (Fig. 4). The following forces act on link 1: the reaction \vec{R}_{10} in the kinematic pair A, the direction and absolute value of which are unknown; the reaction \vec{R}_{12} in the kinematic pair C, which is directed opposite to the found reaction \vec{R}_{21} ; normal inertia force \vec{F}_{in1}^n ; balancing moment \vec{M}_b .

The condition of kinetostatic balance is represented as a system of three equations—the sum of the projections of all forces on the x - and y -axes and the sum of moments relative to point A:

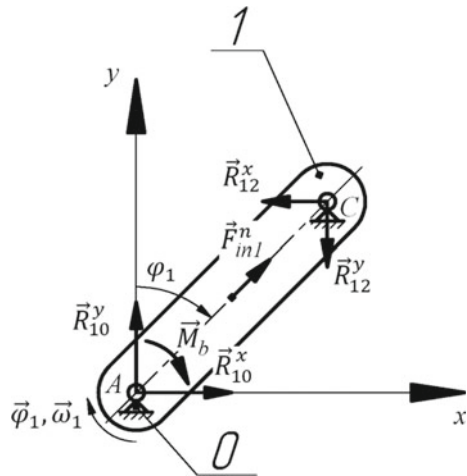
$$R_{10}^x - R_{12}^x + F_{in1}^n \cdot \sin \varphi_1 = 0; \tag{8}$$

$$R_{10}^y - R_{12}^y + F_{in1}^n \cdot \cos \varphi_1 = 0; \tag{9}$$

$$-M_b + R_{12}^x \cdot AC \cdot \cos \varphi_1 - R_{12}^y \cdot AC \cdot \sin \varphi_1 = 0. \tag{10}$$

Unknown values $\vec{M}_b, \vec{R}_{10}^x, \vec{R}_{10}^y$ we find from Eqs. (8–10).

Fig. 4 Design scheme of the link 1



5 Conclusion

Kinestatic analysis is one of the important stages in the design of mechanisms and machines. Studies were conducted in the following sequence:

- design schemes of the planetary gear links with elliptical gears were built;
- in accordance with the D'Alembert principle, forces and moments of inertia forces are applied to the links of the mechanism, as well as external forces and moments;
- balance conditions for each link are obtained, and all reactions in the kinematic pairs of the mechanism are found.

The obtained values of external forces and reactions will allow to carry out the durability calculations of kinematic pairs and links elements, as well as to determine the efficiency of the planetary actuator of the rotationally reciprocating stirred tank.

Acknowledgements The reported study was funded by RFBR according to the research project № 18-31-00256.

References

1. Hemrajani RR, Tatterson GB (2004) Mechanically stirred vessels. In: Paul EL, Atiemo-Obeng VA, Kresta SM (ed) Handbook of industrial mixing: science and practice, John Wiley & Sons, pp 345–390
2. Sterbachek Z, Tausk P (1963) Mixing in the chemical industry. Goskhimizdat, Leningrad
3. Delaplace G, Thakur RK, Bouvier L et al (2007) Dimensional analysis for planetary mixer: mixing time and Reynolds numbers. Chem Eng Sci 62(5):1442–1447. <https://doi.org/10.1016/j.ces.2006.11.039>
4. Hiseman MJP, Laurent BFC, Bridgwater J et al (2002) Granular flow in a planetary mixer. Chem Eng Res Des 80(5):432–440. <https://doi.org/10.1205/026387602320224012>
5. Chusovitin NA, Smelyagin AI, Terskih AA (1996) Mixing device. RU Patent 2,067,535, 10 Oct 1996
6. Wojtowicz R (2014) Choice of an optimal agitated vessel for the drawdown of floating solids. Ind Eng Chem Res 53:13989–14001. <https://doi.org/10.1021/ie500604q>
7. Wojtowicz R (2017) Flow pattern and power consumption in a vibromixer. Chem Eng Sci 172:622–635. <https://doi.org/10.1016/j.ces.2017.07.010>
8. Torubarov NN, Malyshev RM, Kolebanov AV et al (2016) Mixers with nonstationary motion of the stirrers. Chem Pet Eng 52(5–6):327–331. <https://doi.org/10.1007/s10556-016-0194-5>
9. Torubarov NN, Malyshev RM, Serov MV (2016) Apparatus with intracyclic variation of the velocity of the anchor agitator. Chem Pet Eng 52(5–6):379–385. <https://doi.org/10.1007/s10556-016-0203-8>
10. Torubarov NN, Serov MV, Malyshev RM et al (2018) Design of actuator of the drives of nonstationary mixers. Chem Pet Eng 54(7–8):552–559. <https://doi.org/10.1007/s10556-018-0515-y>
11. Senda S, Komoda Y, Hirata Y et al (2014) Fluid deformation induced by a rotationally reciprocating impeller. J Chem Eng Jpn 47(2):151–158. <https://doi.org/10.1252/jcej.13we081>

12. Senda S, Yamagami N, Komoda Y et al (2015) Power characteristics of a rotationally reciprocating impeller. *J Chem Eng Jpn* 48(11):885–890. <https://doi.org/10.1252/jcej.14we392>
13. Prikhodko AA, Smelyagin AI (2015) Dynamic analysis of rotationally reciprocating stirred tank with multiple impellers. In: *Proceedings of 2015 international conference on mechanical engineering, Automation and Control Systems, Tomsk, 2015*. <https://doi.org/10.1109/meacs.2015.7414910>
14. Prikhodko AA (2018) Structural and kinematic analysis of a stirred tank planetary drive. *Matec Web Conf* 226:01012. <https://doi.org/10.1051/mateconf/20182201012>
15. Date T, Komoda Y, Suzuki H et al (2018) Application of a rotationally reciprocating plate impeller on crystallization process. *J Chem Eng Jpn* 41(2):159–165. <https://doi.org/10.1252/jcej.17we015>
16. Smelyagin AI, Prikhod'ko AA (2016) Structure and kinematics of a planetary converter of the rotational motion into the reciprocating rotary motion. *J Mach Manuf Reliab* 45(6):500–505. <https://doi.org/10.3103/s1052618816060108>
17. Prikhodko AA, Smelyagin AI (2016) Development and research of vibromixing reactor with rotationally reciprocating motion of impeller. *Vibroengineering Procedia* 8:102–107
18. Prikhodko AA, Smelyagin AI (2017) Dynamics of rotationally reciprocating stirred tank with planetary actuator. *J Phys: Conf Ser* 858:012026. <https://doi.org/10.1088/1742-6596/858/1/012026>
19. Prikhod'ko AA, Smelyagin AI (2018) Investigation of power consumption in a mixing device with swinging movement of the actuating element. *Chem Pet Eng* 54(3–4):150–155. <https://doi.org/10.1007/s10556-018-0454-7>
20. Ilyin VA, Poznyak EG (2004) *Analytical geometry*. Fizmatlit, Moscow
21. Coxeter HSM (1969) *Introduction to geometry*. Wiley, New York

Automation of Heat Exchanger Shell Holes Machining Operation



A. Yu. Gorelova, M. G. Kristal and V. A. Martynenko

Abstract The design of the shell and tube heat exchanger includes a tubelike shell with holes to which an inlet and outlet pipes are welded. Radial and tangential holes are produced manually by means of plasma cutting with the use of specialized tools, which determines high laboriousness of heat exchanger production. An automatic device is proposed to reduce the laboriousness of this operation. To produce the hole in the heat exchanger shell, two reversible motions are superimposed: linear motion of the cutter along the longitudinal axis of the shell and the shell rotary motion. A mathematical model of the required cutter motion is proposed, which describes the relative trajectories of the plasma cutter and the shell in parametric form. To verify theoretical premises, a prototype of the device was produced using a 3D prototyping technology, a ball screw for the reversible linear motion of the cutter and a stepper motor for the reversible rotary motion of the shell. The shell is fixed by means of a collet chuck and rests on the pipe roller support. The principles of automatic control of the linear and rotary motions of the cutter and the shell are proposed, based on the 3D model of the shell.

Keywords Holes machining · Automatic cutting · Plasma cutting · Automatic device

1 Introduction

Heat exchangers (HEs) are bulky products with shell diameter ranging from 800 to 4000 mm and wall thickness from 10 to 100 mm. HE production includes the production of radial and tangential holes in the shell for inlet and outlet pipes, ranging in diameter from 200 to 1000 mm, to be welded to [1–15]. The operation is performed manually with the use of plasma cutter and specialized tools, what defines the laboriousness of the operation and makes its automation relevant [5–7,

A. Yu. Gorelova (✉) · M. G. Kristal · V. A. Martynenko
Volgograd State Technical University, Lenin Avenue, 28, 400005 Volgograd, Russia
e-mail: asya.gorelova@yandex.ru

10, 12–18]. The automatic cutting device should be designed adaptable for the pieces of varying diameters with the ability of cutting speed control on the basis of the shell material, diameter, wall thickness and the type of the hole (radial or tangential) [12, 16, 17, 19].

Generally, all holes in the HE shell are of either radial or tangential type (Fig. 1). The cutter is placed in the shell’s vertical longitudinal plane of symmetry. Initially, the shell is rotated until the center of the hole reaches the same plane. To preserve the shell’s longitudinal axis’s position with respect to varying diameters of the shell, a three-jaw chuck is used in pair with an adaptable-size pipe roller support (Fig. 2).

The described positioning principle allows to devise a mathematical model, describing the relative motion of the cutter and the shell. Any of the required trajectories are obtainable by the superposition of the reciprocal longitudinal motion of the cutter and the reciprocal rotation of the shell.

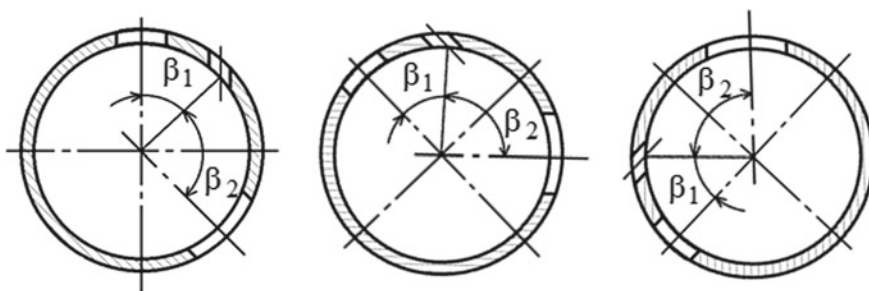


Fig. 1 Different types of the holes in the HE shell

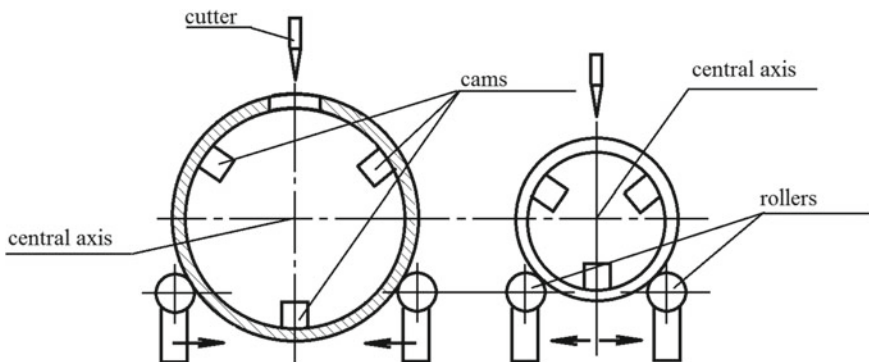


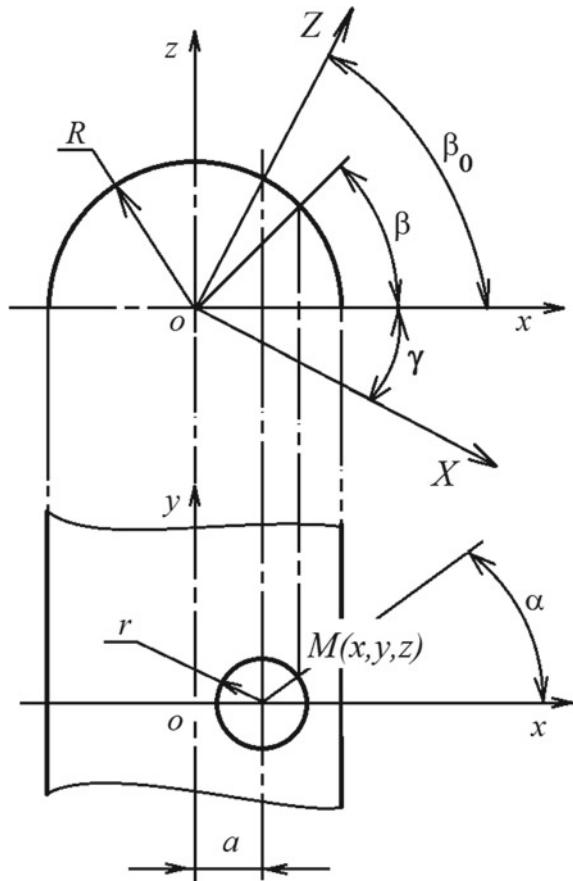
Fig. 2 Positioning of the HE shells of varying diameters

2 Mathematical Model Describing the Trajectory and Kinematic Parameters of the Relative Cutter and Shell Motion During the Hole Formation

Generally, there is displacement a of the hole center from the vertical axis of the shell (Fig. 3). Equation system describing the relation of the motions in planes zox and yox can be written as follows:

$$\begin{cases} x = a + r \cos \alpha, \\ y = r \sin \alpha, \\ z = \sqrt{R^2 - (a + r \cos \alpha)^2}, \end{cases} \quad (1)$$

Fig. 3 Formation of the hole in the HE shell



where R is the radius of the shell, r is the radius of the hole, a is the displacement of the hole axis from the vertical axis of the shell and α is the current angle of the cutting plane yoX .

In the case when the center of the hole lies on the vertical axis of the shell cross section, displacement $a = 0$ and system (1) takes the following form:

$$\begin{cases} x = r \cos \alpha, \\ y = r \sin \alpha, \\ z = \sqrt{R^2 - r^2 \cos^2 \alpha}, \end{cases}$$

The equation of the plane incidental to the axis [9] of the shell can be written as:

$$z = x \operatorname{tg}(\beta) \quad (2)$$

where β is the current angle of the cutting plane zoX .

To avoid the necessity of additional cutter motion in the shell cross-plane which implies additional motor for the case of tangential hole (Fig. 1), the shell rotation is used to bring the hole center to the shell crosscut vertical axis. To achieve this, the frame of reference zoX is rotated to the angle $\gamma = \frac{\pi}{2} - \beta_0$, where $\beta_0 = \arccos \frac{a}{R}$ (Fig. 3).

The equation system in the frame of reference ZoX can be written as follows:

$$\begin{cases} X = \frac{(a+r \cos \alpha)}{\cos \gamma} - Z \operatorname{tg} \gamma = \frac{(a+r \cos \alpha)}{\cos \gamma} - Z \frac{\sin \gamma}{\cos \gamma}, \\ y = r \sin \alpha, \\ Z^2 + X^2 = R^2. \end{cases} \quad (3)$$

System (3) for the coordinate motion $y = r \sin \alpha = r \sin(\omega t)$ allows to achieve the desired equation of the required trajectory of the point of the cut (the point of the contact of the cutter and the shell):

$$Z^2 + \left[\frac{(a+r \cos \alpha)}{\cos \gamma} - Z \frac{\sin \gamma}{\cos \gamma} \right]^2 - R^2 = 0 \quad \text{or}$$

$$\frac{Z^2}{\cos^2 \gamma} - 2 \frac{(a+r \cos \alpha) \sin \gamma}{\cos^2 \gamma} Z - \left[R^2 - \left(\frac{(a+r \cos \alpha)}{\cos \gamma} \right)^2 \right] = 0$$

Multiplying both sides by $\cos^2 \gamma$ gives the final form:

$$Z^2 - 2Z(a+r \cos \alpha) \sin \gamma - \left[R^2 \cos^2 \gamma - (a+r \cos \alpha)^2 \right] = 0 \quad (4)$$

Solving (4) for $Z = R \sin(\beta + \gamma)$ allows to achieve the following equation:

$$\sin(\beta + \gamma) = \frac{(a+r \cos \alpha) \sin \gamma}{R} \pm \sqrt{\frac{(a+r \cos \alpha)^2 \sin^2 \gamma}{R^2} + \frac{R^2 \cos^2 \gamma - (a+r \cos \alpha)^2}{R^2}} \quad (5)$$

which leads to

$$\beta = \arcsin \left[(\varepsilon + \mu \cos \alpha) \sin \gamma \pm \sqrt{(\varepsilon + \mu \cos \alpha)^2 \sin^2 \gamma + \cos^2 \gamma - (\varepsilon + \mu \cos \alpha)^2} \right] - \gamma, \quad (6)$$

where $\mu = \frac{r}{R}$; $\varepsilon = \frac{a}{R}$.

Since $\alpha = \omega t$, the function (6) is the function $\beta(t)$.

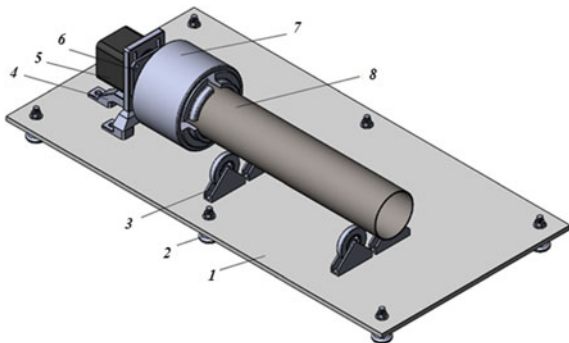
Given that the cutter speed $V = const$, $y(t) = r \sin(\omega t)$ and $V^2 = \left(\frac{dy}{dt}\right)^2 + \left(R \frac{d\beta}{dt}\right)^2$, Eq. (6) allows to define the angular frequency ω , thus making it possible to control the reciprocal motions: longitudinal motion of the cutter and the rotation of the shell. The equations achieved above allow to devise the holes machining control principle aimed to preserve constant cutting speed in an automatic mode.

3 The Device for Heat Exchanger Shell Holes Machining Operation Experimental Rig

The proposed device made with extensive use of 3D prototyping technology includes a collet chuck which fixes the shell resting on the adaptable-size pipe roller, allowing it to rotate about its axis, and plasma cutting head moveable along the axis of the shell. The rig also includes two actuators (linear and rotary), which are acting together to achieve trajectories and velocities of the cutter motion required to produce holes of varying diameters and locations on the shell surface.

Shell rotation unit shown in Fig. 4 is responsible for reciprocal rotation of the HE shell.

Fig. 4 Shell rotation unit:
1–baseplate; 2–adjustable supports; 3–pipe rollers; 4–actuator holder; 5–actuator; 6–bearing unit; 7–collet chuck; 8–shell



Shell rotation unit includes the baseplate (1) mounted on the adjustable supports (2) to ensure the horizontal position of its plane. The shell (8) is fixed by means of collet chuck (7) (Figs. 4 and 5) and rotated by the actuator (5). The collet chuck (7) is mounted on the actuator (5) driveshaft. The actuator (5) is mounted on the baseplate (1) by means of the bracket (4). Actuator's driveshaft (3) rests on the bearing support (6).

Cutter linear motion unit is mounted on the rigid supports (3). Actuator (4), mounted in the holder (5) through the coupling (7), sets the ball screw (8) in motion allowing it to move the cutter assembly (9) along the two cylindrical guides (11) fixed in with the brackets (6) and (13). The screw (8) rests on the ball bearings (12) in the brackets (6) and (13). To trace the cut, the fiber-tipped pen (10) is used instead of the cutter, fixed in the cutter unit (9) (Fig. 6).

The described device action is simulated using CAD program, where the two actuators' motions are set, allowing to achieve the resulting trajectory of the cut (Fig. 7). Experimental rig is shown in Fig. 8.

Fig. 5 Collet chuck

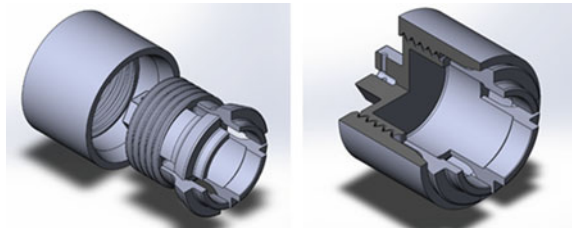


Fig. 6 Cutter linear motion unit: 1-adjustable supports; 2-baseplate; 3-rigid support; 4-actuator; 5-actuator holder; 6-ball bearing unit; 7-coupler; 8-threaded stud; 9-cutter unit; 10-fiber-tipped pen; 11-cylindrical guides; 12-bearing casing; 13-bracket

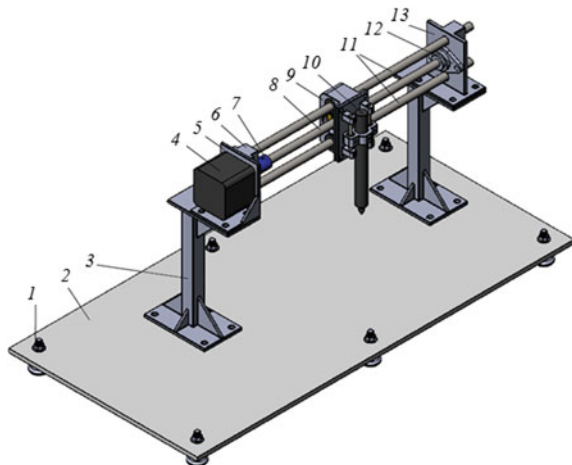


Fig. 7 Trajectory of the cut achieved by computer modeling of the process

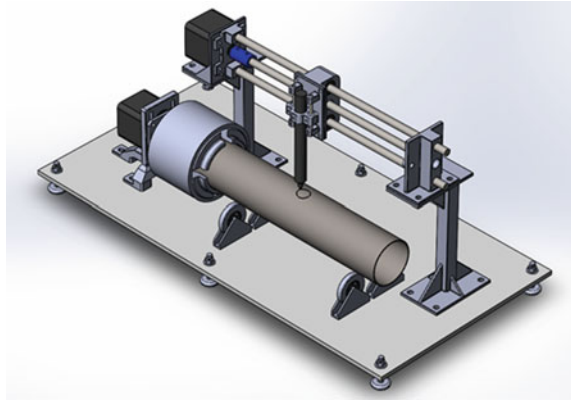
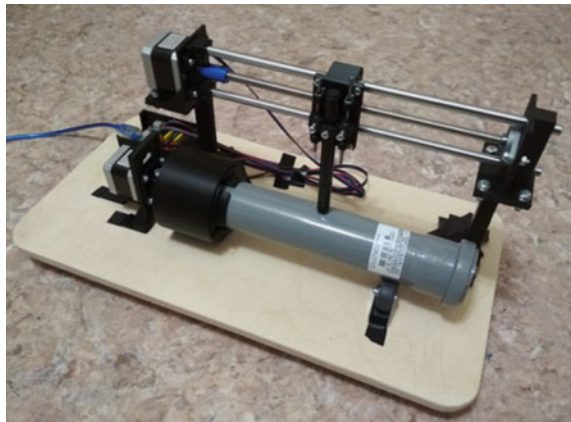


Fig. 8 Experimental rig



4 The Control Principle of Automatic Holes Machining

The control principle of the devised automatic holes machining system is proposed. The shell with its holes is firstly modeled in solid modeling CAE software with respect to given and required parameters of the shell and holes (Fig. 9). The model is then saved as STL file with its surface represented by the list of triangular facets and their corresponding normal lines [1, 8]. Specialized software is used to transform the STL file into the set of layers [11, 20], and the contour of the cut is defined. The G-code is then formed (the set of data containing the information about the movement of the cutter and the shell), which is then loaded into the controller memory, allowing the controller to form signals which set in motion the drivers, producing the cut (Fig. 10).

Fig. 9 Proposed cutting system chart: 1–shell; 2–cutter; 3–drivers

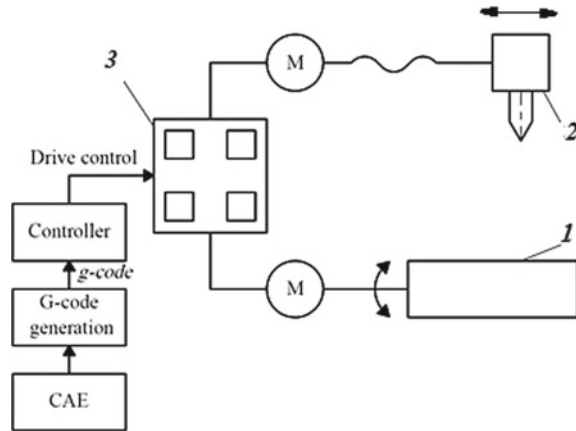


Fig. 10 Solid model of the cutout piece



Acknowledgements The authors express their gratitude to A. M. Makarov (Head of the Department of Technological Processes Automation at Volgograd State Technical University) and Ju. M. Bazhensky (Senior Research Assistant at the same department).

References

1. 3D Printing Industry (2012) 3D Printing processes: free beginner's guide 3D printing industry. Available via DIALOG. <http://3dprintingindustry.com/3d-printing-basics-free-beginners-guide/processes/>. Accessed 10 Nov 2018
2. Baron VG (2018) The heat exchanger. RU Patent 182, 250, 9 Aug 2018
3. Baron VG (2018) The heat exchanger. RU Patent 182, 251, 9 Aug 2018
4. Baron VG (2018) The heat exchanger. RU Patent 182, 252, 9 Aug 2018
5. Bojtler Bit (2014) Laser beam cutting system with variable cutting speed. CH Patent 2, 516, 155, 20 May 2014
6. Clark WT, Partington EC (1978) Machining method. US Patent 4098153, 4 July 1978
7. Delzenne M, Augeraund R (2000) Oxygen arc cutting with plasma pre-heating of ferrous materials, such as structural steel workpieces. FR Patent WO 00/37207 29 June 2000
8. Drobotov A, Avdeev A, Shvets A (2018) Magnetohydrodynamic pump application in complex form aluminum parts additive manufacturing. In MATEC web of conferences international conference on modern trends in manufacturing technologies and equipment 2018 (ICMTME 2018), Sevastopol, Russia, 10-14 Sept 2018, 224:1-6
9. Efimov N (1965) Short course of analytic geometry. Nayka, Moscow

10. Fridel Jens, Irrgang Gerhard, Krink Folker, Ollmann Jens (2015) Method of plasma cutting at plasma cutting unit by pulsating electric current. RU Patent 2, 542, 158, 20 February 2015
11. Gushin I, Avdeev A, Shvets A, Drobotov A (2015) Principles of creating a program for the 3D printing device operation. Izvestia VSTU. 11:50–53. https://doi.org/10.1007/978-981-10-8788-2_11
12. Kovalev OB, Fomin VM (2013) Physical basics of thick sheet materials laser cutting. FIZMATLIT, Moscow
13. Laurisch F, Krink V (2018) Method of plasma cutting of workpieces. RU Patent 2, 647, 959, 21 March 2018
14. Madeja K, Laurisch F, Rueckert R, Krink V (2007) Device and method for the plasma-cutting of workpieces with an additional fusible electrode guided between the nozzle and the workpiece. DE Patent 102005039070, 22 Feb 2007
15. Mokrozub VG, Morozov SV (2013) The Structure of informational and logical model of shell-and-tube heat exchangers. Vestnil TGTU 3:518–525
16. Monaenkov IV (2009) Method for automatic control of laser cutting or hole drilling process and device for its realisation. RU Patent 2, 375, 162, 10 June 2009
17. Rodin AO, Udakov SV, Strizevsky MN (2016) Bulk cutting machine. RU Patent 166, 992, 27 Sept 2016
18. Rudjak EhM, Rudjak EEh (1996) Plasma arc cutting device. RU Patent 9, 510, 23, 66, 20 Nov 1996
19. Tverskoj VS, Tverskoj AV (2006) Method for treatment of surfaces. RU Patent 2, 286, 866, 10 Nov 2006
20. Yakof KSA, Zabudin NF, Sahat IM, Adib MAHM (2018) Development of 3D printed heart model for medical training. In: Hassan M. (ed) Intelligent manufacturing & mechatronics. Lecture Notes in Mechanical Engineering, pp 109–116

Arching Design of Device for Cooling Cutting Zone of Milling Machine Based on Graph Model of Physical Working Principle



A. A. Yakovlev, V. S. Sorokin and S. G. Postupaeva

Abstract The article describes a new method of cooling system searching design, which is based on the physical working principle graph model, based on the thermodynamic description of physical processes. The rationale of the physical working principle graph model has been presented, and basic theoretical propositions concerning the semantic load on the vertices and edges of the graph have been shown. The necessity and sufficiency of this physical working principle graph model for this class of devices have been confirmed by modeling the physical working principle of a technical solution for device for cooling the cutting zone of a milling machine. The example of technical solutions for device for cooling the cutting zone of a milling machine plurality obtainment has been represented. The method can be applied as a means of enhancing the labor efficiency of designers at early stages of designing owing to reduction of labor expenditures when choosing the concept of an engineering system for refrigeration and also as a methodical support for the development of computer-aided design systems.

Keywords Searching design · Physical operating principle · Cooling system · Directed graph

1 Introduction

At present, scientific and technical progress in different fields of industry is characterized by advancing the technical object development compared with the methods of their creation. Traditional design is not able to provide a development time dramatic reduction and improve the object quality. Growing interest in design methodology encourages the creation and development of design methods and the development of computer-aided design (CAD) systems on their basis, all of technical systems' new classes [1, 2].

A. A. Yakovlev · V. S. Sorokin · S. G. Postupaeva (✉)
Volgograd State Technical University, 28, Lenin Ave, Volgograd 400131, Russia
e-mail: posvetlana@mail.ru

In this connection, the purpose of this research is a specialized science-based method of a cooling system (CS) with the searching design creation of a liquid and gaseous working body [3, 4]. This method will increase the quality and efficiency of designer labor quality and efficiency when designing initial stages of CS [5, 6].

The realization of ideas like this is based on different graph models as a rule, which show the main physical processes in technical systems [7, 8]. Consequently, to reach the purpose, it is necessary to solve the following main tasks. The first task is the development of physical working principle (PWP) graph model for the class of technical systems under consideration [9, 10]. The second task is to check the adequacy of the model. The third task is the development of technical solutions' synthesis technique which is based on the PWP model.

2 Physical Working Principle Graph Model

One of the most well-known and theoretically based approaches is functional and physical method of searching design [11–13]. It is based on a model of the PWP, which is represented as a directed graph. The vertices of the graph are physical objects which enable the transformation of input and output material, energy and signal flows. The flows are correlated with graph edges.

Analysis of physical processes, carried out in the CS, has shown that this model requires a significant adjustment for a more adequate PWP reflection of this devices class—it should be verified by the semantic load of graph vertices and edges; also, it provides an opportunity to display the movement routes and the working body interaction sequence.

The most promising way to solve this problem is the use of the phenomenological thermodynamics conceptual apparatus [14, 15]. This is due to three reasons. Firstly, thermodynamics covers the totality of the nature phenomena, making its apparatus extremely versatile and precise and thus opening the possibility of using it to describe all sorts of PWP. Secondly, on the basis of engineering thermodynamics, the description of most energy converters is built. This causes its terminology familiarity when training specialists who design these devices and facilitates their perception of the model. Thirdly, thermodynamics allows the complex real phenomenon substitution to some arbitrary, elementary, which facilitates the process of formalization of the physical working principle description.

In the proposed model, vertices are designated places, the so-called characteristic points where the CS working body is experiencing interactions, for which in thermodynamics a unified formula of the generalized work analytical expression is given:

$$dQ = PdE, \quad (1)$$

where P is the generalized force or so-called intensial which implies physical quantities such as force, speed, pressure, absolute temperature, electric potential difference and chemical potential etc.

E is the generalized coordinate or extensor which implies values such as moving, amount of traffic, volume, entropy, electric charge, mass and material.

The edge semantics is determined by the following considerations. Any interaction between the working bodies is always associated with the change of extensor E that is conditionally compared with the migration process through the control surface of a thermodynamic system, a certain amount dE . For each interaction, there is characteristic parameter E , which uniquely identifies a qualitative and quantitative point of the working body physical properties, insofar as they relate to this interaction [15].

Interactions of the working body are represented on the graph edges labeled of conjugated with them extensors or generalized coordinates. These edges are incident to those vertices (characteristic points), which carried out the relevant interactions [16, 17].

Furthermore, during operation the CS working body substance can move inside the device that necessitates the introduction of edges of a second type—routing connecting characteristic points.

For many cooling systems, functioning characteristic interaction periodicity and working body movement are typical. Examples are a gas cryogenic machine operating on the basis of a reverse Stirling cycle, turbo-refrigerating machines, etc. In this case, the PWP graph is supplemented by a cyclogram for periodic interactions and working body movements.

In developing the PWP model, CS characteristic points, sequence and interaction species in them as well as the order of their passing by the working body are determined. For all the elements of the graph, we will introduce the following notation.

The vertices are marked with letter V with upper and lower indices. Indices indicate the status of the working body and the serial number of characteristic points, respectively. If the working body sequentially passes through several states in one characteristic point, then it can have a composite symbol consisting of several letters. Edges are interaction, marked by letter E with upper and lower indices, which represent the interaction kind and its serial number. Edges are the working body flows marked with letter I , which also has upper and lower indices denoting the components of a working body and the edge serial number.

3 The Physical Working Principle of Cooling System Modeling

In order to verify the adequacy of the proposed PWP graph model for this class of devices, the PWP graph models of the main modern cooling systems have been built [18, 19].

This confirmed its relevance for the class of devices under consideration and provided the basis for the possibility of constructing such models when designing various cooling devices. Figure 1 shows the PWP model, and Fig. 2 design of the device for the supply of lubricating and cooling technological means for cooling the cutting zone of a milling machine, obtained on the basis of this model. On this device, the authors obtained a patent for a utility model RU No. 154326 IPC B23Q11/10, publ. 08/20/2015 [20].

A corona discharge (e^{el}) is maintained between the electrodes 14 and 15 in the ionizer (v_3^1, v_3^2), in which the airflow is ionized (e^{chem}) (Fig. 1). The ionized air (i_1^2) is fed into the annular chamber 8, from which through channels 7 it enters the cavities

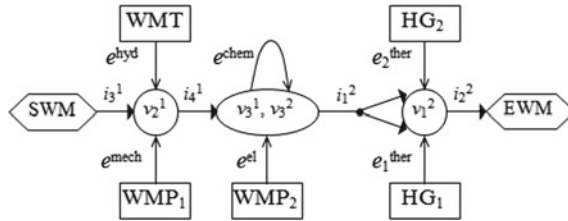


Fig. 1 PWP model of device for cooling the cutting zone of a milling machine tool

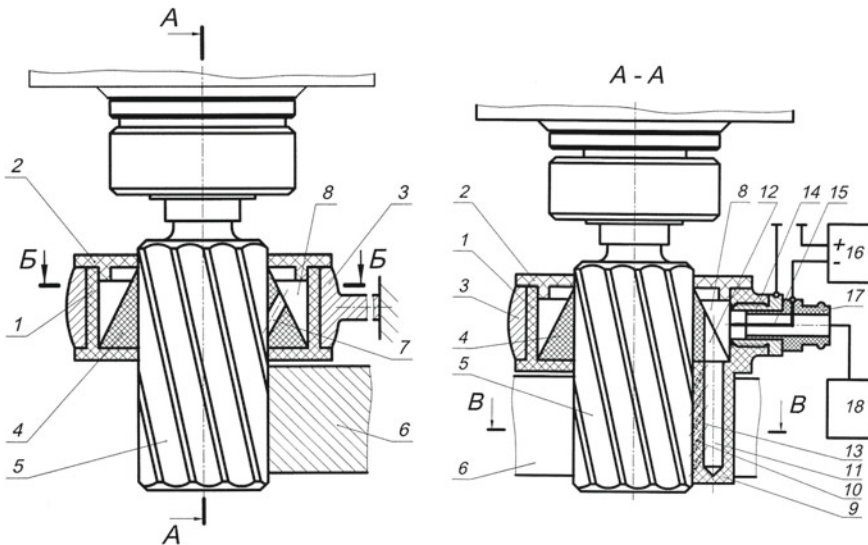


Fig. 2 Device for cooling the cutting zone of the milling machine tool 1—case; 2—cover; 3—kronshane; 4—sleeve; 5—cutter; 6—workpiece; 7—channels; 8—annular chamber; 9—ledge; 10—the inner surface of the protrusion; 11—additional camera; 12—groove; 13—channels; 14—positive cylindrical electrode; 15—negative needle electrode; 16—power supply; 17—fitting; 18—source of compressed air



formed by the inner surface of the sleeve 4 and the outer surface of the mill 5. The streams of ionized air coming out of the channels 7 are reflected from the mill surface ($HG1$) toward the cutting zone, and thus, lubricating and cooling (e_1^{ther}) functions are performed. Another part of ionized air (i_1^2) through the groove 12, made in the sleeve 4, enters the additional chamber 11, from which through the channels 13 it enters the cavities formed by the surface 10 of the protrusion 9 adjacent to the tool teeth 10 and the outer surface of the cutter 5. Outflows' ionized air is reflected from the surface of the cutter in the direction of the cutting zone and carries out lubricating and cooling functions (e_2^{ther}). The sprayed liquid is supplied to the surface of the cutter ($HG1$) and tool ($HG2$) that is not in the cutting zone (Fig. 2).

4 The Synthesis of Technical Solutions Which Is Based on the Physical Working Principle Graph Model

The synthesis of technical solution technique which is based on physical working principle graph model is represented as an algorithm. The algorithm contains the number of procedures and conditional operators (Fig. 3). The structures of input and output data have been implemented for each procedure as relation tables.

Every PWP model's element is associated with structural features identified on the basis of the analysis of thermodynamics abstractions such as "thermodynamic system," "control surface," "external" and "internal degrees of freedom" (Table 1). These functions are presented in papers [15, 16].

In the development of technical solutions to the vertices and edges of the PWP model sets of corresponding them, structural features are compared. Table 2 shows the functions associated with the nodes, and Table 3 shows the functions associated with edges of PWP model for device for cooling the cutting zone of a milling machine. Table 4 contains part of the function to isolate the working fluid from unwanted interactions. These tables have the following structure: m_1^1 —the element of PWP graph identification (vertices and/or edge); m_1^2 —the identification of the elementary function; m_1^3 —elementary function verbal description for the element of the PWP graph; m_1^4 —the identifier of the elementary function; and m_1^5 —necessity for constructive realization.

According to this phase result, technical solution table is filled (Table 5), in which the attributes are the names of elementary functions from Tables 2, 3 and 4. Each row in the table corresponds to a structural element. The table fields contain the values of predicate function $P(f_i)$, which can take a true or false value depending on whether the data element corresponding function f_i is specified in the table header.

In most cases, the structural elements have different feature sets. CS technical solutions are obtained by combining the elements so as to obtain one set of operating all specified functions. One of the technical solution options $\{k_1^2, k_2^3, k_3^2, k_5^2\}$ is highlighted in Table 5 by sparse hatching.

The number of elements in the EC technical solution can vary, which distinguishes this approach from the morphological one.

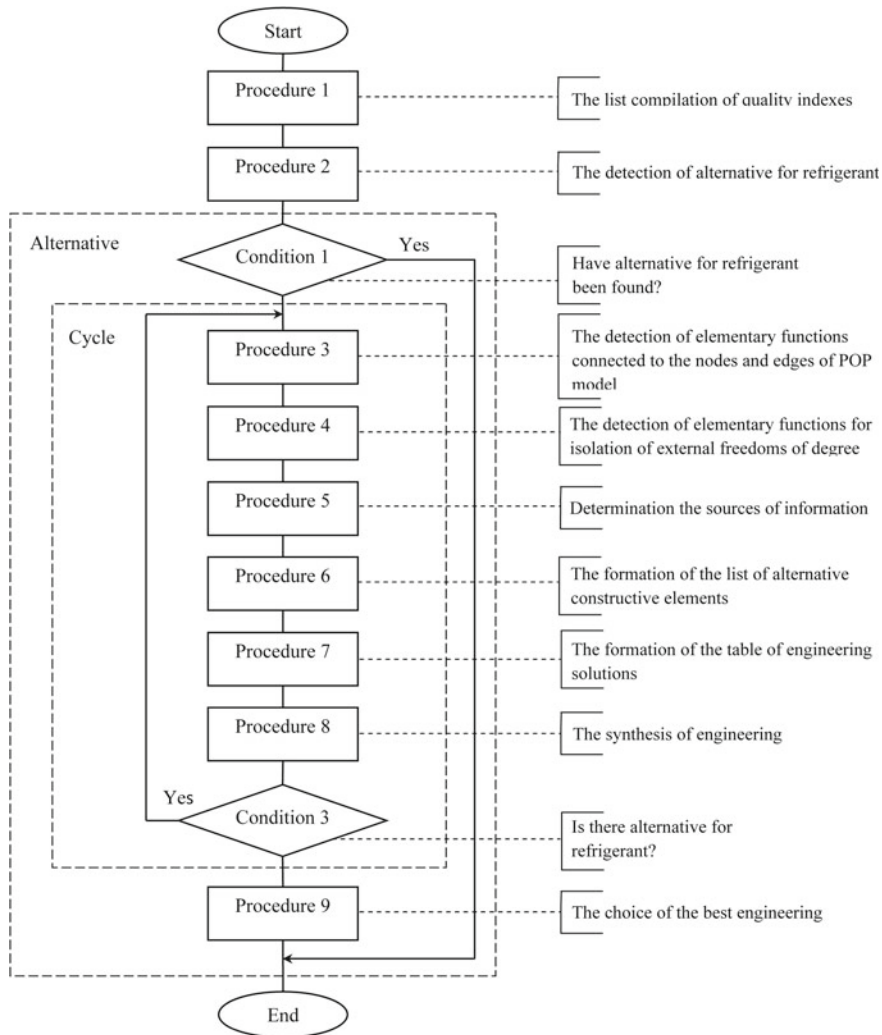


Fig. 3 Method of synthesis of technical solutions

Table 1 Classification of elementary functions of structural elements

Elementary function	Element of PWP graph	Designation
<i>Process maintenance</i>		
1. Providing internal degrees of freedom of the working body	Node (refrigerant)	f_1
2. Providing internal insulation of working body from unwanted interactions	The same	f_2
3. Providing external degrees of freedom of the working body	Node (control surface)	f_3

(continued)

Table 1 (continued)

Elementary function	Element of PWP graph	Designation
4. Providing external insulation of working body from unwanted interactions	The same	f_4
5. Providing an internal degree of freedom for the ongoing factor of extensiveness	Edge	f_5
6. Providing external insulation of conductor extensiveness factor from unwanted interactions	The same	f_6
7. Unions of streams	Hyperedge	f_7
8. Separation of streams	The same	f_8
<i>Process control</i>		
9. Reversal of flow	Edge	f_9^1, f_9^2, f_9^3
10. Change in flow by means of conductive medium resistance	The same	$f_{10}^1, f_{10}^2, f_{10}^3, f_{10}^4, f_{10}^5, f_{10}^6$
11. Change in flow by means of conductive cross section	-//-	$f_{11}^1, f_{11}^2, f_{11}^3$
12. Change of specific flow characteristics	-//-	f_{12}

Table 2 List of functions connected to the nodes of PWP model for devices for supply in lubricating and cooling technological means during milling

m_1^1	m_1^2	m_1^3	m_1^4	m_1^5
v_1, WMP_1	$f_3(e^{mech})$	Providing the ability for air compression	001	0
v_2, WMP_2	$f_3(e^{el})$	Providing the ability for corona formation	003	1
v_3, HG_1	$f_3(e_1^{ther})$	Providing the ability for heat removal from the detail	005	1
v_3, HG_2	$f_3(e_2^{ther})$	Providing the ability for heat removal from the tool	006	1

Table 3 List of functions connected to the edges of PWP model for devices for supply in lubricating and cooling technological means during milling

m_1^1	m_1^2	m_1^3	m_1^4	m_1^5
e^{mech}	$f_5(e^{mech})$	Providing the ability for supplying mechanical extensor to the air	007	0
e^{el}	$f_5(e^{el})$	Providing the ability for supplying electric charge to the electrodes	009	1
i_1^2	$f_5(i_1^2)$	Providing the ability for supply of ionized air to the cutting zone	013	1



Table 4 List of functions to protect the working medium from unwanted interactions of the device for the supply of cooling lubricant technological means during milling

m_2^1	m_2^2	m_2^3	m_2^4	m_2^5	m_2^6
v_2	e_{03}^{el} —voltage supply to the machine tool by ionizer	$f_4(e_{03}^{el})$	Isolation of the electric charge in the ionizer from the machine tool	904	1
v_2	e_{02}^{hyd} —leakage of ionized air in the ionizer	$f_4(e_{02}^{hyd})$	Protection of ionizer against leakage of ionized air	905	1
i_1^2	e_{03}^{hyd} —leakage of ionized air in the conductive channel	$f_6(e_{03}^{hyd})$	Protection of conductive channel against leakage of ionized air	906	1

Table 5 Part of the technical solution table for devices for supplying lubricating and cooling means during milling

Structural elements	The number of elementary functions from tables M1 and M2							
	003	005	006	009	013	904	905	906
k_1^1								
k_1^2								
k_1^3								
k_1^4								
k_1^5								
k_2^1								
k_2^2								
k_2^3								
k_2^4								
k_2^5								
k_3^1								
k_3^2								
k_3^3								
k_3^4								
k_3^5								
k_4^1								
k_4^2								
k_4^3								
k_4^4								
k_4^5								
k_5^1								
k_5^2								
k_5^3								

5 Conclusions

The proposed method can be used when structural elements have different sets of functions, and morphological table’s development is difficult or impossible. This is due to the fact that the model of the PWP allows one to create a table (Table 3), of which the technical solutions’ cooling devices are produced by docking of inter-operable components. The PWP model development process, the definition of constructive functions and tabulation of technical solutions are carried out according to strict rules, which are practically independent of human intuition. The method study does not require the new concept development, and its use is the use of specialized databases. As elements can be used, descriptions of the patent fund technical solutions and other scientific and technical literature.

References

1. Alves JF, Navas HVG, Nunes IL (2016) Application of TRIZ methodology for ergonomic problem solving in a continuous improvement environment. In: international conference on safety management and human factors, Springer, United States, pp 473–485. https://doi.org/10.1007/978-3-319-41929-9_43
2. Berdonosov VD, Kozita AN, Zhivotova AA (2016) TRIZ evolution of black oil coker units. In: chemical engineering research and design. Vol 103. Springer, Komsomolsk-na-Amure, pp 61–73. <https://doi.org/10.1016/j.cherd.2015.08.013>
3. Chani JA, Natasha AR, Che Hassan CH, Syarif J (2016) TRIZ approach for machining process innovation in cryogenic environment. Int J Mater Prod Technol. Inderscience Enterprises Ltd 53:268–297. <https://doi.org/10.1504/ijmpt.2016.079200>
4. Korobkin D, Fomenkov S, Kravets A, Kolesnikov S, Dykov M (2015) Three-steps methodology for patents prior-art retrieval and structured physical knowledge extracting. Commun Comput Inf Sci 535:124–136
5. Glazunov VN (1990) The search of physical operating principles of technical systems, p 143
6. Zaripov M, Zaripova V, Petrova I (2002) Project of creation of knowledge base on physical effects. In 23th international conference on systems engineering. Springer, Las Vegas, pp 365–372. https://doi.org/10.1007/978-3-319-08422-0_54
7. Zaripova V, Petrova I (2014) Knowledge-based support for innovative design on basis of energy-information method of circuit. In: 11th joint conference on safety knowledge-based software engineering. Springer, Volgograd, pp 521–532. https://doi.org/10.1007/978-3-319-11854-3_45
8. Zaripova V, Petrova I (2015) System of conceptual design based on energy-informational model. In: symposium on education in measurement and instrumentation, IMEKO, Wroclaw. https://doi.org/10.1007/978-3-319-08422-0_54
9. Kamaev VA, Yakovlev AA (2006) Information modelling of the physical operating principle and formation of a multitude of engineering solutions of energy converters. Inf Technol 1:2–8
10. Zaripova VM, Petrova IY, Kravets A, Evdoshenko O (2015) Knowledge bases of physical effects and phenomena for method of energy-informational models by means of ontologies. Commun Comput Inf Sci 535:224–237
11. Fomenkov SA, Korobkin DM, Kolesnikov S, Kamaev VA, Kravets AG (2015) The automated methods of search of physical effects. Int J Soft Comput 10(3):234–238
12. Koller R (1976) Konstruktions methode fur den Maschinen. Berlin, Heidelberg, New York, Gerate und Apparateban, p 430
13. Fomenkov SA, Davydov DA, Kamaev VA (2004) Modeling and automated use of structured physical knowledge. Mechanical Engineering-1, Moscow, p 297
14. Veinik AI (1991) Thermodynamics of real processes. Navuka i Tehnika, Minsk, p 576
15. Veinik AI (1968) Thermodynamics. Minsk, Visheysh shcola, p 464
16. Kamaev VA, Yakovlev AA (2006) Physical working principle modeling and developing sets of technical solutions for energy converters. Inf Technol 1:2–8
17. Schevchuk VP, Yakovlev AA (2006) The method for synthesis of conceptual engineering solutions power converters. Industr energ 3:41–46
18. Kurylev ES, Onosovskiy VV, Rumyantsev YD (2000) Refrigerations units. Polytechnic, Spb, p 367
19. Dyachek PI (2007) Refrigerating machines and units Fenix high education, Rostov n/D, p 424
20. Yakovlev AA, Mishustina SN, Sorokin VS, Mishustin OA (2015) Device for supplying of lubricant cooling technological means. Lm 154326 of the Russian Federation, IPC B23Q 11/10, VSTU

Processing of Renewable Wood Biomass into Thermally Modified Pellets with Increased Combustion Value



R. G. Safin, D. B. Prosvirnikov and T. O. Stepanova

Abstract The article deals with the problems of creating new types of fuels based on the processing of renewable forest bioresources and ways of processing wood materials into gaseous, liquid and solid fuels. Solid biofuel, in the form of pellets, is becoming widely used, its production is expanding annually, and that is why much attention is paid to increasing the quality of this type of fuel. KNRTU is conducting research on the integrated processing of wood biomass into liquid and solid fuels. A flow chart of integrated processing of wood biomass into liquid and solid fuels is presented. The authors considered an installation for the production of thermally modified pellets with high heat of combustion. The results of mathematical and physical modelling of thermal modification of pellets obtained by adding lignin are presented. The kinetic curves for the decrease in the specific mass of wood pellets under different temperature conditions, the dependence of the non-condensable gas composition on temperature, the dependence of the heat of combustion of wood pellets on the temperature of the thermal modification process and the concentration of lignin, and the dependence of the hardness of pellets on the initial concentration of lignin are presented. The technology for the production of solid biofuels—thermally modified pellets consisting of shredded wood and lignin—has been developed.

Keywords Wood biomass · Wood waste · Cellulosic ethanol · Combustion gases · Liquid fuels · Solid fuels

1 Introduction

Currently, the problem of creating new types of fuels based on the processing of renewable forestal bioresources is urgent. There are known methods of processing wood materials into gaseous [1] liquid [2] and solid fuel [3, 4]. Currently, solid

R. G. Safin · D. B. Prosvirnikov (✉) · T. O. Stepanova
Kazan National Research Technological University, 68, K. Marx Str., 420015 Kazan, Russia
e-mail: prosvirnikov_dmi@mail.ru

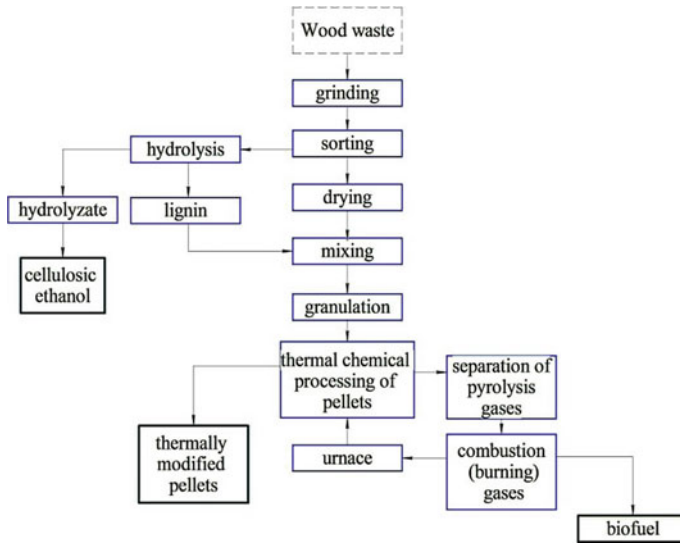


Fig. 1 Technological scheme of complex processing of wood waste

biofuels, in the form of pellets, are becoming more widely used, its production is expanding every year, and thus, much attention is paid to increasing the quality of this type of fuel. KNRTU is conducting research on the integrated processing of wood biomass into liquid and solid fuels [5].

Figure 1 shows a flow chart for the integrated processing of wood biomass into liquid and solid fuels.

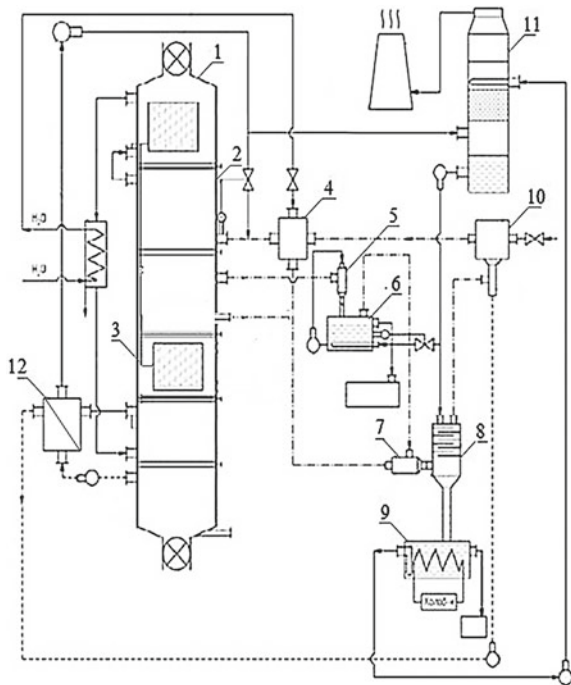
The final products of the presented scheme for complex processing of wood and agricultural waste are the hydrolyzate, which serves as feedstock for the production of liquid fuel and thermally modified pellets with high combustion value, as well as bio-oil obtained by condensation of the resulting vapour–gas mixture. Of all the stages of fuel production, the thermochemical processing of granulose elements is of scientific interest. These are stages of drying, thermal modification, cooling in three steps. Thermochemical processing involves a series of interrelated processes of heat and mass transfer, complicated by chemical transformations, consisting of many parallel reactions, in which endothermic processes with the flowing of thermal energy at the beginning of the process are replaced by exothermic reactions [6]. The works of V. N. Kozlova, V. I. Koryakina, A. N. Koryakina, A. N. Kislitsin, V. N. Pialkina, A. K. Slavic, V. I. Yagodina, E. A. Lebedeva, N. I. Bogdanovich, R. G. Safina, Yu. L. Yuriev, D. A. Ponomareva, A. N. Gracheva, S. N. Bamford, C. Di Blasi, P. S. Maa, C. Briens and F. Thurner, D. Meier are devoted to the issues of thermochemical processing of wood materials. Despite the large number of scientific works, due to the increased complexity of the processes in the field of thermal decomposition of wood, there are no uniform methods for calculating technological processes and devices for the continuous pyrogenic processing of wood materials into thermally modified pellets.

2 Objects and Research Methods

Studies were conducted on the installation for the production of thermally modified pellets (see Fig. 2) [1]. The installation consists of a vertical retort 1, in which, due to gravitational forces, wood pellets move through heating, drying 2, thermal modification, cooling, transforming them into thermally modified pellets, the system for separating the generated gases, the furnace unit, gas cleaning system, recuperative heat exchangers 4, 12. The cooling of the finished product occurs in three steps. In the first stage, the heat from the thermally modified pellets is removed by means of a heat pipe 3 to heat the wood particles in the preheating zone. At the second stage, cooling is carried out by convection by furnace gases discharged from the heating zone of the feedstock 2. At the third stage, the finished product is cooled by air entering the furnace 10.

The pyrolysis gases are separated into high-boiling and low-boiling fractions in mixing condensers 5, 7. Non-condensable gases are burned in the furnace 10. Heat energy from furnace gases is spent on the production of superheated steam and drying wood pellets. The oxidizer is heated before feeding to the furnace due to convective cooling of thermally modified pellets at the third stage and conductive cooling of the furnace gas in the recuperative heat exchanger 12. To cool the refrigerant in the mixing condensers, the used absorbent from the packed column 11 is used [7].

Fig. 2 Installation for the production of thermally modified pellets



The thermal modifying of pellets is carried out by the steam vapour heated up to 300 °C.

Technological zones of the retort are isolated between themselves by sliding gates and from the environment by sectional feeders. Liquefied high-boiling components with a boiling point of more than 100 °C are collected in tanks, and the dehydrated low-boiling components are taken into a container. These components can be used to separate new products from them or in the form of liquid fuels. To launch the installation and maintain the required heat balance, natural gas is supplied to the furnace. The volumetric cooling of the condensate in the separation apparatus 6 by the introduction of the spent absorbent makes it easy to maintain the required temperature of the induced condensate and to separate the vapour phase of the pyrolysis gases into a mixture of high-boiling and low-boiling components.

3 Modelling the Process of Thermal Modification of Pellets

The temperature field in the process zones of the installation is determined by the heat transfer equation [7, 8], which describes the change in temperature of the material over time in layers. For a one-dimensional layer, it can be written as:

$$\rho_{layer} \cdot c_{layer} \cdot \frac{\partial T_{layer}}{\partial \tau} = \frac{\partial T_{layer}}{\partial h} \cdot \left(\lambda_{ef} \cdot \frac{\partial T_{layer}}{\partial h} \right) + q_{layer}, \quad (1)$$

ρ_{layer} is the bulk specific gravity of the pellet layer, kg/m³; c_{layer} is the heat capacity of the bulk layer of pellets, J/(kg·K); λ_{ef} is the effective thermal conductivity of the layer of pellets, W/(m·K); h is the coordinate of a particle in a layer, m; and q_{layer} is the specific heat flow determined by the heating of the pellets and the chemical reactions taking place, J/m² s:

$$q_{layer} = q_{mh} + q_{cr}, \quad (2)$$

where q_{mh} is the heat sink on material heating, J/m² s, and q_{cr} is the heat sink (influx) due to chemical reactions, J/m² s.

The initial temperature in the layer T_H is determined by the final temperature of the material after the previous zone, and the current temperature at the boundary of the layer of material is determined by the temperature of the heat supplying surfaces. At a temperature of more than 180 °C, the thermal chemical decomposition of wood begins. This is accompanied by the formation of coal, steam–gas mixture and a decrease in the mass of wood. The change in mass per volume unit for each of the indicated components can be written as follows [7, 9]:

- For wood,

$$\frac{\partial \rho'_{b,m}}{\partial \tau} = -k_{b,m} \cdot \rho'_{b,m} \quad (3)$$

- For coal,

$$\frac{\partial \rho'_c}{\partial \tau} = \phi \cdot k_{b,m} \cdot \rho'_{b,m} \quad (4)$$

- For vapour–gas mixture,

$$\frac{\partial \rho'_{gv}}{\partial \tau} = (1 - \phi) \cdot k_{b,m} \cdot \rho'_{b,m}. \quad (5)$$

$\rho'_{b,m}$ is the biomass specific weight, kg/m^3 ; ρ'_c is the specific gravity of coal, kg/m^3 ; ρ'_{gv} is the specific gravity of the gas–vapour mixture in the thermal modification zone, kg/m^3 ; and $k_{b,m}$ is the rate constant of chemical reaction of biomass decomposition, s^{-1} .

The degree of thermal modification is determined by the formula:

$$\phi = \frac{\rho'_c}{\rho'_c + \rho'_{b,m_0}}. \quad (6)$$

The change in mass of the vapour–gas phase of the pyrolysis zone is determined by the sum of the mass flows due to convection and the reactions of thermal decomposition of wood:

$$\frac{\partial(\varepsilon \cdot \rho'_{gv})}{\partial \tau} = -\frac{\partial(w_{gv} \cdot \rho'_{gv})}{dh} + (1 - \phi) \cdot k_{b,m} \cdot \rho'_{b,m} \quad (7)$$

where ε the porosity of the particle is determined from the expression, m^3/m^3 .

$$\varepsilon = 1 - \frac{m_{b,m}(1 - \varepsilon_{b,m})}{m_{b,m_0}}. \quad (8)$$

Darcy's law is used to determine the velocity of the gas flow:

$$w_{gv} = -\frac{K_p}{\mu_{gv}} \cdot \frac{\Delta P}{H}, \quad (9)$$

where w_{gv} is the dynamic viscosity of gas, Pa-sec, and K_p is the gas permeability of the particle, which is calculated by the formula

$$K_p = (1 - \phi) \cdot K_{b,m} + \phi \cdot K_c \quad (10)$$

Heat sink during thermal modification of biomass affects the temperature change of the layer. When calculating, we assume that the temperature of the wood particle does not deviate from the temperature of the resulting pyrogases, and the gas and solid phases are in thermodynamic equilibrium [10, 11]. The temperature of the particle is determined from the energy conservation equation:

$$(c_c \rho_c + c_{b,m} \rho_{b,m}) \frac{\partial T_p}{\partial \tau} = \frac{\partial T_p}{\partial \ell} \left(\lambda_p \frac{\partial T_p}{\partial \ell} \right) - \rho_{gv} c_{gv} w_{gv} \frac{\partial T_p}{\partial \ell} + q_{cr}, \quad (11)$$

$$q_{cr} = q_0 \cdot (-k_{b,m} \cdot \rho_{b,m}) \quad (12)$$

where λ_p is the coefficient of thermal conductivity of the particle, W/(m·K); q_0 is the specific heat of chemical reaction, j/kg; w_{gv} is the velocity of gas–vapour mixture, m/s; and ℓ is the current coordinate in particle, m.

The rate constant of a chemical reaction is determined according to the law of Arrhenius:

$$k_{b,m} = k_{b,m_0} \cdot \exp\left(-\frac{E_a}{RT}\right), \quad (13)$$

where k_{b,m_0} is the pre-exponential factor, c-1, and E_a is the activation energy, J/mol.

The initial conditions for solving Eqs. (3–5), (7) and (11) are written as follows:

$$\rho'_{b,m} = \rho'_{b,m_0}; \rho'_c = 0; \rho'_{gv} = 0; \text{ and } T_p = T_H;$$

the boundary conditions for Eq. (11) will be written as follows:

$$T_p|_{\ell=L} = T_{layer}. \quad (14)$$

The effective coefficient of thermal conductivity λ_{ef} in Eq. (1) depends on the porosity and temperature of the layer: $\lambda_{ef} = f(\varepsilon, T_{layer})$; its value is determined experimentally [12, 13].

The coefficient of thermal conductivity for a particle in Eq. (11) is defined as the sum of the thermal conductivities of wood, coal and volatile substances, taking into account the degree of pyrolysis and the radiation of heat through the pores:

$$\lambda_p = (1 - \phi) \cdot \lambda_{b,m} + \phi \cdot \lambda_c + \varepsilon \cdot \lambda_{gf} + \frac{13,5 \cdot c_0 \cdot T^3 \cdot d_{pore}}{\psi_{gf}}, \quad (15)$$

where c_0 is the black body coefficient, W/m²·K⁴; ψ_{gf} is the emissivity factor of gas flow; and d_{pore} is the pore size determined by the formula.

4 Results and Discussion

Figure 3 shows the kinetic curves of the decrease in the specific mass of wood pellets at different temperatures. Analysis of the curves shows that with a decrease in the process temperature below 250 °C, the duration of the process increases significantly [14, 15].

Figure 4 shows the dependence of the composition of the non-condensable gas on temperature. Analysis of the simulation results shows that with increasing temperature there is an increase in the content of combustible gases and a decrease in carbon dioxide, and this, in accordance with Hess’s law, will help to reduce the specific heat of combustion of the finished product; therefore, to obtain pellets with high heat value, the temperature of the thermal chemical process should not be kept above 250 °C [16, 17].

Figure 5 shows the dependence of the heat of combustion of wood pellets on the temperature of the process of thermal modification [18, 19]. This dependence confirms that the value of the rational temperature of thermal modification is 250 °C. Figure 6 shows the dependence of the heat of combustion of thermally

Fig. 3 Kinetic dependence of the pellets’ specific gravity on the heating temperature

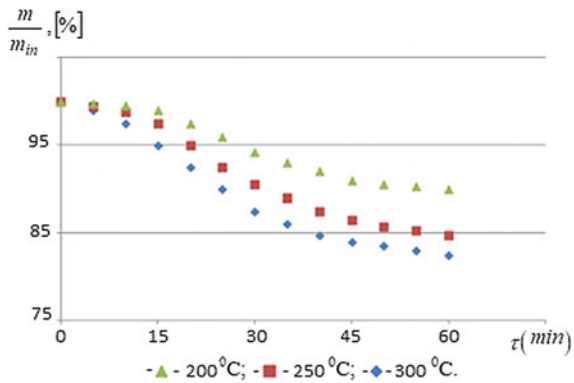


Fig. 4 Experimental dependence of the composition of non-condensable gas on temperature: 1–H₂; 2–CH₄; 3–CO; 4–CO₂

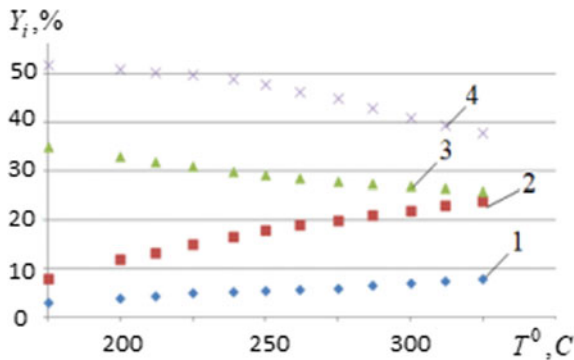


Fig. 5 Dependence of the heat of combustion of pellets with 20% lignin content on the temperature of thermal modification

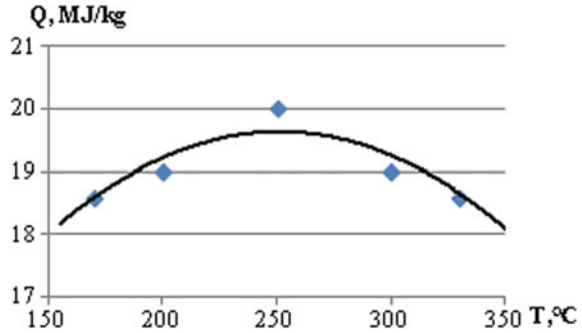
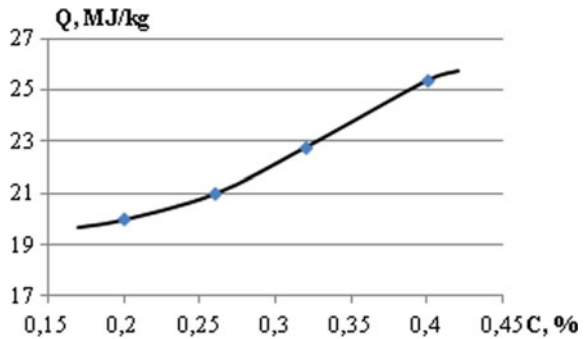


Fig. 6 Dependence of the heat of combustion of thermally modified pellets on the concentration of lignin



modified pellets at 250 °C on the concentration of lignin in them. The analysis of the curves shows a steady proportional dependence of the heat of combustion on the concentration of lignin [20].

Figures 7 and 8 show the dependences of hardness and bending strength and compression of thermally modified pellets on the initial concentration of lignin. The analysis of the obtained dependences shows the efficiency of introducing waste

Fig. 7 Dependence of the hardness of pellets from the concentration of lignin

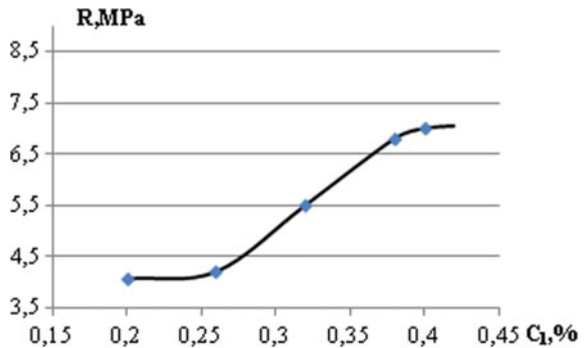
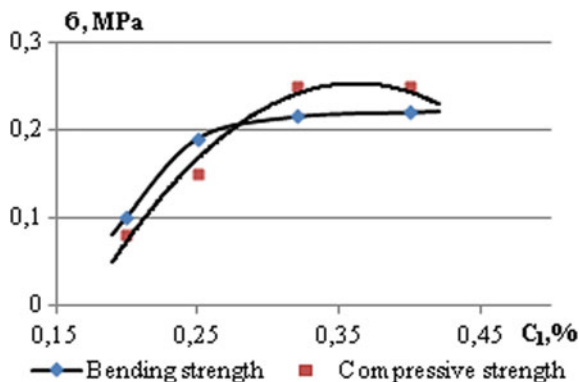


Fig. 8 Dependence of bending strength 1 and compression 2 on the concentration of lignin



lignin into wood waste [21, 22]. This increases not only the heat of combustion of thermally modified pellets, but also their strength characteristics, which is very important when transporting them to their destination.

5 Conclusion

A technology for the production of solid biofuels—thermally modified pellets consisting of wood raw material and lignin—has been developed. The concentration of lignin is 20–40%. The rational temperature of thermal modification is 250 °C. The heat of combustion of thermally modified pellets is 20–44% higher than the heat of combustion made from wood waste [23, 24]. Strength characteristics increase up to 30%. The economic effect from the introduction of the proposed technology is 950 rubles/ton.

Acknowledgements The presented results were obtained within the framework of the state task “Initiative scientific projects” on the theme No. 13.5443.2017/BC “Modification of the physical and chemical properties of wood biomass affecting the performance characteristics of the materials being created”.

References

1. Tuntsev DV, Filippova FM, Khismatov RG, Timerbaev NF (2014) Pyrolyzates: products of plant biomass fast pyrolysis. *Russ J Appl Chem* 87(9):1367–1370
2. Hu G, Li G, Zheng Y, Zhang Z, Xu Y et al (2015) Euler-lagrange modeling of wood chip gasification in a small-scale gasifier. *J Energ Inst* 88(3):314–322
3. Janajreh I, Al Shrah M et al (2013) Numerical and experimental investigation of downdraft gasification of wood chips. *Energ Convers Manage* 65:783–792

4. Timerbaev NF, Safin RR, Safin RG, Ziatdinova DF et al (2014) Modeling of the process of energy-technological treatment of wood waste by method of direct-flow gasification. *J Eng Appl Sci* 9(5):141–146
5. Pakdel H, Roy C et al (1991) Hydrocarbon content of liquid products and tar from pyrolysis and gasification of wood. *Energy Fuels* 5(3):427–436
6. Saravanakumar A, Haridasan TM, Reed TB, Bai RK et al (2007) Experimental investigation and modelling study of long stick wood gasification in a top lit updraft fixed bed gasifier. *Fuel* 86(17):2846–2856
7. Bui T, Loof R, Bhattacharya SC et al (1994) Multi-stage reactor for thermal gasification of wood. *Energy* 19(4):397–404
8. Dasappa S, Paul PJ, Mukunda HS, Shrinivasa U et al (1994) The gasification of wood-char spheres in CO₂ N₂ mixtures: analysis and experiments. *Chem Eng Sci* 49(2):223–232
9. Sadrtidinov AR et al (2016) IOP Conf Ser.: Mater Sci Eng 124:012092. <https://doi.org/10.1088/1757-899x/124/1/012092>
10. Saravanakumar A, Haridasan TM, Reed TB (2010) Flaming pyrolysis model of the fixed bed cross draft long-stick wood gasifier. *Fuel Process Technol* 91(6):669–675. <https://doi.org/10.1016/j.fuproc.2010.01.016>
11. Safin RG, Sattarova ZG, Khairullina ER (2017) Technology of wood waste processing to obtain construction material. *Solid State Phenom* 265:245–249. <https://doi.org/10.4028/www.scientific.net/SSP.265.245>
12. Prosvirnikov DB (2017) IOP Conf Ser: Mater Sci Eng 221:012010. <https://doi.org/10.1088/1755-1315/221/1/012010>
13. Tuncev DV, Prosvirnikov DB, Kozlov RR (2018) Physical and chemical properties of activated lignocellulose and its areas of application. *Solid State Phenom* 284:779–784. <https://doi.org/10.4028/www.scientific.net/SSP.284.779>
14. Prosvirnikov DB, Baigildeeva EI, Sadrtidinov AR, Fomin AA (2017) Modelling heat and mass transfer processes in capillary-porous materials at their grinding by pressure release. In proceedings of 2017 international conference on industrial engineering, applications and manufacturing, ICIEAM 2017, art. no. 8076443. <https://doi.org/10.1109/icieam.2017.8076443>
15. Guseva VG, Fomin AA, Sadrtidinov AR (2018) Adaptation of the methodology of designing cylindrical milling processes to the profile milling processes. *Solid State Phenom* 284:236–241. <https://doi.org/10.4028/www.scientific.net/SSP.284.236>
16. Sadrtidinov AR, Sattarova ZG, Prosvirnikov DB, Tuntsev DV (2015) December) Modeling of thermal treatment of wood waste in the gasifiers. In 2015 International Conference on Mechanical Engineering, Automation and Control Systems (MEACS), p 1–5. <https://doi.org/10.1109/meacs.2015.7414914>
17. Storodubtseva TN, Aksomitny AA, Sadrtidinov AR (2018) Thermal insulation properties of wood polymeric sand composite. *Solid State Phenom* 284:986–992. <https://doi.org/10.4028/www.scientific.net/SSP.284.986>
18. Prosvirnikov DB (2017) IOP Conf Ser: Mater Sci Eng 221:012009. <https://doi.org/10.1088/1755-1315/221/1/012009>
19. Timerbaev NF, Ziatdinova DF, Safin RG, Sadrtidinov AR (2017) Gas purification system modeling in fatty acids removing from soapstock. In proceedings of 2017 international conference on industrial engineering, applications and manufacturing, ICIEAM 2017, art. no. 8076418. <https://doi.org/10.1109/icieam.2017.8076418>
20. Lashkov VA, Sattarova ZG, Taymarov MA, Gerasimov MK, Halitov RA (2016) Modeling of a reduction zone of the gasifier installation. In IOP conference series: materials science and engineering Vol 124(1). IOP Publishing, p 012111
21. Prosvirnikov DB (2016) IOP Conf Ser: Mater Sci Eng 124:012088. <https://doi.org/10.1088/1757-899x/124/1/012088>
22. Stepanov VV, Timerbaev NF (2018) Composite railroad ties obtained by the energy efficient recycle of wooden railroad ties. *Solid State Phenom* 284:981–985. <https://doi.org/10.4028/www.scientific.net/SSP.284.981>

23. Tuncev DV, Sattarova ZG, Galiev IM (2017) Multi-layer wood-polymer composite. Solid State Phenom 265:47–52. <https://doi.org/10.4028/www.scientific.net/SSP.265.47>
24. Timerbaev NF (2017) IOP Conf Ser: Earth Environ Sci 87:082047. <https://doi.org/10.1088/1755-1315/87/8/082047>

Influence Estimate of Spectral Model of Combustion Product Radiation on Results of DKVR-10/13 Steam Boiler Furnace Simulating



D. A. Akhmedzaynov, A. E. Kishalov and V. D. Lipatov

Abstract This article shows the results of studies of heat transfer in the furnace of a DKVR-10/13 steam boiler. The studies were performed using numerical simulation methods. The influence of the computational method of heat exchange by radiation, as well as the spectral model of radiation on the simulation results, was studied. Monte Carlo and discrete transfer methods were chosen as the methods for calculating the heat exchange of radiation. The number of stories and rays for the Monte Carlo and discrete transfer models was 50,000 and 8, respectively. A simple gray-gas model and a weighted-sum gray-gas model were chosen as spectral radiation models. A total of four calculations were performed. For each variant studied, the radiation intensity, maximum temperature, heat removal from the screens, the gas temperature at the outlet of the furnace, and the temperature distribution of gases along the height of the furnace were estimated. Using the engineering method, the results are compared with the results of calculations.

Keywords Numerical simulation · ANSYS CFX · Thermal radiation · Spectral model · Furnace · Monte Carlo model · Gray gas

1 Introduction

Most of the electricity that is generated in the world (about 2/3 of all generated electricity) is produced in traditional thermal stations operating on one of the types of organic fuel. At the same time, one of the main processes of converting the fuel chemical energy into electricity is combustion process. Thus, the quality of the organization of combustion processes, which is determined by a number of parameters (e.g., the design of burner devices and the form of furnaces of power boilers or combustion chambers of ground-based gas turbines), affects the efficiency of the plant as a whole.

D. A. Akhmedzaynov · A. E. Kishalov · V. D. Lipatov (✉)
Ufa State Aviation Technical University, 12, Karl Marx St., Ufa 450008, Russia
e-mail: lipatvadam@gmail.com

The main methods that underlie the design of boiler furnaces [1–3] are based on the results of a large number of experimental studies. When designing nonstandard boiler designs or with substantial modernization of existing ones, this method is applicable only with the carrying out of expensive full-scale experiments. It is possible significantly to reduce the cost of experimentation using modern computational complexes. This approach allows us to evaluate the shape and location of the torch, identify the zones of the most intense heat fluxes and obtain data of the parameters of interest at any point of the installation even before the experimentation. This makes it possible substantially to reduce both the number of experimental studies and their cost, which positively affects the cost of debugging.

The most difficult part of the boiler for numerical simulation is the furnace chamber. It is difficult because of the processes of fuel combustion and radiant heat exchange (as the main type of heat exchange in the furnace). At present, there is a rather large number of studies devoted to the numerical modeling of processes occurring in the boiler furnace [4–10]; however, most of them are devoted to the combustion of solid fuel. In the Russian Federation, a relatively large number of low-capacity steam boilers are working on gaseous fuels, which makes the problem of the numerical study of their furnaces very urgent.

The DKVR-10/13 steam boiler was chosen as an object for research [11, 12].

2 Description of the Research Object

Description of the boiler, as well as its drawing, is given in the article [13] that reflects the initial stage of the present studies.

Two burners of the GMG-5,5 type [14, 15] intended for combined gas and oil fuel combustion are used to supply fuel to the furnace and to organize the combustion process. The air supplied to the combustion chamber is divided into primary and secondary. Primary air (swirler air) is supplied to the furnace in a swirling state (60° tangentially and 30° radially) through the central channel at a flow rate from 10 to 15% of the total airflow. Secondary air is also supplied in a swirling state (45° in the tangential direction) through the peripheral channel. Swirling of both primary and secondary air is carried out with the help of blade swirlers. The number of holes (gas-distributing nozzles–washers) for gas supply located between the primary and secondary air supply zones is 42, and their diameter is 2 mm.

3 Description of Applied Models and Set Parameters

The geometric model of the furnace was built using the Siemens NX System and is shown in Fig. 1, where the names of the given boundary conditions are also shown. In addition, this figure shows in more detail the velocity vectors of fuel and airflows, illustrating their twist.

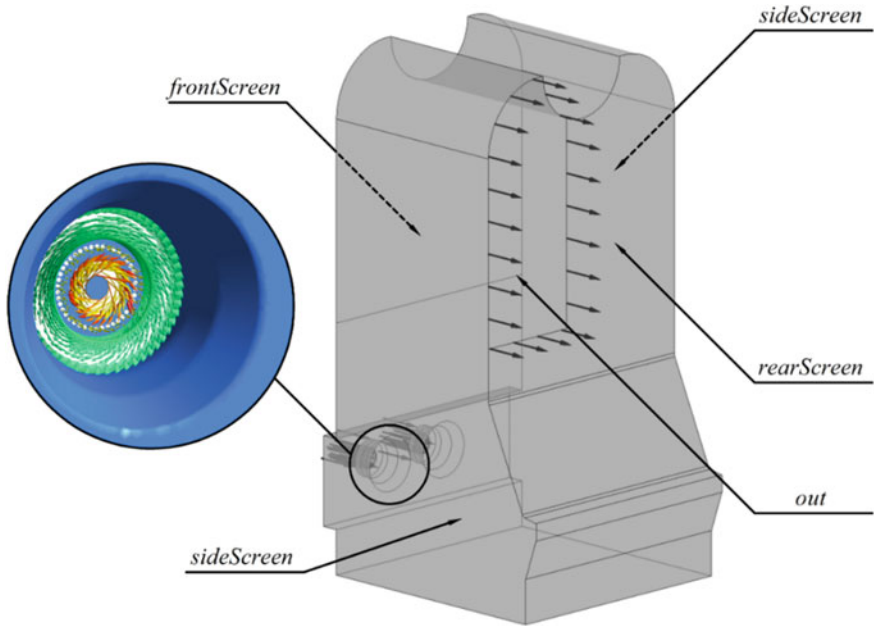
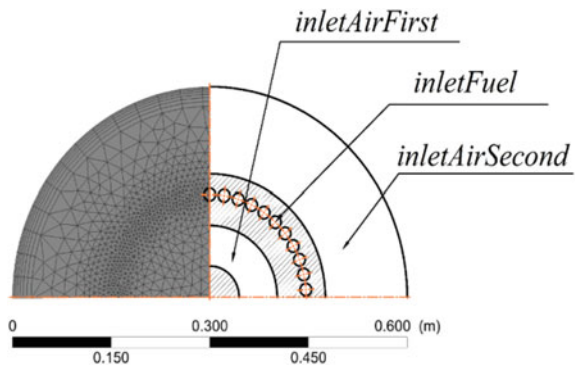


Fig. 1 Furnace geometric model with indication of boundary conditions

Figure 2 shows the location of the boundary conditions of the input section of the furnace (burner output window), and it is shown a finite element mesh. The finite element mesh is represented by unstructured elements with a maximum dimension of 50 mm over the entire volume of the furnace. In the zone of air and fuel outlet from the burners, local refinement of the grid is made by introducing an influencing body (a parallelepiped extending from the exit window of the burners to the opposite wall of the furnace) with an element size of 25 mm. On all surfaces of the furnace, the grid is thickened in the wall regions (to refine the phenomena occurring to the boundary layer) by specifying seven layers of prismatic elements (Fig. 2) with a maximum thickness of 20 mm and a growth factor of 1.2.

Fig. 2 Boundary conditions at the entrance to the furnace



A laminar flamelet model with a kinetic combustion scheme of methane [16] corresponding to the mechanism was chosen as a model of combustion [17].

Owing to the smallness of the gas flow rates, the energy equation was solved in the formulation of thermal energy. Calculations were made taking into account the action of gravitational forces [18]. The turbulence was simulated using Menter's shear stress transport model [19].

Due to the fact that the main type of heat exchange in the furnace is radiant heat exchange, the results of the simulation will depend substantially on both the method used to calculate the radiation and the applied spectral model (due to radiation's selectivity and absorption of combustion products). In this work, Monte Carlo (MC) models [10, 20] with the number of histories at 50,000 and discrete transfer (DT) with eight beams were used to model radiation [21]. As spectral radiation models, a gray-gas model and a weighted sum of gray gases were chosen, the coefficients of which were chosen according to [22, 23]. Thus, four calculations were made during the study.

The airflow for each of the burners through the primary air inlet (inletAirFirst) zone was 0.2095 kg/s, through the secondary zone (inletAirSecond)—1.1870 kg/s. The fuel consumption was selected in such a way as to ensure the required heat load of the boiler according to the results of thermal engineering tests of the boiler and amounted to 0.07862 kg/s for each of the burners. As the calculated fuel, pure methane was used. The temperatures of both fuel and air at the inlet to the calculation volume were 300 K.

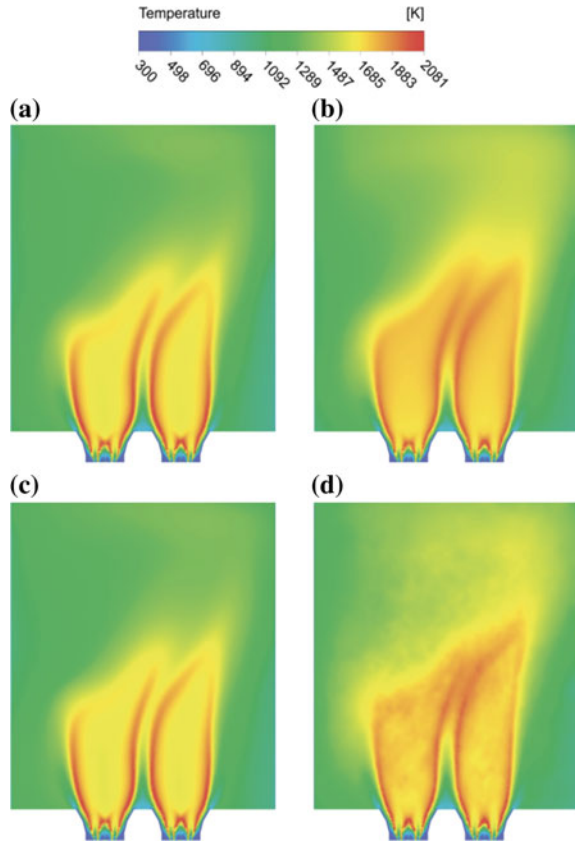
The heat sink in the furnace is organized through the screens, which occupy the corresponding areas on the front (front screen), side (side screen) and rear walls (rear screen). The boundary condition for the screen surfaces was the given temperature of their surfaces, which was assumed to be 450 K, that is somewhat higher than the saturation temperature of the steam–water mixture flowing through the screen tubes.

The output of gases from the furnace is organized through the exit window (out) located in the right upper corner of the combustion chamber. The operation of the boiler is carried out in such a way that a small vacuum is maintained at the outlet from the furnace, amounting to 20–30 Pa. It was assumed in the calculations that at the exit from the furnace the relative static pressure of the combustion products is –30 Pa, relative to the reference pressure assumed to be 1 atm.

4 Results and Discussion

Some results of the calculations are shown in Figs. 3, 4, 5 and 6. Figure 3 shows the temperature contour fields in the horizontal plane of the burner axis. As can be seen from this image, the influence of the radiation model on the shape of the torch is minimal (the almost complete identity of variants a and c in Fig. 3). At the same time, the use of spectral model of the weighted sum of gray gases (WSGG) causes the temperature distribution in the final zone of the flame to become more uniform

Fig. 3 Temperature fields in the horizontal plane of the torch axis: **a** DT method, gray gas; **b** DT method, WSGG; **c** MC method, gray gas; **d** MC method, WSGG



and shifts to a zone of high temperatures (variants b and d in Fig. 3). This circumstance can be explained, obviously, by the specific nature of the spectral model, which makes it possible to consider the radiating medium in intermediate (between thick and thin) optical thicknesses and more fully take into account the absorption of radiation by gases throughout the torch volume, and not only over its delicate boundaries, as, for example, in the cases a and c in Fig. 3. In addition, when using the WSGG spectral model, the differences between the calculation options according to DT and MC methods become more significant. This can be seen, for example, for variants b and d in Fig. 3: The torch calculated by using the MC method acquires a discrete structure, which is due to the essence of the calculation by the MC method (“point” calculation of photons). Thus, in order to obtain a more homogeneous structure when calculating the flame according to the MC emission model, it is necessary to increase the number of histories, which will significantly affect the total calculation time.

In Figs. 4 and 5, the temperature’s contour fields in the vertical plane of the axis of the left and right burners, respectively, are shown. It is obvious that all the conclusions formulated above are also relevant for temperature fields in vertical

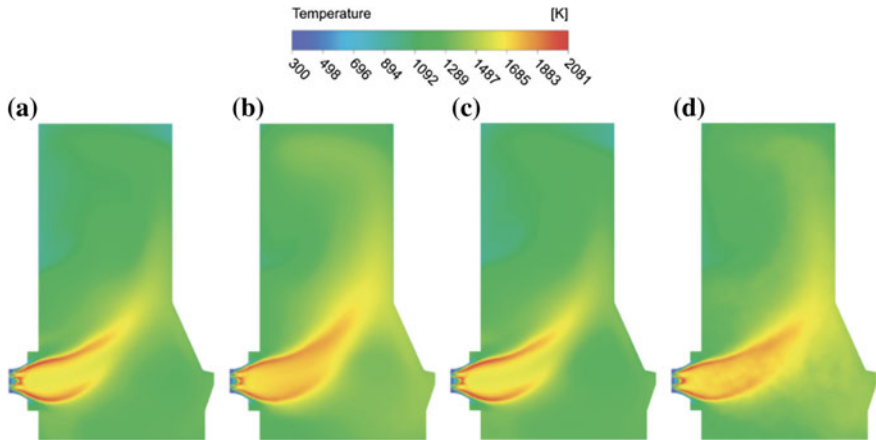


Fig. 4 Temperature fields in the vertical plane of the axis of the left burner: **a** DT method, gray gas; **b** DT method, WSGG; **c** MC method, gray gas; **d** MC method, WSGG

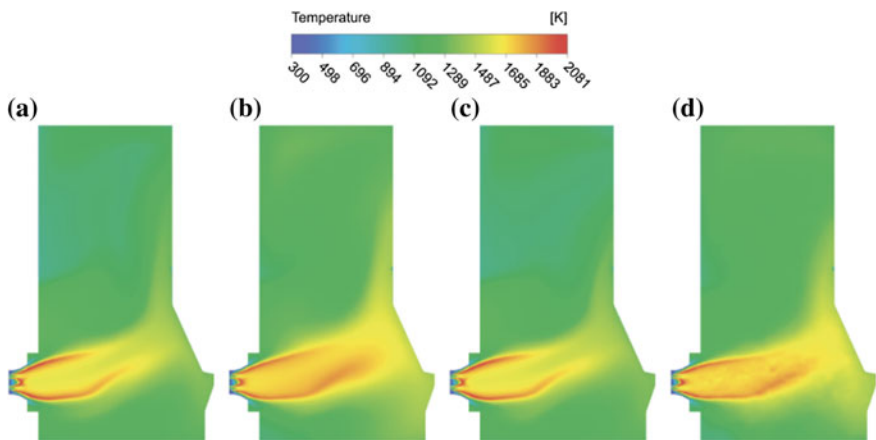


Fig. 5 Temperature fields in the vertical plane of the axis of the right burner: **a** DT method, gray gas; **b** DT method, WSGG; **c** MC method, gray gas; **d** MC method, WSGG

planes. At the same time, it can be seen from these figures that the average temperature over the height of the furnace (and, especially, in its upper part, as seen from variants b and d) will be higher in the case of calculation of radiation with the WSGG spectral model. Also, slightly larger gas temperatures are observed in the zone of the rear screen (inclined plane on the right side of the furnace), which may be important in evaluating the temperature state of the pipes of this screen.

Figure 6 illustrates the contour fields of radiation intensity in the vertical plane of the axis of the right burner. It can be seen that when using the gray-gas approximation, both for the DT method calculation and for the MC method, the gas

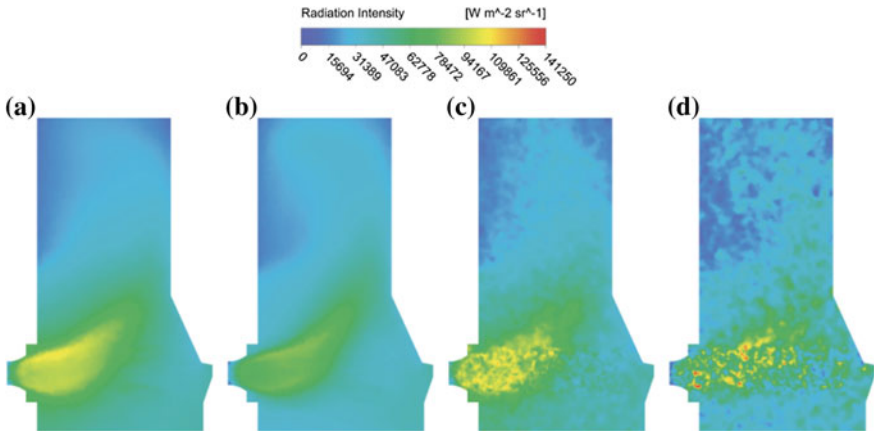


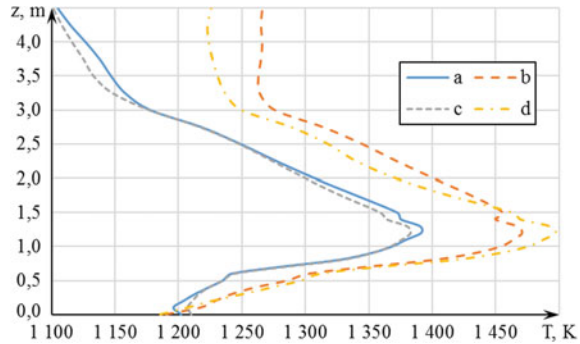
Fig. 6 Radiation intensity fields in the vertical plane of the axis of the left burner: **a** DT method, gray gas; **b** DT method, WSGG; **c** MC method, gray gas; **d** MC method, WSGG

emission is mainly from the central region of the flame (variants a and c). At the same time, using the WSGG model leads to the fact that the greatest intensity (which is greatly smaller than in calculations in the gray-gas approximation) of the gas emission falls on small bands located between the core of the torch and its peripheral part (variant b). In view of the insufficient number of histories in modeling with the MC method and the WSGG model, it is impossible accurately to estimate the radiation intensity distribution over the flame volume, which is observed for variant d in Fig. 6. In addition, for this variant of the calculation, several explicit points of the maximum radiation intensity are observed, which is inconsistent with the rest of the calculation options and may negatively affect the simulation results.

Figure 7 illustrates the distribution of the average (over the area) temperature of the gases along the height of the furnace. As was mentioned above, for the calculation variants with the WSGG model, the average temperature of the gases is higher, which is evident from Fig. 7. Moreover, the maximum difference between the temperatures is observed in the upper part of the furnace. At the same time, for the variants of calculating c and d at an altitude of 3–4 m, the temperature remains almost constant, which is explained by the “temperature swirl” reflected in Fig. 4. This is explained by the fact that for these variants of calculation the radiation intensity is lower and the gases, therefore, cool down more slowly than in the variants of calculating a and d. In addition, the asymmetric location of the output window of the furnace (opposite the right burner) leads to the fact that the gases leaving the left burner have a somewhat longer residence time in the furnace than the gases emanating from the right. This leads to a slight increase in the average temperature in the left part of the furnace due to a more complete burnout of the fuel (variant b in Fig. 4).



Fig. 7 Temperature fields in the vertical plane of the axis of the left burner: **a** DT method, gray gas; **b** DT method, WSGG; **c** MC method, gray gas; **d** MC method, WSGG



A quantitative evaluation of the simulation results is given in Table 1. It can be seen from the table that for the calculation of variant d (MC and WSGG), the maximum temperature of the gases in the furnace is 2107 K, which is somewhat higher than the corresponding temperature for the remaining options. Thus, the influence of the choice of the spectral model on the results of the final calculation should be made only for the DT model. As was mentioned above, when calculating the radiation of gases in the gray-body approximation, the average radiation intensity is higher (by approximately 8%). This leads to a corresponding decrease in the temperature of the gases leaving the furnace (about 10.6%), and an increase in its heat reception (by about 6.0%). In this case, the value of the temperature of the gases, at the outlet from the furnace obtained in calculating the boiler furnace according to [1], is $T_1 = 1218$ K. Consequently, taking into account the radiation and absorption spectrum of gases gives better results than the calculation in the gray-gas approximation: The error in modeling the radiation in the furnace with the DT and WSGG models gives an error of 3.2% for determining the temperature at the outlet from the furnace, and 7.7% for modeling in the gray-gas approximation. In addition, as can be seen from Table 1, when simulating the boiler furnace according to the WSGG model, the heat from the front screen increases (by about 11.1%) and drops from the side and rear screens (by 8.3 and 6.6%, respectively). This circumstance is explained by the fact that the front screen has a smaller area in comparison with the areas of the rear and, especially, the side screens.

This affects the fact that when the temperature fields are redistributed over the height of the furnace (as observed in the WSGG model), the front screen is the most dependent on this change (in comparison with the side and rear screens). At the same time, according to Fig. 7, in modeling according to the WSGG model, a higher radiation intensity is observed at the top of the furnace than for the base version, which also explains the greater heat reception of the front screen. In this case, the error in determining the total heat dissipation (in comparison with the design version) in calculations according to the WSGG model is 2.35 and 3.84% in calculations in the gray-gas approximation.

It should be noticed that when radiation simulating in the boiler furnace in the gray-body approximation, the MC model shows slightly better results than the DT model: The errors in determining the temperature and the total heat flux are

Table 1 Results of modeling

Variant	q_f , kW/m ²	q_s , kW/m ²	q_r , kW/m ²	Q_{total} , kW	Q_{calc} , kW	δQ , %	T_{out} , K	T_b , K	δT , %	I_{ave} , kW/(m ² st)	T_{max} , K
<i>a</i>	-56,070	-90,850	-115,900	4330	4170	3.84	1124	1218	7.72	37,210	2064
<i>b</i>	-62,320	-83,300	-108,200	4072		2.35	1257		3.20	34,250	2040
<i>c</i>	-58,910	-90,380	-110,500	4287		2.81	1133		6.98	36,350	2065
<i>d</i>	-57,280	-82,530	-111,100	4036		2.57	1245		2.22	32,850	2107

6.98 and 2.81%, respectively (vs. 7.72 and 3.84% for the DT model). However, as was noticed above, when using the WSGG model, the MC emission model requires a significant increase in such a parameter as the number of histories, which will negatively affect the calculation time.

5 Conclusions

There are obtained the results of the numerical simulation of the combustion processes in the furnace of the DKVR-10/13 steam boiler for various methods of radiation calculating (DT and MC models) and spectral radiation models (in the gray-gas approximation and WSGG). These results are compared with the thermal calculation of the boiler furnace according to the engineering method. It is determined that the method of radiation calculating has almost no effect on the shape of the flame, and the application of the WSGG spectral model leads to the fact that the temperature of the torch in its volume becomes more homogeneous and shifts toward higher values. In addition, it is found that the application of the WSGG spectral model to the MC calculation method requires a significant increase in such a parameter as the number of histories (since the pattern of the radiation intensity distribution for the same number of histories as for the base version is significantly distorted for the worse), which negatively affects the calculation time. At the same time, for the DT calculation method, this correlation is not observed (no increase in such a parameter as the number of rays is required). Taking into account the emission and absorption of spectra of flue gases according to the WSGG model, the average (in area) of gas temperature over the height of the furnace increases in comparison with the base version. The shape of the curve of this distribution, with the exception of the upper part of the furnace, is retained.

From the point of view of the quantitative evaluation of the calculation results, it has been found that the use of the WSGG model allows obtaining more accurate results that are compared with the calculation by the engineering method. Thus, the error in determining the gas temperature at the outlet from the furnace of the boiler decreased from 7.72 to 3.20%, and the error in determining the total heat flux decreased from 3.84 to 2.35%. At the same time, the use of the WSGG model leads to a redistribution of the calculated heat fluxes through the screens (the increase in the heat perception of the front and decrease in the heat perception of the rear and side screens).

References

1. Teplovoj raschet kotel'nyh ustanovok (Thermal calculation of boiler installations) (1998) NPO TsKTI
2. Mochan SI (1977) Aehrodynamiceskij raschet kotel'nyh ustanovok (normativnyj metod) (Aerodynamic calculation of boiler plants (regulatory method)). Ehnergiya, Leningrad

3. Baldina OM, Lokshin VA, Peterson DF, Semenovker IE, Shvartz AL (1978) *Gidravlicheskiy raschet kotel'nyh ustanovok (normativnyj metod)* (Hydraulic calculation of boiler installations (regulatory method)). Ehnergiya, Leningrad
4. Fan JR, Liang XH, Xu QS, Zhang XY, Cen KF (1997) Numerical simulation of the flow and combustion processes in a three-dimensional W-shaped boiler furnace. *Energy* 22(8):847–857
5. Park HY, Faulkner M, Turrell MD, Stopford PJ, Kang DS (2010) Coupled fluid dynamics and whole plant simulation of coal combustion in a tangentially-fired boiler. *Fuel* 89(8):2001–2010
6. Choi CR, Kim CN (2009) Numerical investigation on the flow, combustion and NO_x emission characteristics in a 500 MWe tangentially fired pulverized-coal boiler. *Fuel* 88(9):1720–1731
7. Backreedy RI, Jones JM, Ma L, Pourkashanian M, Williams A, Arenillas A, Rubiera F (2005) Prediction of unburned carbon and NO_x in a tangentially fired power station using single coals and blends. *Fuel* 84(17):2196–2203
8. Yin C, Rosendahl L, Condra TJ (2003) Further study of the gas temperature deviation in large-scale tangentially coal-fired boilers. *Fuel* 82(9):1127–1137
9. Al-Abbas AH, Naser J, Hussein EK (2013) Numerical simulation of brown coal combustion in a 550 MW tangentially-fired furnace under different operating conditions. *Fuel* 107: 688–698
10. Bloch AG, Zhuravlev AYu, Ryzhkov LN (1991) *Radiative heat transfer: handbook*. Energoatomizdat, Moscow
11. DKVr-10-13GM (E-10-1,4GM). http://www.bikz.ru/production/kotly_paroviye/gaz_zhidkoe_toplivo/serii_dkvr_2_5_4_0_6_5_t_ch/e-10-1_4gmndkvr-10-13gm/. Accessed 21 Jan 2018
12. Zikhov AK (1987) *Parovye i vodogreynye kotly* (Steam and hot water boilers). NPO OBT, Moscow
13. Kishalov AE, Lipatov VD (2017) Trekhmernoe modelirovanie processov gorenija v parovom kotle DKVP-10/13 (Three-dimensional modeling of combustion processes in a steam boiler DKVP-10/13). USATU, Ufa
14. Gorelka GMG-5,0 lev. (Torch GMG-5,0 lev.). http://www.bikz.ru/production/oborudovanie/other4/other14/gmg-5_0_lev/. Accessed 21 Jan 2018
15. GMG-5,5/7—Gorelka jidkotoplivnaya (GMG-5,5/7—oil burner). <http://www.rosteplo.ru/katalog/1/4/1424>. Accessed 21 Jan 2018
16. Peters N (1988) Laminar flamelet concepts in turbulent combustion. In: *International symposium on combustion*, vol 21, no 1. Elsevier, pp 1231–1250
17. Smith GP (1999) GRI-Mech 3.0. http://www.me.berkeley.edu/gri_mech/
18. Lipatov VD, Kishalov AE (2017) Three-dimensional numerical thermogasdynamic modeling of combustion processes in the boiler furnace of a steam boiler DKVR-10/13. In: *The international workshop on computer science and information technologies*, pp 241–247
19. Menter FR (1994) Two-equation eddy-viscosity turbulence models for engineering applications. *AIAA J* 32(8):1598–1605
20. Howell JR (1998) The Monte Carlo method in radiative heat transfer. *J Heat Transf* 120(3): 547–560
21. Lockwood FC, Shah NG (1981) A new radiation solution method for incorporation in general combustion prediction procedures. In: *International symposium on combustion*, vol 18, no 1. Elsevier, pp 405–1414
22. Smith TF, Shen ZF, Friedman JN (1982) Evaluation of coefficients for the weighted sum of gray gases model. *J Heat Transf* 104(4):602–608
23. Yin C, Johansen LC, Rosendahl LA, Kær SK (2010) New weighted sum of gray gases model applicable to computational fluid dynamics (CFD) modeling of oxy-fuel combustion: derivation, validation, and implementation. *Energy Fuels* 24(12):6275–6282

Automated Control of Truck Drive Axle Performance Characteristics



A. Yu. Barykin, M. M. Mukhametdinov and R. Kh. Takhaviev

Abstract The article suggests a method for providing an efficient operation of automated devices in a truck drive axle. An automated blocking of interaxial or inter-wheel differentials eliminates any chance of power circulation occurrence or additional loading of transmission units which makes part service lives longer. The information space of a drive axle control system is determined by external (environment, road) and internal (engine, drive) objects subject to influence each of which can be characterized by a finite number of factors. A drawback linked with a necessity of blocking manual control can be overcome if friction clutches are used as automated mechanisms. The authors present the results of their research of the truck drive axles' operating condition under various conditions. Special emphasis is put on the operation of cars in wintertime. Maintaining the temperature of oil and drive axle parts within a rational range of values provides for an increase in the transmission unit operation efficiency. A possible option is to convert the heat energy of burnt gases into electric power with a subsequent electric power transmission and reverse conversion of such power into heat just in the section of a drive axle.

Keywords Automated blocking · Truck · Drive axle · Differential · Transmission oil · Operating temperature

1 Introduction

A proper operating condition of transmission units can be ensured by means of control parameters' monitoring and automated change in the output characteristics of control mechanisms.

A. Yu. Barykin (✉) · R. Kh. Takhaviev
Naberezhnye Chelny Institute (Branch) of Kazan (Volga Region) Federal University,
68/19, Mira Pr., Naberezhnye Chelny 423812, Russia
e-mail: aleks-jb@rambler.ru

M. M. Mukhametdinov
Regional Institute of Advanced Technologies and Business,
2, Vakhitov Pr., Naberezhnye Chelny 423815, Russia

At the consideration of the operating conditions and peculiarities of the structure of truck drive axle units, the most important control parameters are the following ones:

- Inter-wheel drive blocking degree. This parameter influences a range of performance characteristics—passability, haulage capacity, controllability and sustainability.
- Transmission oil and drive axle operating temperature. This parameter pre-determines the amount of losses in a drive of driving wheels and, consequently, influences the wear intensity and fuel consumption rate.

Here one has to consider a vehicle operation condition as an element of a complex natural and technical system “on-board computer—driving wheel drive—bearing surface—environment.” The evaluation of the mentioned system links’ influence leads the authors to a number of conclusions inconsistent with commonly accepted calculation methods.

One should also take into account the influence of the aforementioned system links on the operation reliability. Let us give the examples of such links for a truck.

- A significant friction torque occurring in the inter-wheel differential influences the values of implemented rotation torques and the possibility of circulating power emergence. Also, moving along a smooth dry road with a rather high adhesion factor increases the possibility of an intensive wear of axle parts.
- Conducting axle technical maintenance with the regulations violation, for example, adjusting gaps and gearings with a deviation from a required range, using transmission oil grades which are hardly suitable for operation under specific conditions, further causes versatile part loading in the automated operation mode. A limited strength of oil film or excessive gap in a gearing can lead to a further failure.
- In case a driver has an insufficient qualification, it may cause resonance phenomena in a transmission unit due to coupling drop, noticeable vibration influence on automated drive mechanisms at a high-speed motion on the road irregularities and profiled obstacles. This factor significantly complicates the operation of an automated control axle.
- Direct environmental influence can manifest itself due to a number of reasons: overheating of drive axle parts and decrease of lubricating properties of transmission oil in hot weather; decrease of part strength and growth in a transmission loss number because of excessive oil viscosity at severe frost. In addition, the environment can exert indirect influence when a car moves through deep snow-banks or along the road with snowdrift, and when a “bulldozer” effect occurs.

The paper [1] points out that the proper evaluation of occurring loads and the necessity of taking them into account while transmission group designing have the highest significance for trucks with a forced blocking of inter-wheel differentials. That is why at movement in difficult driving conditions one shall pay particular attention to the measures providing for transmission unit parts’ non-failure and durability. Transmission unit high reliability can be obtained at optimum values of the performance characteristics of the abovementioned units.

For example, while a car is moving in difficult driving conditions, transmission oil and parts can overheat, dust and wear particles can penetrate a lubricating layer. The listed phenomena cause the necessity to consider the friction torques and differential blocking factors at implementing automated distribution of such torques in a transmission unit [2].

The most significant research stage is selecting a method for external and internal factors arrangement slightly or significantly influencing the wheel drive mechanism output parameters [3]. This influence is not permanent for one and the same structure in various technical states subject to various influences from the automated control mechanisms, driver, etc.

The paper [3] proposed a classification for external influences in a system taking into account a third-party influence on the operation conditions of a truck drive axle. In particular, the authors conducted bench tests of truck units and obtained important experimental data facilitating the specification of the links in the considered system.

The paper [4] evaluates the influence of performance factors with the simulation of influence conditions at the bench tests of a main gear. While bench testing interaxial and inter-wheel differentials, the authors found out the interconnection between various system parameters and evaluation criteria, in the first place, the blocking factor [5]. Such research, due to a comprehensive consideration of system factors and their reproduction in the experiment, provided for an opportunity to identify the unit longevity and fail-free operation under real operation conditions on the basis of these bench tests.

Automated capacity distribution in the driving wheel is quite a complex task due to a large number of external and internal influence factors and a limited range of reasonable characteristics of a distribution unit because of design, cost and other reasons. This problem has been quite widely covered in scientific papers [6, 7].

To some extent, the stated task is performed by distribution mechanisms of vehicles being multi-disk couplings the program control of which is set by certain criteria [8, 9]. However, the capabilities of such systems are very often limited by a registered information space and a number of control criteria. That is why the selection of a rational value of friction torques in the automated differentials or controlled clutches of systems regulating pulling forces is not always optimal.

2 Methods

The information space of a drive axle control system is determined by external (environment, road) and internal (engine, drive) objects subject to influence each of which can be characterized by a finite number of factors. They should include the factors of a vehicle, road, environment, duration, nature and amplitude of one or another factor influence.

The listed factors have various extents of significance depending both on the influence on the necessary blocking degree and mutual influence. Taking into account

the data provided in the paper [10], the key limitations by the value of blocking influence for the main (controlled) groups of operation properties should include:

- The limitation for the case of car movement at the irregular road turn (registered parameters—difference of rotation frequencies of axle wheels, steering wheel rotation angle, suspension dynamic travel)
- The limitation for a case of road turn passing at a high speed (registered parameters—car speed, tire slip angles, steering wheel rotation angle, relative wheel slip)
- The limitation by the condition of road turn passing on a slippery surface (registered parameters—speed and amplitude of rotation torque change at output shafts, steering wheel rotation angle, relative wheel slip)
- The limitation of the emergency situation occurrence (registered parameters—speed and amplitude of rotation torque change at output shafts, value of external lateral efforts, relative wheel slip)
- The limitation for breaking cases, power circulation (registered parameters—presence of negative rotation torques at driving wheels)
- The limitation by the passing ability condition (registered parameters—values of rotation torques on the drive wheels, values of aggregate resistance forces, relative wheel slip)
- The limitation by the condition of providing for an efficient performance of an automated distribution mechanism (registered parameters—values and duration of friction clutch torque action (differential friction torque), friction clutch (differential) operating temperature, relative wheel slip).

The paper [11] demonstrates the practicability of using differentials with discrete type characteristics. This mechanism has the following properties:

- Low degree of self-blocking sufficient for most road situations and providing for optimal performance characteristics (controllability, sustainability, haulage capacity).
- Possibility to automatically or manually increase a blocking torque up to a set value not causing a full differential switching off.

A drawback linked with a necessity of blocking manual control can be overcome if friction clutches are used as automated mechanisms. Also, hard blocking is not necessary even for the driving axle. It is also known that self-blocking differentials at cornering breakaway prevent the wheel de-twisting and further car stop. The paper [5] suggests a method to identify blocking factors necessary to provide passability under the specified conditions.

Such friction torque limitation virtually excludes the circulation of parasitic losses and decreases the power required for blocking mechanisms.

The discrete nature of characteristics helps to significantly stabilize temperature characteristics of friction clutches, enhance operation reliability and durability.

Maintaining the temperature of oil and drive axle parts within a rational range of values provides for an increase in the transmission unit operation efficiency.

However, in this case one observes additional energy consumption determined by a consumed power of a heating device and the environment state.

In this case, the defining external influence factors are the temperature and the degree of motion of atmospheric air. Many regions of the Russian Federation quite often need vehicle transportation under extremely low ambient temperatures [12]. The complexity of operation under specified conditions consists in the following: At first, there is no heating before motion start (so-called cold start), secondly, a drive axle is subject to intense cool air blowing during the car movement.

Main gear and other units' cold start causes additional fuel consumption, intensive wear of part rubbing surfaces due to insufficient lubricating properties of a transmission oil [13].

Part deformation caused by cooling can cause the violation of gaps and negative allowances, in the first place, a preloading of a main gear.

The paper [14] suggests a heat balance model for drive axle parts based on the commonly accepted thermal technology dependencies:

$$W_n = 3.6 \cdot \frac{Q_1 + Q_2 + Q_3 + Q_4}{t_{mn}} \quad (1)$$

where W_n —required power of an onboard heating device; Q_1 —amount of heat required for heating of the main gear parts and some of drive axle parts; Q_2 —amount of heat required for heating of a transmission oil in the main gear casing; Q_3 —amount of heat consumed at the main gear heating for heat exchange with the environment; Q_4 —amount of heat consumed in the unaccounted processes of heat exchange with the environment and car parts; t_{mn} —time of heat supply.

The key peculiarity of a drive axle is its open location which, on the one hand, leads to part cooling, especially in a moving aerial environment and, on the other hand, complicates the design solution for an automated heating system. External heating with hot air described in the paper [15] can be implemented without disturbances; however, its technological complexity makes it efficient under the conditions of a large number of vehicles in rolling stock which is not frequent.

A possible option is to convert the heat energy of burnt gases into electric power with a subsequent electric power transmission and reverse conversion of such power into heat just in the section of a drive axle.

3 Results and Discussion

The heating method selection significantly depends on the heat transmission intensity required under real operation conditions. That is why the relevant problem is to analyze the conditions under which the transmission parts are loaded and select the rational limits for the range of transmission oil and parts operating in the friction couples.

The paper [16] established that the lower limit of such a range should be determined with the account of minimum admissible losses due to friction $N_{V_{\max}}$ for

the oil with the maximum limit viscosity value. The upper limit is restricted by a limit rational power consumption for heating as well as by the decrease of a damping capacity of the $R_{V_{\min}}$ oil with a minimum limit viscosity value. One can suggest that $N_{V_{\max}}$ should be rationally evaluated through the kinematic viscosity value while $R_{V_{\min}}$ —through a dynamic viscosity value, i.e., taking into account the change in oil density within the rational temperature range.

The paper [17] points out to the reasonability of the transmission oil temperature monitoring to provide for the efficient transmission unit operation.

The efficient vehicle operation task during winter is defined by an admissible environmental action expressed by several important criteria. For example, for the trucks the requirement of non-failure operation is specified by limit ambient temperature indicators in various climatic regions.

But, in compliance with the observations [12, 18], average values for absolute temperature minimum indicators in January in most regions from the European part of the Russian Federation fall into the range from -25 to -34 °C, for the regions of Western and Eastern Siberia -38 to -54 °C. Clearly, the probability of extreme transmission oil temperature lowering is quite high for the Russian Federation in the winter period.

The correspondence to the norm values cannot provide for the optimal operation conditions as well. For example, in case of transmission oils corresponding to the viscosity class SAE 80 W, the limit operation temperature is assumed to be -26 °C corresponding to the dynamic viscosity of 150 Pa s. At this, the temperature of such oil freezing corresponds to -30 °C. In case of a less viscous oil SAE 75 W, a maximum permissible operating temperature is equal to -40 °C [19]. However, the drive axle operation at the specified oil dynamic viscosity is performed under unfavorable conditions and results in the following:

- Complex motion start due to a high value of cold oil hydraulic resistance. One should take into account that the driving axle hydraulic resistance is directly proportionate to the oil viscosity, and within the range of low temperatures the viscosity, with the temperature decrease, progressively increases.
- The decrease in oil temperature at movement caused by intense blow-off of a drive axle with cold air.
- The oil temperature drop at long stops (for a drive axle in general) and certain motion modes (for certain parts).

The first and the second events can have a negative influence even at the drive axle preheating. In case an open parking leads to a proportional decrease in the temperature of a whole transmission unit during cold seasons, an irregular intensity of operation of separate units and parts facilitates the occurrence of temperature gradients during movement. For example, in most cases a vehicle straight-line car movement along a smooth road does not facilitate satellite active rotation in its inter-wheel differential and can lead to an increase in internal friction. The same undesirable result can be obtained at the vehicle movement along the road with high adhesive properties providing the drive axle is equipped with multi-disk friction clutches of an automated system for pulling forces' adjustment.

Ensuring an optimal state of transmission oil applied in drive axles with an automated control of pulling forces, in compliance with the paper [20], can be reached by solving the following problems:

- Automated onboard monitoring of temperature gradients under various operation conditions. The information about the heating or cooling of the parts of the wheel drive can be obtained by means of direct temperature measurement on the main gearing casing surface and axle beam surface along the range of unit points. The dynamics of a temperature state within the time is also quite important to determine a rational duration of external control action.
- Oil temperatures' rational range justification. The need of keeping a certain heat oil state is determined by its viscous and temperature characteristics, physical and chemical stability, and its sustainability toward superficial tension and shift voltages.
- Selection of optimal means to maintain temperature modes. One should find out a rational combination of evaluation indicators of a thermal control device for a chosen temperature range and the mode of its maintenance.

According to the authors, the resolution of these problems will facilitate a drive axle resource increase with an automated power distribution under complex operating conditions.

References

1. Barykin AYu, Basyrov RR, Mukhametdinov MM (2015) On influence of external factors on performance characteristics of truck wheel drive. In: Materials of the Xth international virtual scientific and technical conference, Penza, pp 50–55
2. Barykin AYu (2013) Evaluation of performance characteristics influence on blocking properties of small friction differentials. In: Materials of international scientific and technical conference “Innovative mechanical engineering technology, equipment and materials—2013” and the forum “Increasing competitiveness and energy efficiency of mechanical engineering companies under WTO conditions”, Kazan, pp 34–36
3. Barykin AYu, Basyrov RR, Mukhametdinov MM (2014) To issue of system analysis of operating conditions of wheel drives of KAMAZ. *Sci Tech Bull Povolzhye* 6:74–76
4. Mukhametdinov MM (2012) Researching intensity of starting torque drop in rolling-contact bearings of axle drive of KamAZ. In: Mechanical engineering: design, engineering, calculation and repair & production technology. Materials of All-Russian scientific and practical conference, IzhGTU, Izhevsk, pp 113–114
5. Barykin AYu (2001) Basics of modern differentials theory. KamPI, Naberezhnye Chelny
6. Selifonov VV (2011) Automated car systems. Greenlight, Moscow
7. Ziebart E, Ott A (1980) Vergleich und Bewertung verschiedener Arten der Leistungsübertragung im Kraftfahrzeug. *ATZ* 1:9–13
8. Martin H (1993) Elektronisch geregelte elektromagnetische Visco-Lufterkupplungen für Nutzfahrzeuge. *ATZ* 5:240–247
9. Temperaturregelte Visco-Zufterkupplungen mit Zentralbefestigung (1986) *ATZ*, no 2, p 92
10. Barykin AYu (2000) Automated differential: synthesis of structure of blocking properties. In: International conference MSTU MAMI. MAMI, Moscow, 27–28 Sep 2000, pp 35–36

11. Barykin AYu (2002) Synthesis of characteristics of self-blocking differential of wheeled vehicle. In: Priorities of development of national automobile and tractor construction and engineering & scientific staff training. Theses of reports of international scientific & technical conference AAI XXXIX, Moscow, pp 10–12
12. Minimum air temperature (2017) Geography of Russia. <https://geographyofrussia.com/minimalnaya-temperatura-vozduxa/>. Accessed 21 Nov 2017
13. Barykin AYu, Basyrov RR, Mukhametdinov MM (2016) Evaluation of factors determining wheel drive operation conditions. In: Architectural, constructional and road complexes: problems, prospects, innovations. Materials of international research-to-practice conference, SibADI, Omsk, 7–9 Dec 2016
14. Barykin AYu, Takhaviyev RKh (2017) Evaluation of energy consumption during winter operation of truck drive axle. In: Israfilov IKh (ed) Energy saving. Science and Education, Naberezhnye Chelny Institute K(P)FU, Naberezhnye Chelny, pp 52–57
15. YeS Kuznetsov, Boldin AP, Vlasov VM et al (2001) Car technical operation: manual for higher education institutions, 4th edn. Nauka, Moscow
16. Barykin AYu, Mukhametdinov MM, Takhaviyev RKh (2017) Studying reasonable operating conditions of transmission units of trucks at operation in the northern regions. In: Problems of quality and operation of motor vehicles: materials of the XIIIth international virtual scientific and technical conference, PGUAS, Penza, 18 May 2017, pp 25–30
17. Lyandenburskiy VV et al (2015) Diagnostics of truck axle drive gears. In: Problems of quality and operation of motor vehicles: operation and development of motor vehicles: materials of the Xth international virtual scientific and technical conference. PGUAS, Penza, 15 May 2015, pp 199–205
18. Weather files (2017) Weather and climate. <http://www.pogodaiklimat.ru/archive.php>. Accessed 01 Feb 2017
19. Klamann D (1988) Lubricants and other related products. Synthesis, properties, application, chemistry. Khimiya, Moscow
20. Barykin AYu, Takhaviyev RKh (2017) Peculiarities of transmission oil operation in wheel drive. In: Final scientific conference of professors and academics, Naberezhnye Chelny Institute K(P)FU, Naberezhnye Chelny, 3 Feb 2017, pp 61–68

Simulation of Transforming Magnetic Systems Based on Permanent Magnets to Control Microparticles



N. N. Merzlova, A. V. Pashkovskiy and D. V. Boldyrev

Abstract A simulation of the magnetic control system structure of microparticles based on permanent magnets was carried out. Computational experiment results for magnetic field calculation created by the simulated system are presented. Comparative estimates of modern software environment's accuracy based on the finite element method and the SEM software package based on the standard element method are obtained. The authors continued the development of numerical and analytical methods of standard elements and auxiliary functions for the modeling of physical fields in a piecewise-homogeneous and nonlinear media. The introduction of standard elements opens the possibility of applying methods of auxiliary functions and standard elements without combining them with the finite element method. The use of standard elements provides a good approximation of an outer boundary of the computational domain, the interface of its parts with linear and nonlinear properties and complete filling of the computational domain standard elements. Functional representation can be expressed in terms of the nodal values of the solution imposed on the boundaries of standard elements for their bonding with adjacent standard elements.

Keywords Magnetic fields · Mathematical models · Numerical methods · Magnetic systems · Microparticles

1 Introduction

Currently, the use of micro- and nanoparticles is becoming more widely used in industrial, military, space and medical technologies. Targeted delivery of magnetic particles into specified areas of the field is carried out by magnetic control systems (MCS) in which sufficiently strong neodymium magnets can be used, as well as

N. N. Merzlova · A. V. Pashkovskiy (✉) · D. V. Boldyrev
North-Caucasus Federal University, 2, Kulakov Prospect, Stavropol 355029, Russia
e-mail: alecsandr_607@rambler.ru

© Springer Nature Switzerland AG 2020
A. A. Radionov et al. (eds.), *Proceedings of the 5th International Conference on Industrial Engineering (ICIE 2019)*, Lecture Notes in Mechanical Engineering,
https://doi.org/10.1007/978-3-030-22041-9_46

419

electromagnets. In this regard, in the modern practice of solving field problems, the need for more often arises as follows:

- significant increase in calculations accuracy of magnetic fields generated by MCS;
- multi-variant calculations related to MCS structure transformation, when the conditions for microparticles controlling change;
- the formation of the calculated MCS structure in real time;
- saving or slightly increasing the required computational resources to solve them.

As an example, illustrating the complexity and inconsistency of the arising in this case issues, the problem of MCS structure modeling from a set of permanent magnets will be presented, taking into account the necessary personalization.

It is obvious that the requirement of MCS structure personalization is directly related to the size and shape of the area exposed to a magnetic field, its depth and its characteristics as its internal structure (e.g., in cancer medicine it is the patient's body).

Factors complicating the MCS modeling are also:

- (1) The amount of required calculations to change if necessary the MCS structure:
 - (a) on the one hand, the change in MCS structure should be implemented in real time;
 - (b) on the other hand, an exact calculation requires a significant amount of computational resources.
- (2) Problem-solving complexity:
 - (a) on the one hand, the desire to maximize magnetic field localization on the area of impact;
 - (b) on the other hand, the complex form of the area.
- (3) The complexity of the microparticle control technology:
 - (a) on the one hand, the desire for very small particle sizes;
 - (b) on the other hand, a decrease in the influence power of the magnetic field on the particles at their small sizes.
- (4) Security requirements:
 - (a) on the one hand, the desire to strengthen the magnetic field for precise control;
 - (b) on the other hand, compliance with the personnel safety standards and the exposure process by the field, according to the requirements of the protocols.

One can confidently state the existence of such problems by MCS modeling in any of the above-mentioned industries.

2 Formulation of the Problem

In such a situation, the introduction of an standard elements SE with characteristic geometry of permanent magnets used in a magnetic system, which simulate their influence on the magnetic field of the system as a whole, would significantly reduce the degree of decomposition of the computational domain, the dimension of the system of linear algebraic equations (SLAE) to be solved and the accuracy of the calculations. To introduce such SEs, it is necessary to obtain in them analytical representations of boundary value problem solutions taking into account the geometry of the SE, the boundary conditions, the magnetization of the material and also determine the connections at their boundaries between the solution and the normal derivatives, imposed on the border of the SE, in accordance with the methods of SEM [1, 2].

As noted in works [2–10], existing software environments based on the use of the finite element method (FEM) (e.g., FEMM, MATLAB, Maxwell, etc.) often do not provide sufficient accuracy for two-, three-dimensional magnetic fields calculating and force interactions with micro- and nanoparticles in the presence of thin inclusions in the calculated fields, corner points with solution features. Undoubtedly, these conditions occur both in the MCS itself on permanent magnets in the form of cubes or parallelepipeds (corner points of magnets, gaps between them) and in computational areas exposed to a magnetic field. In connection with this, a number of works aimed at solving these problems appear [11–17].

Additional difficulties in using numerical methods based on FEM arise when solving problems that require high speed of calculations, especially in real time. The problem is that in FEMM, MATLAB, Maxwell and other software environments, the main time spent on the calculation is determined by the need to solve SLAE of a large dimension, which can be solved by a boundary value problem. It is the dimension of the SLAE and its structure (tend to tape one) that mainly determine the duration of the computational process. In the conditions of the need to ensure high speed and accuracy of calculation, with the aggravating conditions specified above, it is impractical to use methods based on FEM.

That is why the decision of the following questions is relevant when modeling the MCS:

- partition degree reduction of the computational domain;
- SLAE dimension reduction;
- ensuring high accuracy of calculations in the presence of solution features, the complex internal area structure and various kinds of micro-inclusions.

The results presented in works [1–6, 10] confirm that MCS effectively solves these issues and allows as follows:

- (1) reducing the required computational resources by covering the computational areas with standard elements (SE) and blocks.

- (2) solution smoothness improving in the field through the use of analytical representations of the solution in each SE.
- (3) high accuracy ensuring of normal derivatives gluing of solutions at the boundaries of SE.
- (4) getting block-tape structure SLAE.
- (5) taking into account solution features at internal points with a complex internal structure of the computational domain.

In work [2], a rectangular SE was introduced into the SE library, which simulates a source of a constant magnetic field, and analytical solutions of boundary problems in them were obtained, as well as connections with the normal derivative at their boundaries. It is obvious that the introduction of an SE of geometrically covering sources of a magnetic field in MCS with rectangular permanent magnets and simulating their influence on the magnetic field of the system as a whole allowed:

- to expand the use of SEM on parts of MCS, which are permanent magnets;
- to fill maximally the area of MCS and the surrounding MCS computational areas, minimizing computational costs by simultaneous increasing of calculation accuracy.

3 Rectangular Standard Elements in Modeling of the Field Created by the Magnetic Control System

A plane-parallel magnetic field in the area Ω_1 of permanent magnets and in the outer part of Ω_0 , described by the system of Maxwell's equation, will be considered as follows:

$$\operatorname{rot}H = 0, B = \mu_0 H - \mu_M M \quad \varepsilon \quad \Omega_1; \quad (1)$$

$$\operatorname{rot}H = 0, B = \mu_0 H \quad \varepsilon \quad \Omega_0; \operatorname{div}B = 0 \quad \varepsilon \quad \Omega_0 \cup \Omega_1. \quad (2)$$

On the boundary S_1 of the media section, the following conditions are fulfilled:

$$B_n^+|_{S_1} = B_n^-|_{S_1}; H_x^+|_{S_1} = H_x^-|_{S_1}, \quad (3)$$

where S_1 —is the boundaries of the areas Ω_1 .

As an assumption, the permanent magnets have a constant permeability $\mu_M = \text{const}$ and a uniform magnetization. Let the magnetization vector M of the permanent magnet is oriented along the axis “oy”.

As shown in [10], it can be obtained

$$A_z(x, y) = -m_2x + c. \quad (4)$$

It follows from Eq. (4) that

- (1) The derivative $\partial A_M / \partial n$ is different from zero only on the side parts of the magnet.
- (2) The constant m_2 is chosen taking into account the value of the magnetization vector M .

Similar calculations can be carried out for an SE permanent magnet with a magnetization vector parallel to the horizontal axis.

As shown in [10] when solving in SEs, the Dirichlet problem for the Laplace equation in the construction of the SLAE corresponding to the solved boundary value problem and filling the computational area with SEs, the “connection” equations are used. For a rectangular SE, the “connection” equation between the solution and its normal derivative brought to the boundary of S_1 SE has the form:

$$\begin{aligned}
 & 2/\sqrt{b_2 - b_1} \int_{G_{12}} \frac{\partial A^+}{\partial n} \Big|_{s_2} \sin(n\pi y / (b_2 - b_1)) dy \\
 & = F(cf_{10}, cf_1(k), cf_{20}, cf_2(k), cf_{30}, cf_3(k), cf_{40}, cf_4(k)) \\
 & = 1/(b_2 - b_1) / \text{sh}(n\pi(a_2 - a_1)/(b_2 - b_1)) \cdot \left[\sqrt{2}cf_{10}(1 - (-1)^n) \right. \\
 & \quad \left. + \sum_{k=1}^{nkf} 2cf_1(k) \left(1 - (-1)^{(n+k)} \right) / (1 - k^2/n^2) \right] \\
 & - 1/(b_2 - b_1) / \text{th}(n\pi(a_2 - a_1)/(b_2 - b_1)) \cdot \left[\sqrt{2}cf_{20}(1 - (-1)^n) \right. \\
 & \quad \left. + \sum_{k=1}^{nkf} 2cf_2(k) \cdot \left(1 - (-1)^{(n+k)} \right) / (1 - k^2/n^2) \right] \\
 & + \sqrt{2}/\sqrt{a_2 - a_1} / \sqrt{b_2 - b_1} / \text{sh}(n\pi(a_2 - a_1)/(b_2 - b_1)) \\
 & (\text{ch}(n\pi(a_2 - a_1)/(b_2 - b_1)) - 1)cf_{30} \\
 & + n\pi/\sqrt{b_2 - b_1} / (b_2 - b_1) / \text{sh}(n\pi(a_2 - a_1)/(b_2 - b_1)) \sum_{k=1}^{nkfsh} \text{csh}(k, n) \times cf_3(k) \\
 & - (-1)^n \cdot \sqrt{2}/\sqrt{a_2 - a_1} / \sqrt{b_2 - b_1} / \text{sh}(n\pi(a_2 - a_1)/(b_2 - b_1)) \\
 & (\text{ch}(n\pi(a_2 - a_1)/(b_2 - b_1)) - 1)cf_{40} \\
 & - (-1)^n n\pi / \sqrt{b_2 - b_1} / (b_2 - b_1) / \text{sh}(n\pi(a_2 - a_1)/(b_2 - b_1)) \sum_{k=1}^{nkfsh} \text{csh}(k, n) cf_4(k)
 \end{aligned} \quad (5)$$

It can be noted that the right-hand side of Eq. (5) contains the Fourier coefficients of dissociation into a number of solution traces at the SE boundaries.

The statement of problem (1)–(3) for SE “permanent magnet” is the Dirichlet problem for the Laplace equation and coincides with the statement of the boundary value problem for a rectangular SE from the library, in view of this, using Eq. (5) for SE “permanent magnet,” taking into account the magnetization. In the left-hand side of the equation, an additional term $\partial A_M^+ / \partial n|_{S_2}$ must be added for this. So, the result is as follows:

$$\begin{aligned}
 & 2/\sqrt{b_2 - b_1} \int_{G_{12}} \left(\frac{\partial A^+}{\partial n}|_{S_2} - \frac{\partial A_M^+}{\partial n}|_{S_2} \right) \sin(n\pi \cdot y/(b_2 - b_1)) dy \\
 & = F(cf_{10}, cf_1(k), cf_{20}, cf_2(k), cf_{30}, cf_3(k), cf_{40}, cf_4(k)).
 \end{aligned}
 \tag{6}$$

Then, if considering the “gluing” of a pair of SE, both of which are permanent magnets with the same direction of the magnetization vectors along the common boundary $S_{12} = S_{21}$ (Fig. 1), the equation forming the SLAE will be as follows:

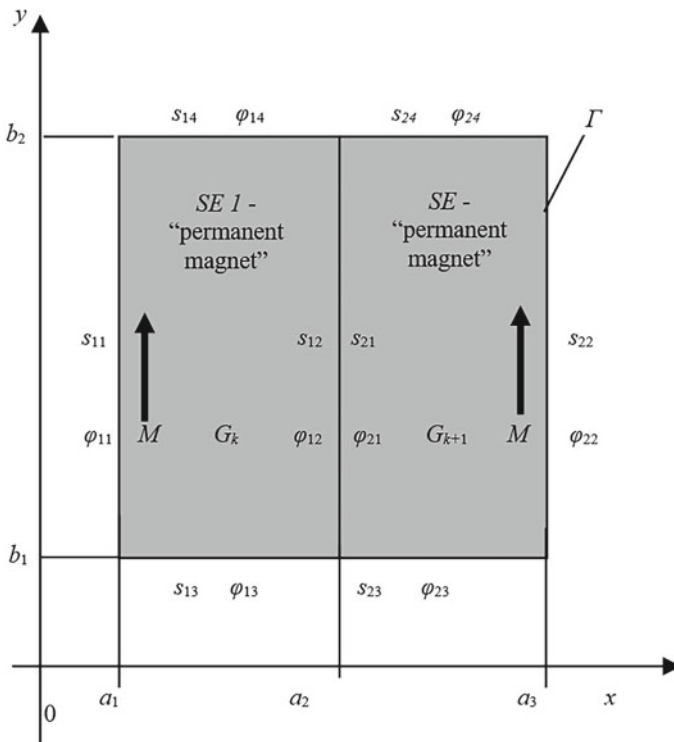


Fig. 1 Pair of SE–SE “permanent magnets”

$$\begin{aligned}
 & 2/\sqrt{b_2 - b_1} \int_{G_{21}} \left(\frac{\partial A^+}{\partial n} \Big|_{S_{21}} - \frac{\partial A_{M^+}}{\partial n} \Big|_{S_{21}} \right) \sin(n\pi y / (b_2 - b_1)) dy \\
 & = 2/\sqrt{b_2 - b_1} \int_{G_{12}} \left(\frac{\partial A^+}{\partial n} \Big|_{S_{12}} - \frac{\partial A_{M^+}}{\partial n} \Big|_{S_{12}} \right) \sin(n\pi y / (b_2 - b_1)) dy.
 \end{aligned} \tag{7}$$

If considering the “gluing” of a pair of SE, both of which are permanent magnets, but with the orthogonal direction of the magnetization vectors, along the common boundary $S_{12} = S_{21}$, the equation forming the SLAE will be as follows:

$$\begin{aligned}
 & 2/\sqrt{b_2 - b_1} \int_{G_{21}} \left(\frac{\partial A^+}{\partial n} \Big|_{S_{21}} - \frac{\partial A_{M^+}}{\partial n} \Big|_{S_{21}} \right) \sin(n\pi y / (b_2 - b_1)) dy \\
 & = 2/\sqrt{b_2 - b_1} \int_{G_{12}} \frac{\partial A^+}{\partial n} \Big|_{S_{12}} \sin(n\pi y / (b_2 - b_1)) dy.
 \end{aligned} \tag{8}$$

In this way:

- (1) The above considered statement of the Dirichlet problem (1)–(3) corresponds to its statement for SE from the created SE library.
- (2) The conditions of “gluing” the SE “permanent magnet” with SE “permanent magnet” are defined by expressions (7) и (8).
- (3) To take into account the magnetization, in the expression (5) when forming the SLAE of the boundary value problem while considering the sides of the “gluing” SE “permanent magnet”–SE “permanent magnet,” it suffices to introduce additional terms: $\partial A_{M^+} / \partial n \Big|_{si}$.

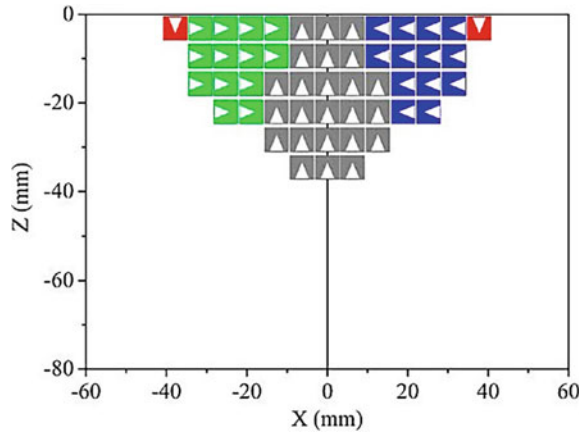
In conclusion, it can be said that the constructed model of a permanent magnet as SE can be applied to the magnetic field calculation both inside a permanent magnet and in the magnetic system as a whole.

4 MCS Application for the Calculation of the Two-Dimensional Magnetic Field of the Magnetic Control System Containing Permanent Magnets

The MCS consisting of permanent magnets set will be considered, laid down in work [18, 19] as a basis for conducting computational test experiments. The MCS design consists of inexpensive, lightweight and accessible cubic permanent magnets with 5×5 mm edges (Fig. 2).

Permanent magnets of class N52 NbFeB with magnetization equal to 1.14×10^6 A/m were used. The directions of the magnetization vectors of magnet groups are orthogonal and are shown in Fig. 2 by arrows. The choice of

Fig. 2 MCS design



magnetization vector directions is determined by the need to minimize the magnetic induction outside the MCS, except for the area above the MCS surface used to control the microparticles.

The task of calculating the magnetic field of MCS is considered in two-dimensional formulation (2)–(3) with linear characteristics of materials. At the outer boundary of the computational domain, the Dirichlet conditions for the vector magnetic potential $A|_{\sigma} = 0$ are satisfied.

To split a computational domain, including fields of permanent magnets, rectangular SE with Dirichlet conditions are used on all edges of the SEM library given in work [10], as well as the SE permanent magnet introduced in work [1]. Selected SE allows to cover completely the settlement area of magnetic system. One of the possible options for filling the SE of the computational region, which was formed automatically, is shown in Fig. 3. For splitting the region, 528 rectangular SEs were used. When forming the SLAE, a pair of SE permanent magnets was glued using Formulas (7) and (8), depending on the direction of the magnetization vectors.

The efficiency and accuracy of the SEM and FEM were estimated on the basis of their efficiency and accuracy with the usual discretization degrees of the computational domain FEM, which can be implemented on a PC, in comparison with the calculation option with a very high degree of discretization. The calculation of the FEM was performed using the packages: FEMM, software MATLAB PDE and ANSYS MAXWELL 16.

The results of the calculation of the magnetic induction vector values in 13 control points above the MCS surface using the SEM and FEM are summarized in Table 1.

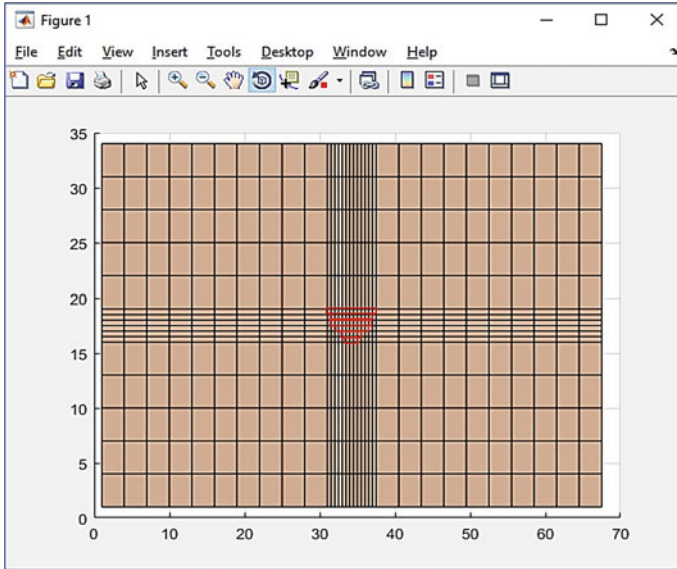


Fig. 3 Filling the magnetic system with 528 standard elements

Table 1 Magnetic induction values at control points above MCS

No	FEMM, B (Tesla)	PDEtool MATLAB, B (Tesla)	SEM, B (Tesla)	Maxwell standard B (Tesla)	δ_{FEMM} (%)	$\delta_{PDEtool}$ (%)	δ_{SEM} (%)
	10000 FE	10000 FE	528 SE	700000 FE (standard)			
	$T = 5$ s	$T = 10$ s	$T = 8$ s	$T = 350$ min			
1	0.6872	0.7079	0.7248	0.7346	6.45	3.63	1.33
2	0.4721	0.4853	0.4911	0.4981	5.22	2.57	1.41
3	0.3296	0.3398	0.3421	0.346	4.74	1.79	1.13
4	0.1644	0.1688	0.1769	0.1815	9.42	7.00	2.53
5	0.1301	0.1316	0.1345	0.1358	4.20	3.09	0.96
6	0.09203	0.1087	0.1009	0.1015	9.33	7.09	0.59
7	0.07497	0.07993	0.08102	0.08189	8.45	2.39	1.06
8	0.06273	0.06477	0.06513	0.06582	4.69	1.60	1.05
9	0.04894	0.05114	0.05201	0.05309	7.82	3.67	2.03
10	0.04081	0.04205	0.04341	0.04435	7.98	5.19	2.12
11	0.03416	0.03633	0.03763	0.03785	9.75	4.02	0.58
12	0.01718	0.01879	0.01931	0.01972	12.88	4.72	2.08
13	0.003989	0.004397	0.005046	0.005278	24.42	16.69	4.40

5 Conclusion

The results of the computational experiment make it possible to draw the following conclusions:

- (1) Rectangular SEs by using precise solutions (analytical formulas) of boundary value problems in SE ensured a high accuracy of calculating the magnetic field in the presence of singularities at the corner points of the computational area.
- (2) The accuracy of SEM in determining the induction is much higher than the accuracy of the FEM packages.
- (3) SEM provided increased accuracy of the solution with significantly smaller dimensions of the expanded SLAE matrices, compared to FEM.
- (4) Introduction pair SE–SE “permanent magnets” allowed the use of SEM without its combination with FEM, which allows the use of SEM programs built for the purpose of calculating the magnetic fields of electromechanical and magnetic systems.
- (5) The SEM provides a significant reduction in the number of elements in the partition of the calculation areas while maintaining high accuracy of calculations.
- (6) SEM provides a significant reduction of temporary costs required for calculations, which reduces the time for reconfiguration and adjustment of the MCS design for a specific technology.
- (7) SEM provides the increased accuracy in the magnetic field calculation, which will allow taking in account weak magnetic fields that also affect microparticles.

References

1. Pashkovskiy AV, Tkachev AN, Bahvalov UA (2018) New standard elements for calculating magnetic fields of electromechanical and magnetic systems with permanent magnets. In: 2018 international conference on industrial engineering, applications and manufacturing (ICIEAM), Moscow, Russia, 15–18 May 2018
2. Pashkovskiy AV, Tkachev AN, Bahvalov UA (2017) New standard element types for magnetic field calculation in the electromechanical system. In: 2017 international conference on industrial engineering, applications and manufacturing (ICIEAM), Saint Petersburg, Russia, 16–19 May 2017. <https://doi.org/10.1109/icieam.2017.8076386>
3. Tkachev AN, Pashkovskiy AV, Burtceva OA (2015) Application of block elements method to calculate the electromechanical systems magnetic field and force characteristics. *Procedia Eng* 129:288–293. <https://doi.org/10.1016/j.proeng.2015.12.064>
4. Pashkovskiy AV, Tkachev AN (2013) Block numerical and analytical method of auxiliary functions for calculating the magnetic field in nonlinear environments. *News of higher educational institutions. Electromechanics* 3:3–7
5. Pashkovskiy AV, Pashkovskiy VI (2012) Block numerical and analytical methods and new mathematical models in the calculation of the force interactions of nanoparticles. *Scientific and technical statements of the St. Petersburg State Polytechnic University. Phys Math* 158:39–44

6. Pashkovskiy AV (2010) The method of standard elements in the operation of heat treatment processes of electromechanical devices. *News of YUFU. Eng Sci* 5(106):74–79
7. Pashkovsky V (2009) Phans in the atomic and nano world, numerical-analytical method SEM in the calculation field of nanotechnology. *Creative search scientists Israel today, Israel, Ashkelon*, vol 13, pp 92–948
8. Pashkovsky V (2010) Creation of antibodies by nanotechnology. *Creative search scientists Israel today, Israel, Ashkelon*, vol 14, pp 90–93
9. Pashkovskiy AV (2010) Combined method of standard and finite elements in the calculation of magnetic field and power characteristics of asynchronous draft-lifting module. *Inf Syst Technol* 4(61):33–42
10. Pashkovskiy AV (2014) Numerical and analytical methods of standard elements for modeling stationary physical fields in linear piecewise-homogeneous and non-linear environments. Dissertation, Platov South-Russian State Polytechnic University
11. Klimenko VV (1998) Modified complex boundary element method for calculating quasistatic electric and magnetic fields. Dissertation, Platov South-Russian State Polytechnic University
12. Tkachev AN (1998) Combined methods for modeling a quasistatic electric field in nonlinear anisotropic ferromagnetic environments. Dissertation, Platov South-Russian State Polytechnic University
13. Shkuropadskiy IV (2005) Combined finite and complex boundary element method for calculating electric and magnetic fields in nonlinear anisotropic environments. Dissertation, Platov South-Russian State Polytechnic University
14. Pahner U, Meztens R, Belmans R, Hameyez K (1998) A parametrica finite element environment tuned for numerical optimization. *IEEE Trans Magn* 34(5):2936–2939
15. Rachowicz W, Demkowicz L (2002) An hp-adaptive finite element method for electromagnetics—part II: a 3-D implementation. *Int J Numer Methods Eng* 53(1):147–180
16. Vassent E, Meunier G, Foggia A (1991) Simulation of induction machines-using complex magnetodynamic finite element method coupled with the circuit equations. *IEEE Trans Magnetics* 27(5):4246–4249
17. Hromadko T, Lai C (1987) The complex variable boundary element method in engineering analysis. Springer Vergas, New York
18. Barnsley L, Carugo D, Stride E (2016) Optimized shapes of magnetic arrays for drug targeting applications. *J Phys D Appl Phys* 49(22). <https://doi.org/10.1088/0022-3727/49/22/225501>
19. Sarwar A, Nemirovski A, Shapiro B (2012) Optimal Halbach permanent magnet designs for maximally pulling and pushing nanoparticles. *J Magn Magn Mater* 324(5):742–754. <https://doi.org/10.1016/j.jmmm.2011.09.008>

Use in Cycle of Biogas Plant Boiler for Waste Disposal



S. A. Naumov, V. Y. Sokolov and A. V. Sadchikov

Abstract This paper presents the results of experiments and calculations of a universal solid fuel boiler that allows one to dispose of waste of hazard class 4–5. A fundamentally new design solution of the furnace chamber and boiler heating surfaces is proposed. A distinctive feature of the proposed design is an inclined sieve that allows the airflow to evenly distribute the burned material in the space of the combustion chamber. As a result of the calculation the optimal shape and size of the sieve were obtained, which allows increasing the efficiency of the combustion process by reducing the time of complete combustion of up to 26%. It is shown that the use of a special screen made of refractory material makes it possible to optimize the directions of movement of the burned material, blast air and combustion products. The heat obtained in the combustion process is used in the cycle of the biogas plant to compensate for the thermal losses of the methanogenesis reactor, which allows ensuring the stability of the plant in the winter period.

Keywords Biogas plants · Waste disposal · Thermal energy

1 Introduction

Current trends in the growth of energy consumption cause the need for more intensive involvement in the economic turnover of alternative renewable energy sources. Among them, biomass energy occupies a special place. The main advantages of biomass are high volumes and stable formation of energy resources, regardless of the time of day and time of year. The most effective from the environmental, energy and economic points of view is the production of methane-containing gas in the processes of anaerobic digestion of biomass, in particular waste of anthropogenic activities with a high content of organic matter.

S. A. Naumov · V. Y. Sokolov · A. V. Sadchikov (✉)
Orenburg State University, 13, Victory Avenue, Orenburg 460018, Russia
e-mail: lyohantron@mail.ru

© Springer Nature Switzerland AG 2020
A. A. Radionov et al. (eds.), *Proceedings of the 5th International Conference on Industrial Engineering (ICIE 2019)*, Lecture Notes in Mechanical Engineering,
https://doi.org/10.1007/978-3-030-22041-9_47

2 The Relevance of the Work

The process of anaerobic fermentation can occur spontaneously, for example, in the body of the landfill. In this case, a landfill gas with a high content of methane is formed (reference to the article in the AEE). Anaerobic digestion of biomass to produce biogas is also produced in artificially created conditions at biogas plants in special reactors and is the main part of the process of organic waste. Modern technologies of biogas production at biogas plants are due to special technological requirements for the main stages of the process, primarily to the fermentation mode. Energy costs in the process of biogas production are mainly related to maintaining the necessary temperature conditions in the reactor. In this regard, the development of new ways to improve the efficiency of biogas production at bioenergy stations is an important scientific direction.

3 Object of Research

The complex, which is located on 23 km from the city of Orenburg on the territory of “Complex of Recycling Systems”, was chosen as an object for the study. The basis of the technological activity of the production and processing complex is a civilized waste disposal (from waste disposal of farms to disposal of expired food products of a wide range). Biogas plant is a whole complex of equipment that allows processing agricultural and food industry waste into biological fertilizers and biological gas, which is further used as the main fuel for gas piston machines that produce both thermal and the electrical energies, as well as motor fuel for converted vehicles [1–4]. Waste disposal stations are now common in countries such as Germany and the Netherlands. In recent years, the number of Chinese farms and food industries using biogas to generate heat and electricity for their own needs has increased.

The layout of energy sources, storage devices and consumers is shown in Fig. 1.

The main purpose of the presented complex is the processing and disposal of waste of 4–5 hazard classes. Currently, the list of waste disposed at the station includes 54 items. Waste containing organic matter is processed in the process of anaerobic fermentation, part of the reactions takes place in the methanogenesis reactor—methane tank (15), while the necessary thermobaric conditions are provided, since the process of methane fermentation takes place with the absorption of heat. Other wastes that do not meet the conditions of anaerobic fermentation are subjected to incineration; to date, a cremator has been used in the complex for this purpose. The practice of waste incineration in the cremator showed that the process is energy inefficient, and the time of complete combustion of hard-to-burn fractions does not meet the technological requirements of the processing. In this regard, the task of creating a highly efficient design of the boiler for burning waste of 4–5 hazard classes is urgent.

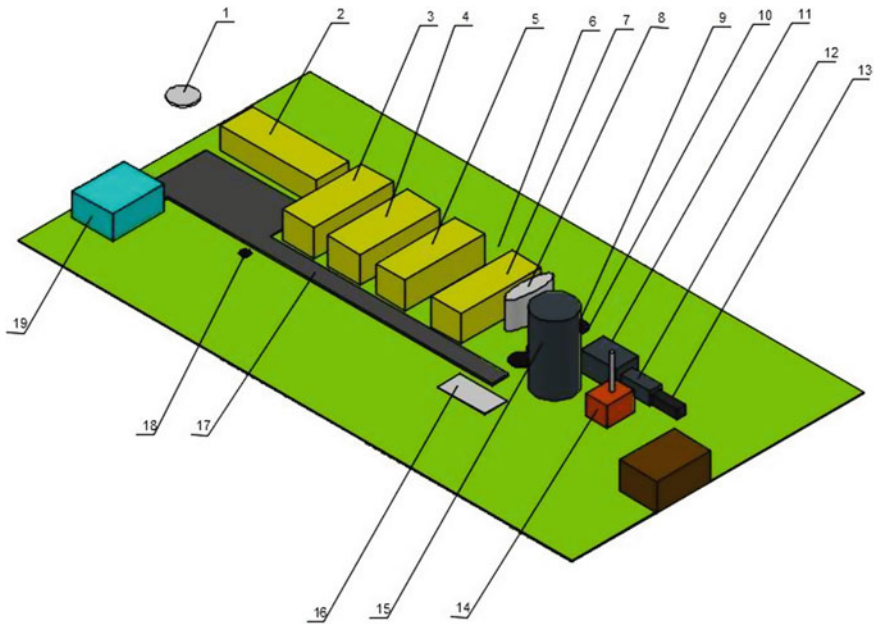


Fig. 1 Layout of energy sources, storage devices and consumers. 1—manhole for sewage, 2—mobile administrator module (MBM), 3—cell module boiler, 4—cell module—a warehouse with solar collectors on the roof of a 5—cell module chopper—podgotovitel products, 6—reservoir storage of crushed products, 7—cell module with fermenter fertilizer, 8—elastic tank, 9—unit wells for receiving and waste transfer in biofermentor, 10—filling up the tank of the extruder, 11—tumbler, 12—extruder, 13—unloading conveyor, 14—boiler, 15—digester, 16—a receiving tank for the unit wells for receiving and waste transfer, 17—a solid surface for transportation of a boot materials, 18—water wells, 19—methane-filling station

At the moment, a large number of utilization plants of low productivity, both domestic and foreign productions, are known [5–8]; however, these plants have lower productivity and in most cases the generated heat is not useful.

To maintain the technological regime of biogas production in the shirt of the methane tank, it is necessary to maintain a positive temperature in the region of 30–45 °C; in this regard, there was a need for heat generation. Currently, the temperature of the upper boundary of the mesophilic regime is maintained in the methanogenesis reactor. As a heat generator in this paper, it is proposed to use a boiler of its own production, the main purpose of which is the disposal of waste 4–5 hazard classes.

The basis of the boiler is the boiler body assembled from rolled steel (Fig. 2). The combustion space is a tank 5.6 m³, to the top of which is mounted a cylindrical pipe with a flange element for fixing the chimney, whose height is 6 m.

According to the technical calculation as a heat exchanger, pipes with a diameter of 50 mm are selected, with a heat exchange surface of 7.53 m². The pipes used as a heat exchanger in the body are not rigidly fixed, but are sealed with

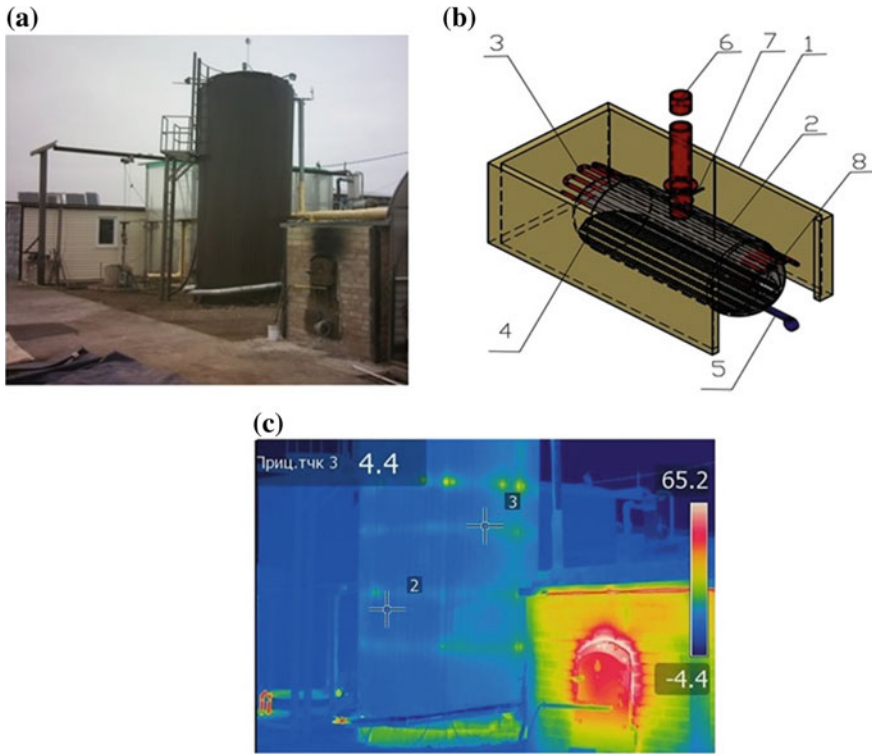


Fig. 2 **a** General view of the installation; **b** boiler design (1—boiler body; 2—tank; 3—heat exchangers; 4—inclined sieve; 5—blast fan; 6—chimney; 7—damper;); **c** thermal imaging of the boiler

non-combustible material to ensure their replacement. For efficient operation of the boiler it is provided a damper that controls the area of the inlet of the exhaust gases.

The heat supply system is equipped with a pressure sensor, temperature sensor and protective. On the front of the stake, there is a cover to fill it. At the bottom of the boiler is a fan blowing power of 0.75 kW. Biogas is used as the initiating fuel. For uniform placement of the incinerated material and increase of completeness of combustion of waste in the boiler, the sieve is provided. To reduce heat losses from the boiler, the body was insulated with mineral wool and brickwork.

The principle of operation of the boiler is as follows: The raw material necessary for utilization is loaded into the boiler, then the initiating fuel is fed into the boiler to ignite the raw material, and at the same time air is supplied through the grate to the boiler to increase the intensity of combustion. The heat generated by the heat exchanger (the heat carrier is water) is directed to the heating of the methane tank in the winter period.

Based on the analysis of flue gases, boiler efficiency is determined by the method of reverse balance [9–13]. At full combustion of fuel, the excess air ratio is

calculated in relation to the nitrogen contained in the dry combustion products, to the nitrogen accompanying oxygen from the fuel consumed for combustion. Hence, the excess air ratio is

$$\alpha = \frac{20.8}{20.8 - O_2} \cdot k_a = \alpha_n \cdot k_a \quad (1)$$

where k_a is the correction factor (determined by the figure. $APR = ; APR - RO_{2max}/RO_2$).

Losses of heat with leaving gases can be determined:

$$q_2 = f \frac{t_{yx} - t_b}{CO_2} \quad (2)$$

where

- f empirical factor (wood = 0.61; paper = 0.74)
- t_{yx} temperature of the leaving gases behind the boiler, °C
- t_b temperature of air at burner, °C
- CO_2 content of carbon dioxide in combustion products, %.

Heat loss from chemical incompleteness of combustion for all solid fuels is defined as

$$q_3 = \frac{k_1 \cdot CO}{CO_2 + CO} \quad (3)$$

CO is the content of carbon monoxide in combustion products, % (for fuel briquettes 70–74, for firewood of natural humidity 58–63, for brown coals 85–90).

Next, we calculate the heat loss to the environment

$$q_5 = \frac{q_{5envir} \cdot Q_n}{Q_a} \quad (4)$$

where

- q_{5envir} heat loss to environment at nominal capacity q_{5envir} taking a generalized curve (Fig. 3)
- Q_n nominal heating capacity (Gcal/h)
- Q_a actual capacity (Gcal/h).

The value of the useful heat or thermal capacity of the boiler is

$$Q_k = G_k \cdot \Delta t \times 10^{-3} \quad (5)$$

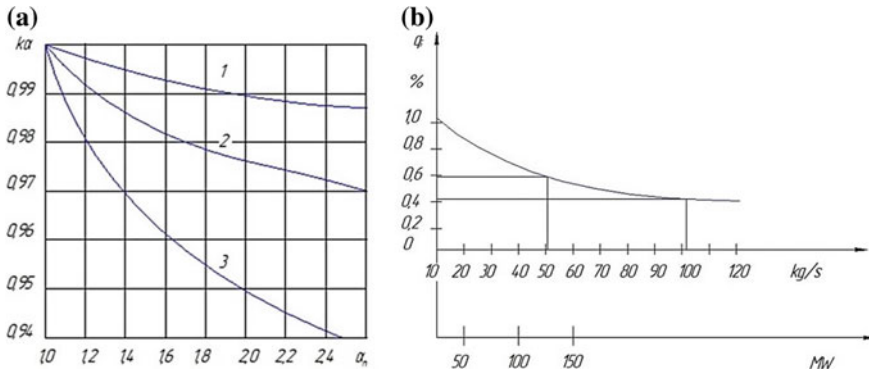


Fig. 3 **a** is a graph of a correction factor k_a (1, 2, 3—respectively, all solid fuels, liquid and gaseous fuels); **b** nominal performance

where

G_k water flow through the boiler (take the pump)

Δt temperature difference of the coolant.

Determine the specific consumption of conventional fuel to produce 1 Gcal at an efficiency of 100%:

$$H_x = \frac{1}{7 \times 10^{-3}} = 142.85 \text{ kg/Gcal} \tag{6}$$

Determination of the efficiency of the boiler unit on the reverse balance is carried out according to the following formula:

$$\eta = 100 - (q_2 + q_3 + q_5) \tag{7}$$

Specific consumption of natural fuel for production of 1 Gcal:

- 1 kg of natural fuel (wood of natural moisture) corresponds to 1620 kcal.
- 1 kg of fuel (paper) matches 3970 kcal.

Therefore, the ideal (at efficiency = 100%) specific consumption of natural fuel for the production of 1 Gcal of heat is:

$$H_x = \frac{1}{1.62 \times 10^{-3}} = 617 \text{ kg/Gcal—wood of natural humidity (50%)}$$

$$H_x = \frac{1}{3.97 \times 10^{-3}} = 251.48 \text{ kg/Gcal—paper}$$

$$H = H_x / \eta_{br} = 617 / 42.67 / 100 = 1481 \text{ kg/Gcal—wood of natural humidity (50%).}$$

The data obtained during the experiment and calculation are presented in Table 1.



Table 1 Data obtained during the experiment and calculation

Parameters	Wood (humidity 50%)	Paper
Average temperature difference (before and after the boiler), °C (water heating)	22	25
The average water temperature to the boiler, °C	46	48
Average water temperature after the boiler, °C	68	73
Outdoor temperature, °C	-5	-5
Weight of fuel loaded into the boiler furnace, kg	190	190
Losses of heat with leaving gases, %	22.87	19
The loss of heat from chemical underburning, %	30.4	20.6
Heat loss to the environment, %	3.86	2.43
Generated thermal energy during testing, kW	128	446
Mass of ash and slag discharged from furnace and sub-grate zone, %	3.4	3.7
Average hourly boiler capacity, kW h	82.5	144
Efficiency of the boiler unit on the reverse balance, %	42.64	57.97
Average temperature of exhaust gases, °C	181	195
Specific fuel consumption for generation of heat Gcal—paper, kg	1481.7	425.2
Specific consumption of equivalent fuel for generation of heat 1	342.9	246.48
The cost of 1 ton of fuel delivered to the boiler, RUB current price	~ 1200 (cutting costs included)	4100

4 Conclusion

In the course of the work carried out, a boiler was designed and constructed to allow the utilization of waste of hazard classes 4–5 [14–17], and the generated heat was directed to the technological cycle and the own needs of LLC “Integrated Recycling Systems.” As a result of the calculation the optimal shape and size of the sieve were obtained, which allows increasing the efficiency of the combustion process by reducing the time of complete combustion of up to 26%. The tests and calculations showed the effectiveness of the proposed installation, and the proposed technological solutions allowed to intensify the combustion process of waste, thereby ensuring the completeness of the combustion of the material to be disposed of.

In fact, in this work one of the oldest methods of waste disposal is implemented—a method of burning large fraction and lump solid fuel. During the manufacture of the design were investigated different versions of models, and the result is a version of the design, which is the most complete destruction of large-scale waste. In the course of research, the most significant variants and the most effective varieties were considered: burning on a fixed inclined grate; burning on a movable inclined grate; and combustion in a fluidized (fluidized) layer, which is used for combustion, located on the grate, through which the air is blown. The experience of

the primary operation of the proposed development has shown that the most effective is the design with a fixed, slightly inclined to the inlet gate grate having in the lower part of the working furnace device to create a non-sharp blast in the form of a fan that provides a breakdown of ash from the burning fuel, but does not create a boiling layer in which the fuel gas is carried away. The development is based on the characteristics obtained during the work on the patent № 2415337 [18–22], obtained by the employees in the Department of Heat Power Engineering of the Electric Power Faculty at the Orenburg State University.

One of the main advantages of the design is that under the pressure of the new incoming portions of fuel, it moves to the sides and upward, filling about a quarter of the furnace space. The direction of movement of the blast air is opposite to the direction of movement of the fuel, so that the air in the combustion space is quickly mixed with volatile combustibles.

The studies also found that in the combustion chamber above the inclined surface of the grate it is advisable to use a special screen made of refractory material that can withstand a temperature of 1800 °C. This screen changes the direction of the combustion gases, and this in turn gives three advantages: The combustion process takes place more intensively and with a higher temperature, the flame goes a longer way than the more complete combustion of the fuel is provided; the amount of sparks reflected over the wet fuel is reduced; the flame dries the feed-stock, reducing to a minimum ash content of the residue.

Acknowledgements The study was performed by a grant of Russian Scientific Foundation (project No. 18-79-10136).

References

1. Biogas Plants by Ludwig Sasse A Publication of the Deutsches Zentrum für Entwicklungstechnologien-GATE. In: Deutsche Gesellschaft für Technische Zusammenarbeit (GTZ) GmbH (1988)
2. Maile I, Muzenda EA (2014) Review of biogas purification through chemical absorption. In: International conference on chemical engineering & advanced computational technologies (ICCEACT'2014), 24–25 Nov, Pretoria, South Africa
3. Lantz M, Svensson M, Björnsson L, Börjesson P (2007) The prospects for an expansion of biogas systems in Sweden-incentives, barriers and potentials. *Energy Policy* 35:1830–1843
4. GOST R53790-2010 Energy biowaste. General technical requirements for biogas plants
5. Zagrutdinov PS, Negaturov VN, Malykhin DG, Senachin PK, Nikishin M S, Filipchenko SA (2013) Preparation and gasification of solid waste in a two-zone gas generators of the direct process, working with the CHP and complexes for the production of synthetic liquid fuels - *polzunovskii Gazette*, No. 4/3
6. Popov AV, Ryzhkov AV, Silin AM (2006) Study of the processes of multi-zone gasification of biomass. In: “Solid fuel Combustion”: collection of reports of the VI all-Russian conference (with the participation of foreign scientists), Part 3, Novosibirsk, pp 126–136
7. Ryzhkov AF, Silin VE, Popov AV, Usov GI (2011) Experimental study of the kinetics of the conversion of highly reactive fuels. *Mod Sci Collect Sci Pap* 3(8):13–20

8. Nagornov AN (2010) Research and development of technology of gasification of low-ash coals in a dense layer under pressure at steam-air blowing. Dissertation, Barnaul, 20 p
9. GOST R 56777-2015 Boiler plants. Method of calculation of energy consumption and efficiency
10. Kuznetsova NV et al (2000) Thermal calculation of boiler units. (Standard method.): Energia, 380 p
11. Andreev AA, Trembovlya VI, Finger EL (1976) Thermal performance testing of boiler plants. Energy, Moscow, 218 p
12. Sorokina L (2004) Fuel and fundamentals of combustion theory: studies. Manual. ISTU Publishing House, Irkutsk, 78 p
13. Practical training in the discipline "Analysis of thermal efficiency of equipment" (2007)
14. GOST R 53691-2009 Resources. Waste treatment. Passport waste I-IV hazard class. Basic requirement
15. Criteria for classifying hazardous waste as a hazard to the environment. Approved by the order of the MPR of Russia from 15 June 2001, no. 511
16. Resolution of the OECD "On the transboundary movement of hazardous wastes destined for recovery operations" (93) 74/Final. Adopted by the Council 23 July 1994 Approved by order of the MPR of Russia from 02.12.2002, no. 786. Registered by the Russian Ministry of justice on 9 Jan 2003, registration number 41907
17. Federal classification catalogue of wastes. Approved by order of the MPR of Russia from 02.12.2002 No. 786. Registered by the Ministry of justice on 9 Jan 2003, registration number 4107
18. Sokolov VYu, Sadchikov AV, Goryachev SV, Naumov SA (2009) Method of operation of the boiler in the mode of solid ash removal C1 2415337 RU f23c 5/24 (2006.01), no. 2009147040/06
19. Ilyasov VA, Khvorov G, Sokolnikov G, Khrustalev GN, Kolomensky SI (2004) Design solutions of JSC "Sibenergomash" translation boilers Kansk-Achinsk coals, with liquid slag removal for slag removal solid. Polzunovskii Bull 1:100–105
20. Volkov EP, Perepelkin AV (1989) Technological and ecological problems of low-grade fuels combustion. Moscow 9:25–28
21. Solovyov TA (2009) Increase in the efficiency of the boiler unit due to the installation of a cyclone-vortex, t. a., t. a
22. Solovyov TA (2016) News of heat supply. In: Publications in the proceedings of scientific and technical conferences, vol 6, pp 30–33

Simulation of Rectification Process Taking into Account Longitudinal Diffusion on Equations of Working Lines



A. B. Golovanchikov, V. N. Karev and N. A. Prokhorenko

Abstract Analytically, on the basis of the differential equations of material balance, the equations of working lines and mass transfer in the distillation column for binary mixtures for the strengthening and exhaustive parts of the packed distillation column with a diffusion structure of the flow in a continuous liquid phase are derived. Comparative examples of the calculation for typical structures of the flow of ideal displacement are given using the derived equations that take into account the longitudinal diffusion for a “ethanol–ethyl alcohol” binary mixture. A calculation algorithm is proposed, and technological and geometrical parameters are compared with similar parameters of the same column and are calculated according to a typical algorithm, when the dispersed gas phase has the structure of an ideal displacement flow, and the continuous liquid phase is an ideal mixing. The scheme of material flows and their concentrations is presented in the exhaustive part of the rectification column taking into account the longitudinal diffusion.

Keywords Longitudinal · Diffusion · Peclet · Displacement · Rectification · Working line · Strengthening · Exhaustive · Column

1 Introduction

The known methods for calculating plate-type distillation columns are based on the model of ideal vapor phase extrusion and perfect mixing in a boiling solution, and packed ones—on ideal pressure in both phases [1–3]. In a number of studies on absorption, extraction, adsorption, and ion exchange, longitudinal mixing is taken into account, which is based on the continuous phase diffusion model of the flow structure [4–7].

The purpose of the article is to derive the working line and mass transfer equations for the binary mixture in the strengthening and exhaustive parts of the

A. B. Golovanchikov · V. N. Karev · N. A. Prokhorenko (✉)
Volgograd Technical University, 28, Lenin Prospekt, Volgograd 400005, Russia
e-mail: natasha292009@yandex.ru

distillation column taking into account the longitudinal diffusion of the liquid phase, as well as comparing the results of calculations of technological and geometrical parameters of the packed methanol–ethanol binary mixture. According to these formulas, which take into account longitudinal mixing, a comparison will be made with a typical calculation corresponding to ideal displacement.

2 Scientific Significance

This topic is relevant because it is used in chemical, oil and gas, oil, oil refining, and energy industries, which is actively developing in Russia.

The development of new technical complexes on the basis of the obtained experimental data will help upgrade existing industrial designs that will have higher productivity and energy efficiency.

The development of new technical complexes based on the experimental data obtained will help to upgrade already having industrial designs that will have higher performance and energy efficiency. One of the main goals of industrial development is resource and energy saving, reducing losses at all stages of the technological process in the preparation of reserves, production, transport, and processing. The energy intensity of Russia's GDP is 2, 3 times higher than the world average, while for EU countries it is 3.1 times. The existing energy-saving potential of Russia ranges from 360 to 430 million tons of conditional fuel or 39–47% of current energy consumption. Almost a third part of it is concentrated in the fuel and energy sectors (including a quarter in the electric power industry and heat supply), another 35–37% in industry and 25–27% in the housing and utilities' sector.

Distillation columns have a complex structure, high metal consumption, and high energy consumption in the form of heating and cooling agents. Energy consumption largely depends on the hardware design, i.e., the effectiveness of contact devices used in the columns. It is known from the theory of rectification that the lower the efficiency of contact devices, the greater the consumption of reflux is required, and consequently, the consumption of heating agent in the column boiler and the cooling in the reflux condenser increases.

3 Theoretical Part

Select the bottom of the column at a distance Z sections I–I from the input of the initial mixture into the column (Fig. 1). According to the scheme shown in the figure, the material balance of the distributed component for sections 0–I, taking into account the rate of longitudinal diffusion, will have the form:

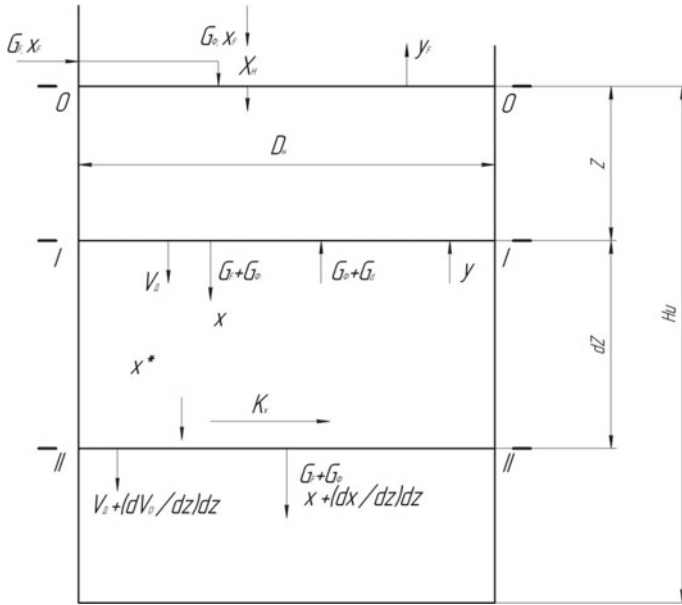


Fig. 1 Scheme of material flows and their concentrations in the exhaustive part of the distillation column, taking into account the longitudinal diffusion sections 0–I height Z to derive the material balance equation (a) for both phases; sections I–II height dz to derive the material balance equation for the liquid phase, taking into account the mass transfer

$$\frac{(G_F + G_f)}{3600M_j} x_H + \frac{(G_f + G_d)}{3600M_g} y + S \frac{\rho_j}{M_j} V_{DH} = \frac{(G_F + G_f)}{3600M_j} x + \frac{(G_f + G_d)}{3600M_g} y_F + \frac{S\rho_j}{M_j} v_D.$$

The rate of longitudinal diffusion through the liquid phase can be written as a modified Fika law [1–4]:

$$V_D = -D_l \cdot \frac{dx}{dz}, \tag{1}$$

where D_l is the longitudinal coefficient of diffusion in the vapor phase, m^2/s .

Then

$$y = y_F + \frac{M_g (G_F + G_f)}{M_j (G_F + G_d)} (x - x_n) + \left[\frac{3600M_g}{(G_f + G_d)} \right] D_l S \left[\left(\frac{dx}{dz} \right)_n - \left(\frac{dx}{dz} \right) \right] \frac{\rho_j}{M_j},$$

Given the fact that

$$\frac{G_F + G_f}{M_j}$$

molar flow rate per hour, their ratio, taking into account the division of each component of the molar flow of the distillate, takes the form:

$$\frac{F + R}{R + 1}.$$

From the known boundary condition at the input for the diffusion model follows (sections 0–0, Fig. 1) [8, 9]:

$$h = 0, \quad x_F = x_n - \frac{1}{\text{Pe}} g_n, \quad (2)$$

i.e., the last equation can be simplified to the form:

$$y_k = y_F + \left(\frac{F + R}{R + 1} \right) \cdot (x_k - x_F) + \frac{g_k}{\text{Pe}}. \quad (3)$$

Since the condition of material balance at the bottom of the column:

$$(R + 1) \cdot (y_F - y_K) = (F + R) \cdot (x_k - x_F), \quad (4)$$

then we obtain an additional boundary condition:

$$h = 1, \quad g_k = 0. \quad (5)$$

Finally, taking into account the conclusions of Eq. (1) can be written as:

$$y = y_F + \left(\frac{F + R}{R + 1} \right) \cdot (x - x_F) + \frac{g}{\text{Pe}}$$

or taking into account Eq. (4):

$$y = x_k + \left(\frac{F + R}{R + 1} \right) \cdot (x - x_k) + \frac{g}{\text{Pe}} \quad (6)$$

The obtained formula (6) is the equation of the working line of the exhaustive part of the distillation column taking into account the longitudinal diffusion through the liquid phase. It (in contrast to the equation of the working line at or, i.e., in a typical calculation, when the structure of the flow of both phases corresponds to the ideal displacement) is not a straight line, but depends on the gradient of dimensionless concentration g in the liquid phase.

We derive a differential equation of the material balance in the liquid phase for the exhaustive part of the column, taking into account its longitudinal mixing and mass transfer to the vapor phase. To do this, select the element of height dz at height z in sections I–II (Fig. 1):

$$\frac{(G_F + G_f)}{3600M_j}x + \frac{S\rho_j}{M_j}V_D = \frac{(G_F + G_f)}{3600M_j} \left(x + \frac{dx}{dz} dz \right) + s \frac{\rho_j}{M_j} \left(V_D + \frac{dV_D}{dz} dz \right) + k_x \sigma S dz (x - x^*).$$

After algebraic transformations, we obtain a differential equation:

$$\left[\frac{G_F + G_f}{3600M_j} \right] \frac{dx}{dh} = S \frac{\rho_j}{M_j} D_{n^2} \frac{d^2x}{dh^2} + k_x \sigma S (x - x^*). \quad (7)$$

Similarly, sections 0–I and I–II can be considered (Fig. 1) for the reinforcing part of the column and get the equation of the working line with the longitudinal diffusion, which has the form:

$$y = \frac{x_f + R_x}{R + 1} - \frac{1}{Pe} g \left(\frac{R}{R + 1} \right), \quad (8)$$

with a boundary condition at the output (3) and a known boundary condition at the inlet of the phlegm nozzle:

$$\left. \begin{aligned} h = 0, \quad x_d = x_n - \frac{1}{Pe} \cdot g_n; \\ h = 1, \quad x = x_F, g_F = 0; \end{aligned} \right\} \quad (9)$$

and mass transfer in the liquid phase having the form identical to Eq. (7), but with the mass transfer coefficients k_x , the number Pe and the ratio (M_j/ρ_j) corresponding to the strengthening part of the column.

Calculation algorithm by formulas (3), (5), (8), and (9) is presented in article [7].

A comparative calculation of the packed distillation column was carried out according to the proposed algorithm, taking into account longitudinal diffusion in the liquid phase, and a typical one, assuming that both phases move in the mode of ideal displacement.

The previously known table dependence for the equilibrium concentration of the binary mixture “methyl alcohol–ethyl alcohol” is processed by the least squares method in the form of the equation [9, 10].

$$y^* = \frac{1}{1 + k \left(\frac{1}{x} - 1 \right)^n}, \quad (10)$$

which is linearized in coordinates:

$$\ln\left(\frac{1}{y^*} - 1\right) = \ln k + n \ln\left(\frac{1}{x} - 1\right),$$

that allows you to find the coefficient k and n least square method (LSM).

4 Results and Discussions

The equilibrium and working lines of both parts of the column are shown in Fig. 2. Here, you can clearly see the effect of longitudinal diffusion on the working lines. First, it is a jump in the concentration of the liquid phase at the inlet to the nozzle: in the reinforcing part with $x_d = 0.965$ to $x_F = 0.951$ and in the exhaustive part with $x_F = 0.403$ to $x_n = 0.394$; secondly, the working lines are no longer direct [see Eqs. (6) and (8)] at:

$$Pe \rightarrow \infty,$$

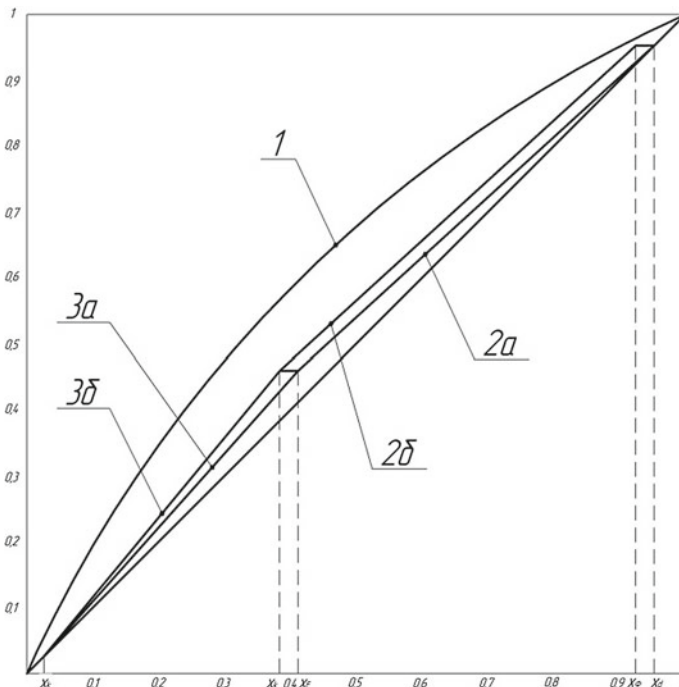


Fig. 2 Equilibrium (1) and working lines of strengthening (2) and exhaustive (3) parts of the distillation column for the binary mixture “methyl alcohol–ethyl alcohol” at phlegm number $R = 6365$: (a) model calculation corresponding to ideal displacement; (b) calculation taking into account longitudinal cross-linking $Pe = 50$

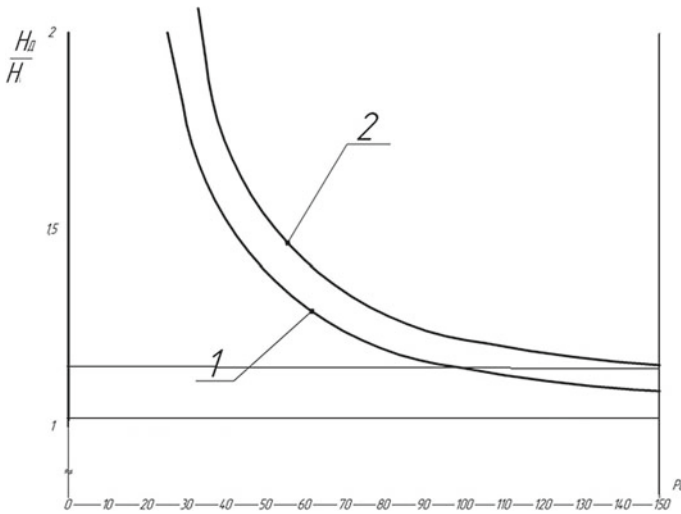


Fig. 3 Dependence of the relative increase in the height of the nozzle in the reinforcing (1) and exhaustive (2) parts of the distillation column on the number of the maximum diffusion furnace

but have a convex form, i.e., as the jumps in the concentrations of the easily volatile at the inlet reduce the local driving force of mass transfer.

This causes an increase in the mass transfer surface, the height of both parts of the column, which leads to an increase in the volume of the nozzle in the column from 138 to 189.5 m³, i.e., 1.37 times. What else should be noted is the unequal effect of longitudinal diffusion on the increase in the surface and height of the nozzle at the same number of Peclet numbers (Pe= 50) in both parts of the column. At the top, they increase by 31%, at the bottom by 43%. Already at Pe= 10, the concentration jump at the input leads to the intersection of the beginning of the working line 2b of the equilibrium line 1,; i.e., x_0 becomes less than $x^* = x^*(y_d)$ and $x_n < x^*(y_F)$, which will require an increase in the working phlegm number so that the working lines 2 and 3 approach the diagonal. Figure 3 presents graphs of the height of the volatile nozzle according to the Peclet number, taking into account the influence of longitudinal diffusion. As can be seen from these graphs for the strengthening of the already when $Pe \leq 150$, and exhaustive of the column with $Pe < 110$, the difference in the calculation of the height of the nozzle by the proposed algorithm taking into account the longitudinal diffusion in the liquid phase in comparison with the model calculation algorithm becomes more than 10% and the calculation should be conducted taking into account the longitudinal diffusion.

Minimal modernization of heat and mass transfer contact devices in some cases can reduce energy consumption by 5–10%. As an upgrade of mass-exchangeable plates, the following changes and additions to the designs can be noted [11–17]:

- improvement of the flow structure due to partitioning (reduced mixing);
- change in the shape and height of the reception and overflow repository;
- installation of chippers and demisters;
- organization of the second phase contact zone;
- optimization of free section of contact devices.

5 Conclusion

Thus, taking into account the longitudinal mixing in the liquid phase of the packed distillation column can lead to a significant reduction in local and medium driving forces, which will require an increase in the height of the nozzle in both parts of the distillation columns and even an increase in the phlegm number, which means the diameter and volume of the column.

The proposed mathematical models of reclamation processes of binary mixtures that take into account longitudinal diffusion allow one to get away from the ideal structures of flows of ideal mixing and ideal displacement through the gas (vapor) and liquid phases and estimate the effect of the Peclet.

The examples show when in the rectification processes, it is possible to ignore the longitudinal diffusion and to perform calculations using standard algorithms.

References

1. Bagaturov SA (1974) Fundamentals of the theory and calculation of distillation and rectification. Chemistry, Russia
2. Pavlov KF, Romankov PG, Noskov AA (1987) Examples and tasks on the course of processes and devices of chemical technology. Textbook for high schools. Chemistry, Russia
3. Nikolaev PI (1987) Processes and apparatus of chemical and petrochemical technology. Textbook for high schools. Chemistry, Moscow
4. Ramm VM (1976) Absorption of gases. Chemistry, Russia
5. Timonin AS (2002) Basics of calculation and design of chemical-technological and environmental protection equipment. Bochkareva Publishing House, Russia
6. Dytnerky YI (2008) The main processes and apparatus of chemical technology. Alliance, Russia
7. Golovanchikov AB, Prokhorenko NA, Karev VN (2016) Algorithm for calculating the packed distillation column with allowance for longitudinal mixing in the liquid phase. *Izv VolgGTU* 3(182):14–17
8. Kafarov VV (1985) Methods of cybernetics in chemistry and chemical technology. Chemistry, Russia
9. Levenshpil O (1969) Engineering design of chemical processes. Chemistry, Russia
10. Timonin AS (2014) Training manual on the course “Chemistry of oil and gas”. UGNTU, Ufa
11. Golovanchikov AB, Reshetova AA, Ostroukhova AS, Fetisov EG (2011) Approximation of tabular dependencies in equilibrium of binary mixtures by a power equation. *News of the Volgograd State Technical University. Series: Rheology, processes and devices of chemical technology* 4(1) (74):37–39

12. Golovanchikov AB, Vasilyeva EV, Ostroukhova AS, Reshetnikov AA (2011) Improving the accuracy of approximation of tabular dependencies on the equilibrium of binary mixtures. Series: Actual problems of computer management and informatics in technical systems 12 (11) (84):9–12
13. Golovanchikov AB, Prokhorenko NA (2018) Material balance modeling taking into account longitudinal diffusion in a distillation column. News of VolgGTU. Series: Actual problems of management, computing and computer science in technical systems 5(215):18–21
14. Golovanchikov AB, Prokhorenko NA (2016) Calculation of the dispersion of reproducibility in the absence of parallel experiments. News of VolgGTU. Series: Actual problems of control, computational engineering and computer science in technical systems 11(190):13–16
15. Golovanchikov AB, Prokhorenko NA (2015) Simulation of rectification process in a packed column with a diffusion structure of the flow in the liquid phase. News of VolgGTU. Series: Actual problems of management, computing and information technology in technical systems 14(178):12–16
16. Bobylev VN (2009) Thermal design of the heater taking into account the structure of the coolant flow. Chem Ind Today 7:45–50
17. Golovanchikov AB (2015) Modeling the operation of a two-pipe heat exchanger taking into account the heat diffusion of the gas coolant. Izv Vuzov Chem Chem Technol 58(9):58–62

Investigation of Process of Cutting Fruit and Vegetable Raw Materials into Slices Using Rotary Chopper



N. Lebed, N. Antonova and G. Rusakova

Abstract A general outline and description of the operation of an automated rotary chopper for horticultural raw material have been presented. Theoretical researches of cutting operation with the device proposed have been carried out, with obtaining a relevant mathematical model, as well as a simplified theoretical model the algorithm of which has been implemented in a computer program. An experimental model of a rotary horticultural raw material chopper has been developed and made. The knife approach angles, as well as the cutting forces of raw materials to be processed with various knife layouts, have been experimentally defined. The experimental data obtained have a high verifiability with mathematical models where the divergence between similar indicators does not exceed 5%. A positive effect of using the chopper includes lowered power consumption during the operation, as well as the minimum destruction of the structure of raw materials processed and high productivity. As a result of the research carried out, methods and calculation algorithms allowing to qualitatively estimate the dynamic condition of the material being processed have been developed and that enabled to analyze the condition of the equipment proposed and achieve rational design parameters and operating modes.

Keywords Operating procedures • Cutting • Slices • Apples • Potatoes

N. Lebed (✉)

Federal Research Center for Agroecology, Russian Academy of Sciences,
97, University Avenue, 400066 Volgograd, Russia
e-mail: nik8872@yandex.ru

N. Antonova

Anapa Industrial Technical School, 2A, Promyshlennaya Street, 353454 Anapa, Russia

G. Rusakova

Volgograd State Technical University, 28, V.I. Avenue Lenin, 400005 Volgograd, Russia

© Springer Nature Switzerland AG 2020

A. A. Radionov et al. (eds.), *Proceedings of the 5th International Conference on Industrial Engineering (ICIE 2019)*, Lecture Notes in Mechanical Engineering,
https://doi.org/10.1007/978-3-030-22041-9_49

451

1 Introduction

An important task for the processing industry, in particular, so as to increase snack production efficiency, is automation of operating procedures and minimization of energy consumption in the most power-intensive area of a chips production processing line, namely in chopping horticultural raw material [1–5] into slices. When chips are produced, a number of processes of fat oxidation and undesirable formation of cancerogenic substances take place and that influence a human body in a harmful way. Besides, a high mass fraction of oil in finished products causes rancidification and a decrease in the qualitative parameters of a product with the subsequent damage to the whole contents of a package. It appears from this that the uniform residual humidity in the material is reached through the identical thickness of all slices [6–11]. At that, equal conditions are created when heat treatment is applied to the material, with a possibility to obtain products being uniform in the oil content.

To decrease the power expenses for cutting fruit and vegetable raw materials into slices [6, 7, 12–14], as well as to improve the quality of the finished slices, we propose an automated rotor chopper [15, 16].

The main design feature of the rotary chopper for horticultural raw material consists in a technical feature of the chopper, which supplies the material to be processed to the radially located knives via a rotor. A positive effect of using the chopper is lowered power consumption during the operation, as well as the minimum destruction of the structure of raw materials processed.

Figure 1a represents the rotary chopper for horticultural raw material, general outline, Fig. 1b—the rotary chopper for horticultural raw material, section A-A, and Fig. 1c—the layout of knives in the knife frame, view A.

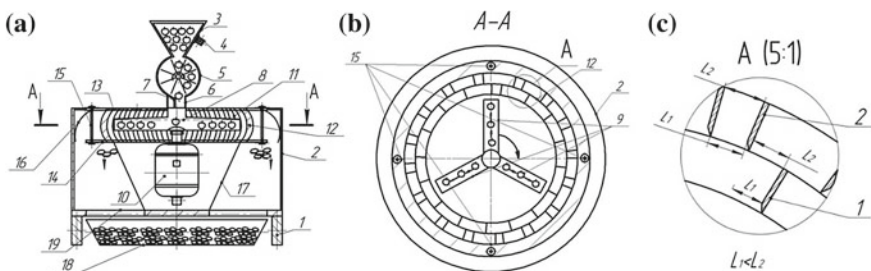


Fig. 1 Automated rotary chopper for horticultural raw material: **a** rotary chopper for horticultural raw material, general layout; **b** rotary chopper for horticultural raw material, section A-A; 1—supports, 2—cylindrical case, 3—feeding hopper, 4—vibrator-stirrer, 5—drum-type batcher, 6—lower neck, 7—fly gate, 8—centrifugal rotor, 9—guide tubes, 10—electrical motor, 11—knife frame, 12—knives, 13—upper disk, 14—lower disk, 15—tie bolts, 16—reflectors, 17—protecting casing, 18—collection container, 19—discharge openings; **c** layout of knives in knife frame, view A; 1—first line knives, 2—second line knives

The device works as follows. Before loading the material, electrical motor 10 of the device was started, to set centrifugal rotor 8 the necessary rotation frequency. The material to be processed entered centrifugal rotor 8 through feeding hopper 3 and drum-type batcher 5. By means of transmitting the turning torque by electrical motor 10 shaft, centrifugal rotor 8 evenly distributed the horticultural material into three guide tubes 9. As a result of the centrifugal force, the material was removed in the direction of arc-shaped knives 12 of knife frame 11 with the linear speed necessary for complete cutting. At that, the horticultural material entered through arc-shaped knives 12, it was chopped into slices of the necessary thickness and further proceeded into the container for collecting material chopped 18 through reflectors 16 and discharge opening 19.

2 Mathematical Modeling

A tuber or a fruit represents a solid body with mass m , moving in a tube with length l , which, in its turn, rotates in the horizontal plane with constant angular speed ω . (Fig. 2).

Let us introduce dynamical frame of reference $Oxyz$ connected to a rotating tube, unite x -axis with the longitudinal tube axis, unite z -axis with the tube rotation axis, and direct y -axis so that we have a rectangular right-oriented Cartesian reference system. As a result of modeling the motion of a body in the tube of the rotary chopper, we will obtain:

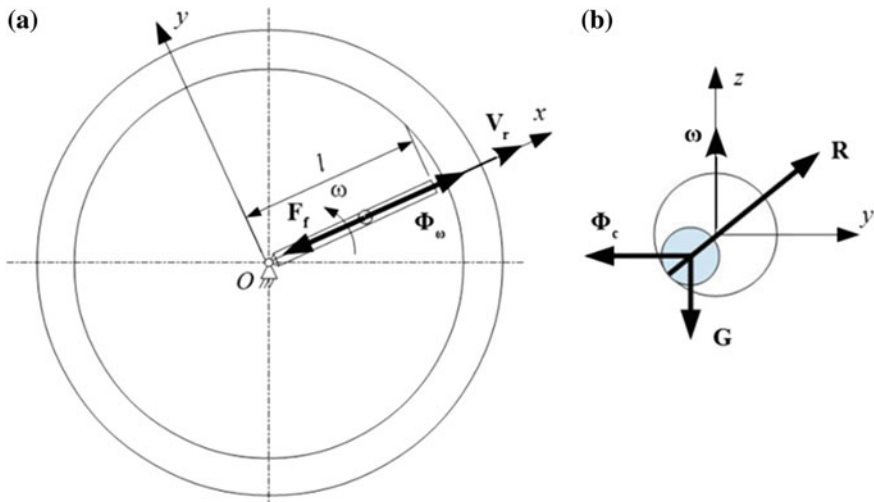


Fig. 2 Calculation model of motion of a potato tuber or an apple in automated rotary chopper for horticultural raw material: a top view; b x-axis end view

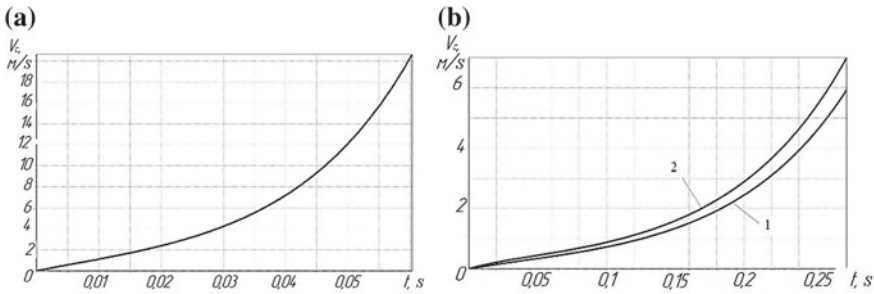


Fig. 3 **a** A change in speed of a body (a potato tuber or an apple) in guide tube of automated rotary chopper; **b** Variation in a body speed in guide tube of automated rotary chopper: 1—solution of exact equation of motion, 2—solution of simplified equation of motion

$$\ddot{x} = \omega^2 x - f \sqrt{4\omega^2 \dot{x}^2 + g^2} \tag{1}$$

where f —effective friction coefficient [4, 17, 18] and g —acceleration of gravity, m/s^2 .

One of the important results of the model obtained is the absence of weight in the differential equation of a body motion (1). It means that, with the assumptions introduced, the weight of the body does not influence its motion.

Figure 3a represents a calculated dependance diagram of a relative speed of the mass center of a body, which moves in the tube with the following starting data: $\omega = 600$ rpm; $f = 0600$; $l = 0.400$ m; $x_0 = 0.030$ m; and $\dot{x} = 0$ m/s.

Believing that the motion of a body relative to the tube of the rotary chopper starts with a zero initial speed, it is possible to obtain a condition for the angular speed:

$$\omega > \omega_{\min} = \sqrt{\frac{fg}{x_0}} \tag{2}$$

where the motion takes place if the condition is fulfilled, and otherwise, the motion of a body does not start.

The analysis of differential equation of motion (1) and the dependance set out in Fig. 3 demonstrates that the speed rapidly increases when a potato moves, the former summand in the radical expression significantly exceeds the latter within nearly all time of motion, and consequently, the latter summand can be disregarded in some cases. Then, Eq. (1) after the transformations takes on the appearance of:

$$\ddot{x} + 2f\omega\dot{x} - \omega^2 x = 0 \tag{3}$$

Such equation has an analytical solution and, to find it, the roots of the characteristic equation are defined:



$$k^2 + 2f\omega k - \omega^2 = 0 \tag{4}$$

Finally, the equation of a body motion in the guide tube of the rotary chopper for horticultural products takes on the appearance of:

$$x = (x_0 - \frac{x'_0 - x_0k_1}{k_2 - k_1})e^{tk_1} + \frac{x_0 - x_0k_1}{k_2 - k_1}e^{tk_2} \tag{5}$$

And, the law of variation in a body speed is expressed by the equation:

$$\dot{x} = (x_0 - \frac{x'_0 - x_0k_1}{k_2 - k_1})k_1e^{tk_1} + \frac{x_0 - x_0k_1}{k_2 - k_1}k_2e^{tk_2} \tag{6}$$

Depending on the parameters of the chopper, the solutions of exact Eq. (1) and simplified Eq. (3) can vary in a wide range. The difference increases when the angular rotation speed of the rotary chopper decreases, and the effective friction coefficient grows. Figure 3b represents the dependences of body motion speeds defined for the parameters: $\omega = 200$ rpm; $f = 0.600$; $l = 0.400$ m; $x_0 = 0.030$ m; and $\dot{x}_0 = 0$ m/s.

When the chopper rotation speeds are high enough (more than 300 rpm) or the friction coefficients are quite low (0,2 or less), the relative accuracy, when the approximate calculation is used, goes down to 5% or lower and that allows to use the simplified technique developed.

The angle, under which the chopper knives should be located, is defined as the angle between the absolute speed vector and x -axis (Fig. 4)—knife approach angle α :

$$\alpha = \arctg \frac{V_e}{V_r} \tag{7}$$

$$V_e = \omega x$$

$$V_r = \dot{x}$$

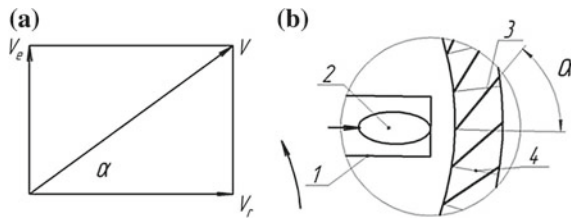


Fig. 4 Diagram to define knife location angle: **a** defining angle between absolute speed vector and x -axis **b** diagram to define angle α ; 1—guide tube, 2—material, 3—knife (according to approach angle location $\alpha > 0^\circ$), 4—knife (according to approach angle location $\alpha = 0^\circ$)

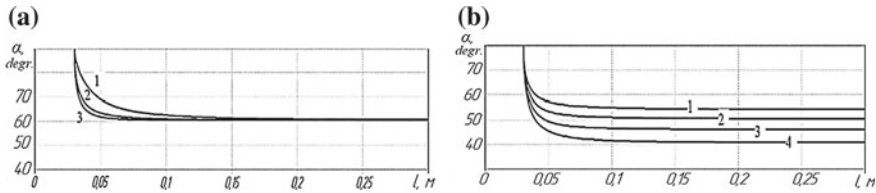


Fig. 5 **a** Dependences of knife approach angle on length of guide tube of rotary chopper with angular rotation speed 200 min^{-1} for various friction coefficients f : 1— $f = 0.5$; 2— $f = 0.3$; 3— $f = 0.1$; **b** Dependences of knife approach angle on length of guide tube of rotary chopper with friction coefficient $f = 0.3$ for different angular speeds ω : 1— $\omega = 100 \text{ min}^{-1}$; 2— $\omega = 200 \text{ min}^{-1}$; 3— $\omega = 300 \text{ min}^{-1}$

The dependences of angle α on the tube length (x -coordinates when a body moves inside the tube) are set out in Fig. 5.

As is seen, when the tube length is sufficient, the angle tends to some constant value. The angular rotation speed of the guide tube does not significantly influence this angle (Fig. 5b). The influence of the friction coefficient is significant (Fig. 5a). However, to all practical purposes, this influence is relatively small: thus, if the friction coefficient varies between 0.1 and 0.5, it results in a variation range of the angle of approximately $48 \dots 58^\circ$.

On the basis of the algorithm of the mathematical models obtained, as well as the design parameters of the chopper and physical and mechanical properties of raw material to be processed [5, 7], a computer program has been developed [19]. The software proposed allows to qualitatively estimate the dynamic condition of the material processed and that enables to analyze the operation of the equipment proposed with rational design parameters and operations modes.

3 Materials and Methods of Experimental Researches, Results, and Discussion

To carry out experimental researches of cutting operation of horticultural raw material, an experimental model of a rotary chopper was used (Figs. 6 and 7).

To define the rational configuration of the knives in the knife frame of the rotary chopper for horticultural raw material, which would satisfy the condition of minimizing the power consumption when cutting the material into slices with preset thickness, experimental researches were carried out, which resulted in the definition of the maximum force in slide and chop cutting [20].

For the purpose of confirming the results of the theoretical researchers, some researches have been carried out to study the jump trajectory of the material processed (a potato tuber or an apple) out of the guide pipe of the rotary chopper, with the real jump angle, which corresponds to the knife approach angle being defined. A high-speed video camera JVC (120 cadre/s) was used for the experimental

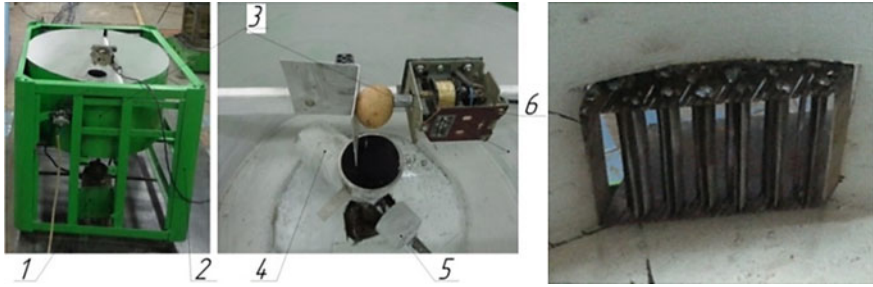


Fig. 6 Automated rotary chopper of horticultural raw material (general view), element of knife frame; 1—drive, 2—stand, 3—case, 4—guide tube, 5—balancer, 6—device to feed material into guide tube

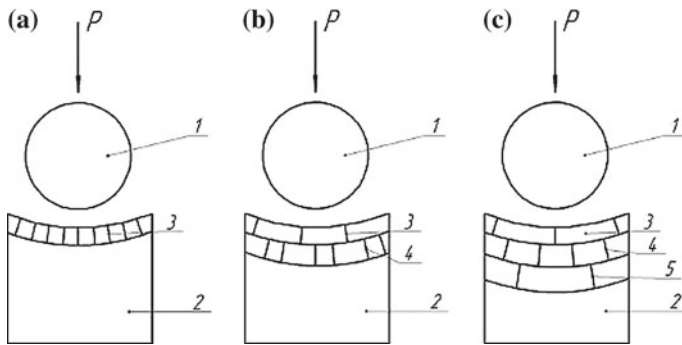


Fig. 7 Cutting options: **a** knives located radially in one line; **b** knives located radially in two lines (in a zigzag way); **c** knives located radially in three lines, making a zigzag; 1—material processed (a potato tuber, an apple fruit), 2—knife frame model, 3—first line knives, 4—second line knives, 5—third line knives

researches, which allowed to record the moment of jump of the material and the position of the guide tube, as well as the impact contact of a fruit or a tuber with the internal part of the case. After filming, the function of frame-accurate rewind of computer program “VLC media player (VideoLAN)” reconstructed the real jump trajectory of the material, and further, the desired angle corresponding to the tube axis and jump direction was made by means of program “COMPAS-3DV13.”

The research results to define the maximum cutting force are set out in Fig. 8a.

As may be inferred from Fig. 8a, the radial knife location allows to lower the cutting force by 20...30% in comparison with the in-line location in a single plane. Locating the knives radially in two lines (one knife between two) demonstrated the best results by decreasing the power consumption yet by 15...25%, which is conditional on the reduction of the constrained cutting effect. The use of the configuration in three lines forming a zigzag increases the duration of the material passage through the knives and, consequently, the cutting operation.

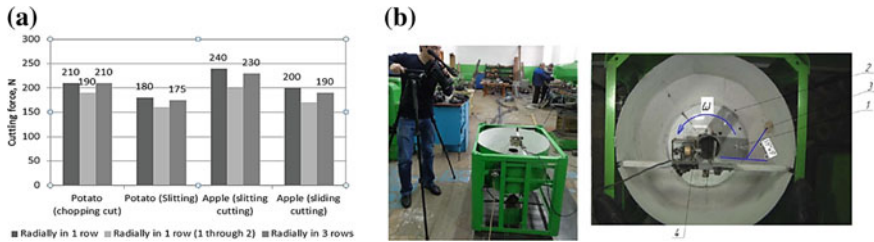


Fig. 8 **a** Research results of influence of knife configuration in knife frame of rotary chopper on maximum cutting force; **b** Experimental researches to define knife approach angle: 1—initial position of guide tube (at moment of material jump), 2—final position of guide tube, 3—material (a potato tuber), 4—material feed unit into guide tube

As a result of the researches carried out to define the actual jump trajectory of the material processed out of the guide tube of the chopper rotor, a high verifiability of the computer simulation with the experimental data has been proven where the difference between the knife approach angles obtained was at most 5%. As it is seen from the example, with the necessary conditions of the tube length, angular rotor speed, and friction coefficient of the material on the working surface, the calculated approach angle was 61° , and the actual one, which was obtained experimentally, was $59^\circ 49'$ (Fig. 8b). Therefore, the difference between the approach angles is less than 2%.

References

- Antonov NM, Lebed' NI, Makarov AM (2014) Influence of a zigzagging location of the knives in the cutting unit on the energy consumption during the cutting process of horticultural produce. Electronic Periodical Scientific Journal "J Food Process Eng". <https://doi.org/10.1111/jfpe.12162>
- Antonov NM, Lebed' NI, Makarov AM (2016) Energetic Calculation of an apple chopper with zigzagging knife location in the cutting unit. Electronic Periodical Scientific Journal "J Food Process Eng". <https://doi.org/10.1111/jfpe.12352>
- Arnaut SA (2010) Thin-sliced apple cutting with the development of a machine to produce chips. Dissertation, Belarusian State Agrarian Technical University
- Khan AA (1990) Mechanical properties of fruit and vegetables. Dissertation, University of Reading (United Kingdom)
- Kurdyumov VI, Ayugin PN (2008) Analysis of factors affecting the energy intensity of cutting. Penza, Penzenskaya GSKHA 3(8):57–59
- Brusenkov AV (2015) Development of operating procedures and a device to chip root crop tubers with a roller prop. Dissertation, Tambov Agricultural Technical University
- Kupreenko AI, Filippov VV (2005) The characteristic of a grinder with the cutting device of reciprocating type. Tekhnika v sel'skom hozyajstve 3:13–17
- Kurochkin AA, Shaburova GV, Baykin SV, Kuchorev ON (2017) Equipment processing industries. Plant material: a textbook. Izdatel'stvo "YUrajt", Moscow
- Kurochkin AA, Shaburova GV, Gordeev AS, Zavrzhnov AI (2017) Equipment and automation of processing industries. Part 2: tutorial. Izdatel'stvo "YUrajt", Moscow

10. Lebed NI, Antonov NM (2014) The processes of grinding fruit and vegetable materials in public catering: a monograph. FGBOU VPO Volgogradskij GAU, Volgograd
11. Lovkis ZV, Arnaut SA (2007) Theoretical and practical results of the process of thin-layer cutting of fruit for apple chips. Sovershenstvovanie tekhnologij i oborudovaniya pishchevych proizvodstv: sbornik dokladov VI Mezhdunarodnoj nauchno-prakticheskoj konferencii. Nesvizh. CH 1:133–136
12. Kurdyumov VI, Ayugin PN, Ayugin NP (2008) Decrease in power consumption of crushing. Vestnik Altajskogo gosudarstvennogo agrarnogo universiteta 5(43):62–68
13. Momot VV, Balabanov VV, Sorokin OV (1988) Mechanization of storage and processing of fruits and vegetables. Directory, Agropromizdat, Moscow
14. Ostal'cev VP (2000) Development and justification of the parameters of the shredder root crops for processing lines for the preparation of feed mixtures on livestock farms. Dissertation, Kirov State Agricultural Academy
15. Antonov NM, Lebed' NI, Minakov VA, Linev NA, Cygankova LS (2016) A chopper for fruits and root crops. RU Patent 163146, 10 Aug 2016
16. Antonov NM, Lebed' NI, Maloletov AV, Mamakhay AK (2017) A chopper for horticultural products. RU Patent 174962, 13 Nov 2017
17. Alvarez MD, Canet W, Lopez ME (2002) Influence of deformation rate and of compression on textural parameters of potato and apple tissues in texture profile analysis. Eur Food Res Technol 1:13–20. <https://doi.org/10.1007/s00217-002-0515-0>
18. Padohin VA, Kokina NR (2007) Physical and mechanical properties of raw materials and food. Ivanovo
19. Antonov NM, Lebed' NI, Maloletov AV, Mamakhay AK (2016) Automated calculation system of dynamic modes of body motion in the rotor of a centrifugal chopper. RU Patent 2016660425, 9 Sept 2016
20. Vysotsky AA (1968) Dynamometer of agricultural machines. Mashinostroyenie, Moscow

Investigation of Kinematics of 3D Printer Print Head Moving Systems



A. R. Avdeev, A. A. Shvets and I. S. Torubarov

Abstract Ensuring the accuracy of the print head positioning plays a significant role in improving the quality of additive parts. However, the factors influencing the accuracy of displacement systems are not sufficiently investigated. The article provides an overview of kinematic schemes of movement of the print head of 3D printer: H-Bot, CoreXY, Markforged, and Ultimaker. According to the schemes considered in this article, the equations of displacement of the print head depending on the direction of rotation of the engines according to these schemes are determined. The authors presented design schemes to determine the rigidity of the leading part of the belt in the longitudinal and transverse movement of the print head in kinematic schemes H-Bot and CoreXY. In the course of the research, dependencies were obtained. Graphs of the accuracy of displacement from the design and operating parameters of the H-Bot and CoreXY kinematic schemes were constructed. The conclusions about their impact on the error are formulated.

Keywords 3D printer · Additive manufacturing · H-Bot · CoreXY · 3D-printing accuracy

1 Introduction

Currently, additive technologies are becoming a means of manufacturing end products. At that, the issue of improving the quality of manufactured parts comes to the fore, a significant role in which is played by ensuring the accuracy of positioning of the tool in the production process [1]. In many ways, the kinematic scheme of movement of the print head and the product is responsible for this.

Unlike the kinematic schemes of tool movement in milling machines, 3D printers have many different variants of construction of such systems, a significant part of which is based on belt transmissions [2]. This is due to the small forces

A. R. Avdeev (✉) · A. A. Shvets · I. S. Torubarov
Volgograd State Technical University, 28, Lenin Avenue, Volgograd 400005, Russia
e-mail: avdartrom@gmail.com

applied to the tool (on the print head in this case) in the process of operation and the low rigidity requirements of the system, respectively. When designing 3D printers, the choice of kinematic schemes based on belt transmission causes the high speed of movement, which is given by such systems, which directly affects the productivity of print. However, the factors influencing the accuracy of the movement of such systems are not sufficiently investigated, there are no practical recommendations for the choice of configuration and kinematic scheme depending on the parameters, that are given by operational characteristics of the 3D printer [3] (construction area, print head mass) and physical characteristics of the structure (backlash of the gantry mount, belt tension, etc.).

Incorrect selection of the parameters of the print head moving system leads to geometrical errors (size and shape) of the printed products [4]. The scientific novelty of this research consists in the offered mathematical models of moving head systems based on belt transmission.

2 Stating the Aim

The aim of the study is to increase the accuracy of products produced by 3D printing method by rational choosing of kinematics of the print head movement system depending on the working parameters of the 3D printer and the physical parameters of its design. To do this, it is necessary to solve the following tasks:

- review known kinematic schemes, identify the most widespread of them;
- to determine the parameters that affect the accuracy of the print head of the 3D printer for the selected schemes;
- mathematical model for determining the accuracy of movement depending on the design and working parameters of the 3D printer should be developed;
- build graphs of displacement error dependencies at different parameters of the 3D printer.

3 Theory

Various variants of kinematic schemes are known to date; 3D printers have increased requirements for the speed of movement of the print head, it is desirable to reduce the inertia of the system to improve the accuracy of movement [5], resulting in widespread application of belt—based schemes. The schemes with the fixed attachment of the engines on the frame are used to further reduce the inertia of the system.

One such pattern of print head movement is described in the patent *US 2013/0078073 A1 of Stratasys Inc* [6]. In this solution, the movement of the print head in

the XY plane is carried out using a single belt (one loop) located in the form of the letter “ H ” and driven by two engines mounted on the base.

This movement mechanism in 3D printers has become widespread. It is used in their products by companies such as *Stratasys* [7], *MakerBot* [8], and others. A description of the kinematic scheme, also known as *H-Bot*, can be found in many articles, for example, in [9, 10].

The general view of the device for moving the print head on the *H-Bot* scheme is presented in Fig. 1a. The movement of print head 1 in the XY plane is carried out by the drive belt 2, by the driving pulleys 3 and 4, rotating clockwise or counter-clockwise by the 5 and 6 engines.

Thus, the *H-Bot* system contains 2 drive pulleys and 6 idle pulleys, placed in one plane, united by one *H*-shaped circuit of the driving belt (Fig. 1a), the ends of which are fixed on the print head carriage. The full description of the displacement device with the *H-Bot* scheme, its implementation, and the mathematical model is described in detail in the source [11].

As it was noted earlier, as the massive motors are fixed on a frame, the scheme *H-Bot* has reduced inertness of moving elements that positively influences at accuracy of positioning. However, in such kinematic scheme, the unidirectional rotation of the motors for moving the print head along the transverse guide causes a multi-directional effect of the resulting forces on the fastening of the portal to the carriage of longitudinal guides. This leads to geometric non-perpendicular longitudinal and transverse rails, and therefore, reduces the accuracy of movement of the print head and causes the error of the shape of the printed parts. This deficiency can be eliminated due to the two-circuit kinematic scheme.

In open sources, the two-circuit kinematic scheme is named *CoreXY* [12]. Figure 1b shows the arrangement of the belts in such a system. The two-circuit scheme of print head moving, in consequence of unidirectional influence on knots of fastening of a portal to carriage of longitudinal directing, provides geometrical

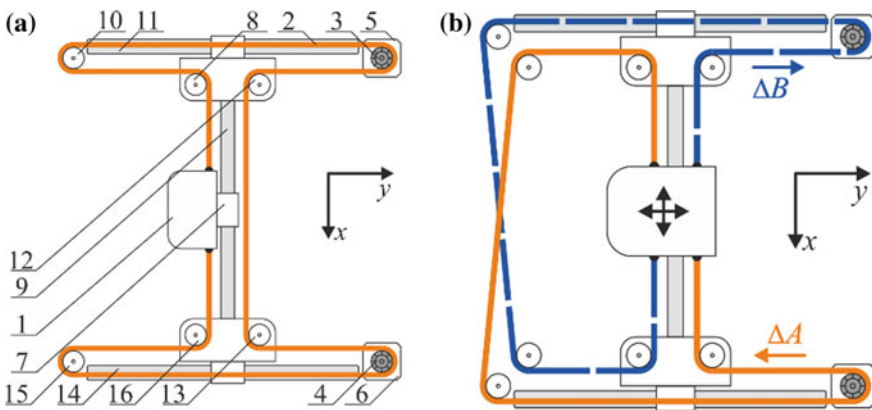


Fig. 1 Kinematic schemes: a *H-Bot* and b *CoreXY*

perpendicular of guides located on axes X – Y . This increases the accuracy of the print head positioning and reduces the error in the shape and size of the part being manufactured.

This movement system in the modernized form is used by the authors of the robotic laser complex [13].

The disadvantages of such a system include the need to ensure equal tension belts of both circuits. The different tension of the belts in movement creates twisting of the movable knot, causes non-perpendicular longitudinal and transverse guides, and reduces the accuracy of movement, as well as uneven wear of these belts, which leads to a decrease in resource of the device.

Another variant of kinematics with stationary arrangement of motors is realized by *Markforged* company [14, 15]. Despite the simplicity of implementation (in the system involved only 5 idle pulleys and 2 drive pulley, belts are located in the same plane and do not have intersections), kinematics has flaws both *H-Bot*, and *CoreXY* (namely, multi-directional moments of forces on the movable knot and the need to ensure the same belt tension). For this reason, this scheme has not been widely spread.

A similar principle, when each motor is responsible for moving only along one axis, is implemented by *Ultimaker* [16]. Due to the fact that the company makes its activities under the *OpenSource* license [17], providing open use of programs and drawings of its products, the kinematic scheme of the printer has become popular [18].

Thus, the review of kinematic schemes allows making the following conclusions:

- The accuracy of movement in the *H-Bot* kinematics significantly depends on the rigidity of the rolling knot and the size of the backlash of the longitudinal guide rails;
- The accuracy of movement in the *CoreXY* kinematics considerably depends on belts contours tension uniformity;
- *MarkForged* kinematics has a simple implementation but shares the disadvantages of both the *H-Bot* scheme and *CoreXY* scheme;
- *Ultimaker* kinematics has a high rigidity of construction and low inertia but has a complex implementation and imposes increased requirements to the accuracy of components;
- The positioning accuracy of *CoreXY* and *H-Bot* schemes is twice as high as the *Markforged* and *Ultimaker*.

Taking this into account, we will investigate the factors influencing the accuracy of the print head positioning in the *H-Bot* and *CoreXY* kinematic schemes.

4 Research of Kinematic Schemes

As noted above, in the H-Bot kinematic scheme, one-directional rotation of motors leads to the appearance of torque forces, which rotates the portal in the plane XY (Fig. 2a). This results in an error in the print head position, which is figured by Fig. 2b: Point N_0 is the desired position of the transverse carriage, point N is the real position.

The rotation angle φ of the portal is determined by the dimensions of the longitudinal guide rails and the size of the gap S in their connection with the guides and the approximately could be determined in relation to:

$$\varphi = \arctg \frac{S}{b}, \tag{1}$$

where b is the length of the longitudinal carriage.

Thus, the error of setting the point N on the coordinates X and Y (Fig. 2b) can be estimated based on geometric considerations:

$$\begin{aligned} \Delta x_{por} &= x - x \cos \varphi, \\ \Delta y_{por} &= x \sin \varphi, \end{aligned} \tag{2}$$

where x is the distance traveled by the transverse carriage on the portal.

Another source of significant error in the print head moving is the elastic stretching of the belt. Let's consider as an example of the moving of a transverse carriage illustrated in Fig. 2a. At the initial moment, the force $\bar{F} = m\bar{a}$, is applied to the carriage caused by the torque from the M2 motor and the force of the elastic stretching of the tight side of the belt $\bar{F}_{upr} = k\bar{x}$.

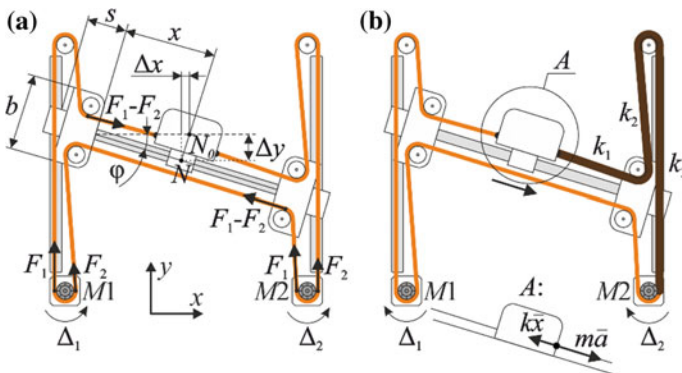


Fig. 2 Calculation scheme to determine the hardness of the tight side of belt in the transverse movement of the portal (H-Bot)



Ignoring the forces of friction, the movement condition of the transverse carriage can be recorded as:

$$m\bar{a} = k\bar{x}_{cr} = 0 \quad (3)$$

where M is the mass of the transverse carriage; A —acceleration of the transverse carriage; k —rigidity of the tight side of belt; x_{cr} —critical lengthening of the tight side of belt.

Hence, the value of the critical extension is defined as the ratio:

$$x_{cr} = \frac{ma}{k} \quad (4)$$

The hardness of the tight side of belt is determined by the hardness of its three successive fragments:

$$\frac{1}{k} = \frac{1}{k_1} + \frac{1}{k_2} + \frac{1}{k_3}, \quad (5)$$

After the transverse carriage reached the desired point the motors stop, but the carriage moves forward to the distance Δx_{belt} , approximate equal to the x_{cr} , under the influence of the force elastic stretching, seeking to return belt the original length. Presenting a belt fragment as a homogeneous rod of approximately constant section, deformed along an axis, it is possible to define a coefficient of its rigidity by the equation:

$$k_i = \frac{EB}{l_i}, \quad (6)$$

where E is Jung's module, depending on the belt material; B —cross-sectional area; l_i —length of the fragment.

In case of longitudinal moving of a portal, the forces of tension of different branches of a belt mutually counterbalance each other that provides translational movement of a portal, however, the error caused by stretching of belts is kept:

$$\Delta y_{rem} = y_{cr} = \frac{m_{por}a_{por}}{k}, \quad (7)$$

where m_{por} , a_{por} —the mass and acceleration of the portal; k —total rigidity of the consecutive connection of three fragments of the belt.

The rigidity of the tight side of the belt in the longitudinal movement of the portal is determined by the ratios depending on the direction of movement in the positive (Fig. 3a) or negative (Fig. 3b) direction of the Y -axis.

In case of transverse moving of a carriage, there will be a print head position error on both coordinates:

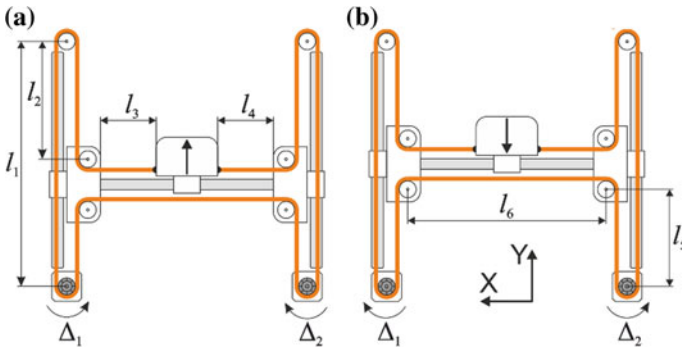


Fig. 3 Calculation scheme to determine the hardness of the tight side of belt in the longitudinal movement of the portal (H-Bot)

$$\Delta x = \Delta x_{por} + \Delta x_{rem} = x(1 - \cos \varphi) + \frac{ma}{k}, \tag{8}$$

$$\Delta y = \Delta y_{por} = x \sin \varphi.$$

In case of longitudinal moving of a portal, there is only an error introduced by elastic stretching of belts and having different values depending on a direction of movement of a portal.

In the present work, the characteristics of 6 mm width GT2 toothed belt elasticity made of neoprene and reinforced [19] were evaluated by an experienced way. The scheme of experience is taken from [20]. According to the results of experiments, the measured value of the Jung module is equal to $E \approx 3,834$ of HPa.

The distribution of the installation errors according to the coordinate X of the transverse carriage depending on its location on the XY plane is depicted in Fig. 4a. The graph family Fig. 4b illustrates the increase of the error by the y coordinate of the transverse carriage with the increase of the longitudinal carriage backlash.

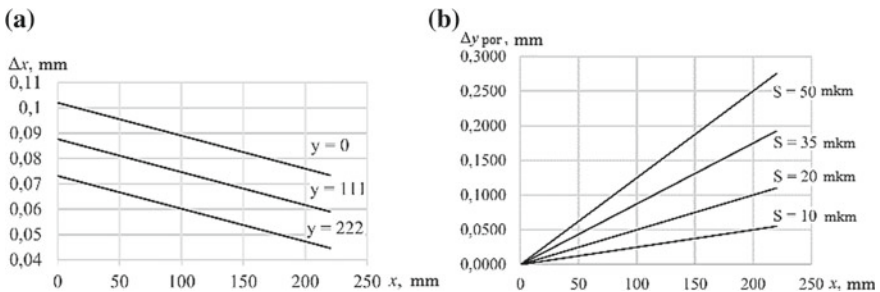


Fig. 4 a Distribution of the error of the print head position on the x coordinate in the carriage transverse in the H-Bot scheme and b the position error of the Y -axis of the print head at the transverse of the carriage at different backlash

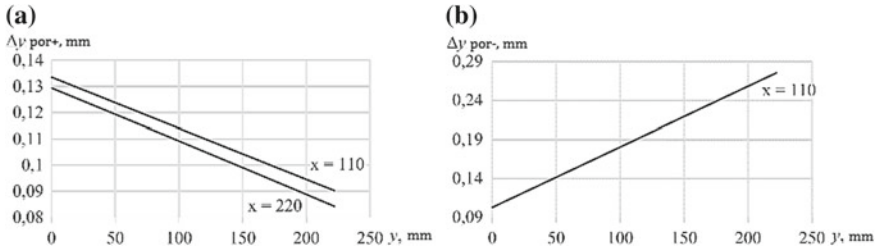


Fig. 5 Distribution of the printing head position errors on the y coordinate in the longitudinal carriage in the H-Bot scheme

The distribution of position errors on the Y coordinate of the portal at its movement in positive (Fig. 5a) and negative (Fig. 5b) directions is depicted. In both cases, the greatest error is achieved at the beginning of the portal when the length of the leading part of the belt maximum.

In the CoreXY kinematic scheme, subject to the equality of the forces of pre-tension in both belt circuits will be only errors from the elastic stretching of belts. However, in the case of unequal tension of belts in the contours, regardless of the ratio between the forces of pre-tension (Fig. 6), there will be a torque, which will be turning the portal to the angle of φ , as in the H-Bot kinematic scheme.

On the other hand, due to a different belt configuration, the dependencies of changing the errors under the effect of their elastic stretching in this scheme will take a different form. At transverse movement of a carriage, the total rigidity of two parallel-connected branches (Fig. 7a) will be determined by the expression:

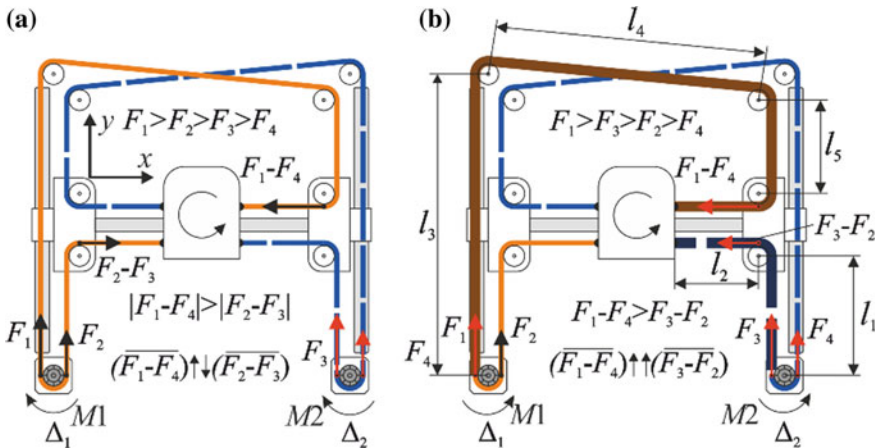


Fig. 6 Calculation scheme to determine the hardness of the tight side of belt in the transverse movement of the portal (CoreXY)



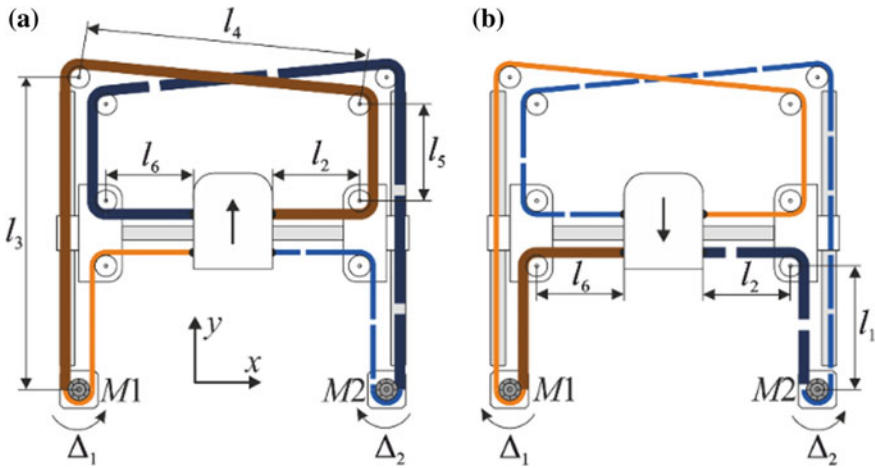


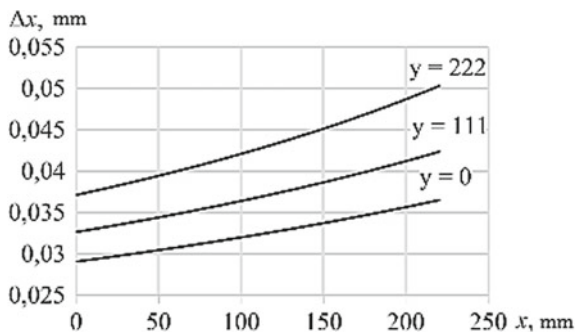
Fig. 7 Calculation scheme to determine the hardness of the tight side of belt in the longitudinal movement of the portal (CoreXY)

$$k = \frac{EB}{l_1 + l_2} + \frac{EB}{l_3 + l_4 + l_5 + l_6}, \tag{9}$$

If the portal is moved in a positive direction (Fig. 7a), the stiffness of the pair is parallel to the connected tight side branches $l_3 + l_4 + l_5 + l_2$ and $l_3 + l_4 + l_5 + l_6$, similar to the formula (9). If the portal is moved in a negative direction (Fig. 7b), the stiffness of the pair is parallel to the connected tight side branches $l_1 + l_2$ and $l_1 + l_6$, similar to the formula (9).

The distribution of the installation errors according to the coordinate X of the transverse carriage depending on its location on the XY plane is depicted in Fig. 8. As in the *H-Bot* scheme, this error is determined by the elasticity of the belts, as well as the position errors in the longitudinal movement of the portal Fig. 9.

Fig. 8 Distribution of the printing head position errors on the x coordinate in the transverse carriage in the CoreXY scheme



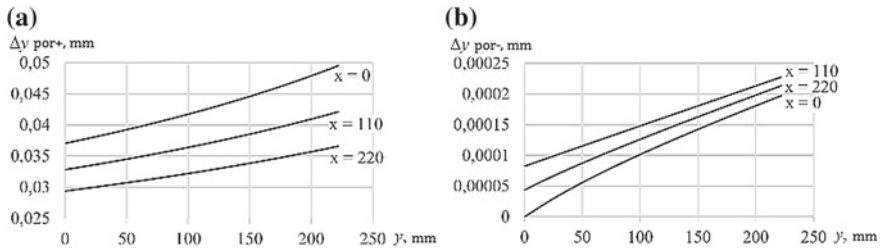


Fig. 9 Distribution of the printing head position errors on the y coordinate in the longitudinal carriage in the CoreXY scheme

However, the dependence of the error on the coordinates of the transverse carriage (and thus the length of the tight side of the belts) has a pronounced nonlinear character, and the maximum error values are smaller twice.

Acknowledgements Thus, mathematical models of determination of movement accuracy in CoreXY and H-Bot kinematics are obtained, depending on the design and working parameters of the 3D printer. The obtained dependences are investigated. The following conclusions are formulated: (1) The error of moving the print head is not linear and depends on the direction of its movement; (2) In transverse movement of the print head, the error is less than the longitudinal; (3) The error of movement in CoreXY kinematics is less, than in H-Bot kinematics; (4) Bending of the portal due to the backlash of the guides introduces an additional error up to 0.1 mm, and in the CoreXY scheme, it can be compensated by equal tension of belt contours.

References

1. Avdeev AR, Shvets AA, Gushchin IA (2016) Perspektivnye napravleniya uvelicheniya proizvoditel'nosti tekhnologij obyomnoj pechati (Upcoming trends of productivity increasing of additive technologies). In: XX Regional Conference of young researchers of the Volgograd region, pp 103–105
2. Gebhardt A (2003) Rapid prototyping. Hanser Verlag, Berlin
3. Serdobintsev YP, Drobotov AV, Gavrilina NV et al (2017) Method of 3D printer selection on the basis of technical and economic indicators. Herald Mech Eng 4:37–40
4. Pham JD, Gault R (1998) A comparison of rapid prototyping technologies. Int J Mach Tools Manuf 38(10–11):1257–1287. [https://doi.org/10.1016/S0890-6955\(97\)00137-5](https://doi.org/10.1016/S0890-6955(97)00137-5)
5. Drobotov AV, Avdeev AR, Shvets AA (2018) Magneto-hydrodynamic pump application in complex form aluminum parts additive manufacturing. In: International conference on modern trends in manufacturing technologies and equipment 2018 (ICMTME 2018). <https://doi.org/10.1051/mateconf/2018.22401076>
6. Comb JW, Swanson WJ, Crotty JL (2011) Gantry assembly for use in additive manufacturing system. In: Google patents. <https://patents.google.com/patent/US20130078073A1/en> (Accessed 28.11.2018)
7. Commercial, Professional, & Industrial 3D Printers | Stratasys. Stratasys Inc. <http://www.stratasys.com/3d-printers>. Accessed 28.11.2018
8. Makerbot 3d Printers. In: MakerBot. <https://www.makerbot.com/3d-printers/>. Accessed 28.11.2018

9. Weikert S, Ratnaweera R, Zirn O et al (2011) Modeling and measurement of H-Bot kinematic systems. ETH Institute for Machine Tools and Manufacturing, Zurich
10. Cenev Z (2014) Design and implementation of double H'-gantry manipulator for TUT microfactory concept
11. Sollmann K, Jouaneh MK, Lavender D (2010) Dynamic modeling of a two-axis, parallel, H-frame-type XY positioning system. IEEE/ASME Trans Mechatron 15:280–290. <https://doi.org/10.1109/TMECH.2009.2020823>
12. Moyer IE (2012) CoreXY. <https://corexy.com/theory.html>. Accessed 28.11.2018
13. Chen Y, Squires A, Seifabadi R et al (2017) Robotic system for MRI-guided focal laser ablation in the prostate. IEEE/ASME Trans Mechatron 22(1):107–114. <https://doi.org/10.1109/TMECH.2016.2611570>
14. Printers|Markforged. Markforged, Inc. <https://markforged.com/>. Accessed 28.11.2018
15. Markforged kinematics. Markforged, Inc. <https://hackaday.io/project/19543-haq-xy/details>. Accessed 28.11.2018
16. Ultimaker BV Ultimaker products. <https://ultimaker.com/en/products>. Accessed 13.11.2018
17. Open Source Initiative. <https://opensource.org/licenses>. Accessed 28.11.2018
18. Ultimaker. RepRap. <https://reprap.org/wiki/Ultimaker>. Accessed 13.11.2018
19. Timing belts, pulleys, chains and sprockets. Designatronics Inc. <http://www.sdp-si.com/PDFS/Technical-Section-Timing.pdf>. Accessed 13.11.2018
20. Gushchin IA, Avdeev AR, Shvets AA et al (2018) Vliyanie himicheskoy obrabotki 3D pechatnyh izdelij na ih prochnost (Influence of chemical processing of 3d printed parts on their strength). Proc VSTU. Ser. Progressive technologies in mechanical engineering 2 (212):58–60

Development of Algorithm for Creating Parametric 3D Models, Controlled by Mathcad Calculations, to Study Parameters of Enclosed Gears Housing



E. Petrakova and V. Sumatokhin

Abstract The article proposes an algorithm for creating parametric 3D models in CAD software using the integration of results of calculation performed in PTC Mathcad. This method may be used to parameterize 3D models, the geometric dimensions of which are determined by complex mathematical formulas associated with the choice of values from tables, standard series, and observance of various conditions and constraints, using logical functions. The research authors have performed a complete automated calculation of an enclosed gear using PTC Mathcad components and have integrated the calculation data into a parametric 3D model of the housing and connected parts created in a CAD software. As a result, a parametric 3D model of the assembly was designed, with automatic geometry updating based on the results of automated calculations. The parameters of the 3D model are controlled by changing the input data in the Mathcad file. This paper presents the examples of studies that were carried out using the developed algorithm. These are the series of graphs and tables of the obtained sizes and masses of gear housings in a wide range of variable input data such as gear ratios, transmitted torque, hardness of the gear pair materials, and a given service life. The developed algorithm for parametrization of 3D models can be used to design a product line of similar configuration, to solve multivariate analysis and design optimization problems and to reach research and development objectives.

Keywords Parametric 3D model · Body parts · CAD · Design automation

E. Petrakova (✉) · V. Sumatokhin
Moscow Polytechnic University, 38, Bolshaya Semyonovskaya str,
Moscow 107023, Russia
e-mail: eka_pet@mail.ru

1 Introduction

In everyday practice, a design engineer does not/rarely encounter the task of redesigning a previously created 3D model of a product due to changes in the input data in the technical specification or the replacement of part materials. At the early design stage, the question of forecasting the overall dimensions, mass, or cost of the developed detail is relevant. To answer this question, an engineer will need to complete work that takes a lot of time and effort.

Parametric 3D modeling of an assembly product that includes body parts that are the most time consuming to design because of their complex shape leads to a reduction in the production time of a product line of similar configuration with different input data and criteria received from the customer.

Often, when designing products, it is necessary to find a rational design using several criteria at once, taking into account the conditions and constraints, as was done in [1]. Obviously, to solve this kind of problems, it is necessary to create a digital mathematical model of the object under study, including automated calculations and the respective parametric model of the product associated with them.

2 Review of Current Methods of Parametric Modeling

Various mathematical packages, spreadsheets, and CAD software may be used to put together computer mathematical models [2–8].

The design and calculation of box-type housing elements such as gearboxes and multipliers are preceded by volumetric design and verification calculations for gears, shafts, bearings, dowels, and other parts according to well-known methods [9, 10].

PTC Mathcad [11, 12] is considered to be the most convenient and frequently used software for engineers to perform complex calculations related to each other. It is important to note that PTC Mathcad data is not supported by the most 3D modeling CAD software like KOMPAS-3D, SolidWorks, Inventor, CATIA, and T-FLEX [7, 8]. The only exception is Creo Parametric, which makes it possible to perform a two-way data exchange [5, 13]. Thus, when designing objects in most CAD systems, there is a gap between the design and checking calculations and the creation of three-dimensional models of products. When changing the input data, it is necessary to manually transfer the resulting geometrical parameters to the created 3D model, as done, for example, in [14, 15].

This problem may be solved by performing calculations in Microsoft Excel [16]. The Microsoft Excel spreadsheet format is supported by all 3D modeling software and, therefore, Microsoft Excel data can be exported to CAD programs to determine the parameters of 3D models. The algorithm of this parameterization method is described in [17–20].

However, this method has a significant drawback. The unique type of formulas and logical functions in table cells of Microsoft Excel is not common to engineers and is difficult to read both by other users and by the product creator, which leads to errors during calculation and parameterization of the 3D model.

It should be noted that many 3D modeling programs have the ability to program and create various macros using Visual Basic or other programming languages. Thus, in [1], the authors parametrized a gear and a shaft via Pro/Engineer macros, and in [21], CATIA macros were used to parameterize models. However, such methods of parameterization require programming skills that a design engineer often does not have.

3 Study Subject, Purpose, and Objectives

Objectives: To automate tasks performed by an engineer (to the extent as huge as possible) during the design of parametric objects created based on complex calculations and minimize the number of errors associated with redesigning of 3D models.

Study subject is a cast-iron housing of a single-stage parallel shaft gearbox designed according to the horizontal scheme.

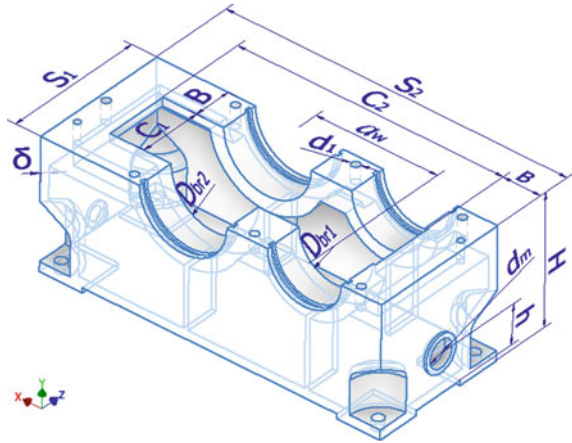
The **purpose** of this study is to predict the size and mass of the gearbox housing when changing the data of the technical specification and technical features of the gear.

4 Study Subject, Purpose, and Objectives

Select Autodesk Inventor as a CAD system to create a parametric 3D model of the housing.

Geometric parameters of the gearbox housing (Fig. 1) are closely linked to the dimensions of its parts [22–24]. The width of the housing's internal cavity C_1 depends on the width of the gear crown and the length of the shaft's thrust shoulders. The length of the internal cavity C_2 depends on the center distance a_w , gear wheel diameter, and the diameter of the bearings of the input shaft D_{br1} . The overall dimensions of the body—height H , width S_1 , length S_2 —are determined by the overall dimensions of the gear pair and the width of flanges B which, in turn, depend on the dimensions of rolling bearings, cuffs, bearing caps, and adjusting rings. The position of the oil gage h and its diameter d_m , as well as the diameter of the drain plug hole, is determined by the required volume of oil in the gearbox and the gear wheel diameter [24]. The diameters of the holes for bearing units D_{br1} and D_{br2} are determined by the bearing size, which are selected by calculating the dynamic load capacity for a given service life using the calculation methods outlined in [9].

Fig. 1 3D model of gear housing



Some dimensions of body elements are found by empirical formulas from [23] depending on the transmitted torque; these dimensions are the gearbox wall thickness δ and the diameter of the clamping screw holes d_1 .

In order to design a mathematical model of the housing based on technical specifications of the gearbox, we have compiled design and checking calculations for the gearbox and shafts, rolling bearing life calculation, and key checking test calculations according to the methods [9, 10], including 160 formulas, 36 Mathcad program blocks with Excel components for selecting factors from standard series and GOST tables and checking various conditions.

Using the Mathcad programming module, the calculations are performed to check the loaded parts for strength, and certain design conditions are specified, which is reflected in the 3D model.

In order to create a connection between the CAD software and the calculation in Mathcad, one must import the calculated data in the third-party Excel document. To achieve this, the WRITEEXCEL function is used in Mathcad, which allows you to export numerical values to an Excel file (Fig. 2). To make data output more convenient, it is preferable to group all the variables into a matrix with one column and specify it as the output variable.

The next stage of design is the creation and parameterization of a 3D model of the housing. When parameterizing, dimensions should be divided into two categories.

Fig. 2 Output of Mathcad calculation data to Excel files

$$\text{WRITEEXCEL}(\text{"Parametr.xlsx"}, \text{Parametr}, \text{"B1"}) = \begin{bmatrix} 28 \\ \vdots \end{bmatrix}$$

$$\text{WRITEEXCEL}(\text{"Korpus.xlsx"}, \text{Korpus}, \text{"B1"}) = \begin{bmatrix} 6 \\ \vdots \end{bmatrix}$$



4.1 Parametric Dimensions of Category A

These are housing parameters which depend on the dimensions of other parts of the gearbox or its technical features. In our case, these are center distance, diameters of the bearing unit holes, housing heights, the width and the length of the gearbox's internal cavity, the width of the upper flanges, wall thickness, the diameter and length of the clamping screw holes, oil gage hole diameter and its location on the wall, and the drain plug hole diameter. The values of these parameters are calculated in Mathcad, displayed in the Excel file, and integrated into the 3D model.

4.2 Parametric Dimensions of Category B

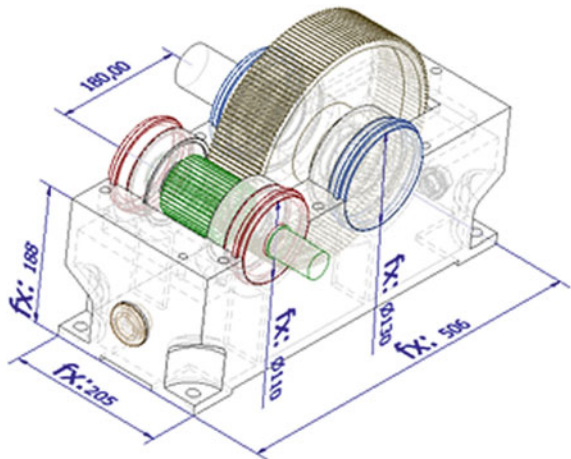
These are the geometric parameters of body parts associated with the dimensions of category A. They are calculated using fairly simple mathematical equations from [22, 23]; therefore, they can be parameterized using the internal capabilities of the CAD software.

For parametrization of 3D models of assembly items, in a similar way, all parts included in it are parameterized (Fig. 3). Note that the design and checking calculations of all gear parts are located in the same Mathcad file.

To control the parameters of the 3D model, one must open the Mathcad calculation file and the file of the body's 3D model in Inventor; change the input data value in Mathcad calculation; press the «Local Update» button in the 3D model in Inventor.

For the assembly unit shown in Fig. 3, the update rate of the 3D model after entering the input data into the Mathcad file is 15–30 s (depending on the performance of the PC).

Fig. 3 Parametric 3D model of the subassembly gear



5 Study Subject, Purpose, and Objectives

Using the developed mechanism for integrating these calculations into a parametric model, you can quickly and accurately carry out a whole range of research and optimization tasks. Research may concern the study of the geometric and physical properties of individual parts included in an assembly, or the analysis of an entire assembly and its optimization according to one or several criteria simultaneously.

Let us demonstrate only some of the conducted studies, having studying the properties of the gearbox housing for the following input data as an example.

Constant input data: The rotational speed of the input shaft is not more than 1500 min^{-1} ; hardness of the gear pair materials is 235 HB. The mode of operation is variable (Fig. 4), the ratio of the minimum transmitted torque to the nominal $T'/T = 0.8$, and the short-term starting torque $T_{\text{start}} = 1.5 \cdot T$. Gearbox operational life: The number of service years is $L = 5$, there are 260 working days per year, the time of work in the first mode $t = 7 \text{ h}$ per day, and in the second mode, $t' = 3 \text{ h}$.

Variable input data: The gear ratio U changes discretely in the range from 2 to 8 according to the first row of GOST 25301-95; nominal torque on the output shaft T varies in the range from 90 to 500 Nm according to the first row of GOST 25301-95; permissible cantilever load—on the input shaft F_1 , on the output shaft F_2 —according to GOST31592-2012:

$$F_1 = 50\sqrt{T} \quad (1)$$

$$F_2 = 125\sqrt{T} \quad (2)$$

Using the considered mechanism for integrating Mathcad's calculation data into the parametric 3D model in the Inventor, 30 standard sizes of the gearbox housing were obtained, the main dimensions of which are the center distance a_w and overall parameters, which are presented in Table 1.

Fig. 4 Daily mode of operation of the gearbox

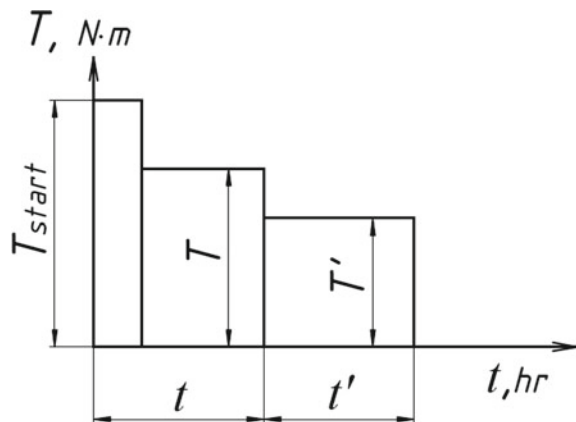


Table 1 Example of a table

U	T (N m)	a_w (mm)	Dimensions of gear housing		
			Height H (mm)	Length S_2 (mm)	Width S_1 (mm)
$U = 2$	90	100	105	304	149
	125	112	113	328	154
	180	125	121	366	171
	250	140	131	395	181
	355	160	145	438	193
	500	180	164	482	205
$U = 3, 15$	90	100	114	305	141
	125	112	123	334	154
	180	125	133	373	171
	250	140	144	414	181
	355	160	159	457	193
	500	180	181	503	205
$U = 4$	90	100	118	302	139
	125	112	128	331	146
	180	125	138	383	171
	250	140	150	420	181
	355	160	166	464	193
	500	180	188	506	205
$U = 6, 3$	90	112	134	331	144
	125	125	146	370	155
	180	140	159	390	157
	250	160	176	444	173
	355	180	193	499	193
	500	200	216	537	201
$U = 8$	90	112	135	331	144
	125	125	149	374	155
	180	140	162	402	161
	250	160	180	448	173
	355	180	198	494	189
	500	200	221	542	201

In some cases, according to the specification, it is necessary to ensure maximum compactness of the future product, in other cases—the lowest cost. It is known that the choice of high-strength materials for a gear pair leads to a reduction in the overall dimensions of the entire gearbox but increases its cost [24, 25]. A product is often designed considering the materials of the workpiece of future parts available at a facility.

Using the developed parameterization algorithm, it is possible to quickly and reliably visualize the dimensions and weight of an assembly product when choosing one or another material for its parts. Figure 5 shows the general dimensions of the housing depending on the hardness of the gear pair materials in the range from 180 to 320 HB for one of the gearbox sizes with a gear ratio $U = 4$ and a torque on the output shaft $T = 250$ N m, obtained using the parameterization algorithm under consideration.

The question of the dependence of the product dimensions on its operational life is equally relevant in the design process. Obviously, the size of the product increases when it is designed for a longer operational life. However, how much the dimensions of the parts and the whole assembly will change when the input data is changed remains unclear without carrying out design and checking calculations and redesigning the 3D model of the assembly. Designing products using automated calculations, with the integration of results into CAD software, allows one to get a quick answer to the questions posed above. Figure 6 shows data on the overall dimensions of gearbox housing with torque on the output shaft $T = 90\text{--}500$ N m and gear ratio $U = 2$, with a set operational life of $L = 5$ years and $L = 10$ years.

The obtained data shows that the length and width of the body vary slightly, and the height remains the same. This is due to the fact that, in order to ensure the gearbox's operational life $L = 10$ years, heavy bearings on both shafts are necessary for all sizes, while for a given operational life of $L = 5$, bearings of medium series are suitable. As a result, for gearboxes with an operational life of

Fig. 5 Graph of dependency of body dimensions and the center distance from the hardness of the gear pair materials

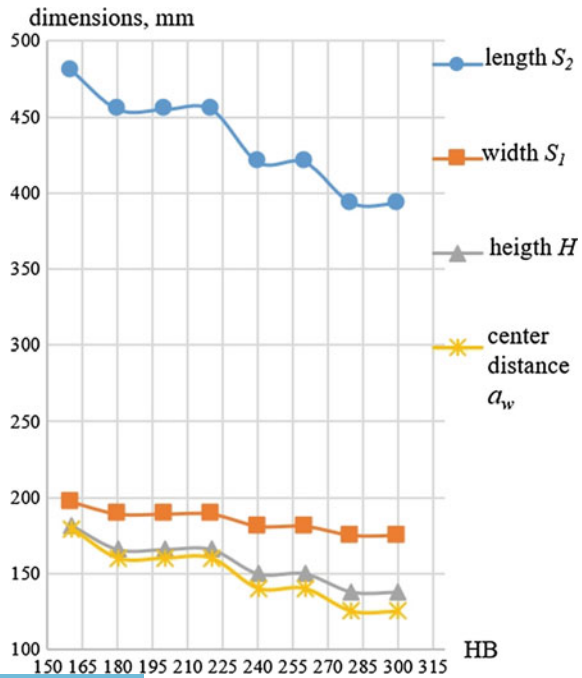
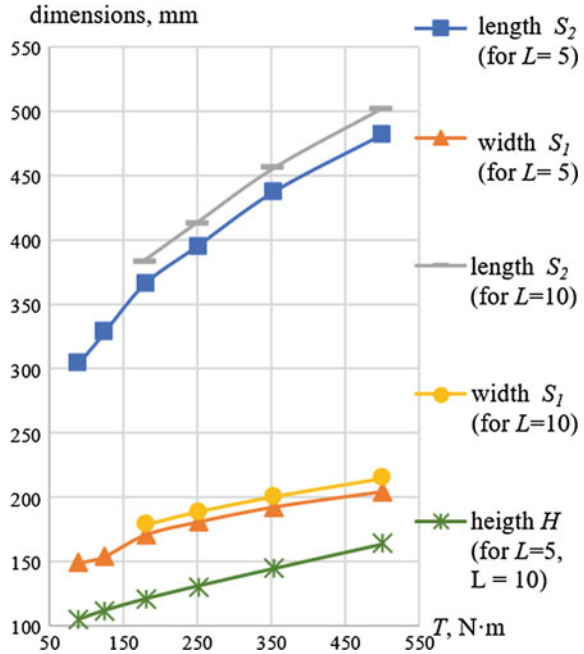


Fig. 6 Graph of dependency of body dimensions from the output shaft torque at set operational life



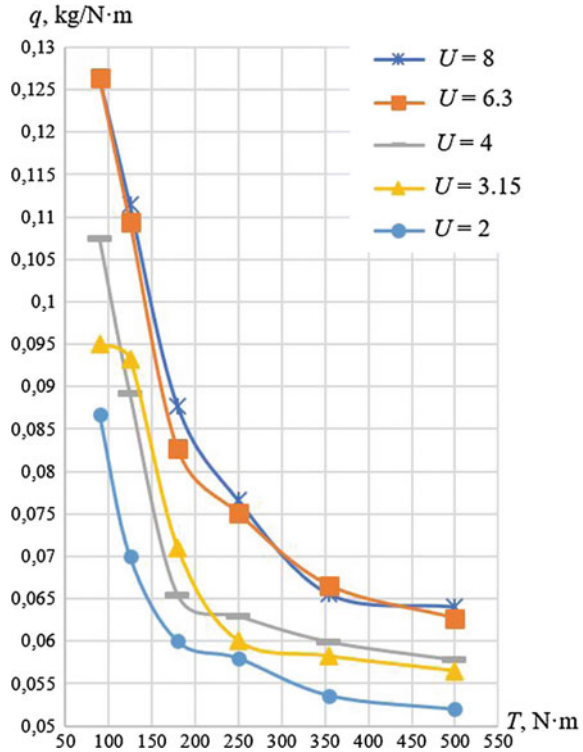
$L = 10$ years, the diameters of bearing housing holes in the housing increase, as well as the width of the flanges associated with the width of the bearings. Increasing the diameters and width of the bearing housing leads to an increase in the length and width of the housing. The height remains constant since it depends only on the diameter of the gear wheel, and the dimensions of which, as shown by the data of automated calculations, do not depend on the change of the gearbox’s operational life from 5 to 10 years.

In addition, visualization of the housing’s 3D model shows that for a gearbox with $T = 90$ N m, the holes for the bearing units intersect, and for a gearbox with $T = 125$ N m, they are so close to each other that there is practically no wall between them. Therefore, manufacturing products for these torques with the operational life $L = 10$ years is not possible (Fig. 6, the absence of two points on the curves “length and width at $L = 10$ years”).

For a comparative assessment of the mass of various sizes of gearboxes, the relative mass index q is usually used. The relative mass of the gearbox housing is the quotient resulting from the division of housing mass (in kg) by the torque at the output shaft (in N m). For 30 sizes in the torque range from $T = 90$ –500 N m and gear ratios $U = 2$ –8 (Fig. 7), the relative mass values of the body are obtained when it is manufactured from cast iron with a density of 7.15 g/cm³.



Fig. 7 Graph of dependency of relative body mass from the output shaft torque at set operational life



6 Conclusion

The developed method of parameterization can be widely used in engineering practice in various fields of technology. It is applicable not only for Autodesk Inventor, but also for other CAD software that support parameterization of models.

Parametric modeling skills and the integration of Mathcad calculations into 3D programs will allow the engineer to eliminate a number of errors associated with the transfer of calculation data to the 3D model and significantly reduce the time to create a product line of the same configuration.

The parametrization algorithm of 3D models under consideration can be applied to design analysis and optimization as well as to solve research problems.

The functionality of the software combination shown in this paper can be expanded by adding new software that supports data integration with Excel tables, for example, ANSYS.

Thus, advanced engineering calculators and new design tools can be created. These software products can be designed in a user-friendly environment and added to sets of software used at enterprises. The created software package will allow engineers to quickly design individual parts or components of the assembly



according to specified parameters. This solution can be used to automate production in the rapidly developing industrial concept of Industry 4.0.

References

1. Zhu L-L, Wang G-X (2009) Optimization design and parametric modelling of gear reducer. In: 2009 second international conference on information and computing science, pp 125–127
2. Tremblay T (2012) Autodesk inventor 2013 and autodesk inventor LT 2013 essentials: autodesk official training guide. Wiley, Hoboken
3. Bol'shakov VP, Bochkov AL, Lyachek YU-T (2015) Solid modeling of parts in CAD systems: AutoCAD, KOMPAS-3D, SolidWorks, Inventor, Creo. Publisher, Piter
4. Tickoo S (2017) Autodesk inventor professional 2018 for designers. CAD/CIM Technologies
5. Verma G, Weber M (2017) Creo parametric 4.0 black book. CAD/CAM/CAE Works
6. Schilling P, Shih R (2015) Parametric modeling with SOLIDWORKS 2015. SDC Publications
7. Bol'shakov VP, Bochkov AL, Sergeev AA (2011) 3D modeling in AutoCAD, KOMPAS-3D, SolidWorks, inventor, T-flex. Publisher, Piter
8. Tickoo S (2016) CATIA V5-6R2015 for designers. CADCIM Technologies
9. Gulia NV, Klokov VG, Yurkov SA (2013) Machine parts. Lan, St. Petersburg
10. Petrakova EA (2012) Machine parts and basic engineering. MGIU, Moscow
11. Maxfield B (2014) Essential PTC mathcad prime 3.0: a guide for new and current users. Elsevier
12. Kir'yanov DV (2012) Mathcad 15/mathcad prime 1.0. BHV-Petersburg, SPb
13. Bekkel' LS, Slominskaya EN (2016) Creo parametric features analysis. Innov Sci 9(21): 47–51
14. Kravchenko AM (2014) Solid-state 3D modeling in problems of engineering design. Bull Ryazan State Agrotechnological University PA Kostycheva 2(22):26–29
15. Stremnev AYU (2014) Parameterization of assemblies autodesk inventor and modules-generators of typical designs. Eng Related Ind 2(86):56–58
16. Larsen RW (2013) Engineering with excel fourth edition. Pearson
17. Petrakova EA, Vlasov AS, Fedorov DYU (2017) Parametric modeling of solid structures in autodesk inventor directory. Eng J Appl 12(249):35–42
18. Lyachek YT, Alkadhi LJ (2016) Methods of creating parametric models of the geometric object in the modern CAD. Kibernetika i programirovanie 2:42–51
19. Petrakova EA (2017) Creating a parametric gear pair in autodesk inventor using external data directory. Eng J Appl 5(242):26–32
20. Randy HS (2017) Parametric modeling with autodesk inventor 2018. SDC Publications
21. Kulikov D, Yablochnikov E, Vostropiyatov A et al (2017) Method of automated design of operating the workpieces in a CAD system environment. In: 2017 IEEE 15th international conference on industrial informatics (INDIN), pp 96–102
22. Kartalis NI, Pronin VA (2016) Features of the design of body parts of standard designs of gearboxes. Textbook.-method. allowance, ITU ITMO, SPb
23. Dunaev PF, Lelikov OP (2000) Designing units and parts of machines. Proc Manual Tehn Specialist Universities. High School, Moscow
24. Kovchegin DA, Petrakova EA (2007) Machine parts: a guide to the implementation of the course project. MGIU, Moscow
25. Petrakova EA, Akhmedov MU, Molokanov MA (2018) The expediency of the choice of high-alloy steel gear pairs in closed gears directory. Eng J Appl 10(259):18–28

Automated Method for Modular Selection of Components for Multi-bearing Unit of Internal Combustion Engine Assembling



V. A. Saninsky, V. V. Korzin and A. V. Petrukhin

Abstract This article is devoted to the creation of elements of a CAD system for internal combustion engines designed for the automated selection of parts for multi-bearing bearing units with more than 4 supports. The basic principles of the proposed approach, based on the use of modified procedures for selective assembly, multiples of the calculation modules consisting of 4 pillars are considered. The article proposed a methodology for determining the optimal assembly option using an automated process control system for assembling multi-support shaft support nodes. It includes a methodology for creating databases and aims at stabilizing the gaps of multi-support shafts. It uses a geometric modeling system based on an invariant computer-aided design system. The proposed method is aimed at organizing diametrical gaps in the range from the minimum functional gap to the optimum. It is also intended to ensure the limits of the minimum and optimum thickness of the oil layer when assembling a multi-support unit of the support shaft and also to ensure reserves for wear and serviceability by compensating for the actual errors of mechanical processing and individual assembly.

Keywords Geometric model · Tolerance system · Selective assembly · Calculation module

1 Introduction

Known methods of obtaining new design solutions for various components of the internal combustion engine (ICE) using computer-aided design systems (CAD), which is reduced to the design of design documentation using a particular software

V. A. Saninsky (✉) · V. V. Korzin
Volzhsky Polytechnical Institute (Branch) of Volgograd State Technical University,
42a, Engels St, Volzhsky, Volgograd Region 404121, Russia
e-mail: saninv@rambler.ru

A. V. Petrukhin
The Volgograd State Technical University, 28, Lenin Ave, Volgograd 400005, Russia

package for two-dimensional or three-dimensional design [1]. It is aimed at automating the technical requirements for the parts of main bearings of an internal combustion engine obtained at the control stage when using them in CAD to achieve the minimum functional clearance $S_{\min F} = S_1$ of the locking link—gap in the friction pair of the main bearing—neck of the crankshaft (Fig. 1).

This article is devoted to the use of automation of the procedure for computer-sized sizing of such components of multi-bearing assemblies of a multi-support shaft (MSS) of the internal combustion engine as a crankcase, upper sleeve of a sliding bearing $t_{vk.vi}$, main crankshaft necks according to actual dimensions $t_{vk.vi}$, $t_{vk.n.i}$ thicknesses of the upper and lower liners, respectively. The result of this selection is to achieve the goal—obtaining the minimum allowable radial gap S_i between the liners of the first each i -th support (in this example, $i = 1-7$).

It is assumed that the technique can be used in the selection of the listed components for crankcases of ICEs with more than 4 supports based on the use of databases of actual dimensions of components in the context of the tasks of the ICE computer-aided design system [1].

This takes into account the harmful technological heredity of mechanical processing of components of the MSS [1]. This has a significant impact on the achievement during assembly of the minimum link gap $S_{\min F}$ and the further interaction of the surfaces of the parts of movable joints: the crankshaft main journals, the plain bearings. At the same time, the reliability of machines and mechanisms is increasingly associated with the disclosure of the relationship between the assembly and operation of machines [2].

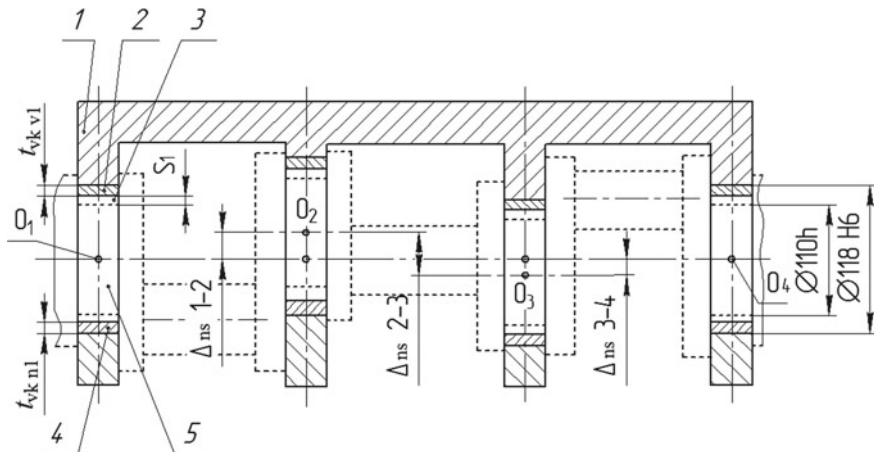


Fig. 1 Scheme of modular multi-support unit of the shaft with the number of supports equal to the number of 4: 1—crankcase, 2—upper liner of the sliding bearing crankcase, 3, 4—lower liner of the sliding bearing, 5—crankshaft; $t_{vk.vi}$, $t_{vk.n.i}$ thickness of the upper and lower liners; S_1 —radial clearance of the liner of the first support

There is also the influence of technological heredity of machining on the tolerances of the links of the dimensional chains of coaxial sliding bearings and the tolerances themselves on the diametrical gaps in coaxial friction pairs and, accordingly, on the parameters of the oil layer of coaxial main diesel sliding bearings [3].

2 Formulation of the Problem

Elimination of harmful technological heredity of the production processes of machines at the assembly stage by compensating for the geometrical errors of the contact surfaces of some parts with the geometrical errors of other contact surfaces of coaxial friction pairs reduces destabilization of gaps in them [3] and reduces the effect of tolerances of dimensional chains of coaxial slide bearings on the parameters oil layer of the coaxial slide bearings [4] due to the selection of components.

The use of CAD elements [5–17] in machine-building technology allows to automate the process of selecting component parts and optimize the diametrical gaps in coaxial friction pairs of the MSS [18].

Creating the conditions for technological support of the process of selective assembly of a multi-support unit for a support shaft based on a personal computer (PC) allows organizing diametrical gaps in the range from the minimum functional clearance $S_{\min F}$ to the optimum S_{optF} . Accordingly, the limits of minimum h_{\min} and optimum h_{opt} of the oil layer thickness will be provided during the assembly of the MSS, as well as the reserves for wear of S_i and efficiency of K_T by compensating for the actual errors of their machining and individual assembly.

The basis of the technological support for the automation of selection is a developed system of designations for tolerances and landings of crankcase core supports, sliding bearing shells and crankshaft journals included in the MSS.

3 Identification of Tolerances and Landings on the Surface of Contact Details MSS

To accomplish the task, a system of notation for tolerances and landings on the contact surface of the MSS parts was developed. This system is used for the automated selection of its components: the diameters of the crankcase main bearings, crankshaft journals and the thickness of the sliding bearing bushings.

To ensure that the bearing wear is minimal and uniform in 7, 10, etc., support MSS, the necessary equal conditions of their work are created based on the application of the schemes in Figs. 2 and 3 and the corresponding method of calculating the gaps and thickness of liners.

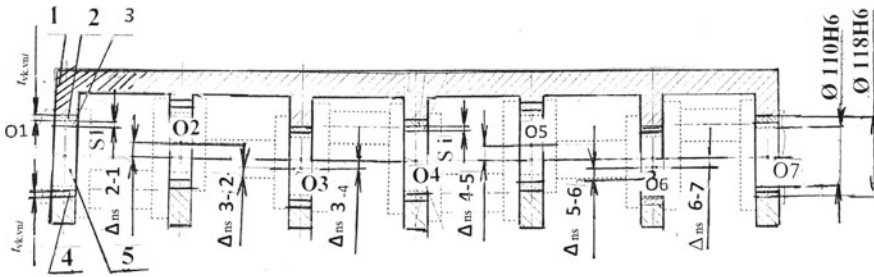


Fig. 2 Scheme of 7-support node shaft support with the number of supports multiple number of module supports: 1—crankcase, 2—upper liner sliding bearing crankcase, 3, 4 is lower liner of the sliding bearing, 5—crankshaft; $t_{vk,vb}$, $t_{vk,n,i}$ is thickness of the upper and lower liners; S_1 is the radial clearance of the liner of the first support; deviations from the coaxiality of each subsequent support relative to the previous one from right to left $\Delta_{n,s,2-1} = \Delta_{n,s,3-2} = \Delta_{n,s,4-3}$

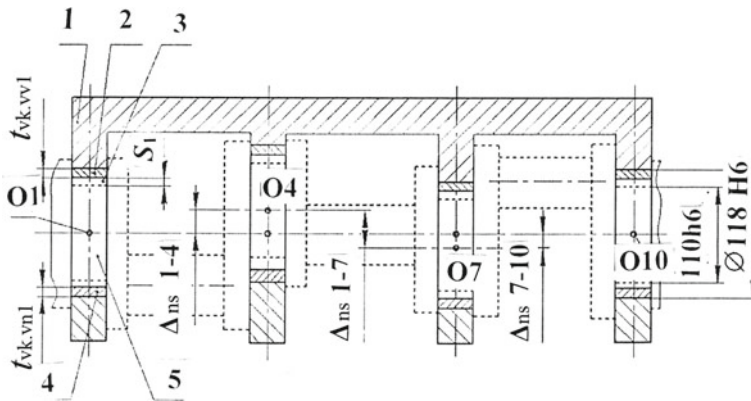


Fig. 3 Scheme of a multi-support shaft with the number of supports multiple of the number of module supports, in which the extreme supports of the module are conditional intermediate supports: $\Delta_{n,s,1-4}$ corresponds to the position in space of the point O_1 according to the scheme of Fig. 1; $\Delta_{n,s,4-7}$ corresponds to the position in space of the point O_7 according to the scheme of Fig. 1; $\Delta_{n,s,7-10}$ corresponds to the position in space of the point O_1 according to the scheme of Fig. 1

The calculation can be achieved by organizing an individual computer assembly that compensates for deviations of the diametrical dimensions and coaxially of the crankcase supports resulting from their mechanical processing, previously presented in the articles [1–6, 18].

As in the traditional technology, the measurement of the main supports crankcase and the thickness of the liners is performed at the input control, and to implement the technology of selection of component parts, the control results are required to be entered into the computer database and used in the selection.



After the creation of the base, the compensating values of the thickness upper and lower liners are automatically selected from the database of the actual dimensions of the liner thickness in the section corresponding to the closest approach friction pairs. This method allows, after laying in bed and tightening the bearing caps, to obtain the required dimensions of the working openings of the bearings with a tighter tolerance of arrangement than with traditional technology. To do this, in the i -th main bearings after boring them on special metal-cutting machines with coaxially $\Delta_{n.s.i-j}$, where j is the number of support from left to right, with a report from the 1st support (Fig. 1). For example, with the misalignment of the second (we denote the j -th) support relative to the first (or i -th) $\Delta_{n.s.2-1} = \Delta_{n.s.j} = \pm 0.03$ mm (similarly to $\Delta_{n.s.1-j} = \Delta_{n.s.1-j} = \Delta_{n.s.3-j}$, etc.), set the upper and lower liners preselected from the database so that their volumes fill the “working gap tP_i ” between the surface of each main bearing and main neck with the formation of the minimum value of the optimal technological gap. (calculated clearances S_i , performed according to the recommendations of the company “Glyko” are within (0.0008–0.001), $d = 0.088$ –0.11 mm.

To implement the automated selection of liners to compensate for errors in crankcase supports (Fig. 1), a mathematical model has been proposed, in which it is considered to be $S_i + D = tP_i$, where D is a variable parameter of the actual thicknesses of the top $t_{vk.vi}$ or lower $t_{vk.n.i}$ liner. At that, in the automated system, the thicknesses of the upper and lower liners are included in one database.

To ensure technological compensation of misalignment of the crankcase main bearings with different thickness of liners, based on the measured values of adverse displacements of the main bearings, it is necessary to have an appropriate system of tolerances and landings.

We assume that the axis common to 1 and 4 of the main journals of the shaft coincides with the axis 1 and 4 of the crankcase main bearings. Then, this axis will be common both for the main bearings of the shaft and for the main neck.

“Working clearances” are determined by the difference of the same size (belonging to one bearing support) of the actual sizes of the main supports and necks and are used to calculate the selectable thickness of the liners. For example, the difference in the size of the actual size D_{p2} of the root support 2 (Fig. 1) and the corresponding sum of the values of the actual size D_{sh2} of the root collar give the value of the actual diametric clearance in the friction pair. It is within the optimum radial clearance in the calculated friction pair and must be equal to the sum of the thicknesses of the upper and lower liners in the plane of the closest approach of the shaft neck and the bearing. The automated selection of liners presented in the article was carried out on this principle and showed satisfactory results.

This approach allows you to create the possibility of improving the accuracy of the assembly due to selective group or individual assembly and to ensure uniformity of the gaps in the friction pairs of the main bearings.

The selection process of components includes the calculation of the mounting gap on the actual dimensions of the contact surfaces of the component parts, which is produced relative to the common axis of the extreme openings of the main bearings and combined with the common axis of the main necks of the crankshaft.

The calculation is performed so that the values of the thickness of the upper and lower liners folded with the lower limit of the gap are equal to the mounting design gap. At the same time, the assembly gap is determined by calculation using modules so that the dimensions of those components that provide the assembly gap, which is technological, are more rigid than the design one which is selected from the database. It must lie in the range between the values of the minimum functional and optimal gaps, which are common to the entire series of coaxial friction pairs of a multi-support unit consisting of a number of individual ones. The position of the forming working surfaces of the lower liners of intermediate bearings and the mounting clearances of the bearing supports are calculated so that they create the minimum allowable diametrical clearances in coaxial friction pairs. For this purpose, a geometric model of the MSS is developed so that the bearing centers are displaced in the direction of their favorable arrangement vectors, and the axes of the outermost and intermediate bearings are located in the plane of the maximum rapprochement friction surfaces of coaxial friction pairs. This creates the possibility of radial displacement of the axis of each main bearing and taking into account the run out of the main bearing by radial displacement of the bearing axis due to the different thickness of the upper and lower liners of the calculated single bearing unit.

The methodology for determining the optimal assembly option using an automated process control system for assembling multi-support nodes includes a database creation method similar to that presented in the article [18] (block of the data storage subsystem). It is aimed at stabilizing the gaps of a multi-support shaft using an invariant CAD-based geometric modeling system.

Step 1 The controller measures the details with a micrometer.

Step 1.1 Liner thickness measurement.

Step 1.2. Measurement of the diameters of the beds of the crankcase main supports.

Step 1.2.1. Measurement of misalignment of axes II, III and IV of crankcase main bearings relative to the main axis.

Step 1.3. Measurement of the diameters of the crankshafts journals.

Step 1.3.1. Measurement of misalignment of axes II, III and IV main supports of the crankshaft relative to the main axis.

Step 2. The controller fills the measurement map, entering the measurement data and the measurements themselves.

Step 3. The administrator of the database management system (DBMS) of multi-support units, using measurement cards and accompanying product documentation, fills the databases of shafts, crankcases and liners.

Step 4. The automated assembly process control system based on measurement data from databases models the crankcase–shaft assembly and calculates the thickness of the “working” gap (clearance during crankcase–shaft assembly between crankcase support and shaft journal) in each of ten

possible cases (let the crankcase have 4 supports and a “working” gap may be located above and below the axis).

- Step 5. The thickness of the “working” gap is recorded in the table “Thickness of the” working “gap,” which is stored in a separate file.
- Step 6. The automated process control system for the assembly fills in the “Pick-up table of the optimal assembly combination” using the data of thickness measurements from inserts from the database and measurement data of “working” gaps from the table “Thickness of” working “gaps.”
- Step 7. Applying the optimization methods (maximal element method, weighting coefficients method, minimax method) to the table “Picking table of optimal assembly options,” the automated process control system of the assembly forms the table “Optimal Assembly Kits,” which contains part numbers from databases that are recommended to be assembled into a node, and for each liner their positions are indicated.

Let us consider in more detail the algorithm of the modeling subsystem.

- Step 1. The module for calculating the thickness of the “working” gap refers to the row m of the database (DB) of crankcases, reads the necessary information on bed diameters and misalignments II–III IV crankcase support relative to the main axis.
- Step 2. Turns to row n of the shafts database, reads information on the diameters of the crankshaft journals, as well as on misalignments of II–II IV of the neck, relative to the main axis.
- Step 3. If the calculation module works with I or IV main support and with I or IV crankshaft journal, then the thickness of the “working” clearance (the gap between the crankcase support and the shaft journal above/below the main axis) is calculated by Formula (1):

$$tP_1 = tP_2 = \frac{D_{mi} - d_{nj}}{2} \quad (1)$$

where $tP_1 = tP_2$ is the thickness of the “working” gaps at a position above the axis/below the axis, respectively (P is the index determining the position of the working gap relative to the I–V main supports and shaft necks, i.e., $P = 1, 2, 3, 4, 5$ and in this case $P = 1$ or $P = 5$); D_{mi} is the diameter of the i -th crankcase bed m (i is the index defining the number of the crankcase’s main support, i.e., $i = 1, 2, 3, 4, 5$; m is the sequence number of the crankcase in the crankcase DB, $m = 1-M$) taken from the database of crankcases; d_{nj} is the diameter of the j -th shaft’s bed n (i is the index determining the shaft neck number, i.e., $j = 1, 2, 3, 4$; n is the ordinal number of the shaft in the database, $n = 1-N$) taken from DB shafts.

Moving on to Step 9, if not, then:

Step 4. If the calculation module works with II–IV main supports crankcase and II–IV crankshaft journal, then the thickness of the “working” gap is calculated by Formula (2):

$$t_{ust} = \frac{D_{mi} - d_{ni}}{2}. \quad (2)$$

Step 5. If in the crankcases DB and in the shafts DB, the misalignment of the i -th bed at the crankcase m and the j -th neck of the shaft n is 0, i.e., $\Delta_{k_{mi}} = \Delta_{sh_{nj}} = 0$ (where $\Delta_{k_{mi}}$ is the misalignment of the i -th bed at the crankcase m , $\Delta_{sh_{nj}}$ is the misalignment of the j -th crankshaft neck n), then $t_{ust.} = tP_1 = tP_2$.

Moving on to Step 9, if not, then:

Step 6. If in the crankcase DB, the misalignment of the i -th bed at the crankcase is $m \neq 0$, and in the shaft database, the misalignment of the j -th shaft is $n = 0$, i.e., $\Delta_{sh_n} = 0$, and $\Delta_{k_{mi}} \neq 0$, then the thickness of the “working” gaps is determined by Formula (3):

$$\begin{aligned} tP_1 &= t_{ust.} + \Delta_{k_{mi}} \\ tP_2 &= t_{ust.} - \Delta_{k_{mi}} \end{aligned} \quad (3)$$

Moving on to Step 9, if not, then:

Step 7. If in the crankcase DB, the misalignment of the i -th bed at the crankcase is $m = 0$, and in the database, the misalignment of the j -th shaft neck is $n \neq 0$, i.e., $\Delta_{sh_{nj}} \neq 0$, and $\Delta_{k_{mi}} = 0$, then the thickness of the “working” gaps are determined by Formula (4):

$$\begin{aligned} tP_2 &= t_{ust.} - \Delta_{sh_{nj}} \\ tP_2 &= t_{ust.} + \Delta_{sh_{nj}} \end{aligned} \quad (4)$$

Moving on to Step 9, if not, then:

Step 8. If in the crankcases DB, the misalignment of the i -th bed at the crankcase is $m \neq 0$ and in the shaft database the misalignment of the j -th shaft is $n \neq 0$, i.e., $\Delta_{sh_{nj}} \neq 0$, and $\Delta_{k_{mi}} \neq 0$, then the thickness of the “working” gaps is determined by Formula (5)

$$\begin{aligned} tP_2 &= t_{ust.} + \Delta_{k_{mi}} - \Delta_{sh_{nj}} \\ tP_2 &= t_{ust.} - \Delta_{k_{mi}} + \Delta_{sh_{nj}} \end{aligned} \quad (5)$$

Moving on to Step 9.

Step 9. Record the obtained value [18] “Thickness of the” working “gaps.” Moving to Step 3, repeat steps 3–9 for $(P + 1)$, $(i + 1)$, $(j + 1)$ until $P = 5$, $i = 4$, $j = 4$.

Go to Step 2, repeat steps 2–9 for the row $(n + 1)$ DB of the shafts until $n = N$.

Go to Step 1, repeat steps 1–9 for the row $(m + 1)$ of the crankcases DB, until $m = M$.

The modeling subsystem performs the following functions:

- (a) refers to the crankcases database and reads the information necessary for the calculation;
- (b) refers to the shafts database and reads the information necessary for the calculation;
- (c) calculates the “working” gap, depending on the position of the gap;
- (d) records the result obtained in the table “Thickness of” working “gaps.”

For the calculation and selection of liners 7-support crankcase (Fig. 2), the above method seems to be difficult and not accurate enough, that is, in this case it is necessary to take measurements on surfaces that are much more distant than it does in the module (Fig. 1).

In this and other variants of calculation, when the number of supports is a multiple of the number of supports of the module, the calculation is proposed according to the scheme shown in Fig. 3 using the methodology and algorithm shown in [18]. For ease of use, symbols can be labeled with an abbreviation corresponding to the number of supports of the calculated crankcase. For example, for a 7-support crankcase in Figs. 2 and 3, symbol 7 is applied. A similar designation is proposed for the calculation of formulas with a large number of supports.

4 Conclusion

The approach proposed in this article for solving the problem of computer selection of component parts of multi-support bearing assemblies for use in the context of the tasks of the computer-aided design of the internal combustion engine as compared to the known methods of selective assembly creates conditions for increasing the efficiency of the selection of component parts by minimizing the assembly gaps in coaxial friction pairs due to automated computer assembly [18].

The novelty of the proposed methodology lies in extending the testing of the methodology presented in the sources [7, 18] to the organization of computerized selection of components of the MSS for crankcases with 7 or more supports multiples of 4 supports (Fig. 1).

The proposed method is aimed at organizing diametrical gaps ranging from the minimum $S_{\min F}$ functional gap to the optimal $S_{\text{opt}F}$, to ensuring the minimum h_{\min} and optimum h_{opt} limits of the oil layer thickness during the assembly of the MSS,

as well as the reserves for wear of S_i and efficiency of K_T by compensating for the actual machining errors and individual assembly.

The technical and economic effect of such an assembly is to improve the accuracy of the gaps and the performance of nodes of the type of MSS and create on this basis increased stocks for wear in coaxial friction pairs using the example of main bearings of heavy diesel engines [18].

The technical and economic efficiency of creating and using the developed system for the selection of component parts of MSS for various methods of ensuring gaps in friction pairs can be estimated from the estimated values of reserves for wear $S_{i \max - \min}$, accuracy K_{TM} and the ratio of K_{IM} accuracy and wear factors for multi-support node for group assembly.

References

1. Dalsky AM, Bazrov BM, Vasiliev AS (2000) Technological heredity in engineering production. Publishing House of the MAI, Moscow
2. Ryltsev IK (2002) Optimization of the interaction of parts of movable joints based on the disclosure of the relationship of the processes of assembly and operation of machines: author. dis. doctors tech. sciences. Samara
3. Saninsky VA (2006) Destabilization of the parameters of the oil wedge coaxial sliding bearings. *Automot Ind* 3:14–16
4. Menshenin GG, Saninsky VA (2006) Influence of tolerances of links of dimensional chains of coaxial sliding bearings on the parameters of the oil layer of coaxial sliding bearings. In: *Mechanical engineering technology*, pp 24–32
5. Berliner EM, Taratynov OV (2011) CAD in mechanical engineering. Forum, Moscow
6. Grover M, Zimmers E (1987) CAD and production automation. Science, Moscow
7. Petrukhin AV, Saninsky VA (2015) The use of CAD elements in the virtual assembly of components of a multi-bearing bearing assembly ICE. In *News of VolgGTU. Ser. Progressive technologies in mechanical engineering: Interst. Sat scientific tr. VolgGTU* 11 (173):29–31
8. Dementiev YuV (2004) CAD in automobile and tractor construction. Academy, Moscow
9. Zuev S, Poleshchuk N (2004) Autocad-based CAD system—how it is done. BHV-Petersburg, Moscow
10. Kazennov GG, Sokolov AG (1989) Basics of building CAD and ASTPP. Higher school, Moscow
11. Klimov VE (1990) Graphic CAD systems. Higher School, Moscow
12. Kureychik VM, Glushan VM, Shcherbakov LI (1990) Combinatorial hardware models and algorithms in CAD. Radio and communications, Moscow
13. Kureychik VM (1990) Mathematical support of design and technological design using CAD. Radio and communications, Moscow
14. Latyshev PN (2010) CAD catalog. Solon-Press, Moscow, Programs and manufacturers
15. Engelke UD (1990) How to integrate CAD and ASTPP. Mashinostroenie, Moscow
16. Petrukhin AV, Saninskiy VA, Moskvicheva NP, Kochkin MV (2015) Automated selection of components in bearing assembly for diesel engines. *Russ Eng Res* 35(7):500–504

17. Petrukhin AV (2005) Methodical bases of the formalized presentation of information on technical objects. In Pedagogical informatics, no. 5
18. Saninsky VA, Petrukhin AV, Moskvicheva NP (2007) Automation of the process of selecting the diametrically compensated machining of coaxial holes in a multi-bearing unit of a diesel engine using liners of different thickness. Mech Eng Technol 7:65–68

Improving Synthesis Accuracy of Topology Elements in Laser Pattern Generators with Circular Scanning Mode



A. V. Kiryanov and V. P. Kiryanov

Abstract Possible ways of improving the accuracy of topology elements in laser pattern generators based on the circular scanning principle are analyzed. The most important sources of errors induced by the system of radial displacements and by the rotation of the rotor of the mechatronic module are studied. For the image generators with circular scanning, the principles of decreasing the main components of the operation instability are described. The method of improving the accuracy of the same generators is proposed. The result is achieved by using two hybrid angular encoders and two-coordinate deflector in it. The use of hybrid angular encoders allows making measurements of the turning angle and current radial deflections of the angular coordinate laser pattern generator rotor axis simultaneously. For that two measuring patterns, radial raster for measuring angular displacement and ring for measuring linear shift raster in a tangential direction are formed on a single glass basis for one technological process. The use of a two-coordinate deflector allows one to make the correction interaction of the laser beam with the photosensitive material.

Keywords Laser pattern generator with circular scanning mode • Optoelectronic angular encoder • Mechatronic module • Hybrid angular encoder

1 Introduction

In recent years, a number of works were made regarding the improving of the metrological characteristics of laser pattern generators with a circular scanning mode (LPG CSM) which are used to manufacture high-precision diffractive optical elements (DOE) and angle measuring structure (AMS) (generic name of optical angular rasters, limbs, and multibit code disks—basic metrology elements of

A. V. Kiryanov (✉) · V. P. Kiryanov
Siberian Branch of the Russian Academy of Sciences (IA&E, SB RAS),
1, Academician Koptyug Ave, Novosibirsk 630090, Russia
e-mail: alexey@iae.nsk.su

angular encoders) [1–6]. In these works, much attention is paid to improving the critical parts of LPG CSM, including the circular movement mechatronic module that is built on the basis of precision aerostatic bearing with a built-in of angular encoder. The use of this module in the design of LPG CSM leads to the appearance of a number of specific errors characteristic only for its. In [7, 8], the method of improving the accuracy of manufacturing the topology of elements by eliminating the drift of the relative position of the axis of the optical recording channel and the axis of rotation of the rotor of the mechatronic module was described. In [9], the problem of reducing the positioning error in angular direction, caused by the limited accuracy control, was decided by using the design of optoelectronic encoder hybrid type (OEHT). However, the task of improving the metrological characteristics of LPG CSM remains an urgent problem.

2 Problem Definition

In [10, 11], the method of increasing the accuracy of element topology manufacturing was described, according to which the test circle is formed on the surface of the photosensitive material deposited on the working surface of the carrier of the future element in the area of the workpiece rotation center. In the selected angular directions, the profile of the trace of the interaction of laser radiation with the photosensitive material arising from the recording of the circle is measured. Based on the results of profile measurements, the coordinates of the formed circle are determined and the value of linear distortions of the applied test circle introduced by the laser image generator is determined, for example, due to the residual imbalance of the spindle rotor. The results of the measurements are used to calculate the values of the corrections that need to be made to the values of the current radial coordinates. These values are entered into the memory block of the processor. Then, during the subsequent recording of the topology of the formed working structures for the selected angular directions, the current interaction radial coordinates are corrected using a deflector which is installed in the optical path of the laser image generator.

Physically, the deflector is used to shift the laser spot in the radial direction by a given value relative to the current coordinates of the spot.

In [10], it is noted that it was obtained experimentally the decrease of the distortion amplitude from 220 to 42 nm, i.e., five times.

However, the author is noted that a number of disadvantages characterizes this approach [10]. The main of them is that it is required to rotate the plate with a test record by 180° and re-carefully adjust the plate after its rotation on the object table of LPG (disk chuck and faceplate). The disadvantages of the method include the fact that the corrective action is obtained only for the radii lying in the selected angular directions, and for the directions lying in the intervals between them, will be required certain methods of interpolation.

The analysis of this technical solution shows that the need to rotate the plate on the faceplate is caused by the fact that the test element is recorded and is read using the same means of LPG CSM: the recording head and the mechanical module of circular movements. As a result, not all defects in the recording are detected by the control scan. Therefore, to make the processes of writing and reading statistically independent (at least partially!) in this mentioned method the measured test object is rotated 180° relative to its recording position.

In addition, it should be borne in mind that in the presence of a wedge in the carrier of the photosensitive layer after turning the plate by 180° , the rotor balancing parameters change, even after the ideal alignment of the plate, which will introduce additional distortions.

The main disadvantage of this method, which was not discussed in [10], is that the interaction trace in the photosensitive material is not always possible to accurately determine the nature of the topology distortions, because at different radii of the surface of the photosensitive layer, the same destabilizing factor can lead to various distortions of the scanning trajectory. And this, in turn, leads to hard-to-predict distortions of synthesized structures, including test ones. This statement is based on the following experimental results.

In [7], it is shown that the rotor imbalance leads to the appearance of complex parasitic movements of the rotor axis. Thus, if the center of mass of the rotor does not coincide with the center of symmetry of the aerostatic bearing, then when the rotor rotates, angular swings of its axis occur, which generate the so-called regular precession of the axis. The resulting gyroscopic accelerations generate another type of forced movements of the rotor axis—the nutation. The combined action of the three components—the rotation of the rotor around the axis, precession, and nutation of the axis itself—leads to the fact that each point on the surface of the plate with a photosensitive material installed on the subject table of the rotor moves along complex trajectories. Moreover, due to the fact that the linear velocity of the surface rotation is different for each of the material surface radius, the resulting trajectory of each point of the surface relative to the fixed recording is different. This situation was simulated on a computer.

Figure 1a shows the field of the displacement instantaneous velocities in the surface points space of the object table, mounted on the upper end of the rotor, while rotating the rotor with a frequency ω and rocking the axis of rotation with a nutation frequency equal to 25ω , is obtained by numerical simulation. In this case, the greater part of the surface of the faceplate scan trajectories are represented as curves, in mathematics are received the name of the elongated epitrochoids [12] (trajectory 1, Fig. 1b). The curvature of the trajectories is increasing continuously by the decreasing of the scan radius and around a certain radius of the scan, the elongated epitrochoids are degenerated into the epicycloids (trajectory 2, Fig. 1b), and as further reducing of the scan radius, the epicycloids degenerate into the shortened epitrochoids. In the case of the shortened epitrochoids, the instantaneous speed of displacement of the surface may change the sign of the offset direction. As a result, loop-like scanning trajectories appear (curve 3, Fig. 1b). The presented results of the analysis of changes in scanning trajectories in the form of quite exotic

curves are not the purely academic interest. In the simulation, the current trajectories were recorded using evenly spaced points. With changes in the linear scanning speed, the distances between them on the surface of the material changed proportionally, which allowed to identify the effect of grouping and, as a consequence, the formation of moire spatial structures. Similar moire spic-like structures are clearly shown in Fig. 1a. In areas where a moire structure has appeared, there will be variable exposure of absorbed power, which will inevitably lead to the appearance of a variable profile in photosensitive materials after its exposure. So, Fig. 2 the real profiles experimentally detected in the central region of the formed DOE are presented. A complex parasitic structure was found in the analysis of a technical failure (green loop) that occurred during the recording of the formed DOE.

Similar results were also registered by German researchers in the analysis of the DOE structure recorded in the chromium film using LPG with circular scanning of the CLWS-300 model [13–16].

Thus, the simulation showed that two circular motions with different frequency and with different amplitude together gave the effect of a very complex modulation of the velocity of motion of the surface points of the photosensitive material, depending on the current value of the scanning radius.

Therefore, it can be argued that the circular scanning of the same perturbation introduced by the residual imbalance of the rotor, correspond significantly different distortions of the exposure of photosensitive material, depending on the current scanning radius of the surface of the material.

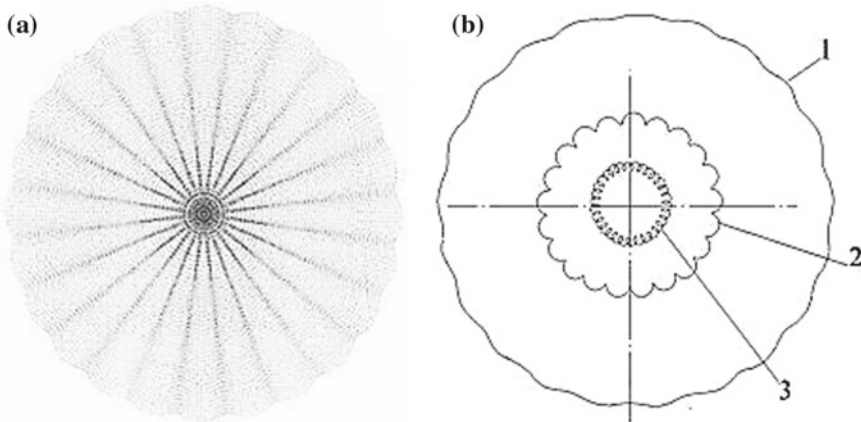
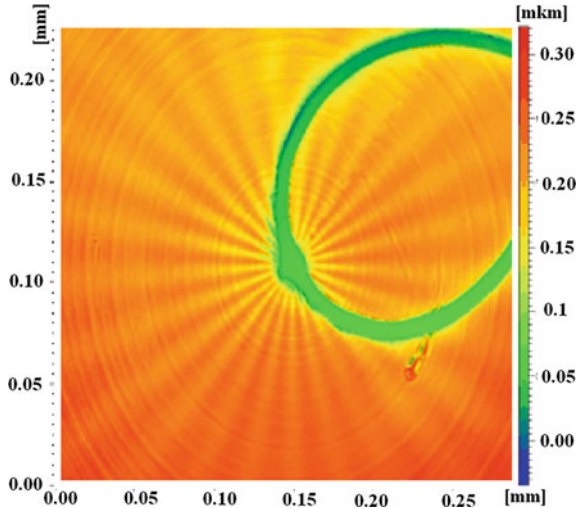


Fig. 1 a Simulation of the velocity field of the faceplate surface points with simultaneous rotation and swing of the rotor axis and b types of trajectories

Fig. 2 Parasitic spic-like structures in the central region of the formed DOE



3 Approaches and Methods of Solving the Problem of Improving the Synthesis Accuracy of Topology Elements in the LPG CSM

Therefore, in order to improve the accuracy of LPG CSM, the authors were proposed [17] to distinguish in explicit form the root causes of distortion of the trajectories of the laser beam on the surface of the photosensitive material and to use them for active compensation of parasitic distortions of the exposure of photosensitive material. The authors distinguish two such reasons.

The first reason is the forced swing of the rotor axis of the aerostatic bearing in the unit of the mechatronic module of circular movements, for example, due to the residual imbalance of the rotor. For unambiguous detection of the nature of the axis swing in the circular scanning unit, two pairs of the rotor axis beat sensors are installed [18–20]. In each pair, both sensors are oriented relative to the axis of rotation with a mutual spatial shift of 90° . In Fig. 3, the variant of the technical implementation of this method is presented. Here, the two hybrid optical sensors 1 and 2 are provided, in which one group of reading heads (meaning heads 3 and 4) is tracking the angular displacements of the measuring rasters 5 and 6, respectively. Two other groups of reading heads (heads 7 and 8 in the sensor 1 and the head 9 and 10 in the sensor 2) are monitoring the linear displacement of the axis of rotation of the raster in two orthogonal-oriented radial directions.

To do this, they are installed in each sensor with a mutual spatial shift of 90° . By registering the output signals of the reading heads 7, 8, 9, and 10, they reveal the nature of the parasitic beats of the rotor 11, which is part of the spindle 12 of the circular scanning unit of the LPG CSM. This is done in the following way. Let read heads 7, 8, 9, and 10 detect the offset of the axis in the corresponding

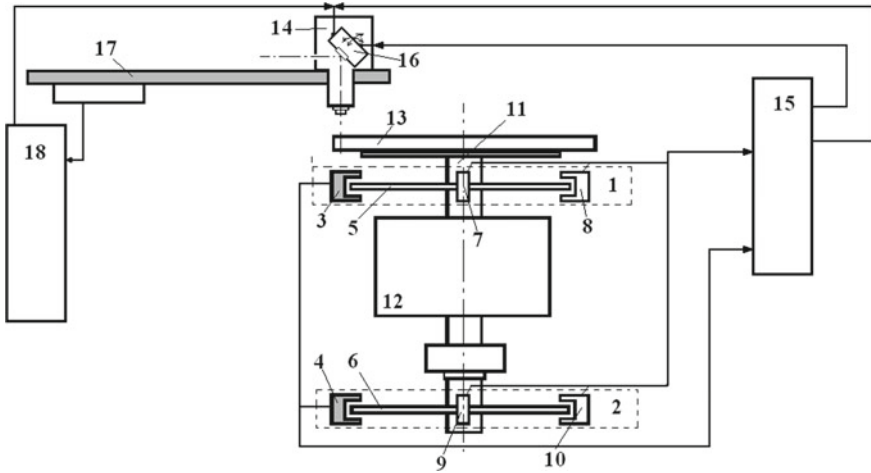


Fig. 3 Laser pattern generators with circular scanning mode with increased accuracy

directions with the sign “+” if the distance between the reading heads and axis is increased, and with the sign “-” if the distance between the reading heads and the axis is reduced. The use of two sensors of the hybrid type (sensor 1 and sensor 2) is due to the fact that the design of the rotation unit does not ensure compliance with the Abbe principle when recording the topology of structures. Its essence is that the measuring device must be in the same plane with the controlled object. In LPG CSM, the recording is carried out with the help of the head 13 on the photosensitive layer applied to the surface of the workpiece 14, using the information is read by the head 3 of the first sensor from the working surface of the raster 5. The plane of the topology record is separated from the plane of measurements at some distance, which can be considered as a certain geometric factor H . Here, $H = H_0 + d$, where H_0 is the distance from the working surface of the raster 5 to the lower surface of the workpiece 14, and d is the current thickness of the workpiece 14.

The parasitic displacement of the rotor axis 11, registered by the sensor 1, may not correspond to the real parasitic displacement of the laser beam on the workpiece surface, if at the moment the rotor axis performs a parasitic motion involving the axis slopes. It is characteristic that with parallel displacement of the axis in space, the parasitic motion of the axis recorded by the sensor 1 will coincide exactly with the parasitic displacement of the workpiece. To distinguish these features, it is necessary to use two sensors spaced at the base distance of the H_B . Then, assessing the displacement of the rotor axis is recorded simultaneously by two sensors, and it is possible to calculate the ΔX —real displacement of the workpiece surface 14 relative to the recording head 13 as follows:

$$\Delta X = \Delta X_1 + (\Delta X_1 - \Delta X_2) \frac{H}{H_B} \quad (1)$$

where $(\Delta X_1 - \Delta X_2) \frac{1}{H_B}$ —the tangent of the angle of the axis of the rotor, the index 1 belongs to a displacement of the axis, was registered by combined sensor 1 and the index 2—by sensor 2.

Using this ratio, it is possible to calculate separately the parasitic displacements of the radiation interaction point with the photosensitive layer caused by the parasitic displacements of the axis, both in the radial and angular (tangential) directions. To do this, it should be taken into account that the rotor 11 of the spindle 12, the workpiece 14, and the measuring rasters 5 and 6 of the sensors 1 and 2 are absolutely rigid. Then, the displacements of all points of the surface of rasters 5 and 6 caused by the parasitic displacement of the axis of rotation for each of the selected directions will be equal to each other in their absolute value.

Accordingly, the distortions of the radial coordinate ΔX_R of the laser radiation point coming out of the head 13 are determined as follows:

$$\Delta X_R = \Delta X_8 + (\Delta X_8 - \Delta X_{10}) \frac{H}{H_E} \quad (2)$$

where ΔX_8 —the phase increment of the output signals of the head 8 at this time, ΔX_{10} —the phase increment of the head 10 output signals at the same time.

Values of the phases of the signals are computed in the DSP 15 of the LPG CSM using, for example, arctangent algorithm. Then, $\varphi = \text{arctg}(\sin \varphi / \cos \varphi)$, where $\sin \varphi$ and $\cos \varphi$ are the output signals of the reading heads 8 and 10.

Accordingly, the distortions in the tangential direction ΔX_Θ the coordinates of the interaction point of the laser radiation coming out of the head 13 are determined as follows:

$$\Delta X_\Theta = \Delta X_7 + (\Delta X_7 - \Delta X_9) \frac{H}{H_E} \quad (3)$$

where ΔX_7 is the phase increment of the output signals of the head 7 at a given time; ΔX_9 —the phase increment of the output signals of the head 9 at the same time.

The phase values of the output signals for the tangential direction are calculated in the processor 15 as $\varphi = \text{arctg}(\sin \varphi / \cos \varphi)$, where $\sin \varphi$ and $\cos \varphi$ are the output signals of the read heads 7 and 9.

Then, based on the selected distortions ΔX_R and ΔX_Θ in the processor 15, taking into account the characteristics of the two-coordinate deflector 16 is installed in the optical path of the laser image generator, and it is necessary to calculate the correction values for both coordinates of the current point of interaction of the laser beam with the photosensitive material. Based on the calculated corrections, real-time control actions on the two-coordinate deflector 16 are formed.

The second possible reason for the distortion of the trajectories of the laser beam on the surface of the photosensitive material is the presence of parasitic movements in the radial direction of the carriage 17 together with the recording head 13, as a consequence of disturbing influences from the spindle. Here, the perturbing effects

are of the beating of the spindle rotor due to residual imbalance, because to suppress external vibrations in the LPG CSM there is a regular vibration isolation system of the optical-mechanical unit, i.e., the residual imbalance of the rotor perturbs not only the spatial position of the axis of rotation of the rotor, but also the position of the carriage 17. The spectral composition of the output signals of the carriage control system 18 was studied, when the recording head was held at a given recording radius. The presence of a significant harmonic contribution in the mismatch signal of the system 18, whose frequency is equal to the rotation frequency of the spindle rotor, was highlighted. And the phase of this harmonic, as a rule, does not coincide with the phase of the perturbation signal detected by the beat sensors in the circular scanning node. According to the authors, this delay is due to the large mass of the plate, which is installed and the carriage 17 linear movements, and the spindle 12, and through which the spindle vibration 12 17 transmitted to the carriage.

Therefore, to improve the accuracy of the synthesis of the topology of elements at their formation with the help of a laser image generator with circular scanning, the authors propose in the system 18 to allocate the current signal of misalignment at the moments when the carriage 17 is steadily in the vicinity of the specified positioning point. On the basis of this signal, it is necessary to calculate an additional correction for the radial coordinate of the interaction point of the laser beam with the photosensitive material and direct the corresponding effect on the input of the radial coordinate of the above-mentioned two-coordinate deflector 16. This control action will compensate for the real-time displacement of the carriage due to the destabilizing effect of the residual imbalance of the spindle rotor in the rotation unit LPG CSM.

4 Conclusion

Estimates of the effect of using the described method of improving the accuracy of the synthesis of the topology of elements in LPG CSM show the possibility of reducing the error of the formation of the topology of elements up to 10 nm or less.

The study was carried out *at* the expense of the subsidy for the financial support of the state task (Project IV.36.1.3 № state registration 031920160009) in the Institute Automation and Electrometry of Siberian Branch of RAS.

Acknowledgements The authors express their gratitude to Dr. V. E. Zyubin and Chief programmer of the laboratory A. D. Petukhov for providing the results of the numerical simulation of the instantaneous velocities field of the carrier surface displacements and to Dr. V. P. Korolkov for providing microphotography of the distorting influence experimentally registered in the photoresist.

References

1. Mukai N, Kono T, Suzuki A et al (2004) High accuracy scale disk for rotary encoder. In: Yoshimoto S, Kim SM (eds) Proceedings of the 1st international conference on positioning technology, ICPT 2004, Hamamatsu, Shizuoka, Japan
2. Bai Zhen, Wei Jingsong et al (2016) High-speed laser writing of arbitrary patterns in polar coordinate system. *Rev Sci Instrum* 87:125118. <https://doi.org/10.1063/1.4973397>
3. Haefner M, Pruss C, Osten W (2011) Laser direct writing of rotationally symmetric high-resolution structures. *Appl Opt* 50(31):5983–5989. <https://doi.org/10.1364/AO.50.005983>
4. Poleshchuk AG, Churin EG, Koronkevich VP, Korolkov VP et al (1999) Polar coordinate laser pattern generator for fabrication of diffractive optical elements with arbitrary structure. *Appl Opt* 38(8):1295–1301. <https://doi.org/10.1364/AO.38.001295>
5. Bowen JP, Michaels RL, Blough CG (1997) Generation of large-diameter diffractive elements with laser pattern generation. *Appl Opt* 36(34):8970–8975. <https://doi.org/10.1364/AO.36.008970>
6. Rhee HG, Song JB et al (2007) Diffractive optics fabrication system for large aspheric surface testing. *J Korean Phys Soc* 50(4):1032–1036. <https://doi.org/10.3938/jkps.50.1032>
7. Kiryanov AV, Kiryanov VP (2010) Improvement of metrological characteristics of laser image generators with circular scanning. *Optoelectr, Instrum Data Process* 46(5):462–475. <https://doi.org/10.3103/S8756699011050098>
8. Kiryanov AV (2010) Accuracy enhancement for precision angle measuring structures. *Key Eng Mater Measur Technol Intell Instrum IX* 437:198–202. <https://doi.org/10.4028/www.scientific.net/KEM.437.198>
9. Kiryanov AV, Kiryanov VP (2012) Increasing of accuracy of angular measurements by using hybrid photoelectric converters. *Optoelectr Instrum Data Process* 48(6):605–611. <https://doi.org/10.3103/S8756699012060088>
10. Korolkov VP (2003) Izmerenie i korekcia traektorii dvizhenia lasernogo puchka v krugovih zapisivaushih sistemah (Measurement and correction of the laser beam trajectory in circular recording systems). *Avtometriya* 9(6):13–25
11. Korolkov VP, Pruss C, Reichelt S et al (2003) Performance improvement of CGHs for optical testing. *Proc SPIE* 5144:460–471. <https://doi.org/10.1117/12.500415>
12. Savelov AA (1960) Ploskie krivye. Sisematika, svoistva, primenenie. Spravochnoe rukovodstvo (Systematization, properties, applications. Handbook), Gosudarstvennoe izdatelstvo fiziko-matematicheskoi literatury, Moscow
13. Pruss C, Reichelt S, Tiziani H, Korolkov VP (2002) Metrological features of diffractive high-efficiency objectives for laser interferometry. *Proc SPIE* 4900:873–884. <https://doi.org/10.3103/S8756699011050098>
14. Annual report (2013/2014) Institut fur Technische Optik Universitat Stuttgart. Stuttgart. http://https://www.ito.uni-stuttgart.de/pdf/jahresberichte/pdf_jahresbericht_13_14/ITO_Report1314_04_Schaal.pdf. Accessed 23 March 2019
15. Guhr J (1997) Test results of the circular laser writing system CLWS-300. *Diffraction Optics EOS Topical Meet Digest Serial* 12:206
16. Freimann R (2000) Aberrations of axially symmetric diffractive optical elements in relation to their fabrication inaccuracies. *Optik* 111(1):485–492
17. Kiryanov AV, Kiryanov VP (2017) Laser pattern generator. RUS Patent 2,017,118,643, 29 May 2017
18. Kiryanov A, Kiryanov V, Chukanov V (2016) The use of hybrid angular encoder in the laser pattern generators with circular scanning. In: 13th International scientific-technical conference on actual problems of electronic instrument engineering, vol. 1. APEIE 2016; Novosibirsk; Russian Federation; 3–6 Oct 2016. *IEEE*, 7802262, p 232

19. Kiryanov AV, Kiryanov VP (2012) Piggyback photoelectric encoder for high-precision angular measurement. In: 11th International conference on actual problems of electronic instrument engineering, APEIE 2012; Novosibirsk, 2–4 October 2012, IEEE. 6628981, p 158
20. Kiryanov AV, Kiryanov VP (2016) Improvement of metrological characteristics of the laser pattern generators with circular scanning mode by the use of hybrid angular encoder. In: International conference on industrial engineering, applications and manufacturing, ICIEAM 2016—proceedings 2016; South Ural State University Chelyabinsk, 19–20 May 2016, 7910973

Estimation of Heat Losses in Fuel Combustion by Analysis of Gas Pressure in the Cylinder of Diesel



E. A. Lazarev, V. E. Lazarev and M. A. Matculevich

Abstract The energy and heat losses reduction in the process of fuel combustion enables the diesel engines' power and fuel efficiency growth by improving the operating cycle indicators. The fuel combustion process efficiency depends on the completeness of the emission and use of the burning fuel heat. The most important factors that determine the level of heat losses are the combustion process duration, the fuel-air mixture composition, and the crankshaft rotation frequency. It is established that the combustion efficiency coefficient increases with the reduction of the combustion process duration; the more intensive the coefficient increase, the lower the crankshaft rotation speed and the greater the excess air ratio. The factors' influence on the combustion process efficiency is determined from the thermodynamic analysis results of the gas pressure indicator diagrams in the diesel cylinder.

Keywords Diesel engine · Work cycle · Mixture composition · Fuel burnout efficiency coefficient · Heat losses · Burnout process duration

1 Introduction

The fuel combustion process is the most important of the processes that the work cycle consists of, and the list of parameters depends on the combustion process: fuel efficiency, power, thermal and mechanical loading of the intra-cylinder space elements, the resource, as well as environmental indicators such as noise, vibration, and emissions exhaust gases of a diesel engine. One of the indicators of the combustion process quality (efficiency) is the level of energy or heat losses that always go with the hydrocarbon fuel oxidation in the conditions of a continuously varying cylinder volume of the operating diesel.

E. A. Lazarev (✉) · V. E. Lazarev · M. A. Matculevich
South Ural State University, 76 Lenin Prospect, Chelyabinsk 454080, Russia
e-mail: lazarevea@susu.ru

© Springer Nature Switzerland AG 2020
A. A. Radionov et al. (eds.), *Proceedings of the 5th International Conference on Industrial Engineering (ICIE 2019)*, Lecture Notes in Mechanical Engineering,
https://doi.org/10.1007/978-3-030-22041-9_54

507

Determination of the dependence of heat losses on the fuel burnout duration, the air-fuel mixture composition, and the speed of the crankshaft lets to evaluate the possibilities of various methods of controlling the combustion process for improving the work cycle indicators of the diesel engine.

2 The Main Criteria for Estimation of Efficiency and Combustion Process Characteristics

Considering the development of the fuel combustion in time, it should take into account that, according to the recommendations of [1–4], we can assume that for $t = 0$ the part of burned fuel $x(t) = 0$, for $t = t$ it is the current value of $x(t) = x$, and at the end of fuel burnout (at $t = t_z$), the part of burnt fuel is assumed to be $x(t) = 0.999 \approx 1$.

It is obvious that the amount of released heat in the fuel combustion process is directly proportional to the part of burned fuel $x(t)$ and can be determined

$$Q_x = \delta \cdot Hu \cdot G_{fc} \cdot x(t) \quad (1)$$

where Q_x —the amount of heat released during the fuel combustion at the time t ; Hu —low heat value; δ —coefficient of heat release, which takes into account the heat losses of fuel combustion due to incomplete burnout (lack of air, imperfect combustion); and G_{fc} —the amount of fuel supplied to the cylinder during the working cycle.

The amount of heat Q , used to increase the internal energy of the working body and to perform the work, is determined

$$Q = Q_x - Q_{\text{loss}} \quad (2)$$

where Q_{loss} —the heat losses during fuel combustion.

Heat losses can be defined as the sum of the following components

$$Q_{\text{loss}} = Q_w + Q_{\text{hl}} + Q_{\text{dis}} \quad (3)$$

where Q_w —the heat losses due to heat transfer to the walls of the cylinder, representing the main part of the heat losses during the fuel combustion; Q_{hl} —the internal hydraulic loss of heat due to the flow of gases; and Q_{dis} —the heat losses for dissociation of combustion products.

The components of the heat losses Q_w , Q_{hl} , and Q_{dis} vary in time according to the heat transfer laws, hydrodynamics, and physical chemistry. Taking into account their relatively small value, it can be assumed that during the whole combustion

process, the sum of the heat losses components is proportional to the fraction $(1 - \psi)$ of the heat Q_x

$$Q_w + Q_{hl} + Q_{dis} = (1 - \psi) \tag{4}$$

where ψ —coefficient of the heat use.

On the basis of the foregoing, it can be assumed that the coefficients δ and ψ are the most important criteria for estimating the efficiency of the fuel combustion process in the working cycle of a diesel engine.

Solving Eqs. (2) and (4) and taking into account the dependence (1), we obtain

$$Q = \psi \cdot Q_x = \psi \cdot \delta \cdot Hu \cdot G_{fc} \cdot x(t) = \xi \cdot Hu \cdot G_{fc} \cdot x(t) \tag{5}$$

where $\psi \cdot \delta = \xi$ —combustion efficiency factor.

The combustion efficiency factor can be considered as an integral criterion for evaluating the efficiency of the fuel combustion process.

On the basis of the foregoing, we can determine the dimensionless integral characteristics: the fuel burnout $x = f(t)$, liberation $x_\delta = f(t)$, using $x_i = f(t)$ and losses $x_{loss} = f(t)$ of heat in the combustion process of the working cycle of a diesel engine. These characteristics are interrelated: $x_\delta = \delta \cdot x$; $x_i = \psi \cdot x_\delta = \psi \cdot \delta \cdot x = \xi \cdot x$; and $x_{loss} = (1 - \psi) \cdot x_\delta$. Current values of x are determined according to the recommendations of work [1], [4]

$$x = 1 - e^{-6.908 \cdot \left(\frac{\varphi}{\varphi_z}\right)^{m+1}} = 1 - e^{-6.908 \cdot \left(\frac{t}{t_z}\right)^{m+1}} \tag{6}$$

where x —the part of fuel burnt by the time t ; m —the indicator of combustion character; and t_z —conditional duration of the combustion process.

3 Research Methodology

Studies on the relationships between the fuel-air mixture composition with duration and the heat losses during combustion were carried out using tools for indicating the gas pressure in a diesel cylinder.

Researches were carried out on diesels with liquid and air cooling, types 1Ch15/16, 1Ch15/20.5, 1Ch15/18 without supercharging and with supercharging, working on various modes of loading and crankshaft rotation speeds. The engine speed range was from 1000 to 2000 min^{-1} . The test diesels had direct injection of fuel, semi-divided and undivided combustion chambers in the piston, in which various methods of mixture formation and combustion were implemented.

The method of investigation assumed the determination of loading characteristics of diesel engines with flow-rate measurement of air, fuel, temperature of exhaust gases, pressure, and charge air temperature. To identify the relationship



between the mixture composition and the combustion process duration, was used the original software package to lead the thermodynamic analysis of almost 600 experimental gas pressure indicator diagrams in a cylinder. As a result of the analysis, were determined the characteristics of fuel burnup and the parameters of the combustion process.

4 Determination of Heat Losses and Combustion Efficiency Coefficient

The mixture composition, characterized by the coefficient of excess air, determines the intensity of the fuel combustion, which affects the combustion process duration [5–11]. In this case, the relative heat losses during the fuel combustion are characterized by a combustion efficiency coefficient ζ .

The coefficient of combustion efficiency takes into account all types of heat losses for the combustion process and is one of the most important parameters that determine the indicator efficiency of the working cycle. The heat losses for the dissociation of gases in diesel, the maximum operating temperature in which rarely exceeds 2000 K, are insignificant in comparison with the losses of heat in the walls of the cylinder. The loss of heat due to incomplete fuel combustion depends mainly on the excess air factor α . The heat losses to the walls of the cylinder are realized both by convection and by radiation. These heat losses are significantly determined by the fuel burnout time—the duration (t_z , s , or φ_z , degrees CA) of the fuel burnout process.

Summarizing the results of the investigations and thermodynamic analysis of the experimental gas pressure indicator diagrams in the cylinder, the duration of the fuel combustion process is determined from the excess air factor at different rotate speeds of the crankshaft n (Fig. 1). An analysis of this dependence shows that with the excess air factor increase, the combustion process duration decreases, and it goes faster, the higher the speed of the crankshaft. With the same value of α , increasing the rotate speed causes an increase in the combustion process duration. The most significant change in φ_z is observed in the region of small excess air coefficient ($\alpha < 2.5$). The excess air factor characterizes the mixture composition and has a significant effect on the fuel burnup rate of the. It was shown above that the combustion process duration is determined by the intensity of fuel burnout, more precisely by its characteristic parameters. Therefore, establishing the relationship between the excess air factor and the combustion process duration, the dependence of the fuel burnup intensity on the mixture composition.

Analysis of the experimental gas pressure indicator diagrams in the cylinder also allows to obtain the dependence of the combustion efficiency coefficient on the excess air factor at different rotate speeds of the crankshaft n (Fig. 2).

The increase in the excess air coefficient leads to an increase in the combustion efficiency coefficient. The greatest change in the combustion efficiency coefficient takes place at values of the excess air factor $\alpha < 2.5$. With an increase in the speed

Fig. 1 Dependence of the combustion process duration on the excess air factor at different rotate speeds of the crankshaft

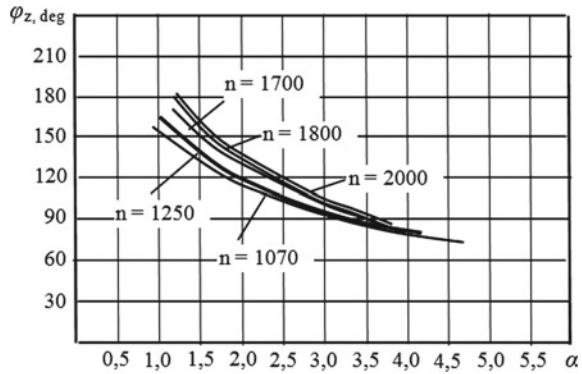
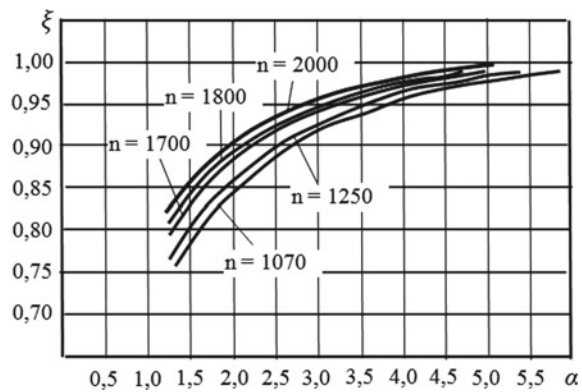


Fig. 2 Dependence of the coefficient of fuel combustion efficiency on the coefficient of excess air at different speeds of the crankshaft



of the crankshaft with a constant value of the excess air factor, the combustion efficiency coefficient increases, which is explained by the decrease in the burnout process time.

Using two empirical dependencies: the combustion process duration and the combustion efficiency factor on the excess air factor, we obtain the desired relationship between the efficiency coefficient and the combustion process duration for different values of the excess air factor and the rotate speed of the crankshaft (Fig. 3). An analysis of this relationship indicates a decrease in α with an increase in the combustion process duration, and this decrease is the more intensive, the lower the speed of the crankshaft.

The dependence in picture three for the convenience of analyzing the obtained results, it is advisable to rebuild taking into account the equation $t = 6 \cdot n/\varphi$, expressing the relative heat losses of the combustion process through the combustion efficiency coefficient $x_{\text{loss}} = 1 - \xi$ (Fig. 4). The heat losses for the combustion process are proportional to the time—the burnout time of the fuel t_z . This dependence can be characterized as linear.



Fig. 3 Dependence of the coefficient of fuel combustion efficiency on the combustion process duration, the coefficient of excess air, and the speed of the crankshaft

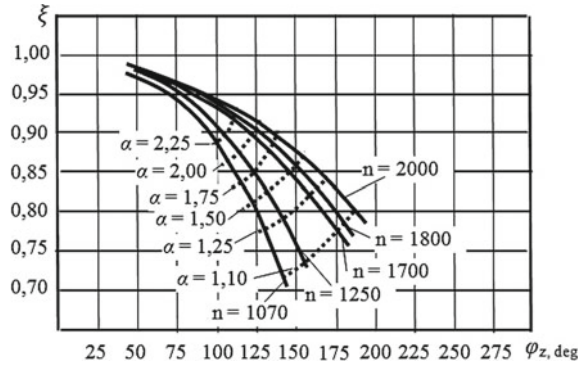
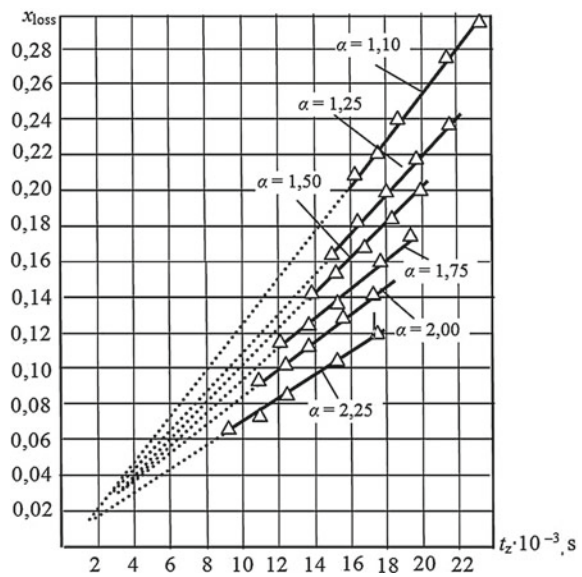


Fig. 4 Dependence of heat losses on the combustion duration and the excess air coefficient



The lower the excess air factor, the more significant the dependence of the heat losses during the combustion process on its duration.

With an increase in the excess air factor, the intensity of the change in the heat losses of the combustion process in the investigated range decreases from 1.29×10^{-5} to $0.62 \times 10^{-5} \text{ s}^{-1}$, i.e., almost 2 times. The obtained dependence can be used in a calculated study of the operating cycle under conditions of changing the excess air factor and the combustion process duration, as well as in the analysis of fuel burnout in the diesel engines with semi-divided combustion chambers.

For ease of use, the graphical representation shown in picture four is approximated by expression



$$x_{\text{loss}} = 1 - \xi = 14.3 \cdot \frac{t_z}{\alpha} = 2.38 \cdot \frac{\varphi_z}{n \cdot \alpha} \quad (7)$$

Here, the combustion efficiency coefficient can be determined

$$\xi = 1 - 14.3 \cdot \frac{t_z}{\alpha} = 1 - 2.38 \cdot \frac{\varphi_z}{n \cdot \alpha} \quad (8)$$

To calculate the combustion efficiency factor in Eq. (8), the duration of the combustion process should be expressed in seconds or in degrees CA with the crankshaft speed in min^{-1} .

5 Conclusion

The coefficient of combustion efficiency in the cylinder should be considered as the most important integral criterion for evaluating the efficiency of the combustion process in the working cycle of a diesel engine since it estimates the completeness of the generation and use of heat.

The generalization of the thermodynamic analysis results of the set of pressure diagrams in the cylinder of various types of diesel engines allows to establish:

- the combustion process duration decreases with increasing excess air factor, the more intensive the higher the rotate speed of the crankshaft;
- the combustion process efficiency increases with the increase in the excess air factor, the more intensive the lower the speed of the crankshaft;
- the combustion efficiency coefficient increases with the reduction of the combustion process duration, the more intensive the lower the rotate speed of the crankshaft and the higher the excess air ratio;
- the dependence of the combustion efficiency coefficient on the combustion process duration, the speed of the crankshaft, and the excess air coefficient, reflecting the physical features of heat transfer in conditions continuously variable volume of the cylinder of the operating diesel, can be used in the synthesis of the operating cycle.

References

1. Vibe II (1970) Brennvlauf und Kreisprozeß von Verbrennungsmotoren. VEB Verlag Technik, Berlin
2. Ivashenko NA, Kuleshov AS (2009) Mathematic modeling of the processes in internal combustion engines. MNTK Turbocharging of Automobile and Tractor Engines, Protvino, pp 5–8

3. Marchenko AP, Osetrov AA, Linkov OY (2013) Mathematical model of the combustion process in diesel. *Internal Comb Engin* 1:3–10
4. Lazarev EA (2010) Basic principles, methods and efficiency of improving the combustion process to increase the technical level of tractor diesel engines: monograph. SUSU Publishing Center, Chelyabinsk
5. Razleytsev NF (1980) Design and optimization of the combustion process in diesel engines. Visha shkola, Kharkov
6. Grekhov LV, Ivashchenko NA, Markov VA (2004) Fuel injection equipment and the systems of control of diesel engines. Legion-Avtodata, Moscow
7. Lazarev EA, Arav BL (1974) Influence of the type of the differential fuel burn-up characteristic on the duty cycle of the diesel engine. In: Questions of designing and researching tractors and tractor engines, pp 200–211
8. Zakharov LA, Sezamin AV, Tarasov AV, Zakharov IL (2013) Method for controlling the combustion process of a high-speed diesel engine and analysis of the results of calculation and experimental studies of reducing thermal loads. *J Autom Eng* 4:24–27
9. Tatschl R, Berg EV, Bogensperger M, Kuensberg ChV, Priesching P (2002) Priesching.CFD in IC-engine spray and combustion simulation-current status and future development. In: Fifth World Congress on Computational Mechanics, Vienna, pp 13–16
10. Malozemov AA (2015) Development of software for calculation and optimization of diesel operating processes and fuel supply. *Proced Eng* 129:724–730
11. Kavtaradze RZ (2008) Theory of piston engines. Textbook for universities, Publishing House MSTU N.E. Bauman, Moscow, Special chapters

Determination of Parameters and Characteristics of Injection in Fuel System of Accumulating Type at Cold Start of the Diesel Engine



V. V. Shishkov and E. A. Lazarev

Abstract To the accumulating type fuel system, a study of fuel delivery processes for low-temperature start-up conditions was performed. The quality deterioration of fuel atomization occurs as a result of the injection pressure decrease and the back pressure in the combustion chamber at low cranking speeds of the crankshaft. Lowering the temperature, increasing the viscosity of the fuel affects the quality of atomization. As a result of the enlargement of fuel droplets, a significant part of it falls on the cold walls of the combustion chamber. The authors estimated the influence of low temperatures and pressures in the high-pressure line of the system on the characteristics of fuel injection and atomization in the combustion chamber. To improve the quality of the distribution of fuel in the volume of the combustion chamber allows multiphase injection. Local fuel heating in the nozzle may have a great influence on the starting characteristics of the diesel. This contributes to a better distribution of fuel in the combustion chamber volume, crushing the fuel into smaller droplets, reducing the time for heating and evaporation of the fuel.

Keywords Diesel · Fuel system · Cold start, fuel injection · Fuel delivery parameters · Electromagnetic nozzle

1 Introduction

The modern scientific and technical level of the engine-building development makes it possible to find solutions for ensuring the running characteristics of diesel engines in areas with harsh climatic conditions. Low ambient temperatures create difficulties for starting diesel engines with unsatisfactory starting characteristics. For a significant part of diesel engines with an electric starter, a reliable start is possible at temperatures not lower than minus 5–10 °C. At lower temperatures, special means are used to facilitate the cold start of a diesel engine [1]. In this case, as a

V. V. Shishkov (✉) · E. A. Lazarev
South Ural State University, 76, Lenin Avenue, Chelyabinsk 454080, Russia
e-mail: shishkovvv@susu.ru

rule, a set of technical solutions and means are used to improve the starting characteristics, in particular, a starting system that ensures the required crankshaft starting frequency, low-viscosity engine oil and tools that facilitate ignition of the fuel. Along with solving the problem of low-temperature diesel starting, more and more attention is paid to solving the problems of reducing acoustic noise levels [2], emissions of unburned fuel, soot, CH, CO, NO_x [3, 4]. The solution of these problems is provided by the parameters and characteristics of the air supply and fuel supply processes, the intensity of the vortex formation of the airflow, the atomization, the distribution of fuel in the volume of the combustion chamber, evaporation, mixture formation, ignition, and combustion of fuel. For a traditional fuel equipment, at start-up, it is typical to see an increase in fuel leakage through the gaps of the plunger pair and a reduction in the cycle fuel supply. The quality deterioration of fuel atomization occurs as a result of the injection pressure decrease and the back pressure in the combustion chamber at low cranking speeds of the crankshaft. Lowering the temperature, increasing the viscosity of the fuel affects the quality of atomization. As a result of the enlargement of fuel droplets, a significant part of it falls on the cold walls of the combustion chamber. To improve the quality of start-up, the cyclic fuel supply is usually increased by 1.5–2 times bigger than the cyclic values at nominal rating power or to the level of 100–120 mg per liter of the cylinder volume. This approach does not tend to solve problems of reducing acoustic noise and harmful emissions. In addition, excessively large cyclic fuel supply can degrade the starting quality of a diesel engine. This happens due to the fact that the evaporation of a larger amount of fuel consumes more heat supplied to the working fluid during compression.

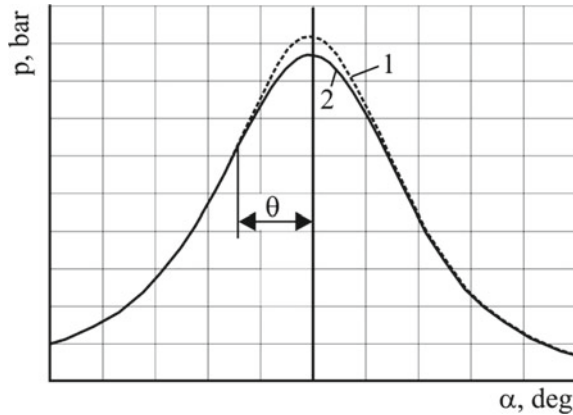
2 The Results of Numerical Simulation

From the beginning of fuel injection θ on the indicator diagram of the working fluid pressure, a decrease in pressure and, consequently, decrease in temperature. It can be observed in comparison with the indicator diagram obtained in cycles without fuel injection under other equal conditions (Fig. 1). The cyclic fuel supply is 170 mm³, the actual injection advance angle is $\theta = 18^\circ$ of crankshaft turn before upper dead center, and the maximum pressure of the working fluid in the cylinder without fuel injection is 26.5 bar (curve 1), with injection of 25 bar (curve 2).

The use of a “Common Rail” accumulator fuel injection system, thanks to efficient control, improves injection parameters during cold start and significantly simplifies the regulation of the actual angle of the injection start and cyclic feed for the period of starting and warming up the diesel engine up to the use of multiphase fuel injection per cycle.

The materials presented in the article were obtained by simulating the fuel supply process in the BOOST HYDSIM software package (licensed by AVL GmbH to South Ural State University under a scientific cooperation agreement).

Fig. 1 Diagram of the working fluid pressure change in the cylinder when starting the diesel



There is an experience of a joint approach to the description of 1D/3D for modeling fuel injection [5]. During the period of the injection process in BOOST HYDSIM, data is generated for 3D modeling of the mixture formation processes and subsequent combustion using the FIRE software package. Such approach considered as modern and advanced for modeling processes in solving problems of ensuring an effective and environmentally safe start-up of a cold diesel engine. At this stage of the research, the adequacy of BOOST HYDSIM in terms of fuel injection modeling during cold-engine start-up was estimated, with the aim of using the results for one-dimensional [6] and 3D modeling of evaporation, mixture formation, and combustion in a diesel cylinder.

During the simulation, the parameters of the fuel injection process in a 6CHN13/15 diesel engine were determined in the rated power mode. The fuel injector nozzle has five nozzle vents with a diameter 0.3 mm. Diesel fuel under normal conditions is characterized by the following parameters: density 865 kg/m^3 ; kinematic viscosity is $1.7 \text{ mm}^2/\text{s}$. The fuel temperature in the rated power mode is $40 \text{ }^\circ\text{C}$ and the cyclic feed reaches 177 mm^3 . For the initial pressure in the fuel accumulator is 150 MPa, the injection duration is 1.681 ms or 21.2° . The open time of the injector solenoid valve is 1.406 ms or 17.7° . The needle lift of the nebulizer was 0.3 mm. Wave phenomena in the fuel system increase the pressure in front of the nozzle orifice up to 140 MPa (Fig. 2).

The parameters of fuel atomization depend on the pressure in front of the nozzle holes: the average diameter of the droplets, the angle of the cone, and the length of the atomized fuel jet. In this case, the calculation should take into account the effect of temperature, kinematic viscosity of the fuel, and other factors on the atomization parameters under study.

Based on the analysis of the existing mathematical calculation models capabilities [7], their reliability, fuel equipment, and simulation conditions for the diesel engine under study, the choice was made in favor of the following models from those offered by the BOOST HYDSIM service. Thus, the average diameter of the sprayed fuel droplets was determined by the dependence [8]

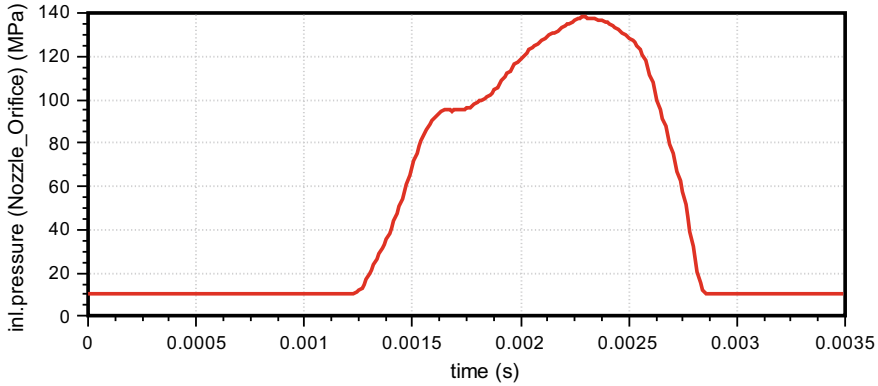


Fig. 2 The dependence of the pressure in front of the nozzle orifice as a function of time during fuel injection

$$d_{32} = \frac{12.392 \cdot d_{\text{hole}}^{0.44} \cdot \rho_D^{0.42} \cdot \sigma_D^{0.28} \cdot \nu_D^{0.28}}{\Delta p^{0.42} \cdot \rho_G^{0.28}} \quad (1)$$

The angle of the cone of the sprayed fuel jet [8] without taking into account the speed of the air vortex in the combustion chamber was determined by the equation

$$\alpha = \frac{320 \cdot \Delta p^{0.15} \cdot \rho_G^{0.25}}{\rho_D^{0.45} \cdot \nu_D^{0.1} \cdot \left(3 + 0.28 \frac{l_{\text{hole}}}{d_{\text{hole}}}\right) \mu_{\text{coeff}}^{0.2}} \quad (2)$$

The length of the sprayed fuel jet was estimated by the equations of [9]

$$t_B = 28.65 \frac{\rho_D \cdot d_{\text{hole}}}{(\rho_G \cdot \Delta p)^{0.5}};$$

$$\text{if } t < t_B \text{ then } S = 0.39 \cdot t \cdot \sqrt{\frac{2}{\rho_D} \Delta p}; \quad \text{if } t \geq t_B \quad (3)$$

$$\text{then } S = 2.95 \cdot \left(\frac{\Delta p}{\rho_G}\right)^{0.25} \sqrt{d_{\text{hole}} \cdot t}$$

In the above formulas: d_{hole} —nozzle hole diameter; l_{hole} —nozzle hole length; ρ_D —fuel density; σ_D —fuel surface tension ratio; ν_D —fuel kinematic viscosity; Δp —pressure difference; ρ_G —gas density; μ_{coeff} —nozzle-discharge coefficient; t —time from start of injection.

The parameters of the sprayed fuel jet for the fuel injection process are as follows: the average diameter of the droplets is 5–6 μm , the fuel jet cone angle is 32–33° of crankshaft turn, and the fuel jet maximum length is 70 mm.

The temperature at which the diesel engines start-up remains possible without preheating, usually not less than minus 20–25 °C. But at these temperatures, special actions are needed to facilitate the start. These include the use of low-viscosity engine oils to provide starting frequencies for cranking the engine and means for igniting the fuel, such as heating the intake air or using glow plugs.

The starting mode of a diesel engine is characterized not only by a lowered fuel temperature, but also by low fuel pressure in the accumulator. From the beginning of cranking the crankshaft for one or two turns, the fuel pump creates a pressure of at least 20–30 MPa, and at low rotation frequencies of the crankshaft, the fuel pressure rises to 50 MPa. Thus, the cold start mode of a diesel engine corresponds to the range of change in the battery fuel pressure from 30 to 50 MPa. The starting frequency for cranking the crankshaft at an ambient temperature of minus 20 °C is 150 min⁻¹. The pressure of the working gas in the cylinder (compression pressure) in this case is 3 MPa. The pressure in the fuel accumulator was set constant at 30, 40, and 50 MPa; the initial pressure at the inlet to the atomizer (Fig. 3) is equal to the pressure in the fuel accumulator. In Figs. 3 through 6, the solid line corresponds to the fuel pressure in the accumulator of 30 MPa, the dotted line—40 MPa, and the dash-dotted line—50 MPa.

The duration of the open state of the injector solenoid valve 0.00333 s or 2.99° of crankshaft turn was set so to get following—when the fuel pressure in the accumulator is 30 MPa, the volume of injected fuel is equal to the cycle supply in the rated power mode (Fig. 4). Compared with the nominal power mode, the injection duration increased in time to 0.00426 s (Fig. 5) and decreased in the angle of rotation of the crankshaft to 3.83° of crankshaft turn. With an increase in fuel pressure up to 50 MPa, the cycle feed increased to 231 mm³, the injection duration remains unchanged.

The accumulator pressure increase leads to the lift speed increase of the nebulizer needle, but the maximum value of the lift changes insignificantly (Fig. 6).

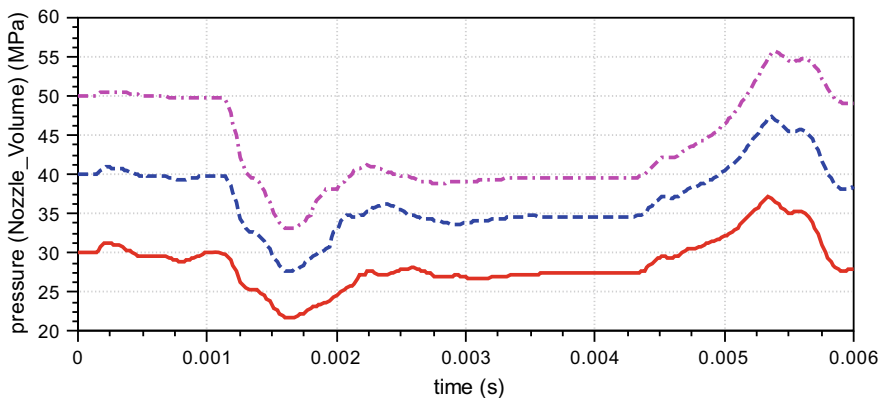


Fig. 3 The dependence of the fuel pressure at the inlet to the sprayer as a function of time during the injection process



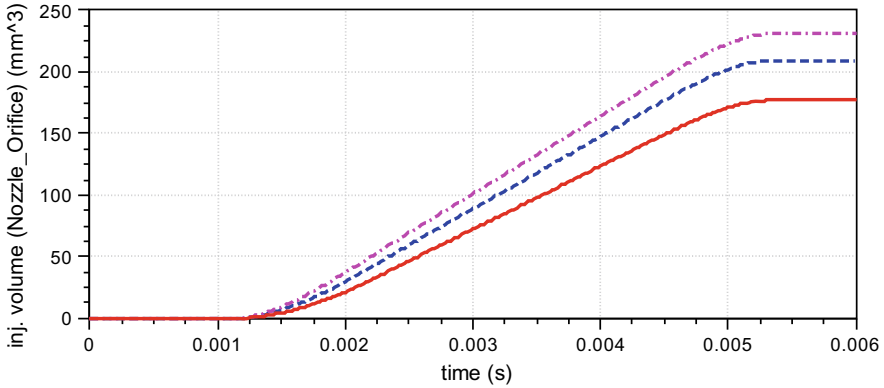


Fig. 4 Integral fuel injection characteristic

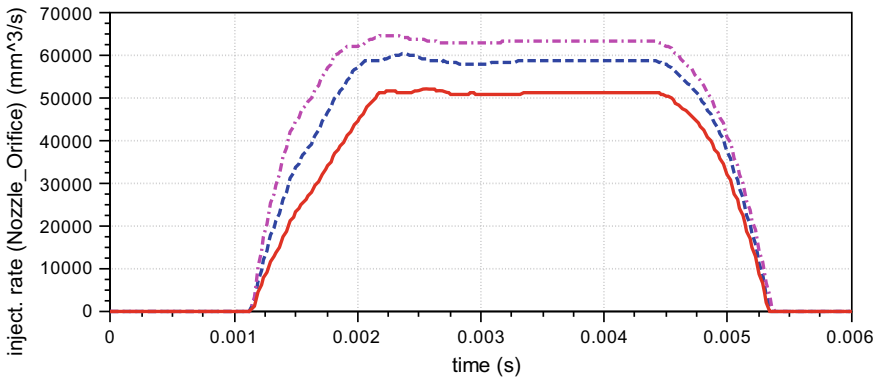


Fig. 5 Differential fuel injection characteristic

Low pressure and temperature of the fuel significantly affect the parameters of the sprayed fuel jet. The average droplets diameter of sprayed fuel in the nominal power mode are 5–6 μm , and under starting conditions 40–47 μm , the cone angle of the sprayed fuel jet, respectively, decreased from 32–33° to 13, and the fuel jet length increased from 70 mm to 105–115 mm. The fuel droplets diameter decreases with increasing injection pressure, and the length of the fuel jet increases. Large fuel drops evaporate slowly. The low angle of the fuel jet indicates an uneven distribution of fuel in the volume of the combustion chamber. Up to 38–43% of the fuel jet length extends beyond the boundaries of the cylinder wall, as a result of which the fuel falls on the cold walls. To improve the quality of the distribution of fuel in the volume of the combustion chamber allows multiphase injection [10, 11]. With a multiphase injection, the fuel jet length in each phase depends on the duration of the injection.

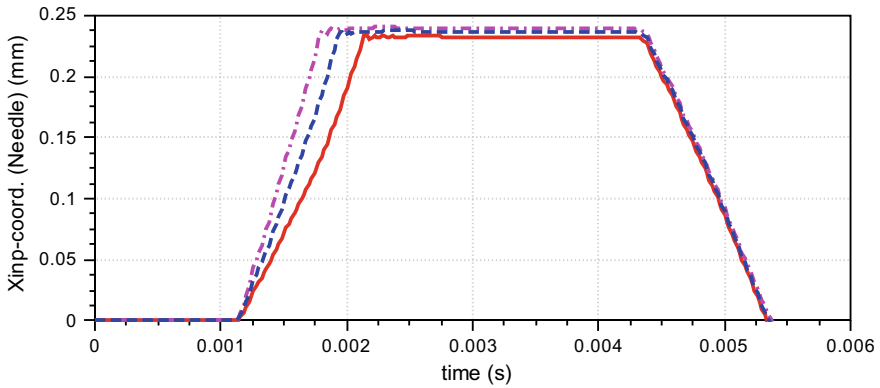


Fig. 6 The dependence of the sprayer needle lift from time

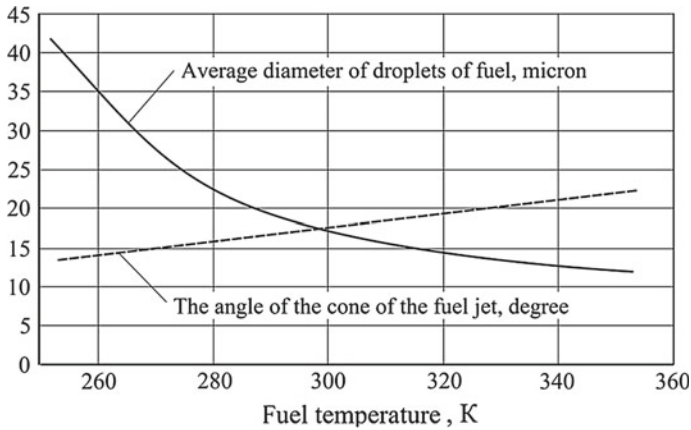


Fig. 7 Effect of temperature on parameters of the fuel injection and atomization

Local fuel heating in the nozzle may have a great influence on the starting characteristics of the diesel. This contributes to a better distribution of fuel in the combustion chamber volume, crushing the fuel into smaller droplets, reducing the time for heating and evaporation of the fuel. As the temperature rises, the angle of the fuel jet cone increases monotonically (Fig. 7), the diameter of the fuel droplets decreases and the most intense change in diameter occurs at low temperatures.

3 Conclusion

The BOOST HYDSIM software package meets the conditions of low-temperature start-up modeling and allows evaluating the influence, primarily, of such factors as fuel temperature and pressure, the influence of structural elements of the fuel supply system on the injection parameters and fuel atomization characteristics in the combustion chamber, and therefore, evaluate the effectiveness of technical measures affecting diesel starting characteristics, fuel injection, and atomization parameters.

The software package allows you to create the necessary databases (fuel pressure before the nozzle orifice during the injection period, average droplet diameter, cone angle, sprayed fuel jet length, etc.) for their implementation in 1D and 3D thermodynamic models for calculating evaporation, mixture formation, ignition and combustion determining the level of acoustic noise, the level of emissions of unburned fuel, soot, HC, CO, NO_x.

References

1. Kwright SM, Mendelevich YA, Chizhkov YuP (1990) Starting qualities and systems of start-up of autotractor engines. Mashinostroenie, Moscow, p 255
2. Alt N, Sonntag H, Heuer S, Thiele R (2005) Diesel engine cold start noise improvement. SAE Technical Paper 2005-01-2490
3. Liu H, Henein N, Bryzik W (2003) Simulation of diesel engines cold-start, SAE Technical Paper
4. Han Z, Henein N, Nitu B, Bryzik W (2001) Diesel engine cold start combustion instability and control strategy. SAE Technical Paper
5. Čaika V, Sampl P, Tatschl R, Krammer J, Greif D (2009) Coupled 1D-3D simulation of common rail injector flow using AVL HYDSIM and FIRE, ICE 2009, Capri, Italy, SAE International, Paper Number 2009-24-0029
6. Shishkov VV (2016) Start cold diesel. Modeling processes in the cylinder. In: In the collection: industrial engineering proceedings of the II international scientific and technical conference, pp 107–110
7. Herzog Peter L (1989) Möglichkeiten, Grenzen und Vorausberechnung der einspritzspezifischen Gemischbildung bei schnelllaufenden Dieselmotoren mit direkter luftverteiler Kraftstoffeinspritzung. Fortschr.-Ber. VDI, Reihe 12 Nr. 127. VDI-Verlag, Düsseldorf
8. Varde K, Popa D, Varde L (1984) Spray angle and atomization in diesel sprays. SAE Technical Paper 841055
9. Arai M, Tabata M, Hiroyasu H, Shimizu M (1984) Disintegrating process and spray characterization of fuel jet injected by a diesel nozzle. SAE Papers 840275:34–36
10. Kukharenek GM, Marchuk AN (2011) The method of determining the parameters of fuel in diesel engines on the start mode. Sci Technol 1:40–47
11. Kukharenek GM, Marchuk AN, Petruchenko AN (2012) Starting qualities of diesel engines with battery fuel supply system. BNTU, Minsk, p 173

Influence of Main Design Parameters of Motion Conversion Mechanism of Crankless Reciprocating Machine (Engine) on Torque Value on Output Shaft



B. A. Sharoglazov and V. V. Klementev

Abstract The paper describes the solution of the problem of determining the relationship of the main design parameters of the motion conversion mechanism with the design and technical parameters of a crankless reciprocating machine (engine) and identifying the influence of these parameters on the machine performance, as well as the value of the developed torque on the output shaft as compared to the crank-rocker internal combustion engine. The comparison is made based on the similarity (identity of the parameters characterizing the conditions for the implementation of the working cycle of a heat engine) of the working processes flowing in a cylinder of a crankless machine and a crank-rocker engine. A conclusion is made on the advantage of the crankless machine concerning the design of high-torque engines. Practical recommendations are given on the choice of design parameters depending on the technical requirements, the purpose, and sphere of application of the crankless machine.

Keywords Heat engine · Combustion engine · Crankless engine · Working cycle · Torque · Conversion mechanism · Design parameter

1 Introduction

The article reviewed influence of the main design parameters of the motion conversion mechanism of a crankless reciprocating machine (Engine) on the torque value on the output shaft under the conditions for the implementation of the working cycle similar to crank-rocker ICs.

The practice of modern engine -building imposes increasingly stringent requirements to the creation of energy- and resource-efficient reciprocating and combined internal combustion engines (ICE) characterized by high technical and

B. A. Sharoglazov (✉) · V. V. Klementev
South Ural State University, 76, Lenin Avenue, Chelyabinsk 454080, Russia
e-mail: sharoglazovba@susu.ru

economic indices and operating characteristics. At the same time, there is a request for the creation of a scientific-technical and design-technological breakthrough in the field of reciprocating engine building. Although there are available reserves for the improvement of “conventional” engines, which basic design contains a crank-and-rod mechanism (CRM) as a system converting the crank motion of the piston (pistons) into the crankshaft rotation, see, for example, [1, 2], but they are exhausted to a large extent. The issues of improving the technical-economic and mass-dimensional indicators of reciprocating and combined internal combustion engines through the use of the opportunities provided by the kinematic diagrams of conversion mechanisms other than the crank-and-rod diagram currently remain relatively underdeveloped both in theory and in practice [3–10].

The department of “Internal Combustion Engines and Electronic Systems of Vehicles” of the South Ural State University developed a crankless reciprocating machine—engine (CRM(E)). The CRM(E) does not contain such expensive, process complicated, overall and massive parts of the “conventional” ICE as a crankshaft and connecting rods. This machine, as opposed to some other internal combustion engines of non-conventional configurations, is reversible and can be implemented as a reciprocating compressor or a pump. The design diagram of the CRM(E) and a number of technical solutions for such a machine are protected by more than 20 utility model patents and certificates of the Russian Federation, for example, [11–13], etc.

Therefore, the works connected with solving the problems of creating promising energy- and resource-efficient internal combustion engines based on unconventional design diagrams (in particular, crankless heat engines) are relevant [14].

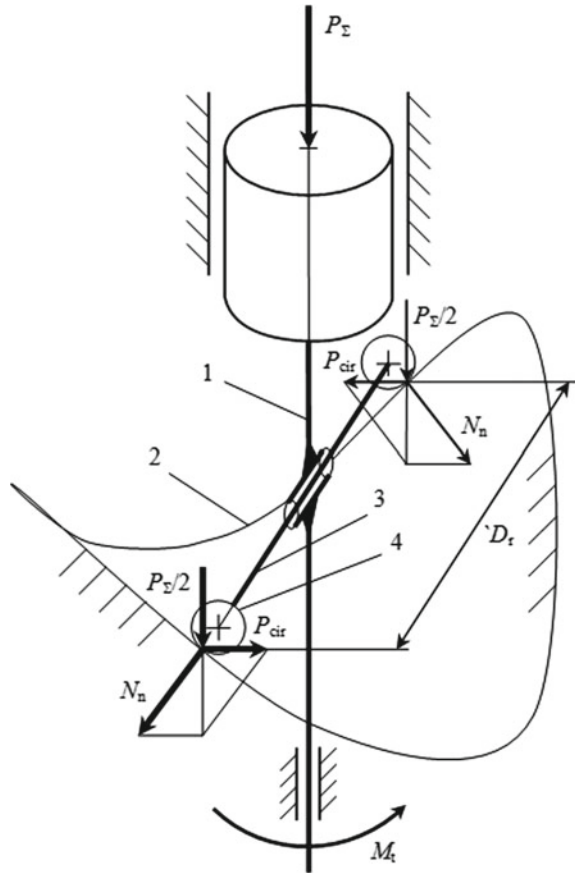
2 Brief Description of the Diagram for Determining the Torque of the Crankless Machine (Engine)

Figure 1 shows a principle diagram of the motion conversion mechanism (MCM) to a crankless reciprocating machine (engine). Other diagrams of machines of this type are published, for example, in [15, 16].

Such a machine is operated as follows. During the combustion and expansion of the working fluid, gases in the cylinder cause the piston to move from one extreme position to another. During its movement, the piston interacts with the curvilinear longitudinal treadmill (TM) made, for example, in a machine body, by means of centrifugal or axially symmetric rotary bodies (balls, rollers, sliders or rolling bearings, etc.). The regular coordination and synchronization of the components of the complex movement obtained in this way are ensured by a relevant profiling of the treadmill. The rotational component of this movement is transmitted to the mechanical energy consumer connected to the output shaft of the machine.

Figure 1 also shows the polygons of the forces acting in the MCM and leading to the appearance of the torque on the output shaft of the machine:

Fig. 1 Principle (isometric) diagram of the CRM(E) and the forces acting in it (as applied to the case of a two-period treadmill): 1—piston rod; 2—treadmill; 3—axis of the MCM carriage (the carriage is not shown in the diagram); 4—rollers mounted on the axis (in the calculations, their radius is assumed to be 0)



- P_Σ total force acting on the piston;
- N_n normal force acting perpendicular to the working surface of the TM at the point of contact between the TM and the rotary body of the MCM;
- P_{cir} circumferential force acting in a plane perpendicular to the axis of the cylinder and directed tangentially to a circle lying in this plane and passing through the point of contact between the TM and the rotary body of the MCM;
- D_r reactive diameter—the diameter of the projection of the TM middle line on the plane perpendicular to the axis of the cylinder;
- M_t torque on the output shaft of the machine.

In the case shown in Fig. 1, when M_t is formed, we take into account two polygons of forces corresponding to the design of the MCM containing two rotary bodies interacting with the TM. In general, depending on the number of periods (“waves”) of the treadmill, the motion conversion mechanism of the CRM(E) may contain one, two or more rotary bodies. In such cases, the corresponding number of polygons of forces forming M_t should be taken into account.

3 Main Design Parameters of the Crankless Machine (Engine) Influencing the Torque Formation

The parameters of the motion conversion mechanism of the CRM(E) reflect the kinematic features of the motion conversion method underlying the design of the machine. Consequently, these parameters have a direct impact on the characteristics of the machine including the developed torque.

The main parameters of the motion conversion mechanism of the CRM(E) include:

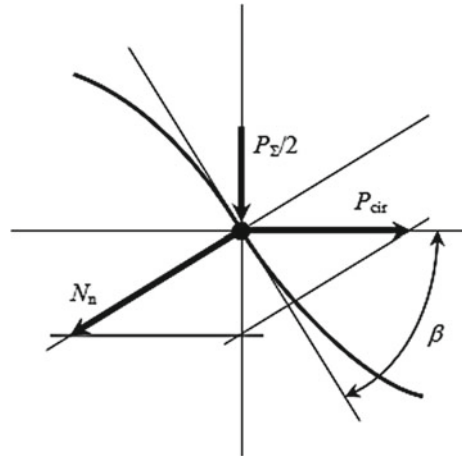
- S_p full stroke of the piston;
- D cylinder diameter;
- D_r reactive diameter (see Fig. 1);
- N number of TM periods equal to the number of rotary bodies (“points of support”) of the MCM (it should be noted that in the paper, the symbol N_n denotes the vector of the roller’s normal action on the TM surface);
- β slope angle of the TM to the plane perpendicular to the axis of the piston (cylinder) determined as an angle between the tangent to the TM at the point of contact between the TM and the rotary body of the MCM through a point of the circle lying in the plane perpendicular to the axis of the cylinder (Fig. 2).

The dependence of angle β on a number of geometrical parameters of the kinematic diagram of the CRM(E) can be expressed by the ratios (as applied to the case of a sinusoidal profile of the TM under the following initial conditions) [17]:

$$\beta = -\operatorname{arctg} \left[2 \left(\frac{S_p}{D_r} \right) \sin 2\alpha \right]; \quad (1)$$

$$\beta = -\operatorname{arctg} [2\mu_\alpha \mu_s \sin 2\alpha]; \quad (2)$$

Fig. 2 Diagram of the decomposition of forces acting at the point of contact of the roller with the surface of the TM (along the axis of the TM)



where $\mu_x = \frac{2}{D_r}$ and $\mu_s = \frac{S_p}{2}$ scale factors of the horizontal and vertical conversions of the TM, respectively, determining the change in the shape of the “theoretical” curve characterizing the treadmill, depending on the actual geometric parameters of the MCM;

α —rotation angle of the rod (output shaft) of the machine; in the written expressions, its initial value, the point of reference, is assumed to be 0 degrees of the MST (main shaft turn), when the piston is at the top dead center (TDC).

In the general case (in case of an N -period TM), expressions (1) and (2) will take the form:

$$\beta = -\arctg \left[N \left(\frac{S_p}{D_r} \right) \sin N\alpha \right]; \quad (3)$$

$$\beta = -\arctg [N\mu_x\mu_s \sin N\alpha]. \quad (4)$$

The expressions for determining the normal force and the circumference force acting at one point of the MCM support have the following form, respectively:

$$N_n = \frac{P_\Sigma}{N \cos \beta}; \quad (5)$$

$$P_{\text{cir}} = \frac{P_\Sigma}{N} \text{tg} \beta. \quad (6)$$

$$P_\Sigma = P_f - P_p + P_j \quad (7)$$

The resulting (total) force acting on the piston of the crankless machine during its operation, where P_f is the pressure force of the working fluid; P_p is the pressure force of gases in the piston chamber; P_j is the inertial force of the reciprocating moving masses of the mechanism.

The torque that appears at one point of the MCM support when all the points of support are located on one and the same diameter D_r (which, in the private case, can be equal to D) is determined by the ratio:

$$M = P_{\text{cir}} \frac{D_r}{2} = \frac{D_r}{2N} P_\Sigma \text{tg} \beta. \quad (8)$$

4 Influence of the Main Design Parameters of the Crankless Machine (Engine) on the Operating Conditions of the Motion Conversion Mechanism

Analyzing dependencies (1)–(4), it can be determined that with an increase in the ratio S_p/D_r of the machine, angle β is also increased, i.e., the angle, at which the forces arising in the conversion mechanism act on the working surface of the

treadmill during operation. Consequently, an increase in the ratio S_p/D_r can result in the fact that the value of this angle goes beyond the allowable limits, and consequently, in a violation of the operability conditions of the conversion mechanism. Thus, there arises the problem of determining the area of the most efficient operation of the conversion mechanism according to the operating conditions of the crankless machine (in particular, according to the parameters S_p , D_r , K , N , β).

The results of the presented, calculated and theoretical study using the developed logical-mathematical tool allowed us to establish that to ensure the performance of the machine, the piston stroke S , the cylinder diameter D , the reactive diameter $D_r = K \cdot D$ and the number of periods of the treadmill N should comply with the ratio (see, for example, [18]):

$$0.577 \cdot \frac{K}{N} \leq \frac{S_p}{D} \leq 1.732 \cdot \frac{K}{N}. \quad (9)$$

The calculated and theoretical study of the influence of the main design parameters of the motion conversion mechanism involved in the formation of the torque of the crankless machine on the operating conditions of its mechanism made it possible to suggest a polygraph of functional parameters (PFP) of the CRM(E). The PFP of the crankless machine mechanism is a multiparameter nomograph that qualitatively and quantitatively reflects the complex interconnection of the main functional parameters of the crankless machine mechanism, such as the piston stroke S_p , cylinder diameter D , reactive diameter D_r , coefficient K , maximum slope angles of the treadmill β_{\max} , and number of periods of the treadmill N . The PFP allows us to determine the most important design ratios and the main geometrical parameters of the MCM elements of crankless machines at the stages of design engineering taking into account their class (dimension), purpose and operating features. One of the variants of the PFP (for crankless machines with sinusoidal tradmills) is shown in Fig. 3.

With an increase in D_r , all other things being equal (constant values of the piston stroke, number of periods of the MCM treadmill, etc.), the TM is smoothed. In other words, the maximum and minimum slope angles of the treadmill to the plane perpendicular to the axis of the cylinder change (decrease) by a nonlinear relationship. In case of an excessive increase in D_r , this can lead to the fact that the values of the angle β_{\max} go beyond the allowable limits ensuring the operability of the mechanism, and to a decrease in the torque of the crankless machine. The inverse result with respect to β_{\max} and similar consequences concerning the functionality of the kinematic diagram gives an increase in the number of periods of the treadmill N while retaining other design parameters of the CRM(E).

At the same time, an increase in N with a growing value of D_r makes it possible to ensure an increase in the power of the crankless machine obtained per one turn of the output shaft, and hence, an increase in the torque generated on the machine shaft and transmitted to the consumer.

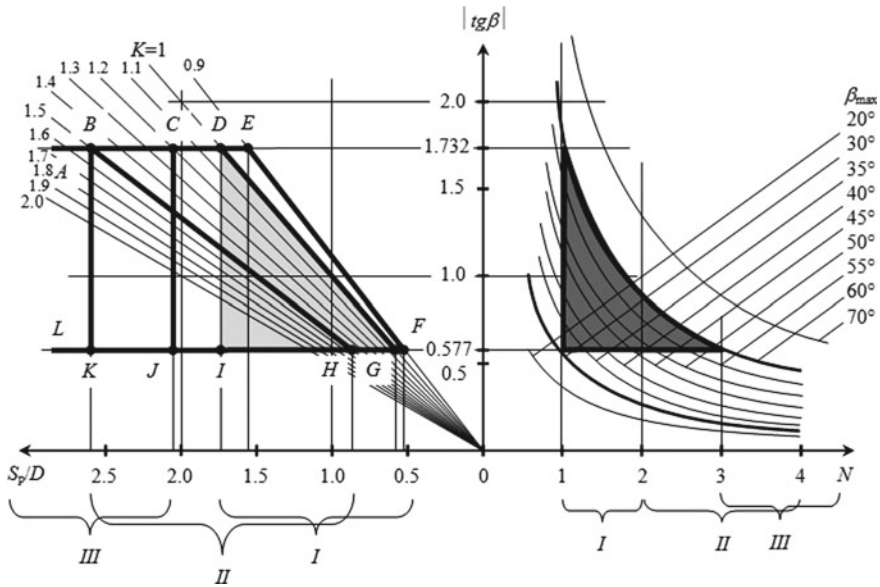


Fig. 3 Polygraph of functional parameters of crankless machines with sinusoidal treadmills: *CEFJ*—high-speed ($S_p > 10$ m/s) machines; *BDGK*—medium-speed machines (S_p about 10 m/s); *ABHL*—low-speed ($S_p < 10$ m/s) machines; *I*—machines with a relatively low M_t (lightly loaded); *II*—medium-loaded machines; *III*—machines with a high M_t (heavily loaded); —area of effective operation of the conversion mechanism; — k -th working area of relative parameters

5 Features of the Formation of the Torque on the Outputs Shaft of the Crankless Machine and Crank-Rocker Engine

Similar conditions for the implementation of the working cycle of the crankless machine-engine and the crank-rocker engine are characterized by the following:

- sameness of design and technical parameters, namely: the diameter of the cylinder, piston stroke, compression degree, number of cylinders, shaft speed (output shaft of the CRM(E) or crankshaft);
- similarity of the conditions ensuring the organization and flow of the working cycle processes in the cylinder of the machine (air excess factor, carburation and combustion conditions, etc.) and the conditions of using the machine—the sameness of the indicator load according to the value of the indicator cycle work.

In conventional, crank-rocker ICEs, one full working cycle can be performed only during one (in two-stroke engines) or two (with a four-stroke cycle organization) revolutions of the crankshaft. A peculiar feature of the kinematic and design diagrams of the CRM(E) mechanism is that, unlike crank-rocker ICEs, more

working cycles can be performed in its cylinder over one revolution of the output shaft of the crankless machine. Consequently, in the CRM(E), it is possible to implement such design solutions that provide a multiple increase in the power as compared to crank-rocker ICEs.

It is shown in [19, 20] that if the indicator cycle operations of a crankless machine and a crank-rocker ICE “corresponding” to it are equal, the power developed by the crankless machine is N times more than the power of the engine with the CRM.

The aforesaid also concerns the torque generated by the crankless machine. A peculiar feature here is that P_{cir} , which is formed in the CRM(E) and is equal to T in ICEs with the CRM, works “on two arms” (other things being equal). This circumstance does not only reduce the load in the MCM but also increases the torque.

At the same time, the limits for increasing the torque of the CRM(E) can multiply increase the corresponding capabilities of engines with the CRM mainly on account of an increase in the periodicity of cycles due to N and the conditions for the formation of P_{cir} .

6 Conclusion

The following main conclusions and practical recommendations were made based on the results of the performed studies.

Based on the proposed logical-mathematical tool for modeling kinematic and dynamic processes, we developed calculation algorithms, which allow us to reveal the peculiar features of the influence of various design solutions of the motion conversion mechanism on the characteristics of crankless machines as applied to different conditions of their use. It is shown that other things being equal, a significantly larger torque can be realized in a crankless machine than in the engine design according to the conventional (crank-rocker) scheme. Thus, for example, the torque of a crankless four-stroke engine with a two-period treadmill, all other things being equal, is twice higher than the torque of a relevant crank-rocker four-stroke engine.

The CRM(E) allows a relatively simple design of high-torque, high-loaded machines, including low-speed, large dimension, etc., in relation to conventional (crank-rocker) engines.

Depending on the class, purpose, and characteristics of the use of crankless machines, it is recommended to use the following ratios of the reactive diameter and the diameter of the cylinder:

- for high-speed and (or) lightly loaded machines, provided that they operate together with the mechanic energy consumer, it is advisable to use motion conversion mechanisms with one- or two-period treadmills at $D_r \approx D$ (see also Fig. 3, areas I , $CEFG$);

- for low-speed, high-loaded, high-torque machines, it is most expedient to use multi-period (with a number of periods of three, four or more) treadmills at $D_r = 1.5-2 D$ in conversion mechanisms (see also Fig. 3, areas III, ABHL);
- in other cases, it may be expedient to use two-period conversion mechanisms with a possible number of treadmills from one to three with $D_r = 1-1.5 D$ (see also Fig. 3, areas II, BDGK).

When determining the area of the most efficient operation of crankless machines by the condition of the MCM operability and effective torque formation, it has been established that the maximum slope angle of the treadmill to the plane perpendicular to the axis of the cylinder should not exceed 60° within the working fluid compression areas, and it should not be less than 30° within the expansion areas. If the value of this angle goes beyond the established limits in the range of $\pm 4-6^\circ$, the conversion mechanism of the machine switches to the self-braking mode. A further increase in the threshold deviations of this angle from the aforesaid limits terminates the normal functioning of the conversion mechanism because the main power elements of the machine's kinematic chain cannot move, regardless of the values of the forces acting on these elements of the mechanism.

Acknowledgements The work was supported by Act 211 Government of the Russian Federation, contract № 02.A03.21.0011.

References

1. Viebe I (1970) Brennverlauf und Kreisprozeß von Verbrennungsmotoren. Vebverlagstechnik, Berlin
2. Viebe I, Farafontov M (1967) Elektronische Analyse der Arbeitspiele von Verbrennungsmotoren. Kraftfahrzeugtechnik 10
3. Axial Internal-Combustion Engines. <http://www.douglas-self.com/MUSEUM/POWER/unusuallCeng/axial-ICeng/axial-IC.htm>. Accessed 07 Nov 2018
4. Rotary Internal-Combustion Engines. <http://www.douglas-self.com/MUSEUM/POWER/unusuallCeng/rotaryIC/rotaryIC.htm>. Accessed 07 Nov 2018
5. Special Types of Internal Combustion Engines. <http://gluedideas.com/encyclopedia-britannica-volume-12-part-1-hydrozoa-jeremy/Special-Types-of-Internal.html>. Accessed 07 Nov 2018
6. Crankless. A new efficient mechanical transmission. <http://crankless.net/index.html>. Accessed 07 Nov 2018
7. Newcastle University. Free piston engine project. <http://www.free-piston.eu>. Accessed 07 Nov 2018
8. The Rotary Engine. http://www.wankelsupertec.de/en_engine.html. Accessed 07 Nov 2018
9. Bensinger W (1973) Rotationskolben. Springer-Verlag, Berlin, Heidelberg, New York
10. Biryukov B (1990) From a water wheel to a quantum accelerator. Mashinostroenie (Machine Building), Moscow
11. Sharoglazov BA, Ponomarev AV, Ivanov GI (1996) Rodless internal combustion engine. Patent of Russia 5063986:1996
12. Sharoglazov BA, Klementev VV, Baranov PN (1998) Rodless internal combustion engine with rotating pistons. Patent of Russia 96117967/06

13. Sharoglazov BA, Klementev VV (2003) Reciprocating machine for transporting (pumping) gaseous and liquid agents (options). Patent of Russia 2002121849/06
14. Klementev V (2003) Prospects of using a new method of converting the reciprocating piston movement into the shaft rotation in piston engines. In: Actual problems of the theory and practice of modern engine-building: proceedings of the international scientific and technical conference, pp 34–37
15. Sharoglazov B, Gofman A (2014) Crankless reciprocating heat machine-engine: kinematics, working cycle, cycle indicators (monograph). SUSU Publishing House, Chelyabinsk
16. Sharoglazov B, Gofman A (2014) Reciprocating heat machine for energy conversion and production of transport operations. Bull South Ural State Univ Series: Mach Build 14:5–11
17. Klementev V (2002) Kinematics and dynamics of an unconventional crankless reciprocating heat machine: dissertation. SUSU Publishing House, Chelyabinsk
18. Sharoglazov B, Klementev V (1999) On some technical requirements to the design elements of the unconventional, crankless reciprocating heat engine. VINITI 3818:99
19. Sharoglazov B, Kuanyshev M, Podsedov K (2018) Analytical evaluation of the ratios of the main indicators of the working cycle of reciprocating crank-rocker and crankless ICEs under similar conditions of use. Transp Urals 1(56):45–48
20. Sharoglazov B, Gofman A (2015) Motion conversion mechanism of a reciprocating two-stroke engine and the characteristic of operating on its strength elements. Int Conf Ind Eng Proced Eng 129:526–534

Research of Dynamic Characteristics of Bearing Structures at Takeaway of Ventilation Equipment on the Workshop Roof



G. Voronkova, N. Borisova and A. Borisov

Abstract There was a need to install additional ventilation equipment with its takeaway on the workshop roof due to change of production schedules. The research showed that the change of a design scheme of bearing structures with organization of additional nodes which it leans on is the way for provision of safe work. This article is researching a dynamic load on bearing structures which is observed at working with additional ventilation equipment. The spectrum of natural frequencies of oscillations was determined. The values of these frequencies were compared with the frequency of forced oscillations of the equipment. The graphs of changes in the spectrum of natural frequencies are constructed when the fans reach the working frequency. According to the graphics, when the frequency of the driving force coincides with the frequency of natural oscillations, the inertial forces increase sharply which indicates the passage of the resonance zone. There was a research of change in dynamic forces due to rotor imbalance. A gap was found that occurs when bearings are worn which will lead to the destruction of the supporting element of the farm.

Keywords Own oscillations · Forced oscillations · Frequencies · Resonance

1 Introduction

Change of technological regulations leads to change of location different equipment in it and making new static and dynamic loads [1–3] which did not consider during the engineering of bearing structures. In that case, there was a need to put additional ventilation equipment at absent place for it. That is why putting ventilation equipment on the roof with bearing on truss elements is the best decision.

G. Voronkova · N. Borisova (✉) · A. Borisov
Volgograd State Technical University, 1, Akademicheskaya Str, Volgograd 400074, Russia
e-mail: borisovani06@mail.ru

Research showed that change of design scheme of bearing structures with organization of additional nodes which it leans on is the way for provision of safe work. This difficult task became more difficult because the customer requested doing work without stop of production process in the workshop.

The design scheme was changed by organization of Sprengel. The ventilation equipment is set up through support racks on the steelwork. Also, additional nodes organized on the steelwork that the center of gravity from ventilations are located on the column axis to exclude appearance of eccentricity so the column continues working as a center compressed element.

2 Main Part

During the dynamic calculation of pivotal systems stand, ordinary design scheme may give very rough result because cubic polynomial describing rod deformation state is not already the solving differential oscillation equations [4, 5].

For solving differential oscillation equations [6]

$$Mz''(t) + Cz'(t) + Kz(t) = q(t), \quad (1)$$

where M —mass matrix, C —deformation matrix, K —system stiffness matrix, $z''(t)$, $z'(t)$, $z(t)$ —vectors of nodal displacements, velocities and accelerations at time, $q(t)$ —time load.

According to Eq. (1) as ordinary differential equations system with constant coefficient follows that finite difference equations in displacements may approximate velocities, accelerations and displacements [7, 8]. For accelerations at time using modified method of central differences may write down the next equation

$$z''(t) = \frac{z(t + \Delta t) - 2z(t) + z(t - \Delta t)}{\Delta t^2}. \quad (2)$$

The computation error in formula (2) has exponent Δt^2 so, there is a need to use equations for calculation velocities and displacements with errors of the same exponent

$$z'(t) = \frac{z(t + \Delta t) - z(t - \Delta t)}{2\Delta t}, \quad (3)$$

$$z(t) = \frac{z(t + \Delta t) + z(t - \Delta t)}{2}. \quad (4)$$

Putting Eqs. (2), (3) and (3) to Eq. (1) and defining vector $z(t + \Delta t) + z(t - \Delta t)$ is made the following equation system

$$\left[\frac{2M}{\Delta t^2} + \frac{C}{\Delta t} + K \right] (z(t + \Delta t) + z(t - \Delta t)) = 2 \left(q(t) + \frac{2M}{\Delta t^2} z(t) + \frac{C}{\Delta t} z(t - \Delta t) \right). \tag{5}$$

The next displacements are determined by early found displacements by means of the solving equations system (5). The solving of rod structure is calculated by the method of finite elements wherein a real system with an infinite number of degrees of freedom is replaced by a system with a finite number of degrees of freedom [9–11]. Distributed mass to the nodes is necessary for researching of free fluctuations of structures (Fig. 1) [12].

Installed engine on the structure because of rotor imbalance the mass of which has eccentricity e relative to axis of rotation due to bearing wear will cause the appearance of centrifugal inertial forces. The gap is variable and may change from 0 to the value at which the structure will be destroyed [13, 14]. Also, vibration loads may appear due to unbalance fan blades. In this case, the amplitude value of the driving force will be the sum of two quantities. Considering that, all rotating elements are balanced during the equipment installing. At the same time, eccentricity $e = 0$.

Bearing wear predetermines the shift of mass from the axis of rotation. In this way, eccentricity is determined by the gap between outer race and balls [15, 16]. Centrifugal inertial force due to eccentricity is calculated by the formula:

$$I = e \cdot \omega^2 \cdot m,$$

where e —eccentricity mass rotation, m —engine mass.

The research of influence of eccentricity on the value of inertial forces is performed in the range $0 \leq e \leq 2.9$ mm.

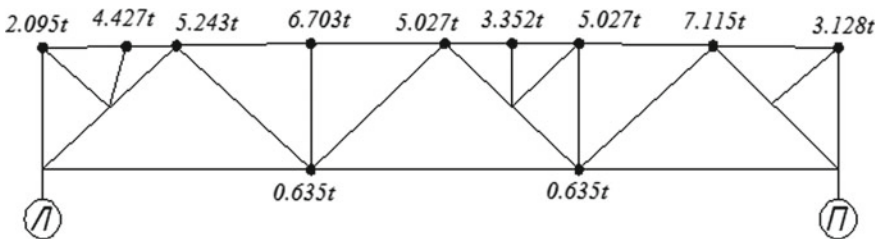


Fig. 1 Distributing mass in design scheme of steelwork



Table 1 Values of natural frequencies of oscillations coinciding with the frequency of the driving force

№	The rotation frequency (rad/s)	The amplitude value of the driving force (t)
3	25.78	0.04776
11	67.78	0.33015
16	111.68	0.89634
17	115.39	0.95688

The centrifugal inertial force at $e = 1.41$ mm, $F = 1.716$ tn. In this way, amplitude value of the driving force [17] will be:

$$F(t) = 1,716 \cdot \sin \theta \cdot t,$$

where θ —the frequency of the driving force.

After calculating the inertial forces where were changed their maximum values (nodes 6, 7, 16) so it's necessary to research of influence of unbalanced mass on them. There was calculated spectrum of the first 30 frequencies. In total, during the acceleration, the frequency of the driving force coincides with the frequency of natural oscillations at four frequencies (Table 1). Consequently, resonance at engine acceleration may appear in these values.

The graphics (Fig. 2) showed change in the magnitude of the inertial forces from the frequency of rotation of the unbalanced mass. The oscillation frequency of the driving force is fixed on every stage. On the axis Y the value of inertial forces in tn. On the axis X the value of the frequency of the driving force in rad/s. Each curve corresponds to a specific node.

According to the graph in the Fig. 2, when the frequency of the driving force coincides with the frequency of natural oscillations, the inertial forces increase sharply which indicates the passage of the resonance zone: there is a sharp leap of inertial forces (the system oscillates in antiphase) when the frequency of the driving force reaches 25.78 rad/s, then change of the inertial forces occurs evenly.

There are no significant changes in the process of increasing inertial forces for the value of the frequency of free oscillations of 67.78 rad/s in the first and second forms of oscillation which observed. According to the graph of the third and fourth frequencies (Fig. 3), there is a sharp leap of inertial forces change evenly when the frequency of the driving force reaches the value of 67.97 rad/s. The graph clearly shows the passage of the resonance zone. Maximum inertial forces occur at the node 7.

There are no significant changes which observed in the process of increasing inertial forces for the first, second, third and fourth modes of oscillation for the value of the frequencies of forces oscillations that coincide with the value of the frequencies of free oscillations 111.68 and 116.39 rad/s (Fig. 4).

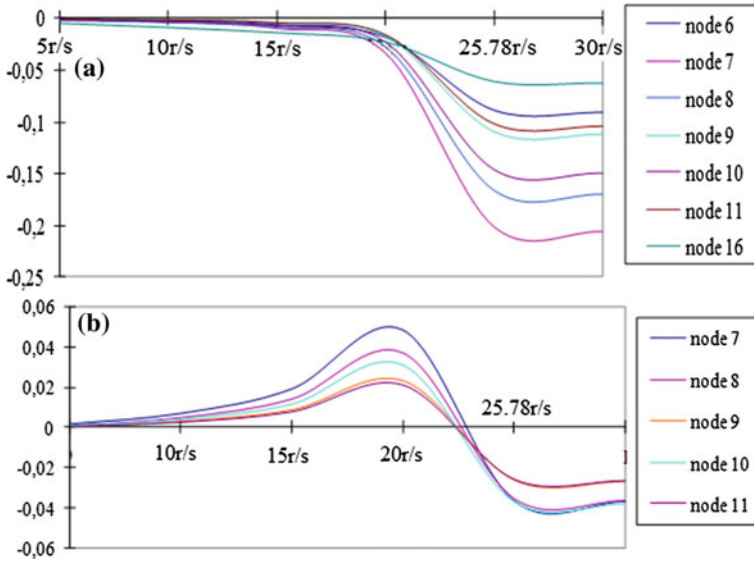


Fig. 2 Frequency of forced oscillations coincides with the frequency of free oscillations 25.78 rad/s: **a** first frequency and **b** second frequency

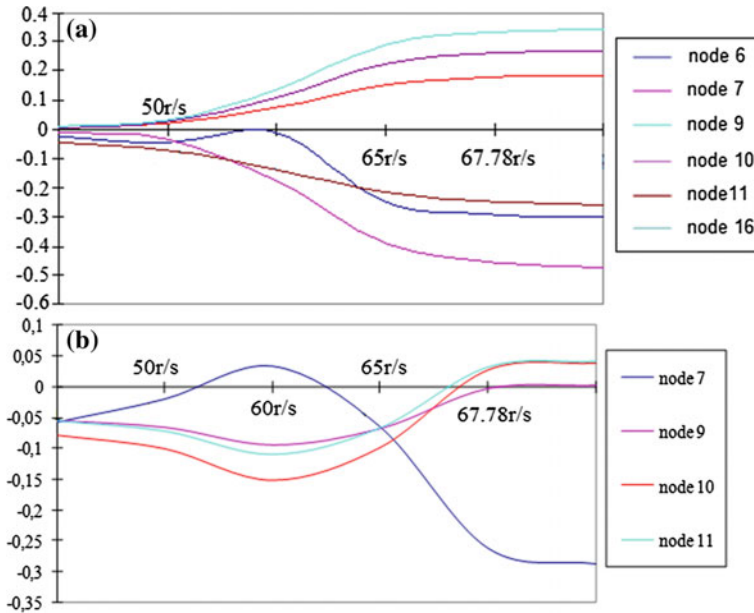


Fig. 3 Frequency of forced oscillations coincides with the frequency of free oscillations 67.78 rad/s: **a** third frequency and **b** fourth frequency

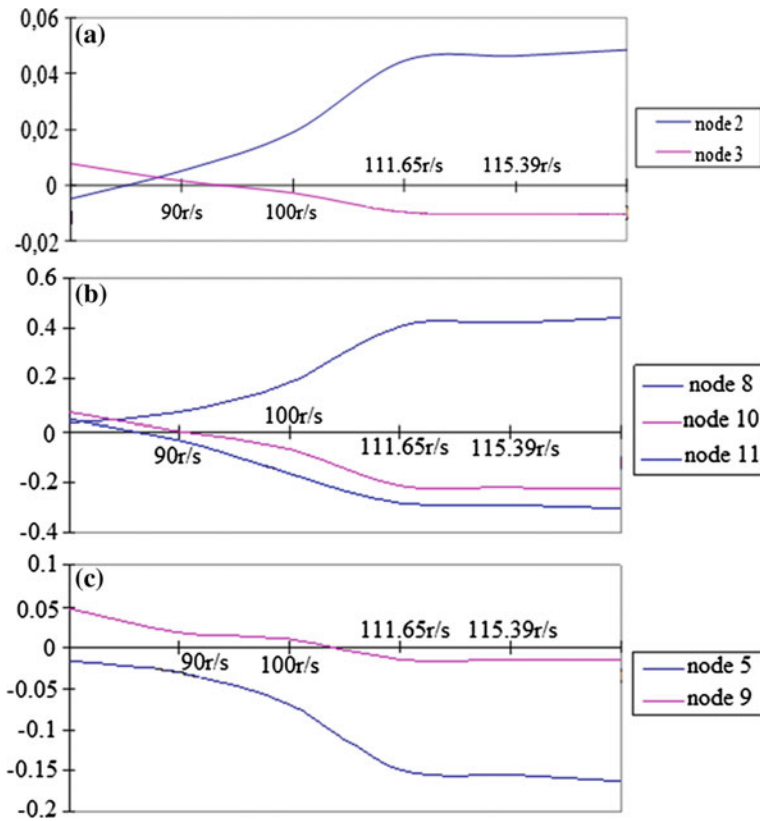


Fig. 4 Frequency of forces oscillations coincides with the frequency of free oscillations 111.68 rad/s: **a** nodes 2, 3 and **b** nodes 8–10; nodes 5, 9

According to the graph, when the frequency of the forcing values reached the natural oscillation frequency of 111.68 rad/s, the increase in the inertial forces is observed, and the further the inertial forces change evenly [18–20].

3 Conclusions

In violation of acceleration speed, when for any reasons speed long time remains less regulated, and at small eccentricities even can coincide with frequencies of free oscillations, increase of internal efforts occurs slowly. This is due to the large difference in the amplitude value of the driving force and its own weight of the structure.

When the eccentricity of the application of the rotating mass increases to 2.9 mm at the imbalance increasing, the support brace of the truss will be destroyed which in turn will cause the structure of the coating to collapse as a whole since this truss is a statically determinable system.

References

1. Evenko V, Evenko V (2006) Chem Pet Eng 42(7–8):451–456
2. Fayrushin Sh, Baykov I, Kitayev S (2016) Oil Gas Bus 14(2):120–124
3. Pashaev A, Dzhanahmedov A, Aliev M (2008) Assembly in mechanical engineering. Instrum Mak 11:31–34
4. Il'in V, Karpov V, Maslennikov A (1990) Chislennye metody reshenija zadach stroitel'noj mehaniki (Numerical methods for solving problems of structural mechanics). High School, Minsk
5. Khudayarov B, Bandurin N (2007) J Appl Mech Tech Phys 48(2):279–284
6. Clough R, Penzien J (1975) Dynamics of structures. New York
7. Ignatev V, Ignatev A (2013) Vestnik Bulletin of the VSUACE. Series: Civil Eng Archit 31-2 (50):337–343
8. Ignatev A, Gabova V (2009) Bulletin of the VSUACE. Series: Civil Eng Archit 14:75–79
9. Ignatev A (2015) Bull MSCEU 1:16–26
10. Klochkov Yu, Nikolaev A, Kiselyev A (2011) Struct Mech Eng Constr Build 3:49–59
11. Rekunov S (2014) Naukovedenie 5(24):56
12. Ivlev V, Nelyubin A, Misyurin S (2017) Mech Mach Sci 44:145–151
13. Shestakov S, Popov A, Dushko O (2007) Welded metal structures, calculation and design. Volgograd State university of Architecture and Civil engineering, Volgograd
14. Zhang B, Zhang J, Zhang N, Jin Q, Yi J (2016) Shock Vibr 2016:5239837
15. Raizer V (2009) Reliability of structures, analysis and applications. Backbone Publishing Company, New York
16. Rekunov S (2016) Russ J Transp Eng 3(2):7
17. Zhao L, Chen Q (1998) Comput Methods Appl Mech Eng 161(3–4):245–255
18. Samarskiy A, Nikolaev E (1978) Metody reshenija setochnyh uravnenij (Methods of solving the mesh equations). Science, Moscow
19. Dushko O, Rekunov S, Alifanov A (2017) Don Eng Bull 2(45):130
20. Uskov Yu, Katerinina S, Katerinina M (2015) Bulletin of the VSUACE. Series: Civil Eng Archit 41(60):130–138

Features of Pulsating Flows Thermomechanics in Exhaust System of Piston Engine with Turbocharging



L. V. Plotnikov, Yu M. Brodov and N. I. Grigor'ev

Abstract The paper presents the results of an experimental study of the influence of a turbocharger turbine on the thermal and mechanical characteristics of gas flows in the exhaust system of a piston internal combustion engine (ICE). The experiments were carried out on a full-scale model of a single-cylinder engine under the conditions of gas-dynamic non-stationarity (pulsating flows). The article describes the laboratory setup and the methodology for conducting experiments. The analysis of the dependences of the instantaneous velocity and pressure of the pulsating flow, as well as the local heat transfer coefficient in time in the exhaust pipe of the piston engine with and without a turbocharger (TC), is presented. It is shown that the placement of the TC turbine in the gas-air path of the piston ICE significantly affects the gas-dynamic, flow and heat exchange characteristics of gas flows in the exhaust system. The installation of the turbocharger causes restructuring of the structure and flow regime in the exhaust system.

Keywords Piston engine · Turbocharger · Exhaust system · Pulsating flows · Gas-dynamics non-stationary · Local heat transfer

1 Introduction

In the literature related to the theory of working processes and the design of piston internal combustion engines (ICE), installing a turbocharger (TC) for boosting is considered solely as an effective way to increase mass flow through the engine cylinders and, accordingly, to improve its technical and economic indicators [1–3]. The works of many authors, in particular [4–8], are devoted to the study of gas exchange processes and optimization of the design of exhaust systems of piston ICEs with and without turbocharging. However, these studies were carried out

L. V. Plotnikov (✉) · Yu M. Brodov · N. I. Grigor'ev
Ural Federal University Named After the First President of Russia B.N. Yeltsin,
19 Mira Str, Ekaterinburg 620002, Russia
e-mail: leonplot@mail.ru

mainly experimentally in static conditions or by methods of numerical simulation in a quasistationary formulation of the problem. Information about dynamic phenomena during the exhaust process is very limited. It is possible to note only a few works [9–12], in which studies of gas exchange processes were carried out taking into account the gas-dynamic unsteadiness inherent in the working cycle of piston engines. It should also be noted that in the literature, the question of the role of the TC in the formation of the gas-dynamic and heat exchange characteristics of the pulsating flow in the exhaust system was not actually addressed. Typically, the TC turbine is simplistically considered a static element of the gas-air path from a hydrodynamic point of view, which creates hydraulic resistance and at the same time is a way of forcing the engine. However, it is obvious that the installation of a turbocharger in the exhaust system of the engine will lead to a significant change in the thermal and mechanical characteristics of the gas flow, which is confirmed by the results of work [13–16].

This article presents the results of studying the effect of a turbocharger turbine on the thermal and mechanical characteristics of a pulsating gas flow in an exhaust system of a piston ICE as applied to an automobile engine (cylinder diameter—82 mm, piston stroke—71 mm).

2 Experimental Installation, Data Acquisition System and Methods

A full-life single-cylinder model of a piston engine (8.2/7.1) with a turbocharger (compressor wheel diameter ≈ 60 mm, turbine wheel diameter ≈ 60 mm) was used for an experimental study. The main elements of the setup are shown in Fig. 1.

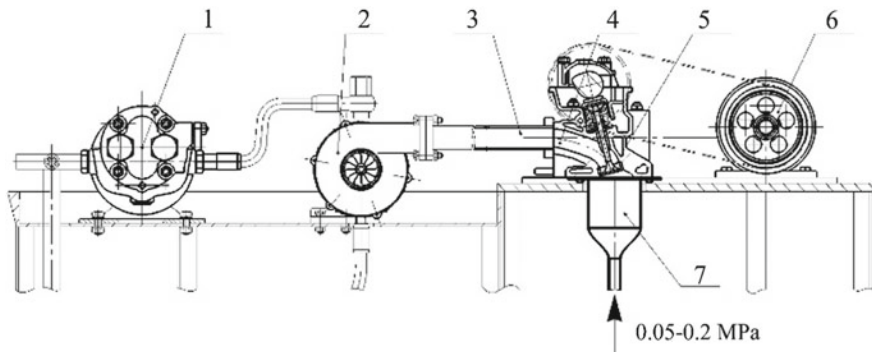


Fig. 1 General view of the experimental setup: 1—oil pump, 2—turbocharger, 3—exhaust pipe, 4—engine block head, 5—exhaust valve, 6—asynchronous motor, 7—cavity imitating engine cylinder

The gas distribution (timing) mechanism in the setup is used from the engine of the VAZ-OKA car. The timing and valve lift corresponded to those for this engine. The camshaft was driven by an asynchronous motor, whose rotational speed was regulated by a frequency converter in the range of 300–1500 rpm; this corresponds to a crankshaft rotational speed of 600–3000 rpm. The turbocharger is a unit with a radial-axial turbine and a centrifugal compressor mounted on the same shaft.

The configuration of the investigated section of the exhaust system of the experimental setup and the installation location of the sensors for measuring instantaneous values of the air flow velocity and the local heat transfer coefficient are shown in Fig. 2. Measurements of the instantaneous values of the static air pressure in the exhaust pipe were also carried out in the course of the research.

The investigated pipeline was attached to the engine cylinder head with a total length of $L = 400$ mm and an internal diameter of $d = 30$ mm. There were three control sections in the pipeline to install pressure sensors and a hot-wire anemometer at distances of 20, 140 and 340 mm. A more detailed description of the experimental setup is presented in [17].

An automated data acquisition system based on an analog-to-digital converter was created for research. The constant-temperature thermo-anemometer was used to determine the instantaneous values of the air flow velocity (w_x) and the local heat transfer coefficient (α_x). The sensitive element of the thermo-anemometer sensors in both cases was a nichrome thread with a diameter of $5 \mu\text{m}$ and a length of 5 mm. The measurement of the camshaft speed (n) was made with a tachometer. Digital non-contact tachometer CEM AT-6 was used to measure the turbocharger rotor rotational speed (n_{TC}). WIKA pressure sensors were used to determine the instantaneous values of the static pressure of the flow in the exhaust channel (p_x), as well as to measure the boost pressure. Signals from all sensors were fed to an

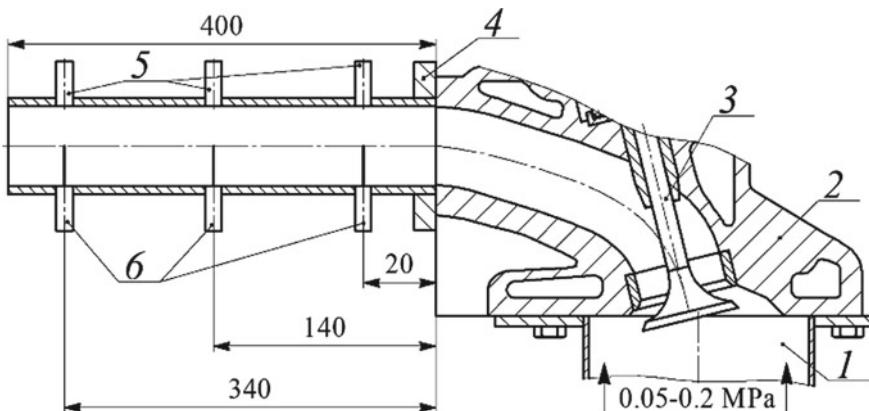


Fig. 2 Longitudinal section of the working section of the piston engine exhaust system: 1—cylinder (cavity), 2—engine block head, 3—the exhaust valve, 4—exhaust pipe under investigation, 5—thermo-anemometer sensors for measuring local heat transfer, 6—thermo-anemometer sensors for measuring the air flow velocity

analog-to-digital converter and then transferred to a personal computer for further processing. Methods for determining the thermal and mechanical characteristics of pulsating flows are described in more detail in [12, 17–20].

Investigations were carried out at crankshaft rotational speeds from 600 to 3000 rpm, at rotor speeds of the turbocharger from 15,000 to 42,000 rpm, and at excessive pressures on the exhaust p_b from 0.05 to 0.2 MPa. The working medium was air with a temperature of 20–25 °C.

3 The Influence of the TC Turbine on Gas-Dynamic Flow Characteristics

Separate results of determining the functions w_x and p_x in time τ with different configurations of the exhaust system and operating modes of the engine model are presented in Fig. 3.

It is shown that the values of the maximum air flow velocity in the exhaust system with a turbocharger, as expected, are lower than in the system without TC. This is most pronounced when the overpressure at the outlet is $p_b = 0.1$ MPa. It is noteworthy that the maximum of the considered characteristic is shifted toward an increase in the crankshaft rotation angle, which is typical of all engine operating conditions. In both cases (with and without a turbocharger), the pulsations of the air flow velocity are most pronounced at low crankshaft speeds ($n < 1500$ rpm). At the same time, the air velocity in the pipeline does not become zero after the exhaust valve is closed (some fluctuations are observed), which is typical for all conditions. This phenomenon is also characteristic of the intake process [21, 22].

Significant differences are observed in the graphs of the flow pressure in the exhaust pipe when installing a turbocharger. The maximum values of the flow

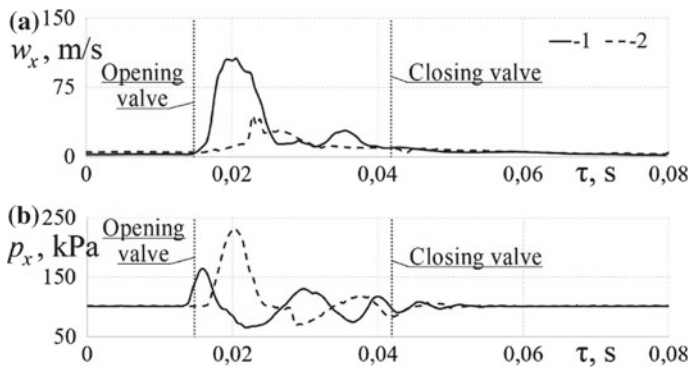


Fig. 3 Dependences of local speeds w_x (a) and pressure p_x (b) of the air flow in the exhaust pipe as a function of time τ at a cylinder overpressure $p_b = 0.1$ MPa and at a crankshaft rotation frequency $n = 1500$ rpm. System configuration: 1—without turbocharger, 2—with TC

pressure in the exhaust system are higher in the case of TC installation than in the system without it. The pressure peaks following the maximum have approximately the same amplitude. There is a shift of the maximum pressure peak in time toward the moment of closing of the exhaust valve. The presence of a turbocharger in the exhaust system results in some smoothing of the flow pressure pulsations under all conditions (especially $p_b = 0.1$ MPa), both during the exhaust process and after the exhaust valve, is closed. It should be noted the presence of flow pressure pulsations after closing the exhaust valve in the exhaust system with and without TC, which also attenuate somewhat faster if there is a turbocharger in the system. Similar results (the presence of pulsations w_x and p_x after closing the exhaust valve) were obtained by studying the influence of hydraulic resistance on the gas-dynamic characteristics of the intake process in the piston ICE.

According to the authors, the above-described changes in the gas-dynamic characteristics of the exhaust process indicate the restructuring of the gas-dynamic structure of the pulsating flow in the exhaust pipeline when the TC turbine is placed in the system. This will inevitably lead to changes in the heat exchange characteristics of the pulsating flow in the exhaust system.

4 The Influence of the TC Turbine on Heat Exchange Characteristics of Flow

It has been established (Figs. 4 and 5) that the presence of a turbocharger in the engine exhaust system leads to a decrease in heat transfer intensity at all values of the exhaust overpressure and rotational speeds of the engine crankshaft and the TC rotor.

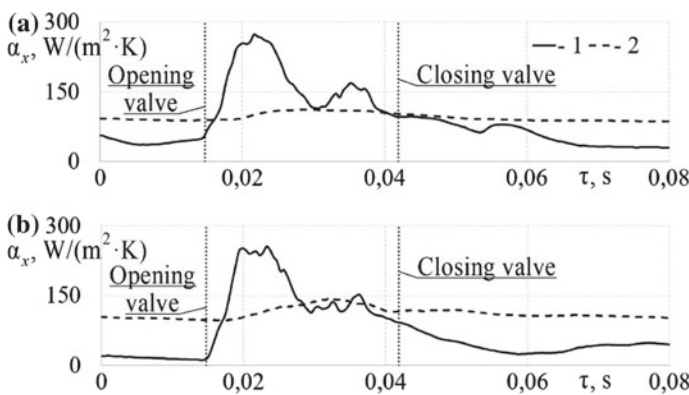


Fig. 4 Dependences of local heat transfer coefficients α_x on time τ in the exhaust pipe at excessive pressures in the cylinder $p_b = 0.1$ MPa (a) and $p_b = 0.2$ MPa (b) at a crankshaft rotation frequency $n = 1500$ rpm. System configuration: 1—without turbocharger, 2—with TC

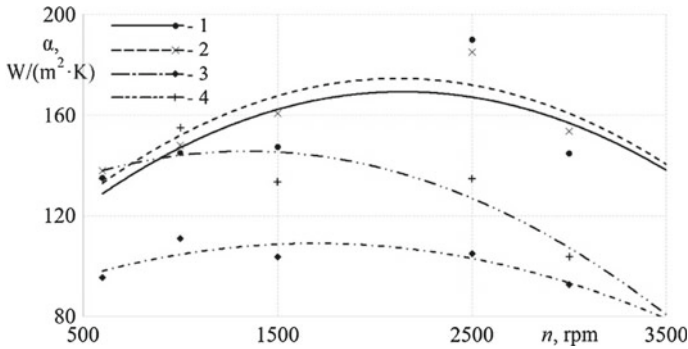


Fig. 5 Dependences of heat transfer coefficient α in the exhaust pipeline on time τ with different configurations and initial conditions: 1—system without the TC, $p_b = 0.2$ MPa, 2—system without the TC, $p_b = 0.1$ MPa, 3—system with the TC, $p_b = 0.1$ MPa, 4—system with the TC, $p_b = 0.2$ MPa

It can be noted that the maximum values of the local coefficient in the exhaust pipe are reduced by about two times when installing a turbocharger (Fig. 4). This trend is typical for all investigated initial conditions. At the same time, the presence of TC causes a significant smoothing of the curve $\alpha_x = f(\tau)$.

It has been established that the heat transfer intensity (averaged heat transfer coefficient over the period of the exhaust process) in the exhaust system with TK is reduced on average by 30% compared with the exhaust system without turbocharging (Fig. 5). This indicates the fact that the heat loss through the pipe wall will be less in this case.

The detected decrease in the intensity of heat transfer to the walls of the exhaust pipe in the presence of TC should have a positive impact on the working process and the technical and economic performance of the engine, since in this case more thermal overshoot will work in the turbocharger and not be lost through the walls of the pipeline.

5 Conclusion

The study showed that the placement of the turbocharger turbine in the gas-air path of the piston ICE significantly affects the gas-dynamic and heat exchange characteristics of the pulsating flow in the exhaust system. This should be taken into account in the calculation of gas exchange processes and in the design of intake and exhaust systems of engines. The presence of TC in the exhaust system of the piston ICE leads to smoothing the pulsations of the speed and pressure of the air flow in the exhaust pipe. At the same time, there is a decrease in the intensity of heat transfer in the exhaust pipeline, which will lead to the triggering of a greater heat differential in the TC turbine, *ceteris paribus*. Installation of the turbocharger causes

restructuring of the structure and flow regime in the exhaust pipe. This complicates the task of creating a method for calculating temperature stresses in the exhaust system, since it is necessary to take into account the dynamics of the exhaust process. In the calculations, it is mainly necessary to apply the empirical equations of heat transfer, which take into account the peculiarities of the exhaust process non-stationarity for specific ICE and TC, as well as the modes of their joint operation.

Acknowledgements The work has been supported by the Russian Science Foundation (Grant No. 18-79-10003).

References

1. Kavtaradze RZ (2016) Theory of piston engines, special chapters. Bauman Press, Moscow
2. Heywood JB (1988) Internal combustion engine fundamentals. McGraw-Hill, New York
3. Khanin NS, Aboltin EV, Lyamtsev BF (1991) Turbocharged car engines. Mashinostroenie, Moscow
4. Liu CM, You JJ, Sung CK et al (2015) Modified intake and exhaust system for piston-type compressed air engines. *Energy* 90:516–524. <https://doi.org/10.1016/j.energy.2015.07.085>
5. Wang TJ (2018) Optimum design for intake and exhaust system of a heavy-duty diesel engine by using DFSS methodology. *J Mech Sci Technol* 21(7):3465–3472. <https://doi.org/10.1007/s12206-018-0650-6>
6. Torregrosa AJ, Broatch A, Arnau FJ et al (2017) On the effect of different flux limiters on the performance of an engine gas exchange gas-dynamic model. *Int J Mech Sci* 133:740–751. <https://doi.org/10.1016/j.iijmecsci.2017.09.029>
7. Torregrosa AJ, Arnau FJ, Piqueras P et al (2017) Phenomenological methodology for assessing the influence of flow conditions on the acoustic response of exhaust aftertreatment systems. *J Sound Vib* 396:289–306. <https://doi.org/10.1016/j.jsv.2017.02.033>
8. Buhl S, Hain D, Hartmann F et al (2018) A comparative study of intake and exhaust port modeling strategies for scale-resolving engine simulations. *Int J Engine Res* 19(3):282–292. <https://doi.org/10.1177/1468087417707452>
9. Grishin YA, Zenkin VA, Khmelev RN (2017) Boundary conditions for numerical calculation of gas exchange in piston engines. *J Eng Phys Thermophys* 965–970. <https://doi.org/10.1007/s10891-017-1644-4>
10. Atanov SN, Enikeev RD (2017) Experimental study of the method of increasing the filling ratio of a four-stroke internal combustion engine by intensifying recharging. *Bulletin Ufa State Aviat Tech Univ* 21(1):38–44
11. Rodrigues MJ, Liburdy JA (2016) Transient heat transfer model and verification for gas cylinder expansion. *Int J Heat Mass Transf* 102:241–250. <https://doi.org/10.1016/j.ijheatmasstransfer.2016.06.036>
12. Plotnikov LV, Zhilkin BP (2017) The gas-dynamic unsteadiness effects on heat transfer in the intake and exhaust systems of piston internal combustion engines. *Int J Heat Mass Transf* 115:1182–1191. <https://doi.org/10.1016/j.ijheatmasstransfer.2017.08.118>
13. Zhao RC, Li WH, Zhuge WL et al (2018) Characterization of two-stage turbine system under steady and pulsating flow conditions. *Energy* 148:407–423. <https://doi.org/10.1016/j.energy.2018.01.125>
14. Petrichenko DA, Korotkov VS, Stukolkin RV et al (2018) Approaches to improvement of turbochargers for automotive engines. *Int J Mech Eng Technol* 9(6):999–1008

15. Plotnikov LV (2017) Features of the gas dynamics and local heat transfer in intake system of piston engine with supercharging. IOP Conf Series: J Phys 899:042008. <https://doi.org/10.1088/1742-6596/899/4/042008>
16. Tang Q, Fu J, Liu J et al (2016) Comparison and analysis of the effects of various improved turbocharging approaches on gasoline engine transient performances. Appl Therm Eng 93:797–812. <https://doi.org/10.1016/j.applthermaleng.2015.09.063>
17. Zhilkin BP, Lashmanov VV, Plotnikov LV et al (2015) Improvement of processes in the gas-air tracts of piston internal combustion engines: monograph. Ural Publishers of the University, Ekaterinburg
18. Bradshaw P (1974) Introduction to turbulence and its measurement. Moscow
19. Foss JF, Peabody JA, Norconk MJ et al (2006) Ambient temperature and free stream turbulence effects on the thermal transient anemometer. Measur Sci Technol 17(9):2519–2526. <https://doi.org/10.1088/0957-0233/17/020>
20. Draganov BKh, Kruglov MG, Obukhova VS (1987) Designing the intake and exhaust channels of internal combustion engines. Visha chkola, Kiev
21. Brodov YM, Zhilkin BP, Plotnikov LV (2018) Influence of intake/exhaust channel lateral profiling on thermomechanics of pulsating flows. Tech Phys 63(3):319–324. <https://doi.org/10.1134/S1063784218030039>
22. Plotnikov LV, Zhilkin BP, Brodov YM (2016) The influence of cross-profiling of inlet and exhaust pipes on the gas exchange processes in piston engines. Proc Engineering 150:111–116. <https://doi.org/10.1016/j.proeng.2016.06.729>

Improvement of Environmental Characteristics of Diesel Locomotive Engine with Turbocharging by Changing Valve Timing (Based on Miller Cycle)



L. V. Plotnikov, S. Bernasconi and P. Jacoby

Abstract The article presents the results of upgrading a diesel locomotive engine with turbocharging and a cylinder with the diameter of 210 mm and a piston stroke of 210 mm through changing the valve timing (based on the Miller cycle). The research was carried out with numerical simulation in the ACTUS programme and based on experimental studies of test benches at the Ural Diesel Motor Plant. In the course of mathematical modelling, the hypothesis of the positive effect of an early closure of the intake valve on the diesel engine's environmental performance was tested. It has been established that an early closure of the intake valve leads to a reduction in NO_x emissions in exhaust gases by up to 20% with a slight change in power and specific fuel consumption ($\pm 3\%$). Based on the experimental research on diesel performance, comparative harmful emission diagrams for the basic and upgraded engines (NO_x, CO and CH) are constructed. It was experimentally established that the change in the gas distribution phases (based on the Miller cycle) leads to a 16% decrease in NO_x content, a 50% reduction in CO and a 54% reduction in CH. At the same time, a decrease in the specific effective flow rate reaches a value of 3.3% for certain operating modes of the diesel engine. The values obtained for the concentration of harmful emissions in exhaust gases are substantially lower than those required by international standards.

Keywords Piston internal combustion engine · Valve timing · Miller cycle · Ecology · Experimental studies · Numerical simulation · ACTUS

L. V. Plotnikov (✉)

Ural Federal University Named After the First President of Russia B.N. Yeltsin, 19,
Mira Str Ekaterinburg 620002, Russia
e-mail: leonplot@mail.ru

S. Bernasconi · P. Jacoby

ABB Turbo Systems Ltd., Bruggerstrasse 71a, 5401 Baden, Switzerland

© Springer Nature Switzerland AG 2020

A. A. Radionov et al. (eds.), *Proceedings of the 5th International Conference on Industrial Engineering (ICIE 2019)*, Lecture Notes in Mechanical Engineering,

https://doi.org/10.1007/978-3-030-22041-9_59

1 Introduction

Today, internal combustion engines (ICE) are the most common source of energy in the world (among thermal engines) and are used in all sectors of the national economy. It is known that the total installed capacity of ICE exceeds by about five times that of all the world's stationary power plants. Therefore, the improvement of the design and development of the operating process of piston ICEs is an urgent task for the development of world energy.

Contemporary trends in the development of reciprocating engines are associated with an increase in fuel efficiency and environmental friendliness [1–3]. There are several methods to achieve these goals. For example, the work of Pesic and Milojevic [4] provided research into the determination of the optimum field of compression ratio values depending on fuel consumption, the minimum amount of nitrogen oxides and the emission of particulate matter in the exhaust gases for a variable-compression diesel engine. Another way to improve the technical, economic and environmental performance of a gasoline engine is presented by Bo et al. [5]. The authors propose physical and mathematical models for the simulation of charge motion in the engine cylinder with a controlled electromagnetic intake valve. In the experimental work of Zhang et al. [6], research into the effects of five different phases of gas distribution on the characteristics of the combustion process and emission of harmful substances under various loads for a super-powerful diesel engine was carried out. One might also highlight the comprehensive work of Schück et al. [7], in which experimental studies into the effect of various engine parameters on the formation of solid particles in exhaust gases under dynamic load changes are carried out.

It can be noted that studies are being actively carried out to compare the efficiency and environmental friendliness of piston ICEs and electric motors [8].

One of the most relevant and effective ways to improve the operating process of piston engines is to use the so-called Miller cycle. A large number of scientific works have been devoted to this field of research. The review article by Zhao [9] presents the main advantages and disadvantages of piston engines operated on the Atkinson cycle and the Miller cycle, and also briefly discuss critical problems, challenges and future solutions for improving ICE. In the theoretical work of Wu et al. [10], the main parameters of a piston ICE were optimised for various operating cycle methods (the Otto, Diesel, Miller and Otto–Miller cycles). One can single out the works connected with the development of mathematical models for modelling processes in piston engines operating on the Miller cycle [11, 12].

There are a large number of experimental works aimed at improving the operating process of piston engines with the Miller cycle. For example, Molina et al. [13] conducted research into the Miller's cycle potential for reducing nitrogen oxide emissions and soot to EURO VI limits while preserving fuel consumption and the average effective engine pressure. Zou et al. [14] describe the results of an experimental study on the effect of an early closure of the intake valve and the magnitude of the diesel engine's fuel injection pressure on the main indicators.

Kim and Bae [15] studied various methods of recirculating exhaust gases and their effect on the environmental performance of a diesel engine running on the Miller cycle.

The efficiency of the Miller cycle for spark-ignited engines is shown in research papers [16, 17].

A separate scientific topic is focused on studying the influence of the Miller cycle on the main parameters of engines operating on gaseous fuels. In the work of Pedrozo et al. [18], the operating process of a high-powered diesel ICE operating on a mixture of ethanol and diesel fuel was improved. To improve the combustion efficiency of the bi-fuel mixture, the Miller cycle and charge-air cooling were used. Zhang et al. [19] presented research results concerning the technical and environmental characteristics of a single-cylinder ICE operated by gaseous fuels (methane). The authors evaluated the effects of a large number of factors on engine performance. Ojapah et al. [20] perfected the operating process of a spark-ignition engine run on gaseous fuel (ethanol) in the Miller cycle.

However, the greatest positive effect in improving the economic and environmental performance of piston ICEs can be obtained with a comprehensive engine upgrade. Imperato et al. [21] present the results of experimental research to reduce NO_x emissions in a marine diesel. Gonca and Sahin [22] presented results associated with upgrading the diesel engine with turbocharging and steam injection into a cylinder operating on the Miller cycle.

This article presents the results of numerical simulation and experimental studies of the operating process of a diesel engine with the dimensions of 21/21 (cylinder diameter—210 mm, stroke—210 mm) in order to improve the environmental performance by optimising valve timing (in particular, early closure of the intake valve). A block diagram of the ICE design and its three-dimensional model are shown in Fig. 1.

The factory designation of the diesel engine is 8DM-21. In the initial configuration, it is a four-stroke, 8-cylinder, V-shaped diesel engine with one turbocharger,

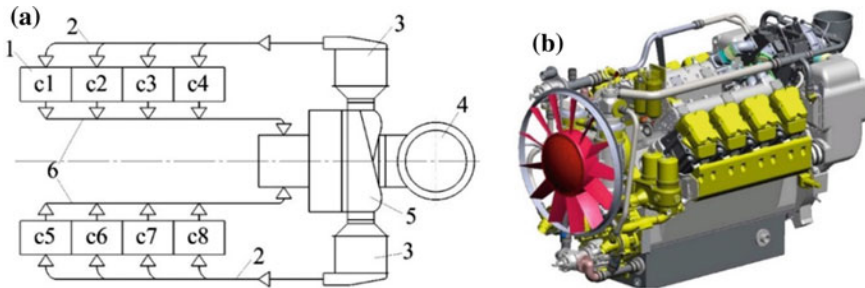


Fig. 1 Flow chart of the diesel design 8DM-21 (a) and 3D model of the engine (b): 1 is the cylinder, 2 is the intake system, 3 is the charge-air cooler, 4 is the air intake, 5 is the turbocharger, 6 is the exhaust system

a cylinder diameter of 210 mm, a stroke of 210 mm and nominal power $N_e = 930$ kW at a crankshaft speed of $n = 1500$ rpm.

2 Modelling the Operating Process of a Diesel Engine

To date, one of the most effective approaches to improving a piston engine is numerical simulation of the workflow in dedicated software systems. Here, numerical simulation of the working process of the 8DM-21 diesel engine in the ACTUS software package developed by ABB Turbo Systems Ltd. was carried out (Baden, Switzerland). The ACTUS programme allows you to define in detail the geometric characteristics of the intake and exhaust systems, turbocharger parameters and other necessary parameters of the cylinder-piston group and turbocharging.

A few more details about the ACTUS programme, its features, capabilities and the results of calculations can be found in articles [23–25].

During the design research, three valve timing options of the diesel engine were simulated (Fig. 2). Figure 2a shows the opening and closing angles of the intake and exhaust valves of the original (basic) engine 8DM-21. Figure 2b shows alternative phases of the gas distribution of the diesel engine with the early closure of the intake valve (21° to bottom dead centre (BDC)), while Fig. 2c shows the third version of the gas distribution phases with an even earlier closure of the intake valve (30° to BDC). During the simulation, only the magnitude of the angle of the intake valve closing was changed: the other parameters of the diesel engine remained unchanged.

Thus, in the first stage of the research, a hypothesis was tested about the positive effect of the Miller cycle (early closure of the intake valve) on the environmental performance of the piston ICE through mathematical simulation of the operating process of the 8DM-21 diesel engine in the ACTUS programme.

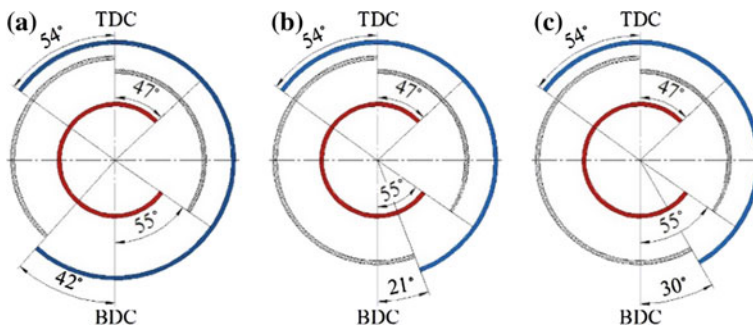


Fig. 2 Valve timing flow charts 8DM-21: **a** is the initial valve timing, **b** is the early closure of the intake valve (21° before BDC), **c** is the early closure of the intake valve (30° before BDC)

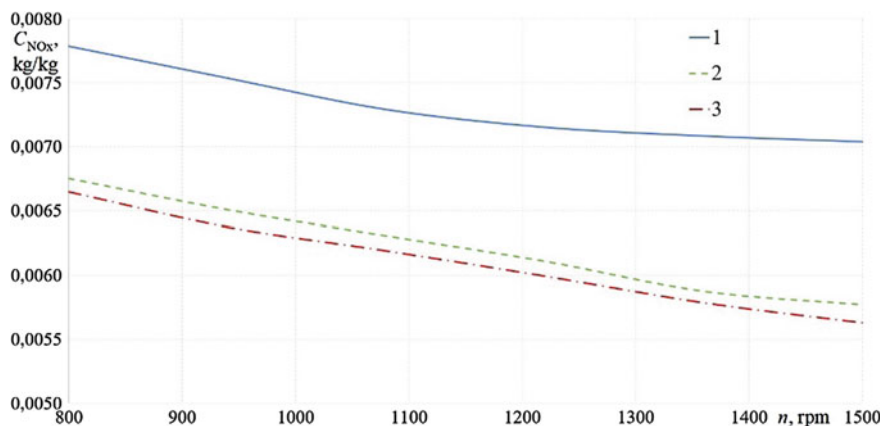


Fig. 3 Dependence of the concentration of NO x emissions on the crankshaft speed at different closing angles of the intake valve: 1 is the basic engine (the intake valve closing angle is 42° after BDC), 2 is the Miller cycle (closing the intake valve 21° to BDC), 3 is the Miller cycle (closing the valve 30° to BDC)

The simulation results showed that the early closure of the intake valve leads to a significant reduction in NO x emissions in the exhaust gases of the 8DM-21 diesel engine (Fig. 3). Thus, if the intake valve is closed 21° to BDC, NO x emissions are reduced by 13–18% compared to emissions in the basic diesel engine. If the intake valve is closed 30° to BDC, the NO x emission concentration is reduced by 20% compared to the original diesel engine.

A decrease in the concentration of NO x in the exhaust gases of a diesel engine operating by the Miller cycle can be explained in two ways. First, by lowering the temperature of the gases in the cylinder at the end of the intake process, the average operating temperature of the piston ICE decreases. Moreover, this should lead to a reduction in the thermal tension of the cylinder-piston group parts and the exhaust system, which will increase the reliability of the engine as a whole. Second, there is a drop in the quality of gas exchange of the engine when operating on the Miller cycle. For example, the scavenging factor decreased by a value of 1–6% in when the intake valve is closed early compared to the basic engine (this indicates a slight deterioration in the cylinder cleaning from the exhaust gases, which leads to a slight decrease in the combustion efficiency of the engine cylinder).

A change in the power of the basic diesel engines and the diesel engines where the intake valve closes early is in the range of $\pm 3\%$. At the same time, a slight decrease in the power of the diesel engines with modified valve timing can be recorded in the range of crankshaft speeds n to 1100 rpm. In contrast, after $n = 1080$ rpm, there is a slight increase in N_e . A similar tendency was also obtained for changing the specific fuel consumption for the basic diesel engine and the diesel engine with early closure of the intake valve. Differences in the specific flow of the

diesel engines in question are in the range of $\pm 3.5\%$. At low speeds of the crankshaft ($n \leq 1080$ rpm), there is a slight increase in the specific fuel flow g_e ; at high values of n , there is a slight decrease in g_e .

3 Experimental Research into the Operating Process of a Diesel Engine

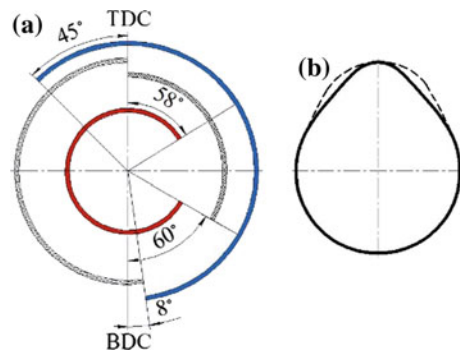
Based on the physical and mathematical simulation of the operating process of the diesel engine 8DM-21, the analysis of reference data and the experience of plants in carrying out experimental research, the gas distribution phases are shown in Fig. 4a. The new valve timing phases differ somewhat from the initial ones (see Fig. 2a).

Thus, the term of the intake process was reduced by 59° of the crankshaft rotation. A sketch of the valve lifting cams for driving the intake valves of the original diesel engine and the upgraded diesel engine is shown in Fig. 4b). The opening and closing moments of the exhaust valves were also changed. The duration of the engine exhaust process increased by 16° compared to the basic engine. It should be noted that the duration of blowing the cylinders was slightly reduced from 109 to 103° of rotation of the crankshaft.

To assess the impact of the new valve timing phases on the environmental performance of the diesel engine 8DM-21, bench tests were conducted with measurements of the specific average weighted emissions of harmful substances in the exhaust gases. These were monitored to check compliance with interstate GOST ISO-8178. During testing, the measured parameters were as follows: the specific weighted average emission of carbon monoxide (CO), the specific weighted average emission of nitrogen oxides (NO_x), the specific weighted average emission of hydrocarbons (CH) and smoking at the exhaust. According to the test results, the specific weighted average emissions of the i -th harmful substances, $g/(kW h)$, were calculated.

The diesel engine test cycles were selected in accordance with the Russian GOST 30574, which determines the operating modes of the engine with a

Fig. 4 Valve timing of the diesel engine 8DM-21 for carrying out experimental research (a) and the camshaft cam profile for driving the intake valve (b): the solid line—new profile, dashed line—the profile of the cam of the original diesel engine



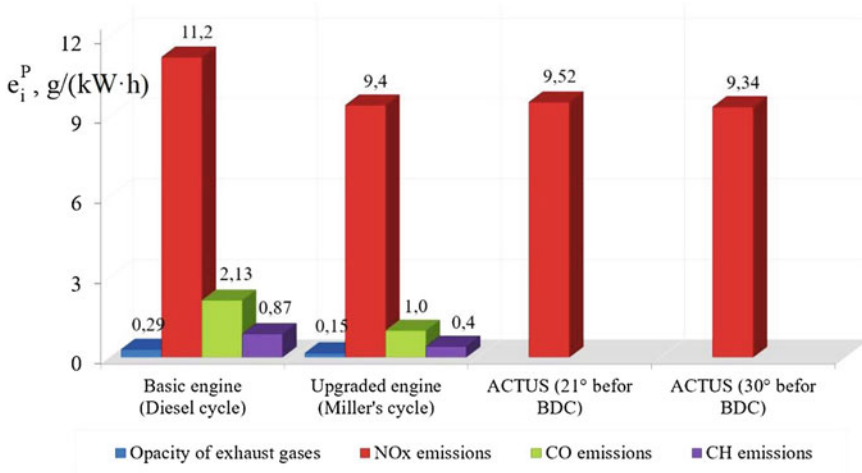


Fig. 5 A comparative diagram of harmful emissions and smokiness of the basic and upgraded diesel engines

certain speed, load and torque. To measure the concentrations of harmful substances (CO, NOx and CH) in the exhaust gases, the gas analyser GIAM-29 and the exhaust gas analyser FEVER were used.

The experimental and calculated data on harmful emissions and smoking at the exhaust for the basic and upgraded diesel engines are shown in Fig. 5. From the data obtained as a result of tests, it is established that the basic engine 8DM-21 meets the requirements of regulatory documents. For example, in accordance with ISO-8178, the smoke exhaust limit value is 0.35 g/(kW h); the limit values of NOx, CO and CH should not exceed 12.0, 3.0 and 1.0 g/(kW h), respectively. However, it should be noted that the backup content of harmful substances and the backup content of the smokiness of exhaust gases is relatively small. At the same time, taking into account the growth trends in the environmental requirements, this backup stock can soon be exhausted quickly, so the basic engine will cease to meet environmental requirements. The use of the new valve timing (based on the Miller cycle) has significantly reduced the volume of harmful emissions in the exhaust gases. For this engine, the NOx, CO and CH content decreased by 16%, 50% and 54%, respectively, compared to the basic engine. It should also be noted that the smoke intensity of the exhaust gases decreased virtually by two times.

Thus, the experimental research has confirmed the results of the mathematical simulation in terms of improving the environmental friendliness of diesel engines through use of the Miller cycle (early closure of the intake valve).

It should be noted that in the course of experimental research, a slight decrease in the specific fuel consumption g_e of the upgraded diesel engine was found in



comparison with the basic ICE. The reduction of g_c in the diesel engine with the new valve timing did not exceed 4% with equal powers of the original and upgraded diesel engines.

4 Conclusion

The numerical and experimental research into valve timing on the environmental and technical performance of the 8DM-21 diesel engine produced the following results:

- The mathematical model of a diesel locomotive engine with supercharging (8DM-21) was developed in the ACTUS software system, taking into account the physical and geometric parameters of the intake and exhaust systems, as well as the intra-cylinder processes of the diesel engine under consideration;
- As a result of numerical simulation, it was established that the application of the Miller cycle (early closure of the intake valve) on the 8DM-21 diesel engine reduces NO_x emissions by up to 20% compared to the basic engine with a slight change in power and the specific flow rate (within $\pm 3\%$);
- As a result of experimental research, it was established that upgrading the 8DM-21 engine due to the change in valve timing (based on the Miller cycle) led to a reduction in harmful emissions: NO_x decreased by 16%, CO by 50% and CH by 54% compared with the initial parameters of the considered diesel engine. This will allow the use of the 8DM-21 engine in the design of advanced diesel locomotives with increased environmental requirements; the obtained values of harmful substance concentration in the exhaust gases are significantly lower than the requirements of international standards;
- During the tests, it was established that the use of new valve timing also leads to a decrease in the specific fuel consumption of the diesel engine 8DM-21 (down to 4% in certain engine operating modes).

References

1. Heywood JB (1988) Internal combustion engine fundamentals. McGraw-Hill, New York
2. Kavtaradze RZ, Zelentsov AA, Iosebidze JS et al (2015) Innovative methods for improvement of technical, economic and ecological efficiency of motor cars. NOVA-Publishers, New York
3. Zhilkin BP, Lashmanov VV, Plotnikov LV et al (2015) Improvement of processes in the gas-air tracts of piston internal combustion engines: monograph. Ural Publishers of the University, Ekaterinburg
4. Pesic R, Milojevic S (2013) Efficiency and ecological characteristics of a VCR diesel engine. Int J Autom Technol 14(5):675–681

5. Bo L, Wenqing G, Binbin S (2015) Benefits of the electromagnetic actuated valve train in gasoline engine application. *Int J Eng Trans B: Appl* 28(11):1656–1662. <https://doi.org/10.5829/idosi.ije.2015.28.11b.14>
6. Zhang X, Wang H, Zheng Z et al (2016) Effects of late intake valve closing (LIVC) and rebreathing valve strategies on diesel engine performance and emissions at low loads. *Appl Therm Eng* 98:310–319. <https://doi.org/10.1016/j.applthermaleng.2015.12.045>
7. Schück C, Samenfink W, Schünemann E et al (2018) Analysis of particulate number emissions during dynamic load changes for port fuel injection on an optically accessible, turbocharged four-cylinder spark ignition engine. *Int J Engine Res* 19(1):78–85. <https://doi.org/10.1177/1468087417731044>
8. Braga LB, Silveira JL, Evaristo Da Silva M et al (2014) Comparative analysis between a PEM fuel cell and an internal combustion engine driving an electricity generator: Technical, economical and ecological aspects. *Appl Therm Eng* 63(1):354–361. <https://doi.org/10.1016/j.applthermaleng.2013.10.053>
9. Zhao J (2017) Research and application of over-expansion cycle (Atkinson and Miller) engines—a review. *Appl Energy* 185:300–319. <https://doi.org/10.1016/j.apenergy.2016.10.063>
10. Wu Z, Chen L, Ge Y et al (2018) Optimization of the power, efficiency and ecological function for an air-standard irreversible dual-miller cycle. *Front Energy* 3:1–11. <https://doi.org/10.1007/s11708-018-0557-z>
11. Wu Z, Chen L, Ge Y et al (2018) Thermodynamic optimization for an air-standard irreversible dual-miller cycle with linearly variable specific heat ratio of working fluid. *Int J Heat Mass Transf* 124:46–57. <https://doi.org/10.1016/j.ijheatmasstransfer.2018.03.049>
12. Brückner C, Kyrtatos P, Boulouchos K (2018) NO_x emissions in direct injection diesel engines: Part 2: model performance for conventional, prolonged ignition delay, and premixed charge compression ignition operating conditions. *Int J Engine Res* 19(5):528–541. <https://doi.org/10.1177/1468087417721558>
13. Molina S, García A, Monsalve-Serrano J et al (2018) Miller cycle for improved efficiency, load range and emissions in a heavy-duty engine running under reactivity controlled compression ignition combustion. *Appl Therm Eng* 136:161–168. <https://doi.org/10.1016/j.applthermaleng.2018.02.106>
14. Zou X, Liu W, Lin Z et al (2018) An experimental investigation of the effects of fuel injection strategy on the efficiency and emissions of a heavy-duty engine at high load with gasoline compression ignition. *Fuel* 220:437–445. <https://doi.org/10.1016/j.fuel.2018.02.035>
15. Kim J, Bae C (2017) Emission reduction through internal and low-pressure loop exhaust gas recirculation configuration with negative valve overlap and late intake valve closing strategy in a compression ignition engine. *Int J Engine Res* 18(10):973–990. <https://doi.org/10.1177/1468087417692680>
16. Wei H, Shao A, Hua J et al (2018) Effects of applying a Miller cycle with split injection on engine performance and knock resistance in a downsized gasoline engine. *Fuel* 214:98–107. <https://doi.org/10.1016/j.fuel.2017.11.006>
17. He Y, Sun D, Liu J et al (2018) Optimization of a turbocharger and supercharger compound boosting system for a Miller cycle engine. *Proc Inst Mech Eng, Part D: J Autom Eng* 232(2):238–253. <https://doi.org/10.1177/0954407017695136>
18. Pedrozo VB, Zhao H (2018) Improvement in high load ethanol-diesel dual-fuel combustion by Miller cycle and charge air cooling. *Appl Energy* 210:138–151. <https://doi.org/10.1016/j.apenergy.2017.10.092>
19. Zhang Q, Xian K, Li M (2017) Investigation of performance and emission characteristics on a large-bore spark-ignition natural gas engine with scavenged prechamber and miller cycle attribute. *J Energy Eng* 143(5):04017026. [https://doi.org/10.1061/\(ASCE\)EY.1943-7897.0000452](https://doi.org/10.1061/(ASCE)EY.1943-7897.0000452)
20. Ojapah MM, Zhao H, Zhang Y (2016) Effects of ethanol on combustion and emissions of a gasoline engine operating with different combustion modes. *Int J Engine Res* 17(9):998–1011. <https://doi.org/10.1177/1468087416634517>

21. Imperato M, Kaario O, Larmi M et al (2018) Emission reduction methods and split fuel injection in a marine four-stroke engine. *J Mar Sci Technol (Japan)* 23(1):94–103. <https://doi.org/10.1007/s00773-017-0458-6>
22. Gonca G, Sahin B (2017) Effect of turbo charging and steam injection methods on the performance of a Miller cycle diesel engine (MCDE). *Appl Therm Eng* 118:138–146. <https://doi.org/10.1016/j.applthermaleng.2017.02.039>
23. Plotnikov LV, Bernasconi S, Brodov YM (2017) The effects of the intake pipe configuration on gas exchange, and technical and economic indicators of diesel engine with the 21/21 dimension. *Proc Engineering* 206:140–145. <https://doi.org/10.1016/j.proeng.2017.10.450>
24. Bernasconi S (2015) Two-stage turbocharging solutions for tier 4 rail applications. In: Internal combustion engine division's fall technical conference ASME ICED 2015, Huston, USA, 08–11 Nov 2015
25. Schurmann P (2013) Contribution of turbocharging solutions towards improved fuel efficiency of two-stroke low-speed engines. In: 27th CIMAC World Congress on Combustion Engines CIMAC 2013, Shanghai, China, 13–16 May 2013

Calculated Analysis of Efficiency of Fresh Charge Heating in Diesel Engine Under Cold-Start Conditions



A. E. Popov, Z. V. Almetova and V. D. Shepelev

Abstract We considered the possibility of calculating the temperature ranges of the fresh charge heating degree, which provides favorable conditions for the self-ignition of the combustible mixture in the diesel cylinder at the end of the compression process, as applied to the “cold”-start conditions. We developed a method to determine the degree of the fresh charge heating and the degree of its oxidizer (air oxygen) impoverishment. We studied that the influence of the degree of the intake air heating on the duration of the diesel engine starts at low ambient temperatures. We calculated that the degree of heating is 40–50 degrees for the ambient temperatures from -30 to $+5$ °C, which ensures the fluid temperature of 287–315 K at the end of the intake. It has been established that the duration of the diesel engine start is reduced intensively up to a certain value of the intake charge heating degree (a 40–60-degree temperature increase), and then, the influence of heating becomes less significant. Thus, at the ambient air temperature of -30 °C, a 60-degree air heating in the intake manifold allows us to reduce the time spent to start the diesel engine from 43 to 22 s. With a further increase in the degree of heating, this time varies slightly.

Keywords Diesel engine · “Cold” start · Air heating · Heating degree · Calculated analysis · Low temperatures

1 Introduction

The rapid development of internal combustion engines (ICE) is currently aimed mainly at improving the power and economic parameters [1, 2]. At the same time, it is also necessary to improve the efficiency of engines, which is largely determined by their starting characteristics. These characteristics are particularly important for diesel engines operated in the conditions of low ambient temperatures. This, in

A. E. Popov (✉) · Z. V. Almetova · V. D. Shepelev
South Ural State University (NRU), 76, Lenin Avenue, Chelyabinsk 454080, Russia
e-mail: popovae@susu.ru

particular, concerns the regions of Russia, where the frost period is over 200 days a year.

At the moment, a significant share of transport mechanisms and diesel engines is operated without any “cold”-start aid means, which results in an increase in the cost of operating the machines. The diesel engine start is already complicated at the temperatures of about +5 °C.

The problem is aggravated by the need for a relatively quick warm-up of a “cold” diesel engine to the level of operating temperatures, which follows from the condition of carburation and self-ignition of diesel fuel in the cylinder.

A high degree of air compression in the cylinder must be provided for self-ignition. Therefore, the minimum crankshaft starting speed of diesel engines is significantly higher than that of gasoline engines. At a low crankshaft speed, there are air leaks through unsound piston rings and valves and an increased heat transfer to the cylinder walls due to a longer cycle period. At a low charge temperature, the temperature of the end of the compression process decreases, and the charge is not heated at the intake, but, on the contrary, cooled by the cold walls of the cylinder [3–5].

This problem can be solved by preheating the fresh charge in the intake manifold. According to the environmental requirements, most modern engines are equipped with exhaust gas recirculation, which can also be used to increase the fresh charge temperature at the intake to the cylinder.

Several studies have dealt with the “cold” start of diesel engines and the influence of the intake charge temperature on their parameters. For example, in [6], the authors Horng-Wen Wu, Tzu-Ting Hsu, Jian-Yi He, Chen-Ming Fan selected the optimal values of the intake air temperature and the degree of the exhaust gas recirculation to improve the engine’s environmental parameters.

In [7, 8], the authors selected threshold intake air temperatures ensuring a stable fuel ignition and engine start. For example, the authors C. Woo, S. Kook, E. R. Hawkes studied the stability of fuel ignition in the engine cylinder at different intake air temperatures [7]. At the same time, they selected pressure and fuel injection characteristics.

A. Broatch, S. Ruiz, X. Margot, A. Gil presented a developed procedure for estimating threshold values of the fresh charge temperature in the engine cylinder during a “cold” start [8]. For the study, they selected two engines with different compression degrees.

In [9], R. García-Contreras, O. Armas, C. Mata, and O. Villanueva developed a procedure for studying the average gas pressure in the combustion process and the heat release rate during a “cold” start. It allows us to adjust the average gas pressure in the engine cylinder from the initial cycle to the subsequent cycle.

A number of works deal with the influence of fuel injection characteristics on the parameters of a diesel engine during a “cold” start [10–12]. Thus, in [10], S. Ezzitouni, J. A. Soriano, A. Gómez, and O. Armas experimented with a diesel car, in which pressure sensors were installed in each engine cylinder. Effective parameters and heat release parameters were evaluated by the first 5–6 cycles. In [11, 12], the main objective was to determine the fuel injection delay period, the duration of the injection process, depending on the fuel viscosity. The visualization

method was also used to determine the flame propagation speed in the combustion chamber.

In [13, 14], much attention was given to the processes of atomization and carburation of fuel when starting a diesel engine in the low ambient temperature conditions. The visualization method was used. The conditions of the experiment corresponded to the engine start conditions at low ambient temperatures.

In [15], A. Broatch, B. Tormos, P. Olmeda, and R. Novella evaluated the possibility of starting an engine on biodiesel fuel at low ambient temperatures and made a comparison with standard diesel fuel.

The authors Y. Deng, H. Liu, X. Zhao, J. E. J. Chen created a digital model of the engine start process, which allows us to select the intake charge heating time based on the analysis of the data on the technical status of the vehicle's auxiliary systems [16].

A distinctive feature of [17] written by H. Peng, Y. Cui, L. Shi, and K. Deng is the use of heat of exhaust gases to heat the intake charge. They studied the influence of the exhaust gas recirculation on the combustion process and emissions during a "cold" start. They determined that in this case, in the first cycle, the maximum gas pressure was about 45% higher than in the normal state without exhaust gas supply.

The purpose of the study is to determine the temperature ranges of the fresh charge heating degree, at which the level of the air charge temperature in the engine cylinder at the end of the compression process meets the requirements of a stable self-ignition.

The implementation of this purpose required to solve the problem of evaluating the possibilities of calculating the numerical values of the intake charge heating degree provides favorable conditions for self-ignition of the combustible mixture in the cylinder of a diesel engine at the end of the compression process.

The practical significance of the study is as follows: based on the results of the calculated and experimental studies as applied to the diesel engine start in the conditions of low ambient temperatures, we determined an expedient temperature range for heating the intake charge with exhaust gases of starting internal combustion engines.

2 Calculated Analyses of the Start Process

The calculated analyses were conducted to identify the peculiar features of changes in the indicators of the operating cycle of a diesel engine at varying degrees of the intake charge heating by hydrocarbon fuel combustion products. The need for such studies is preconditioned by the fact that the work process performance during the diesel engine start is ambiguously influenced by the intake charge parameters (charge temperature, oxygen concentration in it), which, when the intake air is heated, can vary widely, as well as the thermal state of the engine, the ambient temperature, and other parameters.

Heating of the intake air ensures a stable fuel ignition (no missed self-ignition) during the diesel engine start and reduces the ignition delay period. As the degree of

heating, the intake charge with the combustion products increases, and the oxygen concentration in the intake charge and the density of the intake gases decrease, which influence the nature of the combustion process and determines the value of the rated cycle operation. An increase in the concentration of the combustion products in the intake charge increases the ignition delay period.

To accomplish the task, we used a set of two calculation methods:

- a method allowing us to simulate the change in the gas pressure in the engine cylinder in the start mode when using the intake charge heating with exhaust gases, as well as the change in the fluid temperature in the engine cylinder taking into account the heat exchange with the cold walls of the cylinder;
- a method of analyzing the heat use in the engine cylinder in the start mode using the intake charge heating with exhaust gases.

The first method is based on the volume balance method and takes into account the influence of the properties of the intake charge heated by the fuel combustion products, charge leaks from the cylinder through the unsound cylinder and piston group and heat exchange phenomena on the fluid parameters [18].

The second method is meant to determine the parameters of using heat in a diesel engine in the start modes when using the intake charge heating by the hydrocarbon fuel combustion products.

The condition of the study is to ensure that the level of the air charge temperature in the cylinder of the diesel engine at the end of the intake process (at the time of closing the intake valve) corresponded to the engine start conditions in summer ($T_0 \geq +10^\circ\text{C}$).

In case the fresh charge is heated by combustion products, it (the charge) is considered as a mixture of “clean” combustion products ($\alpha = 1$) and air. In this case, the entire volume of the fresh charge is assumed to be equal to one. We introduced the ratio [14] to indicate the excess air proportion:

$$r_\alpha = \frac{M_\alpha}{M} \quad (1)$$

where M_α is the number of moles (amount) of excess air in the intake charge in the intake manifold or in the engine cylinder; M is the total number of moles of gas.

The volume fraction of excess air in the intake charge r_α can be determined based on the percentage of oxygen in it, which (percentage of oxygen) can be outlined based on a chemical analysis of the gases in the intake manifold.

Gas samples are collected directly before the intake valves of the engine. Since the oxygen content in the air is 21%, the volume fraction of excess air is determined from the ratio:

$$r_\alpha = \frac{O_\alpha}{21\%} \quad (2)$$

where O_α is the percentage of oxygen in the intake charge.

As a result, it was determined that the degree of the air charge heating in the intake manifold from 35 to 80 degrees depending on the ambient temperature (the lower the ambient temperature, the higher the degree of the air charge heating) is needed to ensure the fluid temperature at the end of the intake process, at which there are no missed fuel ignitions in the engine cylinder. The temperature at the end of the intake process is $T_{a1} = 310\text{--}315\text{ K}$ (Fig. 1a), the proportion of excess clean air in the intake charge is $r_\alpha = 0.65\text{--}0.94$ (Fig. 1b), and the combustion efficiency coefficient is $\zeta = 0.28\text{--}0.82$ (Fig. 2a).

Heating of the fresh charge of over 80 degrees leads to its oversaturation with exhaust gases and worsening of the self-ignition conditions in the engine cylinder.

Based on the results of the calculated analysis, it was also noted that if the degree of the air charge heating is $\Delta T_S = 40\text{--}50$ degrees at low ambient temperatures ($T_0 \approx -30\text{ }^\circ\text{C}$), the fluid temperature at the end of the intake process is $T_{a1} \approx 287\text{ K}$, the combustion efficiency coefficient is $\zeta \approx 0.55$, and the proportion of excess clean air in the intake charge is $r_\alpha \approx 0.83$.

At the ambient temperature of $+5\text{ }^\circ\text{C}$ and above, such a degree of the fresh charge heating provides $T_{a1} \approx 315\text{ K}$, the combustion efficiency coefficient is $\zeta \approx 0.82$, and the proportion of excess clean air in the intake charge is $r_\alpha 0.91$.

To confirm the correct choice of the degree of the intake air heating, we should determine how its value influences the duration of the diesel engine start at low ambient temperatures.

Such a study was conducted using the empirical dependence of the start duration for tractor diesel engines obtained by Shishkov [19, 20]:

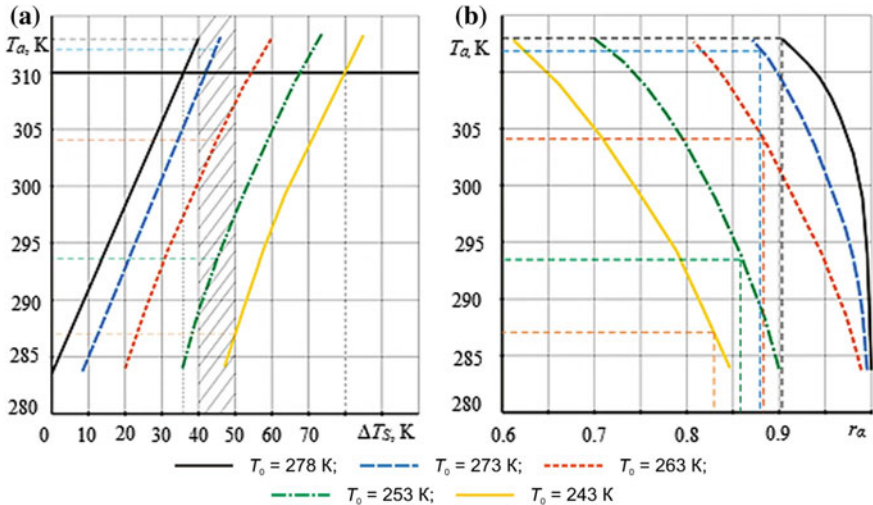


Fig. 1 Influence of the degree of the intake charge heating ΔT_S and the proportion of excess clean air r_α on the fluid temperature at the end of the intake process T_{a1}

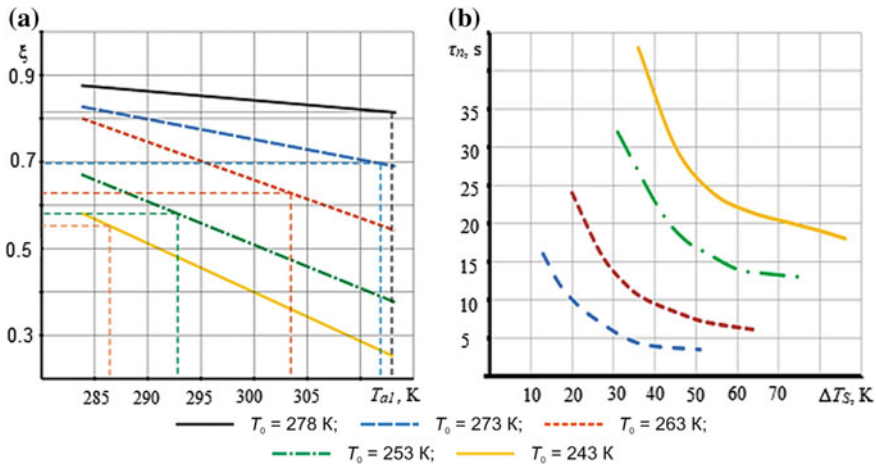


Fig. 2 **a** Influence of the fluid temperature at the end of the intake process on the combustion efficiency coefficient; **b** Influence of the degree of the intake charge heating on the duration of the diesel engine start at various ambient temperatures

$$\ln \tau_n = 175 - 9.05 \cdot \ln T_0 + 0.121 \cdot \ln n - 16.4 \cdot \ln T_c + 1.34 \cdot \ln \Delta \Theta_{Arel} + 1.45 \cdot \ln \Delta G_{Crel} - 0.631 \cdot \ln i - 1.01 \cdot \ln S - 1.99 \ln K - 4.62 \cdot \ln \varepsilon_G \quad (3)$$

where τ_n is the start duration, s; n is the starting speed of the engine crankshaft n_s , min^{-1} ; T_c is the fluid temperature at the end of compression, K; $\Delta \Theta_{Arel}$ is the relative deviation of the adjusting angle of the fuel injection advance from the optimum value when the diesel engine is started; ΔG_{Crel} is the relative deviation of the cyclic fuel supply from the optimum value when the diesel engine is started; i is the number of diesel cylinders; S is the piston distance, cm; K is the quality parameter; and ε_G is the geometric compression ratio.

The results of the study are presented graphically in Fig. 2b.

During the study, it has been established that the duration of the diesel engine start is reduced intensively up to the degree of the intake charge heating of $\Delta T_S \approx 40\text{--}60$ degrees, and then the influence of heating becomes less significant. Thus, at the ambient air temperature of 243 K, a 60-degree air heating in the intake manifold allows us to reduce the time spent to start the diesel engine from 43 to 22 s. At the same time, when heating the intake charge by over 60 degrees, the density of the air charge in the intake manifold decreases significantly, which leads to a decrease in the filling and excess air ratios and creates difficulties in starting the diesel engine.

3 Conclusion

As applied to the diesel engine start modes using the intake charge heating with combustion products, we developed a method for analyzing the engine operating cycle according to an indicator diagram, which takes into account the features of intra-cylinder processes during the start period, to determine the appropriate degree of fresh charge heating. In particular, the degree of its oxidizer (air oxygen) impoverishment in the processes of intake and compression and the influence of this circumstance on the combustion process.

Based on the results of the calculated analysis, we have established an expedient temperature range for heating the intake charge in the diesel engine as applied to various low-temperature start conditions. It is 40–50 degrees for the ambient temperatures from -30 to $+5$ °C, which ensures the fluid temperature at the end of the intake equal to 287–315 K. This corresponds to the conditions of starting a diesel engine (by the intake charge parameters) at the ambient temperature $T_0 = 10$ –15 °C.

We carried out the calculated analysis of the influence of the degree of the intake air heating on the duration of the diesel engine start at low ambient temperatures. Based on the results, it has been established that the duration of the diesel engine start is reduced intensively up to a certain value of the intake charge heating degree (a 40–60-degree temperature increase), and then, the influence of heating becomes less significant. Thus, at the ambient air temperature of -30 °C, a 60-degree air heating in the intake manifold allows us to reduce the time spent to start the diesel engine from 43 to 22 s. With a further increase in the heating degree, this time varies insignificantly.

References

1. Mukhopadhyay S, Badavath SS, Henein N (2017) Direct injection compression ignition engine: cold start on gasoline and diesel. In: SAE World congress experience, WCX 2017 Cobo Center, Detroit, USA, 4–6 Apr 2017. <https://doi.org/10.4271/2017-01-0699>
2. Zhong L, Gruenewald S, Henein NA et al (2007) Lower temperature limits for cold starting of diesel engine with a common rail fuel injection system. In: World congress, Detroit, MI, USA, 16–19 Apr 2007
3. Bielaczyc P, Merksiz J, Pielecha J (2001) Investigation of exhaust emissions from DI diesel engine during cold and warm start. In: World congress, Detroit, MI, USA, 5–8 Mar 2001. <https://doi.org/10.4271/2001-01-1260>
4. Blackwood A, Tidmarsh D, Willcock M (1998) The effect of an oxidation catalyst on cold start diesel emissions in the first 120 seconds of running. In: SAE International congress and exposition, Detroit, MI, USA, 23–26 Feb 1998. <https://doi.org/10.4271/980193>
5. Zahdeh A, Henein N, Bryzik W (1990) Diesel cold starting: actual cycle analysis under border-line conditions. In: International congress and exposition, Detroit, MI, USA, 26 Feb–2 Mar 1990. <https://doi.org/10.4271/900441>

6. Horng-Wen W, Tzu-Ting H, Jian-Yi H et al (2017) Optimal performance and emissions of diesel/hydrogen-rich gas engine varying intake air temperature and EGR ratio. *Appl Therm Eng* 124:381–392
7. Woo C, Kook S, Hawkes ER (2016) Effect of intake air temperature and common-rail pressure on ethanol combustion in a single-cylinder light-duty diesel engine. *Fuel* 180:9–19
8. Broatch A, Ruiz S, Margot X et al (2010) Methodology to estimate the threshold in-cylinder temperature for self-ignition of fuel during cold start of diesel engines. *Energy* 35:2251–2260
9. García-Contreras R, Armas O, Mata C et al (2017) Impact of gas to liquid and diesel fuels on the engine cold start. *Fuel* 203:298–307
10. Ezzitouni S, Soriano JA, Gómez A et al (2017) Impact of injection strategy and GTL fuels on combustion process and performance under diesel engine start. *Fuel* 200:529–544
11. Wang Z, Ding H, Wyszynski ML et al (2015) Experimental study on diesel fuel injection characteristics under cold start conditions with single and split injection strategies. *Fuel Process Technol* 131:213–222
12. Pastor JV, García-Oliver JM, Pastor JM et al (2011) Ignition and combustion development for high speed direct injection diesel engines under low temperature cold start conditions. *Fuel* 90:1556–1566
13. Wang Z, Li Y, Wang C et al (2016) Experimental study on primary breakup of diesel spray under cold start conditions. *Fuel* 183:617–626
14. Desantes JM, García-Oliver JM, Pastor JM et al (2011) Influence of nozzle geometry on ignition and combustion for high-speed direct injection diesel engines under cold start conditions. *Fuel* 90:3359–3368
15. Broatch A, Tormos B, Olmeda P et al (2014) Impact of biodiesel fuel on cold starting of automotive direct injection diesel engines. *Energy* 73:653–660
16. Deng Y, Liu H, Zhao X et al (2018) Effects of cold start control strategy on cold start performance of the diesel engine based on a comprehensive preheat diesel engine model. *Appl Energy* 210:279–287
17. Peng H, Cui Y, Shi L et al (2008) Effects of exhaust gas recirculation (EGR) on combustion and emissions during cold start of direct injection (DI) diesel engine. *Energy* 33:471–479
18. Sharoglazov BA, Shishkov VV (1993) Analysis of the diesel working cycle during start-up according to the indicator diagram. *Engine Build* 3(12):25–27
19. Sharoglazov BA, Popov AE, Shishkov VV (2009) Estimation of the numerical values of the excess air coefficient at the low-temperature start of diesel engines using the intake charge heating. *Bull SUSU Ser Mach Build* 11(144):64–68
20. Shishkov VV (2000) Improving the performance of the diesel working cycle when started by the intake charge heating. Dissertation, South Ural State University, Chelyabinsk

Theoretical Studies of Automobile Smooth Running on High-Safety Wheels



V. V. Mazur

Abstract The tendency of scientists and engineers to enhance automobile safety led to appearance of high-safety wheels able to keep stable and steerable vehicle movement at the loss of excess air pressure even in several pneumatic tires. In case of loss of excess pressure in one of the pneumatic tires, the modern high-safety wheels producers guarantee safe non-stop vehicle running at a speed up to 80 km/h for a distance within 200 km. However, the loss of excess air pressure even in one pneumatic tire results in noticeable deterioration of factors for majority operational properties including smooth running specified by the automobile sway intensity when running on the uneven surface roads and under off-road conditions. Scientific studies aimed at the enhancement of smooth running and keeping vibration loading levels to normative limits for cars forced to continue movement without the excess air pressure in one or several pneumatic tires ensure their urgency.

Keywords Run flat • Air pressure • Rigidity coefficient • Vertical vibrations • Mathematical model

1 Relevance

The operational properties of high-safety wheels with inner emergency supporting bodies at a nominal excess air pressure in pneumatic tires do not differ from traditional wheels, and are widely used in armored vehicles that are designed to transport valuables or high-ranking passengers.

The inner emergency supports can be rigid, non-deforming, made of metal or hard plastic and resilient, and made of rubber or elastic polyurethane [1–9].

For example, Fig. 1 shows the automobile high-safety wheels with inner emergency supporting bodies.

V. V. Mazur (✉)

Bratsk State University, 40, Makarenko, Bratsk 665709, Russia

e-mail: mazurvv@yandex.ru

© Springer Nature Switzerland AG 2020

A. A. Radionov et al. (eds.), *Proceedings of the 5th International Conference on Industrial Engineering (ICIE 2019)*, Lecture Notes in Mechanical Engineering,

https://doi.org/10.1007/978-3-030-22041-9_61

567



Fig. 1 Automobile high-safety wheels with inner emergency supporting bodies: **a** Michelin PAX; **b** Pirelli PAX; **c** Continental CSR; **d** Hankook with support ring Rodgard

Scientific research is relevant and aimed at improving the design of high-safety wheeled propulsion as elements of the suspension system and to assess their impact on the operational properties of the car.

2 Formulation of the Problem

Traction properties, fuel efficiency, throughput, stability, and controllability of a car with high-safety wheels are sufficiently studied. However, they were studied in most cases only from the results of field or laboratory tests of specific experimental or serial samples [10–18]. The smooth running of the car with high-safety wheels is not investigated at all. Therefore, the main task of the research is to reduce the level of vibrations of the car with the loss of excess air pressure in one or more pneumatic tires.

3 Building a Mathematical Model

For theoretical studies of automobile smooth running on high-safety wheels, a mathematical model of a vibratory system equivalent to the tested wheeled vehicle suspension was developed. Known automobile theory terms and limitations were taken into account in development of the math model.

Figure 2a represents a layout of vibration system equivalent to suspension of the tested vehicle on high-safety wheels at nominal excess air pressure in pneumatic tires. The layout takes up the following symbols: M as sprung mass; m_R and m_L as non-sprung masses centered on the right and left wheels of the vehicle; c as rigidity coefficient of springing element of suspension; η_a as inelastic resistance coefficient of hydraulic shock absorber; c_R and c_L as normal rigidity rates of right and left wheels in assembly; η_R and η_L as inelastic resistance coefficient of right and left wheels in assembly; K as track; S as a span between suspension springing elements;

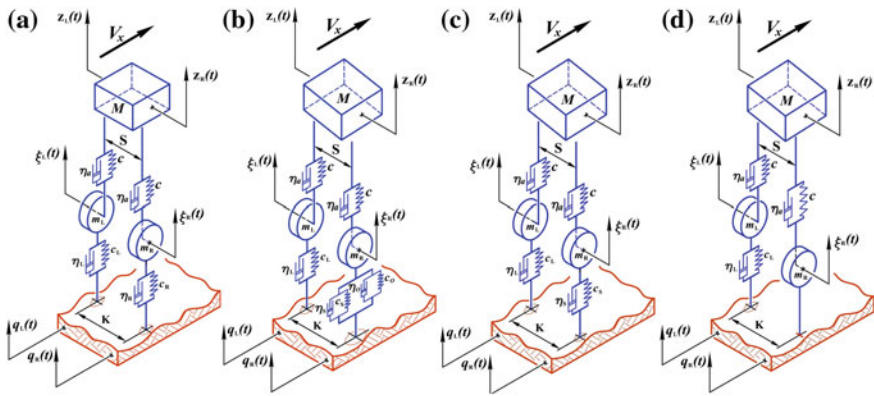


Fig. 2 Layouts of vibration systems equal to vehicle suspension with high-safety wheels: **a** with excess air pressure in pneumatic tires; **b** without excess air pressure in the right pneumatic tire; **c** at running with support on springing inner emergency element of the right wheel with completely damaged pneumatic tire; **d** at running with support on rigid inner emergency element of the right wheel with completely damaged pneumatic tire

$z_R(t)$ and $z_L(t)$ as vertical displacement of right and left centered parts of sprung mass; $\xi_R(t)$ and $\xi_L(t)$ as vertical displacement of right and left non-sprung masses; $q_R(t)$ and $q_L(t)$ as ordinates for road surface microprofile; V_x as vehicle speed.

The equation $q_R(t) = q_L(t) = q(t)$ is fair under condition of symmetrical impact on the road surface irregularities on the vehicle left and right wheels.

It is obvious that at excess air pressure in pneumatic tires of high-safety wheels, the layout given in picture 1, a does not differ principally from the automobile theory known schemes of vibratory systems equal to vehicle suspension with traditional wheeled propulsion. At this, the normal rigidity coefficients of the right and left high-safety wheels in assembly are accepted equal to the normal rigidity coefficient of a pneumatic tire at nominal excess air pressure: $c_R = c_L = c_T$, and inelastic resistance coefficients to the inelastic resistance coefficient of a pneumatic tire by the same pressure: $\eta_R = \eta_L = \eta_T$.

Sprung and non-sprung vehicle mass vibrations are described by the system of differential second-order equations in compliance with the Herman-Euler-d'Alembert principle:

$$\begin{cases} M\ddot{z} + \eta_a(\dot{z}_R - \dot{\xi}_R) + \eta_a(\dot{z}_L - \dot{\xi}_L) + c(z_R - \xi_R) + c(z_L - \xi_L) = 0 \\ J\ddot{\alpha} + \eta_a(\dot{z}_R - \dot{\xi}_R)\frac{S}{2} - \eta_a(\dot{z}_L - \dot{\xi}_L)\frac{S}{2} + c(z_R - \xi_R)\frac{S}{2} - c(z_L - \xi_L)\frac{S}{2} = 0 \\ m_R\ddot{\xi}_R + \eta_T(\dot{\xi}_R - \dot{q}) - \eta_a(\dot{z}_R - \dot{\xi}_R) + c_T(\xi_R - q) - c(z_R - \xi_R) = 0 \\ m_L\ddot{\xi}_L + \eta_T(\dot{\xi}_L - \dot{q}) - \eta_a(\dot{z}_L - \dot{\xi}_L) + c_T(\xi_L - q) - c(z_L - \xi_L) = 0 \end{cases} \quad (1)$$

where $z = z(t)$ as vertical displacement of the sprung mass; J as moment of the sprung mass gyration about the longitudinal axis; α as lateral angular sprung mass displacement.

The mentioned parameters are defined as follows:

$$z = \frac{z_R + z_L}{2}, \quad J = \frac{MS^2}{4}, \quad \alpha = \frac{z_R - z_L}{S}. \quad (2)$$

At the loss of excess air pressure in one of the pneumatic tires, for instance, in the right, the differential equation describing the vertical vibrations in also the right non-sprung mass in compliance with the layout given in Fig. 2b will have the following view:

$$\begin{aligned} m_R \ddot{\xi}_R + \eta_s (\dot{\xi}_R - \dot{q}) + \eta_o (\dot{\xi}_R - \dot{q}) - \eta_a (\dot{z}_R - \dot{\xi}_R) \\ + c_s (\xi_R - q) + c_o (\xi_R - q) - c(z_R - \xi_R) = 0, \end{aligned} \quad (3)$$

where c_s as normal rigidity coefficient of the inner extra elastic support; c_o as normal rigidity coefficient of a pneumatic tire under atmospheric inner pressure; η_s as inelastic resistance coefficient of the inner extra elastic support; η_o as inelastic resistance coefficient of the pneumatic tire under atmospheric inner pressure.

In other words, at the loss of excess air pressure in one of the pneumatic tires due to mechanical damages, the parameters of the right wheel effecting the smoothness of running include the normal rigidity coefficient c_R and the inelastic resistance coefficient η_R will be defined as $c_R = c_s + c_o$ and $\eta_R = \eta_s + \eta_o$.

It is worth mentioning that mathematical presentation of a pneumatic tire without the excess air pressure in the form of separate elements including sidewalls and tread [19, 20] did not give practical results due to impossibility of experimental definition of reliable values necessary for theoretical study of parameters.

It is known from operational experience that by sustained run of the vehicle without the excess air pressure in a pneumatic tire, the complete destruction of the cover is most probably due to increased heat generation caused by the inner and outer friction in the process of tire rolling. The speed of heat destruction of a depressurized tire, first of all, will be influenced by the availability and antifriction properties of special smearing material and manner of fastening of the inner emergency support which, depending on the high-safety wheel design, can rotate or be fixed toward the rim. In that case, further vehicle run will be exercised with support on the inner emergency element of a high-safety wheel.

When the vehicle runs with the support on the inner elastic emergency element of the right wheel with completely destroyed pneumatic tire, the layout of the vibration system presented in Fig. 2c is fair. The differential equation describing vertical vibrations of the right unsprung mass will look as follows:

$$m_R \ddot{\zeta}_R + \eta_s (\dot{\zeta}_R - \dot{q}) - \eta_a (\dot{z}_R - \dot{\zeta}_R) + c_R (\zeta_R - q) - c(z_R - \zeta_R) = 0. \quad (4)$$

At that, the right wheel parameters effecting the smoothness of running will be defined as $c_R = c_s$ and $\eta_R = \eta_s$.

In case of the vehicle running with support on inner rigid emergency element, it is possible to use the vibration system layout presented in Fig. 2d and for description of vertical vibrations of the right unsprung mass to use a differential equation

$$m_R \ddot{\zeta}_R - \eta_a (\dot{z}_R - \dot{\zeta}_R) - c(z_R - \zeta_R) = 0, \quad (5)$$

in which $\zeta_R = q_R(t) = q(t)$.

To solve the received systems of differential equations, the method of operational calculus was applied, namely direct Laplace transformation, which allows receiving the transfer functions of the developed vibration systems and amplitude–frequency characteristics of vertical vibrations.

4 Theoretical Studies

By means of the developed mathematical model, theoretical studies were carried out concerning the smooth running of a passenger car with high-safety wheels forced to continue movement without the excess air pressure in one of the pneumatic tires. The parameters of rear suspension of a small class passenger car were taken for calculations.

Figure 3 shows the calculated amplitude–frequency characteristics of vertical vibrations of VAZ-2115 automobile sprung mass during its running on uneven road in different technical states specified by the degree of damaged pneumatic tires and availability of excess air pressure in them.

The loss of excess air pressure in the pneumatic tire leads to a sharp increase in the amplitude of the vertical accelerations (2.27 times) of the sprung mass of the car. The greatest deterioration in smooth running is observed with the intact rubber-cord sheath of a pneumatic tire at atmospheric pressure.

5 Experimental Studies

Experimental studies [21] of the smooth running of the VAZ-2115 with high-safety wheels were conducted to check the adequacy of the developed mathematical model.

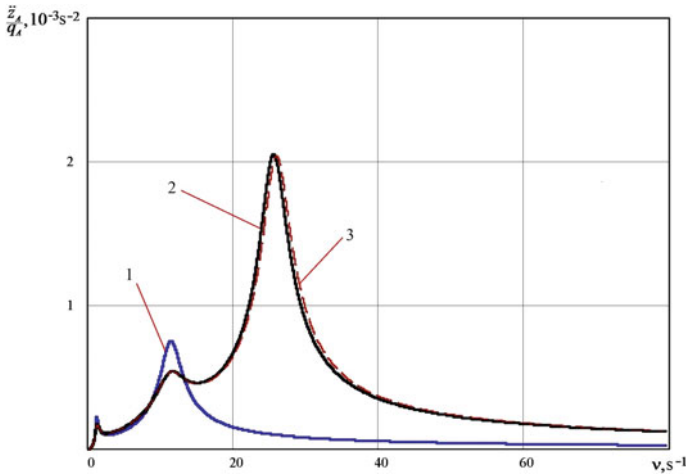


Fig. 3 Amplitude–frequency characteristics of vertical accelerates of automobile sprung mass: (1) with excess air pressure in pneumatic tires; (2) without excess air pressure in the right pneumatic tire; (3) at running with support on springing inner emergency element of the right wheel with completely damaged pneumatic tire

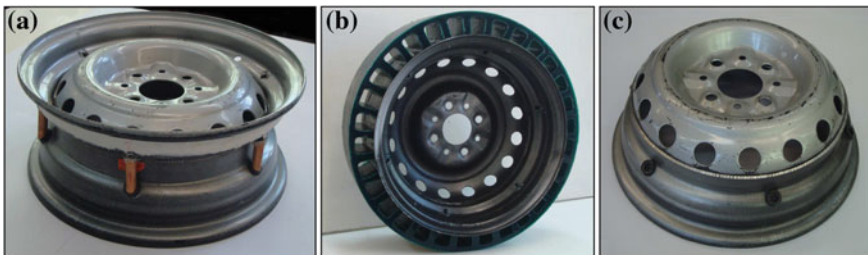


Fig. 4 Full-scale model of a wheel with springing inner emergency element from elastic polyurethane: **a** standard 5JX13H2 disk wheel with a deep rim assembly; **b** assembled with an elastic support ring of elastic polyurethane; **c** wheel disk with the inner part of the detachable rim

The car was equipped with full-scale models of high-safety wheels with springing inner emergency element made of elastic polyurethane (Fig. 4).

Car tests were carried out on a broken dirt road and asphalt road in accordance with OST 37.001.275-84 *Motor vehicles. Test methods for smooth running*.

The measurement and registration of the vertical vibration accelerations of the sprung mass of the test vehicle was carried out using a set of vibration measuring equipment, which includes: ZET 017-U2 portable low-frequency spectrum analyzer with ZETLab software, VS 110 and VS 201 piezoelectric and capacitance accelerometers, ZET 410 preamplifier, Lenovo IdeaPad S10-2 netbook, and Ritmix

RPI-4001 12/230 V 400 W automobile voltage converter. At the same time, the accelerometers BC 110 and BC 201, duplicating each other, were mounted on the right-hand mounting bracket of the rear row seats without an intermediate base plate.

6 Conclusion

The percentage difference between the calculated and experimental values of the vertical vibration acceleration on the right rear seat of the VAZ-2115 with a nominal air pressure in the pneumatic tires is 4.39% on a broken dirt road and 18.99% on an asphalt concrete road. The percentage difference with atmospheric air pressure in the pneumatic tire of the right rear wheel is 8.86% on the dirt and 12.85% on the asphalt road.

The results of experimentally proved theoretical studies of smooth running of a vehicle with high-safety wheels supplement and enlarge the theory of automobile running abilities. The developed mathematical models enable to carry out calculations of parameters influencing the smooth running of high-safety wheels as well as sprung systems characteristics at the stage of design.

References

1. Glinz M et al (1998) Luftbereiftes Fahrzeugrad. EP Patent 0860304, 26 Aug 1998
2. Glinz M et al (2002) Vehicle wheel with emergency running support body. US Patent 6463976, 15 Oct 2002
3. Pompier Z-P et al (2005) Protecting bearing for air tire. RU Patent 2261180, 27 Sept 2005
4. Naito M (2008) Tire/wheel assembly. US Patent 0295938, 4 Dec 2008
5. Tercha MJ et al (2011) Run-flat device. US Patent 0146872, 23 June 2011
6. Anderson B et al (2011) Run-flat device. US Patent 0180194, 26 June 2011
7. Chistov MP et al (2011) Safe wheel air tire internal support. RU Patent 2461468, 10 Jan 2011
8. Glejzbruk EM (2014) Serviceable noninflated tire. RU Patent 2513161, 20 Apr 2014
9. Tercha MJ et al (2015) Run-flat device. US Patent 9108470, 18 Aug 2015
10. Chistov MP et al (2005) Some test results of domestic fighting wheels. Problems of tires and rubber-cord composites. Tire Industry Research Institute, Moscow, pp 53–63
11. Veselov IV et al (2007) The trend to create high-safety tires. Problems of tires and rubber-cord composites. Tire Industry Research Institute, Moscow, pp 96–121
12. Abramov VN, Konkov MY (2008) Influence of thermal radiation of tires on indicators of military vehicle noticeability. Problems of tires and rubber-cord composites. Tire Industry Research Institute, Moscow, pp 64–69
13. Abramov VN, Chistov MP (2008) Prospects for the creation of armor tires for military vehicles. Automobile Industry
14. Sdobnov KS, Veselov IV (2008) On the issue of ensuring tire. Problems of tires and rubber-cord composites. Tire Industry Research Institute, Moscow, pp 166–172
15. Chistov MP et al (2009) The relevance of a complete set of armored wheels with high fighting resistance and a generalized analysis of the design solutions of such wheels. Problems of tires and rubber-cord composites. Tire Industry Research Institute, Moscow, pp 194–201

16. Babakin AN (2010) Increasing the survivability of military vehicles using modern combat-resistant car tires. Automobile and tractor construction in Russia: development priorities and personnel training. MAMI, Moscow, pp 22–28
17. Abramov VN, Aipov TA (2011) A model for calculating the estimated parameters of the possibility of an army vehicle when the wheel propulsion is damaged. Problems of tires and rubber-cord composites. Tire Industry Research Institute, Moscow, pp 49–57
18. Eremin GP (2016) Method of ensuring the mobility of a wheeled vehicle in case of failure of pneumatic tires by using internal additional supports made of polymer composite materials in tires. Dissertation, Bauman Moscow State Technical University
19. Mazur VV (2013) Dynamic model of the vibration system, equivalent to a car with combat wheels when driving on roads with uneven surfaces. Bull Acad Mil Sci
20. Mazur VV, Mazur MA (2014) Vibrations of a wheeled vehicle with combat wheels as it moves along roads with uneven surfaces. Automobile Industry
21. Mazur VV (2015) Experimental evaluation of the smooth running of the car with high-safety wheels without excessive air pressure in one of the pneumatic tires. Transp Sci Technol Manage

Computer Simulation of Numerical Description of Closed Curve Using Fourier Coefficients



S. Ibrayev, Zh. Bidakhmet and Ay. Rakhmatulina

Abstract This article specifies the numerical description of the closed curve using the Fourier series. Fourier analysis of closed curve is used in order to find the appropriate guidance mechanism by electronic catalog. This method is based on optimization methods and allows taking into account the additional requirements of synthesis and limits. The most important role in the study of problems including their computer modeling is assigned to the methods of presenting the obtained results and, above all, the methods of graphic imaging and visualization of the phenomena under study. The main method of computer modeling is writing of proprietary software in algorithmic programming language C++, which gives a fundamental versatility of possibilities and direct comprehension of computer-oriented nature of the used modeling methods. By taking into account the identified shortcomings, it was formulated the setting of research problems, the solution of which allows achieving the goal to be sought—the method for representing of lever mechanisms in the database using Fourier series coefficients for decomposition of the mechanism coupler curve. The methodology offered in this paper represents an effective way to select the first approximation for the synthesized mechanism that allows, on the one hand, the most effective way to create the library of mechanisms and quickly find the right mechanism.

Keywords Fourier series • Guidance mechanism • Coupler curve • Parameter • Analysis • Machine learning

S. Ibrayev

Institute of Mechanics and Engineering, 28, Shevchenko Street,
Almaty 050010, Republic of Kazakhstan

Zh. Bidakhmet (✉)

Almaty University of Power Engineering and Telecommunications,
126/1, Baitursynov Street, Almaty 050013, Republic of Kazakhstan
e-mail: zhanarbi@rambler.ru

Ay. Rakhmatulina

The Kazakh National Technical University after K. I. Satpayev,
22a, Satpayev Street, Almaty 050013, Republic of Kazakhstan

© Springer Nature Switzerland AG 2020

A. A. Radionov et al. (eds.), *Proceedings of the 5th International Conference on Industrial Engineering (ICIE 2019)*, Lecture Notes in Mechanical Engineering,

https://doi.org/10.1007/978-3-030-22041-9_62

1 Introduction

The last ten years are marked by a surge of interest in the automatic manipulators and mechanisms controlled by electronic computing machines where the advanced robotic systems have significant qualitative differences from similar systems of the twentieth century. At the same time, the requirements for mechanical–mathematical models specifying the kinematics and dynamics of their work have been increased.

For example, it is not enough to make a “simple” accounting of the system links elastic properties, it is necessary to provide “sensing” of robots at least at the elementary level using a microcomputer. Machines and mechanisms’ computerized modeling technologies are used not only in industry but in the public health service [1, 2]. The given literature review states that the majority of modern analytical methods of kinematic analysis and synthesis of lever mechanisms is based on the use of extensive capabilities of computer machines, and appropriate software is developed for this purpose [3, 4]. Currently, there is a large number of software packages dedicated to the kinematic analysis and synthesis of lever mechanisms [4–10]. For mechanisms of rather complex structure, the kinematic analysis problem solving is almost impossible. Synthesis of lever mechanisms has a still higher complexity and depends on the task set by the design engineer, and structure of synthesized mechanism, and set of conditions (limits). The existing programs of synthesis of lever mechanisms for the most part are focused on solving the problems of certain particular class. For example, the synthesis of four-link transfer mechanism, six-link mechanism with dwell [11], etc., have been studied. In the works of Drezig and Gaull [9], the authors refer to the works of S. M. Ibrayev, and indicate that the mathematical apparatus of the theory of approximate mechanism synthesis provides new opportunities [10]. Based on the above, it follows that in the future for new rather complicated lever mechanisms, it is necessary to develop new software packages for solution of specific problems of analysis and synthesis depending on technological and structural requirements imposed on them. The classic methods of synthesis of lever mechanisms are divided into accurate and approximate. As is known, the methods of synthesis of mechanisms for accurate reproduction of the given finite-distant positions of the output object are of limited use. As the number of predetermined positions is limited, the methods of synthesis were developed as per the 3, 4 and 5 positions, where it is impossible to take into account the form of the coupler curve between the specified finite-distant positions, and it is also impossible to put not only the limits on the links length and dimensional limitations but also such important limitations as the quality of the motion transmission, etc. It is known that the existing methods of synthesis of lever mechanisms for accurate reproduction of the specified positions of the point in the plane have found quite limited application. The following may be specified as the main reasons:

- (1) Limitedness of the number of specified positions of the point on the coupler curve, which can be reproduced accurately: the known methods of synthesis allow making synthesis of mechanism only as per the 3, 4 and 5 accurate positions.
- (2) Infeasibility of accounting of the form of the coupler curve between the specified finite-distant positions of the synthesis.
- (3) These methods do not allow taking into account the limitations on the link's length and dimensional limitations, the quality of the motion transmission in the finally obtained mechanism, and other additional requirements of synthesis [12, 13].

The most convenient method to represent a closed loop in the form of numerical data is the use of Fourier coefficients. Even the first few Fourier coefficients perfectly represent the curve shape. This method of presentation is also indispensable from the point of view of search of desired curve in the catalog because the search is reduced to the comparison of two sequences of Fourier coefficients, for what no computational costs are required due to the linear nature of Fourier series.

By taking into account the identified shortcomings, it was formulated the setting of research problems, the solution of which allows achieving the goal to be sought—the method for representing of lever mechanisms in the database using Fourier series coefficients for decomposition of the mechanism coupler curve.

The analysis of the mechanisms functional capabilities allows determining the problems which may be solved by mechanical means only, and problems which may be solved by combination of mechanical and non-mechanical means (i.e., control tools, S. M. Ibrayev).

Link mechanisms have two or more variants of position of the assemblage. However, the real mechanism works in one assembly and the problem of assembly identification arise during the study of functional possibilities of the mechanism.

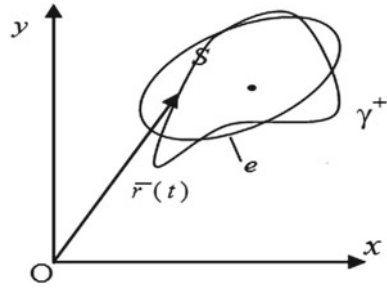
It is known that the most convenient method to represent a closed loop in the form of numerical data is the use of Fourier coefficients. Even the first few Fourier coefficients perfectly represent the curve shape. This method of presentation is also indispensable from the point of view of search of desired curve in the catalog because the search is reduced to the comparison of two sequences of Fourier coefficients, for what no computational costs are required due to the linear nature of Fourier series.

2 Formulation of the Problem

The objective is to represent the method to select the first approximation for synthesized mechanism which allows creating the database of mechanisms in the most efficient way and quickly find the right mechanism.

Parameterized radius-vector $\vec{r}(t)$ of closed curve γ , see Fig. 1 may be represented in the form of Fourier series as follow

Fig. 1 Parameterized radius-vector $\vec{r}(t)$ of closed curve γ



$$\vec{r}(t) = \vec{a}_0 + \sum_{k=1}^{\infty} \left(\vec{a}_k \cos kt + \vec{b}_k \sin kt \right) \tag{1}$$

where $\vec{a}_k = [a_k^x, a_k^y]^T$, $\vec{b}_k = [b_k^x, b_k^y]^T$.

Assume the parameter varies from 0 to 2π . The angle of rotation of a crank or time can act as parameter t .

It is required to determine the Fourier coefficients. For the pure geometrical representation of the curve independent of time, the parameter t of selection varies in proportion to the arc length circumscribed from the curve point $M_0(x_0, y_0)$ to the current position $M(x, y)$.

If the curve γ is represented by discrete sequence of points $M_0, M_1, M_2, \dots, M_n \equiv M_0$ on it with the radius-vectors $\vec{r}_0, \vec{r}_1, \vec{r}_2, \dots, \vec{r}_{n-1}, \vec{r}_n = \vec{r}_0$, i.e., in the form of polygon, then the parameterization independent of time may be acquired at $t_0 = 0$ recursively using the formula:

$$t_i = t_{i-1} + \frac{2\pi}{L} \cdot \|\vec{r}_i - \vec{r}_{i-1}\| \tag{2}$$

where L is the sum of length of polygon edges $M_i M_{i-1}$

$$L = \sum_{i=1}^n \|\vec{r}_i - \vec{r}_{i-1}\| \tag{3}$$

The Fourier series coefficients for acquired polygon have the following form:

$$\begin{aligned} \vec{a}_0 &= \frac{1}{\pi} \int_{t_{i-1}}^{t_i} \vec{r}^*(t) dt = \frac{1}{\pi} \int_{t_{i-1}}^{t_i} \left[\vec{r}_{i-1} + \frac{t - t_{i-1}}{t_i - t_{i-1}} \cdot (\vec{r}_i - \vec{r}_{i-1}) \right] dt \\ &= \frac{1}{\pi} \left[\vec{r}_{i-1} t + \frac{1}{2(t_i - t_{i-1})} \cdot (\vec{r}_i - \vec{r}_{i-1})(t - t_{i-1})^2 \right] \Big|_{t_{i-1}}^{t_i} \\ &= \frac{1}{\pi} \left[\vec{r}_{i-1}(t_i - t_{i-1}) + \frac{1}{2}(\vec{r}_i - \vec{r}_{i-1}) \cdot (t_i - t_{i-1}) \right] = \frac{1}{2\pi} (t_i - t_{i-1})(\vec{r}_i + \vec{r}_{i-1}) \end{aligned} \tag{4}$$



and for $k > 0$.

$$\begin{aligned}\vec{a}_k &= \frac{1}{\pi} \int_{t_{i-1}}^{t_i} \bar{r}^*(t) \cos kt dt = \frac{1}{\pi} \int_{t_{i-1}}^{t_i} \left[\bar{r}_{i-1} + \frac{\bar{r}_i - \bar{r}_{i-1}}{t_i - t_{i-1}} \cdot (t - t_{i-1}) \right] \cos kt dt \\ &= \frac{1}{k\pi} (\bar{r}_i \sin kt_i - \bar{r}_{i-1} \sin kt_{i-1}) + \frac{1}{k^2\pi} \frac{\bar{r}_i - \bar{r}_{i-1}}{t_i - t_{i-1}} (\cos kt_i - \cos kt_{i-1})\end{aligned}\quad (5)$$

$$\begin{aligned}\vec{b}_k &= \frac{1}{\pi} \int_{t_{i-1}}^{t_i} \bar{r}^*(t) \sin kt dt = \frac{1}{\pi} \int_{t_{i-1}}^{t_i} \left[\bar{r}_{i-1} + \frac{t - t_{i-1}}{t_i - t_{i-1}} \cdot (\bar{r}_i - \bar{r}_{i-1}) \right] \sin kt dt \\ &= \frac{1}{k\pi} (-\bar{r}_i \cos kt_i + \bar{r}_{i-1} \cos kt_{i-1}) + \frac{1}{k^2\pi} \frac{\bar{r}_i - \bar{r}_{i-1}}{t_i - t_{i-1}} (\sin kt_i - \sin kt_{i-1})\end{aligned}\quad (6)$$

Thus, the coefficients of the Fourier series for the resulting polygon are of the form

$$\vec{a}_0 = \frac{1}{4\pi} \sum_{i=1}^n [(t_i - t_{i-1})(\vec{r}_i + \vec{r}_{i-1})] \quad (7)$$

and for $k > 0$.

$$\begin{aligned}\vec{a}_k &= \frac{1}{k^2\pi} \sum_{i=1}^n \left[\frac{\cos kt_i - \cos kt_{i-1}}{(t_i - t_{i-1})} (\vec{r}_i - \vec{r}_{i-1}) \right] \\ &\quad + \frac{1}{k\pi} \sum_{i=1}^n [(\vec{r}_i \sin kt_i - \vec{r}_{i-1} \sin kt_{i-1})]\end{aligned}\quad (8)$$

$$\begin{aligned}\vec{b}_k &= \frac{1}{k^2\pi} \sum_{i=1}^n \left[\frac{\sin kt_i - \sin kt_{i-1}}{(t_i - t_{i-1})} (\vec{r}_i - \vec{r}_{i-1}) \right] \\ &\quad - \frac{1}{k\pi} \sum_{i=1}^n [(\vec{r}_i \cos kt_i - \vec{r}_{i-1} \cos kt_{i-1})]\end{aligned}\quad (9)$$

The last term in the expression (8) and (9) equal to zero because we have a closed polygon, i.e., $M_n \equiv M_0$ and $\vec{r}_n = \vec{r}_0$.

As a result, the approximate form of the coefficients of the Fourier series for the resulting polygon is of the form:

$$\vec{a}_0 = \frac{1}{4\pi} \sum_{i=1}^n [(t_i - t_{i-1})(\vec{r}_i + \vec{r}_{i-1})] \quad (10)$$

and for $k > 0$.

$$\vec{a}_k = \frac{1}{k^2\pi} \sum_{i=1}^n \left[\frac{\cos kt_i - \cos kt_{i-1}}{(t_i - t_{i-1})} (\vec{r}_i - \vec{r}_{i-1}) \right] \tag{11}$$

$$\vec{b}_k = \frac{1}{k^2\pi} \sum_{i=1}^n \left[\frac{\sin kt_i - \sin kt_{i-1}}{(t_i - t_{i-1})} (\vec{r}_i - \vec{r}_{i-1}) \right] \tag{12}$$

Only a few members of the Fourier series already characterize the form of closed curve in sufficiently high degree. Assume, for example, the curve γ is a coupler curve of the hinge four-link chain ABCD see, Fig. 2, i.e., the curve circumscribed by link point p in the plane.

When using only the first five members of the Fourier series, the deviations approximating the curve γ_F from the coupler curve γ make 0.38%. This ellipse is described by the expression:

$$\vec{r}_e = \vec{a}_0 + \vec{a}_1 \cos t + \vec{b}_1 \sin t$$

Point S in Fig. 2 represents the “gravity center” of the curve γ and has radius-vector $\vec{r}_s = \vec{a}_0$. It is also the center of ellipse e , which corresponds to the first harmonics $k = 1$.

This ellipse is described by expression:

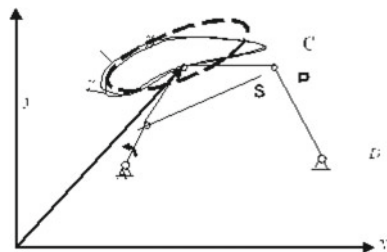
$$\vec{r}_e = \vec{a}_0 + \vec{a}_1 \cos t + \vec{b}_1 \sin t \tag{13}$$

Semi-axes are as follows:

$$h_{1,2} = \frac{\sqrt{2}}{2} \sqrt{|\vec{a}_1|^2 + |\vec{b}_1|^2 \pm \left[\left(|\vec{a}_1|^2 - |\vec{b}_1|^2 \right)^2 + \left(2\vec{a}_1 \vec{b}_1 \right)^2 \right]^{1/2}} \tag{14}$$

Ratio of $\lambda_F = \frac{h_1}{h_2}$, where $0 \leq \lambda_F \leq 1$, represents the parameter characterizing the form of closed curve. This parameter is independent of the position of the curve, shift and turn both of entire and used scale.

Fig. 2 Coupler curve of hinge four-link chain ABCD



Other parameters normalized in relation to the position of n curve length also as mid-radius of the curve measured from the gravity center, or area moment of the swept curve and others are well correlated with the parameter λ_F under study, so their use does not give essentially more precise information about the curve.

Numerical experiment and results of comparative analysis.

If the input curve during the program test is defined in the following form:

$$x = a \cos \phi_i,$$

$$y = b \sin \phi_i$$

at coefficients $a = 8, b = 4$, where ϕ_i varies from 0 to 2π , then may be acquired the following data at $k = 5$.

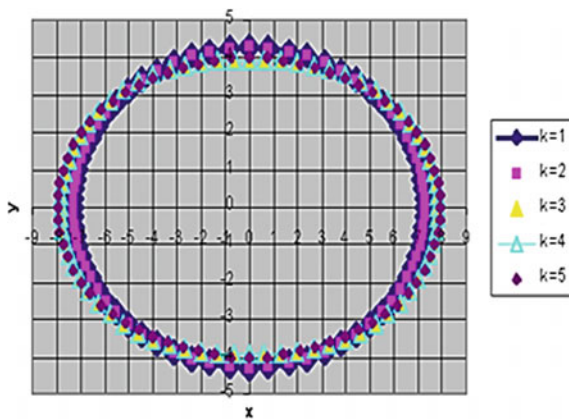
Table 1 presents the results of the Fourier coefficient's given ellipse. In Fig. 3, example of four-link hinge mechanism shows the change in relative frequency $f(\lambda_F)$ depending on the value of the shape parameter λ_F , i.e., standard differential is the relative frequency, with which are encountered mechanisms with the magnitude of the shape parameter λ_F .

The position of point P on the conrod plane varies inside the square size $l \times l$ and with center, located in center connecting rod AB . A close to the evenly distribution obtained when $l = 4|BC|$. At this value, the number of the mechanisms

Table 1 Fourier coefficients of the ellipse where $k = 5$

k	$a0x = -0.0000007331$		$a0y = 0.0000005295$	
	a	Ay	bx	By
1	7.3099274635	-0.0000027036	0.0000046335	4.2890157700
2	0.0000006859	0.0000001233	-0.0000009895	0.0000006688
3	0.5149865746	-0.0000006058	0.0000009236	0.3564125896
4	0.0000001913	-0.0000000397	0.0000004173	0.0000005028
5	0.1136770025	-0.0000001791	0.0000003015	0.0849042758

Fig. 3 Found more coefficients Fourier a given of the ellipse and corresponding them curves



with the value λ , near to zero (completely cohesive mechanism $h_2 \ll \lambda_1$ and with value λ close to unity) with circular conrod curve, $h_1 \approx h_2$, about the same.

Besides, the deviation of a function $f(\lambda_F)$ by the case of uniform distribution frequencies $f(\lambda_F) = 1$ is the smallest.

Comparison of several Fourier series coefficients for two closed curves completely represents the curve shape. Thus, the program of this method is recorded in C++ that is used in the synthesis of the guidance mechanism. The relevant parameters for the guidance mechanisms in the kinematic synthesis are selected from the data design file or by solution of determinants using the random search method [10].

3 Conclusion

This method is based on optimization methods and allows taking into account the additional requirements of the synthesis and limitations. As a result, the computing speed is increasing since the use of Fourier coefficients allows avoiding the time-consuming kinematic analysis at each step of descent to the minimum.

An important advantage of the proposed method is the fact that it is not necessary to store the dimensions of the mechanism in the database. Because the Fourier coefficients depend on the method of the curve parameterization, and for the pure geometric representation of the curve, it is proposed to use a parameter that varies in proportion to the arc length circumscribed from the curve point to the current position.

As a result, the Fourier analysis of the plane closed curve is used to find a suitable guidance mechanism by means of the electronic catalog.

The analysis of the mechanisms functional capabilities allows determining the problems which may be solved by mechanical means only, and problems which may be solved by combination of mechanical and non-mechanical means (i.e., control tools, S. M. Ibrayev). It is assumed that the expert system of the functional analysis will open up new vistas for the creation of scientific bases for development of new mechatronic devices using mechanisms “with built-in intelligence” as the basis of simple and cheap process automation.

References

1. Ibrayev S, Peisach E, Schoenherr J (2000) Synthese von hoehergliedrigen Koppelgetrieben. *Verarbeitungsmaschinen und Verpackungstechnik*, Dresden, pp 270–280
2. Dzholdasbekov AU (1981) Optimum synthesis of plane lever mechanisms of high classes. *Bulletin of the Academy of Sciences of the Kazakh SSR Alma-Ata*, pp 35–41
3. Nesterov VA, Peisach EE (1995) The knowledge base on the analysis and synthesis of lever mechanisms in the computer system LINKAGES. *Bulletin of the Moscow Aviation Institute*, pp 51–58

4. Bawab S, Sabada S, Srinivasan U, Kinzel G, Waldron K (1997) Automatic synthesis of crank driven four-bar mechanisms for two, three or four-position motion generation. *Trans ASME J Mech Transm Autom* 225–231
5. Christem G, Quast V, Buchheem A (1994) Auswahl funfgliedriger Koppelmechanismen fur Bewegungsaufgaben mittels schneller Bahnkurvensimulation. *Konstruktion*, pp 155–160
6. König F (1995) Verdichtung im Erd- und Strassenbau. Wiesbaden. Bauverlag, Berlin, p 253
7. Ibrayev SM, Koishybayeva Zh (2011) Method for presentation of coupler curve lever mechanisms in e-catalog based on Fourier coefficients. *Herald of Central-Asian University*, Almaty, pp 88–91
8. Ibrayev SM (1988) Functional synthesis and analysis of plane parallel manipulators. Almaty, p 198
9. Dresig H, Golle A (2001) Synthese sechsgliedriger Mechanismen fuer periodische Erregerkraefte. *Tradition und Moderne. Wiss. Zeitschrift der TV, Dresden*, pp 65–68
10. Ibrayev SM (1999) Synthesis of planar adjustable 4 bar mechanisms with variable length of two-element. *Kolloquium Getriebetechnik Technische Universitaet Muenchen*, pp 111–120
11. Tussupova AE, Bidakhmet Zh, Rakhmatulina AB (2013) Dynamic synthesis of pulse action vibration exciter on foundation. In: *International conference on industrial engineering. Procedia engineering*, pp 471–479
12. Jomartov A (2013) Research of dynamics picking mechanism of Sulzer Projectile Loom. In: *International conference on mechanical engineering, Paris, France*, pp 1991–1996
13. Joldasbekov SU, Jomartov A (2015) Typical dynamic models of the cyclic mechanism on the software SimulationX. In: *Proceedings of 2015 IFToMM world congress, Taipei, Taiwan*

Simulation of Fuel Ignition Chemical Kinetics in Diesel Engine at Cold Start with Modelica Language



A. Malozemov, A. Savinovskikh and G. Malozemov

Abstract The article presents the results of a mathematical model and software development for numerical simulation of fuel ignition chemical kinetics in a diesel engine combustion chamber at cold start with Modelica language. The study aims at ensuring that diesel engines meet the requirements of regulatory and technical documents for starting characteristics. In the course of the study, the mathematical model of the fuel ignition and combustion chemical kinetics in the diesel engine combustion chamber, which can be used for starting characteristics predicting, was created and implemented as software. In the course of numerical studies, it was determined that to ensure ignition of diesel fuel in the combustion chamber, the required value of local gas temperatures should be at least 1350 K. The permissible proportion of carbon dioxide in the gases, when engine can start, with simultaneous intake air heater operation, should not exceed 40%. The developed mathematical model and software are used in current research and development work of South Ural State University to create new and modernize existing diesel engines of various types and purposes, produced by Chelyabinsk tractor plant.

Keywords Diesel engine · Cold start · Fuel ignition · Chemical kinetics · Mathematical model · Software · Modelica language

1 Introduction

One of the main internal combustion engines' characteristics is the possibility of starting in any conditions, specified in the design and operational documentation. If engine does not start, the machine, on which it is installed, will completely lose its

A. Malozemov (✉) · G. Malozemov
South Ural State University, 76, Lenin Avenue, Chelyabinsk 454080, Russia
e-mail: malozemov@gmail.com

A. Savinovskikh
South Ural Institute of Management and Economics, 1, Kozhavodskaya Street,
Chelyabinsk 454084, Russia

ability to function. Therefore, ensuring a guaranteed engine cold start is one of the main tasks facing the developers in creating new and modernizing existing diesel engine models. One of the components of this task is to carry out computational studies in order to predict the effect of different changes in the diesel engine design on its starting qualities.

2 Problem

It is generally accepted that starting is possible if the total torque, including starter torque, moment created by gases pressure (including air in starting system) in the engine combustion chamber and friction torque in the mechanisms and engine units, is a positive value [1]. If there is no fuel burning in the combustion chamber, then engine start becomes impossible. Determination of the heat relies rate on starting modes using traditional mathematical models, for example, Razleytsev [2] or Hiroyasu [3] is impossible, because they do not take into account the spatial distribution of working fluid state parameters in the combustion chamber, presence of start facilitating tools, and very simply describe the fuel oxidation chemical kinetics. The purpose of the study, results of which are presented in this article, was to develop a mathematical model of the fuel ignition chemical kinetics in a diesel engine at cold start. This model can be used as a basis for creating software for kinetics of the ignition and combustion numerical simulation, as well as working processes in a engine combustion chamber, including CFD (Computational Fluid Dynamics) software.

3 Mathematical Model and Software

The chemical kinetic mechanism, taken as a start and developed by the Engine Research Center of Wisconsin-Madison University [4], based on the oxidation equations of normal heptane (29 reagents and 52 reactions) and the Arrhenius equation system for each reaction, was used [5]:

$$k_f = A \cdot T^b \cdot \exp\left(\frac{-E_a}{R \cdot T}\right) \quad (1)$$

here k_f —reaction rate coefficient; A —preexponential coefficient; b —exponent; E_a —activation energy; T —temperature.

The scheme of the kinetic mechanism is not given here because of its large size, it can be found in the special literature [6]. The initial concentrations of the reactants depend on the fuel and air concentrations in combustion chamber, taking into

account presence of the inlet air heater combustion products. The reaction rate (the rate of reagents concentration change) is determined by the equation:

$$\frac{dC_{12}}{dt} = -k_f \cdot C_1^c \cdot C_2^d \quad (2)$$

here c, d —exponents; C —reagents concentration.

To determine the thermodynamic properties of reagents, NASA polynomials are used [5, 7, 8]:

$$\frac{c_p}{R} = a_1 + a_2 \cdot T + a_3 \cdot T^2 + a_4 \cdot T^3 + a_5 \cdot T^4 \quad (3)$$

$$\frac{H}{R \cdot T} = a_1 + a_2 \cdot \frac{T}{2} + a_3 \cdot \frac{T^2}{3} + a_4 \cdot \frac{T^3}{4} + a_5 \cdot \frac{T^4}{5} + \frac{a_6}{T} \quad (4)$$

$$\frac{S}{R} = a_1 \cdot \ln(T) + a_2 \cdot T + a_3 \cdot \frac{T^2}{2} + a_4 \cdot \frac{T^3}{3} + a_5 \cdot \frac{T^4}{4} + a_7 \quad (5)$$

here c_p —specific heat at constant pressure; R —individual gas constant; H —enthalpy; S —entropy; a_1 – a_7 —coefficients.

Since the coefficients of polynomials depend on temperature range, when gas mixture temperature changes, there is a transition from one range to another, which results is a nonlinear (intermittent) change of the reaction rate and instability or calculation error. To eliminate this drawback, some polynomials coefficients (Eqs. 3–5) were corrected, which did not affect calculation accuracy. The system of differential equations (Eq. 2) is super-stiff, therefore, to solve it, using of traditional numerical methods (Euler, Runge-Kutta, Adams-Bashfort, etc. [9]) is impractical because it requires significant calculation step reduction and leads to unacceptable increase in computational experiment complexity. For this reason, the DASSL solver (differential/algebraic system solver [10]) was used.

To enable determination of a various factors influence on the chemical kinetics of diesel fuel ignition and combustion, software was created [11] that implements the mathematical model described above. This software is program class, created with Modelica language [12, 13] (Fig. 1). For verification, the mathematical model of chemical kinetics was implemented into the free OpenFOAM code [14], in which computational fluid dynamics methods are used in a three-dimensional formulation. Detailed description of the CFD-model is omitted due to very large volume, more detailed information is given in [15]. The verification of created model was carried out by comparing the test calculation results with experimental data and results of calculation performed with AVL FIRE software, widely used in engine industry (Fig. 2).

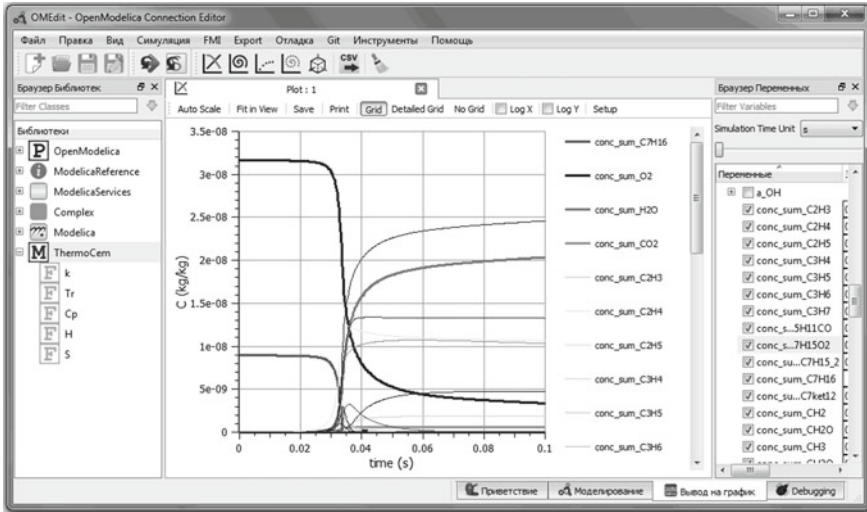


Fig. 1 OMEdit [13] editor window with the results of reagents concentration calculation

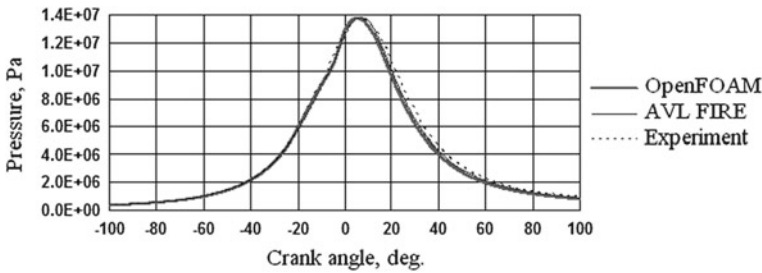


Fig. 2 Comparison of experimental and calculated gas pressure in combustion chamber of 12CHN13/15 diesel engine

4 Theoretical Research

The numerical study of fuel combustion chemical kinetics at diesel cold start was carried out to assess influence of various factors on chemical processes in combustion chamber and determine conditions of diesel fuel ignition. The initial data, used for calculation, corresponded to the diesel engine with cylinder diameter of 150 mm, produced by Chelyabinsk tractor plant.

Figure 3 shows change of normal heptane (*n*-heptane) concentration at different constant gas temperatures in combustion chamber, while Fig. 4—dependence of the time to reach *n*-heptane concentration of 1.2×10^{-8} mol/cm³ (this value is conditionally chosen, it approximately corresponds to 7% of the reacted fuel, that can indicate a combustion reaction visible start) on the gas temperature in combustion



chamber. It can be seen in Figs. 2 and 3 that reaction rate increases significantly with increasing temperature, and 7% of fuel reacts during 0.02 s (which corresponds to 24° of engine crank angle) at gas temperature of 1315 K.

The apparent maximum of the reaction rate takes place at a local gas temperature of 1350–1400 K at the time 0.02 s that corresponds to 10° of crank angle after top dead center, with injection start angle—14° before top dead center (Fig. 5). To clarify the conditions for fuel ignition [16], chemical kinetics modeling was performed at a linearly increasing gas temperature in engine combustion chamber (Fig. 6). The beginning of a visible change in the reaction rate is observed at temperature of 1350–1400 K.

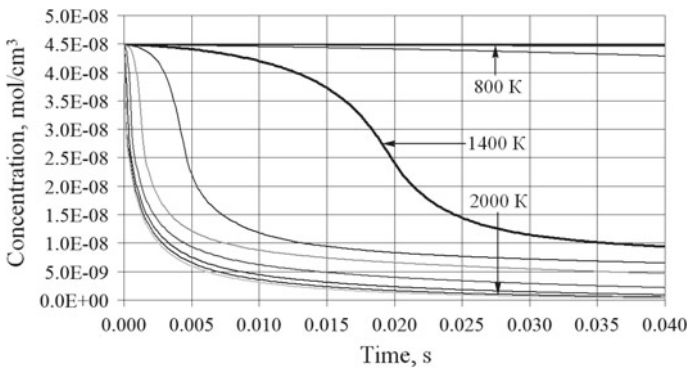


Fig. 3 Change of *n*-heptane concentration at different (step—100 K) gas temperatures in engine combustion chamber (piston at top dead center, compression ratio—12.5, engine speed—200 min⁻¹)

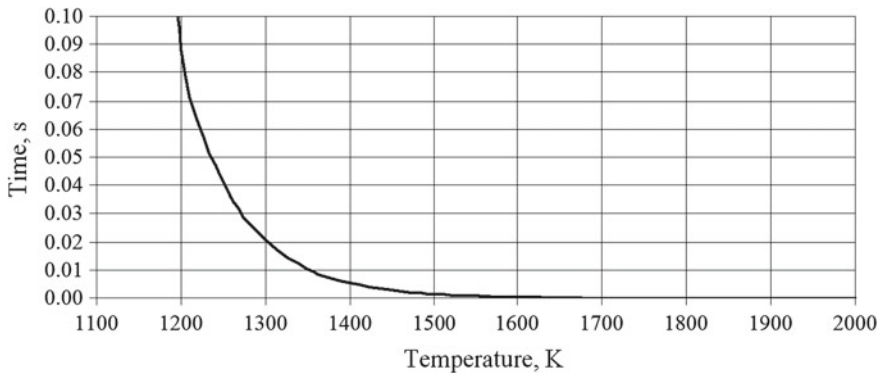


Fig. 4 Dependence of time to achieve *n*-heptane concentration values of 1.2×10^{-8} mol/cm³ on gas temperature in combustion chamber

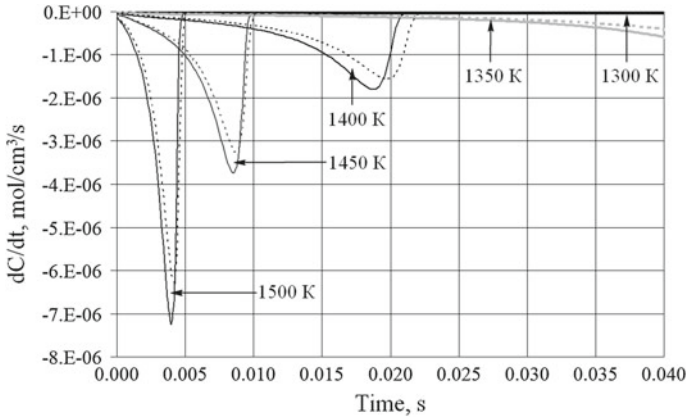


Fig. 5 Rate of reagents concentration change at different gas temperatures in engine combustion chamber (piston at top dead center, compression ratio—12.5, engine speed—200 min⁻¹): — *n*-heptane; ... oxygen

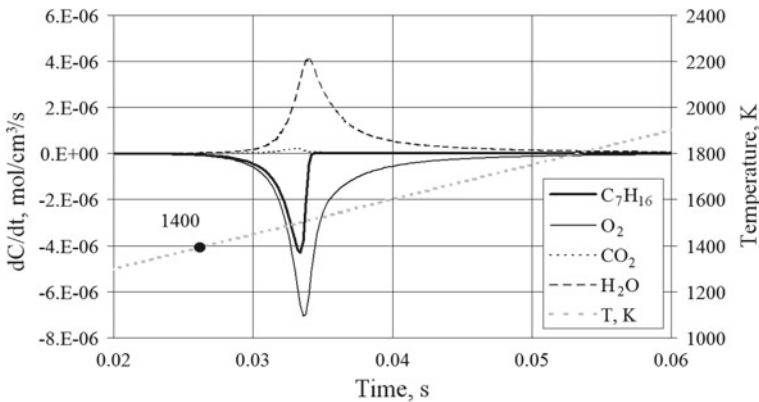


Fig. 6 Rate of reagents concentration change at linearly increasing gas temperature in engine combustion chamber (piston at top dead center, compression ratio—12.5, engine speed—200 min⁻¹): — *n*-heptane; ... oxygen

Figure 7 shows change of the reagents concentration at different initial carbon dioxide mass fractions in combustion chamber, which illustrates the chemical kinetics of the fuel oxidation reaction when diesel engine is running simultaneously with intake air heater. The figure shows that increase of the carbon dioxide mass concentration over 40% leads to incomplete fuel combustion. With smaller proportions of carbon dioxide, its influence on the reaction rate cannot be called significant.



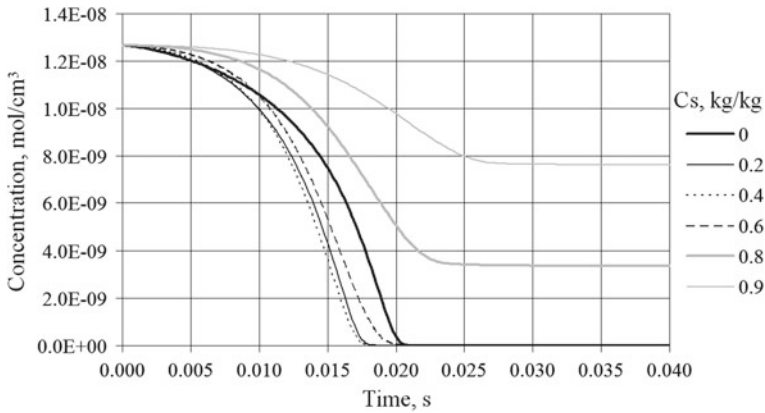


Fig. 7 Change of *n*-heptane concentration at different carbon dioxide initial concentrations (Cs) in engine combustion chamber (piston at top dead center, compression ratio—12.5, engine speed—200 min⁻¹)

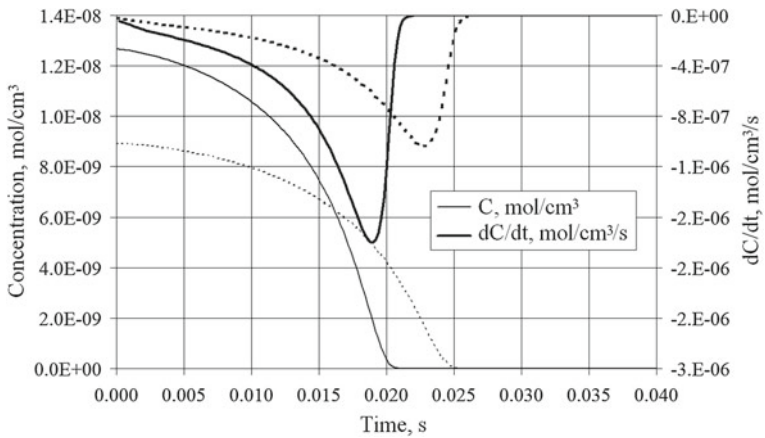


Fig. 8 Change of *n*-heptane concentration (compression ratio—12.5, engine speed—200 min⁻¹): — constant combustion chamber volume; variable combustion chamber volume

The previous calculations were performed at a constant volume of engine combustion chamber based on the assumption that at low engine speed at cold start, main reaction occurs near top dead center and volume change can be ignored [17, 18]. To assess validity of this assumption and introduced error, concentration of *n*-heptane was calculated at constant and variable combustion chamber volume (Fig. 8). It can be seen from the figure that, despite the almost double difference in the reaction rate, duration of visible combustion in variable combustion chamber volume increased from 24° to 28° of crank angle (by 17%).



5 Conclusion

Thus, in course of this study, the mathematical model and software for numerical simulation of fuel ignition chemical kinetics in a diesel engine combustion chamber at cold start were created and implemented as software. In the course of fuel combustion reaction chemical kinetics' computational studies at diesel cold start, it was determined:

- To ensure the fuel ignition in the combustion chamber, required value of gas local temperatures must be at least 1350 K;
- The permissible proportion of carbon dioxide in the gases, when engine is started, with simultaneous intake air heater operation, should not exceed 40%.

The results of this study are used in current research and development work of the South Ural State University to create new and modernize existing diesel engines of various types and purposes, produced by Chelyabinsk tractor plant, in order to ensure their compliance with the regulatory and technical documents requirements for engine starting characteristics [19, 20].

Acknowledgements This work was performed with methodical and scientific support of AVL List GmbH (Graz, Austria) (Agreement for Use of Simulation Software AVL BOOST, AVL CRUISE, AVL EXCITE and AVL FIRE between SUSU (Chelyabinsk, Russia) and AVL LIST GmbH (Graz, Austria)) in part related to the mathematical model and developed software verification.

References

1. Kuperschmidt VL (1968) Uluchsheniye puskovykh kachestv dizeley (Improving the starting quality of diesel engines). Trudy NATI, Moscow
2. Razleytsev NF (1980) Modelirovaniye i optimizatsii protsessa sgoraniya v dizelyakh (Simulation and optimization of the combustion process in diesel engines). Vyscha shkola, Kharkov
3. Hiroyasu H, Kadota T, Arai M (1983) Development and use of a spray combustion modeling to predict diesel engine efficiency and pollutant emissions. Bull JSME 26(214):576–583
4. Pitz W, Cernansky N, Dryer F et al (2007) Development of an experimental database and chemical kinetic models for surrogate gasoline fuels. SAE paper 2007-01-0175, pp 1–25
5. Burcat A, McBride B (1993) Ideal gas thermodynamic data for combustion and air-pollution use. Techno report TAE, p 697
6. Potekhin VM (2007) Osnovy teorii khimicheskikh protsessov tekhnologii organicheskikh veshchestv i neftepererabotki (Fundamentals of the chemical processes, organic substances technology and oil refining theory). Khimizdat, Moscow
7. McBride B, Gordon S, Reno M (1993) Coefficients for calculating thermodynamic and transport properties of individual. NASA report TM-4513
8. Daubert T, Danner R (1994) Physical and thermodynamic properties of pure chemicals: data compilations. Taylor & Francis, Abingdon

9. Kolesov YB, Senichenkov YB (2007) Modelirovaniye sistem. Praktikum po kompyuternomu modelirovaniyu (Modeling systems. Computer modeling workshop). BKHV-Peterburg, Saint-Peterburg
10. Petzold LR (1983) A description of DASSL: a differential/algebraic system solver. *Sci Comput* 65–68
11. Malozemov AA (2018) Barelyef-termokhimiya: svidetelstvo o gosudarstvennoy registratsii programmy (Bas-relief thermochemistry: certificate of software state registration). Russian Federation patent 2018616031, 21 May 2018
12. Fritzon P (2014) Principles of object-oriented modeling and simulation with Modelica 3.3: a cyber-physical approach. Wiley, New-York
13. OpenModelica (2018) Available via DIALOG. <https://openmodelica.org>. Accessed 17 Nov 2018
14. OpenFOAM Foundation (2018) Available via DIALOG. www.openfoam.com. Accessed 17 Nov 2018
15. Malozemov AA (2015) Development of software for calculation and optimization of diesel operating processes and fuel supply. In: International conference on industrial engineering. *Procedia engineering*, vol 129. Elsevier Ltd., pp 724–730
16. Semyonov NN (1967) Samvosplamneniye i tsepnyye reaksii (Auto ignition and chain reactions). *Usp Khim* 36:3–22
17. Mitchell K (1993) The cold performance of diesel engines. SAE paper 932768, pp 678–687
18. Park JK (2007) Simulation of starting process of diesel engine under cold condition. *Int J Autom Technol* 8(3):289–298
19. Malozemov AA, Bondar VN, Kukis VS (2016) Improvement of the forced diesel engines cold starting characteristics using oil injection into the cylinder. In: International conference on industrial engineering. *Procedia engineering*, vol 150. Elsevier Ltd., pp 1149–1155
20. Malozemov AA, Bondar VN, Cherepanov SI (2016) Experimental research of forced diesel engine with oil temperature control system in cold ambient conditions. In: International conference on industrial engineering. *Procedia engineering*, vol 150. Elsevier Ltd., pp 1143–1148

Dynamic Pattern of Safe Operation Indicators for Heavy-Duty Machines



Yu. A. Izvekov, V. V. Dubrovsky and A. L. Anisimov

Abstract This article studies the dynamic pattern of safe (hazardous) operation indicators for heavy-duty machines. A load-carrying structural member of metal-lurgical overhead crane with a frame manufactured from 09G2S steel and having 50 ton lifting capacity was selected for the study. A generalized limit-state equation for the structural crane element represents hypersurface, which distinguishes the safety zone and the hazard zone. Safety and hazard functions are presented as integral functions of probability distribution density, resulting from various factors that affect the likelihood of occurrence of emergencies, accidents and machine break-downs. The indicators with the greatest influence on the probability of safe and hazardous states of the structural element or the structure itself can be identified. It is accepted to investigate probabilistic features of stress and deformation fields. The stochastic boundary-value problem of the structural element's stress-strain behaviour under random load is addressed in this case. The problem can be resolved by obtaining correlation and spectral functions of stress and deformation under given load functions. Considering that heavy-duty machines are operated in steady state, it can be assumed with sufficient assurance that such random processes represent steady Gaussian processes. The probabilistic dynamics of safe operation indicators are studied by using computer-based simulation modelling. The obtained modelled curves of probabilistic machine load allowed one to deduce equations of stress and deformation probability density. Every coefficient of the obtained models is probably significant based on Fisher's criterion. The obtained relationships allow one to construct graphs of limit and acceptable states when evaluating durability and operating life of heavy-duty machines and the probability density for operating and rupturing loads and stresses.

Keywords Safe operation · Heavy-duty machines · Random processes · Probability density · Limit-state graph · Stress · Deformations

Yu. A. Izvekov (✉) · V. V. Dubrovsky · A. L. Anisimov
Magnitogorsk State Technical University n.a. Nosov, 38, Lenin Ave.,
Magnitogorsk 455000, Russia
e-mail: yurij.izvekov@mail.ru

© Springer Nature Switzerland AG 2020
A. A. Radionov et al. (eds.), *Proceedings of the 5th International Conference on Industrial Engineering (ICIE 2019)*, Lecture Notes in Mechanical Engineering,
https://doi.org/10.1007/978-3-030-22041-9_64

595

1 Introduction

Heavy-duty machines operate in severe environment with, normally, high stresses and deformations, sudden temperature changes, multitude cycles, long service life and continuance of defect concentration. All these factors are associated with risks of accidents and emergencies that can be resulted from operating such machines. Therefore, it is important to study the dynamic pattern of safe operation indicators from the perspective of the system's probabilistic dynamics.

2 Study Purpose

Based on the concepts described in [1–3], the following generalized limit-state equation for the rupture zone of a structural loaded heavy-duty machine's element can be generated:

$$F(\sigma_{ij}, \varepsilon_{ij}, l, N, t, T) = 0 \quad (1)$$

where σ_{ij} —stresses; ε_{ij} —deformations; l —defect type and dimensions; N —number of cycles; t —service life; and T —temperature.

Equation (1) represents hypersurface, which distinguishes the safety zone and the hazard zone.

By entering n -dimensional probability distribution density $f(\sigma_{ij}, \varepsilon_{ij}, l, N, t, T) = f(X)$, functions of safety and hazard can be presented as follows:

$$P_S(t) = P\{F(\sigma_{ij}, \varepsilon_{ij}, l, N, t, T)\} = \int f(X)dX; \quad (2)$$

P_S is the probability of safe state (time-based function);

$$P_R(t) = 1 - P\{F(\sigma_{ij}, \varepsilon_{ij}, l, N, t, T)\} = 1 - \int f(X)dX; \quad (3)$$

P_R is the probability of hazard (hazardous state, time-based function).

Thus, the purpose of this article is to quantitatively study the above functions.

3 Study Materials and Methods

The presented formulas enable to evaluate the hazard of out-of-limit stresses, deformations, defects, temperatures, number of cycles and service life in terms of structure-related risk analysis [4–7] from the perspective of rupture and safety [8–25].

Identifying probabilistic properties of potential rupture zones as a compatible function of probability distribution $f(\sigma_{ij}, \varepsilon_{ij}, l, N, t, T)$ represents quite a time-consuming task. By using principal component analysis, indicators with the greatest influence on the probability of safe and hazardous states of the structural element or the structure itself can be identified. It is accepted to investigate probabilistic features of stress and deformation fields. The stochastic boundary-value problem of the structural element's stress-strain behaviour under random load $q(t)$ is addressed in this case. The problem can be resolved by obtaining correlation and spectral functions of stress and deformation under given load functions.

The properties of functions $f(\sigma_{ij}, t), f(\varepsilon_{ij}, t)$ can be described by making a certain assumption about the nature of random processes. Considering that heavy-duty machines are operated in steady state, it can be assumed with sufficient assurance that such random processes represent steady Gaussian processes with the following expectation values:

$$\sigma_{ij} = \int_{-\infty}^{\infty} \sigma_{ij} f(\sigma_{ij}) d\sigma_{ij}, \tag{4}$$

$$\varepsilon_{ij} = \int_{-\infty}^{\infty} \varepsilon_{ij} f(\varepsilon_{ij}) d\varepsilon_{ij}, \tag{5}$$

and dispersions:

$$\sigma_{ij}^2 = \int_{-\infty}^{\infty} \sigma_{ij}^2 f(\sigma_{ij}) d\sigma_{ij}, \tag{6}$$

$$\varepsilon_{ij}^2 = \int_{-\infty}^{\infty} \varepsilon_{ij}^2 f(\varepsilon_{ij}) d\varepsilon_{ij}. \tag{7}$$

Probability distribution density in this case is subject to the normal law of distribution:

$$f(\sigma_{ij}) = \frac{1}{\sqrt{2\pi\sigma_{ij}^2}} e^{-\frac{(\sigma_{ij}-\sigma_{ij}^0)^2}{2\sigma_{ij}^2}}, \tag{8}$$

$$f(\varepsilon_{ij}) = \frac{1}{\sqrt{2\pi\varepsilon_{ij}^2}} e^{-\frac{(\varepsilon_{ij}-\varepsilon_{ij}^0)^2}{2\varepsilon_{ij}^2}}. \tag{9}$$



Calculations will be made for the heavy-duty production equipment element—i.e. the supporting frame of the metallurgical overhead crane with 50 ton lifting capacity. The supporting frame of the crane during load lifting, movement and lowering is subject to varying effective bending stresses, which represents random steady-state differentiated process with normal distribution. Frame material is 09G2S steel. Normal constant expectation values of stresses σ_{ij} and deformations ε_{ij} equal 165 MPa (megapascal) and 0.785×10^{-3} , respectively; dispersion $\sigma_{ij}^2 \approx 8300 \text{ MPa}^2$, (megapascal²) limit stresses $\geq 256 \text{ MPa}$ (megapascal) and limit deformations equal 1.219×10^{-3} . Probabilistic dynamics of safe operation indicators will be studied by using simulation modelling.

4 Study Findings and Their Discussion

Hence, the dynamics of safe and hazardous operation indicators can be presented as follows:

$$P_S(t) = P\{F(\sigma_{ij})\} = \int \frac{1}{\sqrt{2\pi\sigma_{ij}^2}} e^{\frac{-(\sigma_{ij}-\sigma_{ij})^2}{2\sigma_{ij}^2}} d\sigma_{ij}; \quad (10)$$

$$P_S(t) = P\{F(\varepsilon_{ij})\} = \int \frac{1}{\sqrt{2\pi\varepsilon_{ij}^2}} e^{\frac{-(\varepsilon_{ij}-\varepsilon_{ij})^2}{2\varepsilon_{ij}^2}} d\varepsilon_{ij}; \quad (11)$$

$$P_R(t) = 1 - P\{F(\sigma_{ij})\} = 1 - \int \frac{1}{\sqrt{2\pi\sigma_{ij}^2}} e^{\frac{-(\sigma_{ij}-\sigma_{ij})^2}{2\sigma_{ij}^2}} d\sigma_{ij}; \quad (12)$$

$$P_R(t) = 1 - P\{F(\varepsilon_{ij})\} = 1 - \int \frac{1}{\sqrt{2\pi\varepsilon_{ij}^2}} e^{\frac{-(\varepsilon_{ij}-\varepsilon_{ij})^2}{2\varepsilon_{ij}^2}} d\varepsilon_{ij}. \quad (13)$$

Simulation findings are presented in Figs. 1 and 2.

The obtained modelled curves of probabilistic machine load enabled to deduce the following probability density equations:

$$f(\sigma_{ij}) = 0.008e^{-0.006\sigma_{ij}}, \quad (14)$$

$$f(\varepsilon_{ij}) = 0.597e^{\varepsilon_{ij}}. \quad (15)$$

Every coefficient of the obtained models is probably significant based on Fisher's criterion.

Fig. 1 Probability distribution density as function of effective stresses

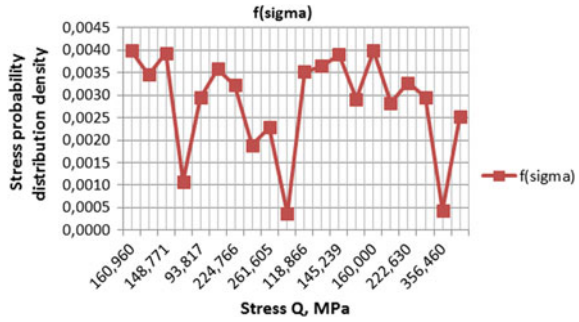
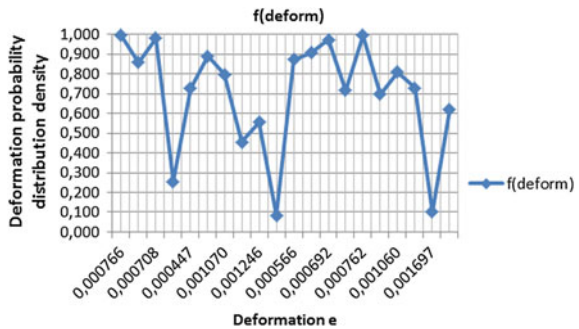


Fig. 2 Probability distribution density as function of deformations



Hence, the dynamic pattern of safe operation indicators for the heavy-duty machine elements under study can be formulated as follows:

$$P_S(t) = P\{F(\sigma_{ij})\} = \int 0.008e^{-0.006\sigma_{ij}} d\sigma_{ij}; \tag{16}$$

$$P_S(t) = P\{F(\varepsilon_{ij})\} = \int 0.597e^{\varepsilon_{ij}} d\varepsilon_{ij}; \tag{17}$$

$$P_R(t) = 1 - P\{F(\sigma_{ij})\} = 1 - \int 0.008e^{-0.006\sigma_{ij}} d\sigma_{ij}; \tag{18}$$

$$P_R(t) = 1 - P\{F(\varepsilon_{ij})\} = 1 - \int 0.597e^{\varepsilon_{ij}} d\varepsilon_{ij}. \tag{19}$$

The resulting relationships allowed to construct the graphs of limit and acceptable states when evaluating durability and operating life of heavy-duty machines and the probability density for operating and rupturing loads and stresses, as shown in Fig. 3.

Dips in the above graph represent potentially hazardous zones of risk, when operating or rupturing stresses and deformations exceed limit values.



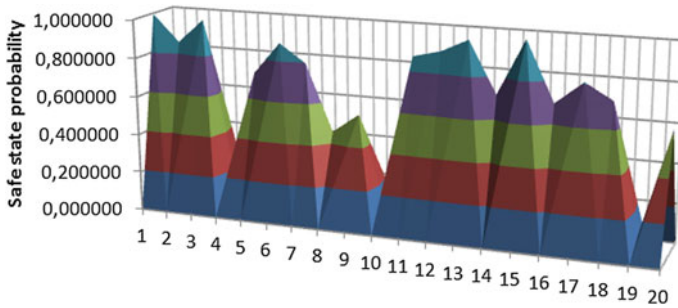


Fig. 3 Graphs of limit and acceptable states for operating and rupturing stresses and deformations

5 Conclusions

The presented multidisciplinary approach to evaluating the dynamics of safe operation indicators for heavy-duty machines represents promising area of risk analysis. This is particularly important when quantitative safety or hazard evaluation is required.

Considering that the identification of probabilistic properties of potential rupture zones as a compatible function of probability distribution represents quite a time-consuming task, it was accepted to study probabilistic properties of stress and deformation fields. Mathematical apparatus of stochastic process was applied in this study.

The equations of safe and hazardous operation functions for the heavy-duty structural element of metallurgical overhead crane—i.e. the frame manufactured from O9G2S structural steel with its known mechanical properties and limit loads—were deduced. Popular mathematical apparatus of nonlinear regression was used. The models were probably significant. The graph of limit and acceptable states for operating and rupturing stresses and deformations were presented based on the analysis of obtained equations of structure-related probabilistic dynamics.

The obtained results demonstrate functionality of risk analysis for different structures and, certainly, constitute useful materials for executive operators of such machines, engineers and researchers. Safe operation of heavy-duty machines results in the improvement of their quality and, consequently, economic efficiency.

References

1. Izvekov YuA (2012) Modelirovanie prognozirovaniya riska nesushchikh konstruksiy kranov metallurgicheskogo proizvodstva (Model operation of prediction of risk of load-bearing frames of cranes of metallurgical production). *Curr Probl Mod Sci Tech Educ* 70:6–8
2. Izvekov YuA (2013) Risk-analiz oborudovaniya metallurgicheskikh proizvodstv. Podkhod, kontseptsiya, analiz (Risk analysis of an inventory of metallurgical productions. Approach, concept, analysis). Saarbrucken, Deutschland

3. Frolov KV, Makhutov NA (2006) Bezopasnost Rossii. Pravovye, sotsialno-ekonomicheskie i nauchno-tekhnicheskie aspekty (Safety of Russia. Legal, socio-economic, and scientific and technical aspects). In: 4 Parts. Part 1: the basic concepts of the analysis and regulation of safety. Znanie, Moscow
4. Anon (1989) Risk criteria for land use planning in the vicinity of major industrial hazards. U. K. Health and Safety Executive, London
5. Anon (1993) Risk analysis, perception, management. The Royal Society, London
6. Bagrov AV, Murtazov AK (2010) Tekhnogennyye sistemy i teoriya riska (Technogenic systems and risk theory). Ryazan State University named for S.A. Yesenin, Ryazan
7. Izvekov YuA, Kobelkova EV, Loseva NA, Dubrovsky VV, Khamutskikh EYu (2015) Mathematical evaluation of mechanical construction safe loading. J Ind Pollut Control 1:115–118
8. Biryukov MP (1980) Dinamika i prognoziryuyushchiy raschet mekhanicheskikh system (Dynamics and the predicting calculation of mechanical systems). Vysheyshya shkola, Minsk
9. Boulding KE (1956) General systems theory—the skeleton of science. Manage Sci 2:197–208
10. Brushlinsky NN, Hall JR, Sokolov SV, Wagner P (2003) Fire statistics, June 2003. Academy of State Fire Service, Moscow
11. Taguchi G (1985) Quality engineering in Japan. Bull Jpn Soc Precis Eng 4:237–242
12. Hammad DB, Shafiq N, Nuruddin MF (2014) Criticality index of building systems using multi-criteria decision analysis technique. In: MATEC web of conferences, vol 15. EDP Sciences, pp 01018
13. Izvekov YuA (2012) Analiz tekhnogennoy bezopasnosti kranovogo khozyaystva Rossii (Analysis of technogenic safety of crane economy of Russia). Mod High Technol 12:18–19
14. Kumamoto H, Henley EJ (1996) Probabilistic risk assessment and management for engineers and scientists. IEEE Press, New York
15. Lepikhin AM (2000) Risk analysis of designs of potentially dangerous objects on the basis of probability models of mechanics of destruction. Dissertation, RAS, Siberian Office, Institute of Computing Model Operation, Krasnoyarsk
16. Malinetsky GG, Potapov AB (2000) Sovremennyye problemy nelineynoy dinamiki (The modern problems of non-linear dynamics). Editorial of URSS, Moscow
17. Sorensen AG (1973) A statistical analysis of product reliability due to random vibration. In: Proceedings of the annual reliability and maintainability symposium, Philadelphia
18. Stepanov VV (2006) Kurs differentsialnykh uravneniy (The course of the differential equations). KomKniga, Moscow
19. Bezopasnost truda v promyshlennosti (Safety of work in the industry) (2010) Moscow
20. Gilmore R (1993) Catastrophe theory for scientists and engineers. Dover, New York
21. Poston T, Stewart I (1998) Catastrophe: theory and its applications. Dover, New York
22. Prigozhin I, Stengers I (1994) Poryadok iz khaosa. Vremya, khaos, kvant (Order out of chaos. Time, chaos, quantum). Progress, Moscow
23. Sanns W (2000) Catastrophe theory with mathematica: a geometric approach. DAV, Germany
24. Saunders PT (1980) An introduction to catastrophe theory. Cambridge University Press, Cambridge
25. Thompson J, Michael T (1982) Instabilities and catastrophes in science and engineering. Wiley, New York

Influence of Spherical Body Diameter on Impact Interaction Dynamics



V. Lapshin, V. Yashenko and A. Eliseev

Abstract A mechanorheological viscoelastic–plastic model was applied to study the influence of a spherical body diameter on the impact duration. With an increasing spherical body diameter, the body mass and the surface curvature radius increase. Simultaneous and separate effects of both factors were studied. Impact interaction was simulated using a mathematical model. The study identified that a simultaneous increase in both factors (body mass and surface curvature radius) increases the impact duration. An increase in the body mass leads to a more significant increase in the impact duration because at the same initial impact speed, body deformation and deformation time increase. An increase in the surface curvature radius decreases the impact time because of the rigidity of the elastic body, i.e. elastic resistance to deformation, increases in the deformation zone. At the same initial speed, body deformation and deformation time decrease. Therefore, under the simultaneous influence of two factors, an increase in impact duration is less significant. At various values of model parameters, an increase in plasticity increases impact duration. This phenomenon is accounted for an increase in full deformation and impact time due to the influence of the plastic unit. Thus, the mechanorheological model identified that impact time depends on impacting body parameters (mass and surface curvature radius) influencing the dynamics of body movement and deformation. To improve simulation and research result accuracy and reliability, it is necessary to account for the influence of these factors on the dynamics of impact interaction when solving practical tasks.

Keywords Viscoelastic–plastic model · Impact interaction · Mathematical simulation of impact interaction

V. Lapshin (✉) · V. Yashenko

Irkutsk National Research Technical University, 83 Lermontov Street, Irkutsk 664074, Russia
e-mail: lapshin@istu.edu

A. Eliseev

Irkutsk State Transport University, 15, Chernyshevskogo Street, Irkutsk 664074, Russia

© Springer Nature Switzerland AG 2020

A. A. Radionov et al. (eds.), *Proceedings of the 5th International Conference on Industrial Engineering (ICIE 2019)*, Lecture Notes in Mechanical Engineering,

https://doi.org/10.1007/978-3-030-22041-9_65

603

1 Introduction

When studying behavior of machines and processes, key dynamics parameters are identified. These include forces of impact interaction, impact duration, speed, and deformation values for individual elements, etc. Loads depend on braking acceleration and impact duration. Large accelerations and forces of inertia are typical of short impact processes. They often destroy machines and structures. Mechanical properties of materials, impact speed, and body parameters affect the behavior dynamics.

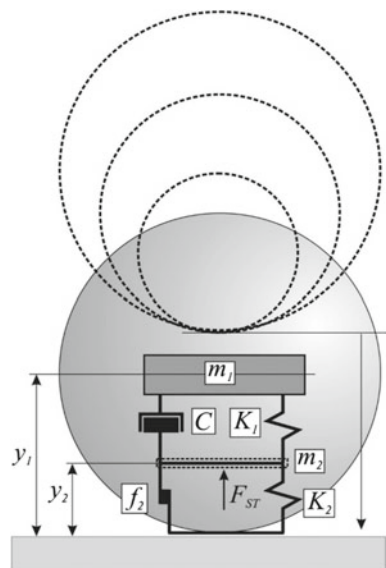
Thus, studies on dynamic processes using mathematical models are important and relevant. To develop mathematical models, a mechanorheological approach is often used. A lot of research papers deal with this issue [1–5].

The present article studies the dynamics of impact interaction of a spherical body using a mechanorheological viscoelastic–plastic model. Effects of a spherical body diameter on the impact duration are studied.

The issue was studied in [4, 6–8]. The researchers used simpler and less accurate viscoelastic models. The present study uses a more advanced viscoelastic–plastic model [9] consisting of viscoelastic and plastic units which describes plastic deformations. To develop model control methods, a number of studies, including studies on the influence of viscoelastic and plastic parameters of the model on impact duration, were carried out [10–14].

Figure 1 is a schematic view of the mechanorheological viscoelastic–plastic model. The model consists of two units: viscoelastic unit $K_1 - C$ and elastic–plastic unit $K_2 - f_2$.

Fig. 1 Scheme of the viscoelastic–plastic model



The whole-body mass is concentrated in inertia element m_1 . The mass of element m_2 is taken as negligibly small ($m_2 \rightarrow 0$). It was introduced for convenient development of the mathematical model with two second-order differential equations.

At the initial interaction stage, only elastic deformations occur. Only the viscoelastic unit $K_1 - C$ becomes deformed. It describes elastic deformations and controls energy losses due to energy dissipation. When the dynamic force has a target value of F_{ST} , corresponding to intensive development of plastic (residual) deformations, the viscoelastic unit $K_2 - f_2$ comes into operation. By modifying values of F_{ST} , one can deform the viscoelastic unit or the viscoelastic plastic unit. One or both units will work.

At the unloading stage, the impact force is maximum N_{max} . At this stage, elastic deformations disappear, and the process describes the viscoelastic unit.

2 Purpose Statement

Similar studies are described in [4, 6–8]. Computer experiments aimed to study and analyze the dynamics of interaction of a spherical body with a flat surface by simulating real impact processes. The experiments aimed to study the effects of rheological properties of the surface and diameters of the spherical body on the impact duration. The results obtained prove that the body diameter influences the impact time.

A simplified model can be used at the initial research stage. After the research task has been solved, more sophisticated models have to be used.

The present research was carried out using a more advanced viscoelastic–plastic model which helps study the influence of material plasticity on the dynamics of impact interaction of bodies. One of the important practical tasks is to adapt the model to real impact processes. The task can be solved by using experimental parameters of the dynamic process: impact time, impact interaction force, etc. The developed methods control the dynamics of model movement [15, 16]. During the experiments, viscoelastic–plastic parameters of the model were modified in order to assess the effect of material plasticity on the dynamics of impact interaction. Spherical bodies of different diameters (9.5; 14.25; 19 mm) were used.

With an increase in the body diameter, the body mass and the body surface curvature radius increase. Both factors influence the dynamics of impact interaction. The simultaneous influence of two factors and the influence of each factor separately were studied.

3 Theoretical Background

The mathematical model is based on the mechanorheological model. Differential equations of the viscoelastic model movement can be written as

$$m_1 \ddot{y}_1 + C_1 \dot{y}_1 y_1 + K_1 y_1^{3/2} = -m_1 g \quad (1)$$

Viscoelastic–plastic model movement can be described by two equations:

$$m_1 \ddot{y}_1 + C_1 (\dot{y}_1 - \dot{y}_2) (y_1 - y_2) + K_1 (y_1 - y_2)^{3/2} = -m_1 g; \quad (2)$$

$$m_2 \ddot{y}_2 + K_2 y_2^{3/2} + f_2 y_2 + C_1 (\dot{y}_2 - \dot{y}_1) (y_2 - y_1) + K_1 (y_2 - y_1)^{3/2} = -m_2 g + F_{ST} \quad (3)$$

where $y_1, y_2, \dot{y}_1, \dot{y}_2$ are the shift and speed of mass m_1 and mass m_2 ; K_1 is the ratio of stiffness of the elastic element of the viscoelastic model unit; C is the ratio of viscosity of a viscous element of the viscoelastic model unit; F_{ST} is the force at the beginning of plastic deformation occurrence; K_2 is the ratio of stiffness of an elastic element of the elastic–plastic unit; f_2 is the ratio of shift of the elastic–plastic unit or the ratio of ductility.

The shift from the viscoelastic model to the viscoelastic–plastic model occurs when the force of normal response $N = C_1 \dot{y}_1 y_1 + K_1 y_1^{3/2}$ has the target value of F_{ST} .

Elastic element K_1 has nonlinear properties [2–4]. Viscous resistance C was proportional to the speed and value of elastic deformation [10]. Equations (1)–(3) can be solved by the Runge-Ku.

4 Analysis of Research Results

The impact process was simulated using steel spherical bodies of different diameters: 9.5; 14.25; 19 mm. The radii of curvature were 4.75; 7.125; 9.5 mm, respectively. The values of body mass were 3.5; 11.82; 28.01 g. Four calculation variants were analyzed. Variant 1: $F_{ST} = N_{max}$ —elastic deformations only. Variant 2: $F_{ST} = 2N_{max}/3$. Variant 3: $F_{ST} = N_{max}/3$. Variant 4: $F_{ST} = 0$ —plastic deformations since the beginning of the impact process. The impact duration T_K was taken as an impact interaction parameter. Model parameters K_1, K_2, f_2 , and C were modified within the limits.

Figures 2 and 3 show the dependence of the impact duration on diameters of the spherical body at different values of F_{ST} and simultaneous influence of two factors (body mass m_1 and radius of surface curvature R). Figure 2 shows that elastic

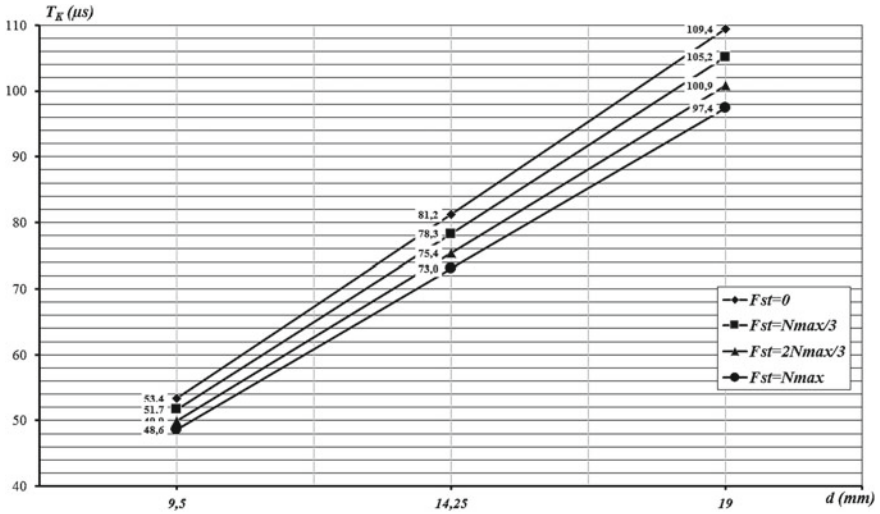


Fig. 2 Dependence of the impact duration T_K on the body diameter d at K_1 -min

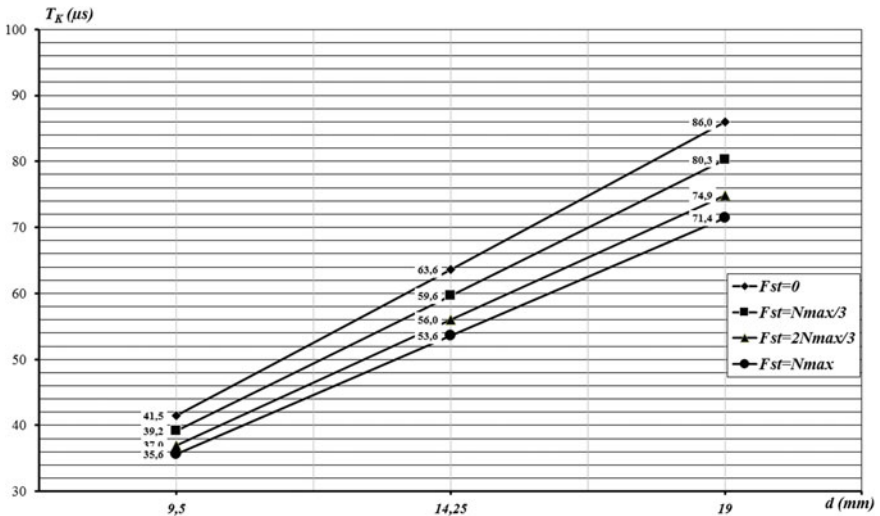


Fig. 3 Dependence on the impact duration T_K on the body diameter d at K_1 -max

parameter K_1 took the minimum value. Figure 3 shows that elastic parameter K_1 took the maximum value. Other parameters $K_2, f_2,$ and C changed in a similar way.

Figures 4 and 5 show the influence of the impact duration on body mass m_1 and surface curvature radius R .



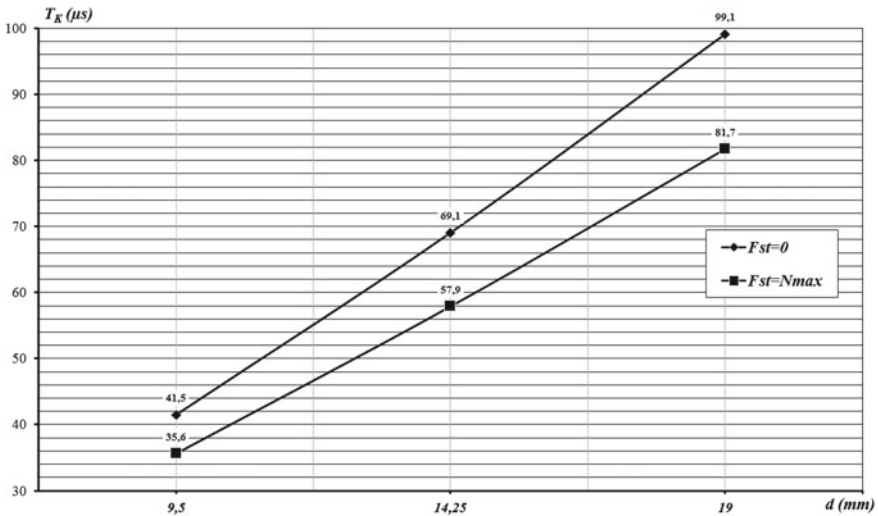


Fig. 4 Dependence on the impact duration T_K on the body diameter d at $R=const$

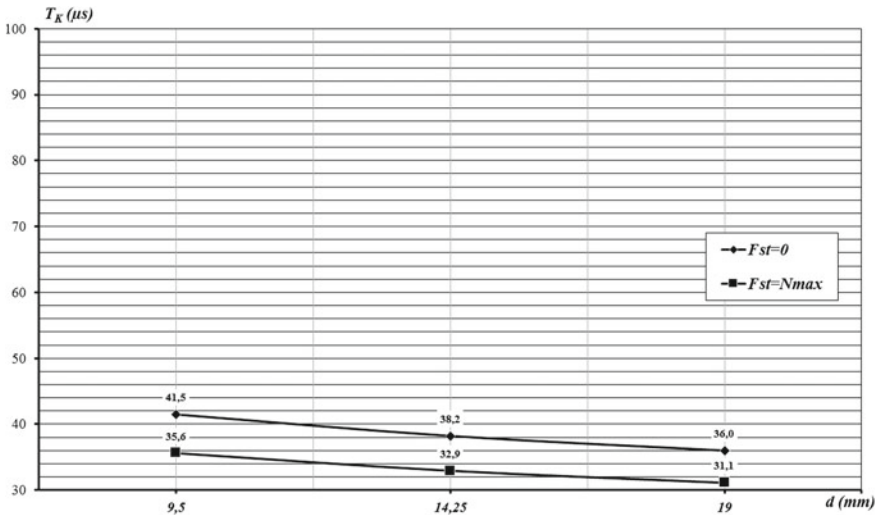


Fig. 5 Dependence on the impact duration T_K on the body diameter d at $m_1=const$

The analysis allowed for the following conclusions. Under the simultaneous increase in two factors (body mass and surface curvature radius), impact duration T_K increases (Figs. 2 and 3). An increase in the body mass at $R=const$ (Fig. 4) causes a more significant increase in the impact duration. The influence of the body mass on the impact duration is due to increasing body deformation and deformation time at the same initial impact speed.

An increase in the radius of body surface curvature at m_1 -const reduces impact time (Fig. 5). The influence of the radius on impact time is due to the elastic body rigidity increasing in the deformation zone of the contact area which increases elastic resistance to deformation. Increasing resistance increases elastic parameter K_1 . At the same initial impact speed, it decreases deformation of the bodies and deformation time. Therefore, under the simultaneous influence of two factors, the impact duration increases slightly.

An increase in plasticity of the model ($F_{ST} = N_{max} \rightarrow F_{ST} = 0$) increases impact duration T_K at various parameters of the model K_1 , K_2 , f_2 , and C . It can be accounted for full deformation increased by the plastic component increasing the impact time.

5 Conclusion

Thus, research results using a mechanorheological model show that the impact duration depends on a body diameter. It can be accounted for the influence of the body mass and surface curvature radius on body movement and deformation dynamics. At the same time, these factors have different effects on the impact duration. To improve simulation and research result accuracy and reliability, it is necessary to take into account the influence of these factors on the impact interaction dynamics when solving practical tasks.

References

1. Panovko YaG (1990) Fundamentals of fluctuation and impact theory. Polytechnic Publ., Leningrad
2. Batuev GS, Golubkov YuV, Efremov AK, Fedosov AA (1977) Engineering methods of studying impact processes. Mashinostroenie Publ., Moscow
3. Kilchevskiy NA (1976) Dynamic contact compression of solid bodies. Naukova Dumka Publ., Kiev
4. Lapshin VL, Yatchenko VP, Rudykh AV (2006) Research model for impact interaction of a spherical body with a plane surface of ore materials. Bull ISTU 2(26):110–115
5. Lapshin V, Rudykh A, Glukhov A (2017) Experimental studies of mechano-rheological model simulating shock interactions. Institute of Electrical and Electronics Engineers IEEE Xplore. <https://doi.org/10.1109/icieam.2017.8076457>
6. Lapshin VL, Rudykh AV (2006) Computer studies on impact duration for interaction between the spherical body and body flat surface. In: Proceedings of the international scientific and engineering conference “Computer solids mechanics”, MIIT, Moscow
7. Lapshin VL, Rudykh AV (2006) Studies on the dynamics of interaction between the non-linear viscoelastic model and flat mounting surface. In: Ore concentration: collection of research works, ISTU, Irkutsk

8. Lapshin VL, Yashchenko VP, Rudykh AV (2006) Studies on the influence of parameters of the elastic nonlinear element of the viscoelastic model on the impact duration for the system “model-flat surface”. In: Proceedings of the 5th interregional scientific and engineering conference with international participation “Mechanics of the 21st century”, BSU, Bratsk
9. Lapshin VL, Demakov EI (2007) Elastic viscous plastic mechanorheological model for assessing the properties of minerals when simulating vibro separation processes. In: Mechanics for the XX century, All-Russian conference proceedings, Bratsk
10. Lapshin VL, Glukhov AV (2011) Studies of a viscous element of the elastic viscous plastic model. Syst Methods Technol 4(12):14–19
11. Lapshin VL, Rudykh AV, Glukhov AV (2012) Use of non-linear viscous and plastic elements in a mechanorheological model of the impact process. Syst Methods Technol 3(15):21–25
12. Lapshin VL, Glukhov AV (2011) Computer studies of the elastic viscous plastic mechanorheological model. In: Modern machines and technologies: studies and developments, Lipetsk, pp 20–27
13. Lapshin VL, Glukhov AV (2011) Regression analysis of the impact interaction strength for a mechanorheological model. Bull ISTU 10(57):44–49
14. Lapshin VL, Glukhov AV (2011) Analysis of residual deformations in impact interaction of an elastic viscous plastic mechanorheological model. Mod Technol Syst Anal Model 4(32): 39–45
15. Lapshin VL, Rudykh AV, Glukhov AV (2014) Methods for determining the modulus of elasticity. RF Patent 2526233, MPK G 01 N 3/48, 20 Aug 2014
16. Lapshin VL, Glukhov AV, Rudykh AV (2015) Development of the impact method for determining the modulus of elasticity of a material. Syst Methods Technol 2(26):37–43

Indicative and Efficient Parameters of the Engine Operating Cycle When Using Fuels with Various Octane Numbers



V. E. Lazarev, M. A. Matculevich and E. A. Lazarev

Abstract The permanent increase in the octane number of gasoline fuel is one of the modern ways of developing the building and exploitation of internal combustion engines. Increasing the gasoline's octane number brings to perfection of exploitation properties of gasoline engines with a simultaneous improvement of proof from detonation processes. The nomenclature of fuels with different octane numbers is quite wide. There are the fuels with octane number 92, 95, 98 and even 100 with different additives and components. However, till now, the information about exact parameters of an operation cycle using the fuel with an octane number of 100 units in comparison with other types of fuels is not enough. In this investigation, the indicative and efficient parameters of the engine's operating cycle are estimated and analyzed by means of an experimental test-bench machine and using the fuels with different octane numbers. The gasoline fuels with octane numbers 95 and 100 units are analyzed with indicative diagrams and various ignition timing. As a result, the duration of a combustion process as well as the values of maximal pressures and temperatures is received for different types of fuels. The conclusions on the results of investigations are proposed and represented.

Keywords Fuel's octane number · Ignition timing · Duration of combustion process · Pressures and temperatures of combustion process · Parameters of operation cycle

1 Introduction

Engine technology is developing in the following main areas: increasing power capacity, fuel efficiency and reducing emissions of harmful substances of exhaust gases. The specific success in these areas is ensured by the improvement of the operating cycle [1, 2], in particular, its main process—fuel combustion process.

V. E. Lazarev (✉) · M. A. Matculevich · E. A. Lazarev
South Ural State University, 76, Lenin Avenue, Chelyabinsk 454080, Russia
e-mail: lazarevve@susu.ru

Available reserves in this area have not yet been depleted [3–5]. Increasing the detonation resistance of fuel by increasing the octane number is an effective measure contributing to the improvement of performance of modern fuel engines [6–9]. The use of high-octane fuels allows increasing the degree of compression without the risk of detonation combustion, which contributes to increased efficiency, efficiency of the operating cycle and engine reliability.

In this regard, a comparative assessment of indicator and effective indicators of a fuel engine when using AI-95-K5 (state standard symbols) base fuel and AI-100-K5 high-octane fuel as an engine fuel is relevant. At the same time, indicator and effective parameters are estimated using a thermodynamic analysis of indicator diagrams of gas pressure in the engine cylinder. These indicators are determined experimentally in the process of motor-bench testing of a gasoline engine equipped with standard fuel injection and fuel ignition systems [3, 10].

All represented investigations are performed for four-cylinder, four-stroke gasoline engine with operation volume 1.6 L.

2 The Purpose, Objectives, and Methods of Research

The main purpose of this research is to experimentally confirm the effectiveness and safety of using AI-100-K5 gasoline with an octane number of 100 units as an engine fuel for a gasoline engine. To achieve this goal, it is necessary to solve the following main tasks:

- evaluation of effective and indicator parameters of the engine when operating on the studied fuels;
- thermodynamic analysis of pressure-diagrams to determine the maximum pressure, gas temperature, moment of start, and duration of the combustion process in the engine's operating cycle when operating on the studied fuels.

In order to determine the moments of the beginning and duration of fuel combustion process, the obtained indicator diagrams are processed by a special technique, which allows evaluating the main parameters of the operation cycle. A correlation between the end of the combustion process and the advance phase of the opening of the outlet valve allows concluding that fuel burns out in the exhaust pipe, the danger of valve burning out, etc.

It should be noted that since the tests are carried out using a gasoline engine having an external air–fuel mixing process, at the time of the ignition, the air–fuel mixture is a well-mixed homogeneous gaseous medium. This circumstance is due to both the method of mixing process and its duration, since the preparation and mixing of fuel and air, starting in the inlet pipe, continues in the processes of intake, and compression until the moment of ignition. Analysis of heat generation by the indicator diagram allows estimating the start time and duration of the fuel combustion process and the moment on the expansion line at which the combustion can be considered as completed.

During engine operational process, detonation occurs during transient conditions (acceleration, a sharp increase of load, etc.) and is targeted at engine parameters that differ from the optimal ones. In this situation, the most convenient variable parameter—ignition timing (θ)—allows you to simulate the conditions for the occurrence of detonation in transient modes of engine operational process. Forced change of the ignition timing in a high-load engine is used to record the beginning of detonation combustion.

It is advisable to receive the engine pressure-diagram together with the determination of, for example, load characteristics. The indicator diagram characterizing the change in gas pressure during the operating cycle, with a total length of 720 crank angle, is divided into sections with a length of 1 crank angle. The obtained indicator diagrams characterizing the change in gas pressure in the engine cylinder in the range from -180 crank angle to $+180$ crank angle relative to top dead center (TDC) were subjected to thermodynamic analysis to determine heat generation.

The detection of the start of the combustion process, as a result of the processing of indicator diagrams, is based on the following theoretical principles. The peculiarity of the operating cycle of a fuel engine is that the ignition of the air–fuel mixture is carried out forcibly from a source of electric spark (ignition spark plug). The angle formed by the axis of the crankshaft and the axis of the cylinder at the time of filing an electric spark is called the ignition timing (IT). From the moment the spark is supplied by the igniter until the start of the combustion process, a certain period of time passes, which is called the inflammation delay period (IDP). The crankshaft during this time manages to rotate at a certain angle. Thus, the angle between the axis of the crankshaft and the axis of the cylinder at the time of ignition of the air–fuel mixture is determined by the difference between the ignition advance angle and ignition delay and is called the inflammation moment (IM). This angle characterizes the beginning of the combustion process and is one of the desired quantities based on the results of processing indicator diagrams and determining the indicator values of the operating cycle.

To identify the beginning of the combustion process, the pressure-diagram of the operating cycle is divided into elementary sections with a length of 1 crank angle. At each site, an analysis of heat dissipation is performed and the dependence of the change in the difference in the amount of specific heat used in the operation cycle (Δq) on the angle of rotation of the crankshaft is plotted. Considering that the heat admission in the compression process is characterized by relative monotony and stability of changes in parameters, the combustion process is characterized by a sharp increase in absolute values and, accordingly, expansion of specific heat (Δq). Thus, the inflammation moment (IM) is one of the determined parameters by the pressure-diagram and can be found from the values of the specific heat.

The duration of the combustion process φ_z is determined using a refined method for calculating and analyzing the operation cycle of gasoline engines, the author of which is Vibe [11–14]. According to the main provisions of this technique, the combustion process continues until the fraction of burned-out fuel is 0.999. At this moment, the combustion process can be considered complete, and the interval from the start of combustion to its completion can be taken as the duration of the combustion process.

3 The Results of Thermodynamic Analysis of Indicator Diagrams of Gas Pressure in the Engine Cylinder

Indicator diagrams of pressure changes in the engine cylinder for the studied fuels are presented in Figs. 1 and 2, and diagrams of changes in the temperature as a function of rotation angle of the engine crankshaft are shown in Figs. 3 and 4.

The analysis of the change expansion in the specific heat in the operating cycle suggests that with increasing engine load, the ignition timing slightly increases, both for AI-95-K5 and AI-100-K5.

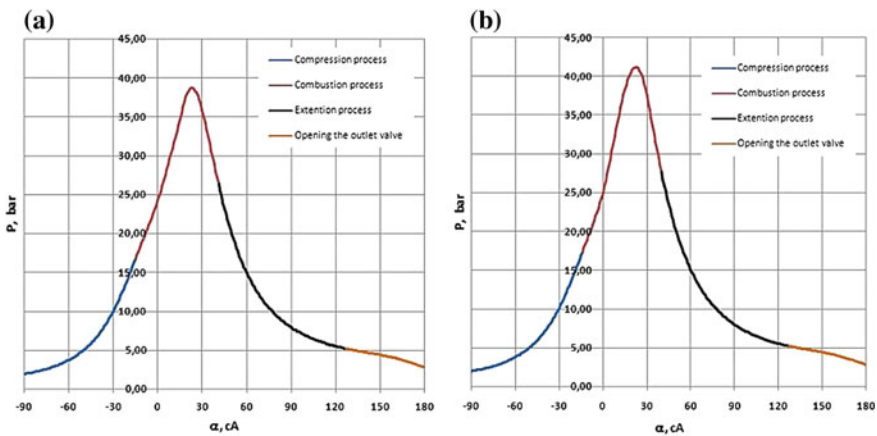


Fig. 1 Engine’s indicative diagram using the different fuels: **a** AI-95-K5 and **b** AI-100-K5 at torque of crankshaft $M = 105 \text{ N m}$ and $n = 3500 \text{ min}^{-1}$

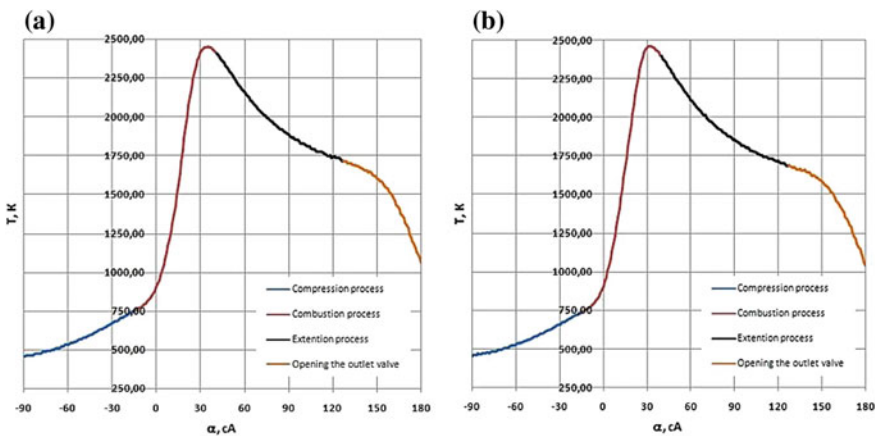


Fig. 2 Engine’s temperature diagram using the different fuels: **a** AI-95-K5 and **b** AI-100-K5 at torque of crankshaft $M = 105 \text{ N m}$ and $n = 3500 \text{ min}^{-1}$

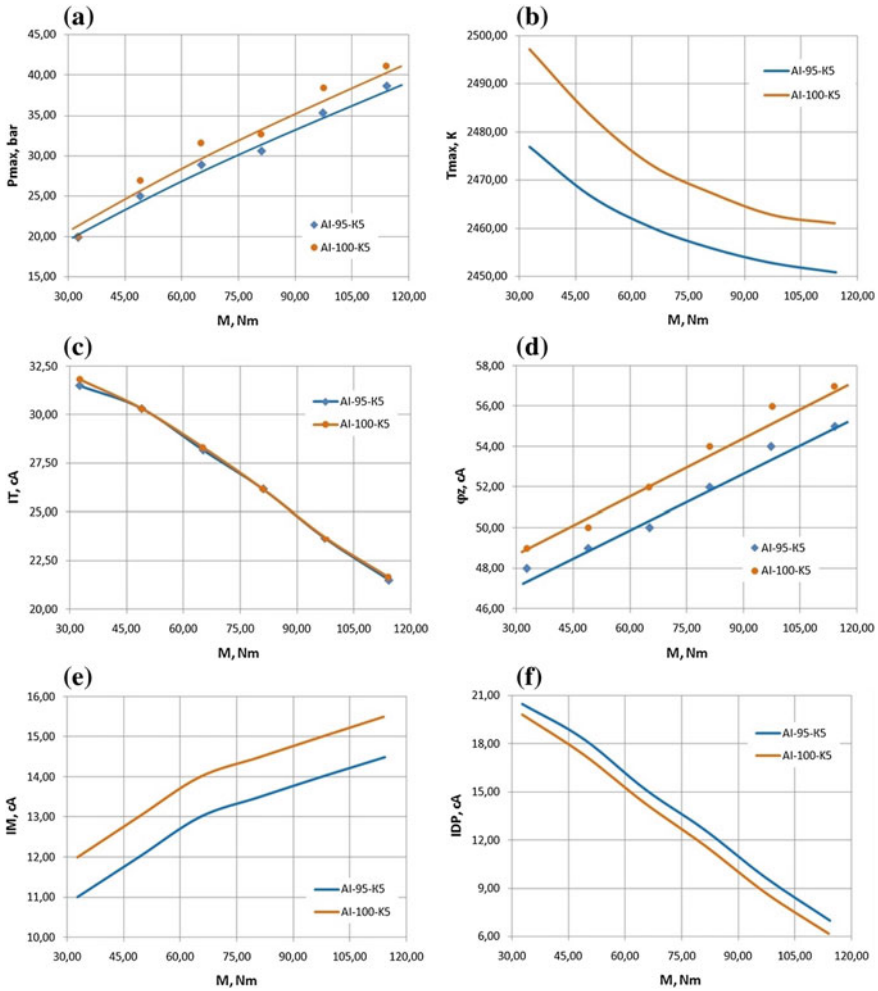


Fig. 3 a Maximal pressure and b temperature, c ignition timing, d duration of combustion, e inflammation moment, and f inflammation delay period in function to engine’s loading ($n = 3500 \text{ min}^{-1}$)

The values of the ignition timing and inflammation moment are 1–1.5 crank angle higher for AI-100-K5 as compared with AI-95-K5. Considering such a slight increase in the angle, this difference can be considered insignificant. Summary data on the ignition timing and inflammation moment values, as well as the inflammation delay period for the studied fuels under various loading conditions are presented in Table 1.

According to the data presented in Table 1, the AI-95-K5 fuel, like the AI-100-K5 fuel, demonstrates approximately equal values of the ignition timing

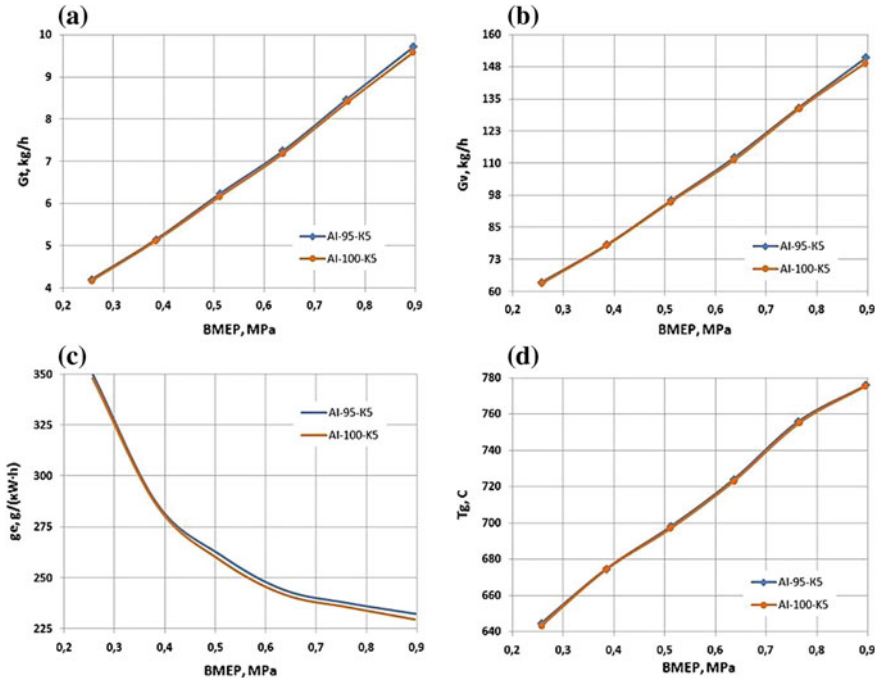


Fig. 4 a Fuel consumption and b airflow, c specific effective fuel consumption, and d temperature of exhaust gases in function to brake mean effective pressure (BMEP)

Table 1 Ignition timing (IT), inflammation moment (IM), and inflammation delay period (IDP) for investigating fuels

Type of the fuel	Parameter	Torque of crankshaft of, N m					
		30	45	60	75	90	105
AI-95-K5	IT	31.50	30.33	28.17	26.17	23.67	21.50
	IDP	20.50	18.33	15.17	12.67	9.67	7.00
	IM	11.00	12.00	13.00	13.50	14.00	14.50
AI-100-K5	IT	31.83	30.33	28.33	26.17	23.67	21.67
	IDP	19.83	17.33	14.33	11.67	8.67	6.17
	IM	12.00	13.00	14.00	14.50	15.00	15.50

(IT), regulated by the engine system controller in automatic mode [15]. The change in the IT for gasoline AI-95-K5 (Fig. 3) with a change in engine load from 30 to 105 N m was from 31.5 to 21.5 crank angle, respectively. The change in the IT for AI-100-K5 with a change in the engine load in the considered range of values ranged from 31.83 to 21.67 crank angle.

On the contrary, when the load changes, the inflammation moment (IM) slightly increased and was determined according to the results of processing indicator



diagrams when the engine is running on various fuels and loading modes (Fig. 3). The IM for AI-95-K5 fuel when changing engine load from 30 to 105 N m ranged from 11 to 14.5 crank angle, and the time for AI-100-K5 changed values from 12 to 15.5 crank angle.

The inflammation delay period (IDP) monotonously decreases with increasing engine load, which is caused by an increase in the rate and degree of turbulence of the fresh air stream with an increase in load (respectively, with an increase in the throttle angle) and a decrease in the residual gas ratio, which characterizes the fraction of the exhaust gases of the previous cycle as part of the fresh inlet gas of the current cycle. Some reduction in the IDP for AI-100-K5 compared to AI-95-K5, in addition to the natural measurement error, should be attributed to the chemical composition of octane-containing fuel at 100 units (change in oxygen content and ester-containing products). The IDP for AI-95-K5 when the engine load changed from 30 to 105 N m varied in the range of values from 20.5 to 7 crank angle, and for AI-100-K5, the value change was from 19.83 to 6.17 crank angle.

The results of processing indicator diagrams obtained during the determination of the load characteristics during operating cycle of the engine using the studied fuels make it possible to identify and analyze changes in the following indicators: maximum pressure (P_{\max}) and cycle temperature (T_{\max}), as well as the duration of the combustion process (φ_z).

The maximum pressure P_{\max} of the combustion process (Fig. 3) increases monotonically with increasing engine load, both when using AI-95-K5 and AI-100-K5 fuels. The maximum pressure for AI-100-K5 when the engine load changes from 30 to 105 N m varies in the range of values from 2.1 to 4.1 MPa, and for AI-95-K5, the change in values ranged from 2 to 3.9 MPa.

Unlike the maximum combustion pressure, the maximum cycle temperature T_{\max} tends to decrease, both for AI-95-K5 and AI-100-K5. This circumstance is explained by a slight increase in the air coefficient (α) with increasing engine load and is in satisfied agreement with the general notions on the parameters of the combustion process that occurs in modern fuel engines. The decrease in the absolute values of the maximum temperature when the engine load changes from 30 to 105 N m ranged from 2497 to 2461 K for AI-100-K5 and 2447 to 2451 K for AI-95-K5.

In relation to the results of this study, the duration of the combustion process (Fig. 3) increases with increasing engine load, both when using AI-95-K5 and AI-100-K5. The duration of combustion φ_z for AI-95-K5 in the engine load range from 30 to 105 N m varies in the range from 48 to 55 crank angle; while for AI-100-K5, this change ranges from 49 to 57 crank angle. The obtained values of the duration of combustion for the tested fuels, as well as other indicator values of the engine, are in satisfied agreement with the basic principles of the theory of operating cycles in modern gasoline engines [3, 5, 6, 8, 9]. The existing differences in the duration of combustion processes for AI-95-K5 and AI-100-K5 are explained by insignificant differences in their physicochemical properties.

The test results to determine the effective performance of the engine when working on AI-95-K5 and AI-100-K5 fuels in the form of graphical dependencies

fuel consumption G_t and airflow G_v , specific effective fuel consumption g_e , and temperature of exhaust gases T_g from the brake mean effective pressure (BMEP) for each loading mode are presented in Fig. 4.

During the tests, it was found that the maximum fuel consumption is typical for AI-95-K5, and at the maximum loaded mode, it was 9.72 kg/h. The minimum value of fuel consumption at a power of 12 kW for this fuel type was 4.2 kg/h. When using AI-100-K5, the maximum value of hourly fuel consumption was 9.59 kg/h, and the minimum value at a power of 12 kW was 4.17 kg/h.

Specific effective fuel consumption g_e (Fig. 4), as the ratio of fuel consumption in each engine operation mode to the amount of generated power, has a minimum value when operated on the load characteristic indicating the section of the most economically efficient engine loading mode at a given crankshaft rotation speed $n = 3500 \pm 25 \text{ min}^{-1}$. The results obtained experimentally make it possible to identify the minimum values of g_e at BMEP = 0.9 MPa for both tested fuels, and the nature of the dependences obtained corresponds well with the general provisions of the engine theory [3, 5, 6, 8, 9], as well as the nature and dynamics of changes in the specific effective flow rate fuel in engines with forced ignition.

In accordance with the test results, AI-100-K5 is characterized by the best economic efficiency, the minimum specific fuel consumption for which was 229.48 g/(kWh). The results of the AI-95-K5 tests revealed the value of the specific effective fuel consumption at BMEP = 0.9 MPa equal to 232.27 g/(kWh).

In accordance with the engine load characteristic, the change in airflow rate G_v (Fig. 4) is recorded in the range from 60 to 150 kg/h for AI-95-K5 and AI-100-K5 with differences in 2–4 kg/h. At the same time, to achieve the required power, approximately equal share opening the throttle was required at a maximum airflow rate of 151.1 kg/h for AI-95-K5 and 149.1 kg/h for AI-100-K5. Differences in the share of opening the throttle in this mode do not exceed 1.5%.

Similar to the change in airflow, the exhaust gas temperature T_g (Fig. 4) monotonously increases with increasing engine load, which is caused by an increase in the cycle supply of the air–fuel mixture with increasing power. The maximum value of the exhaust gas temperature at a maximum engine power of 42 kW was 775–776 °C for AI-95-K5 and AI-100-K5. The minimum value of the exhaust gas temperature at an engine power of about 12 kW was 643–645 °C for AI-95-K5 and AI-100-K5. Thus, there were no significant differences in the value of the exhaust gas temperature for the tested fuels.

The insignificant differences between indicator and effective indicators when using tested fuels confirm the reasonability of using AI-100-K5 as an engine fuel.

4 Conclusions

1. The use of AI-100-K5 fuel in the operation of modern automobile engines makes it possible to achieve such indicators as effective power, torque, exhaust gas temperature, etc. with a slight improvement in fuel efficiency compared with

the use of AI-95-K5. A slight decrease in the specific effective fuel consumption, indicating an improvement in the fuel efficiency of the engine when using AI-100-K5, is accompanied by an insignificant increase in the maximum gas pressures in the cylinder in most of the studied loading conditions.

2. The results obtained experimentally and in the process of analyzing the operating cycle testify the regular indicator values of the investigated engine when working on AI-100-K5 fuel and confirm the possibility of using this fuel as an engine fuel.
3. The data obtained in the course of testing the performance properties of fuels suggests that engine fuels AI-100-K5, AI-95-K5 and AI-98-K5 are interchangeable when used as engine fuel. Automobile fuel AI-100-K5 has slightly improved performance characteristics.
4. The duration of the combustion process in the operating cycle using AI-100-K5 and AI-95-K5 fuels differs by no more than 4–5%.
5. The period between the end of the combustion process to the opening of the outlet valve is 87.5 crank angle for AI-95-K5 and 86.5 crank angle for AI-100-K5. Consequently, the effects of fuel burnout in the exhaust pipe, the transfer of the combustion process to the section of expansion, and thermal destruction of outlet valves when using AI-100-K5 as a engine fuel are not expected.

References

1. Asmus TU, Borgnakke K, Clarky CK (1988) In: Hillard D, Springer JS (eds) Fuel economy of cars with gasoline engines (Translation from English, trans: Vasiliev AM, ed: Kostorov AV). Mechanical Engineering, Moscow
2. Kutlar OA, Arslan H, Calik AT (2005) Methods to improve efficiency of four stroke, spark ignition engines at part load. *Energy Convers Manage* 20(46):3202–3220 (Original Research Article)
3. Kavtaradze RZ (2008) Theory of piston engines. Special chapters: textbook for universities. Publishing House MSTU named after N.E. Bauman, Moscow
4. Kumar RH, Antony AJ (2008) Progressive combustion in SI-engines—experimental investigation on influence of combustion related parameters. *Sadhana* 33(6):821–834. <https://doi.org/10.1007/s12046-008-0036-z>
5. Sharoglazov BA, Farofontov MF, Klementev VV (2004) Internal combustion engines: theory, modeling, and calculation of processes. Publishing SUSU, Chelyabinsk
6. Lukanin VN, Morozov KA, Khachiyan AS (2005) Internal combustion engines. In 3 books. Book 1. Theory of working processes. Higher School, Moscow
7. Safonov AS, Ushakov AI, Grishin VV (2007) Chemotology of fuels and lubricants. NPKITS
8. Heywood JB (1988) Internal combustion engine fundamentals. McGraw-Hill Book Co, New York
9. Orlin AS (1983) Engines of internal combustion: theory of piston and combined engines. Mashinostroenie, Moscow
10. Barlow TJ, Latham S, McCrae IS, Boulter PG (2009) A reference book of driving cycles for use in the measurement of road vehicle emissions. Published project report PPR354

11. Vibe II (1970) Brennvlauf und Kreisprozeß von Verbrennungsmotoren. VEB Verlag Technik, Berlin
12. Lavrik AN (1985) Calculation and analysis of ICE's operating cycle across different types of fuels. Irkutsk University Press, Irkutsk
13. Kuleshov AS (2004) Diesel-RK internal combustion engine calculation and optimization program. Description of mathematical models, the solution of optimal problems. Moscow State Technical University named after N.E. Bauman, Moscow
14. Lukanin VN, Shatrov MG, Kamfer GM (2000) Thermal engineering. Textbook for universities. Higher School, Moscow
15. Tweg R (2004) Gasoline injection systems. Device, maintenance, repair: a practical guide. Publishing House "Za Rulem", Moscow

Interaction of Elastic Wheel with Bumps of Rectangular Shape



A. Startcev, S. Romanov and O. Vagina

Abstract The article presents a mathematical model of the interaction of an elastic wheel with bumps of a rectangular shape. In the study of the process of movement of a wheeled machine is of great importance to calculate the forces applied to the wheel of the vehicle. These forces determine the nature of the movement of the wheeled vehicle. With an increase in the speed of wheeled vehicles and the deterioration of road increase the dynamic load on the elements of the running system. In this regard, there is a need to develop a mathematical model describing the interaction of the wheel of the wheeled vehicle with the road. The proposed mathematical model describing the rolling of a wheel equipped with a pneumatic tyre through a rectangular obstacle can be used for practical calculations. The results of the calculation are in good agreement with the results of experimental studies, taking into account the complexity of the processes and fairly rough assumptions. The average error of calculation of forces of interaction of a wheel with an obstacle of the rectangular form makes 7.71%.

Keywords Road bumps · Mathematical model · Pneumatic tyre

1 Introduction

With the deterioration of road conditions and an increase in the speed of wheeled vehicles increase the dynamic load on the elements of the running system. In this regard, there is a need to develop a mathematical model describing the interaction of the wheel of the wheeled vehicle with the road.

A. Startcev (✉) · O. Vagina
South Ural State Agrarian University and South Ural State University,
75, Lenin Avenue, Chelyabinsk 454080, Russia
e-mail: sav.63.10.04@mail.ru

S. Romanov
State Agricultural University of the Northern Trans-Ural Region, 7,
Republic Street, Tyumen 625003, Russia

In the study of the process of movement of a wheeled machine is of great importance to calculate the forces applied to the wheel of the wheeled vehicle. These forces determine the nature of the movement of the wheeled vehicle. The main reason for the change in the magnitude and direction of the forces of interaction between the wheel and the road is the bumps. The term “the bumps” [1–19] includes quite a wide range of concepts. The analysis showed that the bumps can be divided into several characteristic groups:

- protrusions and depressions—irregularities with wavelengths from several meters to 10 cm—the main source of forces that cause vibrations of the wheeled vehicle and change the specified direction of movement in the horizontal plane;
- roughness—small irregularities in the structure of the road surface with a wavelength of less than 10 cm—usually completely smoothed elements of the running system due to deformation of the tyres and do not have a significant impact on the stability of the course of wheeled vehicles;
- bumps—irregularities caused by accidental destruction and poor maintenance of the road surface (potholes, protrusions, etc.), distinguished by the unpredictability of their occurrence in the process of movement of the wheeled vehicle.

Thus, the micro-profile of the road is a random set of protrusions and depressions of different heights and depths located at different distances from each other [2, 6, 12–14]. In this regard, when driving a wheeled vehicle, there are forced random fluctuations in the vertical plane. These fluctuations become a source of transverse fluctuations which affect the stability of the vehicle in the horizontal plane. Particularly dangerous are the single bumps of a rectangular shape.

2 Theoretical Studies

The interaction of the wheel with bumps of rectangular shape is complex. Complication of the situation is also facilitated by the use of pneumatic tyres and springs [1, 4, 5, 11, 17, 20]. Pneumatic tyres and springs soften and neutralize the dynamic loads arising in the chassis of wheeled vehicles in the process of interaction of the wheel with the bumps. Especially difficult is the process of running the wheel on the bump (initial stage). Moreover, the shape of the bump has a determining effect on the radial stiffness of the pneumatic tyre. The radial stiffness of the pneumatic tyre when interacting with a rectangular obstacle is several times greater than when interacting with a flat surface. In this case, the radial stiffness of the pneumatic tyre can be related to the type

$$C'_z = k_c C_z, \quad (1)$$

C_z —radial stiffness of the tyre, when interacting with a flat surface; C'_z —radial stiffness of the tyre, when interacting with an obstacle of rectangular shape; k_c —coefficient of proportionality.

At the same time, in the final stage of rolling the wheel through the obstacle, the trajectory of the centre of the wheel passes close enough to the trajectory of the centre of the hard wheel (Fig. 1).

The above reasoning, as well as the results of experimental studies, suggests that the trajectory of the centre of the wheel, equipped with a pneumatic tyre, can be described by an expression of the form

$$q = q_0 \left[1 - \cos \left(\frac{2\pi \cdot x}{2 \cdot l_0} \right) \right], \tag{2}$$

q_0 —wave amplitude, $q_0 = \frac{h}{2}$, m; h —the height of the obstacle of rectangular shape, m; x —the abscissa of the point for which q is defined; l_0 —half-length of the wave equal to the distance from the transverse vertical plane passing through the wheel axis to the point of contact of the wheel tyre with the obstacle of rectangular shape: $l_0 = r \cdot \sin \varphi_0$, r —free radius of the wheel, m.

The above assumption does not contradict the assumptions made in [2, 3, 7, 9, 10, 18, 19, 21] that the contact of the wheel with the road surface occurs at one point. In this regard, the value of the angle φ_0 can be determined from the expression

$$\cos \varphi_0 = \frac{r_{cm} - h}{r}, \tag{3}$$

r_{st} —static wheel radius: $r_{st} = r - \frac{G_w}{C_{tyre}}$, m; G_w —radial load on the wheel, N.

Consider the forced oscillations of the spring-loaded mass of the wheel machine. Note that, an accurate analytical study of such oscillations is impossible due to the practically unlimited number of degrees of freedom. This forces us to resort to a

Fig. 1 Scheme of overcoming the obstacle of rectangular shape: 1—hard wheel; 2—wheel equipped with pneumatic tyre

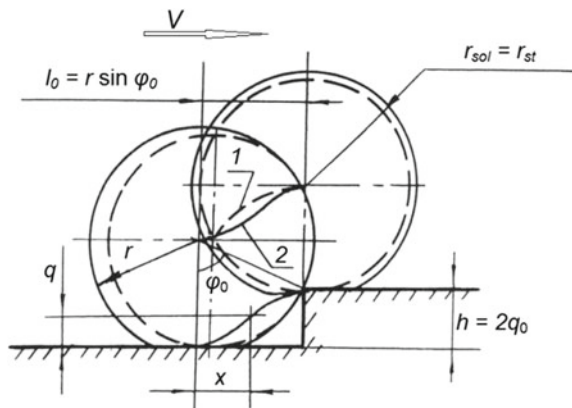
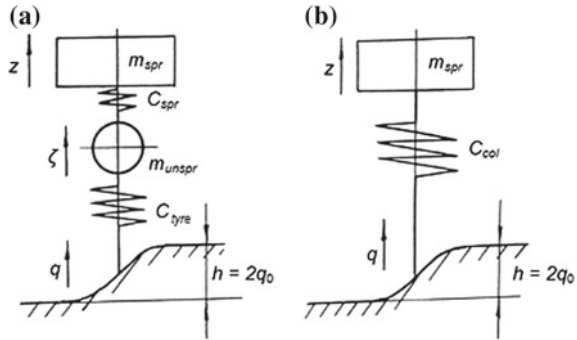


Fig. 2 Calculation scheme for the study of forced oscillations: **a** calculation scheme and **b** equivalent to the calculation scheme

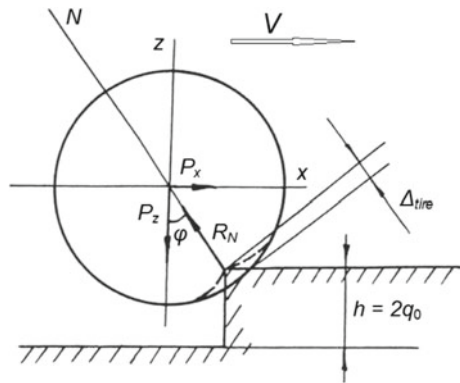


number of additional assumes: fluctuations of the front and rear wheel wheeled vehicle will be considered independent from each other; the skeleton of the wheeled vehicle—absolutely hard; resistance forces depending on the speed are not taken into account. Taking into account the accepted assumptions, we will make a calculation scheme (Fig. 2).

When drawing up the equation of motion of unsprung mass, it should be taken into account that simultaneously with the movement of unsprung mass by the value of ζ , the point of contact of the wheel with the road moves by the value of q . In the calculation scheme, the lower end of the spring replaces the pneumatic tyre (Fig. 3). In connection with the above, equation of motion of unsprung mass is as follows

$$m_{unspr}\ddot{\zeta} - C_{spr}(z - \zeta) + C_{tyre}(\zeta - q) = 0. \tag{4}$$

Fig. 3 Scheme of forces acting on the wheel when overcoming obstacles of rectangular shape: R_N —normal reaction to the wheel from the side of the obstacle wall edge; P_z —force equal to the vertical component of the normal reaction to the wheel; P_x —the pushing force required to move the wheel, equal to the force of resistance to movement or the horizontal component of the normal reaction to the wheel



The obtained Eq. (4) indicates the mutual influence of the oscillations of the unsprung and sprung masses. However, as the analysis of literary sources shows [3, 5, 7, 9, 10, 12, 14, 18, 19, 21], in many practically important cases, such mutual influence can be neglected. This is true in the study of both free and forced oscillations. Thus, both elastic elements (C_{spr} and C_{tyre}) can be replaced by one having collective stiffness C_{col}

$$C_{col} = \frac{C_{spr}C_{tyre}}{C_{spr} + C_{tyre}}. \quad (5)$$

The weight of the sprung masses should be considered equal to the weight per axis, which can be calculated from the equilibrium equations.

Thus, an oscillatory system with one degree of freedom is obtained. Forced oscillations of such a system can be described by the equation of the form

$$m_i\ddot{z} + C_{coli}(z - q) = 0. \quad (6)$$

We accept the movement of the wheeled vehicle uniform ($V = \text{const}$). The value of the abscissa of the point for which q is defined can be found: $x = Vt$. Then Eq. (2) takes the form

$$q = \frac{h}{2} \left[1 - \cos\left(\frac{2\pi \cdot V \cdot t}{2 \cdot l_0}\right) \right] \text{ or } q = \frac{h}{2} [1 - \cos(pt)], \quad (7)$$

p —frequency of action of the disturbing force: $p = \frac{2\pi \cdot V}{2 \cdot l_0}$.

Taking into account the above, the differential Eq. (6) takes the form

$$m_i\ddot{z} + C_{coli}z = C_{coli}\frac{h}{2}[1 - \cos(pt)] \text{ or } \ddot{z} + k^2z = k^2\frac{h}{2}[1 - \cos(pt)]. \quad (8)$$

As it is known, the solution of the obtained Eq. (8) can be found as the sum of the general solution of the corresponding homogeneous equation

$$\ddot{z} + k^2z = 0 \quad (9)$$

and the particular solution of Eq. (8), that is $z = z_1 + z_2$.

The general solution of the corresponding homogeneous equation can be written as

$$z_1 = C_1 \cos(kt) + C_2 \sin(kt). \quad (10)$$

The particular solution of Eq. (10) will be found in the form

$$z_2 = A + B \sin(pt) + C \cos(pt). \quad (11)$$

To find a particular solution to Eq. (8), the expression (11) must be differentiated twice

$$\dot{z} = Bp \cos(pt) - Cp \sin(pt); \quad (12)$$

$$\ddot{z} = -Bp^2 \sin(pt) - Cp^2 \cos(pt). \quad (13)$$

Substitute the obtained values of \dot{z} and \ddot{z} in Eq. (8) and determine the constants A , B and C :

$$\begin{cases} B(k^2 - p^2) = 0 \\ C(k^2 - p^2) = -k^2 \frac{h}{2} \\ A = \frac{h}{2} \end{cases} \quad (14)$$

Accept the condition: $k^2 \neq 0, p^2 \neq 0, p \neq k$, then

$$\begin{cases} B = 0 \\ C = -\frac{k^2 h}{2(k^2 - p^2)} \\ A = \frac{h}{2} \end{cases} \quad (15)$$

Taking into account (15), the solution of Eq. (8) has the form

$$z = C_1 \cos(kt) + C_2 \sin(kt) + \frac{h}{2} - \frac{k^2 h}{2(k^2 - p^2)} \cos(pt). \quad (16)$$

We define the integration constants C_1 and C_2 under initial conditions $t = 0, z = 0, \dot{z} = 0$ from the system of equations

$$\begin{cases} z = C_1 \cos(kt) + C_2 \sin(kt) + \frac{h}{2} - \frac{k^2 h}{2(k^2 - p^2)} \cos(pt) \\ \dot{z} = -C_1 k \sin(kt) + C_2 k \cos(kt) + \frac{k^2 h \cdot p}{2(k^2 - p^2)} \sin(pt) \end{cases} \text{ or } \begin{cases} 0 = C_1 + \frac{h}{2} - \frac{k^2 h}{2(k^2 - p^2)} \\ 0 = C_2 k \end{cases} \quad (17)$$

Hence

$$\begin{cases} C_1 = \frac{k^2 h}{2(k^2 - p^2)} - \frac{h}{2} \\ C_2 = 0 \end{cases} \quad (18)$$

Taking into account (18), the solution of Eq. (8) finally takes the form

$$z = \left(\frac{k^2 h}{2(k^2 - p^2)} - \frac{h}{2} \right) \cos(kt) + \frac{h}{2} - \frac{k^2 h}{2(k^2 - p^2)} \cos(pt). \tag{19}$$

Let’s determine the forces of interaction of the wheel with the support surface using the calculation scheme (Fig. 3). To do this, we project all forces on the normal coordinate axis N . As a result, we obtain the equation

$$R_N - P_x \sin \varphi - P_z \cos \varphi = 0. \tag{20}$$

Let’s take the angular velocity of the wheel is constant, then $\dot{\varphi} = \frac{\omega_0}{\Delta t}$, Δt —the length of time f which the value of the angle φ varies from φ_0 to 0: $\Delta t = \frac{h}{v}$. In this case, the current value of the angle φ can be defined as $\varphi = \dot{\varphi}t$.

In view of the above, the force of P_z is defined as

$$P_{zi} = G_{ki} + C_{npi}(q - z). \tag{21}$$

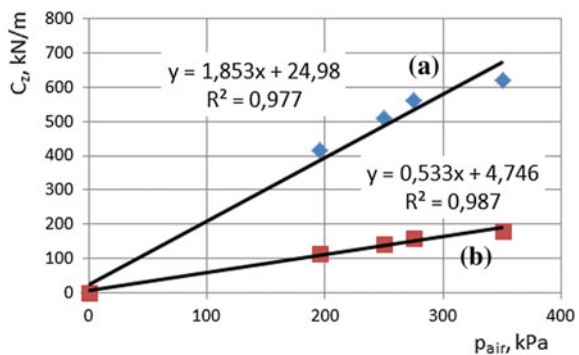
The forces of P_z and P_x are related by dependence

$$P_x = P_z \operatorname{tg} \varphi. \tag{22}$$

3 Results of Experimental Researches

In order to check the adequacy of the mathematical model, the authors conducted experimental studies. The tractor trailer 2 PTS-4 in the unit with tractor MTZ-80 was chosen as an experimental setup. Before carrying out the main experimental studies in the laboratory, the stiffness characteristics of the pneumatic tyres and springs used on this trailer were determined. The results of laboratory experimental studies are shown in Figs. 4 and 5.

Fig. 4 Dependence of the radial stiffness of the tyre 8.25–15 on air pressure: **a** when interacting with a flat reference surface and **b** when interacting with a rectangular obstacle



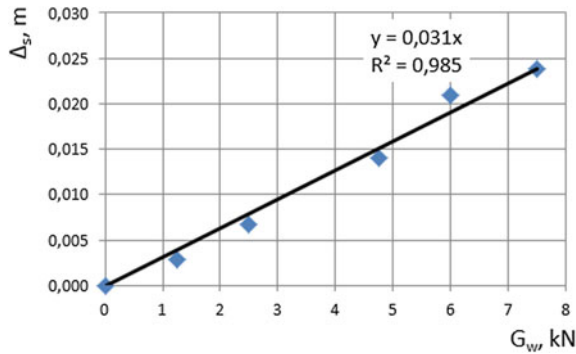


Fig. 5 Deflection of the spring depending on the load on the wheel

Table 1 Results of the experimental studies

Variable factors		Experienced data, kN	Theoretical data, kN	Absolute deviation, kN	Relative deviation, %
Speed, m/s	The height of the obstacle, m				
2.04	0.12	6.01	5.82	0.19	3.16
2.04	0.08	4.01	3.62	0.39	9.72
1.33	0.12	4.62	5.17	0.55	11.90
1.33	0.08	3.08	3.34	0.26	8.44
1.91	0.10	4.32	4.09	0.23	5.32
Average value				0.32	7.71

During the field tests, the main variable factors were chosen: the speed of the unit and the height of the obstacle. In order to ensure the safety of experimental studies, experiments were carried out with a trailer without cargo. The results of the experimental studies are presented in Table 1.

Analysis of the comparison results shows that the average relative error of the mathematical model is 7.71%. This suggests that the results of the calculation are in good agreement with the results of experimental studies, taking into account the complexity of the processes and fairly rough assumptions. It should be noted that the theoretical results are somewhat inflated at low and understated at high speeds.

4 Conclusions

Thus, the proposed mathematical model describing the rolling of a wheel equipped with a pneumatic tyre through a rectangular obstacle can be used for practical calculations. The average error of calculation of forces of interaction of a wheel with an obstacle of the rectangular form makes 7.71%.

References

1. Abdulrahim M (2006) On the dynamics of automobile drifting. SAE World Congress, SAE-2006-01-1019, Detroit, MI, 3–6 Apr 2006
2. Benzit P (1982) Transient dynamic behaviour of a vehicle by mathematical simulation. ISAE technical paper series, vol 820764, pp 1–9
3. Franken G, Glass Z (2007) Advanced state estimation and control of an autonomous ground vehicle using a priori knowledge of vehicular dynamics. Princeton University Junior Independent Project, Princeton, NJ, p 40
4. Grytsenko AV (2013) Concept of development of methods and means of diagnosis of cars. In the collection: Achievements of science-agro-industrial production LII international scientific and technical conference, pp 42–49
5. Gudcov VA, Tarnovsky VN, Ustarov RM (2010) Approaches to choosing a complex characteristic of tyre loading. *Int Polym Sci Technol* 37(6):41–42
6. Henry J, Meyer W (1989) The simulation of tyre traction on wet pavements. *VDS Berichte* 369:121–128
7. Abdel Hady MBA, Crolla DA (1992) Active suspension control algorithms for a four-wheel vehicle model. *Int J Veh Des* 13(2):144–158
8. Nosov VP, Osipov IA, Volkov AB (2015) Analysis of the influence of the initial road surface longitudinal flatness on the intensity of its deterioration 2:235–246
9. Olson BJ (2001) Nonlinear dynamics of longitudinal ground vehicle traction. M.S. thesis defense, Michigan State University, p 53
10. Olson BJ, Shaw SW, Stepan G (2004) Nonlinear dynamics of longitudinal vehicle traction. In: Proceedings of the 9-th mini-conference on vehicle system dynamics, identifications and anomalies, Budapest, pp 537–545
11. Plaksin AM, Gritsenko AV (2013) Constructive relationship improving mobile power tools with the methods of diagnosing their technical condition. *Fundam Res* 10–15:3373–3377
12. Pushkin AV (2004) Simulations of the effects of the micro-profile of roads on the movable ground object. *Tula Instrum Control* 2:81–85
13. Segel L (1994) Tire traction on dry, uncontaminated surfaces. In: *The physics of tire traction: theory and experiment*. New York, London, pp 65–98
14. Short M, Pont MJ, Huang Q (2004) Simulation of vehicle longitudinal dynamic. Technical report ESL 04-01, Embedded Systems Laboratory, University of Leicester, p 18
15. Sikachenko VM, Akhmetov SA, Timakov SY (2006) Methods of determining the statistical characteristics of the micro-profile of road surface. The problems of design, construction and operation of transportation facilities. *SibARI*, Omsk, vol 1, pp 78–86
16. Startcev AV (1997) Results of experimental studies of the micro-profile of roads. *Bull ChSAU* 22:32–35
17. Startcev AV (2001) Justification of the possibility of using the linear characteristics of tyres in the study of the movement of wheeled vehicles with speeds up to 10 m/s. *Bull ChSAU* 34:93–95
18. Verma MK, Gillespie TD (1989) Roll dynamics of commercial vehicles. *Veh Syst Dyn* 9(1): 1–17
19. Wong JY (2001) *Theory of ground vehicles*, 3rd edn. Wiley, New York, p 488
20. Woods E (1972) *Pneumatic tire design*. Cambridge, pp 117–132
21. Wang Z, Reecet A (1984) The performance of free rolling rigid and flexible wheels on sand. *J Terramech* 347–360

Opportunities for Using Spline Method to Calculate Orthotropic Plate Under Bending Conditions



V. S. Zhernakov, V. P. Pavlov and V. M. Kudoyarova

Abstract Composite materials (CM) along with metals at present are widely used. They are characterized by the anisotropy of the mechanical properties, so in some cases CM can be considered as orthotropic materials. Orthotropic materials are characterized by the presence of three mutually orthogonal planes with symmetry properties in each elementary volume. For example, such materials can consist of a plastic binder (matrix) reinforced with fibers, possessing high strength, rigidity, etc. The combination of heterogeneous components leads to the creation of a new material with quantitatively and qualitatively different properties from the original properties of its components. This paper develops a new numerical method based on two-dimensional spline functions of degree 5 defect 1, which allows obtaining the calculation results of the stress-strain state of orthotropic plates with high accuracy. The paper presents a method for constructing a discrete analogue of the differential equation for bending of an orthotropic plate, forms a number of exact solutions for test problems, solves test problems using the numerical spline method, compares numerical solutions with exact ones, and presents quantitative accuracy estimates of the proposed spline method.

Keywords Composite materials · Orthotropic plate · Mathematical modeling · Numerical methods · Splines

1 Introduction

There are many constructions that can be considered as plates. The differential equations are used in partial derivatives of two-fourth order variables the stress-strain state description of plates. To this should be added that CM along with metals at present are widely used, which are characterized by the anisotropy of the mechanical

V. S. Zhernakov · V. P. Pavlov · V. M. Kudoyarova (✉)
Ufa State Aviation Technical University, 12, K. Marx St.,
Ufa 450000, Russia
e-mail: Kudoyarova@inbox.ru

properties, so in some cases CM can be considered as orthotropic materials. All this leads to the need having any methods for calculating of orthotropic plates. The main method for calculating such structures at present is the finite element method (FEM), implemented in modern software such as ANSYS, SolidWorks, etc.

The main prerequisite for the development of any business field is competition; therefore, the development of alternative methods is also needed, one of which is the spline method, which possibilities are presented in this article.

Many products made of CM can be considered as orthotropic plates and the equations from [1, 2] can be used to calculate their stress-strain state. But at the same time, it is necessary to determine the stiffness characteristics of the composite plate in accordance with its reinforcement scheme. This can be performed using the methods described in [3–5].

This paper develops a new numerical method based on two-dimensional spline functions of degree 5 defect 1, which allows to obtain the calculation results of the stress-strain state of orthotropic plates with high accuracy. This method is based on one-dimensional spline functions, which effectiveness had been studied in detail at solving various differential equations for deformed and thermal state of solids [6–20].

2 Problem Definition

A rectangular plate of orthotropic material with sides parallel to the axes X and Y , see Fig. 1, is under consideration. The plate has equal thickness h and dimensions along the axes X and Y equal to l_x, l_y in Fig. 1.

3 Basic Relations for a Two-Dimensional Spline Function of Degree 5 Defect 1

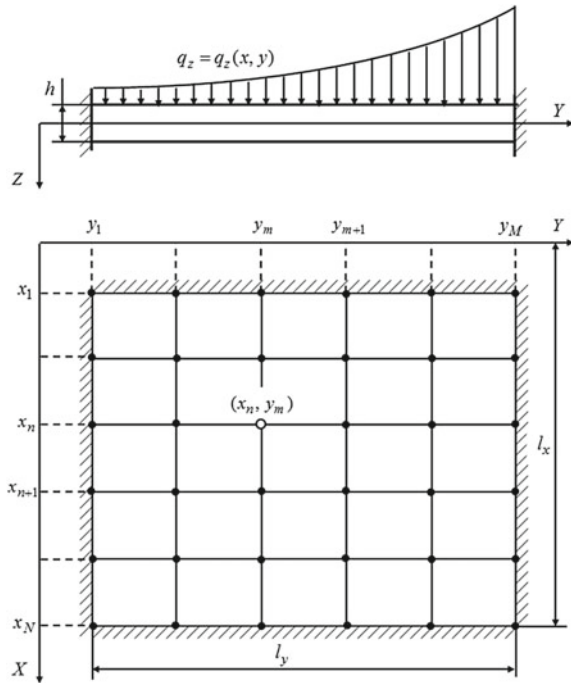
For constructing a two-dimensional spline function, a rectangular area $\Omega = [a, b] \times [c, d]$ is considered where a rectangular mesh of lines $\Delta = \Delta_x \times \Delta_y$ is formed:

$$\begin{cases} \Delta_x : a = x_1 < x_2 < \dots < x_N = b, \\ \Delta_y : c = y_1 < y_2 < \dots < y_M = d. \end{cases} \quad (1)$$

The two-dimensional spline $W_{5,5,1,1}(x, y)$ is defined by the expression

$$\begin{cases} W_{5,5,1,1}(x, y) = \sum_{r=0}^5 \sum_{s=0}^5 a_{n,m}^{(i,j)} (x - x_n)^r (y - y_m)^s, \\ x \in [x_n, x_{n+1}], \quad n = \overline{1, N-1}, \\ y \in [y_m, y_{m+1}], \quad m = \overline{1, M-1}, \end{cases} \quad (2)$$

Fig. 1 Rectangular plate of orthotropic material



and has continuous derivatives up to the fourth order inclusive in the x, y coordinates.

Spline derivatives in nodes x, y are defined by the expressions:

$$\begin{cases} W_{n,m}^{(\alpha,\beta)} = \frac{\partial^{(\alpha+\beta)} W_{5,5,1,1}(x_n, y_m)}{\partial x^\alpha \partial y^\beta} \\ n = \overline{1, N}, \quad m = \overline{1, M}, \quad \alpha = \overline{0, 5}, \quad \beta = \overline{0, 5}. \end{cases} \quad (3)$$

The matrix $Q = \|Q_{i,j}, i = \overline{1, N+4}, j = \overline{1, M+4}\|$ with components $Q_{i,j}$ are shown in Table 1 is selected as the basis of the spline.

This spline is determined by independent parameters $(N+4)(M+4)$. It is necessary to build a system of the same number of equations to determine the spline.

The spline of degree 5 defect 1 is a fifth-degree polynomial on each segment $[x_n, x_{n+1}], n = \overline{1, N-1}$ that is formed on the mesh $\Delta_x : a = x_1 < x_2 < \dots < x_N = b$ [16]:

$$W_{5,1}^{(x)} = \sum_{r=0}^5 a_n^{(i)} (x - x_n)^r, \quad x \in [x_n, x_{n+1}], n = \overline{1, N-1}. \quad (4)$$



Table 1 Matrix components

$W_{1,1}^{(0,0)}$	$W_{1,1}^{(0,1)}$	$W_{1,1}^{(0,2)}$	$W_{1,1}^{(0,3)}$	$W_{1,1}^{(0,4)}$...	$W_{1,m}^{(0,4)}$...	$W_{1,M}^{(0,4)}$
$W_{1,1}^{(1,0)}$	$W_{1,1}^{(1,1)}$	$W_{1,1}^{(1,2)}$	$W_{1,1}^{(1,3)}$	$W_{1,1}^{(1,4)}$...	$W_{1,m}^{(1,4)}$...	$W_{1,M}^{(1,4)}$
$W_{1,1}^{(2,0)}$	$W_{1,1}^{(2,1)}$	$W_{1,1}^{(2,2)}$	$W_{1,1}^{(2,3)}$	$W_{1,1}^{(2,4)}$...	$W_{1,m}^{(2,4)}$...	$W_{1,M}^{(2,4)}$
$W_{1,1}^{(3,0)}$	$W_{1,1}^{(3,1)}$	$W_{1,1}^{(3,2)}$	$W_{1,1}^{(3,3)}$	$W_{1,1}^{(3,4)}$...	$W_{1,m}^{(3,4)}$...	$W_{1,M}^{(3,4)}$
$W_{1,1}^{(4,0)}$	$W_{1,1}^{(4,1)}$	$W_{1,1}^{(4,2)}$	$W_{1,1}^{(4,3)}$	$W_{1,1}^{(4,4)}$...	$W_{1,m}^{(4,4)}$...	$W_{1,M}^{(4,4)}$
...
$W_{n,1}^{(4,0)}$	$W_{n,1}^{(4,1)}$	$W_{n,1}^{(4,2)}$	$W_{n,1}^{(4,3)}$	$W_{n,1}^{(4,4)}$...	$W_{n,m}^{(4,4)}$...	$W_{n,M}^{(4,4)}$
...
$W_{N,1}^{(4,0)}$	$W_{N,1}^{(4,1)}$	$W_{N,1}^{(4,2)}$	$W_{N,1}^{(4,3)}$	$W_{N,1}^{(4,4)}$...	$W_{N,m}^{(4,4)}$...	$W_{N,M}^{(4,4)}$

Let us introduce the notation for derivatives of spline functions $W_{5,1}^{(x)}(x)$:

$$W_{5,1}^{(x)(s)}(x) = \frac{d^s W_{5,1}^{(x)}(x)}{dx^s} = \sum_{r=s}^5 \frac{r!}{(r-s)!} a_r^{(i)}(x-x_n)^{r-s}, \quad s = \overline{0,5}. \tag{5}$$

The vector of parameters $Q_x = (q_i^{(x)}, i = \overline{1, N+4})^T$ uniquely determines the spline $W_{5,1}^{(x)}(x)$, where

$$q_i^{(x)} = W_{5,1}^{(x)(i-1)}(x_1), \quad i = \overline{1,4}; \quad q_{n+4}^{(x)} = W_{5,1}^{(x)(4)}(x_n), \quad n = \overline{1, N}. \tag{6}$$

In the mesh nodes Δ_x , the values of the spline function $W_{5,1}^{(x)}(x)$ and its derivatives up to the fourth order inclusive are considered:

$$f_n^{(x)(s)} = W_{5,1}^{(x)(s)}(x_i), \quad n = \overline{1, N}, \quad s = \overline{0,4}. \tag{7}$$

Column vectors are formed from them:

$$V_{dsf}^{(x)} = (f_n^{(x)(s)}, \quad n = \overline{1, N})^T, \quad s = \overline{0,4}. \tag{8}$$

The vectors of the spline-function nodal values $W_{5,1}^{(x)}(x)$ and its derivatives are determined according to [16] by matrix expressions:

$$V_{dsf}^{(x)} = M_{dsf}^{(x)} Q_x, \quad s = \overline{0,4}, \tag{9}$$



where $M_{dsf}^{(x)}$, $s = \overline{0, 4}$ —rectangular matrices of size $N \times (N + 4)$,

$$M_{dsf}^{(x)} = \left\| M_{n,i}^{(x)(dsf)}, \quad n = \overline{1, N}, \quad i = \overline{1, N + 4} \right\|, \quad s = \overline{0, 4}, \quad (10)$$

formed by the method described in [16].

In a similar way, the spline $W_{5,1}^{(y)}(y)$ is defined on the partition $\Delta_y : c = y_1 < y_2 < \dots < y_M = d$, and then the matrix relation is written as a

$$V_{drf}^{(y)} = M_{dsf}^{(y)} Q_y, \quad r = \overline{0, 4}, \quad (11)$$

between vector Q_y of spline parameters $W_{5,1}^{(y)}(y)$ with the vector $V_{drf}^{(y)}$ of the derivatives of this spline along the coordinate y . There are rectangular matrices of size $M \times (M + 4)$ here

$$M_{drf}^{(y)} = \left\| M_{m,j}^{(y)(drf)}, \quad m = \overline{1, M}, \quad j = \overline{1, M + 4} \right\|, \quad r = \overline{0, 4}, \quad (12)$$

also formed by the method described in [16].

4 Discrete Analogue of the Equilibrium Equation of a Plate in Bending

The bending of an orthotropic plate is described by the differential equilibrium equation [2]:

$$D_x \frac{\partial^4 w}{\partial x^4} + 2H \frac{\partial^4 w}{\partial x^2 \partial y^2} + D_y \frac{\partial^4 w}{\partial y^4} = q_z, \quad (13)$$

where $w = w(x, y)$ —the function of the transverse displacement of the plate points, q_z —the transverse distributed load acting on the plate; D_x , D_y , H —plate stiffness coefficients.

When constructing a discrete analogue of the equilibrium Eq. (13), let us implement the spline-collocation method, in which the exact load q_T equals to its numerical values, obtained on the basis of the spline function in considered mesh nodes:

$$D_x W_{n,m}^{(4,0)} + 2HW_{n,m}^{(2,2)} + D_y W_{n,m}^{(0,4)} = q_T(x_n, y_m), \quad n = \overline{1, N}, m = \overline{1, M}. \quad (14)$$

The external calculated load at each nodal point $q_{n,m} = q(x_n, y_m)$ is expressed through the matrix components Q at the forming a system of discrete equilibrium Eq. (14).

To do this, the expression for the spline derivative $W_{(n,m),(i,j)}^{(s,r)}$ in the node (x_n, y_m) , taking into account only the component $Q_{i,j}$ of matrix Q , is written as:

$$W_{(n,m),(i,j)}^{(s,r)} = M_{n,i}^{(x)(dsf)} M_{m,j}^{(y)(drf)} Q_{i,j}, \quad s = \overline{0,4}, r = \overline{0,4}. \tag{15}$$

On the base of Eq. (14), the contribution $q_{n,m}^{i,j}$ from the component $Q_{i,j}$ of vector Q to the load $q_{n,m}$ for the node (x_n, y_m) is determined:

$$\begin{aligned} q_{n,m}^{i,j} &= D_x W_{n,m}^{(4,0)} + 2HW_{n,m}^{(2,2)} + D_y W_{n,m}^{(0,4)} = a_{n,m}^{i,j} Q_{i,j} \\ &= \left(D_x W_{(n,m),(i,j)}^{(4,0)} + 2HW_{(n,m),(i,j)}^{(2,2)} + D_y W_{(n,m),(i,j)}^{(0,4)} \right) Q_{i,j}. \end{aligned} \tag{16}$$

On the basis of expressions (16), a complete system is formed of $(N + 4)(M + 4)$ linear algebraic equations, having the form:

$$AP = B. \tag{17}$$

In (17), a vector $P = (P_k, k = \overline{1, (N + 4)(M + 4)})^T$ is used, which is formed from the matrix Q components, where

$$P_k = Q_{n,m}, \quad k = \overline{1, [(j - 1)(N + 4) + i]}, \quad i = \overline{1, (N + 4)}, \quad m = \overline{1, (M + 4)}. \tag{18}$$

The system of Eq. (17) contains NM equations based on the equilibrium Eq. (14).

The components of the first rows NM of matrix A are determined taking into account (16) by the formula:

$$\begin{aligned} A_{k,l} &= a_{n,m}^{i,j}, \quad k = (m - 1)(N + 4) + n, \quad l = (j - 1)(N + 4) + i, \\ n &= \overline{1, N}, \quad m = \overline{1, M}, \quad i = \overline{1, (N + 4)}, \quad j = \overline{1, (M + 4)}. \end{aligned} \tag{19}$$

The first components NM of the vector B are determined by the right side of the equilibrium Eq. (14):

$$B_k = q_T(x_n, y_m), \quad k = (m - 1)N + n, \quad n = \overline{1, N}, \quad m = \overline{1, M}. \tag{20}$$

The remaining $(N + 4)(M + 4) - NM = 4N + 4M + 16$ equations of system (17) is determined by the boundary conditions, which are also written based on expressions of the form (15).



5 The Test Problem of Bending a Rectangular Plate Made of Orthotropic Material Clamped Along the Contour

In accordance with Fig. 1, let us take into consideration the functions at constructing a solution to Eq. (13):

$$\begin{cases} \psi = \psi(x) = \frac{x^{k+4} - (k+2)l_y^{k+1}x^3 + (k+1)l_y^{k+2}x^2}{(k+1)(k+2)(k+3)(k+4)}, \\ \chi = \chi(y) = \frac{y^{k+4} - (k+2)l_x^{k+1}y^3 + (k+1)l_x^{k+2}y^2}{(k+1)(k+2)(k+3)(k+4)}, \quad k = 0, 1, \dots \end{cases} \quad (21)$$

Function of displacement is constructed on the base of (21)

$$w_T(x, y) = w_0\psi(x)\chi(y), \quad w_0 = \text{const}, \quad (22)$$

where w_0 —a constant parameter.

Solutions (22) and (21) are exact for a rectangular plate clamped along the contour with boundary conditions:

$$\begin{cases} w = \partial w / \partial x = 0 \text{ at } x = 0 \text{ and } x = l_x, \\ w = \partial w / \partial y = 0 \text{ at } y = 0 \text{ and } y = l_y. \end{cases} \quad (23)$$

Determine the partial derivatives of function $w_T(x, y)$ by the coordinate x with order r and by the coordinate y with order s :

$$\frac{\partial^{r+s} w_T}{\partial x^r \partial y^s} = w_0 \frac{d^r \psi(x)}{dx^r} \frac{d^s \chi(y)}{dy^s}, \quad r = 2, 3, 4, \quad s = 2, 3, 4. \quad (24)$$

The expression for the external load $q_{zT} = q_{zT}(x, y)$ is obtained by substituting (24) into (13), at which differential Eq. (13) has the exact solution (22) for a plate with clamped edges.

Series of exact solutions of Eq. (13) for performing test checks is obtained by varying the values D_x, D_y, H, k and w_0 .

6 Results of Analysis

The test problem was solved with the plate dimensions $l_x = l_y = 1$ m and the stiffness $D_x = 2 \times 10^3$ N m, $D_x = 1 \times 10^3$ N m, $D_x = 1.5 \times 10^3$ N m of a number of index values k in expressions (21).

The method capabilities were estimated by relative calculation errors $\delta^{(r,s)}$, $r, s = 0, 1, 2$ for the displacement function and its derivatives:

$$\delta^{(r,s)} = \max_{\substack{n = 0, 1, \dots, N \\ m = 0, 1, \dots, M}} \left| \frac{\frac{\partial^{r+s} w_{n,m}}{\partial x^r \partial y^s} - \frac{\partial^{r+s} w_{T,n,m}}{\partial x^r \partial y^s}}{\left| \frac{\partial^{r+s} w_T}{\partial x^r \partial y^s} \right|_{\max}} \right|, \quad r, s = 0, 1, 2, \quad (25)$$

where $\partial^{r+s} w_{T,n,m} / \partial x^r \partial y^s$ and $\partial^{r+s} w_{n,m} / \partial x^r \partial y^s$ are the exact and calculated values of the derivative of orders r and s of the function w in the considered node (x_n, y_m) .

In Fig. 2, a–e decimal logarithms of the absolute values of the $w = w(x, y)$ displacement function relative errors and its derivatives up to the second order are shown.

It can be seen from Fig. 2a–e that at $k = 0$ and $k = 1$ a small number of nodes $N = M = 5$ the relative error of calculations does not exceed 1×10^{-12} , which indicates the correctness of the software method implementation. Further, with the same values $k = 0$ and $k = 1$, the error increases monotonically and with $N = M = 101$ an error for the second derivatives increases up to 1×10^{-5} . The reason for this is the error of arithmetic calculations at solving a system of equations from $(N + 4)(M + 4) = 105 \times 105 = 11,025$ equations.

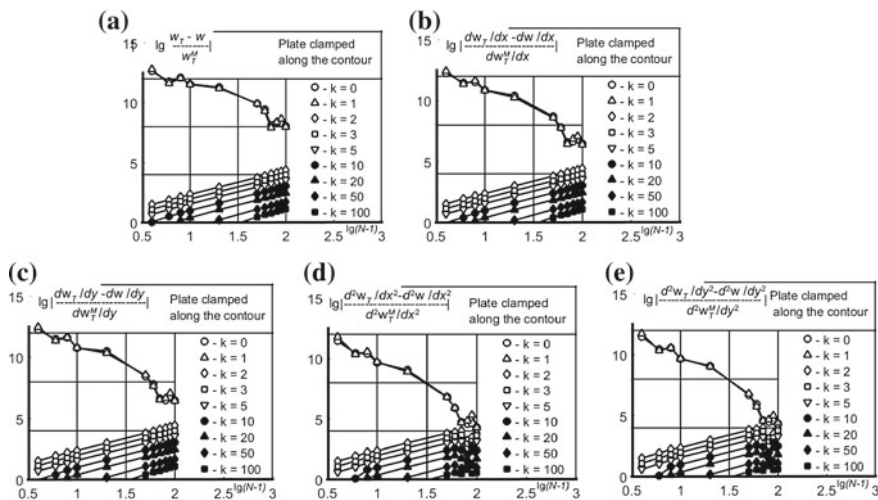


Fig. 2 a Decimal logarithms of the absolute values of the $w = w(x, y)$ displacement function relative errors; b decimal logarithms of derivatives of the displacement function relative errors along X-axis; c decimal logarithms of derivatives of the displacement function relative errors along Y-axis; d decimal logarithms of second order derivatives of the displacement function relative errors along X-axis; e decimal logarithms of derivatives of the displacement function relative errors along Y-axis



As can be seen from Fig. 2a–e: at $k > 0$, the relative error monotonously decreases with the second order of convergence under node number increasing and the upward and downward graphs of error begin to converge in the region $N = 201$.

This particularly leads to the conclusion that it does not make much sense to further increase the node number N and M along the coordinate axes for determine the second and mixed derivatives, which determine the stress state of the plate.

7 Conclusion

This paper has proposed the method of two-dimensional splines of degree 5 defect 1 for the analysis of the stress-strain state of orthotropic plates and its accuracy has been evaluated.

The algorithm for constructing a discrete analogue of the differential equilibrium equation for an orthotropic rectangular plate has been given.

The paper has shown the method, implemented according to the collocation method scheme, has a second order of convergence, which allows obtaining results for fairly complex external load distribution functions with a relative error not higher than 1×10^{-4} , which is quite enough for engineering calculations of many structures.

Acknowledgements The authors acknowledge receiving support base part of funded research program of Russian Foundation for Basic Research (RFBR) and Government of the Republic of Bashkortostan in the framework of a scientific project №_17-48-020824_p_a.

References

1. Lekhnitskiy SG (1977) *Teoriya uprugosti anizotropnogo tela* (Theory of elasticity of an anisotropic body). Nauka, Moscow
2. Timoshenko SP, Voynovskiy-Kriger S (1966) *Plastinki i obolochki* (Plates and shells). Nauka, Moscow
3. Pavlov VP, Kudoyarova VM, Philippov AA (2017) Simulation of boron and carbon fiber composite characteristics of the elasticity. In: MATEC web of conferences, vol 129, pp 1–4. <https://doi.org/10.1051/mateconf/201712902009>
4. Pavlov VP, Kudoyarova VM, Philippov AA (2018) Modeling of the elastic characteristics of a longfiber reinforced composite with an arbitrary orientation of the reinforcing fibers. In: MATEC web of conferences, vol 224, pp 1–7. <https://doi.org/10.1051/mateconf/201822403006>
5. Philippov AA, Pavlov VP, Nikitin SN (2016) Vychislenie ehffektivnykh uprugih harakteristik kompozitsionnogo materiala metodom asimptoticheskogo osredneniya (The method of asymptotic homogenization is applied to the numerical determination of the effective elastic characteristics of the composite material in this article). *Vestnik UGATU* 20–3(73):49–57
6. Kudoyarova VM, Pavlov VP (2016) The spline method for the solution of the transient heat conduction problem with nonlinear initial and boundary conditions for a plate. *Proc Eng* 150:1419–1426. <https://doi.org/10.1016/j.proeng.2017.10.541>

7. Kudoyarova V, Pavlov V (2015) Refining of numerical solution for nonlinear transient heat conduction in a plate made of polymer composite material. *Int J Appl Eng Res* 10–18:39466–39470
8. Smirnov VI (1956) *Kurs vysshej matematiki* (Course of higher mathematics). Gosudarstvennoe izdatel'stvo tekhniko-teoreticheskoy literatury, Moscow
9. Pavlov VP, Kudoyarova VM (2017) Spline based numerical method for heat conduction nonlinear problems solution. *Proc Eng* 206:704–709. <https://doi.org/10.1016/j.proeng.2017.10.541>
10. Zhernakov VS, Pavlov VP, Kudoyarova VM (2017) The enhanced spline-method for numerical results of natural frequencies of beams. *Proc Eng* 176:438–450
11. Zhernakov VS, Pavlov VP, Kudoyarova VM (2017) Spline-method for numerical calculation of natural-vibration frequency of beam with variable cross-section. *Proc Eng* 206:710–715. <https://doi.org/10.1016/j.proeng.2017.10.542>
12. Abdrakhmanova AA, Pavlov VP (2007) Matematicheskoe modelirovanie napryazhenno-deformirovannogo sostoyaniya stekloplastikovogo sterzhnya pri razlichnyh zhestkostyah opor (A fiberglass core's intense condition's mathematical modelling at various rigidities of supports) *Vestnik UGATU* 9–5(23):87–92
13. Pavlov VP (2016) Analiz spektra chastot sobstvennyh kolebaniy sterzhnya metodom splajnov (Analysis of the spectrum of frequencies of own fluctuations of a rod by the method of splines). *Vestnik UGATU* 20–4(74):16–22
14. Pavlov VP (2016) Integral'nyy metod splajnov dlya rascheta chastot sobstvennyh kolebaniy i ego vozmozhnosti (The integral method of splines for calculation of the natural frequencies of the rod and its capabilities). *Vestnik UGATU* 21–4(78):41–49
15. Pavlov VP (2016) Metod splajnov v raschetah sterzhnej na ustojchivost' (The method of splines in the calculation of the studs for stability). *Vestnik UGATU* 20–4(74):45–53
16. Pavlov VP (2003) Metod splajnov i drugie chislennye metody resheniya odnomernykh zadach mekhaniki deformiruemykh tverdykh tel (Method of spline and other numerical methods for solving one-dimensional problems of mechanics deformable solids). UGATU, Ufa
17. Pavlov VP (2017) Opisanie geometrii naruzhnoy poverhnosti pera rabochey lopatki oseвого kompressora GTD dvumernymi splajnymi stepeni 2 defekta 1 (Description of the geometry of the outer surface the pen of the working blades of the axial compressor GTE twodimensional splines of degree 2 defect 1). *Vestnik UGATU* 21–4(78):57–68
18. Pavlov VP (2017) Poperechnye kolebaniya sterzhnya s peremennym poperechnym secheniem i vychislenie ego sobstvennyh chastot metodom splajnov (Transverse vibrations of a rod with variable cross sections and calculation of its eigenfrequencies by the method of splines). *Vestnik UGATU* 21–2(76):3–16
19. Pavlov VP, Abdrakhmanova AA, Abdrakhmanova RP (2013) Zadacha rascheta sterzhnej odnomernym splajnom pyatoy stepeni defekta 2 (The problem of rods calculation by the spline of the fifth degree of defect 2). *Math Notes YSU* 20–1:50–59
20. Kudoyarova VM, Pavlov VP (2018) Analiz temperaturnogo polya v tverdom tele metodom splajnov (Spline-functions method for solving thermal conductivity problems). *Vestnik UGATU* 22–2(80):10–17

Experiments to Find the Rolling Resistance of Non-pneumatic Tires Car Wheels



V. V. Mazur

Abstract Simplicity and high efficiency of a wheeled mover as a mechanism for converting rotational motion into a translatory one have conditioned its wide application in overland machines including motor vehicles. However, a wheel with a non-pneumatic tire has a sufficient drawback lying in termination of a wheeled machine movement at the excess air pressure loss. Moreover, the loss of excess air pressure in a pneumatic tire of traditional design at high speed of movement of a motor vehicle can lead to a traffic accident with heavy consequences. This problem is particularly acute for military purpose motor vehicles as under conditions of combat actions a motionless vehicle becomes a convenient target for grenade launchers and aimed fire of small arms which to a considerable degree influences the chances of military servicemen to stay alive and fulfill the operational mission. The stop of a motor vehicle to change a wheel on a heavy traffic roadway or roadside also poses a threat. These reasons determine the necessity of both well-known design improvements and search for the new wheeled mover design solutions to enhance a motor vehicle safety, the use of wheels with non-pneumatic tires of elastic polymeric materials being one of them. Safety enhancement by means of non-pneumatic tire use along with keeping the high performance of wheeled machine operational properties is an important scientific and technical task that determines the research urgency.

Keywords Polyurethane tires • Rolling resistance coefficient • Runout • Moment of inertia • Stand with running drums • Characteristic of normal rigidity

V. V. Mazur (✉)

Bratsk State University, Makarenko, 40, Bratsk 665709, Russia

e-mail: mazurv@yandex.ru

© Springer Nature Switzerland AG 2020

A. A. Radionov et al. (eds.), *Proceedings of the 5th International Conference on Industrial Engineering (ICIE 2019)*, Lecture Notes in Mechanical Engineering,

https://doi.org/10.1007/978-3-030-22041-9_69

1 Relevance

The irremovable shortcomings of pneumatic tires are associated with the loss of excess air pressure and force to look for fundamentally new design solutions for wheeled movers that can improve the safety of civilian vehicles and the survivability of wheeled armored vehicles. One of these solutions is wheels with airless tires made of elastic polymeric materials.

2 Literature Review

Non-pneumatic tires (NPT) of elastic polymeric materials were first applied in 1991 to wheeled armored machinery by South African company Allthane Technologies International SA (Pty) Ltd. A significant contribution to creation and improvement of non-pneumatic tires was made by such companies as Uniroyal [1], Michelin [2–4] and Resilient Technologies [5] in common with the University of Wisconsin-Madison's Polymer Engineering Center, Polaris [6], Yokohama [7], Bridgestone [8], Hankook [9], Toyo [10], Boeing [11], Amerityre [12], Sumitomo [13], Britek [14] and others. Russia's research on non-pneumatic wheeled movers is conducted by Vescom Research Centre for Tire Industry LLC [15], Bauman Moscow State Technical University [16], South Ural State University, Alekseev Nizhny Novgorod State Technical University and others.

3 Formulation of the Problem

However, the recent interest of domestic and foreign tire companies in airless tires has not allowed to accumulate a sufficient number of published scientific papers, allowing to judge the optimality of structures.

The Department of Automobile Transport (Department of Machine Building and Transport since May 2018) at Bratsk State University has experience in development and research on automobile non-pneumatic tires of elastic polymeric materials. The main task is to create an airless tire made of elastic polyurethane with output parameters and characteristics that are not inferior to pneumatic tires of similar size and carrying capacity.

4 Design of Full-Scale Models of Wheels with Non-pneumatic Tires

The implemented design analysis and patent search allowed to find new technical solutions aimed at the perfection of automobile non-pneumatic tire design and, enjoying the financial backing of Ministry of Education and Science of Russian Federation, manufacture full-scale models of wheels with automobile non-pneumatic tires, one of which is shown in Fig. 1.

Creation of the models was financially supported by the Ministry of Education and Science of the Russian Federation under the Directive on Creating Energy-Efficient Engines and Propulsion Devices for Vehicles, which is part of the Federal Target Program Scientists and Faculty in Innovative Russia (State Contract No. 14.740.11.0319 dd. September 17, 2010 to November 26, 2012).

5 Methods and Results of Tests of Full-Scale Models of Wheels with Non-pneumatic Tires

The program of on-road and laboratory experiments evaluated the carrying capacity, the elastic and damping properties of the NPT wheel models [17, 18] as well as their force heterogeneity and ability to self-clean while rolling [19].

Figure 2 shows the normal rigidity of an NPT model, the elastic properties and the carrying capacity whereof is the closest to same-size pneumatic tires. However, this model has damping, which is 2.98 times higher than that of pneumatic tires.

Further experimental studies are to find the parameters and characteristics of NPT models that may affect the car traction and speed parameters, such as the rolling resistance.

Fig. 1 Automobile wheel with non-pneumatic tire of elastic polymeric materials: (1) flexible spokes; (2) standard 5JX13H2 disk wheel with a deep edge-free band; (3) supporting ring; (4) protector; (5) fitting ring; (6) mounting ring

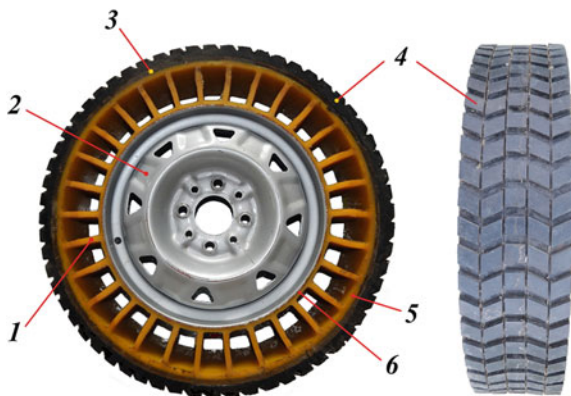
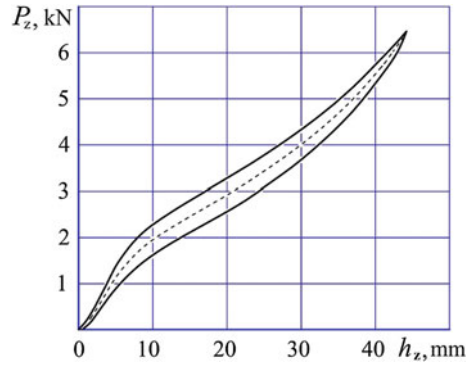


Fig. 2 NPT normal rigidity



Pursuant to GOST 17697–72 *Cars. Wheel rolling. Terms and definitions*, rolling losses may be evaluated by the wheel rolling resistance power N_f , the rolling resistance force P_f , and the wheel rolling resistance factor f .

NPT wheel model parameters:

1. Prepolymer of flexible spokes, protector, fitting and supporting rings	SUREL TF-228
2. Prepolymer of a supporting ring	SUREL TF-682
3. Number of flexible spokes	30
4. Thickness of flexible spokes, mm	8
5. Length of flexible spokes, mm	55
6. Width of tire profile, mm	120
7. Height of tire profile, mm	100
8. Load-free ring radius, mm	265
9. Thickness of supporting ring, mm	8
10. Height of protector, mm	25
including height of protector pattern, mm	5
11. Mass, kg	14
12. Normal rigidity coefficient, kN/m	134
13. Inelastic resistance factor, Ns/m	936

The runout method is one of the best-known and most popular methods for experimental determination of rolling resistance; it can be used both on-road and in a laboratory setting.

The technique of using this method in a laboratory setting to find the rolling resistance experimentally is described in GOST R 52102–2003 *Pneumatic tires. Finding the rolling resistance by the runout method*.

The Department of Machine Building and Transport has a test stand equipped with Cartec LPS 2020 4WD dynamometers for measuring the power at the drive wheels. The specifications of Cartec LPS 2020 4WD meet the requirements to test stands for finding the rolling resistance of car wheels by the runout method;

the stand can be used to carry out tests at speeds of up to 300 km/h with a weight load of up to 3.5 tons per axle.

It must, however, be borne in mind that the rolling resistance of an elastic-tire wheel will differ considerably depending on whether the test setting is a dual dynamometer, a single dynamometer or a hard-paved flat road; in the first case, it can be several times higher [20].

The rolling resistance of the NPT models we had made was determined by the Cartec LPS 2020 4WD stand dynamometers (see Fig. 3) in an acceleration-to-runout mode.

Wheel rolling resistance force was found by the dynamometers as follows:

$$P_f = \left(\sum J_w + \frac{r_d r_k \sum J_s}{r_s^2} \right) \frac{dV_a}{r_d r_k dt} - \frac{M_t}{r_d}, \quad (1)$$

where $\sum J_w$ is the total wheel moment of inertia; $\sum J_s$ is the total moment of inertia of the rotating test-stand bodies; r_d is the dynamic wheel radius; r_k is the kinematic (rolling) wheel radius; r_s is the stand dynamometer radius; dV_a is the speed change; dt is the time change; M_t is drivetrain friction torque.

The car speed by the dynamometers was calculated as

$$V_a(t) = \omega_s(t)r_s \text{ or } V_a(t) = 0.1047n_s(t)r_s, \quad (2)$$

where ω_s is the angular rotation speed of power-stand dynamometers; n_s is the dynamometer rotation speed, rpm.

During the experiments, the wheels of the front-wheel drive VAZ-2115 were accelerated by the dynamometers to 100 km/h; the speed was controlled by the stand instrumentation. The installation was switched to the runout mode by switching the gearbox from the clutch to the neutral gear. The dependence of the stand dynamometer rotation speed on the runout time and, partially, on the acceleration $n_s = n_s(t)$ (Fig. 4) was recorded by a hardware set consisting of a ZET

Fig. 3 VAZ-2115 with non-pneumatic tires on Cartec LPS 2020 4WD dynamometers



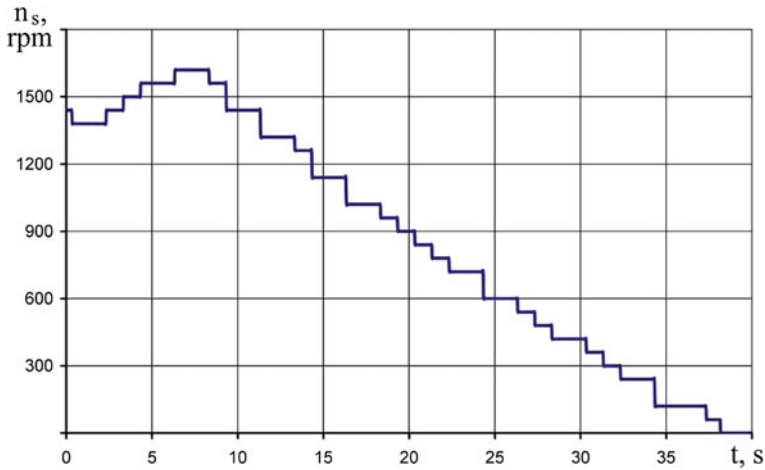


Fig. 4 Stand dynamometer rotation speed as a function of time when running out an NPT VAZ-2115 car

017-U2 portable LF spectrum analyzer with ZETLab software, a BC 401 ICP contactless optical rpm sensor (a tachometric converter) mounted on a tube tripod and a Lenovo IdeaPad S10-2 laptop.

The obtained dependences were approximated by second-degree polynomials for further differentiation. In particular, for the NPT car the dependence $n_s = n_s(t)$ was approximated as $n_s = 0.4793t^2 - 67.467t + 1673.9$, while the one for the pneumatic tires car was approximated as $n_s = 0.4023t^2 - 64.605t + 1654.7$ (Fig. 5).



Fig. 5 Approximated dependences of the stand dynamometer rotation speed on the car runout time: — for NPT; — for BL-85 175/70R13 pneumatic tires

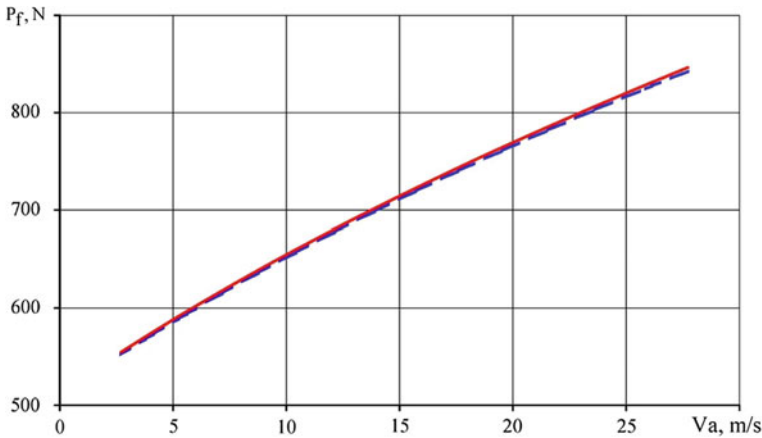


Fig. 6 Plot of the rolling resistance force by the stand dynamometers as a function of speed: — for NPT wheels; - - - for wheels with BL-85 175/70R13 pneumatic tires

The final plot to demonstrate the NPT and pneumatic tires wheel rolling resistance force as a function of speed is shown in Fig. 6.

6 Conclusion

The rolling resistance force of the NPT models, as measured by the stand dynamometers, and its dependence on speed are barely different from the rolling resistance of BL-85 175/70R13 pneumatic tires at a nominal air pressure.

The experimental results do not contradict the foreign manufacturers' statements that NPT feature greater damping properties while boasting lesser rolling resistance.

The new wheel designs with NPT can be in demand by producers of civil and military motor vehicles, wheeled armored machinery [21] and tractors, road-building machines, special motor transport and wheeled planet rovers [22].

References

1. Gajewski VJ (1993) Polyurethane elastomer and non-pneumatic tire fabricated therefrom. US Patent 522359, 29 Jun 1993
2. Dehasse B (1991) Deformable nonpneumatic tire with recesses extending crosswise over the entire axial width of the tire. US Patent 5042544, 27 Aug 1991
3. Rhyne TB et al (2007) Non-pneumatic tire. US Patent 7201194, 10 Apr 2007
4. Dotson ME et al (2013) Non-pneumatic tire with reinforcement band spacer and method of manufacturing same. US Patent 20130278044, 24 Oct 2013

5. Manesh A et al (2011) Tension-based non-pneumatic tire. US Patent 20110079335, 07 Apr 2011
6. Gass DB et al (2017) Non-pneumatic tire. US Patent 9573422, 21 Feb 2017
7. Hanada R et al (2012) Non-pneumatic tire. US Patent 8276628, 02 Oct 2012
8. Abe A et al (2014) Non-pneumatic tire. US Patent 20140251518, 11 Sep 2014
9. Choi SJ et al (2016) Non-pneumatic tire with reinforcing member having plate wire structure. US Patent 9333799, 10 May 2016
10. Iwase M et al (2010) Non-pneumatic tire. US Patent 20100132865, 03 Jun 2010
11. Chadwick DR et al (2014) Non-pneumatic survivable tire, cover and fabrication processes. US Patent 20140034219, 06 Feb 2014
12. Steinke RA et al (2007) Airless spare tire. US Patent 20070119531, 31 May 2007
13. Iwamura W et al (2014) Airless tire. EP Patent 2801485, 12 Nov 2014
14. Russell BA (2015) Wheel system. US Patent 9004120, 14 Apr 2015
15. Veselov IV, Gamlitsky YuA, Zherdetsky AS, Sokolov SL (2016) Calculation and computer optimization of the airless bus. Rubber industry: raw materials, technology. In: Reports of the XXI Scientific and Practical Conference, pp 151–154
16. Kartashov AB (2010) Development of large wheeled propulsions from composite materials based on fiberglass. Dissertation. Bauman Moscow State Technical University
17. Mazur VV (2017) Development and testing of automobile airless tires. Mech Eng Bull 3:86–88
18. Mazur VV (2018) Experimental research in automobile non-pneumatic tire force heterogeneity. In: MATEC web of conferences
19. Mazur VV, Mazur MA (2014) Experimental evaluation of the ability of automobile airless tires self-cleaning of dirt. Syst Methods Technol 3(23):78–82
20. Boyko AV, Fedotov AI, Tsogt D (2011) An experimental study of the forces of rolling resistance of a car wheel on stand rollers. Bull Irkutsk State Tech Univ 8(55):115–121
21. Mazur VV (2014) Wheeled propulsions of military vehicles with enhanced mine protection. Mil Thought 2:55–58
22. Mazur VV (2014) Wheeled propulsions of planetary rovers. Astronaut Rocket Sci 5(78): 86–90.

Peculiarities of Motion of Pendulum on Mechanical System Engine Rotating Shaft



A. I. Artyunin, S. V. Barsukov and O. Yu. Sumenkov

Abstract The authors carried out the mechanical and mathematical modeling of the motion of a pendulum mounted with the possibility of free rotation on the rotor shaft of an electric motor fixed in housing on elastic supports. The peculiarities of the motion of the pendulum within the range from zero to a given value of the angular velocity of the rotor of the electric motor with the presence in this range of natural frequencies of oscillations of the mechanical system are revealed. It is established that when changing the friction moment in the pendulum support or the pendulum mass, a mode of movement is possible and when the rotor rotates with a given angular velocity, the angular velocity of the pendulum rotation is equal to one of the natural frequencies of the mechanical system. The results of a numerical experiment conducted for the first time in a mechanical and mathematical modeling of the motion of a pendulum on a rotating shaft confirmed the results of a previous full-scale experiment on the possible emergence of a pendulum “sticking” effect for such mechanical systems of a general form.

Keywords Mechanical system · Natural frequency · Angular velocity · Pendulum · “Sticking” effect

1 Introduction

At all times, the pendulum has been a remarkable object of research and practical application in mechanics. The pendulum was the subject of research by the founders of the mechanics of Galileo, Newton, Huygens [1, 2].

The pendulum is the main element of the mechanical clock. The Foucault pendulum is used in an experiment to prove the rotation of the Earth, and the

A. I. Artyunin · S. V. Barsukov (✉)

Irkutsk State Transport University, 15, Chernyshevsky Street, Irkutsk 664074, Russia
e-mail: bars_irkutsk@mail.ru

O. Yu. Sumenkov

Tomsk Polytechnic University, 30, Lenin Avenue, Tomsk 634050, Russia

© Springer Nature Switzerland AG 2020

A. A. Radionov et al. (eds.), *Proceedings of the 5th International Conference on Industrial Engineering (ICIE 2019)*, Lecture Notes in Mechanical Engineering,

https://doi.org/10.1007/978-3-030-22041-9_70

Froude pendulum illustrates the possibility of self-oscillations. The torsional pendulum is used in an experiment to determine the density of the Earth and the gravitational constant. Studies of the motion of a pendulum with large deflection angles marked the beginning of a nonlinear theory of oscillations.

Studies of the motion of a pendulum with small deflection angles marked the beginning of a linear theory of vibrations of mechanical systems, and studies with large deflection angles set the stage for the creation of a nonlinear theory of oscillations.

At present, works that focus on the study of the motion of the pendulum can be conventionally divided into two groups. The first group presents studies of the motion of the pendulum on a vibrating base [3–10]. In the other group, the calculation of the motion of a pendulum is an approbation of methods for studying nonlinear oscillations of mechanical systems [11–16].

The pendulum is also the main element of the generalized model of vibration nonlinear mechanics, proposed in [17]. Special cases of the generalized model in this work are a model for studying the phenomenon of stability of the upper position of a pendulum on a vibrating base [3] and a model for studying the process of balancing the rotor using pendulum auto balancers [18].

The basis for the present work was the results of experimental studies of the motion of a pendulum on a rotating shaft [19, 20].

In these works, the experimental unit shown in Fig. 1 was used. The unit was an electric motor 1, mounted on a metal plate 2, which in turn was mounted with four springs 3 on a fixed base 4. A pendulum was mounted with a possibility of free rotation on the motor shaft 5. The pendulum consisted of a threaded rod for hanging loads, a metal ring, and a rolling bearing. An optical tachometer 6 was used to measure the angular velocity of rotation of the pendulum and the motor. This mechanical system, in a plane perpendicular to the plane of the motor shaft, had three natural oscillation frequencies: $k_1 = 44.0$ rad/s; $k_2 = 100.5$ rad/s; $k_3 = 123.1$ rad/s. These frequencies of oscillations of the mechanical system were less than the frequency of rotation of the motor shaft $\omega = 157.0$ rad/s.

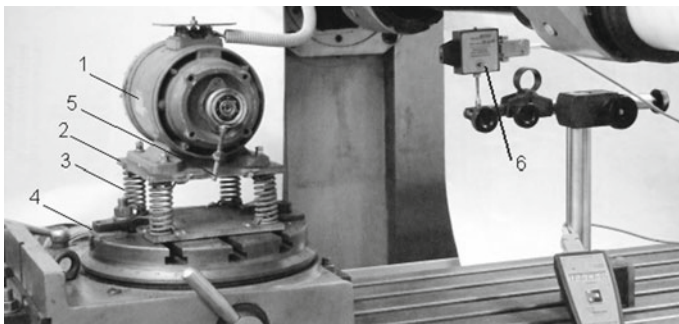
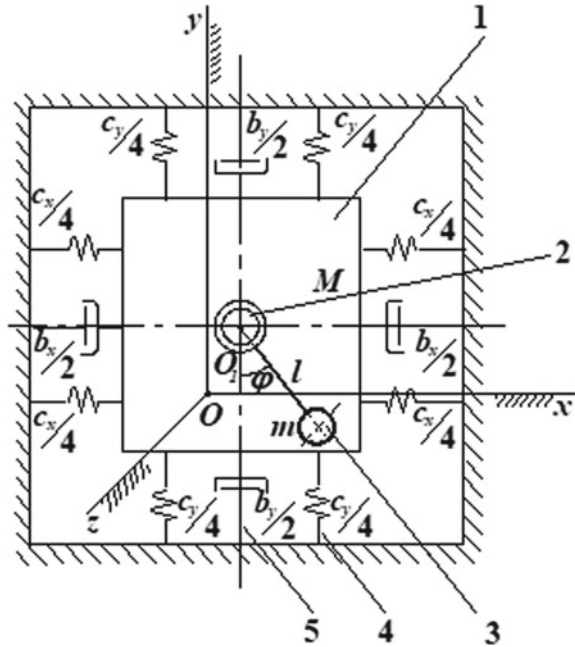


Fig. 1 Experimental unit: 1—electric motor; 2—metal plate; 3—springs; 4—fixed base; 5—pendulum; 6—optical tachometer

Fig. 2 Model of mechanical system with pendulum on rotating shaft: 1—the housing (point O_1 is the center of masses of the housing and the rotor); 2—rotor; 3—the pendulum; 4—weightless elastic supports; 5—dampers



The essence of the experiment was to measure the angular velocity of the pendulum on the rotating motor shaft at various moments of inertia of the pendulum mass.

As a result of the experiment with a constant friction torque in the support of the pendulum, the following was established. With the moment of inertia in the range of $256.8 \leq I \leq 281.2 \text{ g} \times \text{cm}^2$, the pendulum rotated together with the motor shaft and its angular velocity was $\omega = 157.0 \text{ rad/s}$. With the moment of inertia of the pendulum in the range of $304.0 \leq I \leq 369.8 \text{ g} \times \text{cm}^2$, the angular velocity of the pendulum rotation was $\dot{\varphi} = 118.2 \text{ rad/s}$, which with the accuracy of the experiment is equal to the third natural frequency of oscillation of the mechanical system $k_3 = 123.1 \text{ rad/s}$. With the moment of inertia of the pendulum in the range of $394.5 \leq I \leq 506.3 \text{ g} \times \text{cm}^2$, its angular rotation speed was $\dot{\varphi} = 100.5 \text{ rad/s}$. This value of the angular velocity coincided with the second natural frequency of oscillations of our mechanical system, $k_2 = 100.5 \text{ rad/s}$. With the moment of inertia of the pendulum in the range of $531.0 \leq I \leq 603.2 \text{ g} \times \text{cm}^2$, the angular velocity of rotation of the pendulum $\dot{\varphi} = 44.0 \text{ rad/s}$. This value of the angular velocity coincided with the first natural frequency of oscillations of the mechanical system $k_1 = 44.0 \text{ rad/s}$.

Thus, at a constant friction torque in the pendulum support and when its mass moment of inertia changes, there is such a mode of movement in which the rotor rotates at an angular operating speed, and the angular velocity of the pendulum is close to or coincides with one of the oscillation frequencies of the mechanical system. This new phenomenon has been called the “sticking” effect of the

pendulum on the rotating shaft. The purpose of this work is a mechanical and mathematical modeling of the motion of the pendulum on the rotating motor shaft of the mechanical system to detect the “sticking” effect of the pendulum, established in experimental studies [19, 20].

2 The Selection and Description of the Motion Model of the Mechanical System with the Pendulum on the Rotating Shaft

For the study, a model was chosen (Fig. 2), which has a form of housing as a solid body of a symmetrical cubic shape. It is fixed on an immovable base with the help of symmetrically located weightless elastic supports, four vertical and four horizontal ones. The housing is equipped with a balanced rotor with a shaft. A pendulum is mounted on the rotor shaft with the possibility of rotation relative to the shaft. The axis of rotation of the rotor passes through the center of masses of the housing (point O_1 in Fig. 2). Figure 2 also shows dampers, conventionally denoting the presence of resistance proportional to the velocity of the housing.

We will study the motion of the model with respect to the fixed coordinate system $Oxyz$, the beginning of which (point O) coincides with the center of masses of the housing in the position of its static equilibrium. We also assume that the motion along the z -axis and the rotation around the x -, y -, z -axes are absent. Then, to describe the motion of the model, three generalized coordinates can be used: x_1 , y_1 are displacements of the center of masses of the housing; θ_1 is the rotation of the rotor. In addition, the angle of deflection of the pendulum from its lower position is denoted by φ .

To derive the differential equations of motion of the model, we use the Lagrange equations of the second kind in the following form:

$$\frac{d}{dt} \left(\frac{\partial T}{\partial \dot{q}_i} \right) - \frac{\partial T}{\partial q_i} = - \frac{\partial \Pi}{\partial q_i} - \frac{\partial \Phi}{\partial q_i} + Q_\varphi. \quad (1)$$

In this equation, T is the kinetic energy of a mechanical system; q_i the generalized coordinate; Π is the potential energy of the mechanical system; Φ is the Rayleigh function (dispersion function); $Q_\varphi = k(\omega - \dot{\varphi})$. Here ω is the angular velocity of the rotor; $\dot{\varphi}$ is the angular velocity of the pendulum; k is the coefficient of resistance to the relative rotation of the pendulum on the rotor shaft.

With the selected generalized coordinates, the expression for the kinetic energy of the model, which consists of the kinetic energy of the housing, the kinetic energy of the rotor and the kinetic energy of the pendulum, is written as:

$$T = \frac{1}{2}M(\dot{x}_1^2 - \dot{y}_1^2) + \frac{1}{2}I_P\omega^2 + ml(\dot{x}_1\dot{\varphi}\cos\varphi + \dot{y}_1\dot{\varphi}\sin\varphi) + \frac{1}{2}ml\dot{\varphi}^2. \quad (2)$$

In this expression, $M = M_1 + M_2 + m$ (M_1 is the housing mass; M_2 is the mass of the rotor; m is the mass of the pendulum); I_P is the moment of inertia of the rotor; l is the length of the pendulum.

Below is an expression for the potential energy Π , which is the sum of the potential energy of deformation of elastic supports in the horizontal and vertical directions and the potential energy of the gravity forces of the housing, rotor, and pendulum. Given the static equilibrium condition, the expression for potential energy:

$$\Pi = \frac{1}{2}c_x x_1^2 + \frac{1}{2}c_y y_1^2 + mgl \cos\varphi. \quad (3)$$

here, c_x , c_y are the total stiffness of the weightless supports in the horizontal and vertical directions; g is the gravitational acceleration.

The expression for the Rayleigh function with the housing damping will be:

$$\Phi = \frac{1}{2}b_x \dot{x}_1^2 + \frac{1}{2}b_y \dot{y}_1^2, \quad (4)$$

where b_x , b_y are the coefficients of resistance to the movement of the housing in the horizontal and vertical directions.

After the Lagrange procedure (1), we obtain a system of three differential equations to describe the motion of the model.

$$\begin{aligned} M\ddot{x}_1 + ml\ddot{\varphi}\cos\varphi &= ml\dot{\varphi}^2\sin\varphi - c_x x_1 - b_x \dot{x}_1; \\ M\ddot{y}_1 + ml\ddot{\varphi}\sin\varphi &= -ml\dot{\varphi}^2\cos\varphi - c_y y_1 - b_y \dot{y}_1; \\ ml^2\ddot{\varphi} + ml\ddot{x}_1\cos\varphi + ml\ddot{y}_1\sin\varphi &= k(\omega - \dot{\varphi}) - mgl\sin\varphi. \end{aligned} \quad (5)$$

3 The Investigation of the Effect of the Friction Moment in the Support of the Pendulum on Its Angular Velocity

The essence of this study was to find the law of acceleration of the pendulum at different values of the friction coefficient k in the numerical integration of Eq. (5), which was carried out in the Borland Delphi programming. The results of mathematical modeling of the pendulum acceleration for different values of the friction coefficient k are presented in Fig. 3.

The numerical experiment was performed with the following initial data: $M_h = 8$ kg; $M_r = 2$ kg; $m = 0.02$ kg; $c_x = 1 \times 10^5$ N/m; $c_y = 4 \times 10^5$ N/m; $b_x = b_y = 100$ N s/m; $l = 0.221$ m; $0.142 \times 10^{-3} \leq k \leq 0.01$ N m s.

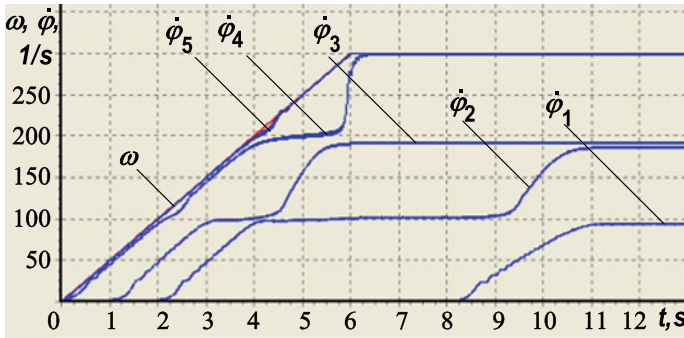


Fig. 3 Laws of motion of the pendulum at different values of the friction coefficient k : 1—at $0.143 \times 10^{-3} \leq k \leq 0.494 \times 10^{-3}$ N m s; 2, 3—at $0.494 \times 10^{-3} \leq k \leq 0.01$ N m s; 4, 5—at $k > 0.01$ N m s

The adopted initial parameters set two natural frequencies of oscillations of the studied mechanical system:

$$k_1 = \sqrt{c_x/M} = 100 \text{ rad/s}; k_2 = \sqrt{c_y/M} = 200 \text{ rad/s}. \quad (6)$$

It was also assumed that for $0 \leq t \leq 10$ s, the angular velocity of the rotor changed according to the law $\omega = 30t$, and for $t > 10$ s, the angular velocity had a constant value $\omega = 300$ rad/s.

The first experiment: The friction coefficient k changed from 0 to 0.142×10^{-3} N m s. In this case, the pendulum immediately or, having made several turns, deflected by some angle from the lower position, making small oscillations relative to this equilibrium position.

The second experiment: The friction coefficient k changed from 0.143×10^{-3} to 0.494×10^{-3} N m s. In this case, the pendulum initially retained its fixed state, as in the first experiment and then was “entrained” by the shaft into rotation, and its angular velocity was $\dot{\varphi} = 100$ rad/s (curve 1 in Fig. 3), which was equal to the first natural frequency of oscillations of the mechanical system. With a further increase in the coefficient of friction k , the time delay of the pendulum rotation decreased. The limiting value of the coefficient k , at which the stable rotation of the pendulum with an angular velocity $\dot{\varphi} = 100$ rad/s was still maintained, was 0.494×10^{-3} N m s.

The third experiment: The friction coefficient k changed from 0.494×10^{-3} to 0.01 N m s. Within this range, the angular velocity of the pendulum initially with a delay of about 4 s reached an angular velocity $\dot{\varphi} = 100$ rad/s, which was equal to the first natural frequency of oscillations of the mechanical system.

After 9 s, the pendulum accelerated and began to rotate at an angular velocity $\dot{\varphi} = 200$ rad/s, which was equal to the second natural frequency of the mechanical system (curve 2 in Fig. 3).

With a gradual increase in the friction coefficient k from 0.494×10^{-3} to 0.01 N m s , the pendulum was entrained into rotation by the rotor of the engine with a smaller delay and shifted from the first natural frequency of oscillations of the mechanical system (100 rad/s) to the second frequency (200 rad/s) earlier.

The limiting mode in which the pendulum is still shifting from the first frequency to the second one is shown in Fig. 3 (curve 3). This behavior of the pendulum was observed when the friction coefficient was $k \leq 0.01 \text{ N m s}$.

With a gradual increase in the friction coefficient k from 0.494×10^{-3} to 0.01 N m s , the pendulum was entrained into rotation by the rotor of the engine with a smaller delay and shifted from the first natural frequency of oscillations of the mechanical system (100 rad/s) to the second frequency (200 rad/s) earlier.

The fourth experiment: The coefficient of friction k became greater than 0.01 N m s . The pendulum accelerated to angular velocity $\dot{\varphi} = 300 \text{ rad/s}$, that is, to the rotor speed $\omega = 300 \text{ rad/s}$ and rotated further along with the rotor (curves 4, 5 in Fig. 3). The line $\omega(t)$ in this figure shows the time variation of the rotor angular velocity over time.

4 The Study of the Influence of the Pendulum Mass on Its Angular Velocity

As in the previous section, the study consisted in finding the law of acceleration of the pendulum for different values of its mass m in the numerical integration of Eq. (2). The results of mathematical modeling of the acceleration of the pendulum with different values of its mass are presented in Fig. 4. The numerical experiment was carried out with the same values of the mass of the rotor and the housing, with the same values of the stiffness and damping coefficients, with the same

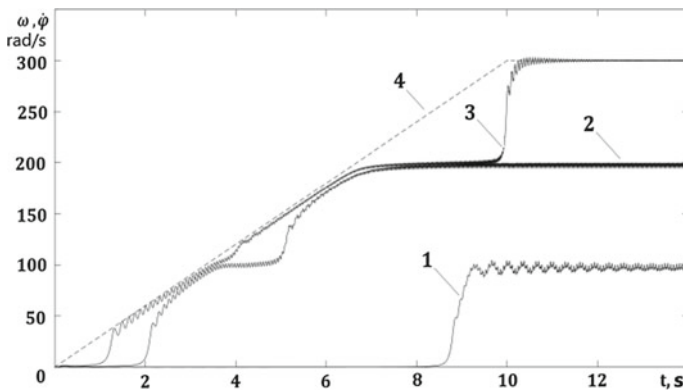


Fig. 4 Laws of motion of the pendulum with its different mass: 1—at $0.020 \leq m \leq 0.060 \text{ kg}$; 2—at $0.005 \leq m < 0.020 \text{ kg}$; 3—at $m < 0.005 \text{ kg}$; 4—is the law of acceleration of the rotor

acceleration mode of the rotor as in previous studies. The friction coefficient in the pendulum support was assumed to be $k = 0.1 \times 10^{-3}$ N m s.

First experiment: The mass of the pendulum did not exceed 0.060 kg. In this case, the pendulum deflected at a certain angle, making small oscillations relative to this equilibrium position.

The second experiment: The mass of the pendulum changed in the range of $0.020 \leq m \leq 0.060$ kg. In this case, the pendulum initially kept its stationary state as in the first experiment, and then, 8 s after the start of the rotor movement, it accelerated and began to rotate with the angular velocity $\dot{\varphi} = 100$ rad/s, almost equal to the first natural frequency of the mechanical system (curve 1 in Fig. 4).

The third experiment: The mass of the pendulum changed in the range of $0.005 \leq m < 0.020$ kg. Here the pendulum accelerated and began to rotate with the angular velocity $\dot{\varphi}$ of 200 rad/s, which was equal to the second natural frequency of the mechanical system (curve 2 in Fig. 4).

The fourth experiment: With the pendulum mass $m < 0.005$ kg, it accelerated to the angular velocity $\dot{\varphi} = 300$ rad/s, that is, to the rotor rotation speed $\omega = 300$ rad/s and rotated along with the rotor (curve 3 in Fig. 4). The law of acceleration of the rotor in this figure is indicated by 4.

Thus, the results of the numerical experiment carried out with a simplified model of motion of the pendulum on the rotating motor shaft fixed in the housing on elastic supports confirmed the results of a full-scale experiment described in [17, 20].

The full-scale experiment using a real model, as well as the mathematical modeling with a simplified model, showed that, with the same angular velocity of rotation of the rotor, the angular velocity of the pendulum rotation, depending on the friction in its support, may coincide with one of the natural frequencies of the mechanical system.

5 Conclusions

As a result of the numerical modeling, the motion of the pendulum on the rotating rotor shaft of the electric motor is fixed in the housing on elastic supports, and it has been established that, when friction changes in the pendulum support or the pendulum mass, a mode of movement is possible when the rotor rotates at a given angular speed, and the angular speed of rotation of the pendulum is equal to one of the natural frequencies of the mechanical system oscillations. Thus, the results of the numerical experiment with the chosen model confirmed the results of the field experiment described in [19, 20].

References

1. Newton I (2017) *Matematicheskie nachala natural'noy filosofii (Mathematical principles of natural philosophy)*. LENAND, Moscow
2. Huygens H (1951) *Tri memuara po mekhanike (Three memoirs on mechanics)*. AS of Lith. SSR, Moscow
3. Kapitsa PA (1951) *Dinamicheskaya ustoychivost' mayatnika pri koleblyushcheysya tochke podvesa (The dynamic stability of the pendulum with an oscillating point of suspension)*. *J Exper Theor Phys* 21(5):588–597
4. Ragulskis KM (1963) *Mekhanizmy na vibriruyushchem osnovanii (Mechanisms on a vibrating base)*. AS of Lith. SSR, Kaunas
5. Valeev KG, Dolya VV (1974) *O dinamicheskoy stabilizatsii mayatnika (On the dynamic stabilization of the pendulum)*. *Appl Mech* 10(2):88–99
6. Chelomey VN (1989) *Izbrannye trudy (Selected Works)*. Mashinostroenie, Moscow
7. Strizhak TG (1991) *Metody issledovaniya dinamicheskikh system tipa "mayatnik" (Research methods for dynamic systems of the "pendulum" type)*. Nauka, Alma-Ata
8. Bardin BS, Markeev AP (1995) *Ob ustoychivosti ravnovesiya mayatnika pri vertikal'nykh kolebaniyakh tochki podvesa (On the stability of the pendulum equilibrium with vertical oscillations of the suspension point)*. *Appl Math Mech* 9(6):922–929
9. Morozov AD (1995) *K zadache o mayatnike s vibriruyushchei tochkoi podvesa (To the problem of a pendulum with a vibrating point of suspension)*. *Appl Math Mechs* 59(4): 590–598
10. Seyranyan AA, Seyranyan AM (2006) *Ob ustoychivosti perevyornutogo mayatnika s vibriruyushchei tochkoi podvesa (On the stability of an inverted pendulum with a vibrating point of suspension)*. *Appl Math Mech* 70(5):835–843
11. Malkin IA (1951) *Nekotorye zadachi teorii nelineinykh kolebaniy (Some problems of the theory of nonlinear oscillations)*. Gostekhizdat, Moscow
12. Bogolyubov NN, Mitropolsky YuA (1974) *Asimptoticheskie metody v teorii nelineinykh kolebaniy (Asymptotic methods in the theory of nonlinear oscillations)*. Nauka, Moscow
13. Moiseev NN (1969) *Asimptoticheskie metody nelineinoy mekhaniki (Asymptotic methods of nonlinear mechanics)*. Nauka, Moscow
14. Volosov VM, Morgunov BI (1971) *Metod osredneniya v teorii nelineinykh sistem (Averaging method in the theory of nonlinear systems)*. Moscow University Press, Moscow
15. Grebennikov EA (1986) *Metod usredneniya v prikladnykh zadachakh (Averaging method in applied problems)*. Nauka, Moscow
16. Blekhan II (1994) *Vibratsionnaya mekhanika (Vibration mechanics)*. Fizmatlit, Moscow
17. Artyunin AI, Khomenko AP, Eliseev SV, Ermoshenko YuV (2015) *Obobshchennaya model' vibratsionnoy nelineinoy mekhaniki i effekt "zastrevaniya" mayatnika na rezonansnykh chastotakh mekhanicheskoi sistemy (The generalized model of vibration nonlinear mechanics and the effect of "sticking" of the pendulum at the resonant frequencies of the mechanical system)*. *Sci J. Eng and Eng Educ* 1:61–67
18. Artyunin AI (1993) *Issledovanie dvizheniya rotora s avtobalansom (Study of the movement of the rotor with autobalance)*. *Proceedings of Higher Educational Institutions. Machi Build* 1:15–19
19. Artyunin AI, Ermoshenko YuV, Popov SI (2015) *Eksperimental'nye issledovaniya efekta "zastrevaniya" mayatnika na rezonansnykh chastotakh mekhanicheskoi sistemy (Experimental studies of the effect of "sticking" of the pendulum at the resonant frequencies of the mechanical system)*. *Mod Techn Sys Analys Model* 2(46):20–25
20. Artyunin AI, Eliseev SV, Sumenkov OYu (2018) *Experimental studies on influence of natural frequencies of oscillations of mechanical system on angular velocity of pendulum of rotating shaft. Dynamics of Machines and Lecture Notes. Working Processes in Mechanical Engineering ICIE 2018*, pp 159–166

Reducing Dynamic Loads in Hoisting Mechanism of Excavator Based on Feedbacks on Elastic Torque



N. K. Kuznetsov, I. A. Iov and E. S. Dolgih

Abstract The article is devoted to the problem of reducing the dynamic loads in the hoisting mechanisms of an electric mining shovel. In this article, by the example of the EKG-8I excavator, the results of studies of the electric drive control algorithm of hoisting mechanisms based on feedbacks on the elastic torque in the hoist cable, allowing one to limit the value of this torque, are presented. In this case, the synthesis of control algorithms is based on the solution of the inverse dynamic problems according to the given law of elastic torque variation, which allows directly determining the structure and parameters of feedback. The equations of motion of the electromechanical system of the hoisting mechanism of the excavator and the results of numerical simulation confirming the effectiveness of the proposed control algorithms are given. It is shown that the synthesized feedbacks allow reducing the dynamic loads in the hoisting mechanism of the excavator and to approach the curve of change of the elastic torque to the shape of the mechanical characteristic of the excavator drive. Possible ways for implementing the proposed motion control algorithms are discussed.

Keywords Mining shovel · Hoisting mechanism · Elastic oscillation · Control system · Electromechanical system · Inverse problem

1 Introduction

Modern digital electric drive control systems allow providing high speed, optimal trajectories of movement of actuators in various technological operations, monitoring, recording, and online setting of parameters of control system [1–6]. The

N. K. Kuznetsov (✉) · E. S. Dolgih
Irkutsk National Research Technical University, 83, Lermontov St.,
Irkutsk 664074, Russia
e-mail: knik@istu.edu

I. A. Iov
SLC-JH, Ltd., 101, Mira St. Moscow 129085, Russia

increase of displacement rate of the actuators leads to increase of dynamic loads in transient modes of operation which have a negative impact on the mechanical and electrical equipment of the excavator, lead to the accumulation of fatigue damage in mechanical elements, reducing productivity and reliability. The dynamic loads are particularly dangerous in the digging mechanisms of excavators operating at low negative temperatures, due to the deterioration of the viscosity properties of structural steels, more obvious impact of structural defects (cracks) and the probability of brittle fracture of actuator equipment [7, 8]. As shown in [9–11], the magnitude of dynamic loads is determined by the magnitudes of accelerations and inertia moments of rotating and translationally moving masses, as well as the rate of change of load on the actuator.

Since the actuators of excavators are complex controlled mechanical oscillatory systems due to the presence of elastic elements, the problem of reducing dynamic loads in them is solved by the methods of machine mechanics and methods of the theory of automatic control. Currently, the main way to limit dynamic loads is to use soft unstressed driving modes with a limitation of the maximum speed of the actuator or rigid and flexible feedbacks on the load in an elastic element [12–16]. The main problem that should be solved when using this method of reducing dynamic loads is the problem of synthesizing the optimal structure and parameters of feedback. For example, in [14], a modified method of normalized transfer functions was used to solve this problem, and studies were carried out based on a simplified two-mass model of the mechanical system of an excavator. Studies of efficiency of feedback on load based on a refined electromechanical model traction mechanism, which took into account not only the elastic properties of the gearbox, but also the backlashes in it and changes in the kinematic parameters of the mechanism during operation, made in [15] revealed undesirable phenomena in the operation of the electric drive associated with an increase in the recovery time of the steady-state value of the speed of the actuator under certain operating modes, which may lead to decrease in reliability mechanical parts and productivity traction mechanism. In [16], it was found that the alternating sign nature of the torque of the electric drive, due to the effect of feedback on the load in an elastic element leads to the opening of backlashes in the gearbox, undesirable phenomena in the drive operation and reduce the reliability of its work.

As the analysis of the well-known works devoted to the problem of the synthesis of the electric drive control system showed, the proposed methods allow to solve the problem parametric synthesis of control actions for a given controller structure only, which does not allow to sufficiently realize the capabilities of a modern electric drive and its control system. In this regard, of particular interest is the application of the method of synthesis of control actions based on solving the inverse problem by using a mathematical model of the control object by defining the desired character of the motion proposed in [17, 18]. The action obtained in this way does not impose any restrictions on the structure of the controller and can be implemented with the help of open and closed control systems.

In this paper, using the example of the EKG-8I mining shovel hoist mechanism, the results of studies of the efficiency of electric drive control algorithms based on

elastic torque feedbacks, which were synthesized by solving the inverse dynamic problems according to given law of elastic torque variation, are presented.

2 Object and Method of Investigation

We will synthesize the control actions of the electric drive, which allow limiting dynamic loads, using the example of the EKG-8I mining shovel hoist mechanism equipped with a double-loop control system with main speed and current feedback [19]. When choosing a calculating scheme for a hoisting mechanism, we accept the following assumptions: the masses are concentrated, and the mechanical elastic connection (cable) is weightless and has constant stiffness. Then dynamic processes can be described quite accurately with a two-mass calculation scheme in which the first mass represents the total inertia moment of the motors, gearbox, and drum, and the second mass is the inertia moment of the bucket filled with rock [14, 16].

Differential equations describing the motion of a mechanical system will have the form:

$$\begin{cases} J_1 s \omega_1 = M_{dv} - M_{12} - M_b - M_t; J_2 s \omega_2 = M_{12} + M_b - M_C; \\ M_{12} = \frac{c_{12}}{s} (\omega_1 - \omega_2); M_b = b(\omega_1 - \omega_2); M_t = a \omega_1. \end{cases} \quad (1)$$

Here J_1 is the inertia moment of first mass; J_2 is the inertia moment of second mass; c_{12} is the stiffness of the elastic element; a is the coefficient of proportionality; b is the coefficient of viscous friction in elastic element; ω_1, ω_2 are the angular velocities of the masses; M_{dv} is the drive torque; M_C is the load of mechanism; s is a Laplace operator.

The control system of the electric drive of the digging mechanism is implemented in the form of a double-loop control system; a static high-speed transistor converter with pulse-width modulation is used as the power unit. The behavior of the electrical part of the electromechanical system of the digging mechanism can be described using the following differential equations:

$$\begin{cases} U_{SR} = \left(U_{ref} - \frac{K_{SS} \cdot \omega_1}{T_b s + 1} \right) \cdot K_{SR}; U_{SR} \leq U_{lim} = \left(K_1 - \frac{K_{SS} \cdot \omega_1}{T_b s + 1} \right) \cdot (\cos a / \sin a) + K_2; U_{lim} \leq U_{ST}; \\ U_{CR} = \frac{\left[U_{SR} - \left(\frac{K_{CS}}{T_{CS} s + 1} + \frac{0.3 K_{CS} s}{T_{CS} s + 1} \right) I_a \right] \cdot (T_a s + 1)}{T_{CR}}; E_p = \frac{U_{CR} \cdot K_b}{T_b s + 1}; E_{dv} = C_e \cdot \omega_1; I_a = \frac{E_p - E_{dv}}{T_a s + 1} \cdot K_a; \\ M_{dv} = C_e \cdot I_a. \end{cases} \quad (2)$$

where U_{SR} is the voltage at the output of the speed controller; U_{ref} is the reference voltage; U_{lim} is the constraint voltage to form a falling section of the mechanical characteristic; U_{CR} is the voltage at the output of the current controller; U_{ST} is the constraint voltage to form a vertical section of the excavator characteristic; E_p is the converter voltage; E_{dv} is the DC machine voltage; I_a is the armature current; K_1 is

the tuning coefficient of mechanical characteristics; K_2 is the limitation of the falling part of mechanical characteristic; K_{SS} is the gain of the speed sensor; K_{SR} is the coefficient of the speed controller; K_{CS} is the gain of the current sensor; K_a is the gain of the armature circuit; K_b is the converter gain; α is the angle of inclination of the falling part of the mechanical characteristic; T_a is the time constant of the armature circuit; T_{CR} is time constant of the current controller; T_b is the converter time constant; T_{fs} is the time constant of the speed sensor; T_{fc} is the time constant of the current sensor; C_e is the voltage constant.

For the synthesis of control actions that limit the dynamic loads in the hoisting mechanism, we use the solution of the inverse dynamic problems according to given law of change elastic torque, which we take in the form

$$M_{12} = M_\gamma(1 - e^{\lambda_1 t} - e^{\lambda_2 t}), \quad (3)$$

where M_γ is the constant component of the elastic moment; λ_1 and λ_2 are the roots of the equation, the real part of which is $\text{Re } \lambda_i < 0$ [20].

When choosing the roots of Eq. (3), it is necessary to be guided by the following, since positive feedbacks reduce the stability margin the feedbacks should be negative; therefore, for a two-mass calculation scheme, the roots must be multiple and their product must be less than the square of the fundamental frequency of oscillation of the mechanical system [17]. Solving the system of Eq. (1) for an elastic torque M_{12} , provided that $M_t = 0$, we find the required law of change of the drive torque for the mechanical system of the hoisting mechanism

$$\ddot{M}_{12} + b\gamma_{12}\dot{M}_{12} + \omega_{12}^2 M_{12} = \frac{c_{12}M_{dv}}{J_1} + \frac{c_{12}M_C}{J_2}, \quad (4)$$

where $\gamma_{12} = \frac{J_1 + J_2}{J_1 J_2}$ is a coefficient of proportion mass; $\omega_{12} = \sqrt{\frac{c_{12}(J_1 + J_2)}{J_1 J_2}}$ is the fundamental frequency of oscillation.

Differentiating (3) twice, we get

$$\dot{M}_{12} = -M_\gamma\lambda_1 e^{\lambda_1 t} - M_\gamma\lambda_2 e^{\lambda_2 t}; \quad (5)$$

$$\ddot{M}_{12} = -M_\gamma\lambda_1^2 e^{\lambda_1 t} - M_\gamma\lambda_2^2 e^{\lambda_2 t}. \quad (6)$$

Substituting (3), (5), and (6) into (4), we determine the required law of variation of the drive torque for the formation of a given type of elastic torque

$$M_{dv} = \frac{J_1}{c_{12}} M_\gamma (-\lambda_1^2 - bJ'_{12}\lambda_1 - \omega_{12}^2) e^{\lambda_1 t} + \frac{J_1}{c_{12}} M_\gamma (-\lambda_2^2 - bJ'_{12}\lambda_2 - \omega_{12}^2) e^{\lambda_2 t} + \frac{J_1 + J_2}{J_2} M_\gamma. \quad (7)$$

To find the control structure and feedback parameters, from Eqs. (3) and (5), we express the exponential functions in terms of the elastic torque and its derivatives:

$$M_\gamma e^{\lambda_1 t} = \frac{\dot{M}_{12} - \lambda_2 M_{12} + \lambda_2 M_\gamma}{\lambda_2 - \lambda_1}; \tag{8}$$

$$M_\gamma e^{\lambda_2 t} = \frac{-\dot{M}_{12} + \lambda_1 M_{12} - \lambda_1 M_\gamma}{\lambda_2 - \lambda_1}. \tag{9}$$

Substituting (8) and (9) into (7), we find an expression that determines the required control action

$$M_{dv} = K_V \dot{M}_{12} + K_A M_{12} + M'_\gamma, \tag{10}$$

where $K_1 = -\lambda_1^2 - b'_{12}\lambda_1 - \omega_{12}^2$; $K_2 = -\lambda_2^2 - bJ'_{12}\lambda_2 - \omega_{12}^2$; $K_V = \frac{J_1(K_1 - K_2)}{c_{12}(\lambda_2 - \lambda_1)}$; $K_A = \frac{J_1(K_2\lambda_1 - K_1\lambda_2)}{c_{12}(\lambda_2 - \lambda_1)}$ and $M'_\gamma = \left(\frac{J_1(K_1\lambda_2 - K_2\lambda_1)}{c_{12}(\lambda_2 - \lambda_1)} + \frac{J_1 + J_2}{J_2}\right)M_\gamma$.

In expression (10), K_V and K_A can be represented as coefficients of rigid and flexible feedbacks on the load in an elastic element, and M'_γ as a new value of the constant component, the value of which is determined by the parameters of the mechanical system and the roots of a given law of elastic torque variation.

Figure 1 shows a structural scheme derived from Eqs. (1), (2), and (10), in which the transfer of feedback from the adder of torque to the input of the control system is performed. In this scheme, the dash and dot lines show the initial state of the synthesized feedbacks, and the dash lines indicate the state after the transfer. As

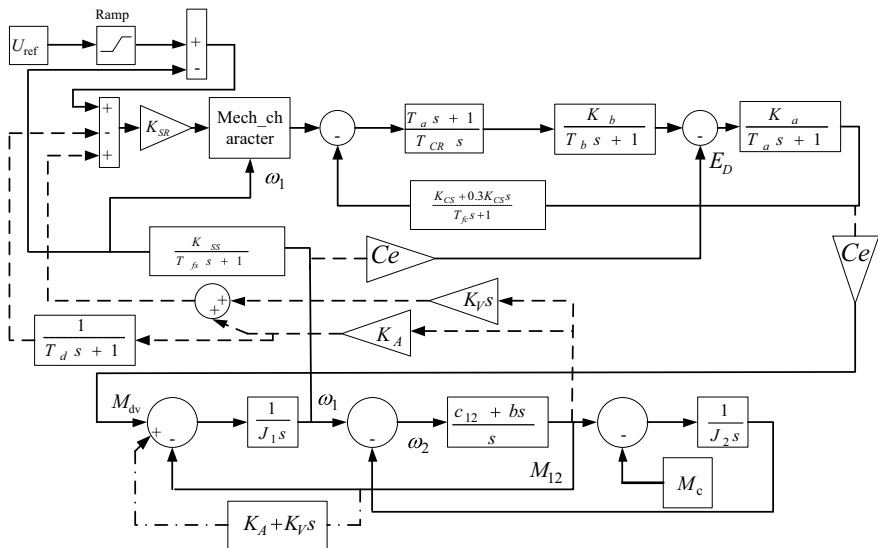


Fig. 1 Electromechanical structural scheme of the hoist mechanism of the excavator with feedbacks on the elastic torque



a feedback signal, a force sensor in the cable of the hoisting mechanism can be used, the elastic torque on which is measured in accordance with the equation $M_{12} = c + bs$.

The control system is adjusted to the technical optimum, and the motor voltage constant feedback [14, 16] is not taken into account when setting. With the exclusion of flexible feedbacks, the transfer function of the optimized current loop will be described by an aperiodic link with gain $1/K_{CS}$ and non-compensable time constant $T_\mu = T_b$. Carrying out the transfer of feedbacks through the voltage constant, the current loop link, and the gain of the speed controller, we obtain the values of the feedback coefficients delivered to the control system at the input of the adder before the speed controller (Fig. 1) and we obtain the transfer function of feedback signals

$$\Delta U_M = \frac{K_V T_\mu M_{12} s^2 + (K_V + K_A T_\mu) s M_{12} + K_A M_{12}}{K_{SR} C_e \frac{1}{K_{CS}}}. \quad (11)$$

Neglecting quantity of the second order of smallness of the derivative of the elastic moment in (11), we find the values of the feedback gains. Since in the control system the acceleration is formed by a power-up control and the shape of the mechanical characteristic, the constant component of the driving torque in (10) providing the specified acceleration of the second mass can be ignored. Reducing the set point speed due to the effect of rigid feedback on the load can be compensated for by a positive signal through the aperiodic function with a time constant T_d .

Perform a test of the effectiveness of the synthesized feedbacks by numerical simulation of an electromechanical system (Fig. 1) in the MATLAB–Simulink environment with the following parameters $U_{ref} = 10$ V/s, $Ramp = 5$ V/s, $K_{SR} = 6$, $K_1 = 10$, $K_2 = 6$, $\cos a = \sin a = 1.05$ rad, $U_{ST} = 10$ V, $T_{fs} = 0.005$ s, $K_{CS} = 0.00657$ V/A, $K_{SS} = 0.1291$ V/rad, $T_a = 0.0635$ s, $T_{CR} = 2T_b K_a K_b K_{CS} = 0.2$ s, $K_b = 76.8$, $K_a = 19.68$, $T_b = 0.01$ s, $T_{fc} = 0.005$ s, $C_e = 6.838$ V s, $T_d = 0.5$ s, $J_1 = 51.1$ kg m², $J_2 = 5.4$ kg m², $c_{12} = 160$ N m/rad, $b = 8$ N m s/rad. With the adopted parameters of the mechanical system, the values of the roots of the equation will be $\lambda_1 = -6$; $\lambda_2 = -12$. Then the feedback gains are determined by the values: $K_V = -0.000837$, $K_A = -0.002$.

3 Research and Discussion

Studies of the effectiveness of the proposed feedbacks on the elastic torque were carried out by comparing with the standard control system for the start-up mode of the mechanism in idle ($M_C = 0$) at the rated speed, followed by a step loading ($M_C = 1.2M_{rate}$) and locking the mechanism at $M_C = 3.2M_{rate}$. The speed of the

bucket ω_2 and the elastic moment M_{12} , torque M_{dv} and speed ω_1 of the drive-in transient operating conditions were registered, the values of which are reduced to relative parameters.

Studies have shown high efficiency of the proposed feedbacks on the elastic torque. They allow to reduce the magnitudes of oscillations of the torque and speed and to reduce the time of transients. An illustration in Fig. 2 shows oscillograms of transients, which show curves of changes in the elastic torque M_{12} (Fig. 2a), bucket speed ω_2 (Fig. 2c), torque M_{dv} (Fig. 2b), and speed ω_1 (Fig. 2d) of the drive. The numbers denote the curves corresponding to standard (1) and synthesized (2) control systems.

Based on the research, we can draw the following conclusions:

- (1) in the start-up mode, the synthesized system (curve 2) ensures a smooth change of the bucket speed ω_2 (Fig. 2c) during acceleration to the rated speed, with fewer oscillations compared with the standard system (curve 1). The change in the elastic moment M_{12} (Fig. 2a) in the process of acceleration for the system (1) and (2) is monotonic;
- (2) in the mode of step loading $M_C = 1.2M_{rate}$, the magnitude of oscillations of the elastic torque in the system (2) exceeds the steady-state value by 9% and in the system (1) by 22%. The time of the transient process of elastic oscillations for the compared control systems is almost the same and amounts to 2 s, while for the system (2) the elastic oscillation curve approaches an aperiodic form. The curve of bucket speed ω_2 in the system (2) reaches a steady-state value with an overshoot of 7%, while in the system (1) an overshoot reaches 48%, and the time of the transient process does not change. It is necessary to note that for the system (2) the path traveled by the bucket from the time of step loading to locking is 30% less than in the system (1), which leads to an increase in the

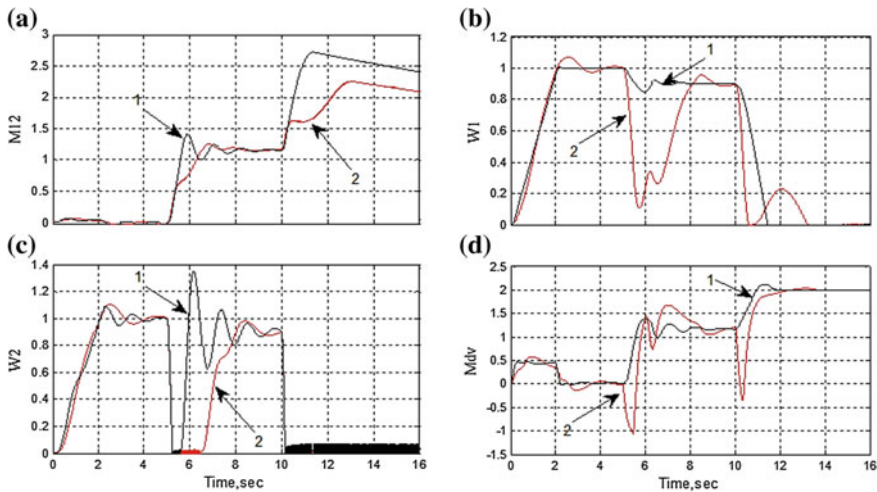


Fig. 2 Oscillograms of transients

time of filling the bucket and reducing the productivity of the digging mechanism;

- (3) in the bucket locking mode, the magnitude of the elastic torque M_{12} in the system (2) is 12% higher than the maximum torque developed by the drive in the steeply falling section of the mechanical characteristic, and in the system (1) the torque release is 136% of the locking force. The oscillations of the elastic torque in the compared systems do not occur, and the increase of torque in the cables is monotonic. In system (2), the change in the elastic torque M_{12} in the locking mode approaches the form of the mechanical characteristic of the drive;
- (4) for the system (2), the oscillatory nature of the drive torque in the mode of step loading and locking is characterized. The magnitude of the braking torque reaches the nominal value, and the maximum value of the rate of change of the armature current is $8 \dots 9 I_n/s$. It should also be noted that such significant values of the braking torque of the drive can lead to the opening of backlashes in the gearbox, and the high rate of change of the armature current in a transient mode can reduce the reliability of the brush unit of the DC motor.

The proposed method of synthesizing feedbacks on the elastic torque by specifying the desired nature of its change, compared with the method of normalized transfer functions [14], allows to directly determine the structure and parameters of feedback and to approach the curve of the elastic torque to the shape of the excavator mechanical characteristics.

4 Conclusion

The proposed method of synthesizing the control system of the digging mechanism of the excavator, based on solving the inverse dynamic problems according to given law of elastic torque variation, allows determining not only parameters but also the structure of feedbacks. The resulting control actions do not impose any restrictions on the structure of the controller and can be implemented using open and closed motion control systems, which allows formalizing the procedure of their structural-parametric synthesis. Their application is a more complete realization of the capabilities of the modern electric drive and its control system. The proposed control algorithms make it possible to reduce the dynamic loads in the hoisting mechanism of excavator and to approach the curve of change in the elastic torque to the mechanical characteristic in the most difficult mode of operation (bucket locking). The observed undesirable effects in the form of drive braking torque and an increase in the bucket filling time are compensated for an increase in the reliability of the actuators a reduction in the downtime and an increase in trouble-free operation time.

References

1. Alekseev VV, Emelyanov AP, Kozyaruk AE (2016) Analysis of the dynamic performance of a variable-frequency induction motor drive using various control structures and algorithms. *Russian Electr Eng* 87(4):181–188
2. Kozyaruk AE, Taranov SI, Samolazov AV (2014) The direction of operation effectiveness increase of excavating and automobile complexes on open-pit mining. *Min Equip Electromech* 1:6–11
3. Siemens AG (2007) Mining shovels SIMINE SH Mining Technologies (Brochure), p 7
4. Malafeev SI, Novgorodov AA, Serebrennikov NA (2012) New excavator EKG-18R: the system of direct current motor drive with the pulse-width modulation control. *Min Equip Electromech* 6:21–25
5. Malafeev SI, Tikhonov YV (2015) Intellectualization of a career excavator. In: Reports of the XXIII international scientific symposium “Miner’s week—2015”. Moscow, 26–30 Jan 2015
6. P&H Joy Global Inc. (2012) Centurion shovel control system product overview, 8 p
7. Leonenko AS (2010) Methods and technical solutions to increase the efficiency of operation of mining machines in cold area: a monograph. Irkutsk State Technical University, Irkutsk, p 280
8. Hendricks C (1990) Performance monitoring of electric mining shovels, Ph.D. thesis. Monreal, McGill Univ, p 386
9. Lyakhomsky AV, Fashilenko VN, Pavlenko SV (2012) Improving the efficiency of electrotechnical systems of mining excavators. TNT, Stary Oskol, p 248
10. Li Ying and Liu Wenyuan (2014) Comparison of advanced dragline dynamics models for efficient engineering analysis. *Int J Adv Manuf Technol* 72(5–8):757
11. Kong WK, Liu JX, Ma MH (2012) Research on dynamic characteristics of implement mechanism of mining excavator. *Appl Mech Mater* 229–231:512–516
12. Caterpillar Inc. (2013) 7495 HF electric rope shovel AEH06960 (03-2013), p 32
13. Kolga AD, Sharipov RH (2010) The effect of the change in hoisting speed on the reliability of the dipper-stick of a mining shovel. Technological equipment for mine and oil and gas industries. *Coll. Scien. Pap. USMU, Yekaterinburg*, pp 370–374
14. Lyakhomskiy AV, Fashilenko VN (2004) Control of electromechanical mining machine systems. Moscow State Mining University, Moscow, p 294
15. Kuznetsov NK, Iov IA, Iov AA (2018) Investigation of efficiency of the electric drive control system of excavator traction mechanism based on feedback on load. *IOP Conf Ser: J Phys*: 1015. 032176
16. Kuznetsov NK, Iov IA, Iov AA (2018) Investigation of the control system of traction electric drive with feedbacks on load. *IOP Conf Ser: Mater Sci Eng* 327. 052023
17. Krut’ko PD (1987) Inverse dynamics problems of control systems: Linear models, Science, Moscow
18. Kuznetsov NK, Iov IA, Iov AA (2018) Investigation of dynamics of excavator digging mechanism with an additional drive. *IOP Conf Ser: Earth Environ Sci* 194. 032014
19. Joint Power Co. Lim. (2012) Low voltage equipment for the electric drive control system. Excavator EKG-8T, p 45
20. Gerasimyak RP, Leshev VA (2008) Analysis and synthesis of crane electromechanical systems. Smil, Odessa

Determination of Magnetization Efficiency of Wheel-Rail Contact Zone



D. Ya. Antipin, V. O. Korchagin and M. A. Maslov

Abstract Railroad transport has a leading position in the country's transport network. Similarly to land transport, rail wheels do the following: braking, rolling, and load transmission. The reliability of a wheel-rail system has a direct impact on the traffic safety. Major energy losses in the mechanical part of a rail-mounted locomotive account for the wheel-rail contact region. Hence, the wheel/rail interface is considered fundamental to the performance of railroad transport. The article considers the results of studies of the distribution of the magnetic field between the wheel and the rail, the criteria for evaluating the efficiency of magnetization of the wheel-rail contact zone. It was found that the saturation of the contacting surfaces of the wheel and rail occurs in different ways. For the saturated state at the two-point comb contact, the greatest value of the magnetic field induction on the crest is less than the induction on the riding surface. For the saturated state in the presence of an air gap between the wheel crest and the rail, almost all the magnetic flux is redistributed to the surface of the wheel.

Keywords Magnetic field · Contact magnetization · Wheel profile · Contact spot · Wheel contour · Wheel-rail contact · Magnetization efficiency

1 Introduction

In most countries, railway transport takes the leading place due to the provision of high carrying capacity. The tractive capability of locomotives is formed by the axial loading and the value of the coefficient of friction. The adhesion is affected by the condition and the shape of the surfaces to be contacted, the speed as well as the

D. Ya. Antipin (✉) · M. A. Maslov
Bryansk State Technical University, 7, 50-Let Oktyabrya, Bryansk 241035, Russia
e-mail: adya2435@gmail.com

V. O. Korchagin
Russian Open Academy of Transport of the Russian University of Transport (ROAT RUT MIIT), 22, Chasovaya, Moscow 175468, Russia

transmitted forces. The coefficient of adhesion of the locomotive wheels to the rails is determined by the tribological processes on the contact spot. Numerous studies show that the friction interaction in the contact zone is the basis of the adhesion of the wheels of the railway vehicle to the rails, and the coefficient of adhesion depends significantly on the friction coefficient. The phenomenon of friction of bodies is accompanied by processes having thermal, mechanical, electrical, magnetic, and chemical nature. The studies of friction by I. V. Kragelsky and N. B. Demkin show that the coefficient of friction strongly depends on the actual contact area, and the actual contact areas are distributed within the contour contact [1–10].

To apply the effect of the magnetic field on the steel friction pair in the tribosystem wheel-rail, the micro-steps of the single platforms of the actual contact should be magnetized. Since the magnetic susceptibility of ferromagnetic and paramagnetic substances is of the same sign, it is not possible to achieve selective magnetization in the contact zone. Together with the micro-steps of the actual contact, the contour contact areas are magnetized, and with sufficient magnetic voltage, the nominal contact of the wheel with the rail is saturated.

2 Materials and Methods

The boundaries of the saturation region take a close to elliptical shape, a large half-axis of the saturation region between the wheel and the rail can be directed both along and across the axis of rotation of the wheel. On contact, when both profiles are new or worn, the saturation regions have a longitudinal orientation. The contact zone of the new profile with the worn one is characterized by transverse stretching of the saturation region. The shape of the saturation region is associated with the distribution of the magnetic lines in the wheel and the rail as well as with a change in magnetic resistance. The analysis of the change in magnetic permeability shows that the resistance increases when the contact of the wheel with the rail is removed from the spot. If we consider that the magnetic resistance is mainly due to the air clearance, the clearance has a significant effect on the formation of the saturation region [11–13].

Let us consider the change in the clearance between the wheel and the rail Δ in mutually perpendicular longitudinal and transverse sections. In the longitudinal section, the clearance between the wheel and the rail is determined by the formula.

$$\Delta = a^2/D_w \quad (1)$$

where D_w is the wheel diameter; a is a half of the saturation region in the longitudinal direction.

The clearance in the cross section depends on the wear of the wheel and the rail, as well as the transverse position of the wheel pair in the track, Fig. 1.

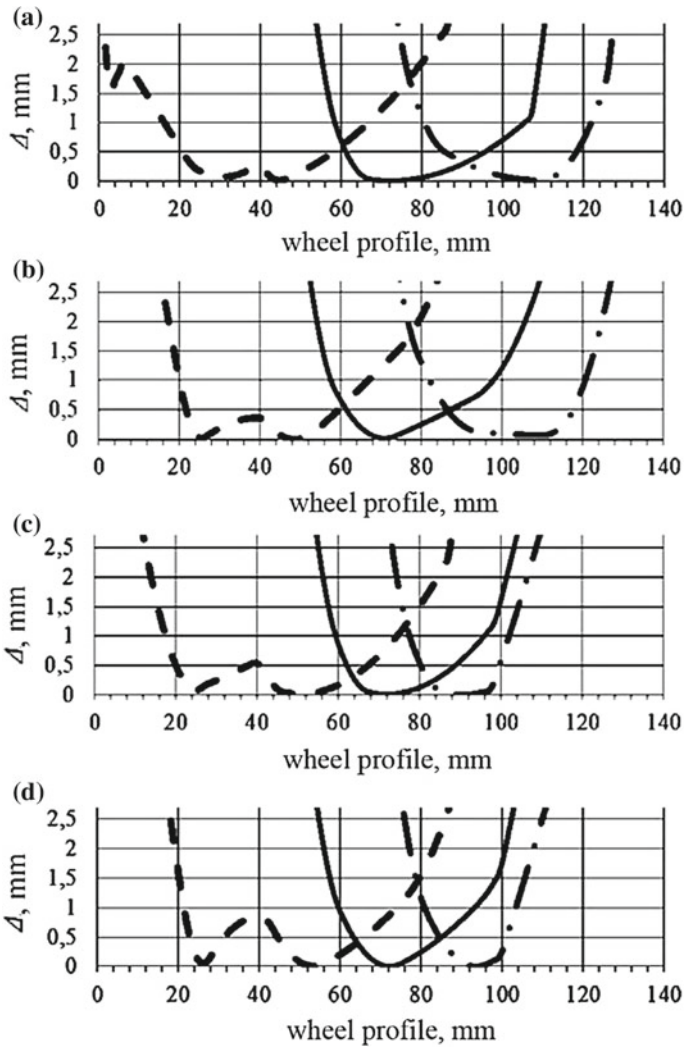


Fig. 1 Clearance between the wheel and the rail in the cross section. **a** The worn wheel and the worn rail; **b** the worn wheel and the new rail; **c** the new wheel and the worn rail; **d** the new wheel and the new rail; - · - · the greatest clearance between the crest and the rail; — the central position of the wheel; — · — the ridge point-to-point contact

The rotation of the magnetic saturation region is explained by the fact that the air clearance around the contact spot varies unevenly. The comparison of the graphs of changes in the clearance between the wheel and the rail with the induction graphs shows that the distribution of induction on the wheel surface is inversely dependent on the clearance between the bodies. The monotonicity of the clearance graphs and the induction varies at the same points of the profile; the maximum induction

corresponds to the minimum clearance. By connecting consistently the equidistant points on the surfaces of the wheel and the rail, we obtain a closed boundary at which the induction takes a constant value.

The application of the magnetic voltage $U_M = 257$ A saturates the wheel contact with the rail and the precontact area [13–15]. The boundary of the saturation region with an induction of 1.3 T is located within the clearance between the wheel and the rail from 0.1 to 0.2 mm, while in the epicenter of the saturation region (the contact spot) the induction reaches a value of 1.5 T. Thus, the contact spot on the riding surface is overlapped by the saturation region.

Next, the saturation region on the rolling surface, where the induction of the magnetic field is greater than the induction of the initial saturation, we call the area of the magnetic contact of the wheel with the rail S_M . By introducing the concept of the magnetic overlap coefficient of the wheel-rail contact as the ratio of the magnetic contact area to the contact spot area S_K , we can characterize the magnetization efficiency of the wheel-rail contact zone.

Inefficient magnetization regimes include the cases where the magnetic contact area is less than the contact spot area ($S_M/S_K < 1$), Fig. 2a. Such modes arise at the extreme positions of the new wheel relative to the worn rail, when the wheel crest is in contact with the rail, as well as at $U_M < 123$ A.

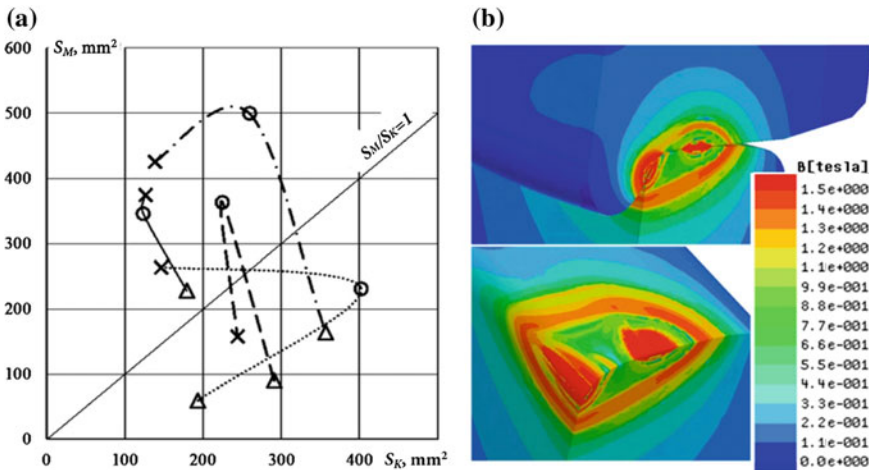


Fig. 2 Dependence of the area of the magnetic contact ($U_M = 257$ A) on the area of the contact spots at different positions of the wheel relative to the rail (a), supersaturated condition of the wheel-rail contact zone when $U_M = 400$ A (b). $\Delta\Delta\Delta$ the ridge point-to-point contact; $\circ\circ\circ$ the central position of the wheel; $\times\times\times$ the greatest clearance between the crest and the rail; — — — the wheel and the rail are new; the new wheel and the worn rail; the wheel and the rail are worn; the worn wheel and the new rail; the wheel and the rail are new; — — — the new wheel and the worn rail; — — — the wheel and the rail are worn; — — — the worn wheel and the new rail



When significant magnetic stresses occur the saturated wheel-rail contact zone appears and there are additional regions of saturation with the induction of 1.3 T. Figure 2b shows the distribution of the field at magnetic $U_M = 400$.

At the first stage of simulation the contact spot areas and the transverse positions of the wheel pairs of the locomotive CHME3 when accelerating from 0 to 12 km/h are defined. At the second stage, the obtained data were imported to MATHLAB, where the system of regulation set the magnetizing current of inductor to maintain the clutch due to the friction between the surfaces of wheel and rail. At the final stage, UM Loco repeated the calculation with the given values of friction coefficients on the surfaces of rolling, fillets, and ridges.

The movement of the locomotive CHME3 occurred within the S-curve laid by the rails of the P65 type, the simulation was performed for new and worn profiles. Part of the rolling surface of the worn rail head is outlined by a line of variable radius from 280 to 310 mm. Rolling on the rolling surface of the worn locomotive wheel approached the permissible value of 5 mm, instead of the slope of 1:20, a convex curvature with a radius of 630–660 mm was formed closer to the ridge fillet. New profiles of the locomotive wheel and the rail head R65 are taken according to [16–20]. The graphs of changes in the total contact area of the left and right wheels depending on the transverse position of the wheel pair in the rail track are shown in Fig. 3.

Each position of the locomotive wheel pairs in the rail track corresponds to a corridor of area values, this is due to the variability of the speed and the forces transmitted to the wheels. When determining the area of contact between the wheel and the rail, a set of features of the contacting profiles should be taken into account, which requires complex programming and a long time of calculations. The exact solution to the contact problem using the methods of the theory of elasticity leads to the integral equations, the solution of which is difficult and sometimes impossible analytically. In the first approximation, with a sufficient degree of accuracy, it is allowed to move from the integral equations to the algebraic ones when solving the contact problem due to simplifications [21, 22].

3 Conclusion

The calculation results show that the saturation of the wheel and the rail surfaces are different. For the saturated state at the two-point comb contact, the greatest value of the magnetic field induction on the wheel crest is 1.4–2 times less than the induction on the riding surface. This difference is particularly figured for worn wheels and depends mainly on the contact spot area. If there is an air clearance between the wheel crest and the rail, 98% of the entire magnetic flux of the contact zone passes through the wheel's rolling surface. With a two-point comb contact, the flow of the rolling surface decreases, its part is from 60 to 70%, due to this, the area of the magnetic contact and the coefficient of the magnetic overlap of the wheel contact with the rail are reduced.

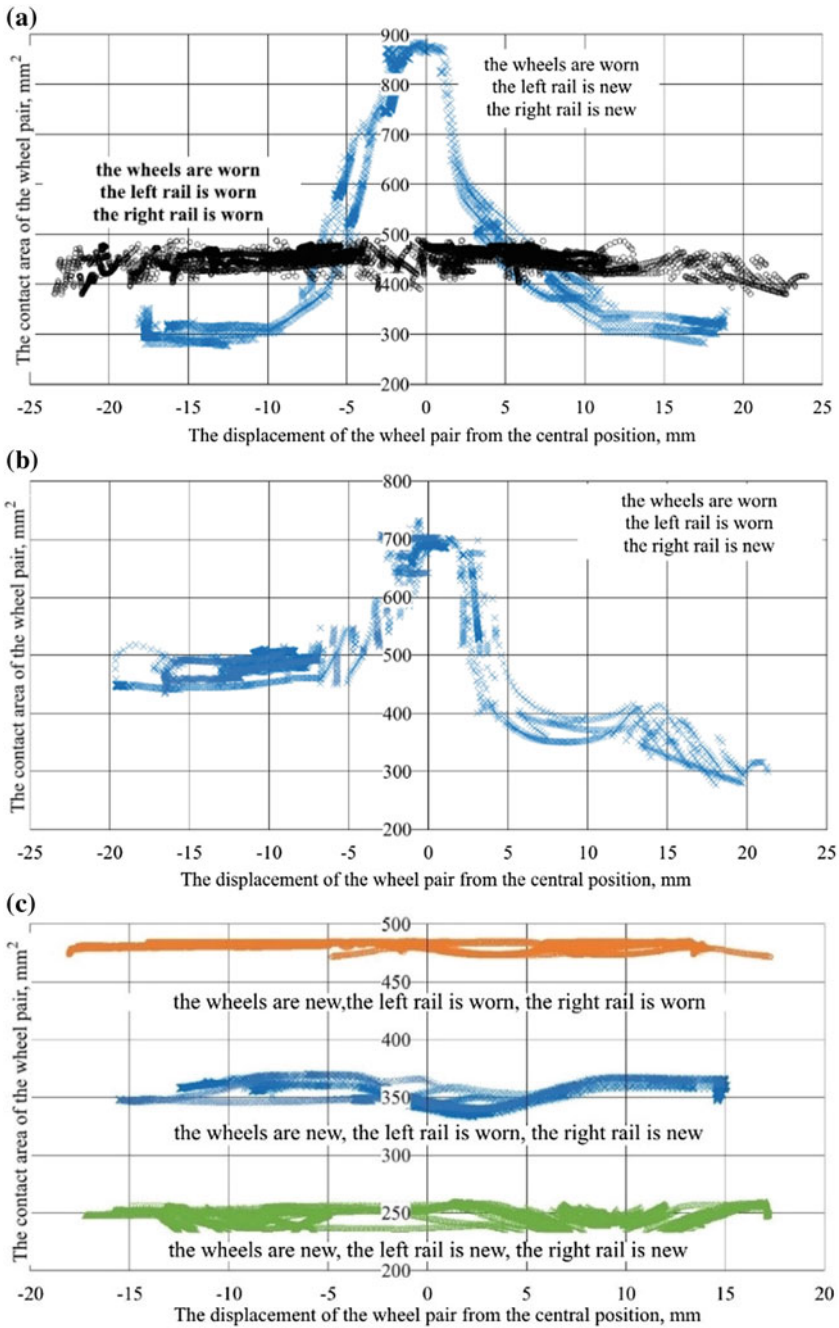


Fig. 3 Contact spot areas of the wheel pairs with the rails from the transverse position in the track

References

1. Kragelsky I, Alisin V (2016) Friction wear lubrication: tribology. Elsevier, Amsterdam
2. Straffelini G (2015) Friction and wear: methodologies for design and control. Springer, Berlin
3. Sarkar A (1980) Friction and wear. Academic Pr, Massachusetts
4. Ludema K (1996) Friction, wear, lubrication: a textbook in tribology. CRC Press, Boca Raton
5. Bhushan B (2013) Principles and applications of tribology. Wiley, Hoboken
6. Lundberg O (1975) On the influence of surface roughness on rolling contact forces. Dissertation, KTH Royal Institute of Technology
7. Golenko A (2010) Fundamentals of machine design. A Coursebook for Polish and foreign students. Wroclaw University of Technology, Wroclaw
8. Ivkovic B, Djukljanovic M, Stamenkovic D (2000) The influence of the contact surface roughness on the static friction coefficient. Tribol Ind 22:41–44
9. Fenga B (2017) Effects of surface roughness on scratch resistance and stress-strain fields during scratch tests. AIP Adv 7:38–42. <https://doi.org/10.1063/1.4979332>
10. Keropyan A, Gorbatyuk S (2016) Impact of roughness of interacting surfaces of the wheel-rail pair on the coefficient of friction in their contact area. Procedia Eng 150:406–410. <https://doi.org/10.1016/j.proeng.2016.06.753>
11. Wang W, Zhang H, Liu Q, Zhu M, Jin X (2016) Investigation on adhesion characteristic of wheel/rail under the magnetic field condition. J Eng Tribol 230:235–239. <https://doi.org/10.1177/1350650115606480>
12. Wang H, Wang W, Liu Q (2016) Numerical and experimental investigation on adhesion characteristic of wheel/rail under the third body condition. J Eng Tribol 230:128–132. <https://doi.org/10.1177/1350650115591232>
13. Zhu Y (2013) Adhesion in the wheel-rail contact. Dissertation. KTH Royal Institute of Technology
14. Foo C, Omar B, Jalil A (2018) A review on recent wheel/rail interface friction management. J Phys 1049:17–21. <https://doi.org/10.1088/1742-6596/1049/1/012009>
15. Blanco-Lorenzo J, Santamaria J, Vadillo E, Correa N (2016) On the influence of conformity on wheel-rail rolling contact mechanics. Tribol Int 103:647–667. <https://doi.org/10.1016/j.triboint.2016.07.017>
16. BS EN 13979-1:2003+A2:2011 Railway applications. Wheelsets and bogies. Monobloc wheels. Technical approval procedure. Forged and rolled wheels. BSI 54p
17. BS EN 13103-1:2017 Railway applications. Wheelsets and bogies. Design method for axles with external journals. BSI. 52p
18. BS EN 13104:2009+A2:2012 Railway applications. Wheelsets and bogies. Powered axles. Design method. BSI. 50p
19. BS EN 13260:2009+A1:2010 Railway applications. Wheelsets and bogies. Wheelsets. Product requirements. BSI. 40p
20. BS EN 13674-1:2011+A1:2017 Railway applications. Track. Rail. Vignole railway rails 46 kg/m and above. BSI. 17p
21. Kovalev R, Yazykov V, Mikhalchenko G, Pogorelov D (2003) Railway vehicle dynamics: some aspects of wheel-rail contact modeling and optimization of running gears. Mech Based Des Struct Mach 31:315–334
22. Kovalev R, Lysikov N, Mikheev G, Pogorelov D, Simonov V, Yazykov V, Zakharov S, Torskaya E (2009) Freight car models and their computer-aided dynamic analysis. Multibody SysDyn 22:399–423

Forecasting of Life Service of Hopper Car Body Load-Bearing Structure on Basis of Mathematical Modeling Methods



D. Ya. Antipin, V. V. Kobishanov and A. S. Mitrakov

Abstract Life service forecast of the hopper car body welded load-bearing structure of the design loading in operation is made on the basis of mathematical modeling. The elastic properties of the car body are taken into account when modeling the load alongside the longitudinal forces appearing in the process of car's movement when a part of the train or shunting is specified. The problem is solved in a dynamic formulation by using hybrid dynamic models of cars movement in conditions of real railway track irregularities and detailed plate finite element models. The fatigue life of the most loaded load-bearing structures of the hopper car was assessed within the framework of the determined Serensen-Kagayev model of multicycle fatigue, which is the basis of the normative calculation. In assessing the durability of the welded load-bearing structure of the body, using the updated methodology, the authors evaluated the influence of stress concentration in the area of welded joints.

Keywords Car load-bearing structure life service · Mathematical modeling · Hopper car · Dynamic loading · Hybrid dynamic models · Shunting collisions, fatigue life

1 Introduction

The task of life service forecasting of rolling stock (RS) welded bearing structures is traditionally solved in a quasi-static formulation that meets the requirements of existing standards. However, such approaches lead to significant errors of the obtained results and do not take into consideration the influence of a number of

D. Ya. Antipin (✉) · V. V. Kobishanov
Bryansk State Technical University, 7, 50-Let Oktyabrya, Bryansk 241035, Russia
e-mail: adya2435@gmail.com

A. S. Mitrakov
Ural State University of Railway Transport (USURT), 66, Kolmogorova St.,
Ekaterinburg 620034, Russia

important factors, including the peculiarities of the operation of the rolling stock unit. All these disadvantages in traditional techniques are compensated due to the introduction of inflated safety factors that result finally in worse technical and economic performance of rolling stock units. Another direction of solving this problem is the use of techniques based on a significant amount of data obtained in expensive field experiments. A compromise solution in this situation is the use of mathematical modeling methods for operating conditions of the investigated rolling stock unit [1–5]. At the same time, the reliability of the data obtained in the simulation should be confirmed by their satisfactory compliance with the data of field experiments conducted in a minimal amount [6–10].

2 Materials and Methods

Based on the analysis of modern scientific research related to the solution of similar problems, it showed that the most reasonable way here is a three-stage scheme of RS welded bearing structure life service analysis [11–15]. At the first stage, the dynamic forces acting on the load-bearing structure of the car during the operation, including longitudinal forces when moving as a part of the train and shunting collisions, are estimated. In determining the dynamic forces, it is advisable to use hybrid dynamic models of the car, which let to take into account the influence of the stiffness characteristics of the body supporting structure while loaded or empty changes in the stress–strain state of the body as a result of influence of dynamic forces obtained at the first stage are analyzed at the second stage. At the third stage, the fatigue and service life of the most loaded welded joints of the body load-bearing structure is evaluated and it is based on the processing obtained at the second stage of the history of body loading in operation.

The operational model of the car includes moving on real track irregularities obtained during track recording movement within a segment of the 25 km way. This model provides for the car movement in the speed range of 10–120 km/h in increments of 10 km/h minding that 50% of the track conforming to the track gauge quality assessment of “satisfactory” criteria [16, 17], 40% is rated as “good,” and 10% is rated as “excellent.” In addition to moving on straight sections of the track, the operation model provides for also moving on curved sections with a radius of 350–1200 m and turnouts R65 of the brand 1/11. The paper assumes that 70% of the time, the hopper car moves along a straight section of the path, 25% in curves, and 5% through turnouts. The elastic-dissipative characteristics of the upper structure of the track were taken in accordance with the recommendations [18] for the summer period with a good condition of the track and rails of type R65 (version I) GOST 8161-75 25 m long, laid on wooden sleepers and crushed stone ballast.

The contact interaction of the wheel with the rail is modeled taking into account the possibility of two-point contact (railcar wheel riding circle and along its crest). Creep forces count in the contact is carried out with the use of the FASTSIM algorithm, based on linear theory of Caulker [19].

Shunting works were taken into account in the form of a car collision with arm strut weighting 300 tons at speeds from 2 to 14 km/h.

The analysis of stresses appearing in the supporting structure of the body when applying dynamic forces to the appropriate nodes obtained at the first stage of the investigation was carried out by using the finite element method in the dynamic formulation. The calculation was made by the method of direct integration of the equations of the nodal displacements of the finite element model.

The estimation of the load-bearing structure service life was made on the basis of the model of multicycle fatigue using the linear hypothesis of summation of fatigue damages under unsteady loading conditions. The calculation of fatigue life is based on the results of dynamic load assessment of the load-bearing structure of the body dynamically, which were obtained by using a detailed finite element model.

3 Analysis of the Dynamic Loading of the Hopper Car Body

Evaluation of the dynamic loading of the body of the hopper car in operation is carried out on the basis of computer simulation, applying a software package for modeling the body system dynamics, known as “universal mechanism” [20].

Dynamic hybrid model of the car (Fig. 1) is a body in the form of an elastic body, pos. 2, described on the basis of the detailed finite element model developed in the design part. The inclusion of the elastic model of the body in the computer model of the car was performed using the software module UMFEM of “universal mechanism” complex. The elastic body model is formed in the Siemens PLM Software Femap software package and connected with the subsystems pos. 1 and through special hinges with a subsystem “automatic coupling equipment.”

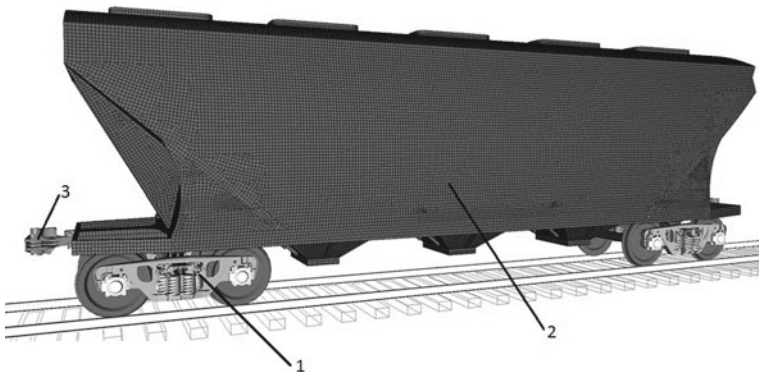


Fig. 1 Hybrid computer model of hopper car: 1—subsystem “truck”; 2—body; and 3—subsystem “automatic coupling equipment”

The body resting on the truck center plate is modeled by using a rotary joint and a power contact elements of type point—plane, allowing to take into consideration “rolling from side to side” of the body on the center bowl if there are some clearance points in the side bearings.

The subsystem “truck” is a system of rigid bodies connected by force elements and joints. When analyzing the dynamic characteristics of the car, either empty body or loaded one with the implementation of the axial load up to 23.5 t/axis is considered.

The dynamic model of the subsystem “automatic coupling device” consists of absolutely rigid bodies connected by rotational hinges, contact, and bipolar elastic-dissipative power elements. Interaction of two subsystems “automatic coupling device” in the coupled state (coupling of cars) is described like introduction of contact power elements between the solids, modeling the bodies of automatic couplers. The location of the contact power elements corresponds to the conditions of interaction between the bodies of couplers (when coupled) minding the contour of the gear in accordance with GOST 21447-75 and taking into account all allowable clearances for new beds.

To determine the forces influencing the body of the car when it moves as a part of the train, a dynamic model of three cars coupling is developed (Fig. 2). It consists of two solid-state models of gondola car being both in the head and tail of the coupling 2, and a hybrid dynamic model of the hopper car 1. Such inclusion of the gondola car can be explained by the fact that this type of cars is very popular in the railway network of Russia.

The weight of the load corresponds to the carrying capacity of the car being 71.6 is equally distributed over the nodes of the body shell of the hopper car. The position of the center of gravity is taken in accordance with the data obtained from three-dimensional model of the body.

As a result of modeling, dynamic force spectra acting on the body were obtained in the process of operation.

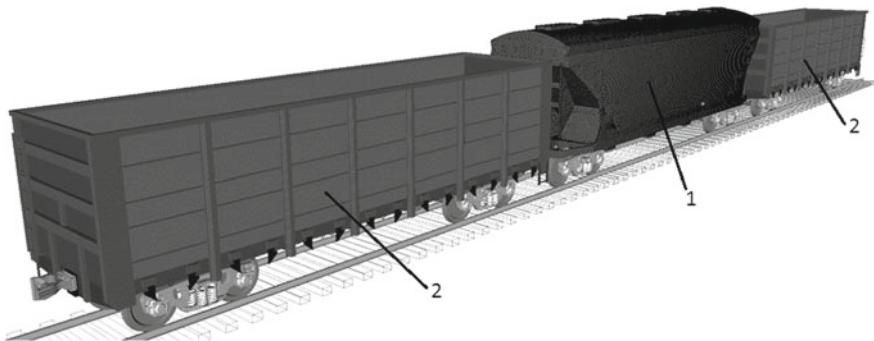


Fig. 2 Dynamic model of the coupling: 1—a hybrid model of the car-hopper; 2—solid-state model of the gondola

The reliability of the simulation results is confirmed by their satisfactory compliance with the data obtained during full-scale tests on the line and impact tests conducted during the certification of the hopper car.

4 Estimation of the Stress–Strain State of the Load-Bearing Structure of the Hopper Car Body

To estimate the stress–strain state of the supporting structure of the hopper car body, a detailed plate finite element model has been developed. It is formed by three- and four-node isotropic plate elements that take into account membrane, shift, transverse, and bending force factors and allow to model plates of considerable thickness. The total number of plate elements with an average size of 50×50 mm was 182 thousand. Thick-walled castings of the body of the car (car center plate, front draft lugs combined with the automatic coupler striker, and rear draft lugs) were simulated by 60 thousand tetragonal, pentagonal, and hexagonal three-dimensional elements.

Three-dimensional element interaction with a plate finite element scheme was carried out by introducing absolutely rigid rod parts into suitable finite element model nodes, being in the zones of three-dimensional and plate element interaction. All final elements of the scheme are combined in 137 thousand nodes with the number of model degrees of freedom up to 819 thousand.

Verification of the developed finite element model was performed by the data of full-scale bench tests of the hopper car body.

Dynamic forces obtained at the first stage were applied to the suitable nodes of the body finite element model. All calculations concerning all operating conditions of adopted operating car modification resulted in oscillogram of equivalent stress changes taking place in elements of design schemes.

Timeline changes of equivalent stresses in the pivoted area of the loaded hopper car moving along the straight track at a speed of 80 km/h (a) and during shunting collisions at a speed of 10 km/h are presented in Fig. 3.

The analysis of the obtained results concludes about the most loaded nodes of the supporting structure when operating. It refers to welding area where frame braces are welded to molding and center bearer (1), (2) and welding area of the sidewall vertical braces welded to center bearer (3) (Fig. 4).

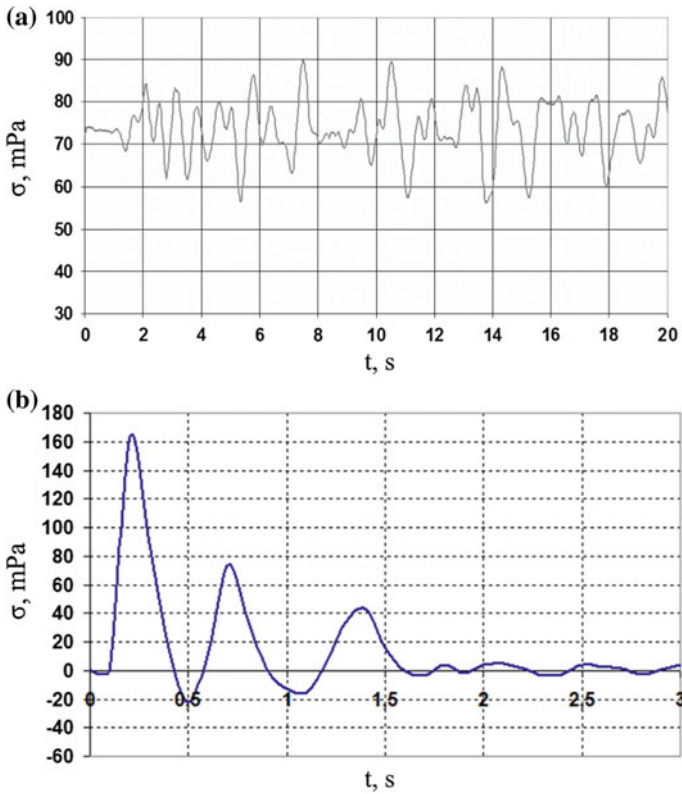


Fig. 3 Equivalent stresses in the carriage pivoted area: **a** when moving on a straight track at a speed of 80 km/h; **b** shunting collisions at a speed of 10 km/h

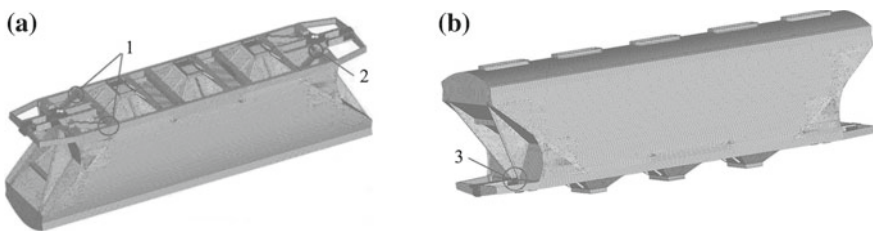


Fig. 4 Location of the most loaded nodes of the hopper car

5 Service Life Forecasting of the Hopper Car Body Load-Bearing Structure

The estimation of fatigue life of the welded load-bearing structure of the hopper car body is carried out on the most loaded nodes presented in Fig. 4. In these nodes, the most loaded elements are angular seams of the t-welded joint with cathetus 8, made in carbon dioxide environment using melting electrode. As a criterion for failure of a welded joint becomes the fatigue, crack element with a length of 10–15 mm appearing in the area of the joint as it can be seen in the figure.

Assuming that the limit state occurs when the reduction of the safety factor of fatigue resistance is below the allowable limit, we have a dependency for welded joint endurance in the loading cycles N_c .

$$N_c = \frac{\left(\frac{\sigma_{a,N}}{[n_y]}\right)^m \times N_0}{\sum_{i=1}^{k_v} (\sigma_{ai}^b)^m P_{vi} + k_n^p \left[\sum_{i=1}^{k_{sv}} (\sigma_{ai}^{sv})^{m_c} P_i^{sv}\right] + k_n^{cf} \left[\sum_{i=1}^{k_{cf}} (\sigma_{ai}^{cf})^{m_c} P_i^{cf}\right]}, \quad (1)$$

where $\sigma_{a,N}$ —the value of the endurance limit of the full-scale car limb calculated for a symmetrical loading cycle; $[n_y]$ —the permissible value of the fatigue resistance factor; N_0 —the base number of test cycles; σ_{ai}^b —the level of stress amplitude when the car moves in the i th speed interval; P_{vi} —the probability of movement of the car in the i th speed interval; k_v —the number of speed intervals of the car; $\sigma_{ai}^{sv}, \sigma_{ai}^{cf}$ —the stress values of effective longitudinal tensile and compressive forces of the i th level; P_i^{sv}, P_i^{cf} —probabilities of longitudinal stretching and compressing forces of the i th level, respectively; k_{sv}, k_{cf} —the number of levels of effective longitudinal tensile and compressive forces, respectively; m —the degree of the fatigue curve equation in amplitudes; m_c —the degree of the fatigue curve equation of the low-cycle fatigue model; k_n^p, k_n^{cf} —reduction ratios taking into account the relationship between the number of cycles of vertical forces active during the car movement for a period of a year and the number of longitudinal tensile or compressive forces acting on the car during the year, respectively.

The welded joint endurance time is calculated according to the dependence

$$T_k = \frac{N_c}{B f_e} \quad (2)$$

where f_e —the central (effective) frequency of the process of dynamic stresses changes; B —the coefficient converting service life period expressed in years to continuous movement in seconds.

The effective stress concentration coefficient in the area of the examined welded joints is determined by the refined method [20].

Table 1 Coefficient estimated

Draft gear condition	Service life (years)	Safety factor (n)
Area a	29.8	1.67
Area b	36.3	2.04
Area c	42.1	2.36

The calculations resulted in the following life service values of the most loaded areas in the bearing structure of the body, including the values of the fatigue resistance reserve coefficient estimated on the basis of the recommendations [7] (Table 1).

Analysis of the results of life service forecasting of the hopper car body load-bearing structure shows that the main factor influencing the life service is the welding unit of the frame bracing pieces to the molding (a) (Fig. 3) that coincides with the results of full-scale bench tests of the structure carried out during certification and proves the reliability of the results obtained due to proposed method.

6 Conclusions

The proposed method of forecasting of the load-bearing structure service life of the hopper car body on the basis of mathematical modeling methods allowed obtaining of the results concerning examined object, which satisfactorily corresponds to the data obtained during the full-scale running and bench tests. Hereinafter, this method gives the chance to estimate the service life of the car by using new design solutions. They are aimed first of all at car improving taking into consideration all the changes appearing under operating conditions of the car minding significant resource saving for conducting a great number of field tests.

References

1. Petrov G, Tarmaev A (2018) Modeling of railway vehicles movement having deviations in the content of running parts. AETS: Adv Eng Res 158:410–415. <https://doi.org/10.2991/avent-18.2018.79>
2. Ballew B (2008) Advanced multibody dynamics modeling of the freight train truck system. Thesis of Master of Science in Mechanical Engineering, Virginia Polytechnic Institute
3. Ghazavi M, Taki M (2008) Dynamic simulations of the freight three-piece bogie motion in curve. Veh Syst Dyn 46:955–973. <https://doi.org/10.1080/00423110701730737>
4. Simpson M (2016) Real-time simulation of rail vehicle dynamics. Dissertation, Newcastle University
5. Kovalev R, Lysikov N, Mikheev G, Pogorelov D et al (2009) Freight car models and their computer-aided dynamic analysis. Multibody Sys Dyn 22:399–423

6. Wang C, Liu C, Jiang Y (2018) Research on fatigue test method of car body for high-speed trains. *IOP Conf Ser: Earth Environ Sci* 189:421–426. <https://doi.org/10.1088/1755-1315/189/6/062011>
7. Miao B, Zhang W, Zhang J, Jin D (2009) Evaluation of railway vehicle car body fatigue life and durability using a multi-disciplinary analysis method. *Int J Veh Struct Syst* 4:85–92. <https://doi.org/10.4273/ijvss.1.4.20>
8. Sepe R, Pozzi A (2015) Static and modal numerical analyses for the roof structure of a railway freight refrigerated car. *Frattura ed Integrità Strutturale* 33:451–462. <https://doi.org/10.3221/igf-esis.33.50>
9. Song Y, Wu P, Jia L (2016) Study of the fatigue testing of a car body underframe for a high-speed train. *Proc Inst Mech Eng* 230:1614–1625. <https://doi.org/10.1177/0954409715618425>
10. Myamlin S, Ten O, Neduzha L (2014) Experimental research of dynamic qualities of freight cars with bogies of different designs. *Visnik Dnipropetrovs'kogo Nacional'nogo Universitetu Zalizničnogo Transportu* 51:136–145
11. Kassner M (2012) Fatigue strength analysis of a welded railway vehicle structure by different methods. *Int J Fatigue* 34:103–111. <https://doi.org/10.1016/j.ijfatigue.2011.01.020>
12. Lysikov N, Kovalev R, Mikheev G (2007) Stress load and durability analysis of railway vehicles using multibody approach. *Transp Prob* 3:49–56
13. Moaaz A, Ghazaly N (2014) A review of the fatigue analysis of heavy duty truck frames. *Am J Eng Res* 3:01–06
14. Savkin A, Gorobtsov A, Badikov K (2016) Estimation of truck frame fatigue life under service. *Load Procedia Eng* 150:318–323. <https://doi.org/10.1016/j.proeng.2016.07.020>
15. Ashurkova S, Kobishchanov V, Kolchina E (2017) Methods used to analyze the impact of passenger cars bodies design features on their stiffness and strength characteristics. *Procedia Eng* 206:1623–1628. <https://doi.org/10.1016/j.proeng.2017.10.688>
16. BS EN 13674-1:2011 + A1:2017 Railway applications. Track. Rail. Vignole railway rails 46 kg/m and above. BSI. 17p
17. The instruction on decoding of tapes and an assessment of a condition of a rail track on indications of the way measuring car of TSNII-2 and measures for safety of the movement of trains approved by Ministry of Railways of the Russian Federation No. CP-515 of 14.10.1997
18. Dahlberg T (2004) Railway track settlements—a literature review. Report for the EU project SUPERTRACK. Linköping University, 41p
19. Rovira A, Roda A, Lewis R, Marshall M (2012) Application of Fastsim with variable coefficient of friction using twin disc experimental measurements. *Wear* 27:109–126. <https://doi.org/10.1016/j.wear.2011.08.019>
20. Cai S, Zhang Q, Xu X, Hu D, Qu Y (2014) Calculation about stress concentration coefficient of welded cruciform joints of magnesium alloy based on FEM. *Adv Mater Res* 994:931–934

Evaluation of Heat Mechanical Loading of Piston of Gasoline Engine 4CH8,2/7,56 When It Is Forced at Average Effective Pressure



G. V. Lomakin and V. M. Myslyayev

Abstract Through the synthesis of the working cycle, the nature of changes in the pressure and temperature of gases in the engine cylinder is determined. According to the results of the kinematic and dynamic analysis of the crank mechanism, the resulting force acting on the piston and applied to the axis of the piston pin is determined. The estimation of the thermal and mechanical loading of the engine piston 4CH8,2/7,56 was carried out, when forcing at the average effective pressure using a universal method for estimating the boundary conditions, allowing to take into account all the components of the heat balance and gas-dynamic loading features during the working cycle. Evaluation of the thermal state of the investigated piston at steady-state operation is reduced to determining its temperature field in the selected critical section. Finding the temperature field of the piston involves solving the differential heat equation. According to the results of the calibration calculation estimates of the thermal and stress-strain state of the piston when the engine was forced to 4CH8,2/7,56 at the mean effective pressure, recommendations and restrictions were formulated.

Keywords Piston · Crank mechanism · Boundary conditions · Gas-dynamic loading · Working cycle

1 Introduction

Improvement of internal combustion engines with spark ignition is associated with an increase in fuel efficiency, an increase in liter capacity, a decrease in mass and dimensional parameters, and so on. For mass-produced engines, the nominal crankshaft rotation speed is 4000–7000 min^{-1} , and its further increase is not expedient; since inertial loads and mechanical losses increase, the wear rate of the cylinder-piston group (CPG) and crank mechanism increases. The promising areas

G. V. Lomakin (✉) · V. M. Myslyayev
South Ural State University, 76, Lenin Avenue, Chelyabinsk 454080, Russia
e-mail: lomakingv@susu.ru

of development of spark-ignited engines are to force them at a medium effective pressure, for example, gas turbine boost. This technical solution is limited by a number of factors, including increased thermal and mechanical loading on the KSHM parts and the risk of detonation combustion.

2 Background to the Assignment of the Study

The thermal loading of the piston, as one of the most loaded elements of the cylinder-piston assembly with operating temperatures up to 300 °C and higher, limits the operation of the compression rings, limits the service life and deteriorates the properties of lubricating oil, causes cracks with subsequent melting of the piston edge, and inhibits the increase in engine power. The design features of the pistons are due to the configuration of the combustion chamber and measures that intensify heat removal from the thermally loaded elements: the placement of thermal barriers in the form of slots above the upper compression ring and an increase in the cross section of the piston at the transition point from the inner bottom to the skirt. For example, nonresistive or steel austenitic ring holders (inserts) are used as thermal barriers. In this case, a decrease in the piston temperature is a consequence of an increase in the thermal resistance of the compression ring zone [1–5].

3 Setting a Research Problem

Improving the design of high-powered engines pistons, in accordance with the tendency to reduce compression rings, is being developed in the following directions: intensification of local cooling, the use of materials with high resistance to heat changes, and composite structures. Serious attention is paid to the height of the “hot” belt of the piston head, determined by the distance from the bottom to the upper compression ring.

Application of various types of oil channels to the surface to evenly distribute the oil and the formation of oil trap grooves in the piston head helps to improve the lubrication conditions of the “piston-cylinder liner” interface, reduce specific pressures, and increase heat transfer from the piston [6–12].

Thus, the assessment of the thermal condition of the engine piston 4CH8,2/7,56, by the method of finite-element analysis, provides for the following sequence of actions:

- determination of the nature of changes in the pressure and temperature of gases in the engine cylinder through the synthesis of a working cycle;
- determination of heat exchange parameters from the side of working gases in the cylinder of the engine, lubricant, and associated elements of the cylinder-piston group;

- a description of the geometric characteristics of the element, the creation of a finite-element model, and the determination of heat exchange conditions at the boundaries of the computational domain;
- an indication of the thermophysical properties of materials and the implementation of calculation procedures for solving the heat conduction equation to find the temperature distribution in the element being analyzed.

4 Method of Defining Boundary Conditions

The boundary conditions of thermal loading of the engine piston 4CH8,2/7,56 are determined by the universal method, which allows to take into account all the components of the heat balance and features of gas-dynamic loading during the working cycle [1].

When assessing the piston strength parameters, as applied to the finite-element model, the boundary conditions of the force action on the nominal power modes are specified, the main of which are gas pressure and inertial force arising during reciprocating piston motion. The resulting force acting on the piston and applied to the axis of the piston pin is determined from the results of the kinematic and dynamic analysis of the crank mechanism.

To assess the temperature distribution over the surface and in the volume of the piston, solid-state and finite-element models have been created and are presented as a set of finite elements (Fig. 1).

It should be noted that the values of specific heat capacity and thermal conductivity coefficient for the piston material must be corrected depending on their temperature when estimating the temperature distribution on the surface and in the volume of the piston head and skirt.

The solution of the thermal problem is formed by a set of boundary conditions for heat transfer, including: the thermophysical properties of materials, equivalent heat transfer coefficients, and the resulting temperature of the medium [13–17].

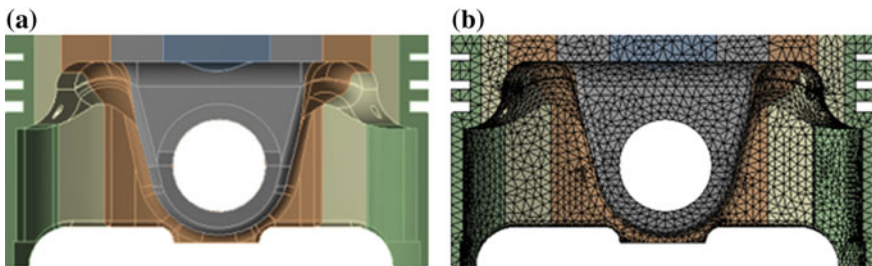


Fig. 1 a Solid piston model; b finite-element piston model

To preserve the adequacy of the shape of the model to the real object under study, the linear dimensions of the elements are chosen in such a way as to eliminate their influence on the geometrical characteristics of the piston and to ensure acceptable accuracy when performing the iterative process.

When determining the temperature distribution over the surface and in the volume of the piston, in accordance with the finite-element method, the functional equivalent to the differential heat equation and the boundary conditions is minimized. For this, the piston model is represented as a system of finite elements of a certain shape. Within each element, material properties are specified, under the assumption that when crossing the boundaries of adjacent elements, they change discretely and taking into account temperature dependence. As a function of the form describing the temperature distribution in the element, a polynomial is usually used. The system of unknowns is the temperature at the nodes of the faces of the elements, through which the temperature distribution within their limits is then expressed. Substituting the function of the form into the expression of the functional, find its minimum with respect to the temperatures of the nodes of the finite-element model under the given boundary conditions and, consequently, the temperature [18–20].

5 Evaluation of Calculation Results

The temperature level in the region of the first compression ring, unforced standard engine (Fig. 2) at the rated power mode at $P_e = 0,895$ MPa corresponds to a value of about 220–230 °C and seems acceptable. With an increase in the average effective pressure up to 1,815 MPa (Fig. 3) at a mode corresponding to the nominal power, temperatures in the region of the first compression ring increase by about 40–45 °C and seem excessively high from the point of view of ensuring acceptable operating conditions for lubricating oil. High-temperature coking, carbon formation, and possible “burning” of lubricating oil in the region of the first compression ring create prerequisites for the loss of mobility of the latter, which are unacceptable.

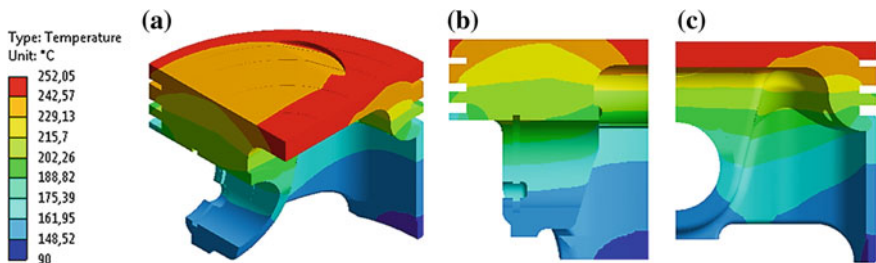


Fig. 2 Piston temperature distribution in isometric (a) longitudinal, (b) and transverse, (c) sections of an unforced 4CH8,2/7,56 engine in rated power mode ($F_e = 0,895$ MPa, $n = 5200$ min⁻¹)

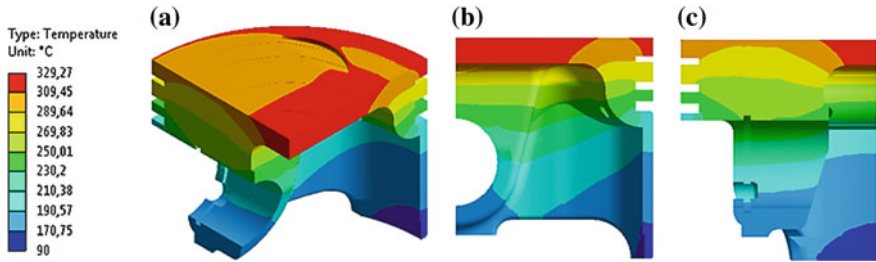


Fig. 3 Temperature distribution of the piston in isometric (a) longitudinal (b) and transverse, (c) sections of the forced 4CH8,2/7,56 engine by the effective pressure at the rated power mode ($P_e = 1,815 \text{ MPa}$, $n = 5200 \text{ min}^{-1}$)

One solution to this problem is to consider the possibility of using materials with improved mechanical properties, using oil cooling under pressure, developing a cooling cavity in the piston, putting a charge air cooler on the engine, and using specialized lubricants that work satisfactorily at elevated temperatures.

Static strength calculation of the piston was carried out at the crankshaft position; the corresponding angle of rotation is 390° . PKV tact expansion. According to the results of the synthesis of the operating cycle of the engine, at this moment, the maximum gas pressure in the cylinder is reached. In the course of the calculation, the total and axial deformations, normal, and equivalent stresses, the values of which were used to assess the safety margins, were determined.

To obtain the correct solution of the thermal-strength problem of estimating the level of deformations and stresses, a complex model of a fragment of a crank mechanism of the engine 4CH8,2/7,56 was used. An integrated model includes a piston, a piston pin, a connecting rod with a piston head bushing and liners and a fragment of a crankshaft.

Accounting for the force effect from the side of working gases in the cylinder of the 4CH8,2/7,56 gasoline engine is performed by applying maximum pressure to the corresponding piston surfaces, and taking into account the inertial force from the reciprocating moving masses (piston, piston and stop rings, piston pin, sleeve piston pin, and part of the mass of the rod) is made by reducing the maximum pressure by an amount corresponding to the specified force.

The use of a complex model when performing thermal analysis of strength is advisable, since it allows to take into account the rigidity of the KSHM fragment when transferring the force from the piston to the crankshaft and to ensure the correct solution of contact problems in the “piston—piston pin,” “piston pin—piston rod bushing” interfaces, “The connecting rod liner is the crankshaft connecting rod journal.”

To solve the problem, the method of static thermal-strength analysis was chosen under the assumption that the action of inertial loads and the processes of dissipation of thermal and mechanical energy do not have a significant effect on the behavior of the material of the coupling elements in the complex model under consideration.

As the resolving equation of the method of iterations used:

$$[K] \cdot \{U\} = \{N\},$$

where $[K]$ is the stiffness matrix; $\{N\}$ —force vector; $\{U\}$ —displacement vector.

When determining the deformation fields (Fig. 4) and stresses (Fig. 5) in the course of static strength analysis corresponding to a single-piston loading, it is assumed to find such a system for moving the points of the elastic material of the piston for which its total potential energy is minimal. The piston model is also replaced with a system of finite elements connected by nodal points on boundaries. The movements of these nodes constitute the main system of unknowns. Then select the form of the form function that determines the movement of any point in the element and on its faces. To set the system for external loads, a system of nodal displacements of the elastic body of the piston is determined, at which the minimum potential energy is achieved. The action of all external and internal force factors is replaced by the action of statically equivalent efforts at the nodes. For the elastic body of the piston, constraints are specified that limit its displacement as a whole. Determining the field of nodal displacements, approximating the field of displacements of points of an elastic body, determine the strain and stress in the element.

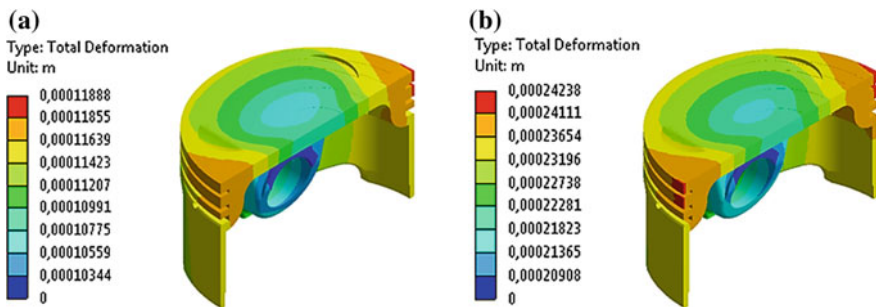


Fig. 4 The distribution of the total deformations of the piston gasoline engine 4CH8,2/7,56. **a** $P_e = 0,895 \text{ MPa}$, $n = 5200 \text{ min}^{-1}$; **b** $P_e = 1,815 \text{ MPa}$, $n = 5200 \text{ min}^{-1}$

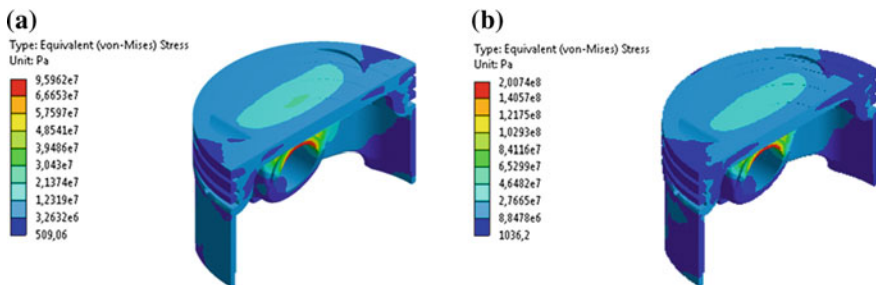


Fig. 5 Distribution of equivalent piston voltages (gasoline engine 4CH8,2/7,56. **a** $P_e = 0,895 \text{ MPa}$, $n = 5200 \text{ min}^{-1}$; **b** $P_e = 1,815 \text{ MPa}$, $n = 5200 \text{ min}^{-1}$

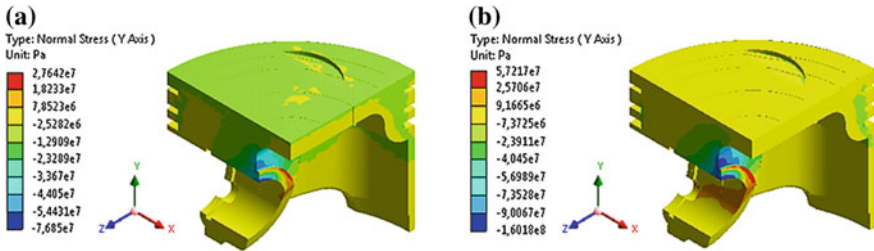


Fig. 6 Distribution of normal stresses (Y-axis) of the piston petrol engine 4CH8,2/7,56. **a** $Pe = 0,895 \text{ MPa}$, $n = 5200 \text{ min}^{-1}$; **b** $Pe = 1,815 \text{ MPa}$, $n = 5200 \text{ min}^{-1}$

It should be noted that the maximum total deformations of 0.11 mm and 0.24 mm for the mode of the terminal power when the engine is 4CH8,2/7,56 with different Pe ($Pe = 0,895$ and $Pe = 1,815$) are observed in the central part of the piston head, which has this section as the most loaded, which is quite consistent with the existing ideas about the mechanical loading of the piston, and at a given level of temperatures, and the mechanical loading achieved during the working cycle is quite acceptable.

The level of equivalent voltages of 96 and 200 MPa for the nominal power mode when the engine is 4 CH8,2/7,56 with different Pe , respectively (Fig. 5) indicates an acceptable level of mechanical loading, the values of which do not exceed the allowable values of point of view of the ultimate strength of the material used. The physical properties of the aluminum alloy AL-35 were set as the material of the piston in the calculation.

The distribution of normal stresses along the Y-axis of the piston is shown in Fig. 6.

The maximum level of normal compression stresses is approximately 77 and 160 MPa, respectively, for the modes of the nominal engine power at different Pe . The distribution of normal piston stresses along the Y-axis indicates an acceptable level of its mechanical loading, the values of which do not exceed the allowable values in terms of the tensile strength of the material used.

6 Conclusions and Recommendations Based on Research Results

Carrying out piston calibration calculations when forcing an engine to 4CH8,2/7,56 at an average effective pressure, characterized by elevated values of specific indicators, allows to predict the behavior of the piston under conditions of real thermal loading and force action, and, if necessary, to introduce restrictions on the degree of forcing of the engine 4CH8,2/7,56 by Pe .



As a result of carrying out calibration calculations of the thermal and stress-strain state of the engine piston 4CH8,2/7,56, the following recommendations can be formulated:

- improve the piston cooling efficiency with lubricating oil and use special lubricating oil that meets the requirement of reduced coking at high temperatures;
- use of a charge air cooler at a pressure of pressurization more than 0.15 MPa;
- reduction of compression ratio to 9–9.5 units;
- the cross section of the second compression ring is recommended to be made in the form of a trapezoid in order to increase its efficiency at high operating temperatures;
- to reduce the level of thermal loading, to increase the heat removal from the cylinder liner by intensifying the movement of the cooling fluid washing its upper region in the cavity of the cooling system.

References

1. Lomakin GV, Matsulevich MA (2014) Method of estimating boundary conditions for solving the problem of determining the thermal state of a piston of a gasoline engine. *Bull SUSU Ser Mashinostroenie* 14(1):26–31
2. Lazarev EA (2011) Guidelines for practical training on the discipline of thermal and mechanical tension of piston engines. Chelyabinsk, Russia
3. Kostin AK, Larionov VV, Mikhailov LI (1979) Heat density of internal combustion engines. USSR, Leningrad
4. Woschni G, Anisitis F (1973) Eine Methode zur Vorausberechnung der Änderung des Brennverlaufs mittelschnellaufender Dieselmotoren bei geänderten Betriebs. *MTZ* No 4:160–165
5. Chaynov ND, Zarenbin VG, Ivaschenko NA (1977) Thermomechanical intensity of engine parts. USSR, Moscow
6. Rosenblit GB (1977) Heat transfer in diesel engines. USSR, Moscow
7. Yudaev BN (1988) Technical thermodynamics. Heat transfer. USSR, Moscow
8. Zhdanovsky NS, Nikolaenko AV (1981) Reliability and durability of automotive engines. USSR, Leningrad
9. Petrichenko RM (1983) Physical bases of intra-cylinder processes in internal combustion engines. USSR, Leningrad
10. Vyubov DN, Ivaschenko VI, Ivin NA et al (1983) Internal combustion engines. Theory of piston and combined engines. USSR, Moscow
11. Lee HS, Cholewczynski W (2003) A study on convection and boiling heat-transfer modes in a standard engine cooling system. Brighton, UK
12. Menter FR et al. (2004) A correlation based transition model using local variables. *ASME TURBO EXPO ASME-GT2004-53452*
13. Zaitsev LK (1978) Study of the working cycle when forcing a tractor diesel engine using mathematical modeling. Dissertation, Chelyabinsk Polytechnic Institute of Chelyabinsk
14. Mikheev MA, Mikheeva IM (1977) Basics of heat transfer. USSR, Moscow
15. Chernyshev GD, Khachiyani AS, Picus VI (1986) Workflow and thermal density of engine parts. USSR, Moscow

16. Warriar GR, Dhir VK (2006) Heat transfer and flux partitioning during subcooled flows nucleate boiling. *Heat Transfer* 128:1243–1256
17. Zieher F, Langmayr F, Jelatancev A et al. (2005) Iron cylinder heads thermal mechanical fatigue simulation. SAE World Congress—12
18. Menter FR, Langtry RB, Völker S (2006) Modeling for general CFD applications in aeronautics. *Flow Turbul Combust* 77:277. <https://doi.org/10.1007/s10494-006-9047-1>
19. Xu X, Ul Weiss (2002) Integrated CAD/CAM/CAE based on multi-model technology. *Int J Autom Technol* 3(2):47–52
20. Frank Th (2006) Multiphase modeling and simulation of the radiation reagent technology. Stockholm, Sweden

Losses Analysis in Gas Turbine Engines Flow Parts



I. A. Krivosheev, N. B. Simonov and K. E. Rozhkov

Abstract The methods of loss in the flow parts of power plants (PP) of aircraft, gas-pumping units (GPU), gas turbine engines (GTE), and gas turbine plants (GTP) accounting are considered. A new method for approximating gas-dynamic characteristics and calculating the efficiency coefficients of the units including compressors and turbines optimizing their geometry and modes is proposed. To verify the method, the results of factory tests, 2D and 3D CAD/CAE-simulation of the flow and gas-dynamic characteristics of the flow part components, including blowing of the blade profile gratings were used. It is shown that this method can be effectively used to optimize the flow parts geometry and to select the modes of operation of input and output devices, blade rims as part of compressors and turbines, and transitional ducts between cascades. It is suggested to use the method to control the change in the characteristics of the GTE units during operation. This can significantly improve the accuracy of parametric diagnostic GTP and GTD. The proposed method can be used to monitor the state of aggregates and systems in the power engineering, in transport, and in other areas.

Keywords Flow · Compressor · Turbomachinery · Turbine · Characteristics · Losses · Efficiency · Parameters · Modes · Diagnostics · Simulation

1 Introduction

Currently, when choosing the geometry [1–10] and operating modes [11–20] of the flow parts of the aircraft PU and GPU, GTE and GTP in their composition, as well as their units—compressors, turbines, and transition ducts between cascades, conditional optimization is carried out. At the same time, the permissible levels of efficiency and losses, the reserves of gas-dynamic stability and strength in compressor and turbine, the required throughput (G_{dp} and A_t), pressure ratio (in

I. A. Krivosheev · N. B. Simonov (✉) · K. E. Rozhkov
Ufa State Aviation Technical University, 12, K. Marx Str., Ufa 450008, Russia
e-mail: sventigo@yandex.ru

© Springer Nature Switzerland AG 2020
A. A. Radionov et al. (eds.), *Proceedings of the 5th International Conference on Industrial Engineering (ICIE 2019)*, Lecture Notes in Mechanical Engineering,
https://doi.org/10.1007/978-3-030-22041-9_75

697

compressors), and the power N_T (in turbines) are considered as limitations, and dimensions (diameters and length) and mass are considered as the goal function (with their minimization). In the number of cases, when designing blades (DBs) in turbines and compressors (with the choice of reactivity ρ , angles of attack i , distribution of work in stages ...), the geometry of the transition ducts between compressor and turbine cascades losses is minimized, and the coefficient of total pressure recovery ratio and efficiency are maximized. In this case, losses in the interblade channels (IBC) of the compressors are taken into account with the use of the coefficient of hydraulic losses ζ (in RB—rotary blade, in GV—guide vane)

$$\zeta_{w_{RB}} = 2(P_{w_1}^* - P_{w_2}^*) / (\rho w^2)_1 \quad (1)$$

$$\zeta_{GV} = 2(P_2^* - P_3^*) / (\rho c^2)_2 \quad (2)$$

In the turbines IBC are used speed coefficients (in the NA-nozzle apparatus $\psi_{NA} = c_1/s_{1s}$, in the RB—rotary blade $\varphi_{RB} = w_2/w_{2s}$), energy ξ (in GV $\xi_{GV} = c_1^2/c_{1s}^2$, in the RB rotary blade $\xi_{RB} = w_2^2/w_{2s}^2$). In addition, for all flow parts elements, the total pressure reduction coefficient $\sigma = P_{i+1}^*/P_i^*$ is used. Here, P is the pressure, c is the velocity in absolute motion, w is the velocity in relative motion, $*$ is the total value of the parameter, indices: in the compressor, one is the input to the RB, 2 is the output from the RB and the input to the GV, and 3 is the output from GV; in the turbine, 1 is the output from the NA, and 2 is the output from the NA. Index i —input in the IBC, index $i+1$ —exit from the IBC. With the use of these coefficients, the efficiency (η) of the nodes and flow parts components is calculated during optimization. However, the initial approximations with this optimization are still selected on the basis of insufficiently precise recommendations, with a fairly wide range of parameters. In addition, for full-fledged optimization, these are not the values of these coefficients “at the point,” only for a particular mode or combination of parameters, but in the form of the gas-dynamic characteristic (GDC) of the flow part element.

2 The Proposed Method of Loss Analysis in the Elements of the GTE

In this paper, it is proposed to use the streamline tracking method, proposed by the authors, to analyze the losses in the elements of the flow part and calculate the efficiency of the units. It is based on the simultaneous consideration of streamlines in relative and absolute motion when particles move along the current surfaces in flow parts, GTEs and GTPs, and units in their composition. All the elements of the flow part in the composition of the aircraft PU and GPA, GTE and GTP, as well as units in their composition work in the mode of diffusers (with braking of the flow) and confusers (with acceleration of the flow). At the same time, the aircraft air

intake (AI) during the operation of the GTE on a fixed aircraft and at the beginning of acceleration during takeoff, at the end of braking during landing and when taxiing at the aerodrome operates in a confusor mode. During the flight of the aircraft, the AI performs the function of a diffuser. All the other elements of the aircraft PU and GPA (input and output devices), GTE and GTP in their composition, as well as their components—compressors, turbines, and transitional ducts between cascades in all modes, perform the functions of either diffusers or confusors. For example, in the absolute movement in the IGV of the compressor or NA of the turbine

$$\zeta_{IGV,NA} = 2(P_0^* - P_1^*)/(\rho c^2)_1. \quad (3)$$

For such flow part components, the transition to the total pressure reduction coefficient σ is performed by the formulas: in absolute motion for the diffuser

$$\sigma = 1 - \zeta \varepsilon(\lambda_i) \lambda_i^2 (k/(k+1)) \approx 1 - \zeta [1 - \pi(\lambda_i)] \quad (4)$$

Differ in equation for confusor is that instead of (λ_i) use (λ_{i+1}) .

For example, in absolute motion for the compressor IGV and turbine NA, for GV of the compressor, In the relative motion for the compressor RB, for turbine RB

$$\sigma_{NA(IGV)} = 1 - \zeta_{NA(IGV)} \varepsilon(\lambda_1) \lambda_1^2 (k/(k+1)) \approx 1 - \zeta_{NA(IGV)} [1 - \pi(\lambda_1)] \quad (5)$$

$$\sigma_{GV} = 1 - \zeta_{GV} \varepsilon(\lambda_2) \lambda_2^2 (k/(k+1)) \approx 1 - \zeta_{GV} [1 - \pi(\lambda_2)] \quad (6)$$

$$\sigma_{wRB} = 1 - \zeta_{wRB} \varepsilon(\lambda_{w1}) \lambda_{w1}^2 (k/(k+1)) \approx 1 - \zeta_{wRB} [1 - \pi(\lambda_{w1})] \quad (7)$$

$$\sigma_{wRB} = 1 - \zeta_{wRB} \varepsilon(\lambda_{w2}) \lambda_{w2}^2 (k/(k+1)) \approx 1 - \zeta_{wRB} [1 - \pi(\lambda_{w2})] \quad (8)$$

Figure 1 shows the correlation between the magnitude of the loss coefficient and the efficiency for the lattice profiles.

3 Analysis of Losses in the Elements of the Flow Part of the GTE Using the Streamline Tracking Method

The streamline tracking method, proposed by the authors, suggests simultaneous consideration of the motion of particles in the compressors and turbines flow part along trajectories in relative and absolute motion. In this case, the change in the relative motion T , along the slow part of the total temperature in the relative motion T , is determined by the theoretical pressure factor of the stator guide vanes, which in turn is determined by the geometry of the blade profiles (BP) of the GV and IGV

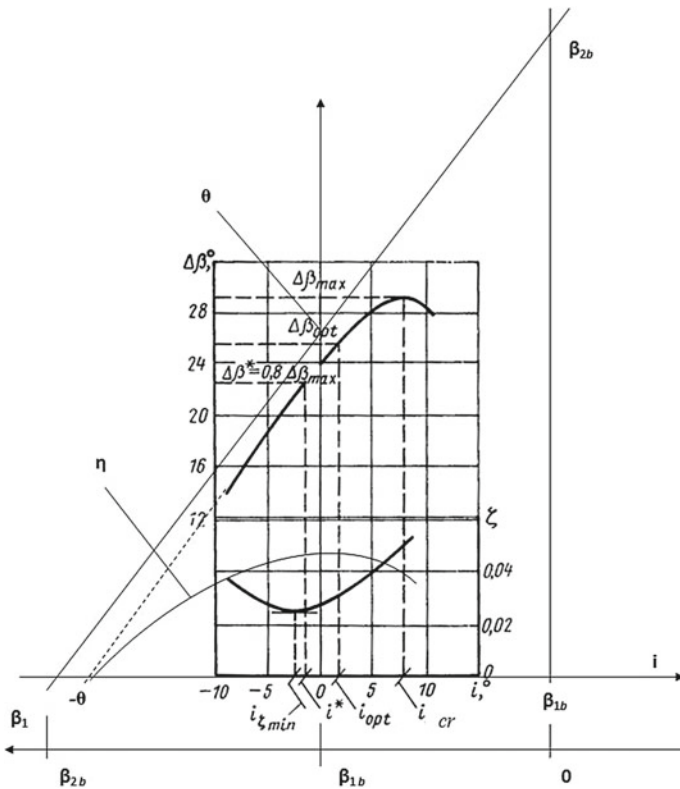


Fig. 1 Correlation between the magnitude of the loss coefficient and the efficiency for the lattice profiles

in the compressor, NA in the turbine, while in relative motion the stator rotates with that same frequency as the rotor, but in the opposite direction, in each section, the virtual circumferential velocity of the stator $u_w = -u$. Trajectories of motion along the current surfaces, along the rotor hub (cross-sections “w”), along the inner surface of the body (section “k”), and along the intermediate current surfaces are considered (for example, the effective “eff” surface for which at the entrance to the one stage

$$D_{\text{eff}} = D_{\text{sh}} \sqrt{(1 + \bar{a}^2)/2} \tag{9}$$

Along each current surface for the compressor,

$$\sigma = \prod \sigma_i. \tag{10}$$



Here, σ_i is the indices for the individual steps. For each i -stage

$$\sigma_i = [\sigma_{IGV} \sqrt{\sigma_{AG_1} \sigma_{AG_{1w}}} \sigma_{RB_w} \sqrt{\sigma_{AG_2} \sigma_{AG_{2w}}} \sigma_{GV}]_i \tag{11}$$

Here, σ_{IGV} , σ_{AG_1} , σ_{AG_2} , σ_{GV} —indices in absolute motion for the elements of the flow part stator (IBC IGV, axial clearance between IGV and RB, RB and GV, GV), $\sigma_{AG_{1w}}$, $\sigma_{AG_{2w}}$, σ_{RB_w} are the indices in relative motion for the elements of the inverter rotor (IBC RB, axial gaps between IGV and RB, RB and GV). In this case, σ_{AG_1} and σ_{AG_2} are determined in absolute motion with respect to λ_{w_1} and λ_{w_2} . and are determined in relative motion with respect to λ_{w_1} and λ_{w_2} . Similarly, in a turbine for each stage

$$\sigma_i = [\sigma_{NA} \sqrt{\sigma_{AG} \sigma_{AG_w}} \sigma_{RB_w}]_i \tag{12}$$

Here σ_{NA} , σ_{AG} —are indicators in absolute motion for the elements of the flow part stator (IBC NA, axial gaps between NA and RB), σ_{AG_w} , σ_{RB_w} —are indicators in relative motion for the elements of the rotor flow part (IBC RB, axial gaps between NA and RB). σ_{AG} is determined in absolute motion with respect to λ_1 . σ_{AG_w} is determined in the relative motion with respect to λ_{w_1} .

The authors proposed to determine the idealized change in the total pressure by the actual change in the total temperature T^* in the blade profile gratings, the stage and the multistage compressor or turbine.

In the compressor RB, in the compressor GV, in the compressor stage, in MSC,

$$\pi_{RB_{ID}}^* = (T_2^*/T_1^*)^{(k-1)/k} \tag{13}$$

$$\pi_{GV_{ID}}^* = (T_3^*/T_2^*)^{(k-1)/k} = 1 \tag{14}$$

$$\pi_{ST_{ID}}^* = (T_2^*/T_1^*)^{(k-1)/k} \tag{15}$$

$$\pi_{C_{ID}}^* = (T_C^*/T_1^*)^{(k-1)/k} \tag{16}$$

The actual value of the total pressure ratio in the RB

$$\pi_{RB}^* = \pi_{RB_{ID}}^* \sigma_{RB_w} \tag{17}$$

If there is an IGV before RB, then total pressure ratio should be determined in the IGV-RB system and $\pi_{RB_{ID}}^*$ should be multiplied at

$$\sigma_{IGV} \sqrt{\sigma_{AG_1} \sigma_{AG_{1w}}} \sigma_{RB_w} \tag{18}$$



In GV

$$\pi_{GV}^* = \pi_{GV_{ID}}^* \sigma_{GV} = \sigma_{GV} \quad (19)$$

Total pressure ratio in compressor stage is

$$\pi_{ST}^* = \pi_{ST_{ID}}^* \sigma_{ST}. \quad (20)$$

Here,

$$\sigma_{ST} = \sigma_{IGV} \sqrt{\sigma_{AG_1} \sigma_{AG_{1w}}} \sigma_{RB_w} \sqrt{\sigma_{AG_2} \sigma_{AG_{2w}}} \sigma_{GV}. \quad (21)$$

In MSC

$$\pi_C^* = \pi_C^* \sigma_C. \quad (22)$$

Here,

$$\sigma_C = \prod \sigma_{ST_i}. \quad (23)$$

Similarly, in the turbine in NA, in turbine RB, in turbine stage are

$$\pi_{NA_{ID}}^* = (T_0^*/T_1^*)^{(k_G-1)/k_G} = 1 \quad (24)$$

$$\pi_{RB_{ID}}^* = (T_1^*/T_2^*)^{(k_G-1)/k_G} = (T_0^*/T_2^*)^{(k_G-1)/k_G} \quad (25)$$

$$\pi_{ST_{ID}}^* = (T_0^*/T_2^*)^{(k_G-1)/k_G} \quad (26)$$

Given the total pressure loss, the actual total pressure ratio in NA, in RB, in turbine stage, and in MST, is:

$$\pi_{NA}^* = \pi_{NA_{ID}}^* \sigma_{NA} = \sigma_{NA} \quad (27)$$

$$\pi_{RB}^* = \pi_{RB_{ID}}^* / \sigma_{RB_w} \quad (28)$$

$$\pi_{ST_T}^* = \pi_{ST_{ID}}^* / \sigma_{ST_T}; \quad (29)$$

$$\pi_T^* = \pi_{T_{ID}}^* / \sigma_T. \quad (30)$$

$$\sigma_{ST_i} = \sigma_{NA} \sqrt{\sigma_{AG} \sigma_{AG_w}} \sigma_{RB_w}, \quad (31)$$

$$\sigma_T = \prod \sigma_{ST_i}. \quad (32)$$

In compressor, in the stage, in the stage are

$$\left(T_{C_S}^*/T_1^*\right) = \left(T_C^*/T_1^*\right) \sigma_C^{(k-1)/k}. \quad (33)$$

$$\left(T_{3_S}^*/T_1^*\right) = \left(T_C^*/T_1^*\right) \sigma_{RB_w}^{(k-1)/k}. \quad (34)$$

$$\left(T_{2_S}^*/T_1^*\right) = \left(T_C^*/T_1^*\right) \sigma_{RB_w}^{(k-1)/k}. \quad (35)$$

With this in mind, the “scapular” (“channel”) efficiency along the selected current surface: for the compressor, for stage, for RB, for GV, is

$$\eta_{Cu}^* = 1 - \left(1 - \sigma_C^{(k-1)/k}\right) \left(c_p T_1^*/H_{T_C} + 1\right), \quad (36)$$

$$\eta_{STu}^* = 1 - \left(1 - \sigma_{ST}^{(k-1)/k}\right) \left(c_p T_1^*/H_{T_{ST}} + 1\right) = 1 - \left(1 - \sigma_{ST}^{(k-1)/k}\right) \left(c_p T_1^* u^2 / \bar{H}_{T_{ST}} + 1\right) \quad (37)$$

$$\eta_{RBu}^* = 1 - \left(1 - \sigma_{RB_w}^{(k-1)/k}\right) \left(c_p T_1^*/H_T + 1\right) = 1 - \left(1 - \sigma_{RB_w}^{(k-1)/k}\right) \left(c_p T_1^* u^2 / \bar{H}_T + 1\right) \quad (38)$$

$$\begin{aligned} \eta_{GVu}^* &= 1 - \left(1 - \sigma_{GV}^{(k-1)/k}\right) \left(c_p T_1^*/H_{T_{ST}} + 1\right) \\ &= 1 - \left(1 - \sigma_{GV}^{(k-1)/k}\right) \left(c_p T_1^*/H_{T_w} + 1\right) = 1 - \left(1 - \sigma_{GV}^{(k-1)/k}\right) \left(c_p T_1^* u^2 / \bar{H}_{T_w} + 1\right) \end{aligned} \quad (39)$$

wherein

$$\bar{H}_{T_w} = 1 - \bar{c}_{2_a} / \tilde{c}_{3_a} \quad (40)$$

here

$$\bar{c}_{2_a} = 1 / (\text{ctg} \beta_2 + \text{ctg} \alpha_2), \quad \tilde{c}_{3_a} = 1 / (\text{ctg} \beta_2 + \text{ctg} \alpha_3). \quad (41)$$

Similarly, in the turbine, in the turbine stage, in turbine NA, in turbine RB are

$$T_{TS}^*/T_0^* = \left(T_T^*/T_0^*\right) (\sigma_T)^{(k_G-1)/k_G} \quad (42)$$

$$T_{2_S}^*/T_0^* = \left(T_2^*/T_0^*\right) (\sigma_{ST_T})^{(k_G-1)/k_G} \quad (43)$$

$$T_{1S}^*/T_0^* = (T_1^*/T_0^*)(\sigma_{NA})^{(k_G-1)/k_G} = (\sigma_{NA})^{(k_G-1)/k_G} \quad (44)$$

$$T_{2S}^*/T_0^* = (T_2^*/T_0^*)(\sigma_{RB_w})^{(k_G-1)/k_G} \quad (45)$$

With this in mind, the “blade” (“channel”) efficiency along the selected current surface: for the turbine, for stage, for RB, for NA, is

$$\eta_{T_u}^* = 1/\left[1 + (1 - \sigma_T^{(k_G-1)/k_G})(c_p T_0^*/L_u + 1)\right] \quad (46)$$

$$\eta_{T_s}^* = 1/\left[1 + (1 - \sigma_{ST}^{(k_G-1)/k_G})(c_p T_0^*/L_u + 1)\right] \quad (47)$$

$$\eta_{RB_{T_u}}^* = 1/\left[1 + (1 - \sigma_{RB_{T_w}}^{(k_G-1)/k_G})(c_p T_0^*/L_u + 1)\right] \quad (48)$$

$$\eta_{NA_u}^* = 1/\left[1 + (1 - \sigma_{NA_T}^{(k_G-1)/k_G})(c_p T_0^*/L_u + 1)\right] \quad (49)$$

Both for the compressor and for the turbine, the internal isentropic efficiency is determined taking into account the end losses (losses in the radial gap and friction losses—disks, friction of the working fluid about the surface of the body, and the rotor hub): in the compressor and in turbine

$$\eta_C^* = \eta_{Cu}^* \bar{\eta}_{Shroud} = \eta_{Cu}^* \bar{\eta}_{rad} \bar{\eta}_f \quad (50)$$

$$\eta_T^* = \eta_{Tu}^* \bar{\eta}_{Shroud} = \eta_{Cu}^* \bar{\eta}_{rad} \bar{\eta}_f \quad (51)$$

The above dependences allow to build the efficiency lines on the characteristics of compressors and turbines, stages and blade profile gratings in their composition and reasonably choose the values of the reactivity ρ , the angles of attack i , the density of the b/t profiles, etc. The analysis of the results of 3D CAD/CAE-modeling, compressor testing allows to organize and accelerate the development of compressors and turbines.

4 Conclusion

The proposed method for approximating the gas-dynamic characteristics and calculating the efficiency coefficients of the units, including compressors and turbines, allows to organize the optimization of their geometry and modes. This method can be effectively used to optimize the flow part geometry and to select the modes of operation of input and output devices, blades in the composition of compressors and turbines, and transitional ducts between cascades. In addition, the proposed method can be used to control the change in the characteristics of the GTE units in

operation. This makes it possible to significantly increase the reliability of the parametrical diagnostics of gas turbine engines in the composition of aircraft PU and gas turbine engines in the GPA. The proposed method can be used to monitor the state of aggregates and systems in the energy sector, in transport, and in other areas.

References

1. Johnson IA (1965) Aerodynamic design of axial-flow compressors. NASA. Revised. Scientific and Technical Information Division
2. Horlock JH (1973) Axial compressors. Butterworth, reprinted with supplementary material, Krieger Publishing Co. Inc
3. Howell AR (1945) Fluid dynamics of axial compressors, proceedings. Inst Mech Eng 153:441–452
4. Moore RD, Reid L (1980) Performance of single-stage axial-flow transonic compressor with rotor and stator aspect ratios of 1.19 and 1.26, respectively and with design pressure ratio of 2.05. NACA
5. Koch CC, Smith LH (1976) Loss sources and magnitudes in axial-flow compressors. Trans ASME J Eng for Power 98A(3):411–424
6. Lieblein S (1960) Incidence and deviation-angle correlations for compressor cascades. J Basic Eng, Trans ASME, D 82:575–587
7. Lieblein S (1959) Loss and stall analysis of compressor cascades. J Basic Eng, Trans ASME, Ser D 81:387–400
8. Lieblein S, Roudeshian WH (1965) Theoretical loss relations for low-speed two-dimensional-cascade flow, NACA
9. Schoeiri MT (1997) Advanced compressor loss correlations. Int J Rotat Mach 3(3):163–177
10. Serovy GK (1981) Axial-flow turbomachine through-flow calculation methods through flow calculations in axial turbomachines, AGARD-AR-175
11. Falck N (2008) Axial flow compressor mean line design, s.l.: Division of Thermal Power Department of Energy Sciences Lund University, Master Thesis
12. Veres JP (2009) Axial and centrifugal compressor mean line flow analysis method, NASA
13. Kuprik VV, Balaban YuN, Hoteenkov IA (2016) Method of assessing the technical condition of the gas turbine engine (A method for assessing the technical state of a gas turbine engine). Gas Turbine Technologies, pp 32–34
14. Chichkov BA (2005) Modeli i parametricheskaya diagnostika aviatsionnykh dvigateley (Models and parametric diagnostics of aircraft engines). MSTU, Moscow
15. Eliseev YS, Krymov V, Malinovsky KA, Popov VG (2002) Tekhnologiya ekspluatatsii, diagnostiki i remonta gazoturbinnnykh dvigateley (Technology of operation, diagnostics and repair of gas turbine engines). Higher School, Moscow
16. Lozitsky LP (1982) Evaluation of the technical condition of aviation GTE (Estimation of technical condition of aviation GTE). Transport, Moscow
17. Stepanenko VL (1985) Prakticheskaya diagnostika aviatsionnykh gazoturbinnnykh dvigateley (Practical diagnostics of aviation gas turbine engines) Transport, Moscow
18. Sheremetev AV (2003) Analiz opyta ekspluatatsii zarubezhnykh gazoturbinnnykh dvigateley po tekhnicheskomu sostoyaniyu (Analysis of operational experience of foreign gas turbine engines according to the technical state). Aviat Space Technol Technol 40(5):5–9

19. Kurochkin VN, Nazarenko SA, Shcherbak NA (2015) Vliyaniye tekhnicheskogo obsluzhivaniya i remontov na resurs oborudovaniya dlya pererabotki maslichnykh kul'tur (Influence of technical maintenance and repairs on the resource of equipment for processing oil-bearing crops). Prog Mod Sci Educ 3:83–91
20. Tarasenko AV, Kondratiev YuV (2016) Otsenka tekhnicheskogo sostoyaniya ustroystv kompensatsii reaktivnoy moshchnosti v tyagovoy seti (Evaluation of the technical condition of reactive power compensation devices in a traction network). Prog Mod Sci Educ 10 (5):155–157

Transfer Functions for Shearing Stress in Nonstationary Fluid Friction



V. Sokolov

Abstract The dependence in the operator form for the shearing stress in nonstationary fluid friction is obtained. The transfer functions for the shearing stress of the velocity of the moving element and the pressure gradient are determined. Based on the analysis of amplitude-frequency characteristics, the boundaries of a quasi-stationary approach are established for calculating the forces of nonstationary viscous friction on the moving elements of hydraulic devices. To calculate the shearing stress, considering the effect of the inertia of the flow structure, we consider a nonstationary plane laminar motion of incompressible fluid in the gap between a moving and a fixed element in the Cartesian coordinate system. The solution of the equation of motion in partial derivatives is fulfilled using the Laplace transform. The estimation of the boundaries of the quasi-stationary approach to the calculation of the forces of nonstationary viscous friction is made from the amplitude-frequency characteristics of vibrations of the moving element and the pressure gradient. As the boundaries of quasi-stationarity, the frequencies at which the amplitude changes by more than 5% are adopted.

Keywords Fluid friction · Shearing stress · Equation of motion · Kinematic viscosity · Transfer function

1 Introduction

The most difficult and responsible stage in the calculation and development of new elements and devices, machines and mechanisms, drives and control systems is the development of the mathematical models of the nonstationary workflows occurring in them [1–4]. It is very important not to allow excessive unjustified complication of the mathematical models as they may not be suitable for practical use. At the

V. Sokolov (✉)

Volodymyr Dahl East Ukrainian National University, 59-a, Central Ave.,
Severodonetsk 93400, Ukraine
e-mail: sokolov.snu.edu@gmail.com

© Springer Nature Switzerland AG 2020

A. A. Radionov et al. (eds.), *Proceedings of the 5th International Conference on Industrial Engineering (ICIE 2019)*, Lecture Notes in Mechanical Engineering,

https://doi.org/10.1007/978-3-030-22041-9_76

707

same time, neglecting phenomena that significantly affect the work processes can make the model too rough, not providing the required accuracy and also not reflecting the main features of the ongoing processes.

The nonstationary hydromechanical processes refer to the complex physical phenomena in which unsteady fluid flows arise with changes in velocities and pressures not only in time but also in the space occupied by flow [5–8]. The direct description of such processes leads to the systems of nonlinear equations in partial derivatives, and the boundary conditions necessary for the solution of these equations are often themselves differential equations describing the dynamic processes in those devices with which fluid flows interact. The use of such complex models requires the implementation of labor-intensive calculations, which may not yield visible results.

The important parameter in calculations of hydromechanical processes is the force of viscous fluid friction, which is characterized by the shearing stress arising in the working medium contacting the surface of the moving element of the actuating, regulating, distributing, or auxiliary hydraulic devices [9–14]. In the presence of a gap between the surfaces of the elements, the shearing stresses arise when relative motion of these surfaces and the motion of the medium are affected by the pressure difference.

2 Literature Review

The traditional approaches [5, 15–20] to the development of mathematical models of nonstationary hydromechanical processes are mainly based on the fact that real flows are replaced by a successive sequence of flows with a quasi-stationary distribution of hydrodynamic quantities over the live flow cross-section. This allows us to introduce into account the coefficients and characteristics obtained for stationary flows. In fact, the structure of nonstationary flows differs from the quasi-stationary flow [1, 5, 8], and it is not always known how and under what conditions such a difference can affect the change in hydrodynamic characteristics.

In real devices, the gap is small in such a way that the flow is considered as a laminar plane between parallel walls (Fig. 1), and the velocity distribution (Fig. 2) has the form [6, 7, 21, 22]

$$\frac{u}{u_0} = \frac{\delta^2}{2\rho\nu} \frac{dp}{dx} \frac{y}{\delta} \left(1 - \frac{y}{\delta}\right) + \frac{y}{\delta}, \quad (1)$$

where x, y —coordinates; u —velocity of the fluid in the gap; u_0 —speed of movement of the moving element (or relative speed of motion of the surfaces); δ —size of the gap; dp/dx —pressure gradient; and ρ, ν —density and kinematic viscosity of the fluid.

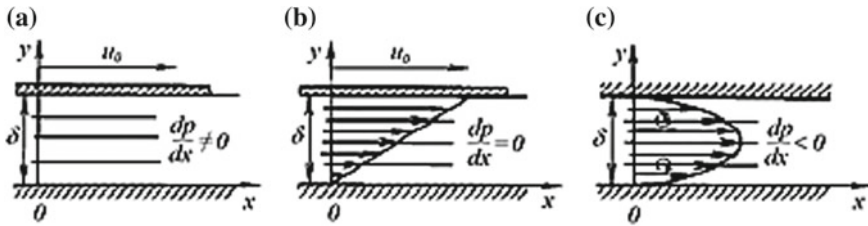
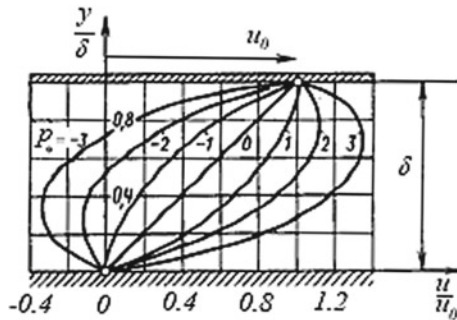


Fig. 1 Laminar flow between parallel planes. **a** Flow scheme; **b** velocity distribution in the absence of a pressure gradient (Couette flow); **c** velocity distribution for fixed boundary planes (flow in a flat channel)

Fig. 2 Dimensionless velocity profiles for the general case of fluid flow between parallel walls ($p_* = -\delta^2 dp/dx / (2\rho\nu u_0)$)



The shearing stress is calculated on the basis of the velocity distribution (1) according to the Newton’s law of viscous friction [7, 19, 21].

The aim of the paper is to obtain dependencies for calculating the shearing stress in nonstationary fluid friction, considering the inertia of the change in the flow structure in the gap, and also estimating the boundaries of the quasi-stationary approach for calculating the forces of nonstationary viscous friction on the moving elements of hydraulic devices.

3 Research of Shearing Stress in Nonstationary Fluid Friction

Let the speed of motion of the moving element (or the relative speed of motion of surfaces) be nonstationary

$$u_0 = V(t). \tag{2}$$

Then, for a quasi-stationary approach, the shearing stress on the moving surface (quasi-stationary shearing stress), taking (1) into account,

$$\tau_{qs}^0 = \rho v \frac{du}{dy} = -\frac{\delta}{2} \frac{dp}{dx} + \frac{\rho v}{\delta} V(t). \quad (3)$$

We transform (3) by the Laplace [23–25] and establish the transfer functions for the quasi-stationary shearing stress with respect to the velocity of the moving element and the pressure gradient

$$W_{\tau V, qs}(s) = \frac{\tau_{qs}^0(s)}{V(s)} = k_{\tau V}. \quad (4)$$

$$W_{\tau p, qs}(s) = \frac{\tau_{qs}^0(s)}{\frac{dp}{dx}(s)} = k_{\tau p}. \quad (5)$$

where s —Laplace variable and transfer coefficients $k_{\tau V} = \rho v/\delta$, $k_{\tau p} = -\delta/2$.

In order to obtain the transfer functions for the shearing stress, considering the influence of the inertia of the flow structure, we consider the nonstationary laminar motion of incompressible fluid in the gap between fixed and moving elements in the Cartesian coordinate system (Fig. 1). Assuming the flow is plane, the equation of fluid motion is represented in the known form [6]

$$\frac{\partial u}{\partial t} = -\frac{1}{\rho} \frac{\partial p}{\partial x} + \nu \frac{\partial^2 u}{\partial y^2}. \quad (6)$$

For the fluid velocity u , which is the function of time t and the coordinate y , we define the boundary conditions:

$$\begin{cases} u = 0, & y = 0; \\ u = V(t), & y = \delta. \end{cases} \quad (7)$$

To simplify the mathematical calculations, we make the change of variables

$$z = y - \delta, \quad (8)$$

and also consider that for the flow under consideration

$$\frac{\partial p}{\partial x} = \frac{dp}{dx}. \quad (9)$$

Taking (8, 9) into account, in place of (6, 7) we have:

$$\frac{\partial u}{\partial t} = -\frac{1}{\rho} \frac{dp}{dx} + \nu \frac{\partial^2 u}{\partial z^2}, \quad (10)$$

$$\begin{cases} u = 0, & z = -\delta; \\ u = V(t), & z = 0. \end{cases} \quad (11)$$

Applying the one-dimensional Laplace transform under zero initial conditions, we obtain instead of the partial differential equation (10) the equation in ordinary derivatives

$$\frac{d^2 u(s)}{dz^2} - \frac{s}{\nu} u(s) = \frac{p(s)}{\rho s}, \quad (12)$$

where $u(s)$, $p(s)$ —Laplacian image of velocity u and the pressure gradient dp/dx .

The solution of Eq. (12) has the form

$$u(s) = A_1 \exp\left(z\sqrt{s/\nu}\right) + A_2 \exp\left(-z\sqrt{s/\nu}\right) - \frac{p(s)}{\rho s}, \quad (13)$$

where A_1 , A_2 —integration constants.

The shearing stress on the surface of the moving element is found according to the Newton's law of viscous friction

$$\tau^0(s) = \rho\nu \left. \left(\frac{\partial u(s)}{\partial y} \right) \right|_{y=\delta} = \rho\nu \left. \left(\frac{\partial u(s)}{\partial z} \right) \right|_{z=0}. \quad (14)$$

Substituting (13) into (14), we have

$$\tau^0(s) = \rho\nu\sqrt{s/\nu}(A_1 - A_2). \quad (15)$$

The value $A_1 - A_2$ is determined using the boundary conditions (11) and the obtained solution (13):

$$\begin{cases} 0 = A_1 \exp\left(-\sqrt{\delta^2 s/\nu}\right) + A_2 \exp\left(\sqrt{\delta^2 s/\nu}\right) - \frac{p(s)}{\rho s}; \\ V(s) = A_1 + A_2 - \frac{p(s)}{\rho s}. \end{cases} \quad (16, 17)$$

We multiply (17) by $\exp\left(-\sqrt{\delta^2 s/\nu}\right)$ and subtract (16), then we have

$$V(s) \exp\left(-\sqrt{\delta^2 s/\nu}\right) = -2A_2 \operatorname{sh}\left(\sqrt{\delta^2 s/\nu}\right) + \frac{p(s)}{\rho s} \left(1 - \exp\left(-\sqrt{\delta^2 s/\nu}\right)\right). \quad (18)$$

The subtraction (16) from (17), multiplied by $\exp\left(\sqrt{\delta^2 s/v}\right)$, gives

$$V(s) \exp\left(\sqrt{\delta^2 s/v}\right) = -2A_1 \operatorname{sh}\left(\sqrt{\delta^2 s/v}\right) + \frac{p(s)}{\rho s} \left(1 - \exp\left(\sqrt{\delta^2 s/v}\right)\right). \quad (19)$$

We summarize (18) and (19)

$$2V(s) \operatorname{ch}\left(\sqrt{\delta^2 s/v}\right) = 2(A_1 - A_2) \operatorname{sh}\left(\sqrt{\delta^2 s/v}\right) + \frac{2p(s)}{\rho s} \left(1 - \operatorname{ch}\left(\sqrt{\delta^2 s/v}\right)\right), \quad (20)$$

and hence, we obtain

$$A_1 - A_2 = \frac{p(s)}{\rho s} \frac{\operatorname{ch}\left(\sqrt{\delta^2 s/v}\right) - 1}{\operatorname{sh}\left(\sqrt{\delta^2 s/v}\right)} + V(s) \operatorname{cth}\left(\sqrt{\delta^2 s/v}\right). \quad (21)$$

We substitute (21) into (15), then we transform to the form

$$\tau^0(s) = -\frac{\delta}{2} p(s) \frac{2}{\sqrt{\delta^2 s/v}} \frac{\operatorname{ch}\left(\sqrt{\delta^2 s/v}\right) - 1}{\operatorname{sh}\left(\sqrt{\delta^2 s/v}\right)} + \frac{\rho v}{\delta} V(s) \left[\sqrt{\delta^2 s/v} \operatorname{vcth}\left(\sqrt{\delta^2 s/v}\right) \right]. \quad (22)$$

This expression is the nonstationary shearing stress on the surface of the moving element in the operator form.

According to Eq. (22), we obtain the transfer function for the nonstationary shearing stress with respect to the velocity of the moving element

$$W_{\tau v}(s) = \frac{\tau^0(s)}{V(s)} = k_{\tau v} \sqrt{T s} \operatorname{cth} \sqrt{T s}, \quad (23)$$

where $k_{\tau v}$ —transfer coefficient, introduced according to the expression (4); $T = \delta^2/v$ —time constant.

Consider the dimensionless transfer function

$$\bar{W}_{\tau v}(\bar{s}) = \frac{W_{\tau v}(\bar{s})}{W_{\tau v, kc}(\bar{s})} = \sqrt{\bar{s}} \operatorname{cth} \sqrt{\bar{s}}, \quad (24)$$

where $\bar{s} = sT$ —dimensionless Laplace variable. By the function (24), we determine the amplitude-frequency characteristic

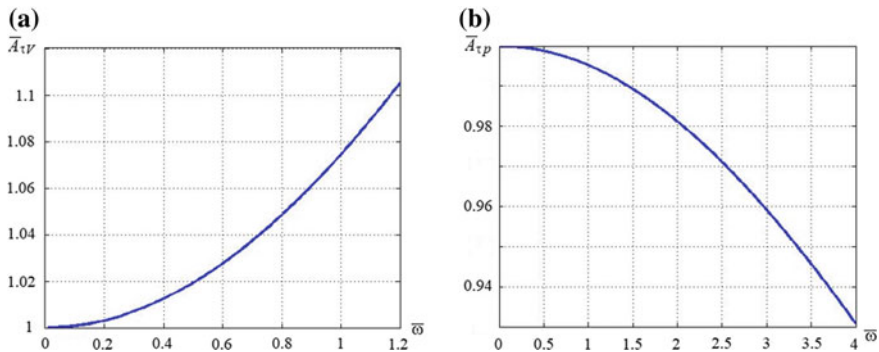


Fig. 3 Shearing stress characteristic. **a** Dimensionless amplitude-frequency shearing stress characteristic (for vibrations of the moving element); **b** dimensionless amplitude-frequency shear stress characteristic (for the pressure gradient vibrations)

$$\bar{A}_{\tau V}(\bar{\omega}) = \text{mod}[\bar{W}_{\tau V}(j\bar{\omega})], \tag{25}$$

where $j = \sqrt{-1}$; $\bar{\omega} = \omega T$ —dimensionless frequency.

The graph $\bar{A}_{\tau V}(\bar{\omega})$, shown in Fig. 3a, shows, that for $\bar{\omega} < 0.81$, the nonstationary of motion leads to an increase in the amplitude of the shearing stresses fluctuations by no more than 5%. Therefore, in this range, it is permissible to use the quasi-stationary transfer function (4) to calculate the frequency characteristics. Thus, this frequency value can be considered as the boundary of a quasi-stationary approach for calculating the viscous friction forces for vibrations of the moving element.

Also, by expression (22), we establish the transfer function for the nonstationary shearing stress with respect to the pressure gradient

$$W_{\tau p}(s) = \frac{\tau^0(s)}{p(s)} = k_{\tau p} \frac{2}{\sqrt{Ts}} \frac{\text{ch}\sqrt{Ts} - 1}{\text{sh}\sqrt{Ts}}, \tag{26}$$

where $k_{\tau p}$ —transfer coefficient, introduced according to the expression (5).

By the dimensionless transfer function

$$\bar{W}_{\tau p}(s) = \frac{W_{\tau p}(\bar{s})}{W_{\tau p,nc}(\bar{s})} = \frac{2}{\sqrt{\bar{s}}} \frac{\text{ch}\sqrt{\bar{s}} - 1}{\text{sh}\sqrt{\bar{s}}} \tag{27}$$

determine the dimensionless amplitude-frequency characteristic

$$\bar{A}_{\tau p}(\bar{\omega}) = \text{mod}[\bar{W}_{\tau p}(j\bar{\omega})]. \tag{28}$$

The graph $\bar{A}_{\tau p}(\bar{\omega})$, shown in Fig. 3b, shows, that for $\bar{\omega} < 3.34$ the decrease in amplitude of the shearing stresses fluctuations by no more than 5%. Therefore, in

this range, it is permissible to use the quasi-stationary transfer function (5) to calculate the frequency characteristics. Thus, this frequency value can be considered as the boundary of a quasi-stationary approach for calculating viscous friction forces for the pressure gradient vibrations.

A good approximation of the transfer functions (23, 26) gives their approximation by the following functions:

$$W_{tv}(s) \approx k_{tv}(1 + 0.387Ts); \quad W_{tp}(s) \approx \frac{k_{tp}}{0.098Ts + 1}. \quad (29)$$

4 Conclusions

Thus, the dependence in the operator form for the shearing stress for nonstationary fluid friction is obtained. The transfer functions for the shearing stress with respect to the velocity of the moving element and the pressure gradient are determined. Based on the analysis of amplitude-frequency characteristics, the boundaries of a quasi-stationary approach for calculating the forces of nonstationary viscous friction on the moving elements are established. The approximate transfer functions for the nonstationary shearing stress are proposed, which allow to establish the connection between the originals in the form of ordinary linear differential equations.

References

1. Popov D (1987) Dynamics and regulation hydro-and pneumatic systems. Machinery Engineering, Moscow
2. Popov D (2005) Mechanics of hydro- and pneumodrives. MGTU, Moscow
3. Sokolov V, Rasskazova Y (2016) Automation of control processes of technological equipment with rotary hydraulic drive. East-Eur J Enterp Technol 2/2(80):44–50. <https://doi.org/10.15587/1729-4061.2016.63711>
4. Popov D (1982) Non-stationary hydromechanical processes. Machinery Engineering, Moscow
5. Sokolov V, Krol O (2019) Determination of transfer functions for electrohydraulic servo drive of technological equipment. In: Advances in design, simulation and manufacturing. DSMIE 2018. Lecture Notes in Mechanical Engineering. Springer, Cham, pp 364–373. https://doi.org/10.1007/978-3-319-93587-4_38
6. Emtsev B (1987) Technical hydromechanics. Machinery Engineering, Moscow
7. Loytsyanskiy L (1987) Mechanics of a liquid and gas. Science, Moscow
8. Sokolov V, Krol O (2017) Installations criterion of deceleration device in volumetric hydraulic drive. Procedia Eng 206:936–943. <https://doi.org/10.1016/j.proeng.2017.10.575>
9. Navrotskiy K (1991) Theory and designing hydro- and pneumodrives. Machinery Engineering, Moscow
10. Sveshnikov V (2008) Hydrodrives of tools. Machinery Engineering, Moscow
11. Shevchenko S, Muhovaty A, Krol O (2016) Geometric aspects of modifications of tapered roller. Procedia Eng 150:1107–1112. <https://doi.org/10.1016/j.proeng.2016.07.221>

12. Shevchenko S, Muhovaty A, Krol O (2017) Gear clutch with modified tooth profiles. *Procedia Eng* 206:979–984. <https://doi.org/10.1016/j.proeng.2017.10.581>
13. Kreynin G, Krivts I (1993) Hydraulic and pneumatic drives of industrial robots and automatic manipulators. Machinery Engineering, Moscow
14. Krol O, Sokolov V (2018) Development of models and research into tooling for machining centers. *East-Eur J Enterp Technol* 3/1(93):12–22. <https://doi.org/10.15587/1729-4061.2018.131778>
15. Sveshnikov V (2007) Hydrodrives in modern mechanical engineering. *Hydraul Pneum* 28:10–16
16. Krol O, Sokolov V (2018) Modelling of spindle nodes for machining centers. *J Phys: Conf Ser* 1084:012007. <https://doi.org/10.1088/1742-6596/1084/1/012007>
17. Abrahamova T, Bushuyev V, Gilova L (2012) Metal-cutting machine tools. Machinery Engineering, Moscow
18. Rasskazova Y, Stepanova O, Azarenko N (2016) Perfection of electrohydraulic drives of machine-building equipment. VDEUNU, Severodonetsk
19. Sokolova Y, Tavanyuk T (2013) Modeling of automatic electrohydraulic drives of special technological equipment. Knowledge, Donetsk
20. Sokolov V, Krol O, Stepanova O (2018) Automatic control system for electrohydraulic drive of production equipment. In: 2018 international Russian automation conference. IEEE. <https://doi.org/10.1109/rusautocon.2018.8501609>
21. Sokolova Y, Azarenko N (2014) The synthesis of system of automatic control of equipment for machining materials with hydraulic drive. *East-Eur J Enterp Technol* 2/2(68):56–60
22. Sokolova Y, Tavanyuk T, Greshnoy D (2011) Linear modeling of the electrohydraulic watching drive. *TEKA. Comm Mot Energ Agric XIB*:167–176
23. Kim D (2003) Theory of automatic control. Vol 1. Linear systems. Fizmathlit, Moscow
24. Lurie B, Enright P (2004) Classical automation control methods. BHV-Petersburg, Saint-Petersburg
25. Pupkov K, Egupov N (2004) Methods of classical and modern theory for automation control. Vol 3. Synthesis of controllers for automation control systems. Publisher Bauman, Moscow

On Splitting of Bending Frequency Spectrum of Geometrically Imperfect Shells



S. V. Seregin

Abstract The relevance of studying the deformation and strength is related to the use of thin circular cylindrical shells in structures exposed to intense dynamic operation. When studying complex dynamics issues, emphasis is made on solving the problems of free oscillations in structural elements. Real shell structures will unavoidably deviate from a perfect cylindrical shape (the initial imperfections) that emerge either in production or in operation. It is known that such imperfections result in specific phenomena as shells oscillate. Splitting of the bending frequency spectrum occurs not only when the number of shaping waves equals that of the shell–shape imperfection waves, as is believed nowadays, but also when the number of shaping waves is half that of the shell-imperfection waves. In the first case, the greater split eigen-frequency equals the frequency of perfect-shape shell oscillations, while the lower frequency is below that. The paper presents studies of how the initial deviations from a perfect circular shape affect the dynamic eigen-parameters of a thin circular cylindrical shell. It discovers the emergence of new splitting zones of the imperfect-shell bending frequency spectrum.

Keywords Oscillations · Shells · Imperfections

1 Introduction

The actuality of studying the deformation and strength is related to the use of thin circular cylindrical shells in structures exposed to intense dynamic operation [1–3]. When studying complex dynamics issues, emphasis is made on solving the problems of free oscillations in structural elements [4–6]. Real shell structures will unavoidably deviate from a perfect cylindrical shape (the initial imperfections)

S. V. Seregin (✉)

Federal State-Funded Educational Institution of Higher Education Komsomolsk-on-Amur State University, 27, Lenin Avenue, Komsomolsk-on-Amur 681000, Russia
e-mail: Seregin-komsHome@yandex.ru

© Springer Nature Switzerland AG 2020

A. A. Radionov et al. (eds.), *Proceedings of the 5th International Conference on Industrial Engineering (ICIE 2019)*, Lecture Notes in Mechanical Engineering,

https://doi.org/10.1007/978-3-030-22041-9_77

717

$w_0(x, y)$ that emerge either in production or in operation. It is known that $w_0(x, y)$ result in specific phenomena as shells oscillate [7].

Many papers have used various theories on, and approaches to, solving this problem [8, 9]. In some papers, initial shape imperfections increase the split eigen-frequencies of shell oscillations [10] as compared to the perfect-geometry shell oscillations; in other papers, a decrease is observed in similar situations [11]. However, all studies have the same finding: Splitting the bending frequency spectrum of a geometrically imperfect shell occurs if the initial imperfections are in resonance with the expected deflection shape or match the shape [8–11].

Papers [12–16] cite a simpler (limiting) problem of oscillations in an infinitely long circular cylindrical shell (ring), which is flat-deformed, to show that the spectrum frequency splitting occurs not only when the number of shaping waves equals that of the shell–shape imperfection waves ($n_0 = n$), as is believed today [8–11], but also in the case when the number of shaping waves is half of the shape imperfection wave number $n_0 = n/2$.

This paper continues the studies [12–16] in the sense that the results obtained for an isolated ring are generalized for the oscillations of a finite-length shell.

2 Imperfect-Shell Oscillation Frequency

MSC Nastran's FEM function is used to simulate and solve the problem of free oscillations in an end-articulated shell with the following geometrical and physical parameters: shell radius $R = 1$ m, $R/h = 200$, where h is the wall thickness; relative shell length $l/R = 10$; Young's modulus $E = 2 \times 10^{11}$ N/m²; mass density $\rho = 7800$ kg/m³; and Poisson's ratio $\mu = 0.3$. The number of finite elements is 157,000. For a perfect shell of such parameters, the lowest spectrum frequency of 12.5 Hz corresponds to the number of circumferential dynamic waves $n_{\min} = 3$.

Let the shell have the deviations from a perfect circular shape n_0 , which are identical to the shape of an expected dynamic deflection in case of oscillations:

$$w_0(x, y) = f_0 \sin \alpha x = (f_{10} \sin \beta y + f_{20} \cos \beta y) \sin \alpha x$$

where $f_{10} = f_0 \cos \varphi_0$; $f_{20} = f_0 \sin \varphi_0$; $\beta = n_0/R$; $\alpha = \pi/l$; x, y are the coordinates along the shell length and circumference; f_0 is the amplitude of initial deviations $f_0 = h$; φ_0 is the starting angle of reference. Oscillations in the vicinity of main resonance are studied, Fig. 1.

Results of calculations for $n_0 = 8$ are shown in the figure, where the solid line stands for the greater split dimensionless frequency of imperfect-shell oscillations $\Omega_{n2} = \lambda_{n2}/\lambda_n$ (λ_{n2} is the absolute value of the greater split eigen-frequency; λ_n is the absolute value of perfect-shell oscillation frequency), the dashed line is for the lower of split dimensionless eigen-frequencies $\Omega_{n1} = \lambda_{n1}/\lambda_n$ (λ_{n1} is the absolute value of the lower split frequency), and the dotted line is for the dimensionless frequency of perfect-shell oscillations $\Omega_n = \lambda_n/\lambda_n = 1$.

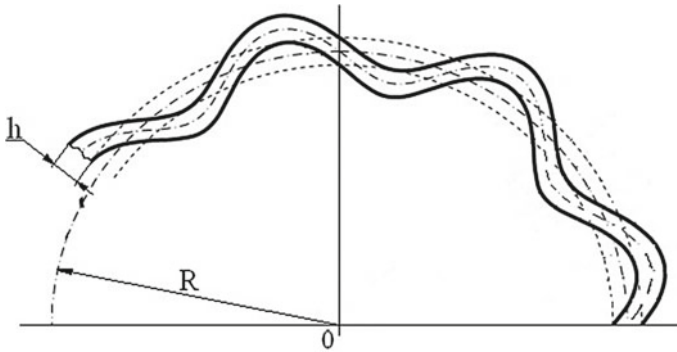


Fig. 1 Schematic representation of the shell imperfections

As can be seen in Fig. 2, splitting of the bending frequency spectrum $\Delta = \Omega_{n2} - \Omega_{n1}$ occurs not only when the number of shaping waves equals that of the shell-shape imperfection waves $n_0 = n$ ($n_0 = n = 8$ in this case), as is believed nowadays [8–11], but also when the number of shaping waves is half that of the shell-imperfection waves $n_0 = n/2$ ($n_0 = n/2 = 4$ in this case). In the first case $n_0 = n$, the greater split eigen-frequency Ω_{n2} equals the frequency of perfect-shape shell oscillations, while the lower frequency is below that. This fact proves the findings of the papers [17, 18], which use a refined approach to the mathematical modeling of oscillations in dynamically asymmetric shells [7, 19].

Frequency spectrum detuning is negligible $\Delta = \Omega_{n2} - \Omega_{n1} = 2\%$. However, these findings contradict the results based on the traditional approach to mathematical modeling [10], where both split frequencies are above the perfect-shape shell oscillation frequency. The paper [10] also notes that the frequency spectrum detuning is significant even if the imperfection amplitude is not.

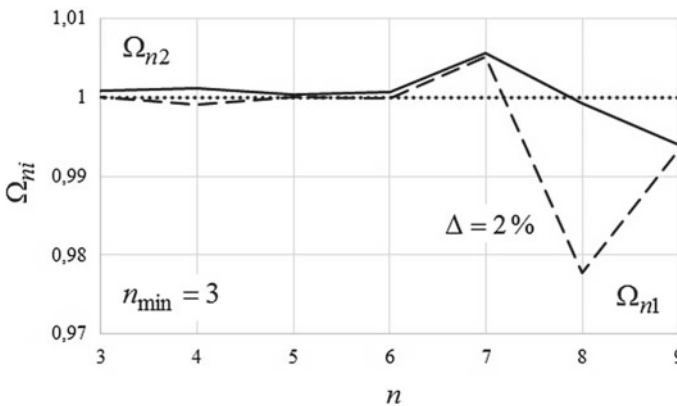


Fig. 2 Split frequencies of imperfect shells



Spectrum splitting at $n_0 = n/2 = 4$ is so little that it might be neglected due to the unavoidable assumptions of the modern theory and analysis methods, as well as due to the permissible errors in various industries. It can therefore be assumed that the theory produces adequate results but no final findings.

Consider a case where $l/R = 3$. $n_{\min} = 5$ corresponds to the minimum spectrum frequency of such a shell. Frequency spectrum splitting is observed in the cases $n_0 = n$ and $n_0 = n/2$ (in this case, $n = 8$ and $n = 4$), Fig. 3. First-zone frequency spectrum detuning is 25%, and second-zone detuning is still $\Delta = 2\%$. If the relative shell length $l/R = 1$, then $n_{\min} = 8$. At $n_0 = n/2 = 4$, frequency spectrum detuning is 25%. Splitting is somewhat higher than in previous calculations at $n = n_0 = 8$ and equals $\Delta = 5\%$.

Consider a case where $l/R = 0.7$. For such a shell, $n_{\min} = 10$ shaping waves correspond to the minimum frequency of the spectrum. In this case, bending frequency spectrum splitting occurs in the cases $n = n_0/2$ and $n_0 = n$ ($n = 4$ and $n = 8$). First-zone frequency spectrum detuning is 30%, and second-zone detuning is $\Delta = 6\%$.

Consider a shell with the following geometrical and physical properties: $l/R = 1$; $R/h = 200$; $R = 1$; $\mu = 0.3$. $n_{\min} = 8$ corresponds to the minimum frequency in the spectrum of such a shell. Let the shell have initial shape imperfections $f_0 = h$, with $n_0 = 8$ being the number of circumferential imperfection waves.

In this case, the bending frequency spectrum is split not only when $n = n_0$, which is conventional, but also when $n = 2n_0$. In case $n = n_0$, both split frequencies are below the oscillation frequency of a geometrically perfect shell, which is inconsistent with the conventional solution [10] but consistent with the new analytical solution as well as with the solution presented in [7]. The frequency $\Omega_{n2} - \Omega_{n1}$ drops by 5%. In the analytical solution, the frequency spectrum detuning ($\varepsilon = 0.102$, $\theta = 0.393$ in the case under consideration) $\Omega_{n2} - \Omega_{n1} = 9\%$. In case $n = 2n_0$, one of the split frequencies Ω_{n2} is greater than the perfect-shell oscillation

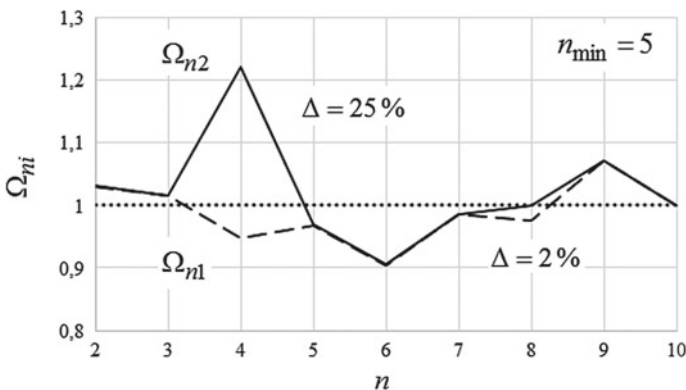


Fig. 3 Split frequencies of the imperfect shell

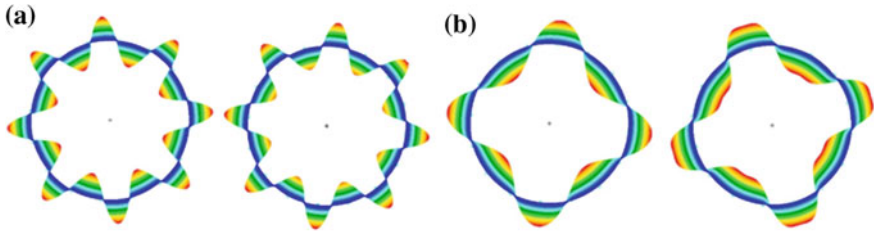


Fig. 4 Oscillation modes and their corresponding split frequencies **a** $n = n_0 = 8$: $\lambda_{81} = 132$ Hz, $\lambda_{82} = 139.2$ Hz; **b** $n_0 = n/2 = 4$: $\lambda_{41} = 265.27$ Hz, $\lambda_{42} = 348.7$ Hz

frequency, while Ω_{n1} is below that. Spectrum detuning can be quite substantial. In this example, it is five times that in the case ($n = n_0$).

Figure 4 presents the oscillation shapes and the corresponding split eigen-frequencies for the case $n = n_0$ and $n = 2n_0$.

If the shell has a perfect geometric surface, both conjugate bending shapes for every n are associated with equal frequencies: $\lambda_4 = 301.5$ Hz and $\lambda_8 = 139.25$ Hz. Apparently, at $n = n_0 = 8$ the higher split imperfect-shell eigen-frequency λ_{82} is nearly equal to the shell oscillation frequency without $w_0(x, y)$ or λ_8 . The lower split eigen-frequency λ_{81} is below the shell oscillation frequency without $w_0(x, y)$ or λ_8 by over 5%. Frequency spectrum detuning $\lambda_{82} - \lambda_{81} \approx 5\%$. In the zone $n_0 = n/2 = 4$, the higher split eigen-frequency of shell oscillations with $w_0(x, y)$ or λ_{42} is higher than the corresponding perfect-shell frequency λ_4 by 15%. The lower frequency λ_{41} is about 12% lower than λ_4 . Frequency spectrum detuning $\lambda_{42} - \lambda_{41} \approx 27\%$.

Note that the analysis of dynamic behavior exhibited by imperfect-shape shells also revealed more complex (ambiguous) oscillation shapes.

3 Equations

The completed studies have produced a finding that the initial shape imperfections result in splitting the bending frequency spectrum of the shell, in which case frequency spectrum detuning occurs not only in cases where the number of shaping waves equals that of the shell-shape imperfection waves $n = n_0$, as is believed nowadays. In case where the number of shaping waves is half that of the shape imperfection waves $n = 2n_0$, frequency spectrum detuning might be significant and numerically in excess of the known case. A similar effect of imperfect-shell bending frequency spectrum splitting occurs at higher-oscillation frequencies.

Additional study has shown that split frequencies are so insignificantly separated from each other that it is reasonable to expect changes in the number of waves of dynamic deformations that correspond to the minimum frequency of the imperfect-shell spectrum.

Acknowledgements The research was financed by the grant of the Russian Science Foundation (project No. 18-79-00057).

References

1. Seregin SV (2014) Free flexural radial oscillations of a thin circular cylindrical shell bearing added mass. *Vestnik MGSU. Proc Mosc State Univ Civ Eng* 11:74–81. <https://doi.org/10.22227/1997-0935.2014.11.74-81>
2. Seregin SV (2014) Numerical and analytical study of free oscillations of circular cylindrical shells carrying the attached mass linearly distributed along the generatrix. *Comput Mech Contin Media* 7(4):378–384. <https://doi.org/10.7242/1999-6691/2014.7.4.36>
3. Seregin SV (2014) About the effect of the splitting of the Flexural frequency spectrum of thin circular cylindrical shells carrying an attached mass. *Constr Mech Calc Struct* 6(257):59–61
4. Seregin SV (2015) Free vibrations of a thin circular cylindrical shell weakened by a hole. *Russian Aeronaut* 58(3):258–262. <https://doi.org/10.3103/S1068799815030022>
5. Leizerovich GS (2015) Influence of attached masses on the dynamic characteristics of thin shell. *Prob Mech Eng Autom* 4:83–89
6. Leizerovich GS, Seregin SV (2016) Free vibrations of circular cylindrical shells with a small added concentrated mass. *J Appl Mech Tech Phys* 57(5):841–846. <https://doi.org/10.1134/S0021894416050102>
7. Seregin SV (2016) Dynamics of thin cylindrical shells with added mass: monograph. Komsomolsk-na-Amure State Technical University, Komsomolsk-on-Amur, pp 175–180
8. Avramov KV, Mikhlin YV (2010) Nonlinear dynamics of elastic systems. Vol. 1. Models, methods, phenomena. SIC “Regular and chaotic dynamics”, Institute of computer research, Moscow, Izhevsk, 704p
9. Amabili M, Païdoussis MP (2003) Review of studies on geometrically nonlinear vibrations and dynamics of circular cylindrical shells and panels, with and without fluid-structure interaction. *Appl Mech Rev* 56(4):349–381
10. Kubenko VD, Koval’chuk PS, Krasnopol’skaya TS (1984) Nonlinear interaction of forms of flexural vibrations of cylindrical shells. *Naukova Dumka, Kiev*, p 220
11. Taranukha NA, Leyzerovich GS (2005) *Dinamika “neppravilnykh” obolochek (Imperfect-Shell Dynamics)*. Dalnauka, Vladivostok, p 423
12. Leyzerovich GS, Prikhodko NB, Seregin SV (2013) On the influence of a small attached mass on the oscillations of a multi-thick circular ring. *Constr Reconstr* 4:38–41
13. Leyzerovich GS, Prikhodko NB, Seregin SV (2013) On the influence of a small attached mass on the splitting of the frequency spectrum of a circular ring with initial irregularities. *Constr Mech Calc Struct* 6:49–51
14. Seregin SV, Leizerovich GS (2014) Free vibrations of an infinitely long circular cylindrical shell with initial imperfections and little added mass. *Sci Notes Komsomolsk-on-Amur State Tech Univ* 4(20):36–43
15. Seregin SV (2017) The influence of shape imperfections on the vibrations of a ring resonator of a wave solid-state gyroscope. *Nonlinear Dyn* 13(3):423–431. <https://doi.org/10.20537/nd1703009>
16. Seregin SV (2017) The splitting features of a frequency spectrum of a gyroscope based on elastic waves in solids: an isolated imperfect ring as an example. *St. Petersburg Polytech State Univ J. Phys Math* 3(3):255–258. <https://doi.org/10.1016/j.spjpm.2017.09.004>
17. Seregin SV (2016) Influence of asymmetric initial imperfection shape on the free vibrations of thin shells. *Vestnik of Samara University. Aerosp Eng, Technol Mech Eng* 15(3):209–222. <https://doi.org/10.18287/2541-7533-2016-15-3-209-222>

18. Seregin SV (2018) On possible zones of splitting of the Flexural frequency spectrum of shells with asymmetric imperfections of shape. News High Educ Inst. Aviat Equip 2:149–152
19. Seregin SV (2017) Qualitative effects on vibrations of annular reinforcing elements with attached mass, as a special case of a thin infinitely long circular cylindrical shell. Proc High Educ Inst. Eng 1(682):31–43. <https://doi.org/10.18698/0536-1044-2017-1-31-43>

Mathematical Model of Spindle Unit Bearing Assembly



E. S. Gasparov and L. B. Gasparova

Abstract The mathematical model which links an information signal with the parameters of technical state of mechanical node in the best way will allow developing methods for diagnosing emerging defects at the operational stage. Development of a mathematical model of spindle unit bearing assembly, which would analytically describe the mechanism of vibration signal formation, linking it to the parameters of the technical state, is a relevant objective at the present time. Perhaps, such a mathematical model will effectively apply the Huang–Hilbert transform to vibration signals, using adaptive decomposition of signals into physically significant components, and also improve the efficiency of currently used analysis methods. The obtained mathematical model qualitatively determines the mechanism of the frequency composition of the vibration spectrum appearing, takes into account the microgeometry of the raceway and ball profiles, when the radial (angular contact) ball bearing works, and gives a quantitative estimate, the error of which will largely depend on the signal/interference ratio of the experimentally obtained time implementation of vibration acceleration (vibration displacement).

Keywords Mathematical model · Spindle unit · Huang–Hilbert transform · Vibration signal · Ball bearing · Contact deformation

1 Introduction

Most of the developed mathematical models of spindle units on rolling contact bearings have no visually understandable mechanisms for the formation of modulated vibration signals. And, accordingly, these models have no changes in the ratio of the spectral amplitudes at frequencies that are divisible by basic excitation frequencies with a change in the parameters of the mechanical system, and with account for inherent amplitude-frequency characteristic of the mechanical system [1–6].

E. S. Gasparov · L. B. Gasparova (✉)
Samara State Technical University, 244, Molodogvardeyskaya Str., Samara 443100, Russia
e-mail: gasparova.lb@gmail.com

From this perspective, the mathematical model that best links information signal with the parameters of technical state of mechanical node will allow to develop methods for diagnosing emerging defects at the operational stage that require a greater depth of diagnosis than diagnostic methods at the stage of manufacturing and assembly more successfully. A large number of those methods are based on octave and fractional-octave analysis of the signal energy spectrum [7–9]. Therefore, development of a mathematical model of spindle unit bearing assembly, which would analytically describe the mechanism of vibration signal formation, linking it to the parameters of the technical state, is a relevant objective at the present time. Perhaps, such a mathematical model will effectively apply the Huang–Hilbert transform [10, 11] to vibration signals, using adaptive decomposition of signals into physically significant components, and also improve the efficiency of currently used analysis methods.

2 Development of a Mathematical Model of Spindle Unit Bearing Assembly

Figure 1 shows the geometric model (a) and the generalized design scheme (b) of the high-speed grinding bearing spindle. The model considers a radial ball bearing, but if necessary, the results can be transferred to the model of angular contact ball bearing [12, 13].

The model has one fixed and several moving coordinate systems, the number of which is equal to the number of balls in the bearing cage. Moving coordinate systems rotate relatively the fixed one with an angular velocity equal to the speed of rotation of the separator; i.e., the geometric center of the ball lies on the axis of the corresponding mobile coordinate system. The path of the inner ring of the bearing is

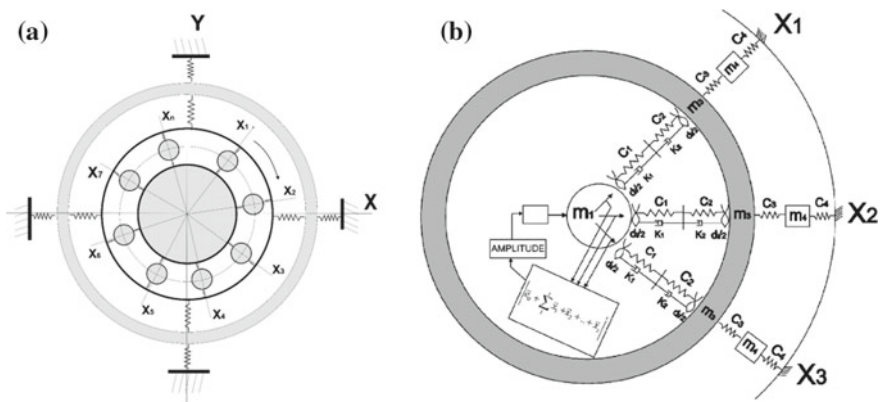


Fig. 1 Geometric model (a) and the generalized design scheme (b) of the high-speed grinding bearing spindle

the surface of the rotor, which is typical for grinding spindles. The model assumes the following assumptions: The balls are not sliding, the profile of the treadmills is permanent, and the angle of contact is constant.

Calculation scheme at Fig. 1b takes into account the influence of the amplitude feedback, i.e., the influence of the rotor displacement on the amplitude of the periodic disturbing force caused by the initial spindle disbalance.

Taking the amplitude feedback into account is defined as the dependence of the instantaneous eccentricity on the displacement, reduced to the bearing, the mass of the rotor (Fig. 2).

The instantaneous eccentricity value is calculated in the way described below [14, 15]:

$$e(t) = e_0 + \sum_1^z x_{1n} \cos\left(\omega_{pc} \cdot t + \phi_{pc0} - \frac{2 \cdot \pi(n-1)}{z}\right) \tag{1}$$

Here, $\sum_1^z x_{1n} \cos\left(\omega_{pc} \cdot t + \phi_{pc0} - \frac{2 \cdot \pi(n-1)}{z}\right)$ is the sum of the displacement projections of the rotor geometric center on the line connecting the rotor geometric center with the gravity center, and $\omega_{pc} \cdot t + \phi_{pc0} - \frac{2 \cdot \pi(n-1)}{z}$ is the rotational phase difference between the rotor and the separator.

We shall consider the mechanical system along one of the movable axes. The mechanical system consists of four elastically bound concentrated masses (Fig. 3a), where m_1 is spindle bearing assembly mass, m_2 is the ball mass, m_3 is the outer ring mass, m_4 is the spindle unit body mass, C_1 is the contact stiffness inner ring–ball, K_1 is the coefficient of viscous contact resistance inner ring–ball, C_2 is the contact stiffness outer ring–ball, K_2 is the coefficient of viscous contact resistance outer ring–ball, C_3 is the contact stiffness outer ring–spindle unit, C_4 is the contact stiffness spindle unit–machine stand, F_{preload} is the preload force, and F_{rotor} is the periodic force due to spindle imbalance.

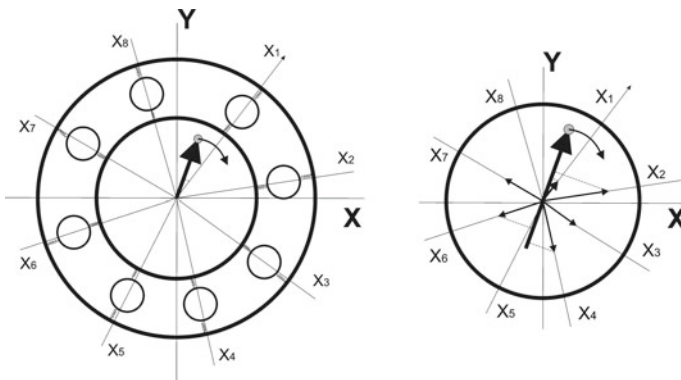


Fig. 2 Graphical explanation of the recording of the instantaneous eccentricity value

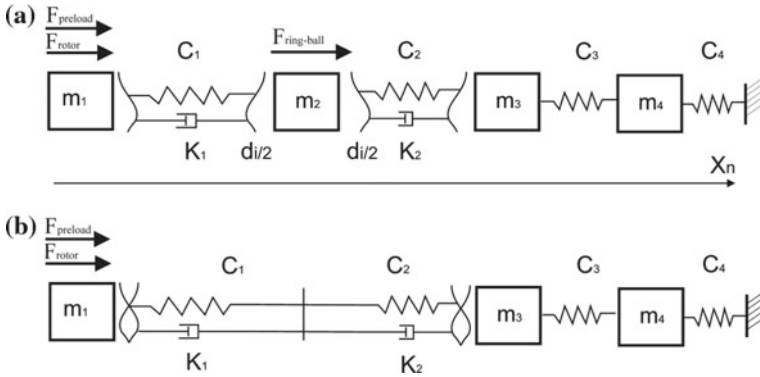


Fig. 3 Mechanical system along one of the movable axes

The mass of the ball m_2 will be neglected and assumed to be zero, since the mass of the ball is less than the masses of the remaining elements by an order of magnitude greater. Therefore, we will simplify the mechanical system to a system of three concentrated masses (Fig. 3b).

A system of differential equations describing the motion of the masses of the simplified mechanical system shown in (Fig. 3b) is given below:

$$\begin{cases} m_1 \ddot{x}_1 = F_{\text{source}} - C_{\text{gen}}(x_1 - x_3 + A(t)) - k_{\text{gen}}(x_1 - x_3 + A(t))' \\ m_3 \ddot{x}_3 = C_{\text{gen}}(x_1 - x_3 + A(t)) + k_{\text{gen}}(x_1 - x_3 + A(t))' - C_3(x_3 - x_4) \\ m_4 \ddot{x}_4 = -C_4 x_4 + C_3(x_3 - x_4) \end{cases} \quad (2)$$

where C_{gen} is the general nonlinear stiffness of the spindle–outer ring contact, equal to $\frac{C_1 \cdot C_2}{C_1 + C_2}$, $A(t)$ is the total kinematic disturbance caused by irregularities in the profiles of the bearing race and the ball, and k_{gen} is the general coefficient of viscous resistance, equal to the sum of the coefficients K_1 and K_2 . F_{source} is the total force on the spindle side.

The components of F_{source} are:

1. Preload force (constant component).
2. Periodic force caused by the rotor imbalance.

$$\omega_p^2 \cdot m_1 \cdot e(t) \cdot \cos\left((\omega_p - \omega_c) \cdot t - \frac{2\pi \cdot (n - 1)}{z} + \phi_{pc}\right) \quad (3)$$

3. The effect of the gravity force mg (depends on the spindle location).

$$\vec{F}_{\text{source}} = \vec{F}_{\text{preload}} + \vec{F}_{\text{period.}} + \vec{F} \quad (4)$$



Stiffnesses C_1 и C_2 are nonlinear quantities; their values depend on the applied load. They are calculated by the formulas according to the Hertz theory:

$$\delta = \frac{2K}{\pi\mu} \cdot \left\{ \frac{3F}{2\sum \rho} \left[\frac{(1 - \epsilon_I^2)}{E_I} + \frac{(1 - \epsilon_{II}^2)}{E_{II}} \right] \right\}^{\frac{2}{3}} \cdot \frac{\sum \rho}{2} \tag{5}$$

$\epsilon_I, \epsilon_{II}$ —are Poisson’s ratios, E_I, E_{II} —are modules of elasticity, $\frac{2K}{\pi\mu}$ —is the numerical coefficient of proportionality which depends on the geometric dimensions of the bearing, $\sum \rho$ is the sum of the difference in curvature, and F is the applied force [14, 16].

Value $A_i(t)$ is a total kinematic disturbance caused by the unevenness of the raceways of the rings and the rolling lines of the balls. The raceway profiles will be represented in Fourier series form as a function of changes in radius and for a ball as a function of changes in diameter.

In view of the above, the expression for the kinematic disturbance will be shown as:

$$A_i(t) = (R_{O_o} - R_{in_o} - D_{b_o}) + \sum_{m,n=1}^{\infty} \left(\begin{aligned} &A_n \cdot \cos\left(n \cdot \psi + \omega_s \cdot t + \frac{2\pi}{z}(i - 1) + \phi_n\right) \\ &- A_m \cdot \cos(m \cdot \psi - (\omega_r - \omega_s) \cdot t + \\ &\frac{2\pi}{z} \cdot (i - 1) + \phi_m) - \sum_{k=1}^{\infty} A_k \cdot \cos(k \cdot \psi + 2 \cdot \omega_b \cdot t + \psi_k) \end{aligned} \right) \tag{6}$$

where $\omega_r, \omega_s, \omega_b$ are a rotational speed of the rotor, separator and spinning balls, respectively, i is the ball number, $R_{in}(\psi)$ is the radius function describing the raceway profile of the inner ring, $R_o(\psi)$ is the radius function describing the raceway profile of the outer ring, and $D_b(\psi)$ is a function describing the change in the balls’ diameter.

It is known that there is a dynamic analogy between mechanical, electrical, acoustic and similar systems based on the formal similarity of differential equations describing the oscillatory movements of these systems. In this regard, studies of the motion differential equation of one system can be extended to dynamically analogous systems of a different nature [17].

Using analogies of mechanical and electrical circuits, methods for calculating circuits with nonlinear elements, and in particular the active two-pole method, taking into account the feedback of the rotor movement with the periodic force generated by it, analytical expressions to accelerate the displacement of the rotor mass applied to a bearing support, expressions to the displacement of the node mass along the axis of the moving coordinate system and expressions to acceleration when the node mass moves along the axis of the moving coordinate system were found.



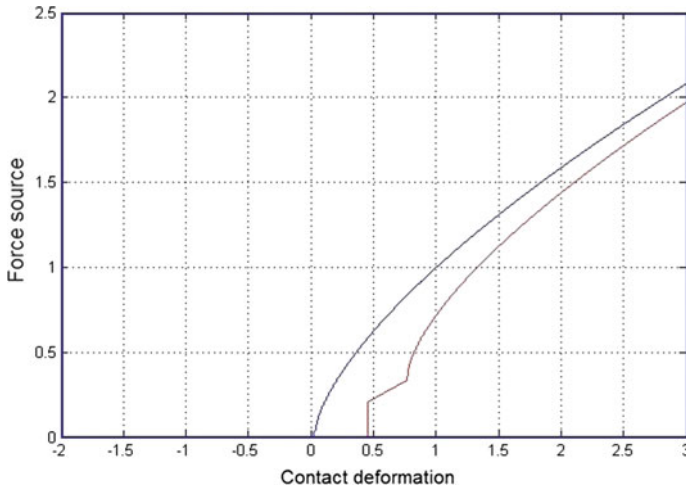


Fig. 4 Contact deformation plots under static loading of the circuit

To check the reliability of the obtained expressions, Fig. 4 shows the graphs of contact deformation under static loading of the circuit, made in the MATLAB package with the values of viscous resistance equal to 0.5, 0.01 and $\rho(\omega) = 1$, $a = 1$ [18, 19].

From the graph in Fig. 4, it can be seen that when the value of the viscous resistance coefficient decreases, the graph U_c degenerates into a graph of equation $\delta = a \cdot U_c^2$, which corresponds to the dependence on the applied force [4, 14, 20].

3 Conclusions

The expressions obtained for the dynamics are valid under the condition that the instantaneous amplitude of the periodic component of the disturbing force is less than the preload, which is quite true for the operating modes of the spindles for precision machining; otherwise, the mode of operation of the bearing becomes significantly nonlinear.

The obtained mathematical model qualitatively determines the mechanism of the frequency composition of the vibration spectrum appearing, takes into account the microgeometry of the raceway and ball profiles, when the radial (angular contact) ball bearing works, and gives a quantitative estimate, the error of which will largely depend on the signal/interference ratio of the experimentally obtained time implementation of vibration acceleration (vibration displacement).

References

1. Galahov MA, Burmistrov AN (1988) Calculation of bearing units. Mechanical Engineering, Moscow
2. Gasparov ES, Denisenko AF, Gasparova LB (2013) Model of spindle assembly on rolling bearings support. Bull Samara State Tech Univ 4(40):96–110
3. Kel'zon AS, Zhuravlev YuN, Yanvarev NV (1977) Calculation and design of rotary machines. Mechanical Engineering, Leningrad
4. Leont'ev MK, Snetkova EI (2012) Nonlinear models of rolling bearings in rotor dynamics. Bull Mosc Aviat Inst 2:19
5. Push AV (1985) Quality evaluation of precision spindle unit drives in areas of output precision parameters states. Mach Tool 2:12–15
6. Push AV (1992) Spindle units: quality and reliability. Mechanical Engineering, Moscow
7. Stribeck R (2002) Die wesentlichen Eigenschaften der Gleit und Rollenlager. Zeitschrift des Vereins Deutscher Ingenieure, vol 36, Berlin
8. de Mul JM, Vree JM, Maas DA (1989) Equilibrium and associated load distribution in ball and roller bearings loaded in five degrees of freedom while neglecting friction- part I: general theory and application to ball bearings. J Tribol 111:142–148
9. Feng NS, Hahn EJ (2000) Rolling element bearing non-linearity effects. ASME Paper 391:2000
10. Norden E Huang, Samuel SP Shen The Hilbert-Huang transform and its applications. World Scientific Publishing Co., Singapore
11. Huang NE, Shen Z, Long SR, Wu MC, Shih HH, Zheng Q, Yen N-C, Tung CC, Liu HH (1998) The empirical mode decomposition and the Hilbert spectrum for nonlinear and non-stationary time series analysis. Proc R Soc London, Ser A 454:903–995
12. IBAG company profile (2015) IBAG Switzerland AG и IBAG North America. <http://www.ibag.ch/en/company-profile.html>
13. SKF Group (2015) General Bearing Corp., Sweden. <http://www.skf.com/ru/index.html?switch=y>
14. Bejzel'man RD, Cypkin BV, Perel' LYa (1975) Rolling bearings, Mechanical engineering, Moscow
15. Barbin AYu, Molodcov VV (2013) Features of the development and use of motor spindles as drives for the main movement of modern machine tools. Mach Tool 1:16–21
16. Iznairov BM, Vasin AN, Iznairov OB (2013) Mathematical model of the interaction of the working elements of a ball angular contact bearing. Mach Tool 4:1–3
17. Chelomej VN, Frolova KV (1981) Protection from vibration and stroke. Mechanical Engineering, Moscow
18. Gul'tyaev AK (2000) Visual modeling in MATLAB: training course. Piter, Saint-Petersburg
19. D'yakov V, Kruglov V (2000) Mathematical Expansion Packs in MatLAB. Special Handbook. Piter, Saint-Petersburg
20. Piskunov NS (1996) Differential and integral calculus for technical colleges. Publishing House "Mifril", Moscow

Evaluation of Contact Stresses in Railway Wheel When Rolling Through Rail Joint



E. S. Evtukh and G. A. Neklyudova

Abstract A computer simulation of the open-top wagon along the track section adjacent to the rail joint is performed taking into account the ballast subsidence in the joint area. At the same time, a number of parameters influencing this process were varied. The range of dynamic forces values that arise between the wheel and the rail when passing the joint by a freight car at operational speeds is determined. The evaluation of stresses obtained as a result of solving the contact problem for the wheel and the rail by the finite element method is estimated. The problem was solved taking into account dynamic efforts found by computer simulation. The intensity of stresses and deformations is determined. The contact pressures in the elements of the rail joint are calculated using three-dimensional finite element models. Contact problems for two variants of the wheel arrangement are considered: above the edge of the joint and at a sufficient distance from it. Based on the results of the solution, an approximating relationship is proposed for the location of the wheel at the rail edge to determine the maximum contact pressure.

Keywords Contact pressure · Modeling · Rail joint · Wagon wheel · Dynamic forces

1 Introduction

The planned increase in the throughput and carrying capacity of railways makes increased requirements for ensuring reliable operation of the units of undercarriage, in particular to elements of the wheel set. The problem of the strength of railway wheels covers a wide range of theoretical and experimental problems, the solution of which has been practiced by scientists from all over the world for decades. In these studies, the issues of strength, durability and increased service life of the

E. S. Evtukh (✉) · G. A. Neklyudova
Bryansk State Technical University, 7, Bulvar 50 Let Oktyabrya,
Bryansk 241035, Russia
e-mail: galinanekludova@yandex.ru

wheel during the movement of a freight car along a continuous rail section of the railroad were solved. On Russian railways, the share of the track with joints is about 60% of the total length, so determining the resource of the wheel, taking into account the current state of the art, requires consideration of the impact of the joint irregularity. When the wheel is rolling through the rail joint, there are dynamic forces between them. Increased dynamic loads on the rail in the area of the joint cause subsidence of the ballast layer resulting in a decrease in the path rigidity. In addition, the ballast subsidence in the joint area leads to an increase in accumulated damage in the wheel. The movement of the wagon in this zone is an oscillatory process, which accompanies the impact interaction of the wheel and rail. The most suitable way to determine interaction forces between the wheel and the rail, which are necessary for solving the contact problem, is the computer simulation. The obtained forces will allow solving a contact problem for a wheel and edge of a rail with the purpose of an estimation of accumulated contact fatigue damages in a wheel of the wagon taking into account rail joints.

1.1 Relevance and Overview of Publications

Rail joints in the “wheel-path” interaction system are usually considered as short irregularities, during the passage of which there are increased dynamic loads on the wheel. The interaction of the rolling stock with a short unevenness of the track, described by the theoretical scheme of a dynamical system with several degrees of freedom, was investigated by G. M. Shahunyants, M. A. Frishman, A. Ya. Kogan, M. F. Verigo, V. F. Grachev [1–5].

Recently, the issues of rolling a wheel through a rail joint have acquired relevance again and have been already considered in a number of works. In the research [6], a mathematical model of impact interaction of a wheel of a freight car and a rail joint is developed, allowing taking into account the contact stiffness of the wheel and rail, the geometric parameters of rail joint defects and the thickness of the rim of the wheel. The developed mathematical model, described by a system of differential equations, allowed the author to determine the additional dynamic effect of the wagon’s wheel on the rolling surface of the railhead, taking into account body oscillations and elastically dissipative parameters of spring suspension. The finite element method was used for calculation of stresses and deformations of the wheel under the influence of impact force, and the values obtained exceed the yield strength of wheeled steel.

For the wheel on the joint-free section of the path in the article [7], an algorithm for modeling the contact stresses in the wheels of the rolling stock using finite element fragments resting on an elastic base was developed and implemented. The proposed algorithm ensures the ease of implementation and speed of the solution of the contact problem. This is fundamental for computer modeling of wear processes and contact fatigue damages in the wheels. In addition, the author developed a program that simulates the accumulation of contact fatigue damages in the wagon’s

wheel when developing and justifying a rational wheel profile by the criterion of contact fatigue.

In work [8], the model of interaction of a wheel and a rail is realized with the purpose of computer modeling of undercarriage dynamics on rail joint. With this model, dynamic forces caused by the shock interaction of the wheel and rail at the junction, as well by the oscillatory process accompanying the movement of the wagon in the area with ballast subsidence at various speeds of movement, depths of subsidence and lengths of sections with ballast subsidence are investigated.

1.2 Formulation of the Problem

The purpose of the study is the computer simulation of the dynamics of the railway undercarriage during the passage of the rail joint and the calculation of the stress-strain state of the wheel of the wagon using dynamic forces obtained as a result of the simulation. The pressures and deformations in the contact area of the wheel and rail during the movement on the joint are determined by the finite element method using the special program ITFEMCP [9]. The obtained results will allow developing a methodology for assessing the effect of rail joints on the accumulation of contact fatigue damages.

2 Motion Modeling

For the computer simulation of rolling process of the wheel on the joint, the “Universal Mechanism” (UM) software package was used [10, 11]. A model is implemented that takes into account parameters of the “undercarriage-way” system and is closest to real conditions.

However, the model development is a complex task due to the large number of factors that must be taken into account in it. Starting from ballast, which is a medium with values of internal friction, modulus of elasticity that are difficult to define and vary within a wide range, and ending with the rail itself, which also has its characteristics. In addition, the track panel is a complex structure containing elements of steel, reinforced concrete, rubber.

In the proposed model, the undercarriage is represented by masses, moments of inertia of masses of frames of carriages, wheel sets, body and connections between them. A number of these criteria are quantitatively identified, and the determination of values of the others is not as difficult as the task of path parameter's identification.

To identify the characteristics of the under-rail base, a laboratory installation was developed that provides the conditions for applying the load on the ballast layer close to actual conditions. With this installation, the dissipative elastic characteristics of the ballast layer are determined [12].

The rail joint is modeled by unevenness. The choice of its shape and its parameters is given in [13] and meets the following conditions: the wheel during the passage of the joint continuously contacts the rail, the contact of the wheel and the rail in the longitudinal direction is single-point, when the joint passage the same dynamic loads are observed as those obtained in carrying out field tests.

The dynamic model diagram of the path in the joint area with ballast subsidence is shown in Fig. 1.

Outside the area with ballast subsidence, the path was modeled by an elastic foundation. The moving undercarriage is represented by rigid bodies connected by elastic-dissipative bonds.

A simulation of the open-top wagon along the track section adjacent to the joint is performed taking into account the ballast subsidence in the joint area. At this, main parameters that determine this process were varied: the amount of subsidence, the length of sections with subsidence and the speed of undercarriage movement. In each case, two values of the dynamic force between the wheel set and the rails were determined: the maximum dynamic force due to the oscillatory process during the movement of the wheel set outside the joint and the force due to impact when passing through the joint. Figure 2 shows oscillograms of dynamic forces with zero subsidence, a speed of 70 km/h and loads on the wheel of 120 kN.

Simulation of the process of railway undercarriage movement on the rail joint section at normalized ballast subsidence values allowed determining the greatest vertical dynamic loads that arise during the impact interaction of the wheel and rail, as well as due to oscillatory processes. It is found that when passing through a joint of a loaded freight car with the permissible speeds, depending on the subsidence, the forces of interaction between the wheel and the rail exceed 300 kN.

If the wheel is located at a sufficient distance from the joint, high contact pressures occur in its contact with the rail with such loads. However, when the wheel is rolling in contact with the receiving rail, the pressure distribution is even more unfavorable, and plastic deformation occurs in the material of the wheel. Such a situation is observed in the first realizations of the contact. In this work, we used the assumption that after this, the material is strengthened and, during further loading, operates within elastic deformations.

To evaluate the pressures in the first case, Hertz's solution can be used. Nevertheless, it is given under the assumption that contacting bodies can be

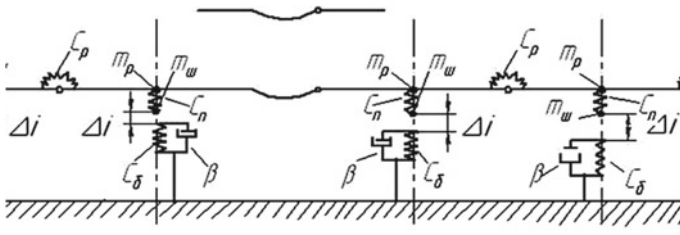


Fig. 1 Dynamic model diagram of the path in the joint area with ballast subsidence

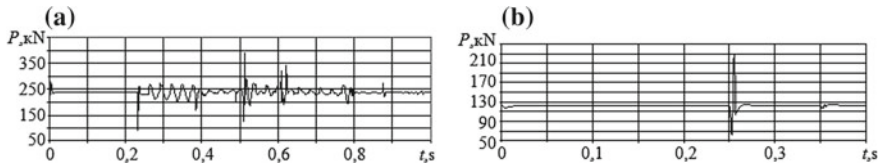


Fig. 2 Oscillograms of dynamic forces arising between rails and wheel sets **a** is a graph of forces on the wheel of the first wheel set when passing an approximate joint irregularity for the path model adopted in the “Universal Mechanism;” **b** on the first wheel set during the passage of the dynamic model of the path in the joint area

represented by computational schemes of half-spaces. In our case, the dimensions of the contact spot are comparable with wheel and rail dimensions. Therefore, the finite element method is used to study the stress state in the contact region. The obtained pressure distributions coincide with Hertz distributions with sufficient accuracy. For the second case, there is no analytical solution, and the finite element method is applied.

3 Materials and Research Results

The solution of contact problems in elastic formulation for cases when the wheel is located above the edge of the joint, as well as at a sufficient distance from it, is performed using the ITFEMCP software complex. The finite element models formed by eight-node finite elements are used. The size of edges of the finite element was assumed to be 1 mm. In the analytic model, fragments of the wheel and rail are used, ensuring sufficient damping of stresses and deformations to the planes of their separation.

An unworn rail R65 was considered the cross section of which is described by radii of 500, 80 and 15 mm. The fragment completely modeled the railhead. The finite element grid was obtained by the “dredge” method by successively displacing the plane matrix along with the generator, parallel to the axis of the rail.

The fragment of the wheel had the same dimensions on length and thickness, and on width, it did not completely model the crest. Such a fragment can be used when the contact is located on the rolling surface. The finite element grid was also obtained by the “dredge” method, and for this purpose, the planar matrix rotated relative to the axis of the wheel set. A fragment of an unworn wagon wheel with a rolling surface profile corresponding to GOST 10791-2011 was considered.

Boundary conditions: The nodes located on the separation planes of the fragments were superimposed with links perpendicular to these planes. A rectangular coordinate system with X , Y , Z -axes directed across the rail is used, along the normal to the initial point of contact and along the rail, respectively. In addition, connections are imposed that ensure the kinematic unchangeability of the analytic model.

The load was applied using boundary conditions of the second kind by assigning displacements to the nodes located on the upper plane of the wheel fragment along the Y -axis. The load from the wheel to the rail was controlled by the sum of contact forces projections on the Y -axis. The specified load values were achieved by selecting node displacements. The nodes immediately received the desired offset, and the iterative procedures were repeated until the specified discrepancy was reached. The solutions were carried out in an elastic formulation.

The processing of the calculation results was carried out using the service programs available in the calculation complex. They provided the ability to visualize the frame finite element scheme, the shadow model of fragments, the representation of any stress component by areas of different colors or isolines, contact pressure diagrams and the representation of contact forces by segments of normals proportional by the length to values of these forces.

In the analysis of information, the main attention was paid to the laws of pressure distributions on contact surfaces, the shape and size of the contact, the maximum pressure in contact and edge effects when the wheel is positioned above the edge of the joint.

The considered problem was solved at the values of loads from the wheel to the rail of 62.5, 110, 150 and 300 kN. The contact pressure distribution obtained from the solution of elastic problem at a load of 110 kN is shown in Fig. 3.

The pressure diagram is very similar to the diagram obtained for the wheel and rail at a distance from the joint and differs from it by the presence of an edge effect at the end of the rail. The edge effect is manifested in a sharp increase in the pressure at the edge. The contact pressure distributions for the considered load cases are shown in Fig. 4.

The evaluation of accumulated damage in the material of the wheel is carried out using the wheel steel fatigue curve. This curve shows the dependence of the number of loading cycles by contact pressures of samples prior to failure, on the maximum contact pressure. In order to determine the accumulated damage, it is necessary to

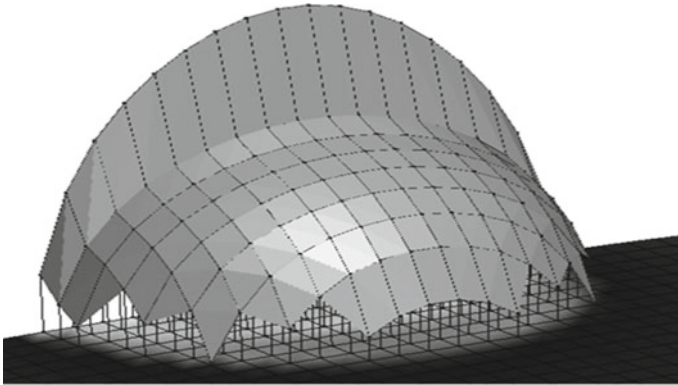


Fig. 3 Distribution of pressures in contact with the wheel and rail edge

Fig. 4 Distributions of contact pressures along the rail when the wheel is placed on the edge of the rail: 1—300 kN, 2—150 kN, 3—110 kN and 4—62.5 kN

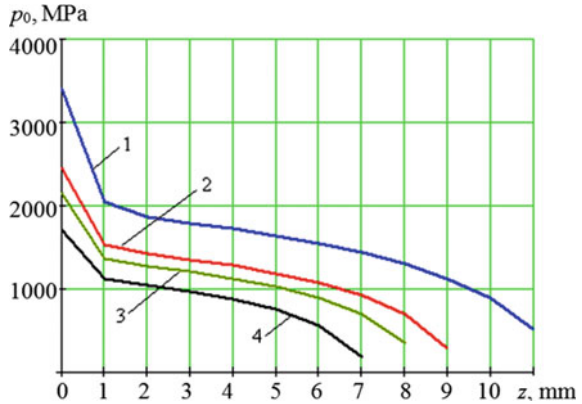
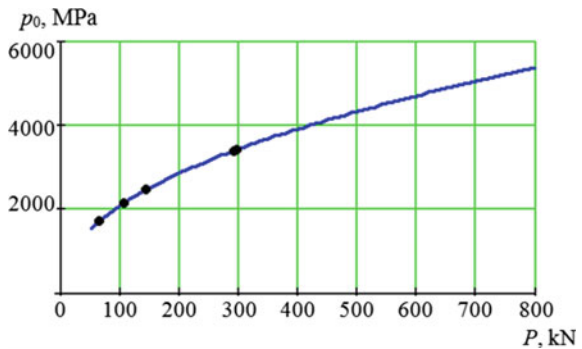


Fig. 5 Graph of the dependence of the maximum pressures on the impact force



obtain a method for determining the maximum pressure, depending on the impact force that occurs when the wheel hits the joint. During an impact, the force can take any values, and the calculation is performed only for four of them, then from the obtained results, it is possible to construct an approximating curve. A good approximation was obtained by using a second-order polynomial:

$$p_0 = 258.285P^{0.454} \tag{1}$$

The values of the normal contact force “*P*” in this formula (1) are substituted in the kilonewtons, and the maximum pressures “*p*₀” are obtained in MPa. The shape of this curve is shown in Fig. 5.



4 Conclusion

When analyzing the obtained solutions, the following conclusions can be drawn:

- A dynamic model has been developed for computer simulation of wagon movement process along a section of the track containing a rail joint, taking into account the ballast subsidence, and also parameters of the rail joint model have been identified.
- Dynamic forces arising during the motion of wagon wheel in the area of rail joint, including the track sections with ballast subsidence, were investigated.
- Analytical and numerical methods have been used to study the stress state in the wheel of the wagon with its different location relative to the rail joint: at the rail edge, at a distance from it at several values of the load from the wheel to the rail.
- For the case of the wheel location at a distance from the joint, the calculation of contact stresses is performed using Hertz solution and the finite element method. In order to determine maximum contact pressures, an approximating dependence was obtained based on Hertz's solution.
- For the variant of wheel position on the rail edge, the solution was obtained using finite element model. Based on the results of the solution for four values of load transferring from the wheel to the rail, an approximating relationship is proposed to determine the maximum contact pressure. The obtained results will allow developing a methodology for assessing the effect of rail joints on the accumulation of contact fatigue damages.

References

1. Verigo MF, Kogan AYa (1986) *Vzaimodeistvie puti i podvizhnogo sostava* (Interaction of the track and rolling stock). Transport, Moscow
2. Kogan AYa, Peich YuL, Poleschuk IV (2003) *Raschety dinamiki udara v yelementah konstrukcii puti* (Calculations of the impact dynamics in the elements of the path construction). In: *Problems of track facilities of Eastern Siberia: coll. of sc. pap. IrGUPS, Irkutsk*, pp 17–29
3. Grachev VF, Alexandrov AI (1983) *Vlijanie mesta prilozhenija nagruzki ot kolesa k rel'su na raspredelenie kontaktnyh davlenii* (Influence of the place of loading from the wheel to the rail on the distribution of contact pressures). *Bull VNIIZHT* 4:43–44
4. Frishman MA (1975) *Kak rabotaet put' pod poezdami* (How does the path work under the trains). Transport, Moscow
5. Shahunyants GM (1987) *Zheleznodorozhnyi put': ucheb. dlja vuzov zh.-d. transp.* (Railroad: Textbook for high schools of railway transport), 3rd edn. revis and suppl. Transport, Moscow
6. Ivanov VV (2008) *Vlijanie defektov v stykovom soedinenii rel'sov na razvitie udarnogo impul'sa v sisteme "koleso – rel's"* (Influence of defects in the joint connection of rails on the development of a shock pulse in the "wheel-rail" system). In: *General and complex problems of technical and applied sciences: interuniversity collection of works of young scientists, graduate students and students. Siberian State Automobile and Highway Academy Omsk* 5–1:117–120

7. Sakalo AV (2011) Modelirovanie nakoplenija kontaktno-ustalostnyh povrezhdenii v kolese vagona s ispol'zovaniem konechno-yelementnyh fragmentov na uprugom osnovanii (Simulation of contact fatigue damages accumulation in the wagon wheel using finite element fragments on an elastic foundation). Bull VNIIZHT 4:44–49
8. Evtukh ES, Neklyudova GA (2012) Computer simulation of the process of passing the wheel through the joint to solve the contact problem. Visnik of the Volodymyr Dahl East Ukrainian National University 176(2):7–11
9. Sakalo VI, Kossov VS (2004) Kontaktnye zadachi zheleznodorozhnogo transporta (Contact problems of railway transport). Mashinostroenie, Moscow
10. Yazykov VN, Pogorelov DYU, Lysikov NN (2012) Computer simulation of train dynamics in real time mode. Visnik Volodymyr Dahl East Ukr Natl Univ 176(2):35–39
11. Yazykov V, Pogorelov D (2010) Simulation of wheel and rail wear in universal mechanism software. In: EUROMECH colloquium 515. Advanced applications and perspectives of multibody system dynamics, Blagoevgrad, 13–16 July 2010
12. Evtukh ES, Agapov DG (2007) Opredelenie uprugih dissipativnyh karakteristik podrel'sovogo osnovanija (Determination of the elastic dissipative characteristics of the under-rail base). In: Materials of the 58th scientific conference of the faculty. BSTU, Bryansk, pp 116–118
13. Evtukh ES et al (2009) Vlijanie prosadki ballasta na dinamicheskie usilija, vznikayushie mezhdru kolesom i rel'som pri prohozhdenii styka (Effect of ballast subsidence on the dynamic forces that arise between the wheel and the rail during the passage of the joint). Trans Urals 23:32–34

Determination of Eigenforms and Frequencies of Transverse Vibrations of a Rod of Variable Cross Section in the Field of Centrifugal Forces



A. P. Levashov and O. Yu. Medvedev

Abstract The authors of the article have developed a unified method for determining the forms and frequencies of free transverse vibrations of a direct rod of variable cross section, taking into account tensile forces caused by the rotation of the rod. The technique is based on finite element approximations where the rod is represented as a set of four-degree bendable elements. The Kirchhoff–Love hypothesis is used while calculating. To obtain the equations of motion of finite elements, the general dynamic equation is applied. The mass matrix, the physical stiffness matrix, and the geometrical stiffness matrix of the final element are obtained taking into account the linear law of variation of the linear mass, flexural rigidity, and tensile centrifugal force along the length of the element. To get the equations of free vibrations of a finite element rod model, the authors have used the general dynamic equation. They have carried out the approbation of the developed technique with the determination of several low natural forms and frequencies of transverse vibrations of a rod of variable thickness rotating around a fixed axis. To determine these forms and frequencies, the iteration method in the subspace is used. This method allows calculating the lower forms and frequencies of natural vibrations of nodes, units, and structures operating in the field of centrifugal forces. The described algorithm is implemented as a program in the MATLAB package.

Keywords Finite element · Centrifugal force · Frequency · Form of vibrations · Geometric rigidity

1 Introduction

Many rotating elements of aviation, engineering, and other structures can be reduced to the calculation of a rod of variable cross section located in the field of centrifugal inertia forces. The most typical of these elements are the rotor blades of

A. P. Levashov (✉) · O. Yu. Medvedev
Vyatka State University, 36, Moskovskaya Street, Kirov 610000, Russia
e-mail: usr06296@vyatsu.ru

helicopters. When a helicopter is flying, the rotor blade under the action of aerodynamic forces can make significant fluctuations. These movements can cause large stresses in the blades or large moments in its root, which are transmitted through the sleeve to the helicopter. Therefore, when designing blades and rotor hubs, it is necessary to make these loads as small as possible. Due to the high flexibility of the blades, their vibrations may be geometrically nonlinear and may have large displacement amplitudes and angles of rotation [1, 2]. In some flight modes, when the frequency of external influences on the propeller coincides with the frequency of natural vibrations of the blade, it may lead to resonance. Elimination of resonance phenomena on the blades is the most urgent task of the helicopter rotor design, which requires the calculation of the shape and frequency of free vibrations of the blade, taking into account its rotation in the screw plane [3]. So, we need available computational techniques and applied software for determining loads on the units of the carrier system [3]. Approximate methods are used [3] to calculate carrier systems which significantly reduce their reliability.

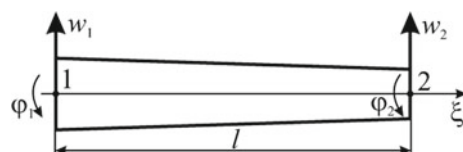
The authors of the article suggest to use the finite element method (FEM) [4] to solve this problem. This method is widely used in order to calculate aircraft, ship structures, and buildings [5–8]. There are several types of FEM: solution in displacement; in strength; mixed wording; hybrid approach. FEM in the form of the displacement method has received the most widespread use in our country and abroad, since it has a number of advantages: simplicity, ease of its programming, natural suitability for solving nonlinear problems [9]. A universal numerical method for solving boundary value problems today is the finite element method in the form of the displacement method. It is often used in problems of mechanics of a deformable solid and in structural mechanics. The finite element method combines universality, a high degree of formalization, and algorithmization. It provides an opportunity to fully automate the computational process. Numerous software systems that use the finite element method have expanded the possibility of a detailed study of the stress–strain state of structures [10].

2 Formation of Free Vibration Equations for a Finite Element Model of a Rod

The finite element method is implemented when solving problems. [4].

The rod is modeled by a set of four-degree bendable finite elements. The nodal parameters of the finite element (FE) are the deflections w_1, w_2 and the angles of rotation ϕ_1, ϕ_2 of its nodes (Fig. 1).

Fig. 1 Four-degree bendable finite element



The element works within the framework of the Kirchhoff–Love hypotheses. The deflection function $w(\xi, t)$ is approximated within an element by the dependence

$$w(\xi, t) = \{N(\xi)\}^T \{r^{(e)}(t)\}. \tag{1}$$

$$\{N(x)\} = \begin{Bmatrix} N_1 \\ N_2 \\ N_3 \\ N_4 \end{Bmatrix}; \quad \{r^{(e)}(t)\} = \begin{Bmatrix} w_1 \\ \phi_1 \\ w_2 \\ \phi_2 \end{Bmatrix};$$

$$N_1 = 1 - 3\xi^2/l^2 + 2\xi^3/l^3; \quad N_2 = \xi - 2\xi^2/l + \xi^3/l^2;$$

$$N_3 = 3\xi^2/l^2 - 2\xi^3/l^3; \quad N_4 = -\xi^2/l + \xi^3/l^2.$$

To obtain the equations of FE motion, we use the general equation of dynamics:

$$\delta A = \delta A_M + \delta A_J + \delta A_S = 0. \tag{2}$$

here $\delta A_M, \delta A_J, \delta A_S$ is the possible work of bending moments M , linear transverse inertial forces J , and longitudinal internal forces $S(\xi)$, caused by the rotation of the rod. The value δA_M is determined by the expression

$$\delta A_M = - \int_0^l \delta k M dx, \tag{3}$$

where k is curvature of the axis in an arbitrary section of the element. Further, we use known dependences:

$$k = \partial^2 w(\xi, t) / \partial \xi^2, \quad M = EI(\xi)k. \tag{4}$$

Taking into account (1) and (4), the expression (3) can be reduced to the form

$$\delta A_M = - \left\{ \delta r^{(e)} \right\}^T \left[K^{(e)} \right] \left\{ r^{(e)}(t) \right\}. \tag{5}$$

where $[K^{(e)}] = \int_0^l EI(\xi) \{N''_\xi\} \{N''_\xi\}^T d\xi \left(\{N''_\xi\} = d^2\{N\}/d\xi^2 \right)$ is physical stiffness matrix FE. We assume that the stiffness $EI(\xi)$ varies within the limits of the FE according to the linear law: $EI(\xi) = EI_1(1 - \xi/l) + EI_2\xi/l$. Therefore, we obtain:

$$\begin{aligned}
 [K^{(e)}] = EI_1 & \begin{bmatrix} 12/l^3 & 6/l^2 & -12/l^3 & 6/l^2 \\ 6/l^2 & 4/l & -6/l^2 & 2/l \\ -12/l^3 & -6/l^2 & 12/l^3 & -6/l^2 \\ 6/l^2 & 2/l & -6/l^2 & 4/l \end{bmatrix} \\
 - (EI_1 - EI_2) & \begin{bmatrix} 6/l^3 & 2/l^2 & -6/l^3 & 4/l^2 \\ 2/l^2 & 1/l & -2/l^2 & 1/l \\ -6/l^3 & -2/l^2 & 6/l^3 & -4/l^2 \\ 4/l^2 & 1/l & -4/l^2 & 3/l \end{bmatrix}.
 \end{aligned}$$

The possible work of transverse inertia forces is:

$$\delta A_J = - \int_0^l \delta w m(\xi) \partial^2 w(\xi, t) / \partial t^2 d\xi. \quad (6)$$

Here $m(\xi)$ is element linear mass. Taking into account the approximation (1), we obtain

$$\delta A_J = - \left\{ \delta r^{(e)} \right\}^T \int_0^l \{N\} \{N\} m(\xi) d\xi \left\{ \ddot{r}^{(e)} \right\}. \quad (7)$$

Expression (7) can have the form:

$$\delta A_J = - \left\{ \delta r^{(e)} \right\}^T [M^{(e)}] \left\{ \ddot{r}^{(e)} \right\}, \quad (8)$$

where $[M^{(e)}] = \int_0^l \{N\} \{N\} m(\xi) d\xi$ is mass matrix FE. We use approximation $m(\xi) = m_1(1 - \xi/l) + m_2\xi/l$. Therefore, we obtain:

$$\begin{aligned}
 [K^{(e)}] = m_1 S_1 & \begin{bmatrix} 13l/35 & 11l^2/210 & 9l/70 & -13l^2/420 \\ 11l^2/210 & l^3/105 & 13l^2/420 & -l^3/140 \\ 9l/70 & 13l^2/420 & 13l/35 & -11l^2/210 \\ -13l^2/420 & -l^3/140 & -11l^2/210 & l^3/105 \end{bmatrix} \\
 - (m_1 - m_2) & \begin{bmatrix} 3l/35 & l^2/60 & 9l/140 & -l^2/70 \\ l^2/60 & l^3/280 & l^2/60 & -l^3/280 \\ 9l/140 & l^2/60 & 2l/70 & -l^2/28 \\ -l^2/70 & -l^3/280 & l^2/28 & l^3/168 \end{bmatrix}
 \end{aligned}$$

To determine the possible work of the force $S(\xi)$, we find the elementary work of this force on an infinitely small segment $d\xi$ when turning it through a small angle

ϕ : $dA_S = -S(1 - \cos \phi)d\xi$. We decompose $\cos \phi$ into a Taylor series in the vicinity of the point $\phi = 0$ up to a value of the second order of smallness: $\cos \phi = \cos 0 - \phi^2/2 = 1 - \phi^2/2 = 1 - (\partial w(\xi, t)/\partial \xi)^2/2$. We obtain:

$$dA_S = -0.5S(\xi)(\partial w(\xi, t)/\partial \xi)^2 d\xi, \quad A_S = -0.5 \int_0^l S(\xi)(\partial w(\xi, t)/\partial \xi)^2 d\xi,$$

$$\delta A_S = - \int_0^l S(\xi) \delta(\partial w(\xi, t)/\partial \xi) \partial w(\xi, t)/\partial \xi d\xi.$$

Taking into account (1), the last expression can have the form

$$\delta A_S = - \left\{ \delta r^{(e)} \right\}^T \left[G^{(e)} \right] \left\{ r^{(e)} \right\}, \tag{9}$$

where $[G^{(e)}] = \int_0^l S(\xi) \{N'\} \{N'\}^T d\xi$ is geometric stiffness matrix FE. We assume that the force $S(\xi)$ is distributed within the element according to a linear law: $S(\xi) = S_1(1 - \xi/l) + S_2\xi/l$. Therefore, after integration we get:

$$[G^{(e)}] = S_1 \begin{bmatrix} 6/(5l) & 1/10 & -6/(5l) & 1/10 \\ 1/10 & 2l/15 & -1/10 & -l/30 \\ -6/(5l) & -1/10 & 6/(5l) & -1/10 \\ 1/10 & -l/30 & -1/10 & 2l/15 \end{bmatrix} - (S_1 - S_2) \begin{bmatrix} 3/(5l) & 1/10 & -3/(5l) & 0 \\ 1/10 & l/30 & -1/10 & -l/60 \\ -3/(5l) & -1/10 & 3/(5l) & 0 \\ 0 & -l/60 & 0 & l/10 \end{bmatrix}.$$

Substituting (5), (8), and (9) into Eq. (2) and taking into account the independence of variations of the components of the vector $\{r^{(e)}\}$, we have the system of equations

$$[M^{(e)}] \{\ddot{r}^{(e)}\} + ([K^{(e)}] + [G^{(e)}]) \{r^{(e)}\} = 0. \tag{10}$$

Summing up (10) by the method of direct rigidity [1, 2], we obtain the equation of free transverse vibrations of a finite element beam located in the field of centrifugal forces:

$$[M] \{\ddot{r}\} + ([K] + [G]) \{r\} = 0, \tag{11}$$

where $[M], [K], [G], \{r\}$ are mass matrix, physical stiffness matrix, geometric stiffness matrix, and nodal displacement vector of the marked model.

The solution of Eq. (11) has the form

$$\{r\} = \{F\}q(t) = \{F\}q_0e^{i\omega t}. \tag{12}$$

here $\{F\}$ is a vibration mode; i —the imaginary unit; q_0, ω —the amplitude and frequency of the normal coordinate $q(t)$, corresponding to the given form.

$$([K] + [G] - \omega^2[M])\{F\} = 0, \tag{13}$$

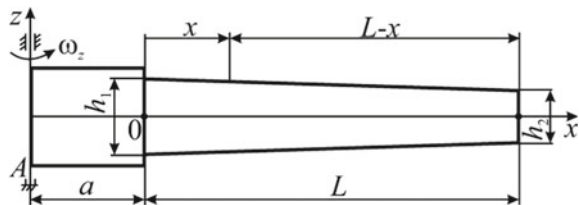
Substituting (12) into (11), we have a system of linear homogeneous equations components of the content of the generalized problem of eigenvalues and eigenvalues [11]. The eigenvalues and eigenvectors are the squares of the eigenfrequencies ω_j and the corresponding forms $\{F\}_j$. To determine the full spectrum of forms and frequencies of the system (13), the well-known Jacobi method of rotations [12–14] can be used. This method is implemented by the built-in functions of the popular mathematics packages MATLAB [12, 14] and Mathcad [15].

However, while determining the dynamic response of a structure, only a few lower eigenforms and frequencies are of interest, and the finding of them is the content of the partial eigenvalue problem [16]. To solve this problem, you can use the methods of matrix iteration. Currently, one of the best methods is the iteration method in the subspace [11, 17]. This method is well combined with the finite element method and finite difference methods [18]. Works [19, 20] propose a modified algorithm that improves the stability and rate of convergence of this method.

3 Numerical Experiments and Analysis of the Results

We consider a variable-thickness rod (Fig. 2) rotating around the vertical axis Az with a constant angular velocity $\omega z = 2262 \text{ s}^{-1}$ (360 rpm). The distance from the root section of the rod to the axis is $Az a = 500 \text{ mm}$. The geometrical parameters of the rod are: $h_1 = 30 \text{ mm}$; $h_2 = 9 \text{ mm}$; $L = 3500 \text{ mm}$. The cross section of the rod is rectangular with a constant width $b = 230 \text{ mm}$. The modulus of elasticity and density of the material are: $E = 72,000 \text{ MPa}$; $\rho = 2700 \text{ kg/m}^3$.

Fig. 2 Variable-thickness core



The longitudinal force $S(x)$ of the centrifugal forces of inertia in an arbitrary section of the rod is determined by the expression

$$S(x) = \omega_z^2 b \rho \int_0^{L-x} (a + x + \eta) h(\eta) d\eta$$

where $h(\eta)$ is

$$h(\eta) = [h_1(1 - x/L) + h_2x/L] \cdot [1 - \eta/(L - x)] + h_2\eta/(L - x).$$

After integration, we get

$$\phi(x) = \omega_z^2 b \rho (c_0 + c_1x + c_2x^2 + c_3x^3)/(6L), \quad c_0 = (h_1 + 2h_2)L^3 + 3a(h_1 + h_2)L^2, \\ c_1 = -6aLh_1, \quad c_2 = 3(-Lh_1 + ah_1 - ah_2), \quad c_3 = 2(h_1 - h_2).$$

We determined 10 lower eigenforms and frequencies of transverse vibrations of the rod by the method of iterations in the subspace. Table 1 shows eigenfrequencies corresponding to these vibrations. Figure 3 shows three lowest forms, obtained with and without rotation of the rod.

Analysis of the results shown in Table 1 and in Fig. 3 shows that the rotation of the rod has the greatest effect on the lower eigenpair (form and frequency). As the form number increases, this effect becomes less significant.

The described algorithm is implemented as a program in the MATLAB package, which allows to define eigenforms of ten lower frequencies of the rod.

Table 1 Frequency of free vibrations of the rod

Rod frequency numbers	Frequencies of free vibrations, 1/s	
	Not taking into account the rotation of the rod	Taking into account the rotation of the rod
1	2.3719	7.5878
2	9.6618	17.9956
3	23.5882	33.2658
4	44.2744	54.6992
5	71.7990	82.6720
6	106.1772	117.3369
7	147.4164	158.7702
8	195.5207	207.0120
9	250.4928	262.0856
10	312.3348	324.0051

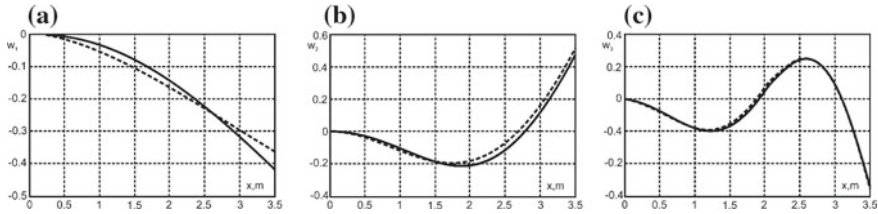


Fig. 3 a–c Three lowest forms of transverse vibrations, taking into account (solid lines) and excluding (dashed lines) rotation of the rod

4 Conclusion

The paper proves it is possible to take into account centrifugal inertia forces when determining the eigenforms and frequencies of transverse vibrations of a rod of variable cross section based on finite element approximations and the iteration method in a subspace to solve a partial eigenvalue problem. To avoid resonance, eigenfrequencies of the blade should be a multiple of the screw rotation frequency [2].

The authors have obtained the mass matrix, the physical stiffness matrix, and the geometric stiffness matrix of the rod-bending element taking into account changes in linear mass, bending stiffness, and tensile force within the element. It improves the calculation accuracy compared to the traditional approach, where all specified parameters within the element are considered constant. The results are similar to those calculated by analytical methods [21].

However, it should be noted that the task of determining the eigenforms and vibration frequencies of real structures (not completely, but only partially) is a rather complicated problem [6, 7].

References

1. Dudnik VV (2005) Helicopter design. Publishing House IUI AP, Rostov-on-Don, p 158
2. Johnson U (2013) Helicopter theory, vol 2. The Book on Demand, Moscow, p 515
3. Averyanov IO (2012) Investigation of the loading and durability of the helicopter rotor blades on menevir and unsteady modes. Dissertation, MATI-RGTU named after K.E. Tsiolkovsky
4. Shishkin VM, Levashov AP (2012) Formation of defining equations for modeling the resonant vibrations of thin-walled composite structures. Bull KSTU 1:82–88
5. Obraztsov IN, Saveliy LM, Khazanov KhS (1985) Finite-element method for structural mechanics of aircraft. High School, Moscow, p 392
6. Parlett B (1983) Symmetric eigenvalue problem. Numerical methods. Mir, Moscow, p 384
7. Clough R, Penzien J (1979) Dynamics of structures. Stroyizdat, Moscow, p 320
8. Ignatiev AV, Gabova VV (2007) Algorithm of static calculation of flat rod systems using the finite element method in mixed form. Bull Volgograd State Univ Arch Civ Eng Ser Nat Sci 6 (23):72–77
9. Levashov AP (2012) Modeling the dynamic response of thin-walled composite structures in resonant loading modes. Dissertation, Vyatka State University

10. Gabova VV (2011) Application of a mixed form of FEM to calculations of core systems. Dissertation, Volgograd State University of Architecture and Civil Engineering
11. Mitchell E, Waite R (1981) The finite element method for partial differential equations. Mir, Moscow, p 216
12. Ketkov YL, Ketkov AY, Schulz MM (2004) MATLAB 6.x: programming numerical methods. BHV-Petersburg, St. Petersburg, p 672
13. Formalev VF, Reznikov DL (2004) Numerical Methods. Fizmatlit, Moscow, p 400
14. Matthews John G, Fink Curtis D (2001) Numerical methods. using MATLAB. Williams, Moscow, p 720
15. Kiryanov DV (2006) Mathcad 13. BHW-Petersburg, St. Petersburg, p 608
16. Shishkin VM, Levashov AP (2017) Modeling of resonant vibrations of an elongated plate with a damping coating. Society, Science, Innovations (NPK-2017): College of Arts: All-Russian annual scientific-practical conference Vyatka State University, Kirov, pp 2439–2450
17. Postnov VA, Kharkhurim IY (1974) The finite element method in the calculations of ship structures. Shipbuilding, Leningrad, p 344
18. Trushin SI (2002) Determination of eigen frequencies and modes of vibrations of plates made of composite material by the method of iterations in a subspace. Bull Peoples' Friendsh Univ Russ 1:102–106
19. Bate K (2010) Finite element methods. Fizmatlit, Moscow, p 1024
20. Bate K, Wilson E (1982) Numerical analysis methods and finite element method. Stroyizdat, Moscow, p 447
21. Girfanov AM (2012) Numerical models and methods for studying the loading of a helicopter with a hinge rotor. Dissertation, Kazan National Research Technical University named after A.N. Tupolev

Problem of Calculation of Reliability of Hierarchical Complex Technical Systems



P. A. Kulakov, D. D. Galyautdinov and V. G. Afanasenko

Abstract Within the framework of ensuring availability at oil and gas processing facilities, an analysis of methods for assessing the reliability of a technical object based on the reliability, availability and maintainability of individual elements was made. The difficulties arising from the complex assessment of the reliability of complex technical objects using different methods are shown: A number of methods did not allow to assess the entire complexity of the object, and other methods led to an increase in the complexity of calculations with an increase in the number of individual elements. The authors propose to use combinations of previously known methods at different hierarchical levels for system analysis. An algorithm for assessing reliability based on dividing a complex object into elements, the evaluation of the reliability of which is determined by one of the most suitable methods, such as the Markov models of states and transitions or statistical models, has been developed. Additional designations are proposed for the unambiguous interpretation and structuring of the reliability assessment system. As an example, the calculation of the failure-free operation of the gas treatment unit of the tar visbreaker was made. The possibility of calculating complex interdependent systems, where linear statistical calculation methods are not applicable, and the labor intensity for the Markov method has power-law dependence, is shown.

Keywords Reliability · Availability · Markov processes · Redundancy · Technical systems · Hierarchical systems · Statistical analysis

1 Introduction

As part of maintaining operational availability of production, the task of the comprehensive assessment of reliability of complex technical facilities at enterprises of the energy complex, petrochemical industry and machine building is quite relevant at present.

P. A. Kulakov (✉) · D. D. Galyautdinov · V. G. Afanasenko
Ufa State Petroleum Technological University, 1, Kosmonavtov Street, Ufa 450062, Russia
e-mail: kulakov.p.a@mail.ru

Works [1–5] present aspects of reliability from the point of view of mathematical statistics and probability theory. In some works, the reliability of identical or elements performing a similar function, but with different reliability parameters, is considered. These can be machines operating in parallel, redundant elements of electrical grids, pumps or radio altimeters and radio altimeter systems for rocket technology. There are articles that consider the reliability of multi-element systems as a combination of parallel and sequential elements. With regard to complex production, transportation and processing of hydrocarbons, some authors propose to build a fault tree, which will show a chain of events leading to the failure of the entire system [6, 7]. By failure, we mean the object's loss of its ability to perform the required function [8]. However, for systems consisting of even a small number of elements, for example, 100 pieces with a failure probability of 0.99, taking into account the rules of mathematical statistics, the reliability will be about 30%.

With an increase in the number of system elements and the operation time of these elements, the probability of failure-free operation $P(t)$ of each element will fall, and the probability of failure-free operation of the entire unit will tend to zero (that is, according to linear calculations of the fault tree, permanent failures of the entire technological system should occur). Some authors introduce correction statistical coefficients [9, 10], but in this case, calculation difficulties emerge, taking into account the loaded and unloaded reserve. Thus, the analysis of the fault tree [6–8] allows you to visualize the paths of development of failures or emergency situations, but is poorly applicable for a correct quantitative assessment of the occurrence of events.

A number of authors propose to consider the system with the Markov theory of processes and states [11–14]. As a rule, as an example, a system of 3–6 elements which has several dozen states or a system of elements of the same type, which makes it possible to combine repeating states into groups in order to simplify calculations, is usually demonstrated.

There are approaches associated with expert assessments [15] and fuzzy logic [16].

Modern enterprises strive for trouble-free and efficient implementation of the main production processes; therefore, a quantitative analysis of the entire system plays an important role [3, 17].

The aim of the work is to propose a mathematical model that adequately evaluates the probability of failure-free operation of a technical system in case of probable failures of its individual elements or subsystems, especially subsidiary ones, and to propose a mechanism for transformation of subsystems reliability to a small risk value or an insignificant risk value, according to the risk matrix.

2 Reliability Assessment Mechanism

Methods for calculating the reliability are described in the following works [18, 19].

Probabilistic risk assessment

In general, reliability can be calculated using the formula [19]

$$P(t) = e^{-\lambda t} \tag{1}$$

where λ the failure rate is determined by the formula:

$$\lambda = \frac{1}{MTTF} \tag{2}$$

where MTTF—is mean time to failure

$$P(t) = e^{-\lambda t} \tag{3}$$

Reliability of complex systems

Complex systems consisting of several elements can be represented as standard models [19]:

1. Consecutive connection of elements
2. Parallel connection of elements
3. *M*-out-of-*n* connection (it is assumed that *m* elements from *n* must work correctly)
4. Models with unloaded reserve
5. Recovery systems.

System of consecutive elements reliability

A consecutive system is operational if all the elements of the system are operational.

The reliability of a system consisting of *n* consecutive elements, each of which is necessary for the system functioning, and the element failures are independent of each other, is equal to [1]:

$$P_{series}(t) = P_1(t) \cdot P_2(t) \cdot \dots \cdot P_n(t) = \prod_{i=1}^n P_i(t) \tag{4}$$

The assumption $\lambda = \text{Const}$ allows to calculate the failure frequency of a linear system by summing the failure rates of individual elements.

$$\lambda = \sum \lambda_i \tag{5}$$

Reliability of parallel elements system

Backup reliability *m*-out-of-*n*

It is considered that *m* of *n* elements should work in order for the whole system to work correctly:

- initially n elements in parallel carry out the functions performed by each element separately;
- m intact elements are necessary to obtain the correct result;
- $(n-m)$ elements are redundant.

The reliability of the m -out-of- n system is determined by the number of i combinations [$m \leq i \leq n$] of correct elements in case of $(n-i)$ elements failure according to the formula:

$$P_{\text{moon}} = \sum_{i=m}^n C_n^i \cdot P^i \cdot Q^{n-i} = \sum_{i=m}^n C_n^i \cdot P^i \cdot (1-P)^{n-i} \quad (6)$$

3 Markov Models. Calculation of the Reliability of the Recovery System

Recovery system models are described using Markov processes [12, 14, 20].

According to the hypothesis of the Russian mathematician Markov:

The probability of getting out of this state depends only on the current state and does not depend on how long the system is in this state, nor on how this state was reached.

States must be:

Mutually exclusive

Collectively exhaustive.

Mathematical description of Markov models. In its most general form, the Markov model consists of a system of interrelated differential equations describing the process in terms of the probabilities $P_i(t)$ of the system's states in predetermined states S , given the initial conditions $P_i(0)$.

Let the model have N states, and the intensity (frequency) of the transition from the S state to the S_i state is defined as λ_i . Then, the system of equations corresponding to this model will look as follows:

$$\begin{aligned} \frac{dP_1}{dt} &= \lambda_{11} \cdot P_1 + \lambda_{12} \cdot P_2 + \dots + \lambda_{1N} \cdot P_N \\ \frac{dP_2}{dt} &= \lambda_{21} \cdot P_1 + \lambda_{22} \cdot P_2 + \dots + \lambda_{2N} \cdot P_N \\ &\dots \\ \frac{dP_N}{dt} &= \lambda_{N1} \cdot P_1 + \lambda_{N2} \cdot P_2 + \dots + \lambda_{NN} \cdot P_N \end{aligned} \quad (7)$$

One of the equations is discarded, and the normalization condition is added to the remaining $(N - 1)$ equation.

$$\sum_{i=1}^N P_i(t) = 1 \quad (8)$$

A stationary solution can be found under the assumption that at infinity, the change in probability is zero. Next, Markov equations are solved using Laplace transformations.

There are two types of models of a redundant recovery system: with an unloaded reserve and with a loaded reserve.

For calculating the reliability of hierarchical complex technical systems the authors propose to use combinations of previously known methods at different hierarchical levels in analyzing the system.

At the lower levels, it is necessary to calculate the failure-free operation of subsystems that will act as basic events at higher levels.

The calculation algorithm is as follows: The whole system (zero level) is divided into first-level subsystems, first-level subsystems are divided into second level subsystems, etc., until we reach atomic or indivisible elements. The minimum hierarchical level is determined by the expert opinion of a specialist.

Statistical models are used to determine the reliability of simple systems consisting of interdependent elements.

To consider the situation with a complex chain of events in the Markov system, a system of Kolmogorov–Chapman equations is compiled.

The concept of transition intensity is used to calculate the transition probability [12, 20]. Simplified, one can denote the failure rate by λ , the recovery intensity—by μ , the time required for switching on (activation) of the reserve—by γ .

Failure rate λ is a parameter characterizing the internal characteristics of the device or technical system. We can determine it through the mean time between failures for devices, using non-destructive testing methods—for technical structures and equipment, using failure statistics.

4 Application of the Method for Calculating the Reliability of Hierarchical Complex Technical Systems on the Example of the Gas Treatment Unit of a Tar Visbreaker Unit

Let us consider the reliability of the gas cleaning unit node of tar visbreaker. The node consists of a column apparatus A-201, level, temperature, pressure sensors, a system of redundant pumps (H-205, H-205a) and a pipeline system (Fig. 1).

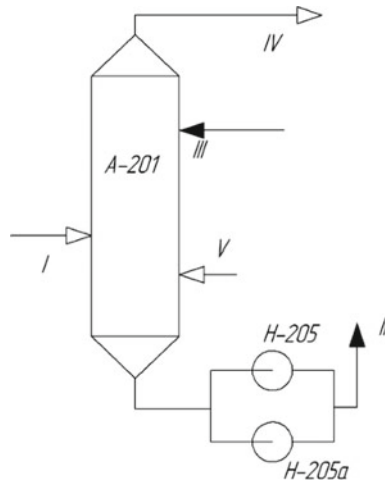


Fig. 1 Schematic diagram of the gas cleaning unit of tar visbreaker. I—hydrocarbon gas with hydrogen sulfide; II—saturated 15% solution of MEA in the regeneration unit; III—regenerated 15% solution of MEA; IV—purified gas in the steam ejector; and V—water vapor

We calculate the reliability of the system consisting of two pumps in the system (one loaded, one in an unloaded reserve), feeding the solution of monoethanolamine from the column for regeneration. If the pump fails, the redundant pump is turned on and the main one is repaired. There may be a situation with the breakdown of both pumps.

The fault tree of the gas cleaning unit of the tar visbreaker is shown in Fig. 2. It can be seen from the figure that event 5 was considered in detail elsewhere. The

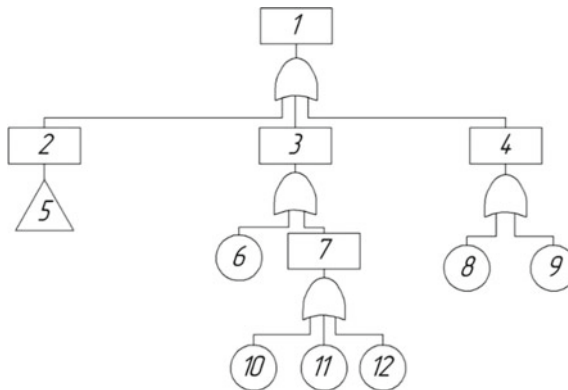
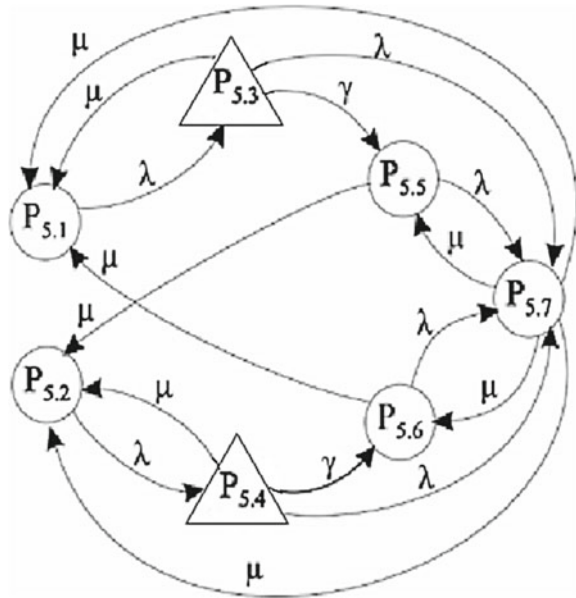


Fig. 2 Fault tree of gas cleaning unit of tar visbreaking unit. 1—system failure; 2—redundant pump failure; 3—column apparatus shut-down; 4—pipeline failure; 5—failure of redundant pump system; 6—depressurization of the absorption column A-201; 7—loss of control over the process; 8—depressurization of the pipeline in places of flange connections; 9—pipeline corrosion; 10—breakage of the manometer; 11—thermometer breakage; and 12—breakage of the level gauge

Fig. 3 Diagram of transitions and states



failure of the redundant pump system is considered as a Markov diagram of transitions and states (Fig. 3). From the diagram of transitions and states, it can be seen that the events P_{5.3} and P_{5.4} are considered in more details separately.

In Fig. 3, a triangle indicates events considered elsewhere (Fig. 4), as in the fault tree (Fig. 1).

Further, the Markov model is considered in the form of a diagram of transitions and states, where the intensity of the occurrence of events 5.3 and 5.4 is found from the fault tree (Fig. 4).

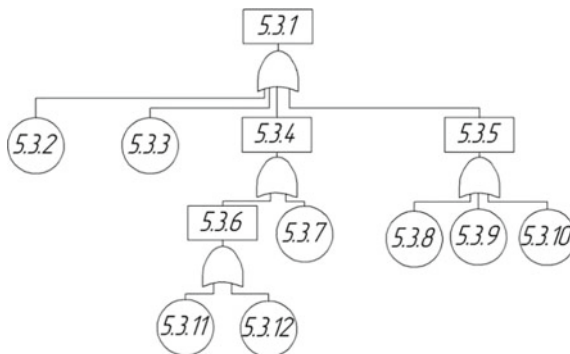


Fig. 4 Pump fault tree 5.3.1—pump failure; 5.3.2—breaker malfunction; 5.3.3—power failure; 5.3.4—engine failure; 5.3.5—overheating of the bearings; 5.3.6—fault winding; 5.3.7—fuse blown; 5.3.8—violation of the centering of the unit; 5.3.9—failure of bearing lubrication; 5.3.10—wear of bearings; 5.3.11—violation of operating conditions; and 5.3.12—operator error

The reliability of switching devices in this research is not taken into account. We introduce the following set of states:

- State 5.1—both pumps are operational, the first is working, and the second is in an unloaded reserve.
- State 5.2—both pumps are operational, the second is working, and the first is in an unloaded reserve.
- State 5.3—the first pump failed, the second is operational, and the production line of the enterprise is reconfigured to activate it as the main pump.
- State 5.4—the second pump failed, the first one is operational, and the production line of the enterprise is reconfigured to activate it as the main pump.
- State 5.5—the first one failed, the second one works.
- State 5.6—the first is working, the second—has failed.
- State 5.7—both pumps failed.

States to Fig. 3 are shown in Table 1.

We take the pump repair time to be 96 h (during this time we must eliminate the repaired damage μ and put the pump in an unloaded reserve): $\mu = 1/96$.

Take the turn-on time of the redundant pump equal to 1 min or 0.017 h: $\gamma = 1/0.017$.

Analysis of the structure and frequency of pump failures (events 5.3 and 5.4) was performed using the fault tree (Fig. 4).

As can be seen in Fig. 4, the pump will fail when one of the eight basic events occurs. For the analysis of the Markov model, we find the pump failure rate according to formula 9 based on the data of the pump certificates:

$$\lambda = \sum \lambda_i = 2 \times 10^{-7} + 2 \times 10^{-7} + 4 \times 10^{-8} + 1 \times 10^{-8} + 1 \times 10^{-8} + 2 \times 10^{-7} + 1.5 \times 10^{-5} + 2 \times 10^{-6} = 1.568 \times 10^{-5}$$

After determining the intensity of the occurrence of all events, a system of Kolmogorov–Chapman equations is compiled:

Table 1 Possible states of pumps and system in general

State	Pump 1	Pump 2	System
5.1	Work	Reserve	Work
5.2	Reserve	Work	Work
5.3	Failure	Activation	Work
5.4	Activation	Failure	Work
5.5	Failure	Work	Work
5.6	Work	Failure	Work
5.7	Failure	Failure	Failure

$$\left\{ \begin{aligned} \sum P_i(t) &= 1; P_1(0) = 1; P_2(0) = 0; P_3(0) = 0; \dots P_7(0) = 0; \\ \frac{dP_1(t)}{dt} &= -\lambda P_1(t) + \mu P_3(t) + \mu P_6(t) + \mu P_7(t) \\ \frac{dP_2(t)}{dt} &= -\lambda P_2(t) + \mu P_4(t) + \mu P_5(t) + \mu P_7(t) \\ \frac{dP_3(t)}{dt} &= -\lambda P_1(t) - (\mu + \gamma + \lambda) P_3(t) \\ \frac{dP_4(t)}{dt} &= -\lambda P_1(t) - (\mu + \gamma + \lambda) P_4(t) \\ \frac{dP_5(t)}{dt} &= \gamma P_3(t) - (\mu + \lambda) P_5(t) + \mu P_7(t) \\ \frac{dP_6(t)}{dt} &= \gamma P_4(t) - (\mu + \lambda) P_6(t) + \mu P_7(t) \\ \frac{dP_7(t)}{dt} &= \lambda P_3(t) + \lambda P_4(t) + \lambda P_5(t) + \lambda P_6(t) - 4\mu P_7(t) \end{aligned} \right.$$

In the stationary case, we have a system of linear algebraic equations with zero left sides.

$$\left\{ \begin{aligned} P_1 + P_2 + P_3 + P_4 + P_5 + P_6 + P_7 &= 1 \\ -\lambda P_1 + \mu P_3 + \mu P_6 + \mu P_7 &= 0 \\ -\lambda P_2 + \mu P_4 + \mu P_5 + \mu P_7 &= 0 \\ \lambda P_1 - (\mu + \gamma + \lambda) P_3 &= 0 \\ \lambda P_2 - (\mu + \gamma + \lambda) P_4 &= 0 \\ \gamma P_3 - (\mu + \lambda) P_5 + \mu P_7 &= 0 \\ \gamma P_4 - (\mu + \lambda) P_6 + \mu P_7 &= 0 \\ \lambda P_3 + \lambda P_4 + \lambda P_5 + \lambda P_6 - 4\mu P_7 &= 0 \end{aligned} \right.$$

To solve the presented system of 8 equations in the C# program complex, a special program has been developed for calculating the probability of occurrence of all events. Event P_7 is the failure state of the system. The results of the calculations are presented in Table 2.

The results of the calculation of the fault tree according to Fig. 1:

$$\lambda = \sum \lambda_i = 2 \times 10^{-5} + 2 \times 10^{-8} + 5 \times 10^{-8} + 2 \times 10^{-7} + 4 \times 10^{-5} + 1.1 \times 10^{-6} = 6.137 \times 10^{-5}$$

Table 2 Calculation results

State	Probability
P_1	0.4992490
P_2	0.4992490
P_3	0.0000001
P_4	0.0000001
P_5	0.0007503
P_6	0.0007503
P_7	0.0000011

The probability of trouble-free operation of the unit during the year is:

$$P = e^{-\sum_i \lambda_i t} = 0.584.$$

The low reliability of the system is explained by the low reliability of the considered elements and their linear evaluation. If we consider the system at a higher level, the failure of an individual element does not always lead to a halt to the entire installation as a whole, since there are backup product delivery paths and there are various techniques for replacing the failed equipment without installation halt.

The above example proved the impossibility of using traditional methods for assessing the reliability of complex systems, since in statistical models, it is impossible to take into account emerging events, such as switching from the main pump to the redundant pump (event 5.5, 5.6), and Markov models are complicated, and for the presented simple example a system of 36 equations will be required.

5 Conclusion

The chapter analyzes the methods for assessing the technical condition and trouble-free operation of individual elements of the system and the entire technical system. It is established that all existing methods in their pure form do not allow to perform the quantitative analysis of hierarchically complex technical systems.

The method proposed by the authors makes it possible to combine standard hierarchical methods for assessing trouble-free operation at different hierarchical levels, in which independent events are evaluated using the methods of mathematical statistics, and Markov models are used for complex sequences of events. As a result, it becomes possible to consider complex technical systems of thousands, tens of thousands of elements with permissible labor input.

References

1. Grishko A, Yurkov N, Goryachev N (2017) Reliability analysis of complex systems based on the probability 13 dynamics of subsystem failures and deviation of parameters. CADSM, pp 179–182
2. Tanasijevic M, Ivezić D, Jovancic P et al (2013) Study of dependability evaluation for multi-hierarchical systems based on max-min composition. Qual Reliab Eng Int 29(3): 317–326
3. Zhang F, Liu T, Liu J (2010) Research on bearing life prediction based on three parameters Weibull distribution. Adv Mater Res 136:162–166. <https://doi.org/10.4028/www.scientific.net/AMR.136.162>
4. Baikov I, Kitaev S, Fayrushin Sh (2016) Evaluation of reliability indicators of pumps of type NC, NCB and PS. Reliability 16:11–16

5. Zhadnov V, Iofin A (2015) Methodological aspects of the calculation of reliability indicators in the practice of designing radio altimeters and radio altimeter systems for rocket technology. *Reliab Qual Complex Syst* 2:42–46
6. Liu J, Wang J, Li G (2017) Evaluation of the energy performance of variable refrigerant flow systems using dynamic energy benchmarks based on data mining techniques. *Appl Energy* 208:522–539
7. Tong Q, Cao J, Han B et al (2017) A fault diagnosis approach for rolling element bearings based on dual-tree complex wavelet packet transform-improved intrinsic time-scale decomposition, singular value decomposition, and online sequential extreme learning machine. *Adv Mech Eng* 9. <https://doi.org/10.1177/1687814017737721>
8. Demichela M, Baldissone G, Camuncoli G (2017) Risk-based decision making for the management of change in process plants: benefits of integrating probabilistic and phenomenological analysis. *Ind Eng Chem Res* 56(50):14873–14887
9. Kelbert M, Sukhov Y (2010) Probability and statistics in examples and problems. Moscow Center for Continuous Mathematical Education
10. Kulakov P, Afanasenko V (2019) Influence of minimally permissible quantity of source materials on the probability of failure of a pump–tank system. *Chem Pet Eng* 54(9–10): 681–686
11. He Q-M, Alfa AS (2018) Space reduction for a class of multidimensional markov chains: a summary and some applications. *Inform J Comput* 30(1):1–10
12. Rakhman PA (2018) A calculation method for estimation of the mean time to first failure of the technical systems on basis of the topological conversion of the markov reliability model. *J Eng Appl Sci* 13(5):1819–1826
13. Rakhman P, Bobkova E (2017) The reliability model of the fault-tolerant border routing with two internet services providers in the enterprise computer network. *J Phys Conf Ser* 803 (1):012124.1
14. Zhao X, Cai K, Wang X et al (2018) Optimal replacement policies for a shock model with a change point. *Comput Ind Eng* 118:383–393
15. Landquist H, Norrman J, Lindhe A (2017) Expert elicitation for deriving input data for probabilistic risk assessment of shipwrecks. *Mar Pollut Bull* 125(1–2):399–415
16. Tanasijevic M, Ivezić D, Ignjatovic D et al (2011) Dependability as criteria for bucket wheel excavator revitalization. *J Sci Ind Res* 70(1):13–19
17. Rykov V, Kozyrev D (2010) Reliability model for hierarchical systems: regenerative approach. *Autom Remote Control* 71(7):1325–1336
18. Emelin N (2015) Analysis and synthesis of systems to ensure the reliability of information management systems (Markov approach). *News Inst Eng Phys* 4(38):3–9
19. Fedorov Yu (2006) Fundamentals of building explosive industries. SINTEG, Moscow
20. Rahman P, Bobkova E (2017) The reliability model of the fault-tolerant computing system with triple-modular redundancy based on the independent nodes. *J Phys Conf Ser* 803 (1):012125.1

Developing Methods for Calculating Gas-Dynamic Parameters in Launch Canister During the Missile Launch



R. A. Peshkov and A. V. Erpalov

Abstract Based on the analysis of various methods for modeling gas-dynamic processes, a methodology has been developed for calculating the main parameters in the launch canister, taking into account the heat exchange processes. The development of the technique includes the choice of physical and mathematical models of gas-dynamic processes in the launch canister, which allow obtaining a stable and convergent solution. The results of FLUENT software package numerical modeling of gas-dynamic processes in the launch canister have been presented, taking into account the heat exchange processes for the given parameters of the heat-shielding coating. The parameters of the MX missile are used as the main parameters for the calculation. Despite a slight increase in the exit time (4%) and the average volume pressure in the launch canister (4–6%), it has been obtained that the effect of heat transfer is increased over time, and for missiles of longer length, it will be more significant. Based on the results obtained, the value of the coefficient taking into account heat transfer was found, and its comparison with known experimental data was made. The obtained coefficient is used to improve the technique on the basis of finding the average volume characteristics in the launch canister. The use of the numerical simulation technique will allow further evaluation of the effect of changes in the parameters of the thermal protection coating and the parameters of the combustion products of the powder pressure accumulator on the dynamics of the missile movement in the canister.

Keywords Heat exchange · Launch canister · Numerical simulation · Technique · Missile launch

R. A. Peshkov (✉) · A. V. Erpalov
South Ural State University, 76, Lenin Avenue, Chelyabinsk 454080, Russia
e-mail: peshkovra@susu.ru

© Springer Nature Switzerland AG 2020
A. A. Radionov et al. (eds.), *Proceedings of the 5th International Conference on Industrial Engineering (ICIE 2019)*, Lecture Notes in Mechanical Engineering,
https://doi.org/10.1007/978-3-030-22041-9_82

765

1 Introduction

One of the main tasks at the launch of a missile is to ensure a given rate of missile exit and to determine the gas dynamic loads on the elements of the design of the launch canister and the missile. The loading study should be carried out at the stage of preliminary design of the launcher, before the production of full-scale units, or with the partial readiness of some units and components of the missile and the launch canister. When considering the period of the missile's movement in the canister, the objective function is the change in pressure in the volume behind the missile, which determines the dynamics of the missile's movement in the canister, the speed of the missile's exit from the canister. Previously, the main tool for obtaining results was a physical experiment, but now with the development of computer technology, another tool complementing it and allowing to reduce the cost of missile production is a numerical experiment. There are many methods for determining gas-dynamic parameters in the launch canister.

2 Analysis of Methods

The most common methods for performing the engineering analysis are the methods based on the solution of a system of differential equations describing the change in the average volume gas-dynamic parameters in the launch canister [1]:

$$\left\{ \begin{array}{l} \frac{dp}{dt} = \frac{k-1}{V} \left[\frac{k}{k-1} \dot{m}RT - \frac{k}{k-1} p \frac{dV}{dt} \right] \\ \frac{dx}{dt} = v \\ m_P \frac{dv}{dt} = \frac{\pi d_k^2}{4} (p - p_h) - m_P g - F_{mp} \\ \frac{dV}{dt} = \frac{dx}{dt} \frac{\pi d_k^2}{4} \\ \frac{d\rho}{dt} = \frac{1}{V} \left[\dot{m} - \rho \frac{dV}{dt} \right] \end{array} \right. , \quad (1)$$

where p —pressure; ρ —density; x —missile position; V —volume of missile sub-space; d_k —canister diameter; p_h —atmosphere pressure; k —adiabatic index; m_P —missile mass; F_{mp} —friction force of the depreciation belts; \dot{m} —mass second flow of gases from the powder pressure accumulator; v —missile speed, R —initial gas constant.

Despite the simplicity, the main drawback of the technique is the problem of accounting for heat transfer processes. In [1], the heat exchange process was taken

into account by introducing a coefficient into the equations of system 1, describing the change in the mean volume pressure in the launch canister:

$$\frac{dp}{dt} = \frac{k-1}{V(t)} \left[\frac{k}{k-1} (1-\eta_t) \dot{m} RT - \frac{k}{k-1} p \frac{dV}{dt} \right], \quad (2)$$

where η_t —coefficient of thermal losses of powder accumulator gases, T —temperature.

This coefficient was determined experimentally and numerically, as the ratio of the total heat flux to the total energy input from the powder pressure accumulators. To find it, it was required to determine the heat transfer coefficients to the surfaces under consideration (of the launch canister and the pallet). The determination of the heat transfer coefficient was made using the method of V. M. Ivlev [2], or a method used in heat engineering for the calculation of thermal conditions in cylindrical pipes with a turbulent mode of gas flow [3]. When calculating these methods, it was problematic to determine the gas parameters near the wall, on which the value of the heat transfer coefficients depends.

Another area of research is related to the development of a structural element method for calculating gas dynamic problems [4], including the gas dynamics of the launch. Much attention is paid to the modeling of ejection processes, in the annular gap between the missile and the launch canister [5]. The main direction of research is connected with the active-reactive launch circuit, and the application of the developed method to other types of launch requires additional verification. This is due to the complexity of determining the boundaries of the allocated subareas and the choice of mathematical models for describing the processes in them.

In connection with the development of computer technology, numerical simulation of gas-dynamic processes using finite-difference methods is becoming popular. To simulate the gas dynamics of the launch, the system of Euler differential equations is applied to the motion of the ideal incompressible gas [6]. To close the resulting system, the equation of state and the equation of missile motion are used. The numerical model of the launch is realized using the method of large particles of Belotserkovsky-Davydov. The main assumption is that the process is considered adiabatic, and the gas is ideal. In the works of *Debin Fu* and *Yong Yu*, the gas dynamic processes were studied in detail at the stationary position of the missile [7] and taking into account the dynamics of movement in the canister [8]. The works of *Rui Shouzhen* are devoted to calculations of a two-phase flow with the help of the Euler-Lagrangian method, on the basis of which conclusions were made on optimization of combined-cycle power systems of missile ejection from the canister and increase of their reliability [9, 10]. In this method, the description of moving boundaries is realized within the framework of the Lagrangian approach, and the description of the motion of a continuous medium is carried out using the Eulerian approach.

In [11, 12], the calculation technique based on solving the equations of conservation of mass, energy, state, and the equation of missile motion recorded in zero-dimensional formulation is presented. One of the main issues discussed in [12]

was the determination of heat losses due to heat exchange of gas with the walls of the canister and the missile pallet. Despite the good agreement between the results of the experiment and the calculation, the developed technique was based on empirical expressions obtained for certain parameters of the missile.

When modeling the dynamics of the missile's motion in the launch canister, a need arose to develop new methods for the reconstruction of grids. In works [13–15], new methods for reconstructing grids have been developed and the results on the three-dimensional modeling of the gas flow from the launching canister, obtained with the use of these methods, are presented.

In [16, 17] the results of numerical modeling of the gas dynamics of the missile exit at the “cold” start are given, obtained using the FLUENT software package and a comparison is made with the experimental data. Despite good agreement with the experimental data on the velocity and acceleration of the missile, the analysis of the criteria for selecting the parameters of the obtained mathematical model is not given in the works [17]. The missile movement was modeled using dynamic grids in three-dimensional setting and built-in user functions (UDF), but the processes of heat exchange of gas with the canister wall are not taken into account, which can greatly affect the final velocity of the missile exit from the canister.

Despite a large number of studies on the gas dynamics of the launch, the questions of accounting for the viscosity of the gas, the effect of temperature factors on the dynamics of the missile's movement in the canister remain topical. A promising direction is the numerical simulation of the gas dynamics of the start with the help of various software packages that will reduce the costs of experimental testing and expand the range of measurements and variable factors.

The article deals with a special case of the gas-dynamic launch, in which the missile's ejection occurs using the combustion products of a powder pressure accumulator that is not on the missile's board. Numerical simulation is performed using the FLUENT software package.

3 Mathematical and Physical Models

The mathematical and physical models of calculation are similar to the models described in [18], but they have their own peculiarities, primarily related to the specification of boundary conditions, the choice of the grid model and the consideration of heat exchange processes. As boundary conditions at the outlet of the powder battery, pressures were set: \dot{m} , T and p [10]. Since the boundary conditions were time-dependent, special user functions were used. As the boundary conditions on the wall, the impenetrability condition and the initial wall temperature were specified.

When solving the heat transfer problem, the heat transfer coefficient was calculated by the formula [19]:

$$h_{\text{eff}} = \frac{\rho c_p C_\mu^{1/4} k_p^{1/2}}{T^*}, \tag{3}$$

where c_p —specific heat; k_p —turbulent kinetic energy in the first wall unit P ; T^* —dimensionless temperature:

$$T^* = \frac{(T_w - T_p) \rho c_p C_\mu^{1/4} k_p^{1/2}}{q} = \begin{cases} \text{Pr} y^* \frac{1}{2} \rho \text{Pr} \frac{C_\mu^{1/4} k_p^{1/2}}{q} U_p^2 (y^* < y_T^*), \\ \text{Pr} y_t \left[\frac{1}{k} \ln(E y^*) + P \right] + \frac{1}{2} \rho \text{Pr} \frac{C_\mu^{1/4} k_p^{1/2}}{q} \{ \text{Pr}_t U_p^2 + (\text{Pr} - \text{Pr}_t) U_c^2 \} (y^* < y_T^*), \end{cases} \tag{4}$$

where

$$\begin{cases} \dot{m} = \varphi F_i \sqrt{\frac{2k}{k-1} p \rho \left(\left(\frac{p_h}{p} \right)^{\frac{2}{k}} - \left(\frac{p_h}{p} \right)^{\frac{k+1}{k}} \right)} & \text{npu} \frac{p_h}{p} \leq \left(\frac{2}{k+1} \right)^{\frac{k}{k-1}} \\ \dot{m} = \varphi F_i \sqrt{k \left(\frac{2}{k+1} \right)^{\frac{k+1}{k-1}} p \cdot \rho} & \text{npu} \frac{p_h}{p} > \left(\frac{2}{k+1} \right)^{\frac{k}{k-1}} \end{cases}$$

was calculated using the formula represented by *Jayatilleke* [19] (for a smooth wall):

$$P = 9.24 \left[\left(\frac{\text{Pr}}{\text{Pr}_t} \right)^{3/4} - 1 \right] \left[1 + 0.28 e^{-0.007 \text{Pr} / \text{Pr}_t} \right], \tag{5}$$

where ρ —pressure; q —heat flow; T_p —temperature in the first wall unit P ; T_w —wall temperature; Pr —Prandtl molecular number $\mu c_p / k_f$; Pr_t —turbulent Prandtl number (0.85 on the wall); A —Van Drist constant (26); U_c —average speed (at $y^* < y_T^*$); E —empirical constant (9.793); k —von Karman constant (0.4187); U_p —average gas velocity near the wall unit P ; y_p —distance from point P to the wall; μ —coefficient of dynamic viscosity; $y^* = \rho C_\mu^{1/4} k_p^{1/2} y_p / \mu$ —dimensionless distance from the wall; y_T^* —dimensionless thickness of the thermal sublayer; $C_\mu = 0.09$ —dimensionless coefficient for the k - ϵ model of turbulence.

In hard areas (heat-shielding coating), the energy equation is [19]:

$$\frac{\partial}{\partial t} (\rho h) + \nabla \cdot (\vec{v} \rho h) = \nabla \cdot (\alpha \nabla T), \tag{6}$$

where h —enthalpy; α —thermal conductivity; T —temperature.

The second term on the left-hand side of Eq. 6 is the convective energy transfer due to the rotation or translational motion of the solid body. The velocity field \vec{v} is calculated from the motion indicated for hard surfaces. The terms on the right-hand side of Eq. 6 characterize the heat flux due to thermal conductivity.

The missile motion parameters were determined with the help of the built-in 6DOF solver while the mass, inertial, and additional power characteristics were set using the user function.

4 Grid Model

The parameters of the MX missile were chosen as the initial data for the calculation [10]: the missile weight—198,000 lb (89,811 kg), the tube and breech diameters are equal at 8.1 ft (2.47 m) and the launch seal to canister muzzle length 70.57 ft (21.51 m), the initial breech volume is 220 ft³ (6.23 m³) has been assumed. The layout of the pallet and the supply of powder gases to the volume is shown in Fig. 1a [10]. To assess the effect of accounting for heat transfer processes on changes in the mean volume pressure in the missile subspace, the speed and time of the missile exit from the canister, a calculation was carried out with the parameters of the heat-shielding coatings used in the design of solid fuel engines [20]: $\rho = 1950 \text{ kg/m}^3$, $c_p = 1700 \text{ J/(kg K)}$, the coefficient of thermal conductivity ($\lambda = 0.4 \text{ W/(m K)}$). The thickness of the thermal protective coating is assumed equal to 0.015 m.

Based on the available geometry (Fig. 1a), a finite-element, two-dimensional grid model, symmetric about the axis of the missile, was constructed. A similar formulation of the problem made it possible to use a hexahedral grid. The use of a tetrahedral grid is possible, but it will require a greater number of elements to obtain results that are comparable in accuracy. For the hexahedral grid, only the *Layering*

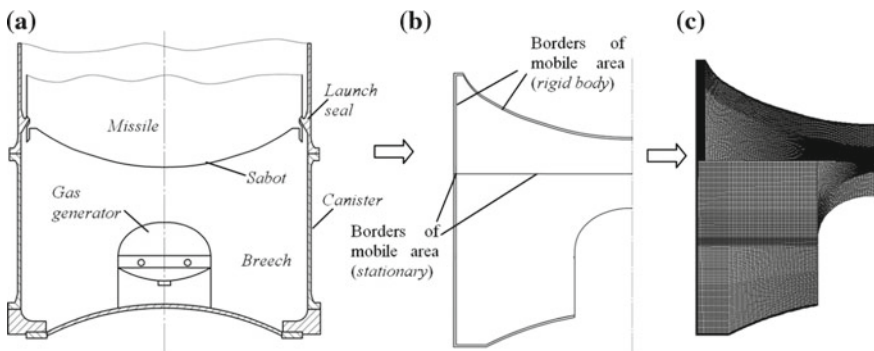


Fig. 1 Stages of grid model formation, **a** layout of the pallet; **b** location of the boundaries of the subarea with the mobile grid; **c** grid model

rebuild method is available. With this method, the entire calculation grid moves along with the body, and the cells are added and destroyed only at the specified static boundaries.

After choosing the rebuilding method, the parameters of the boundaries of the subarea with the moving grid were set (Fig. 1b). The wall conditions for the bottom of the pallet and array of grid cells were set movable. The height of the newly formed cells at the boundary connecting the two areas (near the pallet and near the bottom of the canister) was set in the range from 0.0001 to 0.005 m. This ensured the stability of the count, namely it reduced the divergence in solving the system of algebraic equations using the multigrid method.

In connection with the peculiarities of the chosen model of the dynamic reconstruction of the grid, various grids were constructed for different parts of the calculation model. Further, all these grids were combined in the solver through a special interface that transfers data from one area to another as the calculation is performed. The heat transfer was taken into account by constructing a separate grid for the heat-shielding coating and “sewing” it with a grid constructed for the gas flow area. Separately, a grid was constructed for the upper part of the calculation area (near the pallet) and for the lower (near the canister).

When constructing the grid, condensation was carried out at the surface of the pallet and the bottom of the launch canister. At the same time, to calculate the cell height on these surfaces, the value of the parameter $y^+ = 20 \dots 300$ was adopted. The result of specifying a grid for simulating the motion of the missile in the canister using the developed recommendations is shown in Fig. 1c.

According to the results of the analysis of the thermodynamic parameters of combustion products of solid fuel charges [21], the following parameters were chosen as initial: $k = 1.4$, $R = 297 \text{ J/(kg K)}$.

5 Calculations and Conclusions

As a result of the calculations, we obtained the graphs of the change in the mean volume pressure in the canister (Fig. 2a) and the speed of the missile (Fig. 2b), taking into account (curve 1) and without taking into account (curve 2) the heat exchange processes. All parameters presented in Fig. 2 are written in relative values.

The calculations of gas-dynamic parameters in the launch canister at the launch of the missile with the help of the developed numerical simulation technique have shown that taking heat transfer into account reduces the average volume pressure in the canister by 4–6%. This change led to a decrease in the missile launch speed by 4% and an increase in the exit time by 4%. Despite a small change in the parameters, it has been obtained that, over time, the effect of heat transfer is increased, and for missiles of greater length, it will be more significant. Thus, taking into account the heat transfer process plays an important role in calculating the speed and time of

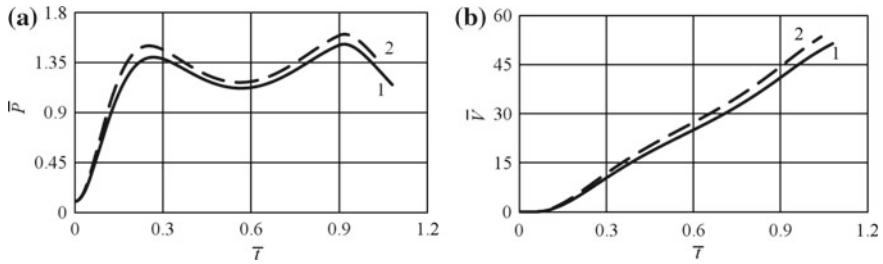


Fig. 2 Charts for changing basic parameters, **a** average volume pressure in the launch canister; **b** speed of the missile

the missile exit from the canister, which are the defining parameters when creating a control system and building a diagram of start commands.

According to the results of numerical modeling of the change in the mean volume pressure in the launch canister (Fig. 2), it is obtained that the coefficient η_t varies little over time and it can be assumed constant as the missile leaves the launch canister. With the selected parameters of heat-shielding coating $\eta_t = 0.131$. The resulting value of the coefficient falls within the range obtained for piston-type machines (the working cycle of the piston engine and the motion of the missile in the launch canister are similar): $\eta_t = 0.13 \dots 0.135$ [22]. The use of the numerical simulation technique will allow further evaluation of the effect of changes in the parameters of the thermal protection coating and the parameters of the combustion products of the powder pressure accumulator on the dynamics of the missile movement in the canister.

References

1. Konyukhov SN (1997) Minometnyiy start mezhkontinentalnykh ballisticheskikh raket (Mortar launched intercontinental ballistic missiles). National Academy of Sciences, Space Agency of Ukraine, Institute of Technical Mechanics, design office "Yuzhnoye", Dnepropetrovsk
2. Avduevskij VS, Galicejskij BM, Glebov GA (1992) Osnovy teploperedachi v aviacionnoj i raketno-kosmicheskoy tehnike (Fundamentals of heat transfer in aviation and rocket and space technology). Mashinostroenie, Moscow
3. JaM Shapiro, Mazing GJu, Prudnikov NE (1966) Teorija raketnykh dvigatelej na tverdom toplive (Theory of solid-fuel rocket engines). Voennoe izdatel'stvo ministerstva oborony SSSR, Moscow
4. Afanas'ev EV, Baloban VI, Bobyshev SV, Dobroserdov IL (1998) Strukturno-jelementnyj metod rascheta gazostrujnykh processov (Structural element method for calculating gas jet processes). Matematicheskoe modelirovanie 10(1):31–43
5. Afanas'ev EV, Bobyshev SV, Dobroserdov IL, Sokolova TT (2001) Strukturno-jelementnoe modelirovanie jezhekcionnykh processov pri starte kosmicheskikh raket-nositelej (Structural element modeling of Jewish processes at the launch of space launch vehicles). Matematicheskoe modelirovanie 13(7):104–109

6. Korolev AA, Komochkov VA (eds) (2010) *Ballistika raketnogo i stvol'nogo oruzhija* (Ballistics of rocket and barreled weapons). Izdatel'stvo Volgogradskogo gosudarstvennogo tehničkog universiteta. Volgograd
7. Fu D-B, Yu D-J, Zhang Z-Y (2012) Lumped parameter model for concentric canister launcher. *J Solid Rocket Technol* 35(3):301–305
8. Fu D-B, Yu Y (2013) Simulation of gas flow and additional thrust with missile launching from concentric canister launcher. *Proc Inst Mech Eng Part G J Aerosp Eng* 227(12):1977–1987. <https://doi.org/10.1177/0954410012464602>
9. Rui S, Xing Y (2009) Comparative studies of interior ballistic performance among several missile eject power systems. *J Beijing Univ Aeronaut Astronaut* 35(6):766–770
10. Rui S, Xing Y (2010) Numerical simulation of two-phase flow and interior ballistic for missile launching system. Paper presented at the 25th international symposium on ballistics, Beijing University of Aeronautics, Beijing, China, 16–22 May 2010
11. Edquist CT (1990) Prediction of the launch pulse for gas generator launched missiles. *J Propul Power* 6(6):705–712. <https://doi.org/10.2514/3.23275>
12. Edquist CT, Romine GL (1980) Canister gas dynamics of gas generator launched missiles. Paper presented at the 16th joint propulsion conference, Hartford, CT, USA, 30 June 1980–2 July 1980
13. Hao J-G, Jiang Y, Han S-Y, Liao Q (2007) New dynamic mesh update method and its applications. *J Ballist* 19(2):88–92
14. Jiang Y, Hao J-G, Fu D-B (2008) 3D unsteady numerical simulation of missile launching. *Acta Armamentarii* 20(29):911–915
15. Zhai X, Chen Y, Jiang Y (2006) Using dynamic grid to simulate interior trajectory of the launching container. *Mod Def Technol* 34:24–28
16. Liu Y, Xi A, Liu H (2012) Numerical study of interior trajectory of missile ejection based on mechanics. Paper presented at the 2nd international conference on information science, automation and material system, Changsha, China, 21–22 Apr 2012. <https://doi.org/10.4028/www.scientific.net/AMR.485.616>
17. Liu Y, Xi A (2013) An interior trajectory simulation of the gas-steam missile ejection. *J Comput (Finl)* 8(5):1321–1326. <https://doi.org/10.4304/jcp.8.5.1321-1326>
18. Peshkov RA, Sidel'nikov RV (2015) Analiz udarno-volnovykh nagruzok na raketu, puskovuju ustanovku i kontejner v processe starta (Analysis of shock-wave loads on the rocket, launcher and container during launch). *Vestnik Juzhno-Ural'skogo gosudarstvennogo universiteta. Serija "Mashinostroenie"* 15(2):81–91
19. Fluent Inc. (2011) *FLUENT 14.0 Theory Manual*
20. Fahrutdinov IH, Kotel'nikov AV (1987) *Konstrukcija i proektirovanie raketnyh dvigatelej tverdogo topliva* (Design and design of solid-fuel rocket engines). Mashinostroenie, Moscow
21. Pavljuk JuS (1996) *Ballisticheskoe proektirovanie raket: Uchebnoe posobie* (Ballistic raket design: tutorial). Izdatel'stvo Cheljabinskogo gosudarstvennogo tehničkog universiteta, Cheljabinsk
22. Kostin AK, Larionov VV, Mihajlov LI (1979) *Teplonaprjazhennost' dvigatelej vnutrennego sgoranija: Spravochnoe posobie* (Thermal intensity of internal combustion engines: a reference manual). Mashinostroenie, Leningrad

The Detection of Electrode Breakage in Electric Discharge Process by Methods of Vibroacoustic Diagnostics



M. Kozochkin, A. Porvatov and D. Allenov

Abstract As a research task, the authors determined an attempt to assess the possibility of applying the methods of vibroacoustic diagnostics to detecting an electrode breakage during electrical erosion processing (EDM). The presence of a diagnostic system allows timely replacing tools and thereby increasing the productivity of the process. During the review of previous research, considerable attention is paid to identifying the main parameters of EDM processing, among which the most important is gap size in the electrode gap. The absence of high-quality automatic control of this gap on the machine makes the EDM process ineffective. Experimental research was conducted on a wire-cut machine “CUT 1000”, the materials being processed were alloys VK 60, T15K6 and VOK60 (WC, TiC and ceramic alloys). The authors proposed a dynamic model of the erosion treatment zone and experimentally showed a change in its frequency characteristics with increasing concentration of erosion products. There was established that the measurement of amplitude-frequency characteristics allows detecting an increase in the concentration of erosion products and determining the moment of electrode breakage with a sufficiently high accuracy. The results of research of vibration signals in the processing of conductive ceramics were given. Monitoring was made directly in the process without removing the tool and the workpiece. The problems of processing conductive ceramics and possible ways to solve them by controlling high-frequency vibrations are shown.

Keywords Electrical discharge machining · Vibroacoustic diagnostics · Electrode breakage · Amplitude-frequency response · Online monitoring

M. Kozochkin · A. Porvatov
Moscow State University of Technology “STANKIN”, 1, Vadkovsky per.,
127055 Moscow, Russia

D. Allenov (✉)
Peoples’ Friendship University of Russia (RUDN University), 6, Miklukho-Maklaya,
117198 Moscow, Russia
e-mail: allenov_dg@rudn.university

1 Introduction

Electrical discharge machining (EDM) occurs when the total immersion in the dielectric, but the workpiece range is so small and remote from the surface that it is difficult to use monitoring tools that automate the functions of a CNC machine operator. Vibroacoustic (VA) methods are increasingly used in mechanical processing methods. They are based on the selection of VA signals generated in the cutting zone, reflecting the quality of the process itself, wear and breakage of the tool in the form of changes of spectral and temporal characteristics. This allows managing the movement of working members, timely change the tool, preventing accidents and defects [1–7].

Experimental researches [6–8] have established that “contactless” electrical discharge machining generates VA signals in a wide frequency range. They can be registered by accelerometers located on the elastic system of the machine in the distance from the cutting zone. Monitoring the parameters of the VA signals allow to reliably track the approach of the moment of separation of the cut product from the workpiece and the moments of cutting the wire into the workpiece. The spectral composition of the VA signals is determined not only by disturbances, but also by the amplitude-frequency characteristic (AFC) of the elements of the machine’s elastic system. Thereby, it is established that reducing the tension of the wire, i.e. reduction its stiffness, increases in the amplitude of the VA signal in a wide frequency range.

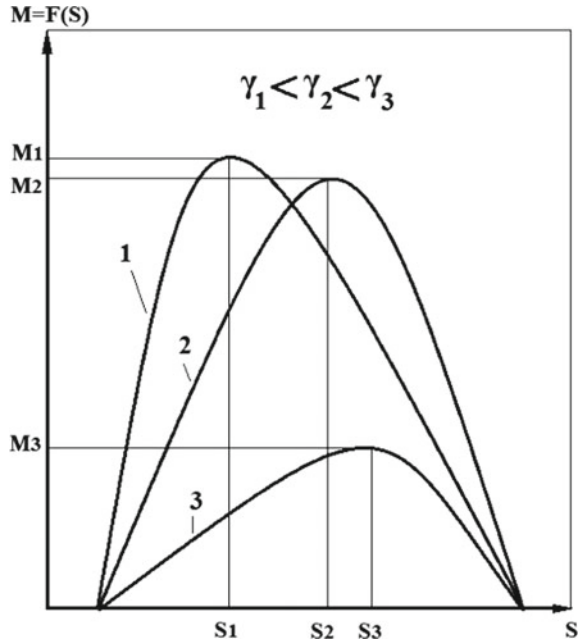
2 Problems and Task Definition

It is necessary to maintain stability or rationally regulate a number of parameters that have a dominant influence on the process during electrical discharge machining to provide optimal conditions (maximum performance, efficiency, best purity, etc.) [6, 9, 10]. The size of the gap, s , in the interelectrode gap is considered as basic, since the quality parameters of the EDM substantially depend on it. A small increase of the gap can change the conditions of breakdown and even stop them completely. The reverse change of the gap leads to the deterioration of the evacuation of erosion products, reduced process performance, slagging of the electrodes and short circuits. The absence of high-quality automatic control of the gap on the machine makes the process of EDM ineffective [8, 11, 12].

Figure 1 shows typical dependencies between process performance of EDM, M , and gap, s . It is seen that this dependence has an extreme character. The dependence, $M = F(s)$, is not stable. It continuously changes in the process of EDM of even one detail on the one mode. This is due to the continuous varying of the concentration of erosion products, γ , in the interelectrode gap.

It can be seen from Fig. 1 that as γ increases the productivity of the process decreases and the extremum shifts, i.e. the value of the optimal gap shifts. This is due to the fact that, for example, as the electrode is introduced into the material, the

Fig. 1 Dependence of the performance of the EDM on the gap and the concentration of erosion products ($\gamma_1 < \gamma_2 < \gamma_3$)



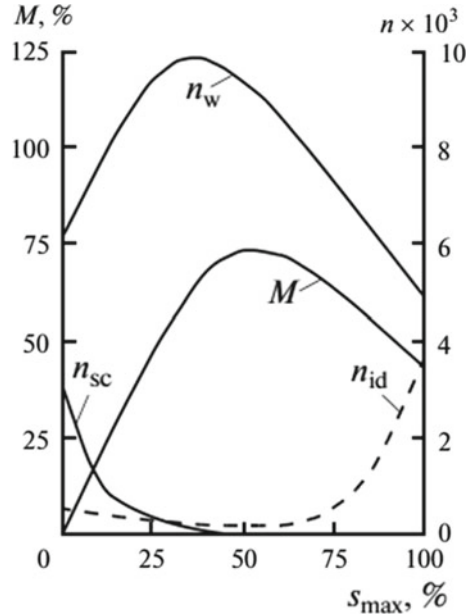
conditions for removal of erosion products may deteriorate that reduces the share of working impulses of the EDM process.

Figure 2 shows, that tuning of the gap regulator affects not only process performance, but number of working impulses, n_w , number of idle pulses, n_{id} , and number of short circuit pulses, n_{sc} . The maximum of performance is shifted relative to the maximum n_w in the direction of greater values of the gap. This is due to the fact that at maximum values of n_w , an excess of erosion products appears and the whole process shifts towards the formation of short-circuit pulses, which breaks the stability of the process. In case of pollution of the working fluid with erosion products, individual working impulses do not spend all the energy on useful metal removal, but spend part of it on additional destruction of erosion products, i.e. among the working impulses a significant part may be defective. This is the main disadvantage of the existing performance evaluation methods of EDM by electrical parameters.

3 The Selection of Diagnostic Signal and Experimental Studies

An attempt was made to use the parameters of the VA signal registered by the accelerometer installed on a device for fixing the workpiece to estimate the useful energy. Researches show that the parameters of the VA signal are related to the

Fig. 2 Dependence of performance (M) of EDM, number of working impulses



performance of the EDM process by a monotonic dependence. In this case instead of dependence $M = F(s, \gamma)$, it is allowed to use similar dependence $A = F_A(s, \gamma)$, and manage the process of EDM based on information, received directly from the treatment area.

The effect of the concentration of erosion products on the parameters of the VA signal can be represented as a dynamic model shown on Fig. 3.

According to the linear properties of the dynamic system amplitude spectrum $U(f)$ of signal perceived by the accelerometer is determined by Eq. 1:

$$U(f) = H_1(f)H_2(f)Q(f) \tag{1}$$

where $Q(f)$ —spectrum of discharge current signals, $H_1(f)$ and $H_2(f)$ —AFR of the workspace and elastic system.

Parallel records of VA signals and discharge current signals were made during the experiment on the EDM machine model “CUT 1000” by Agie Charmilles company in the process of cutting workpiece from WC and TiC alloys. AFR of observation channel $H(f)$ was build according to these records in the process of cutting the electrode into the workpiece and before the moment of the wire electrode breakage (Fig. 4).

To monitor the process of EDM, it is necessary to follow the changes of AFR in a wide frequency range, but it is difficult and inconvenient due to possible interference from the working mechanisms. For control simplification, it is enough to select one or several informative frequency ranges to measure AFR. Changes of



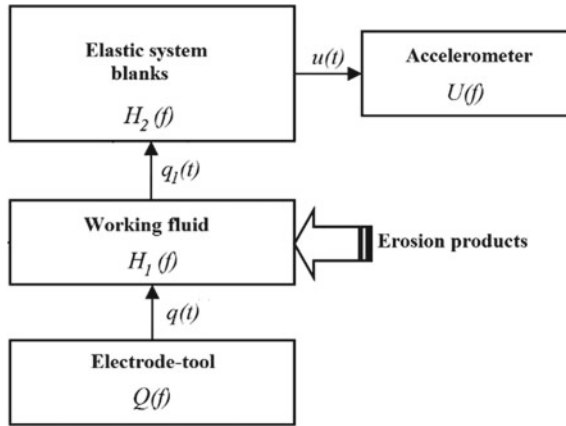


Fig. 3 Dynamic system scheme for EDM (n_w), number of idle pulses (n_{id}) and number of short-circuit pulses (n_{sc}) of gap size (S) at interelectrode gap

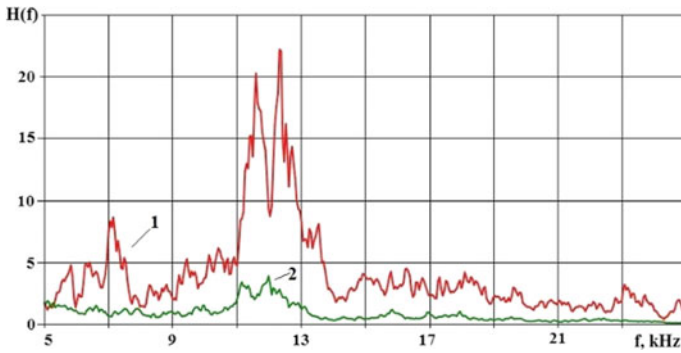


Fig. 4 AFR of the EDM process of WC alloy in the initial processing stage (chart 1) and before electrode breakage (chart 2)

AFR before the electrode breakage (Fig. 4) are sufficient to detect increased concentration of erosion products and for giving a command to change of workspace.

The photograph Fig. 5 taken on a VEGA 3 LMH scanning electron microscope shows that the spot of wire electrode breakage is conical. This form is obtained if tensioned electrode is heated to a temperature close to the melting point. Due the heated, the elastic module of the electrode material falls, there is a plastic flow of wire in the place of heating, which ends in a breakage. The breakage occurred when the diameter of the neck formed in the course of plastic flow became about 7 times smaller than the initial diameter of the wire. It also shows that the conical section of the electrode and part of the cylindrical section from the one side are covered with adhered processing material. This means that the heating was occurred at the moment of short circuit, when the electrode was actually “welded” to the workpiece material.

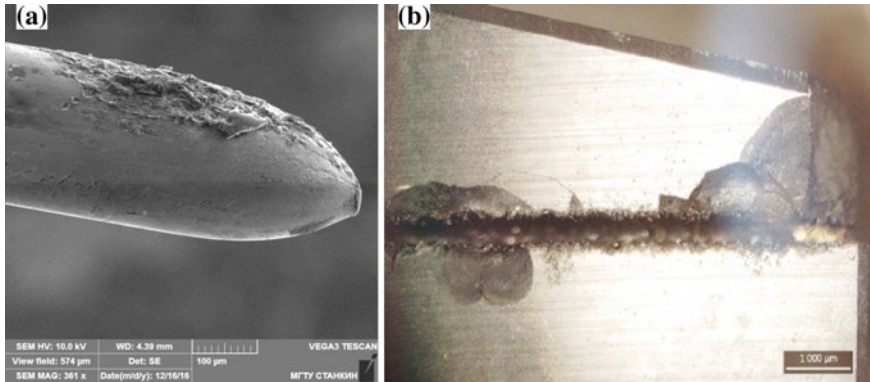


Fig. 5 Photograph of the place of the wire electrode breakage (a) and photograph of the trace from the electrode on the surface of the ceramic workpiece WC (b)

The contact temperature increase of the electrodes affects not only the wire electrode but also the material of the workpiece. Figure 5b shows a photograph of the ceramic workpiece surface with a trace from the wire electrode, where chipped are visible. Due to long-term short-circuit conditions, the ceramic workpiece is heated with the formation of cracks and chips. The control of the VA signals in this situation also allows to operatively detect the moments of the occurrence of short circuits and to conduct a fast electrode reverse [13, 14].

4 Conclusion

Experiments with processing of conductive ceramics show that due to the high resistance of the processed material, the control system is not able to quickly determine the moments of occurrence of short circuits. In this case, the amplitude of the discharge current increases not enough to recognize a short circuit. Instead of a quick reverse, the control system continues wire electrode feed. This causes to electrode breakage. Due to long-lasting short-circuit conditions, the ceramic workpiece is heated to form cracks and chips. Monitoring VA signals in this situation allow to quickly identify the moments of occurrence of short circuits and produce fast reverse of electrode [14].

References

1. Sviridenok AI, Myshkin NK, Kalmykova TF, Holodilov OV (1987) Akusticheskie i jelektricheskie metody v tribotekhnike (Acoustic and electrical methods in tribotechnics). In: Belov VA (ed) Nauka i tekhnika, Moscow
2. Kolubaev EA, Kolubaev AV, Sizova OV (2010) Analiz akusticheskoy jemissii pri trenii skol'zheniya vysokomargancovistoy stali (Analysis of acoustic emission during sliding friction of high manganese steel). Pis'ma v ZhTF 36(16):55–61
3. Malenko PI (2011) Issledovanie metodom akusticheskoy jemissii poverhnostej treniya v usloviyah smazyvaniya (Research of friction surfaces by acoustic emission method under lubrication conditions). Kondensirovannye sredy i mezhfaznye granicy 13(2):164–171
4. Zhang Z, Liu M, Liao Y et al (2018) Contact acoustic nonlinearity (CAN)-based continuous monitoring of bolt loosening: hybrid use of high-order harmonics and spectral sidebands. Mech Syst Signal Process 103:280–294. <https://doi.org/10.1016/j.ymssp.2017.10.009>
5. Jain PS, Ravindra HV, Ugrasen G et al (2017) Study of surface roughness and AE signals while machining titanium grade-2 material using ANN in WEDM. Mater Today-Proc 4(9): 9557–9560. <https://doi.org/10.1016/j.matpr.2017.06.223>
6. Grigor'ev SN, Kozochkin MP, Fedorov SV, Porvatov AN, Okun'kova AA (2015) Issledovanie processa jelektroerozionnoy obrabotki sredstvami vibroakusticheskoy diagnostiki (The research of the process of electroerosive processing by means of vibro-acoustic diagnostics). Izmeritel'naya tekhnika 8:33–37
7. Grigor'ev SN, Kozochkin MP, Fedorov SV, Porvatov AN, Okun'kova AA (2015) Study of electroerosion processing by vibroacoustic diagnostic methods. Meas Tech 58(8):878–884
8. Kozochkin MP, Porvatov AN, Hoteenkov KE, Tokbergenov MZh (2016) Vozmozhnosti akusticheskogo monitoringa processov jelektroerozionnoy obrabotki (Possibilities of acoustic monitoring of EDM processes). Vestnik MGTU "Stankin" 1(36):46–52
9. Grigoriev SN, Volosova MA, Kozochkin MP, Kropotkina EY, Okunkova AA (2016) Study of wire tool-electrode behavior during electrical discharge machining by vibroacoustic monitoring. Mech Ind 17(7):117
10. Gutkin BG (1971) Avtomatizatsiya elektroerozionnykh stankov (Automation of electrical discharge machines). Mashinostroenie, pp 28–29
11. Artamonov BA, Volkov YS (1991) Analiz modelei elektrokhimicheskoi i elektroerozionnoi obrabotki. Chast' 2, Modeli protsessov elektroerozionnoi obrabotki. Provolochnaya vrezka (Analysis of models of electrochemical and electrodischarge treatment, part 2: models of electrodischarge treatment. Wire cutting). Vseross. Nauchno-issled. Inst. Patent. Inform., pp 98–101
12. Fu X, Zhang Q, Gao L et al (2016) A novel micro-EDM-piezoelectric self-adaptive micro-EDM. Int J Adv Manuf Tech 85(1–4):817–824. <https://doi.org/10.1007/s00170-015-7939-8>
13. Conde A, Arriandiaga A, Sanchez JA et al (2018) High-accuracy wire electrical discharge machining using artificial neural networks and optimization techniques. Robot Cim-Int Manuf 49:24–38. <https://doi.org/10.1016/j.rcim.2017.05.010>
14. Kozochkin MP, Porvatov AN, Fedorov SV, Okunkova AA (2015) About possibility of vibroacoustic diagnostics of electrical discharge machining and characterization of defects. Mech Ind 16(7):707

Method of Estimation of Pressure Forces from Power Plant in Microtunneling



E. Y. Kulikova and I. I. Shornikov

Abstract The article describes the method of estimating the values of the pressure forces acting from the power plant when jacking tunnel linings in the microtunneling technology. The assessment carried out for the frictional component of the effort of punching in straight sections when the process is restarted after the punching stops of a certain duration. For the lining, pressed with the use of lubricating solutions, the time evolution of the effect of “sticking” in permeable rocks when the shutdown works is taken into account. This effect allows one to account for the observed increase in effort of pushing when it is restarted. The dependence of the pressure effort of the length of stoppage in time is given. In this relationship, the rate of increase of this area is defined by the time of dissipation of lubricant pressure on contact to initial pressure pore waters. Key parameters, thus, are the module of volume compression and the coefficient of soils permeability. The area of contact is directly proportional to differential pressure, a square of external lining diameter, and inversely proportional to amount of overcut and the module of volume compression of the soil. Resisting force is defined by the areas of contact soil—lining and a lubricant-lining, and shear strengths on these contacts. The received dependence allows considering observable increase in thrust forces at jacking restart after stoppages. New physically well-founded dependences for increase of thrust forces are resulted at duration increase of stoppages. The comparison with experimental data has allowed defining the parameters entering into these dependences.

Keywords Jacking force • Thrust force • Tunnel lining • Time factors • Stoppages • Restart force • MTBM • Shear strength • Sticking • Differential pressure

E. Y. Kulikova (✉) · I. I. Shornikov
National University of Science and Technology MISIS, 4, Lenin Prospekt,
Moscow 119991, Russia
e-mail: fragrante@mail.ru

© Springer Nature Switzerland AG 2020
A. A. Radionov et al. (eds.), *Proceedings of the 5th International Conference on Industrial Engineering (ICIE 2019)*, Lecture Notes in Mechanical Engineering,
https://doi.org/10.1007/978-3-030-22041-9_84

783

1 Introduction

In the practice of tunnel lining punching, the fact of increasing the efforts of punching at restart, when tunneling work is stopped for the installation of the next element of the lining, preventive or emergency work, work to eliminate problems in the face (the appearance of boulders, etc.) or after breaks on weekends or holidays [1–4] is widely known. All these stops, breaks, delays, etc. are further defined by the term “stop.”

The change in the punching forces is characterized by a jump in time with a significant increase at the period of restart, followed by a further decline to the line of the average resistance to punching.

In existing regulations [5], the time factor is not taken into account, which in the microtunneling technology while the design of pipelines prevents the objective selection of the parameters of the lining elements, the jack installation and the design of the thrust wall.

The influence of the time factor takes place both within short (stops for the installation of the next element of the pressed lining) and long periods of time (breaks for the weekend). Experimental studies [1–4] show that when driving with bentonite as a lubricant with long stops (>60 h), the latter can cause a significant increase in static friction. In the most unfavorable cases, the increase in pressure forces after the resumption of the course of punching can reach 70%.

Traditionally, punching forces are divided into two components: downhole and friction [1–6]. Analysis of the values of pressure forces during punching showed that it is advisable to divide the friction component into the end and the residual components. The end component is determined by processes in the shield final area. In this paper, the residual component is of interest. It is distributed over almost the entire length of the lining.

In comparison with the measured ones, predictive estimates of the friction component with the use of available methods gave underestimated values by 2.5 times without taking into account the buoyancy of the lining and by 10 times with full account of its buoyancy [4]. This indicates the need for further study of the behavior of the lining in the presence of a lubricant based on bentonite.

An analogue of the study was the practice of drilling wells for oil production [7, 8]. Thus, the phenomenon of “sticking” under the influence of pressure drop, which leads to a decrease in friction in the system “rock – material lining” and to stabilization of the construction gap is a significant effect on the time factor to reduce the friction component when using lubricants based on bentonite [6]. Such a phenomenon has not been studied for the conditions of pressing the linings.

The works [9–14] are devoted to the problems of filtration of the aqueous component from the solution through the filtration crust into the rock, and the physical behavior of clays [6, 9, 13, 14].

The aim of this work is to conduct assessments of temporal relationships in the formation of the maximum values the efforts of the jacking of tunnel linings when using lubricants on the basis of bentonite.

2 Method of Estimation of Friction Component in Time

To predict the forces of punching after the stoppage of tunneling operations during the effect of stacking when using bentonite suspensions, it is necessary to determine the parameters of the formation of a permeable and deformable clay layer along the contour of the mine working which is the main cause of stacking. At the same time, it is necessary to take into account the fact that the stacking of the lining is formed within a certain period of time when the lining is at rest.

As the clay layer increases, an additional contact area of the tunnel lining with the mine working wall is formed during the stop. There is an increase in adhesion, which corresponds to the laws of formation and behavior under load of the filtration crust in the screening zone with static filtration [13, 14]. The filtration outflow of pore liquid from the screening zone contributes to the growth of contact stress, the introduction of the lining element into the clay layer and, as a consequence, the growth of displacement forces. The main prerequisites for the occurrence of the sticking under the influence of the pressure drop are the difference between the pressure of the lubricant solution in the construction gap p_m and the water pressure in the rock mass p_m , its permeability and the presence of a solid phase in the solution [14].

Taking into account that the lining has an external D_a and internal D_i diameters, the area of its wall can be expressed as follows:

$$A_R = \pi(D_a^2 - D_i^2)/4 = \pi t_R D_a (1 - t_R/D_a) \approx 0.95 \pi t_R D_a.$$

where t_R —the value of the gap between the output circuit and the outer diameter of the lining; R_a —the external radius of the lining.

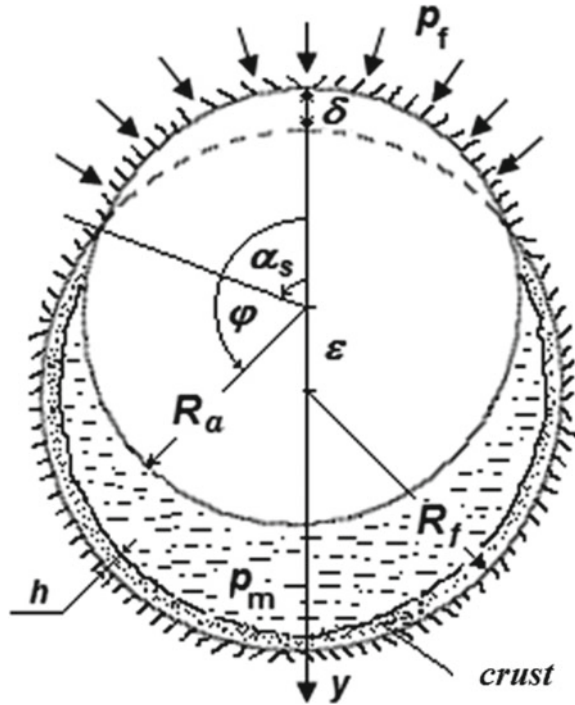
For the applied elements of the lining, the ratio of its wall thickness to the outer radius is $t_R/R_a \approx 0.1$.

In the presence of a lubricant in the construction gap (hereinafter only bentonite solution is considered) under pressure p_m , the lining of reinforced concrete with a specific gravity $\gamma_{rc} = 25 \text{ kN/m}^3$ will be in a state of ascent, since its specific gravity will be equal to $\gamma_R = \gamma_{rc} (4A_R/\pi D_a^2) = \gamma_{rc} (3.8t_R/D_a) = 25 \times 0.19 \approx 5 \text{ kN/m}^3$. This value is less than the specific weight of the bentonite solution $\gamma_m = 11-13 \text{ kN/m}^3$.

In the permeable rock mass as a result of filtration is formed so-called, external filtration crust thickness $h(t)$, which increases in size in the direction of mine working. Promoted lining destroys part of the crust, so a closed circuit is formed. The initial hydrostatic pressure $p_f = 10H_w (\text{kN/m}^2, H_w$ —the height of the water column, m)—occurs at the contact of the edge with the rock.

In permeable rocks on the lining will act pressure equal to the difference $\Delta p = p_m - p_f$. Under the influence of this pressure difference, a zone of sticking is formed at the contact of the lining with the rock [13, 14]. Thus, it is necessary to consider three contact pairs: “lining – rock,” “lining – filtration crust” and “lining – bentonite” with squares A_{ss} , A_{sc} и A_{sm} , respectively ($A_{ss} + A_{sc} + A_{sm} = \pi D_a$). The size of the gap between contour generation radius R_f and lining with external radius R_a denotes as t_g .

Fig. 1 Scheme of the system “lining – crust – grease – rock”



The scheme of interaction in the system “lining – lubricating fluid – crust – rock” is shown in Fig. 1. The scheme takes into account the following parameters: ϵ —displacement of the center of the lining relative to the center of production; δ —depth of penetration of the lining into the rock; φ —coordinate angle of the point at the contacts; α_s —angle of contact “lining – rock” (i.e., $A_{ss} = 2R_a\alpha_s$). The value of h is negligible, so we can simplify the analysis and calculate the increase in the contact area $A_{ss} + A_{sc}$. Due to the increase in the thickness of the external filtration crust, we will present it as a fictitious decrease in the radius of nine working, i.e., reduce the gap from t_g to $(t_g - h)$, and replace approximately $1/t_g$ with $(1/t_g) \cdot (1 + h/t_g)$.

Based on the methods of determining the total force W , acting on the contact of the lining-rock and directed upwards (against the direction of the y -axis) [7, 8] and integrating the pressure distribution along the contour of the lining, we obtain:

$$W = W_{\Delta} - W_R + W_A - W_{ad}.$$

where $W_{\Delta} = \Delta p D_a \sin \alpha_s$ —the downforce is from the pressure difference $\Delta p = (p_m - p_f)$; $W_A = \gamma_m \pi D_a^2 / 4$ —buoyancy force; $W_R = \gamma_r \pi D_a^2 / 4$ —lining weight; $W_{ad} = (\alpha_s / \pi) W_A$ —additional force.

In accordance with [12], the specified force W provides contact with the solution α_s , defined as $\alpha_s^2 \cong (6/\pi)mW(1/t_g) \cdot (1 + h/t_g)$. From this expression and the expressions given for all components of the total force, we obtain an equation to determine α_s :

$$\alpha_s^2 - a \cdot \sin \alpha_s + b \cdot \alpha_s - c = 0. \quad (1)$$

The following symbols are entered here:

$$\begin{aligned} a &= (6/\pi)m\Delta p D_a(1/t_g) \cdot (1 + h/t_g); \\ b &= (6/\pi)m\gamma_m D_a^2(1/t_g) \cdot (1 + h/t_g); \\ c &= 1.5m(\gamma_m - \gamma_R) D_a^2(1/t_g) \cdot (1 + h/t_g). \end{aligned}$$

To determine the dependence of α_s on the parameter k for permeable rocks, we introduce a dimensionless parameter $= 2m\Delta p(D_a/t_g) \cdot (1 + h/t_g)$: $\alpha_s \cong 2.25k$.

Then, the value of immersion of the lining in the rock mass δ with time, according to [12], is determined from the ratio:

$$\delta = E_0 \cdot (8/\pi^2) \cdot \tau.$$

where $\tau = t/(\gamma_w D_a/2kE_*)$ —dimensionless time; $E_0 = [2.25/(2 \cdot 1.7)](\Delta p D_a/E_*)^2 \cdot (1/t_g) \cdot (1 + h/t_g)$; E_* —volumetric modulus of elasticity, k —the filtration coefficient of the rock.

Based on the above dependencies, we can determine the contact area “lining—rock” from the stop time t : taking into account the above dependencies, we determine by the ratio:

$$\begin{aligned} A_{ss} &= D_a \sqrt{\delta/t_g} \\ &= 0.732 \cdot (\Delta p/E_*) \cdot (D_a^2/t_g) \cdot \sqrt{t/(\gamma_w D_a/2kE_*)} \cdot \sqrt{(1 + h/t_g)} \quad (m^2/m) \quad (2) \end{aligned}$$

Due to the small thickness of the crust h (its value is already taken into account in the expression for A_{ss}), we assume that $A_{sc} = 0$ и $A_{sm} = \pi D_a - A_{ss}$.

The increase in the thickness of the external filtration crust h during the time of its formation t is defined as $h = a\sqrt{t}$, where a is the coefficient depending on the shape of the pore channels, grain size, properties of the bentonite solution [8].

Residual stress F_r in the composition of the friction component of the total effort of punching will be determined by the total resistance of friction lining on each of the squares A_{ss}, A_{sm} individually taking into account the total length of the zone of sticking L_{st} . In the first approximation, we assume that the sticking zone is distributed over the entire length of the impacted area and is equal to L .

Table 1 Values of the coefficients depending on the increase in the pressure forces of the duration of the stops when pushing the lining

Sites	Champigny	Montmorency 2
Soils	Sanded clay	Plastic muddy marl
$a \cdot 10^2; b \cdot 10^2$	2; 8.2	11; 5.7
$A \cdot 10^2; B \cdot 10$	3.88; 3.89	4.83; 3.9
R^2	0.9534	0,881

Note (**)—the ratio is established in areas where the use of lubricant was significant

$$F_r = [\tau_{ss}A_{ss} + \tau_{sm}(\pi D_a - A_{ss})]L \quad (3)$$

where τ_{ss} —residual shear strength of “rock contact – lining material” (according to experimental data [2, 3] it was 4.5–7.3 kN/m²), τ_{sm} —contact strength of “bentonite – lining material” (according to [14], $\tau_{sm} = (2-50)10^{-3}$ kN/m²).

According to [2, 3] ratio $F_r/\pi D_a$ for the seven punching sites was a range of values (0.5–3.2) kN/m², so the range of values for $A_{ss}/\pi D_a$ was 0.1–0.6.

According to the same data to plot Champigny, France, the rate of increase of the pressure effort $[F_r(t) - F_r(0)]/(\pi D_a L) \cong \tau_{ss} \cdot [A_{ss}(t)/\pi D_a]$ with increasing section length of rupture L made up for the stopping time $t = 64$ h—2.4 kN/m², для 14 h < t < 20 h—2.0 kN/m², для 1.5 h < t < 3 h—0.8 kN/m². Thus, for this area the ratio $A_{ss}(t)/\pi D_a$ was (kN/m²)—0.45; 0.38 и 0.15, respectively.

In [2–4] according to the experimental data for tunneling with the use of bentonite ratio $\delta F_r/F_r(0) = [F_r(t) - F_r(0)]/F_r(0)$ is represented as a logarithmic $[\Delta f]_{r/(F_r(0))} = a + b \ln t$ proposed by Norris [1]. Processing of data presented in the mentioned works, according to (2), i.e., in the form of $\delta F_r/F_r(0) = A(t/B)^{0.5}$, allowed to determine the coefficients A and B .

In Table 1 for comparison, the values of all coefficients for the three sites are given.

To check the reliability of the obtained dependences (2) and (3) on the basis of a comparison of the values E_* and E_* obtained by calculation in accordance with the above theoretical developments, with full-scale data is currently not possible, in the absence of the latter. In light of this, the accumulation of experimental data seems promising.

3 Conclusion

The presented method of estimation of the friction component of the pressing forces when punching the lining using lubricants based on bentonite in the presence of stops of work on the sinking of a certain duration allows to predict the efforts of punching in straight sections with greater accuracy than in the existing regulations. Taking into account the elastic and filtration characteristics of rocks, as well as the

strength characteristics of the contact between the rock and the lining material, are key in predicting the pressure forces to push the tunnel lining for the design of tunneling works.

References

1. Milligan GWE, Norris P (1999) Pipe-soil interaction during pipe jacking. *Proc Inst Civ Eng Geotech Eng* 137(1):27–44
2. Pellet-Beacour A-L, Kastner R (2002) Experimental and analytical study of friction forces during microtunneling operations. *Tunn Undergr Space Technol* 17(1):83–97
3. Microtunneling and horizontal drilling: French national project “Microtunnels” recommendations. French Society for Trenchless Technology. ISST Ltd, London, 2006, p 343
4. Sheil BB, Curran BG, McCabe BA (2016) Experiences of utility microtunnelling in Irish limestone, mudstone and sandstone rock. *Tunn Undergr Space Technol* 51:326–337
5. Kollektory i tonneli kanalizatsionnyie. Trebovaniya k proektirovaniuu, stroitelstvu, kontrolyu kachestva i priemke rabot. (Sewers and sewer tunnels. Designing, construction, quality supervision and acceptance of works) STO NOSTROI 2.17.66-2012. “BST”, Moscow, 2013, p 101
6. Schoesser B, Thewes M, Peters M, Praetorius S (2011) Practice-oriented guideline for the choice of an adequate bentonite suspension for lubrication in pipe jacking. International No-Dig 2011 29th international conference and exhibition, Berlin, 2–5 May 2011, p 3A-3
7. Outmans HD (1958) Mechanics of differential pressure sticking of drill collars. *Trans Am Inst Min Metall Petrol Eng (Petrol Dev Technol)* 213:267–274
8. Samotoy AK (1986) Prikhvaty kolonn pri burenii skvazhin (Sticking of drill columns in the well boring). Publishing House “Nedra”, Moscow, p 236
9. Kochina IN, Mikhaylov NN (1976) Filtratsiya cherez glinyaniye korki (The seepage through clay cakes). *Izvestiya AN SSSR. Mekhanika tverdego tela (Mech Solids)* 6:70–75
10. Cao Y, Wang X, Du L, Deng K (2014) A method of determining nonlinear large strain consolidation parameters of dredged clays. *Water Sci Eng* 7(2):218–226
11. Nicolaevskiy VN (1996) Geomechanics and fluidodynamics. Kluwer Academic Publishers, London, p 351
12. Johnson KL (1985) Contact mechanics. Cambridge University Press, p 452
13. Budhu M (2010) Soil mechanics and foundations, 3rd edn. Wiley, New York, p 781
14. Broere W (2001) Tunnel face stability and new CPT applications. Thesis, Technical University Delft, p 208

Diesel Work Cycle at Start



V. V. Shishkov

Abstract Despite significant achievements in the diesel engines starting characteristics improvement, there are still problems associated with unstable ignition, poor combustion of fuel during start-up and subsequent warm-up. For the conditions of a diesel engine's cold start, the characteristics of the fuel burnout, heat generation, and thermal management are determined. The inaccuracy in the cylinder pressure measuring was calculated. The patterns of fuel burnup, obtained on the basis of the experimental pressure diagrams analysis, make it possible to obtain a good agreement between the calculated and experimental results. The influence of the start-up conditions, including the increase in the intake air temperature, on the magnitude of the kinetic indicators of combustion characteristics and the completeness of combustion of fuel is established.

Keywords Diesel • Cold start • Combustion process • Kinetic indicators • Combustion efficiency

1 Introduction

Modern diesel engines occupy a significant market share in most countries of the world due to technical and economic indicators, high torque, and low fuel consumption [1]. Despite significant advances in the organization of intra-cylinder processes, including the cold diesel start-up, some aspects remain problems requiring solutions: unstable ignition, uneven combustion, high maximum combustion pressures, and high speeds of pressure increase during the start-up and warm-up of a diesel engine [2–4]. The nature of changes in the working fluid status parameters in the cylinder during start-up indicates the need for using new approaches to planning and conducting an experiment, new methods for analyzing the results of an experiment [5].

V. V. Shishkov (✉)
South Ural State University, 76, Lenin Avenue, Chelyabinsk 454080, Russia
e-mail: shishkovvv@susu.ru

Traditional measurement means in crankshaft engines and engine operating modes during the tests allow to register the parameters maintained constant over a long period of time or representing an average value over a certain number of cycles [6]. The start-up mode differs not only by changing the interframe frequency of the crankshaft, but also by changing the angular velocity of the crankshaft during the cycle [7]. For start-up, increased irregularity of the cycle fuel supply is typical. Direct measurement of a single-cycle feed makes the experiment unnecessarily complex and labor-consuming. For this reason, the actual cycle fuel feed is assumed to be equal to the average cycle over several cycles. The maximum combustion pressure and the indicator operation of the cycle are excessively high in individual cycles; it shows that some part of the fuel can remain on the walls and in the volume of the combustion chamber from previous cycles [7–9]. Low cranking frequency of the crankshaft causes increased leakage through the leakiness of the cylinder-piston group [10]. The cold walls of the combustion chamber increase the heat exchange, as a result of which the temperature and pressure of the working fluid are reduced. Comparison of the results, pressure and temperature calculations in the compression process to experimental data, allows to establish the correspondence between the experimental and calculated mass losses of charge and heat losses in the compression process when the engine crankshaft is cranked [11]. Simulation of the combustion process during the start-up of a diesel engine can be implemented by setting simple linear characteristics of fuel burnout [12]; however, this approach distorts the patterns of the fuel burnout rate change and other parameters, due to which we lose the tool for more detailed study of intra-cylinder processes. In the well-known methods of modeling burnout characteristics, for example, using the equation of Professor Vibe, constants obtained experimentally from the results of processing indicator diagrams are used. The methods of analysis of indicator diagrams used in such cases are oriented to the corresponding methods of synthesis of the engine workflow [13–16], which do not take into account the processes characteristic of the start-up mode. The calculating model for current values of intra-cylinder parameters, taking into account the heat and mass exchange in the cylinder [17], is applicable for the formation on its basis of an analyzing technique for a diesel operating cycle at starting conditions using an indicator diagram. In terms of the use of start-up facilities, such as heating the intake air, there is a change in temperature and composition of the intake charge when starting and warming up the diesel. Heating the intake air shortens the start-up time and allows the development of a start-up strategy [18, 19], which controls the fuel injection pattern taking into account the parameters of the intake charge state and the start-up dynamics in order to reduce harmful emissions from the exhaust gases.

2 Results of the Working Cycle Analysis at Start-up on the Indicator Diagram

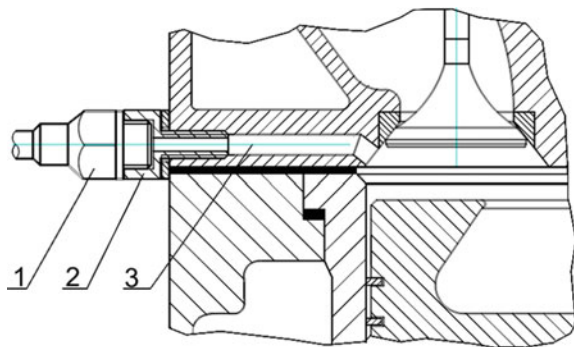
The reliability of results is determined by a number of conditions. Thus, the indicating sensor is usually installed in the combustion chamber without intermediate channels in order to eliminate the displacement of the recorded pressure in the angle of rotation of the crankshaft and eliminate the influence of free gas oscillations in the indicator channel on the actual pressure value. Using the indicator channel is practical, it allows you to install a pressure sensor without significant modification of engine parts (Fig. 1). The proposed sensor placement provides the necessary measurement accuracy for crankshaft starting frequencies of up to 250 min^{-1} . In this case, the natural frequency of gas oscillations in the indicator channel exceeds the required highest frequency of the indicator system bandwidth by no less than 4.7 times. The pressure drop that may occur in the indicator channel does not exceed 0.024 MPa; the phase error of pressure registration does not exceed 0.34 degrees of crankshaft turn (CST).

The method of analyzing the working cycle is formed on the basis of a mathematical model of working cycle synthesis and makes it possible to identify experimental data specifying the mathematical model and necessary to simulate the characteristics of fuel burning. The indicator diagram, taken from the engine when it is started, allows to calculate the elementary amount of heat used.

$$dx_i = \frac{(dp \cdot V)/(k \cdot p) - \partial_{cl}V + dV}{(R \cdot H_u \cdot G_c)/(p \cdot C_p) + \partial_M V}$$

where dp —elementary pressure increment of the working fluid, MPa; V —current cylinder volume, m^3 ; k —adiabatic index; p —working fluid pressure, MPa; $\partial_{cl}V$ —partial change in the volume of the working fluid due to leakage through the leaking of the cylinder-piston group, m^3 ; dV —elementary change in the volume of the working fluid due to the movement of the piston, m^3 ; R —universal gas constant, $\text{kJ}/(\text{kmol K})$; H_u —lower heating value, kJ/kg ; G_c —cycling fuel supply, kg/cycle ;

Fig. 1 Pressure sensor installation diagram: 1—pressure sensor; 2—adapter; and 3—indicator channel



C_p —molar heat capacity at constant pressure, kJ/(kmol K); $\partial_M V$ —particular change in the working fluid volume due to changes in the number of moles of gas in the combustion process, m³.

The reliability of the integral heat use characteristics depends on the accuracy of the leakage calculation of the working fluid and the deviation of the actual fuel-injected value per cycle from the average cycle flow value determined during calibration.

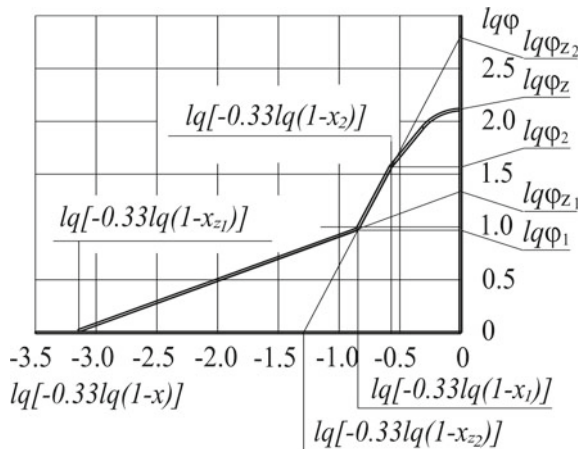
$$dx_\delta = \frac{(dp \cdot V)/(k \cdot p) - (R \cdot dQ_z)/(p \cdot C_p) - \partial_{cl} V + dV}{(R \cdot H_u \cdot G_c)/(p \cdot C_p) + \partial_M V}$$

To calculate the elementary amount of heat released, you must additionally know the heat dQ_z , transferred to the working fluid as a result of heat exchange with the walls of the in-cylinder space. The maximum value of x_δ corresponds to the proportion of fuel burned during the cycle.

The duration of combustion, the conditional duration of combustion, the intensity of the combustion process are determined on the basis of a logarithmic anamorphosis. For the working cycle in the start mode, the S-shaped form of logarithmic anamorphosis is typical, Fig. 2.

The nature of the logarithmic anamorphosis change does not correspond to single-stage combustion. Allocation of two combustion sites [20] allows to simulate more complex patterns of burnout of the fuel. For the S-shaped logarithmic anamorphosis, it is advisable to divide the combustion process into three characteristic sections: kinetic combustion period; the period of diffusion combustion, and the period of burning out. The burnout equation indicators for the first two sections can be determined quite accurately by a logarithmic anamorphosis: for the first section ($0 \leq \varphi \leq \varphi_1$) the conditional duration of combustion $\varphi_{z1} = 10^{\lg \varphi_{z1}}$, burn rate indicator $m_1 = \lg[-0.33 \cdot \lg(1 - x_{z1})]/\lg \varphi_{z1} - 1$, fuel burnout

Fig. 2 Logarithmic anamorphosis



equation $x = 1 - \exp\left[c(\varphi/\varphi_{z1})^{m_1+1}\right]$; for the second section ($\varphi_1 \leq \varphi \leq \varphi_2$) according $\varphi_{z2} = 10^{\lg \varphi_{z2}}$; $m_2 = \lg[-0.33 \cdot \lg(1 - x_{z2})]/\lg \varphi_{z2} - 1$; $x = 1 - \exp\left[c(\varphi/\varphi_{z2})^{m_2+1}\right]$.

For the third section, increases the inaccuracy in determining the pressure on the indicator diagram, and, consequently, the rate of combustion. An insignificant change in the burned fuel proportion occurs according to a rule close to linear. In this regard, to simulate combustion in the afterburning site, it is advisable to set a linear change in the burnout rate from its value at the end of the second section at $\varphi = \varphi_2$ to zero at $\varphi = \varphi_z$.

The logarithmic anamorphosis corresponds to the heat release characteristic x_δ , shown in Fig. 3, which was obtained as a result of the indicator diagram analysis of the first combustion cycle during the start of the diesel engine D160. The experiment shows that the angular velocity of the crankshaft (ω) during the cycle varies from 14.2 to 17.2 s^{-1} , to the arrival of the piston in the upper dead center (UDC) 13% (m_{cl}) of the charge mass (that entered the cylinder during the filling period) is lost during compression through the leakage of the cylinder-piston group, and by the end of the expansion, the amount of charge lost due to leaks reaches 27%.

For the considered cycle are defined: total duration of combustion $\varphi_z = 125^\circ$ CST, the duration of the kinetic combustion period $\varphi_1 = 9.6^\circ$ CST, the duration of the diffusion combustion period $\varphi_2 = 36^\circ$ CST, conditional duration of kinetic combustion period $\varphi_{z1} = 22.4^\circ$ CST, conditional duration of the diffusive

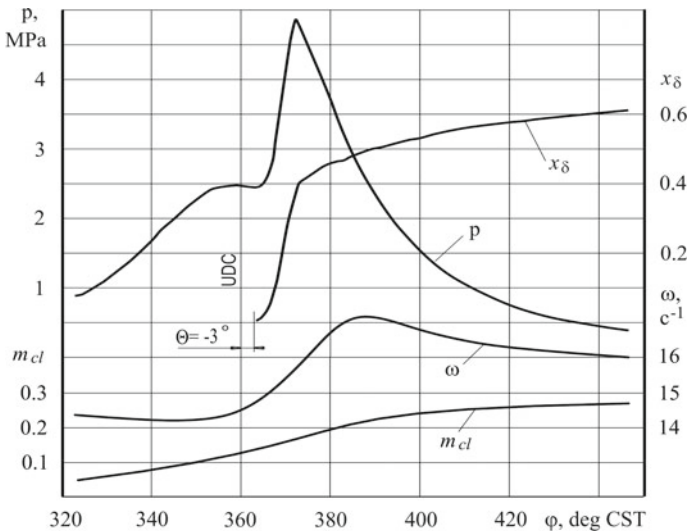


Fig. 3 The results of the analysis of the indicator diagram

combustion period $\varphi_{z2} = 676^\circ$ CST, burn rate for kinetic burn period $m_1 = 1.32$, burn rate indicator for diffusion burn period $m_2 = -0.54$.

The use of data obtained as a result of the analysis of the indicator diagram for comparing the experimental and computational cycle showed a qualitative and quantitative correspondence of pressure changes p and temperature T of the working fluid, emission of heat characteristics x_δ , and the proportion of clean air in the workpiece r_α with the selected method simulation of fuel burn law (Fig. 4). In particular, the indicator work cycle for the computational simulation was 1.40 kJ, and 1.39 kJ when determining the indicator diagram obtained in the experiment. Cycle corresponds to ambient temperature $T_o = 272$ K, cranking frequency $n_s = 143 \text{ min}^{-1}$, cycle fuel supply $G_c = 0.186$ g, and heated intake charge $\Delta T_s = 49$ K (solid lines—synthesis of the working cycle, dotted—analysis).

Kinetic indicators that determine the burnout characteristics of the fuel, as well as the heat release coefficient and a number of other cycle indicators, depend on the ambient temperature and the engine temperature, crankshaft cranking frequency, inlet charge preheat rate, the proportion of combustion products in the intake charge, cyclic fuel supply, and other parameters. To a large extent, the value of the combustion process kinetic indicators is influenced by the duration of the ignition delay period. An increase in the ignition delay period, ceteris paribus, increases the proportion of fuel evaporated before the start of combustion, and, accordingly, increases the duration of the kinetic combustion period φ_1 , and the proportion of fuel that burned during this period.

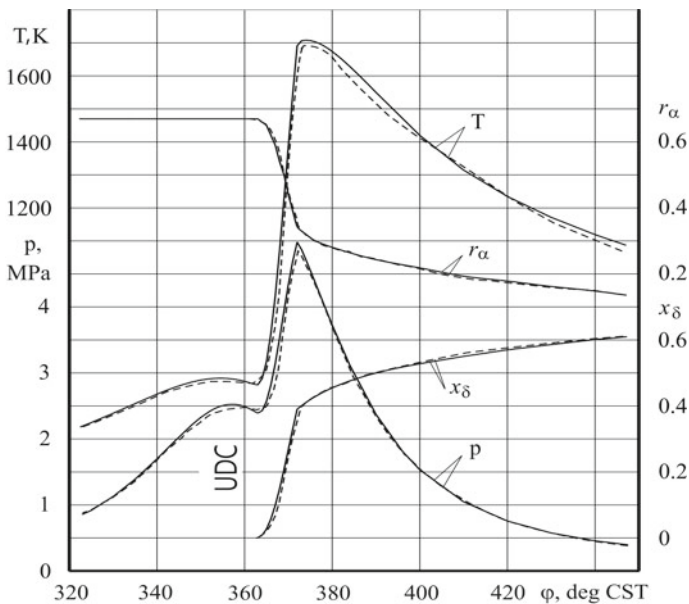


Fig. 4 Synthesis and analysis of the operating cycle

The influence of ambient temperature in different directions. On the one hand, lowering the temperature increases the ignition delay period, and accordingly, the amount of evaporated fuel, on the other hand, the rate of evaporation of fuel decreases.

Under the considered conditions of an equal increase in the temperature of the heated inlet air (70 °C) to a level that ensures fuel ignition, the decrease in the ambient temperature from minus 6 to minus 19 °C (*ceteris paribus*), the combustion process indicators changed slightly, see Table 1. In particular, the ignition delay period increased by two degrees, and the duration of the kinetic combustion period decreased by one degree.

To a somewhat greater degree, the decrease in temperature affected the heat generation coefficient, which decreased from 0.5 to 0.46.

The level of inlet charge heating (Fig. 5) affects the amount of oxygen in the intra-cylinder volume, not only as a result of changes in the heated air density, but also as a result of a change in the proportion of clean air when the intake charge is heated by combustion products. Increasing the intake charge temperature shortens the ignition delay period φ_i until the moment when the decrease in the content of clean air in the intra-cylinder charge r_{α_s} prevents the development of preflame chemical reactions and the ignition delay period begins to increase. The change in the duration of the kinetic combustion period φ_1 corresponds to the character of the φ_i curve, but in a low-burning region r_{α_s} , the duration of combustion increases rapidly. The proportion of heat released during the kinetic combustion period x_{δ_1} decreases from 0.62 to 0.5 as the temperature rises and increases again to 0.62; therefore, over the first period, more than half of the total heat released during the cycle is released. The nature of the change x_{δ_1} is determined, including the magnitude of the ignition delay period. The heat generation coefficient δ varies proportionally r_{α_s} and this pattern corresponds to the equation $\delta = 0.931 \cdot r_{\alpha_s} - 0.161$.

Table 1 The combustion process parameters

The parameter characterizing the combustion	Temperature	
	Minus 6 °C	Minus 19 °C
Ignition delay period, φ_i , deg CST	11	13
The duration of the kinetic period of combustion, φ_1 , deg CST	7	6
Conventional duration of the period of kinetic combustion, φ_{z1} , deg CST	18	15
Duration of the diffusive combustion period, φ_2 , deg CST	48	42
Conventional duration of the period of diffusion combustion, φ_{z2} , deg CST	1100	756
The nature indicator of combustion for the kinetic combustion period, m_1	1.32	1.45
The nature indicator of combustion for the diffusional combustion period, m_2	-0.58	-0.59
Heat generation coefficient, δ	0.5	0.46

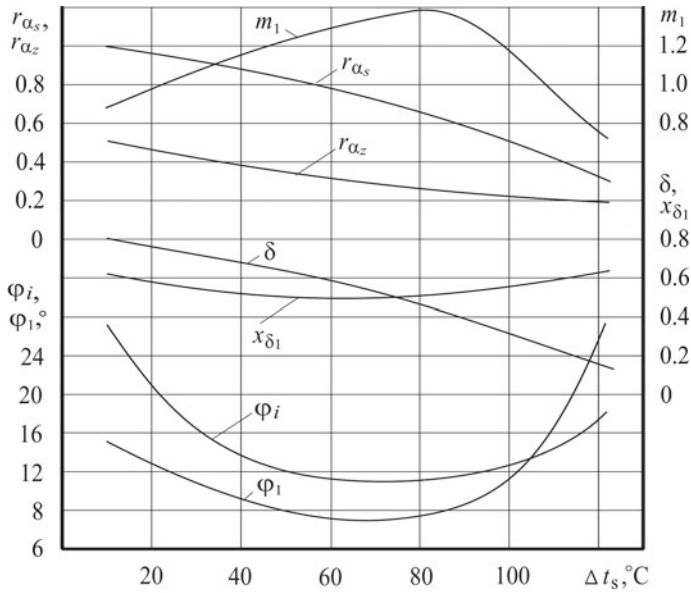


Fig. 5 Influence of heating the intake air on the performance of the combustion process

A decrease in δ as Δt_s increases indicates an increase in the proportion of fuel that does not participate in the combustion process and increases, thereby, the amount of harmful emissions from the exhaust gases.

3 Conclusion

The characteristics of the course of intra-cylinder processes (changes in the amount of working fluid and its composition, heat exchange with the cold walls of the combustion chamber) characteristic of the cold start conditions of a diesel engine, as well as a change in the angular velocity of the crankshaft rotation, take into account regularities reflecting these processes when analyzing the operating cycle instrumental diagram.

Based on the results of processing the indicator diagrams, a regularity of the heat release characteristic was established, which allows to distinguish three characteristic periods of the combustion process, for which the corresponding kinetic parameters were obtained for different start conditions, including when the ambient temperature and the degree of heating of the intake air were changed.

The use of data obtained as a result of analysis of indicator diagrams to simulate the diesel cycle during start-up showed qualitative and quantitative correspondence of changes in pressure and temperature of the working fluid, heat generation characteristics, and other parameters with the proposed method of burning-out modeling fuel.

References

1. Global Diesel Engine Market by Product, market and region, 5th edn. Industry Study 3488. Published Date from Jan 2017
2. Rau B (1975) Versuche zur Thermodynamik und Gemischbildung beim Kaltstart eines direkt einspritzenden Viertakt Dieselmotors. Dissertation, Ing. Fak. Maschininw. Techn. Univ. Hannover, 178 p
3. Ullrich K (1973) Der Einfluss der Ölviskosität auf das Drehmoment beim Kaltstart eines Dieselmotors. Kraftfahrzeugtechnik 5:140–145
4. Kupersmidt VL (1974) Starting qualities and start-up systems of the family of tractor air-cooled diesel engines of the Vladimir Tractor Plant Overview. TSNITEE traktorselkhoz mash, Moscow, 55 p
5. Kadyshovich EK, Miselev MA, Kostin AK et al (1980) Investigation of the process of heat generation during fuel burn-up during the start-up of a diesel engine with compressed air. Dvigatelo stroenie 8:9–13
6. Raykov IY (1975) Tests of internal combustion engines. Higher School, Moscow, 320 p
7. Liu H, Henein N, Bryzik W (2003) Simulation of diesel engines cold-start, SAE Technical Paper
8. Han Z, Henein N, Nitu B, Bryzik W (2001) Diesel engine cold start combustion instability and control strategy. SAE Technical Paper
9. Henein NA, Zahdeh AR, Yassine MA, Bryzik W (1992) Diesel engine cold starting: combustion instability. SAE Technical Paper
10. Malozemov AA, Bondar VN, Kukis VS (2016) Improvement of the forced diesel engines cold starting characteristics by oil injection into the cylinder. Procedia Eng 150:1149–1155
11. Sharoglazov BA, Shishkov VV (1993) Analysis of the diesel cycle on the indicator diagram. Dvigatelo stroeniye 3–12:25–27
12. Boldyrev IV, Smirnova TN, Pushkin SB (1984) Mathematic model of engine start. Dvigatelo stroeniye 6:14–16
13. Vibe II (1962) New about the working cycle of engines. Mashgiz, Moscow, Sverdlovsk, 272 p
14. Stechkin BS, Genkinn KI, Zolotarevsky VS, Skorodinsky IV (1960) Indicator diagram, dynamics of heat generation and the duty cycle of a high-speed piston engine. Because of Acad. Science of the USSR, Moscow, 199 p
15. Farafontov MF (1994) Tests ICE. Types and methods: textbook allowance. Publishing of CSTU, Chelyabinsk, 77 p
16. Bąkowska A, Radziszewska L, Milanb Ž (2016) Determining the polytropic exponent of the process occurring during the working cycle of a diesel. Procedia Eng 136:220–226
17. Shishkov VV (2015) Starting cold diesel. Modeling processes in a cylinder. In: Prom-Engineering: proceedings of the international scientific and technical conference. SUSU Publishing Center, Chelyabinsk, pp 107–110
18. Ramadhas AS, Xu H, Liu D, Tian J (2016) Reducing cold start emissions from automotive diesel engine at cold ambient temperatures. Aerosol Air Qual Res 16:3330–3337
19. Liu D, Xu H, Ramadhas AS, Tian J (2014) Investigation on the performance of diesel oxidation catalyst during cold start at low temperature conditions. SAE Technical Paper
20. Radivoje BPEŠIĆ, Aleksandar Lj DAVINIĆ, Dragan STARANOVIĆ, Danijela MMILORADOVIĆ, Snežana DPETKOVIĆ (2010) Experimental determination of double vibration function parameters in diesel engines with biodiesel. Therm Sci 14:207–218

Dynamic Analysis of Lifting Cranes



N. N. Panasenko and A. V. Sinelschikov

Abstract The finite element method (FEM) which is popular in calculating strength of engineering constructions disposes a long list of basic finite elements (FEs) for building discrete finite element design dynamic models (DDMs) of lifting cranes. The paper presents the general methods of developing equations of motion for crane systems with multiple (n) degrees of freedom and their components in the form of matrixes of stiffness and masses of a thin-walled bar and plate FEs, the latter being analyzed using the Kirchhoff plate theory. The produced final formulas help to analyze the quality of DDM of structural steelworks of the bridge cranes built using bar FEs with a closed profile and plate FEs based on the comparison of general bending stiffness of longitudinal girders and on the comparison of fundamental frequencies (FFs) and eigenforms (EFs) of oscillations of their DDM.

Keywords Lifting bridge crane • Structural steelworks • FEM • Finite element • Thin-walled bar with closed profile • Plate • Design dynamic model • Equation of motion

1 Formulation of a Problem

The intensive development of computer engineering has resulted in a revaluation of traditional beliefs in studying strength of the structural parts of lifting cranes, which allows determining the boundary lines of displacements, deflections, and stresses more accurately in the studied structures. For these purposes, the finite element method (FEM) appears the most popular among the methods oriented to the efficient use of a PC where some basic finite elements (FEs) apply the approximation

N. N. Panasenko (✉)

Astrakhan State Technical University, 16, Tatishchev St., Astrakhan 414056, Russia
e-mail: laex@bk.ru

A. V. Sinelschikov

Astrakhan State University of Civil Engineering, 18, Tatishchev St.,
Astrakhan 414056, Russia

© Springer Nature Switzerland AG 2020

A. A. Radionov et al. (eds.), *Proceedings of the 5th International Conference on Industrial Engineering (ICIE 2019)*, Lecture Notes in Mechanical Engineering,

https://doi.org/10.1007/978-3-030-22041-9_86

801

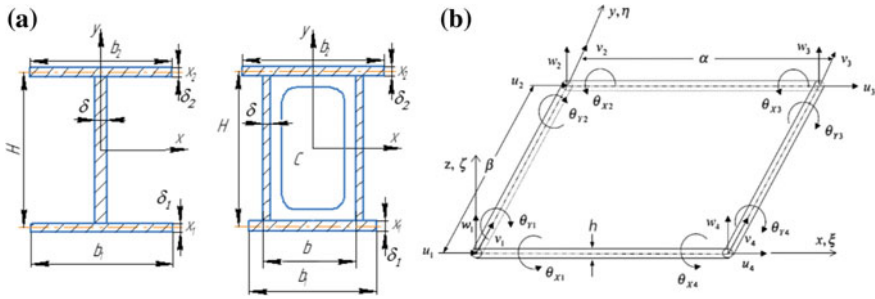


Fig. 1 Basic finite elements: **a** cross sections of thin-walled bars of open and closed profile having $2 \times 7 = 14$ freedom degrees; **b** thin plate with $4 \times 5 = 20$ freedom degrees

of actual structures in the process of building design dynamic models, the most important FEs being considered the thin-walled bars with open and closed profiles and plate FEs (Fig. 1).

In this regard, it becomes obvious that for carrying out the dynamic computation analysis of 3-D structures of the lifting cranes, which are made of bars with open and closed profiles or of plates (shells), as it comes from the theory of consistent FEs in terms of FEM, it is necessary to form a design dynamic finite element model (FEM) of a structure with n degrees of freedom [1] for the combination of loads required for the design. Because the core DDM of a crane is presented by the skeleton axes of longitudinal and end girders, steelwork elements of a load trolley, structural elements of crane connecting passages, etc., its drawing based on a finite element network is considered less difficult and, consequently, more efficient for practicing project analyses. Along with a bar FEM of a crane, its plate model seems more time taking and data consuming, which allows to control computation parameters of DM in any point of a cross section of the model element, especially in welded seams, zones of joining the stiffness diaphragms to the flanges and verticals of the general and end girders of the bridge, etc. Thus, there appears the need to assess the priority of the bar and plate DDMs of a bridge crane in terms of their dynamic portraits, which seems especially appropriate in a seismic design of the lifting cranes using both the linear spectrum method (LSM) and dynamic analysis method (DAM) [2].

2 Finite Element Building Design Dynamic Models

Finite element equation of motion of crane DDM is known [3] as:

$$[M]\{\ddot{V}(t)\} + [\gamma_z([M][K])^{0.5}]\{\dot{V}(t)\} + [K]\{V(t)\} = \{P_{st}\} + \{P_{dyn}\} - [M]\{\ddot{A}(t)\} \tag{1}$$



where γ_z is loss factor [4]:

$$\gamma_z = 2\xi = 2 \left(\delta_z \left[(2\pi)^2 + \delta_z^2 \right]^{-0.5} \right) \approx \frac{\delta_z}{\pi},$$

and δ_3 —logarithmic decrement of oscillations damping, according to which damping ratio in (1) for steel structures of the crane lays within $\xi \leq 0.02 \div 0.04$, which corresponds to logarithmic decrement $\delta_z = 0.125 \div 0.25$.

Obviously, in (1) $[M]_{n \times n}$ and $[K]_{n \times n}$ are mass and stiffness matrixes of a complete system, which are formed of mass and stiffness matrixes of separate FEs in their local coordinate system (LCS), $V(t)$ is vector of displacements of discrete nodes of finite element DDM of the crane of order $1 \times n$, its parameters for separate bar jk FE are as follows:

$$\{V(t)\}_{1 \times n}^{jk} = \left\{ \begin{matrix} \delta_X & \delta_Y & \delta_Z & \varphi_X & \varphi_Y & \Theta_Z & \Theta'_Z \end{matrix} \right\}_{GCS}^{j,T},$$

Here, T is a transposition index, and the first three parameters indicate linear shifting of the node, next three parameters denote angle of rotation, and the last one denoting a derivative from an angle of torsion (deplanation).

The vectors in the right part of equation of motion (1) denote external static, dynamic, and kinematic effects, in which $\{\ddot{A}(t)\}$ can represent accelerogram of a design earthquake [5], and the expression before the vector of velocity $\{\dot{V}\}$ is Martemyanov–Zeitlen attenuation matrix [5].

In the course of the design analysis of crane steelworks, there appears a question of priority of using bar or plate FEs (Fig. 1) in order to build their DDMs, as well as a need to conduct a comparative characteristic of bar and plate DDMs of a crane in terms of their “dynamic portraits,” i.e., on the level of their fundamental frequencies (FFs) and eigenforms (EFs) of oscillations received for the discrete bar and plate dynamic systems (DDM) of the crane construction. The definition of FF and EF can be derived from solving the equation of free oscillations of n -order

$$[M]\{\dot{V}(t)\} + [K]\{V(t)\} = \{0\}, \tag{2}$$

which is following from (1), as a special case.

As it is well known, the matrix of stiffness (mass) in (1) of a complete bar system of the crane structure of order $n \times n$ consisting of Sjk FE is determined by the method of suppositions

$$[K]_{GCS}^{n \times n} = \left(\sum_{jk=1}^{jk=S} \left[\begin{matrix} [K]_{7 \times 7}^{ij} & [K]_{7 \times 7}^{jk} & [K]_{7 \times 7}^{kk} \\ [K]_{7 \times 7}^{kj} & & \end{matrix} \right]_{14 \times 14} \right)_{GCS}^{n \times n}, \tag{3}$$



(mass matrix—with substitution of index K for M), according to which the formula of stiffness (mass) matrix of a separate bar FE jk $[K]_{14 \times 14}^{jk}$ in (3) divides into four blocks (further formulas (10)–(12)) when introducing them into original matrix (3) of order $n \times n$ $[K]_{n \times n}^{GCS}$, according to the numeration of freedom degrees of the discrete nodes j and k of the crane structure DDM.

Let us indicate that in (3)

$$[K]_{7 \times 7}^{kj} = \left([K]_{7 \times 7}^{jk} \right)^T, \tag{4}$$

where T is an index of transposition of matrixes. Besides (4), it should be taken into account that in (3) stiffness (mass) matrix of FE jk is transformed from LCS into GCS using a diagonal matrix

$$[K]_{14 \times 14}^{jk} = \left([T]_{14 \times 14}^{jk} \right)^T \times \left([K]_{14 \times 14}^{jk} \right)_{LCS} \times \left([T]_{14 \times 14}^{jk} \right), \tag{5}$$

where

$$[T]_{14 \times 14}^{jk} = \begin{bmatrix} \left(\begin{matrix} [A]_{3 \times 3} & [0]_{3 \times 3} & 0 \\ [0]_{3 \times 3} & [A]_{3 \times 3} & 0 \\ 0 & 0 & 1 \end{matrix} \right)_{7 \times 7} & [0]_{7 \times 7} \\ [0]_{7 \times 7} & \left(\begin{matrix} [A]_{3 \times 3} & [0]_{3 \times 3} & 0 \\ [0]_{3 \times 3} & [A]_{3 \times 3} & 0 \\ 0 & 0 & 1 \end{matrix} \right)_{7 \times 7} \end{bmatrix}, \tag{6}$$

and matrix $[A]_{3 \times 3}$ in (6) is a matrix of directional cosines of Euler angles β, α, γ (Fig. 2).

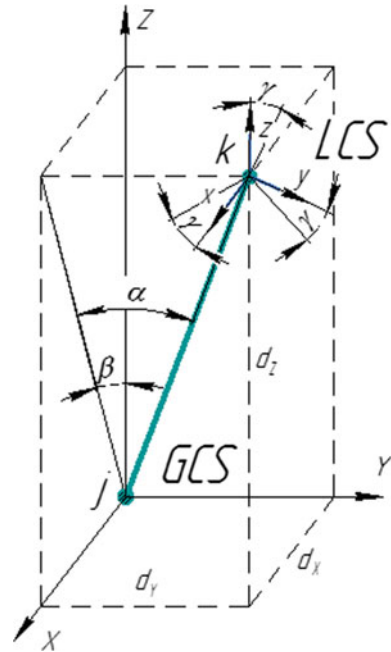
$$[A]_{3 \times 3} = [A_\beta]_{3 \times 3} [A_\alpha]_{3 \times 3} [A_\gamma]_{3 \times 3}, \tag{7}$$

where, according to linear transformation of coordinates of nodes of a separate jk FE from LCS into GCS, using matrix formula (5), the right part of formula (7) executes transformation $LCS \rightarrow GCS$ to angles β, α, γ as three original matrixes $[A_{\beta(\alpha,\gamma)}]_{3 \times 3}$, product (7) of which helps to obtain matrix $[A]_{3 \times 3}$ from (6)

$$[A]_{3 \times 3} = \begin{bmatrix} \cos \beta \cdot \cos \gamma - \sin \alpha \cdot \sin \beta \cdot \sin \gamma & -\cos \beta \cdot \sin \gamma - \sin \alpha \cdot \sin \beta \cdot \cos \gamma & \cos \alpha \cdot \sin \beta \\ \cos \alpha \cdot \sin \gamma & \cos \alpha \cdot \cos \gamma & \sin \alpha \\ -\sin \beta \cdot \cos \gamma - \sin \alpha \cdot \cos \beta \cdot \sin \gamma & \sin \beta \cdot \sin \gamma - \sin \alpha \cdot \cos \beta \cdot \cos \gamma & \cos \alpha \cdot \cos \beta \end{bmatrix}. \tag{8}$$



Fig. 2 Transformation of LCS → GCS for arbitrary in space finite element *jk*



Values of angles α and β in formula (8) are calculated from ratio (Fig. 2):

$$\sin \alpha = \frac{d_y}{\sqrt{d_x^2 + d_y^2 + d_z^2}}; \sin \beta = \frac{d_z}{\sqrt{d_x^2 + d_z^2}}$$

and γ in (8) is angle of clear rotation, which characterizes the turn of finite element around longitudinal axis z . Evidently, backward transformation $GCS \rightarrow LCS$ is described by transposed matrix $[A]_{3 \times 3}^T$ from (8).

For a discrete node with 7 degrees of freedom matrix of coordinate, transformation in (5) will be as follows:

$$[T]_{7 \times 7}^j = \begin{bmatrix} [A]_{3 \times 3}^j & [0]_{3 \times 3} & 0 \\ [0]_{3 \times 3} & [A]_{3 \times 3}^j & 0 \\ 0 & 0 & 1 \end{bmatrix}, \tag{9}$$

where $[0]_{3 \times 3}$ means zero matrix with dimensions 3×3 , and a unit in the seventh component reflects model of deplanation of a thin-walled bar, according to which, sum of bimoments in the node equals to 0.

For a thin-walled bar, FE with 14 freedom degrees matrix of transformation of coordinates subject to (9) can be written as (6)

For practical use matrix $[K]_{14 \times 14}^{jk}$ of bar FE jk from (5) is presented as blocks (3) of matrix formulas (10)–(12) which are determined by elasticity modules E and G (MPa), axial and polar moments of inertia $I_{x(y,\rho)}(M^4)$, length $L(m)$ and cross section area $A(M^2)$. Besides, in Eqs. (10)–(12) parameter D is determined by a formula

$$D = \frac{4EJ_{\bar{\omega}}(J_{\rho}^2 + J_z^2 - 2J_zJ_{\rho})}{LJ_{\rho}^2\mu^4},$$

where $J_{\bar{\omega}}$ is sectorial moment of inertia of a bar FE with closed profile [6], J_{ρ} is its directed moment, and $\mu = 1 - (J_z/J_{\rho})$.

Similar to (10)–(12), matrix of distributed masses of bar FEs jk in LCS is given in blocks [7] of matrix formulas (13)–(15), where p is volume weight of material (kg/m^3) of FE jk , and additionally, analogously to (4),

$$[M]_{7 \times 7}^{kj} = \left([M]_{7 \times 7}^{jk} \right)^T.$$

It should be taken into consideration that concentrated masses of useful load transported by crane and, if any, ballast loads and crane counterweights are considered in DDM nodes in directions of their linear freedom degrees.

$$[K]_{7 \times 7}^{jj} = \begin{bmatrix} \frac{12EJ_y}{L^3} & 0 & 0 & 0 & \frac{6EJ_y}{L^2} & 0 & 0 \\ 0 & \frac{12EJ_x}{L^3} & 0 & -\frac{6EJ_x}{L^2} & 0 & 0 & 0 \\ 0 & 0 & \frac{EA}{L} & 0 & 0 & 0 & 0 \\ 0 & -\frac{6EJ_x}{L^2} & 0 & \frac{4EJ_x}{L} & 0 & 0 & 0 \\ \frac{6EJ_y}{L^2} & 0 & 0 & 0 & \frac{4EJ_y}{L} & 0 & 0 \\ 0 & 0 & 0 & 0 & 0 & \left(\frac{6GJ_z}{5L} + \frac{3D}{L^2}\right) & \left(-\frac{11GJ_z}{10} - \frac{3D}{2L}\right) \\ 0 & 0 & 0 & 0 & 0 & \left(-\frac{11GJ_z}{10} - \frac{3D}{2L}\right) & \left(\frac{17GJ_zL}{15} + D\right) \end{bmatrix}, \tag{10}$$

$$[K]_{7 \times 7}^{kk} = \begin{bmatrix} \frac{12EJ_y}{L^3} & 0 & 0 & 0 & -\frac{6EJ_y}{L^2} & 0 & 0 \\ 0 & \frac{12EJ_x}{L^3} & 0 & \frac{6EJ_x}{L^2} & 0 & 0 & 0 \\ 0 & 0 & \frac{EA}{L} & 0 & 0 & 0 & 0 \\ 0 & \frac{6EJ_x}{L^2} & 0 & \frac{4EJ_x}{L} & 0 & 0 & 0 \\ -\frac{6EJ_y}{L^2} & 0 & 0 & 0 & \frac{4EJ_y}{L} & 0 & 0 \\ 0 & 0 & 0 & 0 & 0 & \left(\frac{6GJ_z}{5L} + \frac{3D}{L^2}\right) & \left(\frac{GJ_z}{10} + \frac{3D}{2L}\right) \\ 0 & 0 & 0 & 0 & 0 & \left(\frac{GJ_z}{10} + \frac{3D}{2L}\right) & \left(\frac{2GJ_zL}{15} + D\right) \end{bmatrix}, \tag{11}$$



$$[K]_{7 \times 7}^{jk} = \begin{bmatrix} -\frac{12EJ_y}{L^3} & 0 & 0 & 0 & \frac{6EJ_y}{L^2} & 0 & 0 \\ 0 & -\frac{12EJ_x}{L^3} & 0 & -\frac{6EJ_x}{L^2} & 0 & 0 & 0 \\ 0 & 0 & -\frac{EA}{L} & 0 & 0 & 0 & 0 \\ 0 & \frac{6EJ_x}{L^2} & 0 & \frac{2EJ_x}{L} & 0 & 0 & 0 \\ -\frac{6EJ_y}{L^2} & 0 & 0 & 0 & \frac{2EJ_y}{L} & 0 & 0 \\ 0 & 0 & 0 & 0 & 0 & \left(-\frac{6GJ_z}{5L} - \frac{3D}{L^2}\right) & \left(-\frac{GJ_z}{10} - \frac{3D}{2L}\right) \\ 0 & 0 & 0 & 0 & 0 & \left(\frac{11GJ_z}{10} + \frac{3D}{2L}\right) & \left(-\frac{GJ_z L}{30} + \frac{D}{2}\right) \end{bmatrix}, \quad (12)$$

$$[M]_{7 \times 7}^{ij} \text{LCS} = \left(\frac{\rho AL}{420}\right) \begin{bmatrix} 156 & 0 & 0 & 0 & -22L & 0 & 0 \\ 0 & 156 & 0 & 22L & 0 & 0 & 0 \\ 0 & 0 & 140 & 0 & 0 & 0 & 0 \\ 0 & 22L & 0 & 4L^2 & 0 & 0 & 0 \\ -22L & 0 & 0 & 0 & 4L^2 & 0 & 0 \\ 0 & 0 & 0 & 0 & 0 & 156\left(\frac{J_x + J_y}{A}\right) & 0 \\ 0 & 0 & 0 & 0 & 0 & 0 & 0 \end{bmatrix}, \quad (13)$$

$$[M]_{7 \times 7}^{kk} \text{LCS} = \left(\frac{\rho AL}{420}\right) \begin{bmatrix} 156 & 0 & 0 & 0 & 22L & 0 & 0 \\ 0 & 156 & 0 & -22L & 0 & 0 & 0 \\ 0 & 0 & 140 & 0 & 0 & 0 & 0 \\ 0 & -22L & 0 & 4L^2 & 0 & 0 & 0 \\ 22L & 0 & 0 & 0 & 4L^2 & 0 & 0 \\ 0 & 0 & 0 & 0 & 0 & 156\left(\frac{J_x + J_y}{A}\right) & 0 \\ 0 & 0 & 0 & 0 & 0 & 0 & 0 \end{bmatrix}, \quad (14)$$

$$[M]_{7 \times 7}^{jk} \text{LCS} = \left(\frac{\rho AL}{420}\right) \begin{bmatrix} 63 & 0 & 0 & 0 & 13L & 0 & 0 \\ 0 & 63 & 0 & 13L & 0 & 0 & 0 \\ 0 & 0 & 70 & 0 & 0 & 0 & 0 \\ 0 & -13L & 0 & -3L^2 & 0 & 0 & 0 \\ -13L & 0 & 0 & 0 & -3L^2 & 0 & 0 \\ 0 & 0 & 0 & 0 & 0 & -156\left(\frac{J_x + J_y}{A}\right) & 0 \\ 0 & 0 & 0 & 0 & 0 & 0 & 0 \end{bmatrix}. \quad (15)$$

By analogy with (2)–(6), two-component matrix of plate stiffness (Fig. 1b) consists of stiffness matrix $[K]_{20 \times 20}^{(1)}$ of plane stress condition

$$[K]_{20 \times 20}^{(1)} = \frac{Eh}{24\alpha\beta(1-\mu^2)} \begin{bmatrix} [K]_{10 \times 10}^{1,1} & [K]_{10 \times 10}^{1,2} \\ [K]_{10 \times 10}^{2,1} & [K]_{10 \times 10}^{2,2} \end{bmatrix}, \quad (16)$$

field of node shifts $\{V\}$ of which is written as vector of axial and traverse motions

$$\{V\} = \{u_1, v_1, \dots, u_4, v_4\}^T, \quad (17)$$

and second component $[K]_{20 \times 20}^{(2)}$ of 3-D deformation of the plate

$$[K]_{20 \times 20}^{(2)} = \frac{Eh}{24\alpha\beta(1-\mu^2)} \begin{bmatrix} [K]_{10 \times 10}^{1,1} & [K]_{10 \times 10}^{1,2} \\ [K]_{10 \times 10}^{2,1} & [K]_{10 \times 10}^{2,2} \end{bmatrix}, \quad (18)$$

field of node shifts $\{V\}$ of which is described as vector of traverse motions (from the plane of plate) and two angle motions (Fig. 1b).

$$\{V\} = \{w_1\theta_{x1}\theta_{y1} \dots w_4\theta_{x4}\theta_{y4}\}^T. \quad (19)$$

Rank of matrixes (16) and (18) 20×20 is determined by total number of freedom degrees of the plate, which follows from (17) and (19), and separate matrix blocks (16) and (18) are correspondingly presented by matrix formulas (20), (21) and (22)–(24), for which the formula similar to (4) applies

$$[K]_{10 \times 10}^{1,1} = \begin{bmatrix}
 4(-\alpha^2 - 2\beta^2 + \alpha^2\mu) & & & & & & & & & & \\
 -3\alpha\beta(\mu + 1) & & & & & & & & & & \\
 0 & 0 & 0 & 0 & 0 & 0 & 0 & 0 & 0 & 0 & \\
 0 & 0 & 0 & 0 & 0 & 0 & 0 & 0 & 0 & 0 & \\
 0 & 0 & 0 & 0 & 0 & 0 & 0 & 0 & 0 & 0 & \\
 4(\alpha^2 - \beta^2 - \alpha^2\mu) & & & & & & & & & & \\
 3\alpha\beta(3\mu - 1) & & & & & & & & & & \\
 0 & 0 & 0 & 0 & 0 & 0 & 0 & 0 & 0 & 0 & \\
 0 & 0 & 0 & 0 & 0 & 0 & 0 & 0 & 0 & 0 & \\
 0 & 0 & 0 & 0 & 0 & 0 & 0 & 0 & 0 & 0 & \\
 \end{bmatrix}, \tag{20}$$

symmetrically

$$[K]_{10 \times 10}^{1,2} = \begin{bmatrix}
 2(\alpha^2 + 2\beta^2 - \alpha^2\mu) & 3\alpha\beta(3\mu - 1) & 0 & 0 & 0 & 2(-\alpha^2 + 4\beta^2 + \alpha^2\mu) & -3\alpha\beta(3\mu - 1) & 0 & 0 & 0 \\
 3\alpha\beta(\mu + 1) & 2(2\alpha^2 + \beta^2 - \beta^2\mu) & 0 & 0 & 0 & 3\alpha\beta(3\mu - 1) & 4(-\alpha^2 + 2\beta^2 + \beta^2\mu) & 0 & 0 & 0 \\
 0 & 0 & 0 & 0 & 0 & 0 & 0 & 0 & 0 & 0 \\
 0 & 0 & 0 & 0 & 0 & 0 & 0 & 0 & 0 & 0 \\
 0 & 0 & 0 & 0 & 0 & 0 & 0 & 0 & 0 & 0 \\
 4(-\alpha^2 + 4\beta^2 + \alpha^2\mu) & 3\alpha\beta(3\mu - 1) & 0 & 0 & 0 & 2(\alpha^2 + 2\beta^2 - \alpha^2\mu) & -3\alpha\beta(3\mu + 1) & 0 & 0 & 0 \\
 3\alpha\beta(3\mu - 1) & 4(-\alpha^2 + \beta^2 - \beta^2\mu) & 0 & 0 & 0 & -3\alpha\beta(\mu + 1) & 2(2\alpha^2 + \beta^2 - \beta^2\mu) & 0 & 0 & 0 \\
 0 & 0 & 0 & 0 & 0 & 0 & 0 & 0 & 0 & 0 \\
 0 & 0 & 0 & 0 & 0 & 0 & 0 & 0 & 0 & 0 \\
 0 & 0 & 0 & 0 & 0 & 0 & 0 & 0 & 0 & 0
 \end{bmatrix}. \quad (21)$$

In addition, it should be noted that open matrixes $[K]_{10 \times 10}^{1,1}$ and $[K]_{10 \times 10}^{1,2}$ from (16) look like matrix formulas (20) and (21) [8, 9], at the same time in (16) it should be noted that $[K]_{10 \times 10}^{1,1} = [K]_{10 \times 10}^{2,2}$, and $[K]_{10 \times 10}^{2,1} = [K]_{10 \times 10}^{1,2}$. Stiffness matrixes (20) and (21) represent reactions of the plate in conditions of plane deflected mode, i.e., from two individual motions of each node shown on design chart of the plate FE (Fig. 1b), namely: $u_i, i = 1, 2, 3, 4$ and $v_i, i = 1, 2, 3, 4$, where i is numeration of plate nodes, and complete matrix of FE plate can be found by summing up matrixes (16) and (18), components (22)–(24) of matrix (18) being stipulated by displacements (19). It should be taken into consideration that in matrixes (20), (21) and (22)–(24) μ is Poisson's ratio, and $\gamma = (\beta/\alpha)$.

Two-component matrix of distributed masses of the plate is calculated similar to matrixes of stiffness (16) and (18)—from mass matrix of the plate $[M]_{20 \times 20}^{(1)}$ under plane DM and mass matrix $[M]_{20 \times 20}^{(2)}$ under 3-D deformation, reduced to one rank 20×20 , which is considered possible, because motions (17) u_{xi} and u_{yi} are components of only plane stress condition and do not depend on motions (19) $w_i, \theta_{xi}, \theta_{yi}$ of bend component.

Thus, component mass matrixes of the plate look like matrix formulas (25) and (26) [8, 9], where p is a volume weight of material of the plate, and α, β, h are its dimensions (matrixes (22), (24)–(26) are symmetric),

$$\begin{aligned}
 & [K]_{10 \times 10}^{1,2} \\
 & = \begin{bmatrix}
 0 & 0 & 0 & 0 & 0 & 0 & 0 & 0 & 0 & 0 \\
 0 & 0 & 0 & 0 & 0 & 0 & 0 & 0 & 0 & 0 \\
 0 & 0 & -2(\gamma^2 + \gamma^{-2}) + \frac{1}{5}(14 - 4\mu) & \left[\gamma^2 - \frac{1}{5}(1 - \mu)\right]\alpha & 0 & 0 & 0 & 0 & 0 & 0 \\
 0 & 0 & \left[\gamma^{-2} - \frac{1}{5}(1 - \mu)\right]\beta & 0 & 0 & 0 & 0 & 0 & 0 & 0 \\
 0 & 0 & \left[\gamma^{-2} - \frac{1}{5}(1 - \mu)\right]\beta & 0 & 0 & 0 & 0 & 0 & 0 & 0 \\
 0 & 0 & \left[\gamma^{-2} + \frac{1}{5}(1 - \mu)\right]\alpha & \left[\frac{1}{3}\gamma^{-2} + \frac{1}{15}(1 - \mu)\right]\alpha^2 & 0 & 0 & 0 & 0 & 0 & 0 \\
 0 & 0 & 0 & 0 & 0 & 0 & 0 & 0 & 0 & 0 \\
 0 & 0 & 0 & 0 & 0 & 0 & 0 & 0 & 0 & 0 \\
 0 & 0 & -2(2\gamma^2 - \gamma^{-2}) - \frac{1}{5}(14 - 4\mu) & 2\left[\gamma^2 + \frac{1}{5}(1 - \mu)\right]\alpha & 0 & 0 & -2(\gamma^2 + \gamma^{-2}) + \frac{1}{5}(14 - 4\mu) & \left[\gamma^{-2} - \frac{1}{5}(1 - \mu)\right]\beta & 0 & 0 \\
 0 & 0 & \left[\gamma^2 - \frac{1}{5}(1 + 4\mu)\right]\beta & \left[\frac{2}{3}\gamma^{-2} - \frac{4}{15}(1 - \mu)\right]\beta^2 & 0 & 0 & \left[\frac{1}{3}\gamma^{-2} + \frac{1}{15}(1 - \mu)\right]\beta & \left[\gamma^{-2} - \frac{1}{5}(1 - \mu)\right]\beta & 0 & 0 \\
 0 & 0 & -2\left[\gamma^2 + \frac{1}{5}(1 - \mu)\right]\alpha & \left[\frac{2}{3}\gamma^2 - \frac{1}{15}(1 - \mu)\right]\alpha^2 & 0 & 0 & \left[\frac{1}{3}\gamma^{-2} + \frac{1}{15}(1 - \mu)\right]\beta & \left[\frac{1}{3}\gamma^{-2} + \frac{1}{15}(1 - \mu)\right]\beta^2 & 0 & 0 \\
 \end{bmatrix}
 \end{aligned}
 \tag{23}$$

$$\begin{aligned}
 & [K]_{10 \times 10}^{2,2} \\
 & \begin{bmatrix}
 0 & 0 & 0 & 0 & 0 & 0 & 0 & 0 & 0 & 0 \\
 0 & 0 & 0 & 0 & 0 & 0 & 0 & 0 & 0 & 0 \\
 0 & 0 & 4(\gamma^2 + \gamma^{-2}) + \frac{1}{5}(14 - 4\mu) & 0 & 0 & 0 & 0 & 0 & 0 & 0 \\
 0 & 0 & -\left[2\gamma^{-2} + \frac{1}{5}(1 + 4\gamma)\right]\beta & \left[\frac{4}{3}\gamma^{-2} + \frac{4}{15}(1 - \mu)\right]\beta^2 & 0 & 0 & 0 & 0 & 0 & 0 \\
 0 & 0 & \left[2\gamma^{-2} + \frac{1}{5}(1 + 4\gamma)\right]\alpha & -\mu\alpha\beta & \left[\frac{4}{3}\gamma^{-2} + \frac{4}{15}(1 - \mu)\right]\alpha^2 & 0 & 0 & 0 & 0 & 0 \\
 0 & 0 & 0 & 0 & 0 & 0 & 0 & 0 & 0 & 0 \\
 0 & 0 & 0 & 0 & 0 & 0 & 0 & 0 & 0 & 0 \\
 0 & 0 & 2(\gamma^2 + \gamma^{-2}) - \frac{1}{5}(14 - 4\mu) & \left[2\gamma^{-2} + \frac{1}{5}(1 - \gamma)\right]\beta & \left[\gamma^2 + \frac{1}{5}(1 + 4\gamma)\right]\alpha & 0 & 0 & 4(\gamma^2 + \gamma^{-2}) + \frac{1}{5}(14 - 4\mu) & 0 & 0 \\
 0 & 0 & -\left[2\gamma^{-2} + \frac{1}{5}(1 - \gamma)\right]\beta & \left[\frac{2}{3}\gamma^{-2} - \frac{1}{15}(1 - \mu)\right]\beta^2 & 0 & 0 & 0 & 0 & \left[\frac{4}{3}\gamma^{-2} + \frac{4}{15}(1 - \mu)\right]\beta^2 & 0 \\
 0 & 0 & \left[\gamma^{-2} + \frac{1}{5}(1 + 4\gamma)\right]\alpha & 0 & \left[\frac{2}{3}\gamma^{-2} - \frac{4}{15}(1 - \mu)\right]\alpha^2 & 0 & 0 & \left[2\gamma^{-2} + \frac{1}{5}(1 - \gamma)\right]\alpha & \mu\alpha\beta & \left[\frac{4}{3}\gamma^{-2} + \frac{4}{15}(1 - \mu)\right]\alpha^2
 \end{bmatrix} \\
 & = \text{symmetrically}
 \end{aligned}
 \tag{24}$$

In the process of developing matrix of stiffness and masses of plate DDM of the crane, stiffness matrix $[K]_{GCS}^{24 \times 24}$ of a separate FE of the plate in GCS 0XYZ looks similarly as (5) for the bar

$$[K]_{GCS}^{24 \times 24} = [T][K]_{LCS}'^{24 \times 24} [T]^T,$$

where index “'” means a parameter in LCS.

In the general case of loading a plane plate FE, when external loads are exerted both on its median surface and along the normal, there applies linear dependency in LCS $oxyz$

$$\{Q\} = [K']\{v\} + \{R'_p\}, \tag{27}$$

where $\{Q\}$ is vector of external forces, and $\{R'_p\}$ is vector of external loads exerted onto FE reduced to its node freedom degrees:

$$\{v\}_i = \{v_{xi} \ v_{yi} \ w_{zi} \ \theta_{xi} \ \theta_{yi} \ \chi_i\}^T, \tag{28}$$

$$\{R'_p\} = \{Q_{xi} \ Q_{yi} \ N_{zi} \ M_{xi} \ M_{yi} \ M_{zi}\}^T \tag{29}$$

Because motions v_{xi}, v_{yi} are the components of plane stress only and do not depend on motions $w_{zi}, \theta_{xi}, \theta_{yi}$ which characterize the bend, let us introduce a turn angle of each node of a plate χ_i that does not take part in motion neither of plane stress, nor of the plate bend. That is why, when studying 3-D metal structures, in every node of which non-coplanar plates join, let us introduce into (28) angle χ_i and corresponding to it null moment M_{zi} , and into stiffness matrix, according to the proper freedom degree, let us introduce a stiffness ratio equal to 0, then the turn angle χ_i of this node will be 0. After that stiffness matrixes of a certain i node of FE plate from (27) will be

$$[K'_i] = \begin{bmatrix} [K_i^n]_{2 \times 2} & 0 & 0 & 0 & 0 \\ 0 & 0 & 0 & 0 & 0 \\ 0 & 0 & [K_i^u]_{3 \times 3} & 0 & 0 \\ 0 & 0 & 0 & 0 & 0 \\ 0 & 0 & 0 & 0 & 0 \end{bmatrix}_{6 \times 6}; \{R_{pi}\} = \begin{bmatrix} R_{pi}^n \\ \dots \\ R_{pi}^u \\ \dots \\ 0 \end{bmatrix}_{1 \times 6}, \tag{30}$$

where indexes “n” and “u” mean “plane” and “bend.” Now it is clear that global matrix $[K]$ of FE and its vector of reactions $\{R_p\}$ are linked to the local matrix $[K']_{6 \times 6}$ and the vector of reactions $\{R'_p\}_{6 \times 6}$ by a dependence

$$[K]_{GCS}^{24 \times 24} = [T][K']_{LCS}^{24 \times 24} [T]^T; \{R_p\} = [T]\{R'_p\}, \tag{31}$$

where



$$[T]_{24 \times 24} = \begin{bmatrix} [T_0]_1 & & & \\ & [T_0]_2 & & \\ & & [T_0]_3 & \\ & & & [T_0]_4 \end{bmatrix} \quad (32)$$

matrix of coordinates transformation LCS \rightarrow GCS of the four-node plate, where $m = 1, 2, 3, 4$, and $[T_0]_m$ in (32) of a separate m -node.

3 Conclusion

Calculations of the dynamic impact onto the crane structures of different types including seismic impact start with developing the design models that constitute a certain hierarchical structure, the quality of these models being very important in the construction design.

In practice, it is required to design crane structures of the new and more complex constructive shapes, so it is necessary to develop new methods in terms of the finite element base of the design models. The demands to work out modern projects of the crane structures are considered satisfied, if there is an accounted 3-D nature of the impact and if the structures are considered as unified 3-D systems; various nonlinearities should be accounted as well.

The paper presents two alternative ways to create the design dynamic models (DDM) of the crane bearing structures based on the plate FE and on the rod FE. Choice of the way should be defined by the assigned task and the design analysis of the load bearing metal structures of the lifting cranes.

References

1. Panasenکو NN (2014) Finite element computer models of lifting mechanisms. In: 4th international science practice conference St. Petersburg State Politechnical University, St. Petersburg, pp 743–756
2. Panasenکو NN (2014) Calculated justification of seismic stability of load-lifting cranes. WSEAS Trans Appl Theor Mech 9:104–123
3. Panasenکو NN (2013) Finite element model of damping oscillations of load-carrying steelworks of lifting cranes. Vest ASTU 2:41–49
4. Kotelnikov VS (2007) Development of model of earthquakes in design analysis of seismic stability of lifting constructions. Ind Saf 9:42–46
5. Zeitleen AI (1981) On taking into account internal friction in regulatory documents on dynamics design of constructions. Build Mech Calc Struct 4:33–38
6. Belkin AE (2008) Design of plates using finite element method. Bauman MSTU, Moscow, p 232
7. Sinelschikov AV (2016) Dynamics of floating crane VOLGAR in heavy sea Vest. ASTU 3:103–115
8. Song K (2000) Development of velocity transformation function of damped flat shell finite element for experimental spatial dynamics modeling: dissertation. <https://vtechworks.lib.vt.edu/bitstream/handle/10919/36091/192>
9. Liu GR (2003) Finite element method: practical course, p 384. <https://www.elsevier.com/books/finite-element-method/liu/978-0-7506-5866-9>

Vibration Isolation Properties of Vehicle Suspension at Optimal Instantaneous Damping Control in Oscillation Cycle



K. V. Chernyshov, A. V. Pozdeev and I. M. Ryabov

Abstract The article is dedicated to the study of anti-vibration properties of vehicle suspension at optimal instantaneous damping control in oscillation cycle. These suspensions in foreign literature are called “semi-active control suspensions.” However, its vibration isolation properties have not been thoroughly analyzed. This article presents ineffective damper zones in the oscillation cycle, mathematical models of vehicle suspension, and the results of theoretical and experimental study of vibration isolation properties of one- and two-mass oscillation systems simulating a suspension at optimal instantaneous damping control in the oscillation cycle. The results in the form of amplitude-frequency characteristics of sprung and unsprung masses displacement and accelerations, waveforms of resonant oscillations and elastic-damping characteristics of oscillation systems at resonance proved that optimal instantaneous damping control does not improve vibration isolation properties in response to shocks and noise in the suspension, thus setting a problem of searching and studying the ways of a smooth damping change in the oscillation cycle.

Keywords Vehicle suspension · Vibration isolation · Damping · Optimal control

1 Introduction

Some authors of this article [1–6] analyzed the suspension in operation without damping control in one-mass oscillation system (Fig. 1a).

The analysis particularly showed that oscillation cycles have two intervals (A and B, Fig. 1b), where the damping force is directed toward a sprung mass change increasing its kinetic energy and oscillation amplitudes. Such intervals were called damper ineffective zones. It was demonstrated that the cause of damper ineffective zones is α phase shift between sprung mass vibrations and relative

K. V. Chernyshov · A. V. Pozdeev (✉) · I. M. Ryabov
Volgograd State Technical University, 28, Lenin Ave., Volgograd 400005, Russia
e-mail: pozdeev.vstu@gmail.com

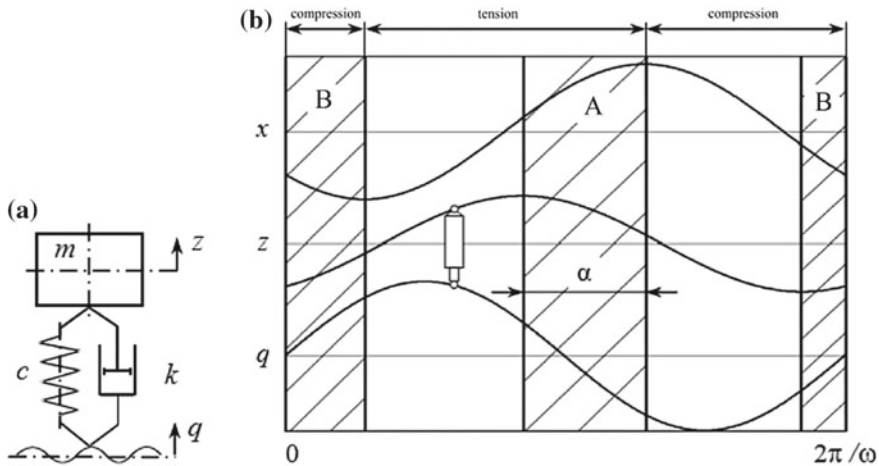


Fig. 1 a Design model of one-mass one-support vibration isolation system with fixed damping: m —sprung mass; c —stiffness of an elastic element (spring); k —damping factor; **b** waveform of an oscillation cycle of one-mass one-support vibration isolation system with constant damping: q —kinematic disturbance; z —displacement of a sprung mass; x —suspension deformation; A and B—ineffective damper zones; α —width of an ineffective damper zone

vibrations of a damper piston rod, depending on a relative damping coefficient ψ and disturbing frequency value ι :

$$\alpha = -\text{arctg}(2\psi\iota). \tag{1}$$

The performed energy analysis of the damper in oscillation cycle showed that in order to increase its energy efficiency and reduce oscillation amplitudes of the sprung weight, it is necessary to reduce damping in the zones of ineffective damping. In the latter case, damping control corresponds to “semi-active control suspension” principle suggested by Furunzhiev [7], Karnopp and Crosby [8, 9].

R. I. Furunzhiev, using the maximum principle developed by L. S. Pontryagin for the mathematical theory of optimal processes, showed on the example of two-mass vehicle model that in order to reduce oscillation amplitudes of a sprung weight, it is necessary to control damping which includes its instantaneous deactivation in oscillation cycle intervals, when change direction of the sprung and unsprung mass matches, and the absolute rate of an unsprung weight is greater than the rate of a sprung weight in a vertical direction, followed by instantaneous activation under changing these conditions for the opposite one.

A number of papers involving the authors of this article [10–21] are devoted to the study of vibration isolation properties of one-mass oscillation system at optimal instantaneous damping control in oscillation cycle, as well as to the design of controlled dampers. However, the received results have not been summarized and

analyzed. Moreover, vibration isolation properties of two-mass oscillation system at optimal instantaneous damping control have not been studied.

2 Investigation of Vibration Isolation Properties of One-Mass Oscillation System at Optimal Instantaneous Damping Control in Oscillation Cycle

The design model of one-mass single-support vibration isolation system with the controlled damper is provided in Fig. 2. The dynamics of such system with optimal instantaneous damping control are described by the following mathematical model:

$$m\ddot{z} + uk(\dot{z} - \dot{q}) + c(z - q) = 0 \tag{2}$$

where u —control parameter:

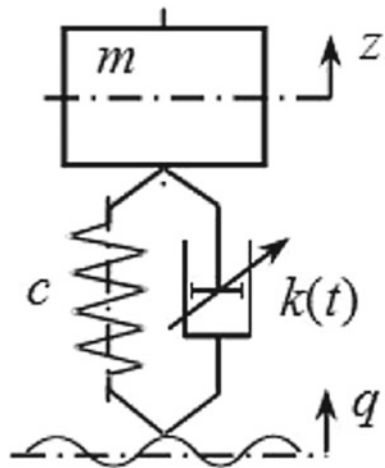
$$u = \begin{cases} u_{\max} = 1 & \text{at } (\dot{z} - \dot{q})\dot{z} > 0; \\ u_{\min} & \text{at } (\dot{z} - \dot{q})\dot{z} < 0, \end{cases} \tag{3}$$

Some results of studying this model are provided in the form of graphics in Figs. 3, 4, and 5.

The analysis results show that:

- damping change from the relative damping coefficient level $\psi_{\max} = \frac{u_{\max}k}{2\sqrt{mc}}$ onto the $\psi_{\min} = \frac{u_{\min}k}{2\sqrt{mc}}$ level in the ineffective damper zones leads to the decrease of amplitudes of sprung mass vertical changes, with the maximum effect at $\psi_{\min} = 0$ ($u_{\min} = 0$), i.e., at a complete damping deactivation;

Fig. 2 Design model of one-mass one-support vibration isolation system with controlled damping: m —sprung mass; c —stiffness of elastic element (spring); k —variable damping factor



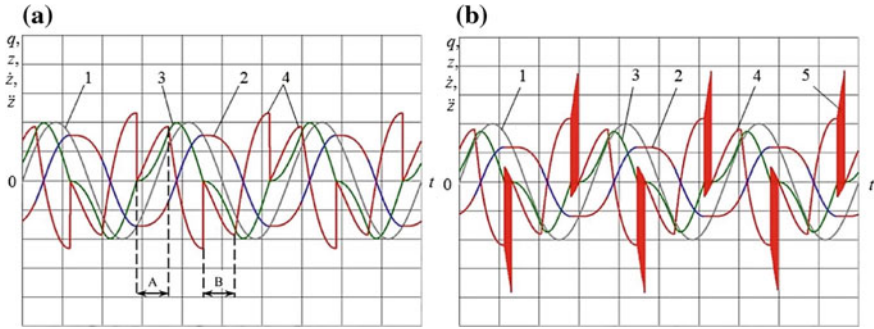


Fig. 3 Waveform of resonant oscillations in one-mass oscillation system **a** with the optimal damping control and **b** with the overcontrol of damping: 1—displacement of disturbing base q ; 2, 3, and 4—displacement z , velocity \dot{z} , and acceleration \ddot{z} of the sprung mass; 5—areas of the overcontrol; A and B—zones of the damper switching off

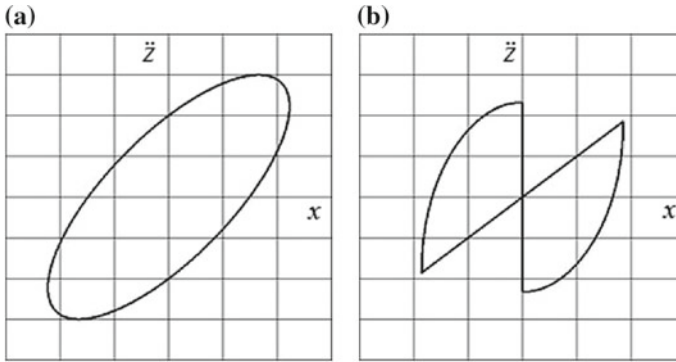


Fig. 4 Elastic-damping characteristics (diagrams) of one-mass oscillation system at a resonance: **a** without the damping control at $\psi = 0.45$; **b** with the optimal damping control at the resonant frequency ($t = 1$)

- the beginning of ineffective zone and consequently damping deactivation moment with optimal control matches with the moment when the sprung mass reaches the extreme upper or extreme lower position ($\dot{z}(t) = 0$), and the end of ineffective zone and the moment of damping activation—with the moment of nulling the suspension deformation rate ($\dot{z}(t) - \dot{q}(t) = 0$);
- at the instantaneous damping deactivation in the moment of reaching an ineffective zone, the function of vertical accelerations for the sprung mass $\ddot{z}(t)$ undergoes simple discontinuities, and when damping is activated in the moment of leaving this zone, the function has a break;
- minimum amplitudes of the sprung mass changes (Fig. 3a) are achieved at instantaneous damping deactivation in the zones of ineffective damping, with a minimum minimorum achieved at zero acceleration $\ddot{z}(t) = 0$ as a result of

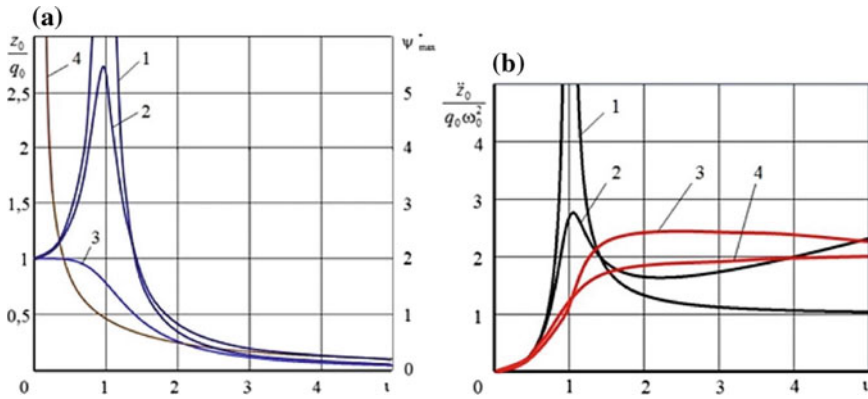


Fig. 5 **a** Characteristics of one-mass oscillation system at harmonic kinematic disturbance: 1, 2, 3 —amplitude-frequency characteristics of displacements of systems: without damping, with constant damping, with the optimal damping control, respectively; 4—function $\psi_{max}^*(t)$ at the optimal damping control; **b** amplitude-frequency characteristics of accelerations of systems: 1—without damping; 2—with constant damping; 3—with damping, variable according to the law 4 (a) without optimal control; 4—with an optimal damping control

damping deactivation (this condition, in particular, defines an optimal damping control at instantaneous deactivation);

- zero vertical acceleration of a sprung mass $\ddot{z}(t) = 0$ in the result of damping deactivation is achieved at a definite (optimal) value of the maximum damping level with a specified disturbing frequency $\psi_{max}^*(t) = \frac{u_{max}^*k}{2\sqrt{mc}}$ (for example, at the resonance disturbing frequency (Fig. 3a) $\psi_{max}^* \approx 0.92$);
- an exceeding maximum level of damping $\psi_{max} > \psi_{max}^*(t)$ causes an overcontrol (Fig. 3b), leading to an abrupt change of vertical accelerations of the sprung mass (dark areas on Fig. 3b);
- introduction of an optimal damping control significantly reduces the heat generation determined by the size of the flowchart area (Fig. 4), which is associated with both a decrease in the amplitudes of suspension deformations and the lack of inefficient damping.

Moreover, using matching of piecewise linear functions, we got an amplitude-frequency characteristic of the sprung mass in one-mass oscillation system at the optimal instantaneous control provided in Fig. 5a (curve 3) and obtained at the optimal dependence $\psi_{max}^*(t)$ (curve 4). This characteristic defines potential opportunities of such method of control in one-mass oscillation system. Figure 5a shows amplitude-frequency characteristics without damping (curve 1), as well as with constant damping (curve 2).

Figure 5b provides amplitude-frequency characteristics of system accelerations without damping (curve 1), with constant damping (curve 2), with damping changed by $\psi_{max}^*(t)$ (curve 3), and with an optimal damping change (curve 4).



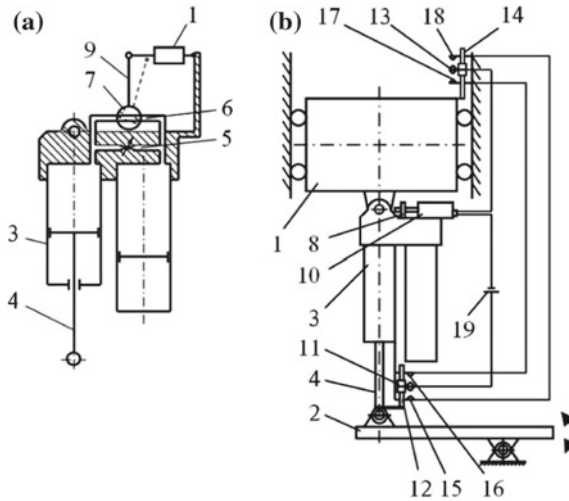


Fig. 6 **a** Scheme of experimental hydro-pneumatic spring with a solenoid valve for damping control in oscillation cycle and; **b** scheme of unit for its testing: 1—sprung mass; 2—disturbing base; 3—hydro-pneumatic spring; 4—rod of a spring; 5—main throttle channel; 6—additional throttle channel; 7—slide valve; 8—axis; 9—lever; 10—electromagnet; 11—contact movable relative to a rod 12; 13—contact movable relative to a rod 14; 15, 16, 17, 18—contacts; 19—source of power

According to the studies, the maximum values of changes of the sprung mass at the optimal damping control are significantly reduced in the entire frequency range (Fig. 5a). However, the value of the sprung mass maximum acceleration is significantly lower only in the resonance zone (Fig. 5b).

Experimental verification of the optimal instantaneous damping control was carried out by the authors on an experimental hydro-pneumatic spring, where damping was controlled by a high-speed solenoid valve (Fig. 6a).

Experimental model based on a test bench for pneumatic tires and elastic vehicle elements [20, 21] with an electrical control circuit with a solenoid valve is shown in Fig. 6b.

Experimental verification of the optimal instantaneous damping control in the resonance zone showed that such control provides a significant decrease in the amplitude of oscillations of the sprung mass (less than the amplitude of the kinematic disturbance), corresponding to the results of a mathematical model study.

However, the participants of this experiment noted the presence of shocks and noise in the suspension in the process of damping change.

3 Investigation of Vibration Isolation Properties of Two-Mass Oscillation System at Optimal Instantaneous Damping Control in Oscillation Cycle

Let us consider the principle of the optimal damping control with instantaneous switching in two-mass oscillation system (Fig. 7a).

A mathematical model of two-mass oscillation system with an optimal instantaneous damping deactivation can be represented as follows:

$$\begin{cases} m_1 \ddot{z}_1 + uk(\dot{z}_1 - \dot{z}_2) + c_1(z_1 - z_2) = 0; \\ m_2 \ddot{z}_2 + c_2(z_2 - q) - uk(\dot{z}_1 - \dot{z}_2) - c_1(z_1 - z_2) = 0, \end{cases} \quad (4)$$

where u —control parameter:

$$u = \begin{cases} 1 & \text{at } (\dot{z}_1 - \dot{z}_2) \dot{z}_1 > 0; \\ 0 & \text{at } (\dot{z}_1 - \dot{z}_2) \dot{z}_1 < 0. \end{cases} \quad (5)$$

The graphs obtained in the process of studying this model are shown in Figs. 7b, 8, and 9.

The analysis of this model shows that the use of optimal instantaneous damping change in two-mass oscillation system leads to a significant decrease in the amplitudes of the sprung mass changes (Fig. 9a, curve 1), but causes a significant

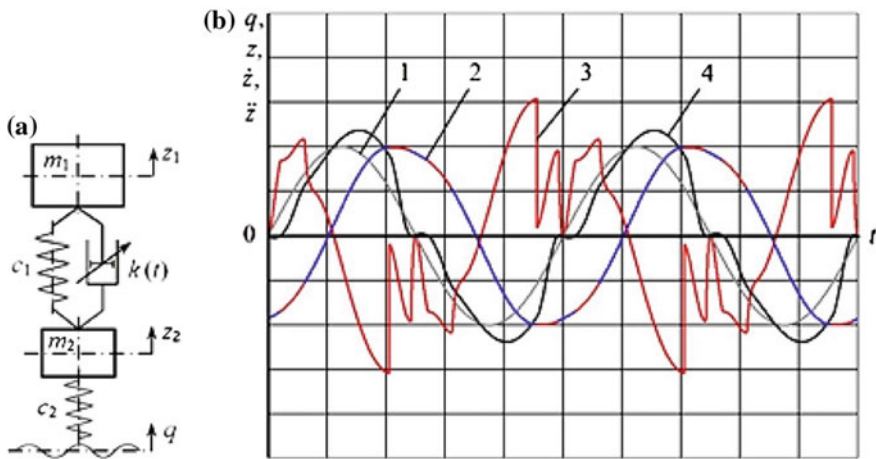


Fig. 7 a Scheme of two-mass one-support vibration isolation system with damping control: m_1 —sprung mass; m_2 —unsprung mass; c_1 —stiffness of an elastic element (spring); $k(t)$ —damping factor; c_2 —stiffness of a tire; q —kinematic disturbance; z_1 —displacement of the sprung mass; z_2 —displacement of the unsprung mass; **b** waveform of resonant oscillations in two-mass oscillation system with the optimal damping control: 1—displacement of a disturbing base q ; 2 and 3—displacement z_1 and acceleration \ddot{z}_1 of the sprung mass; 4—displacement z_2 of the unsprung mass

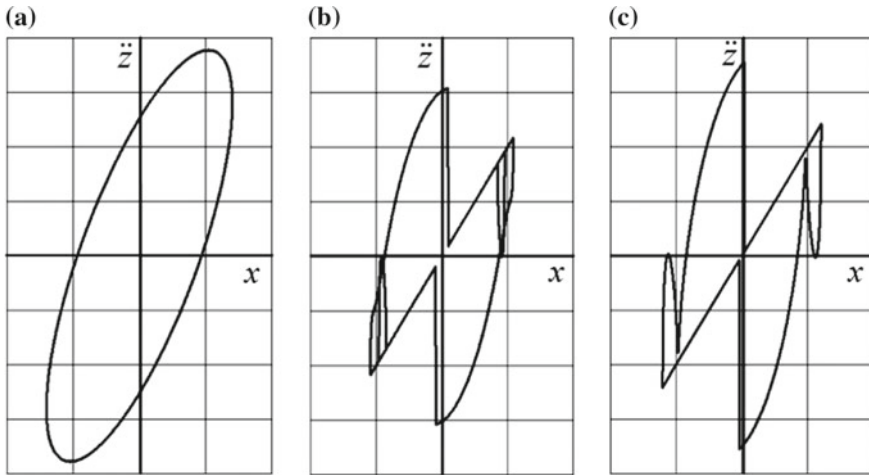


Fig. 8 Elastic-damping characteristics (diagrams) of two-mass oscillation system at the resonance: **a** without the damping control with $\psi = 0.45$ at the resonance; **b** with the optimal damping control at the resonant frequency ($\iota = 1$); **c** with the optimal damping control at a relative frequency of disturbance $\iota = 1.5$

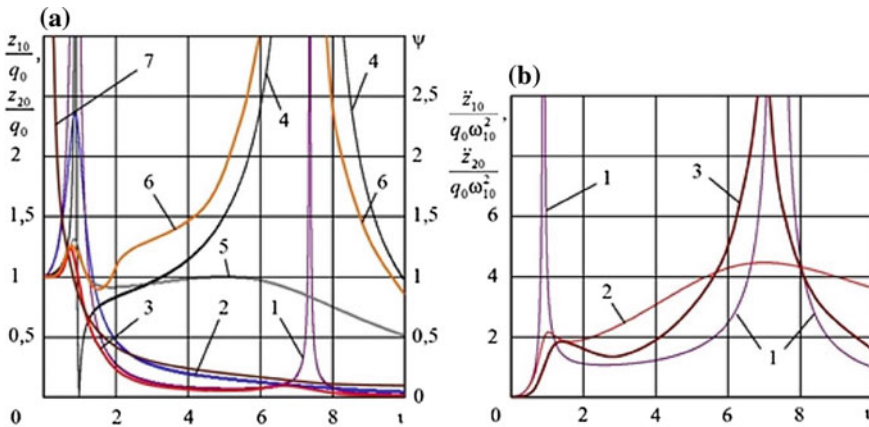


Fig. 9 a Characteristics of two-mass oscillation system at harmonic kinematic disturbance: 1, 2, 3 —amplitude-frequency characteristics of sprung mass displacement of systems: without damping, with constant damping, with the optimal damping control, respectively; 4, 5, 6—amplitude-frequency characteristics of the unsprung mass displacement of systems: without damping, with constant damping, with the optimal damping control, respectively; 7—function $\psi^*_{\max}(\iota)$ at the optimal damping control; **b** amplitude-frequency characteristics of the sprung mass accelerations in two-mass oscillation system: 1—without damping; 2—with constant damping; 3—with the optimal damping control

increase in wheel oscillations (Fig. 9a, curve 2) and significant increase in the acceleration of the sprung mass in the region of the second resonance (Fig. 9b, curve 3), and makes the acceleration change more complex (Fig. 7b), due to the

response of both the sprung and unsprung masses to the instantaneous changes of the damping level, resulting in elastic-damping characteristics of such a system having the shape of a butterfly with clipped wings (Fig. 8).

4 Conclusions

- Optimal instantaneous damping control provides a significant reduction in the amplitudes of the vertical changes of the sprung mass, and, consequently, heat generation in the dampers; however, a significant decrease in the amplitudes of the vertical accelerations occurs in a narrow range of resonant frequencies of the sprung mass.
- To achieve the greatest effect, it is necessary to change the maximum value of the inelastic resistance depending on the oscillation frequency, avoiding overcontrol. The last requirement cannot be fulfilled in practice since the road defines a disturbance spectrum containing many harmonics with different amplitudes and frequencies. Therefore, when driving a car with instantaneous damping change, there will inevitably be a damping overcontrol, leading to additional shocks and shocks in the suspension.
- The use of the optimal instantaneous damping control in two-mass oscillation system determines the complex nature of changes in the vertical accelerations of the sprung mass, which does not contribute to an increase in smoothness.
- A significant decrease in the smoothness of oscillations of the sprung mass was noted when conducting experimental studies of the principle of the optimal instantaneous damping control.

Thus, the optimal instantaneous damping control in the vehicle's suspension provides an increase in vibration isolation properties only in a narrow zone of the resonance of the sprung mass. This circumstance, as well as the presence of shocks and noise in the suspension, associated with instantaneous damping change, sets the problem of finding and studying ways to smoothly change the damping in the oscillation cycle, which ensures high vibration isolation properties of the suspension throughout the entire range of its operating frequencies.

References

1. Ryabov IM et al (1995) KPD amortizatora transportnogo sredstva pri rezonanse (Efficiency factor of vehicle damper at resonance). *EHffektivnost' ehkspluatacii transporta: Mezhvuzovskij nauchnyj sbornik*, Saratov State Technical University, Saratov, pp 81–86
2. Ryabov IM et al (1997) Issledovanie ciklovogo sposobu regulirovaniya neuprugogo soprotivleniya podveski ATS (The study of cyclic control method of inelastic resistance of vehicle suspension). *EHkspluataciya sovremennogo transporta: Mezhvuzovskij nauchnyj sbornik*, Saratov State Technical University, Saratov, pp 96–102

3. Ryabov IM et al (1998) Raspređenje energije v ciklu kolebanij podveski ATS (The distribution of energy in the oscillation cycle of vehicle suspension). *Spravochnik. Inzhenernyj zhurnal* 4:31–33
4. Ryabov IM et al (1998) Novyj sposob gasheniya kolebanij (A new way of oscillation damping). *Motauto'98: Proceeding, Union of mechanical engineering and etc. Sofia* 3:153–156
5. Ryabov IM, Chernyshov KV, Pozdeev AV (2016) Energy analysis of vehicle suspension oscillation cycle. *Procedia Eng* 150:384–392. <https://doi.org/10.1016/j.proeng.2016.06.730>. In: Radionov AA (ed) 2nd international conference on industrial engineering (ICIE-2016), Elsevier Publishing
6. Ryabov IM, Novikov VV, Pozdeev AV (2016) Efficiency of shock absorber in vehicle suspension. *Procedia Eng* 150:354–362. <https://doi.org/10.1016/j.proeng.2016.06.721>. In: Radionov AA (ed) 2nd international conference on industrial engineering (ICIE-2016), Elsevier Publishing
7. Furunzhiev RI (1965) Investigation of some questions of vehicle oscillation damping. Dissertation of Candidate of Technical Science, Minsk
8. Crosby MJ, Karnopp DC (1973) The active damper—a new concept for shock and vibration control. 43rd shock and vibration bulletin, Part H, June 1973, pp 46–73
9. Karnopp DC, Crosby MJ, Harwood RA (1974) Vibration control using semi-active force generators. *Trans ASME J Eng Ind* 96:619–626
10. Ryabov IM, Novikov VV (1999) Amortizator (Shock absorber), RUS Patent 2,142,585, Dec 1999
11. Ryabov IM, Novikov VV (1999) Amortizator (Shock absorber), RUS Patent 2,142,586, Dec 1999
12. Novikov VV, Ryabov IM (2004) Pnevmo gidravlicheskie resory podvesok avtotransportnyh sredstv (Hydropneumatic springs of motor vehicles suspensions). Volgograd State Technical University, Volgograd, 311 p
13. Chernyshov KV, Novikov VV, Ryabov IM (2006) Optimal'noe upravlenie dempfirovaniem podveski na osnove principa maksimuma (Optimal control of suspension damping on the basis of maximum principle). *Traktory i sel'hozmashiny* 2:13–15
14. Novikov VV, Ryabov IM, Chernyshov KV (2009) Vibrozashchitnye svoystva podvesok avtotransportnyh sredstv (The vibration isolation properties of the motor vehicles suspensions). Volgograd State Technical University, Volgograd, 338 p
15. Diakov AS, Pozdeev AV, Pokhlebin AV (2011) Optimal'noe upravlenie zhyostkost'yu i dempfirovaniem podveski ATS na osnove principa maksimuma L.S. Pontryagina (Optimal damping and stiffness control of vehicle suspension based on the maximum principle of L.S. Pontryagin). *Vestnik Akademii voennyh nauk* 2(special edition):132–139
16. Pozdeev AV et al (2011) Sintez algoritmov optimal'nogo upravleniya dempfirovaniem i zhyostkost'yu podveski ATS (Design of algorithms for the optimal control of damping and stiffness of vehicle suspension). *Gruzovik* 6:2–6
17. Dyakov AS et al (2011) Pnevmo gidravlicheskaya resora bystrohodnoj gusenichnoj mashiny (Hydropneumatic spring of high-speed tracked vehicle). *Vestnik Akademii voennyh nauk* 2 (special issue):125–132
18. Pozdeev AV et al (2013) Reguliruemye pnevmaticheskie i pnevmogidravlicheskie resory podvesok avtotransportnyh sredstv (Controlled air and air-hydraulic springs of vehicle suspensions). Volgograd State Technical University, Volgograd, 244 p
19. Chernyshov KV, Khripkov MY (2016) Obzor osnovnyh algoritmov regulirovaniya dempfirovaniya v podveske avtomobilya (Overview of damping control algorithms in vehicle suspension) *Simvol nauki* 4–3:140–144
20. Novikov VV et al (2013) Stendy dlya ispytaniya podvesok nazemnyh transportnyh sredstv (Rigs for testing of suspensions of land vehicles). Volgograd State Technical University, Volgograd, 114 p
21. Novikov VV, Pozdeev AV, Diyakov AS (2015) Research and testing complex for analysis of vehicle suspension units. *Procedia Eng* 129:465–470. <https://doi.org/10.1016/j.proeng.2015.12.153>. In: Radionov AA (ed) International conference on industrial engineering (ICIE-2015), Elsevier Publishing

Monitoring Engine Toxicity Parameters and Selective Control of Its System Operation



A. V. Gritsenko, Z. V. Almetova and V. V. Rudnev

Abstract The change in the technical condition of internal combustion engines in operating such systems as the feed system, ignition system, cylinder-piston group, and intake and exhaust system leads to the deterioration of the combustion process, the growth of toxic components and, as a consequence, the acceleration of the catalyst resource exhaustion. Accordingly, a catalyst failure will lead to a non-compliance of the vehicle's emission standard with the applicable EURO standards, the subsequent replacement of which will not change the situation. It will be necessary to replace some system elements to eliminate the root causes of the catalyst failure. In this regard, when operating ICEs, it is vital to develop ways to control the time history of the concentration of toxic components of CO, CH, CO₂, and O₂ in exhaust gases. It is possible when portable gas analyzers built into the exhaust system are used. The operation of the portable gas analyzer can be organized discretely, in the form of test modes for monitoring the toxicity parameters, for example, at idle speed, in the acceleration mode, in constant power and load conditions, when individual engine cylinders operate selectively. In this study, the cylinders are completely or partially deactivated by the developed portable device—gasoline engine loader. Considering a high selectivity of the load impact on individual cylinders and its significant variation, the catalyst failure can be prevented, including due to the adaptability of the actuating elements to the change in the technical condition of separate unit.

Keywords Engine · Diagnosis · Crankshaft speed · Toxicity · Catalyst converter · Fuel efficiency

A. V. Gritsenko · Z. V. Almetova (✉)
South Ural State University (NRU), 76, Lenin Avenue, Chelyabinsk 454080, Russia
e-mail: almetovazv@susu.ru

V. V. Rudnev
South Ural State Humanitarian-Pedagogical University (CSPU), 69, Lenin Avenue,
Chelyabinsk 454080, Russia

1 Introduction

Motor transport occupies the leading positions in the cargo turnover and passenger turnover among other modes of transport: cargo turnover occupies 68%, passenger turnover—72%. According to the statistics, over the recent decade, the car fleet on the territory of the Russian Federation has increased by 50% [1, 2]. Chelyabinsk is included in top ten regional centers with the largest car fleet (about 323 thousand units). The same list includes: Yekaterinburg, Novosibirsk, Samara, Kazan, Nizhny Novgorod, Omsk, Krasnodar, Rostov-on-Don, and Voronezh.

Naturally, this fact cannot but affect the ecological situation of the city, the region and the country in general. At present, the issue of environmental friendliness of motor transport is one of the main ones. Modern requirements to the emission standard of vehicles require: For the manufacturer on the RF territory, it is permitted to manufacture cars of no less than EURO-5 class, in the leading countries—of no less than EURO-6 standards, which force modern cars to reduce the CO values in 2.7 times, CH—in 2 times, NO_x—in 3 times. All these factors affect the ecological state of the atmosphere, water, and soil. Annually, the world economy emits 350 million tons of carbon monoxide, more than 50 million tons of various hydrocarbons, 150 million tons of sulfur dioxide. Carbon dioxide is accumulated, and the amount of oxygen decreases in the atmosphere [3–5].

Thus, the environmental requirements to the vehicle and its engine are nowadays priority ones. The ecological cleanness of exhaust gases (EG) is laid in the structure of the engine and the vehicle in general in the course of its design, and when the vehicle is operated, the predicted toxicity characteristic should be at a stable level without any changes, which is difficult to observe under the influence of external unrecognized factors [6–9].

The purpose of the research: to develop a method for diagnosing internal combustion engines by the exhaust toxicity parameters in test modes. Research objectives:

- analysis of the methods and measures to reduce toxic emissions;
- analysis of the theoretical studies on the establishment of relationships between the technical condition of the ICE systems and the ICE toxicity parameters;
- establishment of relationships between the number of dead cylinders and individual cycles and the power, torque, and exhaust toxicity parameters;
- development of a procedure for studying the exhaust toxicity parameters in varying loading modes;
- conducting of experimental studies and establishment of the relationship between the loading modes and toxicity parameters when the technical condition of the ICE systems changes;
- economic assessment of the development of the ICE diagnostic method by the exhaust toxicity in test modes.

Research hypothesis: any change in the technical condition of the ICE systems leads to an increase in the exhaust toxicity. When all the ICE cylinders operate

simultaneously, it is impossible to diagnose each cylinder. The application of the test loading method by a full or partial cutout of the ICE cylinders makes it possible to determine the contribution to the overall toxicity of each of the cylinders. Research object: the process of exhaust gas emission during the test loading of the ICE cylinders. Research subject: the relationship between the degree of the cylinders and cycles cutout with the exhaust toxicity parameters.

2 Theoretical Research

There are various methods of diagnostic troubleshooting and ways of reducing the exhaust toxicity [10–13]. The following measures were considered in order to achieve minimum exhaust emissions: improvement of the quality of parts manufacturing, use of alternative fuels and additives, recirculation of exhaust gases, development of low-toxic work processes, thermal neutralization of exhaust gas, liquid neutralization of exhaust gas, catalytic neutralization of exhaust gas, and cutout of several cylinders and cycles [14, 15].

The exhaust purification degree is determined by [16, 17]:

$$\delta = 1 - \exp\left(-\frac{0.41 \cdot a \cdot l}{\text{Re}_n^{0.25}}\right) \quad (1)$$

where δ —exhaust purification degree; a —specific surface area of the catalyst pellets, m^2/g ; l —thickness of the catalyst layer, m ; Re_n —effective Reynolds number.

The pressure drop on the catalyst layer (xP_{cl}) will be [16, 17]:

$$\Delta P_{cl} = \frac{G^2}{F^2 \rho} \cdot \frac{a \cdot l}{2\varepsilon^2} f_r \quad (2)$$

where G —exhaust mass flux, kg/s ; F —area of the reactor, m^2 ; ρ —density, kg/m^3 ; ε —porosity of the catalyst layer; f_r —resistance coefficient.

The resistance coefficient (f_r) can be found from the expression in [16, 17]:

$$f_r = \frac{36.4}{\text{Re}_n} + 0.45 \quad (3)$$

The effective Reynolds number will be [16, 17]:

$$\text{Re}_n = \frac{4G}{F\mu \cdot a} \quad (4)$$

where μ —dynamic gas viscosity, Pa s .

As an example, let us consider the influence of the unsatisfactory technical condition of the exhaust system (increased resistance in the exhaust path) on the ICE power by the parameter of reducing the ICE crankshaft speed [18, 19]:

$$n_{N1} = n_{A1} \pm \Delta n_{A1} \quad (5)$$

where n_{N1} —crankshaft speed of a serviceable ICE (table value), min^{-1} ; n_{A1} —actual value of the crankshaft speed of an unserviceable ICE, min^{-1} ; $\pm\Delta n_{A1}$ —increase or decrease of the ICE crankshaft speed connected with a failure of the exhaust system, min^{-1} .

It is clear from the presented “(5)” that the actual value of the ICE crankshaft speed n_{A1} during diagnosis differs from the table value n_{N1} by the value Δn_{A1} . The value $\pm\Delta n_{A1}$ depends on the technical condition of the exhaust system elements. If the exhaust system elements are serviceable, $n_{N1} = n_{A1}$, which will be $n_{A1}/n_{N1} = 1$ from “(5).” If the exhaust system is unserviceable, $n_{A1}/n_{N1} \neq 1$, and the value of the actual ICE power will differ from the value of the serviceable (reference) ICE power [18–20].

3 Research Methods

The following hardware and software were developed for carrying out the experimental studies: gasoline engine loader, software with an operation interface, a set of artificial resistances, and a holder of the throttle valve in a fixed position. In addition, ZMZ-406 engine specially prepared for the complex studies was used to implement the experimental part. The following failures were set on it according to the simulated algorithms: Ultimate and intermediate values of the cylinder and electromagnetic injectors wear parameters. Thus, the cylinder wear parameters measured by the K-69M air tester are summarized in Table 1, where $U2$ is the air leakage when the piston is at the top dead center (end of the compression stroke); $U1$ is the air leakage when the piston is in the beginning of the compression stroke. It is clear from the data presented in Table 1 that the ultimate value ΔU of the cylinder wear is observed in the 1st and 3rd cylinder, the value of the piston rings and valves wear is observed in the 1st, 2nd, and 3rd cylinder. In the course of the

Table 1 Cylinder wear parameters measured by the K-69M air tester

Indicators	Number of cylinders			
	1 (%)	2 (%)	3 (%)	4 (%)
$U2$	32	22	29	14
$U1$	24	18	20	11
ΔU	8	4	9	3

Table 2 Injector spillage parameters measured on the Forsage stand

Indicators	Number of cylinders			
	1	2	3	4
Capacity (%)	0	-3	-6	+6

complex studies, we installed electromagnetic injectors with the ultimate values of the spillage parameters measured on the Forsage stand (Table 2).

An injector with a reference capacity value was installed in the 1st cylinder (Fig. 1b), the injectors with a feed rate lowered by 3 and 6%, respectively, were installed in the 2nd and 3rd cylinder, and a feed rate maximally increased by +6% was simulated in the 4th cylinder.

We developed the tables of experimental data for resistances $d = 50$ mm, $d = 23$ mm, $d = 15$ mm. The following engine crankshaft speed values were chosen as loading modes:

- all the 4 cylinders are in operation at 880, 1000, 2000, 3000, 4000, 5000 min^{-1} ;
- one cylinder is in operation at 1500, 2000, 2500, 3000, 3500, 3700 min^{-1} ;
- the cycles are partially cut out in one operating cylinder at the ratio from 1 out of 10 to 9 out of 10 [19].

Askon 02.00 gas analyzer was used to measure the exhaust toxicity parameters of CO, CH, CO₂, and O₂, when experimental conditions and resistances were set in the exhaust system.

4 Results of the Experimental Studies

At the first stage, we conducted experimental studies to determine the dependence of the change in the CO concentration (%) in the exhaust gas at the varying ICE crankshaft speed (Fig. 1a). The results of the studies are represented by 5 curves of the dependence with the following options:

- all the cylinders operate simultaneously;
- only the 1st cylinder is used in operation;
- only the 2nd cylinder is in operation;
- only the 3rd cylinder is in operation;
- only the 4th cylinder is in operation [21].

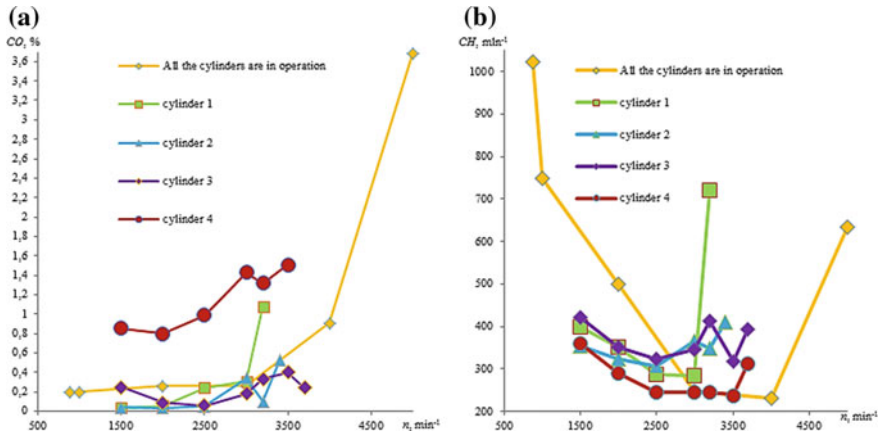


Fig. 1 Diagram of the dependence of the change **a** in the CO concentration (%) in the exhaust gas at the varying ICE crankshaft speed n (min⁻¹); **b** in the CH concentration (min⁻¹) in the exhaust gas at the varying ICE crankshaft speed n (min⁻¹)

It is seen from the data presented in Fig. 1a that there is a sharp difference in the CO concentration when the 4th cylinder is in operation. The installation of the injector with a fuel feed increased by +6% has a prevailing influence on the growth of the CO values in this cylinder, which leads to a significant over-enrichment of the fuel-air mixture (FAM). In this case, the smallest wear of the cylinder-piston group (CPG) is simulated in the 4th cylinder—the charge leakage from the cylinder is 14%. Besides, the growth of CO during the operation of the 1st cylinder stands out from the general trend, which is especially noticeable with an increase in the ICE crankshaft speed of over 3000 min⁻¹. This growth is explained by the extreme wear of the CPG of this cylinder.

Figure 1b shows the relationship between the change in the CH concentration (min⁻¹) in the exhaust gas at the varying ICE crankshaft speed n (min⁻¹). It can be seen from Fig. 1b that the values of the CH concentration at a simultaneous operation of all the four cylinders take a very significant value—more than 1000 min⁻¹. It is explained by a significant wear of individual cylinders in the CPG: 1st—32%; 2nd—22%; 3rd—29%; and 4th—14%. The emphasis should be put on the first cylinder with the maximum wear of the CPG. At a point corresponding to 3000 min⁻¹, the CH concentration sharply increases and reaches the value of over 700 min⁻¹ at 3200 min⁻¹. It can be explained by the growth of charge leakages at an increasing degree of cylinder loading (deformation of the piston rings at an increasing pressure of piston gases).

Figure 2a represents the dependence of the change in the CO₂ concentration (%) in the exhaust gas at the varying ICE crankshaft speed.

As it can be seen from Fig. 2a, the values of the CO₂ concentration have an average trend of about 13% for all the four cylinders. At the same time, the CO₂

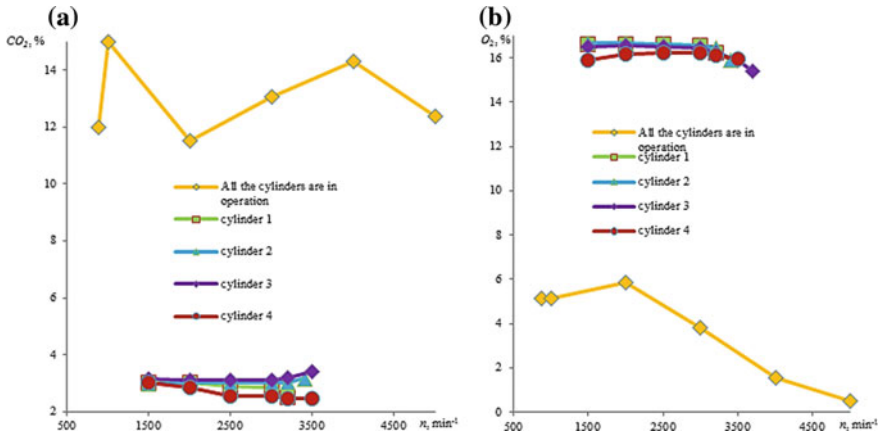


Fig. 2 Diagram of the dependence of the change **a** in the CO₂ concentration (%) in the exhaust gas at the varying ICE crankshaft speed n (min⁻¹); **b** in the O₂ concentration (%) in the exhaust gas at the varying ICE crankshaft speed n (min⁻¹)

concentration takes the value of slightly above 3% for the 2nd and 3rd cylinders (both injectors of the 2nd and 3rd cylinders provide a lean FAM, since their capacity is reduced by -3 and -6%).

Figure 2b represents the dependence of the change in the O₂ concentration (%) in the exhaust gas at the varying ICE crankshaft speed.

When all the four cylinders are in operation, the value of the O₂ concentration reaches the maximum at 2000 min⁻¹ (6%) and tends to the minimum with an increase in the ICE crankshaft speed (Fig. 2b). The diagrams of separate cylinders have an analogous concentration downward tendency with an increase in the ICE crankshaft speed. However, it is clearly seen that when working on a lean FAM, the O₂ concentration is higher for the 2nd and 3rd cylinders than for the 1st and 4th cylinders, which confirms the performance efficiency of the λ -probe, which provides feedback for the O₂ concentration.

5 Conclusions

When studying the change in the CO concentration in the exhaust gas at the varying ICE crankshaft speed by individual cylinders, it has been established that the largest excess of the CO concentration is registered when the 4th cylinder operates on the maximally over-enriched FAM (+6% increased capacity, which is 400% of the nominal value, i.e., 0.8% relative to 0.2%).

When studying the change in the dependence of the CH concentration in the exhaust gas at the varying ICE crankshaft speed by individual cylinders, it has been established that the largest gain in the CH concentration occurs when the 1st

cylinder is in operation, which CPG is worn at the maximum value of 32%. The CH concentration increases to 700 min^{-1} at the point corresponding to 3000 min^{-1} , which is over 3 times more than the nominal value.

When studying the change in the dependence of the CO_2 concentration in the exhaust gas at the varying ICE crankshaft speed by individual cylinders, it has been established that when the 2nd and 3rd cylinders with the injectors of a decreased capacity (-3 and -6%) are in operation, the value of CO_2 is over 3%, which is over 2 times more than the nominal value.

When studying the change in the dependence of the O_2 concentration in the exhaust gas at the varying ICE crankshaft speed by individual cylinders, it has been established that when the 2nd and 3rd cylinders with the injectors of a decreased capacity (-3 and -6%) are in operation, the concentration of O_2 exceeds the nominal value by 0.8–1%.

6 Practical Relevance

We developed hardware and software for carrying out the experimental studies: a circuit breaker for electromagnetic injectors; a software module with an operation interface that allows us to partially cut out the cycles of any operating cylinder at the ratio from 1 out of 10 to 9 out of 10; a holder of the throttle valve in a fixed position, which allows us to stabilize the ICE operation at any crankshaft speed.

7 Recommendations

The studies show that a change in the technical condition of the ICE in operating such systems as the feed system, the ignition system, the cylinder-piston group, the inlet and outlet system leads to the deterioration of the combustion process, the growth of toxic components and, as a consequence, to the acceleration of the catalyst resource exhaustion. Accordingly, a catalyst failure will lead to a non-compliance of the vehicle's emission standard with the applicable EURO standards, and the subsequent replacement of the failed element will not change the situation. It will be necessary to replace some system elements to eliminate the root causes of the catalyst failure. In this regard, when operating ICES, it is vital to develop ways to control the time history of the concentration of toxic components of CO, CH, CO_2 , and O_2 in exhaust gases, which is possible when portable gas analyzers built into the exhaust system are used. The operation of the portable gas analyzer can be organized discretely, in the form of test modes for monitoring the toxicity parameters, for example, at idle speed, in the acceleration mode, in constant power and load conditions, when individual engine cylinders operate selectively.

Acknowledgements The work was supported by Act 211 Government of the Russian Federation, contract № 02.A03.21.0011.

References

1. Khan MI, Yasmeen T, Muhammad M (2016) Research progress in the development of natural gas as fuel for road vehicles. *Renew Sustain Energy Rev* 66:702–741
2. Berdov EI, Fedoseev SYu (2015) Cutout of some engine cylinders as a way to improve the fuel and economic indicators of the tractor-transport unit. *Agric Ind Complex Russ* 72(2): 20–24
3. Karavalakis G, Short D, Russell RL et al (2014) Assessing the impacts of ethanol and isobutanol on gaseous and particulate emissions from flexible fuel vehicles. *Environ Sci Technol* 48(23):14016–14024
4. Gurgenci H, Aminossadati SM (2009) Investigating the use of methane as diesel fuel in off-road haul road truck operations. *J Energy Resour Technol* 131(3)
5. Stein RA, Anderson JE, Wallington TJ (2013) An overview of the effects of ethanol-gasoline blends on SI engine performance, fuel efficiency, and emissions. *SAE Int J Eng* 6(1):470–487
6. Gonçalves M, Jiménez-Guerrero P, Baldasano JM (2009) Emissions variation in urban areas resulting from the introduction of natural gas vehicles: application to Barcelona and Madrid greater areas (Spain). *Sci Total Environ* 407(10):3269–3281
7. Milkins EE, Allen RG, Edsell VD (1990) Gaseous fuel injection system for the operation of heavy duty engines on natural gas. In: Society of automotive engineers, eighteenth Fisita congress—the promise of new technology in the automotive industry, Torino, Italy, 7 May 1990
8. Pasechnik DV (2004) Gas fuel supply system for injection engines ZMZ. *J Autom Ind* 5: 12–15
9. Gaidar SM, Svechnikov VN, Usmanov AYu et al (2013) Improving the engine performance characteristics based on the use of nanotechnologies. *Proc GISNITI* 111:4–8
10. Eck C, Konigorski U, Cianflone F et al (2011) Fault detection system for the air path of common rail diesel engines with low pressure EGR. *SAE Technical Papers, World Congress and Exhibition, Detroit, MI; United States; 12 Apr 2011*
11. Kimmich F, Isermann R (2002) Model based fault detection for the injection, combustion and engine-transmission. *IFAC Proc* 15(1):203–208
12. Hajari SC (1996) Diagnosis and repair of excessively emitting vehicles. *J Air Waste Man Assoc* 46(10):940–952
13. Gumus M, Ugurlu A (2011) Application of phase change materials to pre-heating of evaporator and pressure regulator of a gaseous sequential injection system. *Appl Energy* 88 (12):4803–4810
14. Grebennikov AS (2002) Diagnosis of car-and-tractor engines by the intra-cycle changes in the crankshaft angular speed. Dissertation, University of Saratov
15. Ivanov RV (2010) ICE diagnosis by the parameter of the mechanical loss power. Dissertation, University of Volgograd
16. Leshakov IA, Kravchenko IN, Erofeev MN (2013) Mathematical model for calculating the basic parameters of catalyst converters. *Mod Sci-Intensive Technol* 5:76–80
17. Isaenko PV, Isaenko VD (2006) To the calculation of the hydraulic resistance of the neutralizer-purifier for exhaust systems of vehicles of the motor transport complex. *Bul. of Tomsk State University of Architecture and Const. Tomsk* 1:95–106
18. Gritsenko AV, Kukov SS, Tsyganov KA et al (2011) A method for diagnosing the exhaust path of the reciprocating internal combustion engine. *RUG01M* 15/04, 2011139288, 26 Sept 2011

19. Isaenko VD, Isaenko AV, Isaenko PV (2007) Fundamentals of the reliability theory and car diagnostics. Teaching guide. Federal Agency for Education, State Educational Institution of Professional Education Tomsk State University of Architecture and Construction, Tomsk
20. Patrakhaltsev NN, Strashnov SV, Kornev BA et al (2011) Diesel control by the method of switching on-off of cylinders or cycles. Engine Build 3:7–12
21. Khimchenko AV, Mishin DG, Buzov AV (2013) Reduction of the unevenness of the engine's torque with the cylinder cutout in partial loading modes. Intern Combust Engines 1:46–51

Finding Stable Region of Torsional Vibrations of Agro-Industrial Rotary Cultivators



S. A. Partko, L. M. Groshev and A. N. Sirotenko

Abstract Numerous factors affect the quality of soil cultivation. The modeling of the cultivation-affecting processes requires considering the parameters of the implement as well as those of the machine with a transfer link. The research team has found the stable region of torsional vibrations for tractors and cultivators. The implement drive is considered to be a single-mass dynamic system engaged in torsional vibrations. The moment of inertia and the system rotation angle is applied to the tiller axis. The paper presents a differential equation of torsional vibrations written in the operator form and in the characteristic form to study the effects of process parameters on the elasto-dissipative characteristic of the drive. The condition of ensuring stable torsional vibrations and zero self-oscillations in the drive has been defined.

Keywords Torsional vibrations · Stability · Aperiodic link · Moment of inertia · Elasto-dissipative

1 Introduction

The quality of soil treatment is a complex indicator that depends on the machine characteristics [1–8], the implement drive characteristics [9, 10], and the implement parameters [11, 12]. Rotary cultivators are designed for tillage and weed control in the interrows of tilled crops cultivated on heavy podzolic and loamy soils as well as in flood lands; they are also used to treat the interrows of berry beds. Implements used with such cultivators are plate-like knives bent to the right or to the left and fixed on a removable flange. Torque is transmitted from the tractor shaft to the tiller via the power train, the main gearbox, and transmission shafts [11]. The research team has analyzed the stable region of torsional vibrations, considering the drive as a dynamic system; the unit under analysis consists of a tractor and a cultivator.

S. A. Partko (✉) · L. M. Groshev · A. N. Sirotenko
Don State Technical University, 1 Gagarin Square, Rostov-on-Don 344000, Russia
e-mail: parlana@ramler.ru

2 Main Part

It is generally assumed that the tiller torque M_f is linked to the tiller angular velocity ω_f and the unit linear speed v by the following function:

$$M_f = k_p \frac{v}{\omega_f} \tag{1}$$

where k_p is a coefficient that links the mean tiller torque values M_f and the mean values \bar{v} and $\bar{\omega}_f$; the coefficient can be found experimentally.

Apparently, the tiller torque is generally a non-linear function of the angular velocity ω_f . Expand the expression (1) as a function of two variables (v and ω_f) in a Taylor series [13] to the first term of the series, assuming that the residual term is zero, to get:

$$M_f = \frac{k_p}{\omega_f} \cdot v - \frac{k_p \bar{v}}{\bar{\omega}_f^2} \omega_f \tag{2}$$

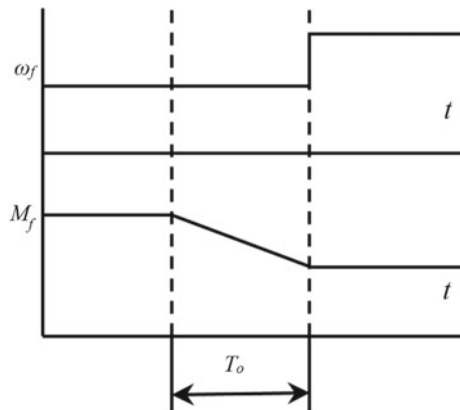
With the assumptions made, the tiller torque is a linear function of the implement angular velocity and the unit travel speed for as long as these values change insignificantly against \bar{v} and $\bar{\omega}_f$. This enables a linear solution of the problem.

Consider the time lag between M_f and ω_f . Figure 1 shows that instantaneous change in the angular velocity ω_f alters the tiller torque by a portion of the tiller turn, i.e., over time:

$$T_o = \frac{2\pi}{\omega_f \cdot z} \tag{3}$$

where z is the number of tiller teeth.

Fig. 1 Tiller torque velocity graph



Apparently, such lag will be observed under other ω_f change laws as well. Write these processes as aperiodic second-order links [14, 15] and write the dynamic component M_f in the operator form as follows:

$$M_f(p) = M_o - \frac{k_p \cdot \bar{v} \cdot \omega_f(p)}{\bar{\omega}_f^2(1 - T_o \cdot p)} \quad (4)$$

where p is the differentiation operator.

Consider the implement drive as a single-mass dynamic system engaged in torsional vibrations. Apply the moment of inertia J_n and the rotation angle φ_n of the system to the tiller axis. The differential equation of torsional vibrations occurring in such as system can be written in the operator form as follows:

$$c \cdot \phi_n(T^2 p^2 + 2\xi T p + 1) = M_o - \frac{k_p \cdot \bar{v}_p}{\bar{\omega}_f^2(1 - T_o \cdot p)} \quad (5)$$

where T is the system time constant, ξ and c are the attenuation coefficients and the system stiffness.

The characteristic equation is then written as:

$$T^2 p^2 + 2\xi T p + 1 + \frac{k_p \cdot \bar{v}_p}{\bar{\omega}_f^2(1 - T_o \cdot p)} = 0 \quad (6)$$

This equation can be used to study how the process parameters (T_o , k_p , \bar{v} , ω_f) affect the elasto-dissipative characteristics of the drive (T , ξ), the soil treatment process stability, as well as the lack of torsional self-oscillations in the drive, which are caused by M_f lagging against ω_f .

Plot the stable regions [16–19]. For the indeterminate parameters of Eq. (5), consider T_o and $\frac{k_p \cdot \bar{v}}{\bar{\omega}_f^2}$ while assuming the values T and ξ to be constant.

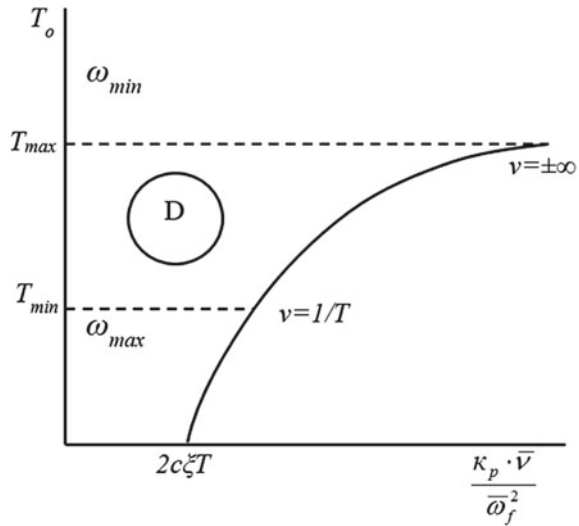
The stable region is built in the plane of two real parameters (T_o and $\frac{k_p \cdot \bar{v}}{\bar{\omega}_f^2}$). To do this, apply D -partitioning to the space of the characteristic equation [14]. The D -partitioning boundary shown in Fig. 2 is a reflection of the imaginary axis on the root plane of spaces formed by the parameters T_o and $\frac{k_p \cdot \bar{v}}{\bar{\omega}_f^2}$ of the characteristic equation. Equating the real and the imaginary parts of the characteristic equation produces:

$$T_o = \frac{1 - v^2 \cdot T^2}{2\xi \cdot T \cdot v^2}; \quad \frac{k_p \cdot \bar{v}}{\bar{\omega}_f^2} = 2c \left[\xi T - \frac{1 - v^2 T^2}{4\xi T v^2} \right] \quad (7)$$

Set v range of $-\infty \div +\infty$ by the formula (7) to find pairwise parameters on the D -partitioning boundary.

Figure 2 shows the values ω_f on the ordinate axis.

Fig. 2 Stable region



As can be seen in the graph, the stability condition can be written as follows:

$$\frac{k_p \cdot \bar{v}}{\bar{\omega}_f^2} \leq 2c \cdot \xi \cdot T \tag{8}$$

This condition links the soil treatment process parameters by the elasto-dissipative characteristics of the drive.

The condition (8) can be used to configure the drive design [5, 7].

3 Conclusion

The derived stability conditions (8) enable linking the linear speed of the unit \$v\$ to the tiller angular velocity \$\omega_f\$ at which there are no parasitic angular accelerations in the system.

This condition can be used to configure the tillage parameters and to set the mass-elastic and dissipative characteristics of the drive.

References

1. Partko SA (2011) O chuvstvitelnosti k sinkhronizatsii i zakhvatyvaniyu kolebany privoda koles i korpusa mobilnykh mashin (APKAgro-Industrial Complex Machine Housing and Wheel Drives: Sensitivity to Synchronization and Capturing of Vibrations). *Advanced Technologies in Mechanical Engineering (Sovremennye tekhnologii v mashinostroyenii)*. In: *Proceedings of the XV international applied research conference*, Penza, pp 168–170
2. Groshev LM, Partko SA, Sirotenko AN (2017) Effect of longitudinal-angular oscillations of the harvester-thresher separator on smooth motion of the reaper. *Vestnik Don State Tech Univ* 17(2):131–135
3. Groshev LM, Partko SA, Sirotenko AN (2016) Application of mathematical simulation methods in the study of mobile agricultural machines frames dynamics. *Sci Rev* 23:92–95
4. Partko S (2008) Vibratory parameters optimization of harvester's running gear system. *Vestnik Don State Tech Univ* 8(2):141–144
5. Groshev LM, Partko SA (2017) Vliyaniye variatsii massovo-geometricheskikh i uprugo-dissipativnykh kharakteristik mobilnogo agregata na ego dinamicheskuyu nagruzhenost (How the Mass, Geometry, and Elasto-Dissipative Characteristics of a Mobile Unit Affect Its Dynamic Load). In: *State-of-the-art and prospects of agricultural mechanical engineering (Sostoyaniye i perspektivy razvitiya selskokhozyaystvennogo mashinostroyeniya)*. *Proceedings of the X international anniversary applied research conference hosted as part of the 20th international agro-industrial convention interagromash 2017*, Rostov-on-Don, pp 39–41
6. Groshev LM, Partko SA, Sirotenko AN, Dyachenko AG (2013) Sravneniye parametrov razgona mobilnoy mashiny s mekhanicheskim i gidromekhanicheskim (privodom Comparing the acceleration parameters of a mobile machine: mechanical vs hydromechanical drive). In: *State-of-the-art and prospects of agricultural mechanical engineering (Sostoyaniye i perspektivy razvitiya selskokhozyaystvennogo mashinostroyeniya)*. *Proceedings of the 6th international applied research conference hosted as part of the 16th international agro-industrial convention interagromash 2013*, DSTU Publ., Rostov-on-Don, pp 74–76
7. Groshev LM, Partko SA (2016) Issledovaniye ratsionalnogo spektralnogo sostava kolebany khodovoy sistemy zernouborochnogo kombayna (Studying the rational spectral composition of vibrations in the harvester undercarriage). In: *State-of-the-art and prospects of agricultural mechanical engineering (Sostoyaniye i perspektivy razvitiya selskokhozyaystvennogo mashinostroyeniya)*. *Proceedings of the 9th international applied research conference hosted as part of the 19th international agro-industrial convention interagromash 2016*, Rostov-on-Don, pp 53–55
8. Androssov AA, Galadzhewa MR, Groshev LM, Partko SA (2010) Research of refusals and reliability of the mobile machines. *Vestnik Don State Tech Univ* 10(1):102–105
9. Groshev LM, Galadzhewa MR, Vislousova IN (2015) Prognozirovaniye pokazateley nadezhnosti pochvoobrabatyvayushchikh mashin s aktivnymi rabochimi organami (Predicting the reliabilities of tillage machines with active implements). In: *Innovative technologies in science and education (Innovatsionnye tekhnologii nauke i obrazovanii)*. ITNO 2015. *Proceedings of the research and methodology conference dedicated to the 85th anniversary of DSTU/SKNIIMESH of Rossselkhozakademiyi*. Rostov-on-Don, Zernograd, pp 475–478
10. Syromyatnikov YuN, Kharmov NS, Voynash SA (2018) Gibky element v sostave rabochikh organov rotornoy pochvoobrabatyvayushchey rykhlytelno-separiruyushchey mashiny (Flexible components in the implements of rotary tillage cultivators and separators). *Tract Agric Mach* 5:32–39
11. Groshev LM, Vislousova IN, Mikhalev AI (2017) Dinamicheskaya nagruzka v frezernom pluge pri ispolzovanii v privode podvizhnykh tsepnykh muft (Dynamic loads in tiller plows with movable chain-coupling drives). In: *Innovative technologies in science and education (Innovatsionnye tekhnologii nauke i obrazovanii)*. ITNO 2017. *Proceedings of the V*

- international applied research conference, 11–15 Sept 2017, Don State Technical University, DSTU-Print, Rostov-on-Don, pp 74–76
12. Voynash SA, Voynash AS, Zharikova TA (2012) Pakhotny agregat na baze malogabaritnogo avtotraktora (Cultivator based on small-size automotive tractor). *Tract Agric Mach* 8:15–16
 13. Smirnov VI (1956) *Kurs Vyshey matematiki (A course of higher mathematics)*. T2. Gostekhteorizdat, Moscow, 628 p
 14. Chemodanov BK (1971) *Matematicheskiye osnovy teorii avtomaticheskogo regulirovaniya (Mathematical foundations of automatic control theory)*, Vysshaya shkola, Moscow, 808 p
 15. Malkin IG *Teoriya ustoychivosti dvizheniya (Movement Stability Theory)*. Nauka, Moscow, 208 p
 16. La Salle J, Lefschetz S (1964) *Stability by Liapunov's direct method with applications*. Mir, Moscow, 305 p
 17. Lure AI (1950) *Operatsionnoye ischisleniye i ego prilozheniya k zadacham mekhaniki (Operational calculus and its applications in mechanics)*. Gos. izd-vo tekhn.-teoret. lit., Moscow, Leningrad, 432 p
 18. YeS Wentzel (2001) *Teoriya veroyatnostey (Probability theory)*, 7th edn. Vysshaya shkola, Moscow, p 575
 19. Gnedenko BV (2005) *Kurs teorii veroyatnostey (Probability theory course)*, 8th edn. revised and updated. Editorial URSS, Moscow, 448 p

Improvement of Fuel Injection and Atomization Processes in Transport Diesel Engine



V. A. Markov, S. N. Devyanin and V. G. Kamaltdinov

Abstract The design of injector nozzles providing improvement of the fuel injection and atomization processes quality in diesel engines is suggested. This is achieved by making grooves on the injector nozzle, each of which forms an expansion of the output channel of the corresponding spray hole. Experiments have been carried out for the D-245.12S diesel engine, alternately equipped with experimental and serial injector nozzles, and operated on diesel fuel, and on 80% diesel fuel and 20% rapeseed oil mixture. The possibility is demonstrated in terms of improving the exhaust gases toxic characteristics using the diesel engine equipped with the experimental injector nozzles and operated on 80% diesel fuel and 20% rapeseed oil mixture. The combination of the experimental nozzles and composite biofuel, containing 80% of diesel fuel and 20% of rapeseed oil, resulted in lower emissions of nitrogen oxides by 8.1%, of carbon monoxide—by 12.4%, and of unburned hydrocarbons—by 15.9%.

Keywords Diesel engine • Mixture formation • Injector • Nozzle • Diesel fuel • Rapeseed oil

V. A. Markov (✉)

Bauman Moscow State Technical University, 5/1, 2-Aya Baumanskaya St.,
Moscow 105005, Russia
e-mail: vladimir.markov58@yandex.ru

S. N. Devyanin

Russian State Agrarian University—Moscow Timiryazev Agricultural Academy,
49, Timiryazevskaya St., Moscow 127550, Russia

V. G. Kamaltdinov

South Ural State University, 76, Lenin Ave., Chelyabinsk 454080, Russia

© Springer Nature Switzerland AG 2020

A. A. Radionov et al. (eds.), *Proceedings of the 5th International Conference on Industrial Engineering (ICIE 2019)*, Lecture Notes in Mechanical Engineering,
https://doi.org/10.1007/978-3-030-22041-9_90

845

1 Introduction

The indicators of fuel efficiency and toxicity of the exhaust gases of transport diesel engines are to a large extent defined by the quality of the processes of fuel injection and atomization. High quality of these processes is achieved through improving the atomization fineness of fuel and its more uniform distribution within the combustion chamber [1–3]. Thus, one of the main factors of the fuel system influencing the diesel engine parameters is the design of the injector, which forms the required characteristics of fuel supply [4, 5]. First and foremost, this refers to the nozzles, is the design of which considerably defines the quality of the mixture formation process [6–8]. Meanwhile, the equivalent flow cross section of the assembled nozzle, the number of holes, their diameter and length, the needle diameter, and the sac volume are of prime importance in the design parameters of the injector nozzles [9–12]. A number of research works indicate that when improving the processes of fuel injection and atomization, it is necessary to ensure the fuel flow turbulence in the nozzles channel [2, 13–15]. The best effect here is achieved when turbulizers are located in the nozzle channels [15–19].

2 Improving the Design of the Injector Nozzles

One of the possible ways of ensuring flow turbulence of the fuel at the nozzles' holes output is to make grooves 2 on the nozzle 1 (Fig. 1a), each of which forms an expansion of the corresponding hole channel 3. Each groove has a shape of a segment and width b , which is equal to the diameter of hole d_p ; groove length l is 2.5–3 times bigger than diameter d_p ; and groove depth is $h = 0.3$ mm. Meanwhile, the groove axes are oriented across and along the nozzle axis [20, 21]. This make of the grooves on the nozzle allows to ensure different lengths of the channel in the plane passing through the groove generatrix, and in the plane perpendicular to this generatrix. As a result, the fuel jet expands in the plane passing through the groove generatrix, and the fuel jet front transforms into an ellipsis with length C and width B (Fig. 1b). This leads to the increase of the fuel jet volume. Moreover, reducing the length of the nozzle hole in the plane passing through the groove generatrix leads to reducing of jet length L , what decreases the part of the fuel sprayed over the relatively cold walls of the combustion chamber, and such hydraulic resistance at the nozzle hole results in additional fuel jet turbulence.

3 Experimental Study of the Diesel Engine with Experimental Injector Nozzles

To assess the indicators of the diesel engine with such nozzles, grooves were made on serial nozzles of 145.1112110 type manufactured by Noginsk Fuel Equipment Plant, as shown in scheme in Fig. 1. Some of the characteristics of the serial nozzles of 145.1112110 type are given in Tables 1 and 2. These nozzles are made with output of the holes 3 (Fig. 1) to the injector sac volume 4 and needle 5 diameter $d_n = 6.0$ mm (along the directrix).

The influence of the design of injector nozzle flow channel on the efficiency and ecological indicators is assessed using the results of experimental studies for turbocharged 4-cylinder four-stroke (110 mm of piston diameter \times 125 mm of piston stroke) D-245.12S diesel engine, being manufactured by Minsk Motor Plant and installed in ZIL-5301 "Bychok" small trucks. This diesel engine features direct injection combustion chamber of CNIDI type (Central Research and Development Diesel Institute) with volume and wall film mixture formation. D-245.12S diesel engine had a fuel system, which included a fuel injection pump of type PP4M10U1f by Motorpal, with $d_{pl} = 10$ mm of plunger diameter and $h_{pl} = 10$ mm of full stroke plunger, fuel pipes with length $L_p = 540$ mm, and injectors FDM-22, which were adjusted to start of injection pressure $p_{inj0} = 21.0$ MPa. The injectors were

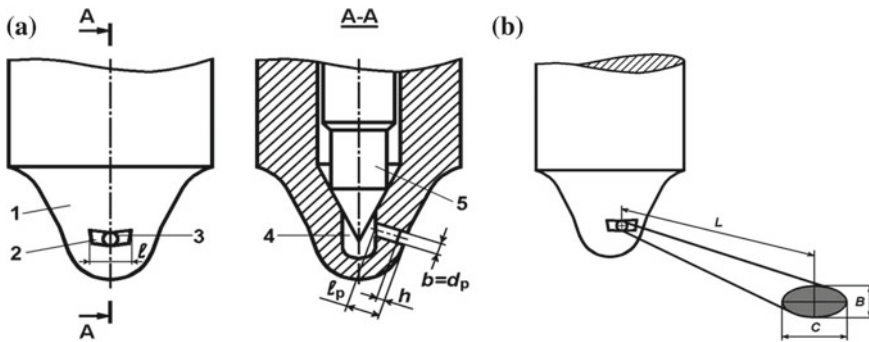


Fig. 1 Scheme of the injector nozzle with the grooves made on the nozzle tip, the output cross section of the spray jet (a) and geometry of the fuel jet formed by such spray hole: 1—nozzle tip; 2—groove; 3—spray hole; 4—injected fuel chamber; and 5—needle

Table 1 Parameters of the nozzles under study

Spray holes diameter d_p , mm	Spray holes number i_p	Maximum needle lift h_n , mm	Total effective area of the assembled nozzle μ_{pf} , mm ²
0.32	5	0.26	0.278

Note Values μ_{pf} are given for the maximum injector's needle lift; average values h_n and μ_{pf} are indicated for a set of nozzles



Table 2 Location of the spraying holes in the atomizers under study

Hole no.	Angular hole location as related to the pin, degree	Hole tilt angle as related to the nozzle axis, degree
1	8	62
2	90	71.5
3	172	62
4	237	52
5	303	52

alternately equipped with serial nozzles of 145.1112110 type by Noginsk Fuel Equipment Plant, and with experimental nozzles with grooves on the nozzle tips by Noginsk Fuel Equipment Plant. The studies were carried out for the modes of full load and in a 13-mode test cycle under ECE regulation No. 49 (ECE R49). During the tests, the timing angle of fuel injection, equal to $\theta = 13^\circ$ of crank angle before the top dead point, as well as the position of the stop of maximum fuel supply remained unchanged. To assess the possibility of using the experimental nozzles when the diesel engine is operated on composite biofuels, studies were carried out for the diesel engine operated on diesel fuel under GOST 305-82, and on a mixture of diesel fuel with rapeseed oil in proportion of 80% to 20%, respectively. The properties of these fuels are given in Table 3.

Table 3 An example of a table

Physical and chemical properties	Fuels		
	Diesel	Rapeseed oil	80% diesel + 20% rapeseed oil
Density at 20 °C, kg/m ³	830	916	848
Kinematic viscosity at 20 °C, mm ² /s	3.8	75	9
Surface stress factor at 20 °C, mN/m	27.1	33.2	–
Lower heating value, kJ/kg	42,500	37,300	41,500
Cetane number	45	36	–
Autoignition temperature, °C	250	318	–
Cloud point temperature, °C	–25	–9	–
Pour point temperature, °C	–35	–20	–
Amount of air required for combustion of 1 kg of fuel, kg	14.3	12.6	13.9
Content, % by mass			
C	87.0	78.0	–
H	12.6	10.0	–
O	0.4	12.0	–
Total content of sulfur, % by mass	0.20	0.002	–
Coking ability of the 10% residue, % by mass	0.2	0.4	–

Note “–” means that the properties were not determined; for the diesel–rapeseed fuel mixture the volume percentage content of components is indicated

The motor test bed was equipped with a set of the required measurement instruments. The exhaust gases smoke was measured using a manual MK-3 smoke meter by Hartridge (United Kingdom), accurate to within $\pm 1\%$. The concentrations of NO_x , CO, and CH_x in the exhaust gases were measured with SAE-7532 gas analyzer by the Japanese company YANACO with the errors in measurements of the components within $\pm 1\%$.

During the testing of D-245.12S diesel engine at the modes of full load, a dependency between the engine indicators and the types of the used nozzles was revealed (Fig. 2). When serial nozzles were replaced with the experimental ones, brake specific fuel consumption (*BSFC*) showed relatively a little change. Thus, at the maximum power at $n = 2400 \text{ min}^{-1}$, the fuel consumption *BSFC* decreases from 285.4 to 283.1 g/(kW h), and at the maximum torque at $n = 1500 \text{ min}^{-1}$ *BSFC* increases from 248.9 to 253.5 g/(kW h). When using the experimental nozzles, there is a tendency to decrease in the exhaust gases smoke K_x . First and foremost, this concerns the high engine speed regimes. Thus, at the regime with $n = 2400 \text{ min}^{-1}$, the installation of the experimental nozzles resulted in the decrease of exhaust gases smoke from 40 to 37% on Hartridge smoke units. Considerable decrease in the exhaust gases smoke of the diesel engine with the experimental nozzles may be achieved if it is operated on rapeseed oil composite biofuels.

The low calorific value of the composite biofuel resulted in the fact that in case of D-245.12S diesel engine's operation on a mixture of diesel fuel and rapeseed oil, *BSFC* slightly increases, as compared to operation on diesel fuel (Fig. 2). If the engine equipped with the experimental nozzles was operated on the composite biofuel at the maximum power at $n = 2400 \text{ min}^{-1}$ *BSFC* increased from 283.1 up to 289.8 g/(kW h), and at the maximum torque at $n = 1500 \text{ min}^{-1}$ —from 253.5 up to 255.2 g/(kW h). However, in this case, the engine net efficiency η_e did not decrease: at $n = 2400 \text{ min}^{-1}$, the efficiency did not change and stayed equal to $\eta_e = 29.9\%$, and at $n = 1500 \text{ min}^{-1}$ efficiency η_e even increased from 33.4 up to 34.0%. The use of diesel–rapeseed fuel mixture resulted in considerable decrease in exhaust gases smoke K_x . When D-245.12S diesel engine equipped with the experimental nozzle was operated on composite biofuel instead of diesel fuel at the maximum power at $n = 2400 \text{ min}^{-1}$, the decrease in the exhaust gases smoke from 37.0 to 30.0% on Hartridge smoke units was registered; at the maximum torque at $n = 1500 \text{ min}^{-1}$ —from 54.5 to 44.0%; and at the full load with $n = 1080 \text{ min}^{-1}$ —from 50.0 to 31.0% (characteristics 2 and 3 in Fig. 2).

The results of testing of D-245.12S diesel engine equipped with the serial and experimental nozzles, at the 13-mode test cycle are given in Fig. 3. The characteristics of total fuel consumption TFC given in Fig. 3a are proof to the fact that replacing the serial nozzles with the experimental ones leads to a slight increase in TFC. The biggest variation between the values of TFC was registered at the maximum torque at $n = 1500 \text{ min}^{-1}$. At this mode, the replacement of the serial nozzles with the experimental ones is accompanied by growth of TFC from 13.95 up to 14.41 kg/h, but this maximum increase in TFC amounts to only about 3%.

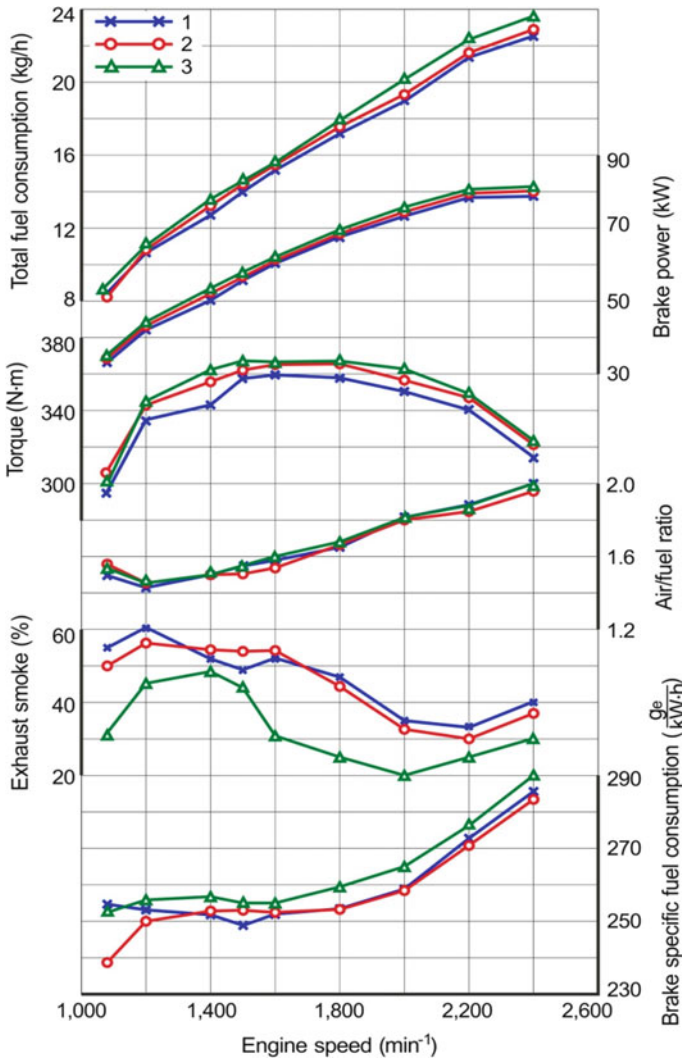


Fig. 2 Dependency of brake power N_e , torque M_e , total fuel consumption C_f , air ratio α , exhaust gases smoke K_x , and brake specific fuel consumption g_e on engine speed of D-245.12S diesel engine at full load when using different nozzles and different fuels: 1—serial nozzles, diesel fuel; 2—experimental nozzles, diesel fuel; 3—experimental nozzles, 80% diesel fuel and 20% rapeseed oil mixture

Further increase in TFC is registered when instead of diesel fuel the diesel engine is operated on composite biofuel, which is characterized with lower calorific value.

The testing of D-245.12S diesel engine performed at the 13-mode test cycle became proof of the influence of the used nozzle type on the exhaust gases toxicity. The dependency of nitrogen oxides C_{NO_x} concentration in the exhaust gases on the

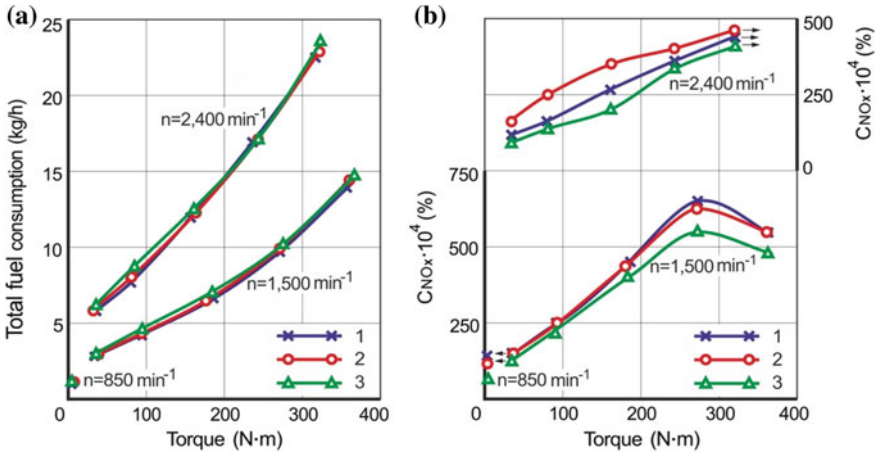


Fig. 3 Dependency of total fuel consumption G , **a** and volume concentration of nitrogen oxides C_{NO_x} in the exhaust gases **b** on engine speed n and torque M_e of D-245.12S diesel engine: 1—serial nozzles, diesel fuel; 2—experimental nozzles, diesel fuel; 3—experimental nozzles, 80% diesel fuel and 20% rapeseed oil mixture

Table 4 An example of a table

Nozzle type, fuel type	Specific mass emission of toxic components, g/(kW h)		
	e_{NO_x}	e_{CO}	e_{CH_x}
Serial nozzles, diesel fuel	5.749	7.872	2.207
Experimental nozzles, diesel fuel	5.723	6.893	2.040
Experimental nozzles, 80% of diesel fuel + 20% of rapeseed oil	5.285	6.900	1.855

nozzle type is ambiguous (Fig. 3b). Thus, at the idle mode at $n = 850 \text{ min}^{-1}$, bigger contents of NO_x in the exhaust gases were registered in case of the serial nozzle— $C_{NO_x} = 0.0140\%$, against $C_{NO_x} = 0.0125\%$ with the experimental nozzle. At $n = 1500 \text{ min}^{-1}$, the content of NO_x in the exhaust gases depends on the nozzle type relatively a little. At the modes with $n = 2400 \text{ min}^{-1}$, the installation of the experimental nozzles is accompanied by slight increase in the NO_x content in the exhaust gases. However, at the 13-mode test cycle, the integral specific mass emission of nitrogen oxides, when using the experimental nozzles, turned out to be lower— $e_{NO_x} = 5.723 \text{ g/(kW h)}$, against $e_{NO_x} = 5.749 \text{ g/(kW h)}$ in case of the serial nozzles (Table 4). As a result, the NO_x emission reduced by 0.5%.

The notable decrease in the nitrogen oxides emission is achieved by operation of D-245.12S diesel engine with the experimental nozzles, on the mixture of 80% of diesel fuel and 20% of rapeseed oil. This effect was registered for all modes of the 13-mode test cycle (Fig. 3b). When replacing diesel fuel with composite biofuel,

the specific mass emission of nitrogen oxides at this cycle e_{NO_x} reduced from 5.723 to 5.285 g/(kW h), that is by 7.7% (Table 4).

The type of the used nozzle notably influences the concentrations of carbon monoxide C_{CO} and unburned hydrocarbons C_{CH_x} in the exhaust gases of D-245.12S. Meanwhile, at the 13-mode test cycle, the integral specific mass emissions of these toxic components reduce if the serial nozzles are replaced with the experimental ones, and the engine is further operated not on diesel fuel, but on the mixture of 80% of diesel fuel and 20% of rapeseed oil (Table 4).

4 Conclusion

The testing performed for D-245.12S diesel engine with the serial and experimental nozzles has proven the possibility of improving the quality of the operation process of the diesel engine equipped with the experimental nozzles with grooves, each of which forms an expansion of the output channel of the corresponding spray hole. The replacement of the serial nozzles with the experimental ones is accompanied with reduced emission of nitrogen oxides by 0.5%, of carbon monoxide—by 12.4%, and of unburned hydrocarbons—by 7.6%. Additional improvement of the exhaust gases toxicity indicators of D-245.12S diesel engine with the experimental sprayers has been achieved by replacing diesel fuel with composite biofuel. Using the mixture of 80% of diesel fuel and 20% of rapeseed oil has resulted in additional reduction of the emission of nitrogen oxides by 7.7%, and of unburned hydrocarbons—by 9.1%, while carbon monoxide emission practically did not change. The combination of using the experimental nozzles and the mixture of 80% of diesel fuel and 20% of rapeseed oil has allowed to reduce the emission of nitrogen oxides by 8.1%, of carbon monoxide—by 12.4%, and of unburned hydrocarbons—by 15.9%.

References

1. Grekhov LV, Ivashchenko NA, Markov VA (2005) Fuel systems and diesel engine control systems: text book for higher school, 2nd edn. Legion-Autodata Press, Moscow
2. Markov VA, Devyanin SN, Mal'chuk VI (2007) Fuel injection and spraying in diesel engines. Bauman Moscow State Technical University Press, Moscow
3. Astahov IV, Golubkov LN, Trusov VI et al (1990) Fuel systems and diesel engines efficiency. Mashinostroyeniye Press, Moscow
4. Fainleib BN (1990) Fuel equipment of auto tractor diesel engines: reference book. Mashinostroyeniye Press, Leningrad
5. Lyshevskiy AS (1981) Fuel systems for diesel engines. Mashinostroyeniye Press, Moscow
6. Trusov VI, Dmitrienko VP, Maslyanyj GD (1977) Injektors of auto tractor diesel engines. Mashinostroyeniye Press, Moscow
7. Dmitrienko VP (1970) Research influence of a sprayer constructive elements on its hydraulic characteristic. In: Proceedings MADI. Moscow, pp 110–114

8. Trusov VI, Mal'chuk VI, Zryachkin MV (1979) Choice of sprayer design data under given characteristics of fuel injection and spraying. In: Proceedings MADI, vol 178, pp 58–62
9. Fainleib BN, Baraev BI (1973) Influence of design data on spraying, torch development, and fuel evaporation in high-speed diesel engines. TsNIITEItraktorosel'khoz mash, Moscow
10. Galgovskiy VR (1970) way of choosing nozzle holes number. Higher School News. Mashinostroyeniye 3:5–12
11. Bae C, Kang J (2006) The structure of a break-up zone in the transient diesel spray of a valve-covered orifice nozzle. Int J Engine Res 7:1–14
12. Payri R, Salvador FJ, Gimeno J (2009) Effects of nozzle geometry on direct injection diesel engine combustion process. Appl Therm Eng 29:2051–2060
13. Korotnev AG, Kulchitskiy AR, Chestnov YI (2002) A sprayer flowing part design and parameters of a diesel engine. Automobile Ind 2:15–17
14. Mal'chuk VI (2003) Methods of perfection of fuel spraying in a high-speed diesel engine. Piston Engines and Fuels in XXI Century, Proceedings MADI (GTU). Moscow, pp 30–36
15. Goney KH, Corradini ML (2000) Isolated effects of ambient pressure, nozzle cavitation and hole inlet geometry on diesel injector spray characteristics. SAE Technical Paper Series 2000-01-2043:1–17
16. Kutovoy VA (1981) Fuel injection in diesel engines. Mashinostroyeniye Press, Moscow
17. Trusov VI, Mladenov MB (1976) Influence of cavitation and eddy formation in nozzle holes on fuel spraying quality. In: Proceedings MADI, vol 126, pp 46–53
18. Bae C, Yu J, Kang J (2002) Effect on nozzle geometry on the common-rail diesel spray. SAE Technical Paper Series 2002-01-1625:1–13
19. Ganipa LC, Andersson S, Chomiak J (2003) Combustion characteristics of diesel sprays from equivalent nozzles with sharp and rounded inlet geometries. Combust Sci Technol 175: 1015–1032
20. Markov VA, Mal'chuk VI, Devyanin SN, Zenin AA (2007) Diesel engine injector. RU Patent 2005120719, 20 Jan 2007
21. Markov VA, Mal'chuk VI, Devyanin SN et al (2006) Diesel engine injector sprayer. RU Patent 2004120241, 10 Jan 2006

Finding New Component in Displacement of Normal Supporting Surface Reaction to Car Wheels



T. A. Golubeva and E. V. Balakina

Abstract It is known that when an elastic wheel, e.g., a car tire, moves on a solid supporting surface, its normal reaction is displaced longitudinally. The direction of such displacement in relation to the forward speed vector of the wheel depends on the wheel movement. The magnitude of such displacement (drift) is important as it determines the center of the friction-at-rest area in the contact spot, which triggers a lateral reaction of the supporting surface that determines the stability of wheel and car movement to a great extent. There used to be known only two components of such a drift. The first component characterizes hysteresis losses (radial and tangential) due to the wheel rolling. The second component characterizes the longitudinal elastic displacement of the wheel axis in relation to the geometric center of the contact spot. The authors have experimentally identified a new, i.e., the third component that characterizes elastic angular deformations in the tire, which cause the curve of normal stresses in the contact spot to be asymmetric. This third component has been found to have much greater magnitude than the two other components.

Keywords Elastic wheel · Contact area · Normal reaction · Coefficient of adhesion · Reactions in contact · Displacement

1 Introduction

It is known that when an elastic wheel, e.g., a car tire, moves on a solid supporting surface, its normal reaction is displaced longitudinally [1–22]. The direction of such displacement in relation to the forward speed vector of the wheel depends on the wheel movement. The magnitude of such displacement (drift) is important as it determines the center of the friction-at-rest area in the contact spot, which triggers a lateral reaction of the supporting surface that determines the stability of wheel and car movement to a great extent.

T. A. Golubeva (✉) · E. V. Balakina

Volgograd State Technical University, 28, Lenin Prospekt, Volgograd 400005, Russia
e-mail: golybeva_tat9na@mail.ru

© Springer Nature Switzerland AG 2020

A. A. Radionov et al. (eds.), *Proceedings of the 5th International Conference on Industrial Engineering (ICIE 2019)*, Lecture Notes in Mechanical Engineering,

https://doi.org/10.1007/978-3-030-22041-9_91

There used to be known only two components of such drift. The first component, defined by Coulomb, characterizes hysteresis losses (radial and tangential) due to the wheel rolling. The second component, introduced by V. A. Petrushov, characterizes the longitudinal elastic displacement of the wheel axis in relation to the geometric center of the contact spot. The authors have experimentally identified a new, i.e., the third component that characterizes elastic angular deformations in the tire, which cause the curve of normal stresses in the contact spot to be asymmetric.

2 Methods and Approaches

Figure 1 presents the diagrams of an elastic wheel in different movements.

The figure uses the following legend:

- V_a for the wheel axle forward speed;
- ω for the angular velocity of the wheel;
- l_c for the contact spot length;

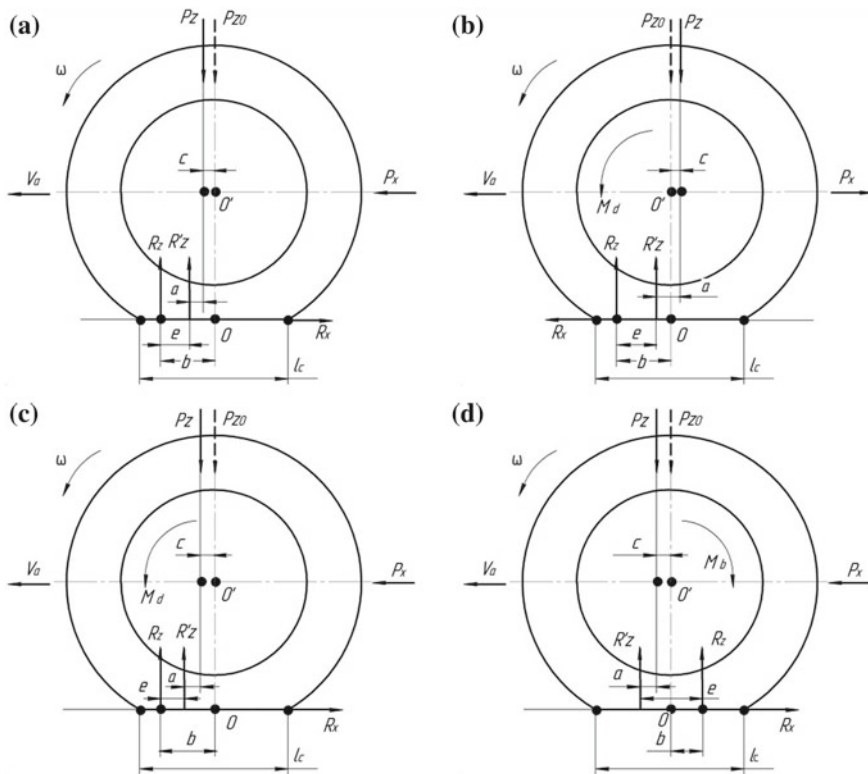


Fig. 1 Diagrams of an elastic wheel in different movements: **a** for driven wheels; **b** for drive wheels; **c** for neutral movement; and **d** for braking

- P_x for the pushing (tractive) force of the wheel;
 P_{z0}, P_z for the normal wheel load;
 R_z, R'_z for the normal reaction of the supporting surface;
 R_x for the tangential reaction of the supporting surface;
 M_d for torque;
 M_b for braking torque;
 b for the longitudinal drift of the normal supporting surface reaction, i.e., the distance from the normal reaction of the supporting surface R_z to the geometric center of the contact spot;
 c for the longitudinal elastic displacement of the wheel axle in relation to the geometric center of the contact spot;
 a for the longitudinal drift of the normal reaction due to hysteresis losses in the wheel;
 e for the longitudinal drift of the normal reaction due to elastic angular deformations in the tire.

Following the principle of superpositions, the ratio of the values a , c , and e determines the total magnitude of the longitudinal drift of the normal supporting surface reaction b .

The direction coincident with that of the wheel axle forward speed V_a is assumed to be the positive displacement direction a, b, c, e .

The direction of longitudinal elastic displacement of the wheel axle c in relation to the geometric center of the contact spot can be both positive and negative depending on the direction of the force P_x . This causes a normal load displacement from the position P_{z0} to the position P_z .

Longitudinal drift a of the normal reaction due to hysteresis losses in the wheel is the distance between the load effect line P_z and the current normal reaction line R'_z . The direction a is always positive and determines the wheel rolling resistance:

$$a \approx f \cdot r_k,$$

where f is the wheel rolling resistance coefficient; r_k is the wheel rolling radius [4, 18].

Longitudinal drift e of the normal reaction is the distance between the current normal reaction line R'_z and the final line R_z . It occurs due to elastic angular deformations of the tire, which cause asymmetry in the contact spot normal stress curves. For driven wheels, drive wheels, or neutral movement, the drift e has a positive direction; when braking, the direction is negative [4, 18].

Evaluate the components of the total longitudinal drift of the normal supporting surface reaction.

Table 1 presents computations of the total longitudinal drift of the normal supporting surface reaction, caused by hysteresis losses in the wheel.

Table 2 presents the results of computing the longitudinal elastic wheel axle displacement c in relation to the geometric center of the contact spot.

Table 1 Total longitudinal drift a of the normal supporting surface reaction, caused by hysteresis losses in the wheel

Vehicle type	Wheel radius r_k , mm	Rolling resistance coefficient f	Longitudinal hysteresis loss normal reaction drift a ,mm	a_{max} , mm
Passenger cars	220...350	0.007...0.015	1.54...5.25	5
Trucks	450...600	0.008...0.06	3.6...36.0	36

Table 2 Total longitudinal drift a of the normal supporting surface reaction, caused by hysteresis losses in the wheel

Vehicle type	Tire seating radius r_0 , mm	Torsional stiffness coefficient of tires [3] $C_{t\beta}$, Nm/rad	Longitudinal stiffness coefficient of tires [3] $C_{tx} \approx \frac{C_{t\beta}}{(r_0)^2}$, N/rad	Maximum possible pushing force, P_x N	c_{max} , mm
Passenger cars	152...216	17,200...45,800	745...1100	2800...6050	3...5
Trucks	254	86,000...200,500	1330...3110	11,600...27,900	8...9

Table 3 Magnitudes of the components a , c of the total longitudinal drift in the normal supporting surface reaction

Vehicle type	a_{max} , mm	c_{max} , mm
Passenger cars	5	5
Trucks	36	9

Here $c_{max} = \frac{[P_x]}{C_{tx}}$, where $[P_x]$ is the maximum possible pushing force of the wheel; C_{tx} is the longitudinal stiffness coefficient of tires.

$$[P_x] = [P_z] \cdot \varphi_{max},$$

where φ_{max} is the maximum coefficient of tire adhesion to dry asphalt.

Table 3 presents the computation results.

In this paper, the longitudinal drift magnitude e of the normal reaction has been found experimentally, see below. The basic assumption is that the wheel rolling is a quasi-static process.

3 Experiment Methods and Results

VSTU has designed an equipment to find the longitudinal drift e of the normal reaction experimentally; the drift occurs due to the elastic angular deformations of tires, which causes asymmetry in the normal contact spot stress curves.





Fig. 2 Experimental equipment

Figure 2 shows the equipment picture.

The wheel hub is hinge-joined to a horizontal frame connected unilaterally to the hinges, with the wheel axle being placed horizontally; the beams of the wheel are exposed to radial load force factor that generates radial loads in the wheel rotation plane passing through the geometric center of the wheel. The horizontal frame is parallel to the rotating supporting pad used for measurements. The rotation axis of the pad is placed in the hinges and is always parallel to the wheel axle interacting with the wheel tire. The weight of this axle triggers a normal supporting surface reaction in the contact area, which is proportional to the radial load force factor in case there is no other force factor. The reaction is calculated based on the primary supporting pad force sensor readings. The frame is not parallel to the rotating supporting pad if there is an additional torsional load force factor that causes the normal supporting surface reaction application point to be displaced in the horizontal plane perpendicular to the wheel axle. Such displacement is proportional to such additional torsional load force factor and can be calculated based on the secondary readings of the supporting pad force sensor.

The setup shown in Fig. 2 used a 3.25/3.00-8 tire. This is similar to other tires not only in geometry, but also in terms of elastic properties.

The setup measures only the third component e , as:

- the first component a is absent due to lack of wheel rotation;
- the third component e is absent as the wheel axle is immobile.

Experiment results are shown in Fig. 3.

Table 4 presents the computed e_{\max} values for passenger cars and trucks, proportional to the normal wheel load.

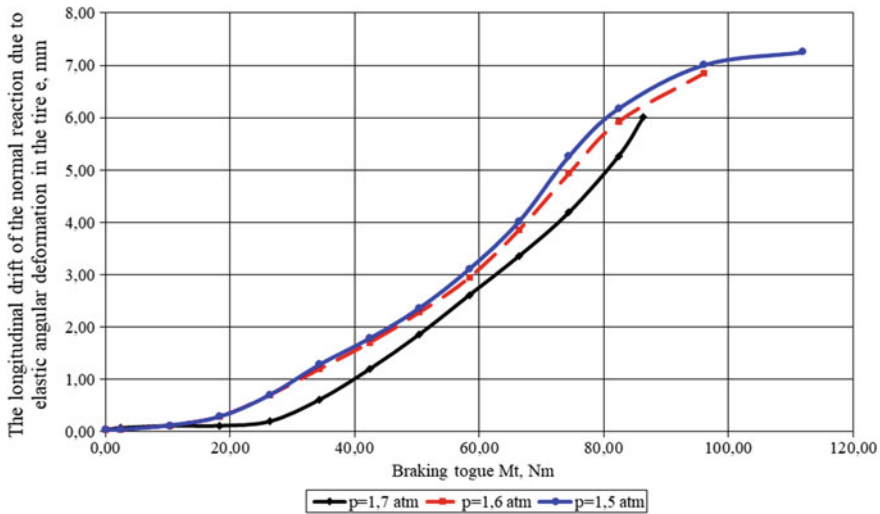


Fig. 3 Experimental results

Table 4 Experimental and computed magnitudes of the longitudinal drift e_{max} in the normal reaction as caused by elastic deformations of tires

Tire	Permissible normal load $[P_x]$ on the wheel, N	e_{max} , mm
Experimental value	800	6.3
Passenger cars	3000...6500	24...51
Trucks	12,500...30,000	99...236

Table 5 summarizes the components of the longitudinal drift b of the normal supporting surface reaction against the geometric center of the contact spot.

Apparently, the direction of such longitudinal drift b is positive in any movement except braking. It is negative when braking, see Fig. 1d. The maximum longitudinal drift e_{max} of the normal reaction is approximately an order of magnitude greater than the other components a_{max} and c_{max} .

The authors' theoretical investigations show that

- for passenger cars $e_{max} \approx 12 \cdot h \cdot \varphi$;
- for trucks $e_{max} \approx (13 \dots 16) \cdot h \cdot \varphi$.

where h is the vertical deflection of the tire; φ is the adhesion coefficient in wheel slip.

The obtained expressions mean that the longitudinal drift of the normal supporting surface reaction depends on the elastic and adhesive properties of the tire. On an asphalt concrete pavement, its maximum magnitude e_{max} is approximately an order higher than the radial deflection of the tire.



Table 5 Components of the longitudinal drift b of the normal supporting surface reaction against the geometric center of the contact spot

Tire	Longitudinal elastic displacement of the wheel axle in relation to the geometric center of the contact spot c_{max} , mm	Longitudinal drift of the normal reaction due to hysteresis losses d_{max} , mm	Longitudinal drift of the normal reaction due to elastic deformations in the tire. e_{max} , mm	Longitudinal drift of the normal supporting surface reaction $ b_{max} $, mm			
				Unrestrained movement	Drive wheel	Braking	
Passenger cars	3...5	1.54...5.25	24...51	5...10	21...53	29...61	14...47
Trucks	8...9	3.6...36.0	99...236	12...45	94...264	111...281	54...224

4 Findings

1. Below are the maximum absolute magnitudes of the total longitudinal drift b of the normal supporting surface reaction against the geometric center of the contact spot:
 - for passenger car tires:
 - 5...10 mm in unrestrained movement;
 - 21...53 mm for drive wheels;
 - 29...61 mm in neutral movement;
 - 14...47 mm when braking.
 - for truck tires:
 - 12...45 mm in unrestrained movement;
 - 94...264 mm for drive wheels;
 - 111...281 mm in neutral movement;
 - 54...224 mm when braking.
2. The longitudinal drift b of the normal supporting surface reaction against the geometric center of the contact spot is positively directed in any movement except braking. It is negative when braking.
3. Elastic angular deformations of the tire cause asymmetry in the contact spot normal stress curves, which is why the third normal reaction longitudinal drift component e_{\max} has a maximum magnitude that is approximately an order of magnitude higher than that of the two other components a_{\max} and c_{\max} .
4. When solving a car movement stability problem, one must assume that the lateral reaction of the supporting surface to the wheel is applied to the geometric center of the friction-at-rest area in the contact spot, while the normal reaction application point depends on its total drift b from the geometric center of the contact spot.

References

1. Balabin IV, Putin VA, Chabunin IS (2012) Automobile and tractor wheels and tires. MGTU MAMI, Moscow
2. Balakina EV (2017) Calculation of the geometric position and the sizes of the static friction and sliding friction zones at the point of contact between an elastic wheel and a firm surface. J Friction Wear 38(2):144–149
3. Balakina EV, Kochetkov AV (2017) Friction coefficient of tire with road surface. Mechanical Engineering, Moscow, 292 p
4. Balakina EV, Zotov NM (2015) Determination of the mutual arrangement of forces, reactions, and friction zones in the contact zone of an elastic wheel with a solid surface. J Friction Wear 36(1):29–32
5. Balakina EV, Zotov NM, Fedin AP (2018) Modeling of the motion of automobile elastic wheel in realtime for creation of wheeled vehicles motion control electronic systems. In: IOP conference series: materials science and engineering, vol 315, p 012004

6. Balakina EV et al (2015) Modeling techniques for tires based on diagram. *Acta Technica CSAV (Ceskoslovensk Akademie Ved.)* 60(2):173–178
7. Balakina E et al (2013) Problems of modelling of dynamic processes in real time (on the example of vehicle brake dynamics). *Mechanical Engineering, Moscow*, 299 p
8. Emami A et al (2017) Physics-based friction model with potential application in numerical models for tire-road traction. In: *Dynamic systems and control conference*, 6 p
9. Fedotov AI (2015) Dynamic method of diagnostics of pneumatic brake drives of motor vehicles: monograph. Publ. IrNITU, Irkutsk, p 514
10. Khaleghian S et al (2017) A technical survey on tire-road friction estimation. *Friction* 5 (2):123–146
11. Khaleghian S, Ghasemalazadeh O, Taheri S (2016) Estimation of the tire contact patch length and normal load using intelligent tires and its application in small ground robot to estimate the tire-road friction. *Tire Sci Technol TSTCA* 44(4):248–261
12. Knoroz VI (ed), Klennikov EV, Petrov IP (1976) *Operation of automobile tires*. Transport, Moscow, 240 p
13. Koskinen S (2010) *Sensor data fusion based estimation of tyre-road friction to enhance collision avoidance*. Dissertation, Tampere University of Technology
14. Kravets VN, Selifonov VV (2011) *Automobile theory*. College textbook. OOO Greenlight, Moscow, p 884
15. Minca C (2015) The determination and analysis of tire contact surface geometric parameters. *Rev Air Force Acad Romania* 1:149–154
16. Morris de Beer et al (2012) Tyre—pavement interface contact stresses on flexible pavements—quo vadis? In: *8th Conference on asphalt pavements for Southern Africa*, June, 2012
17. Pacejka HB (2012) *Tire and vehicle dynamics*. Published by Elsevier Ltd, USA
18. Petrushov VA (2008) *Automobiles and road trains: new technologies of research of rolling and wind resistance*. Torus Press, Moscow, p 352
19. Jazar RN (2008) *Vehicle dynamics: theory and application*. Springer Science+Business Media, LLC, London, p 1015
20. Tomaraee P et al (2015) Relationships among the contact patch length and width, the tire deflection and the rolling resistance of a free-running wheel in a soil bin facility. *Span J Agric Res* 13(2):7
21. Turenko AN, Lomaka SI, Ryzhikh LA, Leontiev DN (2010) Calculation of realized traction coefficient at wheel floating in braking mode. *Automobile Transp* 27:7–12
22. Woodward D et al (2014) The static contact patch of some friction measuring devices. In: *4th International safer roads conference*. Cheltenham, United Kingdom, May 2014

Numerical Research of Combustible Mixture Inert Components Influence on Compression-Ignition Engines Combustion Process



V. G. Kamaltdinov, V. A. Markov and K. S. Leonov

Abstract An expression is suggested for determining the coefficient of the oxygen reaction activity K_1 when modeling the process of fuel combustion in the compression-ignition engine. Using coefficient K_1 allows modeling the decrease in the rate of combustible mixture combustion due to the inert components in case of the changes in mixture composition caused by combustion and exhaust gases recirculation (EGR). The numerical research has been performed for the process of combustion of the homogeneous mixture of air and dimethyl ether in the constant volume chamber. The increase in the inert components content in the combustible mixture in case of the EGR (increase of the residual gases coefficient from 0 up to 0.5) results in the slowdown of the dimethyl ether combustion process, decrease in the maximum combustion rate and postponed achieving of this rate. The maximum calculated combustion rate without consideration of the inert components decreases by 23.8%. Taking into account the inert components, it decreases 2.52 times by using coefficient K_1 . In the first case, the maximum combustion pressure decreases only by 0.3 MPa and is registered 0.04 ms later. In the second case, the maximum combustion pressure decreases by 0.46 MPa and is registered 0.41 ms later, though the initial amount of oxygen decreases identically—1.86 times. The main causes of the slowdown of the dimethyl ether combustion in conditions under study are the decrease in the initial amount of the oxygen molecules and the 1.53 times decrease in the reaction activity of oxygen.

Keywords HCCI engine · Dimethyl Ether · Inert components · Oxygen activity · Combustion rate · EGR · Nitrogen oxides

V. G. Kamaltdinov (✉) · K. S. Leonov
South Ural State University, 76, Lenin Avenue, Chelyabinsk 454080, Russia
e-mail: kamaltdinovvg@susu.ru

V. A. Markov
Bauman Moscow State Technical University, 5/1, str. Baumanskaya 2-ya,
Moscow 105005, Russia

1 Introduction

One of the main factors, which determine the paths of development of modern engine building, is the strict requirements to the toxicity of the internal combustion engines exhaust gases [4, 14]. Manufacturers of internal combustion engines are using more and more complex systems to reduce hazardous emissions and the exhaust gases toxicity.

The most toxic components in the exhaust gases of internal combustion engines of any type are nitrogen oxides NO_x [12, 15]. The proportion of NO_x in the total toxic emissions from the exhaust gases of diesel engines amounts to 30–80% as per mass and 60–95% as per toxicity equivalent [18]. Meanwhile, about 42% of nitrogen oxides emitted into the atmosphere are generated by motor transport [15].

Nitrogen oxides are produced as a result of nitrogen oxidization, contained in the air charge of the cylinder in an internal combustion engine. In the combustion chamber of an internal combustion engine, nitrogen (which is chemically inert in normal conditions) under high pressure and temperature above 2000 K reacts with the air oxygen, as a result producing mostly nitrogen monoxide NO , which is an unstable component. During expansion and temperature dropping below 650–700 K, nitrogen monoxide NO undergoes oxidization and transforms into dioxide NO_2 . Meanwhile, the toxicity of NO_2 is seven times higher than that of NO . The concentration of other gaseous nitrogen oxides (N_2O , N_2O_3 , N_2O_4 , and N_2O_5) in the exhaust gases is negligible [14].

The temperature of combustion has a certain influence on the NO emission with the exhaust gases. The highest NO concentration is registered in local zones of the combustion chamber with low coefficients of the air excess λ and maximum combustion temperatures (the gas temperatures in the combustion chambers of diesel engines reach 2800 K, and in the combustion chambers of spark-ignited engines—3000 K). That is why decreasing the maximum temperatures in the combustion chambers of internal combustion engines is an efficient way to reduce nitrogen oxide emissions into the atmosphere.

At present, the exhaust gases recirculation [14] is considered as one of the most efficient methods of reducing the emissions of nitrogen oxides with the exhaust gases from internal combustion engines [16, 21]. Inert gases, injected to the engine cylinders, decrease the combustion rate and, therefore, reduce the maximum local temperatures. For that purpose, the exhaust gases from an internal combustion engine are used, part of which is injected from the outlet system of the engine to its inlet. The main inert components of the exhaust gases are nitrogen, carbon dioxide, and water vapor. The carbon dioxide and water vapors content in the diesel engines exhaust gases reaches 12 and 9% (as per mass), respectively. The nitrogen concentration in the exhaust gases varies within the range of 74 up to 78%, and the oxygen content fluctuates from 2 up to 18% (air composition: nitrogen—about 78%, oxygen—about 21%, carbon dioxide—0.03–0.04%, and other inert gases—about 0.94%) [14].

For advanced homogeneous charge compression-ignition (HCCI) engines, a whole series of research studies have been performed in Russia and abroad on numerical and experimental modeling of the operation process, including with the exhaust gases recirculation [1, 3, 5–8, 16, 17, 19, 20, 22, 23]. However, the issue on the influence of the content of the inert components in the fuel–air mixture on the combustion process in general, and on the indicators of HCCI engines in particular, still remains insufficiently studied. One of the reasons for this is that the used mathematical models lack the qualitative assessment of the content of these components in the combustible mixture.

2 Mathematical Model of Fuel Combustion with Consideration to the Inert Components Content

To perform this analytical study, a mathematical model of fuel combustion in an internal combustion engine was used, based on the provisions described in detail in works [9–11]. The suggested mathematical model differs from the well-known ones by the fact that it allows to make qualitative assessment of how the combustion rate is influenced not only by the decrease in the oxygen content, but by the increase in the inert components content as well, what is characteristic of the real process of combustion.

According to the adopted scheme of the combustion process in an internal combustion engine, the rate of combustion is determined by expression:

$$w = \frac{dN}{d\tau} = \frac{Z_E}{\tau_y} \quad (1)$$

Here, dN —change in the quantity of substance resulting from the reaction; $d\tau$ —time interval; Z_E —quantity of active fuel molecules calculated using the well-known Arrhenius equation, depending on the energy of activation and temperature; τ_y —conditional duration of the active fuel molecules group oxidation reaction [9–11].

Value τ_y is determined by expression:

$$\tau_y = \frac{V}{\text{const} \cdot K_1 \cdot Z_F^{p-1} \cdot Z_{O_2}^q} \quad (2)$$

Here, const—constant, which takes into account the quantity of active collisions of molecules of the reacting substances, per unit time per unit volume; K_1 —coefficient of the oxygen reaction activity, which takes into account the influence of the inert components of the working medium (nitrogen and combustion products); Z_F , Z_{O_2} —quantities of molecules of fuel and oxygen in volume V , respectively; p , q —power exponents, meanwhile $p + q = n$ —the kinetic order of reaction, $n = 2$.

Thus, to obtain the numerical value of the combustion rate at any moment of time, it is sufficient to determine the quantity of active and simultaneously reacting fuel molecules and divide it by the conditional duration of their oxidization reaction.

The coefficient of the oxygen reaction activity K_1 is determined using the expression obtained based on the analysis of the dependency of the fuel ignition delay period [2] on the oxygen concentration in the oxidation agent CO_2 :

$$K_1 = 1 - \left(1 - \frac{Z_{\text{O}_2}}{Z_{\text{O}_2} + Z_{\text{N}_2} + Z_{\text{CO}_2} + Z_{\text{H}_2\text{O}} + Z_{\text{CO}}} \right)^6 \quad (3)$$

Here, Z_{N_2} , Z_{CO_2} , $Z_{\text{H}_2\text{O}}$ and Z_{CO} —quantities of the molecules of nitrogen, carbon dioxide, water, and carbon oxide in the volume V , respectively.

3 Numerical Research on the Influence of Inert Components on the Dimethyl Ether Combustion Process

Using the developed model, the calculated studies were performed for the combustion process of the homogeneous air mixture of dimethyl ether in case of its autoignition in the constant volume combustion chamber at the following initial conditions: pressure $p = 1.5$ MPa, temperature $T = 700$ K, and injection of dimethyl ether— 0.053×10^{-3} kg per cycle. The residual gases coefficient γ changed from 0 up to 0.5. The volume of the mixture corresponded to the volume of the combustion chamber of the HCCI engine with the cylinder diameter of 0.13 m and the piston stroke of 0.15 m at the compression ratio of 14 units. The constant volume of the combustion chamber was adopted in order to exclude the influence of the mixture ramming or expansion, resulting from the piston motion, on the process of combustion. The calculations were performed at the condition of the absence of the influence from the inert components (coefficient K_1 was assumed as equal to 1) and with consideration to the influence from the inert components by the value of coefficient K_1 , determined with expression (3). As a result of the combustion process, calculation graphs were built for changes in the pressure within the combustion chamber (Fig. 1) and the rate of dimethyl ether combustion (Fig. 2).

Figure 1a shows that for all the studied values of the residual gases coefficient without consideration to the inert components ($K_1 = 1$), the pressure in the combustion chamber grows faster and reaches a higher value. The maximum pressures equal from 4.68 MPa (at $\gamma = 0$) to 4.38 MPa (at $\gamma = 0.5$). The maximum pressure growth occurs in over 0.43–0.47 ms from the beginning of the combustion process. This corresponds to the moments of time in which the maximum rate of dimethyl ether combustion is reached (Fig. 2a). That is, in case when the influence only from the reacting components is taken into account, and the inert components influence on the conditional duration of the oxidization reaction τ_y is excluded, according

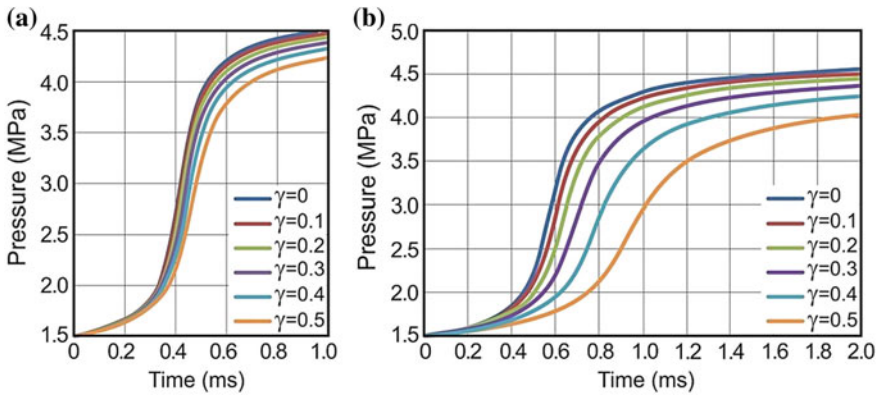


Fig. 1 Changes in the pressure in case of the combustion of the air mixture of dimethyl ether in the constant volume combustion chamber at different residual gases coefficients: **a** at the condition of $K_1 = 1$; **b** at the coefficient K_1 , calculated with expression (3)

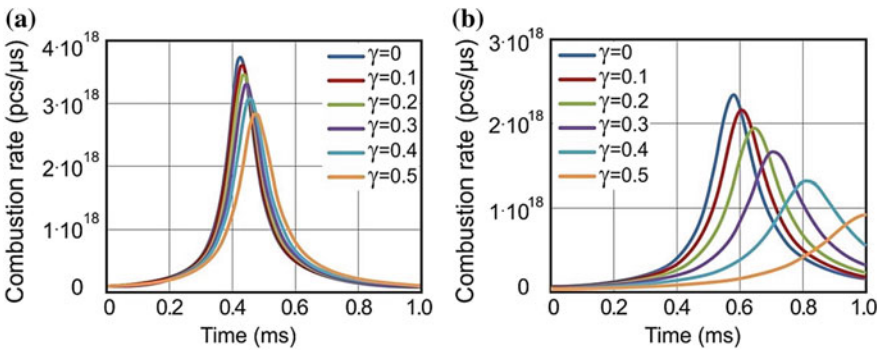


Fig. 2 Changes in the rate of combustion of dimethyl ether in the constant volume combustion chamber at different residual gases coefficients: **a** at the condition of $K_1 = 1$; **b** at the coefficient K_1 , calculated with expression (3)

with expression (2) (at the condition of $K_1 = 1$), the maximum values of the combustion rate and the moments of reaching it change insignificantly (Fig. 2a). At $\gamma = 0$, this rate equals 3.73×10^{18} molecules per 1 μ s, which is the equivalent of 8.2 J/ μ s in heat release rate. At $\gamma = 0.5$, the maximum combustion rate equals 2.84×10^{18} molecules per 1 μ s, which is the equivalent of 6.25 J/ μ s in heat release rate. That is, in case the residual gases coefficient increases from 0 up to 0.5 without consideration to the influence of the inert components according with expression (3), the combustion process slows down insignificantly. The maximum pressure reduces only by 0.3 MPa (6.4%) and occurs 0.04 ms (by 9.3%) later (Fig. 1a). And the maximum rate of combustion (heat release rate) decreases by 23.8% (Fig. 2a). Such results do not get confirmed by the experimental studies of the influence of the



degree of the exhaust gases recirculation on the combustion process in internal combustion engines [7, 8, 17, 21].

When taking into account the inert components by the coefficient K_1 , calculated according with expression (3), the pressure within the combustion chamber grows considerably more slowly and to lower values (Fig. 1b). The maximum pressures equal from 4.62 MPa (at $\gamma = 0$) to 4.16 MPa (at $\gamma = 0.5$). The maximum pressure growth occurs much later: in over 0.59 ms (at $\gamma = 0$) and in over 1.0 ms (at $\gamma = 0.5$) from the beginning of the combustion process. This corresponds to the moments of time in which the maximum rate of dimethyl ether combustion is reached (Fig. 2b). That is, in case when the simultaneous influence from the reacting and the inert components is taken into account using coefficient K_1 , a considerable slowdown in the combustion process is obtained (Fig. 2b). At $\gamma = 0$, this rate equals 2.34×10^{18} molecules per 1 μs , what is the equivalent of 5.15 J/ μs in heat release rate. At $\gamma = 0.5$, the maximum combustion rate equals 0.92×10^{18} molecules per 1 μs , which is the equivalent of 2.04 J/ μs in heat release rate. That is, in case the residual gases coefficient increases from 0 to 0.5 with consideration to the influence of the inert components as per expression (3), the combustion process slows down significantly. The maximum pressure reduces by 0.46 MPa (10%) and occurs 0.41 ms (by 69.5%) later (Fig. 1b). And the maximum rate of combustion (heat release rate) decreases 2.52 times (Fig. 2b).

Such degree of influence is confirmed by the results of the experimental studies of the influence of the degree of the exhaust gases recirculation on the combustion process in internal combustion engines [7, 8, 17, 21].

Figure 3 gives the graphs of the changes in the quantities of the oxygen molecules (Fig. 3a) and coefficient K_1 (Fig. 3b), obtained according to expression (3), with consideration to the influence of the inert components of the working medium.

Figure 3 demonstrates that the value of coefficient K_1 changes within the first 2.0 ms of the combustion similar to the quantity of the oxygen molecules. At $\gamma = 0$, the quantity of the oxygen molecules reduces from 4.2×10^{21} to 2.26×10^{21} , i.e., 1.86 times. And coefficient K_1 decreases from 0.75 to 0.49, i.e., 1.53 times. At $\gamma = 0.5$,

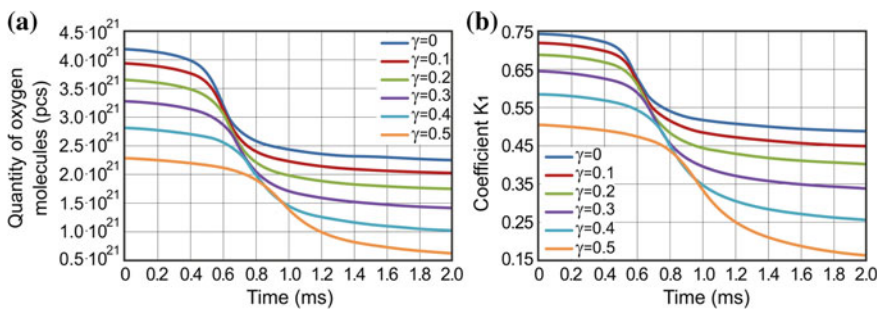


Fig. 3 Changes during the combustion process in the quantities of the oxygen molecules Z_{O_2} **a** in the constant volume combustion chamber and the coefficient K_1 and **b** at different residual gases coefficients

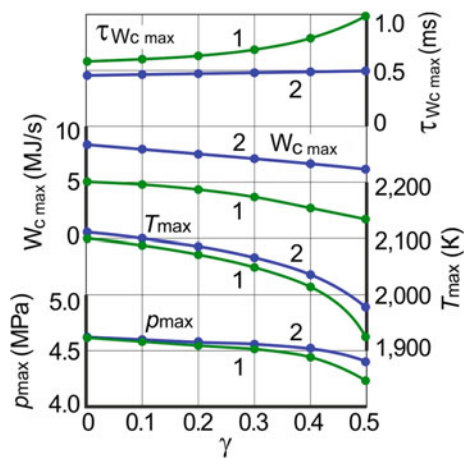
the quantity of the oxygen molecules reduces from 2.3×10^{21} to 0.6×10^{21} , i.e., 3.83 times. And coefficient K_1 decreases from 0.5 to 0.15, i.e., 3.33 times. This decrease leads to the increase in the conditional duration of the reaction of oxidization of the active fuel molecules τ_y (expression 2) and to respective slowdown in the rate of dimethyl ether combustion.

The use of coefficient K_1 allows to model the slowdown in the generation and duration of oxidization of the active fuel molecules in the process of combustion according to the changes in the composition of the combustible mixture (decrease in the oxygen content and increase in the inert components content) at different residual gases coefficients. For example, in case of the absence of residual gases ($\gamma = 0$), the initial value of the coefficient of the oxygen reaction activity K_1 within the duration of the combustion of 1 ms decreases from 0.75 down to 0.52, i.e., 1.44 times. This increases the conditional duration of the oxidization of the active fuel molecules, as compared to the absence of the inert components, 1.32 times in the beginning of the combustion and 1.92 times in the end of the combustion process (Fig. 2b does not show the end of the combustion).

As a result, the conditional duration of the reaction of oxidization of the active fuel molecules, calculated with consideration to coefficient K_1 , in the process of combustion increases faster when the inert components are not taken into account. At the studied maximum residual gas coefficient of 0.5, the coefficient of the oxygen reaction activity K_1 decreases from its initial value of 0.5 to less than 0.1, i.e., more than five times (Figs. 2b and 4 do not show the end of the combustion). This leads to significant slowdown in the combustion process, despite the mixture enrichment to $\lambda = 1.03$.

Thus, introducing the coefficient of the oxygen reaction activity K_1 to the expression for determining the conditional duration of the oxidization reaction of the active fuel molecules τ_y (2) has allowed to correct the calculated quantity of active collisions of molecules of the reacting substances (per unit time per unit volume) due to the increase in the quantity of the inert molecules being generated in

Fig. 4 Influence of the residual gases coefficient γ on the indicators of the combustion process: 1—at the coefficient K_1 , calculated with expression (3); 2—at the condition of $K_1 = 1$



the process of combustion. As a result, the calculated combustion process with consideration to the influence from the inert components has become “softer” and more durable in time, for instance, at $\gamma = 0$, the value of the calculated maximum combustion rate decreased ~ 1.6 times and shifted in time by $\sim 37\%$.

The summary of the results of the residual gas coefficient influence on the indicators of the combustion process of the homogeneous air mixture of dimethyl ether in the constant volume combustion chamber is given in Fig. 4. It is demonstrated that with the increase in the residual gas coefficient γ , the maximum values of the combustion rate, as well as of the pressure and temperature within the combustion chamber decrease, and the moments, when the maximum combustion rate is reached, increase. The taking into account of the inert components influence by the coefficient of the oxygen reaction activity K_1 has made the dependency of these indicators on the residual gases content in the combustible mixture more obvious, which agrees with the available data on their influence on the processes of ignition and combustion [7, 8, 13, 16, 17, 21].

4 Conclusions

Based on the described analysis of the numerical research results on the influence of the inert components on the process of dimethyl ether combustion in the constant volume combustion chamber, the following conclusions have been made.

1. Using the coefficient of the oxygen reaction activity K_1 allows to model the slowdown in the rate of combustion of the combustible mixture by means of the inert components in case of the changes in the mixture composition caused by combustion and recirculation of the exhaust gases.
2. The increase in the inert components content in the combustible mixture in case of the exhaust gases recirculation (increase of the residual gases coefficient from 0 up to 0.5) results in the slowdown of the development of the process of dimethyl ether combustion, decrease in the maximum combustion rate and postponed achieving of this rate. The maximum calculated combustion rate without consideration to the inert components decreases by 23.8%. And taking into account the inert components by coefficient K_1 , it decreases 2.52 times. In the first case, the maximum combustion pressure decreases only by 0.3 MPa (6.4%) and is registered 0.04 ms (9.3%) later. In the second case, the maximum combustion pressure decreases by 0.46 MPa (10%) and is registered 0.41 ms (69.5%) later, though the initial amount of oxygen decreases identically—1.86 times.
3. The main causes of the slowdown of the dimethyl ether combustion in the conditions under study are the decrease in the initial amount of the oxygen molecules and the (1.53 times) decrease in the reaction activity of oxygen.
4. The developed mathematical model of the combustible mixture inert components influence on the combustion process allows to obtain close-to-real-life

results at different modes of operation. This will allow to study the possible methods of influencing it for the purpose of reducing the toxicity of the exhaust gases in compression ignition engines.

References

1. Chen Z, Konno M, Oguma M et al (2000) Experimental study of CI natural-gas/DME homogeneous charge engine. SAE technical paper series 2000-01-0329:1-10
2. Dubovkin NF (1962) Handbook of the thermophysical properties of hydrocarbon fuels and their products of combustion. Gosenergoizdat, Moscow-Leningrad
3. Flowers D, Aceves S, Smith R et al (2000) HCCI in a CRF engine: experiments and detailed kinetic modeling. SAE technical paper series 2000-01-0328:1-13
4. Grekhov LV, Ivashchenko NA, Markov VA (2005) Fuel systems and diesel engine control systems: text book for higher school, 2nd edn. Legion-Autodata Press, Moscow
5. Gusakov SV, Mohamed M, El Hagar EG (2003) Algorithm of processing indicator diagrams for HCCI-process on mixed fuel: dimethyl ether/natural gas. Series 'Automobile Transport', vol 7. Tidings of the Tula State University, pp 179-184
6. Gusakov SV, Mohamed M, El-Hagar EG (2003) Simulation of combustion process reciprocating engine with homogeneous charge compression ignition. Series 'Automobile Transport', vol 7. Tidings of the Tula State University, pp 173-179
7. Jang J, Lee Y, Cho C, Woo Y, Bae C (2013) Improvement of DME HCCI engine combustion by direct injection and EGR. Fuel 113:617-624
8. Jung D, Iida N (2017) Thermal and chemical effects of the in-cylinder charge at IVC on cycle-to-cycle variations of DME HCCI combustion with combustion-phasing retard by external and rebreathed EGR. Appl Therm Eng 113:132-149
9. Kamaltdinov V (2011) Combustion process modeling in HCCI engine. SAE technical paper series 2011-01-1789:1-10
10. Kamaltdinov VG (2008) New model of fuel combustion in diesel engines. Dvigatelistroyeniye 3:17-20
11. Kamaltdinov VG, Markov VA (2010) Influence of the cylinder hot surface temperature on the combustion process and on the HCCI engine working cycle characteristics. Truck 12:38-47
12. Kind W, Jacob E, Muller W (2001) NO_x—Verminderung bei Dieselmotoren. MTZ 62:70-78. <https://doi.org/10.1007/BF03227083>
13. Lima O, Jamsran N, Iida N (2014) A computational study of the effects of initial conditions on DME autoignition characteristics. Energy Procedia 61:1577-1580
14. Markov VA, Bashirov RM, Gabitov II (2008) The toxicity of diesel engines exhaust gases. Bauman Moscow State Technical University Press, Moscow
15. Markov VA, Gayvoronskiy AI, Grekhov LV et al (2008) Diesel engines operation on alternative fuels. Legion-Autodata Press, Moscow
16. Nishi M, Kanehara M, Iida N (2016) Assessment for innovative combustion on HCCI engine by controlling EGR ratio and engine speed. Appl Therm Eng 99:42-60
17. Putrasari Y, Jamsran N, Lim O (2017) An investigation on the DME HCCI autoignition under EGR and boosted operation. Fuel 200:447-457
18. Smaylis VI (1991) Current state and new problems of diesel engine production ecology. Dvigatelistroyeniye 1:3-6
19. Yao M, Chen Z, Zheng Z et al (2005) Effect of EGR on HCCI combustion fuelled with dimethyl ether (DME) and methanol dual-fuels. SAE technical paper series 2005-01-3730:1-8

20. Yao M, Zheng Z, Qin J (2006) experimental study on homogeneous charge compression ignition combustion with fuel of dimethyl ether and natural Gas. Transactions of the ASME. J Eng Gas Turbines Power 128:414–420
21. Yoon SH, Han SC, Lee CS (2013) Effects of high EGR rate on dimethyl ether (DME) combustion and pollutant emission characteristics in a direct injection diesel engine. Energies 6:5157–5167. <https://doi.org/10.3390/en6105157>
22. Zheng Z, Yao M, Chen Z et al (2004) Experimental study on HCCI combustion of dimethyl ether (DME)/methanol dual-fuel. SAE technical paper series 2004–01–2993:1–9
23. Zheng Z, Yao M, Wang Y et al (2003) Experimental study on HCCI combustion process fueled with DME. J Combust Sci Technol 9:561–565

Results of Bench Tests of Pneumatic Suspension with Air-Hydraulic Damping



V. V. Novikov, A. V. Pozdeev and D. A. Chumakov

Abstract The chapter presents a brief description of the experimental unit made on the basis of a dynamic test bench and the results of bench tests of a single-support pneumatic suspension, including sprung and unsprung masses, pneumatic spring with a sleeve-type rubber-cord casing, air damper mounted in the piston of the air spring, receiver and hydraulic shock absorber. The chapter contains the following: elastic characteristics of air springs with different operating volumes, damping characteristics of the hydraulic shock absorber, oscillograms of free damped oscillations of the sprung mass of 0.5 t after the push of the suspension from the bottom up and down by 100 mm, amplitude-frequency characteristics of oscillations of the sprung and unsprung masses at a harmonic kinematic disturbance with an amplitude of 12 mm. The maximum temperature and the time of reaching the steady-state temperature of the various surfaces of the air spring are determined with the help of a permanently installed professional thermal imaging camera.

Keywords Air spring · Air damper · Hydraulic shock absorber · Bench tests · Heating

1 Introduction

One of the ways to improve the vibration-protective properties of the mechanical transport vehicle suspensions is the use of pneumatic (air) springs with sleeve-type rubber-cord casings [1], which works together with air dampers and hydraulic shock absorbers [2–29]. However, the lack of research in this area hinders the implementation of such cushion systems.

Below is a brief description of the experimental unit [28–30] and the results of bench tests of the air suspension, which are presented in the form of diagrams of elastic characteristics of air spring with different operating volumes, damping

V. V. Novikov · A. V. Pozdeev (✉) · D. A. Chumakov
Volgograd State Technical University, 28, Lenin Ave., Volgograd 400005, Russia
e-mail: pozdeev.vstu@gmail.com

characteristics of hydraulic shock absorber, oscillograms of free damped oscillations of the sprung mass, amplitude-frequency characteristics of the swing of vibrations of the sprung and unsprung masses, as well as diagrams of the temperature dependence on the time of the steady-state temperature for different air spring surfaces.

2 Experimental Unit

The experimental unit (Fig. 1) consists of a sprung mass 1 and unsprung mass 2, spring 3, simulating the wheel tire, air spring 4 and hydraulic shock absorber 20 made by KYB, which with the help of the guide arms of the suspension can be installed with a different gear ratio, that provides a change in its force reduced to the axis of suspension.

The basic elements of air spring: sleeve-type rubber-cord casing 4; elongated hollow piston 6; air damper 7, which is a choke with a diameter of 6 mm and a check valve open during the compression. The operating volume of rubber-cord

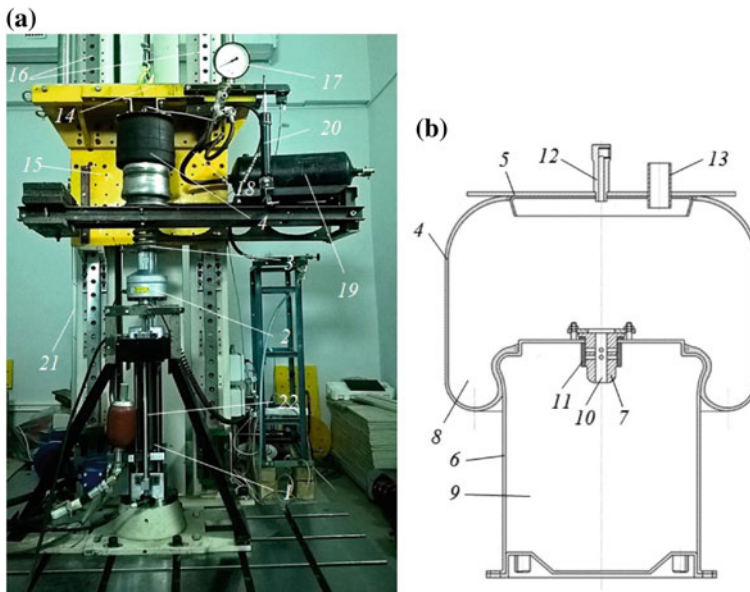


Fig. 1 Experimental unit for bench tests of air spring with air damper and hydraulic shock absorber: **a** general form; **b** design of air spring; 1—hydraulic pulsator; 2—force sensor; 3—support plate of hydraulic pulsator; 4—rubber-cord casing of air spring; 5—top cover; 6—hollow piston of air spring; 7—air damper; 8—over piston cavity; 9—piston cavity; 10—throttle; 11—check valve; 12—filling fitting; 13—pipe; 14—traverse; 15—sprung mass; 16—vertical guides; 17—manometer; 18—hose; 19—receiver; 20—hydraulic shock absorber; 21—displacement and velocity sensor; and 22—position sensor

casing under static load was 11 L, and the piston volume was 7.6 L. In addition, rubber-cord casing cavity can be connected by means of a hose to the receiver with a volume of 20 L. The cross-sectional diameter of the hose is 20 mm.

Tests were carried out at the dynamic test bench of “Automatic installations” Department of Volgograd State Technical University developed together with the companies BISS-ITW (India) and “Test benches,” LLC (Russia). The main power elements of the test bench are a horizontal support base, a hydraulic pulsator, a vertical guide rack with a movable frame and loads simulating a sprung mass, a winch. In addition, the test bench includes: pumping station with the radiator and servo-hydraulic valves, stand with control unit of electronic modes of test bench operation and recording the registered parameters. This test bench allows you to test different types of suspensions in a wide range of power and kinematic loading.

During the tests, the following parameters and loading modes were set: Sprung mass is 500 kg; unsprung mass is 130 kg; pressure in air spring is 0.12 MPa; height of air spring under static loading is 450 mm; value of a push of a hydraulic pulsator up and down is 100 mm; and amplitude of harmonic fluctuations of a hydraulic pulsator is 12 mm. Tests were carried out in the laboratory at the temperature of 22...23 °C without the use of forced air blowing for air spring cooling.

3 Results of Bench Tests

The test results are shown in Figs. 2, 3, 4 and 5.

Figure 2a shows that with an increase in the operating volume of air spring from 11 to 38.6 L, the stiffness of the suspension decreases sharply. From Fig. 2b, it follows that hydraulic shock absorber force during the rebound is much greater than during the compression.

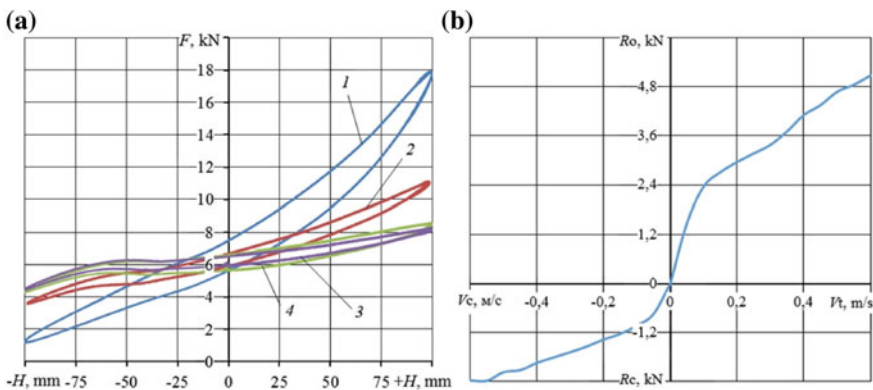


Fig. 2 Characteristics of the elements of the tested suspension: **a** elastic characteristics of air spring with different operating volumes; **b** damping characteristic of hydraulic shock absorber KYB; 1—11 L; 2—18.6 L; 3—31 L; and 4—38.6 L

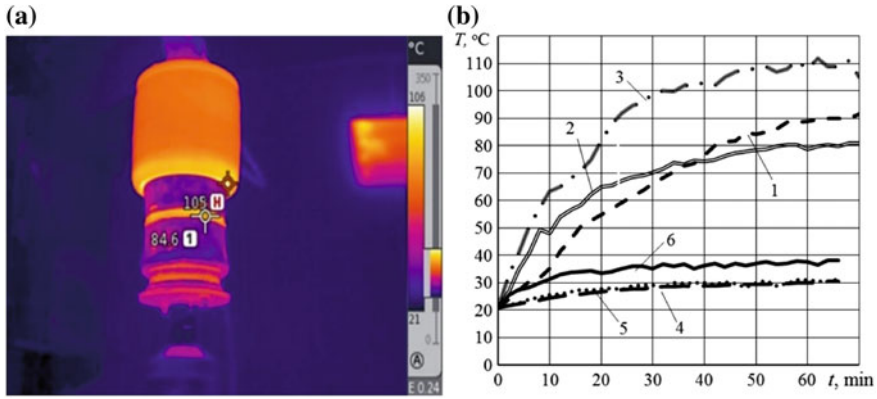


Fig. 3 Results of thermographic tests of the air spring: **a** thermogram of the air spring with operating volume of 18.6 L, with a 6 mm throttle and a check valve; **b** heating curves of the air spring at different operating volumes with a damping unit in the form of the throttle and the check valve; 1, 2, 3—air spring with a displacement of 18.6 L; 4, 5, 6—air spring with operating volume of 38.6 L; 1, 4—heating of the piston side; 2, 5—heating the surface of the middle part of the rubber-cord casing; 3, 6—heating of the belt inversion of the rubber-cord casing

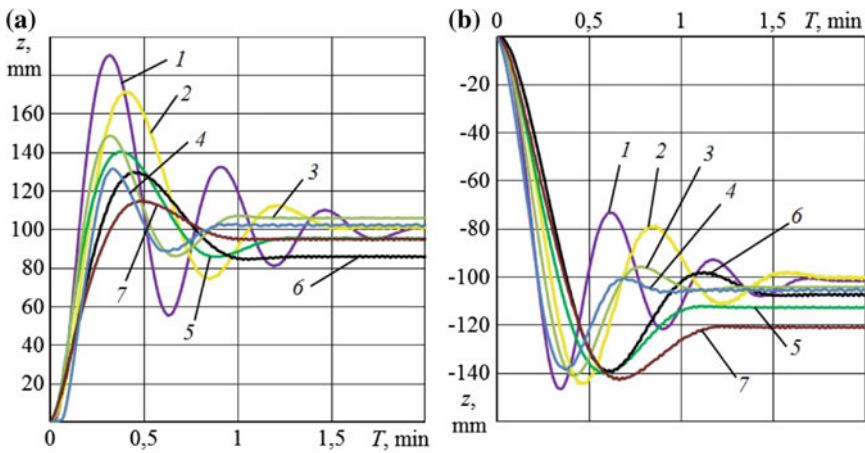


Fig. 4 Oscillograms of free damped oscillations of the sprung mass on the air spring with different operating volumes in the absence and presence of a hydraulic shock absorber and air damper: **a** after pushing up 100 mm; **b** after pushing down 100 mm; 1—air spring with operating volume of 11 L; 2—air spring with operating volume of 18.6 L; 3—air spring with operating volume of 18.6 L and the air damper; 4—air spring with operating volume of 18.6 L, the air damper and the hydraulic shock absorber; 5—air spring with operating volume of 31 L; 6—air spring with operating volume of 38.6 L; 7—air spring with operating volume of 38.6 L and the air damper

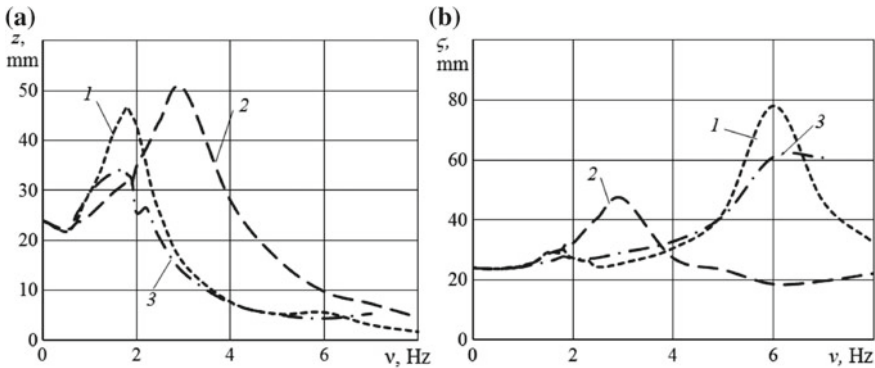


Fig. 5 Experimental amplitude-frequency characteristics of displacement of sprung mass **a** and unsprung mass **b** on the air suspension with operating volume of 18.6 L and dampers: 1—weak hydraulic shock absorber; 2—powerful hydraulic shock absorber; 3—air damper and weak hydraulic shock absorber

In Fig. 3a, zones of the greatest heating of air spring elements surfaces are shown by brighter color. From Fig. 3b, it follows that the highest maximum heating temperature is reached when the piston throttle with a check valve is installed. Upon that, the maximum piston heating temperature (curve 1) is higher than the rubber-cord casing (curve 2). With an increase in the operating volume of air spring from 18.6 to 38.6 L and installation of the throttle with a check valve in the piston, the piston heating temperature decreases from +90 to +30 °C, the middle part of rubber-cord casing—from +80 to +30 °C and the belt inversion of rubber-cord casing—from +110 to +37.2 °C, that is 2.5...3 times (Fig. 3b).

Figure 4a shows that after pushing the piston of air spring up to 100 mm, the increasing of the operating volume from 11 L (curve 1) to 18.6 L (curve 2) reduces the damping time of sprung mass from 1.92 to 1.5 s and reduces the natural oscillation frequency of air spring from 1.67 to 1.25 Hz. The increase in the operating volume of air spring to 31 L (curve 5) and 38.6 L (curve 6) reduces the damping time of air spring to 1.23 and 1.0 s, respectively. Upon that, the character of free damped oscillations approaches the aperiodic law. In addition, with an increase in the volume of air spring from 11 L (curve 1) to 38.6 L (curve 6), the amplitude of the first half-period of oscillation decreases from 88 to 29 mm. In this case, the installation of air damper in the piston (curves 3 and 7) practically does not affect the damping time of air spring oscillations. With an operating volume of 18.6 L, the installation of air damper in the piston (curve 3) reduces the amplitude of the first half-period of oscillation from 70.8 to 48 mm that is almost 1.5 times. The use of weak hydraulic shock absorber together with air damper (curve 4) reduces almost 2 times the amplitude of air spring and the nature of free damped oscillations approaching the aperiodic law.

Figure 4b shows that after pushing air spring piston down by 100 mm with an increase in the operating volume from 11 L (curve 1) to 18.6 L (curve 2), the

damping time and the amplitude of sprung mass oscillations decrease slightly, and the natural oscillation frequency decreases from 1.81 to 1.28 Hz. This corresponds to an increase in the relative attenuation coefficient from 0.18 to 0.25. The increase in the operating volume of air spring to 31 L (curve 5) and 38.6 L (curve 6) reduces the damping time of the oscillations to 1.1 and 1.5 s, respectively. Upon that, the character of free damped oscillations approaches the aperiodic law. The increase in the operating volume of air spring from 11 L (curve 1) to 38.6 L (curve 6) slightly affects the oscillation amplitude. Upon that, the installation of air damper in the piston at operating volumes 18.6 (curve 3) and 38.6 L (curve 7) reduces the damping time of air spring to 1.36 and 1.17 s and practically does not affect the reduction of the vibration amplitude. Efficiency of air spring working together with hydraulic shock absorber during the descent of a 100 mm is reduced compared with a rise of 100 mm.

Figure 5 shows the experimental amplitude-frequency characteristics of vertical oscillations of sprung mass and unsprung mass on a pneumatic suspension with an operating volume of 18.6 L at a harmonic kinematic perturbation with amplitude of 12 mm.

Figure 5 shows that the suspension with a weak hydraulic shock absorber (curve 1) provides the sprung mass oscillation damping in the area of low frequencies with a coefficient of vibration, equal to 1.9. This corresponds to the relative attenuation coefficient $\psi = 0.32$, which is typical for most modern car suspensions. Upon that, the oscillations of unsprung mass in the zone of high-frequency resonance of the wheel are quenched much worse—with a coefficient of vibration protection equal to 3.2. In comparison with light damping, the increase in hydraulic shock absorber power (curve 2) leads to a shift of resonance toward higher frequencies by 1 Hz and an increase in the amplitude of resonant oscillations of sprung mass more than 2.5 times. However, the oscillations of unsprung mass in the zone of high-frequency resonance of the wheel become less than the kinematic perturbation. Application of the air damping (curve 3) in air suspension with weak hydraulic shock absorber provides additional reduction in oscillations in low-frequency resonance of air spring by 28% and in high-frequency resonance of unsprung mass by 23%.

4 Conclusions

- The experimental unit allowing to carry out bench tests of a pneumatic suspension with the combined air-hydraulic damping is developed.
- The use of air-hydraulic damping with an increase in the operating volume of the air compressor leads to a significant increase in the vibration properties of vehicle air suspension.
- Heating elements of the air compressor even with no air cooling does not exceed the permissible limits, the maximum values of which are sharply reduced when connecting the receiver, which makes it possible to recommend the use of the air damper to increase the vibroprotective properties of the vehicle air suspension.

References

1. Pevzner YM, Gorelik AM (1963) Pnevmaticheskie i gidropnevmaticheskie podveski (Pneumatic and hydropneumatic suspensions). Moscow, p 319
2. Novikov VV (2007) Stendovye ispytaniya pnevmopodveski avtobusa VZTM-32731 s gidroamortizatorami raznoj moshchnosti (Bench tests of the pneumatic suspension of the bus VZTM-32731 with hydraulic shock absorbers of different power). Gruzovik 6:41–44
3. Novikov VV (2007) Stendovye ispytaniya pnevmopodveski s vozdushnym dempferom v vide drosselya i obratnogo klapana (Bench tests of pneumatic suspension with air damper in the form of a throttle and a check valve). Gruzovik 7:43–46
4. Novikov VV, Bukaev SO, Diyakov AS (2008) Sovmestnaya rabota vozdušnogo dempfera i gidroamortizatora (Joint operation of the air damper and hydraulic shock absorber). Avtomobil'naya promyshlennost' 1:20–22
5. Kalashnikov BA (2008) Sistemy amortizatsii ob'ektov s diskretnoj kommutatsiej uprugih ehlementov (Systems of depreciation of objects with discrete switching of elastic elements). Omsk State Technical University, Omsk, p 344
6. Novikov VV, Ryabov IM, Chernyshov KV (2009) Vibrozashchitnye svoystva podvesok avtotransportnyh sredstv (The vibration isolation properties of the motor vehicles suspensions). Volgograd State Technical University, Volgograd, p 338
7. Novikov VV et al (2009) Zadnyaya podveska koles avtomobilya (Rear suspension vehicle wheels). RUS Utility model, vol 85, p 403, Aug 2009
8. Novikov VV, Pozdeev AV (2010) Opredelenie optimal'nyh algoritmov regulirovaniya aktivno-upravlyаемых pnevmopodvesok (Determination of optimal control algorithms for actively-controlled pneumatic suspensions). Gruzovik & 5:6–10
9. Chernyshov KV et al (2010) Opredelenie uslovij optimal'nogo regulirovaniya zhyostkosti pnevmaticheskoy podveski ATS (Determining the conditions for the optimal regulation of the stiffness of the pneumatic vehicle suspension). Gruzovik 11:2–5
10. Novikov VV et al (2011) Pnevmaticheskaya podveska (Pneumatic suspension). RUS Utility model, vol 109, p 698, Jun 2011
11. Ryabov IM et al (2011) Podveska kolesa avtomobilya (Car wheel suspension). RUS Utility model, vol 109, p 697, Jul 2011
12. Pozdeev AV et al (2013) Reguliruemye pnevmaticheskie i pnevmogidravlicheskie resory podvesok avtotransportnyh sredstv (Controlled air and air-hydraulic springs of vehicle suspensions). Volgograd State Technical University, Volgograd, p 244
13. Pozdeev AV et al (2013) Issledovaniya dvuhkamernoj pnevmaticheskoy resory s kommutatsiej polostej (Studies of a two-chamber air spring with cavity switching). Gruzovik 1:35–37
14. Pozdeev AV et al (2013) Samoreguliruemye dvuhkamernye pnevmaticheskie resory s kommutatsiej polostej (Self-regulating two-chamber pneumatic springs with cavity switching). Gruzovik 9:2–5
15. Pozdeev AV (2015) Vibrozashchitnye svoystva dvuhpolostnyh pnevmaticheskikh resor na osnove sinteza optimal'nyh algoritmov kommutatsii polostej (Vibroprotective properties of dual-chamber air springs based on the synthesis of optimal cavity switching algorithms). Tekhnologiya kolyosnyh i gusenichnyh mashin 1:27–31
16. Novikov VV et al (2015) Vibrozashchitnye svoystva pnevmaticheskoy podveski s dinamicheskim gasitelem kolebanij kolyos i suhim treniem (Vibroprotective properties of pneumatic suspension with a dynamic vibration damper and dry friction). Oboronnaya tekhnika 9–10:102–106
17. Klimentiev EV, Korneev VS, Korneev SA (2015) Matematicheskoe modelirovanie ter-modinamicheskikh processov v pnevmaticheskikh ehlementah s vozdushnym dempfirovaniem (Mathematical modeling of thermodynamic processes in pneumatic elements with air damping). Omskij nauchnyj vestnik 3(143):130–138

18. Klimentiev EV, Korneev VS, Korneev SA (2015) Chislennyj analiz raboty pnevmati-cheskogo amortizatora pri standartnom rezhime nagruzeniya i raznyh algoritmah upravleniya (Numerical analysis of pneumatic shock absorber operation under standard loading mode and different control algorithms). Omskij nauchnyj vestnik 3(143):138–145
19. Korneev SA, Korneev VS, Klimentiev EV (2015) Gas-dynamic processes mathematical modeling in pneumatic components with air damping. In: Radionov AA (ed) Procedia engineering, international conference on industrial engineering (ICIE-2015), vol 113. Elsevier publishing, pp 276–281. <https://doi.org/10.1016/j.proeng.2015.07.265>
20. Korneev SA et al (2016) Osnovy tekhnicheskoy teorii pnevmaticheskikh amortizatorov (Fundamentals of the technical theory of pneumatic shock absorbers). Omsk State Technical University, Omsk, p 147
21. Zubarev AV et al (2016) Sposob tekhnicheskogo obespecheniya tem-peraturnogo rezhima raboty amortizatora vozdušnogo dempfirovaniya (The method of technical support of the temperature mode of operation of the air damping shock absorber). Dinamika sistem, mekhanizmov i mashin 1:43–45
22. Novikov VV et al (2017) Sovmestnaya rabota pnevmaticheskoy podveski ATS s dinamicheskim gasitelem kolebanij kolyos i gidroamortizatorom (Joint operation of an pneumatic vehicle suspension with a dynamic vibration damper and a hydraulic shock absorber). Vestnik mashinostroeniya 7:34–39
23. Korneev SA, Korneev VS, Adonin VA (2017) Termodinamicheskij metod postroeniya rabochih harakteristik pnevmaticheskikh ehlementov (vozdušnyh pruzhin) s uprugou deformiruemoj rezinokordnoj obolochkoy (Thermodynamic method for constructing the performance characteristics of pneumatic elements (air springs) with an elastically deformable rubber-cord casing). Sovremennyye tekhnologii. Sistemnyj analiz. Modelirovanie 4(56):8–18
24. Novikov VV et al (2018) Zadnyaya pnevmopodveska kolyos avtomobilya s kombinirovannoj dempfiruyushchej sistemoy (Rear pneumatic suspension of car wheels with a combined damping system). Progress transportnyh sredstv i sistem—2018, Volgograd, pp 65–67
25. Chernyshov KV et al (2018) Matematicheskaya model' pnevmaticheskoy podveski s kombinirovannoj dempfiruyushchej sistemoy (Mathematical model of pneumatic suspension with combined damping system). Progress transportnyh sredstv i sistem—2018, Volgograd, pp 57–59
26. Novikov VV et al (2018) Pnevmaticheskaya podveska s uprugoj harakteristikoj v vide «babochki» (Pneumatic suspension with elastic characteristics in the form of “butterfly”). Progress transportnyh sredstv i sistem—2018, Volgograd, pp 75–77
27. Novikov VV, Pozdeev AV, Chumakov DA (2018) Termograficheskie issledovaniya rezi-nokordnoj pnevmaticheskoy resory na stende-gidropul'satore (Thermographic studies of rubber-cord pneumatic spring on a bench-hydropulsator). Progress transportnyh sredstv i sistem—2018, Volgograd, pp 61–63
28. Novikov VV, Pozdeev AV, Chumakov DA (2018) Ehksperimental'noe issledovanie vliyaniya dopolnitel'nogo ob"yoma i dempfiruyushchego ustrojstva na svobodnye zatu-hayushchie kolebaniya diafragmennyh pnevmaticheskikh resor (Experimental study of the effect of the additional volume and damping device on the free damped oscillations of diaphragm air springs). Vestnik Irkutskogo gos. tekhnicheskogo un-ta 10:212–226
29. Novikov VV et al (2018) Ehksperimental'noe issledovanie pnevmaticheskoy podveski s kombinirovannym dempfirovaniem (Experimental study of pneumatic suspension with combined damping). Gruzovik 9:3–7
30. Novikov VV, Pozdeev AV, Diyakov AS (2015) Research and testing complex for analysis of vehicle suspension units. In: Radionov AA (ed) Procedia engineering, international conference on industrial engineering (ICIE-2015), vol 129. Elsevier publishing, pp 465–470. <https://doi.org/10.1016/j.proeng.2015.12.153>

Investigation of Stress-Strain State of Ball Mill Trunnion



Ju. A. Bondarenko, S. I. Khanin and O. V. Bestuzheva

Abstract The article discusses the trunnion of a ball mill in the framework of the theory of elasticity, which is subjected to uneven thermal effects due to the heating load. Long-term operation of the mills leads to a significant wear of mainly mechanical parts of the supporting rotating parts—pins. There are various defects on the working surface of the trunnion, which, under the action of dynamic loads, contributes to the loss of working capacity and long downtime during repair. The study of the stress-strain state will determine the parameters for restoring the cylindrical surface of the trunnion. The equations describing the radial displacement of a point inside the trunnion of a ball mill are obtained. The equations describing the movement of the trunnion points of the ball mill are derived. The stress-strain state of the trunnion of the ball mill was determined depending on the temperature of the inner and outer surfaces of the trunnion. Deformations and stresses arising on the surface of a pin are investigated by numerical methods.

Keywords Ball mill · Trunnion · Stress-strain state

1 Introduction

In the production of building materials, main equipment for grinding raw materials is a ball mill. As a result of impact of free-falling grinding bodies, which are used as balls, grinding of raw materials takes place in a rotating drum along with material to be grounded under the action of centrifugal forces.

Long-term operation of the mills leads to a lot of wear and tear mainly to the mechanical parts supporting the rotating parts—trunnions. There are various defects

Ju. A. Bondarenko (✉) · S. I. Khanin
BSTU named after V.G. Shukhov, 46, Kostyukov Str., Belgorod 308012, Russia
e-mail: kdsm2002@mail.ru

O. V. Bestuzheva
Belgorod National Research University, 85, Pobedy Str., Belgorod 308015, Russia

on the working surface of the trunnion. Dynamic loads contribute to the loss of efficiency and long downtime during repair. The study of the stress-strain state will determine the parameters for restoring the cylindrical surface of the trunnion.

2 Getting the Source Data for Mathematical Description of the Stress-Strain State of Trunnion

In the framework of the theory of elasticity, we consider a ball mill, which due to the heating of the loading materials, is subjected to an uneven thermal effect in terms of volume. As a result, there is a temperature field, which in turn, will lead to thermal deformations and stresses.

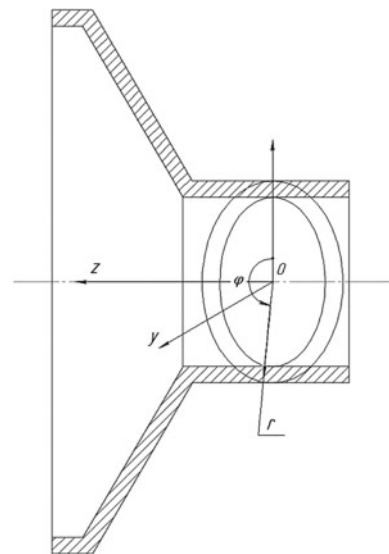
This section is devoted to the mathematical description of the deformation field and stresses in the ball mill axle. Among other reasons that cause stress-strain state of ball mill axle is the temperature field, which changes in the radial direction:

$$T = T(r), \quad (1)$$

where r varies in the following limits $R_1 \leq r \leq R_2$ (R_1 —inner radius of trunnion of ball mill; R_2 is the external radius of the axle).

In virtue of the axial symmetry, we introduce cylindrical coordinate system (r, φ, z) according to the design scheme presented in Fig. 1. The trunnion of ball mill will be considered as a thick-walled cylindrical tube with radial temperature change (1). Neglecting the influence of the ends can be assumed that in the perpendicular to the axis OZ of the sections are equal and are flat.

Fig. 1 Calculation scheme for choosing a coordinate system



On the basis of the made assumptions, we can conclude that the radial displacement of the point U in the trunnion of the ball mill depends only on one coordinate r , moving in the azimuthal direction, and elongation in the direction of OZ axis is constant:

$$\varepsilon_z = \text{const.} \quad (2)$$

In turn, relative elongations in radial direction:

$$\varepsilon_r = \frac{dU}{dr}, \quad (3)$$

in azimuthal direction:

$$\varepsilon_\phi = \frac{U}{r}. \quad (4)$$

The physical equations describing voltage field in cylindrical coordinates have following form [1]:

$$\sigma_z = 2G\varepsilon_z + \lambda\phi_0 - \eta T(r), \quad (5)$$

$$\sigma_r = 2G\varepsilon_r + \lambda\phi_0 - \eta T(r), \quad (6)$$

$$\sigma_\phi = 2G\varepsilon_\phi + \lambda\phi_0 - \eta T(r), \quad (7)$$

where $\sigma_z, \sigma_r, \sigma_\phi$ —respectively diagonal components of voltage tensor. For brevity, the following notation is entered as follows:

$$\phi_0 = \varepsilon_z + \lambda\varepsilon_r - \varepsilon_\phi, \quad (8)$$

$$\eta = 2G\alpha \frac{1+\nu}{1-2\nu}, \quad (9)$$

$$\lambda = \frac{2\nu G}{1-2\nu}, \quad (10)$$

$$G = \frac{E}{2(1+\nu)}. \quad (11)$$

where E —module of elasticity; ν —coefficient of Poisson; and α —coefficient of linear thermal expansion.

Substitutions (3), (4) in (6) and (7) allow to take next proportion:

$$\sigma_r = 2G \frac{dU}{dr} + \lambda\phi_0 - \eta T(r), \quad (12)$$

$$\sigma_{\phi} = 2G \frac{U}{r} + \lambda \phi_0 - \eta T(r), \quad (13)$$

Suppose that, as in the case of the solution of the thick-walled ring problem [2], the following equilibrium condition must be satisfied:

$$\sigma_r - \sigma_{\phi} r \frac{dU}{dr} = 0. \quad (14)$$

Expressions (2)–(14) are the starting point for obtaining the equations describing stress-strain state of trunnion of ball mill.

3 Getting the Source Data for Mathematical Description of the Stress-Strain State of Trunnion

According to the result of [2], if the inner and outer surfaces of the thick-walled pipe are maintained, respectively, constant temperature T_{R_1} and T_{R_2} , then for such a steady flow of temperature distribution over the wall thickness is the following formula:

$$T(r) = \frac{T_{R_1} \ln \frac{R_2}{r} + T_{R_2} \ln \frac{r}{R_1}}{\ln \frac{R_2}{R_1}}. \quad (15)$$

The motion of the point U is conveniently represented as an Integral with a variable upper limit:

$$U(r) = \frac{C_{10}}{r} + C_{20} \cdot r + \frac{\alpha}{r} \cdot \frac{1+\nu}{1-\nu} \int_{R_1}^r \chi T(x) dx. \quad (16)$$

To determine the arbitrary constants C_{10} and C_{20} , it is necessary to use the boundary conditions, which are superimposed on the stress values, acting on the inner R_1 and outer R_2 radiuses of the mill axle:

$$\sigma_r(r = R_1) = \sigma_0, \quad (17)$$

$$\sigma_r(r = R_2) = 0, \quad (18)$$

where σ_0 —the value of the voltage tested by the inner radius of the mill axle under the action of loading.

Substitution (15) in (16) and the application of boundary conditions and the condition of the absence of the axial load of the ball mill written as follows:

$$2\pi \int_{R_1}^{R_2} \sigma_z r dr = 0. \quad (19)$$

Allows to obtain unknown values C_{10} and C_{20} :

$$C_{10} = \frac{\alpha R_1^2 (1 + \nu)}{4(1 - \nu)} \left[\frac{2(R_1^2 T_{R_1} - R_2^2 T_{R_2})}{R_2^2 - R_1^2} - \frac{T_{R_2} - T_{R_1}}{\ln\left(\frac{R_2}{R_1}\right)} \right], \quad (20)$$

$$C_{20} = \frac{\alpha}{2} \cdot \frac{(1 - 3\nu)}{(1 - \nu)} \left[\frac{R_2^2 T_{R_2} - R_1^2 T_{R_1}}{R_2^2 - R_1^2} - \frac{T_{R_1} - T_{R_2}}{2 \ln\left(\frac{R_2}{R_1}\right)} \right]. \quad (21)$$

The obtained Eqs. (20) and (21) allow to obtain a solution for (12)–(14):

$$\sigma_r = \frac{\alpha E}{2(1 - \nu)} \left[\frac{r^2 (R_2^2 T_{R_2} - R_1^2 T_{R_1}) + R_1^2 R_2^2 (T_{R_1} - T_{R_2})}{r^2 (R_2^2 - R_1^2)} - \frac{T_{R_1} \ln\left(\frac{R_2}{r}\right) + T_{R_2} \ln\left(\frac{r}{R_1}\right)}{\ln\left(\frac{R_2}{R_1}\right)} \right], \quad (22)$$

$$\begin{aligned} \sigma_\phi = & - \frac{\alpha E}{(1 - \nu)(R_2^2 - R_1^2) \ln\left(\frac{R_2}{R_1}\right)} \cdot \left\{ \left[\frac{R_1^2 R_2^2}{r^2} (T_{R_1} - T_{R_2}) + R_1^2 T_{R_1} - R_2^2 T_{R_2} \right] \ln\left(\frac{R_2}{R_1}\right) \right. \\ & \left. + (R_2^2 - R_1^2) \left(T_{R_2} \ln\left(\frac{r}{R_1}\right) + T_{R_1} \ln\left(\frac{R_2}{r}\right) \right) + T_{R_2} - T_{R_1} \right\}, \end{aligned} \quad (23)$$

and solution for (2)–(4):

$$\begin{aligned} \varepsilon_r = & \frac{\alpha}{2(1 - \nu)} \left[\frac{(1 - 3\nu)(R_2^2 T_{R_2} - R_1^2 T_{R_1})}{(R_2^2 - R_1^2)} + \frac{2\nu(T_{R_2} - T_{R_1}) + (1 + \nu)(T_{R_1} \ln\left(\frac{R_2}{r}\right) + T_{R_2} \ln\left(\frac{r}{R_1}\right))}{\ln\left(\frac{R_2}{R_1}\right)} \right. \\ & \left. + \frac{(1 + \nu)R_1^2 R_2^2 (T_{R_1} - T_{R_2})}{r^2 (R_2^2 - R_1^2)} \right], \end{aligned} \quad (24)$$

$$\begin{aligned} \varepsilon_\phi = & \frac{\alpha}{2(1 - \nu)} \left[\frac{(1 - 3\nu)(R_2^2 T_{R_2} - R_1^2 T_{R_1})}{(R_2^2 - R_1^2)} - \frac{(1 - \nu)(T_{R_2} - T_{R_1}) - (1 + \nu)(T_{R_1} \ln\left(\frac{R_2}{r}\right) + T_{R_2} \ln\left(\frac{r}{R_1}\right))}{\ln\left(\frac{R_2}{R_1}\right)} \right. \\ & \left. - \frac{(1 + \nu)R_1^2 R_2^2 (T_{R_1} - T_{R_2})}{r^2 (R_2^2 - R_1^2)} \right], \end{aligned} \quad (25)$$

$$\varepsilon_z = \frac{\alpha \left[(T_{R_2} - T_{R_1})(R_2^2 - R_1^2) + 2(R_1^2 T_{R_1} - R_2^2 T_{R_2}) \ln\left(\frac{R_2}{R_1}\right) \right]}{2(R_2^2 - R_1^2) \ln\left(\frac{R_2}{R_1}\right)} \quad (26)$$

The obtained ratios (22)–(26) determine the change in the stress-strain state of the ball mill axle depending on the temperature and the change in the radial distance from the axis of symmetry of the mill axle.

Based on the formulas (22, 23), find the stress values on the inner surface of the ball mill axle. To perform this operation, let $r = R_1$:

$$\sigma_z(r = R_1) = \sigma_\phi(r = R_1) = \frac{\alpha E(T_{R_2} - T_{R_1})}{1 - \nu} \left[\frac{R_2^2}{R_2^2 - R_1^2} - \frac{1}{2 \ln\left(\frac{R_2}{R_1}\right)} \right]. \quad (27)$$

When substituting $r = R_2$ in the ratio (22) and (23), we obtain the stress values for the outer surface of the ball mill axle:

$$\sigma_z(r = R_2) = \sigma_\phi(r = R_2) = \frac{\alpha E(T_{R_2} - T_{R_1})}{1 - \nu} \left[\frac{R_1^2}{R_2^2 - R_1^2} - \frac{1}{2 \ln\left(\frac{R_2}{R_1}\right)} \right]. \quad (28)$$

To find the deformation of the inner surface of the ball mill axle in the obtained ratios (24) and (25), substitute $r = R_1$:

$$\varepsilon_r(r = R_1) = \frac{\alpha}{1 - \nu} \left[\frac{T_{R_1}(R_2^2 - R_1^2) + \nu T_{R_1}(R_2^2 + R_1^2) - 2\nu T_{R_2} R_2^2}{R_2^2 - R_1^2} + \frac{\nu(T_{R_2} - T_{R_1})}{\ln\left(\frac{R_2}{R_1}\right)} \right], \quad (29)$$

$$\varepsilon_\phi(r = R_1) = \frac{\alpha}{2(1 - \nu)} \left[\frac{(1 - 3\nu)(R_2^2 T_{R_2} - R_1^2 T_{R_1}) + (1 + \nu)T_{R_1}(R_2^2 - R_1^2)}{R_2^2 - R_1^2} - \frac{(1 - \nu)(T_{R_2} - T_{R_1})}{\ln\left(\frac{R_2}{R_1}\right)} \right]. \quad (30)$$

To find deformations on the outer side of the ball mill axle in formulas (24) and (25), it is necessary to put $r = R_2$:

$$\varepsilon_r(r = R_2) = \frac{\alpha}{2(1 - \nu)} \left[\frac{(1 - 3\nu)(R_2^2 T_{R_2} - R_1^2 T_{R_1}) + (1 + \nu)T_{R_2}(R_2^2 - R_1^2)}{R_2^2 - R_1^2} + \frac{2\nu(T_{R_2} - T_{R_1})}{\ln\left(\frac{R_2}{R_1}\right)} \right], \quad (31)$$

$$\varepsilon_{\phi}(r = R_2) = \frac{\alpha}{2(1-\nu)} \left[\frac{(1-3\nu)(R_2^2 T_{R_2} - R_1^2 T_{R_1}) - (1+\nu)(R_1^2(T_{R_1} - T_{R_2}) + T_{R_2}(R_2^2 - R_1^2))}{R_2^2 - R_1^2} - \frac{(1-\nu)(T_{R_2} - T_{R_1})}{\ln\left(\frac{R_2}{R_1}\right)} \right]. \quad (32)$$

Thus, the obtained expressions (27)–(32) determine the stress-strain state of the inner and outer surface of the axle depending on the temperature inside and outside the ball mill axle.

4 Getting the Source Data for Mathematical Description of the Stress-Strain State of Trunnion

Under the action of the forces of the loading clinker, the potential energy of the inner part of the axle accumulates and in the process of moving the material into the housing turns into heat. When unloading, the thermal energy of the resulting cement from the housing also affects the inner surface of the unloading axle.

To derive the equations of dependence of the temperature of the inner surface along the length of the axle, it should be taken into account that the increase in the distance from the axle axis leads to a decrease in the heat flux density, which in this case is a variable. To calculate the heat loss through a cylindrical wall, the linear heat flux density is applicable:

$$q_l = \frac{Q}{l}. \quad (33)$$

According to the Fourier law, the amount of heat passing through the metal layer is equal to:

$$Q = -k_l \cdot F \frac{dt}{dr} = -\lambda \cdot 2\pi r \cdot l \frac{dt}{dr}. \quad (34)$$

When

$$q_l = -k_l \cdot 2\pi r \cdot \frac{dt}{dr}. \quad (35)$$

Substituting the boundary values of the variables and integrating the expression (34), according to [3], we obtain the following ratio:

$$\Delta t = -\frac{q_l}{2\pi k_l} \ln \frac{R_2}{R_1} + C. \quad (36)$$

Having determined the integration constant C [4], we obtain a calculation formula for determining the temperature change of the inner surface of the axle:

$$T_{R_1} = T_{R_2} - \frac{Q \ln \frac{R_2}{R_1}}{2\pi l k_l}, \tag{37}$$

where T_{R_1} —temperature of the inner surface of the axle, T_{R_2} —surface temperature of the axle, l —axle length, R_1 —inner radius of the trunnion of the ball mill, R_2 —external radius of the axle, and k_l —heat transfer coefficient calculated by the formula [5]:

$$k_l = \frac{1}{\frac{1}{\alpha_1 R_1} + \frac{1}{\lambda} \ln \frac{R_2}{R_1} + \frac{1}{\alpha_2 R_2}}, \tag{38}$$

where α_1 —heat transfer coefficient of the material to the inner surface of the axle, α_2 —heat transfer coefficient of the external surface of the axle to the air, and λ —thermal conductivity coefficient of steel.

The heat energy transferred from the inner to the outer surface of the axle will be equal to the amount of heat loaded from the clinker furnace during loading or cement during unloading [6]:

$$Q = q \cdot \rho \cdot V, \tag{39}$$

where q —specific heat of clinker/cement, ρ —density of the clinker when loading and when unloading cement, and V —volume of loaded and unloaded material.

Substituting all the initial values, the amount of heat during loading and unloading will be equal to [7]:

$$Q_{cl} = q_{cl} \cdot \rho_{cl} \cdot V = 0.88 \cdot 1400 \cdot 1.18 = 1454 \text{ J}, \tag{40}$$

$$Q_{cem} = q_{cem} \cdot \rho_{cem} \cdot V = 0.8 \cdot 1500 \cdot 1.18 = 1416 \text{ J}. \tag{41}$$

Since the magnitude of the heat amount of clinker only is slightly higher than the cement, take the value of the quantity of heat of clinker and look at the axle boot [8, 9].

Then, according to the found expressions (35)–(37), finding the temperature change of the inner surface of the axle along the length is made by the formula [10, 11]:

$$T_{R_1} = T_{R_2} - \frac{Q \cdot \ln \frac{R_2}{R_1}}{2\pi l k_l} = T_{R_2} - \frac{Q \cdot \ln \frac{R_2}{R_1}}{2\pi l \cdot \left(\frac{1}{\frac{1}{\alpha_1 R_1} + \frac{1}{\lambda} \ln \frac{R_2}{R_1} + \frac{1}{\alpha_2 R_2}} \right)}. \tag{41}$$

Consider the change in stresses and strains of the inner and outer surfaces of the axle along the length, substituting (40) depending on (29)–(32).

The change in the stresses of the inner and outer surface of the axle along the length is shown in Fig. 2. The internal surface stress along the longitudinal axis is

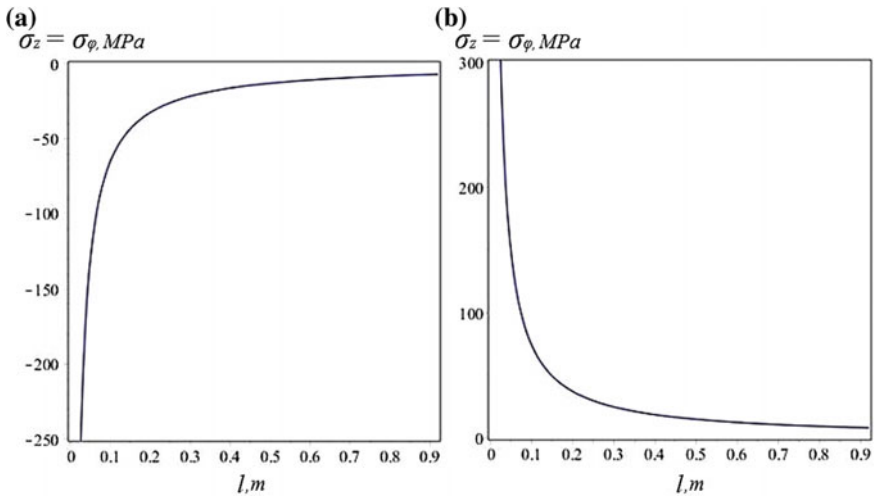


Fig. 2 The change in the voltage of the axle length **a** inner surface; **b** outer surface

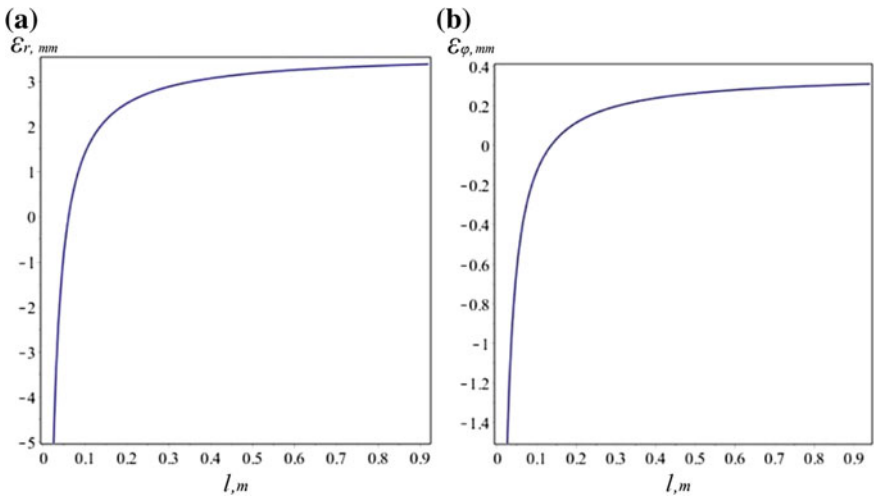


Fig. 3 Change of deformation of the inner surface of the axle along the length **a** in radial direction; **b** in azimuthal direction

only negative, indicating the influence of the internal surface temperature of the axle on the external surface of the axle [12, 13]. The change in the voltage of the outer surface along the length of the axle is characterized by an increase along the longitudinal axis from the bottom to the end [14, 15].

The change in deformations in both the radial and azimuthal direction of the inner surface of the axle along its length, shown in Fig. 3, shows the compression

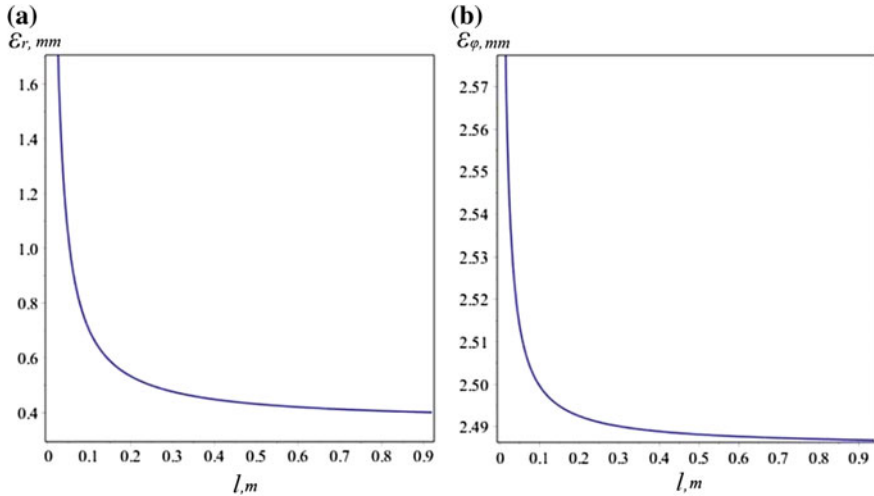


Fig. 4 Changing the deformation of the outer surface of the axle along the length **a** in radial direction; **b** in azimuthal direction

of the surface located closer to the bottom and the tension at the end of the axle [16, 17].

The deformation of the outer surface of the axle along the length in the radial and azimuthal directions is positive, which indicates tension (Fig. 4). In this case, when moving from the bottom to the end of the axle, the deformation of the outer surface decreases [18, 19]. The dependence of the deformation of the outer surface of the longitudinal coordinate is inverse [20].

Thus, the dependency graphs presented in Figs. 2, 3, and 4 characterize the stress-strain state along the length of the axle depending on the temperature of the inner surface.

References

1. Madera A (2005) Modeling of heat transfer in engineering systems. Moscow
2. Kartashov E, Kudinov V, Stefanyuk E (2012) Technical thermodynamics and heat transfer. Moscow
3. Timoshenko S, Gere J (2002) Mechanics of materials. Saint-Petersbourg
4. Bezukhov N (2011) Fundamentals of the theory of elasticity, plasticity and creep. Moscow
5. Birger I, Shorr B, Iosilevich G (2003) Calculation of the strength of machine parts. Moscow
6. Svetlickij V (2002) Mechanics of rods. Moscow
7. Filin A (2008) Applied mechanics of deformable solid. Moscow
8. Bogdanov O (2012) Handbook of ore dressing (in five volumes). Moscow
9. Pisarenko G, Mozharovskij N (2001) Equations and boundary value problems of the theory of elasticity and plasticity. Kiev

10. Bestuzheva O, Bondarenko J, Fedorenko M, Lipchanskaya J (2016) Machine for machining axles grinding mills. Russian Federation Patent 166615, 10 Dec 2016
11. Mukhachev V (2007) Planning and processing of experimental results. Tomsk
12. Rogov V, Poznyak G (2005) Methods and practice of technical experiments. Moscow
13. Daniel K (2009) The application of statistics to industrial experiments. Moscow
14. Afanasyeva N (2016) Computational and experimental methods of scientific experiment. Moscow
15. Research methods and organization of experiments (2013) Humanitarian center. Moscow
16. Bestuzheva O, Fedorenko M, Bondarenko J (2016) Experimental study of the recovery of a surface of revolution of large parts of industrial equipment. Bulletin of Belgorod State Technological University after V. G. Shukhov, vol 11, pp 122–127
17. Bestuzheva O, Fedorenko M, Bondarenko J (2016) Determination of the rational parameters of a rotating processing surfaces of rotation when restoring large parts. Bulletin of Belgorod State Technological University after V. G. Shukhov, vol 12, pp 121–125
18. Bestuzheva O, Fedorenko M, Bondarenko J, Sanina T (2016) Research of dependence of the area of he slice from the technological parameters and modes for the rotary machining of large parts. Technol Mech Eng 5:14–19
19. Bestuzheva O, Fedorenko M, Bondarenko J, Duganov Y (2016) Distortion of the cut surface of the workpiece in the form of a truncated cone with rotary processing. Technol Mech Eng 4:9–11
20. Sidnyaev N (2012) Theory of experiment planning and statistical data analysis. Moscow

Influence of Stiffness of Rear Leaf Spring on Van Vibration Loading



Yu. A. Polyakov

Abstract The influence of the stiffness of the rear leaf spring on the vibration loading of the van is estimated using a spatial model of its dynamic. The new model of spatial oscillations of the van with all-metal body taking into account the dynamics of the movement by road microprofile, nonlinearities of dynamic hysteresis characteristics of elements of the vibroprotective systems and tires, taking into account the deformation of frame and body, is built. The calculations were carried out when moving the van in two weight states: empty and full weight. For analysis of the vibration loading of the van, the spectrums of vertical accelerations at several points of the van construction were obtained. All calculations were performed in the “FRUND” programmatic system. Based on the calculation results, the rational stiffness parameters of the rear spring are proposed. The results obtained in the course of calculations were constructively realized by removing the fourth and sixth leaves from the standard leaf rear spring. This also led to a significant reduction in the weight of the rear leaf spring.

Keywords Vibration loading · Leaf spring · Stiffness of the leaf spring

1 Introduction

Suspensions with elastic elements in the view of leaf springs are widely used in trucks, trailers, and some cars and buses [1–4]. The complex nature of the dynamic interaction of elements of vibroprotective systems, objects of vibration protection and supporting structures of vehicles, moving on roads with hard surface, necessitates the development of methods for calculating the spatial vibrations of their structures at random road impacts [5–10].

Yu. A. Polyakov (✉)
National University of Science and Technology “MISiS”,
4, Lenin Ave., Moscow 119049, Russia
e-mail: polyakov_yu.a@mail.ru

In this case, the actual problem is the rejection of the assumption about small displacements of bodies, usually used in such calculations, and their implementation on the basis of differential equations of large displacements of bodies, without the assumption about the smallness of the rotation angles, that is, with an accurate description in equations of dynamics of the angular orientation and mutual arrangement of bodies [11–30]. This makes it possible to carry out a refined spectral analysis of the vehicle vibration loading.

2 The Spatial Dynamic Model of the Van with a Refined Representation of Leaf Spring Suspensions

The new model of spatial oscillations of the van with all-metal body taking into account the dynamics of the movement by road microprofile, nonlinearities of dynamic hysteresis characteristics of elements of the vibroprotective systems and tires, taking into account the deformation of frame and body, is built.

The calculation scheme of the van (Fig. 1) is a mechanical system, consisting of absolutely solid bodies (in particular, a power aggregate, a front-axle beam, a rear-axle beam, and a subsystem “man—seat”), each of which has six degrees of freedom, and elastic finite element bodies (a frame, a subsystem “cabin—all-metal van”), connected by elements of vibroprotective systems (leaf springs, rubber mountings of body and power aggregate, stabilizers, and shock absorbers).

In the formation of the dynamic model of the van, special attention was paid to the elements of the front and rear leaf spring suspensions. The nonlinearity of the

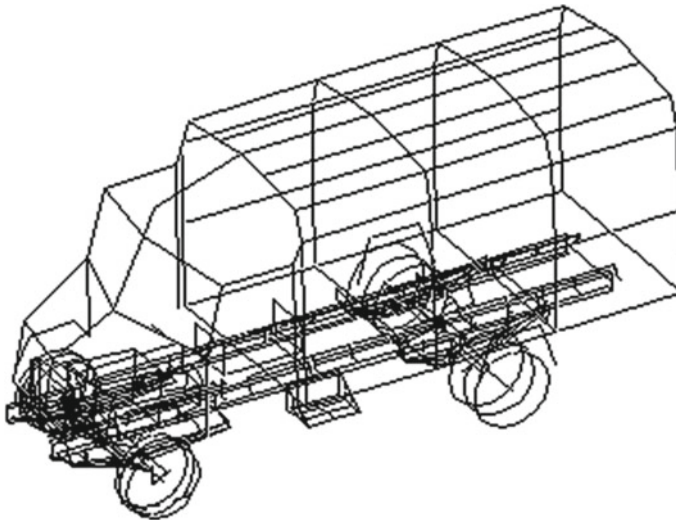


Fig. 1 The calculation scheme of the van with a refined representation of leaf spring suspensions

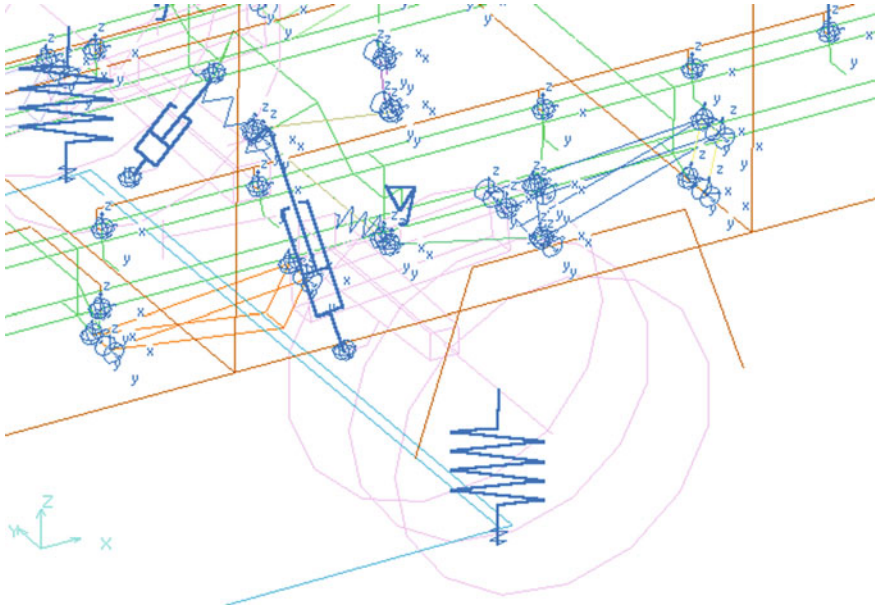


Fig. 2 Inclusion of the rear leaf spring in the calculation scheme of the van

characteristics of the vertical elasticity of the leaf springs is provided by taking into account the interleaf friction, so that these characteristics are hysteresis.

In the described model, each leaf spring is included in the form of three links connected by joints, the characteristics of which are selected from the condition of equivalence to the vertical stiffness of the leaf spring, taking into account the forces of interleaf friction (Fig. 2). In particular, the middle link of the leaf spring is fixed to the front-axle or rear-axle beam, to which two other links are pivotally connected. Moreover, the front link in the course of the van is simultaneously attached to the frame bracket and the rear—to the leaf spring earring. The earring is pivotally attached to the corresponding bracket of the finite element frame.

3 Results and Discussion

The movement of the van on a random road microprofile with a constant speed was simulated. The calculations used time realizations of a standard microprofile in the form of an even cobble. For analysis of the vibration loading of the van, the spectrums of vertical accelerations at several points of the van construction were obtained. All calculations were performed in the “FRUND” programmatic system [6, 7]. The calculations were carried out when moving the van in two weight states: empty and full weight.

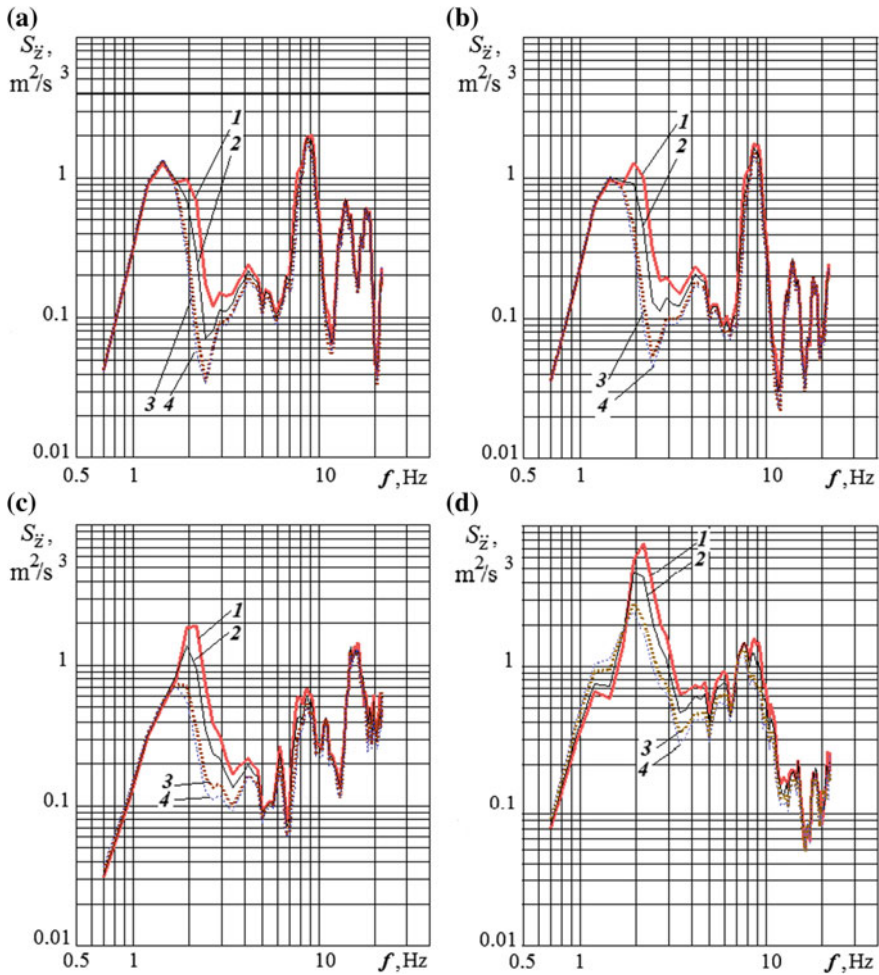


Fig. 3 Spectrums of vertical accelerations during the movement of an empty van on an even cobble at a speed of 60 km/h: **a** on the cab floor, under the driver seat; **b** on the floor of the body, above its third rubber mounting; **c** on the floor of the body, above its fifth rubber mounting (in the middle of the wheelbase of the van); **d** on the rear overhang of the body; static stiffness of the rear leaf spring on the first and second sections of the vertical elasticity characteristic: 1—146.5, 196.7 kN/m; 2—126.5, 176.7 kN/m; 3—106.5, 156.7 kN/m; 4—100, 150.2 kN/m

For an empty van for the points, taken in the front part of the body (Fig. 3a, b), the decreasing stiffness of the rear leaf spring leads to a decrease in the area occupied by the low-frequency spectral maximum, that is, to the occurrence of a more acute spectral peak. Moreover, the location of the maximum, corresponding to the natural frequency of oscillations of the sprung parts of the van on the front leaf springs, remains unchanged in the ordinate and the frequency (because the stiffness

of the front leaf spring is constant), and the formation of a more acute spectral peak is observed due to the reduction of the second low-frequency resonance, arising from the impact of oscillations from the rear leaf springs.

For the points, selected in the middle of the wheelbase of the van and in the rear part of the body (Fig. 3c, d), a decrease in the stiffness of the rear leaf spring entails a decrease in the ordinate of the first low-frequency spectral maximum with simultaneous displacement of its top to the left, to a lower frequency. The displacement of this spectral maximum in frequency is caused by a decrease in the stiffness of the rear leaf spring, and the decrease in its ordinate is due to an increase in the relative damping coefficient with a decrease in the stiffness of the rear leaf spring.

For a full-weight van, the decrease in the ordinate of the first low-frequency spectral maximum for the points taken in the front part of the body and in the middle of the wheelbase of the van (Fig. 4a, b, c) is due to the decrease in the additive to the vertical accelerations of the component from the longitudinal-angular oscillations, due to the displacement of the center of longitudinal-angular oscillations with a decrease in the stiffness of the rear leaf springs. Moreover, with decreasing stiffness of the rear leaf spring, the point, taken in the middle of the wheelbase of the van (Fig. 4c) becomes closest placed to the center of the longitudinal-angular oscillations of the sprung parts of the van.

For points, selected behind the rear axle of the van (Fig. 4d), a decrease in the stiffness of the rear leaf spring causes an increase in the ordinate of the low-frequency spectral maximum with simultaneous displacement of its top to the left, to a lower frequency. The displacement of this spectral maximum in frequency is caused by a decrease in the natural frequency of oscillations of the sprung parts on the rear leaf springs. The increase in the ordinate of this spectral maximum is due to the increase in the additive to the vertical accelerations of the component from the oscillations of the sprung parts of the van in the longitudinal-angular direction. This is due to the displacement of the center of the longitudinal-angular oscillations of the sprung masses with decreasing stiffness of the rear springs.

4 Conclusion

Evaluation of the impact of the stiffness parameters of the rear leaf springs on the vibration loading of the van is largely determined by its weight condition. In this regard, it is advisable to perform calculations for two weight states: for an empty van and with its full weight.

Based on the calculation results, the rational stiffness parameters of the rear spring are proposed. The results obtained in the course of calculations were constructively realized by removing the fourth and sixth leaves from the standard leaf rear spring. This also led to a significant reduction in the weight of the rear leaf spring.

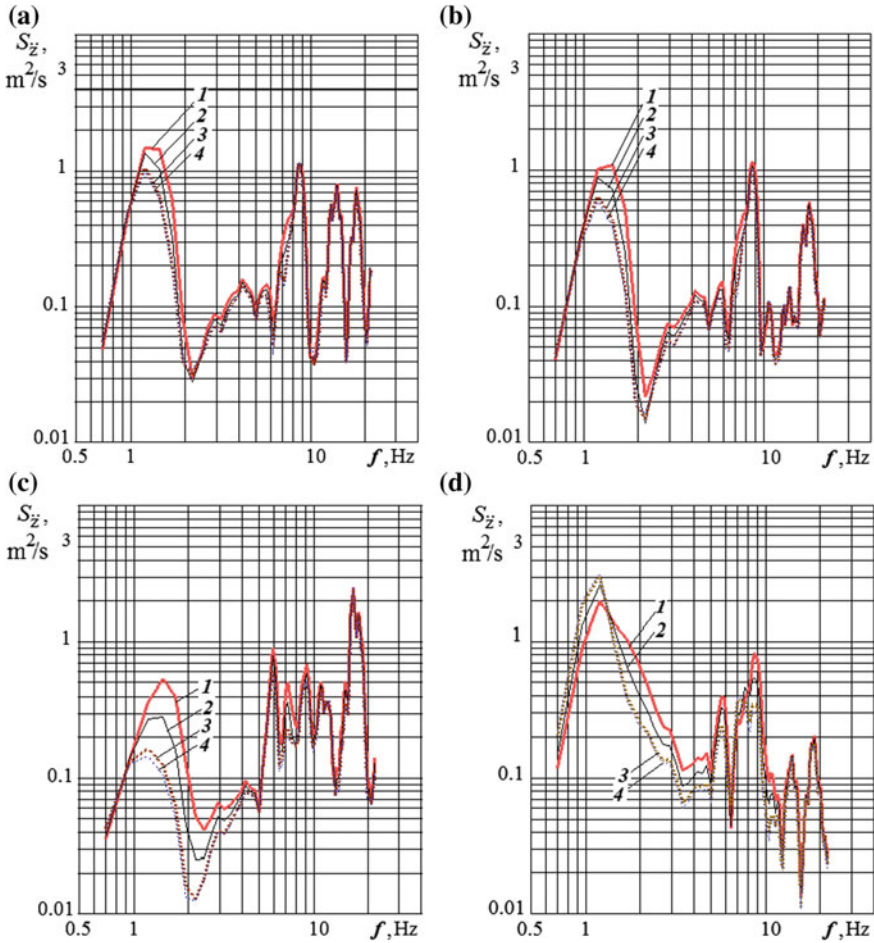


Fig. 4 Spectrums of vertical accelerations during the movement of the full-weight van on an even cobble at a speed of 60 km/h: **a** on the cab floor, under the driver seat; **b** on the floor of the body, above its third rubber mounting; **c** on the floor of the body, above its fifth rubber mounting (in the middle of the wheelbase of the van); **d** on the rear overhang of the body; static stiffness of the rear leaf spring on the first and second sections of the vertical elasticity characteristic: 1—146.5, 196.7 kN/m; 2—126.5, 176.7 kN/m; 3—106.5, 156.7 kN/m; 4—100, 150.2 kN/m

References

1. Reimpel J, Stoll H, Betzler JW (2001) The automotive chassis: engineering principles; translated from the German by AGET Limited, 2nd edn. Elsevier Butterworth-Heinemann, Oxford
2. Parkhilovskiy IG (1978) Avtomobil'nye listovye resory (Automotive leaf springs). Mashinostroenie, Moscow



3. Polyakov YuA (2010) Napravleniya sovershenstvovaniya sistem podressorivaniya avtomobiley (Directions of improvement of vehicle suspension systems). *Avtotransportnoye predpriyatiye* 6:53–55
4. Yatsenko NN (1972) Kolebaniya, prochnost i forsirovannye ispytaniya gruzovykh avtomobiley (Vibrations, strength and forced testing of trucks). Mashinostroenie, Moscow
5. Blundell M, Harty D (2015) The multibody systems approach to vehicle dynamics, 2nd edn. Elsevier Butterworth-Heinemann, Oxford
6. Gorobtsov AS, Kartsov SK, Pletnev AE, Polyakov YuA (2011) Kompyuternye metody postroeniya i issledovaniya matematicheskikh modeley dinamiki konstruktivnykh avtomobiley (Computer methods of construction and research of mathematical models of dynamics of car structures). Mashinostroenie, Moscow
7. Gorobtsov AS, Kartsov SK, Polyakov YuA (2017) Estimation of the vibration loading vehicle with pneumohydraulic suspensions. In: IOP conference series: materials science and engineering, vol 177, p 012086. <https://doi.org/10.1088/1757-899x/177/1/012086>
8. Mitschke M, Wallentowitz H (2004) Dynamik der kraftfahrzeuge (Vehicle dynamics). Springer, Berlin, Heidelberg
9. Popp K, Schiehlen W (2010) Ground vehicle dynamics. Springer-Verlag, Berlin, Heidelberg
10. Schramm D, Hiller M, Bardini R (2014) Vehicle dynamics: modeling and simulation. Springer-Verlag, Berlin, Heidelberg
11. Shabana AA (2005) Dynamics of multibody systems. Cambridge University Press, New York
12. Bathe KJ, Ramm E, Wilson EL (1975) Finite element formulations for large deformation dynamic analysis. *Int J Numer Methods Eng* 9:353–386
13. Bauchau OA, Damilano G, Theron NJ (1995) Numerical integration of non-linear elastic multibody systems. *Int J Numer Methods Eng* 38(16):2727–2751. <https://doi.org/10.1002/nme.1620381605>
14. Bauchau OA, Theron NJ (1996) Energy decaying scheme for nonlinear elastic multibody systems. *Comput Struct* 59(2):317–331. [https://doi.org/10.1016/0045-7949\(95\)00250-2](https://doi.org/10.1016/0045-7949(95)00250-2)
15. Bauchau OA, Xin H, Dong S, Li Z, Han S (2012) Intrinsic time integration procedures for rigid body dynamics. *J Comput Nonlinear Dyn* 8:011006. <https://doi.org/10.1115/1.4006252>
16. Baumgarte J (1972) Stabilization of constraints and integrals of motion in dynamical systems. *Comput Methods Appl Mech Eng* 1(1):1–16. [https://doi.org/10.1016/0045-7825\(72\)90018-7](https://doi.org/10.1016/0045-7825(72)90018-7)
17. Bayo E, Garcia de Jalon J, Serna MA (1988) A modified Lagrangian formulation for the dynamic analysis of constrained mechanical systems. *Comput Methods Appl Mech Eng* 71(2):183–195. [https://doi.org/10.1016/0045-7825\(88\)90085-0](https://doi.org/10.1016/0045-7825(88)90085-0)
18. Bayo E, Garcia de Jalon J, Avello A, Cuadrado J (1991) An efficient computational method for real time multibody dynamic simulation in fully cartesian coordinates. *Comput Methods Appl Mech Eng* 92:377–395. [https://doi.org/10.1016/0045-7825\(91\)90023-Y](https://doi.org/10.1016/0045-7825(91)90023-Y)
19. Bayo E, Ledesma R (1996) Augmented Lagrangian and mass-orthogonal projection methods for constrained multibody dynamics. *Nonlinear Dyn* 9:113–130. <https://doi.org/10.1007/BF01833296>
20. Bayo E, Avello A (1994) Singularity free augmented Lagrangian algorithms for constraint multibody dynamics. *Nonlinear Dyn* 5:209–231. <https://doi.org/10.1007/BF00045677>
21. Blajer W (2001) A geometrical interpretation and uniform matrix formulation of multibody system dynamics. *ZAMM J Appl Math Mech* 81(4):247–259
22. Brenan KE, Petzold LR (1989) The numerical solution of higher index differential-algebraic equations by implicit methods. *SIAM J Numer Anal* 26(4):976–996. <https://doi.org/10.1137/0726054>
23. Gonzalez F, Dopico D, Pastorino R, Cuadrado J (2016) Behaviour of augmented Lagrangian and Hamiltonian methods for multibody dynamics in the proximity of singular configurations. *Nonlinear Dyn* 85(3):1491–1508
24. Lin ST, Hong MC (1998) Stabilization method for numerical integration of multibody mechanical systems. *J Mech Des* 120(4):565–572. <https://doi.org/10.1115/1.2829316>
25. Park KC, Chiou JC (1988) Stabilization of computational procedures for constrained dynamical systems. *J Guidance Control Dyn* 11(4):365–370. <https://doi.org/10.2514/3.20320>

26. Simo JC, Wong KK (1991) Unconditionally stable algorithms for rigid body dynamics that exactly preserve energy. *Int J Numer Method Eng* 31(1):19–52. <https://doi.org/10.1002/nme.1620310103>
27. Shabana AA, Hwang YL, Wehage RA (1992) Projection methods in flexible multibody dynamics. Part I: kinematics. Part II: dynamics and recursive projection methods. *Int J Numer Methods Eng* 35(10):1927–1966
28. Sharp RS (1994) The application of multibody computer codes to road vehicle dynamics modeling problems. *Proc Inst Mech Eng* 208:55–61
29. Schwerin R (1999) *Multibody system simulations: numerical methods, algorithms and software*. Springer, Berlin, Heidelberg
30. Wasfy TM, Noor AK (1996) Modeling and sensitivity analysis of multibody systems using new solid, shell and beam elements. *Comput Methods Appl Mech Eng* 138:187–211. [https://doi.org/10.1016/S0045-7825\(96\)01113-9](https://doi.org/10.1016/S0045-7825(96)01113-9)

Hydroelastic Oscillations of Three-Layered Channel Wall Resting on Elastic Foundation



D. V. Kondratov, V. S. Popov and A. A. Popova

Abstract The hydroelastic bending oscillations of a three-layered wall of narrow parallel-plate channel with viscous flow were studied. We analyze the hydroelastic problem of a plane type and consider the upper channel wall as a rigid vibrating stamp and the bottom channel wall as a three-layered beam resting on elastic foundation. The flow in the channel is studied within the viscous incompressible fluid model. We investigate flow as a creeping one and assume a Winkler model for elastic foundation. The three-layered beam is a sandwich construction, which consists of outer layers and a stiff lightweight core, as well as three-layered beam kinematics is described by using the postulate of broken normal. The mathematical model of the investigated parallel-plate channel consists of dynamic equations of the three-layered beam with stiff lightweight-core, dynamic equations of the creeping flow and boundary conditions. We assume boundary conditions at the channel walls are no-slip ones, as well as boundary conditions at the channel edges are pressure difference. We studied the stationary oscillation problem under loading harmonic vibrating stamp. The analytical solution of the considered problem was obtained. We suggest the frequency-dependent function of three-layered beam deflection distribution along the channel and make calculations of the channel wall amplitude-frequency response.

Keywords Hydroelasticity · Oscillations · Three-layered beam · Viscous flow · Parallel-plate channel · Vibrating stamp · Mathematical modeling

D. V. Kondratov

Russian Presidential Academy of National Economy and Public Administration, 164, Moskovskaya street, Saratov 410012, Russia

V. S. Popov (✉) · A. A. Popova

Yuri Gagarin State Technical University of Saratov, 77, Politechnicheskaya street, Saratov 410054, Russia

e-mail: vic_p@bk.ru

© Springer Nature Switzerland AG 2020

A. A. Radionov et al. (eds.), *Proceedings of the 5th International Conference on Industrial Engineering (ICIE 2019)*, Lecture Notes in Mechanical Engineering,

https://doi.org/10.1007/978-3-030-22041-9_96

903

1 Introduction

Three-layered beams and plates are widely used in different industries. Therefore, the static and dynamic problems of three-layered beams and plates are of actual significance both for the theory of elasticity and contemporary industry. For instance, Reference [1] considers historical development review of zig-zag theories for multilayered beams and plates and Reference [2] deals with the approach to study three-layered beams and plates with incompressible core in the framework of the broken normal hypothesis, as well as static and dynamic problems of three-layered structure elements with compressible core under various loadings. The three-layered construction elements resting on an elastic foundation are often encountered in practice. In a well-known monograph [3], an elastic foundation is studied on the base of a single- or double-layer model, whose properties are described by two or more elastic characteristics. Contemporary studies of homogeneous beams and plates resting on elastic foundation of different types are considered in [4]. The deformations and oscillations of three-layered constructions founding on elastic media under the various loads are considered in [5–8]. Along with that, there are a lot of practical hydroelastic problem of homogeneous constructions interacting with fluid. For example, the hydroelasticity of beams, plates and shells interacting with an ideal fluid is considered in [9–12]. Nevertheless, the viscosity property of the liquid and influence of elastic foundation are not considered in the references mentioned above. The free and forced hydroelastic oscillations of homogeneous beams, plates and shells interacting with viscous liquid were investigated in [13–17]. The hydroelastic models of walls oscillations of thin or tapered gaps containing a viscous fluid are developed in [18–21]. References [22–25] considered vibrations of homogeneous plates resting on Winkler or Pasternak foundation. The problems of three-layered plate hydroelastic response are also relevant. The hydroelastic vibrations of multilayered and composite plates interacting with ideal and viscous fluids are studied in [26–28]. In the present work, we investigate hydroelastic vibrations of narrow channel wall as a three-layered beam resting on Winkler foundation.

2 Hydroelastic Problem Statement

We study the dynamics of parallel-plate gap walls interacting with a flow. The narrow parallel-plate gap is shown in Fig. 1. The channel's length is 2ℓ . The bottom channel wall is rested on an elastic foundation. The elastic foundation is studied within Winkler model. The viscous flow moves due to an assigned pressure difference $\Delta p = p^* - p^{**}$ at the edges of the narrow gap. Let us assume p^* and p^{**} are the static pressures at the left and the right channel edges accordingly. The upper wall of the channel is a rigid vibrating stamp. The bottom wall of the channel is a three-layered beam. The three-layered beam is a sandwich construction consisting of outer layers and a stiff

lightweight core. Thicknesses of outer layers are h_1 and h_2 . Thickness of the core is $2c$. The postulate of broken normal for three-layered beam is accepted according to [2]. The three-layered beam edges are simply supported. We consider Cartesian coordinate system Oxz , the center of Cartesian system is sited in non-deformable beam core center. In an unperturbed state, the flow thickness is $h_0 \ll \ell$, i.e., the channel's length ℓ is significantly greater than h_0 . We suggest the stamp vibrations are along the axis Oz , as well as its amplitude is z_m , and amplitude deflection of the beam is w_m . Further, we assume $h_0 \gg w_m$ and $h_0 \gg z_m$. The liquid layer has high damping properties caused by viscosity. As a result, the transient processes are disappeared quickly [29] and we analysis plane hydroelastic problem for the steady-state harmonic oscillations. Bearing in mind [30], the inertial forces of three-layered beam in a longitudinal direction are not considered and we study the three-layered beam bending fluctuations only.

3 The Theory and Solution

According to [31], the viscous flow in a narrow gap is the creeping one. The equations of creeping flow are represented in the form of

$$\frac{1}{\rho} \frac{\partial p}{\partial x} = \nu \left(\frac{\partial^2 u_x}{\partial x^2} + \frac{\partial^2 u_x}{\partial z^2} \right), \frac{1}{\rho} \frac{\partial p}{\partial z} = \nu \left(\frac{\partial^2 u_z}{\partial x^2} + \frac{\partial^2 u_z}{\partial z^2} \right), \frac{\partial u_x}{\partial x} + \frac{\partial u_z}{\partial z} = 0, \quad (1)$$

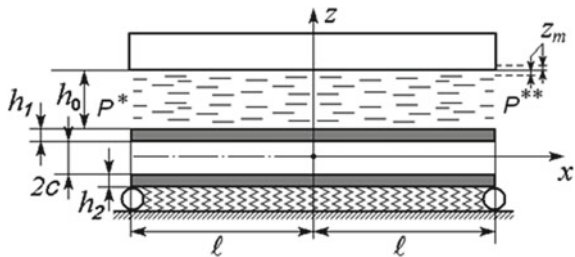
where p is the flow pressure, u_x and u_z are the velocities of the flow along Ox and Oz , ρ is the density of the flow, ν is the kinematic viscosity coefficient of the liquid.

Equation (1) is supplemented by the no-slip conditions at the gap wall and the boundary conditions for the pressure in the form of

$$u_x = 0, u_z = \frac{dz}{dt} \text{ at } z = h_1 + h_0 + c, \quad (2)$$

$$u_x = 0, u_z = \frac{\partial w}{\partial t} \text{ at } z = h_1 + c,$$

Fig. 1 Parallel-plate gap formed by vibrating stamp and three-layered beam resting on Winkler foundation



$$p = p^* \text{ at } x = -\ell, p = p^{**} \text{ at } x = +\ell, \tag{3}$$

where w is the three-layered beam deflection, $z = z_m f(\omega t) = z_m \sin(\omega t)$ is the stamp vibrations law, ω is the stamp vibrations frequency.

Consistent with [2], we obtain the dynamic equations of three-layered beam resting on Winkler foundation in the form of

$$\begin{aligned} a_1 \frac{\partial^2 u}{\partial x^2} + a_6 \frac{\partial^2 \varphi}{\partial x^2} - a_7 \frac{\partial^3 w}{\partial x^3} &= q_{zx}, \\ a_6 \frac{\partial^2 u}{\partial x^2} + a_2 \frac{\partial^2 \varphi}{\partial x^2} - a_3 \frac{\partial^3 w}{\partial x^3} &= 0, \\ a_7 \frac{\partial^3 u}{\partial x^3} + a_3 \frac{\partial^3 \varphi}{\partial x^3} - a_4 \frac{\partial^4 w}{\partial x^4} - \kappa w - m_0 \frac{\partial^2 w}{\partial t^2} &= -q_{zz}, \\ a_1 &= 2K_3^+ c + K_2^+ h_2 + K_1^+ h_1, a_2 = K_2^+ h_2 c^2 + \frac{2}{3} K_3^+ c^3 + K_1^+ h_1 c^2, \\ a_3 &= K_1^+ h_1 (c^2 + 0.5h_1 c) + K_2^+ (c^2 h_2 + 0.5ch_2) + \frac{2}{3} c^3 K_3^+, \\ a_4 &= \frac{2}{3} K_3^+ c^3 + K_1^+ h_1 c \left(c + h_1 + \frac{1}{3} h_1^2 / c \right) + K_2^+ h_2 c \left(c + h_2 + \frac{1}{3} h_2^2 / c \right), \\ a_6 &= cK_1^+ h_1 - cK_2^+ h_2, \\ a_7 &= K_1^+ (ch_1 + 0.5h_1^2) - K_2^+ (ch_2 + 0.5h_2^2), m_0 = \rho_1 h_1 + \rho_2 h_2 + 2\rho_3 c, \\ K_j^+ &= 4G_j / 3 + K_j. \end{aligned} \tag{4}$$

where u and w are the longitudinal displacement and the deflection of three-layered beam, j is the number of the layer, G_j is the j th layer shear modulus, K_j is the j th layer bulk modulus, ρ_j is the density of j th layer material, φ is the angle of rotation of the deformed normal in the three-layered beam core, κ is the foundation modulus, q_{zz} is the normal stress in the viscous liquid, q_{zx} is the shear stress in the viscous liquid.

The normal stress and the shear stress are presented as

$$q_{zz} = -p + 2\rho v \frac{\partial u_z}{\partial z} \text{ at } z = h_1 + c, q_{zx} = \rho v \left(\frac{\partial u_z}{\partial x} + \frac{\partial u_x}{\partial z} \right) \text{ at } z = h_1 + c. \tag{5}$$

The simply supported edges' conditions for Eq. (4) are

$$u = \varphi = w = \frac{\partial^2 w}{\partial x^2} = 0 \text{ at } x = \pm \ell. \tag{6}$$

Taking into account the channel narrowness, we can assume the velocity transverse component u_z is negligible compared to the velocity longitudinal component u_x , and the derivative $\partial^2 u_x / \partial z^2$ is much larger than the derivative $\partial^2 u_x / \partial x^2$. Bearing in mind the above, Eq. (1) is simplified and takes the form of

$$\frac{1}{\rho} \frac{\partial p}{\partial z} = 0, \frac{1}{\rho} \frac{\partial p}{\partial x} = v \frac{\partial^2 u_x}{\partial z^2}, \frac{\partial u_x}{\partial x} + \frac{\partial u_z}{\partial z} = 0, \tag{7}$$

and the expressions for normal and shear stresses are written as

$$q_{zz} = -p, q_{zx} = \rho v \frac{\partial u_x}{\partial z}. \tag{8}$$

By solving Eq. (7) with boundary conditions (2), (3), we obtain

$$\begin{aligned} u_x &= \frac{1}{\rho v} \frac{\partial p}{\partial x} \frac{(z - c - h_1)^2 - h_0(z - c - h_1)}{2}, u_z \\ &= \frac{1}{\rho v} \frac{\partial^2 p}{\partial x^2} \frac{3h_0(z - c - h_1)^2 - 2(z - c - h_1)^3}{12} + \frac{\partial w}{\partial t}, \end{aligned} \tag{9}$$

$$\begin{aligned} p &= \frac{6\rho v}{h_0^3} \left(\frac{dz}{dt} (x^2 - \ell^2) - 2 \int_{-\ell}^x \int \frac{\partial w}{\partial t} d\xi d\zeta + \left(\frac{x}{\ell} + 1 \right) \int_{-\ell}^{\ell} \int \frac{\partial w}{\partial t} d\xi d\zeta \right) \\ &+ \frac{1}{2} [p^* + p^{**} - \frac{x}{\ell} (p^* - p^{**})]. \end{aligned} \tag{10}$$

It follows from Eqs. (9) and (10) that the normal liquid stress at the channel wall is much greater than the shear one; that is, we will assume further $q_{zx} = 0$. Taking into account the above, and considering the first and second equations of Eq. (4), we obtain

$$\frac{\partial^2 u}{\partial x^2} = b_1 \frac{\partial^3 w}{\partial x^3}, \frac{\partial^2 \varphi}{\partial x^2} = b_2 \frac{\partial^3 w}{\partial x^3}, b_1 = \frac{a_2 a_7 - a_3 a_6}{a_1 a_2 - a_6^2}, b_2 = \frac{a_1 a_3 - a_7 a_6}{a_1 a_2 - a_6^2}. \tag{11}$$

By substituting Eqs. (10) and (11) in third equation of Eq. (2), we get

$$\begin{aligned} D \frac{\partial^4 w}{\partial x^4} + \kappa w + m_0 \frac{\partial^2 w}{\partial t^2} &= -\frac{6\rho v}{h_0^3} \left(\frac{dz}{dt} (x^2 - \ell^2) - 2 \int_{-\ell}^x \int \frac{\partial w}{\partial t} d\xi d\zeta \right. \\ &\left. + \left(\frac{x}{\ell} + 1 \right) \int_{-\ell}^{\ell} \int \frac{\partial w}{\partial t} d\xi d\zeta \right) - \frac{1}{2} [p^* + p^{**} - \frac{x}{\ell} (p^* - p^{**})] \end{aligned} \tag{12}$$

where the following notation is used $D = a_4 - a_7 b_1 - a_3 b_2$.

Boundary conditions for Eq. (12) are the simply supported conditions at three-layered beam edges

$$w = \frac{\partial^2 w}{\partial x^2} = 0 \text{ at } x = \pm \ell. \tag{13}$$

According to simply supported boundary conditions (13), we present the three-layered beam deflection in the form of

$$\begin{aligned} w &= \sum_{k=1}^n (R_k^0 + R_k(t))X_k(x) + Q_k^0 Y_k(x), X_k = \cos((2k - 1)\pi x/(2\ell)), Y_k \\ &= \sin(\pi k x/\ell), \end{aligned} \tag{14}$$

We denote the stationary solution due to Δp by the upper index 0. Finally, after solving Eq. (12), we obtain the following expression for three-layered beam elastic deflection in the form of

$$\begin{aligned} w &= -\frac{\Delta p \ell^4}{D} \sum_{k=1}^{\infty} \left(\frac{2(-1)^{k+1}}{(2k - 1)\pi} \frac{X_k}{((2k - 1)\pi/2)^4 + \kappa \ell^4/D} + \frac{(-1)^k}{\pi k} \frac{Y_k}{(\pi k)^4 + \kappa \ell^4/D} \right) \\ &+ z_m A(x, \omega) \sin(\tau + \varphi(x, \omega)). \end{aligned} \tag{15}$$

Here, we introduce the symbols:

$$\begin{aligned} A(x, \omega) &= \sqrt{C^2 + B^2}, \varphi(x, \omega) = \text{arctg}(B/C), \\ C &= \sum_{k=1}^{\infty} \frac{K_k^z K_k^w \omega^2}{(D_k - m_0 \omega^2)^2 + (K_k^w \omega)^2} X_k, B = \sum_{k=1}^{\infty} \frac{K_k^z \omega (D_k - m_0 \omega^2)}{(D_k - m_0 \omega^2)^2 + (K_k^w \omega)^2} X_k, \\ D_k &= \frac{D}{\ell^4} \left(\frac{(2k - 1)\pi}{2} \right)^4 + \kappa, \\ K_k^z &= 12 \frac{\rho v}{h_0 \psi^2} \frac{4(-1)^k}{(2k - 1)\pi} \left(\frac{2}{(2k - 1)\pi} \right)^2, K_k^w = 12 \frac{\rho v}{h_0 \psi^2} \left(\frac{2}{(2k - 1)\pi} \right)^2. \end{aligned}$$

The function $A(x, \omega)$ in Eq. (15) has to be considered as frequency-dependent function of three-layered beam deflection distribution along the gap. When we specify a fixed value of longitudinal coordinate x_0 , this function is transformed into the amplitude-frequency response $A(\omega) = A(x_0, \omega)$ at the specified channel cross section.



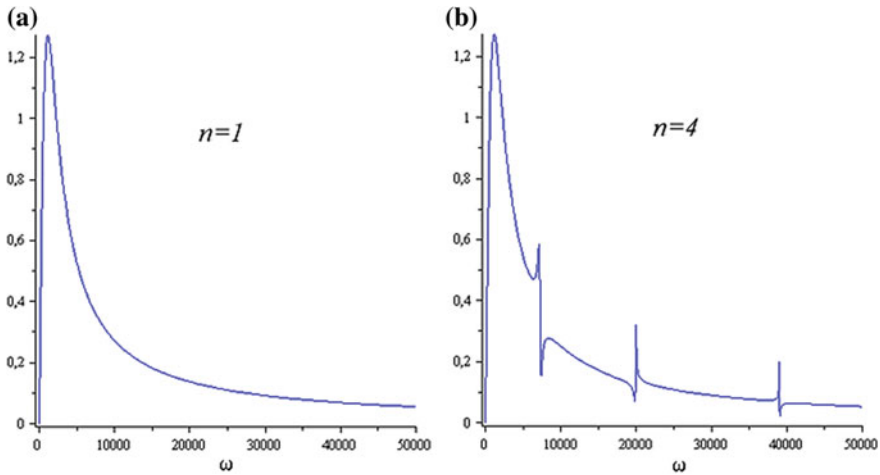


Fig. 2 Charts of channel wall amplitude-frequency response $A(\omega) = A(0, \omega)$ for cases $n = 1$ and $n = 4$

4 Calculation Results

To illustrate the mathematical model usage, we consider the following source data $K_1 = K_2 = 8 \cdot 10^{10}$ Pa, $K_3 = 4.7 \cdot 10^9$ Pa, $G_1 = G_2 = 2.67 \cdot 10^{10}$ Pa, $G_3 = 9 \cdot 10^7$ Pa, $\rho = 1840$ kg/m³, $\rho_1 = \rho_2 = 2700$ kg/m³, $\rho_3 = 2150$ kg/m³, $\nu = 25 \cdot 10^{-5}$ m²/s, $h_0/\ell = 1/15$, $h_1/\ell = 2/100$, $h_2/\ell = 3/100$, $c/\ell = 5/100$, $\ell = 0.1$ m. We make calculations of channel wall amplitude-frequency response $A(\omega) = A(0, \omega)$ for cases of different numbers of terms in the series (15). The charts of $A(0, \omega)$ for cases $n = 1$ and $n = 4$ are presented in Fig. 2.

5 Conclusion

As a result, we suggest the mathematical model for studying the three-layered beam vibrations, for the case the three-layered beam is a part of the narrow parallel-plate gap with viscous incompressible flow. In the framework of the presented model, we can investigate bending oscillations three-layered beam resting on Winkler foundation and determine the beam resonant frequencies. The obtained expression for flow pressure offers an opportunity to study the change of pressure along the gap due to the vibration frequency of the stamp. Therefore, the suggested solution of hydroelasticity problem gives the occasion of modeling and investigating hydroelastic vibrations three-layered elastic elements included in the hydraulic drive systems, lubrication systems, and liquid cooling systems, as well as various machines and devices.



Acknowledgements The study was supported by the Russian Foundation for Basic Research (RFBR) Grant No. 18-01-00127-a and the President of Russian Federation Grant MD-756.2018.8.

References

1. Carrera E (2003) Historical review of zig-zag theories for multilayered plates and shells. *Appl Mech Rev* 56(3):287–308. <https://doi.org/10.1115/1.1557614>
2. Gorshkov AG, Starovoitov EI, Yarovaya AV (2005) Mechanics of layered viscoelastoplastic structural elements. Fizmatlit, Moscow
3. Vlasov VZ, Leontiev NN (1960) Beams, plates, and shells on elastic foundation. Fizmatgiz, Moscow
4. Wang YH, Tham LG, Cheung YK (2005) Beams and plates on elastic foundations: a review. *Prog Struct Mat Eng* 7(4):174–182. <https://doi.org/10.1002/pse.202>
5. Kubenko VD, Pleskachevskii YuM, Starovoitov EI, Leonenko DV (2006) Natural vibration of a sandwich beam on an elastic foundation. *Int Appl Mech* 42(5):541–547. <https://doi.org/10.1007/s10778-006-0118-8>
6. Starovoytov EI, Leonenko DV, Suleyman M (2007) Deformation of a composite plate on an elastic foundation by local loads. *Mech Compos Mater* 43(1):75–84. <https://doi.org/10.1007/s11029-007-0008-0>
7. Starovoitov EI, Leonenko DV (2012) Thermal impact on a circular sandwich plate on an elastic foundation. *Mech Solids* 47(1):111–118. <https://doi.org/10.3103/S0025654412010116>
8. Pradhan M, Dash PR, Pradhan PK (2016) Static and dynamic stability analysis of an asymmetric sandwich beam resting on a variable Pasternak foundation subjected to thermal gradient. *Meccanica* 51(3):725–739. <https://doi.org/10.1007/s11012-015-0229-6>
9. Lamb H (1920) On the vibrations of an elastic plate in contact with water. *Proc Roy Soc A* 98:205–216. <https://doi.org/10.1098/rspa.1920.0064>
10. Indeitsev DA, Polypanov IS, Sokolov SK (1994) Calculation of cavitation life-time of ship engine liner. *Problemy Mashinostraeniya i Nadezhnos'ti Mashin* 4:59–64
11. Bochkarev SA, Lekomtsev SV (2017) IOP conference series: material science engineering, vol 208, p 012009. <https://doi.org/10.1088/1757-899x/208/1/012009>
12. Amabili M (2001) Vibrations of circular plates resting on a sloshing liquid: solution of the fully coupled problem. *J Sound Vib* 245(2):261–283. <https://doi.org/10.1006/jsvi.2000.3560>
13. Mogilevich LI, Popov VS, Popova AA (2008) Oscillations of a cylinder liner of an internal combustion engine with a water cooling system caused by piston group impacts. *J Mach Manuf Reliab* 37(3):293–299. <https://doi.org/10.3103/S105261880803014X>
14. Velmisov PA, Ankilov AV (2017) Dynamic stability of plate interacting with viscous fluid. *Cybern Phys* 6(4):269–277
15. Önsay T (1993) Effects of layer thickness on the vibration response of a plate-fluid layer system. *J Sound Vib* 163(2):231–259. <https://doi.org/10.1006/jsvi.1993.1162>
16. Faria CT, Inman DJ (2014) Modeling energy transport in a cantilevered Euler-Bernoulli beam actively vibrating in Newtonian fluid. *Mech Syst Signal Process* 45(2):317–329. <https://doi.org/10.1016/j.ymssp.2013.12.003>
17. Akcabay DT, Young YL (2012) Hydroelastic response and energy harvesting potential of flexible piezoelectric beams in viscous flow. *Phys Fluids* 24(5). <https://doi.org/10.1063/1.4719704>
18. Ageev RV, Mogilevich LI, Popov VS, Popova AA, Kondratov DV (2014) Mathematical model of pulsating viscous liquid layer movement in a flat channel with elastically fixed wall. *Appl Math Sci* 8(159):7899–7908. <https://doi.org/10.12988/ams.2014.410795>
19. Mogilevich LI, Popov VS, Popova AA (2010) Dynamics of interaction of elastic elements of a vibrating machine with the compressed liquid layer lying between them. *J Mach Manuf Reliab* 39(4):322–331. <https://doi.org/10.3103/S1052618810040047>

20. Ageev RV, Kuznetsova EL, Kulikov NI, Mogilevich LI, Popov VS (2014) Mathematical model of movement of a pulsing layer of viscous liquid in the channel with an elastic wall. PNRPU Mech Bull 3:17–35. <https://doi.org/10.15593/perm.mech/2014.3.02>
21. Mogilevich LI, Popov VS, Popova AA (2018) Longitudinal and transverse oscillations of an elastically fixed wall of a wedge-shaped channel installed on a vibrating foundation. J Mach Manuf Reliab 47(3):227–234. <https://doi.org/10.3103/S1052618818030093>
22. Kondratov DV et al (2018) J Phys Conf Ser 944:012057. <https://doi.org/10.1088/1742-6596/944/1/012057>
23. Mogilevich LI et al (2018) J Phys: Conf Ser 944:012081. <https://doi.org/10.1088/1742-6596/944/1/012081>
24. Mogilevich LI, Popov VS, Popova AA (2017) Interaction dynamics of pulsating viscous liquid with the walls of the conduit on an elastic foundation. J Mach Manuf Reliab 46(1):12–19. <https://doi.org/10.3103/S1052618817010113>
25. Ergin A, Kutlu A, Omurtag MH, Ugurlu B (2012) Dynamic response of Mindlin plates resting on arbitrarily orthotropic Pasternak foundation and partially in contact with fluid. Ocean Eng 42:112–125. <https://doi.org/10.1016/j.oceaneng.2012.01.010>
26. Kramer MR, Liu Z, Young YL (2013) Free vibration of cantilevered composite plates in air and in water. Compos Struct 95:254–263. <https://doi.org/10.1016/j.compstruct.2012.07.017>
27. Ageev RV, Mogilevich LI, Popov VS (2014) Vibrations of the walls of a slot channel with a viscous fluid formed by three-layer and solid disks. J Mach Manuf Reliab 43(1):1–8. <https://doi.org/10.3103/S1052618814010026>
28. Mogilevich LI et al (2017) Mathematical modeling of three-layer beam hydroelastic oscillations. Vibroeng PROCEDIA 12:12–18. <https://doi.org/10.21595/vp.2017.18462>
29. Panovko YG, Gubanov II (1965) Stability and oscillations of elastic systems. Consultants Bureau Enterprises, Inc., New York
30. Vol'mir AS (1976) Shells in fluid and gas flows: aeroelasticity problems. Nauka, Moscow
31. Lamb H (1945) Hydrodynamics, 6th edn. Dover Publications Inc., New York

Use of Vibration Isolation Systems with Negative Stiffness on the Basis of Special Shaped Guides to Reduce Pump Piping Vibration



A. Tokarev, A. Valeev and A. Zotov

Abstract The paper is devoted to the problem of reduction of the vibration level of pipelines, caused by resonance with the disturbing frequency of pumping units. Each case of the occurrence of pipeline vibrations requires a careful and qualified analysis, because no universal methods for reducing the vibration of technological pipelines have been developed. It is offered to use vibration isolators based on the special shaped with negative stiffness area for vibration isolation. A pipeline in this case acts as a stabilizer for a vibration isolator with negative stiffness. The combination of these two elements in a particular area force characteristic “pipeline—vibration isolator” system becomes flat, thereby providing a reduction of its stiffness and thus natural frequencies. Analytical calculations have been made to prove the effectiveness of the proposed solution. Thus, in the case considered in the paper, the natural frequency of the pipeline oscillations is reduced from 33.33 to 9.5 Hz. A passive vibration isolator based on an elastic element moving along the guides of the design form perpendicular to their axis allows creating the force characteristics of a given shape that are necessary for vibration protection in each case.

Keywords Pump unit · Vibration isolation · Pipeline · Negative stiffness

1 Introduction

Technological pipelines at pumping stations are directly connected to high-pressure units and equipment and often operating in non-stationary modes, as a result of which they produce (or are transmitted to them from pumping equipment) increased vibration. Pipeline vibrations can often significantly exceed permissible values and cause damage to the pumping equipment. A common cause of failure in some cases

A. Tokarev (✉) · A. Valeev · A. Zotov
Ufa State Petroleum Technological University, 1, Kosmonavtov Street,
Ufa 450062, Russia
e-mail: art-tokarev@yandex.ru

© Springer Nature Switzerland AG 2020
A. A. Radionov et al. (eds.), *Proceedings of the 5th International Conference on Industrial Engineering (ICIE 2019)*, Lecture Notes in Mechanical Engineering,
https://doi.org/10.1007/978-3-030-22041-9_97

913

is the depressurization of the connections of the pump nozzles and pump piping due to their fatigue damage during vibration [1].

The high level of pipeline oscillations is transmitted to the connected pumping unit, which creates large stresses on its body and increases vibration. This becomes especially important when the frequencies coincide or are close. All this can lead to failures of the pumping equipment in case of damage to its parts and assemblies, as well as to unforeseen expenses for repair work.

No universal methods for reducing the vibration of technological pipelines have been developed. Each case of the occurrence of pipeline vibrations requires a careful and qualified analysis, as the methods of damping implemented in practice without sufficient justification do not always give the expected result.

1.1 Resonance of Natural Frequencies of Pump Piping with Disturbing Frequencies of the Pump

Considering the pump unit as a source of a large number of forced vibrations with different frequencies, it should be noted that in some cases, it is necessary to reduce the natural frequencies of the pump piping. Thus, as a result of examining a number of cases of pipeline oscillations [1–5], it was found that the main reason for this phenomenon is the resonance of the natural frequencies of the piping with the disturbing frequencies of the pump unit.

So, according to the results of vibration diagnostics of horizontal retaining pumping units NMP 5000-90 (Fig. 1) and a rotational speed of 1000 r/min, high values of vibration velocity are noted over a long observation period [2, 3, 6].

The main disturbing frequencies of the pump unit and the natural oscillation frequencies of the pump piping are presented in Table 1.

Fig. 1 Pump unit NMP 5000-90



Table 1 Main vibration frequencies of the NMP 5000-90 pumping unit

No.	Disturbing frequency of the pump unit, Hz	Natural frequency of pump piping, Hz
1	16.67—main rotary frequency	13.03
2	33.33—the second harmonic of the rotor frequency	26.06
3	116.69—the impeller blade frequency	34.5
4	233.38—the second harmonic of the impeller blade frequency	69

Table 2 Ratio of the disturbing frequencies to the natural frequencies of the pump piping

Natural frequencies, Hz	Disturbing frequencies, Hz	The ratio
13.03	16.67	0.78
26.06	33.33	0.78
34.5	33.33	1.04
69	33.33	2.07

The detuning of the natural frequencies f_0 from the disturbing frequencies f_{ip} is the main method of achieving vibration strength of the pipeline. In this case, the condition should be satisfied [7]:

$$f_0/f_{ip} \leq 0.75 \text{ and } f_0/f_{ip} \geq 1.3. \quad (1)$$

Consider the ratio of the disturbing frequencies with the closest natural frequencies of the pump piping vibrations (Table 2).

Thus, the increased vibration of the considered system “pump—pump piping” is caused by exceeding the permissible level of vibrations of the suction pipe in the horizontal section.

The most characteristic resonant frequency is $f_{03} = 34.5$ Hz at the excitation frequency $f_{p2} = 33.3$ Hz. The ratio of the natural and disturbing frequencies, in this case, is $f_{03}/f_{p2} = 1.04 \approx 1$, which causes resonant oscillations.

Under these conditions, detuning from the resonance between natural and disturbing frequencies becomes important to ensure acceptable operating parameters [8–10].

2 Vibration Isolation System with Negative Stiffness Based on Special Shaped Guides

To protect against vibrations of pipelines, systems with negative stiffness [2, 3, 11–14] have the highest efficiency, which make it possible to reduce vibration frequencies of the “pipeline—vibration isolator” system.

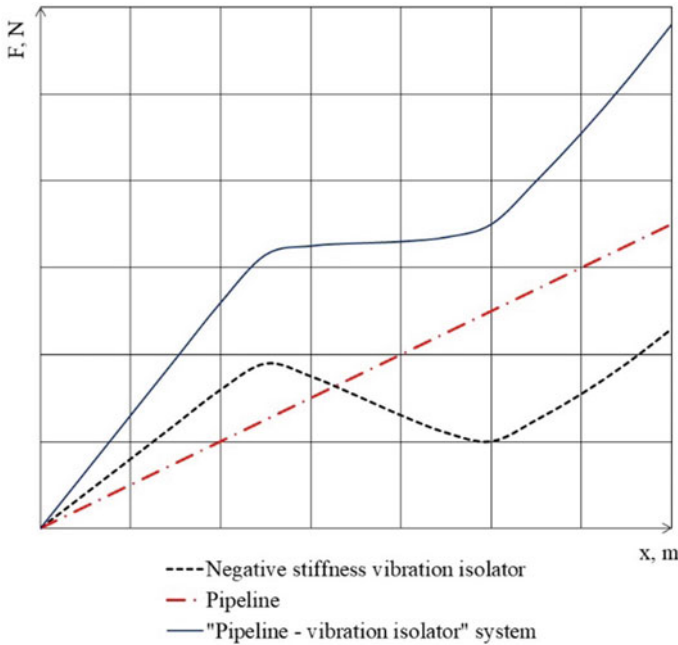


Fig. 2 Force characteristic of the vibration isolation system with negative stiffness

Considering the pipeline as an elastic system (simulating its mass on a spring), we obtain the missing elastic element, working as a “stabilizer” for a vibration isolator with negative stiffness (Fig. 2).

With the combination of these two elements in a particular area force characteristic “pipeline—vibration isolator” system becomes flat [13, 15–20], thereby providing a reduction of its stiffness and thus natural frequencies determined by the equation:

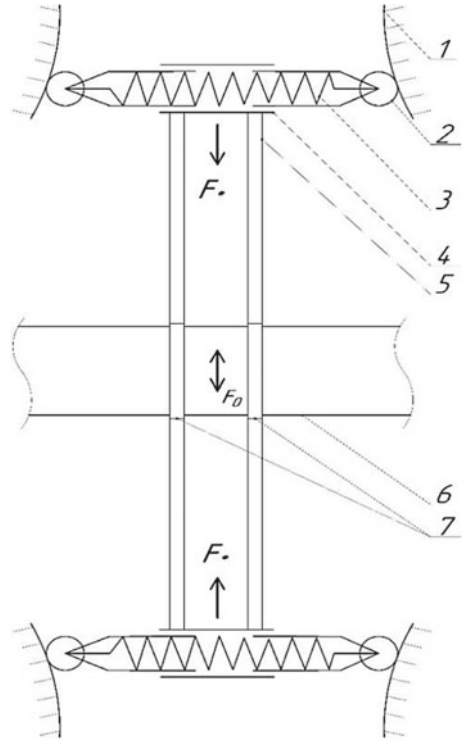
$$f_0 = \frac{1}{2\pi} \sqrt{\frac{c}{m}}, \tag{2}$$

where c is the stiffness coefficient determined by the pipeline itself, N/m; m is the mass of the protected object, kg.

Negative stiffness in this system is obtained on the downward section of the force characteristic of the vibration isolation system (Fig. 2). That is, the working range of the vibration isolation system is set in such a way that its force characteristic decreases with increasing amplitude of the pipeline oscillations. In combination with the linearly growing force characteristic of the pipeline, which acts as a stabilizer with positive stiffness, we obtain a flat section with an almost constant restoring force with increasing values of vibration displacements. When working in this area (with preliminary preload), the stiffness of the “pipeline—vibration isolator” system decreases.



Fig. 3 Negative stiffness system based on special shaped guides 1—special profile guides; 2—roller support; 3—compression spring; 4—guide glass; 5—hard link; 6—pipeline; 7—clamps; F_0 —driving force; and F_* —restoring force



A system with negative stiffness can be built on the basis of guides that have a specially designed shape (Fig. 3).

The elastic element of the system is a compression spring 3, moving perpendicular to the axis of the guides of a specially designed form 1 by means of roller supports 2. The compression spring 3 is connected through a hard link 5 to the pipeline 6 by clamps 7.

For the case under consideration, the value of negative stiffness should be calculated in such a way as to reduce the frequency of oscillations of the “pipeline—vibration isolator” system to a level that does not coincide with the driving frequencies of the pump unit, taking into account (1).

The shape of guides must be calculated for each case separately. The design scheme is presented in Fig. 4.

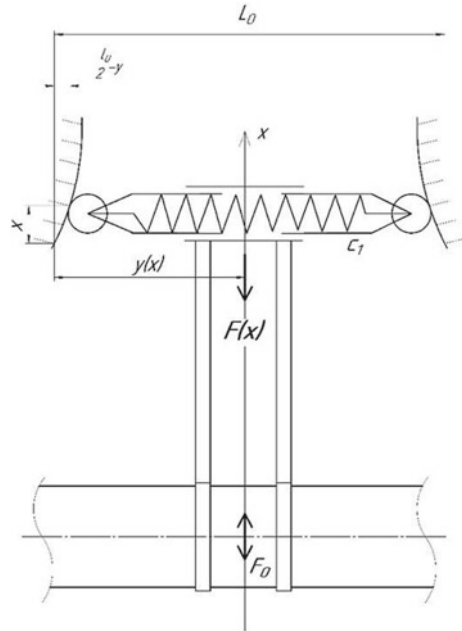
The amplitude of the restoring force $F(x)$ is determined by the equation:

$$F(x) = -\frac{\partial P}{\partial x}, \tag{3}$$

where P is the potential energy of the elastic element; c_1 —is the spring stiffness; $(\frac{l_0}{2} - y)$ is the amplitude of the spring compression.

The potential energy of the compressed spring is

Fig. 4 Design scheme of a vibration isolation system with negative stiffness based on special shaped guides



$$P = \frac{c_1}{2} (l_0 - 2y)^2, \tag{4}$$

where y is the function that determines the shape of the guides; l_0 is the length of the unstressed spring.

In this case, the length of the unstressed spring l_0 is greater than the length of the spring L_0 in the zero position ($x = 0$).

Since the function y depends only on the x -coordinate, it is possible to reduce the partial differential equation to an ordinary differential equation:

$$F(x) = -2c_1(2y - l_0) \frac{dy}{dx} \tag{5}$$

The initial condition for this differential equation: for $x_0 = 0$ $y_0 = L_0/2$.

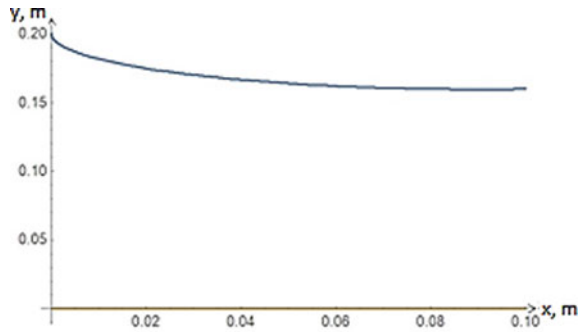
The amplitude of the restoring force $F(x)$ can be written as

$$F(x) = b - c_* \cdot x, \tag{6}$$

where $b = mg$; c_* —required value of negative stiffness.

Solving the differential Eq. (5), you can get the shape of the guides, determined by the function y for a given force $F(x)$. It is required to receive the restoring force, for receiving negative stiffness. The differential Eq. (5) with regard to (6) can be rewritten in the following form

Fig. 5 Profile of the guides for negative stiffness vibration isolation system



$$-(b - c_* \cdot x) = -2c_1(2y - l_0) \frac{dy}{dx}, \tag{7}$$

The initial condition: for $x_0 = 0, y_0 = L_0/2$.

Solving the differential Eq. (7), we obtain a function for determining the profile of the guides:

$$y = \frac{c_1 \cdot l_0 \pm \sqrt{-2c_1 \cdot D_0 + c_1^2 \cdot l_0^2}}{2c_z}, \tag{8}$$

where $D_0 = \frac{c_* \cdot x^2}{2} - bx + c_1 l_0 L_0 - \frac{c_1 \cdot L_0^2}{2}$.

With the minus sign, we get the profile of the guides for the compression spring (Fig. 5).

The profile of the guides was calculated to create the value of negative stiffness $c_* = 19558000$ N/m, at which the stiffness of the “pipeline—vibration isolator” system becomes $c = 1800000$ N/m. Thus, the natural frequency of the pipeline oscillations is reduced to $f_{01} = 9.5$ Hz. The ratio of the natural and disturbing frequencies is $f_{01}/f_p = 0.285$, condition “(1)” is satisfied.

3 Summary

The proposed design of the vibration isolator allows the use of a section with negative stiffness to reduce the vibration of the pump piping, operating in resonance conditions, by reducing the natural frequencies of oscillations of the “pipeline—vibration isolator” system. A passive vibration isolator based on an elastic element moving along the guides of the design form perpendicular to their axis allows to create the force characteristics of a given shape that are necessary for vibration protection in each case.

References

1. Samarin AA (1979) Vibratsii truboprovodov energeticheskikh ustanovok i metodyi ih ustraneniya (The vibrations of pipelines of power equipment and methods of their elimination). *Energia*, Moscow, p 228
2. Tokarev A, Zotov A, Valeev A (2017) The application of passive vibroprotective systems having power characteristics with hysteresis loops of rectangular shape for the main pumping units. *Procedia Eng* 176:118–127. <https://doi.org/10.1016/j.proeng.2017.02.279>
3. Tokarev AP, Zotov AN (2017) Primenenie passivnykh vibroizolyatorov s otritsatelnoy zhestkostyu dlya magistralnykh nasosnykh agregatov. (Application of negative stiffness passive vibration isolators for main pumping units). *Neftgazovoe delo* 15(1):133–139
4. Gumerov AG, Gumerov RS, Akberdin AM (2001) Ekspluatatsiya oborudovaniya nefte-perekachivayushchikh stantsiy (Operation of pumping stations equipment). Moscow, 475 p
5. Gumerov AG, Gumerov RA, Iskhakov RG (2008), Vibroizoliruyuschaya kompensiruyuschaya sistema nasosno-energeticheskikh agregatov (Vibration-isolating compensation system of pump-power units). SUE “IPTER”, Ufa, 328 p
6. Drozyner P (2011) Determining the limits of piping vibration. *Sci Probl Mach Oper Maintenance* 1(165):97–103
7. GOST 32388-20 13 Technological pipelines (2014) Norms and methods of strength analysis, vibration and seismic effects. Introduced for the first time. Standartinform, Moscow, 109 p
8. Nikitin NN (1990) Kurs teoreticheskoy mekhaniki (The course of theoretical mechanics). Vysshaya Shkola, Moscow, p 607
9. YaG Panovko (1990) Osnovyi prikladnoy teorii kolebaniy i udara (Fundamentals of applied theory of oscillations and shock). Politehnika, Leningrad, p 272
10. Andreeva LE (1981) Uprugie elementy priborov. (Elastic elements of devices). Mashinostroenie, Moscow, 391 p
11. Tokarev A, Zotov A, Valeev A (2017) Study of application of vibration isolators with quasi-zero stiffness for reducing dynamics loads on the foundation. *Procedia Eng* 176:137–143. <https://doi.org/10.1016/j.proeng.2017.02.281>
12. Platus DL, McMahon J Negative-stiffness vibration isolators. How they work. Available via DIALOG. https://www.minusk.com/content/technology/how-it-works_passive_vibration_isolator.html. Accessed 14 Jan 2018
13. Alabuzhev P, Gritchin A, Kim L, Migirenko G, Chon V, Stepanov P (1989) Vibration protecting and measuring systems with quasi-zero stiffness. Hemisphere Publishing, New York, 110 p
14. Platus David L, McMahon J Negative-stiffness vibration isolation gains popularity. <https://www.photonics.com/Article.aspx?AID=38385>. Accessed 20.11.2018
15. Ahn H-J (2010) A unified model for quasi-zero-stiffness passive vibration isolators with symmetric nonlinearity. In: 22nd international conference on design theory and methodology; special conference on mechanical vibration and noise, pp 689–693
16. Robertson W, Cazzolato B, Zander A (2013) Planar analysis of a quasi-zero stiffness mechanism using inclined linear springs. In: Conference: acoustics, at Victor Harbour, pp 1–6
17. Carrella A, Friswell MA (2008) A passive vibration isolator incorporating a composite bistable plate. IP ACS Open Access Electronic Library, OpenLi.brary, 6 Euromech Nonlinear Dynamics Conference, ENOC 2008
18. Zotov AN, Akhiyarov DT (2007) Impact protection system with quasi-null rigidity for oilfield equipment. In: Intellectual service for oil & gas industry analysis, solution, perspectives, proceedings, vol 4. Mis-kolc, p 206–212
19. Zotov AN (2008) Systems with quasi-zero-stiffness characteristic. Abstracts. ENOC 2008 Sixth EUROMECH Nonlinear Dynamics Conference, FINAL PROGRAM and ABSTRACTS, June 30–July 4. Saint Petersburg, 5 p
20. Valeev AR, Zotov AN, Kharisov ShA (2015) Designing of compact low frequency vibration isolator with quasi-zero stiffness. *J Low Freq Noise Vib Active Control* 34(4):459–474

Effect of Two Cracks in a Rotor on Stiffness Using the Theory of Fracture Mechanics



Salam Ahmed Abed, Mohammad Reza Bahrami
and Jassim Farij Thijel

Abstract In this paper, a Jeffcott model with an offset disk rotor system with two cracks has been analyzed. By using the theory of fracture mechanics for two cracks in a Jeffcott model, a mathematical model of the rotor shafts with cracks with changing the crack depths has been created. The increase in the growth of the cracks is one of the most dangerous phenomena in rotors. The effect of changing speeds on the dynamic parameters of journal bearings (stiffness and damping) and then on Sommerfeld number has been studied. The relation of the types of stiffnesses ratios of a cracked rotor and stress concentration factor of the crack tip, with the angle of rotation rotor, has been found. The results have been obtained analytically using MATLAB. The results show that when cracks are fully open, the stiffness ratio in all directions reaches to a minimum while the concentration stress reaches to the maximum.

Keywords Rotor dynamics · Stiffness ratio · Cracked rotor · Two cracks · Stress · Concentration factor

1 Introduction

In the last years, because of the high cost of maintenance of rotary machines, the dynamics of rotors turn into a very important issue in the design of rotary machines, based on vibration. The rotor is the most important part in rotary machinery that

S. A. Abed (✉)

Peter the Great St. Petersburg Polytechnic University, 29, Polytechnicheskaya st.,
St. Petersburg 195251, Russia
e-mail: almuhands67@gmail.com

M. R. Bahrami

Innopolis University, 1, Universitetskaya St., Innopolis 420500, Russia

J. F. Thijel

Midland Refineries Company (Al—Daura Refinery), Ministry of Oil, Baghdad 6178, Iraq

© Springer Nature Switzerland AG 2020

A. A. Radionov et al. (eds.), *Proceedings of the 5th International Conference on Industrial Engineering (ICIE 2019)*, Lecture Notes in Mechanical Engineering,

https://doi.org/10.1007/978-3-030-22041-9_98

921

gives the main function of the machine, because of the widely used in industry and power plants. So, this work has been focused on the study of an uncracked and a cracked rotor.

A crack may grow from the small size on the shaft surface or from inside the material, and then it appears because of the high-stress concentration.

The unsymmetrical rotor, which has disk lies on unequal distance from both bearings, has been chosen for investigation. A mathematical model for oil film short bearing has been performed. This mathematical model depends on the clearance, rotational speed, and oil properties and is used for finding stiffness and damping coefficients in horizontal, vertical, and cross-coupling directions due to oil film for each side of the journal bearing. Then one can derive the equation of motion of the uncracked shaft model using all these parameters of bearings (stiffness, damping, and equivalent shaft mass) and solve this equation of motion by using MATLAB.

The theory of fracture mechanics has been used and represented the cracks theoretically. Many cases of cracks have been taken for a study like two cracks that one is a slant and the other is transverse. Each crack is located 15 mm near each side of the disk of the rotor with different depths. $(0.2R, 0.4R)$, $(0.5R, 0.8R)$, and $(0.8R, 0.8R)$ are cracks' depths for first and second crack, respectively that have been used in this study. The slant angles of the first crack are 30° , 60° , and 90° .

1.1 Literature Review

Since 1954 up to now, many experts from many countries in the world published papers in many different areas that deal with cracks in shafts. Crack detection has enticed the interest of researchers in the whole world based on the idea that variation of a rotor's dynamic behavior could be applied for the overall failure exposure from the seventies [1].

The applications of rotors are very wide like all electric motor's rotor, centrifugal pumps, centrifugal compressors, steam turbines in oil refineries, steam, gas, and water turbines used in power plants. and gas turbines in air crafts jet engines. Rotors have been studied analytically and numerically with the presence of cracks in rotor's shaft in order to detect the crack and to find crack depth without using the classical methods like ultrasonic, dye penetration, X-radiography, television viewing, or acoustic emission. Previous studies [2–13] showed that crack development might occur in the case of shrink fit, thermal stresses, and thermal shocks and generates high local stress intensity factor (SIF). This high SIF causes the starting of crack and propagation. The crack may take various shapes. It is commonly perpendicular to the shaft centerline, known as transverse crack, which represented by circular sector shape. The stress concentration factor depends on the geometry of the crack and not on its size. These factors gated from typical engineering reference materials to predict the stresses that could not be analyzed by applying the strength of materials approaches [1, 2, 4, 12, 13].

2 Fundamental Equations

There exist various parameters and physics phenomena which carry the rotors away from stationary structures. However, the key variations are the supports of fluid film, that doing a lot of things more than the friction losses, see Fig. 1. The bearing center C and the journal center \tilde{C} will form an attitude of the bearing and make the angle with the vertical load W , see Fig. 1. The clearance h will be variations between two values, see Fig. 1. Table 1 shows the dimension of the selected model and the properties of the shaft's material (AISI4140).

From the bearing features (geometry, speed, eccentricity, pressure, attitude angle), the Sommerfeld parameter can be derived to give an indication about the bearing eccentricity as [6, 7]:

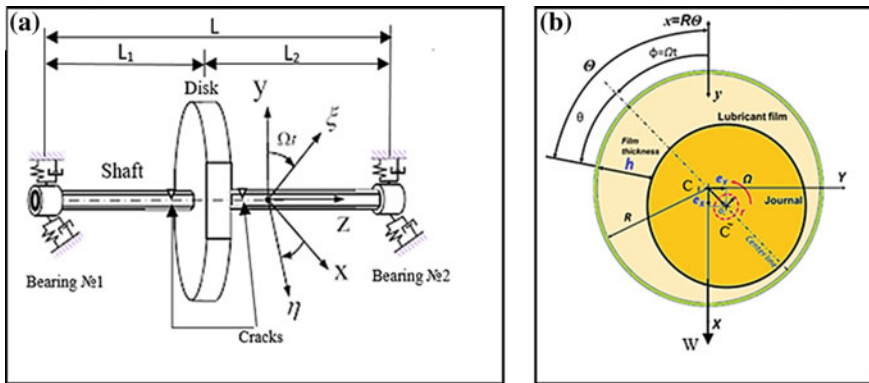


Fig. 1 a Bearings representation by rotor springs and dampers, b Sliding bearing: eccentricity between shaft and bearing

Table 1 Dimensions of model studied and shaft material AISI4140 properties

Description	Dimensions of the selected model
Total shaft length (m)	0.654
Shaft diameter (m)	0.048
Disk diameter (m)	0.34
Distances between disk and bearings (m)	$L1 = 0.414, L2 = 0.24$
Crack depths (m)	0.005, 0.01, 0.015, 0.020
Distances between the left side of disk and crack (m)	0.01
Disk thickness (m)	0.02
Total rotor mass (Kg)	23.25
Young Modulus (E) (N/m ²)	2.05×10^{11}
Poisson's ratio (ν)	0.29
Density (ρ) (Kg/m ³)	7850

$$S = \frac{\mu D L N}{W} * \left(\frac{r}{C_l} \right)^2. \quad (1)$$

The radial and tangential forces F_r , F_t are:

$$F_r = -\frac{D \Omega \mu L^3 \epsilon^2}{2h^2(1 - \epsilon^2)^2}, F_t = -\frac{\pi D \Omega \mu L^3 \epsilon}{8h^2(1 - \epsilon^2)^{3/2}}. \quad (2)$$

The force F_t opposes the sliding motion. The power loss is $F_t \times \Omega D/2$. The resultant force on the bearing is opposite to the applied load on the rotor:

$$F = \sqrt{F_r^2 + F_t^2} = \frac{\pi D \Omega \mu L^3 \epsilon}{8h^2(1 - \epsilon^2)^2} ((16/\pi^2 - 1)\epsilon^2 + 1)^{1/2}. \quad (3)$$

If the load on the bearing is known, then the modified Sommerfeld number will be, [8]:

$$S_s = \frac{D \Omega \mu L^3}{8 F h^2}. \quad (4)$$

The vertical resultant force is a common case, where the load is due to the rotor weight. In this case, the position of a journal in the bearing ensures that the load is indeed vertical. If the magnitude of this load is known, then the bearing eccentricity may be obtained by rearranging “Eq. 3” to give “Eq. 5,” where S_s from “Eq. 4,” is called modified Sommerfeld number and is known for a particular speed, load, and oil viscosity, [10]:

$$\epsilon^8 - 4\epsilon^6 + (6 - S_s^2(16 - \pi^2))\epsilon^4 - (4 + \pi^2 S_s^2)\epsilon^2 + 1 = 0. \quad (5)$$

The value of eccentricity ratio, ϵ , is $\tilde{C}-C/h$ and always is taken between 0 and 1. Here, ϵ has been found by iteration method (Newton–Raphson method) from 0 to 6000 RPM using MATLAB. Then the relation between modified Sommerfeld number and all of stiffness and damping with rotation speed has been found. When a linear bearing model is designed in the machine, displacement must be small since the linear analysis does not include any limitations on the displacement. In this study, short journal bearings have been considered; therefore, the matrices are 2×2 for stiffness and damping matrices could be found as, [7].

$$K = \frac{F}{h} \begin{bmatrix} a_{xx} & a_{xy} \\ a_{yx} & a_{yy} \end{bmatrix} = \begin{bmatrix} k_{xx} & k_{xy} \\ k_{yx} & k_{yy} \end{bmatrix}, c = F/(h \times \Omega) \begin{bmatrix} b_{xx} & b_{xy} \\ b_{yx} & b_{yy} \end{bmatrix} = \begin{bmatrix} c_{xx} & c_{xy} \\ c_{yx} & c_{yy} \end{bmatrix}. \quad (6)$$

All parameters in “Eq. 6” were taken from [7, 14].

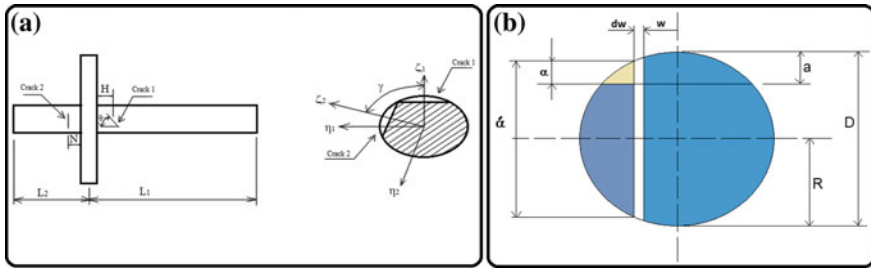


Fig. 2 a Two cracks in rotor one slant and the other straight, b Cracked region cross-sectional area

Figure 2a shows the cracks function of the stresses acting on the crack tip. The stress intensity factor (SIF) denoted by KI mode $\{I\}$ on the crack is used for the crack opening mode and is given by [4]:

$$\begin{aligned}
 K1^{(I)} &= KQ\zeta1^{(I)} + KQ\eta1^{(I)} \text{ (for the first crack),} \\
 K2^{(I)} &= KQ\zeta2^{(I)} + KQ\eta2^{(I)} \text{ (for the second crack),} \\
 KQ\zeta1 &= \frac{Q\zeta1 \times (L1 - H) \times \alpha'}{4I} \sqrt{\pi\alpha} \times F, \\
 KQ\eta1 &= \frac{Q\eta1 \times (L1 - H) \times w}{2I} \sqrt{\pi\alpha} \times \tilde{F} \sin \theta,
 \end{aligned}
 \tag{7}$$

where $KQ\zeta1^{(I)} = \sigma\zeta1\sqrt{\pi\alpha} \times F$, $\sigma\zeta1 = (Q\zeta1 \times (L1 - H) \times \alpha') / (8I)$, $KQ\eta1^{(I)} = \sigma\eta1\sqrt{\pi\alpha} \times \tilde{F}$, $\sigma\eta1 = (Q\eta1 \times (L2 - N)) \times w \times \sin\theta / I$. F and \tilde{F} are the correction factors in ζ and η directions, respectively [4].

From the fracture mechanics theory and from, Fig. 2b may find additional deflection resulting from a crack in $\zeta1-\eta1$ coordinates [12]:

$$ui1 = \frac{\partial}{\partial Qi1} [\int J1(\alpha) d\alpha].
 \tag{8}$$

Substituting the strain energy density, $J1(\alpha) = \frac{1}{E} [KQ\zeta1^{(I)} + KQ\eta1^{(I)}]^2$, in “Eq. 8” and using “Eq. 7” we obtain:

$$\begin{aligned}
 u_{\zeta 1} &= \frac{2}{E} \iint_{A_1} \left(\frac{Q_{\zeta 1} \times (L1 - H) \times \alpha' \times \sqrt{\pi \alpha} \times F}{4I} + \dots \right. \\
 &\quad \left. + \frac{Q_{\eta 1} \times (L1 - H) \times w \times \sqrt{\pi \alpha} \times \tilde{F} \sin \theta}{2I} \right) \frac{(L1 - H) \times \alpha' \times \sqrt{\pi \alpha} \times F}{4I} d\alpha dw, \\
 u_{\eta 1} &= \frac{2}{E} \iint_{A_1} \left(\frac{Q_{\zeta 1} \times (L1 - H) \times \alpha' \times \sqrt{\pi \alpha} \times F}{4I} + \dots \right. \\
 &\quad \left. + \frac{Q_{\eta 1} \times (L1 - H) \times w \times \sqrt{\pi \alpha} \times F \sin \theta}{2I} \right) \frac{(L1 - H) \times w \times \sqrt{\pi \alpha} \times \tilde{F}}{2I} \sin \theta d\alpha dw.
 \end{aligned}
 \tag{9}$$

The same way for deflection in $\zeta 2$ - $\eta 2$ coordinate for the second crack has been utilized where

$$\begin{aligned}
 \begin{pmatrix} Q_{\zeta 2} \\ Q_{\eta 2} \end{pmatrix} &= \begin{bmatrix} \cos \gamma & \sin \gamma \\ -\sin \gamma & \cos \gamma \end{bmatrix} \begin{pmatrix} Q_{\zeta 1} \\ Q_{\eta 1} \end{pmatrix}, \\
 \tilde{u}_{\zeta 1} &= u_{\zeta 1} + u_{\eta 2} \sin \gamma + u_{\zeta 2} \cos \gamma + u_{\zeta 1}^0, \\
 u_{\zeta 1}^0 &= Q_{\zeta 1} L^2 L^2 / 3EIL.
 \end{aligned}
 \tag{10}$$

In the same way for the direction of $\eta 1$, one can write: $\tilde{u}_{\eta 1} = u_{\eta 1} + u_{\zeta 2} \sin \gamma + u_{\eta 2} \cos \gamma + u_{\eta 1}^0$, where $u_{\eta 1}$ is the deflection due to the crack 1 in the direction $\eta 1$, $u_{\zeta 2}$ is the deflection due to crack № 2 in direction $\zeta 2$, $u_{\eta 2}$ is the deflection due to crack 2 in direction of $\eta 2$, and $u_{\eta 1}^0$ is the deflection of uncracked shaft in $\eta 1$ direction.

The direct and cross-coupled flexibilities $g_{\zeta}, g_{\eta}, g_{\zeta \eta}, g_{\eta \zeta}$ could be found as, [13]:

$$g_{\zeta} = \frac{\partial \tilde{u}_{\zeta 1}}{\partial Q_{\zeta 1}}, g_{\zeta \eta} = \frac{\partial \tilde{u}_{\zeta 1}}{\partial Q_{\eta 1}} = g_{\eta \zeta} = \frac{\partial \tilde{u}_{\eta 1}}{\partial Q_{\zeta 1}}, g_{\eta} = \frac{\partial \tilde{u}_{\eta 1}}{\partial Q_{\eta 1}}.
 \tag{11}$$

The above equations have been used to find the flexibilities of the two-cracked shaft of rotors; one is transverse crack and the other one is slant crack. The results are obtained by MATLAB and plotted.

The values of the flexibilities depend on the values of angles γ, θ , and on the cracks' depths [15]. Angle γ is the orientation between two cracks, and angle θ is the slant angle of the first crack. The stiffness could be written as, [4]:

$$K_{\zeta} = \frac{g_{\eta}}{g_{\eta} g_{\zeta} - g_{\zeta \eta}^2}; \quad K_{\eta} = \frac{g_{\zeta}}{g_{\eta} g_{\zeta} - g_{\zeta \eta}^2}; \quad K_{\zeta \eta} = \frac{-g_{\zeta \eta}}{g_{\eta} g_{\zeta} - g_{\zeta \eta}^2}.
 \tag{12}$$

From “Eq. 12,” we can find the values of the stiffness ratios in all directions with the angular rotation of the shaft relative to the cracked rotor.



By taking Newton’s second law in ζ and in η directions, one can get the equation of motion of cracked shaft as:

$$\begin{aligned}
 &M(\ddot{\zeta}_1 - 2\Omega\dot{\eta}_1 - \Omega^2 \zeta_1) + C(\dot{\zeta}_1 - \Omega\eta_1) \\
 &\quad + K_\zeta \zeta_1 + K_{\zeta\eta} \eta_1 = \dots = mec \Omega^2 \cos \beta - Mg \cos \theta', \\
 &M(\ddot{\eta}_1 - 2\Omega\dot{\zeta}_1 - \Omega^2 \eta_1) + C(\dot{\eta}_1 - \Omega\zeta_1) \\
 &\quad + K_\eta \eta_1 + K_{\eta\zeta} \zeta_1 = \dots = mec \Omega^2 \sin \beta - Mg \sin \theta',
 \end{aligned}
 \tag{13}$$

where β is the orientation of mass unbalance from the ζ_1 axis in the direction of shaft rotation and θ' is the angle of rotation of the shaft.

“Equation 13” represents the equation of motion of shaft with two cracks. After solving the equation of motion by MATLAB and finding the maximum response, one can get the forces Q_ζ , Q_η on the crack cross section. Then one can find the variation of SCF with the angular rotation of the shaft.

3 Results

The stiffness of the rotor is derived based on the theory of fracture mechanics. Figures 3 and 4a show that the stiffness in K_ζ , K_η , and $K_{\zeta\eta}$ directions decreases with rotation angle till reaching to the minimum value at rotation angle 180° , and then it decreases to reach a value of uncracked stiffness at 360° because of closing crack in this stage. In Fig. 4b, the stress concentration factor (SCF) in crack tip increases with the angle of rotation till 180° , and then it decreases till 360° as crack breathing case.

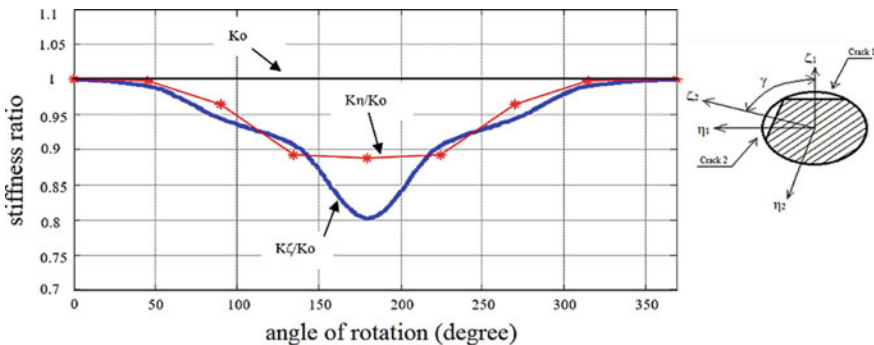


Fig. 3 Stiffness ratio versus angle of rotation of the shaft with two cracks, one slant, and one transverse, with $0.8R$, $0.5R$ crack depth and $\theta_2 = 90^\circ$, $\theta_1 = 30^\circ$, and $\gamma = 0^\circ$

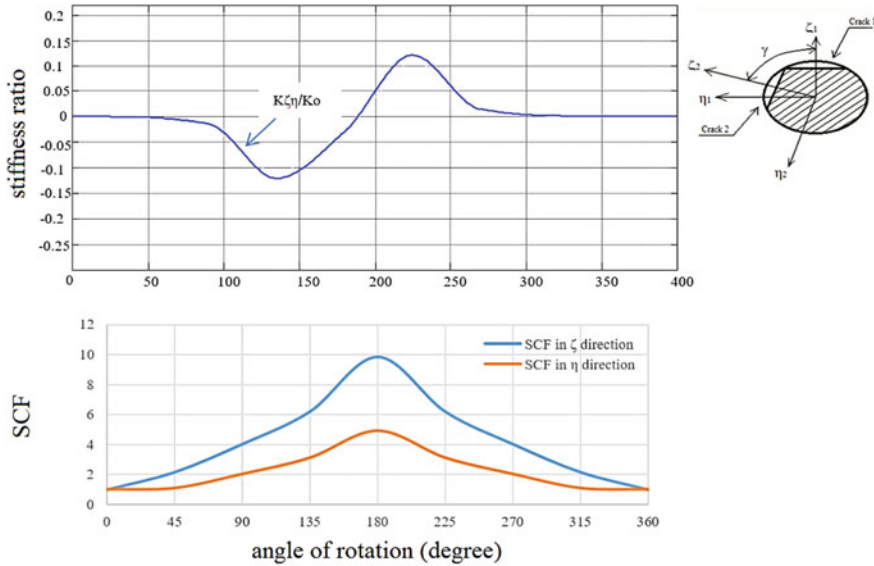


Fig. 4 a Cross-stiffness ratio, b SCF in the crack tip versus angle of rotation of the shaft with two cracks, one slant, and one transverse, with $0.8R$, $0.5R$ crack depth and $\theta_2 = 90^\circ$, $\theta_1 = 30^\circ$ and $\gamma = 0^\circ$

4 Conclusion

The variation of stiffness ratio in horizontal, vertical, and cross-coupling directions with stress concentration factor (SCF) is proportional to the crack depths and the slant angle of the first crack. The results of the study of the two-cracked rotor will be useful in diagnosing fatigue cracks in real rotors.

References

1. Guo C, Yan J, Yang W (2017) Crack detection for a Jeffcott rotor with a transverse crack: an experimental investigation. *Mech Syst Signal Process* 15(83):260–271
2. Upadhyay N, Kankar PK (2017) Dynamic analysis of rotor-bearing system by considering the transverse crack on the rotor. *Eur J Comput Mech* 26(3):336–350
3. Upadhyay DK, Satankar RK (2017) Dynamic behavior of a disc-rotor system subjected to different crack location & different speed—FEM investigation: a review. *IJSRD—Int J Sci Res Dev* 5(6):2321–2613
4. Darpe AK, Gupta K, Chawla A (2003) Dynamics of a two-track rotor. *J Sound Vib* 259(3):649–675
5. Liu Chao, Jiang D (2017) Dynamics of slant cracked rotor for a steam turbine generator system. *J Eng Gas Turbines Power* 139(6):062502



6. Abed SA, Bahrami MR, Thijel JF (2018) Analytical and numerical investigation to the effect of single transverse crack on the dynamic behavior of the rotor-bearings system. *Int J Eng Technol* 7(3.20)
7. Abed SA, Al Draji JF, Bahrami MR (2018) Numerical investigation of a rotary-bearing system with a single crack using harmonic analysis. *St. Petersburg Polytechnic Univ J Eng Sci Technol* 24(03):139–152
8. Xiao-Bo R, Yan-Dong C, Ying-Xiang C et al (2017) Dynamics of a cracked rotor system with oil-film force in parameter space. *Nonlinear Dyn* 88(4):2347–2357 (Springer Science + Business Media, Dordrecht)
9. Ishida Y, Yamamoto T (2012) *Linear and nonlinear rotor dynamics. A modern treatment with applications*, 2nd enlarged and improved edition. Wiley-VCH Verlag, Germany
10. Michael IF, John ET, Seamus DG, Arthur WL (2012) *Dynamics of rotating machines*. Cambridge University Press, 32 Avenue of the Americas New York NY 10013, 2473 p
11. Ignacio RV, Luis MP, Humberto CH (2013) Vibrational response of a rotor supported in hydrodynamics short bearings, *Memories Del Xix International Congress of Her Annual Somim, Pachuca, Hidalgo, Mexico*, pp 1085–1094
12. Abed SA, Bahrami MR, Thijel JF (2018) Analytical and numerical investigation to the effect of two cracks on the dynamic behavior of rotor-bearings system. *Russ Sci J “Sci Bus Ways Dev”* 11(89):8–13
13. Abed SA, Bahrami MR, Thijel JF (2018) Dynamic behavior of rotor-bearings system with changing angle orientation between two cracks. *Russ Sci J “Sci Prospects”* 11(110):26–34
14. Rao JS (2011) *History of rotating machinery dynamics*. Springer Science + Business Media BV
15. Abed SA, Bahrami MR, Thijel JF (2019) Stability of a flexible rotor-bearing system with a transverse crack. In: Uhl T. (ed) *Advances in mechanism and machine science*. IFToMM WC 2019. Mechanisms and machine science, vol 73. Springer, Cham, pp 3363–3373

How Asymmetric Initial Imperfections in Shape Affect Free Oscillations of Thin Shells



S. V. Seregin

Abstract The relevance of studying the deformation and strength is related to the use of thin circular cylindrical shells in structures exposed to intense dynamic operation. When studying complex dynamics issues, the emphasis is made on solving the problems of free oscillations in structural elements. Real shell structures will unavoidably deviate from a perfect cylindrical shape (the initial imperfections) that emerge either in production or in operation. It is known that such imperfections result in specific phenomena as shells oscillate. This paper dwells upon the bending oscillations in thin shells. It demonstrates there may emerge an additional bending frequency spectrum-splitting zone due to the initial shell-shape imperfections. It has been discovered that the bending frequency spectrum splitting occurs not only when the number of circumferential dynamic strain waves equals that of the shell-shape imperfection waves, as is believed nowadays, but also when the number of shaping waves is half that of the shell-shape imperfection waves.

Keywords Shell · Dynamics · Imperfection · Resonance

1 Introduction

Thin circular cylindrical shells are widely used as the basic load-bearing elements in aerospace tech. It is inevitable that such structures initially deviate from a perfect circular shape, which is due to the way they are made.

It is nowadays believed that the axisymmetric part of the dynamic bending affects only the nonlinear behavior of shells, while it is sufficient to consider only the conjugate bending shapes in case of low-amplitude oscillations [1–3].

S. V. Seregin (✉)

Federal State-Funded Educational Institution of Higher Education Komsomolsk-on-Amur State University, 27, Lenin Avenue, Komsomolsk-on-Amur 681000, Russia
e-mail: Seregin-komsHome@yandex.ru

© Springer Nature Switzerland AG 2020

A. A. Radionov et al. (eds.), *Proceedings of the 5th International Conference on Industrial Engineering (ICIE 2019)*, Lecture Notes in Mechanical Engineering,

https://doi.org/10.1007/978-3-030-22041-9_99

931

However, papers [4–7] present a simpler (limiting) problem of oscillations in an infinitely long circular cylindrical shell, which is a ring subjected to flat strain; the example cited there shows that even when the problem is stated as a linear problem, considering the radial oscillations [8] results in the qualitative and quantitative improvements in the results compared to an interaction exclusive to conjugate bending shapes. The results shown in the paper are in qualitative agreement with the computational studies [9, 10]. The proposed mathematical model is now widely applied to solve the dynamics of finite-length shells carrying an attached weight and weakened due to the presence of holes; in such problems, the model eliminates a number of qualitative inconsistencies and reveals new effects and features of how conjugate bending shapes interact with the radial shapes [11–15]. The results of these studies are consistent with the computational studies [16–20], which also outline the contradictions and error in analytical solutions.

This paper continues the studies [4, 6, 7, 9] in the sense that the results obtained for a limiting problem (the oscillations of an isolated geometrically imperfect ring) are generalized for the oscillations of a finite-length shell, which initially deviates from a perfect circular shape.

2 Mathematical Model

Let a butt-hinged circular cylindrical shell of the mass M_0 , radius R , length l , and thickness h execute low bending oscillations near the main resonance zone.

2.1 Linearized Equations of Motion

The analysis is based on the known shallow-shell theory equations, which are written as follows for an isotropic imperfect shell:

$$\begin{aligned} \frac{D}{h} \nabla^4 w &= \frac{\partial^2 w_0}{\partial x^2} \frac{\partial^2 \Phi}{\partial y^2} + \frac{1}{R} \frac{\partial^2 \Phi}{\partial x^2} - \rho \frac{\partial^2 w}{\partial t^2}, \\ \frac{1}{E} \nabla^4 \Phi &= -\frac{\partial^2 w_0}{\partial x^2} \frac{\partial^2 w}{\partial y^2} - \frac{1}{R} \frac{\partial^2 w}{\partial x^2}, \end{aligned} \quad (1)$$

In (1), $D = Eh^3/(12(1 - \mu^2))$ is the cylindrical stiffness, where E is Young's modulus; μ is Poisson's ratio; ∇^4 is the Laplacian biharmonic operator; $w(x, y, t)$ is the dynamic deflection; $\Phi(x, y, t)$ is the function of stress; ρ is the mass density; t is time.

2.2 Boundary Condition and Condition for the Solution Periodicity

As in most cases, the problem is solved by meeting the tangential boundary conditions $N_1 = T = 0$ “on average” [2]:

$$\frac{h}{2\pi R} \int_0^{2\pi R} \frac{\partial^2 \Phi}{\partial y^2} dy = 0; \quad -\frac{h}{2\pi R} \int_0^{2\pi R} \frac{\partial^2 \Phi}{\partial x \partial y} dy = 0 \quad \text{when } x = 0, x = l \quad (2)$$

The circumferential motion continuity condition is written as follows:

$$\int_0^{2\pi R} \frac{\partial v}{\partial y} dy = \int_0^{2\pi R} \left[\frac{1}{E} \left(\frac{\partial^2 \Phi}{\partial x^2} - \mu \frac{\partial^2 \Phi}{\partial y^2} \right) + \frac{w}{R} - \frac{\partial w_0}{\partial y} \frac{\partial w}{\partial y} \right] dy = 0 \quad (3)$$

2.3 Finite-Dimensional Model

In a perfect shell, each point of the circle can be a node of oscillations. It has been discovered experimentally that shell imperfections eliminate this uncertainty and fix the nodes in the circumferential direction. The node positions depend on the shape of initial imperfections [1, 2]. This is why it is assumed that in a linearly stated problem, the dynamic deflection of an imperfect shell can be approximated by an expression that considers only the interaction of conjugate $\sin \beta y \sin \alpha x$, $\cos \beta y \sin \alpha x$, ($\alpha = m\pi/l$, $\beta = n/R$, n —is the number of circumferential dynamic strain waves, m —is the number of longitudinal semi-waves, $n, m = 1, 2, 3, \dots, N$) bending shapes, which are the shapes of eigen-frequencies in a perfect shell that correspond to the same eigen-frequency n . It is known that these shapes correspond to the same eigen-frequency [2]. This approach enables describing the quality of dynamic strain in perfect shells as is shown experimentally; however, in case of real (shape imperfect) shells, the traditional mathematical model may contradict the experimental data [1].

In this paper, a mathematical model earlier proposed for a simpler (limiting) of oscillations in an infinitely long circular cylindrical shell, which is a ring subjected to flat strain [4], is generalized for the oscillations of a finite-length shell.

Refining the finite-dimensional model implies that even when the problem is stated linearly, the dynamic asymmetry results not only in coupling the conjugate bending forms, but also in the low-frequency shell bending oscillations interacting with the high-frequency radial oscillations. In the new approach, the dynamic deflection of shells is written as follows [4, 5, 11–15]:

$$w(x, y, t) = \left(\sum_{n,m}^N f_1^{n,m} \sin \beta y + f_2^{n,m} \cos \beta y + f_3^m \right) \sin \alpha x \quad (4)$$

where $f_1^{n,m}(t)$ and $f_2^{n,m}(t)$ are generalized coordinate; the generalized coordinate $f_3^m(t)$ that is introduced in addition to [2] corresponds to the radial oscillations.

In, the authors use a similar approach to build a finite-dimensional model for shells that deviate in the circumferential direction (the imperfections are not distributed along the entire shell). The difference is that in (4), the coordinate $f_3^m(t)$ that describes the radial oscillation shapes depends on the number of longitudinal semi-waves m , while in, it depends on the number of longitudinal semi-waves m as well as on the number of circumferential direction waves n , which the author believes contradicts the physics of the dynamic behavior demonstrated by real shells. For the problem considered herein (a shell with deviations peculiar to its undulation), the authors of the paper approximated the dynamic deflection by a more complex expression. In this regard, the results presented herein are somewhat similar to those presented in, yet this paper refines them and describes new findings.

2.4 Initial Imperfections

It is known that initial imperfections have the greatest effect on the static and dynamic properties of shells if such oscillations have the same shape as the deflections emerge when shells oscillate or become unstable [1, 2]. This is why, this is the most interesting case, both in theory and in practice.

Let a shell deviate initially from a perfect circular shape, with such deviations following the law:

$$w_0(x, y) = f_0 \sin(\beta_1 y + \phi_0) \sin \alpha x = (f_{10} \sin \beta y + f_{20} \cos \beta y) \sin \alpha x, \quad (5)$$

where $f_{10} = f_0 \cos \phi_0$; $f_{20} = f_0 \sin \phi_0$; f_0 is the amplitude of initial deviations; ϕ_0 is the initial angle of reference; see Fig. 1.

3 Eigen-Frequencies and Shapes of Oscillations in Geometrically Imperfect Shells

Substituting the dynamic deflection function (4) and the initial perfect circle deviation function (5) in the first equation of the linearized system (1) produces a non-homogeneous differential equation, from which the mid-surface stress function can be defined as follows:

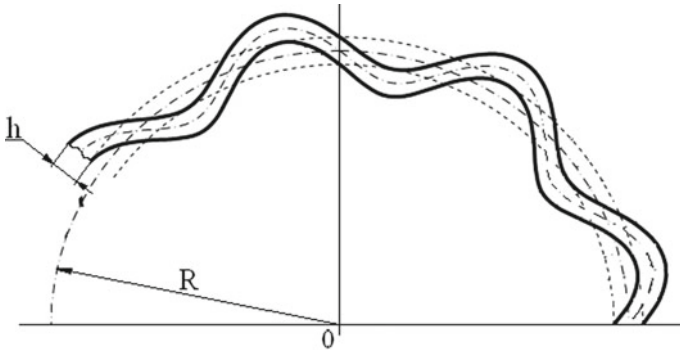


Fig. 1 Schematic representation of the shell imperfections under consideration

$$\begin{aligned} \Phi = E[& \Phi_0 \sin(\alpha x) \sin(\beta y) + \Phi_1 \sin(\alpha x) \cos(\beta y) + \Phi_2 \sin(\beta y) + \Phi_3 \cos(\beta y) \\ & + \Phi_4 \cos(2\alpha x) \sin(\beta y) + \Phi_5 \cos(2\alpha x) \cos(\beta y) + \Phi_6 \sin(\alpha x) + \Phi_7 \cos(2\alpha x) \\ & + \Phi_8 \sin(2\beta y) + \Phi_9 \cos(2\beta y) + \Phi_{01} x^2 / 2]. \end{aligned} \tag{6}$$

The coefficients for (6) can be found by the formulas:

$$\begin{aligned} \Phi_0 &= \frac{h\alpha^2}{R(\alpha^2 + \beta^2)^2} a_1, \quad \Phi_1 = \frac{h\alpha^2}{R(\alpha^2 + \beta^2)^2} a_2, \quad \Phi_2 = -\frac{h^2\alpha^2}{2\beta^2} a_{10}a_3, \\ \Phi_3 &= -\frac{h^2\alpha^2}{2\beta^2} a_{20}a_3, \quad \Phi_4 = \frac{h^2\alpha^2\beta^2}{2(4\alpha^2 + \beta^2)^2} a_{10}a_3, \\ \Phi_5 &= \frac{h^2\alpha^2\beta^2}{2(4\alpha^2 + \beta^2)^2} a_{20}a_3, \quad \Phi_6 = \frac{h}{\alpha^2 R} a_3, \quad \Phi_7 = \frac{h^2\beta^2}{16\alpha^2} (a_{10}a_1 + a_{20}a_2), \\ \Phi_8 &= -\frac{h^2\alpha^2}{16\beta^2} (a_{10}a_2 + a_{20}a_1), \quad \Phi_9 = \frac{h^2\alpha^2}{16\beta^2} (a_{10}a_1 - a_{20}a_2), \end{aligned}$$

Φ_{01} is found from the circumferential motion continuity condition $v(x, y, t)$ provided that the boundary conditions (2) are met as follows:
 $\Phi_{01} = \beta^2(f_{10}f_1 + f_{20}f_2)/4$.

Substituting (4), (5), and (6) and orthogonalizing the motion Eq. (1) as the first approximation produce a system of three coupled dynamic equations in the dimensionless coordinates $a_i = f_i/h$ ($i = 1, 2, 3$):

$$\begin{aligned}
 \ddot{a}_1 + c_{11}a_1 + c_{12}a_{10}a_{20}a_2 + c_{13}a_{10}a_3 &= 0, \\
 \ddot{a}_2 + c_{21}a_{10}a_{20}a_1 + c_{22}a_2 + c_{23}a_{20}a_3 &= 0, \\
 \ddot{a}_3 + c_{31}a_{10}a_1 + c_{32}a_{20}a_2 + c_{33}a_3 &= 0,
 \end{aligned}
 \tag{7}$$

where points stand for derivation with respect to dimensionless time $\tau = \lambda t$ (λ is the eigen-frequency), while the coefficients equal

$$\begin{aligned}
 c_{11} &= 1 + \frac{\varepsilon}{8\omega^2} [(3 + \theta^4)a_{10}^2 + \theta^4 a_{20}^2], \\
 c_{22} &= 1 + \frac{\varepsilon}{8\omega^2} [(3 + \theta^4)a_{20}^2 + \theta^4 a_{10}^2], \\
 c_{12} = c_{21} &= \frac{3\varepsilon}{8\omega^2}, \quad \varepsilon = \left(\frac{n^2 h}{R}\right)^2, \quad \theta = \frac{\pi R}{nl}. \\
 c_{33} &= \frac{1}{\omega^2} \left\{ p^2 + \frac{\varepsilon\theta^4}{8} \left[2 + \frac{1}{(1 + 4\theta^2)^2} \right] (a_{10}^2 + a_{20}^2) \right\}, \\
 c_{13} = c_{23} &= -\frac{8\varepsilon^{1/2}}{3\pi\omega^2} \left[1 + \frac{\theta^4}{(1 + 4\theta^2)^2} \right], \\
 c_{31} = c_{32} &= -\frac{4\varepsilon^{1/2}}{3\pi\omega^2} \left[1 + \frac{\theta^4}{(1 + \theta^2)^2} \right].
 \end{aligned}$$

Below are the formulas for the dimensionless frequency squares corresponding to the bending and radial shapes of circular cylindrical shell oscillations:

$$\omega_n^2 = \frac{\rho}{E} R^2 \lambda^2 = \frac{\varepsilon(1 + \theta^2)^2}{12(1 - \mu^2)} + \frac{\theta^4}{(1 + \theta^2)^2}; \quad p_1^2 = 1 + \frac{\varepsilon\theta^4}{12(1 - \mu^2)};$$

In a conventional solution, the system of modal Eqs. (7) features only the first two equations and $a_3 = 0$. Dimensionless split eigen-frequencies of bending equations $\Omega_{ni} = \omega_{ni}/\omega_n$ ($i = 1, 2$; ω_{ni} are the oscillation frequencies for dynamically asymmetric shells) equal [19]

$$\begin{aligned}
 \Omega_{n1}^2 &= 1 + \varepsilon\theta^4 a_{10}^2/8 \\
 \Omega_{n2}^2 &= 1 + \frac{\varepsilon a_{10}^2}{8} (\theta^4 + 3)
 \end{aligned}
 \tag{8}$$

Therefore, the initial imperfections of the type (5) correspond to the shell undulation and split the bending frequency spectrum. The oscillation frequencies Ω_{n1} and Ω_{n2} are always greater than one. Dimensionless frequencies of a geometrically ideal surface equal $\Omega_{n1} = \Omega_{n2} = 1$.

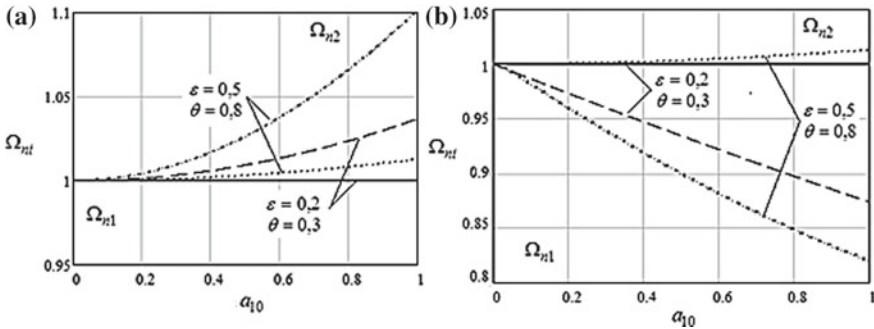


Fig. 2 Split frequencies Ω_{n1} and Ω_{n2} as a function of the imperfection amplitude a_{10}

In the new solution, the system of dynamic equations defines three frequencies Ω_{ni} ($i = 1, 2, 3$). The first two frequencies Ω_{n1} and Ω_{n2} correspond mainly to the bending oscillation shapes. The third frequency Ω_{n3} corresponds mainly to radial shapes. As in the conventional solution [19], the higher split eigen-frequency Ω_{n1} can be found exactly, with its square being equal to $\Omega_{n1}^2 = 1 + \varepsilon\theta^4 a_{10}^2/8$. Unlike in the conventional solution, the lower split eigen-frequency is below the perfect-shell oscillation frequency.

Figure 2a shows the frequencies obtained when solving the problem involving the interaction of conjugate bending shapes (the conventional solutions) for different values of ε , θ , and a_{10} , while Fig. 2b shows the frequencies obtained when solving the problem of conjugate bending/radial shape interaction. In the graphs, the two top lines correspond to the frequencies Ω_{n2} , while the two bottom lines correspond to Ω_{n1} .

Apparently, the bending frequency spectrum-splitting effect depends on the geometric and wave parameters of the shell regardless of the solution. The second frequency in the new solution equals the first one in the conventional solution. One of the split eigen-frequencies is above the perfectly circular shell frequency, while the other one is below that, as noted in. In the conventional solution, both split frequencies are higher than the perfect-shell oscillation frequency. Higher imperfection amplitude increases the spectrum splitting $\Omega_{n2} - \Omega_{n1}$ in both solutions.

3.1 Computational Solution

Consider a shell with the following geometrical and physical properties: $l/R = 1$; $R/h = 200$; $R = 1$; $E = 2 \cdot 10^{11} \text{ MPa}$; $\rho = 7800 \text{ kg/m}^3$; $\mu = 0.3$. $n_{\min} = 8$ corresponds to the minimum frequency in the spectrum of such a shell. Let the shell have initial shape imperfections $f_0 = h$ following the law (5), with $n_0 = 8$ being the number of imperfection waves. Figure 1 is a schematic representation of such a shell. Calculation results are summarized in Fig. 3. The solid line stands for the

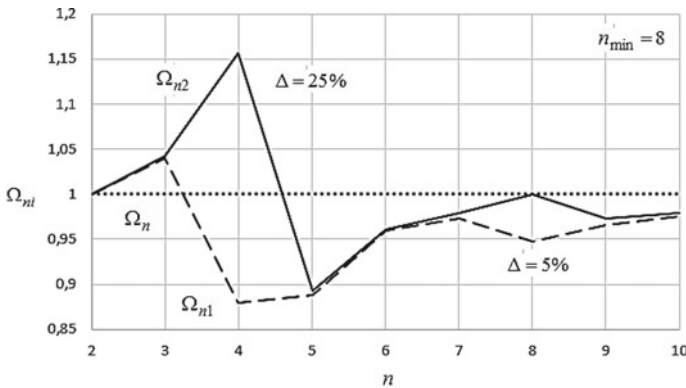


Fig. 3 Split frequencies of mainly bending oscillations as a function of the shaping wave number n

higher split dimensionless eigen-frequency Ω_{n2} , the dashed line stands for the lower frequency Ω_{n1} , while the dotted line stands for the dimensionless perfect-shell oscillation frequency Ω_n .

Apparently, the bending frequency spectrum splits not only at $n = n_0$, as is believed nowadays [17–19], but also at $n = 2n_0$. In case $n = n_0$, both split frequencies are below the oscillation frequency of a geometrically perfect shell, which is inconsistent with the conventional solution [19] but consistent with the new analytical solution as well as with the solution presented in [17]. The frequency $\Omega_{n2} - \Omega_{n1}$ drops by 5%; see Fig. 3. In the analytical solution, the frequency spectrum detuning ($\varepsilon = 0.102$, $\theta = 0.393$ in the case under consideration) $\Omega_{n2} - \Omega_{n1} = 9\%$. In case $n = 2n_0$, one of the split frequencies Ω_{n2} is greater than the perfect-shell oscillation frequency, while Ω_{n1} is below that. Spectrum detuning can be quite substantial. In this example, it is five times that in the case ($n = n_0$).

Notably, a similar effect has been discovered by the author when researching the oscillations of an imperfect ring subjected to flat strain.

4 Equations

This paper is the first to discover there may emerge a bending frequency spectrum-splitting zone due to the initial shell-shape imperfections (deviations from a perfect circular shape). Asymmetric shape imperfections result in splitting the bending frequency spectrum. Frequency spectrum detuning occurs not only at $n = n_0$, as is believed nowadays, but also at $n = 2n_0$. In case $n = n_0$, both split frequencies are below rather than above the geometrically perfect-shell oscillation frequency. In case $n = 2n_0$, one of the split frequencies Ω_{n2} is greater than the perfect-shell oscillation frequency, while Ω_{n1} is below that. Spectrum detuning can



be quite substantial. The spectrum-splitting effect depends on the geometric and wave parameters of the shell in either case: $n = n_0$ and $n = 2n_0$. The frequencies of mainly radial oscillations might be commensurate with those of mainly bending oscillations at specific undulation and shape imperfection amplitudes.

Acknowledgements The research was financed by the grant of the Russian Science Foundation (project No. 18-79-00057).

References

1. Seregin SV (2014) Free flexural radial oscillations of a thin circular cylindrical shell bearing added mass. *Vestnik MGSU*. In: Proceedings of Moscow State University of Civil Engineering, vol 11, pp 74–81. <https://doi.org/10.22227/1997-0935.2014.11.74-81>
2. Seregin SV (2014) Numerical and analytical study of free oscillations of circular cylindrical shells carrying the attached mass linearly distributed along the generatrix. *Comput Mech Continuous Media* 7(4):378–384. <https://doi.org/10.7242/1999-6691/2014.7.4.36>
3. Seregin SV (2014) About the effect of the splitting of the Flexural frequency spectrum of thin circular cylindrical shells carrying an attached mass. *Constr Mech Calculation Struct* 6 (257):59–61
4. Seregin SV (2015) Free vibrations of a thin circular cylindrical shell weakened by a hole. *Russ Aeronaut* 58(3):258–262. <https://doi.org/10.3103/S1068799815030022>
5. Seregin SV, Leizerovich GS (2015) Influence of attached masses on the dynamic characteristics of thin shell. *Probl Mech Eng Autom* 4:83–89
6. Leizerovich GS, Seregin SV (2016) Free vibrations of circular cylindrical shells with a small added concentrated mass. *J Appl Mech Tech Phys* 57(5):841–846. <https://doi.org/10.1134/S0021894416050102>
7. Seregin SV (2016) Dynamics of thin cylindrical shells with added mass: monograph. Komsomolsk-na-Amure State Technical University, Komsomolsk-on-Amur, pp 175–180
8. Avramov KV, Mikhlín YV (2010) Nonlinear dynamics of elastic systems, vol. 1. Models, methods, phenomena. SIC “Regular and chaotic dynamics”. Institute of Computer Research, Moscow, Izhevsk, 704 p
9. Amabili M, Païdoussis MP (2003) Review of studies on geometrically nonlinear vibrations and dynamics of circular cylindrical shells and panels, with and without fluid-structure interaction. *Appl Mech Rev* 56(4):349–381
10. Kubenko VD, Koval’chuk PS, Krasnopol’skaya TS (1984) Nonlinear interaction of forms of flexural vibrations of cylindrical shells. *Naukova Dumka, Kiev*, p 220
11. Taranukha NA, Leyzerovich GS (2005) *Dinamika “nepravilnykh” obolochek (Imperfect-shell dynamics)*. Dalnauka, Vladivostok, p 423
12. Leyzerovich GS, Prikhodko NB, Seregin SV (2013) On the influence of a small attached mass on the oscillations of a multi-thick circular ring. *Constr Reconstr* 4:38–41
13. Leyzerovich GS, Prikhodko NB, Seregin SV (2013) On the influence of a small attached mass on the splitting of the frequency spectrum of a circular ring with initial irregularities. *Constr Mech Calculation Struct* 6:49–51
14. Seregin SV, Leizerovich GS (2014) Free vibrations of an infinitely long circular cylindrical shell with initial imperfections and little added mass. *Scientific notes of Komsomolsk-on-Amur state technical University*, vol 4(20), pp 36–43
15. Seregin SV (2017) The influence of shape imperfections on the vibrations of a ring resonator of a wave solid-state gyroscope. *Nonlinear Dyn* 13(3):423–431. <https://doi.org/10.20537/nd1703009>

16. Seregin SV (2017) The splitting features of a frequency spectrum of a gyroscope based on elastic waves in solids: an isolated imperfect ring as an example. St. Petersburg Polytechnical State Univ J Phys Math 3(3):255–258. <https://doi.org/10.1016/j.spjpm.2017.09.004>
17. Seregin SV (2016) Influence of asymmetric initial imperfection shape on the free vibrations of thin shells. Vestnik of Samara University. Aerosp Eng Technol Mech Eng 15(3):209–222. <https://doi.org/10.18287/2541-7533-2016-15-3-209-222>
18. Seregin SV (2018) On possible zones of splitting of the flexural frequency spectrum of shells with asymmetric imperfections of shape. News of higher educational institutions. Aviat Equip 2:149–152
19. Seregin SV (2017) Qualitative effects on vibrations of annular reinforcing elements with attached mass, as a special case of a thin infinitely long circular cylindrical shell. Proceedings of higher educational institutions. Engineering 1(682):31–43. <https://doi.org/10.18698/0536-1044-2017-1-31-43>
20. Milczyn AM, Olevsky VI, Platin VV (2011) On the forms of supercritical wave generation of inhomogeneously loaded cylindrical shells with technological imperfections. East Eur J Adv Technol 7(53):44–48

Test Bench for Analyzing Adaptability of Foil Gas-Dynamic Bearings to External Changes



A. V. Gorin, R. N. Poliakov and A. V. Sytin

Abstract The article presents a test hydromechanical test bench, methods, and results of testing petal gas-dynamic bearings when the position of the rotor axis of rotation changes in space. A mathematical model of the rotor dynamics in a petal bearing is proposed based on a modified Reynolds equation in a non-stationary formulation for a viscous compressible fluid. The solution of the specified equation allows finding reactions of a lubricating layer. The reactions of the lubricant layer allow us to find the stiffness and damping coefficients necessary to record the equations of motion. The case of a rotor displacement in the vertical direction is considered, and the adaptive behavior of the rotor in a petal gas-dynamic bearing is shown. The principal hydraulic scheme and the description of the test bench operation are presented. The test bench simulates external influences in a wide range. The functional scheme of the information-measuring system is given. The article proposed an interface for interconnection of the operator and the information system. In addition, it provides some graphs of the oscillations of the rotor y-axis during the motion of hydraulic cylinders in the vertical direction.

Keywords Test bench · Load · Mathematical model · Rotor dynamics · Movement trajectory

1 Introduction

An effective way to increase machine productivity is to increase the rotational speeds of rotors [1, 2], the highest values of which can be achieved using gas, mainly air, and lubricants [3, 4]. However, with increasing rotational frequencies, increased vibrations occur [5–7]. Reducing the overall level of vibrations and dynamic stresses is an important task. One of the ways to solve this problem is the

A. V. Gorin (✉) · R. N. Poliakov · A. V. Sytin
Orel State University Named After I. S. Turgenev,
95, Komsomolskaya St., Orel 302026, Russia
e-mail: gorin57@mail.ru

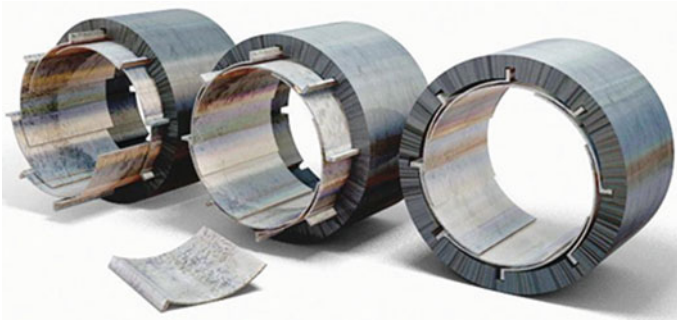


Fig. 1 Foil gas-dynamic bearing

use of elastic-damping supports. Promising in this class is foil gas-dynamic bearings [8–10] (Fig. 1). Their elastic elements create the maximum area of the bearing surface and also serve to suppress instability.

In general, belt and foil supports have prospects for use in light, high-speed turbomachines, spinning spindles, automotive gas turbine bearings, solar-powered water coolers [11–14]. In particular, in the USA, a lot of attention is paid to their use as supports for auxiliary installations in aviation and space systems. The development of high-altitude aviation and space technology has dramatically increased the demand for compact high-speed turbo-generators and turbo-compressors for air cleaning and air conditioning systems [15–17].

The rotor-bearing unit of a modern high-speed turbomachine with plain bearings is a complex hydromechanical system consisting of three main interacting with each other elements: A rotor trunnion, a bearing sleeve, and a lubricating layer connecting them and transmitting force from the rotor to the turbine unit body [8, 10]. Each of these elements, in general, having certain dynamic characteristics (elastic, damping, inertial properties), can have a significant impact on the oscillatory processes in the dynamic system “rotor-sliding bearings.”

2 Theoretical Position

The dynamic behavior of the rotor, which is supported by sliding bearings, is determined by the combination of non-stationary (variable in magnitude and direction) disturbing forces and bearing reactions [2, 6]. Analysis of the possible trajectories of the rotor movements under the action of such a system of forces makes it possible to evaluate the geometrical and operating parameters of the rotor system and the entire turbomachine selected at the design stage, as well as to take an adequate decision to change them if necessary. This contributes to the choice of the right approach in the design of the rotor system in terms of meeting operational

and technological requirements, as well as ensuring the stable operation of the rotor-bearing assembly at operating frequencies and during transients.

In the general case, the equation of motion for a rotor of mass m concentrated at the center of mass is presented in the paper [5]. In the course of transformations, the equations of motion of the rotor using Laplace second type transformations [1] with $c = \infty$ ($X_1 \equiv Y_1 \equiv 0$), we obtain the equalities for the motion of a rigid rotor in the following form:

$$\begin{cases} m\ddot{X} = 2R_X + m\Delta\omega^2 \sin \omega t + F_X(t) \\ m\ddot{Y} = 2R_Y + m\Delta\omega^2 \cos \omega t + F_Y(t) \end{cases} \quad (1)$$

where R_X, R_Y —projections of lubricant layer reactions on the corresponding coordinate axes; ω —rotor speed.

The balanced rotor occupies a stationary position on the moving equilibrium curve (Fig. 2), in which the external load is balanced by the reactions of the lubricating layer [4]. The equilibrium condition is then given by:

$$\begin{aligned} R_{X0} = 0 &\Rightarrow \int_0^L \int_0^{\pi D} p \sin \alpha dx dz = 0; \\ R_{Y0} = -mg &\Rightarrow \int_0^L \int_0^{\pi D} p \cos \alpha dx dz = mg, \end{aligned} \quad (2)$$

where R_{X0} and R_{Y0} —the reaction of the lubricant layer, the index “0” indicates a steady state.

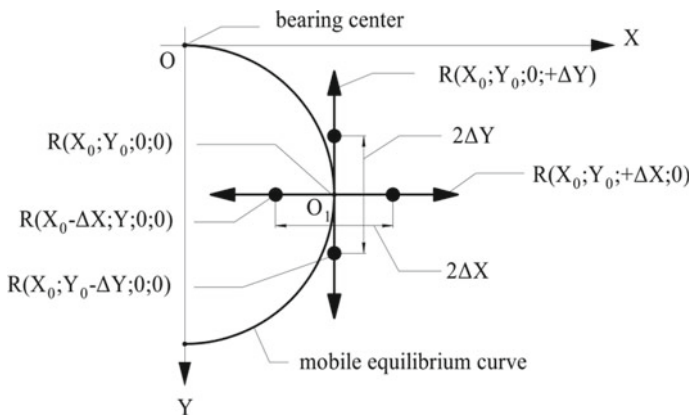


Fig. 2 Calculation schemes of foil bearing determination scheme of the dynamic coefficient

To find the reactions, it is necessary to determine the pressure field on the basis of the Reynolds equation, which is generalized to the case of a two-dimensional turbulent flow of a viscous compressible lubricant:

$$\frac{\partial}{\partial x} \left[\frac{\rho h^3}{\mu K_x} \frac{\partial p}{\partial x} \right] + \frac{\partial}{\partial z} \left[\frac{\rho h^3}{\mu K_x} \frac{\partial p}{\partial x} \right] = 6 \frac{\partial}{\partial x} (\rho U h) - 12 \rho V + 12 h \frac{\partial \rho}{\partial t}, \quad (4)$$

where: U and V —velocity values at points on the trunnion surface velocity values at points on the spigot surface.

A feature of high-speed turbomachines is the work of their rotors with very small eccentricities. In this case, the stationary position of the trunnion can be considered an axis passing through the centers of the bearings. This is true for low- and medium-loaded high-speed rotors ($\bar{e} < 0,3$). In addition, the dynamic coefficients of the lubricating layer in a wide range (up to $\bar{e} = 0,5$) for this type of rotors can be taken at $\bar{e} = 0$, i.e., with concentric arrangement of the trunnion in the bearing [7]. At the central position of the trunnion, the gyroscopic forces (cross section damping coefficients) with a low gas content are non-zero and tend to zero with developed boiling, the direct stiffness and damping coefficients are equal, respectively, and the pseudo-gyroscopic (non-conservative) forces are characterized by one coefficient (cross stiffness coefficients), so at $\bar{e} = 0$:

$$\begin{aligned} \bar{K}_{GXX} &= \bar{K}_{GYY} = \bar{K}_0; \\ \bar{K}_{GXY} &= -\bar{K}_{GYX} = \bar{C}_0; \\ \bar{B}_{GXX} &= \bar{B}_{GYY} = \bar{B}_0; \\ \bar{B}_{GXY} &= \bar{B}_{GYX} = \bar{D}_0 \approx 0. \end{aligned} \quad (5)$$

In the case of an FGDB, the rigidity of the system will look like a “lubricating gas layer–petal–petal” in the OX and OY directions (equivalent rigidity K_{GX} and K_{GY}) can be thought of as the sum of the gas lubricant layer (K_G), connected in series and the rigidity of the elastic petals (K_{ni}) and (K_{ni+1}) [3, 13].

3 Creating an Experimental Stand

The scientific laboratory of the department “Mechatronics, Mechanics and Robotics” of Orel State University named after I. S. Turgenev designed and executed test bench (Fig. 3a) to simulate external influences on bearing units. Test stand combines rotor-bearing units and hydraulic drive. A distinctive feature of the test bench is the simulation of external influences, such as uniformly accelerated microdisplacements in the vertical direction, corresponding to the smooth height gain of the aircraft, as well as sharp alternating loads corresponding to the zones of turbulence. At the same time, the load is applied directly to the bearing units, bypassing the housing where they are installed. Rotating rotor 12 is installed in the

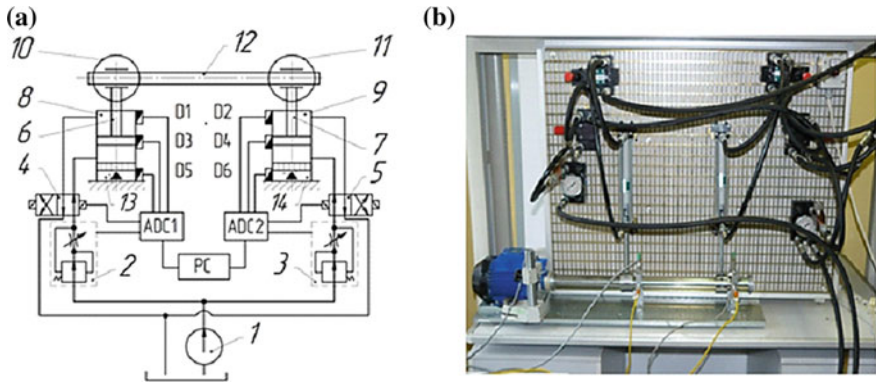


Fig. 3 a Principled hydraulic scheme of the test bench; b The appearance of the test bench

bearing units 10 and 11. The dynamic effect on the bearing units 10 and 11 is modeled by hydraulic cylinders 8 and 9. The hydraulic drive allows steeples and in a wide range to change the speed of movement of the rods 6 and 7 of the hydraulic cylinders 8 and 9. The research stand can operate in manual and automatic mode.

Single external impacts are provided in manual mode. Automatic mode simulates periodic external dynamic effects. At the same time, simple dynamic effects can cause structural damage to the bearing assemblies, as a result of strong, albeit short-term overstress in the material. External effects of a complex nature are accompanied by cyclic or alternating loads, which leads to the accumulation of fatigue micro-deformations.

The operation of the hydraulic circuit of the test bench (Fig. 3a) is as follows. Analytically, using the calculated formulas, the required energy, frequency, and nature of external influence is determined. Based on the magnitude and nature of the external dynamic effects, the speed and direction of movement of the rods 6 and 7 of the cylinders 8 and 9 are determined. The supply of working fluid is provided by a hydraulic pump 1. Flow regulators 2 and 3 set the required speed of movement of the rods 6 and 7. Electromagnetic distributors 4 and 5 go to the position of the working stroke and rods 6 and 7 of the hydraulic cylinders begin their movement. Next is the transfer of external dynamic effects directly on the housing of bearing units 10 and 11.

The value of the energy of the external dynamic effects is controlled by the indications of hydropneumatic dampers 13 and 14 using sensors D5 and D6. The speed of movement of the rods 6 and 7 of the hydraulic cylinders 8 and 9 is controlled by the speed sensors D1 and D2. The position and direction of movement of the rods 6 and 7 are monitored by sensors D3 and D4. The received signals from the sensors and control system of the hydraulic circuit of the test bench are fed to the boards of analog-digital converters ADC1 and ADC2. The measurement results and further control is carried out by a computer (PC). The appearance of the test bench is presented in Fig. 3b.

The joint operation of the hydraulic circuit and control system of the test bench can provide various directions of external dynamic effects.

External dynamic loads are characterized by a rapid release of energy, as a result of which local elastic or plastic deformations, stress waves, and other effects occur, which in some cases can lead to disruption of the rotor-support unit and the entire aggregate. Therefore, for automatic control of the experimental stand, as well as for collecting and processing the obtained experimental data, an information-measuring system (IMS) (Fig. 4) was developed on the basis of the “National Instruments” software and hardware complex [1].

The basis of IMS is the NI6052E multifunction board, which has the capability of multi-channel digital and analog I/O and counters-timers. The functional purpose of the board is to provide I/O signals, digitizing and executing commands, and controlling the power modules of the stand. Signals from various sensors are fed to single- or dual-channel analog matching SCC modules.

The control of the electric motor and the pump, as well as the implementation of the functions of the emergency shutdown of the stand, is carried out through the relay modules SC-RLY01. For a more compact arrangement and subsequent signal processing, the SCC and SC-RLY01 modules are mounted into a single SC-2345 block-module, where the unified signals from the sensors are converted into a range perceived by the analog-to-digital converter (0.5 V).

In our particular case, displacement sensors and power modules of the experimental stand are connected to the SC-2345 via the BNC, 9-Pin D-sub, and Strain Relief interface connectors. The SC-2345 module requires an external 5 V power supply, the source of which is the SCC-PWR01 power supply unit. The NI6052E

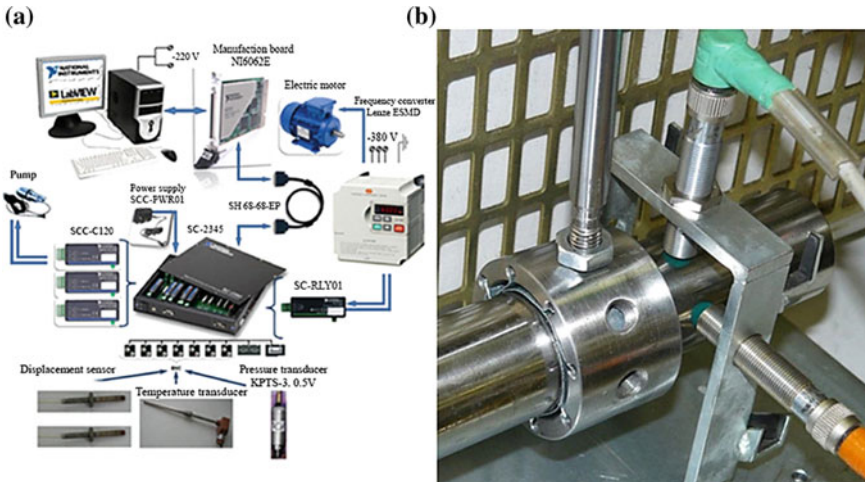


Fig. 4 Information-measuring system and bearing unit based on foil bearing

board and SC-2345 module are commutated using a single SH 68-68-EP cable. The data from the multifunctional NI6052E board with advanced synchronization and clocking capabilities is fed to the controller for further processing or writing to the hard disk.

The experiment program includes at least three tests for the same operating parameters. Each test consists of accelerating the rotor to the operating speed, running for some time in steady state, impact effect, and stopping. The capabilities of the experimental stand allow recording the rotational speed, the trajectories of the center of the rotor trunnion in the PS gap, the time-frequency characteristics of the rotor on the acceleration and coasting modes, and other important parameters. The interface of the information-measuring system is presented in Fig. 5.

In Fig. 6 shows graphs of rotor oscillation along the y-axis.

When the hydraulic cylinders move down (a, b) and in the case of the hydraulic cylinders move up (c, d), foil gas-dynamic bearing are adapted to external influences and the magnitude of the oscillation amplitude does not exceed 20 μm .

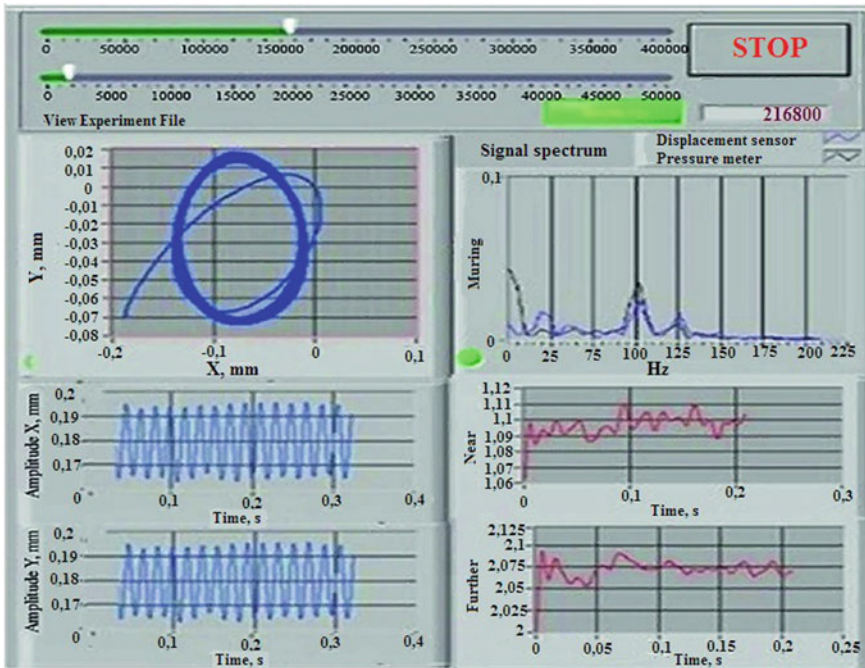


Fig. 5 Interface of information-measuring system

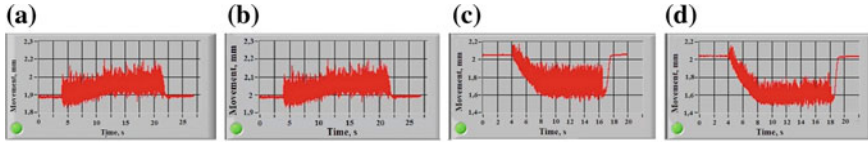


Fig. 6 Graphs of rotor oscillation along the y -axis when the hydraulic cylinders move in the vertical direction (10^{-5} m)

4 Conclusion

The test bench with controlled external dynamic effects presented in the article allows to study the influence of external force factors on the trajectory and stability of the rotor in sliding bearings based on foil bearings in manual and automatic mode, with the possibility of recording and subsequent analysis of the trajectories. A flexible change in the speed and magnitude of the impact (according to a pre-determined law of change) allows you to cover a wide range of possible external influences on the rotary unit.

Acknowledgements This work was supported by the Ministry of Education and Science of the Russian Federation under the project No. 9.2952.2017/4.6.

References

1. Solomin OV (2007) Method development for dynamic analysis of rotor systems with hydrodynamic bearings. Dissertation, Orel State Technical University
2. Poznyak E (1980) Rotors vibrations. Machines, structures and their elements vibrations. *Vibr Mach* 3:130–189
3. Pugachev AO (2004) Transient modes dynamics of rotors with journal bearings. Dissertation, Orel State Technical University
4. Savin LA (1998) Theoretical basis of calculation and dynamics of sleeve bearings with liquid-vapor lubrication. Dissertation, Orel State Technical University
5. Aleksandrov A, Filippov V (1995) Dynamics of rotors. MEI, Moscow
6. Antipov V, Duletskiy M, Komarov R (2003) The influence of force factors on the characteristics of the “rotor-body”. *Dynamic system Bulletin of the Orel State Technical University. Mech Eng* 3:6–9
7. Voskresenskiy V, D'yakov V (1980) Calculation and design of sleeve bearings with liquid lubrication. Mashinostroenie, Moscow
8. Gaevik D (1985) Bearing supports in modern machinery. Mashinostroenie, Moscow
9. Kostyuk A (2000) Dynamics and durability of turbomachinery. MEI, Moscow
10. Barkov A, Barkova N, Azovtsev A (2000) Vibration monitoring and diagnostics of rotary machines. Spb GMTU, Saint Petersburg
11. Gorin A, Eshutkin D, Gorina M (2015) Hydraulic impact devices utilization for ground wells development. State University-UNPK, Orel

12. Kotylev U, Eshutkin D (2007) Applied hydraulic impact devices theory. Mashinostroenie, Moscow
13. Ushakov L, Kotylev U, Kravchenko V (2000) Hydraulic impact devices. Mashinostroenie, Moscow
14. Bashta T (1992) Hydraulic machines and hydraulic drives. Mashinostroenie, Moscow
15. Gorin A, Eshutkin D, Zhuravleva A (2011) Simulation of the drive of a static-dynamic machine for trenchless construction of pipelines. Fundamentals and applied problems of engineering and technology. Oryol 3(287):20–26
16. Gorin A, Eshutkin D, Gorina M (2015) Volumetric hydraulic drive of combined machines for ground wells development. State University-UNPK, Orel
17. Gorin AV (2012) Pressure and shock mechanisms with volumetric hydraulic drive parameters of the machines for ground wells development. Dissertation, Orel State Technical University

Automatic System of Low-Pressure Gas Recycling at Liquid Removal from Wells and Gas Collectors



M. Yu. Prakhova, A. N. Krasnov and E. A. Khoroshavina

Abstract It means that all gas well parameters such as pressure, temperature and gas flow decrease. As a result of all these factors influence, there is a liquid accumulation which occurs in the wells and gas-collecting system (GCS) pipelines. That is why GCS pressure loss increases, and ice and hydrate plugs' formation risk increases too. There are many methods used to remove liquid. In fact, the most useful ways are a well, flowline, and gas gathering line header blowdown. But it leads to significant gas loss and field environmental degradation. It is offered in this paper to use low-pressure gas line to blow down. The low pressure is made by low power compression unit. The low-pressure gas feeds through this line to the complex gas treatment plants. Designed automated instrumentation and control system allow one to use existing temperature and pressure-measuring means. We also offer to use existing equipment which was earlier decommissioned because of falling production. Conducted research on the offered blowdown methods and control system showed their efficiency.

Keywords Field development · Final stage · Flowline water cut · Blowdown to the flare · Low-pressure gas · Control system

1 Introduction

At present, many of the largest gas fields of Western Siberia, such as Vyngapurskoye, Medvezhye, Urengoisskoye, are either under the final development stage or have been already finished. The key peculiarity of this stage is a significant decrease of formation pressure which makes the operation of wells and gas-collecting systems (GCSs) difficult. The reason of such complication is the increase in the formation fluid content in gas at simultaneous decrease of not only pressure but also the temperature and gas consumption.

M. Yu. Prakhova (✉) · A. N. Krasnov · E. A. Khoroshavina
Ufa State Petroleum Technological University, 1, Kosmonavtov Street, Ufa 450044, Russia
e-mail: prakhovamarina@yandex.ru

This factors facilitate the arrangement of conditions for liquid accumulation in the gas buster station pipelines which, in its turn, forms a whole set of operation problems [1], such as the increasing pressure losses along the line length, occurrence of liquid burst releases into inlet separators of the complex gas treatment plants (CGTPs), increase of ice and hydrate formation risk.

Thus, for example, the facilities for arrangement of Urengoiskeye Oil and Gas Condensate Field (OGCF) were designed to provide the maximum volumes of gas recovery the peak of which was reached 25 years ago [2]. Since that time, the volumes of recovered gas have been reduced several times. The parameters of pumping and compressing tubes of the well and pipelines at gas buster stations were designed on the basis of minimum hydraulic losses at maximum gas consumption with a continuous water removal from all the system sections. At the moment, in the final development stage, under the conditions of reducing the volumes of recovered gas and the existing parameters of the GSS, there are no conditions for continuous water removal (in a set mode). Apparently, it leads to the increase in the number of the stock of wells and gathering lines operated with liquid accumulation. In course of time, the situation both at the Urengoiskeye field and other fields will keep aggravating which makes gas-producing enterprises consider and test various technologies and methods allowing either for the adaptation of the existing GSS for a significantly reduced gas consumption or crucially change the gas recovery technology. The complex nature of the projects connected with a reconstruction of the existing system of gas collection consists not only in the fact that they require significant expenses but also in the necessity to consider wells and gas-collecting facilities as a whole. This paper considers the system allowing efficient water removal from wells and GSSs by means of the existing gas-collecting system adaptation to the operation at the decreased values of wellhead pressures with minimum expenses.

2 Literature Review

At the moment, there are several typical technical solutions and methods for preventing liquid accumulation and removal from wells and gas-collecting systems.

Liquid removal from a gathering line is conducted either from time to time, i.e., upon the fact of its accumulation or in a continuous mode which allows preventing the accumulation of large amounts of water at any section of the gathering line [3–12]. Frequent cleaning is most of times conducted by the blowdown of gathering lines at the flare at the wellhead or at the gas field [3, 5]. In addition, non-destructive of destructive pistons is also used for frequent cleaning conduct.

In [11], routine liquid removal from the well bottom is conducted by means of a recovered gas blowing gathering lines through a gas ejector. Each well is occasionally connected to the ejector mixing chamber to the input of which a HP gas is fed from a boosting compressor station (BCS), and after that, a mixed flow is directed to the BCS input. The blowdown period of each well is determined by the

inside temperature stabilization. This method actually stipulates for heating gathering lines and wells by means of pumping a dried high-pressure gas from a gas field through a gathering line into a formation with a simultaneous feed of sprayed methanol (through the ejector). The main drawback of this method is that the liquid accumulated in the gathering line is not removed from the gas buster station and is returned back to the formation, which later will lead to plugs and well squeezing.

To provide a continuous gathering line cleaning, it is necessary to increase the rate of a gas and liquid flow. This can be done by means of adding surface active agents [13] or through the structural changes of the existing collecting system, e.g., by means of making a pipeline with a smaller diameter inside an existing one (“pipe in a pipe”) [1] by a simple change of existing gathering lines with the ones having a smaller diameter [5, 6] or uniting two gathering lines into one [8]. As a result of such measures the liquid removal conditions become better, that is why the issue of its accumulation at any sections is not raised.

The source [1] conducts a detailed analysis of the mentioned methods allowing for the assessment of their advantages and disadvantages. The gathering lines were combined and successfully tested in the gas field conditions, but the authors [1] point out to the limited possibilities of the technology application at field GSSs as the number of gathering lines in one corridor and the length of such corridors, as a rule, are quite small comparing with the GSS length.

It should be mentioned that liquid plugs do not pose a serious problem in themselves as they do not have a significant impact on the gathering line resistance [2]. However, they become a problem during a winter period when a liquid plug transforms into an ice one decreasing or blocking a gathering line cross section and thus increasing its resistance. With the account of this, it is possible to approach the issue of liquid accumulation in the gathering line in the other way, providing for the positive temperatures of the gas and liquid flows along the gathering line. It can be implemented, e.g., with the help of a heat tracer [14].

From a technical point of view, this method reminds the technology “pipe in a pipe”; however, the inside pipe is installed not for the increase of the gas movement rate but for its continuous heating. A heat tracer—coiled tubing—is placed inside a GSS main pipeline. This coiled tubing is used for the circulation of a water and methanol solution heated by a rejected heat from gas air-cooling units (ACUs). This helps preventing liquid freezing in the main pipe.

Nevertheless, until the present time the key method for the periodic liquid removal from wells and gathering lines is the blowdown of wells and connecting pipelines (gathering lines, collectors) to the flare for 15–30 min. The gas rate at the well bottom shall reach 3–6 m/s. This method is very simple and applied in those cases when the flow rate is recovered for a long period of time (several days). However, this method has such drawbacks as an incomplete liquid removal from the well bottom; increased depression on the formation leading to the intense inflow of new water portions, formation destruction, sand plug forming; environment pollution and gas irretrievable losses. Besides, this method cannot be applied at a permanent basis and at a higher number of points, requiring simultaneous blowdown [15].

Water can be removed by the BCS operation mode control as well. In [16], the authors perform a short-time stop of gas recovery at the field by means of the BCS switch into an idle mode (“ring unloading”) with its subsequent commissioning in the normal operation and the feed of produced gas into a main pipeline. During the period of gas recovery liquid plugs stops tend to form inside connecting pipelines at lower areas of the route while the liquid in the well is accumulated at the bottom and partially absorbed by the formation. A subsequent and quite fast BCS switch to the operation into a pipeline results in the removal of a liquid phase from wells and connecting pipelines. The drawback of this method is that it stipulates for a necessity to fully stop a BCS for a short time with a subsequent kick start at a full capacity, and it should be done quite often. Thus, e.g., for the field “Medvezhye” it is necessary to stop a BCS for 10 min once in a day [5, 16]. However, the stop of gathering line and well in a winter period may cause the freezing of liquid accumulated in gathering lines. In addition, today at the fields which are at the final stage of their operation gas fields are being united; gas from some gas fields is finally compressed at others. In this case, even a short stop of one gas field can cause the stop of all the cluster.

With the help of a BCS, it is also possible to organize a low pressure line to which the gathering lines are switched from time to time when excess watering problems occur in them [17]. However, in this cases, despite the fact that no full stop of a BCS is performed, one still needs to change the operation mode of the whole station which is not desirable from the technological point of view. At the Cenomanian stations of the Urengoiskoye OGCF, there is a practice of water removal from gathering lines by means of recurrent input pressure lowering [2]. In this case, pressure decreases simultaneously for a whole well stock and over the whole gas-collecting system. However, to provide a controllable action at the problem section of a proper scope and duration is impossible with the help of its method; on the contrary, the action is mostly provided at the sections where it is not desirable.

3 Research Problem Statement

As the analysis of literature references shows, the principle of water removal, underlying the blowdown method and stipulating for the generation of local pressure drops of necessary values in the system, is the most efficient at present time.

At the Urengoiskoye field, there is a practice of operation of low-pressure Valanginian gas fields by means of continuous or recurrent gas feed to the gathering lines operated at lower pressures than a main part of the gas-collecting system. The gas intake to the CGTP from these gathering lines is performed for dedicated low-pressure technological process trains bypassing a common collector of the valve station. An additional pressure difference for gathering lines with low parameters is provided by means of ejection. It is understood that the energy of the main gas flow is sufficient for the provision of the low-pressure collector operation.

In case of Cenomanian fields, the energy for water removal is not sufficient for a whole well contour, because making a similar low-pressure train, it is required to use additional technological means included into the system of automatic control by means of gathering line blowdown.

The purpose of this research is to develop an automatic system for recycling low-pressure gas at liquid removal from wells and gas collectors.

4 The Theory

The nature of the suggested technology consists in a remotely controlled of high-performance wells' capacity limit for a period of blowdown of the killed wells through a gathering line. This technology implementation is possible because of a low-capacity compressor unit allowing recurrent blowdown as the problems accumulate at the sections of GBS sections. A mandatory condition is the availability of the system for control and automatic management of such contiguous areas as gas collectors because it is impossible to control the action of the actuating unit (compressor) on the remote object (well of gathering line) without feedback.

The low pressure line is generated with the help of a screwed oil-free compressor (compressor group) in relation to a low production (20–30 thousand of nmc per hour) which is capable of lowering the pressure sufficient for liquid removal from wells and gathering line problem sections in a wide range.

To evaluate the possibility of introducing a similar scheme at Cenomanian CGTPs, gas field tests were conducted with the blowdown of the Cenomanian well through a gas-collecting pipeline at the CGTPs where the compressor operation was simulated with the help of a horizontal flare unit (HFU). The telemetering system of pressure and temperature parameters of the wells and gathering line on the basis of the technological parameters' registering devices RTP-4 with an increased resolution and a minimum measurement error (0.05% of the pressure measurement scale) [18], intended for the most accurate measurement of low pressure differences (up to 0.0003 at) against relatively high (up to 18 at) of absolute pressures.

The tests of well operation were conducted at the cluster No. 510 of the CGTP-5. The selection of this gas field is explained by the presence of a horizontal flare unit providing for the possibility to model the well cluster and gas collector operation at low pressures; i.e., simulate the operation of a low-capacity compressor. The gathering line of the cluster No. 510 is 3552 m long has the diameter of 325 mm and the wall thickness of 14 mm. This cluster includes three wells No. 5101, 5102, and 5103. The cluster No. 510 was selected because of the well operation with difficulties: Here, the wells were frequently stopped, as a rule, in winters. At this, the wells of the cluster No. 510 were blown 5–6 times in a month. The well No. 5103 is characterized by the worst operation conditions with the lowest gas rate in the oil well tubing along the cluster: 1.7 m/s.

Figure 1 shows the change in pressure difference between wells and the valve stations. It is synchronous for all cluster wells as it depends on the pressure at the

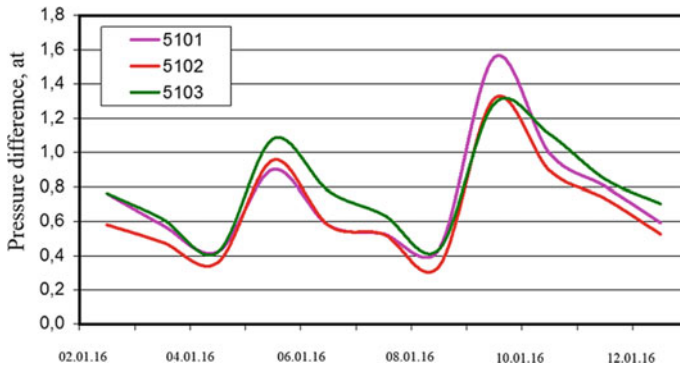


Fig. 1 Change of the pressure difference between the valve station and the wells of the cluster No. 510 (5101, 5102, 5103 well numbers)

valve station and a hydraulic resistance of the gathering line which can change at the change of gas consumption in the pipeline and ice plug formation. The well blowdowns do not allow a final freezing of a gathering line because the release of the accumulated liquid column leads to the decrease of the head pressure and a temporary increase of the well rate (Fig. 1). The diagrams clearly show a periodic occurrence of head pressure growth and gathering line pressure difference within 3–6 days, and the range of pressure drops changes within 0.7–1.2 at. The pressure difference between a well cluster and a valve station exceeding 0.4 at. shows the beginning of ice formation [2]. The main pressure difference within 0.25–0.3 at. from 0.4 is registered at the section from the wellhead to the cluster collector.

Figure 2 demonstrates the scheme of the tests of the gathering line blowdown through a gas collector to the CGTP flare simulating the blowdown with a help of the compressor. The gas from the wells No. 5101 and No. 5102 passed to the gas collector from the cluster No. 510 to the CGTP-5. For the well No. 5103, an operation into the gathering line was stipulated with the gas rate measurement by means of a clamp-on ultrasound flow meter. The pressure adjustment in the system “wells–gas collector–valve station” was performed with a help of the fitting located before the CGTP flare.

To control temperature and pressure parameters at the wellhead, the devices for registering industrial parameters RTP-4 were installed on the cluster pipeline after the section of mixing gas flows from wells and on the gas collector. The devices RTP-4 were also installed on the gas collector at the start of the pipeline, in the lowered pipeline section, where liquid accumulation occurs, and at the end of the pipeline before the valve station.

The increase of water content in gas until the moment of the well killing was simulated by the well capping and pumping of 100 m³ of the 15% water and methanol solution inside. After the well was opened, it did not start its operation again (Fig. 3).

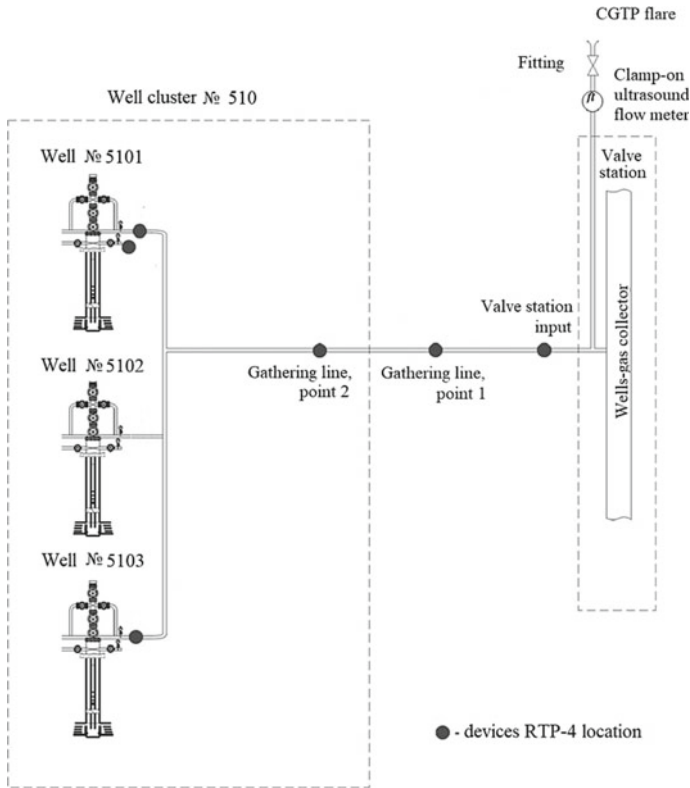


Fig. 2 Scheme of the gathering line blowdown through a gas collector to the CGTP flare

Before starting blowdown through a gathering line, the wellhead pressure was virtually equal to the pressure at the CGTP valve station. The gathering line of the well cluster No. 510 was switched to the operation through a flare collector of the valve station resulting in the pressure decrease at the gathering line end and the start of the well No. 5101 operation. At the well blowdown through a gathering line, one can register a 1.1 at pressure decrease at the valve station comparing with the initial one (Fig. 4) in the first stage. At the well No. 5101, a 0.6 at pressure decrease was registered down to 13 at.

Further, in the course of liquid removal from the well, the pressure at the valve station flare collector increased up to 14.1 at, while at the well up to 14.5 at.

Therefore, the conducted field tests on the blowdown of the well No. 5101 through a gathering line to a HGU proved the possibility to blowdown wells and gathering lines with the help of a low-capacity compressor as in terms of the generated pressure differences its operation is similar to the HGU operation. The working capacity of a killed well was recovered within an hour.

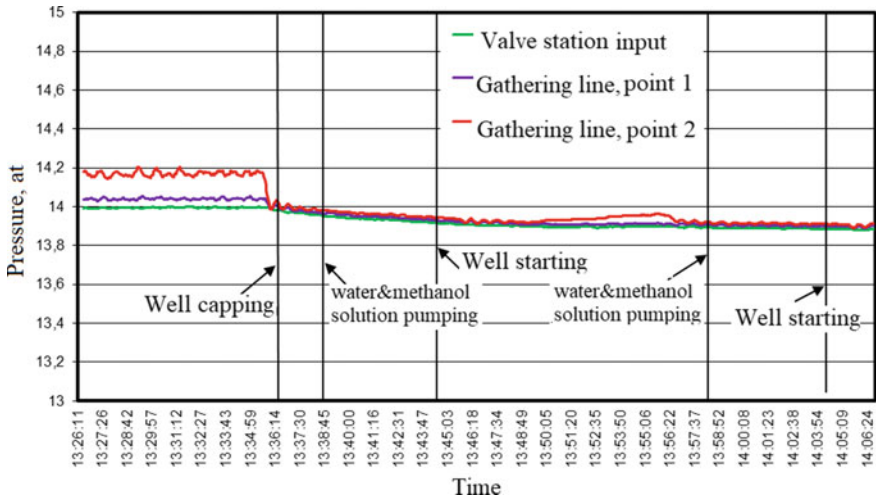


Fig. 3 Change of the gas flowline pressure and control and safety valves pressure while 510 well self-kill

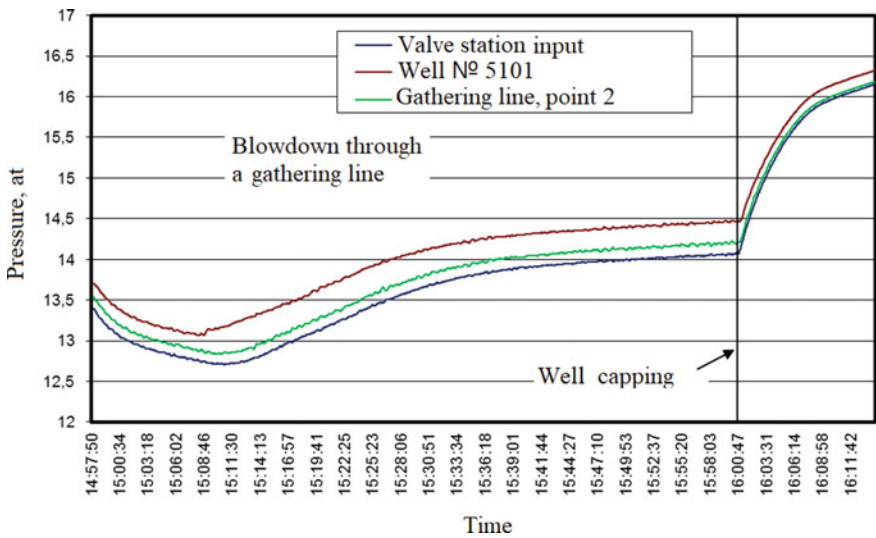


Fig. 4 Change of the wellhead gas pressure and control and safety valves pressure while 510 well blowdown

5 Practical Significance of Research Results

Figure 5 shows the scheme of gas recycling at water removal from wells and gas collectors.



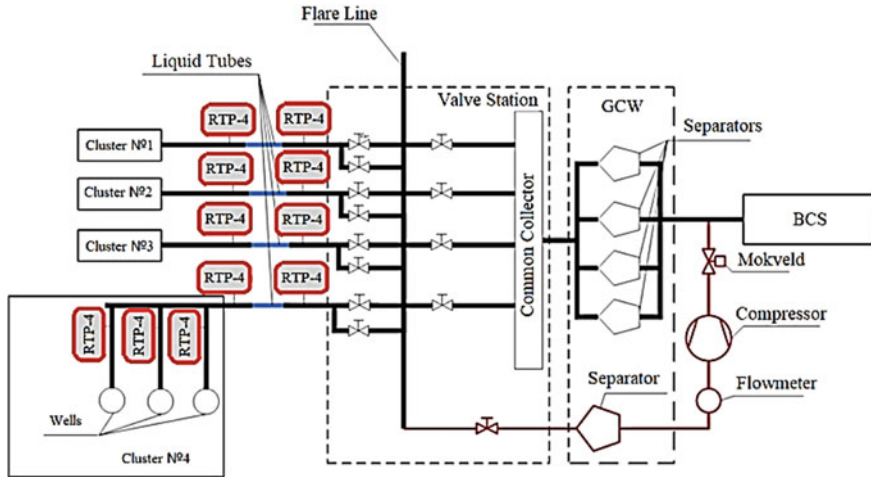


Fig. 5 Scheme of gas recycling at water removal from wells and gas collectors

The well products pass into a common collector of the valve station of the CGTP through gathering lines. A gathering line of a well cluster, at which it is necessary to conduct water removal from a well (wells) or to conduct a survey, is connected to a flare line. As it is seen in Fig. 5, it is possible for all well clusters as at the valve station before and after the flare line, each gathering line is equipped with gate valves.

From the common collector gas, depending on the CGTP, is directed to the gas cleaning workshop (GCW) or the technological workshop (TW) of gas drying. Along the flare line from the well cluster, at which well (wells) blowdown or their survey are conducted, the gas will pass into a separation equipment of the GCW of TW with the help of pipelines. After the separator, gas is fed to a low-capacity compressor through flowmeter. The pressure at the low-capacity compressor would increase up to the gas pressure level before the first stage of the Cenomanian BCS.

To provide the possibilities of the blowdown of one well from several cluster wells, gas rate limiters are installed on them.

The suggested technology advantage is the possibility to use already existing equipment standing because of the reduction of production volumes. Thus, e.g., for the CGTP-5 at the Urengoiskeye OGCF, at which the blowdown process was simulated, it is possible to implement the procedure of low-pressure gas recycling showed in Fig. 6.

The CGTP operation is conducted as follows. The gas from well clusters passes into the valve station common collector and further passes into the first–the fourth technological trains (TT) of the TW-1 for pre-drying. The gas from a low-pressure cluster or well clusters passes to the valve station and, bypassing a common collector, is directed to the sixth technological train TW-1. At this, the gas passes through a multifunctional device GP 365 for cleaning from liquid in the separating

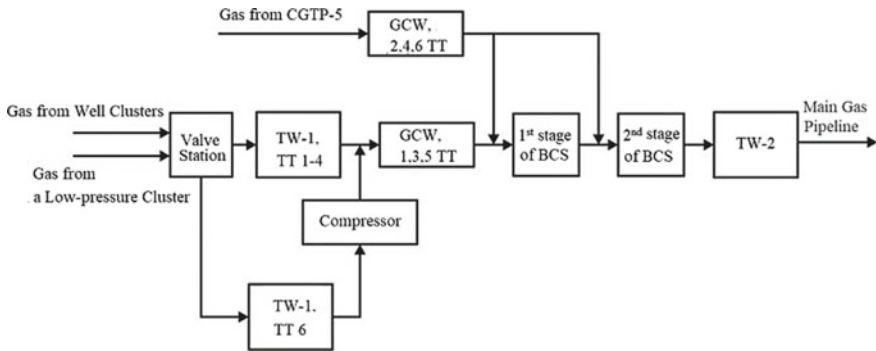


Fig. 6 Operation procedure of the CGTP-5 at the implementation of gas recycling technology at water removal from wells and gas collectors

and filtrating parts of the device. Further, the low-pressure gas passes into the compressor, after which it is mixed with a pre-dried main gas flow.

The proposed gas recycling procedure allows connecting up to five wells. Taking into account that, at well blowdown through a gas collector, it is planned to connect one cluster to the gas recycling scheme and that the well clusters of the Urengoiskoye OGCF include up to five wells, the proposed scheme provides for the well blowdown without gas release into the atmosphere.

6 Conclusions

1. The well blowdown through a gas collector with gas feed to the CGTP, performed with a help of an additional low power compressor, is an efficient way to recover well operational capacity. This process lasts for about an hour, and gas does not released into the atmosphere. This improves both the economic indicators of the company and the environmental situation in the oilfield.
2. The recycling procedure for low-pressure gas at liquid removal from wells and gas collectors uses an existing piping of a flare line and a common collector of the valve station allowing directing the gas of a low-pressure cluster into a flare line from which one is able to direct gas through pipelines for the separation and compressing up to the pressure level at the inlet to the first stage of the Cenomanian BCS.
3. To compress gas for a cluster of five wells, it is sufficient to use compressors with the capacity 500–750 kW. It is recommended to use an electrical drive for them as it can provide for a wide range on the compressed gas consumption.

References

1. Rotov A, Suleimanov V, Istomin V et al (2015) Key technical solutions on preventing liquid accumulation in gas-collecting systems. *Sci-Tech Collection of Papers "News of Gas Science"* 3(23):109–115
2. Report on conduct of complex inspection of CGTP-5 of Urengoisky oil, gas & condensate field of LLC "Gazprom Dobycha Urengoi" (2016) LLC "Znaniye, Scientific & Production Center". Saint-Petersburg, 188 pp
3. Prakhova M, Krasnov A, Khoroshavina E (2016) Method of diagnosing gas well water content. *Scientific Papers of NIPI Neftegas, State Oil Company of Azerbaijan* 3(3):19–26
4. Krasnov A, Prakhova M, Suleimanov I et al (2017) Continuous monitoring of gas well water content. *Nat Tech Sci* 10(112):40–46
5. Skorobogach M (2011) Problems of operation of gas collection systems at field Medveshye. *Oil Gas Technol* 6:42–47
6. Guzhov I, Rotov A, Trifonov A (2010) Evaluation of efficiency of engineering solutions on reconstruction of gas-collecting system at final stage of Urengoisky field development. *Efficiency of Hydrocarbon Reserves' Development: Scientific & Technical Collection of Papers, Ukhta*, pp 62–69
7. Prakhova M, Krasnov A, Khoroshavina E (2016) The automatic diagnostic system of gas well flooding. In: *2nd International Conference on Industrial Engineering, Applications and Manufacturing, ICIEAM 2016*: 7910954
8. Koryakin A, Nikolayev O, Guzov V et al (2013) Relevant issues of final stage of development of main basic fields of LLC "Gazprom Dobycha Urengoi". transition to abandon operations and procedure of their conduct. *Priority Areas of Development of Urengoisky Complex: Collection of Scientific Papers, Moscow*, pp 58–62
9. Buleiko V, Buleiko V, Salyukov V (2008) Technology of gathering line cleaning with use of gel pistons. *Development of Hydrocarbon Fields: Collection of Scientific Papers. Gazprom VNIIGAZ, Moscow*, p 290–297
10. Istomin VA, Astafyev EN, Baidin II et al (2009) Method of operations of wells and gas collection systems in compressor period of gas & gas and condensate field development. *RF Patent 2346147*
11. Minigulov RM, Shadrin VI (1994) Method of eliminating liquid from gas well and gathering lines. *RF Patent 2017941*
12. Kolovertnov GYu, Krasnov AN, Prakhova MYu, Fedorov SN, Khoroshavina EA (2015) Method of control of gas well watering. *RF Patent 2604101*
13. Miguel A. Liquid loading process in gas wells. <http://www.ingenieriadepetroleo.com/liquid-loading-process-gas-wells.html>. Accessed 12 Dec 2018
14. Kolovertnov GYu, Krasnov AN, Prakhova MYu et al (2018) Innovative technology of operation of gas collectors under far north conditions. *Territory "NEFTEGAZ"* 4:12–17
15. Kolovertnov G, Krasnov A, Kuznetsov Yu et al (2015) Automation of Liquid Elimination from Gas Wells and Gathering Lines. *Territory "NEFTEGAZ"* 9:70–76
16. Astafyev YN, Baidin II, Istomin VA et al (2009) Method of operations of wells and gas collection systems in compressor period of gas & gas and condensate field development. *RF Patent 2346147*
17. Kolovertnov GYu, Krasnov AN, Fedorov SN et al (2016) Method of operation of gas field at collector & radial organization of collection chart at final state of field development. *Patent RF 2597390*
18. Device for Registering Industrial Parameters RTP-4. Description of measurement tool type. <https://all-pribors.ru/opisanie/29581-12-rtp-04-28908>. Accessed 13 Dec 2018

Improvement of Procedure for Determining Antioxidant Additive (Ionol) in Insulating Oils



M. Lyutikova and S. Korobeynikov

Abstract The content of the antioxidant additive ionol in mineral transformer oil within the limits of normalized values (0.08–0.40 wt%) provides reliable operation of oil-filled high-voltage electrical equipment. One of the methods of an inhibitor concentration control in a liquid dielectric is gas-liquid chromatography. However, in the option offered by certified methods based on gas chromatography, it is impossible to ensure high accuracy in determining the amount of inhibitor. In order to reduce the analysis processing time, as well as to increase the reliability of the measured concentration of ionol in a complex hydrocarbon matrix of oil, a new method of chromatography mode using the distribution coefficient of ionol in the oil-ionol-solvent system is proposed in this article. In Russia, the most widely used brands of mineral insulating oil are such as GK, ТКр, Nytro 10XN, Nytro 11GX, and T-750. The value of the distribution coefficient for the listed brands of oils differs from each other (from 2.30 to 2.61), which indicates the unevenness of the distribution of ionol between the molecules of carbohydrates of different chemical compositions and, in general, because of the chemical composition of various brands of oils.

Keywords Insulating oil · Additive · Ionol · Inhibitor · Gas-liquid chromatography · Distribution coefficient

M. Lyutikova (✉)

Federal Grid Company of Unified Energy System, 10, Entuziastov St.,
Noyabrsk 629806, Russia
e-mail: m.lyutikova@mail.ru

S. Korobeynikov

Novosibirsk State Technical University, 20, K. Marx St., Novosibirsk 630092, Russia

© Springer Nature Switzerland AG 2020

A. A. Radionov et al. (eds.), *Proceedings of the 5th International Conference on Industrial Engineering (ICIE 2019)*, Lecture Notes in Mechanical Engineering,

https://doi.org/10.1007/978-3-030-22041-9_102

1 Introduction

In high-voltage electrical equipment, liquid dielectrics are mostly used as transformer oils of various brands (GK, VG, TKp, T-1500U, Nytro 11GX, Nytro 10XN, etc.). As a product of oil refining, mineral oils have a complex chemical composition. During the operation oils usually oxidize and age. The complex blend composition is replenished with polar, ionic, condensed compounds, which can decrease performance properties of liquid insulation. One of the ways to slow down the radical chain oxidation of hydrocarbons and preserve the dielectric properties of the oil is their inhibition by special additives. In Russia, as in many other countries, ionol (2,6-di-tert-butyl-4-methylphenol) has become widespread as an antioxidant, which has several dozens more trade names (Dibunol, Agidol, Dibunol, Agidol I, Alkofen B), topanol-O, kerobit, antioxidant 4, BHT, 2,6-di-tertiary butyl-4-methylphenol, 2,6-di-tertiary butyl paracresol, etc.). In this work [1], it was shown that the additive works as an oxidation inhibitor at a concentration of not less than 0.05 wt%. And, the injection of ionol in the oil more than 0.8% of the mass is unreasonable. In the specifications [2, 3] indicated, controlled level of ionol is in the range of 0.08–0.40% of the mass. Therefore, according to the procedure to maintain the necessary ionol content in the oil, it should be controlled at least 1 time in 2 years. When the additive is depleted to a certain value, the specialists of the insulation services give recommendations on how to bring the oil-insulating characteristics up to standards, including adding the required amount of ionol.

2 Formulation of the Problem

In world practice, methods based on thin-layer chromatography (TLC), high-performance liquid chromatography (HPLC), gas chromatography (GC), chromatography-mass spectrometry (gas chromatography with a mass selective detector—GC/MS), infrared (IR) and ultraviolet (UV) spectrometry [4–11] are used to quantitatively determine the concentration of ionol in the oil. Each of these methods has its own advantages and disadvantages. Using the methods of TLC, HPLC, IR, UV, the reliability of quantitative analysis of the additive in old oils can not be high because of the presence of a large number of oxidized compounds that interfere with the identification of the target analyte (ionol). According to the selectivity of measuring the oxidation inhibitor in both fresh and operating oils, the methods—GC, and especially GC/MS [12] have many advantages. In Russian electrical grid chemical laboratories, detection of ionol in insulating oils is mainly carried out by gas chromatography [7, 8]. Extraction of ionol from the oil matrix is carried out with 96% ethanol. The concentration is recommended to calculate by absolute graduation, which is based on the standard ionol solutions in the cleared transformer oil with concentration range of 0.10–0.40 wt%. In this case, there are two main disadvantages. The first is that the fixing of a calibration factor using

calibration solutions of ionol in oil takes a long time. The second disadvantage is in practice, we deal with different brands of oils, and, therefore, not the same structural group composition, which will affect the distribution of ionol between oil and solvent in the extraction processes.

Therefore, the goal of this work is to improve the gas–liquid method of ionol analyzing in oils using absolute calibration based on calibration solutions of the additive in a solvent and fixing of the ionol distribution coefficients in the “dielectric-ionol–ethanol” system with a single extraction.

3 Theory

The basis of the chromatographic process is the distribution of ionol between the mobile phase (carrier gas) and the stationary liquid phase of the packed column. The distribution itself is due to the adsorption and desorption of the substance.

The gas chromatograph schematically consists of a source of carrier gas (1), a gas purification unit (2), an evaporator (3) with adjustable temperature, a chromatographic column (4) in a thermostat (7), a detector (5) with adjustable temperature (Fig. 1). The liquid sample injected in evaporator is converted into vapor, which is transferred to the chromatographic column by a carrier gas stream. Due to the different distribution coefficients, each compound of vapor mixture moves along the column with its datum speed and overcomes the column in a characteristic time called the retention time. The greater the distribution coefficient, the greater the proportion of the analyzed adsorbate is in the stationary phase and the longer the substance is retained in the column. After column, the substance goes to the flame ionization detector (FID), burning in a hydrogen flame, causes a current flow between the collector electrode and the detector burner with applied voltage. The flowing current is proportional to the amount of organic matter burned in the flame of the detector.

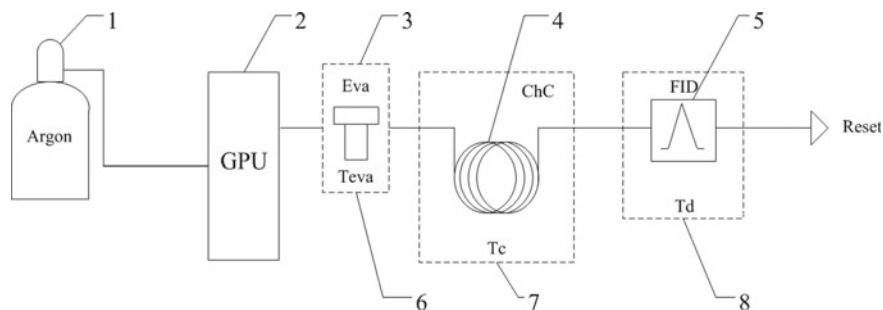


Fig. 1 Example of a chromatograph functional diagram for the determination of ionol in transformer: 1 carrier gas (Argon); 2 GPU—gas purification unit; 3 Eva—evaporator; 4 ChC—chromatographic column; 5 FID—flame ionization detector; 6 Teva—evaporator thermostat; 7 Tc—column thermostat; 8 Td—Detector thermostat

The liquid–gas determination of ionol content C_{ionol} in insulating oil can be carried out using the equation of a single-solvent extraction and the value of the distribution coefficient K_d for ionol in the equilibrium system “oil–ionol–extractant”.

$$C_{\text{ionol}} = K_{\text{grad}} \cdot K_d \cdot S_i \quad (1)$$

where C_{ionol} is the mass concentration of ionol in the test oil, %; S_i is the ionol peak area on the chromatogram of the analyzed transformer oil, mV * s; K_{grad} is a calibration coefficient characterizing the detector linear response in a known concentration range, fixed by the method of absolute calibration using calibration solutions in ethanol.

$$K_d = \frac{C_{\text{ionol}}^{\text{oil}}}{C_{\text{ionol}}^{\text{solvent}}} \quad (2)$$

The distribution coefficient K_d is the ratio of the total analytical concentration of a substance in the oil phase ($C_{\text{ionol}}^{\text{oil}}$) to the total analytical concentration of this substance in the organic solvent phase $C_{\text{ionol}}^{\text{solvent}}$ without taking into account the substance form in each phase.

4 Terms of Conducting Experiments

4.1 Test Objects

Transformer oils of various grades (GK, TKp, T-750, Nytro 11GX, Nytro 10XN) widely used in the Russian power grid equipment were chosen as objects of study.

4.2 Measuring Equipment

Experiments with the determination of the ionol distribution coefficients between two non-miscible liquids and the adjustment of gas–liquid method for determining the additive in oil were performed by a gas chromatograph “Chromatec-Crystal 5000.2” with a flame ionization detector (FID). Packed column (length—1.5 m, ID—3 mm) with a stationary liquid phase—5% SE-30 on the N-AW chromatone with a film thickness of 0.16–0.2 mm. Carrier gas (mobile phase) is high purity argon brand “5.0” (component volume ratio is not less than 99.999%).

4.3 Programmable Chromatography Mode

Evaporator temperature $T_{\text{evap}} = 200\text{ }^{\circ}\text{C}$, column thermostat temperature $T_{\text{chc}} = 140\text{ }^{\circ}\text{C}$, detector temperature $T_{\text{fid}} = 220\text{ }^{\circ}\text{C}$ for FID, temperature programming range is from 140 to 200 $^{\circ}\text{C}$ at a speed of 3 $^{\circ}\text{C}/\text{min}$ after the release of the chromatographic ionol peak. The carrier gas flow rate is 25 ml/min, hydrogen—25 ml/min, air—500 ml/min. The volume of injected extract sample is 2 μl . The chromatography time of one measurement is 40 min.

4.4 Concentration Method

The calibration function “analytical signal—concentration” was based on solid ionol solutions with the main substance content—99.8 wt% in 96% ethyl alcohol. For the prepared solutions of ionol in alcohol, the peak area linearly depends on the inhibitor concentration in the range—0.05–0.60 wt% with a correlation coefficient—0.9999 (Fig. 2), this indicates an analytical approximation. The relative error of determination at $P = 0.95$ was no more than 2%.

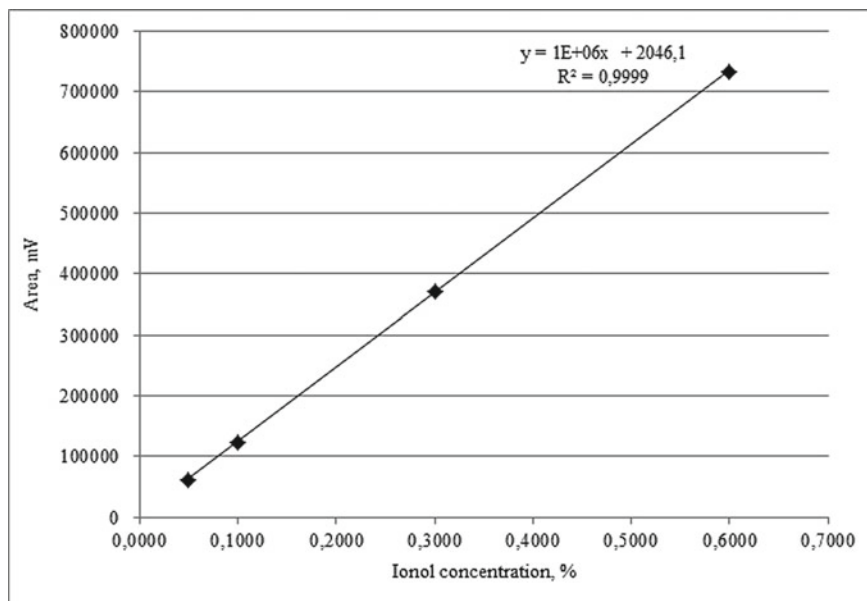


Fig. 2 Calibration dependence of the area of the ionol peak on the chromatogram from its concentration in 96% ethyl alcohol

4.5 Method of Determining the Distribution Coefficient of “Oil–Ionol–Ethanol”

Studies for determination of the ionol distribution coefficient were performed at an indoor temperature of (21 ± 2) °C, oil-to-solvent ratio of 1:1. The principle of this method was to determine the inhibitor concentration in an experimental oil sample with a random content of the additive, and in the same sample oil with added ionol.

The distribution coefficient in the system “transformer oil–ionol–ethanol” was calculated by the following formula:

$$K_d = \frac{C_{\text{ionol}}^{\text{additive}}}{(C_2 - C_1)} \quad (3)$$

where K_d is the distribution coefficient of ionol between the two phases “oil-extractant”; $C_{\text{ionol}}^{\text{additive}}$ —the concentration of ionol added to the oil, %; C_2 —concentration of ionol in ethanol extract from oil after its addition, wt%; C_1 is the concentration of ionol in the ethanol extract from the oil before injection of the additive in the oil, wt%.

5 Test Results and Discussion

The chromatograms of an ethanol extract of ionol from transformer oil sample measured on different chromatography modes are shown in Fig. 3.

Using the chromatographic mode specified in certified methods [7, 8], the process of analyzing antioxidant additives takes a long time (5–9 h). The main reason for such a long analysis is that ethanol is a universal solvent for many chemicals of different polarity. When we extract ionol from the sample, other polar impurities also pass from the oil to the ethanol extract. During the analysis of such an extract, heavy polar impurities enter the chromatographic column and strongly pollute it. The adsorption of undesirable heavy components by the stationary liquid phase of the column leads to a high background of the flame ionization detector (Fig. 3, Mode 1) and the appearance of extraneous peaks, which makes it difficult to reliably determine the concentration of the inhibitor. Ionol is on the “crest” of oil heavy hydrocarbon. To minimize the error in the determination of the additive, chemists spend very long time (at least 2 h) to purge or regenerate the column after the main analysis (recording one chromatogram, and they should be done two or three times to produce the “correct” result), raising the temperature of the column thermostat and FID to several degrees above working temperatures, pointed in a technique. The situation is especially aggravated by the analysis of “old” oxidized oils, which have been used in transformers for several years.

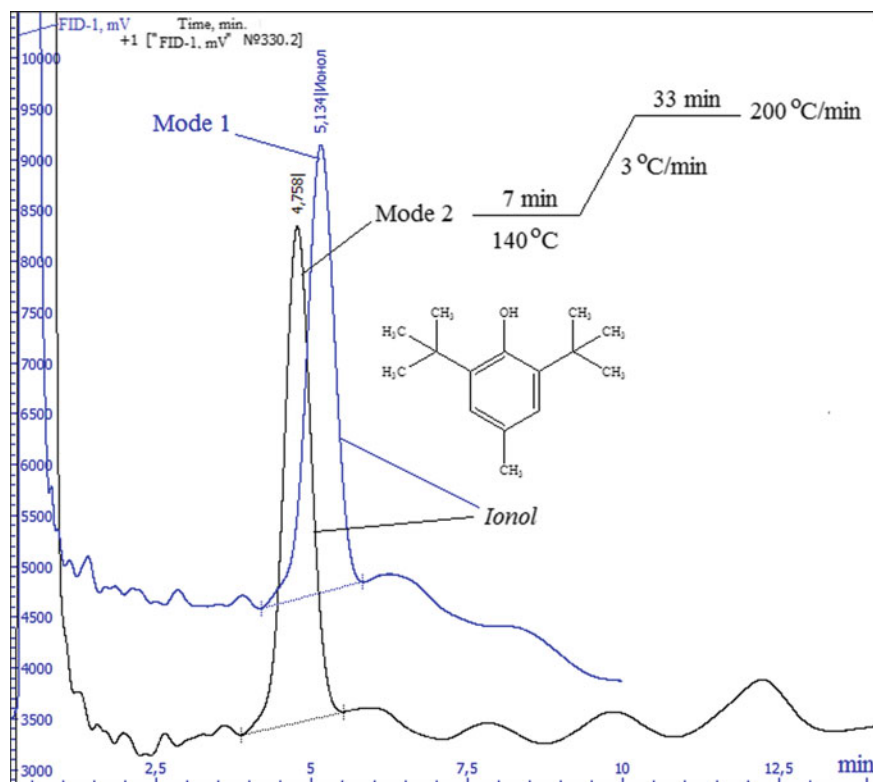


Fig. 3 A typical chromatogram of an ethanol extract of an oil additive. Mode 1—the usual mode indicated in the procedures [8]; Mode 2—isothermal mode (suggested)

Therefore, in this work, we have used a programmable isothermal chromatographic mode (Fig. 3, mode 2), which allows not to carry out a continuous regeneration of the column after each analysis. By increasing the temperature of the thermostat after the target component (ionol) yield, it is possible to remove contaminants in the column, and, therefore, do not allow the zero line of the detector to shift and avoid high background noise at the output. When using the usual chromatographic mode (Fig. 3, mode 1), over time, highly polar compounds accumulate in the column, which, due to their polar nature, are held longer by the stationary liquid phase of the column and lead to a shift in the ionol yield time. Mode 2 helps to quickly clean the column and the detector itself from contaminants during the analysis and also prevents the layering of interfering heavy hydrocarbons on the phase of the chromatographic column.

Table 1 presents the determination results of the ionol distribution coefficient between two non-miscible phases (oil and 96% ethanol) performed by the proposed method of gas-liquid chromatography using the isothermal mode (mode 2).

Table 1 Distribution coefficient (K_d) of ionol in the system “insulating oil–ionol–solvent” at the temperature (21 ± 2) °C

Oil grade	Solvent	Phase ratio (Oil:Solvent)	K_d
GK	96% ethyl alcohol	1:1	2.53
TKp	96% ethyl alcohol	1:1	2.30
Nyro 10XN	96% ethyl alcohol	1:1	2.40
Nyro 11GX	96% ethyl alcohol	1:1	2.44
T-750	96% ethyl alcohol	1:1	2.61

Table 1 shows that the distribution coefficients as the ratio of the ionol concentration in the oil phase to the concentration of ionol in alcohol (Formula 2), for different grades of oils have different values in the range from 2.30 to 2.61. First of all, this is explained by the difference in the structural group composition of insulating oils, as well as by the presence of polar compounds that appear as a result of the thermal and electrochemical aging of liquid dielectrics. It follows that the degree of ionol extraction from calibration mixtures and from oil production samples are different. In the published paper [13], the author has noted that calibration mixtures prepared on the basis of various transformer oils have different calibration coefficients from each other. It means that for each brand of oil, it is necessary to create its calibration function on the ionol solutions in the test oil, previously carried out a whole complex operations, which consists in processing a portion of a liquid dielectric by concentrated sulfuric acid to purify it from ionol and then prepare inhibitor solutions with previously predetermined concentration, by dissolving solid ionol in the purified base oil.

Using the obtained K_d value in calculating the concentration of ionol in an oil sample with an unknown additive concentration according to Formula (1), firstly, helps to avoid such a time-consuming procedure as the creation of absolute calibration with solutions of a certain brand of oil. Secondly, it increases the reliability of the result, which is relevant, especially when determining the minimum allowable concentration of ionol in the mineral transformer oil at a level of 0.1% mass fraction to make a decision about the need of ionol injection into the insulating oil being in operated.

6 Conclusion

The combination, proposed by us, of the chromatography isothermal mode of an additive ethanol extract from oil and the fixed distribution coefficients of ionol in the system “oil–ionol–solvent” allows us to reduce the laboriousness of operations during gas–liquid analysis, and also to increase the reliability of the obtained ionol concentration in the insulating transformer oils in use, which necessarily contain oxidized forms of hydrocarbons.

References

1. Lipshteyn RA (1968) On the mechanism of action of oxidation inhibitors. In: Proceedings of the Second All-Union Scientific and Technical Meeting "Additives to oils". Moscow, pp 169–177
2. STO 34.01-23.1-001-2017 Organization Standard (2017) Scope and standards of electrical equipment testing, PSC "Rosseti". Moscow, 262 pp
3. IEC 60296 International standard. Fluids for electrotechnical applications—Unused mineral insulating oils for transformers and switchgear, 19 p
4. STO 70238424.27.100.053-2009 Organization Standard (2010) Energy oils and oil facilities of power plants and networks. Organization of operation and maintenance. Norms and requirements, INVEL, Moscow, 166 pp
5. RD 34.43.208-95 Method of quantitative chemical analysis Determination of the content of additives in energy oils by HPLC. RAO "UES of Russia", Moscow, 1995, 6 pp
6. ASTM Standard D 4768-96 standard test method for analysis of 2,6-ditertiary-butyl para-cresol and 2,6-ditertiary-butyl phenol in insulating liquids by gas chromatography. ASTM International, 1996, 3 pp
7. Method of quantitative chromatographic analysis. Determination of the content of furan derivatives and additions of ionol in transformer oils by the gas-liquid chromatography method. No. MKHA 01-99. Part 2. Determination of the content of ionol in transformer oils, NPO "Electrum", Moscow, 2010, 9 pp
8. STO 56947007-29.180.010.008-2008 Organization Standard (2007) Methodological guidelines for determining the content of ionol in transformer oils by gas chromatography. PSC "FGC UES", Moscow, 24 pp
9. GOST R MEK 60666-2013 State Standard (2014) Insulating oil oils. Detection and determination of specified additives in mineral insulating oils. Standartinform, Moscow, 28 pp
10. ASTM Standard D 2668—07 (2013) Standard Test Method for 2,6-*di-tert*-Butyl-*p*-Cresol and 2,6-*di-tert*-Butyl Phenol in electrical insulating oil by infrared absorption. ASTM International, 2013, 6 pp
11. Kozlov VK, Valiullina DM, Murataeva GA (2010) Determination of the antioxidant additive ionol in transformer oil by the spectral method. *Energ Tatarstan* 2:55–58
12. Lyutikova MN, Korobechnikov SM, Tretyakov NYu, Marchenko OYa (2017) Determination of ionol in transformer oil from high-voltage oil-filled equipment by gas chromatography with a mass-selective detector. *Ind Serv* 4:33–41
13. Moseva EV, Srednitskaya NI, Kolodko TM (2000) Determination of the ionol in industrial oils. International scientific and technical conference "Resource-saving ecotechnologies: renewal and saving of energy, raw materials and materials". Grodno, pp 145–146

Resource-Saving Multifunctional Apparatus for Autonomous Energy and Water Supply Systems



I. V. Dolotovskij and N. V. Dolotovskaya

Abstract The article proposes a concept of utilizing steam, gas, and wind energy techniques to improve existing autonomous energy and water supply systems by adding new resource-saving multifunctional heat, electric power, cold, and water generating apparatus. The proposed apparatus is fueled by hydrogen produced in its wind energy unit, thus reducing the rate of consumed hydrocarbon fuel, while thermal decontamination of industrial and utility wastewater helps in improving environmental safety of the facility. The article contains a schematic for such apparatus as well as several equipment variations for energy and water supply systems with preset parameters such as electric and heat energy loads and amount of cold and wastewater produced. The proposed set of parameters allows evaluating production, technological, and economic efficiency of the apparatus by considering various interrelations between production facilities and external energy and water supply sources. The comparative analysis of existing energy and water supply systems with autonomous energy and water supply units that utilize the proposed multifunctional apparatus has shown that its installation at various production facilities improved production, technological, and economic efficiency of such facilities.

Keywords Autonomous sources · Energy and water supply · Multifunctional module · Wind generator · Resource-saving · Wastewater utility

1 Introduction

Current trends in development and upgrading of energy production facilities and energy supply systems, that utilize internal power generating sources and on-site generation facilities, are concurrent with evolutionary changes in energy resource

I. V. Dolotovskij · N. V. Dolotovskaya (✉)
Saratov State Technical University Named After Gagarin Yu. A.,
77, Politekhnikeskaya, Saratov 410054, Russia
e-mail: dnw50@yandex.ru

(ER) generation technologies and structure of energy system [1, 2] and undergoing development and implementation of new energy resource-saving techniques. A growing number of industrial enterprises now include autonomous energy sources utilizing the potential of secondary energy resources and industrial wastes [3–6], internal electric power stations with combined cycle gas turbine (CCGT) units [7–9] or power-producing facilities that utilize low-pressure gas and renewable energy sources [10–12] into the structure of their energy complex (EC). Methods of multi-criterial assessment of energy supply systems efficiency [13–15] and development strategies for such systems [16–18], as well as mathematic simulation models for complex energy production facilities [18–20] have also been consistently improving. It should be noted that there are two key factors that must be accounted for in the course of development of multifunctional autonomous energy sources effective over the whole operational period of the facility. The first factor is the directive interrelation between ER supply systems and production units of the primary production facility; this factor is the cause of various problems during structural and parametric integration of such units. The second factor determines the interactions between energy and water supply systems (EWSS) with various operation modes, external ER and water supply systems, and waste recycling systems. These two factors can be represented as a series of general structural and parametric requirements to energy facilities with various degrees of centralization including:

- high reliability of electric power supply to process loads, especially to critical and essential loads;
- highly efficient operation over the whole production cycle starting from facility construction period when there are no internal ER generating sources, and ending with facility decommissioning;
- maximal integration with existing energy process units including formation of closed cycles of ER generation and consumption as well as water consumption and removal;
- integration of automated control systems for ER generation processes with a single system controlling the whole production process;
- maximal consistency between energy generation modes of autonomous and external energy supply sources and ER consumption mode of industrial facilities that is aimed to solve the problem of accumulation of heat and energy power energy.

We have performed theoretical and experimental evaluation of EC of various oil and gas industrial facilities [17, 18] and found out that creation of highly efficient, reliable, and environmentally safe ECs that comply with aforementioned requirements can be achieved by integrating production and energy units into multifunctional modular apparatus.

2 Schematic and Hardware Configuration of Multifunctional Energy and Water Supply Apparatus

Our concept of creating optimal autonomous EWSS is founded on the principle of assembling a resource-saving multifunctional apparatus (RSMA, see Fig. 1) from combined ER (heat, electric power, and cold) and process water generation unit, combustible industrial waste recycling unit, and wastewater recycling unit. The figure depicts one of RSMA modules with parallel connection in EWSS. Modules are connected via process flows of overheated steam, exhaust steam from turbines 5 and 25, and feed water supplied to exhaust heat boilers 3 and 4.

Module depicted on the figure and separate units of RSMA are not only included into autonomous energy supply system structure (RU Patent 164323) but can be also combined with various process units such as hydrocarbon transportation and storage units (RU Patent 118360), absorbent regeneration units of raw oil and gas

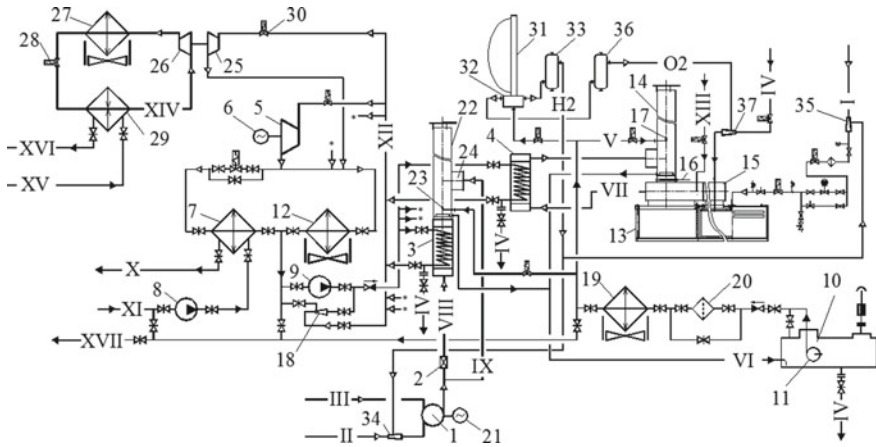


Fig. 1 Schematic of multifunctional energy and water generation module. 1—gas turbine unit (GTU)—thermal engine; 2—smoke gate; 3, 4—exhaust heat boilers; 5—steam extraction turbine; 6, 21—electric power generators; 7—condenser—heat exchanger; 8, 9, 11, 18—pumps (8—network circulation pump, 9, 11—feed pumps, and 18—steam jet pump); 10—condensed water de-aeration (de-carbonization) unit; 12, 27—air conditioning condensers; 13—thermal neutralizer of industrial wastewater; 14, 22—smokestack; 15—gas pipe; 16—smoke gate; 17, 23—nozzles; 19—condensed water cooler; 20—filter; 24—by-pass pipe junction; 25—steam drive of compression refrigerator; 26—compressor; 28—thermal expansion valve; 29—evaporator; 30—steam flow regulator; 31—wind power generator; 32—electrolysis cell; 33—hydrogen storage circuit; 34, 35—fuel and hydrogen mixing vessel; 36—oxygen storage circuit; 37—industrial wastewater and oxygen mixing vessel; I, II—fuel gas (hydrocarbon fuel); III—air; IV—industrial and utility wastes (effluents); V—condensed water; VI—unpurified condensed waster steam; VII, VIII, IX—combustion gases; H₂—hydrogen; O₂—oxygen; X, XI—direct and reverse water flows of heat supply system; XII—overheated steam; XIII—reagent (sulfur oxides absorbent) solution; XIV—cooling agent; XV, XVI—heated and cooled coolant; XVII—water flow going to utility water pre-processing unit; and *—module connection

condensate extraction, pre-processing and processing facilities (RU Patent 138474, RU Patent 114424) and gas turbine engine power stabilization units of process injectors, and CCGT units of electric power stations (RU Patent 149419). The most prominent example of a multifunctional unit constructed in accordance with described principles is a binary energy process module that generates ER, black carbon, and water (RU Patent 2652237). Thermal disposal of combustible wastewaters, drainages from equipment, and effluent is carried out in a thermal neutralizer of industrial waste (hereinafter—in the neutralizer; RU Patent 2523906) with injector burner (RU Patent 135080) providing full combustion of gas- and liquid-phase hydrocarbon mixtures. A general view of the neutralizer is shown in Fig. 2. The advantage of the developed design of the neutralizer is the possibility of continuous operation at all stages of the life cycle RSMA.

As fuel for the neutralizer, it is provided to use diesel fuel during construction, and gaseous or liquid combustible waste of the enterprise during its operation (gases of degassing of oil or gas condensate, low-pressure process gases, and unstable gas condensate).

When using the proposed neutralizer, the lowest specific fuel consumption among the known structures is provided, which does not exceed 200 kg of f. e. per 1 m^3 of utilized industrial effluents (without combustible substances). In the presence of waste streams of fuel, specific fuel consumption is reduced accordingly.

During the operation of the neutralizer, the fuel is supplied through the “A” fitting to the armature fuel block, and then the burners are switched on alternately on each of the container sections (Fig. 2 shows eight container sections, the number of which is determined by the required performance). The burners are switched on in advance, before the industrial effluent is supplied. When the optimum operating temperature of the walls of the working container (about $400 \text{ }^\circ\text{C}$) is reached, industrial effluents are fed through the “B” fitting to the reinforcing block of effluents, and then, through the fittings of the supply of the neutralized liquid, to the working containers.

Heating, evaporation, steam-air gasification, and thermal neutralization of industrial wastewater are carried out under the influence of thermal radiation of the emitting surface, on which the combustion of the gas-air mixture flowing from each injector of the emitting burners is carried out, as well as in contact with the flame torches of burners with drops, foam, and vapors of industrial waste.

Dry residues left in the neutralizer can be removed mechanically.

The regulation of the heat output of the thermal utilizer along the gas path is performed by changing the flow rate of the flue gases by the gate, as well as by regulating the temperature of the flue gases by changing the fuel consumption on the burners with priority provision of a given optimal temperature regime of the neutralization process.

Regulation of the neutralizer performance on industrial effluents is carried out smoothly by changing the fuel pressure in front of the burners within the range of their regulation, as well as stepwise, by switching on/off the container sections.

Power generation unit of CCGT-based RSMA can utilize both natural and associated gas as fuel. Waste and wastewater recycling unit can use low-pressure

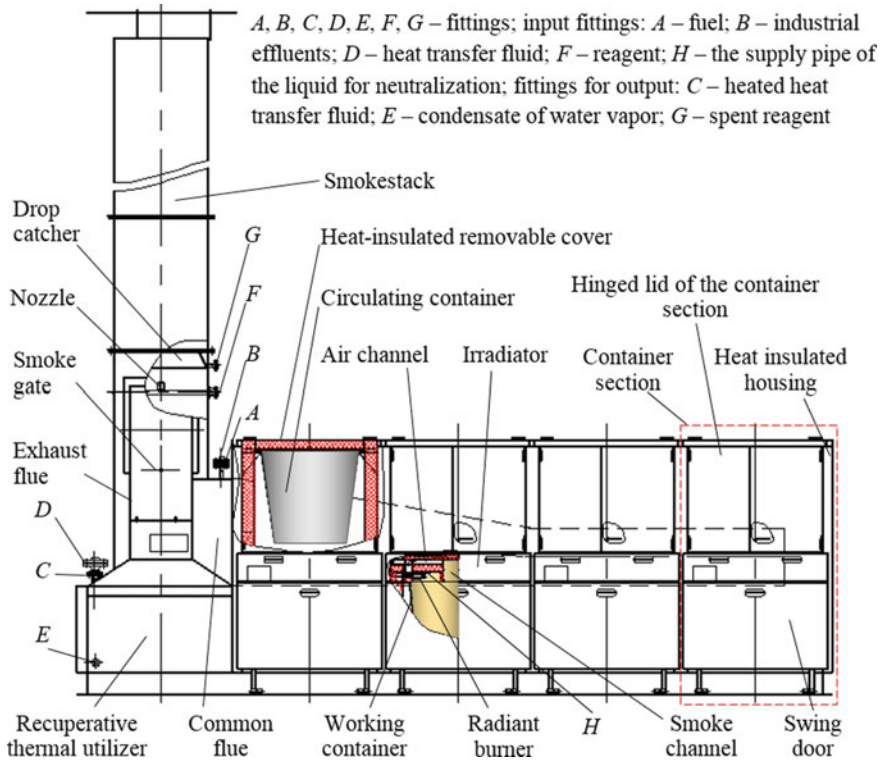


Fig. 2 Thermal neutralizer of industrial wastewater

hydrocarbon gases, combustible wastes (gaseous and liquid) of primary and secondary production processes, and hydrogen generated by RSMA as fuel. Decontamination of wastewater with subsequent utilization of purified process water allows creating water supply system that requires only minimal amount of water to be provided by external sources.

RSMA consists of five primary units (positions of the equipment's of blocks correspond to Fig. 1).

- Thermal decontamination unit processes industrial wastewater and combustible wastes within the neutralizer 13 by utilizing the heat of steam–gas mixture formed in exhaust heat boiler 4 to produce the steam. This unit can also be used for thermal decontamination of sulfur-containing wastes by utilizing a special reagent to absorb sulfur oxides produced as a result of decontamination process. Heat and mass exchange between the flow of combustion gases formed at exhaust heat boiler and water flow coming from nozzle 17 lead to condensation of water vapor formed as a result of wastewater evaporation and combustion of hydrocarbon fuel and hydrogen mixture. Condensed water then goes into de-aeration unit 10 of water pre-processing unit.

- Steam power unit generates electric power and heat at nominal and peak electric loads. Its primary components include thermal engine 1, exhaust heat boiler 3, and steam extraction turbine 5 with electric power generator 6. Allocation of additional condensed water nozzles 23 within smoke funnel 22 of exhaust heat boiler 3 leads to increased process water output of RSMA due to condensation of water vapors from exhaust gases of thermal engine 1. Steam power unit provides for recuperative heating of heating water flow of heat supply system and for utilizing exhaust steam produced by turbine 5 to heat the object. Part of produced steam can be used for other process units of the facility.
- Process water pre-processing unit includes de-aeration (de-carbonization) unit 10 with feed pump 11, filter 20, and condensed water cooler 19. Condensed water produced by the unit does not contain any mineral impurities or salts and can be used to fill and feed exhaust heat boilers and heat supply system network. The quality of condensed water also makes it suitable as feed water for utility and portable water pre-processing unit as well as electrolysis cell 32.
- Electric power generation unit also produced hydrogen and oxygen and includes wind power generator 31, electrolysis cell 32, hydrogen storage circuit 33 and oxygen storage circuit 36. Hydrogen produced by this unit partially replaced hydrocarbon fuel in flame neutralization tank and thermal engine, thus improving energy performance of RSMA. Produced oxygen can be mixed with industrial wastewater leading to increased boundary surface and decreased period of complete waste combustion.
- Cold generation unit includes coolant compressor 26, with steam drive 25, air conditioning condenser 27, evaporator (or process heat exchange unit) 29, and thermal expansion valve 28.

Steam drive of the compressor is connected to steam output flows of exhaust heat boilers 3 and 4 via steam flow regulator 30, while steam drive output is connected to input flow of exhaust steam of condenser-heat exchanger 7 and air conditioning condenser 12. This helps to decrease capital costs of RSMA as the primary equipment can be used to produce electric power, heat energy, process water, and cold at the same time.

Due to its modular and multifunctional structure, RSMA can be easily combined with process and energy systems of various power-consuming units and can be adjusted for their dynamically evolving parameters. At the same time, RSMA units are mostly comprised of standard equipment [21]. For example, RSMA-based EWSS with total electric power and heat output of 4.2 MW (including wind power generator with average power output of 190 kW) and 8 MW, respectively, can be equipped with the following units:

- steam power unit—gas turbine power plant; total electric power output: 2.5 MW, heat output: 4.5 MW;
- thermal decontamination unit—for wastewater flow of 5.4 m³ per hour: six flame neutralization tanks with a capacity of 5 m³; one G-250 exhaust steam boiler with a total output of 3.1 tons of overheated steam per hour (pressure:

1.4 MPa, overheating temperature: 240 °C), and a K-2.5-3.4 condensation drive turbine;

- cold generation unit—propane horizontal compressor; two air conditioning condensers (heat exchange surface area of one condenser is 1588 m²); and two evaporators with heat exchange surface area of 580 m².

EWSS with lower need for ER can utilize a RSMA base module with the following parameters: electric power output of steam power unit: 1.9 MW; heat power output: 0.7 MW; cold power output of vapor compression refrigerating machine: 0.4 MW; rate of processed industrial wastes: 1.1 m³ per hour; and output capacity of wind power generator: 96 kW.

3 Production, Technological, and Economic Efficiency of RSMA

In order to assess production efficiency of the apparatus and its constituent part, we propose using a set of partial and vector efficiency parameters [16, 17] including:

- balance efficiency coefficients (for production and process balance, water consumption balance, and water disposal balance) that characterize the capacity for improving EC via optimization of its structure and parameters and maximal utilization of its internal potential for all types of resources, minimization of ER and water consumption from external sources, and decrease of demand (M_N) for each type of resources to its optimal value (M_{opt}):

$$h_p = 1 - (M_{opt}/M_N); \quad (1)$$

- amount of ER and water consumed from external systems and amount of wastewater produced by the unit measured in natural units of measurement (M_j);
- combined parameters encompassing partial energetic, process, and economic efficiency parameters u_i into vector function;

$$U = Sa_i u_i^0; \quad (2)$$

where a_i is the range coefficient of a parameter determined via hierarchic analysis approach; $u_i^0 = u_i/\Delta u_{i\text{extr}}$ is the relative value of partial efficiency parameter; and $\Delta u_{i\text{extr}}$ is the difference between maximal and minimal value of such parameter measured for alternative variations of EWSS.

Economic efficiency of EC improvement via incorporation of RSMA-based EWSS into its structure can be evaluated by using partial and combined criteria such as net present value (NPV), discounted capital costs, operational costs, and the payback period.

Table 1 Specific resource consumption of alternative EWSS

Specific indicator	Technological installations of the enterprise for preparation and processing of oil and gas condensate raw materials			
	Preprocessing	Purification of gases from H ₂ S and CO ₂	Hydro treating diesel fractions	Reforming
Fuel consumption (commercial gas network), kg of f. e./t	$\frac{79.6-80.5}{58.5-33.4}$	–	$\frac{25.3-27.6}{10.4-12.3}$	$\frac{19.9-22.8}{7.9-13.7}$
Water consumption (external source), kg/t	$\frac{36-70}{3.3-6.3}$	$\frac{167-171}{15-16}$	$\frac{34-48}{4-7}$	$\frac{24-28}{3-4}$
Water disposal, kg/t	$\frac{46-64}{1.4-1.9}$	$\frac{34-56}{2-3}$	$\frac{34-36}{1.6-2.1}$	$\frac{21-26}{2-3}$

Results of comparative analysis of production, technological, and economic efficiency parameters of several alternative variations of EWSS incorporated into the structure of various production facilities and ECs are shown in Table 1 (the numerator shows the indicators of the existing systems of ER and water supply and drainage systems, in the denominator—autonomous resource-saving multifunctional systems).

For specific objects with a certain technological structure and installed equipment, technical solutions to improve the efficiency of the energy complex with an autonomous system of energy and water supply are developed and implemented in stages: the variants of technological schemes for different productivity are formed; optimization of structure, parameters and modes of equipment, devices and systems with the use of information and analytical support is performed; and development of technical specifications for the design of devices and systems.

4 Conclusion

Proposed multifunctional apparatus for autonomous energy and water supply systems for production facilities significantly improves their production, technological, and economic efficiency; provides for combined output of electric power, heat energy, and cold that complies with operational requirements of process loads; improves environmental safety of the facility area due to thermal decontamination of wastewater and creating of almost complete closed water consumption circuits; and helps reducing the consumption of hydrocarbon fuel by substituting it with hydrogen produced by wind energy power unit of the apparatus.

References

1. Bushuev VV, Gromov AI, Belogoriev AM et al (2016) Energetika Rossii: post strategicheskii vzglyad na 50 let vpered (Russian energy: post-strategy look 50 years ahead). IATS "Energiya", Moscow
2. Stennikov VA, Zharkov SV (2015) Osnovy tekhnicheskoy politiki v energosnabzhenii (Fundamentals of technical policy in energy supply). Delovoy zhurnal Neftegaz. RU 9:14–26
3. Bushuev VV, Kulagin AYu, Kartavtsev SV (2014) Otsenka pokazateley effektivnosti avtonomnoy sistemy energoobespecheniya elektrostaleplavil'nogo proizvodstva (Evaluation of performance indicators of an autonomous power supply system for electric steelmaking). Promyshlennaya energetika 6:24–29
4. Kormilitsyn VI et al (2015) Avtonomnyye istochniki kompleksnogo energosnabzheniya dlya lokal'nykh potrebiteley (Autonomous sources of integrated power supply for local consumers). Energoberezheniye i vodopodgotovka 2(94):25–29
5. Director LB et al (2014) Analiz effektivnosti skhem energeticheskikh kompleksov maloy raspredelennoy energetiki (Analysis of the effectiveness of the schemes of energy complexes of small distributed energy). Promyshlennaya energetika 2:41–46
6. Philipp M, Schumm G, Peesel RH et al (2018) Optimal energy supply structures for industrial food processing sites in different countries considering energy transitions. Energy 146:112–123. <https://doi.org/10.1016/j.energy.2017.05.062>
7. Karasevich AM et al (2012) Effektivnost' primeneniya gazoturbinykh tekhnologiy pri razrabotke nebol'shikh neftegazokondensatnykh mestorozhdeniy (Efficiency of application of gas turbine technologies in the development of small oil and gas condensate fields). Teploenergetika 2:41–45
8. Sultanguzin IA et al (2012) Energosnabzheniye gazopererabatyvayushchikh zavodov na osnove gazovykh turbin i teplovykh nasosov (Energy supply to gas processing plants based on gas turbines and heat pumps). Nauka i tekhnika v gazovoy promyshlennosti 3(51):96–101
9. Silva P, Lamberti M, Campanari S et al (2018) Trigenenerative solution for natural gas compressor stations: a north Italian test case. Energy 166:1–10. <https://doi.org/10.1016/j.energy.2018.02.154>
10. Shatrov AF et al (2015) Kombinirovannaya sistema teplosnabzheniya ob"yektov, raspolozhennykh v rayonakh so slozhnymi klimaticheskimi usloviyami (Combined heat supply system for facilities located in areas with difficult climatic conditions). Energoberezheniye i vodopodgotovka 1(93):30–32
11. Khosrav A, Koury RNN, Machado L, Pabon JJG (2018) Energy, exergy and economic analysis of a hybrid renewable energy with hydrogen storage system. Energy 148:1087–1102. <https://doi.org/10.1016/j.energy.2018.02.008>
12. Dolotovskii IV (2018) Production of technical carbon and energy carriers from low-pressure hydrocarbon gases. Chem Pet Eng 54:322–326. <https://doi.org/10.1007/s10556-018-0482-3>
13. Denisov VI, Dzyuba AA (2015) Evolyutsiya obosnovaniy ekonomicheskoy effektivnosti proyektov v elektroenergetike (Evolution of the justification of the economic efficiency of projects in the electric power industry). Elektricheskiye stantsii 1(1002):3–8
14. Agababov VS, Timoshenko NI, Baydakova YuO (2013) Estimation of the effectiveness of investment in the construction of fuel-free generation of electricity generation based on detander-generator units and heat pump installations of vapor compression and air types. Energoberezheniye i vodopodgotovka 3(83):63–65
15. Karasevich VA, Kirshina IA, Vereshchinskaya TV (2013) Metodicheskii podkhod k otsenke effektivnosti energosberegayushchikh meropriyatiy na predpriyatiyakh toplivno-energeticheskogo kompleksa (Methodical approach to assessing the effectiveness of energy-saving measures at the enterprises of the fuel and energy complex). Nauka i tekhnika v gazovoy promyshlennosti 1(53):98–104

16. Filippov SP (2010) Prognozirovaniye energopotrebleniya s ispol'zovaniyem kompleksa adaptivnykh imitatsionnykh modeley (Predicting energy consumption using a set of adaptive simulation models) *Izvestiya Rossiyskoy akademii nauk. Energetika* 4:41–55
17. Dolotovskij IV, Larin EA, Dolotovskaya NV (2017) Analysis and synthesis of optimal supply systems for gas-chemical complexes. *Pure Appl Chem* 89(10):1567–1577. <https://doi.org/10.1515/pac-2016-1114>
18. Dolotovskii IV (2016) Energeticheskiy kompleks predpriyatiy podgotovki i pererabotki gaza. Modelirovaniye i strukturno-parametricheskaya optimizatsiya (Energy complex of gas preparation and processing enterprises. Modeling and structural-parametric optimization). Amirit, Saratov
19. Prina MG, Cozzini M, Garegnani G et al (2018) Multi-objective optimization algorithm coupled to energy-plan software: the EPLANOPT model. *Energy* 149:213–221. <https://doi.org/10.1016/j.energy.2018.02.050>
20. Plis M, Rusinowski H (2018) A mathematical model of an existing gas-steam combined heat and power plant for thermal diagnostic systems. *Energy* 156:606–619. <https://doi.org/10.1016/j.energy.2018.05.113>
21. Summary Catalog 01-04 (2005) Energeticheskoye oborudovaniye dlya vyrabotki i transportirovki energonositeley i energosberezheniye (Energy equipment for the production and transportation of energy carriers and energy saving). Institut promyshlennykh katalogov “Inpromkatalog”, Moscow

Slag Cut-off During Steel Casting



Yu. I. Eremenko and D. A. Poleshchenko

Abstract In this paper, the results of the ladle–tundish system were studied for the timely slag cut-off during steel casting. Accelerometers were installed to provide the access of the protective tube to the manipulator of the steel ladle and the body of the tundish. The search for regularities of the vibration acceleration signal was carried out in order to determine the state, which precedes the beginning of the slag flow from the steel ladle to the tundish. The filtering methods (Chebyshev filter), spectral, and wavelet analysis were applied for the signal processing. This fact can be seen in the Fourier and wavelet spectra of transformations at certain frequencies. The signal itself is quite noisy with the vibrations of the workshop; it is not possible to analyze the signal only using the amplitude. In this paper, a basic algorithm for the diagnostics of the beginning of the slag flow has been developed focusing on the effect of the vibration level reduction in the spectra of the vibration acceleration signal. To implement the algorithm, a Fourier transformation was performed for the signal from the manipulator of the protective tube, and the wavelet transformation was carried out for the signal from the surface of the tundish, and then the signal was integrated in the frequencies defined by the study and the moving average filter was applied.

Keywords Steel casting ladle · Accelerometer · Spectral analysis · Wavelet analysis · Slag · Tundish

1 Introduction

There are two tasks that ensure the casting quality in the system of the casting ladle–tundish in terms of automation. The first is the task of steel level maintaining at a certain value in the tundish by throttling the gate of the casting ladle [1]. The second is to control the moment of steel bucket gate closing for the purpose of slag cutting.

Yu. I. Eremenko (✉) · D. A. Poleshchenko
Sary Oskol Technological Institute n.a. A.A. Ugarov (Branch) National University
of Science and Technology “MISiS”, 42, Makarenko Str., Sary Oskol 309516, Russia
e-mail: Erem49@mail.ru

In this paper, they develop the method for the second problem solution. When liquid metal is poured from a steel ladle, an important process that affects steel quality is to prevent the entering of slag into the tundish.

When slag gets into the tundish, the upper “crust” of the slag is broken, which protects the metal from oxidation and cooling. There is also the possibility of slag falling into the cast billet, which can lead to the finished product rejection [2].

Today, slag cut-off control is carried out manually at most metallurgical enterprises of Russia. In this case, an operator cuts off the slag when a characteristic luminescence occurs that accompanies the rupture of the tundish protective slag crust [3]. The negative aspect of this approach is that a certain amount of slag is entered the tundish. The gravimetric method is used for more important steel grades, which leads to excessive metal losses. In most cases, it is too much in advance, since if errors in measurements and calculations are only 0.5%, and ladle volume is 150 tons, amount of pure metal losses (not teemed from the ladle) will be approximately 750 kg. If annual production volume is three million tons, then the metal losses will be 14 thousand tons of pure metal. Thus, the problem solved in the work is quite relevant in view of the substantial losses incurred by steel mills during steel casting at this technological redistribution.

One of the important operational stages of the electric arc steelmaking is the process of metal casting using continuous casting machines. The quality of this process ensures the process of metal casting from the steel ladle into the tundish. The quality of the cast billet and, subsequently, the quality of the finished product depend on this operation.

When the casting has finished, a funnel forms in the steel ladle pulling the slag [4–6] and slag enters the tundish. To ensure that the slag does not get into the tundish, it is necessary to close the steel slide gate in a timely manner [7].

The entry of slag into the tundish results in the destruction of the protective slag crust of the tundish, which leads to cooling and oxidation of steel. In addition, the penetration of slag can disrupt the laminar flow of the metal flow into the crystallizer [8, 9] that would lead to the entry of the non-metallic inclusions into the cast billet [10, 11].

The main problem in this process is the lack of an exact method, which would be capable to determine when the slag began flowing in order to close the slide gate in a timely manner. Today, the operator visually determines penetration of slag to the surface, being guided by the light difference between metal and slag. However, this method of control causes a certain mass of slag penetrates into the tundish [12].

If to talk about the automatic cut-off of slag, there are approaches such as infrared [13, 14], inductive [15], gravimetric [16], and vibrational [17, 18].

Each of them has own advantages and disadvantages. According to our opinion, the most promising is the vibrational method [19–23], which is capable to provide the required accuracy of the determination of the moment of the slag flow and requires the least costs for the implementation and subsequent operation.

These findings are confirmed and performed in the work [16] studies where in the simulation, the water is in the process of casting along with the vibration, they analyzed the effectiveness of these methods as a weighting method, based on infrared radiation, electromagnetic, and on the basis of the supersonic reflection.

In [20], the authors installed three-axis accelerometers on the arm of the protective tube and the surface of the intermediate bucket. The readings of both sensors were similar, including different axes. Operator began to decline in the measured value of acceleration on the pipe manipulator on the wall of the tundish five seconds before the closing of the gate valve of the ladle with steel. In this paper, only the amplitude of the vibration signal was analyzed, which in the conditions of the real shop is clearly not enough because of the interference, the strongest of which are the movements of the slide gate to control the flow of steel.

In [24], the authors propose to analyze the power spectral density and the discrete wavelet decomposition of the manipulator vibration acceleration signal in the protective tube. They highlight the most informative ranges in the frequency domain and the ranges of wavelet transformation coefficients. They note that the results of both approaches correlate with each other and this is the indicator of effectiveness. However, the authors judge the result not by a series, but by one experiment. The fact is that the signal spectra, as experience shows [25, 26], may differ significantly from melting to melting even for one steel grade with the same casting speeds. This leads to the fact that the areas informative for one melting are useless for another.

By now, many researchers are solving considered problem by joint usage of spectral and wavelet analysis methods with the neural network technologies. Neural networks are able to identify flexible functions and find with their help hidden interdependencies between technological parameters. This is shown in a number of research works [27–30].

The foregoing analysis suggests the need for more complicated processing of information, since in such a nonstationary process, there is probably a cross interference of one parameter to another, which makes information in the spectrum significantly nonlinear and uncertain. Therefore, spectral or wavelet analysis should be used for preliminary information processing, namely, the signal conversion from the time domain into the frequency one. Only after that an attempt to describe the assumed hidden dependencies of process parameters with the function should be made.

An objective of this work was to study the vibration acceleration signal of the manipulator of the protective tube and tundish in order to determine the regularities in the spectrum of the signal characterizing the beginning of the slag flow, and development of an algorithm for the identification of this state.

Here introduce the paper. The paragraphs continue from here and are only separated by headings, subheadings, images, and formulae. The first paragraph after a heading is not indented.

2 Methodology

The accelerometers were installed on the surface of the intermediate ladle and manipulator of the protective tube to obtain the experimental data in real production conditions. They are indicated as ZE in the scheme of the installation presented in Fig. 1.

ADC and a laptop with the software NI LabVIEW 2013 was set near the steel teeming operator panel. This software was used to record and store data.

During the measurements, a short-term penetration of slag in the tundish was intentionally allowed, while the operator reported the moment of slag flow that was recorded in the data collection system.

Within the framework of these measurements, four experiments were conducted to determine the general behavior of an object operating under different casting speeds and under the conditions of the interference in real production. One experiment corresponded to one casting of metal from a ladle.

During research of an experiment for the vibration acceleration signals from the manipulator of the protective tube of the ladle and the surface of the tundish, the following types of analysis were carried out: an amplitude–time analysis of the signals, spectral Fourier analysis in the frequency range 0.5–15 kHz with the separation of individual harmonics and spectral subbands, wavelet analysis for Daubechies wavelet functions of 2–14 orders, Haar wavelet, biorthogonal wavelet, and wavelet of the simplest. A detailed description of all the experiments is not

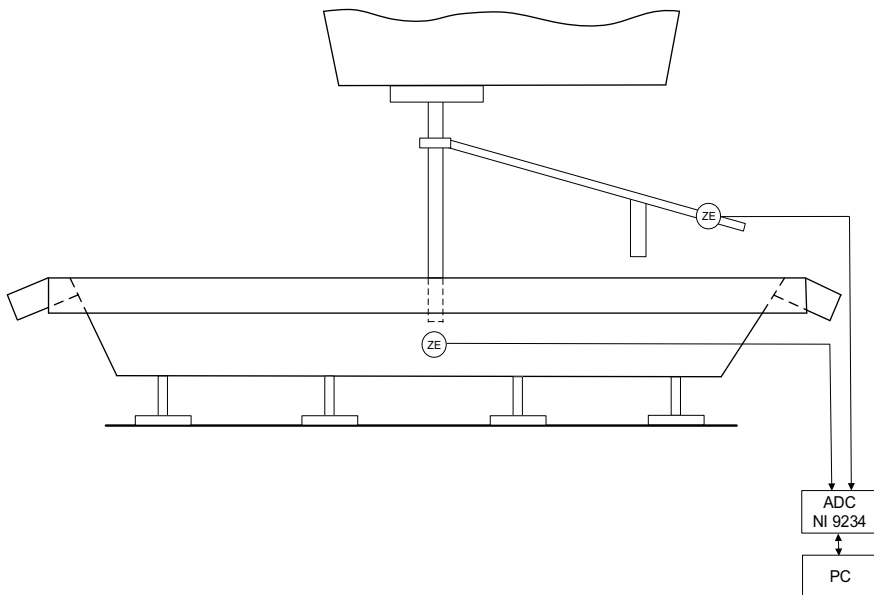


Fig. 1 Scheme of the unit for the experiments

provided in this paper; only the results of the most informative frequency bands for the first casting revealed during research are demonstrated. For the other three casting operations, the results correlate with the results of the first casting.

3 Results and Discussion

Initially, the vibration acceleration signal from the tundish and the manipulator of the protective pipe were filtered by a Chebyshev filter in different frequency bands. In Fig. 2, strong amplitude spikes are visible since 94 beat, which are associated with vibration of the gate valve of the ladle with steel, with the cut-off slag. The abrupt change in amplitude to 94 bars is also associated with the movement of the gate to control the level of steel in the intermediate bucket.

Only in some experiments, there was a slight decrease in the overall level of vibration relative to the previous values of the signal, signaling the beginning of the formation of the funnel. Thereby, it was concluded that under interference conditions a purely amplitude analysis of the vibration acceleration signal is not perspective.

Subsequently, the original signal from the manipulator was processed; it was transformed with Fourier transform:

$$X_i(f_k) = \Delta t \sum_{n=1}^{N-1} x_{in} \cdot e^{-j2\pi k n / N}$$

where $X_i(f_k)$ —is a discrete Fourier image of the vibration acceleration signal (amplitude of the spectrum harmonics),

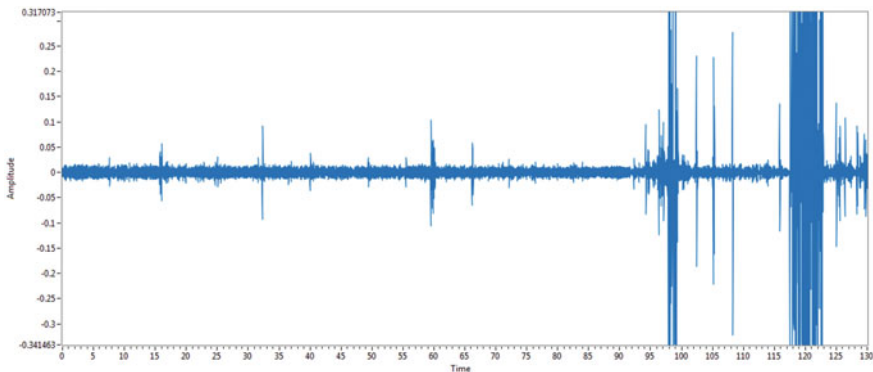


Fig. 2 Signal from the manipulator ladle with steel, filtered Chebyshev



X_{in} —value of the measured signal,
 $n = 0, 1, K, N - 1$ —is the number of points in the time series,
 N —is the number of time series values.

Afterward, the spectrum was integrated in the frequency range 0–15,000 Hz, and then a moving average filter for three values was applied. As a result, the curves for the frequency ranges of the vibration acceleration signal were plotted, which the best way to track the flow time of the slag, Fig. 3. The message that the slag began flowing was received from the operator at 94-th cycle relative to the origin, which was indicated by a vertical green line.

On the basis of the analysis of graphs, it is possible to conclude that in general, before the moment of the slag flow, the vibration level decreases. The greatest difference among the states shown in Fig. 3 is in the minimum value of the signal 30 s before the slag flow and the minimum value of the signal in the vicinity of the point, when it is advised to carry out the slag cut-off; it is observed in the range 1–5 kHz, Graph 1, points (81; 0.07431) and (87; 0.0701).

Experiments with spectral analysis of the signal from tundish did not allow determination of the informative component. As a result, an attempt was made to investigate the signal using the wavelet analysis. Thereby, a number of frequencies were found, and the processing of them has given a stable result.

The signal of vibration acceleration from tundish was subjected to the following processing: it was transformed by the wavelet transformation, i.e. the function of the second order, and then the wavelet spectrum was integrated in different frequency bands with the choice of the best: 26–38 Hz and 300–450 Hz. Then a

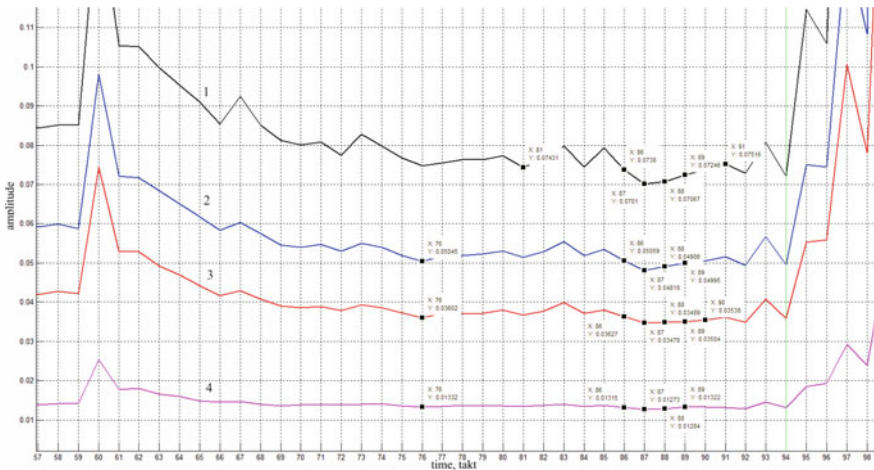


Fig. 3 Graphs of the vibration acceleration signal for the frequencies: (1) black—1–5 kHz; (2) blue—2–5 kHz; (3) red—3–5 kHz; (4) pink—4–5 kHz



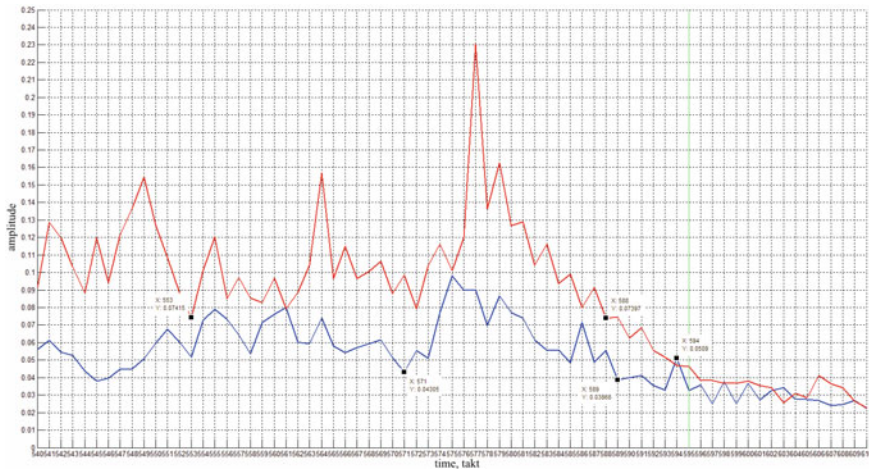


Fig. 4 Graph of the vibration acceleration signal for the wavelet frequencies: (1) blue—26–38 Hz, (2) red—300–450 Hz

moving average filter for the three values was applied to the obtained curves. As a result, the obtained graphs were shown in Fig. 4. The message that the slag began to flow was received from the operator at 595-th cycle relative to the origin.

It is seen from Fig. 4 that the tendency in level reduction of the analyzed signal before the moment of the slag flow has remained.

On the basis of the obtained results, the algorithm was proposed for determination of the moment preceding the slag flow in order to implement the slag cut-off by the glide gate. After achievement of a certain threshold value of metal in ladle, it is needed to launch the algorithm for analysis of the vibration acceleration signal for the time-adjusted width of the signal analysis (40–50 iterations, that correspond to 23–29 s) that to fix the minimum value in amplitude and continuously monitor the signal comparing its current value with the minimum value. In the case of a certain number of iterations (3–1.7 s) with amplitude less than the fixed minimum value of the signal (thereby, the monotonic decrease in the level of vibration is taken into account), the slag cut-off should be performed.

Otherwise, it is required to move the analysis time frame by three iterations ahead and redefine the fixed minimum signal value.

According to the algorithm, the slag cut-off would occur at the following moments: for frequencies 26–38 Hz, 592-nd cycle and for frequencies 300–450 Hz, 591-st cycle.



4 Conclusions

In the results of the experiments, it was found that the slag flow is preceded by decrease in the amplitude of vibration of the manipulator of steel ladle and tundish in certain frequency ranges, which is connected with the formation of a funnel.

The frequency ranges defined by the signal analysis are distinctive for each of the four experiments; that enables to talk about the possibility of generalization of the results and development of the method for determination of the moment of the slag cut-off for different conditions.

References

1. Zhang R, Zhang JY (2004) Physical simulation of level fluctuations in tundish. *J Chin Rare Earth Soc* 22(z1):273–277
2. Ho YH, Chen CH, Hwang WS (2001) Three-dimensional analysis of molten steel flow in slab continuous casting mould with rotated ports in submerged entry nozzle. *Ironmaking Steelmaking* 28(3):258–265
3. Trotter DJ, Duncan G, Camplin JM (1991) Development of a ladle/tundish slag detector. *Iron Steelmaking* 18(10):57–60
4. Morales RD, Dávila-Maldonado O, Calderón I, Morales-Higa K (2013) Physical and mathematical models of vortex flows during the last stages of steel draining operations from a ladle. *ISIJ Int* 53(5):782–791
5. Sankaranarayanan R, Guthrie RIL (2002) Slag entraining vortexing funnel formation during ladle teeming: similarity criteria and scale-up relationships. *Ironmaking Steelmaking* 29(2): 147–153
6. Singh Pavan K (2004) Scale model experiments and numerical study on a steel teeming process. University of Kentucky Master's Theses, 317 pp
7. Koffron RJ (1989) Vortex inhibitor for molten metal discharge. US patent 4871148 A, 09.08.1988
8. Sinha SK, Godiwalla KM, Shaw DK (2001) Fluid flow behaviour in a water model tundish under open, submerged and modified inlet conditions. *Scand J Metall* 30(2):103–107
9. Solorio-Diaz G, Ramos-banderas A, Barreto JJ (2007) Fluid dynamics of vortex formation in tundish operations: Physical modeling. *Steel Res Int* 78(3):248–253
10. Tan DP, Univ ZJ, Zhou H, Li PY, Xu L, Yao GC (2006) Steel water continuous casting slag detection system based on VQ. *Syst Man Cybern* 10:1315–1319
11. Yokoya S, Jönsson PG, Sasaki K (2004) The effect of swirl flow in an immersion nozzle on the heat and fluid flow in a billet continuous casting mold *Scand. J Metall* 33(1):22–28
12. Zhi JJ, Qiu SM, Hou AG (2004) Application of the ladle slag-carry-over detection technology in baosteel. *Bao Steel Technology*, 5 pp
13. Sakashita T, Yamazaki I (1980) Molten steel outflow automatically controlling device. US patent 4,222,506, Sep 1980
14. Kemeny FL, Walker DI (2005) System and method for minimizing slag carryover during the production of steel. US patent 6,929,773, Jul 2005
15. Jalk M, Ohlsson W, Kelvesjö H (2006) Method and a device for detecting slag. US patent 20060219052 A1, Oct 2006
16. Tan DP, Ji SM, Li PY, Pan XH (2010) Development of vibration style ladle slag detection methods and the key technologies. *Sci China Technol Sci* 53(9):2378–2387

17. Davidkhanian A, Kemeny FL, Langari A, Walker DI (2004) Slag detector for molten steel transfer operations. US Patent 6,737,014 May 2004
18. Tan DP, LI PY, Pan XH (2009) Application of improved HMM algorithm in slag detection system. *J Iron Steel Res* 1:1–6
19. Eremenko YI, Poleshchenko DA, Tsygankov YuA, Kovriznich YuA (2017) Determination of slag outflow moment during steel teeming using competitive neural network. *SIBCON*. <https://doi.org/10.1109/sibcon.2017.7998588>
20. Semenov MV, Krasilnikov SS, Shvidchenko DV, Pishnograev RS (2015) Vibratory detection of slag during refluxing steel from ladle to tundish. *Autom Technol Prod* 2:40–42
21. Chen D, Xiao H, Ji Q (2014) Vibration style ladle slag detection method based on discrete wavelet decomposition. In: *Proceedings of IEEE 26th Chinese Control and Decision Conference*, pp 3019–3022. <https://doi.org/10.1109/ccdc.2014.6852692>
22. Uhlenbusch J, Stajduhar MC, Krajcik WJ et al (2003) Trial of the R.A.D.A.R. [trademark] vibra-acoustic ladle slag detection system at a European steel plant. *Iron Steelmaking* 30(7): 19–21
23. Tan Da-Peng, Li Pei-Yu, Ji Yi-Xuan, Wen Dong-Hui, Li Chen (2013) SA-ANN-based slag carry-over detection method and the embedded WME platform. *IEEE Trans Industr Electron* 60(10):4702–4713
24. Chen D, Xiao H, Ji Q (2014) Vibration style ladle slag detection method based on discrete wavelet decomposition. In: *26th Chinese Control and Decision Conference*, pp 3019–3022. <https://doi.org/10.1109/CCDC.2014.6852692>
25. Kovrizhnykh YuA, Poleshchenko DA (2017) Slag control system development for the pouring of steel from a steel ladle into a tundish. *Abstracts of the International Scientific and Technical Conference “Metal-2017”*, pp 12–14
26. Eremenko YI, Poleshchenko DA, Glushchenko AI, Tsygankov YA, Kovriznich YA (2017) ART-2 neural network usage to determine moment of slag discharge during steel teeming process. In: *Proceedings of 2017 XX IEEE International Conference on Soft Computing And Measurements*, pp 547–550. <https://doi.org/10.1109/scm.2017.7970646>
27. Patel M, Lal SKL, Kavanagh D, Rossiter P (2011) Applying neural network analysis on heart rate variability data to assess driver fatigue. *Expert Syst Appl* 38:7235–7242
28. Tibau E, Valencia M, Soriano J (2013) Identification of neuronal network properties from the spectral analysis of calcium imaging signals in neuronal cultures. *Front Neural Circuits* 7: Article 199
29. Sao P, Hegadi R, Karmakar S (2015) ECG signal analysis using artificial neural network. In: *International Journal of Science and Research, National Conference on Knowledge, Innovation in Technology and Engineering*, pp 82–86
30. Bhattacharya A, Chakraborty C (2011) A shunt active power filter with enhanced performance using ANN-based predictive and adaptive controllers. *IEEE Trans Industr Electron* 58(2):421–428

Arresting Longitudinal Cracks in Steel Pipelines: Computational Analysis Technique



Baraa M. H. Albaghdadi and A. O. Cherniavsky

Abstract This research aims to study the arrest of crack propagation in oil or gas steel pipelines by using circumferential ribs as arresters. The use of ribs is much cheaper than high-grade steel with high fracture toughness. It has been shown that two ribs per pipe could prevent the most dangerous type of the pipeline fracture, which is a large length longitudinal crack. In this paper, two types of simplified estimations were used: the first is by calculations of stress intensity factors (K_I) and the second is by analysis of perfectly viscous (plastic) fracture. Both estimations were done on a pipe with plane wall and a pipe with ribs. The results showed that the sizes of ribs that can be technologically obtained increase the resistance of pipes to cracking by 30–50% and could be useful in preventing longitudinal crack propagation. Experimental verification of the results obtained on small-scale models has shown that there are some difficulties that can make direct transfer of results from small-scale model to full-scale structure impossible, and these difficulties are also discussed in this paper.

Keywords Pipeline • Crack arrest • Long crack • FEM • Modeling

1 Introduction

Natural gas and petroleum transmission pipeline systems are one of the most important types of infrastructure. One of the challenges facing the oil and gas industry is assuring more reliable and fail-safe operation of the infrastructure for oil and gas production and transportation [1]. The most severe accidents on trunk

B. M. H. Albaghdadi (✉)

University of Technology, Al-Sinaa' Street, Baghdad 10066, Iraq
e-mail: baraa.albaghdadi@gmail.com

A. O. Cherniavsky

South Ural State University, 76, Lenin Ave, Chelyabinsk 454080, Russia

© Springer Nature Switzerland AG 2020

A. A. Radionov et al. (eds.), *Proceedings of the 5th International Conference on Industrial Engineering (ICIE 2019)*, Lecture Notes in Mechanical Engineering,

https://doi.org/10.1007/978-3-030-22041-9_105

993

pipelines are caused by the appearance of long cracks, which lead to large volumes of oil leakage or large-scale fires. There have been a number of catastrophic instances where cracks have propagated in a rapid manner over a few kilometers in steel gas transmission pipelines.

To prevent such accidents, the steel used for trunk pipelines must meet strength and fracture resistance requirements [2, 3], which impose appropriate restrictions on pipe production technology (see for example, [4, 5]). At the same time, taking into account, the length of main pipelines, the cost of pipes, and economic efficiency of crack preventing solutions become paramount.

Pipe fracture is a complex multi-factor process. When describing it, one should take into account the gradual accumulation of defects of various shapes (relatively “smooth” corrosion defects, crack-like defects including stress-induced corrosion cracking, etc.), changes in material properties due to aging, low climatic temperatures, etc. [6, 7]. This article is devoted only to one aspect of the problem—the rapid propagation of long cracks; the issues of gradual changes in properties, and accumulation of damages are not considered here.

The ability of pipes to resist the rapid propagation of cracks of considerable length is verified experimentally and by calculation. For example, experimental checks are carried out in accordance with the Russian standard [8]. Furthermore, a number of studies have been also devoted to computational examination of this problem.

Computational modeling shows that there are some restrictions on the plasticity and fracture toughness of the material, ensuring the absence of extended cracks [9]. However, it is difficult to meet such requirements with modern high-strength pipe steels, since an increase in strength is often accompanied by a decrease in plastic properties. That is why long crack prevention is still relevant, despite notable efforts and successes in creating viscous pipe steels.

Another method that can be used together with the improvement of material properties is using special devices designed to arrest (stop) the crack and limit its length. For example, O’Donoghue and Zhuang [10] discuss the usage of steel rings as crack arrestor devices to prevent the possibility of long-running axial cracks in steel gas transmission pipelines.

The use of such “crack arrestors” requires additional devices and complicates pipeline construction. At the same time, there is a cheap technology [11] that allows for the creation of ribs—ring thickenings of the pipe walls (Fig. 1). Ribs are created from the pipe material as a result of small shortening of the pipe at cyclic thermal loading. Existing standards demand a crack stop within the length of one pipe, so the number of ribs on one pipe can be limited to two. The cost of creating such ribs is small compared to the cost of improving the properties of the pipe metal by alloying. Since the ribs are made as one piece with the pipe, they do not complicate the construction of the pipeline. This article is devoted to a computational study of the effectiveness of such ribs, i.e. determination of their influence on the propagation of long cracks.

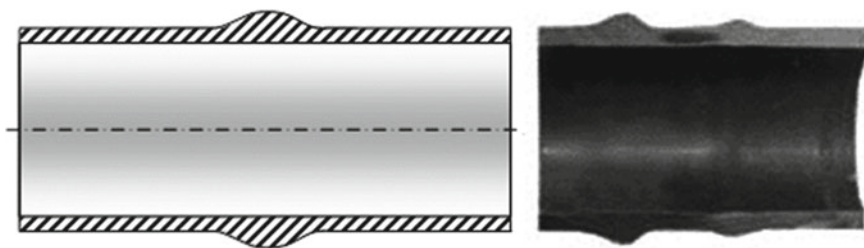


Fig. 1 Pipe with ribs

2 Existing Methods of Crack Parameters Estimation

A large number of papers are devoted to the technology of calculating the parameters responsible for crack growth [12–14]. The main tool for solving this problem is linear and/or nonlinear fracture mechanics, which uses a number of different criteria: stress intensity factor K_I , J-integral, CTOD, CTOA, Charpi test, and DWTT. The presence of a number of approaches (instead of a universal one) is caused by different specific features of the problem that have varying importance in different situations.

First, long cracks in structures where the nominal stresses are elastic (often not greater than 0.7–0.75% of yield strength), should be described by the linear fracture mechanics and K_{IC} . Second, the usage of ductile steels requires accounting for the role of nonlinearity—CTOD criteria, CTOA [15], J-integral, or even just a resource of plasticity accounting for the stress state type near the crack tip [16, 17]. Third, the desire to use thick-walled pipes of high-strength materials, as well as low-temperature conditions in northern Russia [18] or Alaska [19], again “shift” the situation in the direction of brittle fracture and force the use of DWTT [20]. There are various options for 2-parametric criteria, which take influence of the plasticity on the crack resistance into account, i.e. limit fracture toughness, KQ, and R-curve [21, 22].

Moreover, description of the dynamic propagation of long cracks requires knowledge of the material properties depending on the strain rate, accounting for inertia forces, and a possible change of loads during the crack growth due to leakage and pressure drop near the crack. The main tool for numerical modeling here is the finite element method.

There are a number of options to describe the crack growth: by removing the finite elements, by breaking the bonds using special “cohesive” elements, and/or special elements with exact description of the stress field near the crack tip (one of the first papers of this kind was that of Nicolas et al. [23], while Song et al. [24] compared the methods). For example, dynamic analysis relating to rapid crack propagation (RCP) and arrest in gas pipelines was made by Zhuang and O’Donoghue [25], basing on a fluid/structure/fracture interaction package, PFRAC, to simulate the behavior of the fractured pipes. Dynamic crack growth has been

studied by Ortiz and Pandolfi [26], who have developed a three-dimensional finite-deformation cohesive element and a class of irreversible cohesive laws to enable the accurate and efficient tracking of growing cracks.

There are also combined experimental–numerical methods. These methods have been proposed by Kryzhaniv’skyi et al. [27], for the estimation of the conditions of gas pipelines fracture. This study experimentally demonstrated the efficiency of the numerical–analytic approach for evaluating the kinetics and changes in the shapes of corrosion fatigue defects throughout their propagation along the pipeline wall. They determined the conditions under which catastrophic failures of pipes become possible after long operation.

3 Simplified Estimations of the Rib Effectiveness

Accurate modeling of the mixed-mode (brittle and ductile) dynamical fracture is a complex task. As a first step, a two-sided estimation could possibly be useful. The first assumes the pipe material to be brittle (some small plasticity can be considered by using K_{IQ} instead of K_{IC}). The second assumes the material to be perfectly plastic (the criteria is a plastic strain without account for K_I , CTOD).

The stress intensity factor K_I for pipes with and without ribs was calculated using ANSYS finite element code with special elements near the crack tip accounting for the stress singularity, Fig. 2a. In this stage, the calculations were done in quasi-static formulation.

Examples of the results are shown on Fig. 2b. For the pipe without ribs, the stress intensity factor K_I increases with the crack length up to 10–15 of the pipe diameter. Presence of the rib notably decreases the stress intensity factor for long cracks. Bending stiffness of the rib is not as high as tensile stiffness, so after the rib

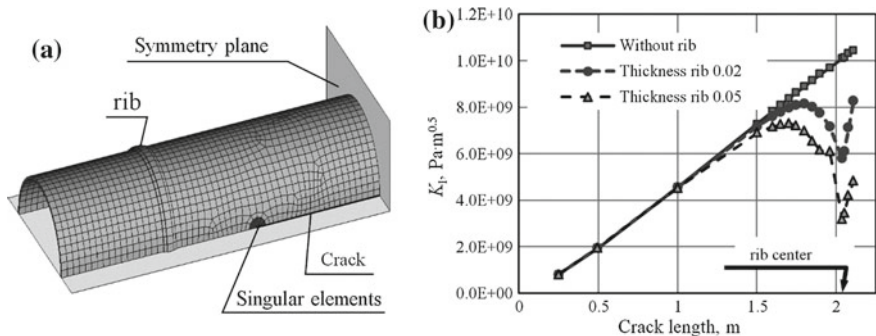


Fig. 2 **a** Numerical model (finite elements enlarged for clarity); **b** stress intensity factor vs. crack length for pipes with and without ribs (pipe of diameter 0.5 m with wall thickness of 0.01 m loaded by 5 MPa internal pressure)



is cut by a crack, the stress intensity factor rises again (right part of curves on Fig. 2b), but a decrease of the minimal stress intensity factor allows for possible crack arrest.

A 30% or even 50% decrease in the stress intensity factor seems very promising. But the calculated level of the stress intensity factor for long cracks significantly exceeds the fracture toughness of pipeline steel. At the same time, cracks in pipeline are usually stopped after they have reached some length. It means that the linear scheme of the task is not correct and more precise calculations are required.

4 Plasticity, Dynamics, and Related Difficulties

To make the previous solution more accurate, the next features of the problem must be considered: plasticity of the pipe material, inertial forces in case of fast crack propagation, change of internal pressure due to leakage through the crack, different velocities of the crack, stress waves in the pipe wall, and pressure waves in internal gas or liquid. LS-DYNA finite element code seems to be a suitable instrument, as LS-DYNA can take all of these features into account. However, LS-DYNA (unlike, for example, ANSYS) cannot directly calculate fracture mechanics criteria—stress intensity factor, J-integral, or crack tip opening displacements CTOD (crack tip opening angle CTOA). LS-DYNA has a set of pre-defined fracture criteria based on stresses or strains in a finite element, so suitable criteria must be chosen and calibrated.

Fracture parameters of the LS-DYNA finite element model were calibrated using comparison of the crack length and the pressure corresponding to the crack start, calculated by LS-DYNA and by $K_I = K_{IQ}$ condition (the stress intensity factor K_I was calculated using ANSYS). The formulation of the task was quasi-static. As a methodical example, a typical steel for pipelines in Russia 17GS was considered (chemical composition 0.14–0.2% C; 0.4–0.6% Si; and 1–1.4% Mn, yield strength $\sigma_{0.2} = 345$ MPa, tensile strength $\sigma_u = 510$ MPa, transverse strain in necking at fracture $\psi = 60\%$). The “true stress σ —logarithmic plastic strain ε_p ” diagram of the steel under consideration was described by the Ramberg–Osgood relationship $\sigma = A\varepsilon_p^n$ with $A = 753$ MPa, $n = 0.126$ [28]. Experiments on samples after a certain operating time [29] show fracture toughness $K_{IQ} = 130$ MPa m^{0.5}, which can describe the fracture at nominal stress level up to $0.7\sigma_{0.2}$.

Calculations were done for nominal stresses $0.36\sigma_{0.2}$, $0.58\sigma_{0.2}$, $0.70\sigma_{0.2}$, and $0.87\sigma_{0.2}$ (the last is obviously incorrect and was used for comparison only). For the selected pipe model of 500 mm diameter and 10 mm wall thickness, it corresponds to pressures 2.5, 4, 5, and 6 MPa while the crack half-length, providing the $K_I = K_{IQ}$, are equal, respectively, to 100, 65, 50, and 40 mm.

Correct fracture modeling must be independent from finite element size. Without special measures, the results are very sensitive to the element size because of large strain gradients near the crack tip. LS-DYNA offers two methods to eliminate the results’ dependencies on finite element size: (1) regularization, i.e. element-size-dependent factor for equivalent plastic strain to failure; and (2) non-local material,

where the failure criterion depends on the state of the material within a radius of influence surrounding the integration point:

$$\bar{d} = \frac{1}{V} \int_V d(\mathbf{r})w(\mathbf{r} - \mathbf{r}_0)dV \approx \frac{\sum d_i w(\mathbf{r}_i - \mathbf{r}_0)V_i}{\sum V_i}, \tag{1}$$

$$w(\mathbf{r}_i - \mathbf{r}_0) = \left[1 + \left(\frac{\|\mathbf{r}_i - \mathbf{r}_0\|}{L} \right)^p \right]^{-q}$$

Here, d is “damage” (fracture parameter—for this task this is plastic strain intensity); \mathbf{r} is the position vector of an arbitrary point in volume V ; \mathbf{r}_0 is the position of the analyzed point; i is the finite element number; and $L, p,$ and q are the parameters. These parameters were found by minimization of the relative variation.

$$\delta = \frac{\max_{m,n}(\varepsilon^*(p, q, L)) - \min_{m,n}(\varepsilon^*(p, q, L))}{\min_{m,n}(\varepsilon^*(p, q, L))} \rightarrow \min \tag{2}$$

Here, ε^* is the plastic strain intensity, calculated using (1) with defined $p, q,$ and L at a pressure for which the ANSYS predicts $K_I = K_{IQ}$ and m and n correspond to a set of crack length and a set of characteristic finite element size. Solution of task (2) is ill-conditioned (Fig. 3a), nevertheless it is possible to find the values of $p, q,$ and L which provide independence of ε^* on the element size (Fig. 3b). There is still some dependence of the results on the crack length l , but this dependence is weak enough in the case of long cracks, so this approach can be used for analysis of the task under consideration—prevention of catastrophic fracture.

The next problem is the fracture mode. If the fracture criteria are maximum plastic strain intensity, then direction of crack growth corresponds to “direction 1”

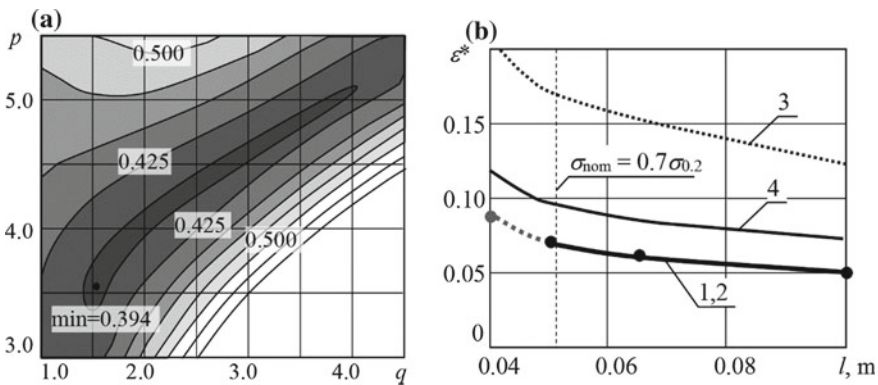


Fig. 3 a Dependence of the variation δ (Eq. 2) on p and q at $L = 2.1$ mm; b value of ε^* (see Eq. 2) for different crack length l and different element size: 1, 2—finite element size 1 and 2 mm with account of Eq. (1); 3, 4—the same without account of (1)

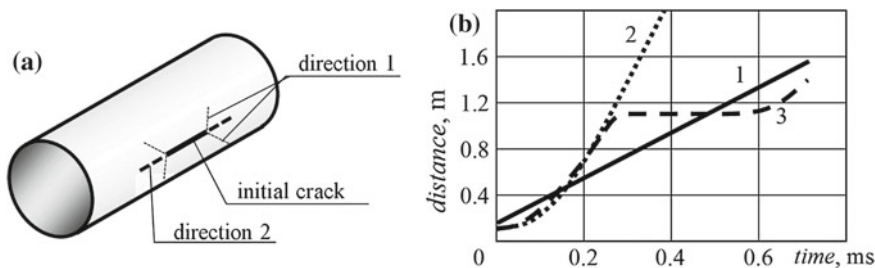


Fig. 4 **a** Fracture mode; **b** propagation of cracks and a decompression wave: 1 decompression wave, 2 crack in a plain pipe (without ribs), 3 crack in a pipe with ribs and auspicious residual stresses

on Fig. 4a, while the typical fracture mode for pipeline is “direction 2.” Criteria based on the stress intensity factor or J-integral predict “direction 2,” but such criteria cannot be used in LS-DYNA directly. To obtain the correct fracture mode for long cracks, an artificial technique could be used: analyzing the fracture criteria only in those finite elements that are placed on a continuation of the initial crack.

The next factor is accounting for leakage through the opening crack and consequent pressure drop. This was determined by use of the fluid–structure interaction (FSI) approach. The pipe was modeled by Lagrangian shell elements, while the filling fluid (oil) and surrounding air were modeled using Eulerian solid elements. Lagrangian and Eulerian meshes were coupled using a standard LS-DYNA “constrained Lagrange in solid” method. This model is not perfectly correct because it does not take into consideration the roughness of the crack faces that can influence the leakage speed, but for a crack opening that is big enough this factor is not very important.

Calculations show that the speed of the decompression wave in oil is less than the crack speed in a plane pipe (without ribs)—Fig. 4b. It means that the crack will outrun the decompression wave and continue to propagate just like under constant pressure. Ribs provide some “delay” in crack propagation. Moreover, the rib formation technique described by Gohfeld et al. [11] produces not only a rib of increased thickness, but also residual stresses near the rib. If these residual stresses are auspicious (compressive near the rib and tensile inside the thick part of the rib), then this delay can be enlarged. In this case, the decompression wave can outrun the crack. The pressure near the crack will decrease and the crack will possibly stop. Whether the crack stops or not depends on the material fracture toughness, but the necessary toughness of a pipe with ribs is distinctly less than that of a plain pipe. Thus, ribs could be useful to stop long cracks in pipelines.

In case the pipe is filled with gas, the decompression influence on the crack growth condition is small due to the low speed of the decompression wave (the crack delay near the rib becomes insufficient for decompression and unloading), unlike an oil-filled pipeline.

Calculations reveal a difficulty in possible experimental verification: using a small-scale model instead of full-scale main pipes at the same material properties



requires a different relationship between pipe diameter and crack length, which leads to a different relationship between tensile and bending stresses near the crack tip. Proportional size change is not sufficient for the similarity of the model to the real structure if material properties are unchanged, and experimental simulation will be insufficient without numerical simulation and interpretation.

5 Conclusion

The proposed ribs could be an inexpensive way to prevent catastrophic fracture of pipelines from long cracks even in case of using steel with relatively low fracture toughness. Simplified numerical estimations demonstrate the potential utility of ribs. A more detailed research shows that ribs could be potentially useful to prevent long cracks in oil pipelines, while for gas pipelines ribs are less effective.

There are some additional factors that can help to improve the rib effectiveness:

- The formation of favorable residual stresses near the rib that can occur during rib production (compressive circumferential stresses to arrest a crack);
- The possibility of increasing the plasticity of the rib material. Due to the greater thickness of the rib it is not necessary to have the same material strength as the rest of the pipe. The material could be tempered with a corresponding increase in plasticity and fracture toughness.

These methods also must be carefully examined.

Experimental verification is complicated due to a highly nonlinear character of the task and, consequently, the absence of “scaling criteria” for small-scale tests.

References

1. Makhutov NA (ed) (2000) Safety of Russia. Legal, social-economic, and scientific-technical aspects (energy safety). Znanie Publ., Moscow
2. Rivalin F, Besson J, Pineau A, Di Fant M (2001) Ductile tearing of pipeline-steel wide plates II. Modeling of in-plane crack propagation. *Eng Fract Mech* 68(3):347–364
3. Hari Manoj Simha C (2016) A model for arrest of rapid cracks in gas-pressurized ductile steel line pipe. *Eng Fract Mech* 154:245–261
4. Shabalov IP, Solov'ev DM, Filippov GA, Livanova OV (2015) Mechanical properties of a pipe workpiece at the stages of JCOE pipe forming. *Russ Metall (Metally)* 2015(4):309–316
5. Makino H, Kubo T, Shiwaku T, Endo S, Inoue T et al (2001) Prediction for crack propagation and arrest of shear fracture in ultra-high pressure natural gas pipelines. *ISIJ Int* 41(4):381–388
6. Kucheryavyi VI, Mil'kov SN (2014) Statistical modeling of the residual life of an oil and gas pipeline with axial crack-like defects. *J Mach Manuf Reliab* 43(1):82–87
7. Matvienko Yu G (2011) A damage evolution approach in fracture mechanics of pipelines. In: Integrity of pipelines transporting hydrocarbons: corrosion, mechanisms, control, and management. Springer Science+Business Media, pp 227–244. https://doi.org/10.1007/978-94-007-0588-3_15

8. Company standard 01297858 0.0024.0-2007 (2007) Full-scale testing of notched pipes aimed to determine the static crack resistance characteristics of metal (fracture toughness) in a pipe structure. Program and methodology of testing. M: VNIIST (Russian research institute for pipeline construction), p 22
9. Makarov GI (2013) Requirements for the fracture toughness of metal pipes in trunk gas pipelines that ensure its continuous operation without fractures. *Pipeline Transp Theory Pract* 5(39):12–17
10. O'Donoghue PE, Zhuang Z (2002) A finite element model for crack arrestor design in gas pipelines. *Fatigue Fract Eng Mater Struct* 22(1):59–66
11. Gohfeld DA, Chernyavsky OF, Ilin AV (1989) Inventor's certificate No. 1506719, method for corrugating pipe billets. Registered in the USSR State Register of Inventions 08 May 1989
12. Mitsuya M, Motohashi H, Oguchi N, Aihara S (2014) Calculation of dynamic stress intensity factors for pipes during crack propagation by dynamic finite element analysis. *J Press Vessel Technol Trans ASME* 136(1):011207
13. Murtagian GR, Ernst HA (2005) Dynamic axial crack propagation in steel line pipes. Part II: theoretical developments. *Eng Fract Mech* 72(16):2535–2548
14. Leis BN (2015) Arresting propagating shear in pipelines. *Steel Transl* 45(1):1–17
15. Pussegoda LN, Verbit S, Dinovitzer A, Tyson W, Glover A, Collins L, Carlson L, Beattie J (2000) Review of CTOA as a measure of ductile fracture toughness. *Int Pipeline Conf* 1:247–254
16. Oh C-K, Kim Y-J, Baek J-H, Kim W-S (2007) Development of stress-modified fracture strain for ductile failure of API X65 steel. *Int J Fract* 143:119–133
17. Abakumov AI, Abdullin MF et al (2009) Numerical modeling of magisterial crack propagation in pipelines. *Sci Tech Nat Gas Ind* 1:42–49
18. Alekseev AA (2014) Crack branching in fractured large-scale metal structures. *Issues Contemp Sci Educ* 9(27):15–16
19. Tyson WR (2009) Fracture control for northern pipelines. In: *Damage and fracture mechanics*, Dordrecht, pp 237–244. https://doi.org/10.1007/978-90-481-2669-9_25
20. Talemi RH (2016) Numerical simulation of dynamic brittle fracture of pipeline steel subjected to DWT using XFEM-based cohesive segment technique. *Fract Integr Struct* 10(36):151–159
21. Anderson TL (2004) *Fracture mechanics: fundamentals and applications*, 2nd edn. CRC Press, Boca Raton, FL
22. Pestrikov VM, Morozov EM (2002) *Fracture mechanics of solids: a lecture course*. Professia Publ., St.-Petersburg
23. Nicolas M, Dolbow J, Belytschko T (1999) A finite element method for crack growth without remeshing. *Int J Numer Meth Eng* 46(1):131–150
24. Song JH, Wang H, Belytschko T (2008) A comparative study on finite element methods for dynamic fracture. *Comput Mech* 42(2):239–250
25. Zhuang Z, O'Donoghue PE (2000) The recent development of analysis methodology for rapid crack propagation and arrest in gas pipelines. *Int J Fract* 101(3):269–290
26. Ortiz M, Pandolfi A (1999) Finite-deformation irreversible cohesive elements for three-dimensional crack-propagation analysis. *Int J Numer Meth Eng* 44(9):1267–1282
27. Kryzhaniv's'kyi EI, Hrabov's'kyi RS et al (2015) Evaluation of the kinetics of fracture of elements of a gas pipeline after operation. *Mater Sci* 51(1):7–14
28. Gokhfeld DA, Getsov LB, Kononov KM et al (1996) *Mechanical properties of steels and alloys*. Reference book publ. of the Ural Branch of the Russian Academy of Sciences, Yekaterinburg
29. Timashev SA, Chernyavsky OF, Rebyakov YN (2003) Experimental assessment of material strength of two operating main oil pipelines. *Am Soc Mech Eng Press Vessel Pip Div (Publ) PVP* 464:141–145

Improvement of Operational Characteristics of Aggregates by Nanostructuring Surfaces of Tribounits



M. Yu. Karelina, T. Yu. Cherepnina and N. Yu. Bugakova

Abstract The article presents a solution to the problem of improving the operational characteristics of agricultural machinery aggregates by applying a monomolecular protective film on the surface of tribounits. In accordance with the strategy for the development of agriculture, one of the priority areas of which is import substitution, an analysis has been made of existing methods for improving the performance of agricultural machinery aggregates by modifying the interface surfaces with surface-active substances (surfactants). The article presents the theoretical justification and the results of the experiment, confirming the rationale for increasing the operational wear resistance of gears and life by changing the magnitude of the friction on the interface surfaces. The properties of molecules of surface-active substances are used to change the surface energy at the interface and thereby affect the physicochemical processes: wetting, wear, friction, corrosion (Gaidar et al. in Increasing wear resistance of friction units, Works of GOSNITI, pp 40–47, 2016 [1]; Volkov et al. in Improving the tribological properties of lubricants based on gear oil, innovative directions of development of technologies and technical means of agricultural mechanization: materials of the international scientific-practical conference dedicated to the 100th anniversary of the Department of Agricultural Machines of the faculty of Agricultural Engineering of the Voronezh State Agrarian University named after Emperor Peter I, pp 115–119, 2015 [2]; Karelina et al. in Improving the tribological characteristics of lubricating compositions based on gear oil, innovative technologies and technical means in the agricultural sector: materials of the international scientific-practical conference of young scientists and specialists, pp 228–233, 2015 [3]; Gaidar and Karelina in Fluorine-surfactant adsorption and its effect on the lubrication of friction in the conditions of boundary and hydrodynamic friction, from nanostructures, nanomaterials and nanotechnologies to nanoindustry, pp 44–45, 2015 [4]). The methods of

M. Yu. Karelina (✉) · T. Yu. Cherepnina
Moscow State Automobile and Road Technical University (MADI),
Leningradsky Prospect 64, Moscow 125319, Russia
e-mail: karelinamu06@gmail.com

N. Yu. Bugakova
Kaliningrad State Technical University, Sovetsky Prospect 1, Kaliningrad 236022, Russia

forming a monomolecular protective film are presented as well as the technology of modifying the surfaces of friction pairs by surfactants is optimized, based on a model of the behavior of a drop on the surface and an estimate of the wetting angle. The results of experimental studies of the effectiveness of the modifier, evaluation of its physicochemical and operational properties are presented.

Keywords Surface-active substance · Monomolecular film · Surface energy

1 Introduction

Improvement of the performance of agricultural machinery units, including reducing friction losses in friction equipment, is one of the priorities of both scientific and applied research and also development. First of all, high importance of solving the problem is determined at present by the need to search for import-substituting technologies and materials that adequately replace foreign analogues and improve the performance characteristics of units and equipment in general. Due to the objective reduction in purchases of new machines as well as modifiers for various purposes of foreign production and also due to insufficient production volumes of domestic technology, improvement of performance characteristics of technology is an urgent task requiring an operational and high-quality solution.

The decrease in the reliability of a unit of equipment is mainly determined by the intensive wear of parts. Improving wear resistance in gears is one of the ways to increase the reliability of their operation.

2 Actuality of the Problem

The search for new methods to reduce wear of friction pairs in the mode of boundary friction due to reduction of hydrodynamic friction is currently relevant, since solving problems associated with reducing wear of friction pairs is one of the ways to increase the economic efficiency of the operation of agricultural equipment by reducing fuel consumption and increasing resource equipment [5].

The main objective of the State Program for the Development of Agriculture and Regulation of Agricultural Products, Raw Materials and Food Markets for 2013–2020 is to ensure the creation of agricultural equipment in the Russian Federation which would meet the international standards by modernizing existing production facilities and creating competitive domestic equipment corresponding with modern requirements of operation and labor safety [6, 7].

In the study of trends and prospects for the development of agricultural engineering in the Russian Federation, the program presents four scenarios that are

determined by the share of imports in the domestic market and the ratio of exports of agricultural equipment to the domestic market.

The most acceptable one for Russia is the third model—“Global Exporter.” The model is characterized by the protection of the domestic market and large-scale government support for the export of domestic products. This model ensures respect for the interests of all groups and is the most economically attractive. It is more in line with the stated goals of the Strategy for the Development of Agricultural Engineering in Russia until 2020—reducing dependence on product imports and developing the export potential of the industry’s products [8, 9]. Currently, there is such a situation in the market for the production of agricultural machinery (Fig. 1) that Russia accounts for less than 6% of world production, while China provides 14%.

According to the Ministry of Agriculture of the Russian Federation, in the AIC, as of 10/01/2018, there were 3,003,469 self-propelled vehicles and trailers [10].

Ensuring the high performance of agricultural machinery requires the creation and efficient functioning of a material and technical base for maintenance and repair of machines.

The repair and technological equipment available in the production workshops are outdated, and new technologies for carrying out repair work are not applied. Virtually no restoration of worn parts occurs. All this leads to an increase both in the cost of repairing equipment and the timing of repairs, deterioration of its quality and, ultimately, a decrease in the technical readiness of the machine and tractor fleet.

The existing standard technologies for maintenance and repair of machines are not fully implemented and do not sufficiently cover the whole complex of processes for ensuring their operability. A number of technologies for repair and maintenance, in connection with modernization and acquisition of new equipment by farms, require new developments [11–13].

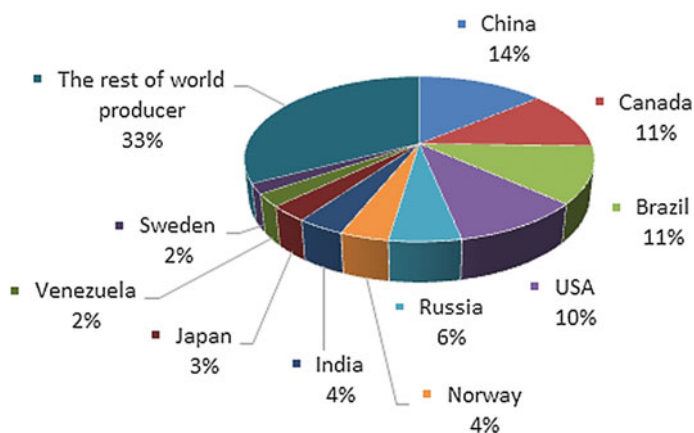


Fig. 1 Shares of leading countries producers of agricultural machinery

Maintenance of equipment in working condition should be carried out due to a significant increase in the resource of repaired equipment based on the development of modern technologies of repair and maintenance with a wide use of new technological equipment, fuel, and lubricants.

The greatest wear of parts is observed under boundary friction, the intensity of wear in the interfaces is determined by the influence of the lubricating medium, friction, properties of materials and characteristics of interacting surfaces. At boundary lubrication, adhesion, corrosion-mechanical, and fatigue wear mainly occur [14, 15].

There is an obvious need to develop a new technology for modifying surfaces, which would make it possible to influence the lubrication conditions of parts of friction pairs in both boundary and hydrodynamic mode in order to increase operational performance [16, 17].

The interphase boundary is an integral part of all material objects, so it is a major participant both in implementation of technological processes and in creation of new materials and technologies, since some physicochemical processes such as friction, wear, adhesion, chemical and electrochemical corrosion affecting the reliability and efficiency of technology occur at the interphase boundary: solid–solid, solid–liquid, gas–solid. Due to the fact that the state of atoms and molecules at the interface differs from the state in the bulk of the phases because of uncompensated force fields at the interface, it is possible to influence the physicochemical processes by changing surface energy. The dependencies of physicochemical properties of surfactants and their ability to reduce surface energy on the composition and structure of a molecule, packing density at the interface, the type of bond of the polar group of molecules with the surface and the number of polar groups in the molecule allow the scientific research to significantly reduce the surface energy [18].

3 Problem Statement

To reduce the magnitude, stabilize the conditions of friction, and reduce the intensity of wear in friction equipment, it is necessary to provide the following:

- provide a layer of lubricant of sufficient thickness between the surfaces of tribounits to ensure the absence of contact between the tops of the surfaces;
- determine the surfactant that changes the surface energy;
- propose a technology for modifying the surfaces of tribounits by means of fluoride surfactants;
- provide a high-quality monomolecular protective film;
- provide quality control of nanomodification.

4 Optimization of Surfactant Ratio in a Composition

Perfluoropolyoxopropylencarboxylic acid is the main material for extreme pressure and antiwear additives in oils and greases, as well as in compositions for processing metalworking tools and friction units in order to increase their service life [19, 20].

The disadvantage of these compounds is that they do not dissolve and slightly emulsify in lubricating oils, and their emulsion in oil is possible only with the use of scarce and expensive fluorine-containing emulsifiers. In addition, the method of obtaining these compounds is very complicated and time-consuming.

As a surfactant, it is proposed to use an organofluorine compound that would allow its use in friction units of machines and mechanisms (diesel, carburetor engines, gearboxes, transmissions, etc.). To do this, it must have the following characteristics:

- easy emulsification in lubricating oils;
- high heat resistance;
- high adhesive, antiwear, anti-seize, and anti-corrosion properties [21–23].

This compound has a fluorocarbon and hydrocarbon radical, an amide functional group instead of carboxyl, and is a colorless or slightly yellow liquid with a viscosity of $6\text{--}35 \cdot 10^{-6} \text{ m}^2/\text{s}$ and a density of $1620\text{--}1810 \text{ kg/m}^3$. The structure of the compound was proved by infrared spectroscopy, nuclear magnetic resonance spectroscopy, and elemental analysis.

The adsorption of this compound on solid surfaces leads to a decrease in their surface energy from $1800\text{--}6000 \text{ mN/m}$ to $4\text{--}6 \text{ mN/m}$, the coefficient of friction and the moment of friction of rest decreases, respectively, $10\text{--}20$ and $100\text{--}104$ times, the tangential force of an oil shift on a solid surface decreases by $70\text{--}75$ times; moreover, the compound is thermostable up to a temperature of $450 \text{ }^\circ\text{C}$, not combustible, explosion, and fireproof and also non-toxic (hazard class 4).

The most important factor is the availability of the considered compound, as well as the ability to synthesize its derivatives with different solubility and emulsifying ability in lubricating oils. In addition, to obtain the proposed connection one does not require the use of scarce raw materials [24].

The task to determine in advance and obtain the required size of the organic molecule by means of synthesis and, as a consequence, achieve proper effectiveness of the protective molecular film, is solved by introducing a different amount (from 0.5 to 3 mol) of H_2BO_3 into the reaction mixture.

Thus, we obtain the target product with a different molecular weight. The length of the molecule affects the structure of the protective molecular layer on the surface of a solid; upon saturation, a quasicrystalline structure is obtained. The solubility of fluoride surfactant depends on the length of the fluorocarbon radical.

5 Optimization Technology for Modification of Friction Pair Surfaces by Perfluorinated Surfactants

The next task of the study was to evaluate the optimal technology for modifying surfaces of friction pairs by perfluorinated surfactants. The baseline optimization characteristic studied was assumed to be the amount of lubricant held on the surface— Y , which naturally depends on the concentration of the solution C most significantly and also the surface roughness R .

A second-order regression model was used in the test plan:

$$y = b_0x_0 + b_1x_1 + b_2x_2 + b_{12}x_1x_2 + b_{11}x_1^2 + b_{22}x_2^2 \quad (1)$$

using the orthogonal three-level Box–Behnken plan for triple repetition (Table 1). The response surface built (Fig. 2) and the graph of predicted values relative to the observed ones (Fig. 3) show that a quadratic approximation is quite an adequate model for this dependence.

As a part of the factor plan analysis, values of all regression parameters were obtained (Fig. 4).

Thus, the conducted studies allow us to draw the following conclusions:

1. as a result of adsorption of a fluorine-surfactant molecule, a MPF of 3–6 nm is formed on the surface, which does not affect the dislocation surface structure, hardness and microhardness of metals;
2. forming a different structure of the MPF on the surface of tribounits, it is possible to increase the oil absorption of the surface at the boundary MPF-metal;
3. a monomolecular protective film assumes the role of a “compensator” in tribounits with different lubrication conditions and protects the surfaces of friction pairs in both hydrodynamic and boundary friction;

Table 1 Lubricant volume test results' table

No. of test	Factor levels		Test results Y for parallel experiments, mg		
	Concentration of fluorine-surfactants, $C, \%$	Roughness R_a , mcm	Blok ₁	Blok ₂	Blok ₃
1	0.1(–)	0.1(–)	0.49	0.47	0.48
2	0.5(+)	0.1(–)	0.33	0.30	0.30
3	0.1(–)	0.3(+)	1.84	1.91	1.86
4	0.5(+)	0.3(+)	1.13	1.15	1.11
5	0.3(0)	0.2(0)	2.35	2.38	2.38
6	0.5(+)	0.2(0)	1.66	1.68	1.67
7	0.1(–)	0.2(0)	1.90	1.92	1.91
8	0.3(0)	0.3(+)	2.23	2.27	2.22
9	0.3(0)	0.1(–)	0.67	0.65	0.69

2 3-level factors, 3 Blocks, 27 Runs; MS Residual=,0259722

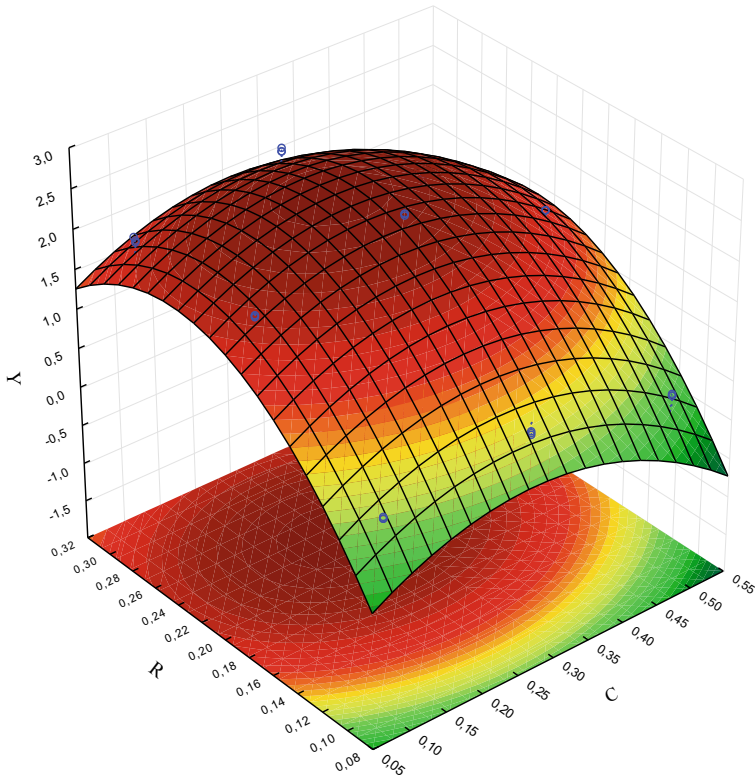


Fig. 2 Surface response of the amount of lubricant concentration and roughness

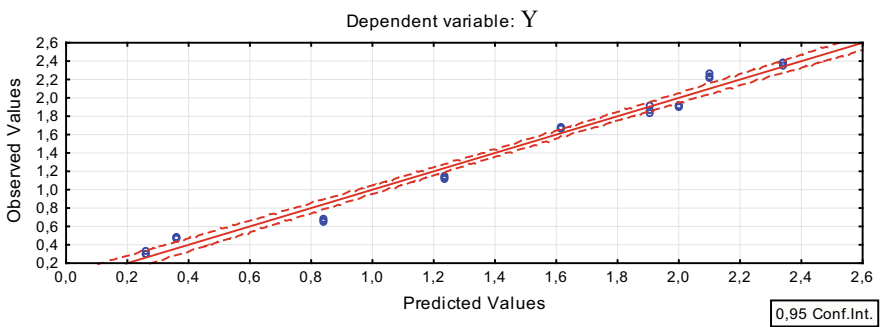


Fig. 3 Graph of predicted values relative to the observed ones

		Effect Estimates; Var.: Y; R-sqr=,96425; Adj.:95352 (CR_5_sta) 2 3-level factors, 3 Blocks, 27 Runs; MS Residual=,0259722 DV: Y				
Factor	Effect	Std.Err.	t(20)	p	-95,% Cnf.Limt	+95,% Cnf.Limt
Mean/Interc.	1,406	0,031	45,318	0,000	1,341	1,470
Bl ok(1)	0,018	0,088	0,203	0,841	-0,165	0,201
Bl ok(2)	-0,007	0,088	-0,076	0,940	-0,190	0,176
(1) C (L)	-0,383	0,076	-5,046	0,000	-0,542	-0,225
C (Q)	0,532	0,066	8,081	0,000	0,394	0,669
(2) R (L)	1,260	0,076	16,585	0,000	1,102	1,418
R (Q)	0,867	0,066	13,173	0,000	0,729	1,004

Fig. 4 Regression estimation table

- the oil holding on a surface is influenced by the concentration of fluoride surfactant in the working solution and also by roughness. The maximum effect is achieved at a concentration of 0.346% and a roughness of 0.238 μm .

6 Method of Determining the Quality of Molecular Protective Film

The method of determining the quality of a protective molecular film is designed to assess the presence of a protective molecular film, as well as the sufficiency of thickness and uniformity of the film deposited from a solution of fluoride surfactant on a solid surface.

The indicator of presence of high-quality protective molecular film on the surface of a solid is the magnitude of the wetting angle θ of an oil drop MN-60, applied onto a clean modified surface with a calibrated oil dosing. This value of the contact angle must be at least 45° .

To quantify the effect of using a solution of fluoride surfactant, solutions of different concentrations were prepared using volatile substance freon 112 as a solvent. Specially prepared metal plates were lowered into the solution. After soaking in the solution and subsequent drying of the metal plates, the values of the wetting angle were measured.

According to the single-factor model (Figs. 5 and 6), there is a clear tendency to increase the angle to 0.5%. After this, the values within the statistical significance range practically do not change.

While considering the influence of two factors at once (the solution percentage and the number of washes), a two-factor analysis model was used.

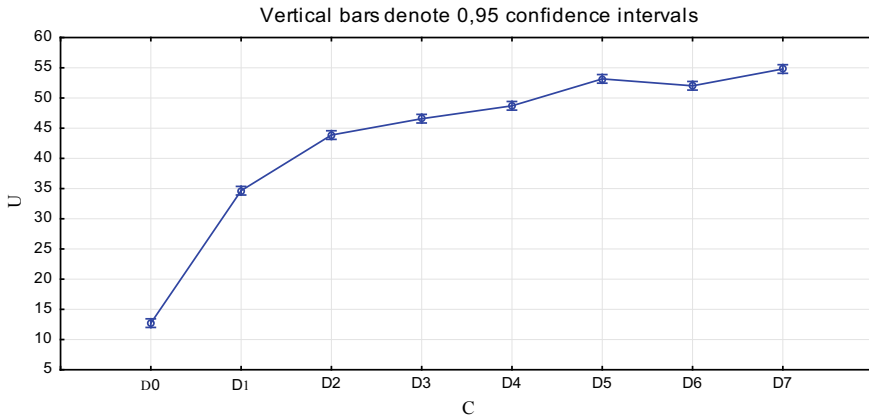


Fig. 5 Univariate experimental dependence of the wetting angle on solution concentration

C ; Weighted Means (Yron_2.sta)						
Current effect: F(7, 472)=1470,9, p=0,0000						
Effective hypothesis decomposition						
Cell No.	C	U Mean	U Std.Err.	U -95,00%	U +95,00%	N
1	D0	12,72	0,90	10,91	14,52	60
2	D1	34,65	0,12	34,40	34,90	60
3	D2	43,86	0,15	43,56	44,17	60
4	D3	46,57	0,14	46,29	46,85	60
5	D4	48,70	0,15	48,40	49,01	60
6	D5	53,16	0,15	52,87	53,45	60
7	D6	52,02	0,28	51,46	52,58	60
8	D7	54,80	0,25	54,30	55,29	60

Fig. 6 Descriptive statistics of wetting angle values for various concentrations

7 Experimental Investigation of the Modifier Efficiency

Laboratory tribotechnical studies have shown that the use of fluoride surfactant additive provides a significant reduction in friction torque and temperature, a more than twofold decrease in wear rate as well as a rather weak relationship between wear rate and normal load. The effectiveness of fluorine-surfactant additives in lubricating compositions based on transmission oils TM5-18 has been proven [25].

The results of the bench tests on the Sh-3 gearbox showed that the working surfaces of gear teeth remained in satisfactory condition after tests using the modifier. At the same time, the loss of mass of gears was almost two times less, well below the established norms. In addition, during the tests, the physicochemical properties of the oil itself slightly changed.



Bench tests of SHVM models allowed to determine the resource of the mechanism, which amounted to 4530 cycles, and also to fix a constant value of the friction zone temperature not exceeding 40 °C. In addition, the use of technology for modifying the surfaces of friction pairs made it possible to reduce the burn-in speed in the initial period by more than 4 times and also to reduce wear after a run-in by 1.5 times.

The test results on a roller stand showed that the addition of fluoride surfactant can reduce mechanical losses in gears and power plants, providing an increase in tractive effort by almost 13%.

It should also be noted that studies in the field of keeping equipment during the operational period and in the period of conservation in terms of protection against corrosion give positive results [26, 27]. Inhibitor compositions have been developed and optimized to ensure the persistence of agricultural machinery [28]. Certain work was carried out and reliable and adequate results were obtained in the field of research of coating-base systems and the formation of equally thick gas-thermal coatings [29, 30].

8 Conclusion

The article reflects the basic points of the study and also describes the solution of the problem of improving performance characteristics of agricultural machinery units by applying a monomolecular film consisting of a surfactant onto the surface of tribounits.

The results of experiments and field tests, as well as the introduction in the State Space Research and Production Center named after M. V. Khrunichev and also others confirm that the results of the research, can be applied in solving the main tasks outlined in the Program “Strategy for the Development of Agricultural Engineering in Russia until 2020.”

References

1. Gaidar SM, Karelina M Yu, Petrovskaya EA, Ziyatdinov EA (2016) Increasing wear resistance of friction units. Works of GOSNITI, pp 40–47
2. Volkov AA, Karelina M Yu, Ziyatdinov EA (2015) Improving the tribological properties of lubricants based on gear oil, innovative directions of development of technologies and technical means of agricultural mechanization: materials of the international scientific-practical conference dedicated to the 100th anniversary of the Department of Agricultural Machines of the faculty of Agricultural Engineering of the Voronezh State Agrarian University named after Emperor Peter I. Voronezh, 25 Dec 2015, pp 115–119
3. Karelina M Yu, Petrovskaya EA, Pydrin AV (2015) Improving the tribological characteristics of lubricating compositions based on gear oil, innovative technologies and technical means in the agricultural sector: materials of the international scientific-practical conference of young scientists and specialists. Voronezh, 26–27 Nov 2015, pp 228–233

4. Gaidar SM, Karelina M Yu (2015) Fluorine-surfactant adsorption and its effect on the lubrication of friction in the conditions of boundary and hydrodynamic friction, from nanostructures, nanomaterials and nanotechnologies to nanoindustry. In: Abstracts of the fifth international conference, Izhevsk, 2–3 Apr 2015, pp 44–45
5. Gaidar SM, Karelina M Yu (2015) Study of the effectiveness of tribological products based on nanomaterials. *Gruzovik*, pp 17–19
6. State Program for the Development of Agriculture and Regulation of Agricultural Products, Raw Materials and Food Markets for 2013–2020. Approved by the Decree of the Government of the Russian Federation of July 14th, 2012, 717. <http://government.ru/programs/208/events/> (reference date: 01.11.2018)
7. Vinogradov VV, Karelina M Yu, Kolomeychenko AV, Petrikov IA, Podzharskaya KS, Titov NV (2015) Import-substituting technology for restoring and hardening the working equipment of construction and road machines. *Construction and road machines*, pp 34–37
8. Golubev IG, Nosikhin PI, Fadeev A Yu (2010) Experience of import substitution of foreign agricultural machinery spare parts. FGSU “Rosinformagrotekh”, Moscow, p 30
9. The Development Strategy of Agricultural Engineering in Russia until 2020. Approved by the Decree of the Government of the Russian Federation dated July 7th, 2017. №1455-r. <http://static.government.ru/media/files/Ba4B6YDTiuOitleLkDQ05MCbz4WrfzJA.pdf> (reference date 01.11.2018)
10. http://usmt.mcx.ru/opendata/7708075454-statistika_po_aktualnoy_tekhnike_po_vidam_vladeltsev (reference date 01.11.2018)
11. Agafonov NI (2010) Economic and engineering forecast of creating an optimized technical service system in a modern AIC. *Agricultural machinery and technology*, pp 23–27
12. Cherepanov SS (1985) A comprehensive system of maintenance and repair of machines in agriculture. GOSNITI, Moscow, p 143
13. Federal Register of Technologies for Technical Service of Agricultural Machinery and Vehicles (1999). *Informagrotech*, Moscow, p 106
14. Karelina M Yu (2015) The effect of organofluorine surfactants on the performance of internal combustion engines. *Technical and technological problems of service*, pp 12–17
15. Karelina M Yu (2015) The mechanism of action of surfactants at the interfaces of phases in the conditions of boundary and hydrodynamic friction. *Bulletin of the Moscow State Automobile and Road Technical University (MADI)*, pp 25–33
16. Zubrilina EM, Karelina M Yu, Kolomeychenko AA, Kravchenko IN (2015) Resource-saving technologies for producing functional nanostructured coatings by high-speed deposition methods. *Bulletin of the Don State Technical University* 15:19–27
17. Gaidar SM, Karelina M Yu (2015) Technology for improving the wear resistance of the surfaces of tribounits by means of physicochemical methods, *Gruzovik*, pp 12–16
18. Volkov AA, Gaidar SM, Karelina M Yu (2015) Fluorine-surfactant adsorption and its effect on the lubrication of friction in the conditions of boundary and hydrodynamic friction. *Works of GOSNITI* 118:113–124
19. Ryabinin NA, Ryabinin AN (1995) Amides and perfluoropolyoxyalkylsulfo- or perfluoropolyoxy-alkylenecarboxylic acids and methods for their production. Russian Patent 2045544
20. Ryabinin NA, Sergeeva G, Volodkov VN, Ryabinin AN (1995) Method for producing polyperfluoropropylene oxide. Russian Patent 2046127
21. Gaidar SM, Karelina M Yu, Pydrin AV (2015) Investigation of the effect of nanostructuring of the surfaces of tribounits on the performance characteristics of engines. *Gruzovik*, pp 29–37
22. Karelina M Yu (2015) Improving the performance of internal combustion engines using nanomaterials. *Construction and road machinery*, pp 16–19
23. Karelina M Yu (2015) Lyophobicization of the fuel system surfaces of internal combustion engines. *Bulletin of the Moscow State Automobile and Road Technical University (MADI)*, pp 20–24

24. Karelina M Yu (2016) Improvement of the durability and efficiency of power plants and gears by modifying compounds with surface-active substances. Dissertation for the degree of Doctor of Technical Sciences. Moscow, p 342
25. Karelina M Yu, Petrovskaya EA, Pydrin AV (2015) Tribo characteristics of lubricating compositions based on gear oil TM5-18. Country Mechanic, pp 30–31
26. Gaidar SM, Karelina M Yu (2015) Innovative technical tool for applying a protective molecular film onto the surface of machines. Machinery and equipment for the village, pp 26–28
27. Bykova EV, Gaidar SM, Karelina M Yu (2015) Prospects for using paintwork materials modified with fluorine-containing surfactants for protection of agricultural equipment. Machinery and equipment for the village, pp 34–37
28. Karelina M Yu, Petrovskaya EA, Pydrin AV (2015) Optimization of the inhibited composition for ensuring the persistence of agricultural machinery. Works of GOSNITI 121:89–93
29. Karelina M Yu, Kolomeychenko AA, Kravchenko IV (2015) Computational-experimental method for studying the thermal state of the coating-base system with a moving boundary. Engineering 3:3–8
30. Gaidar SM, Karelina M Yu, Kravchenko IV, Salyaev NI (2015) Optimization of the process of formation of equally thick gas-thermal coatings. Machinery and equipment for the village, pp 38–42

Advantages of Using Wheel Rolling Radius for Calculating Friction Characteristics in Wheel-to-Road Contact Patch



E. V. Balakina, E. Y. Lipatov and D. S. Sarbayev

Abstract When improving the design of electronic control devices and car stability control system algorithms based on maximizing the road–tire friction coefficients, one has to evaluate the friction between the elastic wheel and the bearing surface. φ – s_x -diagrams are simulated to that end. These are the dependencies of the friction coefficients on the wheel sliding. What they look like depends, aside from external conditions (type of coating, lateral forces, etc.), on the law of contact-patch sliding increase, which in its turn depends on multiple factors including the estimated radius of the wheel. As of today, free radius, dynamic radius, and rolling radius values are used to that end. In this case, the difference between them can reach up to 20%, depending on the value of the tire radial deformation. Despite the large number of studies on the theory of rolling wheels, experts still have not developed a consensus on what radius should be used for these purposes, which, naturally, is accompanied by a difference in the calculations in which these radii are used. The researchers prove the advantages of using the estimated kinematic radius and propose a correlation for calculating it. Herein are presented φ – s_x -diagrams for different radii.

Keywords Elastic wheel · Solid surface · Contact patch · Free · Dynamic and rolling radius · Longitudinal wheel sliding · Friction in contact · Forms φ – s_x -diagrams

1 Introduction

How a car tire interacts with the road surface affects a wide range of car properties, first of all, its stability and controllability, which is fundamental to the safety of driving.

E. V. Balakina (✉) · E. Y. Lipatov · D. S. Sarbayev
Volgograd State Technical University, 28, Lenin Avenue, Volgograd 400005, Russia
e-mail: fahrgestell2011@yandex.ru

© Springer Nature Switzerland AG 2020
A. A. Radionov et al. (eds.), *Proceedings of the 5th International Conference on Industrial Engineering (ICIE 2019)*, Lecture Notes in Mechanical Engineering,
https://doi.org/10.1007/978-3-030-22041-9_107

1015

One of the ways to stabilize the car motion and make it more controllable is to improve the design of electronic controls as well as to enhance the algorithms of car stability systems. This is why evaluating the friction between the elastic wheel and the bearing surface is of interest for vehicle and tire manufacturers.

There are numerous studies and models for describing this or that property of the wheel, including models of the tire–road friction coefficient [1–22]. These models can be both empirical like the ones by A. B. Dick and Y. B. Pacejka, or they can be based on mechanical equivalents. Figure 1 shows the author-compiled classification of basic models. There are simpler models that neglect the lateral-force effects on the coefficient of friction, as well as more complex models that also take into account the sequence, in which lateral forces and braking torque emerge on the wheel.

Cars stability control system algorithms are based on maximizing the tire–road friction coefficients.

How the road–tire friction coefficient φ correlates to the longitudinal wheel sliding coefficient s_x is referred to as the φ – s_x -diagram. What this correlation is written as and how it is numerically characterized has a considerable impact on the estimated parameters of car stability, controllability, and braking dynamics.

$$s_x = \frac{V_s}{\omega \cdot r_k}, \tag{1}$$

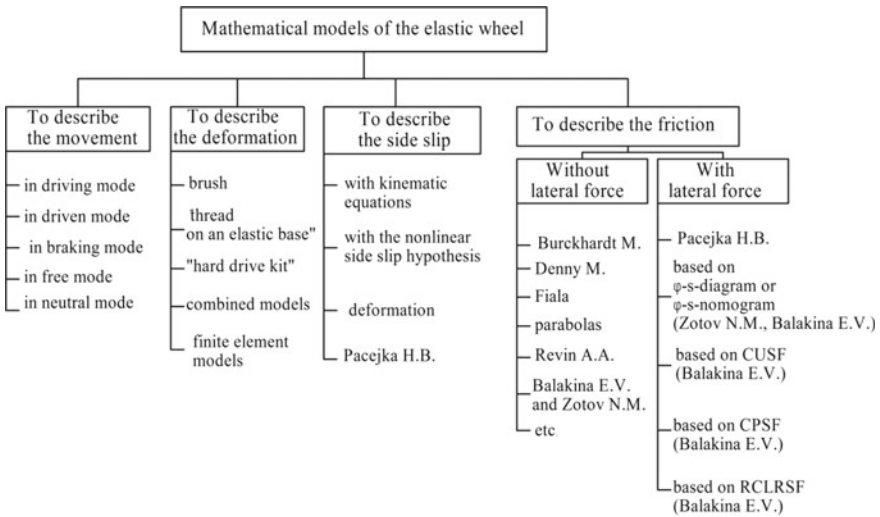


Fig. 1 Wheel model classification: CUSF is the ratio of the share of static friction in the contact patch, used for the realization of longitudinal reaction of a surface, to the general share of static friction in the contact for the same sliding; CPSF is the ratio of the static friction share in the contact patch, remaining to realize the friction properties in the longitudinal direction, to the static friction coefficient; CUSF is the ratio of the share of static friction in the contact patch, used for realization of longitudinal reaction of a surface, to the static friction coefficient



where V_s is the speed of longitudinal wheel sliding ($V_s \approx V_x - \omega \cdot r_k$); ω is the angular velocity of the wheel; r_k is the wheel rolling radius; V_x is the longitudinal component of the wheel-axle forward speed.

In order to exclude simulation problems related to the emergence of a “0” in the denominator and “ ∞ ” in the numerator, as well as to adhere to the physics of the process, assume that:

when accelerating $s_x = 1 - \frac{V_s}{\omega \cdot r_k}$; when braking $s_x = 1 - \frac{\omega \cdot r_k}{V_x}$.

The alteration range $s_x = 0-100\%$.

The rolling radius is sometimes referred to as the kinematic radius [14].

Many authors calculate the value s_x by this correlation (1), i.e. by the rolling radius. Some authors due to lack of rolling-radius data use other value such as the free radius or the dynamic radius. This is why the authors hereof have compared the effects of using different radii on the obtained $\varphi-s_x$ -diagrams when calculating the LWSC. Computational experiments have been carried out in Excel.

2 Goal of the Research

The purpose hereof is to find how the elastic-wheel radius affects on the car tire $\varphi-s_x$ -diagrams.

3 Methods and Approaches

The authors have computed the wheel rolling radius geometrically by using the diagram in Fig. 2. The figure uses the following notation: R_0 is the free radius of the wheel; R_d is the dynamic radius of the wheel; P_z is the normal wheel load; l_c is the contact-patch length; Δz is the radial tire deflection (20% of the profile height at max); ω is the angular velocity of the wheel; and α is the angle.

Wheel rolling radius

$$r_k \approx r_{k0} \approx \frac{L_t}{2\pi},$$

where L_t is the distance traveled per turn; r_{k0} is the rolling radius in free operation [18].

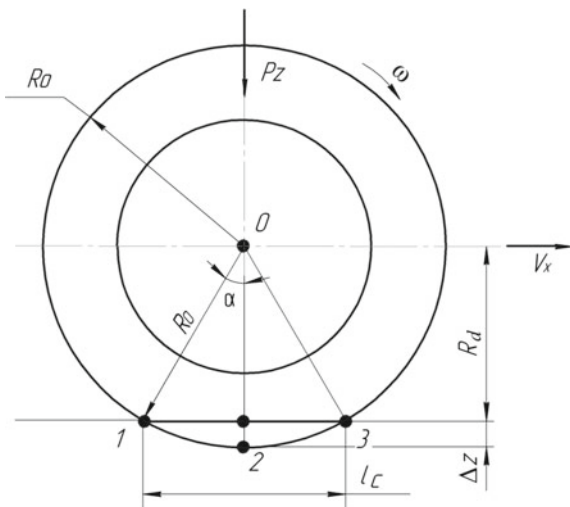
$$R_d = R_0 - \Delta z.$$

Let us introduce the concept of relative radial deformation of the tire and denote it as n :

$$n = \frac{\Delta z}{R_0}; \quad \Delta z = \frac{P_z}{C_{tz}},$$

where C_{tz} is the radial tire stiffness, H/mm.

Fig. 2 Wheel rolling radius calculation diagram



Radial stiffness can be found experimentally, which is expensive and labor intensive; or it can be found by a universal correlation that matches the tire design [3].

$$R_d = R_0(1 - n); \quad L_t = 2\pi R_0 - \cup 123 + l_c; \quad l_c \approx 2\sqrt{\Delta z(2R_0 - \Delta z)} = 2R_0\sqrt{n(2 - n)};$$

$$\cup 123 \approx 2R_0 \cdot \alpha = 2R_0 \left(\arcsin \left(\frac{l_c}{2R_0} \right) \right).$$

Transform to obtain an approximate equation for calculating the wheel rolling radius. Let rolling radius be defined as the dimensionless value

$$\frac{r_k}{R_0} \approx \left(1 - \frac{\arcsin(\sqrt{n(2 - n)})}{\pi} \right) + \frac{\sqrt{n(2 - n)}}{\pi} \tag{2}$$

Figure 3 shows the relative estimated rolling radius and dynamic radius for various relative tire deformations.

As can be seen in Fig. 3, increasing the radial tire deformation reduces the wheel rolling radius calculated by the formula (2) to 2%, while the dynamic radius is reduced to 20%. The rolling radius can be found with a greater precision experimentally by reference to a real-wheel 10-turn travel, an approach used by Professor Fedotov’s school [9]. Experiment shows that increasing the radial tire deformation reduces the wheel rolling radius not to 2% like herein but to 3% [9]. However, experimental determination of the rolling radius does not seem possible when projecting the car safety properties, which is why it is permissible to neglect the error and calculate it by the proposed theoretical dependency (2).



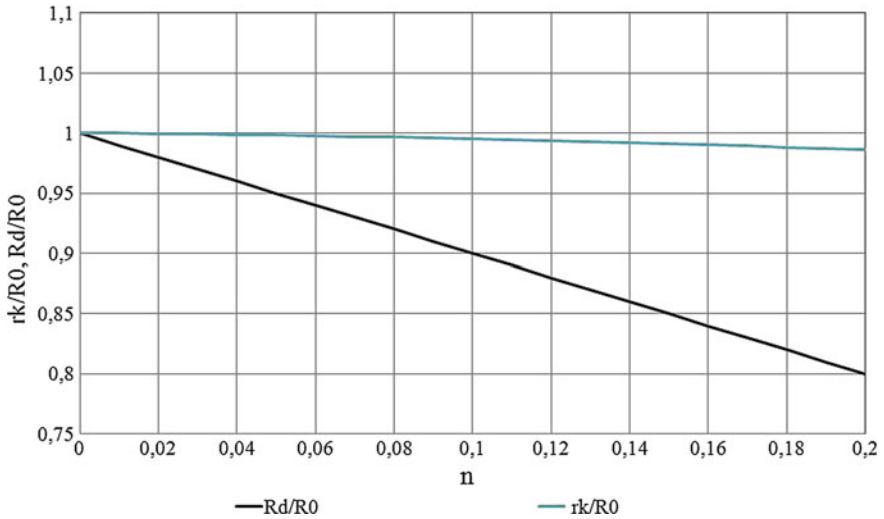


Fig. 3 Estimated relative radii: dynamic radius and rolling radius for different relative tire deformations n

Figure 4 shows the calculation $\varphi-s_x$ -diagrams for various lateral-force P_y values as emerging before braking and obtained when calculating the value s_x by the free radius, the dynamic radius, or the rolling radius of the wheel. Calculation is done by the CUSF methodology [2–4, 7] in Excel. As can be seen in Fig. 4, if one uses the free radius or the rolling radius to calculate the value s_x (see Fig. 4a), the obtained $\varphi-s_x$ -diagrams correspond to the same lateral force, are virtually coincident, and look conventionally. If the dynamic radius (Fig. 4b) is used to that end, then a more intense sliding increase in the contact patch as shown in Fig. 5 results in $\varphi-s_x$ -diagrams that are quantitatively and qualitatively non-conventional in the pre-critical area. In addition, the dynamic radius alters while the car is moving, and the calculation diagram becomes non-smooth.

This means that using the free radius or the rolling radius is appropriate for calculating the LWSC s_x . Approximate calculation of the rolling radius that would be precise enough for real-world calculations can be done by the author-obtained dependency (2) above.

When deriving the formula (2), the theoretical contact-patch length l_c was calculated on the basis of geometric considerations. Experiments show that it is actually smaller:

$$l_{ce} = k_1 \cdot l_c,$$

where l_{ce} is the experimental contact-patch length value; k_1 is the contact-patch length correction factor.



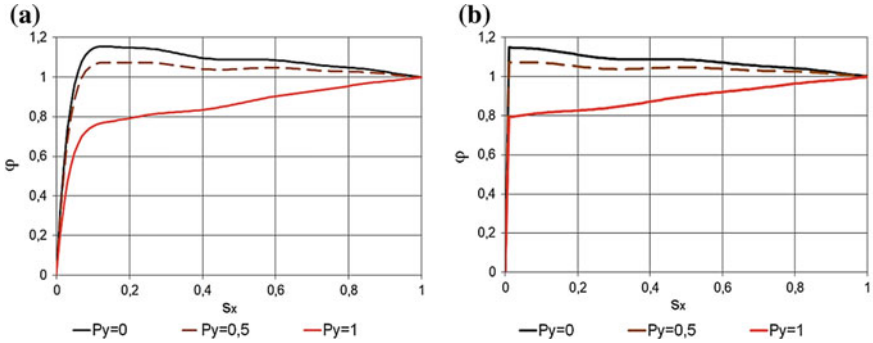
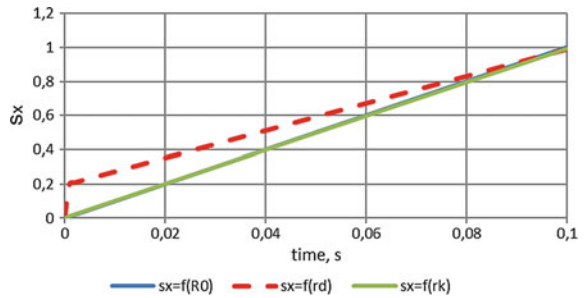


Fig. 4 Calculation $\varphi-s_x$ -diagrams for various lateral-force values as emerging before braking and obtained when calculating the value s_x : **a** by the free radius and the rolling radius; **b** by the dynamic radius

Fig. 5 Sliding increase over time for various estimated wheel radii



According to Balakina [3], for most car and truck tires $k_1 \approx 0.7$. Exception is low-profile radial car tires, for which this value is 0.6.

4 Conclusion

What $\varphi-s_x$ -diagrams look like depend, aside from external conditions (type of coating, lateral forces, etc.), on the law of contact-patch sliding increase, which in its turn depends on multiple factors including the estimated radius of the wheel. It has been proven that if calculations of the sliding value s_x use the rolling radius or the free radius (which are close), then the obtained $\varphi-s_x$ -diagrams for the same lateral force are virtually coincident while looking traditionally. When using the dynamic radius, a more intense increase in the contact-patch sliding results in $\varphi-s_x$ -diagrams that are qualitatively and quantitatively non-conventional in the pre-critical area. In addition, the current dynamic radius alters while the car is moving, and the calculation diagram becomes non-smooth.



This finding holds for both the pre-braking lateral force and for the lateral force emerging after braking torque is applied.

Acknowledgements The reported study was funded by RFBR according to the research project No. 19-08-00011.

References

1. Balabin IV, Putin VA, Chabunin IS (2012) Automobile and tractor wheels and tires. MGTU MAMI, Moscow
2. Balakina EV (2017) Calculation of the geometric position and the sizes of the static friction and sliding friction zones at the point of contact between an elastic wheel and a firm surface. *J Frict Wear Allerton Press Inc N Y* 38(2):144–149
3. Balakina EV, Kochetkov AV (2017) Friction coefficient of tire with road surface. *Mechanical Engineering, Moscow*, p 292
4. Balakina EV, Zotov NM (2015) Determination of the mutual arrangement of forces, reactions, and friction zones in the contact zone of an elastic wheel with a solid surface. *J Frict Wear Allerton Press Inc N Y* 36(1):29–32
5. Balakina EV, Zotov NM, Fedin AP (2018) Modeling of the motion of automobile elastic wheel in realtime for creation of wheeled vehicles motion control electronic systems. In: *IOP Conference Series: Materials Science and Engineering*, vol 315, p 012004
6. Balakina EV et al (2015) Modeling techniques for tires based on $\varphi-s_x$ diagram. *Acta Tech CSAV (Ces Akad Ved)* 60(2):173–178
7. Balakina E et al (2013) Problems of modelling of dynamic processes in real time (on the example of vehicle brake dynamics). *Mechanical Engineering, Moscow*, p 299
8. Emami A et al (2017) Physics-based friction model with potential application in numerical models for tire-road traction. *Dynamic Systems and Control Conference*, p 6
9. Fedotov AI (2015) Dynamic method of diagnostics of pneumatic brake drives of motor vehicles. *Monograph. Publications IrNITU, Irkutsk*, p 514
10. Khaleghian S et al (2017) A technical survey on tire-road friction estimation. *Friction* 5 (2):123–146
11. Khaleghian S, Ghasemalizadeh O, Taheri S (2016) Estimation of the tire contact patch length and normal load using intelligent tires and its application in small ground robot to estimate the tire-road friction. *Tire Sci Technol TSTCA* 44(4):248–261
12. Knoroz VI, Klennikov EV, Petrov IP (eds) (1976) *Operation of automobile tires*. Transport, Moscow, p 240
13. Koskinen S (2010) Sensor data fusion based estimation of tyre-road friction to enhance collision avoidance. A dissertation for the degree of doctor of science in technology of the faculty automation, *Mechanical and Materials Engineering, The Tampere University of Technology*, 12 Mar 2010, 209 p
14. Kravets VN, Selifonov VV (2011) *Automobile theory*. College textbook, OOO Greenlight, Moscow, p 884
15. Minca C (2015) The determination and analysis of tire contact surface geometric parameters. *Rev Air Force Acad Romla* 1:149–154
16. De Beer M et al (2012) Tyre—pavement interface contact stresses on flexible pavements—quo vadis? In: *8th Conference on asphalt pavements for Southern Africa*, June 2012
17. Pacejka HB (2012) *Tire and vehicle dynamics*. Published by Elsevier Ltd., USA
18. Petrushov VA (2008) *Automobiles and road trains: new technologies of research of rolling and wind resistance*. Torus Press, Moscow, p 352

19. Jazar Reza N (2008) Vehicle dynamics: theory and application. Springer Science+Business Media, LLC, London, p 1015
20. Tomaraee P et al (2015) Relationships among the contact patch length and width, the tire deflection and the rolling resistance of a free-running wheel in a soil bin facility. Span J Agric Res13(2):7
21. Turenko AN, Lomaka SI, Ryzhikh LA, Leontiev DN (2010) Calculation of realized traction coefficient at wheel floating in braking mode. Automob Transp 27:7–12
22. Woodward D et al (2014) The static contact patch of some friction measuring devices. In: 4th International Safer Roads Conference, Cheltenham, United Kingdom, May 2014

Lubrication Conditions and Development of Pre-failure State of Crankshaft Bearings



A. T. Kulakov, E. P. Barylnikova and I. P. Talipova

Abstract Most researchers attribute the failure of bearings of a cranked shaft of the engine with the violation of hydrodynamic lubrication. Under normal engine operating conditions, the main oil line maintains the pressure required to ensure optimal lubrication of the friction surfaces. As the bearings of the crankshaft wear out and, consequently, increase the gaps in them, the flow of oil through the bearings is facilitated; in this regard, the pressure in the oil line decreases. The pressure and oil flow through the connecting rod bearings are due to a large number of factors: the performance of the oil pump, the operating mode of the engine, and the degree of wear, as well as design features of lubrication systems, individual components and parts, the method of supplying oil to them. In addition, the oil flows in the rotating crankshaft are subject to centrifugal forces, resulting in pressure loss in the channels up to 50% of the nominal value, which leads to a decrease in oil flow through the connecting rod bearings. Negatively affect the modes of rupture of the oil flow supplied to the connecting rod cavity, which actually precede the failure of the crankshaft bearings. Their research is devoted to this work.

Keywords Diesel engine · Crankshaft bearings · Failures · Lubrication system · Pressure · Flow gap · Hydrodynamics · Methods · Experiment · Pre-failure condition

1 Introduction

The reliability of the diesel engine is largely determined by the technical condition of the crank mechanism parts, especially the crankshaft bearings. The main reason for the low life of 25% of engines in operation is the cranking of the connecting rod inserts [1]. In most studies, the failure of the connecting rod bearings associated

A. T. Kulakov (✉) · E. P. Barylnikova · I. P. Talipova
Naberezhnye Chelny Institute, Kazan (Volga Region) Federal University,
10A, Prospekt Syuyumbike, 423812 Naberezhnye Chelny, Russia
e-mail: altrak09@mail.ru

with the wear of journals and bearings to the limit values. At the same time, the process of oil supply to the bearings of the crankshaft, the kinetics of the oil involved in various forms of motion, as well as the effect of changes in the gap in the main and connecting rod bearings on the conditions of their lubrication are not sufficiently studied. Studies [2, 3] have shown that one of the main parameters affecting the wear rate of crankshaft bearings is the pressure in the lubrication system. The relationship of reducing the oil supply to the connecting rod bearings due to the increase in oil consumption through the main bearings during wear is revealed. Violation of hydrodynamic lubrication due to insufficient amount of oil entering the connecting rod bearings can be a criterion for bearing failure, i.e., a sign of a change in the technical condition of the internal combustion engine, in which the crankshaft bearings are not able to perform the specified functions. Experience in the operation of KAMAZ vehicles after implementation in the previous period of structural and technological activities [4, 5] caused the need for a more thorough study of the changes in the modes of lubrication in operating conditions and their impact on reducing the life of the engine. Therefore, studies aimed at studying the pre-failure condition of the crankshaft bearings on the parameters of the lubrication process to ensure durability in operation are relevant.

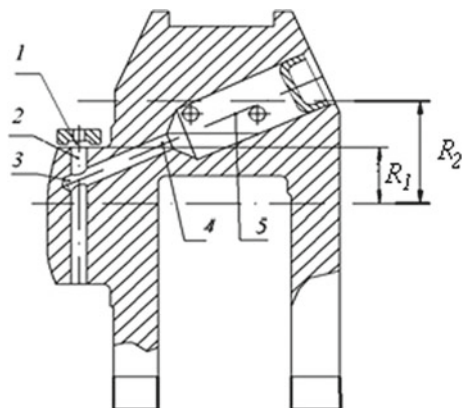
2 Analytical Study

The reliability of the crankshaft bearings is determined by various factors. One of the main factors is the organization of oil supply to the crankshaft bearings. The article considers the scheme of oil supply to connecting rod bearings, which is used on KAMAZ-740 engines [4]. Oil through the channels in the cylinder block is fed into the annular groove 1 and made in the upper root liner (Fig. 1). From it, one or diametrically opposite channels 2 oil enters the crankshaft. In this case, the oil supply can be pulsating or continuous. After passing through channels 3 and 4, the oil enters the centrifugal cavity 5, from which through two holes drilled opposite to each other in a plane perpendicular to the crank, the oil enters the connecting rod bearing of one and the other cylinders.

The measurement of pressure in the annular channel of the main bearing made it possible to determine the value of pressure loss on leaks and hydraulic resistances to the annular channel, which was at $n = 2930 \text{ min}^{-1}$ 0.12 MPa. The calculation determined the pressure loss from the annular channel of the main bearing to the crankshaft axis, which at $n = 2930 \text{ min}^{-1}$ amounted to 0.18 MPa [6].

Consequently, at a nominal pressure in the lubrication system equal to 0.45 MPa [4] at a frequency of $n = 2930 \text{ min}^{-1}$ to point 3 (Fig. 1) the pressure loss will be $\Delta P_{\Sigma} = 0.3 \text{ MPa}$ or 67% and it will be $P_3 = 0.15 \text{ MPa}$. The pressure increment from the centrifugal forces in the area 3–5 (Fig. 1) up to connecting rod bearings at $n = 2930 \text{ min}^{-1}$ is $\Delta P_{cf} = 0.15 \text{ MPa}$. Upon reaching the equality $P_3 = \Delta P_{cf}$, or when ΔP_{cf} exceeds P_3 , it is a break of flow, which leads to a decrease of the oil flow through the bearing. Under these conditions, heat dissipation from connecting rod

Fig. 1 Scheme of supply of lubricant to the connecting rod bearings of the engine KAMAZ-740: 1—the ring channel; 2—the channel in the radical neck; 3—the entry point into the channel of supply to the connecting rod neck; 4—the channel of supply to the connecting rod neck; 5—the cavity of the centrifugal trap; R_1 —the radius of the crank; R_2 —connecting rod radius



bearings, stress-strain state of connecting rod inserts significantly deteriorates, and the probability of their forming and hydrodynamic disturbances increases, and as the completion of the process—turning the inserts.

3 Experimental Study

Experiments on the original methods investigated different parts of the lubrication system by oil pressure. The phenomena of flow rupture at certain modes were found, which is a little-known phenomenon today, which is not taken into account in the design and operation of internal combustion engines. During operation, the pressure in the engine lubrication system is reduced, so the pressure in the annular channels is estimated at different pressure levels in the system at different speeds with the load in the bench conditions. The results are presented in Fig. 2 and Table 1.

From these data, it follows:

- the pressure in the annular channels of the main supports is much lower than the standard pressure gauge on average 74% at idle, 67% with load;
- pressure loss to the main oil channel (point in the area of the first root support) are insignificant and make 3% at idle, 8% with load;
- the amount of pressure loss is determined mainly by the pressure in the lubrication system and the speed of the crankshaft depends slightly;
- the lowest pressure in comparison with the rest have the second and fourth supports in the entire range of pressures and speeds;
- slight non-uniformity of pressure on the supports (less than 10%) indicates a uniform load of supports by consumers.

The oil supply to the connecting rod bearings is determined by the pressure at point 3 (Fig. 1). Up to this point, there are losses due to the action of centrifugal

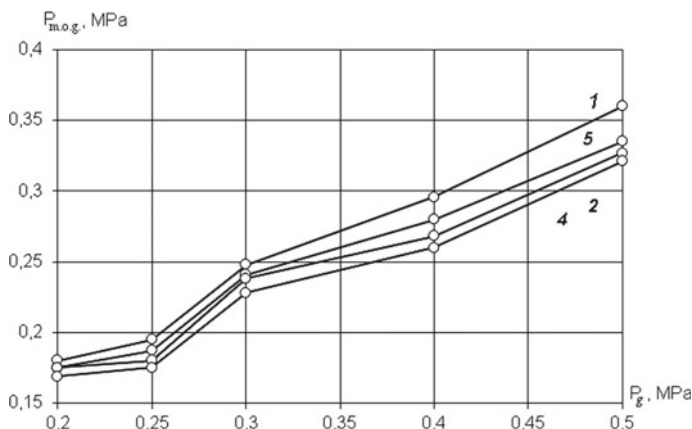


Fig. 2 Dependence of the pressure in the annular channels of the main supports on the oil pressure in the system: 1, 2, 4, 5—number of main supports

Table 1 Pressure change in annular channels at idle speed and external speed characteristic

n	M_t	t_{oil}	P_g	$P_{m.o.g.}$	P_1	P_2	P_4
min^{-1}	$\text{N}\cdot\text{m}$	$^{\circ}\text{C}$	MPa	MPa	MPa	MPa	MPa
2930	Idling	85	0.460	0.444	0.356	0.336	0.316
2600	Idling	100	0.440	0.416	0.312	0.292	0.292
2200	Idling	96	0.440	0.420	0.328	0.308	0.308
1800	Idling	87	0.430	0.400	0.320	0.316	0.316
1400	Idling	83	0.380	0.364	0.296	0.296	0.296
1000	Idling	80	0.270	0.268	0.220	0.224	0.228
600	Idling	74	0.160	0.160	0.136	0.140	0.144
Pressure, %			100	95	76	74	73
<i>With the load</i>							
2600	496	98	0.460	4,200	0.312	0.276	0.276
2200	560	101	0.430	3,960	0.300	0.272	0.284
1800	608	96	0.380	3,620	0.288	0.272	0.280
Pressure, %			100	92	71	64	66

Note n —crankshaft speed; M_t —torque; t_{oil} —oil temperature; P_g —oil pressure on the bench pressure gauge; $P_{m.o.g.}$ —pressure in the main oil channel; P_1 , P_2 , P_4 —pressure in the annular channel of the first, second, and fourth main bearings

forces, the estimated value of which is 0.18 MPa [6–8]. An experiment was conducted to confirm these losses. The technique consists of the output of the probe tube from the oil channel along the axis of the crankshaft to the outside (Fig. 3) and evaluation of the oil flow out of the tube. The absence of expiration indicates that the pressure in the channels along the axis of the crankshaft is zero, and there is a rupture of the flow.

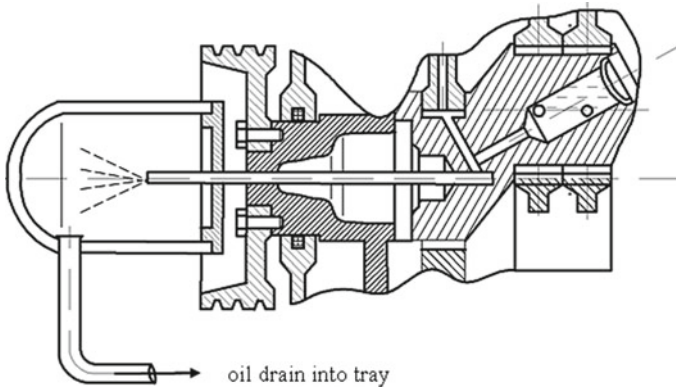


Fig. 3 Detection scheme interrupting the flow and determine the pressure drop from the centrifugal force of the crankshaft axis

Table 2 Pressure loss in the crankshaft channel from the action of centrifugal forces (to the axis of rotation) on the first crank

n	t_{oil}	P_g	P_1	P_6	$P_1 - P_6$	$P_g - P_6$
min^{-1}	$^{\circ}C$	MPa	MPa	MPa	MPa	MPa
2000	80	0.100	0.100	0	0.100	0.100
2100	78	0.130	0.128	0	0.128	0.130
2200	87	0.140	0.124	0	0.124	0.140
2300	86	0.160	0.148	0	0.148	0.160
2400	85	0.170	0.156	0	0.156	0.170
2500	85	0.180	0.160	0	0.160	0.180
2600	86	0.182	0.168	0	0.168	0.182
2700	86	0.200	0.176	0	0.176	0.200
2800	89	0.230	0.196	0	0.196	0.230
2930	92	0.270	0.216	0	0.216	0.270

Note P_g —oil pressure on the bench pressure gauge; P_1 —pressure in the annular channel of the first main bearing; P_6 —pressure along the crankshaft axis; $P_1 - P_6$ —losses from centrifugal forces; $P_g - P_6$ —total losses

Forced reduction of pressure in the lubrication system (with bypass filter in the pan) was achieved at different frequencies of rotation of the termination of expiration of oil from the tube. The results are shown in Table 2.

From Table 2, it follows the value of losses in the crankshaft channel from the action of centrifugal forces is significant and is at frequencies more than 2000 min^{-1} from 20 to 50% of the nominal pressure ($n = 2600 \text{ min}^{-1}$, $\Delta P_{1-6} = 0.168 \text{ MPa}$, $\Delta P_{g-6} = 0.182 \text{ MPa}$). The flow rupture was detected by stopping the oil flow from the end of the tube.



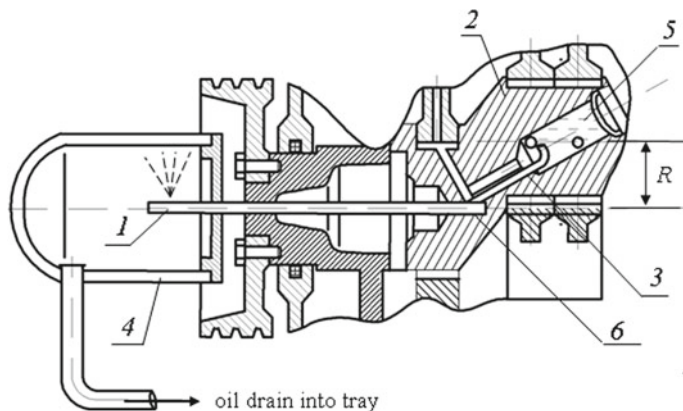


Fig. 4 Scheme for determining the loss of pressure to the connecting rod of the cavity and its filling: 1—probing tube; 2—the connecting rod neck; 3—the oil channel; 4—cap; 5—connecting rod cavity; 6—channel along the axis of the crankshaft; R —the radius of the rod

At the next stage of research, the value of pressure loss during the oil supply to the connecting rod cavity was determined (Fig. 4). For this purpose, the cavity was administered tube 1. The end of the tube, located inside the connecting rod cavity, was opposite the hole. Draining the oil reduced pressure until, until the various frequencies of rotation of the crankshaft from the tube did not stop the outflow of oil. Since at the point 5 of the oil intake pressure is equal to $P_5 = P_{ct} + P_{din}$, where P_{ct} —static pressure inside the connecting rod cavity channels; P_{din} —pressure generated by centrifugal forces at a radius of $R = 60$ mm, and when the oil exits the tube on the section of the inclined channel, it overcomes the action of centrifugal forces ($-P_{din}$), the expiration of the tube means the presence of static pressure in the connecting rod cavity, that is the filling of the connecting rod cavity with oil. The absence of expiration suggests that the connecting rod cavity is not filled, the static pressure in it is zero, all the pressure developed by the pump went to overcome the losses in the previous sections.

Table 3 presents the obtained values of the pressure at which the terminated end of the hollow rod journal on the strand gauge and in the root pole at the frequency of rotation of a cranked shaft of 2000 min^{-1} and above.

Table 3 shows

- there are modes of breaking the flow when approaching the connecting rod in the cavity when the cavity is not filled with oil (this mode let us call the first critical). Engine operation in this mode is not allowed;
- termination of the oil flow into the connecting rod cavity occurs when the pressure in the annular channel of the root support and losses from the centrifugal forces in area 1–3 (Fig. 1).

Table 3 Loss of pressure to the connecting rod cavity

n	t_{oil}	P_g	P_1	P_5	P_1-P_5	P_g-P_5
min^{-1}	$^{\circ}\text{C}$	MPa	MPa	MPa	MPa	MPa
2000	86	0.100	0.100	0	0.100	0.100
2200	86	0.130	0.120	0	0.120	0.130
2400	93	0.140	0.136	0	0.136	0.140
2600	92	0.160	0.156	0	0.156	0.160
2930	90	0.220	0.196	0	0.196	0.220

Note P_1 —static pressure in the annular channel; P_g —pressure on the bench pressure gauge; P_5 —static pressure in the connecting rod cavity; P_1-P_5 —losses from centrifugal forces; P_g-P_5 —total losses

Table 4 Modes periodic filling rod journal

n	M_t	t_{oil}	P_g	P_1	T_c	τ_3	τ_o
min^{-1}	N•m	$^{\circ}\text{C}$	MPa	MPa	s	s	s
2000	20.6	80	0.177	0.160	63	48	15
2425	22	86	0.198	0.188	80	44	36
2418	22	87	0.200	0.176	73	41	32
2608	24	91.5	0.220	0.208	65	29	36
2644	25	98	0.246	0.220	115	55	60
2800	33	103	0.298	0.240	51	27	24
2777	32.4	101	0.275	0.236	92	39	53
2904	42.2	105	0.293	0.248	57	24	33
2910	39.6	105	0.290	0.240	74	27	470

Note T_c —cycle period, s; τ_3 —duration of filling; τ_o —duration of emptying

Pressures in the lubrication system are higher than indicated in Table 3. The connecting rod cavity is filled with oil (e.g., at $n = 2600 \text{ min}^{-1}$, $P_g \geq 0.160 \text{ MPa}$). Moreover, in the pressure interval between the state when the cavity is empty and filled, the regime of periodic filling and emptying of the cavity is found. This mode occurs, obviously, with the alternating balance of oil flow from the connecting rod cavity through the bearings and the inflow into it. Expiration modes were observed on the trace on the transparent cap 4 (Fig. 4). The cycle duration was measured by a stopwatch for at least seven cycles.

In order to detect intermittent expiration, the expiration termination mode was set (Table 3), then a small decrease in the frequency of rotation of the crankshaft sought to start the expiration. The cavity is filled periodically. The results are presented in Table 4.

Table 4 shows

- there are modes of breaking the flow with periodic fill connecting rod cavity with the oil, at which time a cavity is not filled. The operation of the engine in this mode is also not allowed (this mode comes before the first, although it is detected later and is called the second critical);

- the pressure in the lubrication system at which the second critical mode (periodic filling) occurs is higher than at the empty cavity by 0.05–0.07 MPa (the first critical mode);
- constant filling of the connecting rod cavity occurs when the pressure increases by 0.02–0.03 MPa relative to the pressure in the second mode of periodic filling.

The KAMAZ engine plant has made significant improvements to the engine design [8–12]. The number of failures in operation decreased; however, there was a change in the design of the crankshaft through the oil channels, and where the lubrication system increased engine power, and the crankshaft bearing capacity remains low.

Therefore, the physical process of flow rupture (periodic filling and emptying of the connecting rod cavity) requires further study and explanation.

Further studies of the oil supply conditions to the crankshaft bearings were carried out using ANSYS Workbench ver. 12 [12]. The aim of this study was to reproduce the lubrication conditions of the crankshaft bearings and to observe the change in pressure at characteristic points in different operating modes of the engine. This was developed for the three-dimensional model of root channels and connecting rod journals, input parameters corresponding to the modes, and working conditions of crankshaft bearing: the geometric dimensions of the channels of the crankshaft; the oil; oil temperature; engine speed; intake pressure in the crankshaft bearing.

In the course of the research, it was found that at the maximum speed of the crankshaft, the action of centrifugal forces on the moving oil flow becomes essential. In the root neck channel, a centrifugal force arises that acts on the oil supplied and is directed from the center of the root neck, which tends to dynamically lock the incoming oil at the entrance to the root neck channel. On the other hand, in the inclined channel of the oil supply to the connecting rod neck, the oil flow is accelerated under the action of pressure from the centrifugal force and seeks to break the continuity of the oil flow. Thus, the effect of centrifugal forces on the formation of the locking pressure from 0.184 to 0.206 MPa at the inlet to the channel and the accelerating pressure up to 0.249–0.271 MPa is confirmed (Fig. 5) in the centrifugal trap, leading to the imbalance of oil supply and the rupture of the oil flow.

The conducted research allowed to explain the physical meaning of the oil flow rupture. The physical process of periodic filling and emptying of the connecting rod cavity requires further study. For this purpose, the study of the conditions of oil flow through the crankshaft rod bearings from the third crank, most often having turning inserts.

Between the third and fourth root support in the cylinder block an isolated compartment is made, allowing to catch and measure the oil flow from the third connecting rod neck (Fig. 6).

In order to avoid oil ingress into the isolated “compartment” from the third and fourth bushings of the camshaft between the partitions of the cylinder block, a metal plate 1 was fixed and on the supports of the third and fourth main necks of the

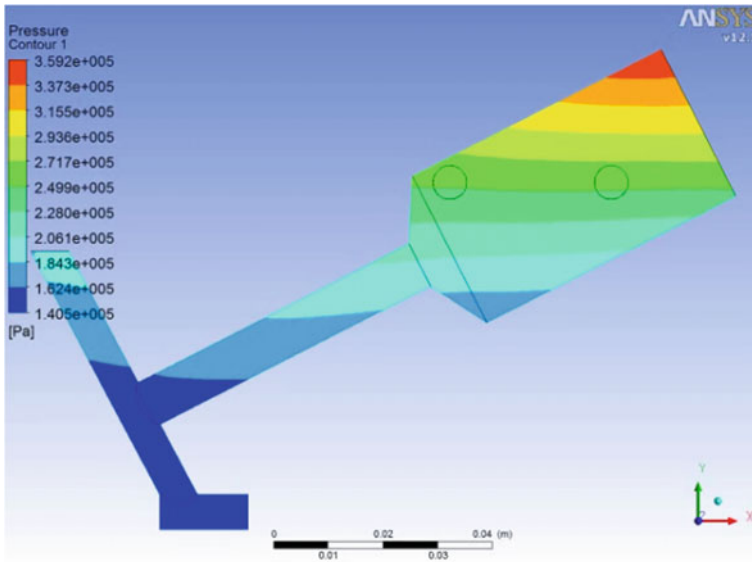


Fig. 5 Distribution of oil pressure in the feed channels at the maximum speed of the crankshaft

crankshaft, the sealing cuffs 2 were installed. In the lower part of the block between the third and fourth root supports, an isolated pallet 3 was mounted, the drain tube of which was brought out through the main engine tray. These improvements were carried out in order to ensure that only oil is collected in the insulated pallet, which merges through the connecting rod bearings of the third and seventh cylinders of the engine.

The oil flow rate through the connecting rod bearings of the third and seventh cylinders was determined by weighing the oil received in one minute from the isolated pallet 3 to the measuring container 4 at different operating modes of the engine.

The studies were carried out on the test stand of the company “AVL,” with the hydraulic brake of the company “SCHENCK.” The stand is equipped with the necessary equipment and devices, the accuracy of which meets the requirements of GOST 14846. All test bench devices are certified and calibrated.

When assembling the engine, the micrometer of the third connecting rod neck and connecting rods with inserts was carried out. At the first stage, the oil flow rate was determined at a nominal gap of 0.10 mm.

The engine is filled with oil M 8 G2K; the pressure control valve is fully open; the adjustment set the pressure in the lubrication system $P = 0.2$ MPa. The external high-speed characteristic of the engine was removed, recording all the readings of devices and sensors, as well as measuring the amount of oil to drain from the third connecting rod neck. Then, the pressure in the lubrication system was raised to

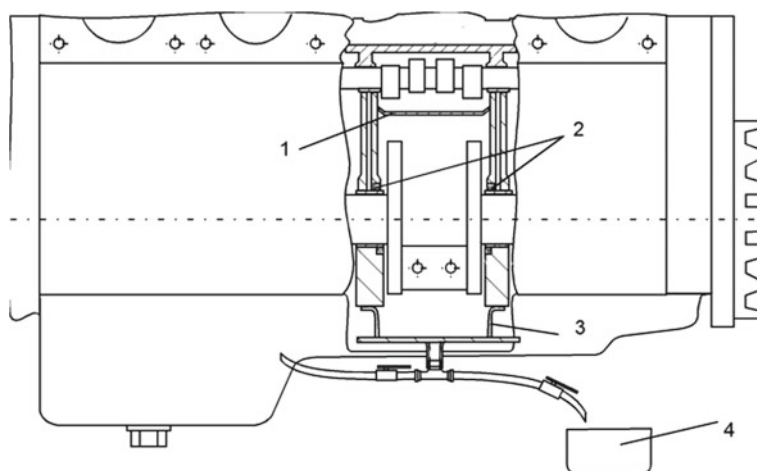


Fig. 6 Scheme of measurement of the actual oil flow rate from the third connecting rod neck to the drain on the running engine: 1—metal partition; 2—sealing sleeve; 3—insulated tray; 4—dimensional capacity

$P = 0.3$ MPa and the external velocity characteristic was removed. So repeated the research, gradually raising the pressure to $P = 0.7$ MPa. At all modes of operation of the engine, the amount of oil on the drain from the third connecting rod was measured. The results are shown in Fig. 7.

The actual oil flow rate to drain 1 in the pressure range from 0.26 MPa below the required 2 [12] and even reaches zero (crosses the abscissa axis). This is nothing more than a flow break in different modes (Fig. 7).

When measuring the oil flow through the connecting rod bearings, the effect of “pulsation” of the oil flow flowing out of the compartment with the termination and restoration of the expiration is revealed. The effect of the “surge” is a periodic cessation of the expiration of oil and then increases the intensity after a certain period of time. The duration of the flow intensity is 3–4 s. This ripple was observed at the speed of the crankshaft, starting from 1600 min^{-1} and above, in the region of inflection of the actual flowchart (Fig. 7).

Depending on the set oil pressure in the engine lubrication system, the nature of the “pulsation” of the oil flow varies. By reducing the set oil pressure from 0.5 to 0.25 MPa, the beginning of the ripple is shifted from the speed of the crankshaft 1600 to 2000 min^{-1} . The amplitude of the “ripple” is also changing. The number of “pulsations” of the oil flow for the same periods of measurement time increases with the increasing speed of the engine crankshaft. When the pressure in the lubrication system is higher than the inflection point, the connecting rod cavity is filled with oil.

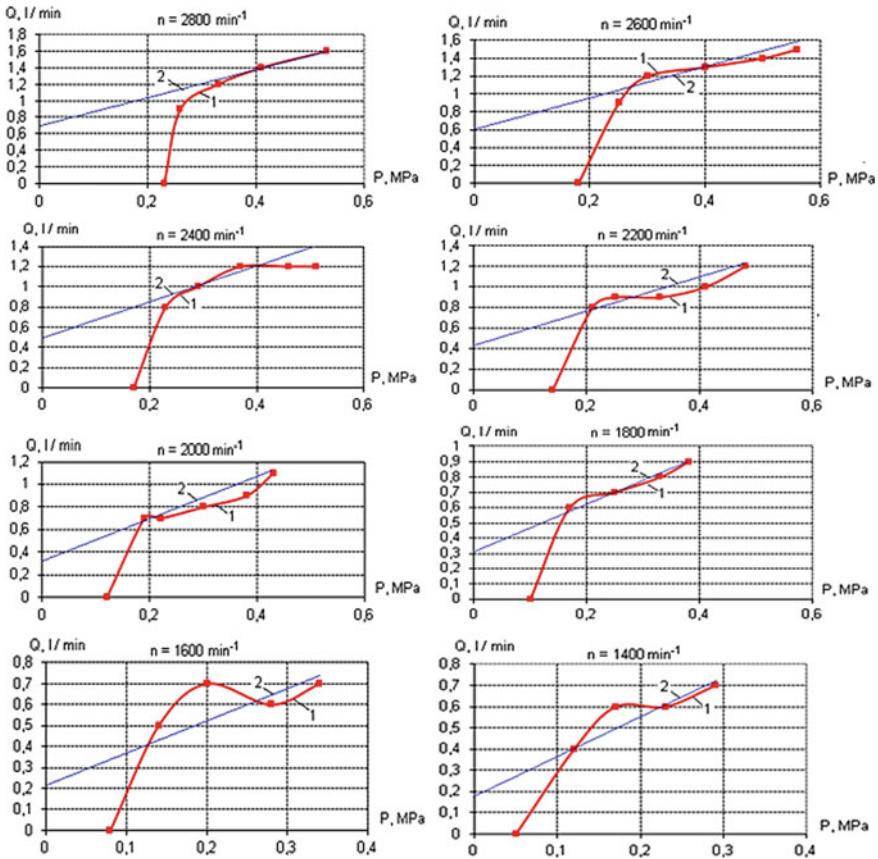


Fig. 7 Oil flow through the connecting rod bearings of the third neck at different frequencies and set pressures in the lubrication system: 1—oil flow from the third connecting rod neck, measured on the drain (actual); 2—the required oil consumption

4 Conclusion

1. Are the modes of rupture of the oil flow supplied to the connecting rod cavity? This occurs when the pressure in the annular channel of the main bearing is equal to the pressure of the losses from the centrifugal forces, and when the pressure on the crankshaft axis is zero.
2. Very significant pressure loss in the channels of the crankshaft from the action of centrifugal forces and is at frequencies more than 2000 min^{-1} from 20 to 50% of the nominal pressure, which acts to reduce the flow of oil to the connecting rod bearings.



3. The pressure in the annular channels of the main bearings is much lower than the standard pressure gauge (74% at idle and 67% under load). The unevenness on the main bearings is 10%. The most significant decrease in pressure is due to wear of the main bearings with a general decrease in pressure in the lubrication system.
4. Critical regimes of the oil supply to the connecting rod bearings are the cause of their failure in the process of operation and come on the runs of 120–150 thousand km when the pressure in the lubrication system below 0.26 MPa.
5. The reason for the “pulsation” and the frequency of oil consumption on the drain from the connecting rod bearings can be the form of connecting rod inserts.
6. In connection with the change in the design of the crankshaft by oil channels, lubrication system and engine power KAMAZ need to conduct research on the above methods for currently produced engines.

References

1. Kulakov AT, Denisov AS (1981) Analysis of the causes of service failures of the connecting rod liners of engines KAMAZ-740. *Engine Eng* 9:37–40
2. Barylnikova EP, Kovrikov IT, Kovalenko SYu (2014) The increase in online automobile engines by stabilization of a greasing mode of the connecting rod bearing in operation. *Bull Oren-Burg State Univ* 10(171):15–22
3. Kulakov AT, Denisov AS, Kulakov OA (2012) The kinetics predating condition and maintainability of the crankshaft. LAP LAMBERT Academic Publishing, Saarbrücken
4. The Engine KamAZ-740.11-240 (1977) The user manual for 740.11-3902001PЭ. Naberezhnye Chelny
5. Kulakov AT, Denisov AS, Makushin AA, Barylnikova EP (2015) Design-technological methods of ensuring reliability of automotive bearings operating results. Kazan Publishing House UN-TA, Kazan
6. Kulakov AT (1986) Development of a method for diagnosing connecting rod bearings of engines and practical recommendations to reduce their failures in the process of operation (for example, KAMAZ-740). Dissertation, Saratov
7. Smirnov VG, Luchinin BN (1980) Increasing the durability of automotive engine parts by improving the design of lubrication systems. Neonatorum, Moscow
8. Kulakov AT, Barylnikova EP, Gafiyatullin AA (2014) Providing normal conditions of lubricating of diesel engine during its operation. IOP conference series: materials science and engineering. <https://doi.org/10.1088/1757-899x/69/1/012027>
9. Kulakov AT, Barylnikova EP, Talipova IP, Kulakov OA (2018) Self-regulating lubrication system that takes into account the wear of the bearings of internal combustion engines in process of operation. *Nat Tech Sci* 4(118):161–163
10. Kulakov AT, Barylnikova EP, Kulakov OA (2017) Adaptive system of supplying lubricant to the internal combustion engine. IOP conference series: materials science and engineering. <https://doi.org/10.1088/1757-899x/240/1/012010>
11. Kulakov AT, Svetlichnyi NI, Gafiyatullin AA (2003) Improvement of the design of a crankshaft of the engine KAMAZ. *Engine Eng* 3:24–26
12. Barylnikova EP (2013) The increase in online automobile engines by stabilization of a greasing mode of the connecting rod bearing to use. Dissertation, Orenburg State University

Investigations of Antifriction Films Formation in Dioctyl Sebacate Medium with Cholesteryl Esters



M. V. Boiko, A. P. Sychev and I. V. Kolesnikov

Abstract In the article, investigations of antifriction films formation at friction in dioctyl sebacate (DOS) medium with additives of cholesteryl esters of caproic and oleic acids. The relevance of the study is due to the development of biodegradable lubricants. The time required to achieve a friction coefficient of 0.02 in DOS medium occurs after 20,000 s from the start of the test, in DOS with 3% LCKA medium after 13,000 s, and DOS with 3% LCOA medium after 1000 s. The elemental analysis of antifriction films showed that the films contain organic and inorganic components. The organic part consists of dioctyl sebacate molecules. The inorganic part includes iron compounds. Cholesteryl esters are capable of planar orientation on friction surfaces and form layered structures in the zone of tribocontact. This provides an additional reduction in the friction coefficient and an increase in the energy-saving properties of the lubricant. This effect is achieved due to the realization in the friction zone of the mesomorphic state of a lubricant, which is characterized by an ordered oriented arrangement of the molecules of the mesogenic additive.

Keywords Antifriction film · Lubricants · Cholesteryl ester of caproic acid · Cholesteryl ester of oleic acid · Dioctyl sebacate · IR spectroscopy · Scanning electron microscopy

1 Introduction

Currently, virtually all areas of technology use lubricants. Lubricants in various friction units have many important functions, in particular, they reduce wear of friction parts, protect machine parts from corrosion, reduce operating temperature, noise, remove wear particles from the contact area, thereby preventing abrasive

M. V. Boiko (✉) · A. P. Sychev · I. V. Kolesnikov
Rostov State Transport University, 2, Rostovskogo Strelkovogo Polka Narodnogo
Opolcheniya Sq, Rostov-on-Don 344038, Russia
e-mail: m2487328@yandex.ru

wear of surfaces, and also reduce the coefficient of sliding friction [1–4]. The latter discloses the energy-saving function of lubricants. Lowering the frictional force, we accordingly reduce the energy loss for friction and, thus, reduce fuel or electric power consumption for the operation of the device. A large number of high-performance lubricants for various friction units have been developed, allowing to save significant quantities of fuel or other forms of energy; however, even a slight further improvement in the energy-saving properties of the lubricant results in even greater savings, which in the total, taking into account the long-term use of the device produce tangible economic effect. Thus, it seems advisable to carry out research in the field of technologies that allow achieving high antifriction properties of lubricants. The process of formation of antifriction films on friction surfaces can be attributed to such technologies. These films provide high antifriction and, as a consequence, energy-saving properties of lubricants, however, their nature, and patterns of formation are not fully understood.

We have found that during friction of steel bodies in a medium of dioctyl sebacate (DOS), a film is formed on the friction surface. Film formation leads to a significant (up to 2–3 times) reduction of the friction coefficient. Dioctyl sebacate can be obtained using enzymatic synthesis [5] or from castor oil, which belongs to renewable sources. The use of oils from renewable sources as lubricants is a promising direction in the development of the science of lubricants, since natural reserves of hydrocarbons are depleted every year. In addition, dioctyl sebacate belongs to biodegradable lubricants [6–8]. This suggests that if released into the environment as a result of leakage from the friction unit, this lubricant will biodegrade over time and will not harm the environment.

In addition, the main classes of lubricant additives currently used are also often poorly biodegradable and can cause significant environmental damage.

The purpose of this work is to study cholesteryl esters of caproic (LCKA) and cholesteryl esters of oleic acids (LCOA) as additives to biodegradable oils based on dioctyl sebacate.

Cholesteryl esters are a popular object of study as additives to oils and greases [9–15]. They have shown their effectiveness in petroleum-based lubricants. At the same time, their use in ester oils has not been studied.

2 Materials and Methods

Tribological tests of lubricants were carried out on the end friction machine according to the scheme “three pins on the steel disk.” Pins and disk were made from AISI 420S steel, roughness was $R_a = 1.5$. The diameter of each pin was 1 cm, and the distance from the center of the disk to the middle of the friction track was 35 mm. For the repeatability of the tribological tests, the pins previously were repeatedly polished to the steel surface of the disk with same roughness. All tests began without running-in of rubbing surfaces, considering that the antifriction film formed during the experiment will smooth out the surface roughness of the disk,

thereby reducing the friction coefficient. Among the all friction parameters, we controlled only the friction coefficient. The load on the friction unit was 2 MPa and the sliding speed was 0.5 m/s for all tests.

The presence of the film on the friction surface was confirmed by a scanning electron microscope Zeiss EVO-18 MA equipped with BSD, SE, and X-Max 50 sensors. The accelerating voltage varied from 5 to 15 kV. The film is an insulator, and therefore its presence on the metal is clearly detectable. The steel surfaces were pre-treated with a solvent to remove excess of lubricant. Elemental microanalysis of the surface was performed with an X-Max SDD detector. The active area of the detector crystal was 50 mm². SDD detector X-Max allows count rate, imaging, and analytical performance all at the same time. Its parameters: up to 80 mm² active area; count rates > 500,000 cps; throughput > 200,000 cps; MnK_α typically 125 eV.

Antifriction films were studied using FTIR spectroscopy with an ATR attachment on a Nicolet 380 instrument.

Objects of research were dioctyl sebacate (DOS), dioctyl sebacate with 3% cholesteryl esters of caproic acid (LCKA), and dioctyl sebacate with 3% cholesteryl esters of oleic acid (LCOA). The additive concentration of 3% is selected as the most effective according to the results of previous studies [16].

3 Results and Discussion

Tribinological tests performed on the pin-on-disk friction machine showed that adding cholesteryl esters of caproic and oleic acids reduces the friction coefficient in the system, Fig. 1. At the same time, cholesteryl ester of oleic acid is most effective. The time required to achieve a friction coefficient of 0.02 in DOS medium occurs after 20,000 s from the start of the test, in DOS with 3% LCKA medium after 13,000 s, and DOS with 3% LCOA medium after 1000 s.

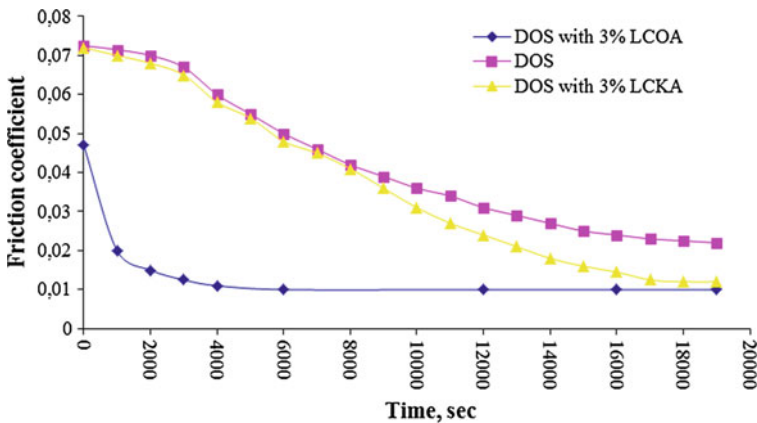


Fig. 1 Results of tribological tests

Using SEM, an image of the friction surface in DOS with 3% LCOA medium was obtained, Fig. 2.

An element analysis of the disk surface without friction (area 1 in Fig. 3), the surface of the antifriction film on the friction track (area 2 in Fig. 3), and the friction track (area 3 in Fig. 3) were carried out. The results of the study of the elemental composition of the surface using the X-Max SDD detector are shown in the Table 1. The content of each element is given in atomic percent.

For element analysis, the disk was pre-cut on a cutting machine and a 1 cm 1 cm sample containing an antifriction film was obtained. The obtained sample was thoroughly washed with deionized water 5–6 times.

The surface without friction (area 1 in Fig. 3), in addition to the elements inherent in steel, contained some amount of carbon and oxygen related to organic contamination of the surface.

The surface of the antifriction film on the friction track (area 2 in Fig. 3) contains a large amount of carbon, oxygen, and iron. The presence of sodium, magnesium, sulfur, chlorine, potassium, and calcium on the surface is explained by the interaction of the disk with the cutting fluid during cutting. The high content of aluminum and silicon is associated with contamination of the surface with residues of abrasive particles. Area in Fig. 3 contains both surface without friction and areas covered with an antifriction film. Elemental analysis of this area shows the average value between areas 1 and 2 (Fig. 3).

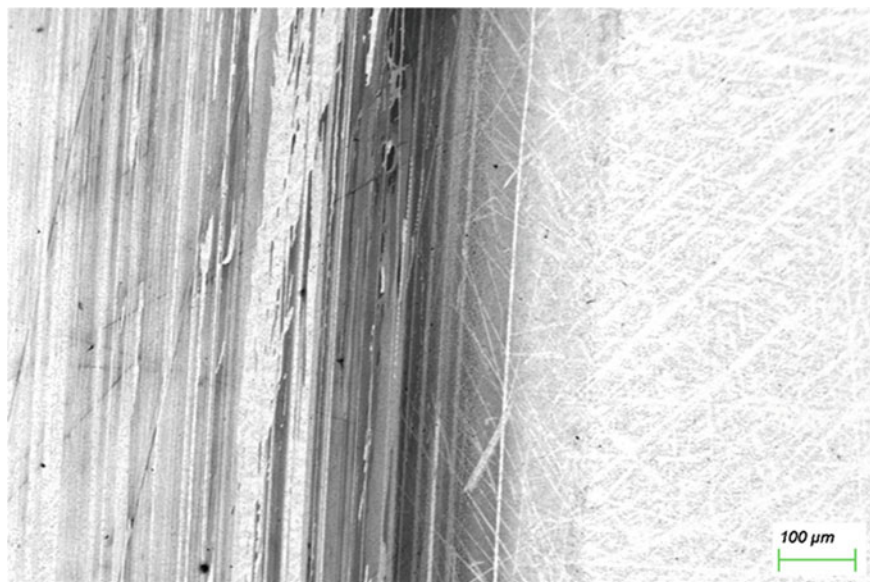


Fig. 2 SEM image of the friction track formed in DOS with 3% LCOA medium

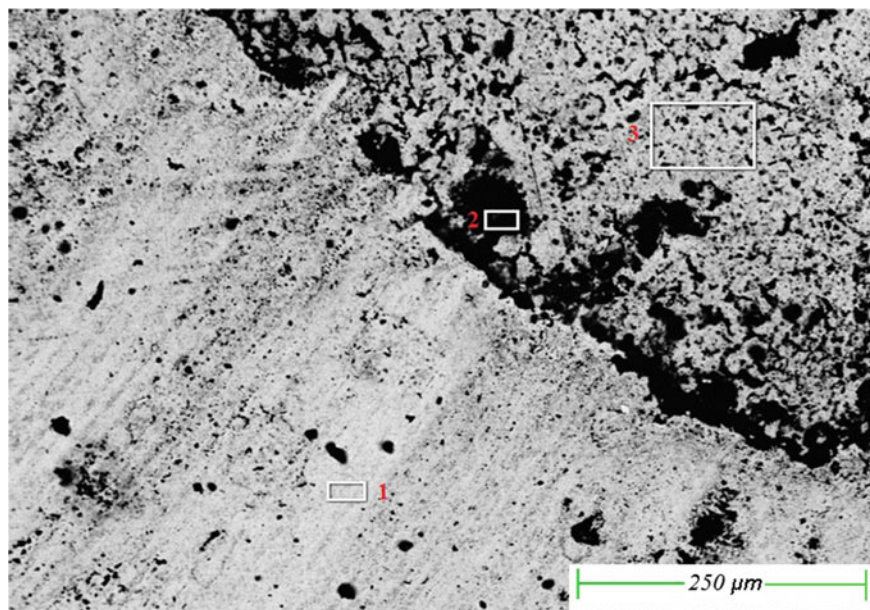


Fig. 3 SEM image of the areas in which elemental analysis was determined

Table 1 Results of the study of the elemental composition of the surface

Surface area number	C	O	Na	Mg	Al	Si	S	Cl	K	Ca	Cr	Fe
1	3.19	2.5	-	-	0.08	0.29	-	-	-	-	15.65	78.29
2	54.02	19.75	3.22	0.33	1.49	3.63	1.42	1.42	2.18	1.85	-	10.68
3	8.5	3.55	0.39	-	-	0.33	0.12	0.16	-	-	13.33	73.62

The data obtained indicate that the antifricition film contains both the organic and inorganic components. The organic part consists of dioctyl sebacate molecules. The inorganic part includes iron compounds, for example, oxides.

Antifricition films were studied using IR spectroscopy with an ATR attachment. Pre-gasoline removed excess oil from the friction surface. The spectra of antifricition films formed in the DOS with 3% LCKA medium and DOS with 3% LCOA medium environment completely coincide with the spectrum of the friction track formed in the DOS medium, Fig. 4. This indicates that the antifricition film is formed from DOS molecules. At the same time, cholesteryl esters are capable of planar orientation on friction surfaces and form layered structures in the zone of tribocontact. This provides an additional reduction in the friction coefficient and an increase in the energy-saving properties of the lubricant. This effect is achieved due to the realization in the friction zone of the mesomorphic state of a lubricant, which

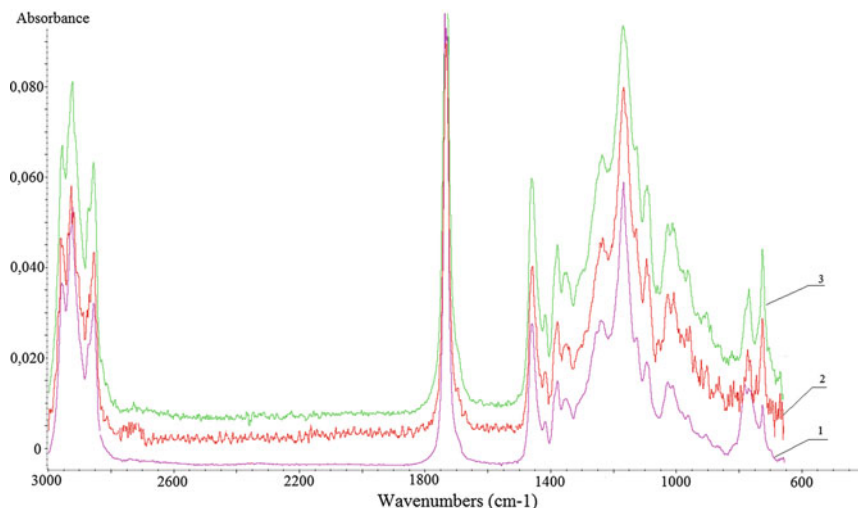


Fig. 4 IR spectra of antifriction films formed in the medium: 1—DOS, 2—DOS with 3% LCKA, and 3—DOS with 3% LCOA

is characterized by an ordered oriented arrangement of the molecules of the mesogenic additive. LCOA is more effective for reducing friction due to better solubility in DOS, which is provided by the longer hydrocarbon radical of the acid residue.

4 Conclusion

1. The addition of cholesteryl esters of fatty acids to dioctyl sebacate-based lubricants improves their energy-saving properties.
2. The most effective additive cholesteryl ester of oleic acid.
3. Antifriction film is formed from DOS molecules.
4. The increase in the energy-saving properties of the lubricant occurs due to the formation in the friction zone of the mesomorphic state of the lubricant, which is characterized by an ordered oriented arrangement of the mesogenic additive molecules.
5. Antifriction film contains both the organic and the inorganic components. The organic part consists of dioctyl sebacate molecules. The inorganic part includes iron compounds.

Acknowledgements The study has been supported of the Russian Science Foundation (project No. 18-19-00292).

References

1. Persson BNJ (2000) Sliding friction. In: Physical principles and applications. Berlin, Heidelberg
2. Chan C-H, Tang SW, Mohd NK et al (2018) Tribological behavior of biolubricant base stocks and additives. *Renew Sustain Energy Rev* 93:145–157. <https://doi.org/10.1016/j.rser.2018.05.024>
3. Colyer CC (2017) The SAE Lubricants Review Institute—purpose and operation. Society of Automotive Engineers Inc
4. Turner CH, Oldridge K (1987) Rolling lubricants in today's environment. *Steel Times* 9:462–466
5. dos Santos Corrêa IN, da Silva SSP, de Queiroz DS et al (2016) Enzymatic synthesis of dioctyl sebacate. *J Mol Catal B Enzym* 133:S166–S171. <https://doi.org/10.1016/j.molcatb.2016.12.011>
6. Renewable Lubricants Inc. (2006) Understanding biobased/biodegradable and the industry's standardized tests and definitions. <http://renewablelube.com/files/4514/4734/8222/standardized.pdf>. Accessed 07 June 2006
7. Zainal NA, Zulkifli NWM, Gulzar M, Masjuki HH (2018) A review on the chemistry, production, and technological potential of bio-based lubricants. *Renew Sustain Energy Rev* 82:80–102. <https://doi.org/10.1016/j.rser.2017.09.004>
8. Mannekote JK, Kailas SV, Venkatesh K, Kathyayini N (2018) Environmentally friendly functional fluids from renewable and sustainable sources—a review. *Renew Sustain Energy Rev* 81:1787–1801. <https://doi.org/10.1016/j.rser.2017.05.274>
9. Biresaw G et al (1990) Tribology and the liquid-crystalline state. In: American Chemical Society, Symposium Series, I, vol 441
10. Chen H, Xu C, Xiao G et al (2018) Ultralow friction between steel surfaces achieved by lubricating with liquid crystal after a running-in process with acetylacetone. *Tribol Lett* 2:68. <https://doi.org/10.1007/s11249-018-1020-3>
11. Rodnenkov VG, Kupchinov BI (2000) Tribological behavior of liquid crystalline cholesterol compounds. *Trenie Iznos* 1:41–46
12. Iglesias P, Bermúdez MD, Carrión FJ, Martínez-Nicolás G (2004) Friction and wear of aluminium-steel contacts lubricated with ordered fluids-neutral and ionic liquid crystals as oil additives. *Wear* 3–4:386–392. [https://doi.org/10.1016/S0043-1648\(03\)00442-3](https://doi.org/10.1016/S0043-1648(03)00442-3)
13. Ermakov SF, Parkalov VP, Shardin VA, Shuldykov RA (2004) The effect of liquid crystalline additives on the triboengineering characteristics of dynamically contacting surfaces and the mechanism of their friction interaction. *Trenie Iznos* 2:213–218
14. Ermakov SF, Beloenko ED, Eismont OL (2004) The role of liquid crystals in tribomechanical properties of joint cartilages. *Trenie Iznos* 5:486–491
15. Berezina EV, Godlevskiy VA, Usol'Tseva NV (2016) Investigation of cholesteric liquid crystals and carbon nanotubes additives on mineral oil antifrictional and rheological characteristics. *Procedia Eng* 150:579–583. <https://doi.org/10.1016/j.proeng.2016.07.044>
16. Ermakov SF, Kolesnikov VI, Sychev AP (2016) Lubricity of cholesteric liquid-crystal nanomaterials in friction of solids. *J Friction Wear* 2:136–140. <https://doi.org/10.3103/S1068366616020057>

Dependence of Automatic Installation of Tool Carrier Process on Orientation Errors and Their Effect on Performance Characteristics of Spindle-Tool Subsystem



O. Yu. Kazakova and L. B. Gasparova

Abstract The mandrel taper errors connected with its manufacture may be added by the operation errors emerging as a result of wearing out caused by friction in the mating conical surfaces. Depending on the ratio of deviations from parallelism and alignment of mandrel taper and spindle socket and their directions, the initial tool carrier contact may occur at the point of a large spindle socket diameter (intensive wearing out of the mandrel taper bottom part and the spindle socket) or at the point of a small diameter of the mandrel taper (intensive wearing out of the upper part of the mandrel taper and the spindle socket). The formation of the friction path will depend on the initial contact of the mandrel taper and the spindle socket. The result of the study includes obtaining dependencies that allow determining the areas of intense wearing out and contacting pressures when using the automatic tool changer system, depending on the deviations of the mandrel axes and the spindle socket from alignment and parallelism at the moment of initial contact determined by the auto operator's work errors.

Keywords Automatic tool change · Errors · Tool carrier/mandrel · Spindle · Machine tool · Wearing out

1 Introduction

The deviations of the linear and angular dimensions of the tool carriers significantly affect the spindle-tool subsystem accuracy characteristics [1–3]. It is also important to ensure minimal errors in the shape which lead to a decrease in the rigidity of the system due to a significant reduction in the contact area. Errors in the shape of the tool carriers are formed during manufacture and operation.

O. Yu. Kazakova (✉) · L. B. Gasparova
Samara State Technical University, 244, Molodogvardeyskaya Str., Samara 443100, Russia
e-mail: kzakova8080@mail.ru

The shape errors that occur during manufacturing are easier to control and minimize. The shape errors may also occur during operation time due to wearing out arising from the friction of conical surfaces. And the surface unevenly wears out. Therefore, it is difficult to control this process, taking into consideration the complicated wearing out mechanism during operation.

However, detecting intensive wearing out zones depending on the features of the automatic tool changer systems will allow predicting the change in the shape of the contacting surfaces as well as the change in performance characteristics of spindle-tool subsystem [4–7].

2 Intensive Wearing Out Zones Depending on the Features of the Automatic Tool Changer Systems

To assess wearing out, we assume that the mandrel axes and spindle sockets do not cross, that is, lie in the same plane. We also assume that the rotation of the mandrel during basing occurs around the axis that coincides with the axis of the manipulator arm [8, 9].

Depending on the ratio of the deviation from parallelism and the alignment of the mandrel tool and the spindle socket and their directions, the initial contact of the mandrel and the spindle can be at the point of a large spindle socket diameter (Fig. 1a) (intensive wearing out of the mandrel taper bottom part and the spindle socket) or at the point of a small diameter of the mandrel taper (Fig. 1b) (intensive wearing out of the upper part of the mandrel taper and the spindle socket).

In order to determine the friction path for the cases under consideration, we find the position of the corresponding cones at their initial contact. As for the case shown in Fig. 1a, the axes of the mandrel and the socket deviate from alignment by the value; the mandrel is at the position shown in Fig. 2, at the initial contact. The

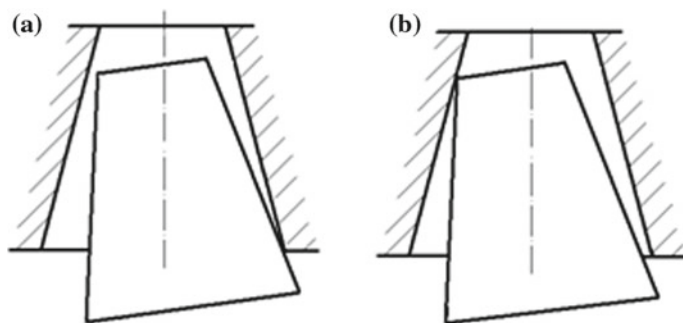


Fig. 1 Diagram of the initial contact of the mandrel and the spindle socket: **a** contact at the point of a large spindle socket diameter; **b** contact at the point of a small diameter of the mandrel taper

Fig. 2 Position of the mandrel tool with the initial touch of the spindle socket if there is a deviation of their axes from alignment

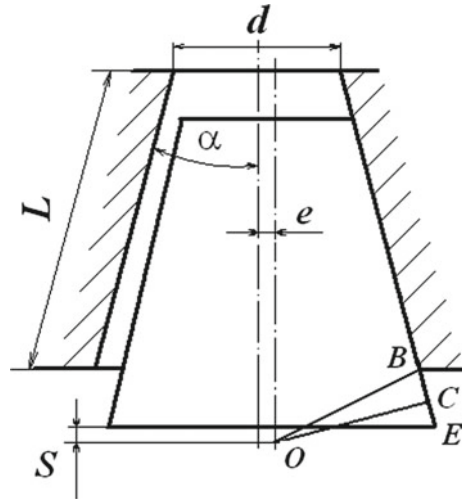
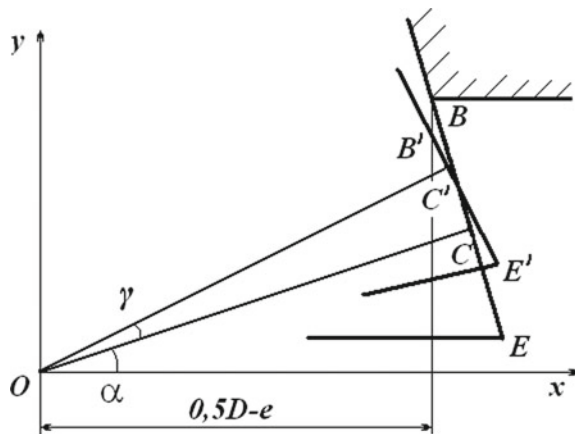


Fig. 3 Position of the mandrel tool and the spindle socket if there is a deviation of their axes from alignment and parallelism



further rotation of the axis of the mandrel relative to the axis of the spindle socket occurs according to the angle of the initial contact is shown in Fig. 3.

From the figures, it is clear that with both errors given in the axial shift of the mandrel in the socket point *B* at the point of a large spindle socket diameter is tangent to the mandrel taper at the point *B'* and then the path of friction on the mandrel will correspond to the distance.

$$B'E' = B'C' + C'E' \tag{1}$$

$$C'E' = CE = (0.5d + L \sin \alpha + Stg \alpha) \cos \alpha \tag{2}$$

The point C corresponds to the intersection of the perpendicular from the point of rotation of the mandrel O (Fig. 2) on the forming taper. Writing down the equation of the mandrel forming in the XOY coordinate system (Fig. 3), we shall find the coordinates of the points B' and C' .

$$x_{B'} = 0.5d + L \sin \alpha - e \quad (3)$$

$$y_{B'} = \frac{(0.5d + L \sin \alpha + \text{Stg } \alpha) \cos \alpha - (0.5d + L \sin \alpha - e) \cos(\alpha + \gamma)}{\sin(\alpha + \gamma)} \quad (4)$$

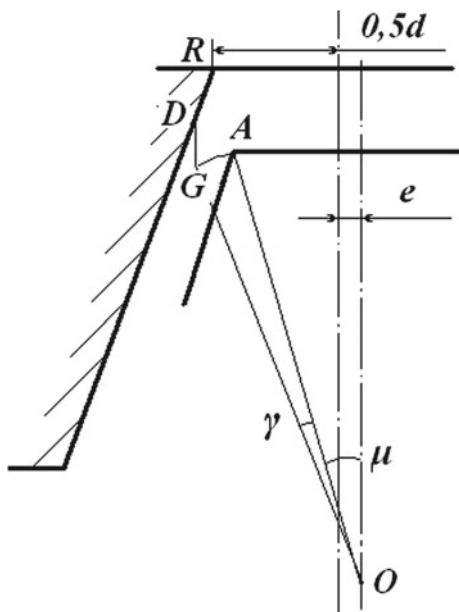
$$x_{C'} = \frac{(0.5d + L \sin \alpha + \text{Stg } \alpha) \cos \alpha}{\sin(\alpha + \gamma) [\text{ctg}(\alpha + \gamma) + \text{tg}(\alpha + \gamma)]} \quad (5)$$

$$y_{C'} = \frac{(0.5d + L \sin \alpha + \text{Stg } \alpha) \cos \alpha}{\cos(\alpha + \gamma) [\text{ctg}(\alpha + \gamma) + \text{tg}(\alpha + \gamma)]} \quad (6)$$

$$B'C' = \sqrt{(x_{C'} - x_{B'})^2 + (y_{C'} - y_{B'})^2} \quad (7)$$

The scheme of the slip distance formation for the case shown in Fig. 1b is presented in Fig. 4, where the point A corresponds to the position of the upper left angle of the mandrel with a given deviation from the axis by the value e , and the point G with given deviations from the axis by the value e and from the parallelism by the angle γ . With both these errors given when moving the mandrel into the

Fig. 4 Scheme of the slip distance formation for the case shown in Fig. 1b



spindle socket, their initial contact will occur at a point D and the slip distance will be equal to the segment DR in the further movement of the mandrel.

$$DR = \frac{\gamma \cos \mu \sqrt{4(L \cos \alpha + S)^2 + d^2} - 2e}{2 \sin \alpha} \quad (8)$$

$$\mu = \arctg \frac{d}{2(L \cos \alpha + S)} \quad (9)$$

Realization of the specific scheme presented in Fig. 1 cases will be determined by comparing the sizes of segments BB' (Fig. 3) and GD (Fig. 4): if $BB' < GD$, the scheme shown in Fig. 1a will be represented; if $BB' > GD$, the scheme shown in Fig. 1b will be represented.

As it is widely known [10–12], the wearing out the intensity in connection parts depends on the contact pressure. The estimation of pressures in the zone of the considered contacts can be carried out taking into account various assumptions based on the evaluation of the contact physical nature: consideration of elements of the automatic tool change system as absolutely rigid bodies with absolutely rigid surfaces; consideration of the links of the automatic tool changer system as absolutely rigid bodies with elastic surfaces; solution of the problem under the condition of elastic deformation of the automatic tool changer elements and its contacting surfaces; solution of the problem taking into account elastic–plastic deformation in the automatic tool changer connections [13, 14].

There are significant contact pressures associated with the necessity of providing high rigidity upon fixing the mandrel [15–20]. As it is shown in [1], at significant specific contact pressures (preliminary stresses), it is possible to consider

$$\delta = c\sigma, \quad (10)$$

where

- δ is an elastic deformation;
- σ is a pressure in the connection;
- c is the coefficient.

Thus, to determine the pressure at the connection of the mandrel and spindle, it is necessary to define the elastic contact deformation, determining the spatial position of the mandrel during fixing. In general case, the spatial position of the body in a static load application can be determined from the zero of the main vector condition and the main moment of the external forces affecting the body relative to the arbitrary center. These conditions are necessary and sufficient for the balance of the spatial system of forces. The following external forces affect the mandrel during fixing in the spindle socket: the clamping force which can be taken in a concentrated form; distributed load which occurs due to the elastically deformed surface

layers at the contact point of the mandrel and the spindle; elastic reactions from the manipulator; friction forces in contact.

For working out the estimated model, we shall substitute the distributed load by the concentrated one, considering that for each connection point the same dependence fair is as for the flat connections.

$$P = kV \quad (11)$$

$$V = \delta F, \quad (12)$$

where

V is elastically deformed volume;
 k is coefficient of contact stiffness;
 P is a concentrated load;
 F is a contact area.

We also assume that the resulting elastic strain load is focused at the gravity center of the spatial plot pressure. Since fixing the tool into the spindle is an axisymmetric task, it can be considered on the basis of a two-dimensional (2D) model. However, in this case it is necessary to determine the coefficient as applied to the 2D problem. This can be done from the condition that the net load is equal to the elastic deformation in a 2D and 3D setting:

$$\delta Lk_f = FLk_v \quad (13)$$

where

L is length of the contact.

For a diameter equal to the average diameter of the mandrel tool, we obtain

$$k_f = 0.5k_v(d + L) \sin \alpha, \quad (14)$$

where

d is a small diameter of mandrel tool;
 α is a half angle of mandrel tool.

If there are deviations from alignment e and parallelism γ of the mandrel axes and the spindle socket after the manipulator arrives at the loading position and if the reactions from the manipulator side are preserved while fixing the mandrel, the spatial position of the mandrel relative to the spindle socket will be evaluated by the elastic contact deformations shown in Fig. 5.

To estimate these deformations, we use the equations of forces equilibrium affecting along and perpendicular the axis of the mandrel (projections of the frictional forces on the horizontal axis due to their smallness due to negligibility of angle α are neglected) and equate the moments of forces exerted to the point O .

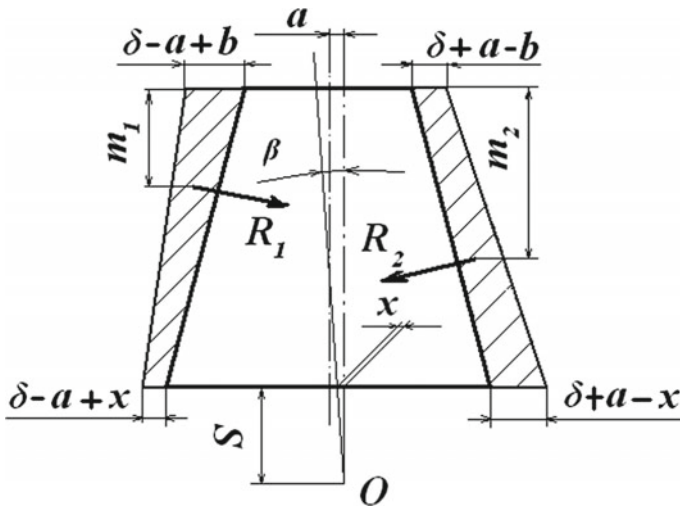


Fig. 5 Spatial position of the mandrel tool and elastic contact deformations upon fixation

$$(R_1 + R_2)(\sin \alpha + f \cos \alpha) - P = 0 \tag{15}$$

$$(R_1 - R_2) \cos \alpha + c_L(e - a) = 0 \tag{16}$$

$$R_1 \left[(L \cos \alpha + S) \cos \alpha - m_1 - \frac{d}{2} \sin \alpha \right] - R_2 \left[(L \cos \alpha + S) \cos \alpha - m_2 - \frac{d}{2} \sin \alpha \right] - c_U(\gamma - \beta) + (R_2 - R_1) \left(\frac{d}{2} + L \sin \alpha + \text{Stg} \alpha \right) f \cos \alpha = 0 \tag{17}$$

$$m_1 = \frac{L}{3} \left(\frac{3(\delta - 2) + b + 2x}{2(\delta - 2) + b + x} \right) \tag{18}$$

$$m_2 = \frac{L}{3} \left(\frac{3(\delta + 2) - b - 2x}{2(\delta + 2) - b - x} \right) \tag{19}$$

$$x = b \left(\frac{S}{L \cos \alpha + S} + 1 \right) \tag{20}$$

$$\delta = \frac{P}{2(\sin \alpha + f \cos \alpha) k_f L \cos \alpha}, \tag{21}$$

where

R_1 and R_2 are reactions of elastically deformed layers;



c_L and c_U are linear and angular manipulator rigidity, respectively;
 f is friction coefficient.

In Fig. 5, the elastic deformations that determine the pressure after fixing the tool are shown. Since from the contact moment to the values shown in Fig. 5, the elastic deformations and the corresponding voltages increase gradually, and then to estimate the wearing out at the corresponding points, we will take into account the pressures equal to 50% of the final ones.

3 Conclusion

Thus, based on the above studies, we obtained dependencies that make it possible to determine the areas of intense wearing out and contact pressures when using the automatic tool changer system depending on the deviations of the mandrel axes and the spindle socket from alignment and parallelism at the moment of initial contact determined by the error of the auto operator. The developed technique allows to determine the dimensions of zones of intensive wearing out of conical surfaces that are located in the upper or lower parts of the mandrel tool and the spindle socket.

We found areas of intensive wearing out of the conical surfaces of the mandrel and the spindle socket in the presence of their axes deviation from alignment and parallelism.

References

1. Levina ZM (1971) Contact rigidity of machines. Mechanical Engineering, Moscow
2. Levina ZM (1970) Calculation of rigidity of cylindrical and conical joints. *Mach Tool* 3:3–7
3. Orlikov ML, Kuznetsov YuN (1977) Designing clamping mechanisms of automated machine tools. Mechanical Engineering, Moscow
4. Levina ZM, Kornienko AA, Boim AG (1973) Investigation of the rigidity of conical joints. *Mach Tool* 10:13–17
5. Petrunin VI (1982) The study of the accuracy of the positioning of the tool on machines of the “machining center” type. Dissertation, Moscow Machine Tool Institute
6. Denisenko AF, Kazakova OYu (2007) Formation of operational characteristics of the mechanism of automatic tool change. *Bull Volgogr State Tech Univ* 2:26–30
7. Denisenko AF, Petrunin VI, Kazakova OYu (2011) Accounting of contact processes in assessing the accuracy of anchoring the mandrel in the machine spindle. *Bull Samara Sci Cent Russ Acad Sci* 4(3):713–716
8. Pronikov AS (2000) Designing of metal-cutting machines and machine-tool complexes. Mechanical Engineering, Moscow
9. Kazakova OYu, Petrunin VI, Kazakov AA (2016) Increase in accuracy when processing blanks on CNC machines. *High Technol Eng* 2(56):44–48
10. Lizogub VA (2003) Influence of the parameters of the spindle unit of the machine on the accuracy of processing parts. *Mach Tool* 3:16
11. Averyanov OI (1981) Systems of automatic tool change. *Mach Tool* 2:4–8

12. Kuznetsov YuI, Maslov AR, Baikov AN (1990) Tooling for CNC machine tools. Mechanical Engineering, Moscow
13. Belyakovskiy VP, Seligey AM, Goldreich GM (1979) Investigation of instrumental conical joints with small gradient angles. Mach Tool 6:15–17
14. Vragov YuD, Evstigneev VN, Ustinov BV (1977) Analysis of directions of cutting force and calculation of rigidity of multi-operation machines. Mach Tool 8:12–14
15. Denisenko AF, Kazakova OYu (2013) Formation of the error of tool holder with automatic tool change. Bull Samara State Techn Univ 2(38):111–116
16. Kazakova OYu, Kazakov AA (2016) Increase of accuracy of processing on machine tools due to minimization of errors of tool systems. High Technol Eng 12(66):35–39
17. Denisenko AF, Abulhanov SR, Kazakova OYu (2011) Rod tool with conical shank. Russian Federation Patent 2009103387/02, 20 Aug 2011
18. Maslov AR, Balkov VP (2004) The use of shanks with a 7:24 taper and possible alternatives. Shavings 1:30–32
19. Kazakova OYu, Gasparova LB, Kazakov AA (2018) The effect of the radial component of the cutting force and the geometrical parameters of the tool mandrel on its position in the spindle. Bull Bryansk State Techn Univ Bryansk 1(62):18–23
20. Burkov VA (2002) Device for fixing tool holders with a ball grip. Mach Tool 2:38–39

Automated Calculation and Control of Body Wear in Friction Pair



V. A. Saninsky, V. V. Korzin and M. A. Kononovich

Abstract It has been established that with the same initial data of deviations of the covered and spanning surfaces of a hydraulic sliding bearing, the value of the calculated diametral clearance depends, in general, on the law of the distribution of errors. It is not always possible to guarantee the fulfillment of these errors, as a result of which destabilization of the gaps of the multi-support shaft support nodes is characterized by the relation $h_{1\min} \neq h_{2\min} \neq h_{3\min} \neq h_{4\min}$. To calculate the diametral gaps in a cylindrical hydraulic sliding bearing, a model was proposed based on the condition that the circumscribed and enveloping surfaces are made on the limiting dimensions that can be combined in an unfavorable and favorable direction of contact pairing. The obtained values of the volume of worn material with both options, showing the possibility of using automated calculation in the software tool COMPAS-3D.

Keywords Friction pair · Sliding bearing · Limiting diameters · Diametral clearance · Automated calculation · Automated control

1 Introduction

During functioning of the shafts, installed in slide bearings, where lubrication is carried out by supplying a lubricating fluid or air to the annulus, over time, the inner surface of the sliding bearing and the gap between the bearing rings increase. It is necessary to know the permissible operating time of this friction pair, as well as the amount of metal carried away from the liner of the bearing and the speed of this

V. A. Saninsky (✉) · V. V. Korzin
Volzhsky Polytechnical Institute (Branch) of Volgograd State Technical University,
42a, Engelsa Street, Volzhsky, Volgograd Region 404121, Russia
e-mail: saninv@rambler.ru

M. A. Kononovich
The Volgograd State Medical University, 1, Square Pavshikh Bortsov,
Volgograd 400131, Russia

drift. A calculation to determine these parameters can be performed by an automated method in the computer program KOMPAS-3D.

In addition, the current state of a friction pair during operation can be monitored with the use of an automated measurement system for the size of the gap in the bearing.

2 Relevance

It is known that actual deviations are random variables, and the gaps in bearings of the considered sizes can lie in the range from 0.1 to 0.385 mm. After assembling units with such gaps, the reserves for wear S_f [1] will lie within the same limits; as a result, machines of the same design may have different values of service life. To calculate the unit operation time before overhaul, according to [1], it is required to know the volume ΔV and the speed of the metal carried from the surface of the liner (the volume embedded in the bearing surface of the main neck) and, accordingly, the contact area and angle $2\varphi_0$ (Fig. 1) [1, 2]. To determine the values of these initial data for calculating the wear time, you can use Formula (1) for calculating ΔV for nominally flat bodies, one of which is abradable, smooth, deformable, and the other is rigid rough.

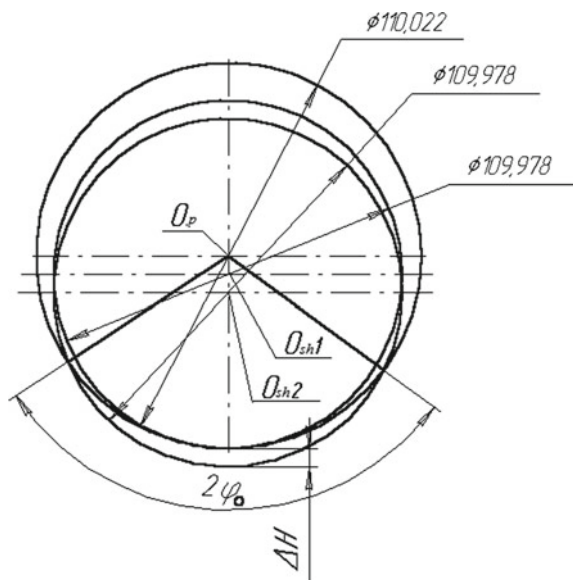


Fig. 1 Scheme for determining the wear ΔH at the contact of the largest limiting size of the hole conditional bearing-sleeve $\text{Ø}110,022$ mm with the smallest limiting size of the neck $\text{Ø}109,978$ mm: O_p —the center of the conditional bearing-sleeve, O_{sh1} —the center of the neck at the beginning of wear; O_{sh2} —center of the neck at the end of wear; $2\varphi_0$ —angle of contact of the friction surfaces of the neck and the conditional bearing-sleeve

$$\Delta V = \alpha A_c R_{\max} b \int_0^\varepsilon x^\nu dx = \frac{A_c b \varepsilon^{\nu+1} R_{\max} \alpha}{\nu + 1} = \frac{\varepsilon R_{\max} A_c}{\nu + 1}, \quad (1)$$

where

ε is convergence bodies;

α is the coefficient taking into account the difference in the cross-sectional area of the protrusions at level x from the value of another level for the same rapprochement value. This coefficient depends on the irregularity configuration and the type of contact; for a spherical model of surface irregularities $\alpha = 0.5$ and $\alpha = 1$ with plastic contact (for a friction pair, the liner—neck, when the liner can be considered ductile, and the hardened and nitrated neck is solid);

A_c, A_r, R_{\max} —geometrical parameters of friction surfaces;

b and ν are the parameters of power approximation.

Formula (1) is difficult for practical application and the values obtained on its basis will differ from the real ones, since the coefficients α, ε , etc. change their value during operation, which makes it difficult to determine their change over time [1].

3 Formulation of the Problem

The purpose of this work is to improve the accuracy of calculating the amount of body wear in a friction pair.

To achieve this goal is required to solve the following tasks:

- Determine the wear parameters of cylindrical surfaces: the main neck and the bearing.
- To calculate the values of the reserve factors for wear of $K_{p,k,p}$ and $K_{p,k,p}^{min}$.
- Form a body model with wear of the material.
- Develop a mathematical model of the gap between the measuring nozzle and the wall of the part.

4 Definition of Wear

To answer the question about the magnitudes of volumes ΔV in each specific case, it is necessary to solve the problem on the basis of dependence (2), since the clearance for the oil wedge of a cylindrical sliding bearing with liquid lubricant has a sickle shape.

For example, the force in the entire hydrodynamic base layer of this form lying in the sector from φ_1 to φ_2 is equal to [2]

$$P = \frac{3\mu\omega}{\psi^2} ld \int_{\varphi_1}^{\varphi_2} \cos[\pi - (\varphi' - \varphi_0)] d\varphi' \times \int_{\varphi_2}^{\varphi'} \frac{\chi(\cos \varphi - \cos \varphi_m)}{(1 + \chi \cos \varphi)^3} d\varphi \quad (2)$$

Denote

$$P = \frac{3\mu\omega}{\psi^2} ld\Phi \quad (3)$$

From this equation, the formula for determining the hydrodynamic load capacity is obtained in terms of—bearing load factor Φ , where Φ is the load factor of the bearing

$$\Phi = \frac{P\psi^2}{ld\mu\omega} = \frac{K\psi^2}{\mu\omega} \quad (4)$$

This value determines the position of the shaft in the bearing and hence the minimum thickness of the oil layer. In the special literature, there are values of Φ depending on the relations $\frac{l}{d}$, which are built on the basis of numerous experiments.

To determine Φ , it is necessary to know m , the viscosity of the oil, which depends on the temperature in the bearing. Therefore, it is necessary to determine the heat balance of the bearing T , which for diesel engines does not exceed 110 °C.

To determine the wear parameters of cylindrical surfaces: The main neck and the bearing, you can use the geometrical model of wear shown in Fig. 1 and calculations of geometric parameters performed on a computer using computer-aided design systems [1, 2]. The proposed method for determining ΔV is not related to the calculation of the coefficients α and ε , etc., but only with the geometrical parameters of wear, which are determined in the KOMPAS-3D system (Fig. 1).

The calculations made according to the recommendations of [1] showed a variation in the values of the reserve factors for wear of the $K_{p,k,p}$ and $K_{p,k,p-min}$ ranging from 0.95 to 4.45. The scatter limits are due to the scatter of the recommended values of the wear rate at $I_h = -1.6 \times 10^{-12} - 1.8 \times 10^{-11}$ [1]. It is possible to use them for approximate calculations in a feasibility study of assembling an assembly unit based on the presented analysis of the calculated values of bearing wear parameters calculated in the KOMPAS-3D system.

The calculation is made taking into account the fact that the main neck is in the process of engine operation under the alternate force action of the left and right connecting rods standing side by side.

It is possible to determine the expected wear of the main neck using the KOMPAS-3D automated designing system. In this case, as mentioned above, it is

necessary to determine the contact angle of the shaft with the bearing journal $2\varphi_0$, the contact area A_m and the volume of worn material ΔV .

This case can create a model of the body with the wear of the material. To do this, on the sketch we form the contour of the cross section of the shaft journal and the contour of the cross section of the bearing shell, taking into account the limiting sizes of the diameters of the conditional bearing-sleeve and neck, which form the fit $\text{Ø}110 \text{ H6/h6}$.

Paired upper and lower liners can take these diameters when tightening them in bed with bolts. Then we build the contour of the shaft, taking into account the displacement ΔH , which the shaft can get as a result of the wear of the bearing surface. The sketch is two intersecting circumferences.

Execute the Cut command and get a sector bounded by two arcs (Fig. 2). It should be noted that the geometrically manual construction of such a sector is practically impossible since the diameter difference of the circles and the displacement due to wear are values measured by micrometers.

Therefore, only a computer with high accuracy will be able to build a sector bounded by arcs with such a small offset and calculate an angle of $2\varphi_0$ with an error of a few seconds. Perform a sketch extrusion operation and obtain a model that represents the body of worn material.

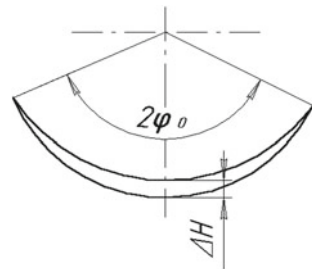
In the automatic mode, using the capabilities of the KOMPAS-3D system, it is possible to obtain the values of the area of the contact surface and the amount of wear. A similar experiment was conducted in AutoCAD by simulating cylindrical intersecting bodies. The amount of worn material was obtained by subtracting one body from another.

Various variants of conjugate pairs of friction were investigated $\text{Ø} 110 \text{ H6/h6}$: D_{\max}/d_{\max} , D_{\max}/d_{\min} , D_{\min}/d_{\max} , D_{\min}/d_{\min} .

The results obtained in the two systems have a discrepancy of less than 0.3% and can be used in calculating the parameters of wear of the surfaces bearings of the 8 $\Phi VN 15/16$ diesel engines when predicting their performance. It is possible to use the presented experience in similar studies of other sliding bearings, for example, camshaft bushings and axles of levers (rockers) of the internal combustion engine and multi-bearing bearing assemblies in compressors, machine tools.

The use of computer systems for design is also considered in [3–13].

Fig. 2 Scheme of creating a cross section of the body worn material



5 Measurement of the Value of Clearance in Sliding Bearings

In the course of operation of a friction pair, over time, the abrasion of sliding bearings occurs, in which lubrication is carried out by supplying air to the annulus. In order to determine the maximum permissible degree of abrasion in time and to replace the sliding bearings in time, preventing their destruction and pneumatic spindle failure, measurement of the gap size is used with a jet meter of linear dimensions combined with an air supply nozzle. The measured value of air pressure is amplified by a pneumatic amplifier and fed to a pneumatic controller, or converted into an electrical signal and fed to the input of an electronic control device. In an electronic or pneumatic control device, the change in the size of the gap is monitored due to the generation of a change in the input signal, and upon reaching a predetermined value, a signal is generated indicating the maximum allowable value of the gap. During further operation, and further increasing the gap, the controller generates a signal prohibiting the operation of the pneumatic spindle.

The strict definition of dependence $p_I = \phi(z)$ is very complex, so for practical analysis of pneumatic measuring circuits, this dependence is determined approximately.

For the calculation, the equation of flow continuity is used

$$s_1 \rho_1 v_1 = s_2 \rho_2 v_2,$$

where ρ_1, v_1 and $\rho_2 v_2$ are the air densities and the flow velocities passing, respectively, through the inlet and measuring nozzles, and s_1 and s_2 are the cross-sectional areas, respectively, of the inlet and measuring nozzle.

Taking the assumption that the air passing through the nozzles is not compressed; that is $\rho_1 = \rho_2 = \rho$, we get the formulas for calculating the flow velocity, in the inlet and measuring nozzles:

$$v_1 = \xi_1 \sqrt{\frac{2(p_p - p_I)}{\rho}}; \quad (5)$$

$$v_2 = \xi_2 \sqrt{\frac{2p_I}{\rho}}, \quad (6)$$

where ξ_1 and ξ_2 are the expiration factors, respectively, through the input and measuring nozzles.

Based on the above, the approximate dependence of the measuring pressure on the gap is as follows:

$$p_I = \frac{P_p}{1 + \left(\frac{\xi_1}{\xi_2} \cdot \frac{s_1}{s_2} \right)^2}, \quad (7)$$

where $s_2 = \pi d_2 z$ (d_2 is the diameter of the measuring nozzle) [14].

After performing mathematical transformations, the expression for calculating the gap between the part and the measuring nozzle is:

$$z = \frac{1}{4\sqrt{\frac{P_p}{p_I} - 1}} \cdot \frac{d_1^2}{d_2} \cdot \frac{\xi_1}{\xi_2}. \quad (8)$$

6 Temperature Measurement in Sliding Bearings

With the prolonged operation of the shaft in conjunction with the sliding bearings, their temperature increases. Increasing the temperature above, the permissible value may lead to overheating of the bearing and its failure. It is advisable to use the measurement of the temperature of the bearings with the help of an aerodynamic-electronic measuring system, considered in [15]. The results of theoretical and experimental studies of the aerodynamic pulsed temperature transducer are given in [16, 17].

7 Work Algorithm for Electronic Computing Block of the Information Measurement System

When an automated system for measuring the gap in a friction pair is in operation, the measuring air pressure R is amplified by a pneumatic amplifier and converted by an pneumatic-electric converter into an electrical signal, which is then fed to computer unit of the automated gap measurement system.

8 Practical Importance Suggestions for Implementation

For the practical confirmation of the results of theoretical studies, methods and devices have been developed, allowing to confirm the results of theoretical studies and to use them in the operation of bearing assemblies.

By the definition of wear, studies were conducted, the results of which were applied for 3 patents, one of which received a positive decision [18].

Automated calculation of the volume of body wear in a friction pair using the computer program KOMPAS-3D can be used to calculate the duration of use of sliding bearings.

The information-measuring system, consisting of an aerodynamic sensor, pneumatic signal amplifier, pneumo-electric converter, electronic computing unit, according to the developed mathematical model of the gap, and the proposed algorithm of operation, allows you to monitor the current state of the gap in a friction pair during operation.

9 Conclusion

The formed model of a worn body of a cylindrical friction pair allows the automated calculation of the volume of material in a worn part of a sliding bearing depending on its size and, in addition to the methods [8, 9], create theoretical conditions for predicting its performance.

Parameters wear cylindrical surfaces for $D = 110$ и $110,022$ мм; $d = 109,978$ и 110 мм can be confirmed by calculating the values of the stock factors for wear of $K_{p,k,p}$ and K_p .

$k, p \cdot \min v$

The developed mathematical model of the gap between the measuring nozzle and the part wall allows it to be used to measure the gap between the surfaces of cylindrical friction pairs and determine the operating time of the bearing assembly before overhaul by determining the volume ΔV of the metal, which is carried away from the surface of the liner (volume embedded in the surface of the bearing of the main neck).

References

1. Saninsky VA (2011) Methodology of increasing the accuracy margin of the main bearings of diesel engines by dimensional machining and computer assembly. VSTU, Volgograd
2. Kragelsky IV, Dobychin MN, Kombatov VS (1977) Basics of calculation for friction and wear. Engineering, Moscow
3. Dementiev YuV (2004) CAD in automobile and tractor construction. Academia, Moscow
4. Zuev S, Poleshchuk N (2004) CAD based AutoCAD software—how it is done. BHV-Petersburg, Moscow
5. Kazennov GG, Sokolov AG (1989) Basics of building CAD and ASTPP. High school, Moscow
6. Klimov BE (1990) Graphic CAD systems. High School, Moscow
7. Kureichik VM, Glushan VM, Scherbakov LI (1990) Combinatorial hardware models and algorithms in CAD. Radio and communication, Moscow
8. Kureichik VM (1990) Mathematical provision technological design using CAD. Radio and communication, Moscow

9. Latyshev PN (2010) CAD catalog. Programs and manufacturers/Solon-Press, Moscow
10. Engelke UD (1990) How to integrate CAD and ASTPP. Engineering, Moscow
11. Berliner EM, Taratynov OB (2011) CAD in mechanical engineering. Forum, Moscow
12. Grover M, Zimmers E (1987) CAD and production automation. Nauka, Moscow
13. Petrukhin AV, Saninskii VA, Moskvicheva NP, Kochkin MV (2015) Automated selection of components in bearing assembly for diesel engines. *J Russ Eng Res* 35(7):500–504
14. Volosov SS, Markov BN, Ped EI (1974) Basics of measurement automation. Standards Publishing, Moscow
15. Korzin VV (2012) Aerodynamic system for measuring the temperature of gaseous media. Abstract of dissertation. VSTU, Volgograd
16. Korzin VV (2007) Theoretical analysis of the workflow of an aerodynamic pulse temperature converter. *J News of VolgGTU. Adv Technol Mech Eng* 3(4):46–47
17. Korzin VV (2007) Experimental studies of the aerodynamic pulse temperature converter. *J News of VolgGTU. Adv Technol Mech Eng* 3(4):47–49
18. Saninsky VA, Kononovich MA (2018) Bearing unit slip. A positive decision on the grant of a patent of Russia dated 10.23.2018 on application No. 2014131750 dated 09.03.2018

Method for Modelling of Circulation of Lubricating Fluid in Models of Machine-Building Products



A. S. Gorobtsov, E. G. Gromov and N. V. Chigirinskaya

Abstract A method for the computation of the lubricating fluid circulation is presented. It uses orthogonal meshes of the inner volume of assemblies and a particle-in-cell method to calculate the flows of lubricant. The lubricating fluid volume consists of a set of particles which can move without interaction in the field of a force of gravity. Particles are sprayed from special areas, move in the inner volume and drain on the border of a volume. Particle movement on the inner surface of a model is calculated using the particle velocity, damping coefficient and normal to this surface. CAD geometry of assemblies is used to generate a mesh of inner volume. The result of calculations can be presented as the movement trajectories of particles or as the accumulation of particles on the border. The charts of movement and velocity of particles can be generated. The program system, which uses this method, is developed. Testing on test samples is performed. The calculation of the circulation of lubricating fluid in the reducer of a cargo vehicle is carried out. Directions of further development are given.

Keywords Computation of the lubricant · Particle-in-cell method · Surface wetting · Particle movement trajectory · Orthogonal mesh · Mesh generation · Grid models

1 Introduction

Numerical simulation of the circulation of lubricating fluid in different assemblies and details of machines is an urgent task because it leads to significantly decreased payments on the experimental elaboration of these assemblies [1]. Methods, based on solving the exact equations of hydrodynamics, use lots of computational resources [2, 3]. For example, hydrodynamic processes in drive axle housing of a cargo vehicle “KAMAZ” were modelled using software product “FlowVision”

A. S. Gorobtsov · E. G. Gromov (✉) · N. V. Chigirinskaya
Volgograd State Technical University, 28, Lenin Avenue, Volgograd 400005, Russia
e-mail: jek_kot@mail.ru

in the work [4]. Analysis of the distribution of transmission oil in the working space of a drive axle housing was made using the model of incompressible fluid flow under the action of rotating details in the field of gravity. Resource-intensive numerical solution of the Navier–Stokes differential equation must be used to solve this task [5–7]. That is why only five full turns of a central wheel of a reducer were simulated. But such simulation does not show the whole picture of lubricant flows. Usage of a more complex model significantly increases requirements for computing resources.

2 Theoretical Part

Particle-in-cell method is used in current work to determine the characteristics of a lubricant circulation in the inner volume, which is presented as a three-dimensional space with complex configuration. The geometry of inner details with normals to surface allows to consider the flows of a lubricant [8]. The geometry is presented by cubic orthogonal meshes, which are generated using CAD geometry of modelled assembly [9]. Such approach allows to get some physical characteristics of modelled object [10]. For example, it can be statistic characteristics of the circulation of lubricant—the intensity of wetting of surfaces and parameters of the flows.

The main rules of the movement of particles, which are used during the development of algorithms for calculation of lubricant, are

- free movement inside the volume without any interaction between the particles;
- movement on the inner surface of a model with particle velocity, damping coefficient and normal to this surface taken into account;
- draining of the lubricant in the field of gravity;
- spraying of the lubricant from the special areas—areas of spraying;
- particles move in orthogonal mesh, which describes modelled volume with channels of lubricant circulation.

Computation of lubricant circulation is an iterative process, which is performed before the maximum quantity of iterations is reached. This quantity is calculated from time step and maximum time. One iteration includes re-calculation of lubricant volume in all cells, re-evaluation of right parts of the equations of the movement and saving the results.

The first step consists of computation of initial level of static volume. Static volume is an area, where all the particles are located in the initial moment. The quantity of cells of a mesh, which take part in initial filling, can be calculated after the division of the volume of lubricant on the volume of a cell. The volume of a cell can be calculated as cube of discretization step of a mesh because of orthogonality of a mesh.

The next step is an iterative process of searching of cells with minimal potential energy and adding these elements in the list of static volume elements. Each cell of

static volume is filled with defined in the parameters of a model maximum quantity of particles per cell. Each particle is also defined by initial velocity and movement along X-, Y- and Z-axles. They are necessary for further computation of particle movement trajectory. The velocity assigned to the particles which are situated in the static volume is defined as average value of its projections along coordinate axles with consideration of variation, which can use either normal distribution or uniform distribution. The type of distribution is defined in the parameters of a model.

The task of calculation of particle movement trajectory is iterative, and last before maximum quantity of iteration is reached. The main and largest stages of this process are recalculation of lubricant volume in all cells and re-evaluation of right parts.

The calculation of lubricant volume in each cell is necessary to avoid the overflow of each cell, because the computational algorithm uses defined maximum quantity of particles per cell. In case of overflow of some cell, the particle is moved to the neighbour cell. Transformation of calculation results (according to output parameters: show trace, show trace only on border, show accumulation in the cells of a mesh) is also performed on this stage.

The re-evaluation of right parts is made after the calculation of lubricant volume in each cell. It consists of assignment of velocity and movement to all the particles and calculation of a new level of static volume. New position of a particle is calculated according to the formula of uniform acceleration of a body. Equation 1 allows to find the distance [11–13], went by the particle.

$$S = s_0 + v_0t + \frac{at^2}{2} \quad (1)$$

where

s_0 initial position of a particle,

v_0 initial velocity of a particle,

a acceleration of a particle,

t time.

In Eq. 1, acceleration is presented by the force of gravity g , which is defined in the parameters of a model by its module and cosines of its angles to coordinate axles. The moment of contact of a particle with border of geometry can be exactly defined because analytical equations for the calculations of particle position are used. If the particle is situated inside the considered volume, the cell of a mesh, which is located on the trajectory of a particle with computed distance along coordinate axles, is calculated and its number is assigned to the particle. So it can be said, that the particle is situated in the cell with given number. If the particle is going to leave the modelled volume, two cases are possible. In the first case, when it is defined in the parameters of a model, that normals are not taken in the consideration, the velocity along the coordinate axle of leaving of a particle is nullified. In the second case, when normal must be taken in the consideration, the calculation of particle movement trajectory includes computation of tangent and normal

components of the velocity of a particle. Projections of a particle velocity on coordinate axes are equal to the tangent velocity of a particle at the moment of leaving modelled volume (Fig. 1).

In Fig. 1, τ is a tangent to the border surface, and n is a normal to this surface. The velocity of a particle at the moment of a contact is denoted as v (velocity vector has blue colour), target velocity— v_τ has red colour. Normal projection v_n of particle velocity v has green colour on the Fig. 1.

It is necessary to calculate both the value of v , and the value of normal component v_n to find v_τ . The value v_n can be calculated as a scalar product of vector v and vector n (n is unitary normal) [14–16]—Eq. 2.

$$v_n = v_x n_x + v_y n_y + v_z n_z \quad (2)$$

Normal projection v_{n_s} of vector v in the coordinate system of a modelled body is calculated as shown in Eq. 3

$$v_{n_s} = (v_{n_x}; v_{n_y}; v_{n_z}) = (v_n n_x + v_n n_y + v_n n_z) \quad (3)$$

Vector of tangent component of particle velocity after inelastic collision (Fig. 1) is calculated according to Eq. 4.

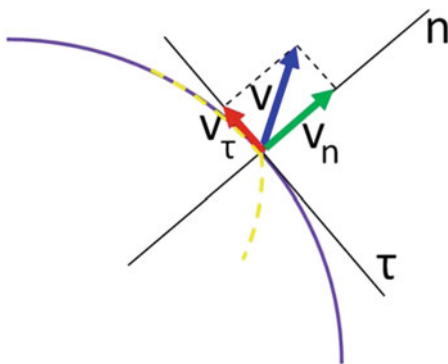
$$v_\tau = (v_x - v_{n_x}; v_y - v_{n_y}; v_z - v_{n_z}) \quad (4)$$

The movement of a particle with consideration of viscous friction and force of gravity is described by Eq. 5 [17, 18].

$$a_\tau + b v_\tau = q_\tau \quad (5)$$

where b is a coefficient of viscous friction; a_t is a projection of acceleration of a particle on tangent τ ; q_t is a projection of the force of gravity on tangent τ .

Fig. 1 Particle velocity definition at the moment of contact with border



Solution of Eq. 5 is presented in Eq. 6 [19–21].

$$s_{\tau_j+1} = -\frac{c_1}{b} e^{-bh} + c_2 h + c_3 \quad (6)$$

where $c_1 = v_{\tau_j} - \frac{q_c}{b}$, $c_2 = \frac{q_c}{b}$, $c_3 = s_{\tau_j} + \frac{c_1}{b}$, s_{τ_j} —initial position of a particle, h — time step.

3 Experimental Part

Modelling of lubricant circulation consists of three stages:

- preparing data for calculations (geometric model selection, mesh generation based on the selected CAD geometries, input parameters definition);
- analytical computation of particle movement trajectories using generated mesh;
- visualization.

Calculation of lubrication fluid circulation in the model of a sphere with cut (Fig. 2a) and reducer of cargo vehicle (Fig. 2b) is considered as an example.

The result of calculation of particle movement trajectories is shown in Fig. 3a, and accumulation of particles on the border is shown in Fig. 3b.

The generation of charts of movements and velocities of a particle with consideration of damping coefficient was performed. Chart of particle movement in OYZ plane is shown in Fig. 4a, and chart of horizontal velocities of a particle is shown in Fig. 4b.

In Fig. 4, point 1 is a point of spraying. The particle begins its movement in the vertical direction (line 1–2) and later meets with the border (point 2). The velocity of this particle along X after repulsion becomes equal to the velocity along Y at the moment of an impact because the normal is nearly horizontal. After that the particle starts free-falling, keeping the velocity along X (line 2–3). In the point 3, the particle reaches the border and starts slithering (line 3–4). In the point 4, the particle stops

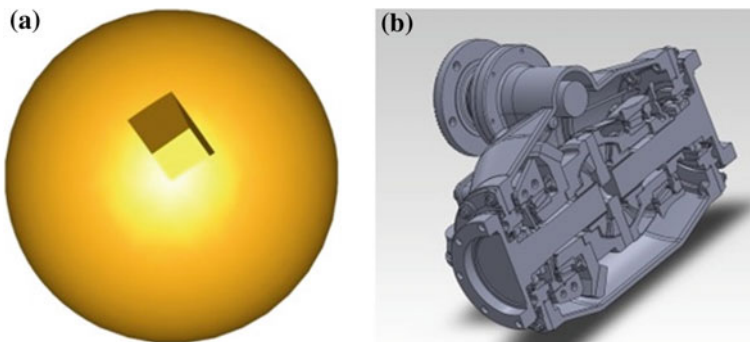


Fig. 2 a Model of a sphere with cut; b model of a reducer of cargo vehicle

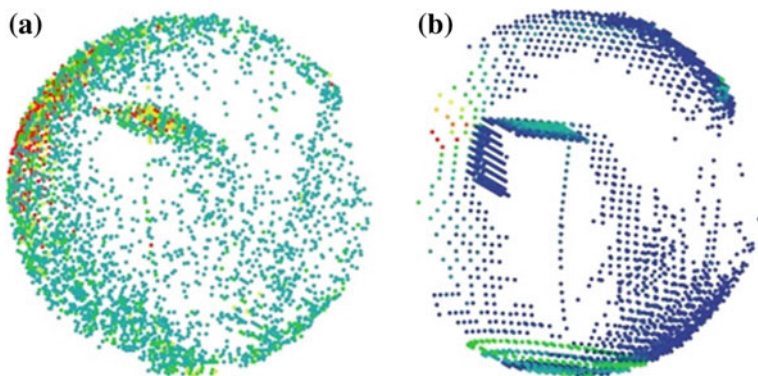


Fig. 3 a particle movement trajectories; b accumulation of particles on the border

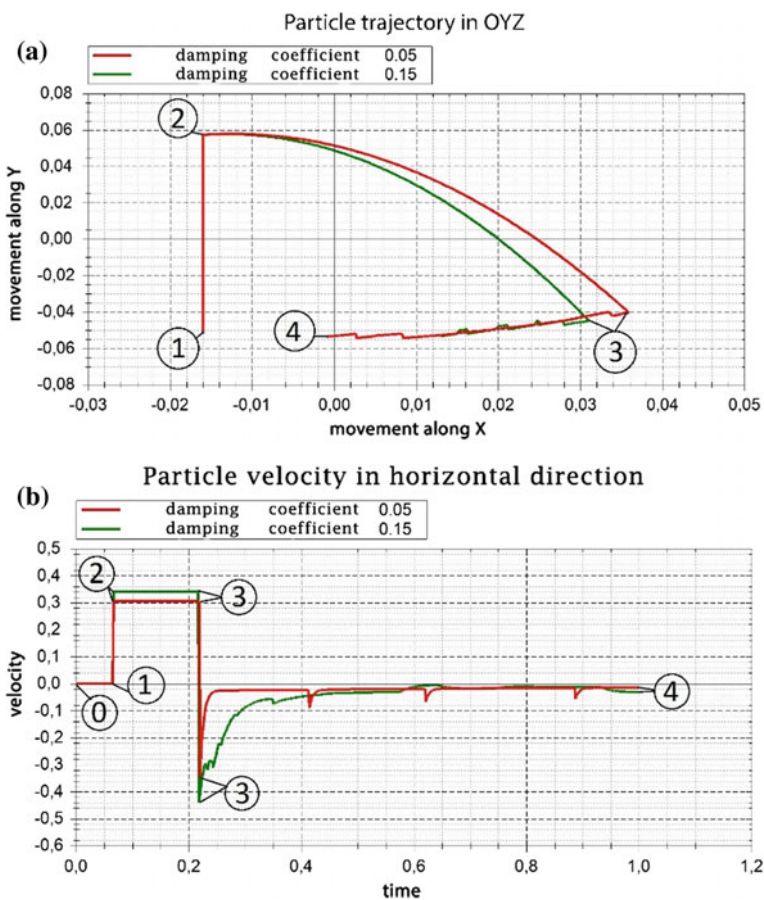


Fig. 4 a Particle movement in OYZ plane; b horizontal velocities of a particle

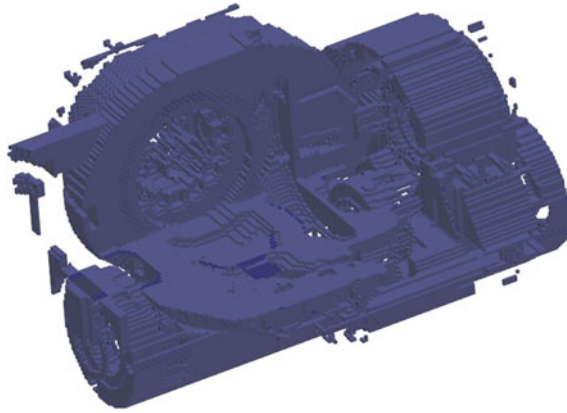


Fig. 5 Inner volume of a reducer

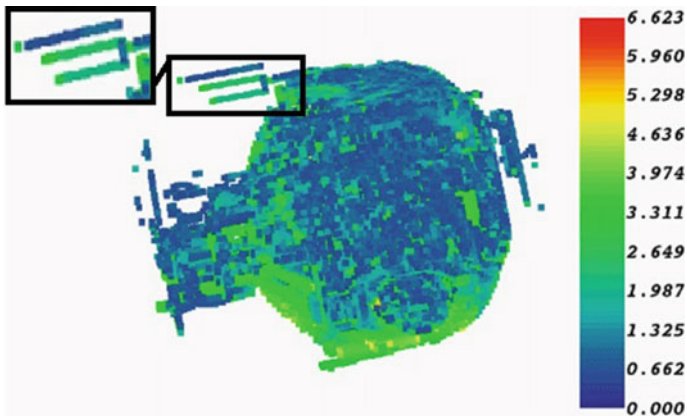


Fig. 6 Lubricant distribution in the reducer

because of damping. Stepped sections of trajectories on the lines 3–4 on Figs. 4 and 5 are explained by discrete interaction between the particle and border cells within the used model.

Program for calculation of lubricating liquid was used to model the reducer of a cargo vehicle. Cut of inner volume of a reducer housing, generated from the geometric model of a reducer with inner parts is shown in Fig. 5.

Lubricant distribution in the reducer is shown in Fig. 6. It can be seen, that the lubricant flows both inside the volume of a reducer and inside the special channels in the housing. Areas with low amount of lubrication fluid can be also seen in Fig. 6. These areas coincide with broken parts of the reducer.

4 Conclusions

The result of this work is a software product which uses particle-in-cell method to calculate the circulation of a lubrication fluid. It allows to make computations of the meshes of higher dimensions for inner volumes of geometric models.

Developed product was used to calculate the circulation of lubrication fluid in the models of real assemblies (reducer of a cargo vehicle). The results of simulation (areas with low amount of lubricant) correspond to the broken parts of assemblies. It allows to make a conclusion about the correctness of used mathematical model.

Further directions of the development are

- description of different models of spraying—gears, tapered roller bearings;
- improvement of algorithm for calculation of initial level of lubrication fluid;
- development of interfaces for binding of spraying elements to the cells of mesh;
- improvement of a subsystem for mesh and calculation results visualization;
- increasing the detalization of a mesh by means of distributed computing.

References

1. Gorobtsov A, Kartsov S, Pletnev A, Polyakov J (2011) Computer methods of building and research of mathematical models of vehicle construction dynamics. Machinebuilding, Moscow
2. Solodenkov S, Gorobtsov A, Lutin K (2008) Mathematical model of hydromechanical system with constant rotation speed. *Autom Ind* 8:21–24
3. Holdeman JT (2010) A Hermite finite element method for incompressible fluid flow. *Int J Numer Meth Fluids* 64(4):376–408
4. Valeev D, Zhestkov M, Iliasov V, Rusakov V, Sazonova V, Shmelev V (2017) Numerical simulation of hydrodynamic processes in drive axle housing of a cargo vehicle “KAMAZ”. In: *Engineering systems*, pp 27–44
5. Launder BE, Spalding DB (1974) The numerical computation of turbulent flows. *Comput Methods Appl Mech Eng* 3(2):269–289
6. Anderson Jr JD (1995) *Computational Fluid dynamics. The basics with applications*. McGraw-Hill Science Engineering Math, 1 edn
7. Huebner KH, Thornton EA, Byron TD (1995). *The finite element method for engineers*, 3rd edn. Wiley Interscience
8. Gromov E, Nasonov A, Novokshenov A, Firsova V (2015) Multiphysical tasks in the dynamics of a system of rigid and flexible bodies. *Kazan*, pp 1080–1082
9. Chibisov D, Ganzha V, Mayr E, Vorozhtsov E (2005) Generation of orthogonal grids on curvilinear trimmed regions. In: *Constant time 8th international workshop, CASC 2005, Kalamata, Greece, September 12–16, 2005, Proceedings*, pp 105–114
10. Andreev A, Gromov E, Reznikov M, Shapovalov O (2009) System of calculation of thermal technological processes in machine building. *Volgograd*, pp 124–126
11. Sivuhin D (2005) *Common course of physics*. Phyzmathlit, Moscow
12. Landau L, Lifshits E (2004) *Mechanics*. Phyzmathlit, Moscow
13. Cassidy DC, Holton GJ, Rutherford FJ (2002) *Understanding physics*. Birkhäuser
14. Pogorelov A (1974) *Differential geometry*. Science, Moscow
15. Lipschutz S, Lipson M (2009). *Linear algebra (Schaum’s Outlines)*, 4th edn. McGraw Hill

16. Kostrikin A, Manin J (1986) Linear algebra and geometry. Science, Moscow
17. Sedov L (1970) Mechanics of continuums. Science, Moscow
18. Landau LD, Lifshitz EM (1987), Fluid mechanics, 2nd edn. Pergamon Press
19. Zill DGA (2000) First course in differential equations, 5th edn. Brooks/Cole
20. Arnold V (1966) Ordinary differential equations. Science, Moscow
21. Polyanin A, Zaytsev V, Zhurov A (2005) Methods of solving of nonlinear equations of mathematical physics and mechanics. Phyzmathlit, Moscow

Influence of Physicochemical Processes on Reliability of Node of Sliding Current Collector of Electric Machines



S. A. Izotov, A. I. Izotov and A. A. Fominyh

Abstract Electric machines are widely used in the assembly, and mechanisms of modern equipment and devices operate in different climatic conditions. These conditions often determine the peculiarities of operation of electric machines, repair and preventive measures. In many ways, the reliability of DC electric machines is determined by the node of a sliding current collector (UST), in which the current-carrying brushes are in dynamic and static contact with the plates of the metal collector or ring. Physical, mechanical, and chemical processes occurring at the interface of the contacting counterbody data determine the switching processes and reliability (UST). The purpose of the article is to analyze and study the impact of probable physical and chemical factors on the operational reliability of the sliding current collector unit of electric machines. The results of scientific and practical work allow determining the measures aimed at eliminating the negative impact of adverse physical and chemical environmental factors on electric machines.

Keywords Electric machine · Brush · Molybdenum disulfide · Solid lubricant · Sliding current collector assembly · Collector wear

1 Introduction

Electric machines with brush materials in the current collection unit may work in different conditions: different atmospheric compositions, temperatures, and operating modes.

Under these conditions, cyclic modes (idle time, work at idle and under load) and the reliability of the operation of electric machines are largely determined by the physicochemical processes in the sliding current collection unit (UST).

S. A. Izotov (✉) · A. I. Izotov · A. A. Fominyh
Vyatka State University, 3b, Moskovskaya Str., Kirov 610000, Russia
e-mail: sergizotov63@mail.ru

UST of an electric machine can have the following types of corrosive phenomena: chemical corrosion (mainly a gas one); electrochemical corrosion; corrosive erosion or sometimes called fretting corrosion—the destruction of the metal with brushes with mutual abrasive effects [1]; contact corrosion of metal collector plates or rings in the junction with carbon brushes having different electrode potentials.

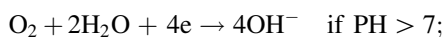
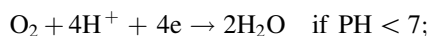
The flow of electrochemical processes is connected with surface ionization of the metal in a water-film electrolyte localized on a metal surface. In this case, reaction products of various structures can be formed. They may be loose, dense, not solid, flooded, etc. [2].

Under the operating conditions of electric machines, the share of corrosive erosion is high in UST. Corrosive erosion (corrosive mechanical wear) can lead to the destruction of the surface of a solid object, in this case, a metal, caused by the mechanical abrasive effect of another solid object (carbon brush) while the corrosive environment acts simultaneously and the total synergistic effect of two factors (electrolyte, mechanical effect) may be more if separately. The fretting corrosion rate (corrosive erosion) is determined by the nature of contacting parts, the corrosivity of the environment, the slip amplitude, the contact pressure, the number and frequency of cycles of relative displacements of contacting parts, the fit of contacting parts, the temperature in the contact zone [2].

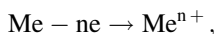
Generally, the necessary condition for the atmospheric corrosion is the presence of a thin layer of water on the surface of the metal of the collector, and its thickness largely depends on the moisture content of the air [3]. The traditional process of atmospheric corrosion occurs in the neutral water-film environment, where oxidizing agents are water molecules and molecular oxygen.

In an acidic atmosphere, especially saturated with vapors of SO_2 , NO , and NO_2 in the moisture film on the surface of the metal collector, the hydroxonium ion H_3O^+ (H^+) becomes an active additional oxidizing agent.

Thus, the main oxidizers (H_2O , O_2 , H_3O^+) of the corrosion process are restored due to the release of electrons upon ionization of the metal according to the equations [4]:



Metal ionization (anodic reaction of the corrosive process) occurs according to the equation:



where Me is collector metal (ring);

In this case, both reactions of the conjugate corrosive process can lead to soluble and insoluble products having different adhesions to the metal base in the form of collector plates or contact rings.

Electrochemical corrosion is characterized by local separation of the conjugated metal ionization reactions and the reduction of the oxidizing component on the metal microrelief and is determined by its structural heterogeneity, for example, by the presence of impurities, while these conjugate reactions are spatially separated on the metal micro profile.

The degree of inhibition in time (kinetics of the process) of the cathodic (reduction of oxidizers) or anodic reaction (metal ionization) of the corrosive process limits the overall rate of flow of the electrochemical corrosive process occurring at a compromise potential (corrosion potential). The corrosion potential is due to the influence of both reactions and occurs when each potential is “imposing” its potential on the metal surface.

The intensity of the electrochemical corrosive process is caused by the thickness of the moisture film on the metal surface of the collector. It depends not only on the relative humidity of the air but is also largely determined by the duration of moistening [4].

It is known that condensed moisture films are divided into adsorption and phase by their thickness and formation conditions [2].

Adsorption films are the thinnest films capable of being formed if relative humidity is more than 30%, and there is no precipitation and dew. In dry air (below 30%), the adsorption layer of moisture can be comparable with the thickness of the molecular layer of water. Adsorption water films systematized as “wet” corrosion are the thinnest moisture films from several dozen molecular layers. They lie within thicknesses from 10^{-5} to 10^{-3} mm and are connected by van der Waals bonds with the friction surface and directly between their molecular monolayers. An adsorption film can serve as the basis for the formation of a so-called phase water film and depends on the chemical activity of the metal with the other conditions being equal.

It should be noted, however, that water films formed during capillary and chemical condensation [2] also belong to “wet” corrosion. Capillary condensation depends on the microrelief of the corroding surface and increases with the growth of porosity and roughness of the latter. Therefore, there is no doubt that this type of condensation in the conditions of the existence of a porous carbon layer on the contact surface of a metal collector or ring is sufficiently heavy. Chemical condensation is due to the hygroscopicity of the resulting corrosion products and other chemical compounds that appear on the metal surface during operation when worn or from air.

Phase films [4] (“wet corrosion”) are thick films of condensed moisture, as a rule, they are weakly connected with a metal surface. The main sources of these films are fogs, thaws, rains, dew, and fogs. Their occurrence and localization on the surface of the contacting parts are associated with the location of the brush-collector unit in unprotected or insufficiently protected natural atmosphere conditions (unheated box, roof, etc.) and is strongly influenced by temperature differences.

Atmospheric corrosion can also occur under insignificant molecular moisture layers (relative humidity of air, as a rule, is up to 50%) and the film thickness is up to 10^{-5} mm. It is “dry” atmospheric corrosion. According to [4], this kind of corrosion is characterized by surface oxidation of the metal by chemical mechanism

during the interaction of any reagent in gaseous form with the metal surface. The processes of “dry” atmospheric corrosion under conditions of natural temperatures do not have a significant effect on the state of the surface, the speed of the process is low, and oxidation of the metal surface is small.

However, it should be noted that if an operational temperature increases in the zone of contact of UST due to heating of the rubbing surfaces of parts or transient processes, active evaporation of moisture occurs and another type of chemical corrosion is realized—a gas corrosion. The main product of this corrosion is oxide films [4]. The state of these oxide films is subject to the Pilling-Bedworth continuity condition. This type of corrosion process is most characteristic for the operation of electric machines in a controlled atmosphere (heated and ventilated conditions). The temperature and gas composition of the working air environment in this case determines the degree of density and protective ability of the film from further oxidation of the metal, and, undoubtedly, the tribological properties of this sliding surface.

The speed of the gas corrosion can be largely determined by the sorption of acid gases by a porous carbon film and the subsequent destruction of the formed oxide (even with insignificant moisture content) of the protective oxide part of the polish film. In this case, the front of the destruction of the metal by air oxygen through this non-continuous film is directed deep into its volume. The latter can lead to severe corrosive erosion under conditions of additional mechanical wear and rotation.

Precipitated at the interface fine particles, especially of the solid state (dust) and of acidic character due to the sorption of an acidic gaseous environment, also affect the rate of surface corrosion [2]. Moreover, it should be expected that these processes are significantly accelerated when heat is dissipated from local heating zones in accordance with the thermal conductivity of the conjugate materials and media.

If electrical machines are poorly protected from air, the rate of atmospheric corrosion at which a continuous film of moisture appears on the metal surface increases, especially after reaching some specific relative humidity (critical humidity usually corresponds to relative humidity of 50–70%).

Critical humidity depends both on the nature of the metal and on the degree of surface contamination since the latter can be hygroscopic and contain large amounts of moisture (chemical condensation).

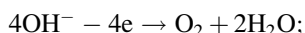
Below a certain level of relative humidity (critical humidity), the moisture film is thin and in most cases, the rate of the electrochemical corrosion is not so significant. It should be noted that since the operation of the electric machine is carried out in the rotation-idle mode, the mass of moisture at the interface of the contacting parts varies cyclically while the corrosion process is controlled by both an electrochemical and chemical mechanism. Their ratio is determined by the amount of heat generated by sliding friction and transient processes, as well as by the intensity of moisture penetration into the air gaps of the contact area of the UST.

Switching processes in UST are also largely dependent on the transition resistance at the friction boundary [5]. The value of relative humidity is the decisive factor in determining the value of surface conductivity. A particularly sharp decrease in surface resistivity is observed if values of relative humidity exceed 50%.

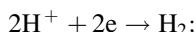
Thus, water in the presence of adsorption or adsorption-phase films most strongly exhibits the properties of an electrolyte at critical humidity, which is of decisive importance for the corrosive process developed by an electrochemical mechanism. Under these conditions, the electrolyte composition of the surface film of moisture significantly affects its corrosivity.

It should be noted that various processes caused by electrolysis between metal of the collector and oppositely polar graphite brushes can occur in a moisture film which is an electrolyte [5]. Electrochemical decomposition of water between the brushes and the collector metal or ring leads to a situation where the hydrogen cations and hydroxyl anions migrate to the cathode and the anode, respectively. These processes have a different effect on the wear of contact parts, depending on the design of UST. So, in the case of UST of a metal collector, the cathode and anode brushes form one sliding surface.

At the same time, a different mechanism of the effect of the brush polarity on the structure of the slip contact surface is clearly manifested on the rings of the turbogenerators. Each ring has its own polar brush. In the contact zone under the anodically polarized electrical brush, hydroxyl ions on its surface ionize to molecular oxygen and water, according to the reaction:



At the same time, the process of hydrogen reduction occurs on the metal of the ring, which is the cathode zone, by the reaction:



Accordingly, under the cathode-polarized brush, these processes change places, and the process of water decomposition occurs at a certain decomposition voltage, the theoretical value of which is 1.23 V [6].

In the latter case, the anodic—polarized positively charged ring actively electro-corrodes, while the metal ions entering the water film can be restored on a cathode—polarized brush in the form of metal. This metal due to weak adhesion to the material of the cathode brush is painted in the contact zone and acts as a strong abrasive. It is confirmed in [7]. The positive ring of UST wears more than a negative one, and its working surface becomes dull and rough. Cathode brushes of the positive ring also wear more strongly. Increased wear of the positive ring of UST increases the instability of transients while sparking on a rough metal surface increases and there are prerequisites for arcing. As a result, it leads to the formation of non-conductive spots (burns) that create significant difficulties during the operation of electric machines. The traditional method of eliminating non-conductive spots is a mechanical groove of the collector, followed by a rather long rubbing of the interface surface of contacting parts. To level this wear, it is recommended periodically (1–2 times a year) change the direction of the current passing through the contact. If there are arc processes, the ring surface can melt and be subject to severe erosion, which is a relatively common negative phenomenon [8].

The process of electrolysis of water is realized under the conditions of additional electricity costs to overcome the electrical resistance of the water-film electrolyte, electrodes, contacts, overvoltage of gas evolution processes, and additional resistance due to concentration and diffusion polarization. Therefore, the applying voltage should be up to 2 V [6]. Thus, the described phenomena in the working area of the contacting elements “brush-collector” are reduced to the visually observed effects when the surface of the ring under the cathode’s electric brush darkens due to more intense oxidation due to the additional molecular oxygen during the decomposition of water. The part of the ring that falls under the electric brush is the lighter anode.

Chemical and electrochemical corrosive processes in UST lead to the formation of a passive oxy-silic acid film on the surface of a collector or ring, which is an integral part of a polished film. The polished film covers the surface of the metal of the collector and consists of oxide-acid copper (65.8%), carbon material of the electric brush (22.1%), and other components (12.1%). Other elements include impurities: SiO_2 , Al_2O_3 , Fe_2O_3 , and CaO . Impurities are introduced into the polish from electric coal products [5].

The magnitude of the transition resistance of the “polishing film” is not standardized by technical conditions, and its thickness is within (5–100) nm. The oxide-acid component of the polished film is formed under conditions of elevated temperatures caused by heating of the rubbing surfaces [9].

Under gas corrosive (vapor-gas) conditions, copper is oxidized to copper (I) oxide (Cu_2O) with a lack of oxygen and up to 200 °C, and to copper (II) oxide (CuO) with an excess of oxygen (rotation) and temperatures of about 400–500 °C [10]. Copper oxide is black and oxide is red-brown. Therefore, taking into account black carbon film, polish can have shades from light red to black.

Taking into account the bulk temperatures of the collector and brushes, on average reaching 150–300 °C [9], the main oxide of the polished film is copper oxide Cu_2O . However, significant amounts of CnO (coke) may form on the surface at high contact temperatures caused by non-optimal switching processes.

The polished film having copper oxide in its composition acts as a solid lubricant protecting the collector and brushes from premature abrasion since it has a low coefficient of friction [11]. If the brush slides along the collector in the absence of current, then a sufficiently thick polish may not form. Therefore, when transporting the locomotive in a “cold” state, brushes are usually removed from the traction motors for a long distance. The latter is obviously related to the mechanical abrasion of the slip plane and the high friction coefficient of a pure metal in comparison with an acidic film.

Thus, in the absence of current during rotation of the collectors and rings at idle, the rate of formation of the polished film and, above all, of the passive oxide-acid film is low. It indicates the exceptional importance of electrical polarization (electrocorrosion, corrosion by electric current) on the speed and depth of formation of protective surface polish.

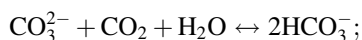
In the presence of a current, the polished film is in dynamic equilibrium, at which the process of film formation occurs simultaneously due to oxidation of the metal surface and its partial abrasion due to friction of the contacting parts [12].

However, in some cases (the operation of electric machines in high-altitude conditions, or during transients, accompanied by intense sparking), this process shifts toward the thickness of the polished film, which causes an increase in wear of brushes, collectors, and contact rings. Too small thickness of the polished film or its absence significantly increases the coefficient of friction in the contact zone and thus creates conditions for increased abrasive wear of the contact surfaces [12]. The latter leads to rapid abrasion of the contact part of the brush and significant problems in the operation of electric machines, especially in cases where frequent replacement of brushes is impossible under the conditions of operation. In addition, the abrasive wear of the collector surface and the associated sparking conditions lead to the need to groove its surface, which greatly complicates the operation.

The specifics of the operation of UST consist in cyclic fluctuations of the humidity level at the interface and in the air, determined by the dissipation of heat of the contacting parts due to friction and transient processes. Under normal conditions of operation of an electric machine, the heating of the airspace of UST and the surfaces of the working parts at a certain point in time become higher than the boiling point of moisture. An increase in temperature leads to the evaporation of moisture and the replacement of electrochemical corrosive processes with chemical ones.

Chemical processes have their own kinetics, and the growth of the oxide film is interpreted by the law of continuity of Pilling and Bedworth [4]. However, even under these conditions, if air humidity is critical, it penetrates into UST due to its replenishment with new portions of air moisture during rotation of the collector or ring. In this case, water vapor plays an undoubted role in the kinetics of the flow of low-temperature gas corrosion.

It should be noted that in addition to electrolysis, carbonate equilibrium is realized in the water film on the contact surface according to the reaction [13]:



If basic carbonate equilibrium is observed, water is stable. Bicarbonate—ions exist in the film solution only in the presence of free carbonic acid. Waters which contain excess free carbonic acid over the equilibrium are aggressive and have a high dissolving ability. Therefore, increasing the relative content of carbon dioxide in the air in a closed room, under conditions of burning various fuels, especially at elevated shop humidity, can increase the water-dissolving ability with respect to the metal and oxide-acid film on the surface of the collector metal or ring of steel and bronze. The reaction of carbon dioxide equilibrium is shifted towards the formation of bicarbonate ions, and the water itself in the presence of an elevated content of carbon dioxide has a weakly acid reaction ($\text{pH} = 5.5\text{--}6.5$). It can easily corrode both oxide films and the metal itself. Especially this process is intensified in conditions of soft water with low salt content up to 2 mg-eq/l of salts since the

solubility of carbon dioxide in it increases dramatically. However, in the operating modes of the electric machine, bicarbonates quickly turn into carbonates when heated by water films from friction and transients. In the future, oxidation of carbonates to oxides is possible, but the process can occur only at high temperatures. For example, for calcium ions, it can occur in the range $T = 900\text{--}1200\text{ }^{\circ}\text{C}$ by the reaction:

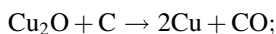
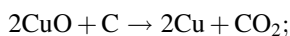


This reaction can be realized in conditions of increased ball sparking. Carbonic acid, even with slight heating, decomposes into carbon dioxide and water, and the process of active degassing from the evaporating moisture of carbon dioxide occurs.

Thus, under conditions of high water hardness, determined by the content of calcium and magnesium bicarbonate in it, thermal processes resulting from friction and transient processes in one degree or another lead to the formation of calcium carbonate and other difficult-soluble salts [14]. Many of them, including calcium oxide and calcium carbonate, have a mild abrasive grinding effect. Soft water in conditions of saturation with carbon dioxide is even more aggressive with respect to the oxide-acid component of the polished film and the collector metal due to the formation of a large amount of carbonic acid.

In some cases, copper collector bronzes can form green insoluble malachite films $\text{CuCO}_3 \times \text{Cu}(\text{OH})_2$ in conditions of prolonged contact with moist air. This phenomenon is typical for electric machines that are especially long idle in the natural atmosphere without sulfates (sulfate—ions) and chlorides (chloride ions) under a roof or in unheated stock [15]. These films are removed by grinding (groove) collectors.

It should be noted that high temperatures in UST can lead to an unfavorable phenomenon—reduction of metal oxides with carbon particles according to the reactions:



The carbon particle film formed by mechanical wear of the brushes during friction is relatively evenly distributed on the surface of the collector or slip ring and has an average thickness of 100–1000 nm [16]. According to the authors [17], there are stages in the reduction reaction of the oxide-acid film according to the scheme: $\text{CuO} \xrightarrow{1} \text{Cu}_2\text{O} \xrightarrow{2} \text{Cu}$. For the first stage, the temperature range of the reaction is from 430 to 650 $^{\circ}\text{C}$, and for the second stage is from 650 to 850 $^{\circ}\text{C}$. The possibility of these reactions depends on the proportion of oxides and carbon. So, the ratio of oxides and carbon characterized by an excess of carbon by the stoichiometric ratio can reduce the temperature of the reduction processes of the first stage to 430 and the second to 650 $^{\circ}\text{C}$. These processes, obviously, can occur in

improper operating modes of electric machines, in the case of not optimally applied electric brushes, pressures on them or with high sparking indices.

High-temperature processes occurring in UST under the conditions of oppositely charged brushes can lead to the existence of conditions for thermionic emission. Under the action of the field, the emission of positively charged ions and microparticles of the anode (ring or collector) toward the cathode occurs after they are separated from the atomic lattice of the anode as a result of electrolysis [5].

With a high concentration of applied voltage in the gap of UST on the sharp cleavage of the brush edge or the sharp edge of the brush, air atoms are ionized by emission electrons and a non-self-sustaining discharge called “dark” appears. Further, a glow discharge can occur and lead to the formation of a “cathode spot” and the discharge turns into a spark. The electrical strength of the air gap is broken, and there is a breakdown and a sharp increase in current between the contacting parts. At some moments, the brush stops contacting the ring due to vibration and an air gap is formed between them, leading to an open circuit and an arc [18]. The strongest arc is formed in the places of the electric field concentrators—on the tops of the microprotrusions of the tracks and on the sharp edges of the tracks along the compression grooves [15].

Also, UST can have processes which are classified by the general name “plasma electrolysis” [19].

Transient electric processes accompanied by the formation of low-temperature plasma begin to occur at 1900 °C. Their impact can lead to the formation of droplet, vapor, and ionized metal phases, contribute to the intensive erosion of the collector metal while the surface of the ring and the collector quickly go beyond the repair parameters.

It should be noted that the processes of strong erosion of steel and bronze collectors and rings of electrical machines are quite common. It requires a careful study of the physicochemical features of these negative processes and also the development of complex measures to prevent their occurrence.

2 Materials and Methods

The work of the engines of electric machines of direct current, intended for operation in high-altitude conditions, is connected with a decrease in the content of moisture and oxygen in the environment. Engines are sealed. To equalize the atmospheric pressure and pressure inside the engine, most of the sealed engines have a drain hole, closed by a grid. Some engines without drainage have increased brush wear, which leads to a decrease in insulation resistance and the need to repair the engine.

To counteract the negative climatic manifestations, to reduce wear of the contacting parts of UST, the authors have proposed to use a composite element consisting of molybdenum disulfide (MD) with a binder. This lubricating brush (LB) is installed in a separate brush holder or in a pocket structurally connected with a

current-carrying brush holder on the working path of the collector. In the experiments, the authors used 5 W engines with and without drainage.

To assess the influence of oxygen and moisture in the environment on the resistance of the polished film (PF) and the wear of the brushes in sealed engines, six 5 W sealed engines were prepared. Two windows were cut for visual assessment of sparking when operating in normal conditions. Windows, if necessary, were closed with hermetic plugs. A regular brush holder was placed between the current-carrying brushes, and if necessary, sensors were placed to measure the resistance of the PF. Engines were tested in conjunction with a gearbox when operating under load. Before the measurements, the brushes were rubbed into obtain 100% of the contact surface. The brushes were weighed on an analytical balance and the engines operated for 150 cycles under normal climatic conditions, after which the wear of the brushes and the resistance of the PF were determined using a sensor installed in an additional brush holder [20]. Then, one pair of engines worked 100 cycles in a thermoelectric chamber with a temperature $t = +120$ °C, and pressure $P = 15$ mm Hg. At the end of the mode, the wear of the brushes was measured (the wear of the brushes was calculated through their specific weight) and the resistance of the PF (it was assumed that the resistance of the PF characterizes its thickness). Using a similar technique, the remaining engines were tested. The second pair worked 200 cycles in the thermo-chamber, and the third worked 300 cycles.

3 Results

Table 1 presents the averaged results of the resistance of the PF and the wear of the current-carrying brushes on two engines after the test modes.

As follows from Table 1 (depressurization due to the removal of the plug on the engine's viewing windows), as far as the time in the thermo-chamber with a pressure of 15 mm Hg is in progress, there is an increase in resistance of PF in relation to normal conditions. The increased wear of the brushes in relation to normal conditions in this case can obviously be explained by the effect of dry friction, which occurs due to a decrease in the content of water vapor in the surrounding atmosphere.

The results of similar tests of four sealed engines with a power of 5 W (only an additional brush holder was installed) are shown in Table 2. They show a decrease in PF resistance and an increase in brush wear by 2.7 times compared to previous results. Obviously, increased sealing of the engine leads to a decrease in the oxygen content inside the engine due to its burning out under the action of switching sparking. It leads, apparently, to a shift in the process of abrasion and the formation of PF in the direction of reducing the dynamics of its formation, causing more intense brush wear.

Table 1 PF resistance and wear of the current-conducting brushes of a 5 W engine with open viewing windows

Initial resistance of the polished film (Ω)	Normal conditions		Thermo-chamber operation mode: $t = +120 \pm 3$ °C, $P = 1.5 \pm 1\%$ mm Hg					
	Number of cycles: 150		Number of cycles: 100		Number of cycles: 200		Number of cycles: 300	
	Resistance of the polished film (Ω)	Brush wear, mm 10^{-3}	Resistance of the polished film (Ω)	Brush wear, mm 10^{-3}	Resistance of the polished film (Ω)	Brush wear, mm 10^{-3}	Resistance of the polished film (Ω)	Brush wear, mm 10^{-3}
0.02	0.821	7.52	1.12	39.27	–	–	–	–
0.02	0.812	8.36	–	–	1.45	68.78	–	–
0.02	0.759	8.36	–	–	–	–	1.79	111

Table 2 PF resistance and wear of current-carrying brushes of 5 W sealed engines

Normal conditions		Thermo-chamber operation mode: $t = 120 \text{ }^\circ\text{C} \pm 3 \text{ }^\circ\text{C}$, $P = 15 \pm 1\% \text{ mm Hg}$.							
Number of cycles: 150		Number of cycles: 50		Number of cycles: 100		Number of cycles: 150		Number of cycles: 200	
Resistance of the polished film (Ω)	Brush wear, $\text{mm} \times 10^{-3}$	Resistance of the polished film (Ω)	Brush wear, $\text{mm} \cdot 10^{-3}$	Resistance of the polished film (Ω)	Brush wear, $\text{mm} \cdot 10^{-3}$	Resistance of the polished film (Ω)	Brush wear, $\text{mm} \cdot 10^{-3}$	Resistance of the polished film (Ω)	Brush wear, $\text{mm} \cdot 10^{-3}$
0.779	5.57	0.657	66	–	–	–	–	–	–
0.755	5.45	–	–	0.564	109	–	–	–	–
0.768	5.49	–	–	–	–	0.493	200	–	–
0.775	5.57	–	–	–	–	–	–	0.384	225

The degree of sparking in the experiments remained approximately constant (no more than $1\frac{1}{2}$ points) and was measured by the PKK-5, the instrument for monitoring the switching of electrical machines [21]. The PKK-5 is designed to assess the degree of sparking of brushes of collector electric machines in stationary modes by a signal from a multi-polar brush indicator.

To test the effect of the collector material on the wear of the current-carrying brushes, the authors studied three 2.5-W sealed DC engines with drainage on the case with collectors made of copper, cadmium and chrome bronze and current-conducting brushes G-21A (Table 3). The research cycle included their work in normal and in high-altitude conditions (pressure 15 mm Hg) in combination with temperatures of $+85\text{ }^{\circ}\text{C}$ and $-60\text{ }^{\circ}\text{C}$, with measurement of the total wear of brushes (the number of cycles for each mode is the same).

The largest total brush wear is observed at the anchor with a copper collector (1.7 times relative to chrome bronze), the smallest is on a chrome bronze collector.

The brush wear of electrical machines designed to work in high-altitude conditions can be reduced by reducing the friction coefficient of the brush-collector by installing the LB made on the basis of the DM [22].

Table 4 presents the results of the effectiveness of the use of PF in a sealed electric engine with a power of 5 W, in which an additional brush holder was placed in an additional brush holder. The use of LB reduces wear on the current-carrying brushes when working in a thermal pressure chamber with temperatures $+120\text{ }^{\circ}\text{C}$ and $-60\text{ }^{\circ}\text{C}$, at a pressure of 15 mm Hg, respectively, 5 and 7 times. While working in normal conditions, wear is reduced by 1.5 times. Table 5 presents the results of the evaluation of the influence of LB on the characteristics of the test engine operating as part of mechanisms with MGS-7 and G-21A brushes under normal conditions and in a thermo-chamber.

Installing LB (one LB on two conductive) leads to a maximum increase in current consumption up to 13% and the time of rotation of the shaft of the mechanism up to 12%. However, the parameters of engines correspond to the specifications for their delivery.

Table 6 presents the results of reducing wear of the current-carrying brushes when installing LB on different types of 2.5 W engine collectors. Installing LB on

Table 3 Brush wear of 2.5 W engine with different collector materials

No.	Experiment conditions	Total brush wear on research cycle (normal + high-altitude conditions) $p = 15\text{ mm Hg} \cdot t = (+85\text{ }^{\circ}\text{C}, -60\text{ }^{\circ}\text{C}), \text{ mm} \times 10^{-3}$
1	Brushes G-21A, copper collector	44.4
2	Brushes G-21A, cadmium bronze collector	36.2
3	Brushes G-21A, chrome bronze collector	25.6

Table 4 Current-carrying brush wear of an electric engine with a power of 5 W when installing a lubricating brush

Experiment conditions	Brush brand	Thermo-chamber operation mode		
		Normal conditions	$t = 120 \pm 3 \text{ }^\circ\text{C}$, $p = 15 \text{ mm Hg}$	$t = -60 \pm 3 \text{ }^\circ\text{C}$, $p = 15 \text{ mm Hg}$
		Brush wear during the test cycle, mm 10^{-3}		
There is no lubricating brush	G-21A	9.74	12.18	80.4
There is a lubricating brush	G-21A	6.09	2.43	10.95

Table 5 Comparative characteristics of a 5 W sealed engine when a lubricating brush is installed

Experiment conditions	Supply voltage, B	Current through brushes, A		Turning time of the shaft, c	
		Right rotation	Left rotation	Right rotation	Left rotation
<i>Brush MGS-7</i>					
Normal conditions	27	$\frac{0.74}{0.77}$	$\frac{0.74}{0.79}$	$\frac{8.03}{8.68}$	$\frac{8.08}{8.18}$
$t = +120 \pm 3 \text{ }^\circ\text{C}$, $p = 15 \text{ mm Hg}$		$\frac{0.73}{0.76}$	$\frac{0.71}{0.75}$	$\frac{8.76}{9.22}$	$\frac{8.69}{9.18}$
$t = -60 \pm 3 \text{ }^\circ\text{C}$, $p = 15 \text{ mm Hg}$		$\frac{0.7}{0.76}$	$\frac{0.66}{0.75}$	$\frac{8.48}{9.22}$	$\frac{8.12}{9.18}$
<i>Brush G-21A</i>					
$t = +120 \pm 3 \text{ }^\circ\text{C}$, $p = 15 \text{ mm Hg}$	27	$\frac{0.62}{0.65}$	$\frac{0.63}{0.65}$	$\frac{8.38}{9.45}$	$\frac{8.5}{9.92}$
$t = -60 \pm 3 \text{ }^\circ\text{C}$, $p = 15 \text{ mm Hg}$		$\frac{0.61}{0.66}$	$\frac{0.61}{0.64}$	$\frac{8.18}{9.33}$	$\frac{8.23}{9.16}$

Note Numerator—engine characteristics without lubricating brush; denominator—engine characteristics when a lubricating brush is installed

Table 6 Current-carrying brush wear of 2.5 W electric engine with different collector materials when LB is installed

No.	Experiment conditions	Brush brand	Total brush wear (normal + high-altitude conditions), mm 10^{-3}
1	There is a lubricant brush, copper collector	G-21A	15.2
2	There is a lubricant brush, cadmium bronze collector	G-21A	10.6
3	There is a lubricant brush, chrome bronze collector	G-21A	6.4

the collector of copper, cadmium and chrome bronze, respectively, reduces the wear of standard brushes in 2.9, 4.2 and 6.9 times relative to a regular collector made of copper. The pressure on LB was the same.

In all cases, there is a slight increase in current and a decrease in rotational speed. Changes in parameters when using cadmium and chromium bronzes are approximately the same. An anchor with a copper collector in the case of a LB installation is characterized in general by a larger value of current consumption. However, all electric engines correspond to the specifications of their delivery.

Thus, a LB installation leads to a decrease in wear of the current-carrying brushes.

4 Conclusion

Thus, when working in high-altitude conditions, the wear of the brushes in the case of a sealed engine increases not only due to a decrease in the moisture content in the environment but also due to a decrease in oxygen in the air. It leads to a decrease in the thickness of the PF and increased wear of brushes. The use of lubricating brushes made on the basis of molybdenum disulfide can significantly reduce the wear of the brushes without significant structural modifications.

5 Recommendations

The issue of improving the systemic reliability of UST electric machines based on counteracting the negative physicochemical processes arising during the operation of electric engines requires finding new technological ways and approaches. One of them is the formation of the interface surface of a brush-collector with effective tribological characteristics [8, 22, 23].

References

1. Safonov AL, Safonov LI (2009) Rectangular electrical connectors. Fretting is corrosion in electrical contacts. *Technologies in the electronic industry* 3:48–54
2. Yanin EP (2007) Corrosion of metals and metal structures as a source of environmental pollution. *Probl Environ Nat Resour* 6:46–92
3. Korolyanchuk DG, Nefedov VG, Ovcharenko VI (2017) About the reasons for the increase in corrosion rate under thin films of water. *Ukrainian State University of Chemical Technology. Metal metallurgy and thermal processing of metals* 4:31–37
4. Stekolnikov YuA, Stekolnikova NM (2008) *Physico-chemical processes in engineering technology. Textbook.* Publishing House of Yelets State University named after I.A. Bunin, Yelets, 136 p

5. Kachin OS (2008) Increasing the resource of the sliding contact of universal collector motors. Dissertation, Tomsk
6. Khokhryakova EA, Reznik YE (2007) Water preparation: handbook. Aqua-Term, Moscow, p 240
7. Kachin SI, Kachin OS (2011) Results of the study of the influence of the mechanical state of collectors and bearings on the processes of wear in the sliding contact of an electric machine. Proceedings of higher educational institutions. Electr Eng 6:5–9
8. Rostik GV (2008) Evaluation of the technical condition of turbine generators: textbook. Federal Education Agency, Institute of advanced training of state employees, department “Operation of energy facilities and energy sales activities”, sector “Technical. Re-equipment, modernization and repair in the energy sector”. IPK of the civil service, Moscow, 489 p
9. Fominyh AA (2015) Evaluation of the influence of solid lubricant on tribo characteristics of sliding current collection sites. Dissertation. Kirov
10. Korshunov AV, Il'in A (2008) Peculiarities of the oxidation of copper nanopowders when heated in air. Polytech Univ Tomsk 313(3):5–13
11. Izotov AI, Fominykh AA, Pokashev DK, Kokhanchuk ND, Izotov SA (2017) On the issue of solid-phase oxidation of metal surfaces of collector-electric machines. In: All-Russian annual scientific and practical conference. Society. Science. Innovations (NPK-2017), 01–29 April 2017, pp 1093–1102
12. Myshkin NK, Konchiz VV, Brownovich MK (2008) Electrical contacts. Intellect, 560 p
13. Kontseva SA (2015) Hydrocarbonate equilibrium in aqueous solutions. Sci Technol Educ 9:7–9
14. Vasileva LV (2017) Formation of the elemental and phase composition of deposits in heat power equipment in the conditions of various water treatment schemes and methods of their removal. Dissertation, Krasnodar
15. Samorodov YuN (2011) Risks of damage to turbine generators. Library of electrical engineering. Is. 3. Part 1. NTF Energoprogress, Energetik, Moscow, 80 p
16. Tsofov GI, Ovsyannikov VN, Elshansky NA (2014) Mechanism of contacting sliding contact from carbon-graphite materials. Volga Reg Bull 1(43):111–114
17. Grigoryan EG, Niazyan OM, Kharatyan SL (2006) Kinetics and mechanism of reduction of copper (II) oxide by various reducing agents in non-isothermal conditions. Yerevan State Univ Chem J Armen 4:44–54
18. Samorodov YuN (2011) Risks of damage to turbine generators due to defects. The library of electrical engineering. Is. 4. Part 2. NTF Energoprogress, Moscow, 64 p
19. Pogrebnyak AD, Kaverina AS, Kilyshkanov MK (2014) Electrolytic-plasma technology for coating and processing of metals and alloys. Sumy State Univ Physicochem Surf Prot Mater 50(1):72–88
20. Izotov AI, Fominykh AA, Timoshenko VN, Izotov SA, Timina NV (2013) Improving the reliability of the brush-contact device of electric motors G. Mech Electr Agric 4:32–33
21. Kharlamov VV, Sergeev RV, Shkodun PK, Akhmedzyanov GG (2005) Device for measuring the intensity of arcing on the collector of an electrical machine. Patent for useful model 53820, IPC H01R 39/58
22. Izotov AI, Izotov SA, Fominykh AA, Timoshenko VN, Sobolev DV (2017) A method of reducing the wear of friction units in electric machines through the use of nanotechnology. In: International scientific and technical conference “the state and prospects for the development of electrical and thermal technologies (XIX) Benardosov readings”, Ivanovo State Energy University, Ivanovo, May 31–02 June 2017, pp 144–147
23. Izotov AI, Fominykh AA, Nikulin SV, Prokoshev DK, Legoti AB, Timina NV (2018) Increasing operational life of brush-contact device in the turbine generator due to using lubricating molybdenum disulphide brushes. IOP Conf. Series J Phys Conf Series 944:012045. Vyatka State University. <https://doi.org/10.1088/1742-6596/944/1/012045>

Bench-Scale Tests Aimed at Finding Rate and Acceleration of Wear Determining Service Life of Thrust Bearing in Submersible Electric Motor



V. A. Butorin, I. B. Tsarev and R. T. Guseynov

Abstract Thrust bearing is one of the main parts of a submersible electric motor and its service life to a large extent determines the reliability of the entire water pump system. However, the problem of thrust bearing service life in submersible electric motors has not been studied appropriately. In this article, an expression, which allows one to estimate the service life of thrust bearing in submersible electric motor through the initial rate and the acceleration of its wear, has been obtained. The results of the bench-scale tests referred to studying the rate of thrust bearing wear depending on operational factors are presented. Bench-scale tests were based on the experimental design theory. The variation levels of operational factors were determined during the experimental studies on the basis of monitoring water supply wells in the Urals Federal District. To reduce the number of experiments, a fractional factorial experiment with threefold replication has been implemented. It has been revealed that the presence of mechanical impurities in water and water hardness have the greatest effect on the wear rate. It has been shown how to find the initial rate and the acceleration of thrust bearing wear, which determine its service life, on the basis of the experimental dependences of the thrust bearing wear rate on the operational factors with two different operating times of a submersible electric motor. The article will be useful for employees of enterprises engaged in repairing submersible electric motors, as well as for companies involved in operation and maintenance of water pumping units.

Keywords Submersible electric motor · Thrust bearing · Service life · Bench-scale tests

V. A. Butorin (✉) · I. B. Tsarev · R. T. Guseynov
South Ural State Agrarian University, 13, Gagarin Str, Troitsk 457100, Russia
e-mail: butorin_chgau@list.ru

© Springer Nature Switzerland AG 2020
A. A. Radionov et al. (eds.), *Proceedings of the 5th International Conference on Industrial Engineering (ICIE 2019)*, Lecture Notes in Mechanical Engineering,
https://doi.org/10.1007/978-3-030-22041-9_114

1089

1 Introduction

Ensuring uninterrupted water supply to agricultural objects is an important task of the national economy. In rural areas, freshwater is often produced using water supply wells from underground sources. Submersible pumps [1] with asynchronous motors of the PEDV brand (water-filled submersible electric motor) have become widely used as water lifters. About 70% of faults in water pumping systems are connected with electric motors [2]. Approximately 30% of PEDV failures are caused by the breakdown of a thrust bearing [3]. Therefore, the service life assessment of the thrust bearing in PEDV is an important task.

Thrust bearing is a plain bearing unit and serves to support the weight of a rotor. It consists of a thrust collar mounted on the motor shaft and a plain thrust bearing fixed in its case [4]. A thrust collar of *PEDV* is a disc made of stainless steel. A plain thrust bearing is a steel ferrule to which a rubber pad divided into segments by a profiled groove is securely vulcanized [5–7] (Fig. 1).

In the stationary operating mode of *PEDV*, due to the hydrodynamic lifting of the rotor, between the thrust collar and the plain thrust bearing, there is a small gap filled with liquid which acts as a lubricant [8, 9]. Intensive wear of the thrust bearing, which reduces its service life, occurs in the process of rotor accelerating during the start of *PEDV* or rotor slowing down during *PEDV* shutoff. The reason for the wear of plain bearing unit surfaces is dry and semi-liquid friction between the thrust collar and the plain thrust bearing, which acts in the transition process of *PEDV* to the stationary operating mode or to the state of rest [10].

2 Theoretical Assessment of Thrust Bearing Service Life in Submersible Electric Motor

In the first approximation, we can assume that the thrust bearing wear, which is understood as the reduction in the thickness of the rubber pad of the thrust bearing, is proportional to the operating time, which is measured in the number of on–off cycles:

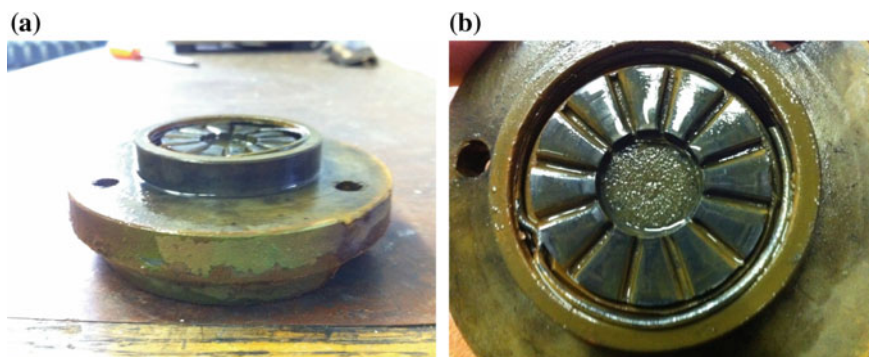


Fig. 1 Plain thrust bearing in submersible electric motor: **a** side view and **b** top view

$$h = Vt, \quad (1)$$

where h is the wear of the thrust bearing, microns; t is the work, cycle; V is the wear rate, $\mu\text{m}/\text{cycle}$.

However, preliminary studies suggest that the wear rate V is not constant and in order to characterize the rate of its change, it is advisable to introduce the acceleration a [11], which by definition is the first derivative of the rate by operating time:

$$a = \frac{dV}{dt}, \quad (2)$$

where a is the acceleration of wear, $\mu\text{m}/\text{cycle}^2$.

To determine the service life of thrust bearing, it is necessary to find the law of change in wear h depending on the operating time t . For this purpose, we shall use the definition of the wear rate (3):

$$V = \frac{dh}{dt}. \quad (3)$$

When solving the system of differential Eqs. (2) and (3), we find the dependence of wear h on the operating time t :

$$h = V_0t + \frac{at^2}{2} \quad (4)$$

where V_0 is the initial wear rate, $\mu\text{m}/\text{cycle}$.

When the wear h reaches the maximum permissible value H , the operating time t will be equal to the service life T . Therefore, when solving the quadratic Eq. (4) regarding the maximum operating time, we find how the thrust bearing service life T is expressed through the initial rate V_0 and the acceleration of wear:

$$T = \frac{V_0}{a} \left(\sqrt{1 + \frac{2aH}{V_0^2}} - 1 \right) \quad (5)$$

The initial rate V_0 and the acceleration a of the thrust bearing wear can be found from the experimental dependence of the amount of wear h on the operating time t as follows: we measure the wear h_1 after operating time t_1 and the wear h_2 after operating time twice as large $2t_1$. Substituting these quantities in (4) results in a system of two equations with two unknowns V_0 and a . When solving this system, we obtain expressions for calculating the initial rate V_0 and the acceleration a of wear.

$$V_0 = \frac{4h_1 - h_2}{2t_1}; \quad (6)$$

$$a = \frac{h_2 - 2h_1}{t_1^2}. \quad (7)$$

The initial rate V_0 and the acceleration a of wear are random variables depending on the conditions of the PEDV operation. Therefore, as follows from (5), the service life T of the thrust bearing will also be a random value.

3 Bench-Scale Tests Aimed at Determining the Initial Rate and the Acceleration of the Thrust Bearing Wear in a Submersible Electric Motor

According to (6) and (7), in order to find the dependences of the initial rate V_0 and the acceleration of the thrust bearing wear on the operational factors, it is necessary to determine experimentally how the amount of wear depends on these factors for two different operating time of PEDV. For this purpose, a test bench-scale that simulates the operation of PEDV in water supply wells was developed [3, 12]. As a result of literature analysis and expert assessments, the following factors were chosen as the operational factors that significantly affect the service life of thrust bearing: supply voltage, presence of mechanical impurities in the form of fine sand and chlorine ions in water, as well as hardness and oxidability of water [13].

Bench-scale tests were carried out on the basis of the experimental design theory [14–16], which allows to approximate the unknown, that is the functional dependence, determined experimentally by a polynomial [7]. The levels of variation factors are presented in Table 1.

The upper and lower levels of variation for mechanical impurities and chemical composition of water were selected on the basis of data monitoring provided by the Chelyabinsk branch of the FBI “Territorial Fund of Geological Information in the Urals Federal District.” The factors are encoded in such a way that the maximum value of the natural factor corresponds to 1 of encoded factor, the minimum value corresponds to -1 , and the average value of the natural factor corresponds to 0 [17].

If there are five main factors to reduce the number of experiments, fractional factorial experiment of the type 2_{V}^{5-2} [18] is implemented. Its matrix is presented in Table 2.

The experiments were conducted with a triple repetition. The results of the experiment are presented in Table 3.

The measurements of wear amount were carried out after operating time $t_1=1000$ and $t_2=2000$ of on-off PEDV cycles. The results of bench-scale tests were processed according to the methodology used in the experimental design theory and included: checking the reproducibility of experiments using the Kokhner

Table 1 Levels of operational factors variation during bench-scale testing

Factor	Designation	Dimension	Code	Variation levels		
				Upper (+1)	Average (0)	Lower (-1)
Supply voltage	<i>U</i>	V	X_1	400	380	360
Mechanical impurities	<i>I</i>	mg/l	X_2	200	100	0
Water hardness	<i>H</i>	mmol/l	X_3	10	7	4
Water oxidability	<i>O</i>	mgO ₂ /l	X_4	6.6	3.3	0
Chlorine ions	<i>C</i>	mg/l	X_5	450	350	250

Table 2 Matrix of fractional factorial experiment of the type 2^{5-2}_V

No. of experiment	Factor							
	X_1	X_2	X_3	X_4	X_5	X_2X_3	X_2X_4	$X_2X_3X_4$
1	+	+	+	+	+	+	+	+
2	-	+	+	-	-	-	-	+
3	+	-	+	-	+	-	+	+
4	-	-	+	+	-	+	-	+
5	+	+	-	+	-	+	-	+
6	-	+	-	-	+	-	+	-
7	+	-	-	-	-	-	-	+
8	-	-	-	+	+	+	-	+

Table 3 Results of bench-scale tests

No. of experiment	Wear h_1 , μm after operating time 1000 cycles			Wear h_2 , 10 μm after operating time 2000 cycles		
	1st repetition	2nd repetition	3rd repetition	1st repetition	2nd repetition	3rd repetition
1	90	75	65	18	15	13
2	81	75	50	16	15	10
3	15	17	11	30	36	22
4	35	20	15	71	41	31
5	50	35	45	41	70	90
6	40	35	44	81	70	89
7	32	21	15	65	43	30
8	13	30	22	27	61	45

criterion, calculating regression coefficients, and evaluating their significance using the Student’s criterion, as well as verification of the model using the Fisher criterion [19, 20]. The result was an approximation of the dependence of the PEDV thrust bearing wear on the operational factors using polynomials which in the decoded form has the form:



$$h_1 = 25 - 0.066I - 0.80H + 0.034IH, \mu\text{m}; \quad (8)$$

$$h_2 = 51 - 0.13I - 1.7H + 0.069IH, \mu\text{m}. \quad (9)$$

It should be noted that the supply voltage, the oxidability of water, and the presence of chlorine ions in it turned out to be non-significant factors.

Substituting (8) and (9) into (6) and (7), we find the dependence of the initial rate and the acceleration of the thrust bearing wear on the content of mechanical impurities in water and its hardness.

$$V_0 = (25 - 0.066I - 7.5H + 0.034IH) \times 10^{-3}, \mu\text{m}/\text{cycle}; \quad (10)$$

$$a = (-56 + 10H - 0.007IH) \times 10^{-8}, \mu\text{m}/\text{cycle}^2. \quad (11)$$

Expressions (10) and (11) can be used to assess the basic statistical characteristics of the thrust bearing service life by the formula (5), if you have statistical data on water hardness and the presence of mechanical impurities in it for various water supply wells.

4 Conclusion

1. The expression (5), which helps to estimate the service life of the thrust bearing in PEDV through the initial rate and the acceleration of its wear, has been obtained.
2. As a result of bench-scale tests based on the experimental design theory, the dependences (10) and (11) of the initial rate and the acceleration of the thrust bearing wear in PEDV on operational factors have been found. The presence of mechanical impurities in the water and its hardness proved to be the most significant operational factors.
3. Dependencies (10) and (11) of the initial rate and the acceleration of the thrust bearing wear in PEDV on operational factors can be used to assess the basic statistical characteristics of the thrust bearing service life in PEDV by the formula (5), if you have statistical data on water hardness and the presence of mechanical impurities in it for various water supply wells. This may be a topic for further research.

References

1. Takacs G (2009) Electrical submersible pumps manual: design, operations, and maintenance. Gulf Professional Publishing, Burlington
2. Butorin VA, Guseinov RT (2012) Causes of electric motors failures in submersible pumps and actions for their elimination. In: LI international scientific and technical conference "Science achievements for agro-industrial production". Russia, Chelyabinsk, February 2012, pp 45–49

3. Butorin VA, Guseinov RT (2014) Development of a test-scale bench for carrying out service life tests of thrust bearing in submersible motor by the PEDV brand. *Vestnik BSAU* 2(30):64–68
4. San Andres L, Phillips S, Childs D (2016) A water-lubricated hybrid thrust bearing: measurements and predictions of static load performance. *J. Eng. Gas Turbines Power* 139(2):022506–022506-10. <https://doi.org/10.1115/1.4034042>
5. Aggarwal S, Pandey RK (2018) Performance investigation of micro-pocketed textured pad thrust bearing. *Ind Lubr Tribol* 70(8):1388–1395. <https://doi.org/10.1108/ILT-10-2017-0302>
6. Kumar V, Sharma SC (2018) Influence of dimple geometry and micro-roughness orientation on performance of textured hybrid thrust pad bearing. *Meccanica* 53(14):3579–3606. <https://doi.org/10.1007/s11012-018-0897-0>
7. Aggarwal S, Pandey RK (2017) Frictional and load-carrying behaviours of micro-textured sector shape pad thrust bearing incorporating the cavitation and thermal effects. *Lubr Sci* 29(4):255–277. <https://doi.org/10.1002/lvs.1367>
8. Rohmer M, San Andres L, Wilkinson S (2018) Static load performance of a water-lubricated hydrostatic thrust bearing. *J. Eng. Gas Turbines Power* 140(6):062401–062401-10. <https://doi.org/10.1115/1.4038472>
9. Gao GY, Yin ZW, Jiang D et al (2014) Numerical analysis of plain journal bearing under hydrodynamic lubrication by water. *Tribol Int* 75:31–38. <https://doi.org/10.1016/j.triboint.2014.03.009>
10. Danilov VN, Shinkarenko IV (2001) Justification of the rotation frequency in submersible electric pump of the ECW type during technological breaks of water supply. *Vestnik CSAU* 35:118–121
11. Butorin VA, Tsarev IB, Guseinov RT (2017) Theoretical substantiation of the thrust bearing assembly service life in submersible electric motor. *Agro-Ind Complex Russ* 24(5):1157–1160
12. Butorin VA, Guseinov RT (2014) Development of electrical circuit for carrying out service life tests of the thrust bearing assembly in submersible electric motor. *Bull Sarat State Agrar Univ Honor N.I. Vavilov* 3:46–49
13. Butorin VA, Guseinov RT (2014) Main factors affecting the bearing units service life in submersible electric motors. In: LIII international scientific and technical conference “Science achievements for agro-industrial production”. Russia, Chelyabinsk, February 2014, Part 3. pp 241–246
14. Hinkelmann K, Kempthorne O (2007) *Design and analysis of experiments, vol. 1: introduction to experimental design*, 2nd edn. Wiley, Hoboken
15. Hinkelmann K, Kempthorne O (2005) *Design and analysis of experiments, vol. 2: advanced experimental design*. Wiley, Hoboken
16. Hinkelmann K, Kempthorne O (2012) *Design and analysis of experiments, vol. 3: special designs and applications*. Wiley, Hoboken
17. Morris M (2010) *Design of experiments: an introduction based on linear models*. Chapman and Hall, New York
18. Clarke Geoffrey M, Kempson Robert E (2010) *Introduction to the design and analysis of experiments*. Wiley, New York
19. Tamhane Ajit C (2012) *Statistical analysis of designed experiments: theory and applications*. Wiley, Hoboken
20. Easterling Robert G (2015) *Fundamentals of statistical experimental design and analysis*. Wiley, Chichester

Macromechanism Destruction of Structurally and Crystallographically Textured Titanium Billets



M. A. Skotnikova, G. V. Ivanova and A. A. Strelnikova

Abstract A systematic investigation of fracture features of structurally and crystallographically textured billets in a two-phase Ti-6Al-IV-IMo alloy impact and low-cycle tested with a light metallographic, X-ray, and scanning electron microscopy was carried out. It is indicated that a reduction of the tensile properties is induced by the structurally and crystallographically precipitated fields of basis orientation of the interface boundaries of 20–30 μm in width spaced across the thickness billet by 100–170 μm . They are responsible for increasing the anisotropy of shock values and increasing the scattering of the results of low-cycle tests of samples in two-phase titanium alloys. The lower the applied stress value at the time of the specimen testing (impact or cyclic), the more the contribution of crack initiation period in its life time, the more important is the account of the number and geometry of the location in a bulk of the flat billets of such structurally and crystallographically pronounced fields effecting on the fracture mechanism change of the tested samples.

Keywords Titanium alloys · Structure · Impact values · Fatigue · Electron microscopy · Fracture mechanism

1 Introduction

A fracture of titanium alloy billets at the time of a hot deformation (rolling) is their elevated sensitivity to a temperature and deformation inhomogeneity across the thickness. This induces a concentration inhomogeneity of alloying elements distribution and an inhomogeneity of a recrystallisation process across the thickness of the flat billets and generation of a geometrical-oriented (structurally texted) structure. The structure enhances anisotropy of the mechanical properties of flat billets.

M. A. Skotnikova (✉) · G. V. Ivanova · A. A. Strelnikova
Peter the Great St.-Petersburg Polytechnic University,
29, Polytechnicheskaya Street, St.-Petersburg 195251, Russia
e-mail: skotnikova@mail.ru

An addition to structural texture, the anisotropy of the properties is influenced by a crystallographic texture of deformation represented by a preferred orientation of elemental hexagonal cells of a crystal lattice of a α -phase influenced by rolling stresses [1–13]. The present work aims at an investigation of impact and low-cycle values of the hot deformed billets of the two-phase titanium Ti-6Al-1V-1Mo alloy with structural and crystallographic texture features of the investigated materials.

2 Impact Bend Test

Figure 1 shows the scheme of the cutting impact specimens and coating them with cuts.

The test results indicated that the billets were characterized by a pronounced anisotropy of the impact values KCV and KCU and its base component—a crack propagation energy (see Table 1).

To explain the results, an investigation of volume morphology of a structural and crystallographic texture of the billets with light metallography, X-ray, and electron microscopy was carried out. As X-ray investigations showed in the billets, two components texture of a prismatic $\{10\bar{1}0\}$ type with an $\langle 0001 \rangle$ axes-oriented along and across, the rolling direction had generated. An investigation of the billets by color electrochemical painting allows to suppose that the components of the crystallographic texture across the full thickness of the billet had a lamellar structure (see Fig. 2a).

Within the layer sections of the $\{0001\}$ crystallographic plane of the α -titanium (white color on the figure) were distributed across the thickness of the billet and $\langle 0001 \rangle$ orientation was changed layer by layer and made up 0, degree angle (non-basic component of the order of magnitude of 20%) or 90, degrees (basic component of the order of magnitude of 60%) in respect with the rolling direction.

The metallographic studies showed that in a surface layers of the hot rolled billet the structurally pronounced fields (bands) had formed, the thickness of the bands

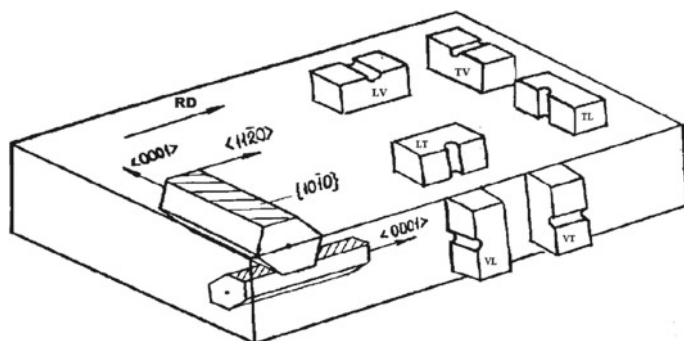
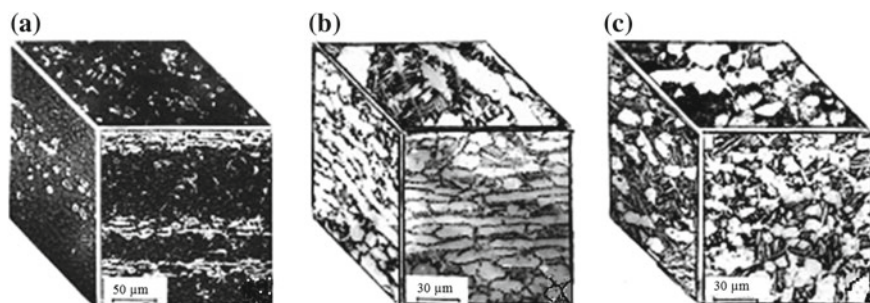


Fig. 1 Scheme of the cutting impact specimenes and coating them with cuts in a bulk of a billet

Table 1 Impact values, KCV, KCU, Mj/m^2 and its components—a crack initiation and a crack propagation energy

Specimen and notch orientation	KCV	KCU	KCU initiation	KCU propagation
TL	0.51	0.76	0.33	0.43
VT	0.45	0.57	0.16	0.41
TV	0.89	0.92	0.06	0.86
LT	0.58	0.74	0.21	0.53
VL	0.73	0.86	0.18	0.68
LV	1.29	1.32	0.06	1.26

**Fig. 2** Volume morphology **a** of crystallographic texture; **b** of structural in surface; **c** an axial layer of billet

was 20–30 μm , they consisted of elongated in two mutually perpendicular directions and tapered in thickness, tightly adjacent to each other α -phase particles (see Fig. 2b).

The preferred orientation of the boundaries of these structurally pronounced fields makes up 90° in respect to the rolling direction (non-basic component) or 0° (basic component) [9, 14–24].

So, in the surface layers of the billet, the structurally pronounced fields seemed to be crystallographically pronounced fields of the basic orientation of the interface boundaries which over regularly distributed across its thickness and spaced by 100–170 μm .

An axial layer of the hot rolled structurally pronounced field of the geometrical orientation the boundaries were not observed, in practice. There was observed small chains of rounded recrystallized grains of the α -phase of the basic orientation across the thickness (see Fig. 2b).

Fractographic investigations of the fracture surfaces of the impact specimens of lamellar structure and of a crystallographic texture allow to understand their fracture mechanisms during the test. The basic micromechanism of a specimen plastic deformation when the applied stress is normal to the $\langle 0001 \rangle$ direction is known to be a prismatic sliding in the $\{1010\}$ plain in $\langle 1120 \rangle$ direction, which induces high values of impact toughness. The deformation of the specimens, where the applied

stresses are parallel to $\langle 0001 \rangle$ direction is activated by a twinning process along $\{10\bar{1}1\}$ plane, and here, the impact values are lower. At the time of destruction, the main crack looks for ways (directions) of the easiest propagation. As for the investigated billets, these directions are extension direction of the large-angle boundaries of structurally pronounced fields out of α -phase primary grains and also a direction along the $\langle 0001 \rangle$ crystallographic axes within the grains. The crack propagates by a minimum energy consumption along these indicated orientations (structural and crystallographic). Kolachev B. A. in 1983 year indicates that the energy to initiate a micro crack will be minimum when dislocation mechanism of its initiation in a metal is retarded and crack generation occurs along the inner interfaces preferably [25].

So, the structural texture of the investigated materials was represented by a preferred orientation of the large-angle interface boundaries of the flattened and elongated particles of the α -phase. The crystallographic texture is represented by a preferable orientation of the elemental hexagonal cells of the crystal lattice of the titanium α -phase. First, the effect of structurally and crystallographically pronounced fields elongated along the rolling direction (basic component) on the fracture micromechanisms of the impact specimens was studied. A contribution of structural texture in these fields is clearly shown on the TL samples (KCU prop. = 0.43 MJ/m^2), for whom large-angle boundary orientation is coincided to the propagation direction of the main crack (see Fig. 3a).

The striations—traces of a ductile destruction along the boundaries of these structurally pronounced fields were observed on the fracture of these specimens type (see Fig. 4a).

The crack initiation in these specimens was preceded by an appreciable plastic deformation along an intersecting under 90° $\{0001\}$ and $\{10\bar{1}0\}$ planes in $\langle 11\bar{2}0 \rangle$ direction which is in line with a direction of an applied load. Because of this, the crack initiation energy is large (KCU init. = 0.33 MJ/m^2). Vertical specimens of VT type (KCU prop. = 0.41 MJ/m^2), the tested section of which was taken out of an axial section of the billets indicate a contribution of the crystallographic texture

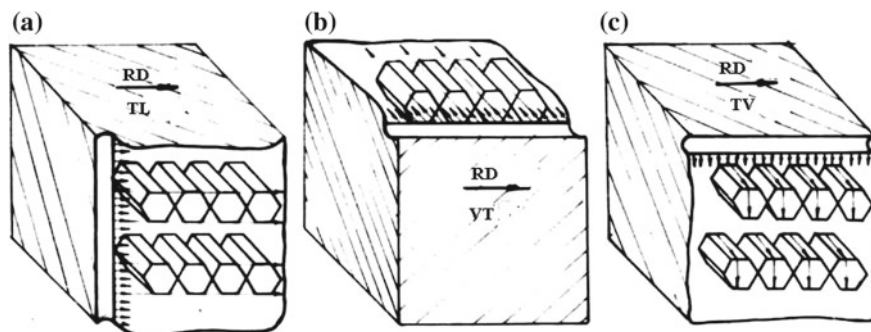


Fig. 3 Fracture mechanism of the impact specimens of structural (a), crystallographic (b), and both types texture (c)

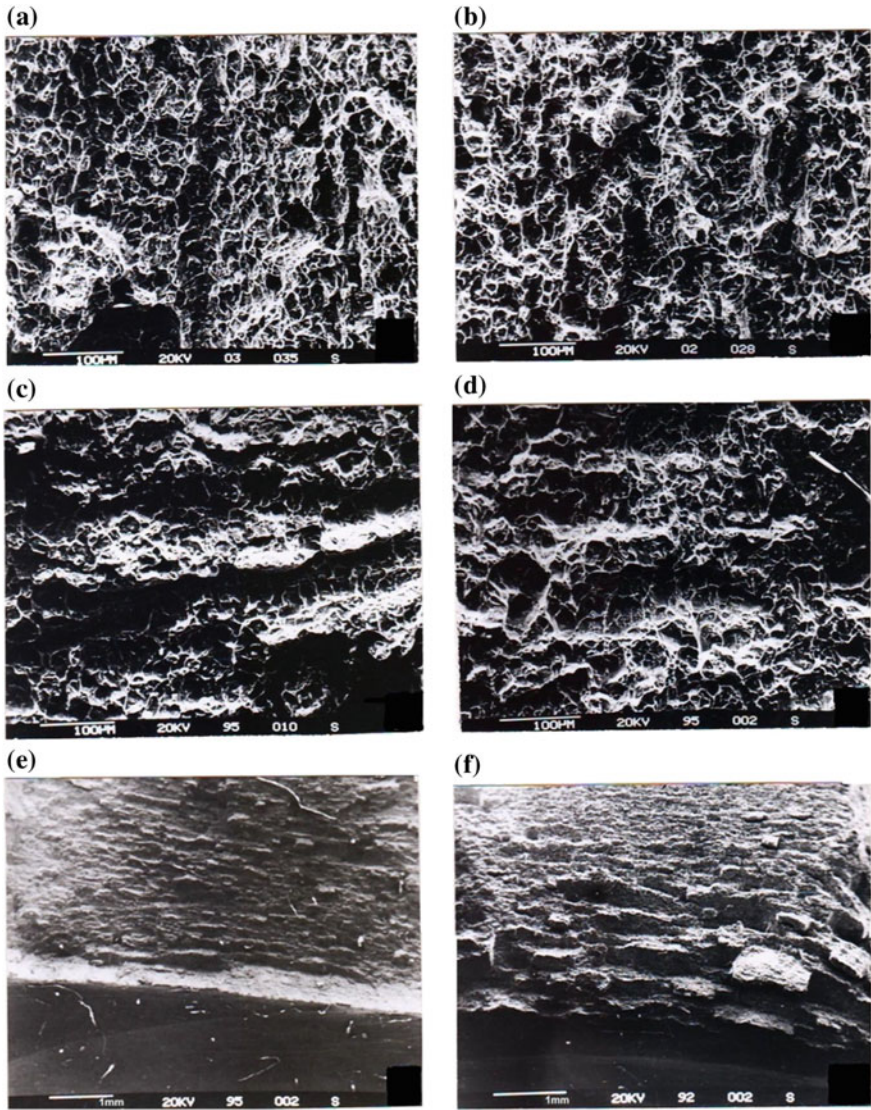


Fig. 4 Characteristic photographs of a microsections of crack propagation zones on fracture surfaces of impact specimens of **a** TL, **b** TV, **c** VL, **d** VT, **e** LT, **f** LV types

only, as the structural texture of the material does not exist in the axial layers. The direction of the propagation of the main crack was in line with the $\langle 0001 \rangle$ crystallographic orientation (see Fig. 3b) and traces of plastic deformation process by microtwinning mechanism were observed on the fracture surfaces of the specimens of this type (see Fig. 4c).

The contribution of the both factors was investigated on the specimens of TV type (KCU prop. = 0.86 Mj/m²). The impact values of these specimens were good related to the total values of impact and energies of the specimens of TL and VT type. In the specimens of TV type with the main crack propagation, the energy was consumed either by a crack opening along the boundaries of the structurally pronounced fields or by a drastic change of its movement direction along the crystallographic axes of <0001> type normal to a front of the crack propagation (see Fig. 3c). Some jogs were observed on the fracture surfaces which is a feature of the crack propagation with large energy consumption (see Fig. 4g). However, the crack initiation energy of the specimens of this type was minimum (KCU init. = 0.06 Mj/m²), as the direction of the operating load was not in the line with either sliding system, and the fracture preceded plastic deformation was not present.

The similar arguments can be put forward for the specimens of LT, VL, and LV type. At the time of their fracture, the main crack meets the structurally and crystallographically pronounced fields oriented across the rolling direction. As the component is not base one (about 20%), its embrittlement effect was smaller, and impact values was higher as compared to the corresponding samples of TL, VT, and TV type (see Table 1). A fractographic analysis of the fracture surfaces of the specimens. Figure 4b, d, f showed, that they fractured by the similar mechanisms (see Fig. 3a–c).

Thus, we can summarize that in the investigated billets after hot deformation, a strong structural (in the surface layers) and crystallographic (across the full plate thickness) texture of material with lamellar structure is generated. These layers of the basic orientation of interface boundaries of the structurally and crystallographically pronounced fields of 20–30 μm in width are regularly distributed across the full thickness of the billet and spaced by 100–170 μm. The existence of these fields in the material results in a change of a fracture mechanism and in an enhancement of the anisotropy of impact values of the specimens in the two-phase titanium alloys.

3 Low-Cycle Tests

A similar combination of the investigations was carried out on a low-cycle specimens with a circumferential notch taken out of the surface layer of a billet in such a manner as its axis was parallel to the rolling direction (see Fig. 5a). 120 specimens tested in a 3% NaCl solution in a regime of a form zero tension under pulsed cycle loading of 2–3 c/min and of applied stress amplitude 0.8 and 0.7 of the average value of the yield strength. Cycles to fracture change in ranges 200–1900 and 700–3800, respectively. Thus, with a reduction of applied stress value, the scatter of cycles number to fracture increases.

A fractographic analyses of macro- and micro topography of the specimens allow to assume that with an increase of the main crack length and a reduction of the gauge section of the specimen four characteristic fracture zones. The zone of the

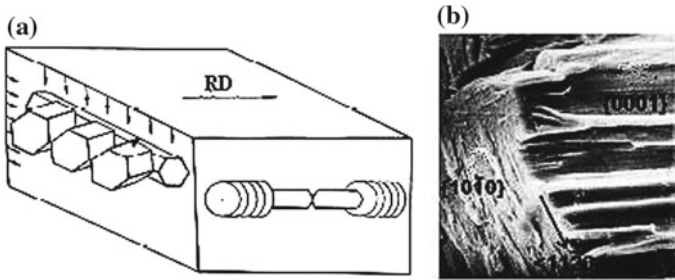


Fig. 5 **a** Fracture scheme and **b** a characteristic appearance of the fracture surface of low-cycle specimens after seawater tests

fatigue crack initiation (zone 1) changed for a zone of stable crack propagation of large fields of regularly fatigue strations (zone 2). Then, a field of an accelerated crack growth followed, where fatigue fracture mechanism was added by a mechanism of a single quasi-static failure (zone 3). And, finally, the field of an after fracture appropriate to a fact static fracture of a final part of the specimen (zone 4). The micrographs of the zone 3, the zone of the accelerated crack growth, represented the mosaic of the misoriented shear facets and microstriction colonies normal to them. This field can be designate a corrosion embrittlement zone (see Fig. 5b) as on the fracture surfaces of the specimens fractured in an air inspite of the existence of microstriction, share facets were not of served.

The zone of corrosion embrittlement was of great area on the fracture surfaces of the samples of low number of cycles to failure and came out on the edge of the sample. The color electrochemical painting of the metal just before the failure aligns to defect the structurally and crystallographically pronounced fields of the basic orientation of the interface boundary at the places of the corrosion embrittlement either does not exist on the fracture surfaces of the samples of high number of cycles to failure or there was in the middle portion of the fracture surface. The color electrochemical painting of this sample detected a non-existence of the elongated a-phase particles of the basic orientation of the interface boundaries in the plane of the main crack propagation.

The above-discussed combination of the investigation allowed to understand the fracture mechanisms of the low-cycle longitudinal samples of structurally and crystallographically pronounced fields oriented across the rolling direction (see Fig. 5a). As the samples were notched circumferentially, the zone of the main crack initiation was potentially over the whole sample perimeter at the same time. However, as it had been shown recently, in places, where structurally and crystallographically pronounced fields randomly occured in the crack initiation zone and were oriented in such a way that the direction of the active load was not in line with either of plastic deformation system (for example, on the samples of LV type (see Fig. 3c), the crack of the minimum energy of crack initiation lazily generated along plane base. Further tare place a drastic change of its movement direction along the crystallographic axis of $\langle 0001 \rangle$ type normal to a front of the crack

propagation, and the same time opening its by mechanism of multiple sliding along an intersecting crystallographic planes of $\{1010\}$ type to the $\langle 1120 \rangle$ direction. The shear facets with misconstruction colonies normal to them appeared on the fracture surfaces (see Fig. 5.b) which are in agreement with the Wanhill R.J.H. in 1976 year suppositions relating to the Ti-6Al-4 V alloy [26].

4 Conclusion

Thus, the structurally and crystallographically pronounced fields of the base orientation of the interface boundaries 20–30 μm in width spaces across the thickness of the hot rolled billet by 100–170 μm is shown to be responsible for the enhancement of anisotropy of impact values and the increase of the scatter of the low-cycle test results of the specimens in the two-phase titanium alloys.

The lower the applied stress value at the time of the specimen testing (impact or cyclic), the more the contribution of crack initiation period in its life time, the more important is the account of the number and geometry of the location in a bulk of the flat billets of such structurally and crystallographically pronounced fields affecting the fracture mechanism change of the tested samples.

References

1. Andreev AA, Anoshkin NF, Bochvar GA (1979) Semi-finished products from titanium alloys. Metallurgy, Moscow
2. Gorynin IV, Chechulin BB (1990) Titanium in mechanical engineering. Mechanical Engineering, Moscow
3. Chechulin BB, Ushkov SS, Razuvaev IN (1977) Titanium alloys in mechanical engineering. Mech. Engin, Leningrad
4. Borisova EA, Bochvar GA, Ya Brun M (1980) Metallography of titanium alloys. Metallurgy, Moscow
5. Belov SP, Brun MYa, Glazunov SG, Ilyin AA (1992) Titanium alloys. Metallurgy of titanium and its alloys. Metallurgy, Moscow
6. Kaganovich IN (1968) Features of production technology of semi-finished products from titanium and its alloys. Titanium alloys for new technology. Nauka, Moscow, pp 230–243
7. Elagina LN, Brun MYa, Evmenov OP (1980) On the role of recrystallization processes in the formation of the structure of semi-finished titanium alloys. Light Alloy Technol 1:45–51
8. Babareko AA, Egiz NV (1982) On the mechanism of deformation and fracture of large-crystal textured α —titanium alloys. News of Academy of Sciences of the USSR. Metals 6:152–157
9. Skotnikova M, Pushkarev V, Kudryavtsev A (1989) Study of micro mechanisms destruction of structurally and crystallographically textured workpieces ($\alpha + \beta$)—titanium alloy. Electron microscopy and strength of materials. Institute of problems of materials, Kiev, pp 142–148
10. Skotnikova MA, Mironova EV, Lanina AA (2013) Structural and phase transformation in material of blades of steam turbines from titanium alloy after technological treatment. Modern Mech Eng 3:256–264. Science and education. Polytechnic University

11. Skotnikova MA, Radkevich MM, Mironova EV (2014) Effect of boron microadditives on the anisotropy of mechanical properties of flat preforms from titanium alloys. *Met Sci Heat Treat* 55(9–10):540–549
12. Skotnikova MA, Krylov NA, Tsvetkova GV (2015) Structural and phase transformation in material of blades of steam turbines from titanium alloy after technological treatment. *Lect Notes Control Inf Sci* 22:93–101
13. Shaboldo OP, Vitorskii YM, Skotnikova MA (2017) Formation of the structure and properties of β -type titanium alloy upon thermomechanical treatment. *Phys Met Metall* 18:75–80
14. Skotnikova M, Pushkarev V, Igoshin C (1990) Study of structural texturing of titanium alloys of plate type in the volume of flat billets. *Fact Lab* 3:32–35
15. Skotnikova M (1992) Features of plastic deformation and fracture of two-phase titanium-based alloys. In: *Physics of strength and plasticity of metals and alloys*, Samara, pp 213–214
16. Skotnikova MA, Kudryavtsev AS (1994) Mechanism of destruction of structurally and crystallographically textured titanium billets. In: *Fracture mechanics: successes and problems*. Indian Institute of science, India, Bangalore, pp 112–1130
17. Betsofen SYa (1977) Study of anisotropy of mechanical properties and texture hardening of industrial titanium alloys. The author's abstract of dissertation. MATI, Moscow
18. Skotnikova MA, Kudryavtsev AS, Medvedeva GV (1991) Identification of the causes of the dispersion of the durability of titanium alloy elements under the corrosive effects of the environment. Improving the reliability and durability of machines and structures. The Institute of materials, Kiev, pp 81–82
19. Skotnikova MA, Kudryavtsev AS (1991) Features of destruction of structurally and crystallographically textual billets from $(\alpha + \beta)$ -titanium alloy. *Metallurgical science and technology of light alloys*. VILS, Moscow, pp 99–103
20. Skotnikova M, Kudryavtsev A (1993) Mechanism of destruction of structurally and crystallographically textured titanium billets. *Fracture mechanics: successes and problems*. Karpenko Physiko—mechanical Institute, Lviv, pp 447–448
21. Chechulin BB, Chesin JD (1987) Cyclic and corrosion strength of titanium alloys. *Metallurgy*, Moscow
22. Chesin JD, Razuvaeva IN, Kopylov VN (1987) Features of recrystallization of a pseudo- α -titanium alloy. *MITOM* 10:39–42
23. Ushkov SS, Razuvaeva IN, Kopylov VN (1988) Features of change of mechanical properties of the textured pseudo-alpha-titanium alloy in a wide temperature range. *FMM* 66(6):1205–1210
24. Skotnikova MA, Martynov MA (2005) Practical electron microscopy in mechanical engineering. St. Petersburg Institute of mechanical engineering, St. Petersburg
25. Kolachev BA, Malkov AV (1983) Physical basis of titanium destruction. *Metallurgy*, Moscow
26. Wanhill RJH (1976) A fractographic analysis of environmental fatigue crack propagation in Ti-6Al-4V sheet. *Corrosion* 32:162–172

Study on Factors Having Influence Upon Efficiency of AC Motor Chain Drive Using Newly Developed Method and Procedure for Identification of Its Friction Losses



V. Belogusev, A. Egorov and I. Polyinin

Abstract The purpose of this paper is to develop a new method, procedure, and measuring system for the identification of friction losses and mechanical characteristics of an asynchronous motor chain drive, as well as to apply them in the study of the impact of its design parameters and other operating factors on its performance. The proposed method allows monitoring the efficiency of a chain drive with a higher accuracy compared to existing methods since it does not require the use of strain gauges and, therefore, eliminates the need for their calibration and allows studying chain transmissions in dynamic operating modes in a wide range of rotational speeds and loads. The results obtained in the experimental part of this paper determine the factors that to a considerable degree affect the efficiency of a chain drive with a single-row sleeve-type chain, which indicates the applicability of the developed procedure and the measuring system for the control of its technical state under different operating conditions.

Keywords Inertia · Friction losses · Mechanical losses · Chain transmission · Performance

1 Introduction

Ensuring high efficiency of power drives remains an important task in the way of improving their quality and technical state. The solution of this problem is directly related to the improvement of the quality and accuracy of methods, procedures, and instruments for monitoring friction losses and the basic mechanical parameters of drives, in particular those with chain transmissions, which are widely used in many mechanical systems. The friction level and inertial characteristics of chain drives

V. Belogusev (✉) · A. Egorov · I. Polyinin
Institute of Mechanics and Machine Building, Volga State University
of Technology, 3, Lenin Sq, 424000 Yoshkar-Ola, Russia
e-mail: vladimir.belogusev@yandex.ru

influence the rate of degradation processes, such as wear and contact endurance, which are criteria for their efficiency, and, as a consequence, have a significant impact on their service life [1–7]. Thus, when developing new methods and improving existing ones, it is also necessary to pay close attention to the possibility of studying the causes leading to the increase in the friction losses in chain transmissions.

The literature review found out that the majority of works in the field of chain drives do not pay enough attention to the issue of measuring mechanical losses in chain transmissions, especially in dynamic modes of operation [2, 8–12]. The strain gauge method, which is currently widely used, has a low level of response speed and a poor accuracy of signal measurement and requires the fine calibration of sensors. In this regard, their use to control mechanical parameters in dynamic modes, in which chain drives are operated most time, seems inappropriate. In addition, there are difficulties associated with the transfer of the signal from the strain element, as well as the high cost of measuring equipment [6, 7, 13–17]. Such methods as a method of registering the reactionary torque on the stators of electric machines and a retardation method are used as well [18, 19]. However, significant methodological errors, the complexity of the measurement process, and the inability to create the rated tension force in the chain during experiments limit their use to solve a wide range of research tasks.

Thus, the purpose of this paper is to develop a new method and tools for measuring the main mechanical parameters of an induction motor chain drive in a wide range of speed modes that do not have the shortcomings inherent in existing methods and techniques. In order to evaluate the developed procedure and instruments, it is also planned to study the impact of operating factors of an asynchronous motor chain drive on its friction losses and efficiency.

2 Materials and Methods

2.1 *Determining the Inertia of an Asynchronous Motor Chain Drive Taking into Account Losses*

Figure 1 presents a scheme of an asynchronous electric drive, which explains the gist of the developed method.

The implementation of the developed method to determine the moment of inertia of a chain drive, taking into account losses, is possible on the basis of a brake-free technique for determining the moment of inertia of rotating elements of electric machines [20, 21]. The concept of the procedure for determining the inertia of an asynchronous motor chain drive taking into account losses is explained in Fig. 1a.

At the first stage, we determine the values of the angular acceleration, $\varepsilon_1(\omega)$, of a chain drive without a disk 9 using an encoder 10. In this case, the torque developed by an asynchronous motor can be determined as follows:

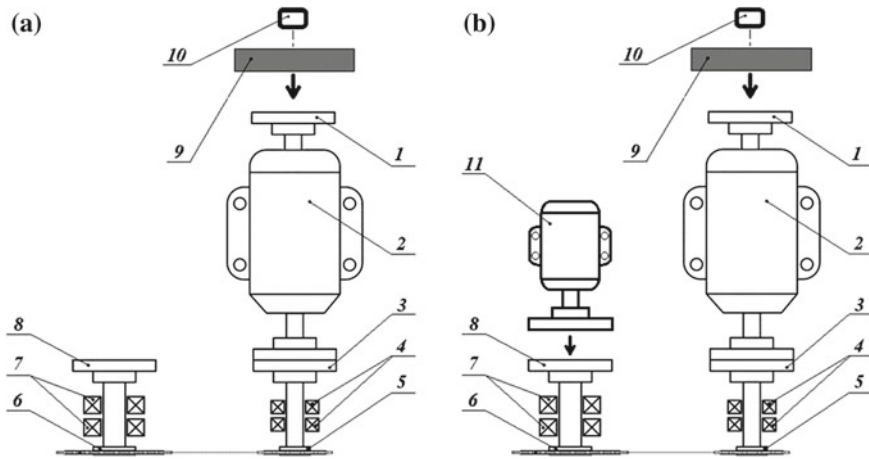


Fig. 1 A scheme of implementation of the method for determining the moment of inertia of an asynchronous motor chain drive: **a** taking into account losses and **b** without taking into account losses: 1 is a half-clutch for mounting a reference moment of inertia; 2 is an asynchronous motor; 3 is a motor overload clutch; 4 are bearing units of a drive shaft; 5 is a drive shaft with a chain wheel; 6 is a driven shaft with a chain wheel; 7 are bearing units of the driven shaft; 8 is a half-clutch of the driven shaft; 9 is a disk with a reference moment of inertia; 10 is an encoder; 11 is an additional induction motor for accelerating the system of rotating elements

$$M(\omega) = J_{CD+loss}(\omega) \cdot \varepsilon_1(\omega) \tag{1}$$

where $J_{CD+loss}(\omega)$ is the moment of inertia of the system of rotating elements of an asynchronous motor chain drive, taking into account losses, kg m^2 .

At the second stage, we determine the angular acceleration of a system of rotating elements with the disk 9 mounted on the drive shaft, $\varepsilon_2(\omega)$. The moment of inertia of the disk 9, J_{ref} , is predetermined either by calculation or experimentally using the method of torsional oscillations.

Given that at constant values of the mains' supply, the speed–torque characteristic of an asynchronous motor remains constant, and then, the product of the moments of inertia and the angular accelerations during the first and the second starts can be equated to each other:

$$M(\omega) = (J_{ref} + J_{CD+loss}(\omega)) \cdot \varepsilon_2(\omega) = J_{CD+loss}(\omega) \cdot \varepsilon_1(\omega) \tag{2}$$

The moment of inertia of the chain drive, taking into account losses, can be found as follows:

$$J_{CD+loss}(\omega) = \frac{J_{ref} \cdot \varepsilon_2(\omega)}{\varepsilon_1(\omega) - \varepsilon_2(\omega)} \tag{3}$$



2.2 *Determining the Inertia of an Asynchronous Motor Chain Drive Without Taking into Account Losses*

To determine the moment of inertia of an asynchronous motor chain drive without taking into account losses, it is necessary to use an additional induction motor to accelerate the test system of rotating elements to the rated velocity, and which is to be disconnected from the system during its rotation. Figure 1b presents a scheme of implementation of the developed procedure.

At the first stage, we mount the reference disk 9 to a half-clutch 1 using fastening elements. With the help of an induction motor 11, we accelerate the presented system of rotating elements with the reference disk up to the rated velocity. Then, when the rated speed is reached, we disconnect the motor 11, and the encoder 10 registers the angular deceleration values, ε_3 , during the retardation of the considered system of rotating elements from the rated to zero rotational speed. The braking torque of friction losses can be found as follows:

$$M_B(\omega) = (J_{\text{ref}} + J_{\text{CD}}(\omega)) \cdot \varepsilon_3(\omega) \quad (4)$$

where J_{CD} is the moment of inertia of the system of rotating elements of the asynchronous motor chain drive without taking into account losses, kg m^2 ; J_{ref} is the moment of inertia of the disk 9, kg m^2 .

At the second stage, we unmount the reference disk 9. It should be noted that in this case, during the process of retardation of the studied system of rotating elements, the resulting angular deceleration increases as the total amount of energy that rotating elements can conserve decreases. The additional induction motor 11 connected to the studied system starts. After the angular velocity of the rotating elements reaches the rated one, the motor 11 is disconnected resulting in self-braking, and the values of the angular deceleration of the asynchronous motor chain drive without the reference disk 9, ε_4 , are registered.

The braking torque of losses can be determined as follows:

$$M_B(\omega) = J_{\text{CD}}(\omega) \cdot \varepsilon_4(\omega) \quad (5)$$

During both retardations of the system of rotating elements (with the reference disk 9 and without it), the magnitude of the friction losses remains unchanged; therefore, we can equate the right-hand sides of Eqs. 4 and 5 and find the moment of inertia of the system of rotating elements of the asynchronous motor chain drive, without taking into account losses, as follows:

$$J_{\text{CD}}(\omega) = J_{\text{ref}} \cdot \frac{\varepsilon_3(\omega)}{\varepsilon_4(\omega) - \varepsilon_3(\omega)} \quad (6)$$

2.3 Determining the Efficiency of a Chain Drive

Based on the results obtained, the efficiency of the asynchronous motor chain drive can be determined according to the following equation:

$$\text{eff}(\omega) = \frac{J_{CD}(\omega)}{J_{CD+loss}(\omega)} \cdot 100\% \tag{7}$$

2.4 A Procedure for Monitoring the Technical State of an Asynchronous Motor Chain Drive and Building Regression Equations

Figure 2 presents a block diagram for the implementation of a multiple-factor experiment to determine the factors affecting the efficiency of an asynchronous motor chain drive and for the assessment of its technical state using the developed method.

2.5 Experimental Setup

To study an asynchronous motor chain drive, a test bench was designed and assembled (see Fig. 3), which allows determining the moment of inertia of the rotating elements system and the efficiency of a test drive during dynamic operating modes.

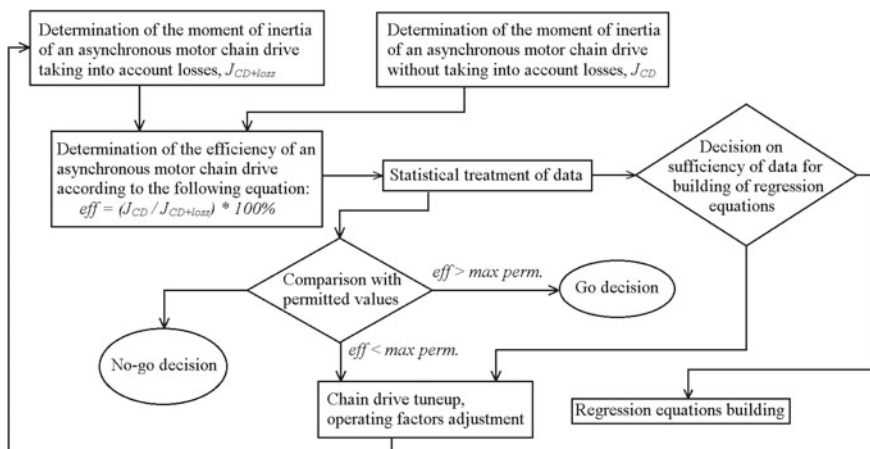


Fig. 2 A block diagram for the implementation of a multiple-factor experiment and the assessment of the technical state of an asynchronous motor chain drive

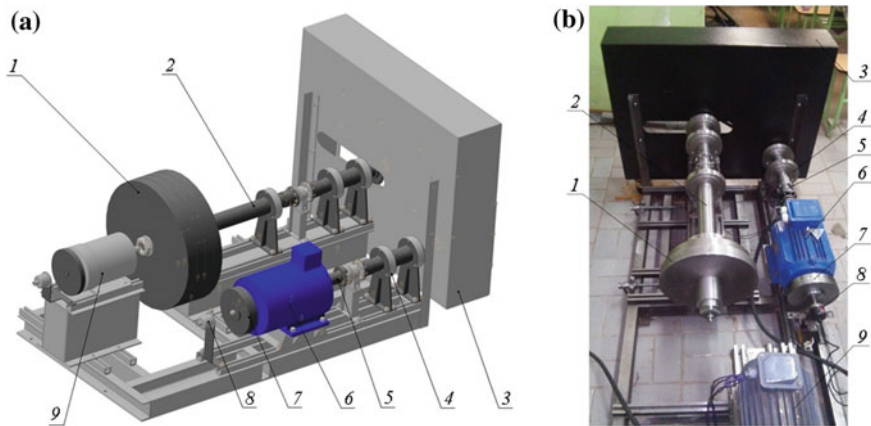


Fig. 3 A test bench for the study of a chain drive: **a** 3D model; **b** photographic image: 1 are loading disks with a total moment of inertia of 0.43939 kg m^2 ; 2 is a driven shaft; 3 is a chain shroud; 4 is a bearing unit; 5 is a drive shaft; 6 is a single-phase asynchronous motor of type AIR 112MV6 (220/380 V, 1.1 kW, $n = 940 \text{ rpm}$); 7 are disks with a total moment of inertia of 0.1792 kg m^2 ; 8 is an encoder of type E40HBP; 9 is a three-phase asynchronous electric motor with a power of 0.75 kW for acceleration of the studied system of rotating elements

The designed bench consists of a single-phase asynchronous motor 6 having the power of 1.1 kW and the rated rotational speed of 940 revolutions per minute. A shaft of a rotor is connected via a clutch to a drive shaft of a chain transmission (a number of teeth of the drive chain wheel are 23). A shaft of a driven chain wheel 2 (a number of teeth of the driven chain wheel are 38) is connected to the shaft, on which loading disks 1 are mounted. These disks allow increasing the acceleration time of the chain drive and create the rated tension force in the chain strand. To determine the moment of inertia of the studied system of rotating elements, taking into account losses and without it, disks with the reference moment of inertia 7 were used, which were freely removable and attachable to the tail section of the drive motor 6. To measure the angular acceleration, an encoder 8 was used.

As a test chain, a single-row sleeve-type chain with the pitch of 9.525 mm was selected.

For the experimental design, based on the theoretical study of chain drives with sleeve-type chains, the following factors were taken as influencing ones: the axial displacement of the chain wheels Δb (x_1), the tension force of the loose strand (the sag value) Δl (x_2), the lubrication method k_1 (x_3), the change of the chain pitch Δt_{ch} (x_4), the distance between axes a (x_5). As an optimization parameter, the efficiency of an asynchronous motor chain drive was used.

3 Results and Discussion

Based on the theoretical analysis of the possible limits of the influence of each of the selected factors on the efficiency of an asynchronous motor chain drive, their levels and coded values for an experimental design were determined (Table 1).

The range of change of factors, $2x_i$, was chosen on the basis of a preliminary qualitative and quantitative analysis of their impact on the optimization parameter.

When determining the levels of the lubrication method, k_i , the following coded values were selected: $k_1 = 1$ is for the crankcase lubrication; $k_1 = 2$ is for the intermittent lubrication (after operation of the chain under nominal conditions for 1 h and 30 min).

In this work, we carried out a full-scale multiple-factor experiment, and in each of the 16 experiments, we carried out at least 5 measurements of the efficiency of the asynchronous motor chain drive. The measurements were carried out according to the procedure described above. During the experiments, blunders were eliminated, random errors were determined, and the average values were found.

Table 2 shows the obtained regression equations.

Figure 4 shows the resulting graphs of the experiments, which characterize the degree of influence of the factors under study on the efficiency of an asynchronous motor chain drive with a single-row sleeve-type chain.

On the basis of the obtained regression equations, we can conclude that the lubrication method has the greatest impact on the efficiency of a chain drive with given features, and as a result, the crankcase lubrication, which provides a sufficient amount of lubricant between the friction elements of the chain, is the most preferred method.

The axial displacement of chain wheels also noticeably influences the optimization parameter, but its impact score is almost two times less than that of the

Table 1 Coded values and levels of factors affecting the efficiency of an asynchronous motor chain drive with a single-row sleeve-type chain

Coded level	Factors				
	Δb (mm) (x_1)	Δl (mm) (x_2)	k_1 (x_3)	Δt_{ch} (%) (x_4)	a (mm) (x_5)
+1	10	2.00	3	2.50	650
0	5	4.50	2	1.50	500
-1	0	7.00	1	0.50	350
$2x_i$	10	5.00	2	2.00	300

Table 2 Regression equations of the efficiency of the asynchronous motor chain drive

Speed range (rev/min)	Regression equations (%)
200–400	$eff=86.93 + 1.77x_1+1.35x_2+5.29x_3+0.65x_4 + 0.41x_5$
400–600	$eff=85.22 + 1.36x_1+1.16x_2+4.23x_3+0.79x_4 + 0.75x_5$
600–800	$eff=84.84 + 1.47x_1+1.05x_2+4.25x_3+0.92x_4 + 1.11x_5$

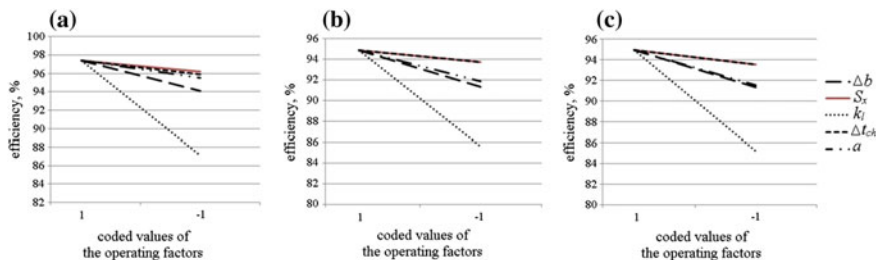


Fig. 4 Graphs characterizing the degree of influence of the factors in different speed ranges: **a** 200–400 rpm; **b** 400–600 rpm; **c** 600–800 rpm

lubrication method. A decrease in the efficiency when the chain wheel is axially displaced is most likely associated with the appearance of the additional friction between an inner side of a chainplate and a wheel tooth.

Based on the obtained experimental results, it can be also concluded that the chain sag, Δl , and the change in the pitch value, Δt_{ch} , do not heavily affect the efficiency of a chain drive.

According to the obtained regression equations, a decrease in the efficiency of a chain drive with an increase in the shaft rotation speed is observed, which may be associated with an increase in the level of oscillations of the loose strand of the chain, which contribute to an increase in the load on the drive chain wheel. In this aspect, it should be noted that at low speeds the impact of the axial distance is insignificant, but it noticeably increases within higher speed ranges.

4 Conclusion

The results of the experimental study presented in this paper allow us to conclude that the application of the proposed method and the software–hardware complex makes it possible to identify the level of friction losses of an asynchronous motor chain drive and to investigate operating factors affecting the efficiency of a chain transmission with a sufficient level of accuracy.

When using a disk with the reference moment of inertia, it is possible to evaluate the impact of design features and operating conditions of a chain drive on its mechanical parameters in a wide range of speed and load modes of operation.

According to the regression equations obtained in the course of the study, it can be concluded that both the chain lubrication method and the chain wheels’ axial displacement heavily affect the performance of a chain drive. In turn, the distance between axes has a noticeable impact on the optimization parameter at the speeds of rotation of the drive shaft above 600 revolutions per minute, which indicates the influence of mechanical system oscillations on its efficiency.

Having determined the acceleration time of an asynchronous motor chain drive, its efficiency, and the tolerance for those indicators, as well as equipping the drive



with the developed software and hardware complex, according to the presented procedure, companies producing and operating chain drives and chain transmissions will be able to continuously monitor their performance, which will lead to not only an improvement of the efficiency parameters of the mechanical system, but also to an increase in its service life.

References

1. Vorobyev NV (1968) *Tsepnye peredatshi (Chain transmissions)*. 4th ed. Mashinostroeniye, Moscow
2. Conwell JC, Johnson GE (1996) Experimental investigation of link tension and roller sprocket impact forces in roller chain drives. *Mech Mach Theory* 31(4):533–544. [https://doi.org/10.1016/0094-114X\(95\)00070-F](https://doi.org/10.1016/0094-114X(95)00070-F)
3. Fuglede N, Thomsen JJ (2016) Kinematics of roller chain drives—exact and approximate analysis. *Mech Mach Theory* 100:17–32. <https://doi.org/10.1016/j.mechmachtheory.2016.01.009>
4. Childs PRN (2014) Belt and chain drives. *Mech Des Eng Handbook*, 1st edn. Butterworth-Heinemann, Oxford, pp 459–512
5. Salgado DR, Del Castillo JM (2014) Analysis of the transmission ratio and efficiency ranges of the four-, five-, and six-link planetary gear trains. *Mech Mach Theory* 73:218–243. <https://doi.org/10.1016/j.mechmachtheory.2013.11.001>
6. Spicer JB, Richardson CJK, Ehrlich MJ et al (1999) Effects of frictional loss on bicycle chain drive efficiency. *J Mech Des* 123(4):598–605. <https://doi.org/10.1115/1.1412848>
7. Spicer JB, Richardson CJK, Ehrlich MJ et al (2000) On the efficiency of bicycle chain drives. *Tech J IHPVA* 50:3–9
8. Huo J, Yu S, Yang J et al (2013) Static and dynamic characteristics of the chain drive system of a heavy duty apron feeder. *Open Mech Eng J* 7:121–128. <https://doi.org/10.2174/1874155x01307010121>
9. Troedsson I, Vedmar L (1999) A method to determine the static load distribution in a chain drive. *ASME J Mech Des* 121(3):402–408. <https://doi.org/10.1115/1.2829475>
10. Zhang L, Zhang C, Hornig J-H et al (2012) Study on simulation of the chain transmission mechanism. *Adv Mater Res* 593(6):797–800. <https://doi.org/10.4028/www.scientific.net/AMR.591-593.797>
11. Liu S-P, Wang KW, Hayek SI (1990) Modeling and analysis of chain drive systems. *J Acoust Soc Am* 87:S136. <https://doi.org/10.1121/1.2027963>
12. Fuglede N, Thomsen JJ (2016) Kinematic and dynamic modeling and approximate analysis of a roller chain drive. *J Sound Vib* 366:447–470. <https://doi.org/10.1016/j.jsv.2015.12.028>
13. Cusimano G (2013) Influence of the reducer efficiencies on the choice of motor and transmission: Torque peak of the motor. *Mech Mach Theory* 67:122–151. <https://doi.org/10.1016/j.mechmachtheory.2013.04.006>
14. Spicer JB (2013) Effects of the nonlinear elastic behavior of bicycle chain on transmission efficiency. *J Appl Mech* 80(2). <https://doi.org/10.1115/1.4007431>
15. Doppelbauer M (2011) Accuracy of the determination of losses and energy efficiency of induction motors by the indirect test procedure. In *Proceedings of 7th international conference on energy efficiency in motor driven systems*, Alexandria, USA, pp 457–469
16. Irimescu A, Mihon L, Pădure G (2011) Automotive transmission efficiency measurement using a chassis dynamometer. *Int J Automot Technol* 12(4):555–559. <https://doi.org/10.1007/s12239-011-0065-1>
17. Levintov SD (1984) *Beskontaktnye magnitoupругiye datshiki krutyashogo momenta (Noncontact magnetoelastic sensors for torque measurements)*. Energoatomizdat, Moscow

18. Russian State Standard GOST 11828-86 (1986) Mashiny elektritsheskiye vrashayushiyesya. Obshnye metody ispytaniy (Rotating electrical machines. General test methods)
19. Katsman MM (2004) Laboratornye raboty po elektritsheskim mashinam i elektroprivodu (Lab research on electric motors and electric drives). Akademia, Moscow
20. Egorov AV, Belogusev VN (2010) Bestormoznoye opredeleniye effektivnykh kharakteristik elektritsheskikh dvigateley vrashatel'nogo deystviya (Brake-free determination of the performance characteristics of rotary electric machines). Test Diagn 7:66–72
21. Egorov AV, Kozlov KE, Belogusev VN (2016) Experimental identification of the electric motor moment of inertia and its efficiency using the additional inertia. ARPN J Eng Appl Sci 10(17):10582–10588

Discrete Contact in Toothed Gearing



Alexander Vladimirovich Titenok and Igor Alexandrovich Titenok

Abstract On the basis of personal inventions and well-known experimental research, the authors proved the characteristic of lubricant filling in the form of microscopic rounds as an antiwear and antifriction additive agent to improve toothed gearing quality. Trying to solve existing technical and economic contradiction, they proposed principally new construction of fixed members with higher kinematic pairs that notably increased wearability of fixed members working surfaces. The discrete contact is proved in the work, so that there is no need to apply special technology to make new gear wheels. Theoretical basis of storability of system-balanced condition on fixed members with higher kinematic pairs is elaborated. The main characteristics for the estimation of quality factors of reciprocating motion fixed member are defined: motion trajectory of the surface plate; ratio of recentering force to vertical load, i.e., rollback angle τ_g ; angle between resultant of forces and its normal projection in the contact points, i.e., meshing angle. In static and dynamic bench tests of the fixed members, estimated characteristics were proved.

Keywords Toothed gearing · Tooth form · Natural wear · Discrete contact · Globules

1 Introduction

Coefficient of performance (COP) is a quantitative indicator of technical efficiency, and its value for toothed gearing is the most important evaluative factor. Tooth shape stability during operation influences the quality of gearing work. In the

A. V. Titenok (✉)

Bryansk State Agrarian University, 5, Sovetskaya Str., Apt. 21, Kokino,
Vygonichsny District 243365, Russia
e-mail: titenok@bk.ru

I. A. Titenok

ABB Ltd, 2-1 Medynskay Str., Apt. 398, Moscow 117546, Russia
e-mail: elproekt-it@yandex.ru

© Springer Nature Switzerland AG 2020

A. A. Radionov et al. (eds.), *Proceedings of the 5th International Conference on Industrial Engineering (ICIE 2019)*, Lecture Notes in Mechanical Engineering,

https://doi.org/10.1007/978-3-030-22041-9_117

1117

involute tooth transmission, the peripheral surface of the wheel tip and fillet is more inclined to aging, and the maximum normal contact voltage is in the pitchpole. An involute tooth takes normal aging shape [1], stable at first and then having negative indicators associated with gear accuracy shift. There is a technical and economic contradiction. From a theoretical position, we have a high gearing COP at the form of a higher pair of kinematic elements. In operation, this factor varies, which is accompanied by many negative manifestations. The article discusses one of the alternative ways to resolve mentioned contradictions by changing the working environment in gearing [2, 3] with the introduction of the concept “discrete contact” that changes the structure and shape in friction process.

In the article uses the method of retrospective engineering analysis, taking into consideration the substantive base known in the engineering and metallurgy and the results obtained by the authors personally.

2 Rational Base

Wide range and diverse combination of loads, rolling and sliding speeds, working temperatures, a variety of materials and processing methods lead to the different character of gear damage and destruction.

Existing classification of tooth damage comes to the following factors: destruction under flexion and impact stress, tooth chipping (pitting); seizure; mechanical wear; plastic deformation of the tooth-working surface; chemical wear.

Among these types of damage, only the first is less connected with the nature of lubricant. All other damages represent different types of wears. They are associated with the nature of lubricant, and their characteristics should be considered in the process of choosing lubricants.

The founder of the theory of hydrodynamic lubrication N. P. Petrov in the work “Friction in machines and its impact on the lubricant” gave a description of the fluid friction importance between surfaces machine parts. Its essence is that the gap between sliding surfaces must have a wedge form. Lubricant should fill the gap and continuously arrive in the required quantity. Speed in relation to the movement of one of the surfaces should be enough to create internal pressure in the oil layer is created due to lubricant wedging. Lubricant should completely separate contacting parts.

The theory of the oil wedge proposed by N. P. Petrov is still actual, and hydrodynamic lubricant is implemented in run-in gears. In the interaction of two contacting surfaces with solid wear particles between them, the latter, due to the specific properties and certain geometry, can be involved in rotational movement [4]. And fluid elements also have the similar rotation. It is connected with simple shift (twist) and is due to kinetic energy of the fluid particles considered as small volumes. In 1956, M. Reiner called this phenomenon [5] the “teapot effect.” Simple shift vortex is not just fluid “sticking,” but its pressure on its surface is due to the kinetic energy of vortex rotation. Fluid swirling contributes to the surface irregularities flow. In the erosion process, rough surface bumps get the optimum form which is rounded.

Violation of the surface layer structure in the friction process leads to the formation of wear particles which are deformed in a specific way. Becoming spherical or cylindrical, these masses have rotational moving. The rotational movement mechanism is typical for fragments of destruction.

In the study of ball bearings using a scanning electronic microscope, the tiny spherical particles were found; similar particles were found on the ferrograph glass. We know about the phenomenon spontaneous rolling caused by sliding friction: In some modes, there were microspheres that rolled grooves like bearing tracks. Coefficient of friction sharply diminished. In such cases, the geometric shape of rolling elements tends to ideal. The value of the mechanism of spontaneous rolling increases when the contact points become smaller and relative surface bearing capacity becomes higher due to the big factor of strength [6, 7].

It was established experimentally that if the size of wear particles (of any shape) does not exceed 5 μm , then they, having a larger developed surface, adsorb the products of oil oxidation, that can reduce the intensity of parts wearing. The particles probably intensify heat transfer between friction surfaces. Small particles serve as antiwear and antifricition additives, preventing direct contact between sliding surfaces.

All this applies to particles less than 5 μm . Large particles are harmful. Spherical metallic particles appear in rolling and sliding systems as a result of different processes. The formation of spherical wear particles with wear-resistant boride coatings on contact surfaces is explained by the aggregation of the smallest wear products and by the reflow of secondary structures consisting mainly of boron oxides and other compounds in the amorphous state.

The elementary composition of spherical wear particles showed that they contain 47% carbon, 34% oxygen, 8.7% iron, 8.2% boron, 1.6% sulfur. Since the temperature of boron oxide melting is 450 $^{\circ}\text{C}$, we can suppose the appearance of spherical wear particles under more severe test conditions. It is characteristic that such relatively high temperatures occur only in the volumes of no more than a few micrometers.

A model in which spherical particles are secondary corresponds to the experimental data. The particles obtained in the experiment do not exceed 5 μm , but the particle size can significantly vary depending on friction conditions and material properties (2.5–16 μm). It is assumed that spherical particle appear when the proportion between oscillation amplitudes and spherical circumference particles is equal to 1 (according to different data, this ratio ranges from 0.2 to 2.4). On practice, spherical particles are very rare in tribosystems with unidirectional motion.

The quality level of gearing rises when the lubricant is supplied with spherical particles of not more than 5 μm [2, 3] that allows to realize the contact mechanism of adjacent surfaces of complex shape using rolling elements. In the process of gearing, microspheres will move to the pitch point. This phenomenon provides the effect discovered by Schulz [1] for wheels with natural wear teeth.

The second positive effect of innovation is that the lubricant microspheres fill the depressions of asperities in the working surfaces of the teeth. Thus, the specific surface load is redistributed and contact voltage is reduced.

The technological aspect of innovation is the following: Spherical microparticles can be produced by the method used in powder metallurgy: by spraying the melt in

inert gases [8]. What should be the size of particles? Intensity of movement over the body surface and the wear of this surface from the pressure of particles depend on their forms [9, 10]. According to foreign studies [11, 12] after reaching a critical particle size, metal wear almost does not depend on their size (particles ranging in size from 0 to 70 μm are analyzed). With changing the size of wear particles from 75 to 250 μm , the wear rate of steel samples at the beginning gradually decreases and then when resizing particles from 250 to 500 μm remains unchanged. Maximum wear is observed at a particle size of about 40 μm or, in another similar study, at a particle size of 600 μm . D. N. Garkunov [13] cites data on the impact of small abrasive particles on wear in the case when the lubricant contains these particles. At different times and independently on each other, such data was obtained by the following researchers: Nikiforov O. A., Vinogradov G. V., Wenzel S. V. and Wenzel E. S., Barabash M. L., Korogodsky M. V., Bortnik G. I., Shpenkov G. P.

The similar effect is possible on macro-level.

The group of authors [14–18] worked up and analyzed a series of mechanisms with higher pair of kinematic elements for reciprocating motion of machine actuating device and diminishing of vibratory action influence on a person and environment using the example of grain combine cutter.

Vibratory action is classified according to the following criteria: The way of impact on a person—general and local; source of origination—transport (in machine movement), transport and technological (in combination with movement and technological processes, e.g., in scything and thrashing with self-propelled combine, in trench excavation, etc.) and technological (in fixed machines, e.g., pump units); vibration frequency—underfrequency (less than 22.6 Hz), midfrequency (22.6–90 Hz), radio frequency (more than 90 Hz); spectrum type—narrow band and broad band; active time—constant and temporary; the latter is divided into modulate in time, dashed and impulsive.

Vibratory norms are defined for three directions normal to each other in orthogonal coordinate system. In general vibration measuring and estimation, it is necessary to remember that x -axis runs from a person's back to his breast, y -axis—from the right shoulder to the left, z -axis—vertically along the body. In local vibration measurement, it is necessary to know that z -axis runs along the hand tool, and x - and y -axes are perpendicular to z -axis.

There are separate norms for transport vibratory movement (category 1), transport and technological (category 2) and technological (category 3); besides the norms for the category 3 are divided into subcategories: 3a—for vibratory movement on permanent facilities working places; 3b—on working places in storage area, mechanical rooms without machines causing vibration; 3c—in rooms for intellectual workers.

In cases of vibration excess allowed for a person, it should be decreased. Vibration influences a worker through such objects as machines, constructions and transport facilities with vibration source (electric motors, explosion engines, machine tool stations, etc.). So, protective measures should embrace all the elements of the system “vibration source object person.”

If the object is under vibration of periodic forces, they should be diminished in vibration source. In this case balance quality of swiveling parts, working accuracy and surface condition of mating parts should be increased, interbalancing mechanisms should be applied, force that influences a shaking detail and rate speed should be decreased, machine rotors loads should be equally divided, work-cycle time should be raised. There is an active method to stimulate vibration in the contrary direction with fundamental oscillations in the construction in order to effectively resist them. Such vibration damping is possible when there is only one fixed or dominant frequency and with strict regard to phase opposition. Besides, vibratory movement influences machine life cycle, especially when voltage is close to endurance strength. Then, high level of vibration accelerates the limit number of cycles, and fatigue stress can appear in a machine too soon.

Thus, the task to elaborate the table balance is actual.

Here is specification for such a mechanism:

- Quantity of motion (mv) of equivalent mass of equilibrator and reaper machine cutter must be equal.
- Kinematic characteristics of equilibrator and reaper machine cutter must be ambidextral.
- Equilibrator drag force must not notably differ from force of rolling friction.

This specification can be realized with positive results of mechanism updating on the fixed members with higher kinematic pairs.

In this regard, there are the following tasks:

- To analyze the possibility of material system-balanced condition rigidity on the fixed members with higher kinematic pairs.
- To elaborate fundamental constructive bearing project where sliding motion is replaced with rolling in order to notably diminish abrasive wear and power waste on friction.
- To define the main characteristics for the estimation of quality factors of reciprocating motion fixed member.
- To elaborate a device that guarantee stable work of a fixed member no matter how the friction angle changes in the sliding contact surfaces.
- To suggest the fixed member for equilibrator of inertial forces and reaper machine cutter weight.

Here are the following gradual results:

Summary 1:

- There is a constructive bearing project of reciprocating motion fixed members with higher kinematic pairs where sliding motion is replaced with external surfaces rolling on internal ones.
- There found the main characteristics for the estimation of fixed member quality factors: motion trajectory of the surface plate; ratio of recentering force to vertical load, i.e., rollback angle tg ; angle between resultant of forces and its normal projection in the contact points, i.e., meshing angle.

- There got theoretical characteristics, and four special cases of influence of fixed member parameters to its characteristics; each special case can be used depending on fixed member application and its exploitation conditions.

Summary 2:

- Amplitude of oscillation of a fixed member with higher kinematic pairs can be notably increased with the help of locking mechanisms that will take tangential forces, if meshing angle exceeds friction angle.
- In locking mechanism installation, there is small sliding motion, if $2 < R/r < 3$; if $1.5 \leq R/r < 2$, sliding motion notably increases approaching to 1.5.
- For the variant, $R/r = 1.5$ angular amplitude must be limited to 20° .

The results of theoretical analysis let us formulate the conclusion: We suggest constructions of reciprocating motion fixed members with higher kinematic pairs and elaborated calculation procedure of the main geometric, kinematic and force parameters; spheres of possible using are proposed; general calculation procedure of contact and strength voltage is elaborated.

Summary 3:

- The results of restoring force theoretical characteristics are proved with the statistic experiments on the testing bench.
- Either derived or experimental curves have nonlinear behavior of restoring force.
- In the experiment, restoring force curve turned out to be lower than theoretical one because of friction forces in the elements of the system.
- While dynamic experiments of vibration on the testing bench, we got oscillating amplitude changing curves of charge depending on frequency and amplitude of exciting force for two variants of nonlinear system.
- Maximum oscillating amplitude of the system depends on amplitude of exciting force, at the same time in kinematic amplitudes 10 and 7 mm there happens "the reset" of the amplitudes in the superresonance zone, with the amplitude 4 mm it does not reach "the reset" point because of notable friction in the system.
- The experiments let us reliably prove that charge behavior on the fixed members with higher kinematic pairs with forced motion does not contradict the general oscillation theory of nonlinear systems.
- In the bench tests of the fixed member full-scale specimen, the restoring force characteristics almost coincided with the design numbers.

Summary 4:

- If reaping machine cutter is not equilibrated, then in reciprocal motion the whole reaping machine vibrates.
- Vibration amplitude depends on the ratio of natural frequency to forced frequency, and if this ratio is close to 1, the amplitude may theoretically increase infinitely.
- Equilibrator stopping excludes vibration of reaping machine cutter.

Finally, the following points are proved:

- Theoretical basis of startability of system-balanced condition on fixed members with higher kinematic pairs is elaborated.
- There proposed principally new construction of fixed members with higher kinematic pairs, in which sliding motion is replaced with rolling of buckled cylindric surfaces on concave surfaces, that notably increased wearability of fixed members' working surfaces.
- The main characteristics for the estimation of quality factors of reciprocating motion fixed member are defined: motion trajectory of the surface plate; ratio of recentering force to vertical load, i.e., rollback angle tg ; angle between resultant of forces and its normal projection in the contact points, i.e., meshing angle.
- Fundamental project and analysis technique of tangential forces locking elements are elaborated. It is a device that guarantees stable work of a fixed member no matter how the friction angle changes.
- The elements of construction of the fixed members with higher kinematic pairs and strength calculation procedure are proposed.
- In static and dynamic bench tests of the fixed members, estimated characteristics were proved.
- The construction of a fixed member with higher kinematic pairs for equilibrator of inertial forces and reaper machine cutter weight is elaborated.

Despite positive results of work, such fixed members are of limited utility because of its design features, so, the device was updated.

The fixed member of reciprocal motion with higher kinematic pairs having baseboard and surface plate with concave surfaces and put between the fixed members with convex surfaces on the flanks differs from the ones examined before in the fact that contact working surfaces of the baseboard, surface plate and fixed member are made with unevenness that can be either teeth of any form, or convex–concave congruent form, or convex–concave tooth form (application for an invention N 2017142218/20(073019) from 04.12.2017). In this project, we analyze the possibilities of “discrete contact” realization in toothed gearing of reciprocal motion.

In some technical spheres, they use suspension tackings with bearing supports with higher kinematic pairs so that their wearing capacity is notably higher than that of sliding supports. Suspension tackings with such bearing supports are positive-acting for more than 20 years. But these bearing supports are too big and heavy that is why they are not so actively used in techniques.

The proposed bearing support with higher kinematic pairs that works in compression and has the advantages of a suspension tacking is not so high and has several times less mass. Besides, as it became clear in the process of working on the project, its band of performance is much wider than that one of the suspension tacking.

V. V. Shultz [1] took into consideration the form of toothed gearing normal aging. In his opinion, mathematical theory of moving matching joints wear-out

should be based on experimental research of microscopic behavior of a wearable contact. During the research on gear teeth wear-out, the rational theoretical teeth profile was found: wear-optimized convex–concave form, that is in fact the form of twice-involute gear. A range of other interesting technical solutions were found taking account of natural aging form.

This toothed gear is called twice involute because the gear teeth have ordinary involute spirals, and the wheel teeth have concave spirals outlined in normal section on rack trochoid or its equidistant. It was technically proved that teeth surface form in energetic optimum is tolerant to wearing.

In fact, this suggestion is a curved flank of wearable involute tooth fillet and point taken from the pitch point, i.e., these wheels are “worn out” involute gearing. Wearing is an inevitable result of gearing use. Starting with running-in phase, wearing leads to progressive loss of kinematic and strength characteristics of involute spur gear and to the loss of only strength characteristics of helical gear. It is known that in the wearing process working surface, involute takes from similar to cycloid outlined profile.

As a result of running-in wear, toothed gearing must tend to keep kinematic characteristics and to level off strength ones. That is why it must be helical gear; have convex and concave teeth profiles in cross-sectional view; be initially point-tracked with almost linear contact, at the same time line of contact must be parallel to axis of instantaneous rotation; be out of poles— at the same, time this effect must be little as well as the meshing angle α ; have as long dimple spherical radius as possible.

As it is obvious that only gearings out of poles are meant, the traces of all the teeth points of one wheel (e.g., with convex profile) will be enlarged epicycloid. Therefore, its doubled concave profile must be either of the closest trochoid or of rack trochoid. Such profiles will slowly move apart in relative motion.

Line of contact is a geometrical place of contact points in fixed coordinate system. The data of a problem to find energetically optimal line of contact is in a curve that corresponds to the least friction forces work and maximal COP of toothed gearing with permanent gearing ratio (this is in fact an attempt to solve the task of L. Eiler). Such curves correspond to involute and cycloid gearing. They were found from geometro-kinematic considerations without taking into consideration the energy of gearing process.

Continuity of these curves does not reflect snapback action from one-pair contact to two-pair contact, when all gearing parameters change in steps. Therefore, involute wheel profiles wearing notably deform the line of contact. Cycloid line of contact is less deformed because it is closer to optimal form. It is proved by the well-known facts of gearing profile deformation.

Gear wheels made with account for natural wear form are more technologically problematical than now dominating wheels with involute profiles. That is why the discrete contact proved in the work, moving the loading material to the gearing pole in the gearing process, imitate natural wear in involute gearing, that there is no need to apply special technology to make new gear wheels.

3 Summary

Small particles (up to 5 μm) were introduced into the lubricant as an additive to improve the quality of toothed gear serve as an antiwear and antifricition additive. Larger particles are harmful. This can be taken as a recommendation to the selection of parameters for spherical filler particles.

References

1. Schulz VV (1990) Form of natural wear of machines parts and tools. Mechanical Engineering, Leningrad, 139 p
2. Titenok AV (1992) Toothed Gear. Russian patent on the invention № 1768849 IPC.F 16H 57/04. Publ. 10.15.1992, Bull. No. 38
3. Titenok IA (2003) Toothed gear. Russian patent on utility model 31157 MPK7.F 16H 57/04. Publ. 07.20.2003, Bull. No. 20
4. Chebdy M, Chichinadze AV (1990) Handbook of tribotechnology. V. 2: Lubricants, lubrication technology, sliding and rolling bearings. Mechanical Engineering, pp 224–227
5. Rayner M (1963) Deformation and flow. In: Introduction to rheology. GNTI of oil and fuel literature, p 44–46
6. Marchenko EA (1979) On the nature of metals surface destruction at friction. Science
7. Labunets VF, Voroshnin LG, Kindrachuk MV (1989) Wear resistant boride coatings. Technique, Kiev, pp 46–54
8. Manokhin AI, Pozhivanov AM, Pancakes KA (1990) New inmaterials technology. Engineering, Hanau: Leibold AG, pp 194–195
9. Ikramov UA (1987) Calculation estimation methods of abrasive wear. Mashinostroenie, pp 78–83
10. Makovetsky PV (1991) Look at the root! Compilation of curious problems and questions. In: Science. Ch. ed. Physical and mat. Lit., p 144–148
11. Wellinger K (1950) Influence of grain size of the wear behavior is different material pairings. VDI-Zisch (15):371–375
12. Gunter H, Besser D (1982) On the impact of Mineral Particles on the nature of wear. Theoretical and practical problems of sliding, wear and tear. In: Science, pp 227–237
13. Garkunov DN (1985) Tribotechnics. Mechanical Engineering, p 170–171
14. Aksyutenkov VT, Titenok AV, Timakov AK (2010) Axle guard with rolling elements. Bull Bryansk State Tech Univ (4):50–54
15. Aksyutenkov VT, Titenok AV, Timakov AK (2009) Reciprocal motion fixed members with higher kinematic pairs. Bull Bryansk State Techn Univ (2):49–52
16. Aksyutenkov VT, Titenok AV, Timakov AK (2010) Band of performance widening in fixed members with higher kinematic pairs. Bull Bryan State Tech Univ (1):31–35
17. Titenok AV (2017) Experimental definition of statistic and dynamic characteristics of fixed members with higher kinematic pairs. Bull Bryan State Tech Univ (2):85–95
18. Titenok AV (2017) Mechanism with higher kinematic pairs. Bull Bryan State Tech Univ (3):11–19

Contact Movement in Mating Conical Joints Within Resting Friction



V. Feropontov, N. Perfileva and A. Maksimenko

Abstract Friction conical conjunctions are considered in the present paper. The physico-mathematical model of dynamic contact interaction under conditions of static friction was taken into account for calculating the axial and diametrical tension of the frictional conical conjunction, taking into account displacements in the contact. The patterns of change in contact compliance in the normal and tangential directions, diametral and axial tightness in the conjunctions of conical contacts have been identified. A numerical–analytical method has been developed for the calculation of frictional conical conjunction, which makes it possible to take into account the contact compliance of the mating parts when designing and calculating. With the help of this method, the calculation of frictional conical conjunctions is made taking into account contact compliance. The results of the calculations were compared with the result of engineering calculations. Based on the comparison, the evaluation of the effect of contact deformations in the conjunction of the conical connection was made. It has been established that the consideration of contact deformations in the calculation of frictional conical conjunctions entails a decrease in the axial tension value by 20% and in some cases by 30%. The application program is developed and the certificate is received. The program allows you to perform a refined calculation of the static and dynamic characteristics of the elastic mechanical contact when designing frictional conical conjunctions. As a result of experiments, confirmation of theoretical calculations was obtained. Recommendations for making design changes have been provided.

Keywords Conical conjunction · Axial tension · Diametric tension · Contact deformations

V. Feropontov (✉) · N. Perfileva · A. Maksimenko
Altai State Technical University, 46, Lenin Avenue, Barnaul 656038, Russia
e-mail: sopromat116@mail.ru

© Springer Nature Switzerland AG 2020
A. A. Radionov et al. (eds.), *Proceedings of the 5th International Conference on Industrial Engineering (ICIE 2019)*, Lecture Notes in Mechanical Engineering,
https://doi.org/10.1007/978-3-030-22041-9_118

1127

1 Introduction

Various connections of parts are widespread in the designs of modern machines and mechanisms. Failure of the connections of parts leads to failure of machines and equipment downtime. This entails economic losses. One of the reasons for damage to parts is wear connections under the influence of static friction. In this case, radical changes in the near-surface volume of the material of the contacting parts occur. Accuracy, vibration resistance, durability, performance, reliability of machine components, and mechanisms are determined by static and dynamic contact stiffness. The constant deformations that occur in the connections of machinery parts are very significant, and in most cases, they prevail over the deformations of the parts themselves [1].

When designing units and mechanisms of machines, the neglect of contact stiffness in a cylindrical connection with tension leads to an error in determining the pressure in the conjunction up to 10–20% for high tension and up to 40% for low tension. The error in calculating the required force of the screw tightening in the calculation of the threaded connection can reach 50%. In precision engineering, the error in the calculations without taking into account contact deformations can reach 70% [2–4]. All the above facts indicate the relevance of this problem. To date, contact deformations have been studied and an assessment of their influence in threaded, rivet, wedge, and cylindrical conjunctions has been given.

The purpose of the study is to develop an improved method for calculating the strength and stiffness of conical conjunctions, taking into account movements in contact before sliding friction, and adaptation of this method to engineering calculations of conical conjunctions. The estimated refined method of calculation makes it possible to take into account the contact compliance when precision instruments and mechanisms are created. Moreover, their parts are connected by contacting. In turn, this will lead to an increase in their reliability and efficiency.

The presented method can be recommended as a non-destructive method of controlling the strength of conical conjunctions.

2 Methods of Solution

The study of contact stresses and displacements is necessary to solve the problems of the strength of responsible conjunctions. These so-called conditionally fixed conjunctions include: threaded, wedge, rivet, slot connections, and connections with tension. The strength and rigidity of such conjunctions largely depends on the processes occurring in the contact parts of the conjunctions. Ivanov [5, 6] found that the share of contact deformations accounts for up to 80% of the total deformation. Therefore, issues related to the contact interaction of parts, primarily dynamic contact stiffness, and energy dissipation are very important. Classical engineering strength analysis should be supplemented by the calculation of contact displacements [7–9].

To develop a refined engineering methodology for calculating conical conjunctions, taking into account dynamic contact displacements and compliance, the choice of a universal dynamic model of elastic mechanical contact was made within the preliminary displacement [10]. The proposed physical–mathematical model of contact interaction of the normal and tangential directions allows to take into account all possible types (schemes) of dynamic loading in the calculations:

- shock loading in the normal or tangential direction;
- complex shock loading, causing free damped oscillations of bodies;
- vibration excitation of various directions, the consequence of which will be forced oscillations of the contacting surfaces.

The deformation is mainly determined by the contact displacements of the rough layer, and this is indicated by [11]. Then, we can assume that deformations under dynamic loading occur only in the areas of protrusions of a rough surface.

Since the mass of the protrusions is very small compared to the masses of the contacting bodies, it can be neglected. Based on this, we can assume that under dynamic loading, the relationship between force and deformation of conjugate bodies can be assumed to be the same as under static loading. Dynamic loading of an arbitrary direction to the surface causes contact displacements simultaneously in both normal and tangential directions. Kragelsky I. V. found that in an elastic contact, the tangential component of the dynamic force does not have a significant effect on vibrations in the normal direction [11]. Calculations made by Demkin N. B. show that the increase in the actual area of the elastic contact under the influence of tangential forces with average values of the friction coefficient does not exceed 5%, i.e., tangential loading on the contact does not lead to significant changes in the approach of two rough bodies [12]. Therefore, the evaluation of contact displacements under complex dynamic loading consists in the study of contact oscillations of the tangential direction.

To determine the normal displacement in the elastic dissipative contact, the solution of static problems was used, as well as the model of the behavior of the contact pair under conditions of free damped oscillations. To determine the tangential contact displacements, the decision of Mindlin was made [13]; for the case of contacting rough surfaces in static conditions, the decision of Maksaka [14, 15] was used. Figure 1 shows the forces acting in a conical conjunction.

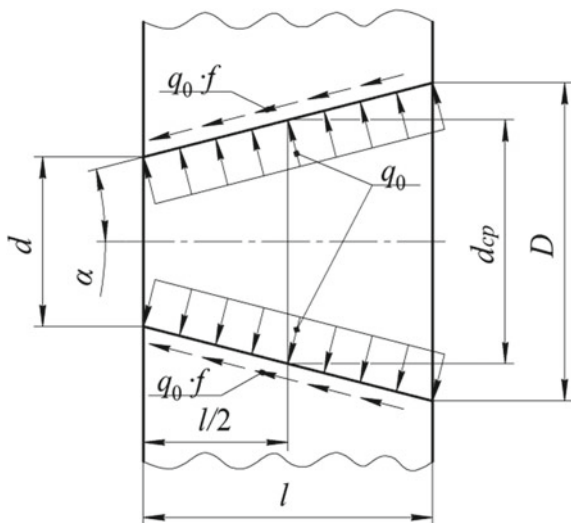
Comparison of engineering calculation and calculation taking into account contact compliance was performed.

The diametric tension that occurs in the conjunction when tightened depends on the radial stiffness of the shaft and the hub is determined by the Lamé formula [16].

$$\Delta = 10^3 \cdot k \cdot d_{cp} \cdot \theta, \quad (1)$$

where k is pressure on the seating surfaces; θ is coefficient determined by the formula:

Fig. 1 Schematic of the conical conjunction



$$\theta = \frac{c_1 - \mu_1}{E_1} + \frac{c_2 + \mu_2}{E_2}, \tag{2}$$

where μ_1, μ_2 are Poisson coefficients for shaft and hub; E_1, E_2 are elasticity modulus of 1 kind for the shaft and hub; c_1, c_2 are coefficients depending on the parameters of thinness;

$$c_1 = \frac{1 + a_1^2}{1 - a_1^2}, \quad c_2 = \frac{1 + a_2^2}{a_1^2}, \tag{3}$$

where a_1, a_2 are defined as:

$$a_1 = d_{cp}/d_0, \quad a_2 = D/d_{cp}. \tag{4}$$

Axial tension h required to obtain the calculated value Δ :

$$h = 10^{-3} \frac{\Delta'}{K}, \tag{5}$$

$$\Delta' = \Delta + 2 \cdot \phi (R_{z_1} + R_{z_2}), \tag{6}$$

where R_{z_1}, R_{z_2} are roughness height for shaft and hole surfaces; ϕ is crushing coefficient of roughness.

All of the above relates to the engineering design of conjunction. However, for responsible conjunction of machines and devices, this is not enough. In the overwhelming majority of cases, the deformations, displacements, and stresses that occur in the surface layers of the mating parts within the limits of static friction, due to the phenomenon of preliminary displacement, are not taken into account.

The limiting force that can withstand the connection will be defined as a tightening force, since it is difficult to determine in advance the actual static load in real conjunctions.

$$N = P_z/f, \quad (7)$$

where f is the friction coefficient.

Nominal pressure is calculated as

$$q_0 = \frac{N \cdot k}{\pi \cdot d_{cp} \cdot l \cdot f}, \quad (8)$$

where d_{cp} is the average diameter; l is length.

The nominal area is determined by the expression:

$$A_0 = \pi \cdot d_{cp} \cdot l. \quad (9)$$

And the value of the normal load will be:

$$N_0 = q_0 \cdot A_0. \quad (10)$$

The contour area of contact in conjugation is determined by the Khokhlov formula [17]:

$$A_c = A_0 \cdot \left(\frac{q_0}{\sigma_T} \right)^{1 - \frac{q_0}{\sigma_T}}, \quad (11)$$

where σ_T is yield strength.

The value of rapprochement is according to the Kragelsky—Demkina formula [11, 18]:

$$\delta = \left[\frac{5 \cdot N \cdot r^{\frac{1}{2}} \cdot (1 - \mu^2) \cdot R_{\max}^v}{A_c \cdot b \cdot v \cdot (v - 1) \cdot k_1 \cdot E} \right]^{\frac{2}{2 \cdot v + 1}}, \quad (12)$$

where R_{\max} is the maximum height of the protrusions of the rough layer; r is coerced radius; b, v are approximation parameters of the support surface curve; k_1 is integration constant depending on v .

Normal contact compliance in conjugation is determined as [19, 20]:

$$K_\delta = \delta/q_0. \quad (13)$$

Radial compliance of parts is defined as:

$$\lambda_1 = \frac{C_1 \cdot d}{2 \cdot E_1}, \quad \lambda_2 = \frac{C_2 \cdot d}{2 \cdot E_2}. \quad (14)$$

Nominal circuit pressure will be determined taking into account contact pliability:

$$q_{0 \text{ fact}} = \frac{\Delta}{2 \cdot (\lambda_1 + \lambda_2) + K_\delta}. \tag{15}$$

Then the actual diametric tension will be calculated as:

$$\Delta_{\text{fact}} = q_{0 \text{ fact}} \cdot d_{cp} \cdot (C_1/E_1 + C_2/E_2). \tag{16}$$

The actual axial tension is determined by the expression:

$$\Delta'_{\text{fact}} = \Delta_{\text{fact}} + 2 \cdot \phi \cdot (R_{z_1} + R_{z_2}), \tag{17}$$

$$h = \Delta'_{\text{fact}}/K. \tag{18}$$

3 Results

For comparison, the results of engineering calculation and calculation with regard to contact displacements were performed.

The results showed that not taking into account contact deformations gives a 33% error in calculations. The evaluation of the effect of friction coefficient, taper, and torque on the axial tension with various roughness parameters was made. The axial tension decreases with increasing friction coefficient (Fig. 2a).

This is due to the fact that with an increase in the friction coefficient, the pressure on the seating surfaces decreases and, as a result, the axial tension decreases.

Evaluation of the effect of torque (Fig. 2b) allows the following conclusions. In engineering calculations, the axial tension value has a linear relationship. The value of the axial tension increases in direct proportion to the moment increase. In the case of taking into account contact deformations, the dependence becomes

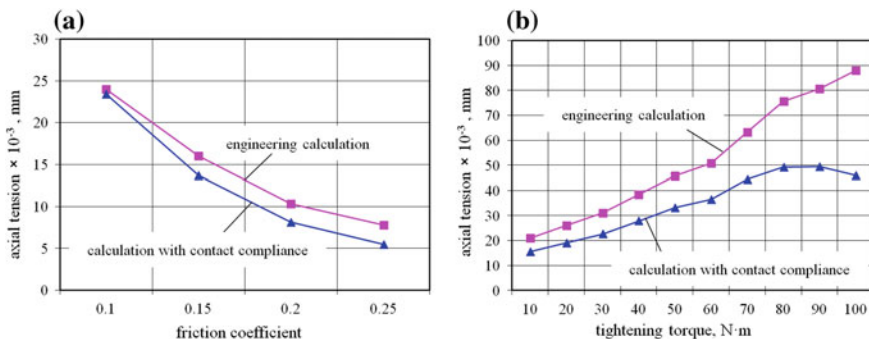


Fig. 2 Dependence of the axial tension on the: a friction coefficient and b axial tension on torque

nonlinear. This clearly allows you to see at what value of torque the deformation from the elastic zone turns into a plastic one and the connection surface will collapse.

This is due to the fact that with an increase in the friction coefficient, the pressure on the seating surfaces decreases and, as a result, the axial tension decreases.

The effect of taper on the axial pressure is reflected in Fig. 3. The results showed that an increase in axial tension occurs with a decrease in the value of the taper. This is due to the fact that the axial reaction force decreases with increasing cone.

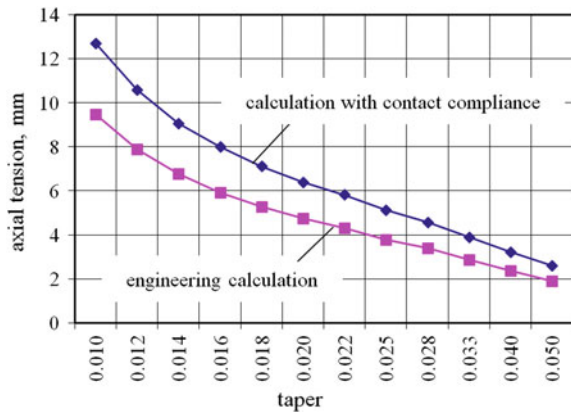
The amplitude–frequency characteristics (AFC) were obtained under various external conditions in the process of studying elastic contact displacements under conditions of forced oscillations and under dynamic loading. They make it possible to estimate the value of the loss of mechanical energy in a contact and to establish resonance zones and zones of stable operation of contact pairs. This helps to create conditional fixed conjunctions as sufficiently reliable and durable in operation, taking into account the recommendations received.

The method used for calculating contact oscillations under dynamic action and under conditions of forced oscillations makes it possible to determine AFC in a wide range of contact conditions. The growth of the normal static contact stiffness leads to the sharp drop in the absorption capacity of the contact and a significant decrease of the maximum amplitudes in the resonance region. Wherein, an increase or decrease in roughness significantly affects the pattern of dynamic processes in conjugation.

In particular, the frequency increases, the amplitudes decrease, the absorption coefficient increases, and, accordingly, the amount of energy is dissipated by the contact.

The results of the influence of the friction coefficient on the contact flexibility of the coupling have practical value. Studies have shown that static and dynamic contact flexibility of coupling increases with increasing friction coefficient. This is due to the weakening of the contact due to changes in friction conditions.

Fig. 3 Dependence of the axial tension on the value of the taper



The influence of micro-geometry parameters on the tension is less pronounced than the influence of friction coefficient and force, but it does occur. Studies have shown that the error between engineering calculation and calculation taking into account contact compliance increases with increasing micro-geometry parameters. This is explained by the fact that a change in micro-geometry parameters leads to a change in the actual contact area and, as a consequence, to a greater change in the tension.

4 Conclusion

The theoretical and experimental studies of the characteristics of the contact of real conical conjugations allow us to draw the following conclusions. The choice of theoretical prerequisites was correct. The model of elastic contact interaction is dynamic within a preliminary displacement. The developed methodology should be used in the updated engineering calculations for the strength and stiffness of the conjugations. All this is one of the methods of non-destructive quality control of generally fixed conjugations.

References

1. Demkin NB, Ryzhov EV (1981) Surface quality and contact of machine parts. Mashinostroenie, Moscow
2. Goryacheva IG (1999) Calculation of contact characteristics taking into account the parameters of macro- and microgeometry of surfaces. *Frict Wear* 20(3):239–245
3. Ivanov AS, Popov BA (2005) Calculation of the interference joint according to contact rigidity of conjugated surfaces. *Vestnik Mashinostroeniya* 4:31–35
4. Ivlev VI, Dmitriev PI (1979) Dynamic method for determining contact stiffness. *Metrology* 10:29–33
5. Ivanov AS (2005) Registration of contact stiffness at calculation of fixed joints. *Vestn Mashinostroeniya* 3:46–48
6. Ivanov AS, Ermolaev MM, Kuralina NN, Murkin SV (2013) Deformation analysis of friction joint loaded with compressive force and random system of moments. *Vestn Mashinostroeniya* 7:17–19
7. Lankov AA, Rogozin GI (1988) Calculation of the actual contact area of two rough surfaces taking into account elastoplastic deformations of microprotrusions. In: *Physicomechanical processes in the contact zone of machine parts*, Kalinin, pp 15–27
8. Lankov AA (1984) Friction contact of machine parts. Kalinin
9. Levina ZM, Reshetov DN (1971) Contact rigidity of machines. Mashinostroenie, Moscow
10. Kragelsky IV (1968) Friction and wear. Mashinostroenie, Moscow
11. Kragelsky IV, Dobychin MN, Kombalov VS (1977) Basics of calculations for friction and wear Mashinostroenie, Moscow
12. Demkin NB (1970) Contacting of rough surfaces. The science, Moscow
13. Mindlin RD (1949) Compliance of elastic bodies in contact. *J Appl Mech* 71(16):947–949
14. Maksak VI (1975) Preliminary displacement and rigidity of mechanical contact. The science, Moscow

15. Maksak VI, Tritenko AN (1978) Energy dissipation during the contacting of elastic solids under complex loading conditions. Energy Scattering with Oscillations of Mechanical Systems: Collected Scientific Works, Kiev, pp 112–118
16. Orlov PI (1977) Basics of design. Reference book. Mashinostroenie, Moscow
17. Khokhlov VM (1990) Calculation of contour areas of contact and pressure. News of universities. Mashinostroenie
18. Demkin NB, Izmailov VV (2008) The development of the theory of contact interaction of machine parts. Vestn Mashinostroeniya 10:28–32
19. Maksimenko AA, Perfilieva NV, Koteneva NV (2009) Contact compliance of precision conditionally fixed joints under dynamic loading conditions to sliding friction. Polz vestn Barnaul 1–2:260–263
20. Perfilieva NV (2003) Dynamic model of elastic mechanical contact within the limits of static friction. The science, Novosibirsk

Forming Laminar Flow of Engine Oil Under Conditions of High-Speed Sliding Friction



V. I. Kubich, E. A. Zadorozhnaya and O. G. Cherneta

Abstract The state of engine oil flow in hydrodynamic couplings is determined not only by geometrical or thermo-mechanical parameters of the interacting friction surfaces, but also by the flow regime. Due to heavy operating conditions of plain bearings in some regimes, self-organization processes on friction surfaces are inefficient. This negatively affects the continuity and damage resistance of forming lubricants. The regime of lubricant flow against the friction surfaces changes during operation. The engine oil flow frequently makes a transition from a laminar flow to a turbulent state. The article reports the results of evaluating possible operating regimes and conditions which enable the engine oil flow in the plain bearing of the turbocharger shaft makes a transition to turbulence. This allowed us to determine the thicknesses of likely boundary layers about the radius of surface roughness and compare them with the total thickness of the possible lubricating layer in a journal-bushing coupling. The proposed approach makes it possible to evaluate the overall state of the oil flow from the point of view of its layer pattern and the motion pattern of its components, which is necessary to improve the methods for ensuring reliability of lubricating the bearing of a particular turbocharger.

Keywords Reynolds number · Turbulent flow · Turbocharger · Boundary layer · Lubricating formations · Oil component

V. I. Kubich

Zaporizhia National Technical University, 64, Zhukogo Str, Zaporizhia 69063, Ukraine

E. A. Zadorozhnaya (✉)

South Ural State University, 76, Lenin prospekt, Chelyabinsk 454080, Russia

e-mail: zadorozhnaiea@susu.ru

O. G. Cherneta

Dniprovsk State Technical University, 2, Dniprobudivska Str, Kamenskoe 51900, Ukraine

© Springer Nature Switzerland AG 2020

A. A. Radionov et al. (eds.), *Proceedings of the 5th International Conference on*

Industrial Engineering (ICIE 2019), Lecture Notes in Mechanical Engineering,

https://doi.org/10.1007/978-3-030-22041-9_119

1137

1 Introduction

The development of measures for improving the reliability of bearing assemblies, operating under the conditions of high-speed sliding friction, implies the availability of data that determine both the surface loading condition and manifestation of the rheological properties of lubricants flowing through clearances of certain sizes. The range of high shaft speed in the friction assemblies of automotive engines is quite wide, for example, from 3000 to 6000 min^{-1} in tribological assemblies of crankshafts and camshafts, and from 75,000 to 220,000 min^{-1} in turbocharger shafts. The state of engine oil flow in such couplings is determined not only by geometrical or thermo-mechanical coupling parameters of the interacting friction surfaces, but also by the flow regime. Due to heavy operating conditions of plain bearings in some regimes, self-organization processes on friction surfaces are inefficient, and this negatively affects the continuity and damage resistance of forming lubricants. This is due to mechanical damage caused by insufficient oil in the friction zone. It should be taken into account that oil is a flowable substance where changing regimes of flow against the friction surfaces in general and the elements of their surface contour in particular can happen, that is, a possible transition of engine oil flow into a turbulent state. A characteristic feature of the turbulent state is vortex motion of lubricant layers. This puts questions about the possibility of forming stable lubricant structures on friction surfaces and their functionality under extreme operating conditions. Answers to the formulated questions make it possible not only to expand the established scope of knowledge about the formation of protective boundary layers on the friction surfaces of engine parts limiting the operational life of critical friction assemblies, but also to develop measures for improving fluid lubricant control.

2 Literature Review

Presently, much attention is paid to the issues of engine oil flow through sliding friction assemblies of automotive engines and, in particular, through the bearing clearances of a crankshaft or a turbocharger shaft [1–7]. For example, [1] developed and presented methods for diagnosing main and connecting rod bearings for automobile and tractor engines by measuring pressure pulsations in the main oil gallery. Having developed some supplementary equipment, the authors managed to establish a correlation between the pressure signal quantity and the technical condition of main bearings. In [2–4, 6], the team of authors conducted a series of theoretical and full-scale experimental studies on installing supplementary equipment into the lubrication system to increase its operational reliability. The turbocharger was equipped with a hydroaccumulator and a brake device to reduce the rotor rundown time, and cooling and lubrication of the shaft during the engine shutdown by forcible inlet of engine oil to the friction zone using a supplementary

pipe and hollow bolts. Research results showed that reduction in the rotor rundown time to 37–57 s, depending on the operational mode, excludes the possibility of semi-dry or dry friction modes, which leads to possible extension of the operational life of the turbocharger.

The research [5] presents a methodology for evaluating and interpreting the diagnostic information, based on the studies presented in [1]. The proposed methodology makes it possible to diagnose engines without disassembling them and to evaluate the wear degree of plain bearings in the slider-crank mechanism according to the parameters of pressure pulsation in the central oil gallery. In [7], the team of authors established the correlation between the rotational speed of a turbocharger and the lubrication criterion λ at different temperatures of engine oil. This research established the correlation between the radial force that loads the bearing and the shaft speed. In general, the obtained results indicate that lubricating formations fail always to withstand the effects of the coupled element, that is, the turbine shaft, caused by the magnitude of the radial force. And this, in turn, leads to switching to lubrication regimes that are adverse to the resistance of bearing material to wear.

When studying the flow state of liquids and gases with different rheological properties in specific operational modes of couplings, it is always necessary to determine the Reynolds number. This will determine above all the laminarity or turbulence of layered flows in the total flow, washing the geometric profiles of surfaces, which determine, for example, the thicknesses of the boundary layers. Hydromechanical problems that are solved using the Reynolds number are considered in various applied and fundamental research and development tasks in different fields of technology, and were published in a number of scientific journals, including [8–11].

Thus, in [12, 13], the authors used the Reynolds number to evaluate the oil flow, which is fed to the friction assemblies of the crankshaft, camshaft, and turbocharger units at different viscosity and temperature parameters of engine oil, geometrical parameters of plain bearings, and operational speed parameters of engine samples. It was found that flow turbulization of the engine oil flow in bearing clearances is theoretically possible in certain operating modes. In [12, 13], the flow through operating clearances was considered. However, discontinuity of the oil flow, which leads to lubrication of surfaces with residual material in the clearance, was not considered, and the possibility of flow turbulization of the residual oil layers was not evaluated. This mode of interaction between surfaces is possible in the general case of delayed oil inlet to the friction zone, and in particular, when the mixed lubrication regime starts. The mathematical model of lubricant material presented in [14] took into account lubricant films in the form of adsorbed layers that are formed straight on the friction surfaces. The effect of polymolecular adsorption on the rheological behavior of lubricating oil in a thin layer was described in [15–17]. However, these research works failed to present an experimental study of friction assemblies in machines where the described lubricant flow regime would be implemented.

Thus, the results of the analyzed works indicate the relevance of evaluating the state of the engine oil flow in the engine friction assemblies, since it determines both the possibility of diagnosing these assemblies in general and the formation of lubricant films straight on the surfaces of engine parts.

2.1 Problem Statement, Goal Setting

The engine oil flow is a structural component of almost every tribological coupling with hydrodynamic, boundary, or mixed lubrication regimes according to the operating conditions. The plain bearings of the turbocharger shaft of automotive engines are considered as tribological “journal-bushing” couplings with a changing pattern of engine oil flow. However, such lubrication regimes are sometimes inconstant, since the thickness of the lubricating layer changes depending on a number of parameters. These are dynamic viscosity η , contact load N , and parameters of surface roughness $R_{a1,2}$.

If plain bearings, where the reverse flow zone is more extensive, have a large length, the static eccentricity is significant ($\varepsilon > 0.3\text{--}0.4$), and the Reynolds number is high ($Re > 200$), then vortex circuits are to be expected in the wide part of the lubricant layer, which disturbs the lubricant flow in the adjacent parts of the lubricant layer.

When Re is more than 2300, the flow is turbulent. Since lubrication systems of automotive engines usually use viscous oils, and the speed in the galleries is low (0.5 l/s), the oil flow is always laminar.

According to Couette, the flow in plain bearings is laminar at $Re < 1900$ and turbulent at $Re > 1900$. Radial bearings with hydrodynamic lubrication are calculated using the method of successive approximation or the method of variation by improving structural and operational factors in order to achieve low work wear and favorable energy costs taking into account the available oils and their viscosity.

The stability of a laminar flow is influenced by breakdown and cavitation of liquid lubricant. These phenomena significantly disturb the evenness of fluid flow and the boundary conditions of flow. Moving cavities and splashes cause significant disturbances in the form of random local eddies. Such eddies do not form the usual disordered turbulent flow, as they are of a larger scale, lower frequencies, and lower stability. Nevertheless, they can significantly increase the viscous resistance and change the acting hydromechanical forces.

The critical values of the Reynolds numbers also depend on the roughness of the bearing surface. Moreover, a rough surface has lower critical Reynolds numbers than a smooth surface. When the bearing surface is washed by oil, a turbulent boundary layer may be formed from the very beginning (there are no laminar zones and transition zones in this case).

Thus, according to [18], the minimum thickness of the lubricant layer, which maintains the conditions for hydrodynamic lubrication, is determined according to the expression:

$$h_{\min} = 0.57 \frac{\eta \cdot U \cdot d \cdot l}{N}, \tag{1}$$

where d is the diameter of the bearing shaft, m; l is the bearing length, m.

Taking into account the established tribological approach to the evaluation of lubrication regimes according to the criterion λ [18], the parameters of expression (1) will determine its numerical values as follows:

$$\lambda = 0.57 \frac{\eta \cdot U \cdot d \cdot l}{N \sqrt{R_{a1}^2 + R_{a2}^2}}, \tag{2}$$

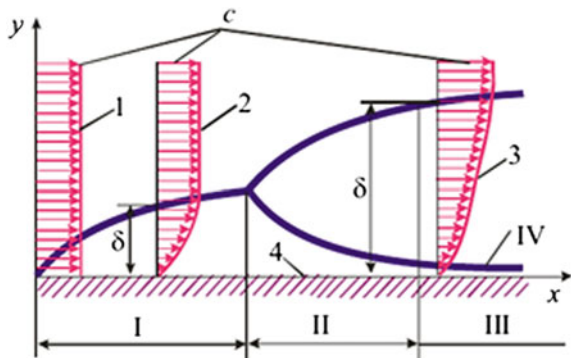
where $R_{a1,2}$ is the arithmetic average value of roughness profile of the contacting surfaces.

As follows from expressions (1, 2), the main parameters that determine the change of lubrication regimes under the conditions of steady regular roughness of interacting surfaces are the directly proportional sliding speed and viscosity, and the inversely proportional load and roughness parameter. In this case, the flow rate v_c of the lubricant will be determined by the rotation speed of the tribo-assembly movable element in this case, by the sliding speed in contact $v_c = f(U)$. However, the movement of separate layers has different velocity gradients depending on the distance from the surfaces of the coupled elements.

Depending on the flow regime, there are laminar and turbulent boundary layers. The latter is characterized by intensive mixing, formation of eddies, velocity pulsations, significant transverse velocity, heat and mass exchange with the external flow [19]. Due to the smooth transition of the boundary layer to the flow core, it is assumed that the boundary layer ends at the thickness δ , where the rate differs from the external flow rate by 1% (Fig. 1).

As the wall is washed by the external flow with a slightly varying velocity, the thickness of the boundary layer δ increases. The layer is laminar at first (Section I), but under certain conditions, it begins to make a transition to turbulence due to the formation and intensification of pulsations. Section II, where this process occurs,

Fig. 1 Diagram of the boundary layer when the flat wall is washed by the flow: I—laminar regime; II—transition zone; III—turbulent regime; IV—laminar sublayer; 1—velocity profile of the ideal flow; 2—the same in the laminar layer; 3—the same in the turbulent layer; 4—the wall that is washed by the flow [19]



is called transitional, and in section III, the layer can be considered turbulent. However, there is also a thin laminar sublayer between the wall and the turbulent layer.

The thickness of the turbulent layer is remarkably larger than that of the preceding laminar layer. The turbulent layer has a more complete velocity profile than the laminar one (see the velocity profiles in Fig. 1), which is explained by intensive mixing inside the layer.

It is difficult to determine the characteristics of the non-laminar lubricant flow experimentally, because different regimes, ranging from ordered Taylor vortex flows to disordered turbulent flows, can intervene.

The vortex zone acts on the rest of the lubricant flow like a solid body of the same configuration that has been put in its layer. This reduces the wedge part of the lubricating layer in its widest part. The lubricant in this area makes a transition to turbulence only in the weakly loaded part of the lubricating layer, and therefore, the flow turbulization has little effect on the magnitude of hydromechanical forces acting, for example, on the shaft journal. Actually, the expanding part of the liquid lubricating layer is usually cavitated due to the lowering pressure in the main flow, and the lubricant part, where eddy currents could occur, breaks down.

Breakdown and cavitation of liquid lubricants—lubricating formations with variable rheological properties—have a great influence on the stability of the laminar flow. These phenomena significantly disturb the evenness of the fluid flow and the boundary conditions for the flow of its layers. Moving cavities and splashes cause significant disturbances in the form of random local eddies. Such eddies do not form the usual disordered turbulent flow, as they are of a larger scale, lower frequencies, and lower stability. Nevertheless, they can significantly increase the viscous resistance and change the acting hydromechanical forces.

The velocity gradients of the lubricating layers may be as follows.

First, they may be increasing $-dv_c/dh > 0$, which is predetermined by a pre-formed boundary layer, that is, lubricant formations of polyatomic carbon-hydrogen molecule chains. The latter are characterized by certain cohesive bonds within the structure and adhesive bonds with a set of active centers of the surfaces. These are polymolecular layers with a different shear strength.

Second, they may be constant $-dv_c/dh = 0$, when $v_c = 0$ or $v_c = \text{const} > 0$, which is predetermined:

- on the one hand, by the lacking boundary layers—when they have been destroyed for some time and have not been formed yet, which is caused by the critical values of contact loading parameters;
- on the other hand, by the laminar state of the flow when the lubricant films are formed again, which is characterized by the constant velocity of conditional points moving along the streamlines. In this case, the conditional points of the streamlines can be considered as the motion of lubricant components in the form of individual polyatomic molecules.

Third, they may be variable $-dv_c/dh \geq 0$, $dv_c/dh \leq 0$, which is predetermined by the transition from the laminar flow state of the lubricant components to the turbulent state.

It is an established fact that in case the laminar flow regime of lubricant fails, the friction moment acting on the journal and on the bearing increases. The hydrodynamic force supporting the journal slightly increases, but reliable measurements of this force for non-laminar lubricant flow regimes are unknown. There are very little data about the components of hydromechanical forces during lubricant fluctuations [20]. According to the known measurements, the pressure profiles of the turbulent lubricant flow do not differ significantly from those of the laminar flow and sometimes are within the margin of measurement error.

The next issue that is important for high-speed shafts in mechanical engineering structures is transition from the laminar flow regime of lubricant, for example, engine oil, to a turbulent one. The latter increases the moment of friction, enhances the heat production, and therefore, has a smaller flow of lubricant components than the laminar regime.

The probability, with which adhesive-cohesive bonds will be formed in new lubricant film structures of certain thicknesses, will be determined by the motion rate of lubricating medium components and, accordingly, by the time spent on energy exchange and interaction of force fields. It seems obvious that the lack of ordered motion of lubricating medium components with different molar masses will cause chaos in the formation of stable bonds. This is especially important for surface-active substances, which, for example:

- are responsible for coordinating the position of polyatomic molecules, for example, $\text{CH}_3(\text{CH}_2)$, with respect to the active centers on the metal surfaces;
- participate in their aggregation process in suspension and form a liquid crystal layer of the boundary film, healing the damaged layers on the surfaces [20].

Thus, the lack of ordered motion of the interaction medium components, that is, additives, can be represented with a model of electrohydrodynamic flows. The higher the intensity and heterogeneity of the field between the electrodes and the concentration of the polar phase in the oil volume are, the stronger they are [21]. We interpret this model as an ordered laminar motion of components, Fig. 2a, and a disordered turbulent motion of components, Fig. 2b, against a conditional surface with active centers. Moreover, the authors discuss the mechanism of boundary lubricating layer formation under the conditions of electromagnetic action on oil additives. The researchers consider a kind of inverse problem, that is, control of forced flow turbulization of the lubricant medium in order to intensify the mixing of lubricant components, which generally leads to increased physical adsorption of additive molecules on metal surfaces, the formation of a more durable multi-molecular boundary layer of lubricant, and the improved tribotechnical indicators of friction couplings.

However, the lubricating medium in the form of engine oil does not consist only of additive compositions with surface-active substances, but also of base oil with

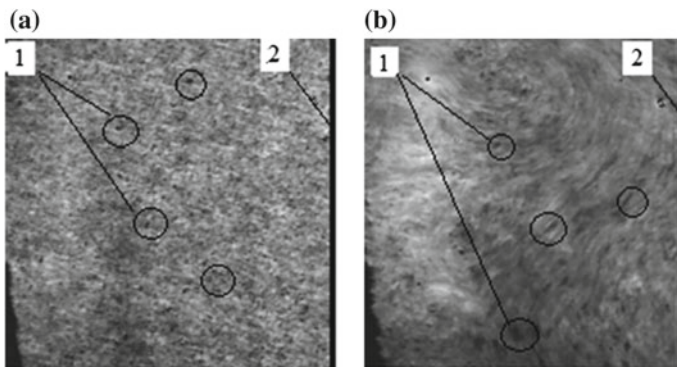


Fig. 2 Photomicrographs of a LiquiMoly 10W40 oil sample on glass in the interelectrode space, magnification— $\times 1000$: **a** voltage on the electrodes $U = 0$; **b** voltage on the electrodes $U = 500$ V; 1—medium components; 2—conditional metal surface

complex molecules that form its structure as a whole. This composition is certainly characterized by viscous friction forces, which make the fluid adhere to the surface of the washed element [22]; that is, they keep the oil components in the rest state. According to the theory of the boundary layer, created mainly by L. Prandtl, under certain flow conditions, the engine oil components form such a boundary layer, where the viscous friction and pressure forces are of the same order and the velocity increases as it gets farther from the body surface [22]. In any case, regardless of breakdown and repair of protective lubricant formations, there are boundary layers on the surfaces that are washed with oil. But it still remains unanswered: What inherent properties of intensity and time of action do they have under the conditions of change of the hydraulic state? It is also interesting to evaluate the percentage of the components of surface-active substances in the boundary layer during transitions from one lubrication regime to another. This knowledge is especially important for controlling the processes when restoring effective boundary layers in tribological systems of materials with different surface activity.

The boundary layer thickness δ is not a well-defined concept, since the layer boundary on the liquid side is not sharply outlined, but it can be determined as follows [22]:

$$\delta \approx \frac{l}{\sqrt{Re}}, \quad (3)$$

where l is the characteristic linear size of the washed element; Re is the Reynolds number.

This approach in evaluating the state of engine oil flow near the washed surfaces theoretically determines the formation of a shielding boundary layer with favorable conditions for the formation of adhesive bonds of oil components with active metal centers. However, the velocity of layers in the boundary layer rapidly increases as it

gets farther from the surface. This together with the variable velocity gradients of components in the bordering zone, which is typical of the flow turbulization effect, causes fragmentary blocking of their direct passage to the surface. Thus, a blocking layer of different density is formed.

The eccentricity of the bearing journal of the high-speed shaft, while it is not large ($\varepsilon < 0.3$), has almost no effect on the stability of the laminar flow. According to some data, such eccentricity slightly (within the range of 10–15%) reduces the critical value of the Taylor number, but, according to other data, it slightly increases it. A more significant eccentricity definitely prevents Taylor vortices, thereby stabilizing the laminar lubricant flow. The turbulence of the lubricant flow manifests itself mainly as an apparent increase in lubricant viscosity and a slight reduction in the relative length of the bearing.

Theoretically, the laminar flow in the lubricating layer is stable at any flow rate if the angular velocity of bushing rotation exceeds the angular velocity of journal rotation, when they rotate in the same direction. This can be explained by the fact that when the bushing rotates, the centrifugal forces press the lubricant to the moving surface. On the contrary, the loss of stability during journal rotation is due to the fact that the centrifugal forces push the lubricant from the rotating surface. Such a simplified idea of forces certainly does not explain all the peculiarities of the stability loss by the laminar flow.

The formation of a blocking layer is determined by the fact that oil components with lower velocities cannot overcome the resistance to the motion of components with high velocities. Based on the above it follows that the boundary layers have smaller thicknesses when the Reynolds number has large values, and, accordingly, the reserve of concentrated surface-active substances that causes restoration of the damaged boundary layers may not be sufficient. Basing on the length of one average molecule, the thickness of the boundary layers will be comparable with the heights of the forming polymolecular lubricant layers; for example, for a fatty acid molecule, it will be 1.7–2.3 nm. We propose to use the outlined approach to evaluate the state of engine oil flow in the plain bearing of turbochargers as a basis for developing measures of improving its reliability under extreme operating conditions.

Thus, from the point of view of evaluating the processes that cause the structuring of boundary layers shielding the interaction surfaces, it seems significant to take into account the velocities of the lubricant components that flow around the friction surfaces during their interaction. It is quite difficult to calculate the velocities of motion of the lubricating medium components in the lines of fluid flow, but it is not difficult to evaluate the flow state with the lines of fluid flow according to the Reynolds number for a plain bearing.

At this stage, the research aims to determine the possible operating regimes and conditions under which the engine oil flow in the plain bearing (s) of the turbocharger shaft transitions to turbulence with corresponding thicknesses of the likely boundary layers. The obtained results will allow us to evaluate the overall state of the oil flow from the point of view of its layer pattern and the motion pattern of its components.

3 Materials and Methods

To calculate the Reynolds number for the plain bearing, we used the mathematical expression [12, 13]:

$$Re = \frac{\pi \cdot d \cdot n \cdot \rho \cdot S}{2 \cdot \mu_{ef}} \leq 41.3 \cdot \sqrt{\frac{d}{S}} \tag{4}$$

where d is the shaft diameter, m; n is the turbocharger shaft speed, s^{-1} ; ρ is the density of the engine oil, kg/m^3 ; μ_{ef} is the dynamic viscosity of the engine oil, Pa s; S is the diameter clearance, m.

Calculations were made in Microsoft Excel. The following values of interference parameters were used as initial data for calculations: the shaft (journal) diameter, m: $d_{max} = 0.012$; $d_{min} = 0.006$; the diameter clearance, μm : $S_{nom} = 16$; $S_{manuf} = 58$; $S_{bound} = 75$; the shaft speed, s^{-1} : $n_{max} = 4100$ ($246,000 \text{ min}^{-1}$); $n_{min} = 20$ (1200 min^{-1}); the dynamic viscosity, Pa s: $\mu_{max} = 0.9$; $\mu_{min} = 0.0024$.

The values of dynamic viscosity were calculated for Lukoil Super 15 W-40 mineral engine oil according to the data given in Table 1.

The diameter clearance was selected based on the fact that it increases from the rated value to the boundary value, as the bearing life diminishes. The shaft diameters were selected based on the design features of turbochargers, determined by the geometrical dimensions of the main parts and the maximum turbine shaft speed. Thus, two average diameters of shafts were selected for analytical studies: $d_{max} = 0.012$ m for turbochargers with maximum shaft speed from $100,000$ to $125,000 \text{ min}^{-1}$, for example, TCR-6 (01), TCR7-00.1 (700-1118010), K-27-543-01, etc., with an operating range of $90,000\text{--}100,000 \text{ min}^{-1}$; $d_{min} = 0.006$ m for turbochargers with maximum shaft speed of $150,000 \text{ min}^{-1}$ and higher, for example, TCR-4, TCR5, Garret G25-555, Garret 15445, etc., with an operating range of $160,000\text{--}180,000 \text{ min}^{-1}$.

The behavior of the Reynolds number value was modeled in Microsoft Excel according to expression (4). To visualize the line of oil transition into the turbulent state and determine the regimes and conditions for maintaining this state, response surfaces were built.

Table 1 Initial data

Parameter	Numerical values							
Temperature T ($^{\circ}C$)	0	20	40	60	80	100	120	140
Kinematic viscosity γ , mm^2/s	1000	215	70	26	18	8	5	3
Density ρ^* , kg/m^3	908	893	878	863	848	833	818	803
Dynamic viscosity μ_{eff} , Pa s	0.9	0.19	0.061	0.022	0.015	0.0066	0.0041	0.0024

Note *the density was calculated according to the expression $\rho = 0.908 - 7.5 \times 10^{-4} T$, which was obtained by processing the data of laboratory research on the change in lubricant mass per volume unit under a thermal effect

To determine the thickness of a likely boundary layer, expression (3) was used. The numerical value of the radius of the surface roughness curve r was used as the characteristic linear size of the washed body. The numerical values of the parameter r are determined by the profile recording data of the working surfaces of the journal and the bushing. To make theoretical calculations, we used the values $r_1 = 30 \mu\text{m}$, for example, for the surface of a steel shaft, and $r_2 = 13 \mu\text{m}$, for example, for the surface of a bronze bushing that correspond to the cylindrical surface finish at $R_{z\text{max}} = 1.2 \mu\text{m}$ and the internal grinding at $R_{z\text{max}} = 4.72 \mu\text{m}$.

4 Results

Figure 3 shows response surfaces for the Reynolds number with the range of shaft rotation speed $n = 20\text{--}2760 \text{ s}^{-1}$ ($1200\text{--}165,600 \text{ min}^{-1}$)

Tables 2 and 3 show turbocharger regimes that maintain the oil flow turbulence transition. Table 4 shows numerical values of the boundary layer.

5 Discussion

Tables 1, 2, 3, and 4 show the calculation results that indicate the following.

Oil flow does not make a transition to turbulence when the operating clearance S is $16 \mu\text{m}$, regardless of the shaft diameters, viscosity change, and shaft speed. The thickness of the boundary layer varies from 1.8 to $9.5 \mu\text{m}$ on the surface with a larger asperity radius, and from 0.78 to $4.1 \mu\text{m}$ with a smaller asperity radius. This determines favorable conditions for the interaction of the oil components both between themselves and with the surfaces, especially at low shaft speed.

When the operating clearance S is $58 \mu\text{m}$ and the shaft diameter d is 0.006 m , the oil flow makes a transition to turbulence when its rotation speed ranges from $138,000 \text{ min}^{-1}$ (with the oil viscosity of 0.0024 Pa s , which corresponds to a

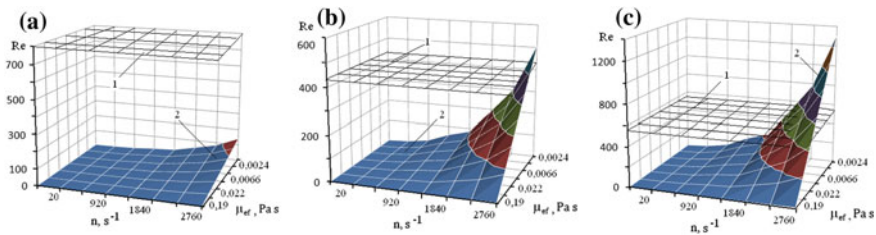


Fig. 3 Response surfaces for the Reynolds number: 1—line of transition into the turbulent state; 2—the response surface; **a** when $d = 0.006 \text{ m}$; $S = 16 \mu\text{m}$; **b** when $d = 0.006 \text{ m}$; $S = 58 \mu\text{m}$; **c** when $d = 0.012 \text{ m}$; $S = 75 \mu\text{m}$



Table 2 Numerical values of the parameters when the shaft diameter $d = 0.006$ m

Clearance S (μm)	Dynamic viscosity μ (Pa s)	Shaft speed n , min^{-1}	Reynolds number Re
16	0.0024–0.9	1200–246,000	799*
	$Re_{\text{max}} = 206$		$Re_i < 799$
58	0.0066–0.9	1200–246,000	420*
	0.0041–0.9	1200–165,000	$Re_i < 420$, $Re_{\text{max}} = 749$
	0.0024–0.0041**	138,000–246,000**	$Re_i > 420$
75	0.0066–0.9	1200–246,000	369*
	0.0041–0.9	1200–138,000	$Re_i < 369$, $Re_{\text{max}} = 969$
	0.0024–0.0041**	110,400–246,000**	$Re_i > 369$

Note *boundary value of the Reynolds number Re of flow turbulization, lower value–maximum value under flow turbulization; **values under flow turbulization

Table 3 Numerical values of the parameters when the shaft diameter $d = 0.012$ m

Clearance S , μm	Dynamic viscosity μ_{eff} , Pa s	Shaft speed n , s^{-1}	Reynolds number Re
16	0.0024–0.9	20–4100	1131*
	$Re_{\text{max}} = 413$		$Re_i < 1131$
58	0.0066–0.9	1200–246,000	594*
	0.0041–0.9	1200–138,000	$Re_i < 594$, $Re_{\text{max}} = 1498$
	0.0024–0.0041**	138,000– 246,000**	$Re_i > 594$
75	0.0015–0.9	1200–246,000	522*
	0.0066–0.9	1200–138,000	$Re_i < 522$, $Re_{\text{max}} = 1930$
	0.0024–0.0041**	138,000– 246,000**	$Re_i > 522$

Note *boundary value of the Reynolds number Re of flow turbulization, lower value–maximum value under flow turbulization; **values under flow turbulization

temperature of 140 °C) to $193,000$ min^{-1} and higher (with a viscosity range between 0.0041 and 0.0024 Pa s, which corresponds to a temperature range between 130 and 140 °C). These ranges of operating parameters of the oil layer in TCR bearings are dangerous, because the contact lubricating layer sharply decreases. This causes the oil burning effect, plaque and sludge formation. Under these operating conditions, the resource reduces by 2–10 times. It may lead to the fusing of the working surfaces of the journal and the bearing, as well as complete jamming of the rotating TCR assemblies. The average thicknesses of the boundary layers are 1.4 and 0.6 μm , which is 1.7 and 1.8 times smaller than under more

Table 4 Numerical values of the boundary layer δ , μm

Clearance S , μm	Diameter $d = 0.006$ m		Diameter $d = 0.012$ m	
	Asperity radius $r_1 = 30$ μm	Asperity radius $r_2 = 13$ μm	Asperity radius $r_1 = 30$ μm	Asperity radius $r_2 = 13$ μm
16	2.5–9.5*	1.1–4.1*	1.8–9.5*	0.78–4.1*
58	1.46–9.5	0.63–4.1	1.23–9.5	0.53–4.1
	1.33–1.46**	0.6–0.63**	0.94–1.23**	0.41–0.53**
75	1.56–9.5	1.41–4.1	1.31–9.5	0.57–4.1
	1.17–1.56**	0.44–0.5**	0.83–1.31**	0.36–0.57**

Note *values were determined for the range of the Reynolds number Re from 10 to Re_{bound} ; **values under flow turbulization (for the clearances of 58, 75 μm , the values in the numerator with zero flow turbulization)

favorable conditions. In this case, the theoretical range of flow turbulization is imposed on the possible operating mode of the turbocharger. This means that the discussed effects, consisting in transition of the oil flow to turbulence, its discontinuity, and cavitation phenomena, are possible. In a coupling with the same clearance, but with a shaft diameter of $d = 0.012$ m, the oil flow makes a transition to turbulence when the oil viscosities are the same, but the shaft speed is $110,400 \text{ min}^{-1}$ and higher. However, turbochargers with a shaft diameter of about 12 mm and more do not operate within this speed range. Therefore, it is unnecessary to consider the mode of flow turbulization.

When the operating clearance S is 75 μm and the shaft diameter d is 0.006 m, the oil flow makes a transition to turbulence:

- when rotation speed is $110,400 \text{ min}^{-1}$ and higher, oil viscosity is 0.0024–0.0041 Pa·s;
- when the rotation speed is $246,000 \text{ min}^{-1}$ and the oil viscosity is 0.0066 Pa s, the temperature is 100 °C.

The thicknesses of the boundary layers get reduced by an average of 6–13%. In this case, the theoretical range of flow turbulization is not only imposed on the operating mode of the turbocharger, but also expands toward a decrease in the shaft rotation speed. Reduction in boundary lubricant layers and discontinuity of flow with the operating clearance $S = 75$ μm lead to an increase in dangerous ranges of TCR shaft speed. Approximate calculations showed that this can lead to a decrease in resource parameters by 1.1–1.6 times in comparison with the TCR operating with clearances of 16, 58 μm .

In a coupling with the same clearance, but with a shaft diameter of $d = 0.012$ m, the oil flow makes a transition to turbulence:

- when the rotation speed is $82,800 \text{ min}^{-1}$ and higher, and the oil viscosity is 0.0024 Pa s;
- when the rotation speed is $110,400 \text{ min}^{-1}$ and higher, and the oil viscosity is 0.0024–0.0041 Pa s;

The thicknesses of the boundary layers also get reduced by an average of 6–13%. This interaction geometry is characterized by the range of oil flow transition to turbulence that is imposed on the operating mode of the turbocharger.

However, in operational modes, the turbocharger bearings have radial clearances that are caused by the efficiency of the oil flows, as well as the direction and magnitude of the radial loading force. These clearances are not equal and even in cross-section.

To evaluate the correlations between the thicknesses of the boundary layers on the shaft and journal (bearing) surfaces and the thickness of the lubricating layer between them in operational modes of the turbocharger, the calculations were made according to expression (1), see Table 5. In this case, we used the radial force value $N = 20H$ that was calculated in [7]. This force loads the friction surface of the plain bearing of the GT1544 turbocharger.

The analysis of changes in thickness fields of the lubricating layer in the coupling and the boundary layers on the friction surfaces of the shaft and bushing (Tables 3, 4, and 5) shows the following.

When operational clearances in the coupling are 58 and 75 μm and the shaft diameter $d = 0.006$ m, there is no possibility of forming stable boundary layers on the surface of the bushing and the shaft in the zone of maximum contact. This is determined by the fact that the average range of thickness of the lubricating layer under possible transition of oil flow to turbulence is 4–5 times smaller than the theoretical boundary layer on the shaft surface and 1.5–2.5 times on the journal surface. Such a correlation seems to be with a “preload.” The conditions for clearly defined thicknesses of the boundary layers, that is, with a “clearance,” are more favorable when the oil temperature is less than 100 $^{\circ}\text{C}$. The area of preload work poses a threat by reducing the resource parameters of TCR assemblies by 1.1–2 times.

When operational clearances in the coupling are 58 and 75 μm and the shaft diameter $d = 0.012$ m, there is a possibility of forming stable boundary layers on the surface of the bushing and the shaft in the zone of maximum contact. This is determined by the fact that the average range of the lubricating layer thickness in the zone of maximum contact is approximately equal to the sum of the possible thicknesses of the boundary layers on the surface of the shaft and the journal. This

Table 5 Effective thickness of the lubricating layer h_{min}

Parameter	Conditions: $d = 0.006$; $l = 0.015$ m; $N = 20$ N							
	$n = 110400 \text{ min}^{-1}$, $v_s = 34.66$ m/s				$n = 165,600 \text{ min}^{-1}$, $v_s = 51.81$ m/s			
M_{eff} , Pa s	0.0024	0.0041	0.015	0.022	0.0024	0.0041	0.015	0.022
T , $^{\circ}\text{C}$	140	120	80	60	140	120	80	60
h_{min} , μm	0.21	0.36	1.33	1.95	0.3	0.54	1.99	2.9
	Conditions: $d = 0.012$; $l = 0.025$ m; $N = 20$ N							
	$n = 82,800 \text{ min}^{-1}$, $v_s = 51.99$ m/s				$n = 110,400 \text{ min}^{-1}$, $v_s = 51.99$ m/s			
h_{min} , μm	1.06	1.8	6.66	9.7	1.4	2.43	8.89	13.8

correlation seems “transitional” with a defined “clearance” under the oil temperature lower than 110 °C. Thus, the work zone above 110 °C can be called transitional, and transition to turbulence is more likely.

In general, the obtained results indicate that the hydraulic tension of the layers formed of engine oil components on the surfaces of the shaft and the bushing may vary depending on the degree of its turbulence and the geometric parameters of the contact. The oil is under threat with a danger of developing additives, overheating of oil layers, or accelerated wear in relation to the bushing and the shaft. And this, in turn, determines the pattern of forming damage-resistant bonds between elementary polyatomic molecules of oil and active centers, that is, ions of metals of the bushing and shaft materials. At the same time, the time component of the contact interaction is decisive for the motion pattern of the components of engine oil when changing modes of force and speed loading of its layers. It must be taken into account when forecasting surface effects when using, for example, repairing and restoring products to improve the technical condition of the elements to be restored.

Further studies can be directed to a comparison of the calculation results with experimental data. For this purpose, experimental stands for research of turbochargers developed by Gritsenko [23–26] and others can be used.

6 Conclusions

The considered approaches allowed us to calculate the estimate of possible operational modes and conditions under which the engine oil flow in the plain bearing(s) of the turbocharger shaft makes a transition to turbulence, which allowed us to determine the thicknesses of probable boundary layers on the surfaces of the shaft and the bushing, and compare them with the thickness of a possible lubricating layer under the loading conditions. It has been established that the boundary layers can have different thickness and correlate with the “preload,” the “clearance,” and be “transitional” depending on the considered parameters. The considered technique can be applied to evaluate the state of engine oil flow in the predicted diameter clearance of any turbocharger. The obtained results may call for ways of ensuring reliability of bearing(s) lubrication in a particular turbocharger. Moreover, the obtained data can be used to simulate the effects of accelerated wear, reduced reliability of frictional couples, and undesired friction modes.

References

1. Glemba K (2014) Diagnosing main and rod bearings of a slider-crank mechanism. *M Bull SUSU* 14(1):63–71
2. Plaksin A, Plaksin A, Gritsenko A et al (2014) Improving the reliability of automotive turbochargers using hydroaccumulators. *T Bull KSAU (Krasnoyarsk State Agrarian Univ)* 8:176–180

3. Burtsev A, Plaksin A, Gritsenko A (2015) Improving the operational reliability of diesel tractor turbochargers. *M AIC Russ* 72(1):23–25
4. Plaksin A, Gritsenko A, Burtsev A et al (2015) A way to improve the performance of diesel turbochargers using an autonomous lubricating-braking device. *T Bull KSAU (Krasnoyarsk State Agrarian Univ)* 6:89–94
5. Gritsenko A, Kukov S (2010) Methods for analyzing diagnostic information in diagnosing bearings of a slider-crank mechanism according to pressure parameters in the central oil line. *M Bull ČGAA* 57:57–62
6. Plaksin A, Gritsenko A, Burtsev A (2014) The results of experimental studies of the rotor run-out time in the turbocharger TCR-11. *Bull CSAA (Chelyabinsk State Agroeng Acad)* 70:130–135
7. Manuilov E, Kubich V (2015) Gas-dynamic evaluation of loading and lubrication regimes of a bearing in the turbo-supercharging unit of an internal combustion engine. In: Proceedings of the 15th international scientific conference “Scientific prospects of the 21st century. Achievements and prospects of the new century”, Novosibirsk MNI “Education”, Russia, 11–12 Sept 2015, 8/15:77–80
8. Krishna V, Suresh C, Panicker M et al (2017) Experimental analysis of multiport averaging device and effect of body shape on flow coefficient. *FME Trans* 45(1):32–37
9. de Lima Rafael, Lemos Rodrigo Spotorno, Vieira et al (2017) Numerical analysis of a turbulent flow with coanda effect in hydrodynamics profiles. *FME Trans* 45(3):412–420
10. Radenković DR, Milićević SS, Stevanović ND (2016) Rarefied gas flow in microtubes at low reynolds numbers. *FME Trans* 44/1:10–15
11. Stevanovic Nevena D, Vladan D et al (2014) An exact analytical solution for the second order slip-corrected reynolds lubrication equation. *FME Trans* 43(1):16–20
12. Kurlikov D, Kubich V (2017) Influence of motor oil turbulence on the ICE life. Problems of energy resources conservation in the industrial region. In: Proceedings of the “Science and practice” annual scientific conference, Mariupol State Pedagogical University “PDTU” 11–12 May 2017: 37–38
13. Kurlykov D, Kubich V (2017) The regression equation of the Reynolds number for couplings of ICE sliding. In: Materials of the “Modern energetic installations in transport, technology, and equipment for their maintenance” 8th international scientific conference, 28–29 Sept 2017, Kherson CDMA:236–240
14. Zadorozhnaya E, Cherneyko S, Kurochkin M et al (2015) A study the axial and radial rotor stability of the turbo machinery with allowance the geometry of the surface and properties of the lubricating fluid. *Tribol Ind* 37(4):455–463
15. Mukhortov E, Zadorozhnaya E, Levanov I (2013) Multimolecular adsorption lubricants and its integration in the theory fluid friction. In: Proceedings of the STLE annual meeting and exhibition, 14–17 May 2013, Detroit, Michigan, USA, pp 147–149
16. Mukhortov E, Zadorozhnaya E, Levanov I et al (2015) The influence of poly-molecular adsorption on the rheological behaviour of lubricating oil in a thin layer. *FME Trans* 43(3): 218–222
17. Zhang C (2002) TEHD behavior of non-newtonian dynamically loaded journal bearings in mixed lubrication for direct problem. *J Tribol* 124(1):178–185
18. Dmitrichenko M, Mnatsatsakanov R, Mikosyanchik O (2006) Tribotechnics and bases of reliability of machines. Educational Guide. K Informavtodor:216
19. Belyaev L (2008) Turbines of thermal and nuclear power plants. Summary of lectures. Tomsk NTL Publisher, p 218
20. Voronin S (2015) Influence of the phase state of the additive on the thickness of the liquid crystal layers of the boundary film. Collection of Scientific Papers UkrDAZT. Kharkiv UkrDazht 151/2:56–62
21. Voronin S, Dunaev A (2015) Effects of electric and magnetic fields on the behavior of oil additives. *J Frict Wear* 36(1):33–39

22. Sivukhin D (1979) Mechanics Volume I. The boundary layer and the breakaway phenomenon. Mechanics of liquids and gases. Access mode. Moscow Nauka:520. http://old.pskgu.ru/ebooks/sdvpdf1/smg112_103.pdf. Accessed 21 Sept 2008
23. Gritsenko A, Zadorozhnaya E, Shepelev V (2018) Diagnostics of friction bearings by oil pressure parameters during cycle-by-cycle loading. Tribol Ind 40(2):300–310. <https://doi.org/10.24874/ti.2018.40.02.13>
24. Gritsenko A, Plaksin A, Shepelev V (2017) Studuing lubrication system of turbocompressor rotor with integrated electronic control. Procedia Eng 206:611–616. <https://doi.org/10.1016/j.proeng.2017.10.525>
25. Gritsenko A, Plaksin A, Almetova Z (2017) Development of combined ICE startup system by means of hydraulic starter. Procedia Eng 206:1238–1245. <https://doi.org/10.1016/j.proeng.2017.10.625>
26. Plaksin A, Gritsenko A, Glemba K (2015) Modernization of the turbocharger lubrication system of an internal combustion engine. Procedia Eng 129:857–862. <https://doi.org/10.1016/j.proeng.2015.12.122>

Study of Dependence of Kinematic Viscosity and Thermal-Oxidative Stability of Motor Oils



V. G. Shram, Yu. N. Bezborodov and A. V. Lysyannikov

Abstract The results of the study of thermo-oxidative stability of mineral and synthetic motor oils in the temperature range from 170 to 200 °C are presented. The indicators of thermo-oxidative resistance are proposed, taking into account optical density, evaporation, and kinematic viscosity. It should be noted that, as an indicator of thermo-oxidative resistance, three variants of a combination of optical density, evaporation coefficients, and relative viscosity were considered. The effect of temperature on the oxidation processes was investigated, and an analytical relationship between optical density, evaporation, and kinematic viscosity was obtained. It is established that the oxidation of mineral oil produces two types of products regardless of the oxidation temperature, which is confirmed by the presence of a branch of dependence with a high rate of change in optical density. It has been established that the change in kinematic viscosity during the oxidation of mineral and synthetic oils occurs according to a general U-shape, regardless of temperature.

Keywords Temperature control · Optical density · Volatility · Kinematic viscosity · Thermal and oxidation resistance

1 Introduction

To assess the thermal-oxidative stability of lubricating oils in the laboratory in [1–10], the method of direct photometry was applied. The main indicators are optical density and evaporation, which characterize the amount of heat energy absorbed by the lubricating oil during thermostating [11–20].

The purpose of this work is to study the effect of kinematic viscosity on the thermal-oxidative resistance index.

V. G. Shram (✉) · Yu.N. Bezborodov · A. V. Lysyannikov
Siberian Federal University, 82/6, Svobodny Ave., Krasnoyarsk 660041, Russia
e-mail: Shram18rus@mail.ru

2 Methodology

Mobil 10 W-40 SC/CC mineral engine oil and synthetic Mobil 5 W-40 SJ/CF as well as the following controls and tests were selected for the study: a device for temperature control of lubricating oils, a photometric device for direct photometry of oxidized oils, a low-volume viscometer, and electronic scales. The test procedure consisted in the following; a sample of oil weighing 100 g was poured into a glass beaker of a temperature control device and thermostatically controlled at a given temperature with stirring with a glass stirrer with a rotation speed of 300 rpm.

After a certain time of testing, a glass with a sample of oxidized oil was weighed, the mass of evaporated oil was determined, a sample was taken for direct photometry at a photometric layer thickness of 2 mm by monochromatic light flux, and optical density and kinematic viscosity at 100 °C were determined.

Selected samples were poured into a glass beaker, which was reweighed. Testing of the oils was continued according to the agreed technology until an optical efficiency rating of 0.75 ... 0.8 units was achieved at temperatures of 170, 180, 190, and 200 °C.

Based on the obtained experimental data, the following parameters were determined:

- optical density of the oxidized oil D

$$D = \lg \frac{\varphi}{\varphi_o}, \quad (1)$$

here φ and φ_o —respectively, the luminous flux incident on the layer of oil in the cell and passed through the layer of oxidized oil;

- K_G coefficient evaporation

$$K_G = \frac{m}{M}, \quad (2)$$

here m and M —respectively, the mass of the evaporated oil when tested and the mass of the remaining oil in a glass beaker, g;

- coefficient of relative viscosity K_μ

$$K_\mu = \frac{\mu_o}{\mu_T}, \quad (3)$$

here μ_o and μ_T —respectively, the viscosity of the oxidized and marketable oils.

3 The Results of Research

When thermostating oils, there is a change in optical density, evaporation, and kinematic viscosity, the latter indicator changing as a result of evaporation, temperature destruction of the base or additives, increasing the concentration of oxidation products. In this regard, as an indicator of thermal-oxidative resistance P , we investigate three options for the combination of optical density, evaporation coefficients, and relative viscosity

$$P_1 = D + K_G, \quad (4)$$

$$P_2 = (D + K_G) \cdot K_\mu, \quad (5)$$

$$P_3 = \frac{D + K_G}{K_\mu}, \quad (6)$$

The indicator P_1 characterizes the amount of heat energy absorbed by the lubricating oil, as a result of which oxidation and evaporation products are formed.

The indicator P_2 characterizes the influence of kinematic viscosity on the indicator P_1 , and the indicator P_3 determines the ratio between oxidation products, evaporation, and kinematic viscosity.

Figure 1a–c presents the dependences of optical density, kinematic viscosity and evaporation of Mobil 10 W-40 SC/CC mineral motor oil on time and oxidation temperature.

Dependencies are described by the equations: at the first stage, linear, and at the second, a second-order polynomial (Fig. 1a), and the regression equations have the form for temperatures:

$$\begin{aligned} 200^\circ\text{C} \quad D &= 0.0163t \text{ (before 12 h of testing)} \\ D &= 0.0095t^2 - 0.213t + 1.383 \text{ (after 12 h of testing)}, \end{aligned} \quad (7)$$

$$\begin{aligned} 190^\circ\text{C} \quad D &= 0.0108t \text{ (before 17 h of testing)}, \\ D &= 0.0023t^2 - 0.076t + 0.819 \text{ (after 17 h of testing)}, \end{aligned} \quad (8)$$

$$\begin{aligned} 180^\circ\text{C} \quad D &= 0.00356t \text{ (before 30 h of testing)}, \\ D &= 0.00102t^2 - 0.062t + 1.055 \text{ (after 30 h of testing)}, \end{aligned} \quad (9)$$

$$\begin{aligned} 170^\circ\text{C} \quad D &= 0.00164t \text{ (before 60 h of testing)}, \\ D &= 0.00041t^2 - 0.0519t + 1.748 \text{ (after 60 h of testing)}. \end{aligned} \quad (10)$$

The correlation coefficients are as follows: for $T = 200^\circ\text{C}$ —0.998; 0.996; for $T = 190^\circ\text{C}$ —0.996; 0.998; for $T = 180^\circ\text{C}$ —0.996; 0.998; for $T = 170^\circ\text{C}$ —0.995; 0.96.

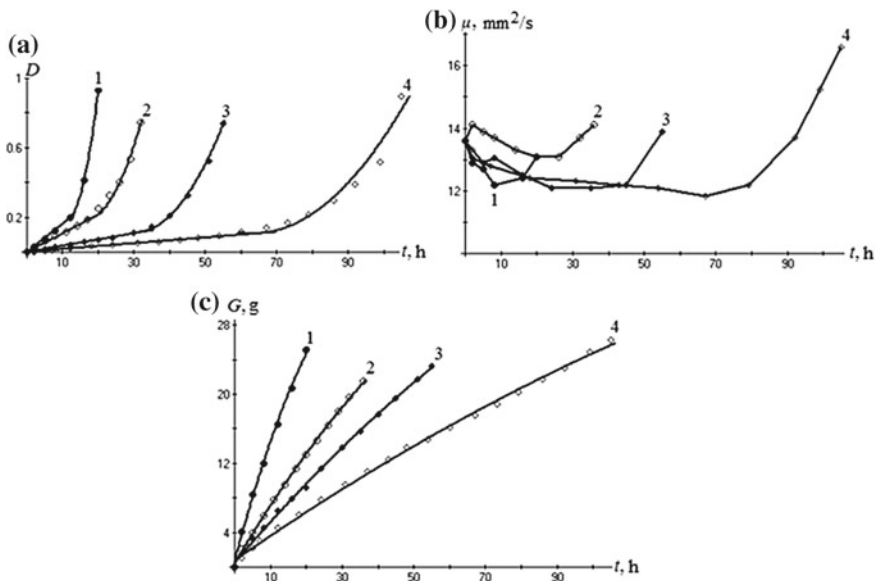


Fig. 1 Dependences of optical density (a), kinematic viscosity (b), and evaporation (c) from time and temperature of oxidation of Mobil 10 W-40 SC/CC mineral engine oil: 1—200 °C; 2—190 °C; 3—180 °C; 4—170 °C

It is established that the oxidation of mineral oil produces two types of products regardless of the oxidation temperature, which is confirmed by the presence of a branch of dependence with a high rate of change in optical density.

The dependences of the kinematic viscosity (Fig. 1b) are described by U-shaped equations having a minimum, the onset time of which increases with decreasing oxidation temperature.

The dependences of evaporation (Fig. 1c) on the time and temperature of oxidation are described by a second-order polynomial, and the regression equations have the form for temperatures:

$$200\text{ °C} \quad G = -0.018t^2 + 1.565t + 0.575, \tag{11}$$

$$190\text{ °C} \quad G = -0.0032t^2 + 0.698t + 0.421, \tag{12}$$

$$180\text{ °C} \quad G = -0.0013t^2 + 0.482t + 0.513, \tag{13}$$

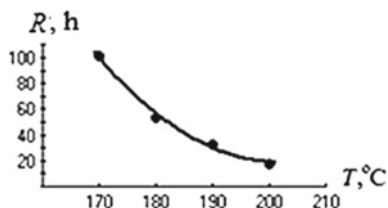
$$170\text{ °C} \quad G = -0.00049t^2 + 0.289t + 0.755. \tag{14}$$

The correlation coefficients are as follows: 0.998; 0.999; 0.999; 0.998.

The potential resource (Fig. 2) determined by the time to achieve an indicator of thermal-oxidative stability of magnitude 1 for temperatures was 200 °C—18 h;



Fig. 2 Dependence of the potential resource on the temperature test Mobil 10 W-40 SC/CC mineral engine oil



190 °C—33 h; 180 °C—54 h; 170 °C—104 h. Evaporation reached 12 grams at temperature: 200 °C in 8 h; 190 °C—18 h; 180 °C—26 h; 170 °C—42 h.

The regression dependence equation is described by a second-order polynomial.

$$R = 0.08T^2 - 32.3T + 3279 \quad (15)$$

The correlation coefficient is 0.995.

Using the dependence, it is possible to predict the potential resource of the test oil with a decrease or increase in the test temperature.

Figure 3a–c presents the dependences of the indicators of thermal-oxidative stability of P_1 , P_2 , P_3 on the time and temperature of oxidation.

All dependencies presented have two stages. The first stage is described by a linear dependence, the second by a second-order polynomial. Regression equations of time and temperature have the following form:

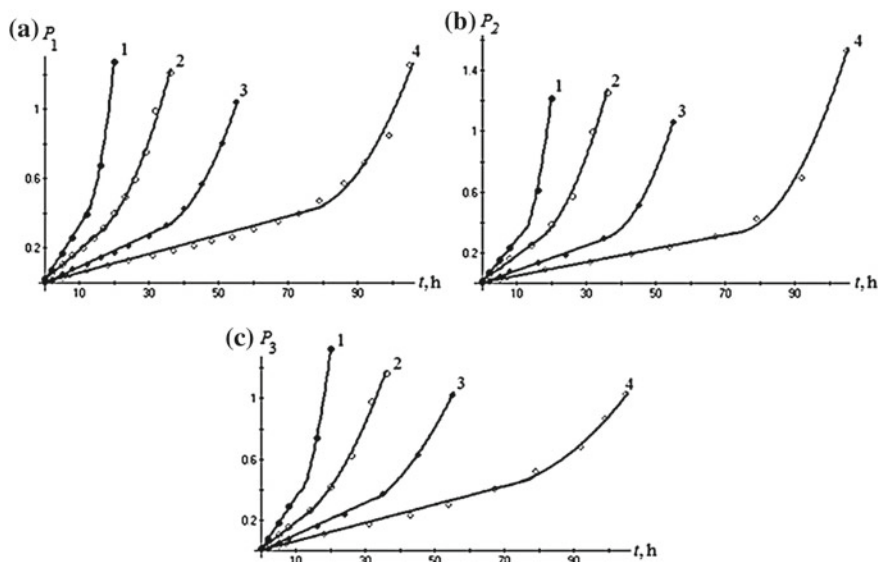


Fig. 3 Dependences of thermo-oxidative dependence of P_1 (a), P_2 (b), and P_3 (c) on the time and temperature of oxidation of mineral motor oil Mobil 10 W-40 SC/CC: 1—200 °C; 2—190 °C; 3—180 °C; 4—170 °C

For indicator P_1 (Fig. 3a):

$$\begin{aligned} 200^\circ\text{C} \quad D &= 0.315t + 0.016 \text{ (before 12 h of testing),} \\ D &= 0.0099t^2 - 0.207t + 1.458 \text{ (after 12 h of testing),} \end{aligned} \quad (16)$$

$$\begin{aligned} 190^\circ\text{C} \quad D &= 0.0172t + 0.018 \text{ (before 17 h of testing),} \\ D &= 0.0014t^2 - 0.027t + 0.368 \text{ (after 17 h of testing),} \end{aligned} \quad (17)$$

$$\begin{aligned} 180^\circ\text{C} \quad D &= 0.0093t - 0.0002 \text{ (before 35 h of testing),} \\ D &= 0.00116t^2 - 0.07t + 1.357 \text{ (after 35 h of testing),} \end{aligned} \quad (18)$$

$$\begin{aligned} 170^\circ\text{C} \quad D &= 0.0054t + 0.004 \text{ (before 73 h of testing),} \\ D &= 0.0008t^2 - 0.1175t + 4.727 \text{ (after 73 h of testing).} \end{aligned} \quad (19)$$

The correlation coefficients are: for $T = 200^\circ\text{C}$ —0.997; 1; for $T = 190^\circ\text{C}$ —0.998; 0.995; for $T = 180^\circ\text{C}$ —0.997; 0.998; for $T = 170^\circ\text{C}$ —0.994; 0.99.

For indicator P_3 (Fig. 3c):

$$\begin{aligned} 200^\circ\text{C} \quad D &= 0.0344t + 0.0085 \text{ (before 8 h of testing),} \\ D &= 0.0073t^2 - 0.119t + 0.771 \text{ (after 8 h of testing),} \end{aligned} \quad (20)$$

$$\begin{aligned} 190^\circ\text{C} \quad D &= 0.0178t + 0.01 \text{ (before 14 h of testing),} \\ D &= 0.00096t^2 - 0.006t + 0.154 \text{ (after 8 h of testing),} \end{aligned} \quad (21)$$

$$\begin{aligned} 180^\circ\text{C} \quad D &= 0.0105t - 0.0005 \text{ (before 35 h of testing),} \\ D &= 0.00065t^2 - 0.0256t + 0.476 \text{ (after 35 h of testing),} \end{aligned} \quad (22)$$

$$\begin{aligned} 170^\circ\text{C} \quad D &= 0.006t + 0.0015 \text{ (before 67 h of testing),} \\ D &= 0.00034t^2 - 0.0425t + 1.73 \text{ (after 67 h of testing).} \end{aligned} \quad (23)$$

The correlation coefficients are as follows: for $T = 200^\circ\text{C}$ —0.999; 1; for $T = 190^\circ\text{C}$ —0.999; 0.996; for $T = 180^\circ\text{C}$ —0.997; 1; for $T = 170^\circ\text{C}$ —0.995; 0.996.

The effect of kinematic viscosity on the indicators of thermal oxidative stability P_2 and P_3 in comparison with the indicator P_1 , in which the viscosity is not taken into account, is determined by the time it takes to reach their values of 1 at different temperatures. So, for the indicator P_1 , the time was: 200°C —18 h; 190°C —33 h; 180°C —55 h; 170°C —101 h. For indicator P_2 : 200°C —19 h; 190°C —32 h; 180°C —54 h; 170°C —97 h. For indicator P_3 : 200°C —18 h; 190°C —33 h; 180°C —54 h; 170°C —104 h. From the presented data it is clear that the differences between the indicators of thermal oxidative stability are insignificant, therefore, any of them can be used to compare different oils.

4 Conclusion

According to undertaken studies, it is found out that:

1. The use of a photometric thermal-oxidative stability control method allows one to obtain additional information about their resistance to temperature effects, substantiate thermal-oxidative resistance indicators taking into account changes in optical density, evaporation, kinematic viscosity, which will make it possible to compare different lubricating oils and choose more heat-resistant with a maximum resource.
2. The processes of oxidation of mineral and synthetic motor oils, expressed by optical density, differ significantly, and for synthetic oil, a period is established at which the optical density decreases. For mineral oil, the oxidation process is described by a second-order polynomial regardless of the oxidation temperature.
3. It is established that the change in kinematic viscosity during the oxidation of mineral and synthetic oils occurs according to a general U-shape, regardless of temperature; however, at temperatures of 180 and 170 °C, the viscosity of synthetic oil decreases exponentially.

References

1. Kowalski BI, Bezborodov YUN, Ananyin NN, Maltseva EG (2011) The method for determining the thermal-oxidative stability of lubricants. Pat RF 240886
2. Kowalski BI, Maltseva EG, Bezborodov YUN et al (2012) The method for determining the thermal-oxidative stability of lubricants. Pat RF 2453832
3. Kowalski BI, Yudin AV, Shram VG et al (2013) The method for determining the thermal-oxidative stability of lubricants. Pat RF 2485486
4. Kowalski BI, Yanovich VS, Petrov ON, Shram VG (2013) Optical method of monitoring the thermal-oxidative stability of gear oils. News of the Tula State University, Technical science, vol 2, pp 302–311
5. Kowalski BI, Petrov ON, Shram VG, Bezborodov YuN, Sokolnikov AN (2015) Photometric method for controlling oxidation of synthetic motor oils. News of the Tula State University, Technical science, vol 7–2, pp 169–184
6. Kowalski BI, Vereshchagin VI, Shram VG, Runda MM (2013) Processes occurring on the frictional contact with the tribological tests running motor oils. Control and Diagnostics 13:172–177
7. Kowalski BI, Vereshchagin VI, Shram VG, Runda MM (2014) Processes occurring in the lubricating oil during incubation, and their effect on the anti-wear properties. News of the Tula State University, Technical science, vol 7, pp 226–232
8. Kowalski BI, Shram VG, Petrov ON, Khimich GN (2015) Evaluation of the bearing capacity of the lubricant boundary layer at a sliding friction. Bull Irkutsk State Tech Uni 10:173–178
9. Petrov ON, Shram VG, Kowalski BI, Sokolnikov AN (2015) A method for improving the lubricity of motor oils. J Mech Eng 4:37–39
10. Kovalsky BI (2005) Methods and means of increasing the efficiency of the use of lubricants. Science, Novosibirsk, 341 p
11. Chichinadze AV, Brown ED, Buyanovsky IA (2003) Directory. Engineering Journal 9:47–51

12. Studt P (1989) Boundary lubrication: adsorption of oil additives on steel and ceramic surfaces and its influence on friction and wear. *Tribol Int* 22(2):111–119
13. Bowden FP, Tabor D (1964) *The friction and lubrication of solids*, pt II. Clarendon Press, Oxford, p 202
14. Hopkins V, Wilson R (1964) Transition temperatures in the four-ball wear tester. *Lubr Eng* 8:305 p
15. Blok H (1937) Theoretical study of temperature at surfaces of actual contact under oiliness lubricating conditions. *Proc Inst Mech Eng (Gen Disc Lubr Lubricants)* London, 22 p
16. Fein R (1964) Effect of lubricants on transition temperatures. In: *International conference on lubrication*, Washington
17. Askwith T, Cameron A, Crouch R (1964) The relation-ship of molecular chain length of lubricant and theory of scuffing. *Conf Inst Petrol Gear Lubr* 37 p
18. Ahmatov A (1963) *Molecular physics of boundary friction*. Gos ed Sci Lite-ture, Moscow, 472 p
19. Matveevsky RM (1971) *Temperature resistance boundary lubricant layers and Tver gut-lubricating coatings in friction of metals and alloys*. Izdatelstvovo Science, Moscow, 228 p
20. Maharramov AM, Akhmedova RA, Akhmedova NF (2009) *Petrochemicals and nefteper-erabotka*. Textbook for higher educational institutions. Baku University, Baku, 660 p

Complex Method for Evaluating Lubricating Properties of Technological Tools and Stresses When Drawing Products from Sheet Steel



G. I. Shulga, A. O. Kolesnichenko and I. Y. Lebedinsky

Abstract The complex method for evaluating the lubricating properties of technological lubricants and stresses when drawing axisymmetric products from sheet steel has been presented. To determine the friction coefficients in friction units during deep drawing the end-face friction, a test machine has been used simulating the contact coupling of friction units during the sheet steel drawing. Determination of the friction coefficients of friction units has been carried out when they were lubricated with technological lubricant RE-18 that contains fractal structures with copper, bronze, and zinc nanopowders adsorbed on these structures. The evaluation of the effectiveness of technological lubricants SL-2M, technical castor oil, and RE-18 during the sheet steel drawing has been performed on a modernized machine for testing the technological properties of sheet metal MTS-10H-1. The effectiveness of lubricants has been evaluated according to the proposed criteria: the force corresponding to the yield strength of the sample material; the maximum tensile force of the sample; the average diameter of the flange after drawing; the coefficient of ultimate strain; the difference between the diameters of the billet and the flange; the coefficient of relative ultimate strain; the drawing depth; the relative drawing depth. The determination of stresses in sheet materials is made using the model of sheet steel drawing in the ANSYS Workbench universal software system for finite element analysis.

Keywords Deep drawing · Stress · Sheet steel · Lubricant · Friction coefficient · Finite element

G. I. Shulga (✉) · A. O. Kolesnichenko · I. Y. Lebedinsky
Platov South-Russian State Polytechnic University (NPI),
132, Prosveshcheniya St., Novocherkassk 346428, Russia
e-mail: g.shulga41@mail.ru

© Springer Nature Switzerland AG 2020
A. A. Radionov et al. (eds.), *Proceedings of the 5th International Conference on Industrial Engineering (ICIE 2019)*, Lecture Notes in Mechanical Engineering,
https://doi.org/10.1007/978-3-030-22041-9_121

1163

1 Introduction

In modern engineering to produce axisymmetric parts from sheet steel with cold deep-drawing technological lubricants, coatings and top-composites are widely used [1–17]. The development of methods for evaluating the lubricating properties of technological lubricants, stresses arising in the process of cold drawing of steel sheets, and the optimization of these processes using the ANSYS Workbench universal software system for finite element analysis is an actual scientific and technical problem.

The scheme of cold deep drawing of an axisymmetric billet of sheet steel is shown in Fig. 1 [12]. Sheet round billet 2 is set in the matrix 4. The workpiece 2 is

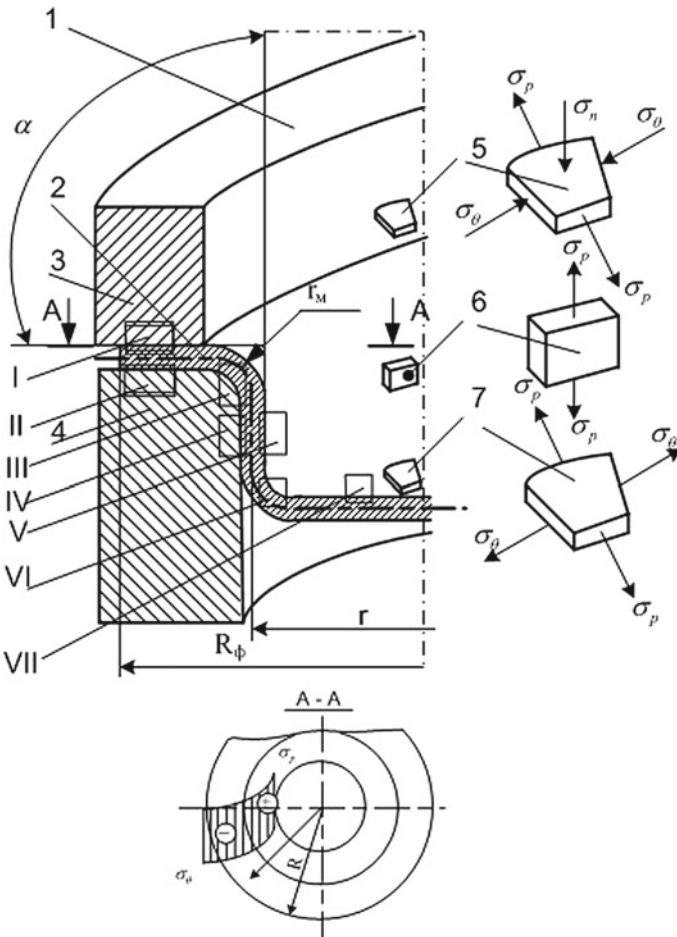


Fig. 1 Deep-drawing scheme of axisymmetric billets from the sheet steel: 1—punch; 2—the billet; 3—clamp; 4—matrix; 5, 6, 7—elements of the billet, I–VII—tribosystem

pressed against the matrix by the clamp 3; the change in the sheet billet in axisymmetric is carried out by the punch 1.

Figure 1 shows 5-, 6-, and 7-billet elements with normal stresses arising in them, acting respectively in the meridional, latitudinal, and normal to the middle surface directions on the flange, the cylindrical section, and the bottom part. During the deep drawing, shear stresses act on the billet's elements (not shown in Fig. 1) caused by the action of friction forces on the contacting surfaces. For the description of the limiting state of deep drawing of sheet steels, the hypotheses of constancy of the maximum tangential stresses and the energy condition (von Mises-Genki) [1] are acceptable.

Figure 1 also shows the tribological systems I–VII: I—clamp-billet; II—billet-matrix; III—billet-radius of the matrix; IV—cylindrical part of the matrix-billet; V—cylindrical part of the punch-billet; VI—radius of the punch-billet; VII—the bottom of the punch-billet. When carrying out deep drawing, the tribosystem I–VII is lubricated with technological lubricants. The operation of these friction units is carried out in the friction boundary mode.

A complex method for evaluating the lubricating properties of process lubricants involves determination of the friction coefficient of tri-shells on the end-face friction test machine [11], simulating contacting pairs of sheet steel-matrix, sheet steel-punch, and sheet steel-clamp. The method of comparative evaluation of the effectiveness of technological lubricants according to the proposed criteria on a modernized machine for testing the technological properties of sheet metal hydraulic MTS-10Y-1 [12–17] has been used. Determination of stresses in the billet during deep drawing of steel sheets has been carried out using the ANSYS Workbench universal software system for finite element analysis [18].

An important element in using the ANSYS Workbench universal software system for finite element analysis is the preliminary determination of the friction coefficient between the materials of a deformable product and a stamping tool with the application of technological lubricants.

On the basis of the generalized law of friction during plastic strain Isachenkova and Isachenkova [3, 4], the specific friction force during plastic strain is determined by:

$$\tau = \mu_{DT} \cdot q \cdot (1 - \gamma) + \eta \cdot \frac{dV}{dz} \cdot \gamma, \quad (1)$$

where τ —specific friction force at the boundary of a deformable material-tool, N/mm²; μ_{DT} —the coefficient of dry sliding friction; q —contact specific load, N/mm²; $\gamma = \frac{S_0}{S_C}$ —the coefficient of the lubricant continuity between the friction surfaces of the processed material and the tool; at $\gamma = 0$ —the dry friction is realized, at $1 > \gamma > 0$ —the boundary friction is realized, $\gamma = 1$ —the hydrodynamic friction is realized; S_0 —the area of lubricated contact surface, mm²; S_C —the entire area of the contact surface, mm²; η —the dynamic viscosity of the lubricant medium, P; V —the sliding speed in the contact zone, mm/c; Z —the average value of the lubricating layer, mm [3].

Based on the theory of friction of *F. Bowden*—welding, cutting, and plowing [5]—the coefficient of friction without a lubricant is determined by:

$$\mu_{DT} = \mu_A + \mu_D = K_A \cdot \frac{S_{SS}}{p^*} + \frac{A_2}{A_1} \quad (2)$$

where μ_A —the adhesive component of the friction coefficient; μ_D —the strain component of friction coefficient;

K_A —the coefficient depending on the shape of the roughness model adopted in the calculation (sphere, horizontal cylinder, cone); S_{SS} —the average shear stress, N/mm²; p^* —yield strength of the deformed material, N/mm²;

A_1 —the grooves plowing area receiving the load, mm²; A_2 —the cross-sectional area of the groove, mm² [5].

Substituting Eq. (2) into (1), we obtain the specific force friction during plastic strain:

$$\tau = \left(K_A \cdot \frac{S_{SS}}{p^*} + \frac{A_2}{A_1} \right) \cdot q \cdot (1 - \gamma) + \eta \cdot \frac{dV}{dz} \cdot \gamma \quad (3)$$

In case of boundary friction, the total friction coefficient consists of liquid, adhesive, and deformable components:

$$\mu_{BF} = \mu_L + \mu_A + \mu_D = S_L \cdot \gamma + \frac{S_{SS}}{\bar{p}} \cdot (1 - \gamma) + \frac{F_{pr}}{S_C \cdot \bar{p}} \cdot (1 - \gamma) \quad (4)$$

where μ_L —the liquid component of the friction coefficient; S_L —the shear resistance of the lubricant in, N/mm²; \bar{p} —the average pressure, N/mm²; $p^* > \bar{p} > p_{hydr}$; p_{hydr} —hydrodynamic pressure in the roughness cavities N/mm²; F_{pr} —the plowing force, *N*.

Maximum tensile stresses $\sigma_{P_{max}}$ during deep drawing determine [1]:

$$\sigma_{P_{max}} = \sigma_s \cdot \left(\ln \frac{R}{r} + \frac{\mu \cdot P_{c.f}}{\pi \cdot R \cdot S \cdot \sigma_s} + \frac{S}{2r_m + S} \right) \cdot (1 + 1,6 \cdot \mu), \quad (5)$$

where σ_s —the yield stress, N/mm²; R —the radius of the billet, mm; r —radius of the drawn cup, mm; $P_{c.f}$ —the clamping force, *N*; μ —the friction coefficient on the matrix radius; S —thickness of the billet, mm; r_m —matrix radius, mm.

The clamping force $P_{c.f}$ is determined by [1]:

$$P_{c.f} = 0,1 \cdot \left[1 - \frac{18 \cdot k \cdot S}{(k - 1) \cdot D} \right] \cdot k^2 \cdot P_{max}, \quad (6)$$

where $k = \frac{D}{d}$, D —the initial diameter of the billet, mm; d —diameter of the draw-able cup, mm; P_{\max} —the maximum drawing force, N.

The maximum drawing force P_{\max} is determined by [1]:

$$P_{\max} = \pi \cdot d \cdot S \cdot (k - 1) \cdot \sigma_{t,s}, \quad (7)$$

where $\sigma_{t,s}$ —tensile strength of sheet steel, N/mm².

The given calculation formulas do not allow to evaluate the overall picture of the stress distribution over the entire volume of the deformable product. The stress distribution pattern in a deformable billet can be received in the ANSYS Workbench universal software system for finite element analysis.

2 Evaluation Methods of Lubricant Properties of Technological Tools

To optimize the process of cold deep drawing of steel sheets using a water-soluble lubricant material RE-18 with the addition of non-ferrous metal nanopowders, the matrix friction coefficient of the stamping tool made of 40X steel and 08U sheet steel has been determined.

Tests on the end-face friction test machine of a 40% aqueous solution of the RE-18 lubricant both without and with additives of 1–2% copper, bronze, and zinc nanopowders (Fig. 2) showed a change in the value of the friction coefficient of the 40X friction pair—08U steel from 0.12 up to 0.16 at specific loads 30 ... 100 MPa. Friction coefficient 0.15 ... 0.16 has been adopted in the computer model in the ASYS Workbench system when receiving axisymmetric parts with a sheet drawing.

Criteria for evaluating the efficiency of technological lubricants on the upgraded machine for testing the technological properties of sheet steel MTS-10H-1 are given in Table 1.

Fig. 2 Dependence of the friction coefficient on the specific pressure when lubricating the friction pair of steel 40X-steel 08Y and the use of lubricants: 1–RE-18; 2–RE-18 with the addition of 1% of the bronze nanopowder; 3–RE-18 with the addition of 2% of zinc nanopowder; 4–RE-18 with the addition of 2% of copper nanopowder

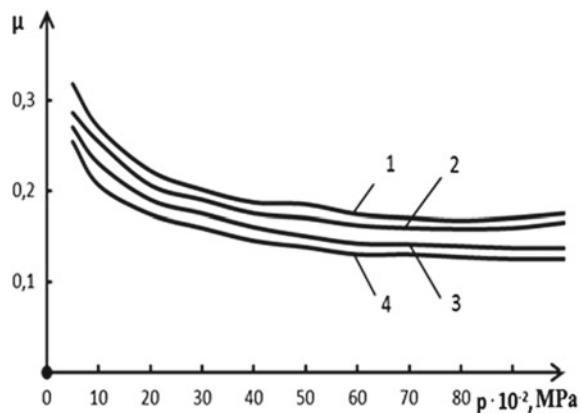


Table 1 Criteria for evaluating the effectiveness of technological lubricants in the sheet steel drawing

Criteria	Dimension	Formula, method definition
	kN	Measurement
The maximum force of rupture of the sample	kN	Measurement
The average diameter of the flange, the angle 120° after exhaust D_{af} .	mm	$D_{af} = \frac{D_{f,1} + D_{f,2} + D_{f,3}}{3}$
The ratio of the ultimate strain K_{us}	–	$K_{us} = \frac{D_b}{D_{af}}$
The difference between the blank diameter and the average diameter of flange ΔD	mm	$\Delta D = D_b - D_{af}$.
The coefficient of relative ultimate strain K_{rus}	–	$K_{rus} = \frac{D_b - D_{af}}{D_b}$
The extrusion depth of the sample, not oil edition lubricants, material H	mm	Measurement
The extrusion depth of the sample, lubricated lubricant $H_{l,1}$	mm	Measurement

Schematic sheet steel drawing with spherical and cylindrical punches samples and the cap formation stages to the rupture are shown in Fig. 2, and the diagrams of the dependences of drawing force and the cap height on time on the modernized machine for testing the technological properties of sheet steel hydraulic MTS-10H-1 are shown in Fig. 3.

Comparative tests of technological lubricants on the modernized machine MTS-10H-1 (Table 2) have shown that the 40% aqueous solution of RE-18 with the addition of the 2% copper nanopowder has better results according to the efficiency criteria compared to the lubricant SL-2 M TU 0254-044-23763315-2006 and technical castor oil GOST 6757-96.

The cap height (Fig. 4) H_y has been determined with the force corresponding to the yield strength P_y of the billet's sheet material; the limiting height H_{sl} has been determined at the maximum rupture force of the sample P_{bfmax} .

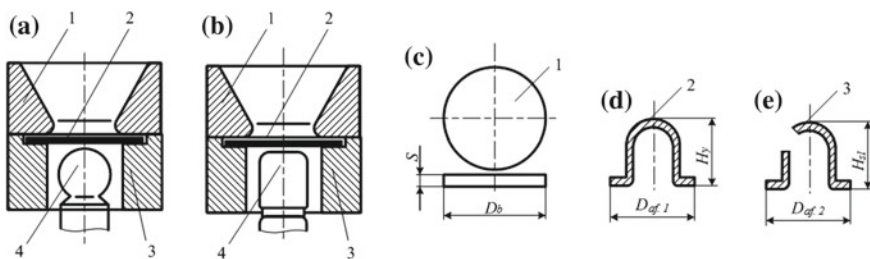


Fig. 3 Schemes of drawing of sheet material: **a** a spherical punch; **b** a cylindrical punch; **c, d, e** formation stages of the cap to the rupture from the sheet material; 1—clamp; 2—billet; 3—matrix; 4—punch

Table 2 Comparative tests of technological lubricants

Technological lubricants	P_y , kN	P_{bfmax} , kN	$H_{l,1}$, mm	ΔD , mm
40% aqueous solution RE-18 with the addition of 2% copper nanopowder	31.5	51.00	13.62	1.45
SL-2 M TU 0254-044-23763315-2006	30.8	49.28	13.21	1.5
Castor oil technical GOST 6757-96	30.7	49.12	13.25	1.4

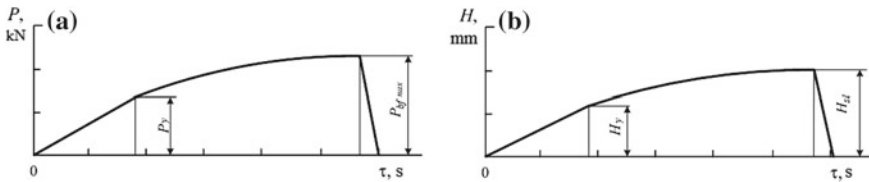


Fig. 4 a, b Diagrams of the dependences of the drawing force, the cap height on the time received (b) on the modernizes machine for testing the technological properties of sheet steel MTS-10H-1

Table 3 Physical and mechanical properties of sheet steels

Material	Density, g/cm ³	The Young's Modulus, GPa	Poisson's Ratio	Yield strength, MPa
St3kp GOST 14637-89	7.85	208	0.26	195
08kp GOST 1050-88	7.87	203	0.26	196
08Y GOST 9045-93	7.8	200	0.26	195

The simulation of the deep-drawing process in the ANSYS Workbench universal software system for finite element analysis has been performed for steel billets: St3kp, 08kp, 08Y, the physical and mechanical properties of which are given in Table 3. The influence of the 40% lubricant RE-18 with the addition of the colored nanopowders on the process efficiency according to the main criteria has been studied: maximum depth of drawing before the rupture and maximum stresses arising in the sample throughout the entire test process.

The problem of determining the stresses in the deep-drawing process in the ANSYS Workbench software package has been solved using the Static Structural Analysis Systems module [18]. The physical and mechanical properties of materials have been set by the parameters: density, Young's modulus of elasticity, Poisson's ratio, and yield strength (Table 3).

The friction units in the model have been set by the frictional coupling type with the specified friction coefficients obtained experimentally and equal to 0.28–0.32,



in the case without the use of a lubricant, and 0.15–0.16, in the case of the use of a lubricant RE-18 with additives of non-ferrous metal nanopowders.

It follows from Fig. 5 that the stresses during the billet strain without a lubricant and using the 40% aqueous solution of RE-18 differ significantly. The thickness of the bottom of the strained billet is also changed. It has been noted that during deep drawing the thickness of the bottom of the tested steels at the dry friction has decreased from 3 to 2.2 mm. When lubricated with the 40% aqueous solution, the thickness of the bottom of the tested steels has decreased from 3 to 1.4 mm. When using the technological lubricant RE-18, the force corresponding to the yield strength of the sheet material increases compared with experiments without the use of a lubricant.

The diagrams of the distribution of total stresses by von Mises (equivalent von Mises stress) in the 08U steel sheet billet at the rupture point without a lubricant (a) and using the 40% aqueous solution of the lubricant RE-18 with the addition of 2% copper nanopowder (b) are shown in Figs. 6, 7. The use of the ANSYS Workbench universal software system for finite element analysis allows to determine the stresses at any stage of the process of deep drawing of sheet steel.

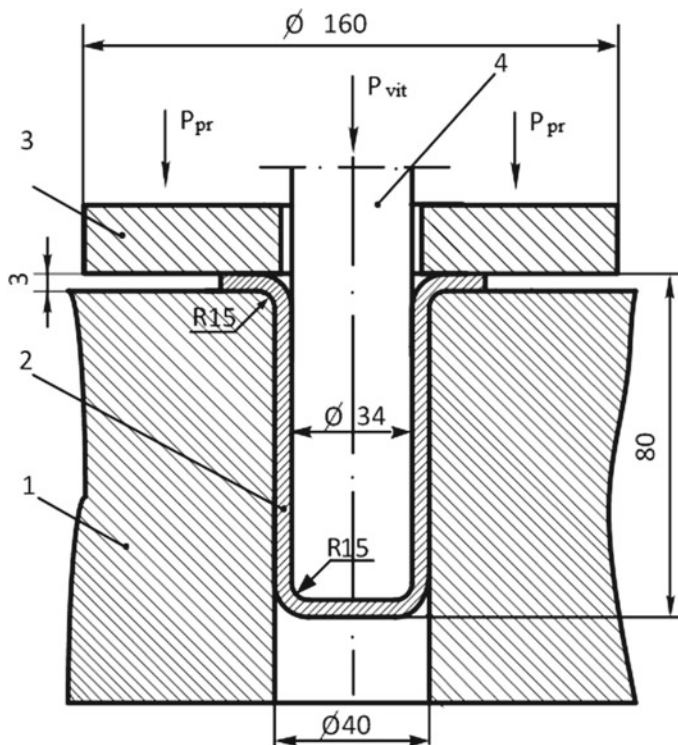


Fig. 5 Geometrical parameters of the stamping tool model at cold deep drawing of sheet steels with a clamp: 1—matrix; 2—preparation; 3—clamp; 4—punch

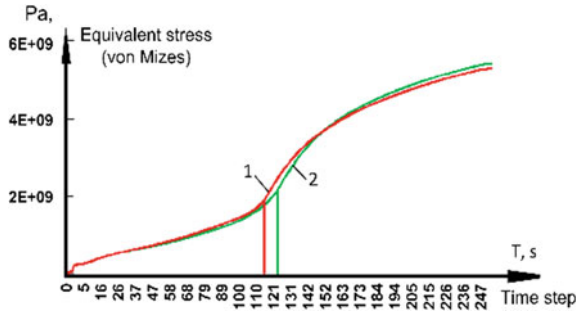


Fig. 6 Time increase in total stresses in the samples according to Mises (equivalent von Mises stress): 1—without using; 2—using the 40% aqueous solution of lubricant RE-18 with deep drawing of sheet steel 08U. *Note* In Fig. 6, the designation 2E+09 corresponds to 2.109 Pa; in Fig. 6, the designation 1 9747e9 corresponds to 19,747.109 Pa

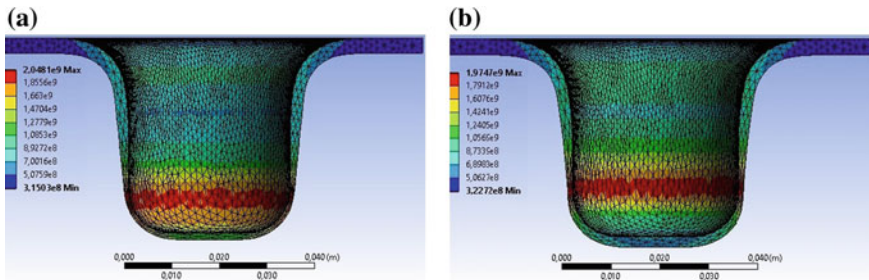


Fig. 7 Diagrams of the total stress distribution according to Mises (equivalent von Mises stress) in the sheet steel 08Y billet at the point of rupture: **a** without a lubricant, **b** using the 40% aqueous solution of lubricant RE-18 with the addition of 2% copper nanopowder

3 Conclusion

A complex method for the evaluation of lubricating properties of technological tools and stresses when drawing axisymmetric products from sheet steel allows:

- to determine friction coefficients on the end-face friction test machine, simulating the contact coupling of friction units of deep-drawing process products from sheet steel when lubricated with the technological lubricants;
- to evaluate the effectiveness of lubricants according to the proposed criteria on the machine for testing the technological properties of sheet metal MTS-10H-1;
- to determine stresses at any stage of the deep-drawing process of sheet steel using the ANSYS Workbench universal software system of finite element analysis;

- to increase the efficiency of the deep-drawing process by the optimization of the curvature radius on the matrix and the punch, the gap between the punch and the matrix, changing the clamping forces, the billet thickness, the use of the lubricant RE-18 due to the formation of complex anti-friction films of increased bearing capacity when coupling with friction units.

References

1. Winkov UP, Johnson W, Kolmagorov VL et al (1983) The theory of plastic deformation of metals. In: Winkov UP, Ovchinnikov AG (eds). Mashinostroenie, Moscow, 598 p
2. Popov EA (1977) Fundamentals of sheet metal stamping theory. Mashinostroenie, Moscow, p 278
3. Isachenkov VE, Isachenkov EI (1972) Generalized theory of friction in the processing of metals by pressure. Forging and Stamping Prod 12:18–21
4. Isachenkov EI (1978) Contact friction and lubrication during the metal forming. Mashinostroenie, Moscow, p 208
5. Bowden FP, Tabor D (1964) Part 2. The friction and lubrication of solids. Oxford at the Clarendon Press
6. Moore DF (1975) Principles and applications of tribology. Pergamon Press, Oxford
7. Moore DF (1972) The friction and lubrication of elastomers. Pergamon Press, Oxford
8. Shulga GI (1994) Continuous tribotechnology for cold sheet metal stamping of stainless steel products. The North Caucasus region. Technical science 3-4:120–134
9. Shulga GI (1996) Continuous tribotechnologies for obtaining thin-walled shells in flexible production systems. In: Proceedings of higher educational institutions. The North Caucasus region. Technical Sciences 2/1:62–73
10. Shulga GI (2001) Water-soluble technological toponomastica for thin-walled shells of composite materials “Science and technology”. In: Proceeding of the XXI Russian school on science and technology, 26–28 June 2001, Miass, Moscow, pp 147–154
11. Shulga GI, Kolesnichenko AO (2002) Tribological testing of aqueous solutions of process lubricants for use in drawing steel sheets. “The New technology of motion control of technical objects”. In: Collection of papers on materials of the 5th international scientific-technical conference December 18–20, Novocherkassk-Rostov-n/D. North Caucasus center of higher education 3/2:92–95
12. Shulga GI (2004) Functional water-soluble lubricant technology for materials processing. Izvestiya vuzov, The North Caucasus region, p 212
13. Shulga GI, Kolesnichenko AO, Skrynnikov EV, Shulga TG (2011) Functional and technological lubricants, structured nanoparticle non-ferrous metals, to more efficient processing of vehicle parts. Vestnik of Don State Technical University 11(10):1867–1873
14. Shulga GI (2014) Improving the surface quality by the application of functional coatings containing fractal nanoclusters. Qual Life Number 1:56–61
15. Shulga GI, Shulga TG (2016) Toponomastica for multijunction drawing of body parts of transport systems. “Mechanics and tribology of transport systems”: collection of reports. Scientific Conference Rostov n/D, 8–10 November 2016, 2:146–150
16. Shulga GI, Kolesnichenko AO, Sirotin PV, Lebedyns'ky IYu, Skrynnikov EV, Vasilyev MA (2018) Optimization of technology for products of deep drawing sheet steels with the use of lubricants in universal software system ANSYS workbench. 10.1051/mateconf/201822601028

17. Shulga GI, Kolesnichenko AO, Sirotn PV, Lebedinsky IY, Skrinnikov EV, Vasiliev MA (2018) Technology of water-Soluble lubricants containing a fractal structure, with the addition of nanoclusters of non-ferrous metals in the processes of drawing sheet steels. In: Tribology mechanical engineering: proceedings of the XII International scientific-technical conference dedicated to the 80th anniversary of IMASH RAS.-Moscow-Izhevsk : Institute of computer science, pp 584–588
18. Bruyaka VA, Fokin VG, Soldusova EA, Glazunova NA, Adeyanov IE (2010) Engineering analysis in ANSYS Workbench: textbook, Part 1, Samara State Tehnical University, Samara, 271 p

Monitoring Technical Status of Engine Bearings by Pressure Parameters in Central Oil Line



A. V. Gritsenko, V. D. Shepelev and A. G. Karpenko

Abstract Design improvement of motor-and-tractor internal combustion engines is aimed at differentiating the operating parameters of the lubrication system depending on the change in the operating modes and conditions, which increase in the precision of parts manufacturing, reduction of difference tolerances of operating process parameters and use of microprocessor control systems. Up to 20% of engine failures are failures connected with the wear of crankshaft friction bearings. Their known diagnostic methods have significant drawbacks: the need to take the engine out of operation, large time expenditures for diagnostics, impossibility of in-place determining the technical status of some elements. Today, the automotive industry is significantly ahead of the production of diagnostic tools. There appear concepts and models of machines, for which it is not enough to use low-sensitive pressure sensors. For such models, it is recommended to control pressure pulsations in the ICE oil line to determine the technical status and lifetime of internal combustion engines. When monitoring the technical status of main bearings, the diagnostics is performed at the crankshaft speed $n = 880 \text{ , min}^{-1}$, when using the complex for diagnosing crank-and-rod mechanisms and mechanisms of the lubrication system. The diagnostic parameter is the difference of minimum pressure amplitudes when the bearing operates through a cycle, with and without load.

Keywords Internal combustion engine · Bearings · Crank-and-rod mechanism · Clearances · Pressure parameters

A. V. Gritsenko · V. D. Shepelev (✉)
South Ural State University (NRU), 76, Lenin Avenue, Chelyabinsk 454080, Russia
e-mail: shepelevvd@susu.ru

A. G. Karpenko
South Ural State Humanitarian-Pedagogical University (CSPU), 69 Lenin Avenue,
Chelyabinsk 454080, Russia

1 Introduction

Statistical data of advanced lines of research show that the number of failures of bearings of the crank-and-rod mechanism (CRM) is from 5 to 25% of all engine failures [1–3]. The main and primary causes of failures are as follows:

- Violation of loading modes [4, 5]
- Complex operating conditions [6, 7]
- Violation of the maintenance intervals of nodes and elements of the lubrication system and the CRM [8–10]
- Violation of maintenance algorithms, procedure and conditions [11]
- Misuse of inappropriate brand and low-quality oils and filters, etc. [12, 13].

Consistent compliance with all these activities is indispensable. The situation can be significantly changed by a continuous monitoring of the complex and element-wise (selectively) technical status of bearings of the CRM and the lubrication system [4, 14].

The scientific literature pays considerable attention to theoretical and experimental studies of the relationship between the size of clearances in rod bearings of the crank-and-rod mechanism and the pressure parameters in a wedge-shaped clearance of the rod journal [5, 9, 15]. At the same time, the relationship between the size of clearances in rod bearings of the crank-and-rod mechanism and the pressure parameters in the central oil line of the internal combustion engine is studied insufficiently [13, 14]. In our work, we conducted theoretical studies to determine the relationship between the size of clearances in rod bearings of the crank-and-rod mechanism and the pressure parameters in the central oil line of the internal combustion engine, which are presented in this paper.

The considered analysis of tools and methods of diagnostics and continuous monitoring shows their low functional capacity and reliability [16–18]. The impossibility of the built-in (built-in control tool—a diagnostic tool in the design of a motor-and-tractor vehicle, which is a standard instrument for diagnosing engine systems) monitoring when using most of these methods and tools makes it impossible to apply them [4, 19]. A promising direction in the field of engine diagnostics is the use of test methods for diagnosing minor components in a dynamic mode [4, 10, 20].

2 Theoretical Research

The task of the theoretical studies was to determine the boundaries of pressure pulsations at their corresponding speeds and loading modes. To this end, we analyzed the data from our earlier studies [4, 14]. Let us analyze the change in the increment value of the minimum pressure amplitude ΔP , MPa, for different clearances in the main and rod journal at the corresponding value of the crankshaft

speed. For this purpose, we will make Table 1 of increments of the minimum pressure amplitude ΔP , MPa, for $Z_R = 0.05$ mm and $Z_M = 0.09$ mm, $Z_M = 0.12$ mm, $Z_M = 0.15$ mm.

Let us also make Table 2 of increments of the minimum pressure amplitude ΔP , MPa, for $Z_R = 0.10$ mm and $Z_M = 0.09$ mm, $Z_M = 0.12$ mm, $Z_M = 0.15$ mm

According to Tables 1 and 2, it is clear that the crankshaft speeds, at which there is an increment in the minimum pressure amplitude, for clearances in the rod journal $Z_R = 0.05$ and $Z_R = 0.10$ are almost the same for all the combinations of clearances in the main and rod journals. Based on this assumption, let us build the dependence of the diagnostic speed mode n , min^{-1} , on the clearance size in the main bearing Z_M , mm (Fig. 1):

The dependence in Fig. 1 is described by the straight line equation:

$$n = -1.667 \times 10^3 \cdot Z_M + 1.85 \times 10^3 \tag{1}$$

Thus, it has been established that the speed mode n , min^{-1} , for determining the technical status of the rod bearing is determined by the “Eq. 1.” Since “Eq. 1” is linear for the clearances in the main journal $Z_M = 0.09$ mm, $Z_M = 0.12$ mm,

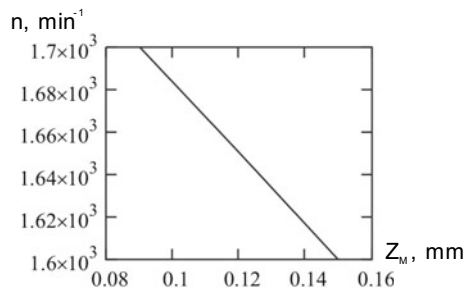
Table 1 Increments of the minimum pressure amplitude ΔP , MPa, for $Z_R = 0.05$ mm and $Z_M = 0.09$ mm, $Z_M = 0.12$ mm, $Z_M = 0.15$ mm

Z_M , mm	$Z_M = 0.09$	$Z_M = 0.12$	$Z_M = 0.15$
Z_R , mm	$Z_R = 0.05$	$Z_R = 0.05$	$Z_R = 0.05$
ΔP , MPa	0.009	0.0171	0.0405
n , min^{-1}	1700	1660	1600

Table 2 Increments of the minimum pressure amplitude ΔP , MPa, for $Z_R = 0.10$ mm and $Z_M = 0.09$ mm, $Z_M = 0.12$ mm, $Z_M = 0.15$ mm

Z_M , mm	$Z_M = 0.09$	$Z_M = 0.12$	$Z_M = 0.15$
Z_R , mm	$Z_R = 0.10$	$Z_R = 0.10$	$Z_R = 0.10$
ΔP , MPa	0.0152	0.0340	0.0627
n , min^{-1}	1680	1640	1580

Fig. 1 Dependence of the diagnostic speed mode n , min^{-1} , on the clearance size Z_M , mm, in the main bearing



$Z_M = 0.15$ mm, it can be assumed that this expression is also valid for the clearances in the main journal of less than $Z_M = 0.09$ mm.

However, the increment values of the minimum pressure amplitude ΔP , MPa, for $Z_R = 0.05$ mm and $Z_R = 0.10$ mm at the same clearance in the main journal are different. According to Table 1, we determine the dependence of increments of the minimum pressure amplitude $\Delta P_{0.05}$, MPa, for $Z_R = 0.05$ mm, which is approximated by a polynomial:

$$\Delta P_{0.05} = 85 \cdot Z_M^2 - 15.15 \cdot Z_M + 0.765 \quad (2)$$

where Z_M is the clearance in the main journal, mm.

According to Table 2, we will build the dependence of increments of the minimum pressure amplitude $\Delta P_{0.10}$, MPa, for $Z_R = 0.10$ mm, which is approximated by a polynomial:

$$\Delta P_{0.10} = 55 \cdot Z_M^2 - 5.283 \cdot Z_M + 0.182 \quad (3)$$

Thus, we determined the influence of the technical status of the rod journal on the increment of the minimum pressure amplitude, which can be calculated using “Eqs. 2–3.”

3 Research Methodology

We propose a device for determining the technical status and lifetime of internal combustion engines [8, 19], which consists of a strain gauge (piezoelectric) pressure sensor.

The object of the tests was a crank-and-rod mechanism (CRM) and a lubrication system of the ZMZ-4062 engine with a drive motor and gearbox.

By comparing the reference oscillograms with the oscillograms with worn-out main and rod bearings, we chose standard pressure oscillogram points that characterize the wear of the CRM bearings.

4 Results of Experimental Studies

The following diagnostic parameters were outlined in the pressure signal: A_{\max} —maximum pressure amplitude, MPa; A_{av} —average pressure value, MPa; A_1 , A_2 , A_3 —minimum pressure amplitudes at the moment of the combustion stroke, MPa; $A_1 - A_2$, $A_1 - A_3$ —difference between the minimum pressure amplitudes of two adjacent cycles, MPa. An analysis of these parameters allowed us to establish a sensitive diagnostic parameter characterizing the technical status of the main bearing: the difference of the minimum pressure amplitudes $A_1 - A_2$, $A_1 - A_3$ of

two adjacent cycles at the moment of the combustion stroke when the diagnosed bearings operate through a cycle, with and without load at a fully opened throttle blade (the correlation ratio was 0.99), as well as the engine operating mode corresponding to 880 min^{-1} of the crankshaft speed [14].

We established an experimental dependence reflecting the relationship between the wear degree of the main bearing and the difference in the minimum pressure amplitudes $A_2 - A_1$, which is approximated by a third-order equation:

$$Z_M = 170.86 \cdot (A_2 - A_1)^3 - 68.87 \cdot (A_2 - A_1)^2 + 8.93 \cdot (A_2 - A_1) + 0.248 \quad (4)$$

where $A_2 - A_1$ is the difference in the minimum pressure amplitudes of two adjacent cycles when the first cylinder is on (2, 3, 4 are disconnected), through the cycle, one cycle is working, the other one is non-working; Z_M is a clearance in the main journal, mm.

Thus, we can determine the actual wear of any main bearing by measuring the difference in the pressure amplitudes of two adjacent cycles when the diagnosed cylinder is on (the other three are disconnected), through a cycle, with and without load, using "Eq. 4."

It has been established that the limiting value of the difference between the minimum pressure amplitudes under load and without load for rejecting the main bearing at the crankshaft speed $n = 880, \text{ min}^{-1}$, is 0.02 MPa.

To establish the relationship of the technical status of the main and rod bearing using the selected diagnostic modes with a minimum pressure amplitude, we planned and conducted a multifactor experiment [19], and the results of which are presented in Fig. 2.

When analyzing the experimental data, it has been established that the cumulative influence of the technical status of the main and rod journal is characterized by a violation of the linearity of the minimum pressure amplitude growth. Moreover, with an increase in clearances in the main and rod journal, considering their mutual influence, the range of the nonlinearity of the minimum pressure amplitude increases. To determine the general regression equation linking the

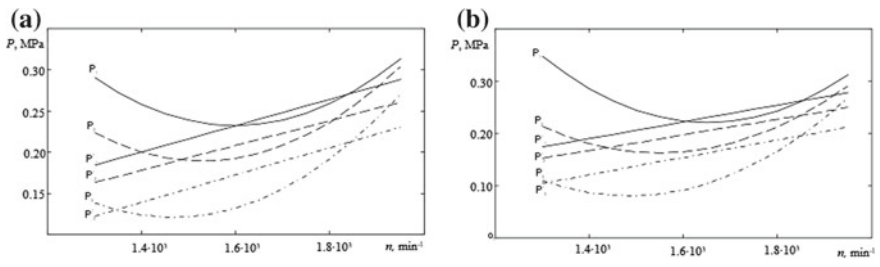


Fig. 2 Dependencies of the minimum pressure amplitude P , MPa, on the crankshaft speed $n, \text{ min}^{-1}$: **a** $Z_R = 0.05 \text{ mm}$ and $Z_M = 0.09 \text{ mm}, Z_M = 0.12 \text{ mm}, Z_M = 0.15 \text{ mm}$; **b** $Z_R = 0.10 \text{ mm}$ and $Z_M = 0.09 \text{ mm}, Z_M = 0.12 \text{ mm}, Z_M = 0.15 \text{ mm}$



technical status of the main and rod journal, as well as the crankshaft speed, we decomposed the experimental data into two components:

- linear component of the change in the minimum pressure amplitude characterizing the beginning and the end of the dependence
- nonlinear component of the change in the minimum pressure amplitude characterizing the nonlinearity range.

Figure 2 shows the results of the dependence decomposition into two components—linear and nonlinear.

After analyzing the experimental data in Fig. 2a and b, we obtained partial regression equations for the clearance in the main journal $Z_R = 0.09$, mm, linking the minimum pressure amplitude P_1 , P_1^1 in the central oil line with the clearance in the rod journal Z_R , mm and the crankshaft speed n , min^{-1} .

$$P_1 = (7.438 \times 10^{-5} \cdot Z_R + 2.852 \times 10^{-6}) \cdot n^2 - (0.26 \cdot Z_R + 8 \times 10^{-3}) \cdot n + (223.8 \cdot Z_R + 7.91) \quad (5)$$

$$P_1^1 = (1.6 \times 10^{-3}) \cdot n - (2 \cdot Z_R + 0.14) \quad (6)$$

For the clearance in the main journal $Z_M = 0.12$ mm,

$$P_2 = (3.048 \times 10^{-5} \cdot Z_R + 5.012 \times 10^{-6}) \cdot n^2 - (0.1 \cdot Z_R + 0.015) \cdot n + (76.44 \cdot Z_R + 13.368) \quad (7)$$

$$P_2^1 = (1.5 \times 10^{-3}) \cdot n - (2.2 \cdot Z_R + 0.21) \quad (8)$$

For the clearance in the main journal $Z_M = 0.15$ mm,

$$P_3 = (4.514 \times 10^{-5} \cdot Z_R + 4.201 \times 10^{-6}) \cdot n^2 - (0.139 \cdot Z_R + 0.012) \cdot n + (98.8 \cdot Z_R + 10.165) \quad (9)$$

$$P_3^1 = (1.66 \times 10^{-3}) \cdot n - (3.6 \cdot Z_R + 0.754) \quad (10)$$

When analyzing the dependencies in Fig. 2, it has been established that the increment of the minimum pressure amplitude ΔP , MPa, changes. Moreover, with an increase in the clearance in the rod journal Z_R , mm from 0.05 to 0.10, the increment of the minimum pressure amplitude ΔP , MPa, increases.

As a result of recalculating the coefficients of “Eqs. 5–10,” we obtained a general regression equation, which links the increment of the minimum pressure amplitude with the clearance size in the main and rod journal:

$$\Delta P = (-600 \cdot Z_R + 115) \cdot Z_M^2 - (-197 \cdot Z_R + 25.017) \cdot Z_M + (-11.66 \cdot Z_R + 1.348) \quad (11)$$

where ΔP is the increment of the minimum pressure amplitude, MPa; Z_M is the clearance in the main journal, mm; Z_R is the clearance in the rod journal, mm.

However, in order to apply the results of the multifactor experiment, we obtained a general regression equation that links the clearance size in the rod journal with the increment of the minimum pressure amplitude ΔP , MPa, and the clearance in the main journal Z_M , mm:

$$Z_R = (243.889 \cdot Z_M^2 - 68.217 \cdot Z_M + 4.97) \cdot \Delta P - (34.898 \cdot Z_M^2 - 8.076 \cdot Z_R + 0.467) \quad (12)$$

where ΔP is the increment of the minimum pressure amplitude, MPa; Z_M is the clearance in the main journal, mm; Z_R is the clearance in the rod journal, mm.

5 Results

Thus, the experimental studies resulted in the dependence “Eq. 4” to determine the wear degree of the main journal Z_M , mm by the difference of the minimum pressure amplitudes $A_2 - A_1$, MPa, of two adjacent cycles when the diagnosed cylinder operates through a cycle, with and without load at the crankshaft speed of the ZMZ-4062 engine $n = 800 \text{ min}^{-1}$. It has been established that the limiting value of the difference between the minimum pressure amplitudes under load and without load for rejecting the main bearing is 0.02 MPa. We obtained “Eq. 1” to determine the speed mode n , min^{-1} , when diagnosing the technical status of the rod bearing. We obtained regression “Eq. 11,” which links the increment of the minimum pressure amplitude with the clearance size in the rod and main journals. We obtained regression “Eq. 12” that allows us to determine the clearance in the rod journal at a known clearance in the main journal and the measured value of the increment of the minimum pressure amplitude. The use of the device and the method allows us to increase the reliability of the engine’s technical status evaluation and to ensure the adaptability of the crankshaft speed regulation.

Acknowledgements The work was supported by Act 211 Government of the Russian Federation, contract № 02.A03.21.0011.

References

1. Hajari SC (1996) Diagnosis and repair of excessively emitting vehicles. *J Air Waste Manag Assoc* 46(10):940–952. <https://doi.org/10.1080/10473289.1996.104675292>
2. Chuepeng S, Saipom S (2018) Lubricant thermo-viscosity effects on turbocharger performance at low engine load. *Appl Therm Eng* 139:334–340

3. Nelson DA (2018) Development of a non-contacting mechanical seal for high performance turbocharger applications. In: ASME Turbo Expo: Turbomachinery Technical Conference and Exposition, Oslo, Norway, June 2018, vol 07B. <https://doi.org/10.1115/gt2018-77126>
4. Gritsenko AV, Zadorozhnaya EA, Shepelev VD (2018) Diagnostics of friction bearings by oil pressure parameters during cycle-by-cycle loading. *Tribol Ind* 40(2):300–310. <https://doi.org/10.24874/ti.2018.40.02.13>
5. Chen Y, Sun Y, Yang D (2017) Investigations on the dynamic characteristics of a planar slider-crank mechanism for a high-speed press system that considers joint clearance. *J Mech Sci Technol* 31(1):75–85. <https://doi.org/10.1007/s12206-016-1209-z>
6. Harnoy A (2003) *Bearing design in machinery: engineering tribology and lubrication*. Marcel Dekker, New York
7. Mishra PC (2013) Modeling for friction of four stroke four cylinder in-line petrol engine. *Tribol Ind* 35(3):237–245
8. Gritsenko AV, Kukov SS, Tsyganov KA, Gorbunov AV (2013) A method for determining the technical state of an internal combustion engine and an electronic device for its implementation. Russia Patent 2474715 RUG01 M 15/00, 2011141374
9. Nikolakopoulos P, Zavos A (2015) Slew bearings damage detection using hilbert huang transformation and acoustic methods. *Tribol Ind* 37(2):170–175
10. Sangha MS, Gomm JB, Dingli Yu (2008) Neural network fault classification of transient data in an automotive engine air path. *Int J Modell Identif Contr* 3(2):148–155. <https://doi.org/10.1504/ijmic.2008.019352>
11. Ünlü BS, Atik E (2007) Determination of friction coefficient in journal bearings. *Mater Des* 28(3):973–977. <https://doi.org/10.1016/j.matdes.2005.09.02>
12. Phung VT, Pacas M (2017) Sensorless harmonic speed control and detection of bearing faults in repetitive mechanical systems. In: 2017 IEEE 3rd International Future Energy Electronics Conference and ECCE Asia, IFEEC—ECCE Asia 2017, pp 1646–1651. <https://doi.org/10.1109/ifeec.2017.7992294>
13. Jing G, Zhang X, Wang B et al (2017) Multiple-axle fatigue analysis of a star engine master conrod. Neiranji Gongcheng. *Chin Intern Combust Engine Eng* 38(1):102–108. <https://doi.org/10.13949/j.cnki.nrjgc.2017.01.017>
14. Plaksin M, Gritsenko AV, Lukomsky KI et al (2014) Development of methods of test diagnostics of working capacity of systems of fuel and lubrication of internal combustion engines. *Agrarian Bull Urals* 7(125):53–58
15. Mănescu B, Ionuț D, Nicolae-Doru et al (2017) Aspects in the synthesis of a variable compression ratio mechanism. *IOP Conf Ser: Mater Sci Eng* 252(1). <https://doi.org/10.1088/1757-899x/252/1/012075>
16. Zadorozhnaya EA, Cherneyko SV, Kurochkin MI et al (2015) A study the axial and radial rotor stability of the turbo machinery with allowance the geometry of the surface and properties of the lubricating fluid. *Tribol Ind* 37(4):445–463
17. Levanov IG, Zadorozhnaya EA, Dudnikov AL (2015) Methods of assessing the resource of the crankshaft bearing of internal combustion engine based on the calculation of hydro-mechanical characteristics. *Tribol Ind* 37(3):360–365
18. Nikolic N, Torovic T, Antonic Z (2012) A procedure for constructing a theoretical wear diagram of IC engine crankshaft main bearings. *Mech Mach Theory* 58:120–136. <https://doi.org/10.1016/j.mechmachtheory.2012.07.009>
19. Gritsenko AV, Kukov SS (2010) Method of in-place diagnostics of the degree of wear of bearings of an internal combustion engine. Russia Patent 2399898 RU G 01 M 15/09, 2009123720
20. Kimmich F, Schwarte A, Isermann R (2005) Fault detection for modern diesel engines using signal- and process model-based methods. *Control Eng Pract* 13(2):189–203. <https://doi.org/10.1016/j.conengprac.2004.03.002>

Evaluation of Thermal Condition of Turbocharger Rotor Bearing



E. Zadorozhnaya, V. Hudyakov and I. Dolgushin

Abstract The thermal state of the sliding bearings has a great influence in calculating the dynamics of the flexible rotor of the turbo-compressor. Experimental studies have shown that the temperature difference between the turbine and compressor bearings can reach twenty degrees. In addition, the temperature is unevenly distributed across the lubricating layer. It increases in the area of elevated pressure. The task of assessing the thermal state of the rotor plain bearings is relevant. The effect of eccentricity on the pressure distribution in a thin lubricating layer of a non-Newtonian fluid was considered. The distribution of temperatures and pressures in the lubricant layer was constructed taking into account the rheological properties of the lubricant. The boundary conditions that were used to solve the problem were taken from the experiment. The results will be used to solve the problem of the dynamics of the turbocharger rotor.

Keywords Rotor · Bearing · Turbocharger · Thermal state · Non-Newtonian fluid

1 Introduction

Internal combustion engines (ICE) are characterized by high efficient and environmental performance. To achieve these indicators, gas turbine charging is used as one of the most promising and widespread methods of boosting. At the current time, boosting for ICE is used in ship and locomotive power facility, engines of cars and trucks, special road or agricultural facility, military equipment and power ones. The percentage of supercharged engines in the production volume reaches 50... 100% for a number of companies [1]. As is known, the trouble-free operation of machines and mechanisms depends on the design of friction units. One of the most important elements determining the operation of the turbocharger is hydrodynamic sliding bearings, which accept radial loads, and thrust bearings, which accept axial

E. Zadorozhnaya (✉) · V. Hudyakov · I. Dolgushin
South Ural State University, 76, Lenin Prospekt, 454080 Chelyabinsk, Russia
e-mail: zadorozhnaiea@susu.ru

loads. In practice, tribo-conjugation with floating rotating rings or floating non-rotating mono-rings are widespread [2–4]. The relevance of studying the bearings performance is confirmed by the statistics of the main causes of bearings failure [5, 6]. The greatest number of breakdowns in turbochargers occurs due to abrasive, adhesive and fatigue wear of bearings.

Another most likely cause of the premature failure of the turbocharger is an increase in temperature. In this case, the lubricant loses its effectiveness, the work of the seals is broken, and the oil consumption increases. Also, the loads acting on the tribo-conjugations in the axial and radial directions increase when the turbocharger is running at higher speeds. This, in turn, leads to an increased thermal loading of the friction units. The rotor position in the bearing space depends on the temperature difference between the turbine wheel and the compressor one. Overheating of the tribo-conjugations leads to an increase in the amplitude of the rotor parts oscillations. As a result of this process, the wheel's blades touch the turbocharger casing, which leads to their destruction and damage to the rotor shaft [2, 3].

Consequently, the resource of the turbocharger is determined by the durability of the bearings, which should ensure operability under conditions of elevated temperatures and an extended range of rotor speeds.

The use of modern high-grade lubricants is the key factor of reducing friction losses in conjugations and improving the power efficiency of an engine as a whole. The majority of hydrodynamic friction units of engines are heavy-loaded; they are loaded by forces whose magnitude and direction vary in time.

A problem of calculating these conjugations is based on the classical hydrodynamic lubrication theory, which describes the behavior of a Newtonian fluid in a thin lubricating film that separates the tribo-unit surfaces. However, state-of-the-art lubricant production methods, as well as the permanent improvement and development of new antiwear and other additives, lead to the impossibility of describing the behavior of lubricating fluids based on the foundations of the lubrication theory. One of the assumptions of this theory as a basis for calculating heavy-loaded conjugations is that the behavior of a lubricant obeys the Newton–Stokes law, which implies the linear dependence of tangential stresses on the shear rate [7]. In this dependence, the dynamic (Newtonian) viscosity μ serves as the coefficient of proportionality; this viscosity depends on the temperature and pressure. In this case, the fluid is called Newtonian or perfectly viscous (purely viscous).

The majority of up-to-date high-grade lubricating oils whose behavior does not obey Newton–Stokes law are non-Newtonian fluids. In the general case, by non-Newtonian behavior is meant any anomalies observed during the flow of fluids. In this case, there is a need to develop calculation methods based on new, non-Newtonian models of the rheological behavior of the lubricant. There are various models of viscoelastic fluids [1], among which the Maxwell model is the best known. In this model, fluids are called Maxwell fluids (viscoelastic Maxwell fluids).

Along with this, when studying the efficiency of conjugations, thermal processes that occur in heavy-loaded fluid-lubricated bearings are of great importance. They are usually considered based on a solution of the generalized equation of energy

(heat transfer) for a thin film of a viscous incompressible fluid, which separates two arbitrarily moving surfaces. This equation allows for both convective heat transfer by the lubricant and heat transfer due to thermal conductivity [8–10].

The three following approaches to the integration of the generalized equation of energy can be used, depending on applied assumptions on the temperature distribution in a thin lubricating film: thermo-hydrodynamic (non-isothermal), adiabatic and isothermal.

In the adiabatic approach, it is assumed that no temperature changes across the lubricating film occur and that the journal and the bearing are perfect heat insulators. Since, in this approach, heat removal to the journal and the bearing is not allowed for, calculated temperatures are highly overestimated, which reduces the validity of the results. In the isothermal approach, it is assumed that the calculation (equivalent) current temperature $T_{eq} = T_{eq}(t)$ is the same at all points of the lubricating films. This temperature is a fairly inertial parameter and determined when solving the equation of heat balance, which reflects the equality of cycle-averaged values of the heat dissipated in the lubricating film and the heat removed by the lubricant flowing out through the bearing ends. In the thermo-hydrodynamic approach, the temperature is assumed to change in all directions [9, 11], including across the lubricating film. In this case, the boundary conditions are the best fit for real thermal processes. This approach yields information on the local characteristics of the temperature field in the lubricating film, i.e., maximum and instantaneous average values of the temperature, as well as zones of increased thermal load.

Deligant [12] in their study proposed a theoretical model for calculating friction losses in turbocharger plain bearings. The author concludes that the cooling of the bearings occurs mainly due to the thermal conductivity of the bearing and convection inside the external clearance.

The method of calculating the dynamics of a flexible asymmetric rotor on a radial sliding bearing was presented in [4]. The calculation results showed that the amplitude of the rotor precession in all modes is less than 11 microns. This indicates that there is no contact between the rotor and the radial support rings. The temperature increment in the bearing is 15–25 °C. At the same time, the conditions of lubricant supply have a slight effect on temperature.

Sharma [13] developed a theoretical model of a slotted hybrid bearing. The model considered a change in viscosity due to thermal effects. The authors found that the minimum thickness of the liquid film is reduced for all bearing configurations due to thermal effects. The authors also pointed out that the coefficients of feed, stiffness and damping of lubricants change significantly when thermal effects are taken into account.

Kucinski and Fillon [14] presented a study that showed the temperature distribution in a plain bearing loaded with a constant force. The main attention was paid to hydrodynamic pressure, temperature distribution at the film/sleeve interface, oil flow rates, power loss and film thickness. The results showed that for high-loaded bearings operating at low speed, the critical parameters are film

thickness and maximum pressure; for high-speed bearings operating at low loads, while the shaft is centered, the heating becomes very significant, and the maximum temperature becomes the critical parameter.

Khatak and Garg [15] analyzed the hybrid bearing in their work taking into account the influence of thermal effects and micropolar lubrication. The results show that increasing the temperature has a significant effect on the bearing. Therefore, it is important to take into account the thermal effects for bearings operating with micropolar lubrication in order to obtain more realistic characteristics of the sliding bearing.

Many researchers attempt to allow for the most realistic properties of lubricants, as well as a number of design, process, operational and other parameters, which affect the operation of tribo-units. The significance and topicality of the thermo-hydrodynamic lubrication problem for heavy-loaded sliding bearings with allowance for the rheological behavior of a lubricating fluid increase are very popular.

Additionally, researchers should take into account the mutual influence of bearings on each other. For example, in paper [16], the authors presented an algorithm for solving the problem of rotor dynamics. The authors take into account the flexibility of the rotor. However, experimental studies [17, 18] had shown that the bearings of the turbine and compressor operate in different thermal conditions. The temperature difference for the turbine and compressor bearings can be 15–30 °C. Studies on thermal aspects of bearings considered with different bearing temperatures are very limited.

Consequently, the evaluation of the thermal state of each bearing and accounting its thermal state in the calculation of the rotor dynamics is an urgent task. At the same time, the position of the rotor relative to the bearing must be determined at each time point. The flexibility of the rotor must be taken into account. The lubrication regime in the thin layer must be taken into account too.

2 Method of Solution

The scope of problems in the theory of hydrodynamic conjugations is characterized by the set of methods for solving the following interrelated problems:

- Solving equations of motion to determine the trajectory of the journal center in the bearing.
- Determining pressures in the lubricating film, which separates the friction surfaces with imperfect geometry with an arbitrary law of their motion with allowance for properties of the lubricant.
- Assessing the temperature state of the “shaft—lubricating film—bearing” system with allowance for properties of the structural materials.
- Determining and optimizing geometrical and hydromechanical characteristics of the bearing.

The complex solution of these problems is a key stage in improving the reliability of conjugations and developing friction units that meet the current requirements. However, this solution involves substantial difficulties, since it requires precise and highly efficient calculation methods and algorithms to be developed.

The result of the modeling of heavy-loaded fluid-lubricated bearings is usually assessed by the calculation of hydromechanical characteristics determined over a bearing loading cycle. The minimum permissible lubricating film thickness and the maximum permissible hydrodynamic pressure are commonly used as the criteria for the efficiency of conjugations [4, 19, 20].

A solution of the above-listed problems in isothermal formulation with allowance for determining the lubricating film thickness is presented in [4, 21, 22]. However, in many cases of calculation, there is a need to find a temperature distribution across the lubricating film, which is only possible in the thermo-hydrodynamic approach. This approach allows one to consider both the non-Newtonian behavior of lubricating oil and the geometry of the friction surfaces, which restrict a thin lubricating film.

Along with this approach to determine the temperature distribution in the lubricant layer, the use of the finite volume method (FVM) is of great interest. The application of this method makes it possible to more accurately obtain the temperature values in each lubricating layer. In this case, the properties of construction and lubricants, as well as the boundary layer on the surfaces of friction mates are taken into account.

The main provisions of the FVM are conveniently stated by considering the “standard” balance equation of a certain value ϕ in the control volume Ω , which is bounded by a surface with an external normal \vec{n} :

$$\int_{\Omega} \frac{\partial \rho \phi}{\partial t} d\Omega + \sum_k \int_{S_k} \vec{n} \cdot \vec{q} ds = \int_{\Omega} Q d\Omega, \quad \vec{q} = \rho \vec{V} \phi - \alpha \nabla \phi, \quad (1)$$

where \vec{q} is the flux density vector of $\vec{\phi}$, which includes the convective and diffusion components, Q is the distribution density of bulk sources; \vec{V} is the velocity vector; ρ is the density of the medium; α is the diffusion coefficient. The ϕ may include, for example, the internal energy of fluid, the additive concentration, the kinetic energy of turbulence, etc.

In the limit, with the volume we compress to a point, based on the Ostrogradsky–Gauss formula, this equation can be rewritten in differential form: $\partial \rho \phi / \partial t + \nabla \vec{q} = Q$.

Calculated areas are divided into small control volumes, for each of which the balance ratio (1) is recorded. One nodal point is located in the centers of control volumes. When solving three-dimensional problems with a complex geometry of the regions, in most cases, the cells of the computational grid are used as a control volume.

There are two options for solving problems with the help of the FVM:

- The boundaries of the control volume coincide with the boundaries of the element.
- The faces of the control volume pass through the centers of the faces of the elements into which the region is divided. The required variables are stored in the vertices of the elements. A control volume is built around each vertex.

FVM has several advantages:

- the main quantities are stored throughout the region, for example, system energy, mass, heat flux and so on. This condition is satisfied even for a coarse computational grid;
- the calculation speed is high. Many calculated values can be calculated by splitting a region into elements, and there is no need to calculate them at each time step;
- the method is easily used for problems with complex geometry and curvilinear boundaries. The ease of using different geometric types of elements—triangles, polygons.

3 Results

The calculations were performed for the radial plain bearing of the turbocharger TKR 50.09.16 produced by NPO “Turbotekhnika.” The rotational speeds of the rotor shaft 50.09.16 TKR were 90,000, 140,000, 180,000 and 195,000 min^{-1} . The design of the radial bearing is shown in Fig. 1.

At the first stage, the pressure contours for the lubricating layer of the sliding bearing were performed. The model was calculated using the ANSYS Academic Fluent software [23, 24]. When creating a computational grid in the Meshing mesh preprocessor, the Sweep method was used for all parts of the model. For the Src/Trg Selection option, the Manual source mode is selected, allowing the user to manually select the source surface, and the receiving surface is automatically detected. This option is relevant if the model cross section along the pull line changes and the cross-sectional dimensions of the source and receiver surfaces do not match.

To simulate the boundary layers, the Number of Divisions option was used, as well as the Sweep Bias Type option, which is used to thicken the grid to one of the surfaces. For certain parts of the model, the so-called domains, the Inflation tool

Fig. 1 Design of the radial plain bearing

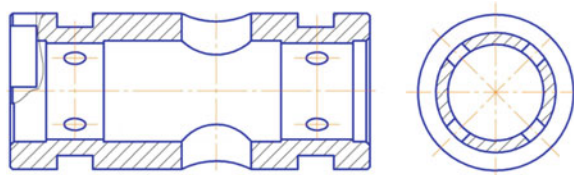
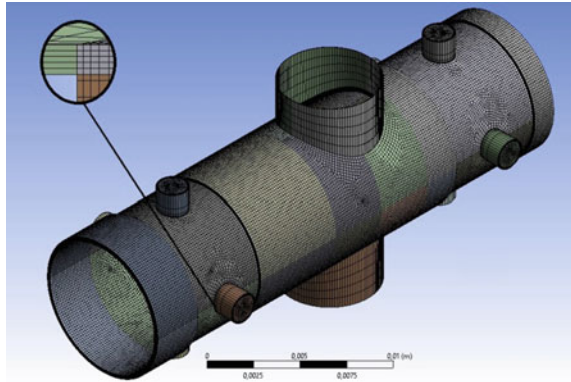


Fig. 2 Computational grid of the fluid model for the radial bearing, taking into account the internal prismatic layers



was used. The tool is responsible for building a computational grid with prismatic cells with thickening layers near the surfaces. The model was divided into 44 parts. This was necessary to improve the quality of the calculation grid. To save computing power and time, most of the cells in the model are hexahedral. The calculated geometric model is presented in Fig. 2.

The calculation in the Fluent software package was carried out for two computational models with different eccentricities, where $\chi = 0,5$ and $\chi = 0,8$. The solution algorithm was chosen as pressure-based, better known in the Russian literature as an implicit establishment algorithm. The model is connected to the energy equation, which takes into account changes in the flow temperature and thermal phenomena. Viscosity model (model Viscous) was chosen two-parameter turbulence model k-epsilon realizable.

Since the two-parameter model of turbulence was used, two additional parameters are required that characterize the turbulence of the incoming flow. In our case, we used turbulence intensity and hydraulic diameter. The value of turbulence intensity is 5%. The value of the hydraulic diameter for the inlets is 1.8 mm, and for the outlets is 0.1 mm.

The solution was made according to the PISO scheme, which is used for non-stationary tasks. At the same time, a second-order upwind sampling scheme was used for most parameters. The parameters of the lubricant are presented in Table 1.

There are ten inlets and four outlets in the model. The radial equilibrium distribution option was enabled at the outlets. It makes it possible to take into account

Table 1 Lubricant parameters

Parameter	Value	Unit of measurement
Density	850	kg/m ³
Heat capacity	1926	J/(kg K)
Thermal conductivity	0,12	W/(m k)
Dynamic viscosity	0,01	Pa s

Table 2 Boundary conditions

Parameter	Gauge pressure, kPa	Turbine temperature, °K	Compressor temperature, °K
Inlet	400	383	363
Outlet	103,325	423	343

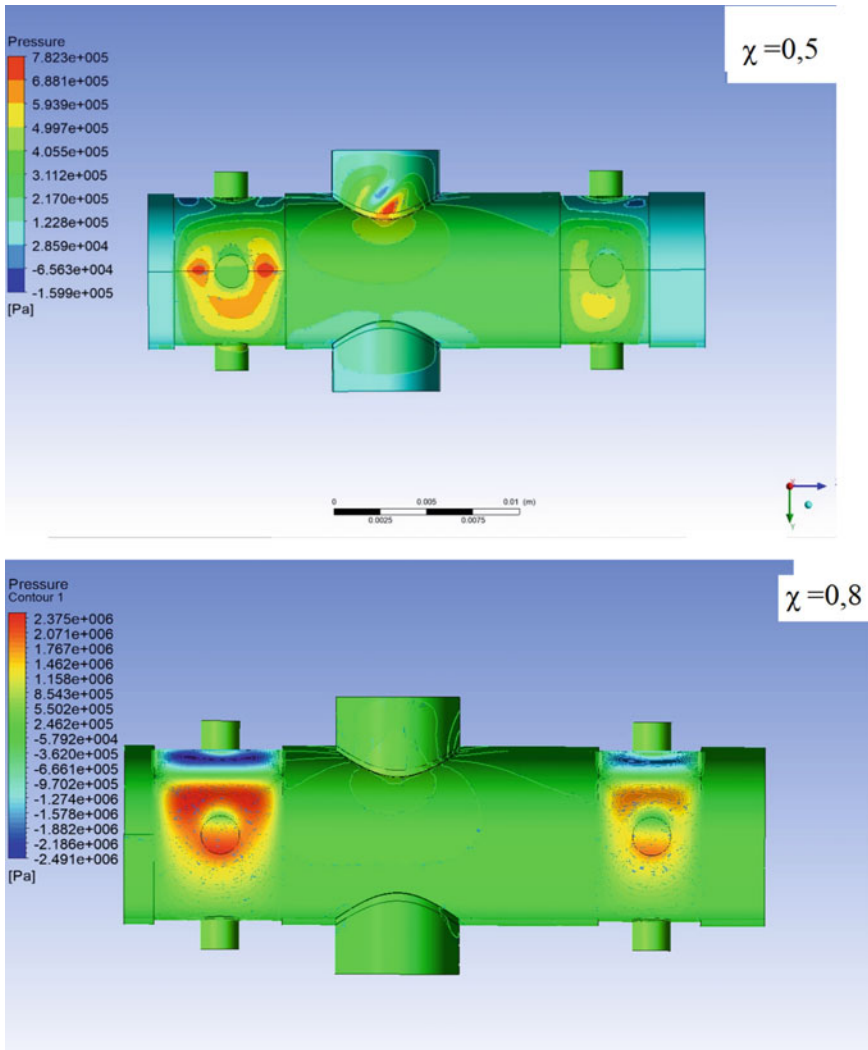


Fig. 3 Comparison of the fields of hydrodynamic pressure at different shaft eccentricities

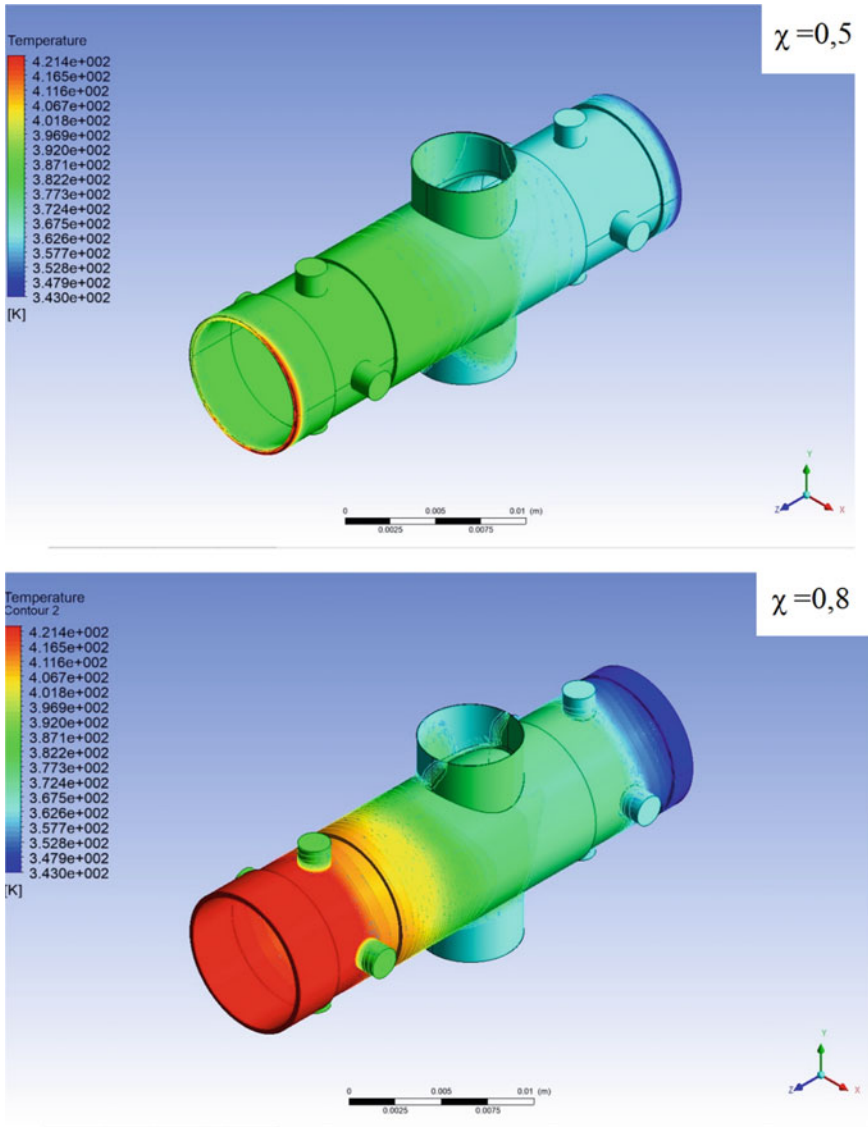


Fig. 4 Comparison of temperature fields in the lubricant layer of the bearing at different eccentricities of the shaft

the pressure distribution over the channel height using the radial equilibrium equation. This improves the accuracy of modeling the lubricant flow in turbomachines. The interior of the model rotates at a speed of 90,000 rpm, simulating the rotation of the lubricant under the action of the turbocharger rotor. Table 2 shows the boundary conditions used in the calculation.

The type of the output parameter was integral, and the solution is converged at 100–200 iterations. Figures 3 and 4 present the results of the calculation of pressure contours, and Fig. 4 presents the results of the calculation of thermal fields.

4 Conclusion

The obtained temperature fields indicate uneven thermal loading of the turbine and compressor bearings. This fact significantly affects the position of the flexible asymmetric rotor in the gap space. The thickness of the lubricant layer decreases with increasing temperature. This leads to a change in the mode of operation of the friction conjugations. From the hydrodynamic mode, the transition to a mixed or boundary friction mode is possible. In areas of high pressure, a local increase in lubricant temperature is observed. The results will be used to solve the problem of the dynamics of the rotor of the turbocharger.

Acknowledgements This work was carried out with the financial support of the Russian Foundation for Basic Research (Project No 16-08-01020\16) and the Ural Branch of the Russian Academy of Sciences (Project No 0407-2015-0005).

References

1. Baturin OV, Baturin NV, Matveev VN (2009) The history of the invention and development of pressurized aggregates of internal combustion engines. *Aircr Space Rocket Eng* 2–3:369–376
2. Lusheko VA, Nikishin VN (2015) The research of distribution of oil flow into the bearing turbocharger. *J Automot Eng* 1(90):30–35
3. Zadorozhnaya E, Sibiryakov S, Hudyakov V (2017) Theoretical and experimental investigations of the rotor vibration amplitude of the turbocharger and bearings temperature. *Tribol Ind* 39(4):452–459. <https://doi.org/10.24874/ti.2017.39.04.04>
4. Zadorozhnaya E, Sibiryakov S, Lukovich N (2017) Calculated estimates for the thermal state and the precession amplitude of the rotor in the turbocharger radial bearing. *Procedia Eng* 206:716–724. <https://doi.org/10.1016/j.proeng.2017.10.543>
5. Smirnov AV (2014) New type of turbocharger bearing support. *Dvigatelistroyeniye* 256:23–25
6. Vencl A, Rac A (2014) Diesel engine crankshaft journal bearings failures: Case study. *Eng Fail Anal* 44:217–228. <https://doi.org/10.1016/j.engfailanal.2014.05.014>
7. Wilkinson WL (1960) *Non-Newtonian fluids*. Pergamon Press, London
8. Kameron A (1962) *Teoriya smazki v inzhenernom dele (Lubrication theory in engineering)*. Gos Nauch Tekh Izd, Moscow
9. Zhang C (2002) TEHD behavior of non-Newtonian dynamically loaded journal bearings in mixed lubrication for direct problem. *ASME J Tribol* 124(1):178–185. <https://doi.org/10.1115/1.1396342>
10. Zadorozhnaya EA (2015) Solving a thermohydrodynamic lubrication problem for complex-loaded sliding bearings with allowance for rheological behavior of lubricating fluid. *J Mach Manuf Reliab* 44(1):46–56. <https://doi.org/10.3103/S1052618814020198>

11. Prokop'ev VN, Karavaev VG (2003) Thermohydrodynamical lubrication problem for complex loaded sliding bearings by means of non-Newtonian fluids. *Vestn Yuzhn Ural'sk. Gos Univ Ser Mashinostr* 1(17):55–66
12. Deligant M, Podevin P, Descombes G (2011) CFD model for turbocharger journal bearing performances. *Appl Therm Eng* 31(5):811–819. <https://doi.org/10.1016/j.applthermaleng.2010.10.030>
13. Sharma SC, Kumar V, Jain SC, Nagaraju T, Prasad G (2002) Thermohydrostatic analysis of slot-entry hybrid journal bearing system. *Tribol Int* 35(9):561–577
14. Kucinski B, Fillon M (1999) An experimental study of transient thermal effects in a plain journal bearing. *J Tribol* 121(2):327–332
15. Khatak P, Garg HC (2016) Performance analysis of capillary compensated hybrid journal bearing by considering combined influence of thermal effects and micropolar lubricant. *J Tribol* 139(1):011707. <https://doi.org/10.1115/1.4033715>
16. Taranenko P, Sliva O, Zadorozhnaya E (2015) Dynamics analysis of flexible rotor supported by floating ring bearings. *Mech Mach Sci* 21:1103–1113
17. Kaminskiy VN (2012) Experience in the development of supercharging systems for KAMAZ EURO-4 engines. *Zurnal AAI* 5:16
18. Kaminskiy VN (2012) Development of test-benches for control and research tests of turbochargers. *Scientific journal "Izvestiya MGTU MAMI" Рисунк 2(14):Рисунок, 143–148*
19. Zakharov SM, Sirotenko VI, Zharov IA (1995) The way to simulate an operation for tribological system "crankshaft_bearings, cylinders block bearing" for combustion engines. *Trenie Iznos* 16(1):47–54
20. Chichinadze AV, Berliner EM, Braun ED (2003) *Trenie, iznos i smazka: Tribologiya i tribotekhnika (Friction, wear and lubrication: tribology and tribological engineering)*. Mashinostroenie, Moscow
21. Prokop'ev VN, Zadorozhnaya EA, Levanov IG (2008) Oils non-Newtonian properties effect onto crankshaft rod bearings loading. *Dvigatelistroenie (Engines Constr)* 3:40–42
22. Levanov IG (2011) The way to calculate hydromechanical characteristics of complex loaded sliding bearings for piston and rotor machines lubricated by non-Newtonian oils. *Vestn Yuzhn Ural'sk. Gos Univ Ser Mashinostr* 31(248):34–43
23. ANSYS Fluent Software: CFD Simulation. <https://www.ansys.com/products/fluids/ansys-fluent>
24. Engineering Simulation and 3D Design Software|ANSYS. <https://www.ansys.com/>

Ensuring Tightness of Sealing Joints at the Design Stage



P. Ogar, A. Kozhevnikov and V. Kushnarev

Abstract The issues of ensuring the tightness of sealing joints are considered. It is indicated that to calculate the tightness at the design stage, it is necessary to know the regime of the outflow of the medium being sealed, which is determined by the Reynolds number. It is shown that the Reynolds number is determined by the ratio of the linear mass flow rate through the sealing joint to the dynamic viscosity of the sealed medium. Dependencies of the relative contact area, the density of gaps in the joint, and the probability of medium flow from the dimensionless force elastic-geometric parameter f_q should be determined taking into account the mutual influence of asperities of the rough surface. Said contact characteristics determine the functional of the permeability C_u which characterizes the sealing capacity of the sealing joint. Their role in various periods of loading of a sealing joint by a dimensionless load is shown.

Keywords Tightness · Contact sealing pressures · Permeability functional · Relative contact area · Gap density · Medium leakage probability

1 Introduction

Tightness is the property of joints to ensure the permissible amount of leakage, determined from the conditions of normal operation of various systems and equipment, the safety of people, and the protection of the environment. For a quantitative assessment of tightness, the leak rate is used that is the mass or volume of the medium in unit time per unit length along the perimeter of the sealing joint. The tightness of the joint between the parts of sealing joints (SJ) is determined by the functional parameters of the sealing surfaces and compressive stresses (the contact pressure of sealing q), and the required contact characteristics are the relative area of contact and the density of gaps in the joint [1, 2]. The norms of

P. Ogar (✉) · A. Kozhevnikov · V. Kushnarev
Bratsk State University, 40, Makarenko St, 665709 Bratsk, Russia
e-mail: ogar@brstu.ru

tightness of valves of pipe fittings are regulated by the state standard; however, there are no regulations for determining the contact pressures of sealing, ensuring the specified tightness.

To assess the sealing ability of the sealing joint, the authors of [1, 2] proposed a dimensionless permeability functional, which depends on the relative contact area, density of gaps in the joint, and the degree of confluence of individual contact spots of microasperities (probability of medium flow). The required value of the permeability functional is determined by the permissible amount of leakage, the parameters of the medium, and the geometrical parameters of compaction.

2 Modes of Flow of the Working Medium Through the Joint of SJ

Let us consider the case that is often encountered in practice—a stationary flow of a viscous fluid (or a gas with Knudsen number $Kn \rightarrow 0$) under the action of a pressure gradient, which is called filtration. At the same time, viscous and turbulent flow regimes are possible. The transition from viscosity to turbulent mode is determined by the achievement of the critical value of the Reynolds number

$$Re = \rho v d / \mu \quad (1)$$

where ρ is the density of the medium, v is the filtration rate, d is the characteristic size, which is used as the average size of microchannels, the equivalent hydraulic radius, the average size of asperities, etc.

According to [3], in tortuous capillaries due to curvature and periodic narrowing and widening of channels, flow turbulization occurs at $20 < Re < 200$. The author [4, 5] found that if $Re < 4 \dots 12$, the mode is laminar; if $Re > 4 \dots 12$ the mode is mode. Thus, it follows that in the sealing joint, the flow turbulization occurs at significantly lower Reynolds numbers than for smooth pipelines.

For a flat sealing joint with an average diameter d_m , filtration rate is

$$v = \frac{Q_v}{A} = \frac{Q_v}{\pi d_m r_h} \quad (2)$$

where Q_v is the volumetric flow rate of the medium and A is the cross-sectional area along the seal perimeter.

If the characteristic radius in Eq. (1) is to use the hydraulic radius r_h , then the Eq. (1) takes the form

$$Re = \frac{\rho Q_v}{\pi d_m \mu} = \frac{G_l}{\mu} \quad (3)$$

G_l is the mass flow rate of the medium.

Since the value of G_l is specified when designing the SJ, it is possible to determine the mode of the working medium outflow and then calculate the leakage value depending on the applied load.

3 Algorithm for Determining Contact Pressure of Sealing

We consider the tightness calculation using the example of a capillary model of a sealing joint and viscous flow of a medium.

To determine the mass flow rate in viscous mode, the Poiseuille formula for a cylindrical circular pipe is widely used

$$G = \frac{\pi r^4 \rho \Delta p}{8 \eta l} \quad (4)$$

where r is the radius of the cross section of the pipeline; ρ , η are the viscosity and density of the medium; $\Delta p = p_1 - p_0$ is the pressure drop; and l is the length of the pipeline.

In [1], it was shown that for pipelines with arbitrary cross sections, such as microchannels in a sealing joint, one can use the concept of a hydrodynamic radius

$$r_h^4 = \frac{4S^3}{\pi P^2} \quad (5)$$

where S and P are the area and perimeter of the microchannel section. Equation (5) agrees well with the data of [6–8].

For a discrete roughness model, the average values of S_l and P_l per unit length of the profile can be determined from the volume of gaps of intercontact space and relative contact area [1]:

$$S_l = \frac{V_3}{A_c} = R_{\max} A; P_l = 2(1 - \eta) \quad (6)$$

We represent the sealing joint of rough surfaces with a multitude of intersecting microchannels as a porous medium formed by two rough surfaces with the initial height $R_{\max} = R_{\max 1} + R_{\max 2}$.

We assume that at steady-state flow, the pressure distribution in all planes coinciding with the pressure gradient is the same and changes from p_1 at r_1 to p_0 at r_2 at the entrance and exit of the porous medium [9]. Since all sections perpendicular to the pressure gradient are ergodic and the flow of the medium through them at a steady flow is constant, the total leakage through the joint

$$G = \sum_{i=1}^N G_i = N\bar{G}K \quad (7)$$

where $N = \pi d_m n v_k$ is the number of microchannels through which leakage occurs; n is the number of microchannels per unit length; v_k is the probability of medium flow; G_i is the leakage through the i -th microchannel; \bar{G} is the mass and volume flow through the microchannel defined through the average values of the functionals S and P ; K is the coefficient taking into account losses due to structural elements and local barriers (narrowing, expansion, etc.), and in the first approximation, you can take $K = 1$.

Taking into account Eqs. (4) and (5), we have

$$\bar{G} = \frac{\pi \rho \Delta p}{8 \eta l} \cdot \frac{4 S_l^3}{\pi P_l^2 n}$$

where the second factor determines the hydraulic radius for a microchannel with an arbitrary cross section.

Substituting the obtained equation into (7) with allowance for (6) and the number of microchannels, for the leak rate, we get

$$G_l = \frac{G}{\pi d_m} = \frac{R_{\max}^3 \rho \Delta p}{2 l \mu} \cdot \frac{A^3 v_k}{4(1 - \eta)^2} \quad (8)$$

where the second factor is the permeability functional C_u , which characterizes the joint sealing ability and depends on the microgeometry parameters and contact pressure, which determines the contact characteristics of the junction A , η , v_k .

The Eq. (9) can be represented as

$$\text{Re}^* \cdot \mu = C_f \cdot C_u \quad (9)$$

where Re^* is the required Reynolds number, defined by Eq. (3)

$$C_f = \frac{R_{\max}^3 \rho \Delta p}{2 l \mu}, C_u = \frac{A^3 v_k}{4(1 - \eta)^2} \quad (10)$$

When designing a sealing joint, it is convenient, based on the specified ρ , p_1 , p_0 , μ and assigned d_m , l , and R_{\max} for the required Re^* value, to determine the required permeability functional from Eqs. (9) and (10)

$$C_u^* = \frac{2 l \mu^2 \text{Re}^*}{R_{\max}^3 \rho \Delta p} \quad (11)$$

and then from the $C_u(f_q)$ dependencies to determine the dimensionless force elastic-geometric parameter f_q (or parameter f_σ), which provides a given level of C_u^* , and therefore, a given amount of leakage G_l [2]. The force elastic geometry parameter f_q is used for the elastic contact of asperities and is determined by the equation

$$f_q = \frac{q a_c}{E^* \omega R_{\max}} \tag{12}$$

where a_c , ω , R_{\max} are the parameters of the discrete roughness model [2]; E^* is the reduced modulus of elasticity; the parameter $\bar{q}_\sigma = q/\sigma_y$ is used for the elastoplastic contact of asperities; and σ_y is the yield point.

4 The Relative Contact Area and the Density of Gaps in the Joint

The issues of determining the relative contact area and density of gaps in the joint, which are part of the permeability functional C_u , for different types of contact of rough surfaces are considered in [1, 2, 10].

Figure 1 shows typical dependences $\eta(f_q)$ and $\Lambda(f_q)$ for the elastic contact of rough surfaces for different values of the parameters p and q of the profile bearing curve, which is described by a regularized beta function.

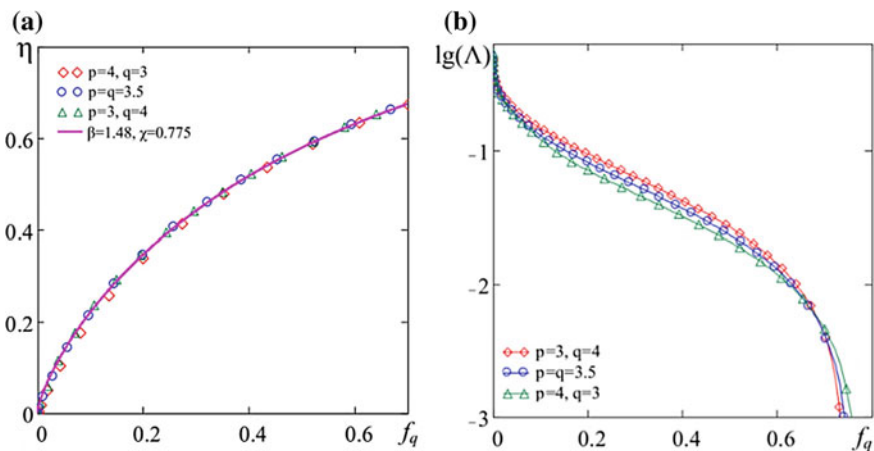


Fig. 1 Dependence of the relative contact area (a) and density of gaps in the joint (b) on the dimensionless parameter f_q



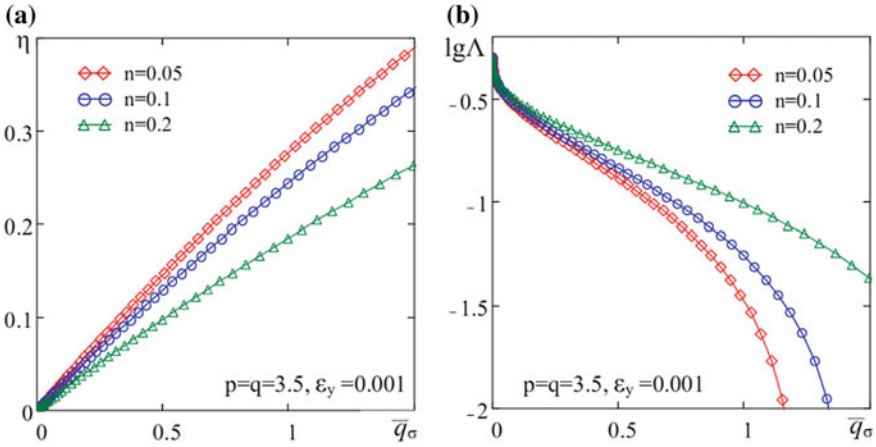


Fig. 2 Dependence of the relative contact area (a) and density of gaps in the joint (b) on the dimensionless parameter \bar{q}_σ

As follows from Fig. 1, the dependences $\eta(f_q)$ for different values of the parameters p and q almost merge into one line. Therefore, for engineering calculations, it is advisable to approximate them by the equation

$$\eta = 1 - \exp\left(-1.48f_q^{0.775}\right) \tag{13}$$

which describes them quite accurately and is recommended for engineering calculations of the relative area in the case of elastic contact. It follows from the proposed dependence that $\eta \rightarrow 1$ with $f_q \rightarrow \infty$, which is consistent with studies of almost complete contact between rough surfaces [11–15].

Figure 2 shows the typical dependences $\eta(\bar{q}_\sigma)$ and $\Lambda(\bar{q}_\sigma)$ for the elastoplastic contact of rough surfaces for different values of the hardening exponent. In this case, the approach proposed by the authors of [16] was used. Similar dependences for the case of unloading of preloaded surfaces are determined according to [17, 18].

5 Medium Flow Probability

The likelihood of the medium flowing through the sealing joint is determined by the degree of confluence of the individual contact spots [2]:

$$v_k(\varepsilon) = \begin{cases} (1 - x^*), & x^* < \frac{1}{3}; \\ 3^{k-1}(1 - x^*)^k, & x^* \geq \frac{1}{3}; \end{cases} \tag{14}$$



where k is the number of rows of asperities across the width of the compaction zone;

$$x^*(\varepsilon) = \int_0^\varepsilon x_i^*(\varepsilon, u) \phi'(u) du, \quad x_i^*(\varepsilon, u) = \begin{cases} 0, & \eta_i(\varepsilon, u) < \eta_i^*; \\ 1, & \eta_i(\varepsilon, u) \geq \eta_i^*; \end{cases} \quad (15)$$

$\phi'(u)$ is the density of the height distribution asperities function; and $\eta_i^* = 0.5 \dots 0.52$ is the critical value of η_i .

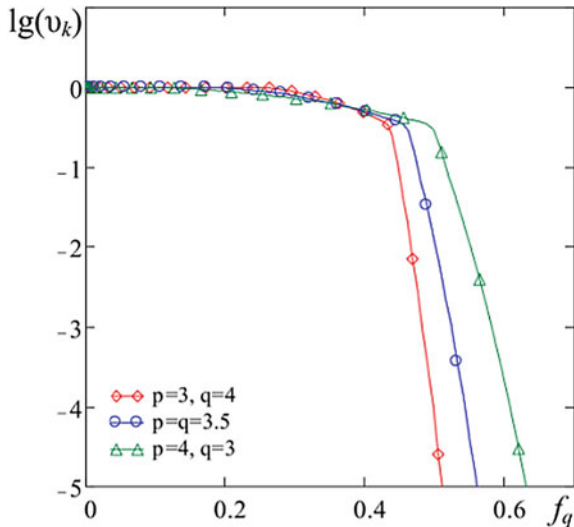
Figure 3 shows the dependences of $v_k(f_q)$ for different values of the parameters p and q of the profile bearing curve.

Typical dependences of $C_u(f_q)$ and $C_u(\bar{q}_\sigma)$ are presented in Fig. 4.

From the graphical dependencies, Fig. 4a follows the presence of three sealing zones: (a) initial ($f_q \leq 0.05$), due to the indentation of the highest asperities; (b) stable ($0.05 \leq f_q \leq f_{qe}$), due to a decrease in the density of the gaps; and (c) effective ($f_q > f_{qe}$), due to the merging of individual contact spots.

The value of f_{qe} is characterized by the onset of a sharp decrease in permeability functional (Fig. 4a) due to a decrease in the probability of medium penetration (Fig. 3). For a given level of probability of flow of the medium, for example, $v_k = 0.0001$, the values $f_{qe} = 0.50 \dots 0.60$. With allowance for Eq. (13), this occurs at a relative contact area $\eta = 0.58 \dots 0.63$, for $p = q = 3.5$, we have $\eta = 0.60$. This result agrees well with the data of [19, 20] obtained using the percolation theory (penetration), which determine the value of the relative actual contact area at which a continuous closed cluster is formed, i.e., overlapping of all microchannels in the joint is ensured.

Fig. 3 The dependence of the probability of flow of the environment v_k from the dimensionless parameter f_q



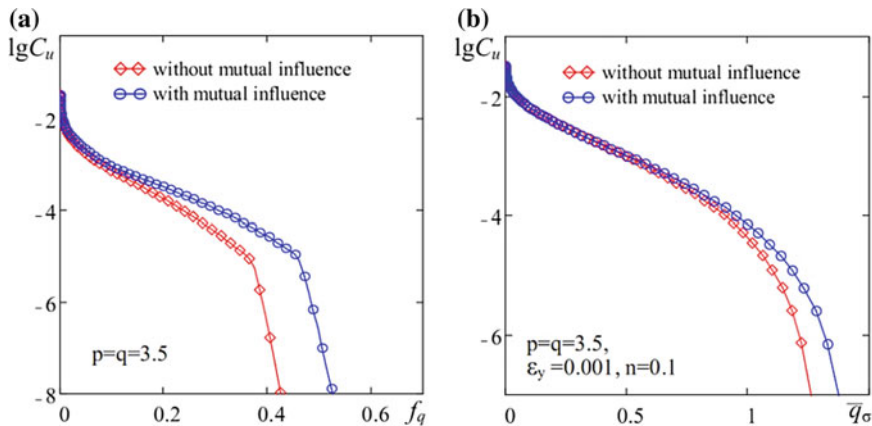


Fig. 4 The dependences of the permeability functional for the elastic (a) and elastic-plastic (b) contacts

6 Conclusion

1. To predict tightness at the design stage, it is necessary to know the flow regime of the medium being sealed, which is determined by the Reynolds number. It is shown that the Reynolds number is determined by the ratio of the specific mass flow rate through the sealing joint to the dynamic viscosity of the medium to be sealed.
2. The sealing ability of sealing joints is determined by the contact characteristics: the relative contact area, the density of gaps in the joint, and the degree of confluence of individual contact spots, which determines the likelihood of the medium to flow and is the most effective characteristic.
3. The relative contact area and the density of the gaps in the joint should be determined taking into account the mutual influence of asperities, the values of which give a margin of tightness in comparison with the values obtained without taking into account the mutual influence.
4. The guaranteed tightness depends on the distribution of asperities along the height of the rough layer and is provided with the relative contact area in the joint $\eta = 0.58 \dots 0.63$. This result is in good agreement with the data obtained using the percolation theory.

References

1. Ogar PM, Tarasov VA (2014) Design of special pipeline valves. BrSU, Bratsk
2. Ogar PM, Belokobylsky SV, Gorokhov DB (2018) Contact mechanics of rough surfaces in hermetic sealing study. In: Contact and Fracture Mechanics. InTechOpen Limited, London

3. Timofeev DP (1962) Kinetics of adsorption. Izd-vo AN SSSR, Moscow
4. Kosinskij VV (2006) Determination of the permeability coefficient of porous bodies impregnated with viscous liquids under pressure. Metallurgy. Proc Zaporozhye State Eng Acad 13:55–59
5. Kosinskij VV (2007) Nonlinear Darcy laws and Reynolds criterion for the flow of compressible fluids under high pressure in porous bodies. In: New materials and technologies in metallurgy and mechanical engineering, vol 1, pp 60–68
6. Bashta TM, Mendelson DA, Shifrin SN (1981) Calculation of gas leaks through the pneumatic valve. In: Operational reliability of the airframe and aircraft systems. KIIGA, Kiev
7. Dehshman S (1964) Scientific basis of vacuum technology. Mir, Moscow
8. Pipko AI, Pliskovskij VA (1979) Design and calculation of vacuum systems. Energy, Moscow
9. Daragan VL, Kotov YA, Melnikov GN, Pustostogarov AV, Starshinov VI (1970) Calculation of pressure loss during gas flow through porous materials. J Eng Phys 26:787–794
10. Ogar PM, Gorokhov DB, Kozhevnikov AS (2015) The density of gaps in the seal joint in elastic contact of microasperities. In 2nd international conference on modelling, identification and control (MIC 2015), Paris
11. Hyun S, Robbins MO (2007) Elastic contact between rough surfaces: effect of roughness at large and small wavelengths. Tribol Int 40:1413–1422
12. Yeo C-D, Katta RR, Lee J, Polycarpou AA (2010) Effect of asperity interactions on rough surface elastic contact behavior: hard film on soft substrate. Tribol Int 43:1438–1448
13. Xu Y, Jackson RL, Marghitu DB. (2014) Statistical model of nearly complete elastic rough surface contact. Int J Solids Struct 51:1075–1088
14. Yastrebov VA, Anciaux G, Molinari J-F (2015) From infinitesimal to full contact between rough surfaces: evolution of the contact area. Int J Solids Struct 52:83–102
15. Xu Y, Jackson RL (2017) Statistical models of nearly complete elastic rough surface contact-comparison with numerical solutions 105:274–291
16. Ogar P, Gorokhov D, Belokobylsky S (2017) The elastic-plastic contact of a single asperity of a rough surface. MATEC Web of Conf 129:06017
17. Ogar PM, Gorokhov DB (2017) Influence of materials hardenability parameters on the machine parts characteristics after unloading. Key Eng Mater 723:369–375
18. Ogar P, Gorokhov D, Ugryumova E (2017) Mechanics of unloading of a rough surfaces pre-loaded joint. MATEC Web of Conf 129:06016
19. Tihomirov VP, Gorlenko OA (1989) Criterion for tightness of flat mates. J Friction Wear 10:214–218
20. Tihomirov VP, Poroshin VV, Gorlenko OA, Izmerov MA (2014) Tightness detachable fixed joints. MGIU, Moscow

Modeling Introduction of Rigid Sphere into Layered Elastic Body



P. Ogar, A. Kozhevnikov and V. Kushnarev

Abstract On the basis of a simplified rigid model of a layered elastic body, an engineering technique for determining the parameters of a contact is proposed for the indentation of a spherical indenter into it. The model is based on the dependence of the displacement of the points of the half-space along the axis of symmetry on the magnitude of the applied distributed load. The reduced elasticity modulus and the Poisson's ratio are determined depending on the elastic properties of the base and coating materials, the thickness of the coating, and the radius of the contact area. Equations are given for determining the parameters of a contact when a spherical indenter is indented into a layered body. The obtained results are compared with the exact solution of the spatial axisymmetric problem for describing the stress-strain state in an elastic layer when a spherical indenter is indented into it, obtained by A. P. Makushkin using the Fourier–Bessel integral transformation method.

Keywords Layered elastic body · Layered half-space · Reduced elastic modulus · Indentation of a sphere

1 Introduction

At present, the possibilities of increasing the service life of the connections of machine parts by changing the design or improving the materials by optimizing their microstructure are practically exhausted. In this regard, one of the promising ways to improve the operational performance of the joints of machine parts, including sealing joints and friction units, is to apply coatings to their working surfaces or to form modified layers based on metals, ceramics, and polymers [1]. Experience in the operation of friction units and seals with such coatings shows that their antifriction properties and sealing ability are determined not only by the

P. Ogar (✉) · A. Kozhevnikov · V. Kushnarev
Bratsk State University, 40 Makarenko St, 665709 Bratsk, Russia
e-mail: ogar@brstu.ru

properties of the coating material, but also by its thickness [2]. Known recommendations on the choice of coating thickness are based on experimental data, often contradictory. The lack of a theory of contact interaction of rough surfaces through the coating layer does not allow developing reliable methods for predicting the friction characteristics of tri-shears and tightness of seals at the design stage, which requires costly and time-consuming experimental tests.

In the framework of the theory of elasticity, the presence of a coating means that an elastic body should be considered with varying values of the elastic modulus and Poisson's ratio depending on the distance to the surface [3].

2 Problem State

Contact problems for bodies with varying depth, mechanical characteristics were considered in [3–7]. However, it is not possible to apply the obtained results for solving practical problems of tribology and hermetology. In [8], an approximate solution of the axisymmetric contact problem for an elastic layer of finite thickness lying on a rigid base is presented, which may be of interest when using polymer coatings.

A separate group should include engineering methods for solving contact problems based on simplifying hypotheses, for example, the representation of a layered body as a topocomposit—structures with special mechanical properties depending on the coating thickness, the mechanical properties of the base, and coating materials [9, 10].

As the method was developed, the authors of [11–15] determined the reduced modulus of elasticity and the Poisson's ratio for any values of coating thickness under axisymmetric loading of a layered half-space based on the rigid model of a layered body.

In general, the axisymmetric load is

$$p(r) = p_0(1 - r^2/a^2)^\beta, \quad 0 \leq r \leq a, \quad (1)$$

where $0 \leq \beta \leq 0.5$, $p_0 = p_m(1 + \beta)$, p_m is the mean pressure, and $P = p_m \cdot \pi a^2$.

Following the classical approach, based on the application of potential Boussinescu functions [16], to move any point along the axis of symmetry inside a homogeneous half-space when loaded with a distributed load (1), we get:

$$u_z = \frac{P_m a}{E^*} K(\bar{z}, \beta, \nu) \quad (2)$$

$$K(\bar{z}, \beta, \nu) = \frac{1}{\sqrt{1 + \bar{z}^2}} \cdot {}_2F_1\left(\frac{1}{2}, 1 + \beta; 2 + \beta; \frac{1}{1 + \bar{z}^2}\right) - \frac{\bar{z}}{2(1 - \nu)} \cdot \frac{d}{d\bar{z}} \left[\frac{1}{\sqrt{1 + \bar{z}^2}} \cdot {}_2F_1\left(\frac{1}{2}, 1 + \beta; 2 + \beta; \frac{1}{1 + \bar{z}^2}\right) \right], \quad (3)$$

where ${}_2F_1$ is the Gauss hypergeometric function, $E^* = E/(1 - \nu^2)$, and $\bar{z} = z/a$.

For Hertz's load distribution with $\beta = 0.5$, the expression for $K(\bar{z}, \beta, \nu)$ can be represented as

$$K(\bar{z}, 0.5, \nu) = \text{arctg}\bar{z} + \frac{\nu}{1 - \nu} \bar{z}(1 - \bar{z} \text{arctg}\bar{z}). \tag{4}$$

Simplify the notation by accepting

$$K_i(0, 0.5, \nu_i) = K_i(0), K_i(\bar{\delta}_1, 0.5, \nu_i) = K_i(\bar{\delta}_1), \tag{5}$$

As the analysis showed, the function $K(\bar{z})$ to a small extent depends on the values of the Poisson coefficient. Moreover, $K_i(0) = \pi/2$, with $\bar{z} \rightarrow \infty K(\bar{z}) \rightarrow 0$.

For a layered elastic body, the reduced elastic modulus and the Poisson's ratio is determined by the expressions:

$$E_{01}^* = E_1^* \cdot F_1, F_1 = \frac{K_{01}(0)}{K_1(0) - K_1(\bar{\delta}_1) + K_0(\bar{\delta}_1)} \cdot I_e; \nu_{01} = \nu_1 + (\nu_0 - \nu_1) \frac{1 - F_1^{-1}}{1 - I_e} \tag{6}$$

Of practical interest for solving problems of tribology and hermetology is the determination of elastic characteristics when introducing a spherical indenter.

3 Layered Model When Describing the Implementation of a Spherical Indenter

Consider the contact of a rigid sphere of radius R with a layered half-space (Fig. 1).

The displacement of the point O (Fig. 1a) can be represented as the sum of the displacements of the coating and the base under the load P .

$$w_0 = w_\delta + w_A.$$

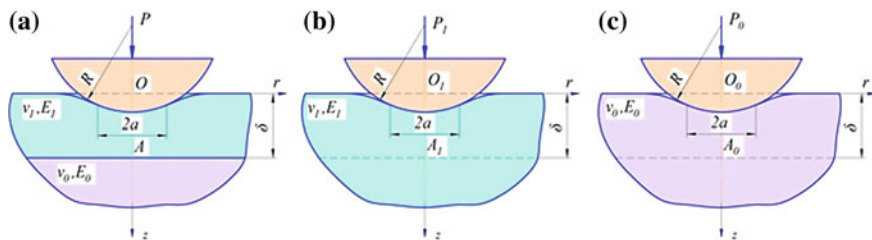
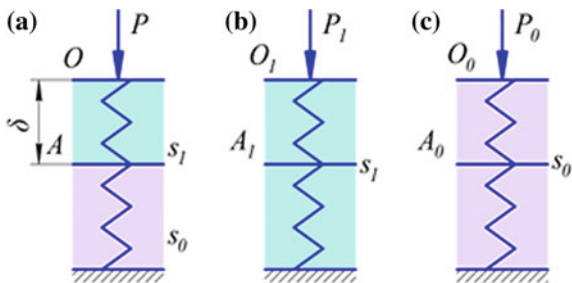


Fig. 1 The design scheme of contacting (a) and the scheme of contact of a sphere with homogeneous half-spaces, having characteristics ν_1, E_1 (b) and ν_0, E_0 (c)

Fig. 2 Modeling a layered half-space: **a**—the original scheme of a layered half-space (Fig. 1); **b, c**—stiffness schemes of homogeneous half-spaces



Scheme 1a can be represented as a stiffness model (Fig. 2a).

Then, the displacement $w_0 = P(s_1 + s_0)$, where s_1, s_0 —stiffness of the layer and the base material, $P = \pi a^2 p_m$.

Consider the insertions of spheres of radius R into two homogeneous half-spaces with elastic characteristics ν_1, E_1 and ν_0, E_0 , under loads P_1 and P_0 (Fig. 2b and 2c) According to [16], the radius of the contact area of a sphere with a homogeneous half-space

$$a = \left(\frac{3PR}{4E^*} \right)^{\frac{1}{3}}. \tag{7}$$

Taking into account (4) and (7), the compression of a homogeneous layer with a thickness of δ (Fig. 2b) and the corresponding rigidity are determined by the equation.

$$\begin{aligned} w_1 = w_\delta &= \frac{1.5P_1}{\pi} \left(\frac{4}{3E_1^*P_1R} \right)^{\frac{1}{3}} [K_1(0) - K_1(\delta)], \quad s_1 = \frac{w_1}{P_1} \\ &= \frac{1.5}{\pi} \left(\frac{4}{3E_1^*P_1R} \right)^{\frac{1}{3}} [K_1(0) - K_1(\delta)] \end{aligned} \tag{8}$$

The displacement of the point A_0 and the corresponding stiffness s_0 are equal to

$$w_{A_0} = w_A = \frac{1.5P_1}{\pi} \left(\frac{4}{3E_1^*P_1R} \right)^{\frac{1}{3}} K_0(\delta), \quad s_0 = \frac{w_{a0}}{P_0} = \frac{1.5}{\pi} \left(\frac{4}{3E_1^*P_1R} \right)^{\frac{1}{3}} K_0(\delta) \tag{9}$$

The value of P_1 is determined from the condition of equality of displacements ($z = \delta$) of a layered elastic body under load P and a homogeneous material under load P_1 :

$$P_1 = \frac{E_1^*}{E_{01}^*} \left(\frac{K_{01}(0) - K_{01}(\delta)}{K_1(0) - K_1(\delta)} \right)^{\frac{3}{2}} P. \tag{10}$$



The value of P_0 is determined from the condition of equality of displacements ($z = \delta$) of a layered elastic body under load P and a homogeneous material under load P_0 . As a result, we get

$$P_0 = \frac{E_0^*}{E_{01}^*} \left(\frac{K_{01}(\bar{\delta})}{K_0(\bar{\delta})} \right)^{\frac{3}{2}} P. \quad (11)$$

From equality of displacements $w_1 = w_\delta$ и $w_{A_0} = w_A$, it is followed that:

$$P = P_1 \frac{s_1}{s_1 + s_0} + P_0 \frac{s_0}{s_1 + s_0}, \quad (12)$$

Substituting the expressions (8), (9), (10), (11) into (12), we have

$$E_{01}^* = E_1^* \cdot F_{1R}, \quad F_{1R} = \frac{K_{01}(0)}{\frac{(K_1(0) - K_1(\bar{\delta}))^{\frac{3}{2}}}{(K_{01}(0) - K_{01}(\bar{\delta}))^{\frac{3}{2}}} + \frac{(K_0(\bar{\delta}))^{\frac{3}{2}}}{(K_{01}(\bar{\delta}))^{\frac{3}{2}}} I_e} \quad (13)$$

In the case of the approximation of the values of $K_{01}(\bar{\delta})$ to $K_i(\bar{\delta})$, we obtain Eq. (6).

The maximum discrepancies in the dependences of $F_{1n}(\bar{\delta})$ and $F_{1Rn}(\bar{\delta})$ in the range $\bar{\delta} = 0 \dots 10$ with $I_e = 0.1$ do not exceed 5%, and the average discrepancies do not exceed 1%.

Assuming the applicability of the Hertz theory for a layered elastic body with a reduced modulus of elasticity $E_{01}^* = E_1^* \cdot F_{1R}$, we determine the relative contact characteristics when introducing a sphere—radius of the contact area $\bar{a} = a/R$, insertion value $\bar{w}_0 = w_0/R$, maximum pressure at the contact area $\bar{p}_0 = p_0/E_1^*$ —depending on the dimensionless load $\bar{P} = P/(E_1^* R^2)$. For $a/R \leq 0.4$ when defining contact parameters, it should use the expression for a paraboloid of rotation [16]:

$$\bar{P} = \frac{P}{E_1^* R^2} = \frac{4}{3} \bar{a}^3, \quad \bar{w}_0 = w_0/R = \bar{a}^2, \quad \bar{p}_0 = \frac{p_0}{E_1^*} = \frac{1}{\pi} (6\bar{P} F_{1R}^2)^{\frac{1}{3}} \quad (14)$$

Equations for the spherical indenter are given in [17].

4 Discussion of the Results

The exact solution of the spatial axisymmetric problem for describing the stress-strain state in an elastic layer with the indentation of a spherical indenter into it is given in [2], which used the method of the integral Fourier–Bessel transform. This problem was also considered in [18–20]. Below, in Table 1, some data of the

Table 1 The results of calculations comparing the values of the relative insertion of a spherical indenter into the elastic layer, rigidly bonded to the base, carried out according to [2] and according to the proposed method

$a \cdot 10^4$, м	P, H	p_0 , МПа	$w_0 \cdot 10^4$, м	$\log \bar{P}$	\bar{w}_0	\bar{w}_{0s}	$\frac{\bar{w}_0 - \bar{w}_{0s}}{\bar{w}_0}$, %
1	2	3	4	5	6	7	8
0.05	0.0002	3.69	0.0106	-7.941	4.24×10^{-6}	3.999×10^{-6}	5.67
0.1	0.0017	7.39	0.0413	-7.012	1.652×10^{-5}	1.6×10^{-5}	3.13
0.2	0.0135	14.8	0.1570	-6.112	6.28×10^{-5}	6.4×10^{-5}	-1.92
0.3	0.0464	23	0.322	-5.575	1.288×10^{-4}	1.21×10^{-4}	6.05
0.5	0.2250	40	0.804	-4.89	3.216×10^{-4}	3.24×10^{-4}	-0.76
0.8	1.04	73	1.842	-4.225	7.368×10^{-4}	7.842×10^{-4}	-6.43
1	2.23	102	2.738	-3.894	1.095×10^{-3}	1.156×10^{-3}	-5.56
2	28.3	359	9.781	-2.79	3.912×10^{-3}	4.225×10^{-3}	-7.98
3	126	804	21.45	-2.142	8.58×10^{-3}	8.464×10^{-3}	1.35
4	427	1440	38.17	-1.612	0.015	0.016	-5.64
5	1046	2267	60.33	-1.222	0.024	0.025	-4.76
8	6962	5824	163.1	-0.399	0.065	0.062	4.2
10	16952	8990	260.4	-0.013	0.104	0.1	4.13
15	82556	19155	616.3	0.675	0.247	0.235	4.56
20	247400	31973	1137	1.151	0.455	0.416	8.51

exact solution from [2] for comparison with the results obtained by the proposed engineering methodology. The elastic moduli and Poisson's ratios of the coating and base materials are, respectively: $E_0 = 201$ GPa, $\nu_0 = 0.3$; $E_1 = 2.39$ GPa, $\nu_1 = 0.38$; Spherical indenter radius $R = 2.5 \times 10^{-3}$ m, and the thickness of the polymer coating is rigidly bonded to the base, $\delta = 10^{-4}$ m.

For given values of a (column 1), the indentation force P , the maximum pressure at the contact area p_0 , and the insertion value w_0 (columns 2–4) were determined. To summarize the results, we compare the dimensionless quantities. For dimensionless load, the relative indentation of \bar{w}_0 is determined according to [2] and according to the proposed engineering technique \bar{w}_{0s} (columns 6 and 7, respectively). The maximum error in absolute value did not exceed 10%, and the average error for the given values of the relative implementation was 4.7%, which indicates the acceptability of the proposed method for engineering calculations of the parameters of contact of a spherical indenter with a layered elastic body.

The corresponding graphical dependences of the relative indentation on the dimensionless load, calculated by different methods, are presented in Fig. 3. Dots indicate dependencies according to the data given in Table 1. The solid line corresponds to the data calculated by Eq. (14) for the values of a given in column 1 of Table 1. The dashed line corresponds to an approximate solution of the axisymmetric contact problem for an elastic layer of finite thickness [8]. As follows from Fig. 3 and Table 1, an approximate solution is acceptable only for $a \leq \delta$.

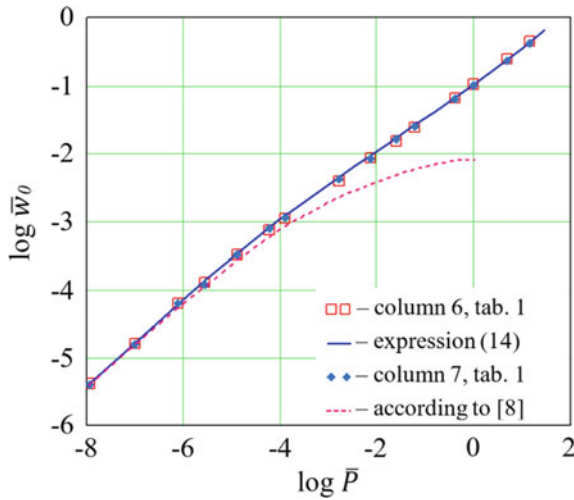


Fig. 3 Dependence of the relative introduction \bar{w}_0 on the dimensionless load \bar{P}

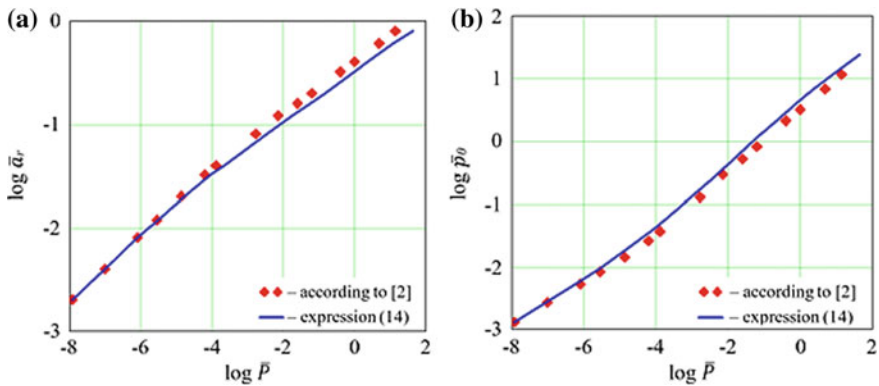


Fig. 4 dependence of the relative radius of the contact area \bar{a}_r and the relative maximum contact pressure \bar{p}_0 on a dimensionless load

Figure 4 shows the dependences of the relative radius of the contact area \bar{a}_r and the relative maximum contact pressure \bar{p}_0 on the dimensionless load \bar{P} obtained from Eq. (14) under the assumption of the Hertz theory.

As follows from Figs. 3 and 4, the best coincidence of the results of the proposed method with the exact solution [2] occurs when determining the indentation of the indenter (Fig. 3). This is quite understandable since the basis of the rigid model of a layered body is the dependence of the displacements along the axis of symmetry on the applied force. The systematic error in determining the radius of the

contact area and the maximum contact pressure is related to the difference in the contact from the Hertz's pressure distribution.

5 Conclusion

1. Using a simplified model of a layered body, an engineering technique has been developed for determining contact parameters when introducing a spherical indenter into it.
2. A comparison was made of the results obtained with the data of an exact solution of a similar problem [2], which presents certain difficulties for its practical application in engineering calculations, due to their complexity and laboriousness. The coincidence of the graphical dependencies of the contact parameters from the dimensionless force, which varies within ten orders of magnitude, with the results of accurate solutions [2] allows us to recommend the proposed engineering technique for practical use.
3. The best coincidence of the results according to the proposed method with the exact solution [2] takes place when determining the implementation value of a spherical indenter (Fig. 3). The maximum error in this case did not exceed 10%, and the average error for the reduced values of the relative implementation was 4.7%. An approximate solution for the indentation of a sphere into an elastic layer of finite thickness [8] is acceptable only for $a \leq \delta$.
4. The proposed method is recommended for use for solving problems of contacting a rough surface through a layer of polymer coating. In this case, the contact of a single asperity should be considered taking into account the influence of the remaining contacting asperities [21].

References

1. Kovalev EP, Ignat'ev MB, Semenov AP et al (2004) J Friction Wear 25:316–336
2. Makushkin AP (1993) Polymers in friction and seal assemblies at low temperatures. Mechanical Engineering, Moscow
3. Torskaya EV (2014) Modeling of frictional interaction of bodies with coverings. Dissertation, Moscow
4. Aleksandrov VM, Mkhitarian SM (1983) Contact problems for bodies with elastic coatings and interlayers. Nauka, Moscow
5. Giannakopoulos AT, Suresh T (1997) Indentation of solids with gradients in elastic properties. J Solids Struct 34:2357–2392
6. Aizikovitch SM, Aleksandrov VM, Vasiliev AS, Krenev LI, Trubchik IS (2011) Analytic solutions of mixed axisymmetric problems for functional gradient media. Fizmatlit, Moscow
7. Potelezhko VP (2006) The Bousinescu problem for a two-layer half-space. Mech Phy Process Surf Contact of Solid Bodies Mach Parts 2:27–32
8. Argatov II (2004) Approximate solution of an axisymmetric contact problem for an elastic layer of finite thickness. Probl Mech Eng Reliab Mach 6:35–40

9. Voronin NA (1993) Application of the theory of the elastic Hertz contact to the calculation of the stress-strain state of a layered elastic body. *Friction and Wear* 14:250–258
10. Voronin NA (2002) Calculation of elastic contact parameters and effective characteristics of the topocomposite for the case of interaction of the latter with a spherical indenter. *Friction Wear* 23:583–596
11. Ogar PM, Tarasov VA, Fedorov IB (2013) Control of stiffness of contact systems of sealing joints modern technologies. *Syst Anal Model* 1:2–27
12. Ogar PM, Tarasov VA (2013) Determination of the elastic characteristics of bodies with thin coatings. *Adv Mater Res* 677:267–272
13. Ogar PM, Gorokhov DB, Kozhevnikov AS (2016) Effective modulus of elasticity of a layered body. *Modern technologies. Syst Anal Model* 4(52):37–42
14. Kozhevnikov AS (2017) Simplified model of a layered body. *Mech XXI Century* 16:211–217
15. Ogar P, Kozhevnikov A, Fedorov V (2018) The reduced modulus of elasticity of a layered half-space. *MATEC Web Conf* 224:02051
16. Johnson K (1989) *Contact mechanics*. Mir, Moscow
17. Argatov II, Dmitriev NN (2003) *Fundamentals of the theory of elastic discrete contact*. Politechnica, St.-Peterburg
18. O'Sullivan TC, King RB (1988) Sliding contact stress field due to a spherical indenter on a layered elastic half-space, *ASME. J Tribol* 110:235–240
19. Peng W, Bhushan B (2001) Three-dimensional contact analysis of layered elastic/plastic solids with rough surfaces. *Wear* 249:741–760
20. Peng W (2001) *Contact mechanics of multilayered rough surfaces in tribology*. Dissertation, The Ohio State University
21. Ogar P, Alpatov Yu, Gorokhov D (2018) Relative contact area in metal-polymer joints. *MATEC Web Conf* 224:02051

Influence of Oxidation Products on Anti-wear Properties of Lubricants



B. I. Kovalsky, N. N. Lysyannikova and E. G. Kravcova

Abstract The article presents the research results of effect of oxidation products on anti-wear properties, including the absorption coefficient of the light flux, evaporation, viscosity, the amount of wear, the coefficient of thermal stress, and the coefficient of resistance to oxidation. The method of research for lubricating oils for thermo-oxidative stability, determining the diameter of a wear spot and the effect of oxidation products on the anti-wear properties of the oils under study are described using test and control tools such as a device for thermal oxidation of oils, a photometer for direct electrophoretic oxidized oils, three-ball friction machine, and electronic scales. The dependences of the light flux absorption coefficient, volatility, and viscosity on the test time were constructed, by which the dominant influence of oxidation products was determined and then the amount of converted thermal energy and the thermal stress coefficient were determined. The article proposes to determine the quality of the lubricant from the graphical dependences of the thermal stress coefficient on the light absorption coefficient. According to the dependences of the change in the anti-wear properties of oxidized oils on the absorption coefficient of the light flux, the authors determine the degree of influence of oxidation products on the anti-wear properties.

Keywords Motor oil · Absorption coefficient of the light flux · Volatility · Viscosity Thermo-oxidative stability · Anti-wear properties

1 Introduction

Motor oils are subject to high viscosity, anti-friction, anti-wear, and anti-oxidant properties. Since automatic boxes include several completely dissimilar units, a complex control system, the range of oil functions is very wide. Engine oil

B. I. Kovalsky · N. N. Lysyannikova (✉) · E. G. Kravcova
Siberian Federal University, Institute of Oil and Gas, 82/6, Svobodny Ave, Krasnoyarsk
660041, Russia
e-mail: Nataly.nm@mail.ru

lubricates, cools, and transmits torque and provides a friction clutch. A variety of materials in friction pairs (steel–steel, steel–metal–ceramic, steel–bronze, and steel–friction gasket) makes it difficult to select anti-friction additives. Diverse materials of parts, oxygen, water, oil, form electrochemical vapors that activate corrosive wear [1].

Thus, during the operation of machines and assemblies, the lubricants are subjected to mechanical, thermal, and chemical degradation and the temperature on the friction surface has an important factor influencing their lubricating properties.

The purpose of these studies is to determine the effect of the degree of oxidation of motor oils on their anti-wear properties.

2 Methodology

For the study used the means of control and testing: a device for determining the thermal-oxidative stability of oils, a photometric device, electronic scales, and a three-ball friction machine.

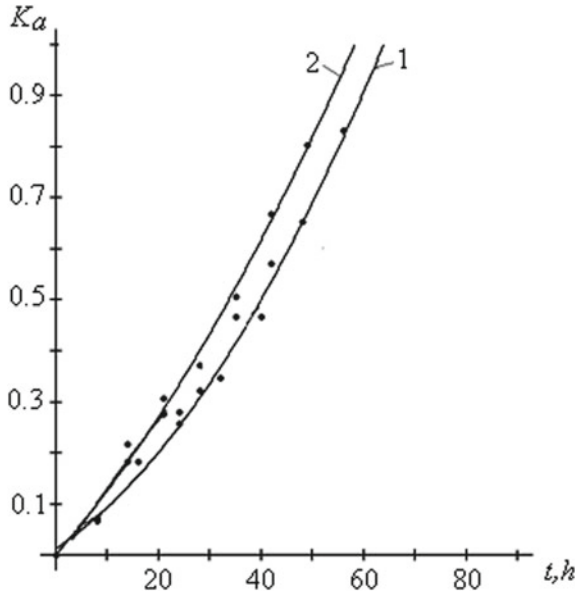
A sample of engine oil weighing $100 \text{ g} \pm 0.1 \text{ g}$ was poured into the glass of the device for determining the thermo-oxidative stability and was subjected to thermal oxidation at a temperature of $180 \text{ }^\circ\text{C}$. After every 8 h of testing, an oil sample was taken; the first part of the sample was used for direct photometry, viscosity, and volatility measurements. The degree of oxidation of the oil was estimated by the absorption coefficient of the light flux, changes in viscosity and volatility. The second part of the test was tested on a three-ball friction machine with a ball-to-cylinder friction scheme [2, 3]. The anti-wear properties of motor oil were evaluated by the diameter of the wear spot and the current flowing through the friction contact from the stabilized power source [4, 5]. The maximum current value was assumed to be 100 μA . The loss of oil for friction was compensated by adding oil up to 100 g, while their mass was recorded and the effect on the oxidation processes was evaluated. The research methodology was tested in [6–20]. According to the obtained data, graphic dependencies were built.

Mobil Super 2000 10 W–40 SJ/SL/CF motor oil semi-synthetic (shown in curve 1) and Mobil Super 3000 5 W–40 SJ/SL/SK/CF synthetic oil (shown in curve 2) were investigated.

3 The Results of Research

The dependences of the absorption coefficient of the light flux on the time of testing are presented in Fig. 1. The process of oxidation of motor oils without adding oil (curves 1 and 2) is described by the regression equation of the second order

Fig. 1 Dependence of the absorption coefficient of the light flux on the time of testing at a temperature of 180 °C of semi-synthetic Mobil Super 2000 10 W-40 SJ/SL/CF (1) motor oil and synthetic Mobil Super 3000 5 W-40 SJ/SL/SK/CF (2)



$$K_a = at^2 + bt + c, \tag{1}$$

where *a*, *b*, and *c*—factors characterizing the influence of oil aging products on the oxidation process.

Regression equations for oils have the form.

$$\text{Mobil Super 2000} \quad K_a = 1.36 \times 10^{-4}t^2 + 0.007t + 0.01 \tag{2}$$

$$\text{Mobil Super 3000} \quad K_a = 9.55 \times 10^{-5}t^2 + 0.01t + 0.002 \tag{3}$$

Correlation coefficient is 0.99.

According to dependencies, it was found that in semi-synthetic Mobil Super 2000 oil, the time of onset of formation of oxidation products that affect the properties of the oil is 10 h, and in Mobil Super 3000 synthetic oil—20 h, and the optical density at 20 h. Mobil Super 3000 is less than semi-synthetic by 10%, therefore, oxidation products have a greater effect on synthetic oil.

The viscosity of the oils was estimated by the coefficient *K_μ* of the relative viscosity, determined by the ratio of the viscosity of the oxidized oil to the viscosity of the original. The effect of oxidation products on the viscosity of oils was estimated by the dependence of the relative viscosity coefficient on the absorption coefficient of the light flux (Fig. 2). It is shown that oxidation products have a slight effect on viscosity, and a decrease in its value is caused by the destruction of a viscous additive at a test temperature of 180 °C.

Volatility for the studied oils varies slightly, however, oxidation products (Fig. 3) for Mobil Super 3000 oil (curve 2) reduce volatility by approximately 5 grams.



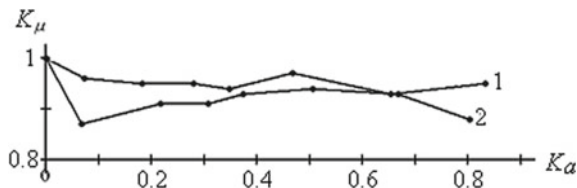
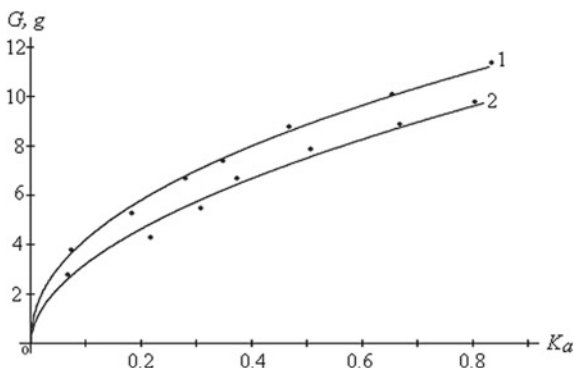


Fig. 2 Dependence of the coefficient of relative viscosity on the absorption coefficient of the light flux when testing a semi-synthetic Mobil Super 2000 (1) and synthetic Mobil Super 3000 (2) engine oils

Fig. 3 Dependence of volatility on the absorption coefficient of the light flux when testing a semi-synthetic Mobil Super 2000 (1) and synthetic Mobil Super 3000 (2) engine oils



Thus, as a result of self-organization processes, during the oxidation of motor oils, excess thermal energy is converted into products that change optical properties and volatility, so if volatility is converted into the volatility factor K_G , determined by the mass ratio of the evaporated oil to the mass of the remaining sample, the amount of converted thermal energy E_t can be expressed by the sum of the coefficients:

$$E_t = K_a + K_G \tag{4}$$

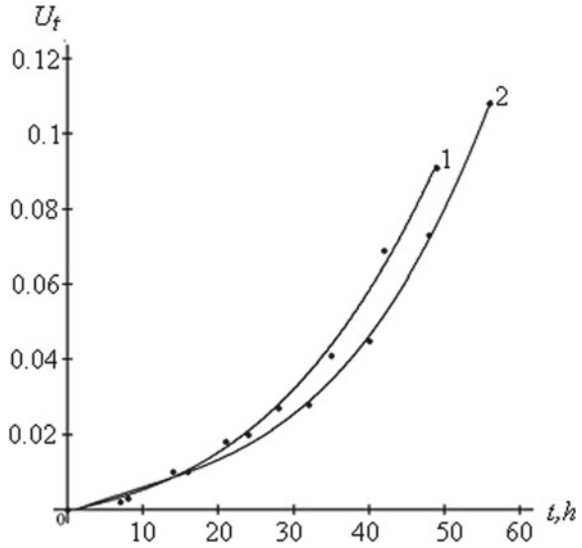
where K_a and K_G —are the absorption coefficients of the light flux and volatility, respectively.

The amount of thermal energy discharged is determined by the values of the absorption coefficient of the light flux and volatility, which in turn determine the resistance of the oil under study to thermal effects. There is a parallel discharge of thermal energy, then the equivalent oxidation resistance R_E is determined by the formula:

$$R_E = (K_a \cdot K_G) / K_a + K_G \tag{5}$$

In the likeness of Ohm’s law, the discharged heat flow is determined by the value of the energy of transformation of the E_t , and the coefficient of thermal voltage U_t , as the coefficient of excess energy is determined by the expression

Fig. 4 Dependence of the coefficient of thermal stress in the process of self-organization from the time when testing a semi-synthetic Mobil Super 2000 (1) and synthetic Mobil Super 3000 (2) engine oils



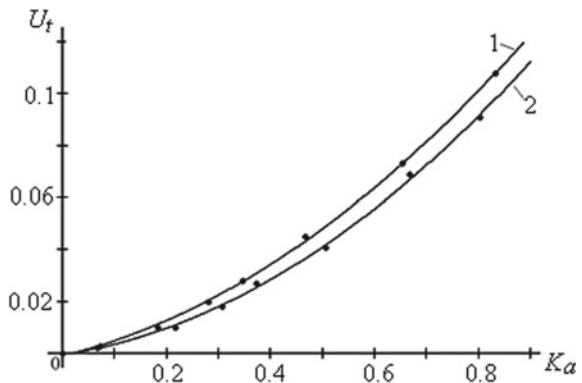
$$U_t = E_t \cdot R_E = K_a \cdot K_G \tag{6}$$

The dependences of the thermal stress coefficient U_t in the process of self-organization during the oxidation of oils on the time of testing are shown in Fig. 4.

In Fig. 4 demonstrates dependence, which shows the increase in heat flux during the test. The intensity of the increase of the coefficient U_t is associated with an increase in the influence of the conversion coefficients of thermal energy E_t and on the oxidation resistance R_E , which depend on the resulting oxidation products and their influence on the overall transformation process.

The dependence of thermal stress on the absorption coefficient of the light flux (Fig. 5) is described by a polynomial of the second degree

Fig. 5 Dependence of the coefficient of thermal stress emitted during the self-organization during oxidation on the absorption coefficient of the light flux when testing a semi-synthetic Mobil Super 2000 (1) and synthetic Mobil Super 3000 (2) engine oils



$$U_t = aK_a^2 + bK_a + c \quad (7)$$

where a , b , and c —coefficients characterizing the intensity of self-organization processes during the oxidation of oils.

Regression equations of these dependencies have the following form:

$$\text{Mobil Super 2000} \quad U_t = 0.1K_a^2 + 0.05K_a - (9.16 \times 10^{-4}) \quad (8)$$

$$\text{Mobil Super 3000} \quad U_t = 0.1K_a^2 + 0.03K_a - (5.56 \times 10^{-4}) \quad (9)$$

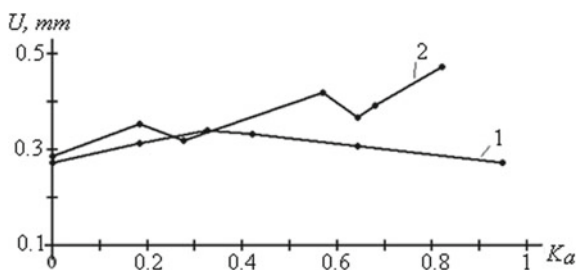
According to the dependences of the coefficient of thermal stress in the process of self-organization during oxidation of oils on the absorption coefficient of light flux (Fig. 5), it was found that the higher the values of the coefficient of thermal stress, the higher the quality of the lubricant, since for the formation of the same concentration of oxidation products requires a greater amount of thermal energy.

In Fig. 6 shows the dependence of the change in the anti-wear properties of oxidized oils on the absorption coefficient of the light flux. For semi-synthetic oil (curve 1), anti-wear properties vary in the range from 0.273 to 0.34 mm, and in synthetic oil from 0.287 to 0.473 mm when the absorption coefficient of the light flux is changed to 0.947.

According to the data (Fig. 6), for semi-synthetic oil (curve 1), at first, the anti-wear properties deteriorate to a value of the coefficient $K_a = 0.32$; however, with values of the absorption coefficient of the light flux greater than 0.32, they increase. The improvement of anti-wear properties can be explained by the appearance of a certain concentration of acidic oxidation products, which have a favorable effect on the formation of protective chemisorption layers on the friction surfaces. To the value of the coefficient $K_a = 0.32$ friction boundary layers were created due to physical adsorption.

A clear dependence of the anti-wear properties of oxidized oils has not been established with the coefficients of resistance to oxidation (Fig. 7a) and thermal stress (Fig. 7b). This is due to the fact that the concentration of oxidation products and additives in the oil is oil top up, and, besides, with different concentrations of oxidation products, physical or chemical adsorption can affect the anti-wear properties of the oil. This is confirmed by the data on topping up. Thus, when

Fig. 6 Dependence of the amount of wear on the absorption coefficient of the light flux when testing a semi-synthetic Mobil Super 2000 (1) and synthetic Mobil Super 3000 (2) engine oils



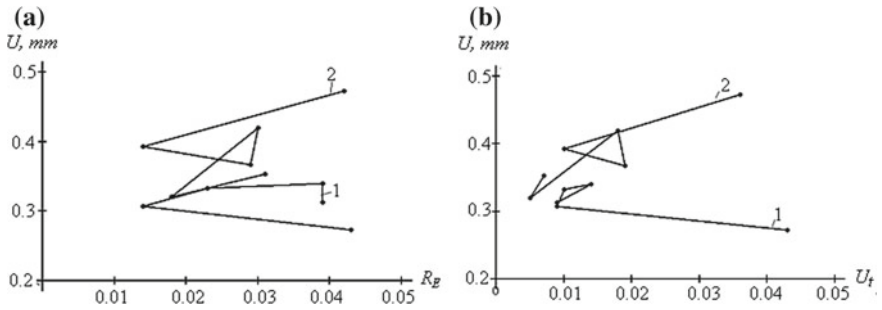
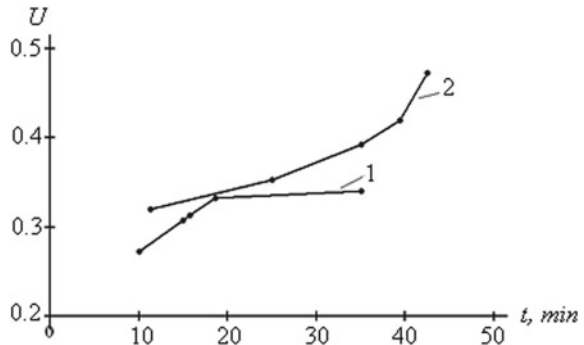


Fig. 7 Dependence of the amount of wear on the resistance coefficient to oxidation (a) and on the coefficient of thermal stress (b) when testing semi-synthetic Mobil Super 2000 (1) and synthetic Mobil Super 3000 (2) engine oils

Fig. 8 Dependence of the amount of wear on the time of formation of protective layers on the friction surfaces in the study of semi-synthetic Mobil Super 2000 (1) and synthetic Mobil Super 3000 (2) engine oils



testing partly synthetic oil Mobil Super 2000, the topping was 49.8 g, and that of synthetic Mobil Super 3000 was 80.3 g.

The general trend in the dependence of anti-wear properties on the duration of the formation of protective boundary layers (Fig. 8) is characteristic of both semi-synthetic and synthetic oils. With increasing time of formation of protective layers, wear increases.

Comparing the data obtained during the testing of semi-synthetic and synthetic oils, it can be seen that with a semi-synthetic oil with an increase in the coefficient K_{ox} , current fluctuations decrease. That is, oxidation products more actively form protective boundary layers, apparently due to the mineral base. In addition, the duration of plastic and elastoplastic deformations of a semi-synthetic oil decreases with an increase in the coefficient K_{ox} , and increases with a synthetic one.

4 Conclusion

Research has shown that oxidation products ambiguously affect the anti-wear properties of oils and the reason for this is their heterogeneous composition, which depends on the basic basis, the quality of additives used and their tendency to oxidation.

References

1. Matveevsky RM (1969) Investigation of the temperature resistance of the boundary layer lubrication in friction, Methods for assessing extreme pressure and anti-wear properties of lubricants, Moscow
2. Kovalsky BI, Griбанov ME (1982) Device for testing rubbing materials and oils. RU A.S. 983522 23 Dec 1982
3. Kowalski BI, Bezborodov YrN, Petrov ON, Tihonov VI (2011) Device for testing rubbing materials and oils. RU Patent 2428677, 10 Sep 2011
4. Kovalsky BI, Titkovsku NN, Mishkin NK (1991) Method for determination of lubricity of oils. RU A.S. 1,054,732, 15 Aug 1991
5. Kovalsky BI, Vasilyev SI, Kovalsky SB, Barkov DG (2002) Method for determination of lubricity of oils. RU Patent 2,186,386, 27 Jul 2002
6. Kovalsky BI, Derevyagina LM, Kirichenko IA (1992) The method for determining the thermal-oxidative stability of lubricants. RU Patent 2,057,326, 04 June 1992
7. Kovalsky BI, Vasilyev SI, Yanaev EYu (2003) The method for determining the thermal-oxidative stability of lubricants. RU Patent 2,219,530, 20 Dec 2003
8. Kovalsky BI, Vasilyev SI, Bezborodov YuN, Gavrillov VV (2004) Method for determination of thermal-oxidative stability of lubricants. RU Patent 2,274,850, 30 Aug 2004
9. Kovalsky BI, Vasilyev SI, Erashov RL et al. (2004) The method for determining the performance of lubricating oils. RU Patent 2,222,012, 20 Jun 2004
10. Kovalsky BI, Vasilyev SI, Bezborodov YuN, Badiina AA (2005) Method for determination of thermal-oxidative stability of lubricants. RU Patent 2,247,971, 10 Mar 2005
11. Kovalsky BI, Danilenko VS, Malysheva NN, Bezborodov YuN (2008) The method for determining the thermal-oxidative stability of lubricants. RU Patent 2,318,206, 27 Feb 2008
12. Kovalsky BI, Malysheva NN, Metelitsa AA, Bezborodov YuN (2008) The method of determining the thermal-oxidative stability of lubricants. RU Patent 2,334,976, 27 Sept 2008
13. Kovalsky BI (2005) Methods and means of improving the effectiveness of use of lubricants: monography. Novosibirsk
14. Bezborodov YuN (2007) Methods and means of increasing the efficiency of use of gear oils: monography. Krasnoyarsk
15. Kovalski BI, Bezborodov YrN, Lysyannikova NN (2011) Controls lubricants for machines and mechanisms of varying degrees of loading: monography. Krasnoyarsk
16. Kovalski BI, Yudin AV, Runda MM, Berko AV (2012) Method for determining anti-wear properties of lubricants. RU Patent 2,454,653, 27 June 2012
17. Malysheva NN, Kravtsov EG, Kowalski BI (2014) Method for determining the quality of lubricating oils. RU Patent 2,528,083, 10 Sept 2014
18. Kovalski BI, Bezborodov YuN, Kowalski SB et al (2010) Method of research anti-wear properties and mechano-chemical processes at the boundary sliding friction. Bull Tomsk Polytech Univ 316(2):42–46

19. Kovalski BI, Bezborodov YuN, Maltseva EG (2011) Influence the electrical potential on the mechano-chemical processes at the boundary sliding friction. J Siberian State Aerosp Univ (Academician M. F. Reshetnev, Krasnoyarsk) 1(34):135–139
20. Kovalski BI, Shram VG, Petrov ON, Sokolnikov AN (2014) The mechanism of formation of the protective boundary lubricating layer. News of the Tula State Univ 3:26–32

Experimental Modeling of Wearing the Friction Surfaces of “Piston-Cylinder” Tribounit



A. Doikin and K. Gavrilov

Abstract Experimental studies of friction and wear for piston skirt and cylinder liner materials at hydrodynamic mode with using a friction machine have been carried out. Influence of initial roughness and lubricant on a final micro-relief of contacting surfaces after experiment was investigated. The experimental studies were carried out according to a “roller-pad” scheme. Three brands of motor oil from the main groups for diesel engines were used. The first is from the group of oils made from the sulphurous oil. The second is from the group of oils containing alkylsalicylate additives. The third is from the group of oils with packages of dealkylation phosphate additives. The wear rate and the friction coefficient in each experiment were determined. Experiment results show that the parameters of the equilibrium roughness do not depend on their initial values, but depend on the applied engine oil. The hypothesis, which explains the reasons of relief change of friction surfaces at hydrodynamic mode, is proposed.

Keywords “Piston-cylinder” tribounit · Friction surfaces wear · Surface roughness parameters

1 Introduction

The interaction of rough surfaces determines many processes in electrical and heat engineering in the transmission of electrical and thermal energy through mobile and fixed contacts, friction, lubrication, and wear processes in mechanical engineering, automobile industry, engine building, and other industries [1–4].

Enhancing tribological properties of engine components are important since nearly one-third of the fuel energy is used to overcome engine friction [5–9]. In 2009, 208 billion liters of fuel were used to suppress friction losses in passenger

A. Doikin (✉) · K. Gavrilov
South Ural State University, 76, Lenin Avenue, Chelyabinsk 454080, Russia
e-mail: doikinaa@susu.ru

cars [3]. Lubrication is important to reduce losses in the mechanical parts. However, friction in lubricated parts still represents about 25% of the power loss in engines [10].

At present, in order to increase the oil capacity of the “piston-cylinder” tribounit, honing of the cylinder liner is used. By honing, a grid of scratches is formed on the cylinder liner, so it is commonly believed that as a result of it happens a reliable retention of grease on the rubbing surfaces of the parts, their running-in comes faster, the wear of the parts decreases and the service life of the engine increases.

Despite the fact that during the operation of the engine in the way “piston-cylinder” hydrodynamic friction mode sets on, also on the surface of the liner and the piston rubbings are formed in the form of clear parallel bands in the direction of friction. When examining them with the microscope it is seen that they constitute the grooves. The surface of these grooves has a smooth fine-grained structure, and there are no traces of cutting, scoring, cracking, plastic deformation. The purpose of this work is to find out the cause of their appearance, as well as to determine the linear integral wear intensity of the materials of the “piston-cylinder” tribounit when it is lubricated with different oils.

2 The Methodology of the Experiments

The experiments were carried out on the friction machine SMC-2. Friction unit (Fig. 1) for experimental studies contains a roller 1 made of a sleeve material (alloy cast iron) with a diameter of 90 mm and a width of 20 mm mounted on the lower shaft of the friction machine. A bronze bushing of the current collector 8 with a semicircular groove for the string 6 is installed on the same shaft. Pad 2 is made of a material of the piston (aluminum alloy AK-4) and has the size of the working surface in terms of 5×10 mm and fixed in the tool holder 3, which is electrically isolated from the body of the friction machine. The load on the pad is set using the lever (not shown in the diagram) and the loading device of the friction machine. The oil is supplied to the friction zone by means of a dropper, which is adjusted to the flow rate of 1 drop in 4–5 s. The thermocouple 5 is clamped between the back of the pad and the holder, which ensures proper thermal contact of the junction and the pad.

The decrease in direct current voltage on the contact “roller-pad” was measured with the aim of determining the metal contact between surfaces of the roller and pads. The load resistance is 11.6Ω excludes the overload of the direct current power source when the metallic contact occurred. The pad is connected to the positive contact of the power supply to minimize the transfer of metal and the effect of direct current on the real characteristics of the oil layer. In addition, the circuit is closed for a short period of time at the time of voltage measurement.

The moment of friction was measured by the friction machine torque sensor and recorded on the tape recorder PSR. The measurement system is set to increased sensitivity.

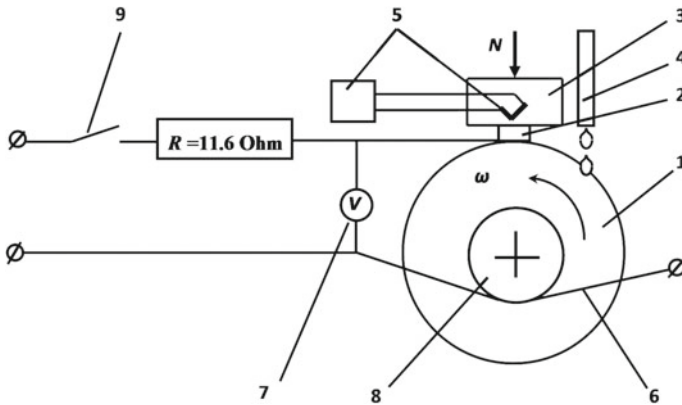


Fig. 1 Experimental scheme of the friction unit: 1—steel roller, 2—pad, 3—holder, 4—oil drip, 5—thermocouple, 6—current collector string, 7—voltmeter, 8—current collector, 9—switch

The friction path was calculated by the known number of turns fixed by the shaft speed counter of the friction machine. Based on the previous experience of the authors [10–13], the friction path required to achieve the wear of the pad is sufficient to measure on the existing equipment, is 200,000 turns of the roller (56,000 m) and is the same for all experiments. The angular velocity of rotation of the roller was maintained constant and equal to 104.6 s^{-1} , which corresponds to the maximum linear velocity of the piston equal to 4.71 m/s. The compression load of the pad and roller was selected in such a way as to provide a constant nominal pressure P_a corresponding to the maximum pressures in the interface and equal to 4.6 MPa. The temperature of the pad was maintained during the tests at the level of the operating temperature of the unit, that is, equal to $140 \pm 10 \text{ }^\circ\text{C}$ with fan and infrared heater. The radial run-out of the working surface of the roller did not exceed 0.01 mm and was provided by the groove of the roller mounted on the shaft of the friction machine, with the following polishing.

The profilograms of the surfaces of the samples were shot using the profilograph-profilometer ABRIS PM-7 in nine points of the circumference of the roller and at one point on the pad in view of its small size. The parameters of the liner and roller roughness were calculated by known methods [14–16]. The initial roughness of the roller (Fig. 2) set based on the profilogram (Fig. 3), removed from the real cylinder liner of the engine type CHN 13/15. The roughness was applied by analogy with the liner, i.e., in cross directions at an angle of $30\text{--}60^\circ$. The values of the parameters of the liner and roller roughness before the experiment (arithmetic mean for three experiments) are given in Table 1, which shows their qualitative coincidence. After installing the pad and roller, the pad was lapped to the roller through the grinding sandpaper M40 thickness 0.15–0.16 mm, which provided a radial clearance required for the supply of engine oil in the friction area.

After every two thousand turns of the roller, the temperature of the pad, the friction moment and the voltage drop on the oil layer between the pad and the roller

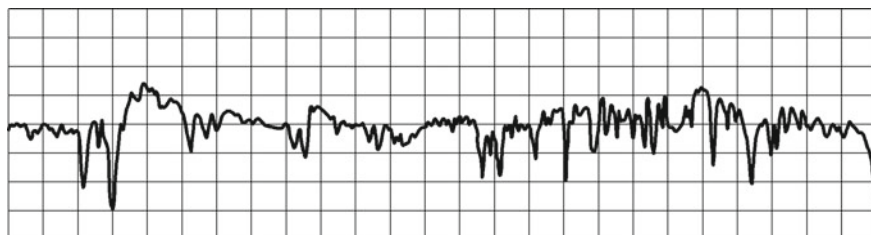


Fig. 2 Profilogram of the roller surface before the experiment. *Division price* horizontal 0.3 mm; vertical 0.0025 mm

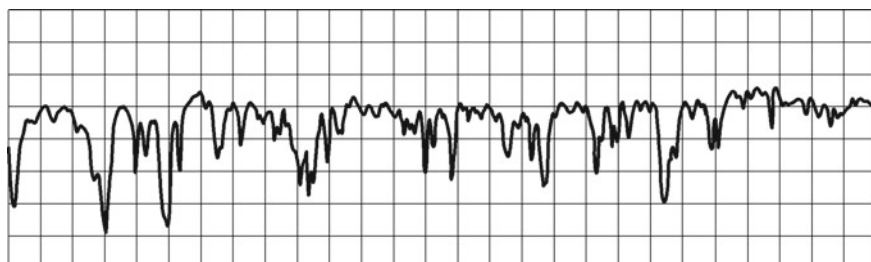


Fig. 3 Profilogram the surface of the liner after honing. *Division price* horizontal 0.16 mm; vertical 0.002 mm

Table 1 Roughness parameters

Parameter	Sample	
	Liner	Roller
The arithmetical mean deviation of profile R_a , μm	1.37	1.16
The height of roughness at ten points R_z , μm	9.75	7.12
The maximum height of the profile R_{max} , μm	10.50	9.79
Arithmetic mean value of the step of micro-irregularities S_m , μm	101.52	86.83

were recorded, for which a DC voltage was supplied for a short time. The measurement results were entered into the test report. After the tests, the obtained data were processed and the friction coefficient and its average integral value f were determined.

The weight of the pad was measured with an accuracy of 5×10^{-5} grams before and after the experiment. The linear integral wear intensity was calculated by the formula:

$$I_h = \frac{\Delta m}{\rho \cdot A_a \cdot L}$$

where $\Delta m = m_1 - m_2$ —the weight changing of the pad as a result of wear; ρ —aluminum alloy density AK-4; A_a —the nominal area of contact; L —friction way.

3 Experimental Result

For testing, three brands of motor oil were selected from the main groups for diesel engines of tractors and road construction equipment. The first M-10DM from the group of oils made from the sulphurous oil. The second—Shell Rimula R3X from the group of oils containing additives that are resistant to thermo-mechanical stress, mainly alkylsalicylate. Third—Mobil Delvac XHP from the group of oils with packages of dealkylation phosphate additives [17–20].

To study the effect of the initial surface treatment of the roller on the roughness parameters, experiments 1 and 2 were carried out (Table 2) on motor oil M-10DM. To study the effect of lubricant properties on roughness parameters, experiments 3 and 4 were carried out on Shell Rimula R3 and Mobil Delvac XHP engine oils. In experiments no. 1, 3, and 4 the surface roughness of the roller was applied as described above, in experiment no. 2 the surface of the roller was polished. The results of the experiments are given in Table 2. Taken after the experiments, the profilograms of the roller and pad is shown on the same scale and combined in Fig. 4.

As shown in Fig. 4, regardless of the initial roughness, the machined surfaces of the roller and pad are complementary. Under the complementarity of the surfaces, we understand the fact that opposite the ledge on the surface of the roller is a cavity on the surface of the pad and opposite the cavity—the corresponding protrusion. The following hypothesis is proposed to explain this phenomenon. When the protrusion moves near the opposite surface, the liquid spreads to the sides, as a result, mass transfer processes between the oil film and the other surface are sharply accelerated near this protrusion. Since the oil has a viscosity, this perturbation spreads over a short distance and quickly fades. The highest rate of fluid movement develops near the protrusion, which provides an increase in the rate of oxidation process. This leads to cavities on the opposite surface.

Table 2 Experimental result

S. No.	Oil	I_h	f	$R_a, \mu\text{m}$	$R_z, \mu\text{m}$	$R_{\text{max}}, \mu\text{m}$	$S_m, \mu\text{m}$
1	M-10DMM	2.248×10^{-10}	0.071	1.29 ^a	6.67	9.68	125.77
				2.58 ^b	17.04	21.28	78.52
2	M-10DM	0.409×10^{-10}	0.136	0.22	2.16	4.10	39.44
				2.91	19.36	25.46	83.92
3	Shell Rimula R3X	1.363×10^{-10}	0.108	0.93	6.69	9.09	65.46
				3.67	17.84	24.75	168.47
4	Mobil Delvac XHP	3.788×10^{-10}	0.116	1.27	8.00	10.60	69.25
				2.61	17.55	25.25	86.48

^aThe value of the parameter before the experiment; ^bThe value of the parameter after the experiment

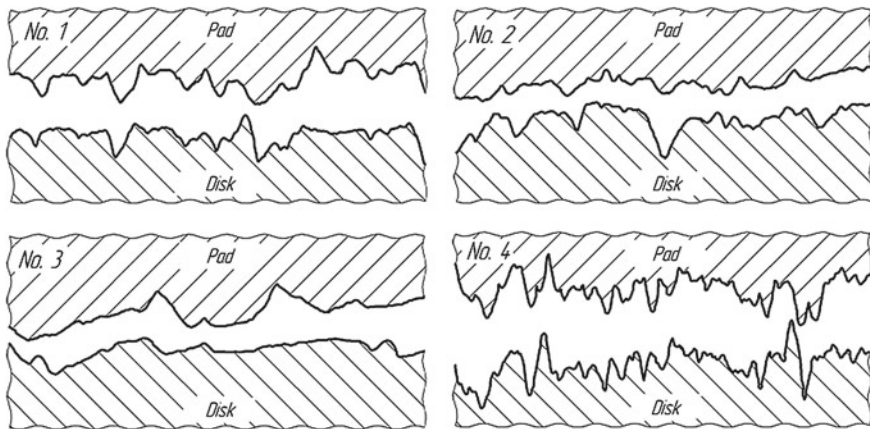


Fig. 4 Profilograms of the roller and pad after the experiments

4 Conclusion

As a result of the experiments, it was found that the parameters of the equilibrium roughness (R_a , R_z , R_{max} , S_m) do not depend on their initial values, but depend on the applied engine oil. Since in all experiments there was no metal contact between the pad and the roller, the most likely cause of the transverse roughness of the roller and the pad are oxidative and cavitation phenomena in the oil film. Thus, the difference in the roughness parameters is explained by the different oxidizing and rheological properties of the tested oils, due, in particular, to the additives introduced into them.

Acknowledgements South Ural State University is grateful for financial support of the Ministry of Education and Science of the Russian Federation (grant No. 9.7881.2017/8.9).

References

1. Vencel A, Rac A (2014) Diesel engine crankshaft journal bearings failures: case study. *Eng Fail Anal* 44:217–228
2. Javorova J, Mazdrakova A, Andonov I, Radulescu A (2016) Analysis of HD journal bearings considering elastic deformation and non-newtonian Rabinowitsch fluid model. *Tribol Ind* 38 (2):186–196
3. Holmberg K, Andersson P, Erdemir A (2012) Global energy consumption due to friction in passenger cars. *Tribol Int* 47:221–234
4. Gavrilov K, Goritskiy Yu, Migal I, Izzatullov M (2017) A numerical model for estimation of service life of tribological systems of the piston engine. *Tribol Ind* 39(3):329–333
5. Rozhdestvensky A, Gavrilov Y, Doikin K (2019) Influence of location of lubrication sources on hydromechanical characteristics of diesel crankshaft bearings. *Lect Notes Mech Eng* 983–991

6. Gavrilov K, Doikin A, Izzatulloev M, Goritskiy Y (2019) Numerical model of mechanical interaction of rough surfaces of journal bearings of piston engine. *Lect Notes Mech Eng* 993–1002
7. Cupillard S, Glavatskih S, Cervantes M (2008) Computational fluid dynamics analysis of a journal bearing with surface texturing. *Proc Inst Mech Eng Part J Eng Tribology* 222(2): 97–107
8. Kango S, Sharma R, Pandey R (2014) Thermal analysis of microtextured journal bearing using non-newtonian rheology of lubricant and JFO boundary conditions. *Tribol Int* 69:19–29
9. Ligier JL, Noel B (2015) Friction reduction and reliability for engines bearings. *Lubricants* 3 (3):569–596
10. Lazarev VE, Usoltsev NA (2010) The wear rate of antifriction layer of bearings of internal combustion engine under boundary friction conditions. *Tyazheloe Mashinostroenie* 9:18–22
11. Lazarev VE, Gavrilov KV, Doikin, AA, Seurd-Base J, Vorlaufer G (2014) Estimation of the tribotechnical parameters of the piston skirt-cylinder liner contact interface from IC-engine for decreasing the mechanical losses. In: 1st International conference on energy production and management in the 21st century: the quest for sustainable energy. *WIT Trans Ecol Environ* 190(1):625–635
12. Levanov I, Doykin A, Zadorozhnaya E, Novikov R (2017) Investigation antiwear properties of lubricants with the geo-modifiers of friction. *Tribol Ind* 39(3):302–306
13. Goryacheva IG, Morozov AV, Rozhdestvensky YV, Gavrilov KV, Doikin AA (2013) Development of method for calculating and experimentally evaluating tribological parameters of piston-cylinder tribosystem of diesel engine. *J Friction Wear* 34(5):339–348
14. Hebda M, Chichinadze A (1989) Handbook of tribotechnology: theoretical foundations. *Mashinostroenie, Moscow*
15. Goritskiy Y, Ismailova Y, Gavrilov K, Rozhdestvensky Y, Doikin A (2015) A numerical model for mechanical interaction of rough surfaces of the “piston-cylinder liner” tribosystem. *FME Trans* 43:249–253
16. Goritskiy Y, Gavrilov K, Rozhdestvensky Y, Doikin A (2015) A numerical model of mechanical interaction between rough surfaces of tribosystem of the high forced diesel engine. *Procedia Eng* 129:518–525
17. Rozhdestvensky Y, Gavrilov K, Doykin A, Mukhortov I (2010) Influence of viscosity-temperature properties of motor oils on hydromechanical characteristics of piston-cylinder tribosystem. *Dvigatelistroyeniye* 2:23–26
18. Rozhdestvensky Y, Gavrilov K, Doykin A, Levanov I (2013) Numerical and experimental investigations of “piston-cylinder” tribosystem of diesel engine. In: 5th world tribology congress, vol 2. WTC, pp 1255–1258
19. Rozhdestvensky Yu, Gavrilov K, Doikin A (2017) Forced diesel piston tribological parameters improvement. *Procedia Eng* 206:647–650
20. Rozhdestvensky Yu, Gavrilov K, Doikin A (2017) Development of technical solutions for forced diesel main tribosystems. *Procedia Eng* 206:651–655

Investigation of Influence of Steel SH 15 on Oxidation and Anti-wear Properties of Mineral Oil



E. G. Kravtsova, B. I. Kowalsky and N. N. Lysyannikova

Abstract The article presents the results of research on effect that SH 15 steel has on processes of oxidation and anti-wear properties of Spectrol Super Universal 15W-40 SF/CC mineral engine oil with the use of a photometric method. This study suggests new factors that account for steel's effect on thermo-oxidative stability, wear, frictional contact conductance coefficient, forming time of frictional contact, and lubricative properties. The effects of steel on oxidative processes and anti-wear properties of oil and steel's influence coefficients on oxidation processes and anti-wear properties were researched. It was established that SH 15 steel influences oxidation processes and wear, it can show both catalytical and inhibitory effects as well as oxidation of mineral oil with steel ambiguously affects the volatility of oil, and the formation time of nominal friction contact area was determined from the current recording diagrams on computer display for the duration of plastic and elastoplastic deformations and its electrical conductivity and lubricity due to the products of chemisorption processes occurring on surfaces.

Keywords Luminous flux absorption ratio · Volatility · Anti-wear properties criteria · Lubricative properties ratio · Motor oil

1 Introduction

Processes which take place in tribosystems are determined by physicochemical properties of friction pair's materials, and these processes lead to the formation of miscellaneous structures on frictional areas. [1–10] Intensity of these processes does not depend on external factors only (load, surface velocity, temperature), and it is also determined by friction pair's materials interference, lubricant oil, and products of its oxidation and thermal destruction [11–20]. In this regard, research on the role

E. G. Kravtsova (✉) · B. I. Kowalsky · N. N. Lysyannikova
Siberian Federal University, Institute of Oil and Gas, 82/6, Svobodny Ave,
Krasnoyarsk 660041, Russia
e-mail: Rina_986@mail.ru

of materials of friction pairs in oxidative processes that occur in lubricating oil and the influence of the products of these processes on the anti-wear properties of oxidized oils is acquiring important scientific and practical significance.

The goal of the research is to determine the effects of SH 15 steel on the indicators of thermo-oxidative stability and anti-wear properties of Spectrol Super Universal 15W-40 SF/CC mineral engine oil.

2 Methodology

The research method consisted of two stages of oil testing: at the first stage, the oil was thermostatted at 180 °C with stirring without steel and evaluating anti-wear properties, and at the second stage, it was tested using the same technology with steel. The following instruments were used as controls: a device for thermostating the oil, a photometer, a three-stroke friction machine with a “ball—cylinder” element, and electronic scales. Thermal stability was evaluated by the absorption ratio of the luminous flux determined by volatility and direct photometry of the oil at a thickness of the photometric layer of 2 mm by passing monochromatic light from the red spectrum through the layer of oil.

Tribotechnical characteristics were determined by the arithmetic mean of the diameter of the wear spot on three balls in two parallel experiments, the electrical conductivity of the friction contact, the time of formation of the nominal area of the friction contact, and the lubricating properties ratio. The friction parameters were: load—13 N; sliding speed—0.68 m/s; oil temperature in the volume—80 °C; and test time—2 h. A constant current of 100 μ A from an external stabilized voltage source of 3 V was passed through one of the balls.

Based on determined errors of measuring instruments, a decision was made to carry out a triple testing of the same oil, which ensured sufficient accuracy of the obtained results. Average relative error of each measurement does not exceed 3% [9].

3 The Results of Research

Figure 1 shows the dependences of the luminous flux absorption ratio K_f and volatility G on the time of oxidation of mineral oil without steel and with steel. An insignificant increase in these parameters in the presence of SH 15 steel at the beginning of the oxidation process, $K_f \approx 0.6$ units, was established. However, with an increase in the oxidation time from 30 to 40 h, oxidative processes slow down during the oxidation of oil with steel, and the volatility of the oil almost coincides with the volatility of the commercial oil.

The anti-wear properties of the oil (Fig. 2) were evaluated by the arithmetic mean value of the diameters of wear spots on three balls (Fig. 2a). It was

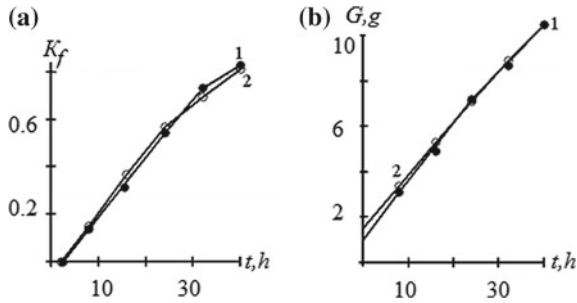


Fig. 1 Dependences of the luminous flux absorption ratio (a) and volatility (b) on the testing time of Spectrol Super Universal 15W-40 SF/CC mineral engine oil: 1—without steel; 2—with SH 15 steel

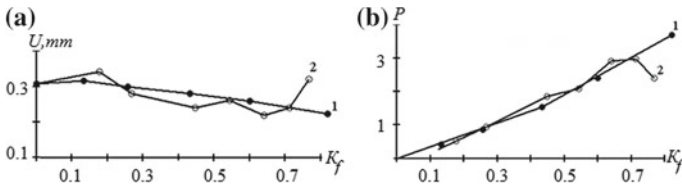


Fig. 2 Dependence of the diameter of the wear spot (a) and the criterion of anti-wear properties (b) on the luminous flux absorption ratio when testing the Spectrol Super Universal 15W-40 SF/CC mineral engine oil: 1—without steel; 2—with SH 15 steel

established that for commercial oil (curve 1), the diameter of the wear spot U decreases with an increase in the concentration of oxidation products, expressed by the coefficient K_f . For oil tested with steel (curve 2), wear is less than the commercial oil tested without steel in the range of K_f variation from 0.25 to 0.7 units.

To assess the anti-wear properties of oxidized oils, criterion P (Fig. 2b) was proposed, which characterizes the concentration of oxidation products in the area of friction contact and is determined by the ratio

$$P = K_f / U \tag{1}$$

where U —arithmetic mean value of the wear spot diameter on three balls, mm.

It was established that for oil tested without steel (curve 1), the function $P = f(K_f)$ has two linear sections with different rate of change of criterion P , which indicates an increase in the anti-wear properties of the oil at values of the coefficient $K_f > 0.4$ units. For oil tested with steel, the values of criterion P (curve 2) fluctuate, increasing anti-wear properties or lowering them. This indicates that steel periodically discharges products formed on its surface into oil. After researching surface of the steel after oxidation processes, two layers were determined, and the top layer can be easily erased.



To assess the effect of steel on the oxidation processes and the anti-wear properties of the oil, the coefficients of the effect of steel on the oxidation processes K_{VSO} and the anti-wear properties K_{VSI} are proposed, which are determined by the ratio

$$K_{VSO} = E_{TOS}^O / E_{TOS}^S \quad (2)$$

$$K_{VSI} = U_O / U_{OS} \quad (3)$$

where E_{TOS}^O and E_{TOS}^S —the coefficients of thermo-oxidative stability of oils tested without steel and with steel, respectively; U_O и U_{OS} —arithmetic mean values of the wear spots diameters of oils tested without steel and with steel, respectively.

Figure 3 shows the dependence of these factors on the time of oxidation of oils. It has been shown that steel has an inhibitory effect (region II) on oxidation processes after 30 h of testing, i.e., when the values of $K_f > 0.7$ units. The inhibitory effect of steel on wear (Fig. 3b, region II) is set in the time range from 13 to 31 h.

The relationship between these coefficients is shown in Fig. 4, and it shows that under the catalytic effect of steel SH15 on the oxidation processes ($K_{VSO} < 1$), the oxidation products have both a catalytic and inhibitory effect on wear. And, under the inhibitory effect of steel on the oxidation processes, oxidation products have a catalytic effect on anti-wear properties, i.e., when oil is oxidized with steel, in relation to the oil tested without steel, the effect of the products on anti-wear properties occurs according to the cycle shown in Fig. 4 in the direction indicated by the arrow.

The tribotechnical characteristics of the mineral oil during oxidation without steel and with steel were estimated by the time of formation of the nominal area of the friction contact t_{ipc} (Fig. 5a) and the coefficient of electrical conductivity of K_E (Fig. 5b). The formation time of the nominal contact area was determined from the current recording diagrams on the computer display by the duration of plastic and elastoplastic deformations.

The formation time of the nominal area of friction contact (Fig. 5a) for oil tested without steel (curve 1) at the beginning of the oxidation process increases to a coefficient $K_f < 0.25$ units, which is explained by the adaptability of the oil to the

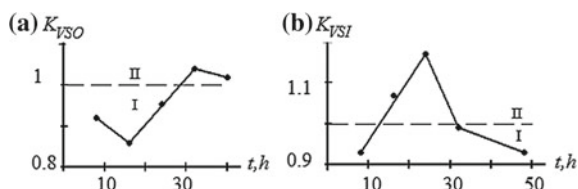


Fig. 3 Dependencies of the coefficient of the effect of steel on the oxidation processes K_{VSO} (a) and the coefficient of influence of steel on the amount of wear of K_{VSI} on the time of oxidation of the Spectrol Super Universal 15W-40 SF/CC mineral engine oil: I—area of the catalytic effect of steel; II—area of inhibitory effect of steel

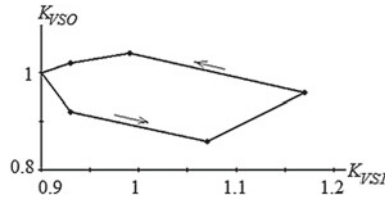


Fig. 4 The relationship between the coefficients of the influence of steel SH15 on the oxidation processes and anti-wear properties of Spectrol Super Universal 15W-40 SF/CC oil

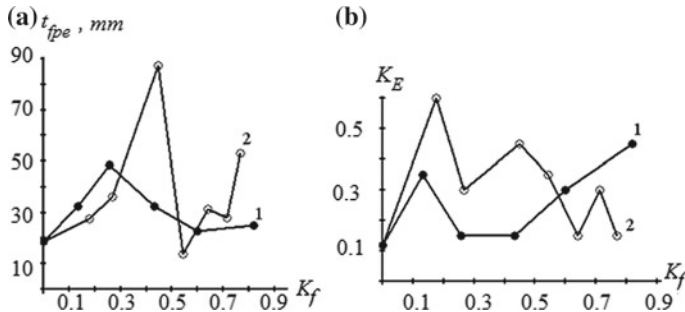


Fig. 5 Dependencies of the formation time of the nominal area of the friction contact (a) and the coefficient of electrical conductivity of the boundary layer (b) on the luminous flux absorption ratio when testing Spectrol Super Universal 15W-40 SF/CC mineral engine oil: 1—without steel; 2— with SkHk15 steel

new operating conditions. Further increase in $K_f > 0.25$ units causes a decrease in the time t_{fpc} by reducing the diameter of the spot of wear.

The test of oil with steel has a similar pattern; however, the time t_{fpc} at the beginning of the oxidation process increases up to the value of the coefficient $K_f < 0.45$ units, and its decrease occurs in the range of the values of the coefficient K_f from 0.45 to 0.55 units. A further increase in the coefficient K_f (concentration of oxidation products) causes another increase in the time t_{fpc} by increasing the area of the wear spot.

The electrical conductivity of the friction contact (the boundary layer separating the friction surface) was estimated by the coefficient of K_E ratio.

$$K_E = I_{FC} / I_G \tag{4}$$

where I_{FC} и I_G —the amount of current flowing through the friction contact during wear and the amount of the given current (100 μ A), respectively.

The frictional contact conductance coefficient is determined at the time of the onset of elastic deformations from current diagrams. For commercial oil tested without steel (Fig. 5b, curve 1), at the beginning of the oxidation process, the value



of the K_E coefficient increases, then decreases, stabilizes, and re-increases. The initial increase in the K_E coefficient is caused by the presence of the adsorption layer of lubricating oil with a low concentration of oxidation products in the contact zone. A further decrease in the K_E coefficient and its stabilization are caused by the formation of chemisorption layers on friction surfaces due to an increase in the concentration of oxidation products. A second increase in the K_E coefficient is caused by an increase in the acidity of the oxidized oil.

At the beginning of the oxidation process for oil tested with steel (Fig. 5b, curve 2), a change in the K_E coefficient is similar to commercial oil, but with an increase in $K_f > 0.3$ units, the conductivity of the friction contact ranges from 0.45 to 0.15 units. This is explained by the fact that the products of chemical reaction of steel with acidic products of oil increase the electrical resistance of the boundary layer once they get released. It can be assumed that the resistance of the boundary layer depends on the concentration of oxidation products on the nominal area of the friction contact and the chemisorption layer on the friction surfaces, and since the concentration of oxidation products in the contact determines the anti-wear properties of oils P, then this indicator will characterize the boundary resistance layer separating the friction surface. Therefore, the product of the anti-wear properties criterion P and the coefficient of electrical conductivity of the frictional contact in the zone of elastic deformations will determine the voltage drop at the boundary layer, which characterizes the lubricating properties of the oxidized oil, indicated by the K_{SS} coefficient.

It could be considered that the resistance of the boundary layer depends on the concentration of oxidation products on the nominal area of the friction contact and the chemisorption layer on the friction surfaces. And, since the concentration of oxidation products in the contact determines the anti-wear properties of oils P, then this indicator will characterize the boundary resistance layer separating the friction surface. Therefore, the product of the anti-wear properties criterion P by the coefficient of electrical conductivity of the frictional contact in the zone of elastic deformations will determine the voltage drop at the boundary layer, which characterizes the lubricating properties of the oxidized oil, indicated by the K_{SS} coefficient.

$$K_{SS} = P \times K_E \quad (5)$$

The dependences of the coefficient of lubricating properties on the concentration of oxidation products for oils tested without steel and with steel are presented in Fig. 6. For oil tested without steel (curve 1), lubricating properties are constant in the range of K_f below 0.45 units, and when the coefficient $K_f > 0.45$ units, properties are increasing, which are confirmed by the function $U = f(K_f)$ (Fig. 2a).

For oil tested with steel (curve 2), lubricating properties vary from 0.3 to 0.9 mm^{-1} , but in the range of K_f under 0.55 units, lubricating properties of the oil tested with steel exceed that of the oil tested without steel.

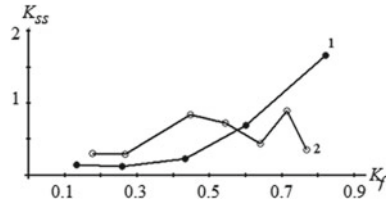


Fig. 6 Dependences of the lubricative properties ratio on luminous flux absorption ratio during the oxidation of the Spectrol Super Universal 15W-40 SF/CC mineral engine oil: 1—without steel; 2—with steel SH15

4 Conclusion

1. Based on the conducted research, it was established that oxidation of mineral oil with steel ambiguously affects oxidation processes, oil volatility, anti-wear properties, the formation time of the nominal area of frictional contact, its electrical conductivity, and lubricating properties due to products of chemisorption processes occurring on surfaces of steel.
2. Coefficients of effect of steel on oxidation processes and anti-wear properties of oxidized oils were suggested. The relationship between them occurs cyclically, and the catalytic effect of steel on the oxidation processes has an inhibitory effect on wear and vice versa.

References

1. Rebinder PA, Petrova NN (1959) Physico-chemical basis of the phenomenon of wear of rubbing surfaces and lubricants at high pressures. USSR, p 450
2. Akhmatov AS (1963) Molecular physics of boundary friction. Moscow, p 472
3. Sanin PI (1980) Chemical aspects of boundary lubrication. Moscow, pp 45–57
4. Chichinadze AV, Buyanovsky IA, Gursky BE (2002) Transition diagram and shielding effect of the lubricating layer. Moscow, pp 334–341
5. Buyanovsky IA (1992) The role of surface interactions in the tribological process. Chem Technol Fuels Oils 11:7–13
6. Lerner YuN (2005) On the strength of adhesive non-conductive films on the surface of metals under friction. Mech Eng Bull 7:42–45
7. Bilyakovich ON, Bohayskaya EV (2010) Modern views on the formation of boundary lubricating layers with the participation of active components of lubricating media. Bulletin HNADU, Kiev, vol 51, p 95
8. Konchits VV, Korotkevich SV, Sautin SD (2002) Lubricating properties of organic deposits on the friction surface at elevated temperatures. Frictionandwear 2:170–175
9. Kowalsky BI, Shram VG, Kravtsova EG, Malysheva NN (2013) The system of methods for controlling lubricants. Ind Serv 2(47):17–20
10. Malysheva NN, Kravtsova EG, Kowalsky BI (2014) Method for determining the quality of lubricating oils. RU Patent 2,528,083, 10 Sept 2014

11. Kowalsky BI, Maltseva EG, Bezborodov YuN et al (2012) The method for determining the thermal-oxidative stability of lubricants. RU Patent 2,453,832, 12 June 2012
12. Kowalsky BI (2005) Methods and means of increasing the efficiency of the use of lubricants. Novosibirsk, No 3, p 341
13. Kowalsky BI, Maltseva EG, Malysheva NN, Kowalsky SB, Vishnevskaya EA (2011) Change in wear resistance of steel SH15 when it is thermostatted in the medium of mineral oil M-10G2K. *VestnikSibGAU* 2(35):154–160
14. Kowalsky BI, Bezborodov YuN, Malysheva NN, Kowalsky SB, Maltseva EG (2011) Effect of electric potential on mechanochemical processes during boundary friction. *Bull SibSAU* 34:135–139
15. Kowalsky BI, Bezborodov YuN, Kowalsky SB, Malysheva NN, Maltseva EG (2009) Methods of research on the anti-wear properties of commercial motor oils and mechanical chemical processes under boundary sliding friction. *Izvestia Tomsk Polytech Univ* 316(2):42–46
16. Kowalsky BI, Bezborodov YuN, Kravtsova EG, Malysheva NN (2012) Effect of steel SH15 on oxidative processes of engine oil Lukoil Super 15W-40 CD/SF Herald of Ir-Kut State Technical University. *Irkutsk* 7:126
17. Kowalsky BI, Bezborodov YuN, Maltseva EG (2011) Effect of direct current through frictional contact on the anti-wear properties of a lubricant. In: *Oil and gas of Western Siberia: materials of the International Scientific and Technical Conference dedicated to The 55th anniversary of the Tyumen State Oil and Gas University*, vol 3, pp 43–45
18. Kowalsky BI, Bezborodov YuN, Malysheva NN, Kravtsova EG (2012) Method of quality control of lubricating oils. *Proceedings of the international scientific-practical conference "Modern problems and their solutions in science, transport, production and education 2012"* 5:67–70
19. Kowalsky BI, Kowalsky SB, Bezborodov YuN, Maltseva EG (2009) Control system for lubricants. *Interstroyemeh: Mater Int Sci Techn Conf* 345–349
20. Kowalsky BI, Bezborodov YuN, Malysheva NN, Metelitsa AA, Maltsev EG (2010) Investigation of the relationship of oxidation processes of lubricants with their anti-wear properties. In: *Proceedings of the fourth international symposium on the transport-tribo-technology "transtribo-2010"*, St. Petersburg, pp 71–73

Theoretical Research of Kinematic Pair “Shaft-Sleeve” of Friction Bearing of Gas-Compressor Unit at Variable Speeds of Shaft Rotation



Y. P. Serdobintsev, M. P. Kukhtik and A. M. Makarov

Abstract The article is devoted to the development of theory of tribotechnical interaction of a kinematic pair “shaft-sleeve” of the friction bearing of a gas-compressor unit (GCU) on the basis of molecular physics of boundary friction. The aim of the research is achievement and securing of a high level of reliability and safety during the lifecycle of high-loaded friction supports of GCU. A mathematical model describing contact deformations in the pair “shaft-sleeve” of friction bearing has been proposed. The stage of dynamical sliding of the shaft in a bearing sleeve has been considered. The mathematical model of boundary friction of porous heterogeneous surfaces taking into account their geometrical, force and physical and mechanical parameters has been proposed. Lubricating ability of porous heterogeneous surfaces has been researched. The parameters determining contact interaction of surfaces of high-loaded friction support of GCU have been brought out.

Keywords Tribotechnical modeling · Kinematic pair · Friction bearing · Gas-compressor unit · Lubricant · Boundary friction

1 Introduction

The predominating parameter for the satisfactory operation of support assemblies in gas-compressor units for main gas pipelines is the minimum wear of the parts and the absence or minimum presence of defects that can be caused by both corrosive processes and fatigue effects, low-quality lubrication and incorrect assembly of the support elements. The most widespread defects of friction supports are destructions of the sleeve surfaces, fatigue damages of the babbitt, cavitation wear, temper

Y. P. Serdobintsev (✉) · M. P. Kukhtik · A. M. Makarov
Volgograd State Technical University, 28, Lenin Av, Volgograd 400005, Russia
e-mail: serdobintseyup@mail.ru

© Springer Nature Switzerland AG 2020
A. A. Radionov et al. (eds.), *Proceedings of the 5th International Conference on Industrial Engineering (ICIE 2019)*, Lecture Notes in Mechanical Engineering,
https://doi.org/10.1007/978-3-030-22041-9_129

1241

colors in the friction zone, evacuation of babbitt alloy from the bearing, damages due to the misalignment and dis-balance of a shaft, and entry of foreign particles between the sleeve and the bearing saddle and possible reasons of such malfunctions [1–5].

2 Contact Deformations in the Pair “Shaft-Sleeve” of a Bearing

To analyze the tribotechnical processes in the pair “shaft-sleeve” of a friction bearing in a gas-compressor unit, let us consider the rotation of a turbine shaft with acceleration from zero speed [6, 7]. Initially, there is a contact between the shaft and the bearing sleeve (placed in a case) and the sleeve turns over for a narrow angle before sliding starts, owing to the compliance of the system. Rolling friction takes place in this period (the shaft rolls in the bearing like a roller). Sliding occurs between the shaft and the sleeve when friction torque M_S increases. The condition for sliding is the excess of Coulomb friction torque value by torque M_S in a contact between the turbine journal of the gas-compressor unit and the bushing sleeve:

$$M_S > f_m \cdot R \cdot W_{el}, \quad (1)$$

where M_S is the torsion torque between the turbine shaft and the antifriction sleeve (in a support), f_m is Coulomb friction coefficient, R is the shaft radius, W_{el} is the reaction due to a normal load in the contact area between the shaft and the bearing.

Most often [1, 7], sleeves of friction bearings for centrifugal gas-compressor units are made by means of babbitt lining (as a rule, that of grade B83) on a surface with elements of mechanical fastening or by means of babbitt lining on a smooth surface [6] with the following machining of the interior operation surface.

The elastic structure of any bearing support must admit some angular compliance. To simplify, an elastic bearing support is represented as a set of springs (Fig. 1) [6, 7].

The “rotation,” i.e., the angular displacement of a bearing jointly with the shaft, causes countertorque M_{OP} in the direction, which is opposite to the rotation, due to the angular compliance of the system “shaft-bearing”:

$$M_{OP} = K \cdot \theta_{OP}, \quad (2)$$

where K is the angular stiffness of a support; θ_{OP} is the rotation angle of a bearing.

When a shaft rotates jointly with the bearing, elastic deformation occurs in the micro-relief of the operation surfaces of the shaft and sleeve. As a result, a preliminary (tangential) displacement is observed in the contact area. Consequently, the shaft torque can be expressed as [6, 7]:

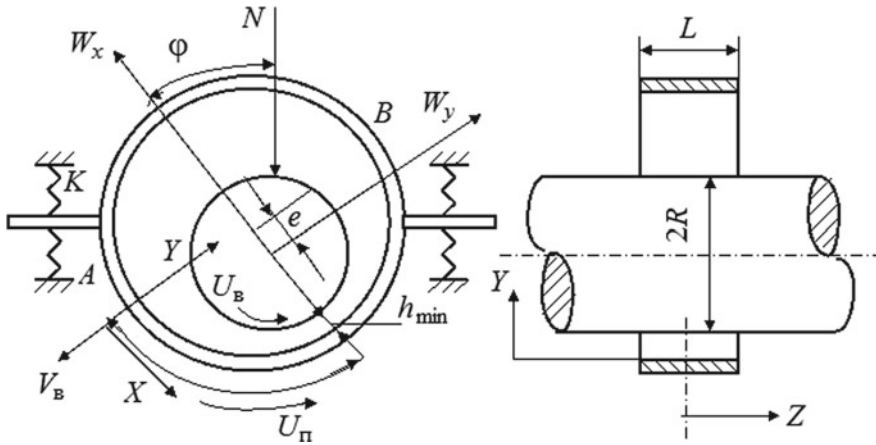


Fig. 1 Diagram of a bearing support with angular compliance

$$M_S = K_1 \cdot (\theta_S - \theta_{OP}), \tag{3}$$

where K_1 is the equivalent stiffness of the system “shaft-sleeve”, θ_S is the rotation angle of the shaft.

The resultant of torques M_S and M_{OP} is a function of acceleration in the bearing system (support-sleeve):

$$K_1 \cdot (\theta_S - \theta_{OP}) - K \cdot \theta_{OP} = I_{EQ} \cdot \frac{d^2\theta_{OP}}{dt^2}, \tag{4}$$

where I_{EQ} is the equivalent moment of inertia in the bearing system.

Equation (4) is an equation of differential motion for the preliminary (tangential) displacement mode. It can be integrated for variable u_S —the shaft rotation speed:

$$\theta'_S = \omega_0 \cdot \sin \alpha, \tag{5}$$

where ω_0 is the amplitude of the shaft angular speed; α is the speed oscillation frequency.

The transition criterion from the preliminary displacement to the shaft sliding mode in the bearing sleeve should be considered at each integration step of Eq. (4). The minimum value of shaft torque M_S should be chosen at each integration step.

When the shaft brakes, i.e., when transition from sliding to preliminary displacement takes place, value θ_S in Eq. (4) should be replaced by value of initial rotation angle θ'_S at the moment of transition to the preliminary displacement:

$$\theta'_S = \theta_{OP} + f_m \cdot R \cdot W_{el}/K_1. \quad (6)$$

3 Dynamical Sliding Friction

The next stage of the bearing operation can be characterized as the stage of dynamical sliding of the shaft in the bearing sleeve.

The beginning of sliding is characterized by a too low shaft rotation speed where the lubricating material does not completely divide the operation surfaces of the sleeve and shaft. It is a stage of boundary friction where a “metal” contact of the micro-roughnesses—traces of machining of the operation surfaces with a cutting tool—takes place [8–10].

When the shaft rotation speed increases, minimum thickness of lubricating film h_0 (Fig. 1) becomes less than critical value h_{tr} , i.e., the thickness of the oil film when the bearing switches from the mixed friction to the hydrodynamic operation mode where the operation surfaces of the sleeve and shaft are divided by a layer of lubricating liquid. Speed ω_{const} of the transition into the hydrodynamic lubrication mode can be determined with the help of Stribeck curve in the point of the minimum frictional force [6, 7].

In the area of mixed friction, response of bearing W to the load imposed is determined by adding reaction contact vectors of micro-asperities W_{el} and those of lubricating film W_f :

$$\bar{W} = \bar{W}_{el} + \bar{W}_f. \quad (7)$$

Frictional force F_{fr} is equal to the sum of the resistance force to sliding due to the deformation of the micro-asperities and the force of viscous resistance of the lubricant. Assuming that the density of the micro-asperities in the “mixed” area (mixed friction mode) is rather low and does not play any essential part in the hydrodynamic friction, we will represent the equation for full friction torque $M_S = F_{fr} \cdot R$ between the shaft and bearing

$$M_S = \frac{f_m \cdot K_n \cdot R \cdot \Delta}{C} + \frac{L \cdot \mu \cdot R^3}{C} \cdot \frac{2\pi}{\sqrt{1 - \epsilon^2}} \cdot \left(\frac{d\theta_S}{dt} - \frac{d\theta_{OP}}{dt} \right), \quad (8)$$

where K_n is a normal contact stiffness, L and R are the length and radius of the bearing (Fig. 1), μ is the dynamic viscosity of the lubricant, C is the average value of the radial clearance, ϵ is the relative eccentricity, $\epsilon = e/C$, where e is the eccentricity of the shaft (Fig. 1), Δ is the coefficient in the mixed or boundary friction:

$$\Delta = 1/|b_{eq} \cdot (\epsilon_{tr} - \epsilon)^{v_{eq}}|, \quad (9)$$

where C_{tr} is the relative eccentricity, which corresponds with value h_{tr} of the thickness of the lubricating film, b_{eq} and v_{eq} are the equivalent parameters, which characterize the micro-geometry of both contact surfaces (the bearing and the shaft).

As the parameters of the initial part of bearing area curve b and v determine the distribution of the height parameters of the micro-asperities, coefficient Δ allows to determine the number of the micro-asperities whose height exceeds the thickness of the lubricating film at the moment.

b_{eq} and v_{eq} allow to determine the values of the relative actual contact area and the relative number of the micro-asperities in contact, with this average elastic deformation of micro-asperities δ [6, 7]:

$$b_{eq} = \frac{b_1 \cdot b_2 \cdot (R_{p1} + R_{p2})^{v_1 + v_2}}{R_{p1}^{v_1} \cdot R_{p2}^{v_2}}, \quad (10)$$

$$v_{eq} = v_1 + v_2, \quad (11)$$

where b_1, b_2, v_1, v_2 are the parameters of the initial part of the contact bearing area surfaces (the bearing and the shaft); R_{p1}, R_{p2} are the heights of smoothing the first and the second surfaces.

Thus, there appears a possibility to introduce the geometric parameter of the contact surfaces into the mathematical model of friction in a friction bearing and express the dependence of the friction torque in the system “shaft-bearing” on the quality of processing the contact surfaces.

4 Boundary Friction

According to theory of Bowden and Tabor [11], force of boundary friction T can be expressed as a sum of two items, which represent the force necessary to overcome the shift resistance of the lubricating film and the force for cutting the roughnesses on the surfaces, which is proportional to the actual contact area:

$$T = aS_a + Bp, \quad (12)$$

where a is the average intensity of the molecular constituent of the frictional force; S_a is the actual contact area; B is the coefficient, which characterizes the mechanical constituent of the frictional force; p is the normal pressure.

A decrease in the metal transfer in the presence of lubrication testifies that the major portion of its transfer is explained by a shift in the lubricant itself where resistance takes place at the moment of friction, not by a cut of the metallic bonding through the lubricating film.

It is important for practice that the friction coefficient cannot serve as a criterion when we estimate the antiwear properties of a lubricant. According to the data of

work [12], the wear with an equal force of boundary friction can differ by 20 times, depending on a type of a lubricating material. One should aim at reducing S_a and a to decrease the molecular constituent of the frictional force.

The friction coefficient usually decreases in discrete steps when it transits from rest to motion. It decreases parabolically with the increase in speed. When the speed has some critical value, the friction coefficient reaches its minimum and the motion goes into the area of liquid friction [13].

The mechanism of boundary friction takes place at the conditions of insufficient lubrication (when the shaft is started) at low sliding speeds (a lack of the hydrodynamic effect), when the rubbing surfaces of the shaft and sleeve of a bearing are covered with adsorbed molecules only in the areas with increased adsorption potential close to the actual contact patterns. The molecules adsorbed are located in separate islets on the rest of the surface [14–16].

When friction of the surfaces occurs, the boundary lubricating layer wears down owing to the sublimation, chemical aging, and evacuation of the lubricant outside the friction area. It is necessary to periodically supply oil into the friction area to recover the boundary lubricating layer (healing). After wearing, its regeneration occurs as a result of adsorption filling of the bare surfaces of the metal from the lubricant volume (lubricating pockets) and owing to the centripetal migration of the molecules of the boundary layer from the perimeter, which limits the area of destruction. Thus, the presence of lubricating “tanks” on the friction surfaces is one of the necessary conditions for fast recovery of the boundary lubricating film [17].

The time necessary for the boundary lubricating layer to regenerate [18]

$$t \leq \sqrt{\frac{d_n}{2c}}, \quad (13)$$

where d_n is the average statistic distance between the centers of the lubricating pockets

$$c = 2D_s^{0.5} \left[\ln \left(\frac{m_s}{4\pi D_s C_0 t} \right) \right]^{0.5}, \quad (14)$$

where D_s is the coefficient of surface diffusion (to be determined experimentally); m_s is the weight of the source; C_0 is the concentration of the diffusible substance.

The formation speed of the monolayer, which consists of adsorbed molecules within the crystallite surface of polycrystalline solids, is found from the condition for determining the average statistical speed of the lubricant molecules [17]

$$\bar{v} = \sqrt{\frac{\pi \cdot kT}{2m_m}}, \quad (15)$$

where k is Boltzmann's constant; T is the absolute temperature; m_m is the molecular weight.

If then it is necessary to estimate the diffusion speed on the surface outside the crystallite, the energy spent on overcoming the boundary energy barriers is taken into account. The flow speed will be far lower in this case.

The formation speed of the poly molecular boundary layer depends on both the factors related to the physical nature of the adsorbent and adsorbate and the relative position of the contact areas of the shaft and sleeve, i.e., on a change in the adsorption potential of the adsorbent.

The time, which is free from a direct contact of the micro-asperities within the nominal contact of the shaft and sleeve of a bearing, is characterized by the time of progress of the sorption processes [19],

$$t_{c,fr} = \frac{\pi \cdot HB \cdot d_a}{8p_n v}, \quad (16)$$

where HB is Brinell hardness of a less hard material; d_a is the average diameter of the actual contact pattern; p_n is the nominal pressure in a contact; v is the linear shaft rotation speed.

By solving Eqs. (13) and (16) jointly, we will find the average statistic distance between the centers of the lubricating pockets, whereby the monolayer to be adsorbed recovers at certain values of HB , p_n , and v provided that d_a is known [17]:

$$d_n = 2c \left(\frac{\pi \cdot HB \cdot d_a}{8p_n v} \right)^2. \quad (17)$$

When an elastic unsaturated contact of rough surfaces, which is modeled by spherical segments, takes place:

$$d_a = 2 \left(\frac{3}{8} \cdot \frac{NR}{E^*} \right)^2, \quad (18)$$

where N is the compression force; R is the radius of the spherical segments; E^* is the effective elastic modulus of the shaft and sleeve.

The approximate value of the diameter of the contact patterns can be calculated taking into account the area occupied by the pores, which are formed in the heterogeneous plasma coating of the bearing sleeve [17],

$$\frac{\pi \cdot d_a}{4} = A_{ri} = A_c / \int_1^n d_n = \frac{\varepsilon^v 2\pi R \cdot R_{\max}}{(x')^{v-1} v} (1 - \gamma_p), \quad (19)$$

where A_{ri} is the actual contact area, which falls on a single asperity; A_c is the contour contact area (in the absence of undulation and macro deflections); $A_c = A_a$ is the nominal contact area; $\varepsilon = h/R_{\max}$ is the relative approach; h is the thickness of the lubricant layer; R is the radius of the curvature of the interacting micro-asperities; R_{\max} is the maximum height of the micro-asperities; x' is the

coordinate of the asperity peak at random section; γ_p is the specific volume of the pores in the plasma coating of a bearing sleeve.

Where the elastic saturated contact (when all the asperities contact) takes place, $n_c = n_r$ and

$$n_c = \frac{A_c b v \varepsilon_H^{v-1}}{2\pi R \cdot R_{\max}}, \quad (20)$$

where ε_s is the relative approach in the elastic saturated contact [20].

Parameters b and v depend on the type of machining of a shaft and sleeve. Since the conditions of the external friction $0 < \varepsilon < 0, 2$, and assuming that $\varepsilon_s \cong \varepsilon$, let us determine the average value of the diameter of the contact pattern:

$$\frac{\pi \cdot d_{a.av}^2}{4} = \frac{A_r (1 - \gamma_p)}{n_c} = \pi R \cdot R_{\max} \varepsilon v^{-1} (1 - \gamma_p); \quad (21)$$

$$d_{a.av} = 2\sqrt{RR_{\max} \varepsilon v^{-1} (1 - \gamma_p)}. \quad (22)$$

The value obtained of the diameter of the contact pattern differs from the actual diameter maximum 5–7% [20].

Then, taking into account (15) and (19), the average distance between the centers of the lubricating pockets is

$$d_{n.av} = 2c \left[\frac{\pi \cdot HB \sqrt{RR_{\max} \varepsilon v^{-1} (1 - \gamma_{\Pi})}}{4p_H v} \right]. \quad (23)$$

By using formulas (11) and (22), and the equation for the mathematical expectation of a discrete random value and neglecting the influence of porosity on the contact area, it becomes possible to determine the specific volume of the pores, which corresponds to the optimum lubricating ability of the real heterogeneous plasma coatings of a bearing sleeve, taking into account the geometric, power, physical, and mechanical parameters of the rubbing surfaces, as well as the parameters of lubrication at the stage of boundary friction between the shaft and sleeve of a friction bearing.

Acknowledgements The reported study was funded by RFBR and the government of the Volgograd region according to research project no. 18-48-342001.

References

1. Kunina PS et al (2016) Analiz defektov opornykh ehlementov gazoperekachivayuschikh agregatov kompressornykh stantsiy magistral'nykh gazoprovodov (Analysis of the supporting elements' defects of gas pumping units of the main gas pipeline compressor stations). *Territorya Neftegas* 4:68–75
2. Barszcz T, Zimroz R, Urbanek J, Jabłoński A, Bartelms W (2013) Bearings fault detection in gas compressor in presence of high level of non-Gaussian impulsive noise. *Key Eng Mater* 569–570:473–480
3. Muzakkir SM, Lyesh KP, Hirani H (2014) Tribological failure analysis of a heavily-loaded slow speed hybrid journal bearing. *Eng Fail Anal* 40:97–113
4. Sverdlov AB (2014) Povyshenie nadezhnosti gazoperekachivayuschikh agregatov putem primeneniya tekhnologii ehpilamirovaniya (Reliability of gas pumping machinery and application of fluorine-containing film coatings). *Nauchno-tekhnicheskie vedomosti SPbPU. Estestvennye i inzhenernye nauki* 3(202):62–69
5. Shapovalov VV, Sladkovski A, Ehrkenov AC (2015) Aktual'nye zadachi sovremennoy tribotekhniki i puti ikh resheniya (Actual problems of modern tribotechnology and ways of solution). *Izvestiya vuzov. Mashinostroenie* 1(658). <https://cyberleninka.ru/article/n/aktualnye-zadachi-sovremennoy-tribotekhniki-i-puti-ih-resheniya> . Accessed 21 Nov 2018
6. Serdobintsev YP, Burlachenko OV (2005) Obespechenie ehffektivnosti upravleniya ehkspluatatsionnymi svoystvami tribosopryazheny tekhnologicheskogo oborudovaniya v protsesse zhiznennogo tsikla (Securing of effectiveness of control of operation properties of tribocouplings of processing equipment in the process of lifecycle). *RPK Politehnik, Volgograd*
7. Serdobintsev YP, Burlachenko OV, Skhirtladze AG (2017) Povyshenie kachestva funkcionirovaniya tekhnologicheskogo oborudovaniya (Increase of quality of functioning of processing equipment). *TNT, Staryj Oskol*
8. Wen S, Huang P (2012) Principles of tribology. Wiley, Hoboken
9. Hutchings I, Shipway P (2017) Tribology: friction and wear of engineering materials. Butterworth-Heinemann, Oxford
10. Rahnejat H, Gohar R (2018) Fundamentals of tribology. World Scientific, London
11. Bowden FP, Tabor D (2001) The friction and lubrication of solids. Oxford University Press, London
12. Matvievsky RM, Buyanovsky IA, Lazovskaya OV (1978) Protivozadimaya stoykost' smazochnykh sred pri trenii v rezhime granichnoy smazki (Antiscuff durability of lubricating mediums at friction in the mode of boundary lubricant). *Nauka, Moscow*
13. Reshetov DN (ed) (1972) Detali i mekhanizmy metallorezhuschikh stankov (Parts and mechanisms of machine tools), vol 1. *Mashinostroenie, Moscow*
14. Ukonsaari J (2003) Wear and friction of synthetic esters in a boundary lubricated journal bearing. *Tribol Int* 36(11):821–826
15. Kerr I, Priest M, Okamoto Y, Fujita M (2007) Friction and wear performance of newly developed automotive bearing materials under boundary and mixed lubrication regimes. *Proc Inst Mech Eng Part J J Eng Tribol* 221(3):321–331
16. Gebretsadik DW, Hardell J, Prakash B (2015) Friction and wear characteristics of different Pb-free bearing materials in mixed and boundary lubrication regimes. *Wear* 340–341:63–72
17. Serdobintsev YP, Podshipkov AA (2002) Tribotekhnicheskoe modelirovanie i issledovanie modifitsirovannykh par treniya tekhnologicheskogo oborudovaniya (Tribotechnical modeling and research of modified friction pairs of processing equipment). *RPK Politehnik, Volgograd*

18. Ahmatov AS (1963) Molekulyarnaya fizika granichnogo treniya (Molecular physics of boundary friction). Fizmatgiz, Moscow
19. Drozdov YN (1980) Obobshchennye kharakteristiki dlya otsenki iznosostojkosti tverdykh tel (Generalized characteristics for estimation of wearing capacity of solids). *Trenie i Iznos* 3:417–423
20. Kragel'sky IV, Dobychin MN, Kombalov VS (1977) Osnovy raschetov na trenie i iznos (Basics of friction and wear calculations). Mashinostroenie, Moscow

Design Engineering and Manufacturing of Technology of Bearings for Heavy-Duty Friction Units



R. V. Yudin, D. A. Parinov and I. N. Medvedev

Abstract The description of the construction of a self-lubricating sliding bearing of modified wood for heavy-duty friction units and manufacturing technology of it are presented in this article. To determine the coefficient of wood friction on steel, the technique was developed and MI-1M machine friction was modernized. Depending on the load the coefficient of sliding is in the range 0.06–0.11. The designed bearing construction allows one to replace not only sliding bearings, but also the rolling bearings in friction units. The main advantage of such bearing constructions is uniform density over a cross section. This density provides a low coefficient of friction and high wear resistance, as well as the ability to absorb abrasive particles and wear products that provides a long-term zero wear of a rider. To reduce the friction coefficient, the lubricant such as the Biol type is put in the metalized timber in the amount of 7–8% by weight of the wood. To impart the increased rigidity of wood, the hardness and wear resistance nanocrystalline cellulose (NCC) in the amount of 0.5–0.8% by the weight of wood is added into the timber together with the lubricant.

Keywords Sliding bearing · Machine · Test · Unit · Wood · Friction

1 The Technology of Bearing Production for Heavy-Duty Friction Units

The new possibilities of obtaining materials for friction units appeared together with a development of nanotechnology, when it was found that by introducing nanocrystalline pulp into the wood its strength and wear resistance can be increased by 1.5–2 times. Thus, there is a real opportunity to develop the design of wear-resistant sliding bearings for heavy-duty friction units where static loads

R. V. Yudin (✉) · D. A. Parinov · I. N. Medvedev
Voronezh State University of Forestry and Technologies named after G.F. Morozov, 8,
Timiryazev St., 394087 Voronezh, Russia
e-mail: romanyudin1@yandex.ru

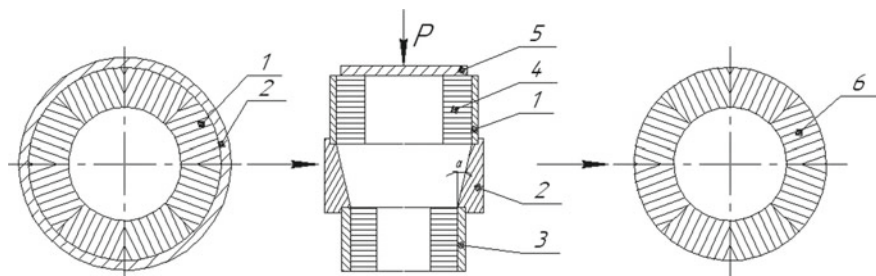


Fig. 1 Production of the bearing from segments. 1—segments; 2—false yoke; 3—cone; 4—the final yoke; 5—punch; 6—finished bearing

exceed 50 MPa. Figure 1 shows a flow diagram for production of the bearing from the compressed wood bar with fibers located along the radius [1–4].

Pressed wood, which is used to make bearings has a brand Drevstal and contains Biol lubricant and is ceresine thickened.

Low competitiveness of sliding non-metallic bearings versus ball and roller bearings of high-alloy steel is explained by the fact that the non-metallic bearings have 2–3 times less hardness and consequently less wear and a low thermal conductivity, which severely limits the range of acceptable speeds. To increase the thermal conductivity in the bearing into timber intended for pressing the nickel metal in an amount of 4–6% by weight of the timber is added, that in a volume of 0.3–0.4% by volume of wood in the form of a continuous film of 0.8 m thick lining the entire inner surface of the timber by the process described in Patent № 23390505 [5–7].

To reduce the friction coefficient into metalized timber Biol type lubricant in an amount of 7–8% by weight of the wood is added. To impart increased rigidity wood, the hardness and wear-resistant nanocrystalline cellulose (NCC) in an amount of 0.5–0.8% by weight of the wood is added into timber together with a lubricant. The final operation producing compressed wood is pressing the bars to 1250–1300 kg/m³ density [8–12].

The nickel content in the wood in an amount of 4–6% provides a thermal conductivity of compressed wood of 12–15 W/m K (thermal conductivity of natural wood is of 0.5 W/m K), which is sufficient to remove the heat from the friction zone. If nickel content is less than 4% thermal conductivity decreases several times due to discontinuities nickel film and increasing the nickel content of more than 6% increases the duration of the metallization process from three hours to 10.8 h, and slightly increases the conductivity.

When NCC content is less than 0.5% the hardness of the particle board slightly increases, and to receive the compressed wood with NCC content exceeding 0.8% is not technically possible due to the large volume of NCC gel [13–16].

Compressed wood with the best strength properties is obtained in a density range of 1250–1300 kg/m³. In this method, you may get the density to 1400 kg/m³, but the defect of fractures increases several times, and the process becomes a non-technological [17, 18].

Production of sliding bearing according to the proposed method is as follows:

First, on semi-automatic machine for cutting segments of the compressed wood bar first side edges are cut, and then the segment with the radius of the future of the bearing is cut off, as shown in Fig. 1. The adhesive is applied on the side edges of segments and is collected in a yoke 2. The false yoke 2 is set on the cone 3, in turn, mounted on the receiver 4. The angle of the cone depends on the initial density of the segments 1 and defined by the formula (1):

$$\lambda = tg \frac{\rho^k}{\rho^0} \sqrt{D^2 - d^2} \quad (1)$$

where ρ^k —density of segment, kg/m^3 ; ρ^0 —bearing density, kg/m^3 ; D —the inside diameter of false yoke, mm; d —the inside diameter of receiver, mm.

Then the workpiece 5 of the segments 1 through cone 3 is repressed on a hydraulic press to a receiver 4 by punch. After hot curing of adhesive, the ready bearing is removed from the holder and if necessary, grinded to the inner diameter with a minimum stock of 0.4–1.0 mm. Property characteristics of bearing are given in Table 1.

Developed bearing design allows to replace not only sliding bearings, but also the rolling bearings in friction units.

The main advantage of such bearing construction is uniform density over a cross section. This density provides a low coefficient of friction and high wear resistance,

Table 1 Bearing properties indicators

No/ №	Properties' indicators	The analog— auth. inventor's certificate No. 409854	The proposed method
1.	Density, (kg/m^3)	1200	1350
2.	Humidity, (%)	2	2
3.	Biol lubricant, (%)	8	8
4.	Content of NCC	–	0.7
5.	Nykel content, (%)	–	5
6.	Thermal conductivity, (W/m K)	0.9	16
7.	The stress limit at pressing along the fibers at static load, (MPa)	150	222
	At dynamic load, (MPa)	35	90
8.	Friction coefficient at $P = 5(\text{MPa})$, $V = 1,0$ (m/s)	0,06	0,05
9.	Frontal hardness, (MPa)	160	350
10.	Wear, mom per 1000 m path	28	4
11.	Permissible temperature in the friction zone, ($^{\circ}\text{C}$)	100	150
12.	Bearing life in friction units of conveyor belts, years (serial w/n number 208 serves for 1.8 years)	1.2	2.4

as well as the ability to absorb abrasive particles and wear products that provide long-term lack of rider wear [19–21].

Getting a new bearing material—a modified wood required the development and changes in methods and apparatus for determining the tribotechnical characteristics.

The most important indicators of performance of sliding bearings are wear resistance and friction coefficient. To determine the wear resistance of the modified wood, holes cut method was used, but largely upgraded [22–24].

2 Methods of the Experiment to Determine the Wear Resistance and Friction Coefficient

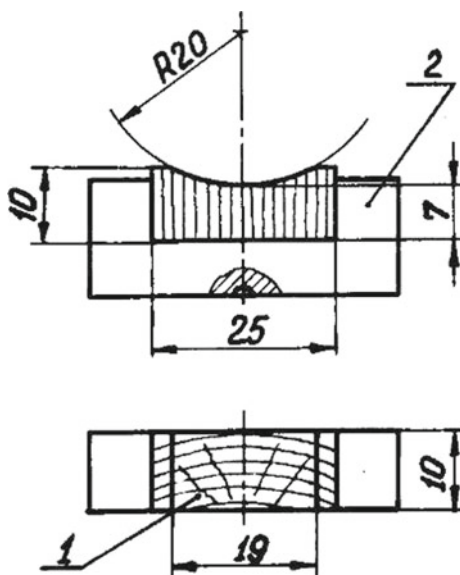
Test samples should have a cylindrical shape or a buckle with frontal working surface, with dimensions and forms given in mm in Fig. 2.

Test samples are made from workpieces of modified wood according to NSS P 54577, trimmed on the edges by at least 20 mm NSS P 54912.

Test samples (items) must meet the requirements of NSS 2140. The roughness of the sample surface at the site of the hole should be no more than $R_a = 0.63$ – 0.40 mm in accordance with NSS 2789. Humidity—in the range of 2–4%. The surface roughness of the rider is 0.16–0.1 microns.

To cut holes on flat samples (details), it is recommended to use a device designed on the basis of MIS-II microscope (Fig. 3).

Fig. 2 The size and shape of samples. 1—a sample of the modified wood; 2—mandrel



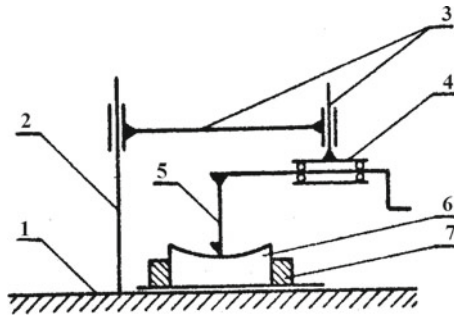


Fig. 3 Device for cutting holes. 1—the base of the device; 2—front; 3—the links to move the cutter; 4—a device for fixing and rotating the cutter; 5—cutter; 6—sample (part); 7—a device for fixing a sample (detail)

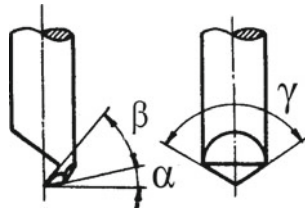


Fig. 4 Form of a working part of the tool. β —wedge angle cutter ($35 \pm 1^\circ$); α —back angle ($12 \pm 1^\circ$); γ —frontal approach angle ($130 \pm 1^\circ$); deviation of the top of the cutter from the mandrel axis is not more than 0.2 mm

The device is equipped with a cutter made of P18 tool steel according to NSS 19265. The shape of the working part of the cutter is shown in Fig. 4.

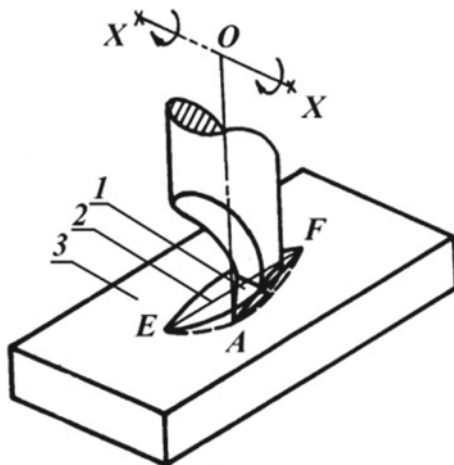
Note: The devices made in accordance with NSS 23.301, instead of a diamond cutter, RAI-I it is needed to use the proposed cutter.

Cutter is mounted in the device in the way that the hole is turned to a depth of 0.2 mm and a length of 4 mm, a symmetrical shape with respect to its longitudinal axis. The radius of rotation of the cutter top is 12.5 ± 0.1 mm. There should not be a backlash in the rotation mechanism. On the sides and top of the cutter notches and chips, distinguishable when viewed under a microscope with a $35\times$ increase are excluded.

To cut the hole on the sample (detail) the tool should provide movement of the cutter relatively to the sample in three dimensions. To measure the size of the hole and determine wear the tool microscope or special equipment models 965 and 966 are used.

Burn-in of samples (details) is performed prior to cutting holes for at least 4 h. Marks are put by the lead pencil on the sample working surface in the form of two parallel lines which reflect the longitudinal length of the hole. The friction surface at

Fig. 5 Scheme of cutting the hole by the cutter. 1—steel cutter; 2—hole; 3—the surface of the friction of part (sample); XX—the rotation axis of cutter; EF—the length of the hole; OA—radius of rotation of cutter top



the site of the holes before measurement should be thoroughly cleaned with a cloth dampened with ether in accordance with NSS 20370.

The size of the holes and their location on the surface of friction depends on the expected wear and task. The recommended length of the hole is 2.5–4.0 mm; the longitudinal axis of symmetry must be perpendicular to the direction of relative movement of the friction surfaces. Experimental determination of the wear resistance and friction coefficient is performed in the following sequence [25–27].

The holes are cut by rotating cutter (scheme is shown in Fig. 5), observing the process through a magnifying glass. Cutter feed is of 0.01–0.05 mm/rev. Cutting speed is of 0.1–0.2 m/s.

Upon reaching a predetermined length the surface of the hole is adjusted by rotating the tool in both directions without feed. After finishing, and after each step of wear the holes are measured in length, the part wear (sample) is calculated at the site of its marking. Measuring accuracy is of ± 5 microns.

In the case of reducing the length of the hole to less than 1.5 mm, the further holes' cut at a distance of 2–5 mm from the same or a new hole cut on the existing site for subsequent wear measurements is acceptable. Wear of flat and cylindrical surfaces at the hole located on the cylinder generating line is calculated from the formula (2) or at Table 1 as the difference between the hole's depth before and after the wear:

$$\Delta h = h_1 - h_2 = \frac{0,125}{r} (l_1^2 - l_2^2) = 0,01 (l_1^2 - l_2^2) \tag{2}$$

where Δh —linear wear at the site of the hole, in mm;

r —cutter top radius of rotation, $r = 12.5$ mm;

l_1, l_2 —the length of the hole before and after a certain stage of wear, mm.



3 Summary

1. A sliding bearing design for heavy machines, equally strong throughout the whole section with high thermal conductivity was developed.
2. The coefficient of friction and linear are determined by the machine MI-1M modified for testing of eight samples at the same time with the installation of a thermocouple to a depth of 0.3–0.5 mm from the surface friction.
3. The sliding bearings of the modified wood were successfully tested in rolling mills of JSC Severstal, screw crushers of feed stuff and conveyor belts of processing plants.

Acknowledgements The research materials presented in this article were obtained as a part of the state task of the Ministry of Education and Science of Russia, № 11.3960.2017/4.6.

References

1. Fomin AA et al (2016) Mechanical treatment of raw waste lumber an effective way to preserve the ecology and resources. IOP Conf Ser Mater Sci Eng 142:012091. <https://doi.org/10.1088/1757-899x/142/1/012091>
2. Safin RG, Lashkov VA, Golubev LG, Safin RR (2002) Mathematical model of vacuum-oscillating drying of lumber. Inzh-Fiz Zh 75(2):95–98
3. Lashkov VA, Levashko EI, Safin RG (20010) Heating of production wood chips in a saturated-steam medium. Inzhenerno-Fizicheskii Zhurnal 74(1):80–83
4. Timerbaev NF, Safin RR, Safin RG, Ziatdinova DF (2014) Modeling of the process of energy-technological treatment of wood waste by method of direct-flow gasification. J Eng Appl Sci (EAAS) 9(5):141–146
5. Timerbaev NF et al (2016) The development of experimental setups and experimental studies of the process of energy technological processing of wood. IOP Conf Ser Mater Sci Eng 142:012096. <https://doi.org/10.1088/1757-899x/142/1/012096>
6. Prosvirnikov DB et al (2016) Mathematical modelling of the steam explosion treatment process for pre-impregnated lignocellulosic material. IOP Conf Ser Mater Sci Eng 124:012087. <https://doi.org/10.1088/1757-899x/124/1/012087>
7. Saldaev VA, Prosvirnikov DB, Stepanov VV, Sadrtidinov AR, Kapustin AN (2016) Equipment for the production of wood-polymeric thermal insulation materials. IOP Conf Ser Mater Sci Eng 142(1):012097. <https://doi.org/10.1088/1757-899x/142/1/012097>
8. Fomin AA (2013) Vibrational motion of a complex mill under the action of the cutting force. Russ Eng Res 33(1):57–60
9. Fomin AA (2013) Kinematics of surface formation in milling. Russ Eng Res 33(11):660–662
10. Sadrtidinov AR, Sattarova ZG, Prosvirnikov DB, Tuntsev DV (2015) Modeling of thermal treatment of wood waste in the gasifiers. In: Proceedings of 2015 international conference on mechanical engineering, automation and control systems, MEACS 2015. Art. No. 7414914. <https://doi.org/10.1109/meacs.2015>
11. Sadrtidinov AR, Safin RG, Timerbaev NF, Ziatdinova DF, Saprykina NA (2016) The development of equipment for the disposal of solid organic waste and optimization of its operation. IOP Conf Ser Mater Sci Eng 142(1):012095. <https://doi.org/10.1088/1757-899x/142/1/012095>

12. Lashkov VA, Sattarova ZG, Taymarov MA, Gerasimov MK, Halitov RA (2016) Modeling of a reduction zone of the gasifier installation. IOP Conf Ser Mater Sci Eng 124(1):012111. <https://doi.org/10.1088/1757-899X/124/1/012111>
13. Safin RR, Khasanshin RR, Timerbaeva AL, Safina AV (2015) Study of the physical and energy properties of fuel granules based on a thermomodified wood raw material. J Eng Phys Thermophys 88(4):958–961. <https://doi.org/10.1007/s10891-015-1270-y>
14. Safin RR, Khasanshin RR, Shaikhutdinova AR, Safina AV (2014) Research of heating rate while termo modification of wood. World Appl Sci J 30(11):1618–1621. <https://doi.org/10.5829/idosi.wasj.2014.30.11.14223>
15. Galyavetdinov NR, Safin RR, Voronin AE and Shaikhutdinova AR (2015) The mathematical modeling of the wood greenery extraction processes. In: 2015 international conference on mechanical engineering, automation and control systems (MEACS), pp 1–5. <https://doi.org/10.1109/meacs.2015.7414885>
16. Galyavetdinov NR, Khasanshin RR, Safin RR, Safin RG, Razumov EY (2015) The usage of wood wastes in the manufacture of composite materials. In: 2015 international multidisciplinary scientific geoconference surveying geology and mining ecology management (SGEM) 1(4):779–786
17. Bardovsky A, Gerasimova A, Aydunbekov A (2018) The principles of the milling equipment improvement. MATEC Web Conf 224. <https://doi.org/10.1051/mateconf/201822401019>
18. Gerasimova AA, Radyuk AG, Titlyanov AE (2016) Wear-resistant aluminum and chromonickel coatings at the narrow mold walls in continuous-casting machines. Steel Trans 46(7): 458–462. <https://doi.org/10.3103/S0967091216070068>
19. Nekrasov RY, Tempel YA, Starikov AI, Proskuryakov NA (2018) Fuzzy controllers in the adaptive control system of a CNC Lathe. Russ Eng Res 38(3):220–222. <https://doi.org/10.3103/S1068798X18030188>
20. Rezhnikov AF, Kochetkov AV, Zakharov OV (2017) Mathematical models for estimating the degree of influence of major factors on performance and accuracy of coordinate measuring machines. MATEC Web Conf 129:01054
21. Yemelyanov V, Tochilkina T, Vasilieva E, Nedelkin A, Shved E (2018) Computer diagnostics of the torpedo ladle cars. In: AIP Conference Proceedings, vol 2034. P 020008. <https://doi.org/10.1063/1.5067351>
22. Sharkov OV, Koryagin SI, Velikanov NL (2016) Design models for shaping of tooth profile of external fine-module ratchet teeth. IOP Conf Ser Mater Sci Eng V.124:012165. <https://doi.org/10.1088/1757-899x/124/1/012165>
23. Gromov VE, Kormyshev VE, Glezer AM et al (2018) Microstructure and wear properties of Hardox 450 steel surface modified by Fe-C-Cr-Nb-W powder wire surfacing and electron beam treatment. IOP Conf Ser Mater Sci Eng 411(1)
24. Kononov S, Chen X, Sarychev V et al (2017) Mathematical modeling of the concentrated energy flow effect on metallic materials. Metals 7(1)
25. Grechnikov FV, Rezhnikov AF, Zakharov OV (2018) Iterative method of adjusting the radius of the spherical probe of mobile coordinate-measuring machines when monitoring a rotation surface. Meas Tech 61:347–352
26. Sharkov OV, Koryagin SI, Velikanov NL (2018) Shaping cutter original profile for fine-module ratchet teeth cutting. IOP Conf Ser Mater Sci Eng V327:042102. <https://doi.org/10.1088/1757-899x/327/4/042102>

Surface Films Formation on Steel During Friction of Polymer Composites Containing Microcapsules with Lubricant



A. V. Sidashov and M. V. Boiko

Abstract Microcapsules based on the product of the interaction of 2,4-toluene diisocyanate and 1,6-hexamethylenediamine containing DOS lubricant inside were synthesized by the method of interfacial polycondensation in an oil-in-water emulsion. Adding microcapsules containing lubricant to phenylone FS-2 improves its tribological properties. The friction coefficient for composite containing 7% microcapsules is three times lower than that of phenylone without additives. When the friction composite contains microcapsules with a lubricant, the formation of transfer films occurs on the surfaces of friction of AISI 420 steel. The elemental composition of the friction surfaces of AISI 420 steel with FS-2 polymer contained 7% DOS microcapsules composite was investigated by XPS. The presence of the N1s spectrum in the survey spectra indicates the presence on the surface of friction of fragments of the phenylone molecule. On the surface of the steel, there are atoms of the alloying element of chromium, which are partially oxidized. Spectra N1s from the surface without friction and after friction and then from the surfaces after ion etching, demonstrate the preservation of fragments of the phenylone molecule to 15 min of ion etching.

Keywords Antifriction film · XPS spectroscopy · Polymer composites · Phenylone FS-2 · Microcapsules · Lubricants · Dioctyl sebacate

1 Introduction

Polymer composite materials are widely used in many areas of modern technology. The development of technique and technology makes new demands on the properties of polymeric materials. One of the most promising polymeric material is phenylone, which is a copolymer obtained by the polycondensation of isophthalic

A. V. Sidashov · M. V. Boiko (✉)
Rostov State Transport University, 2, Rostovskogo Strelkovogo Polka Narodnogo
Opolcheniya Sq., 344038 Rostov-on-don, Russia
e-mail: m2487328@yandex.ru

acid chloride with μ -phenylenediamine. Phenylone S-2 (FS-2) possesses high heat and frost resistance, and has high hardness, rigidity, strength, resistance to shock loads, which allows its wide application.

The purpose of this work is to increase the antifriction properties of phenylone FS-2 by modifying it with microcapsules with a dioctyl sebacate (DOS) lubricant.

Improving the performance properties of polymeric materials produced by introducing into their structure various additives and fillers. However, the introduction of additives can adversely affect the mechanical properties of the polymer matrix, and this is especially true for the addition of liquid lubricants. The most promising lubricants are synthetic oils based on esters. These oils are capable of forming antifriction films on friction surfaces, which significantly reduces the friction coefficient in the system. In addition, these oils are eco-friendly. To solve this problem, we used the method of preliminary encapsulation of a lubricant.

2 Materials and Methods

Microcapsules based on the product of the interaction of 2,4-toluene diisocyanate and 1,6-hexamethylenediamine containing DOS lubricant inside were synthesized the method of interfacial polycondensation in an oil-in-water emulsion [1–4]. The capsules were separated from the solution by centrifuging in a Beckman Coulter Allegra Centrifuge at a rotor speed of 10,000 rpm. Next, the microcapsules were mixed with phenylone FS-2 and the composite was pressed. Received samples contain 3, 5 and 7% of the capsules in the polymer.

Tribological tests of lubricants were carried out on the end friction machine according to the scheme “three pins on the steel disk”. Disks are made from AISI 420 steel, and roughness was $R_a = 1.0$. Pins are made from phenylone FS-2 or phenylone composite. The diameter of each pin was 1 cm, and the distance from the centre of the disk to the middle of the friction track was 35 mm. All tests began without running-in of rubbing surfaces, considering that the antifriction film formed during the experiment will smooth out the surface roughness of the disk, thereby reducing the friction coefficient. Among the all friction parameters, we controlled only the friction coefficient. The load on the friction unit was 0.9 MPa, and the sliding speed was 0.5 m/s for all tests.

3 Results and Discussion

The results of the tribological tests of the initial phenylone FS-2 and of phenylone with the addition of microcapsules are shown in Fig. 1. Adding microcapsules containing lubricant to phenylone improve its tribological properties. The friction

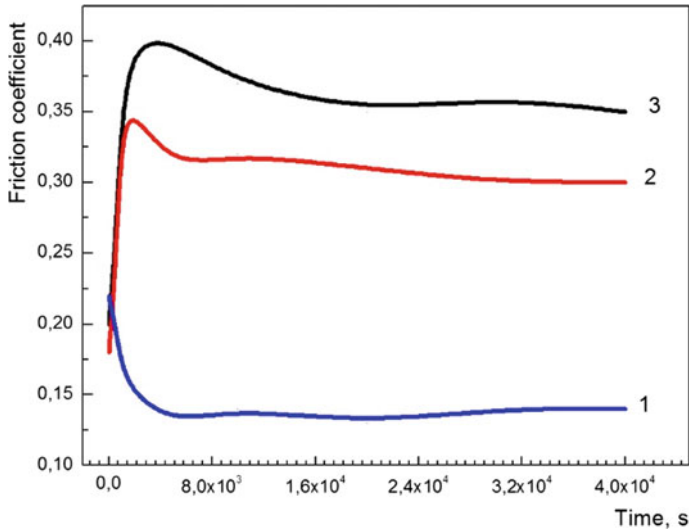


Fig. 1 Results of tribological tests on phenylone FS-2 (3); FS-2 + 3.5% DOS capsules composite (2); FS-2 + 7% DOS capsules composite (1)

coefficient for composite steel containing 7% microcapsules is three times lower than that of phenylone without additives. The obtained data are consistent with the results of previous studies [5–9].

The elemental composition of the friction surfaces of AISI 420 steel with a composite consisting of FS-2 polymer filled with 7% DOS microcapsules was investigated by XPS. Both the initial surfaces and the friction surfaces obtained after etching with argon ions for 5, 10 and 15 min, respectively, were investigated. In accordance with the structural formula of the polymer, Fig. 2, after the tribological interaction of the surfaces of steel and polymer, the transfer film on the steel surface contained only carbon and oxygen compounds belonging both to polymer and oil, and to air.

As can be seen from Fig. 3, already after 5 min of etching with Ar⁺ ions, the friction surface is mainly the surface of steel AISI 420, which contains, in addition to the main element of iron, also the alloying element chrome. The presence of traces of polymer and lubricant on the friction surface is indicated by the C1s, O1s and N1s lines of the spectra, the number of which on the surface decreases with

Fig. 2 Structural formula of phenylone FS-2

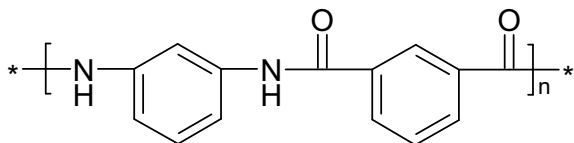
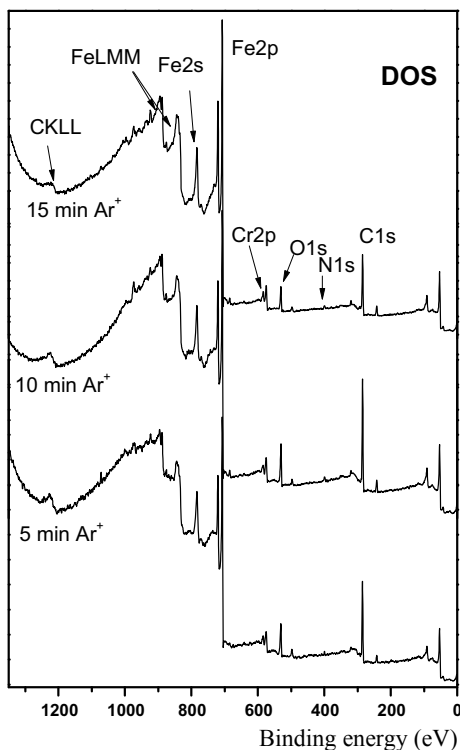


Fig. 3 XPS survey spectrum of friction steel AISI 420 with composite FS-2 + 7% DOS capsules after etching with Ar^+ ions for 5, 10 and 15 min



increasing time of ion etching. It is worth noting that the spectrum of N1s, which can be considered in this case as a kind of marker, indicating the presence on the surface of fragments of the phenylone molecule, is present on the friction surface up to 15 min of etching.

The spectra of C1s, O1s, N1s, Fe2p and Cr2p of internal lines were recorded on each of the friction surfaces studied before and after ion etching. The spectra were decomposed into components and the chemical state of atoms at each etching depth was estimated. In Fig. 4, the spectra of the initial friction surfaces, as well as the friction surfaces after ion etching (for 5, 10 and 15 min) internal lines C1s and O1s, respectively, are shown. Table 1 shows the binding energies of the components of the C1s and O1s spectra, which indicate chemical bonds on the initial friction surface and along its depth.

As can be seen from Fig. 4, C1s spectra of the original surface contain three components A, B and C. After ion etching, component C disappears. The presence of the N1s spectrum in the survey spectra in Fig. 3 indicates the presence on the surface of friction of fragments of the phenylone molecule. At the same time, the friction surface before installing the sample in the spectrometer chamber was in the conditions of air. Therefore, we interpret the origin of components A and B

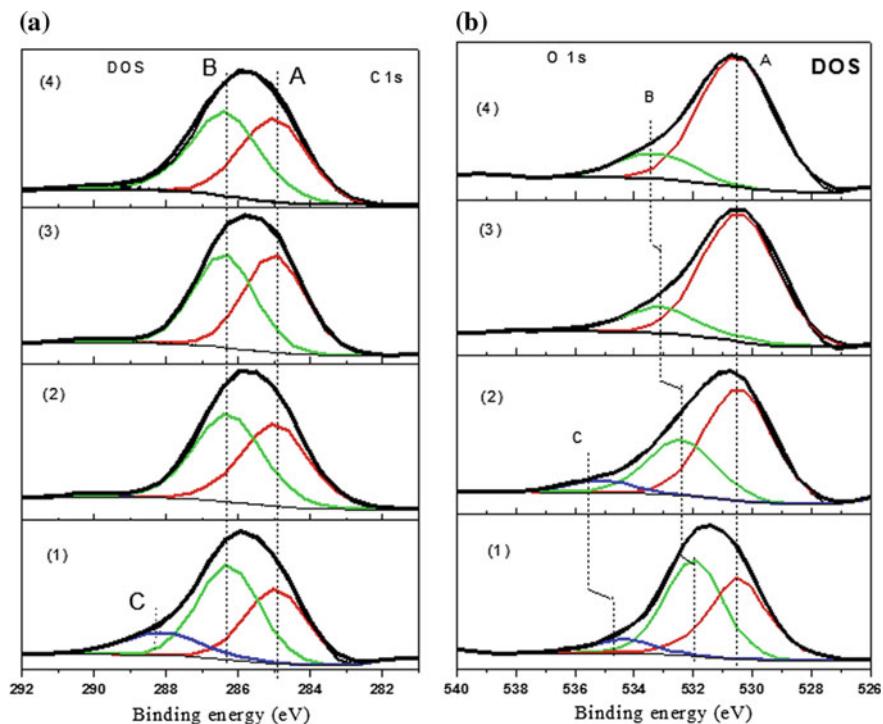


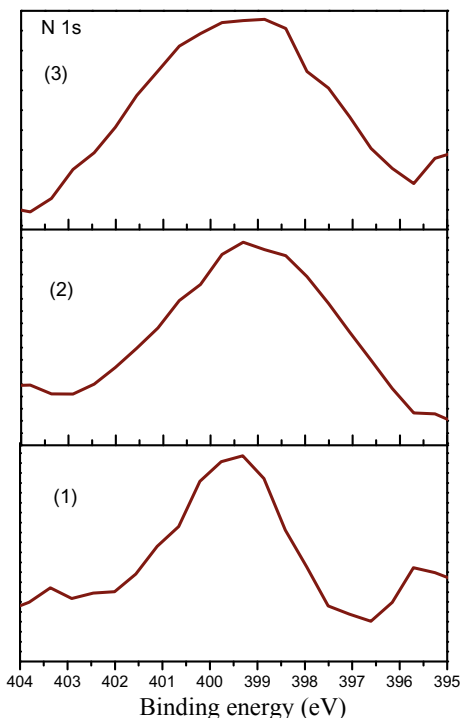
Fig. 4 C1s spectra (a) and O1s spectra (b) friction surfaces of steel AISI 420 with FS-2 + 7% DOS capsules composite (1), as well as friction surfaces after ion etching for 5 min (2), 10 min (3) and 15 min (4)

Table 1 Bond energies of the C1s and O1s components of the spectra of the original friction surface of steel AISI 420 with the FS-2 + 7% DOS capsules composite, as well as the friction surface after ion etching for 5, 10 and 15 min

Time etching, min	C1s			O1s		
	A	B	C	A	B	C
0	285.0	286.3	288.1	530.5	532.0	534.6
5	285.0	286.3	–	530.5	532.4	535.0
10	285.0	286.5	–	530.4	533.2	–
15	285.0	286.4	–	530.5	533.4	–

according to these two factors. Component A, we refer to the C–C bonds. This relationship may relate to hydrocarbon contaminations typical of the steel surface in the air and under vacuum conditions of the analytical chamber of the spectrometer [10–18]. At the same time, it is belonging to the fragments of the polymer shell of the capsules and the oil contained in the capsules cannot be excluded [19, 20]. Usually

Fig. 5 N1s spectra of the original friction surface of steel AISI 420 with FS-2 + 7% DOS capsules composite, as well as friction surface after ion etching for 5 min (1), 10 min (2) and 15 min (3)



[15], the C1s component of the spectra with an energy of about 286.3–286.5 eV is interpreted as belonging to the C–OH and C–O–C groups. Nitrogen detected on the friction surface refers to the C = N bond fragments of the phenyl molecule, where the bond is formed by sp^2 hybrid carbon orbitals lying on the surface [19, 20]. We refer component C to fragments of the phenylone molecule of the C–N bond [19, 20]. Component A in the O1s spectra in Fig. 4, and also in Table 1, we refer to metal oxides on the surface of steel [10–14]. Component B is the C–O bond; however, –OH groups can also give this energy region [19–21]. We uniquely relate component C to water molecules located on friction surfaces [15, 21].

Figure. 5 shows the N1s spectra from the initial friction surface and from the surfaces after ion etching, demonstrating the preservation of fragments of the phenylone molecule up to 15 min of ion etching. Table 2 presents data on the elemental composition of the surface of steel AISI 420 after their interaction with the FS-2 + 7% of DOS capsules composite, including after different times of etching with argon ions.

As can be seen from Table 2, the nitrogen content on the surface is in the range from 1.4 to 2.2% at. And it practically does not decrease with depth. We believe that the fragments of the phenylone molecule, which are indicated by the presence of spectra on the N1s surface, may be contained in the intergranular space of the material of steel AISI 420 or in microcracks on its surface, where they may fall during friction.

Table 2 Composition of the surface (at. %) friction after interaction with the FS-2 + 7% DOS capsules composite

Time etching, min	O1s	C1s	N1s	Fe2p	Cr2p
5	11.76	62.50	1.60	21.14	3.00
10	11.72	55.43	2.00	27.65	3.20
15	8.70	50.40	2.16	34.93	3.81

Table 3 Volumetric chemical composition of steel AISI 420 (at. %)

Fe	C	Si	Mn	P	S	Cr	Mo	Ni	Cu
84.2	1.81	0.5	0.7	0.03	0.01	12.2	0.02	0.4	0.13

Consider the chemical state of iron and the main alloying element of steel AISI 420—chromium, whose internal line spectra appear in the overview spectra in Fig. 3 after etching with argon ions. We have additionally determined the composition of the steel using an FOUNDRY-MASTER Optical Emission Spectrometer. The composition of the steel of the counter body in the initial state is given in Table 3.

Comparing the compositions of the friction surfaces (Table 2) and the composition of the steel volume (Table 3), we see that they differ due to the presence of hydrocarbon-containing films on the surfaces of hydrocarbon and nitrogen. Nitrogen is not included in the composition of steel AISI 420.

In Fig. 6, we give Fe2p and Cr2p spectra's obtained from the surface of steel AISI 420 after 5, 10 and 15 min of etching with argon ions.

Table 4 shows the energy positions of Fe2p_{3/2} and Cr2p_{3/2} peaks. The Cr2p_{3/2} spectra were additionally decomposed into components. The binding energies of these components are shown in Table 5.

Iron on the surface of steel AISI 420 after ion etching is practically in a non-oxidized state. This is evidenced by the value of the binding energy of the Fe 2p_{3/2} peak. At the same time, the weak component with an energy of about 710 eV, especially in Fig. 6 steel AISI 420 after friction with the FS-2 + 7% DOS capsules composite, indicates the presence of divalent iron atoms, possibly in the composition of FeO oxide [10, 11].

As follows from Table 4, chromium on the friction surface is oxidized more strongly than iron. Table 5 shows the concentrations of chromium atoms. We attribute component A to metallic chromium and component B to oxidized chromium [10, 11, 15]. At the same time, it cannot be excluded that the Cr2p_{3/2} spectrum from the chromium bond to the fragments of the phenyl molecule can also contribute to the B component.

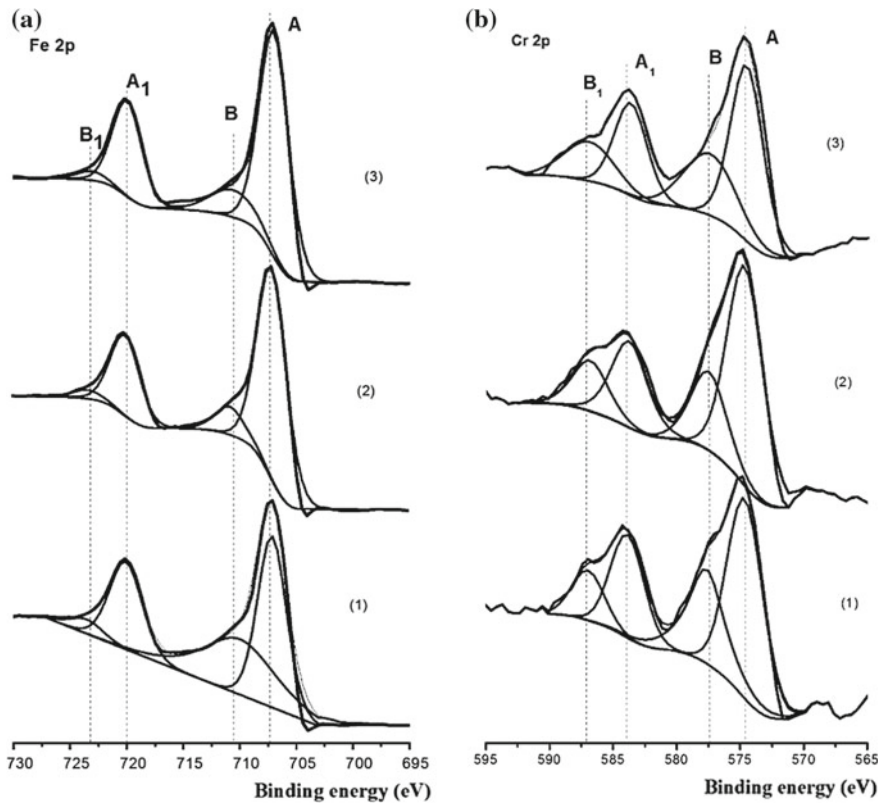


Fig. 6 Fe2p spectra (a) and Cr2p spectra (b) from the friction surface of steel AISI 420 with FS-2 + 7% DOS capsules composite, after ion etching for 5 min, 10 min and 15 min

Table 4 Energy positions of Fe2p_{3/2} and Cr2p_{3/2} peaks of the spectra of iron and chromium on friction surfaces after their etching with argon ions for 5, 10 and 15 min

Time etching, min	FS-2 + 7% DOS capsules composite	
	Fe 2p _{3/2}	Cr 2p _{3/2}
5	707.0	574.5
	710.6	577.4
10	707.2	574.4
	710.7	577.5
15	707.1	574.6
	710.7	577.4

Table 5 Binding energies (eV) of the components in the decomposition of Cr2p3/2 X-ray photoelectron spectra and their concentration (at.%) obtained from the friction surface after interacting with the FS-2 + 7% DOS capsules composite

	5 min etching		10 min etching		15 min etching	
	A	B	A	B	A	B
Bond energy	574.63	577.64	574.65	577.48	574.56	577.48
Concentration	1.9	1.1	2.34	0.86	2.44	1.37

4 Conclusion

1. The addition of DOS lubricants to phenylone microcapsules improves its tribological properties. The friction coefficient for steel with FS-2 + 7% DOS capsules composite is three times lower than that of phenylone without additives.
2. When friction on steel AISI 420 composite containing microcapsules with a lubricant on the friction surfaces of the formation of transfer films, which we recorded from the spectra of the inner lines C1s, O1s and N1s.
3. On the surface of the steel are atoms of the alloying element of chromium, which are partially oxidized. The compound of the chromium substrate with the transfer film can contribute to the region of the Cr2p3/2 spectrum component.

Acknowledgements The study has been supported of the Russian Science Foundation (project No. 18-19-00292).

References

1. Sun D, An J, Wu G, Yang J (2015) Double-layered reactive microcapsules with excellent thermal and non-polar solvent resistance for self-healing coatings. *J Mater Chem A* 3 (8):4435–4444. <https://doi.org/10.1039/c4ta05339g>
2. Jyothi Sri S, Seethadevi A, Suria Prabha K, Muthuprasanna P, Pavitra P (2012) Microencapsulation: a review. *Int J Pharma Bio Sci* 3:509–P531
3. Nakagawa K, Iwamoto S, Nakajima M, Shono A, Satoh K (2004) Microchannel emulsification using gelatin and surfactant-free coacervate microencapsulation. *J Colloid Interface Sci* 278:198–205. <https://doi.org/10.1016/j.jcis.2004.05.031>
4. Arshady R (1990) Microspheres and microcapsules, a survey of manufacturing techniques Part II: coacervation. *Polym Eng Sci* 30:905–914. <https://doi.org/10.1002/pen.760301505>
5. Kolesnikov VI, Myasnikova NA, Myasnikov FV, Boiko MV, Novikov ES, Avilov VV (2018) Physicomechanical and tribological properties of polymer composites filled with lubricant-containing microcapsules. *Russ J Appl Chem* 91:1617–1625. <https://doi.org/10.1134/S1070427218100087>
6. Kolesnikov IV, Lebedinskii KS, Boiko MV (2018) Investigation of the effect of some organic compounds on the formation of an antifriction film in a dioctyl sebacate medium. *MATEC Web Conf* 226:03025. <https://doi.org/10.1051/mateconf/201822603025>

7. Kolesnikov IV, Lebedinskii KS (2017) Ways of improving the tribological characteristics of composite polymeric materials and lubricants in friction units. *J Mach Manuf Reliab* 46:567–571. <https://doi.org/10.3103/S1052618817060097>
8. Kolesnikov IV, Bardushkin VV, Myasnikov PV (2017) Calculation of stress-deformed condition in polymer nanocomposites filled with microcapsules with lubricant. *J Theor Appl Mech* 47:37–47. <https://doi.org/10.1515/jtam-2017-0019>
9. Kolesnikov IV (2016) Metal–polymer tribosystems: basic recommendations for creating composites. *J Friction Wear* 37:507–511. <https://doi.org/10.3103/S1068366616050093>
10. Briggs D, Seach MP (1983) *Practical surface analysis by Auger and X-ray photoelectron spectroscopy*. Wiley, Chichester
11. Watts JF, Wolstenholme J (2003) *An introduction to surface analysis by XPS and AES*. Wiley, Chichester, West Sussecs, England
12. Hüfner S (1995) *Photoelectron spectroscopy*. Springer-Verlag, Berlin
13. Nefedov VI, Cherepin VT (1983) *Fizicheskie Metody Issledovaniya Poverkhnosti Tverdykh Tel (Physical methods to investigate the solids surface)*. Nauka, Moscow
14. Nefedov VI (1984) *Rentgenoelektronnaya Spektroskopiya Khimicheskikh Soedinenii: Spravochnik (X-ray electron spectroscopy of chemical compounds: handbook)*. Khimiya, Moscow
15. Hueso JL, Espinós JP, Caballero A, Cotrino J, González-Elipse AR (2007) XPS investigation of the reaction of carbon with NO, O₂, N₂ and H₂O plasmas. *Carbon* 45:89–96. <https://doi.org/10.1016/j.carbon.2006.07.021>
16. Sidashov AV, Kolesnikov IV (2017) Nonequilibrium processes of segregation and diffusion in metal-polymer tribosystems. *AIP Conf Proc* 1915:020007. <https://doi.org/10.1063/1.5017319>
17. Sidashov AV, Kozakov AT, Yaresko SI (2016) Auger and X-Ray photoelectron spectroscopy study of the tribocontact surface after laser modification. *Mater Sci Forum* 870:298–302. <https://doi.org/10.4028/www.scientific.net/MSF.870.298>
18. Myasnikova NA, Sidashov AV, Myasnikov PV (2016) The formation and functioning of surface nanostructures at tribocontact. *Mater Sci Forum* 870:303–308. <https://doi.org/10.4028/www.scientific.net/MSF.870.303>
19. Susi T, Pichler T, Ayala P (2015) X-ray photoelectron spectroscopy of graphitic carbon nanomaterials doped with heteroatoms. *Beilstein J Nanotechnol* 6:177–192. <https://doi.org/10.3762/bjnano.6.17>
20. Kumar N, Kozakov AT, Dash S, Tyagi AK, Lin IN (2013) Microstructure, chemical bonds, and friction properties of nanocrystalline diamond films deposited in two different plasma mediums. *Phys Solid State (Russian J)* 55:2076–2087. <https://doi.org/10.1134/S1063783413100181>
21. Gupta B, Kumar N, Kozakov AT, Kolesnikov VI, Sidashov AV, Dash S (2017) Lubrication properties of chemically aged reduced graphene-oxide additives. *Surf Interfaces* 7:6–13. <https://doi.org/10.1016/j.surfin.2017.02.005>

Fabrication and Triboengineering Properties of Aluminum Composite Ceramic Coatings



A. N. Bolotov, V. V. Novikov and O. O. Novikova

Abstract The paper presents the basics of the technology for fabrication of solid lubricant composite ceramic coatings that are basically a ceramic matrix with antifriction fillers based on magnetite, graphite, and molybdenum disulfide, which are formed on the aluminum alloy using the micro-arc oxidation method. It also shows the features of electrophoretic implantation of dispersed particles of magnetite, graphite, and molybdenum disulfide into a ceramic matrix. The authors have experimentally studied the dependence of coating triboengineering properties on the concentration of solid lubricant particles in the electrolyte and temperature conditions in the friction zone. As a result, they have formed the requirements for the composition of the electrolyte used to apply these coatings. The comparative triboengineering tests have shown that synthesized solid lubricating composite ceramic coatings with antifriction fillers have higher antifriction characteristics, a lower friction coefficient, and are more wear resistant compared to unsupported ceramic materials obtained by a traditional technology of anodic spark oxidation. The new synthesized coatings can improve antifriction characteristics of friction surfaces for units operating in the absence of a lubricant by several times. The wear analysis of the obtained coatings has shown that the obtained ceramic coating with the molybdenum disulfide as a filler has the highest antifriction properties. The triboengineering tests of molybdenum disulfide coatings (as a solid lubricant) confirmed the need for the adsorbed protective films on the dispersed phase particle surface during the microarray application of these coatings to improve antifriction properties of the particles.

Keywords Micro-arc oxidation · Solid lubricant · Ceramic coating · Antifriction filler · Friction · Wear

A. N. Bolotov · V. V. Novikov · O. O. Novikova (✉)
Tver State Technical University, 22, A. Nikitin Emb., Tver 170026, Russian Federation
e-mail: onvk@mail.ru

© Springer Nature Switzerland AG 2020
A. A. Radionov et al. (eds.), *Proceedings of the 5th International Conference on Industrial Engineering (ICIE 2019)*, Lecture Notes in Mechanical Engineering,
https://doi.org/10.1007/978-3-030-22041-9_132

1269

1 Introduction

Due to high specific strength, low density, and corrosive resistance, aluminum and its alloys are widely used as an engineering material in engineering and medical industry [1–3]. Their low wear resistance holds the use of aluminum alloys in friction units back. Specialists pay much attention to studying wear resistance of aluminum alloys. However, the analysis of the latest studies shows that traditional methods of improving wear resistance of aluminum products are ineffective.

A promising method for improving the surface properties of aluminum alloys that are important for friction is to create a protective oxide layer on its surface by the micro-arc oxidation method [4–7]. This method assumes that when high-density current passes through the valve metal–electrolyte interface, it creates the conditions for micro plasma discharges to occur on the metal surface in micro volumes with high local temperatures and pressures. The electrochemical action of discharges forms the surface layer consisting of the oxidated forms of base metal elements and electrolyte components [8, 9]. Depending on the micro-arc oxidation mode and electrolyte composition, it is possible to obtain ceramic coatings with a wide range of physico-mechanical properties [10–13]. The structure of the coating obtained by micro-arc oxidation is porous ceramics with a complex composition, which is formed due to metal surface oxidation and inclusion of electrolyte elements in the coating composition. The studies in this field made it possible to obtain oxide layers with a thickness of several hundred micrometers on aluminum. However, that coatings properties were not optimized for friction conditions without a liquid or plastic lubricant (“dry” friction) [14]. At the same time, self-lubricating materials in friction units are in demand in various modern assemblies of machines and mechanisms.

Micro-arc oxidation coatings obtained in suspension electrolytes have a wider range of physico-mechanical properties [15]. In order to obtain solid ceramic coatings, we propose to include micro- and nano-sized particles of an antifriction filler into an oxide matrix. A similar approach allowed obtaining oxide composite coatings with unique abrasive properties [16–18].

1.1 Work Objective

The work objective is to develop some basics of the technology for fabrication of solid lubricant composite coatings, which are ceramic matrix with antifriction fillers based on magnetite, graphite, and molybdenum disulfide formed by the method of micro-arc oxidation on aluminum alloy. To study the antifriction characteristics of the obtained oxide composite coatings by experiment.

1.2 Methodical Issues of Experimental Research

The base material for the study is D1 aluminum-based alloy, which is widely used in engineering (about 4% copper, less than 1% iron, silicon, and manganese). We conducted the synthesis of oxide coatings with antifriction powders in electrolytes containing dispersed solid lubricant materials as a filler. These materials have modified the structure of the hardened surface layer when oxidized.

The installation for the synthesis of coating micro-arc oxidation consisted of a condenser current source of and a bath with a cooling jacket filled with an experimental electrolyte. The electrolyte consists of alkali (NaOH), liquid glass, and the main component—distilled water.

The nanodispersed phase of the ceramic coating was a magnetite that is able to improve mechanical properties of the coatings and reduce friction by reducing adhesive bonds between contacting surfaces. Highly dispersed magnetite (a typical size is about 7 nm) has been obtained by chemical precipitation [16, 19]. The peptization process in a liquid glass solution was carried out in order to protect highly dispersed magnetite particles from oxidation and to prevent their coagulation.

An antifriction coating dispersed phase (in addition to a magnetite), we used finely dispersed graphite and molybdenum disulfide powders (with 2–10 μm particle size) that have high antifriction properties. A surfactant to modify a particle surface was glycerin.

During oxidation, dispersed particles were placed into the coating composition through the arc electrophoresis. Electrolyte particles have been transported to the processed alloy surface by a inhomogeneous electric field, entered the spark discharge burning zone and are included into the coating composition.

We used an MTP friction machine [20] to conduct triboengineering tests of composite coatings in the field of medium pressures. The friction scheme is the following: disk-finger (coated). The counter body materials for testing the obtained antifriction coatings were U8A tool steel and KhVG hardened alloy tool steel (45–50 HRC). An inductive indicator continuously was recording linear wear values. During the research, a sliding speed was 0.15–0.95 m/s and contact pressures were 0.5–15 MPa without using any additional lubricant. The measurement error for the linear wear intensity did not exceed 17%, for the friction coefficient did not exceed 10%.

The thickness of non-conductive coatings has been determined using an eddy current thickness gauge.

2 A Background Technology for Coating Production

The background technology for producing composite coatings is based on the existing technology of oxide coating micro-arc synthesis on an aluminum alloy [4]. The known coatings obtained in an electrolyte that contains alkali and a sodium

silicate has a sufficient thickness for practical use (up to 0.3 mm), good adhesion with the substrate material, and high hardness. The main disadvantage of the base coating is a high coefficient of dry friction that causes friction pair jamming and quick fatigue failure of contacting surfaces with a high probability. Considering this disadvantage, we modified the coating to reduce the friction coefficient without using a lubricant.

We have solved the problem using electrophoretic injection of solid lubricant particles into the ceramic matrix of the coating. Energizing leads to the growing barrier oxide layer on the surface of the coated aluminum sample, which forms a refractory ceramic matrix. At the same time, in the electrolyte solution, fine solid lubricant particles drop out and are kept by electromagnetic forces on the sample surface. They are gradually placed into the matrix.

However, the inclusion of graphite particles into the coating is complicated due to its good conductive properties. When electrical current is connected, graphite particles subside on the coated workpiece surface and cause its corrosion. They disturb the passive surface layer. Therefore, sites of non-discharge current flow appear.

In order to solve this problem, there are two approaches to form a coating. According to the first approach, the electrochemical process of coating production is divided into two stages. At the first stage, a sample is coated in the electrolyte without graphite particles during 15 min under the voltage of 450–500 V. It is sufficient to create a thin dielectric coating of 3–10 μm . Further, the process is carried out in the electrolyte containing graphite particles with an end-point voltage of 500–600 V and current density of 3 A/dm^2 during 1 or more hours. Hydrophobized graphite particles in the suspension electrolyte can coagulate and subside, which lowers their concentration in the coating. In order to avoid conglomerates, the electrolyte is actively stirred using compressed air barbotage. The obtained ceramic coating has a concentration gradient of a dispersed graphite filler, which is absent in the layer bordering aluminum.

A distinguishing feature of the second method of forming a coating is the fact that graphite is coated by a dielectric layer from glycerin adsorbed on its surface in order to decrease electrical conductivity of the contact graphite—aluminum surface. To prevent glycerin decomposition and changing its properties as a polar liquid at high temperatures, the electrolyte is cooled to a temperature of 5–10 $^{\circ}\text{C}$. Figure 1 shows the coating microstructure (black dots represent inclusions of graphite particles).

Another material of the dispersed phase is a molybdenum disulfide MoS_2 . It has good lubricating properties. Additionally, it is a dielectric according to its electro-physical features. A disadvantage of molybdenum disulfide is its relatively low chemical stability. During coating synthesis, due to high temperature and oxidizing environment, it can turn into molybdenum dioxide and trioxide that do not have solid lubricant properties. In order to prevent oxidation of molybdenum disulfide, we also used the protective properties of glycerin adsorbed on the particles. The electrochemical coating process included initial voltage of 470 V and final one of 580 V, the current density of 2.4 A/dm^2 , and it lasted for several hours.

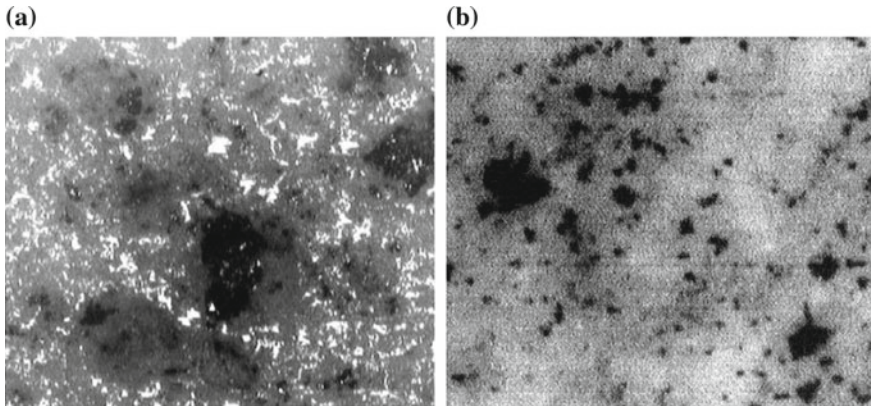


Fig. 1 Surface microstructure of the ceramic composite coating with a graphite filler on D1 aluminum alloy: **a** in typical light; **b** in polarized light ($\times 500$)

The introduction of nano dispersed magnetite particles into the composite coating composition did not cause any technological difficulties and did not significantly affect the micro-arc oxidation process.

The base distilled water electrolyte contains 0.1%wt of NaOH alkali and 1.1%wt of sodium silicate (the suspension electrolyte with MoS₂ contains 1.5%wt of sodium silicate). We also added dispersed particles of graphite, molybdenum disulfide, and magnetite to the base electrolyte (2–6%wt).

3 The Results of Experimental Studies and Their Discussion

It is established that the friction coefficient of a ceramic coating with a dispersed filler MoS₂, which is not treated in glycerin, is 0.25–0.3. This is typical for coating micro-arc oxidation without antifriction fillers. This confirms that it is reasonable to use glycerin or a surfactant with similar ionic properties.

Figure 2 shows time dependences of the friction coefficient for the studied materials. Test conditions are the following: the contact pressure is 1.5 MPa and the sliding speed is 0.47 m/s. At the beginning of the test, there is running in of coating materials, therefore the friction force decreases. The friction coefficient increases due to the gradual abrasion of coatings and the appearance of metal contact areas. The friction force value for composite coatings with a molybdenum disulfide is lower than the one of coatings with dispersed graphite (curves 2 and 3) at permissible operating temperatures of the friction unit not above than 150 °C.

Figures 3 show the effect of the concentration in an antifriction filler electrolyte on triboengineering properties of ceramic coatings. The increase in the concentration of MoS₂ particles and graphite leads to an almost linear decrease of the friction

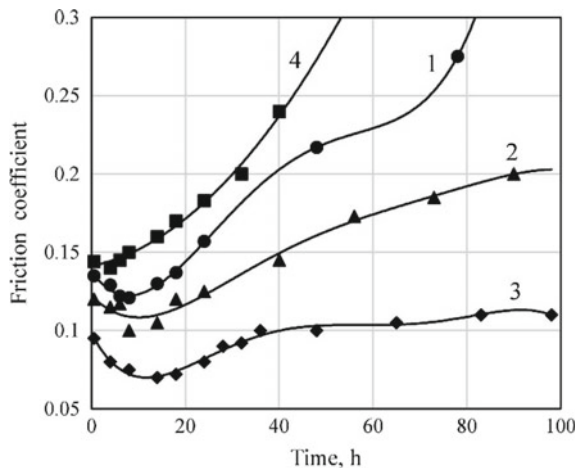


Fig. 2 Friction coefficients of composite ceramic coatings depending on test duration. Antifriction fillers: 1—no filler, 2—graphite, 3—molybdenum disulfide, and 4—magnetite

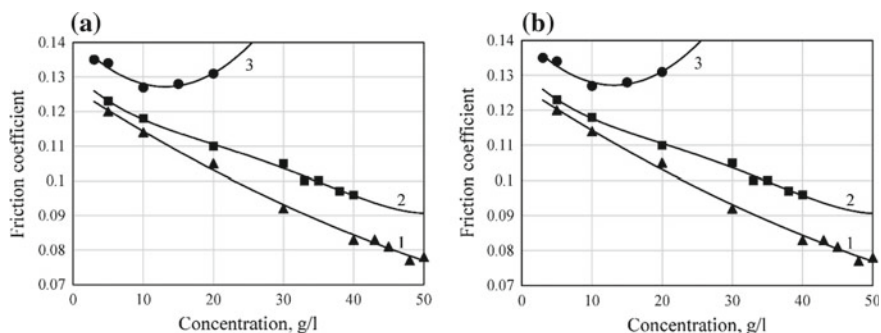


Fig. 3 Dependence on MoS₂ particle concentration (1), graphite (2), and magnetite (3) in the electrolyte: **a** friction coefficient; **b** linear wear intensity

coefficient (Fig. 3a). The dependence of the linear wear intensity on MoS₂ concentrations (Fig. 3b, curve 1) is extreme. The optimal concentration of MoS₂ in the electrolyte is about 45 g/l, which provides about 25% vol of MoS₂ concentration in the formed coating. Further increase in the concentration of molybdenum particles in the electrolyte (over 50 g/l) and in the finished coating leads to a decrease in its strength, wear resistance, and degradation of adhesive properties of adhesion with a substrate material.

Graphite lubricating properties in air are lower than those of MoS₂. Considering this fact, increasing its concentration in the electrolyte leads to a less significant decrease in the friction coefficient. The optimal concentration is 30 g/l in the electrolyte and, consequently, about 20% in the coating composite material.

Table 1 Properties of composite coatings with various antifriction fillers

Dispersed phase	Friction coefficient	Linear wear rate	Coating hardness (GPa)	Oxide layer thickness (mm)
Molybdenum disulfide	0.07–0.11	5×10^{-9}	10–12	0.1–0.50
Graphite	0.10–0.16	7×10^{-9}	12–14	0.1–0.45
Magnetite	0.15–0.26	9×10^{-9}	14–17	0.1–0.30
No filler	0.11–0.25	15×10^{-9}	12–14	0.1–0.40

The critical concentration value is defined as 35 g/l (Fig. 3b, curve 2). Above this value, there is a sharp increase in the linear wear intensity due to a decrease in coating thickness and its discontinuity. A further increase in the concentration of graphite particles in the electrolyte to 40 g/l leads to breaking the coating formation process due to the catastrophic growth of corrosion spots on the composite sample surface.

Table 1 presents the results of triboengineering tests of the obtained coatings. It also considers the properties of coatings without fillers. The data in the table shows that the inclusion of nano dispersed magnetite particles into the coating composition increases coating micro hardness. This is due to the fact that the coating becomes less loose as porosity decreases by twice. Frictional properties of magnetite coatings have improved under unlubricated friction. However, their overall level is lower than the level of coatings with solid lubricants.

Figure 4 presents photographs of friction tracks on the coating with MoS₂ particles. Dark areas on the friction surface of a ceramic antifriction coating sample and a steel counter sample indicate the formation of a protective MoS₂ lubricating film on them.

We have studied how contact pressure affects the linear wear intensity of coatings with graphite and molybdenum disulfide particles. The ceramic coating with the MoS₂ filler has shown the highest antifriction characteristics in the entire range of working pressures (0.5–7 MPa).

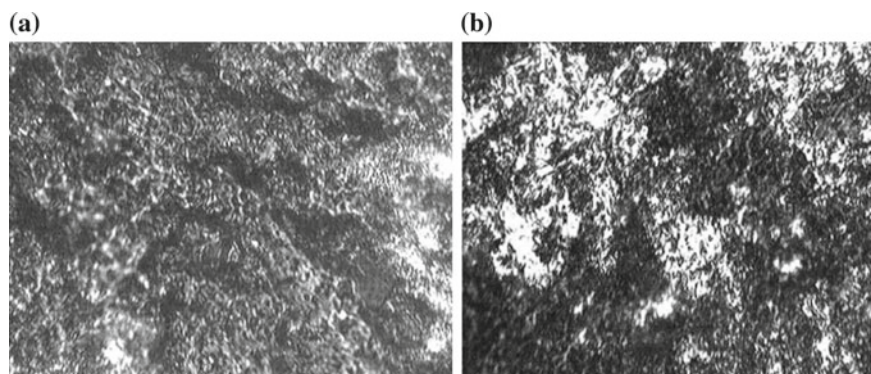


Fig. 4 Composite coating friction surfaces with molybdenum disulfide: **a** A coating surface; **b** A counter body (KhVG steel)

The increased temperature in the friction zone significantly affects coatings with molybdenum disulfide and to a lesser extent on the coating with graphite. At temperatures up to 150 °C, coatings with molybdenum disulfide particles show better triboengineering properties than coatings with graphite particles, while at temperatures of 200–450 °C coatings with graphite particles have some advantages due to different thermal stability of dispersed phase particles and a different lubricating mechanism.

In real friction units, we can often see counter body material heavy wear, not an antifriction material. In the above-mentioned experiments, the steel counter body wear was of the same order as the coating wear. The higher its hardness, the smaller it was.

Triboengineering studies have confirmed the effectiveness of dispersed solid lubricants in the synthesis of ceramic coatings used in dry friction units. They have also shown the feasibility of using surfactants (glycerin) to produce coatings.

4 Conclusion

We propose a new approach to fabrication of solid lubricant composite ceramic coatings on aluminum and its alloys using micro-arc oxidation. The method assumes the additional injection of a finely dispersed molybdenum disulfide, which is modified by a surfactant, into an electrolyte.

It is shown that oxide ceramic coatings obtained by micro-arc oxidation have higher antifriction and antiwear properties. Therefore, they are suitable to apply in slide bearings without additional lubrication with liquid or consistent materials. A composite ceramic coating with a solid lubricant filler MoS_2 has a linear wear rate and a friction coefficient 1.5–2 times lower than a coating with dispersed graphite particles. Oxide coatings with a nano dispersed magnetite have substantially better triboengineering characteristics than traditional aluminum oxide coatings have. However, they are not as good as ceramic solid lubricants filled with MoS_2 .

Acknowledgements The work has been financially supported by RFBR (Grant 18-48-690001).

References

1. Vityaz PA, Basinyuk VL, Belotserkovskii MA et al (2012) Application of nanostructured materials and the activated methods of surface engineering for advanced technology. *Mekhanika mashin, mekhanizmov i materialov (Mechanics of machines, mechanisms and materials)* 3–4(20–21):46–66
2. Tikhonenko VV, Shkilko AM (2012) Method of microarc oxidation. *Vostochno-evropeyskiy zhurnal peredovykh tekhnologiy (East Euro J Adv Technol)* 2(56):13–18

3. Gnedenkov ST, Sinebryukhov SL, Sergienko VI (2013) Kompozitsionnye mnogofunktsionnalye pokrytiya na metallakh i splavakh, formiruemye plazmennym elektroliticheskim oksidirovaniem (Composite multifunctional coatings on metals and alloys formed by plasma electrolytic oxidation). *Dal'naya nauka, Vladivostok*
4. Suminov IV, Epelfeld AV, Lyudin VB, Krit BL, Borisov AM (2005) Mikrodogovoe oksidirovanie (teoriya, tekhnologiya, oborudovanie) (Microarc oxidation (theory, technology, equipment)). *EKOMET, Moscow*
5. Belevantsev VI, Terleeva OP, Markov GA (1998) Microplasma electrochemical processes. *Zashchita metallov (Metal protection)* 34(5):471–486
6. Bozza A, Giovanardi R, Manfredini T et al (2015) Pulsed current effect on hard anodizing process of 7075-T6 aluminium alloy. *Surface Coating Technol* 270:139–144
7. Bayati MR, Zargar H, Molaei R et al (2010) One step growth of W03-loaded Al₂O₃ micro/nano-porous films by micro arc oxidation. *Colloids Surface A Physicochem Eng Aspects* 355:187–192
8. Matykina E, Arrabl R, Mohamed A et al (2009) Plasma electrolytic oxidation of pre-anodized aluminium. *Corros Sci* 51:2897–2905
9. Yerokhin AL, Nie X, Leyland A et al (1999) Plasma electrolysis for surface engineering. *Surface Coating Technol* 122:73–93
10. Gordienko PS, Dostovalov VA, Efimenko AV (2013) Mikrodogovoe oksidirovanie metallov i splavov (Microarc oxidation of metals and alloys). *DVFU, Vladivostok*
11. Timoshenko AV, Magurova VYu, Artemova SYu (1996) Influence of additives in an electrolyte, oxidation of complex compounds on the process of microplasma application of coatings and their properties. *Fizika i himiya obrabotki (Phys Chem Mater Process)* 2:57–63
12. Yerokhin AL, Snizhko LO, Gurevina NL et al (2004) Spatial characteristics of discharge phenomena in plasma electrolytic oxidation of aluminium alloy. *Surf Coat Technol* 177–178:779–783
13. Yerokhin AL, Shatrov A, Samsonov V et al (2005) Oxide ceramic coatings on aluminium alloys produced by a pulsed bipolar plasma electrolytic oxidation process. *Surf Coat Technol* 199:150–157
14. Malyshev VN, Markov GA, Fedorov VA et al (1984) Features of the structure and properties of coatings applied by microarc oxidation. *Himich. mashinostroenie (Chem Eng)* 1:26–27
15. Borisov AM, Krit BL, Lyudin VB, Morozova NV, Suminov IV, Epelfeld AV (2016) Microarc oxidation in electrolyte suspensions (review). *Elektronnaya obrabotka materialov (Electr Mater Process)* 1:50–77
16. Bolotov AN, Novikov VV, Novikova OO (2006) The use of microarc oxidation for the production of ceramic diamond-containing material. *Uprochnyayushchie tekhnologii i pokrytiya (Strengthening Technol Coatings)* 3:13–16
17. Bolotov AN, Novikov VV, Novikova OO (2005) Analysis of work of tribo-couplings on the basis of ceramic diamond-containing materials. *Trenie i iznos (J Friction Wear)* 26(3):279–284
18. Bolotov AN, Novikov VV, Novikova OO (2017) Dependence of wear of friction pair composite diamond-containing material-ceramics. *Mekhanika i fizika processov na poverkhnosti i v kontakte tverdykh tel, detaley tekhnologicheskogo i ehnergeticheskogo oborudovaniya (Mech Phys Process Surface Contact solids Parts Technol Power Equip)* 10:153–157
19. Fertman VE (1988) *Magnitnye zhidkosti: spravocnoe posobie (Magnetic liquids: a reference book)*. Vysheysh, Shk, Minsk
20. Bolotov AN, Novikova OO, Novikov VV (2017) Studying tribotechnical properties of nanostructured lubricating oils with various dispersive media. *J Friction Wear* 38(2):121–125

Formation and Properties of Multilayer Composite Solid Lubricant Coating



I. N. Shcherbakov, A. A. Korotkiy and E. V. Egelskaya

Abstract Based on the experimental data on a composite solid lubricant coating, which can be applied within a wide temperature range and under high loads, has been developed. The coating consists of several layers. The layers differ from each other by the physical and chemical composition and the method of application to the steel surface. The first layer of the composite solid lubricant coating has been obtained using the method of chemical deposition of the nickel-containing layer. The first layer obtained consists of the coating with a polyphase structure, such as nickel-phosphor, nickel, etc. The following layer has been obtained by the application of the water solution of aluminum phosphate and chrome to the surface of the first layer. The last layer is applied on the second layer in the form of the solid lubricant coating. The last layer is a binder with a composition of particles of solid lubricants. The universal technology to form the multilayer composite solid lubricant coating has been developed and its properties have been studied.

Keywords Coating · Friction · Technology · Composition · Aqueous solution · Chemical precipitation

1 Introduction

At the end of the twentieth century, the advances in theoretical physics and chemistry as well as in the theory of dissipative structures offered many opportunities for the increase of reliability and durability of the modern and prospective equipment.

It is known that solid lubricant coatings are used in different moving friction assemblies and are among the most promising coatings applied to steel parts operating under high contact pressure, in vacuum, in inert media, some aggressive

I. N. Shcherbakov (✉) · A. A. Korotkiy · E. V. Egelskaya
Don State Technical University (DGTU), 1, Gagarin Square, Rostov-on-Don 344000, Russia
e-mail: spravka_n@mail.ru

media, in quite wide temperature range, and they are extremely stable in severe operating conditions and nuclear reaction [1–6].

Wear-resistance coatings based on solid lubricant coatings are used in cases, where application of ordinary lubricants is not efficient or impossible [2–4]. Improved wear resistance, low friction coefficient, abrasability, and uniform thickness of the coating make it possible to use solid lubricant coatings to increase durability of parts in hydraulic, pneumatic, fuel, and other systems.

Many composite solid lubricant coatings were developed and studied throughout the world [6–8], but there are just a few coatings, which can be used within wide temperature and load range.

2 Experimental Data and Their Discussion

Based on the experimental studies conducted in the laboratory of the Special Technological Bureau Federal State Unitary Enterprise (ORION), one developed the composite coating applied to steel items, characterized by good adhesion to the surface, good contact, and low friction coefficient allowing for considerable increase in the surface wear resistance when used at high temperatures and under high loads, consisting of three layers.

Each layer represents a composite coating, performing specific functions and applied according to the developed technology. The first layer consists of the coating obtained by application of the composite coating containing in the course of friction the nickel phases and phases of nickel and phosphor compound. This coating is subject to water solution deposition.

The technology of the first layer application from the water solution includes the following processes: part surface preparation for the coating application; preparation of the working solution; application of the coating to the item; heat treatment of the coating; coating quality control.

Before application of the first layer of the coating on steel samples, the surface is prepared using standard methods [5–27].

The working solution was prepared according to specific sequence to prevent nickel formation in the solution in the absence of parts in the tank. For this purpose, the required quantity of distilled water was added to the chemical deposition plant and heated up to 55–60 °C. Then, at intimate mixing (until complete decomposition of components) the estimated quantity of nickel salts, buffering, complexing additives, and modifying agents was added successively. The solution was heated up to 80–85 °C and the estimated quantity of hypophosphite was added after heating. Before putting the parts into the tank, the working solution temperature was increased up to 90 °C. A distinctive feature of the coating first layer deposition is the adding to the solution of 5–6 g/l of molybdenum disulfide 2–3 min after the deposition starts. Deposition time—from 0.2 to 1 h depending on steel grade, item configuration, and further use of the item. Then the items with deposited coating were washed with cold running water, underwent heat treatment at 200–210 °C,

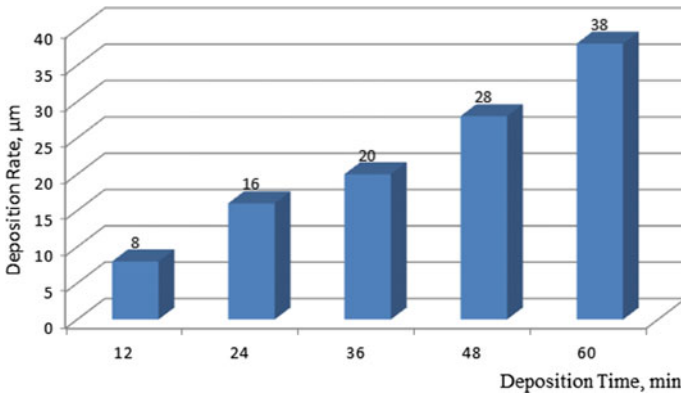


Fig. 1 First layer deposition rate against deposition time

and cooled down in the air within 10–15 min. This optimum temperature was determined with consideration for research data on deposition time, deposition rate, porosity, and adhesion. The results of experimental data on the deposition time and rate are provided in Fig. 1. Adhesion and porosity of the first layer meet the requirements, established for this type of coatings.

The composition of the developed solution is presented in the next form (by pH 4,8–5,5), g/l:

$\text{NiCl}_2 \cdot 6\text{H}_2\text{O}$ —20–30;
 $\text{NaH}_2\text{PO}_2 \cdot \text{H}_2\text{O}$ —10–15;
 Thiocarbamide—0.002;
 $\text{K}_2\text{O} \cdot n\text{TiO}_2$ MoS_2 —5–6.

The second layer of the composite solid lubricant layer is applied by dipping the steel part with the first layer applied into the solution containing the aluminum phosphate and chrome and having pH from 1 to 3. The surplus of the second layer was carefully removed from the part surface. Then, heat treatment was performed at 400–410 °C within 40–45 min. [4, 5]. When heated, the polycondensation reaction takes place in the second layer, resulting in formation of various types of polymer phosphates and hardening of the first and second layers. The resulting phosphate layer has good physical and mechanical properties, durability, is resistant to heat shocks and high temperatures [9].

The final layer of the composite solid lubricant coating is applied to the surface of the second layer in the form of solid lubricant layer. Suspension of the solid lubricant layer is prepared in advance and is mechanically agitated until complete decomposition of components in the distilled water and is applied to the second layer using a brush or dispenser. Upon application of the third layer, the heat treatment in the heating cabinet was performed at 300 °C during 20–120 min.

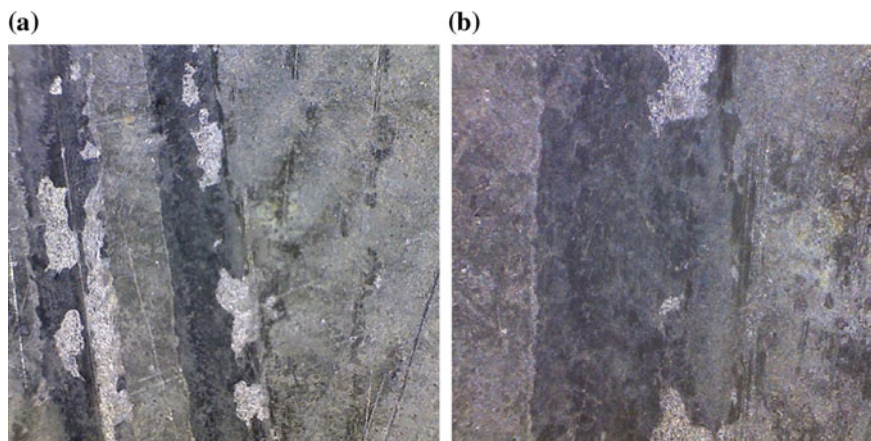


Fig. 2 Pictures of surface of the solid composite lubricant coating: **a** $\times 20$ zoom; **b** $\times 200$ zoom

The ratio of components in suspension of the solid lubricant layer, g/l:

Cadmium chloride—10–30;
 Zinc nitrate—20–50;
 Magnesium oxide—12–36;
 Silver nitrite—10–20;
 Orthophosphoric acid—200–280;
 Nitric acid—5–20;
 Molybdenum disulfide—200–250;
 Distilled water—up to 1 l.

Appearance of the coating is shown in Fig. 2.

The composite solid lubricant coatings of the same thickness obtained from three compositions were tested at reciprocating friction ball-and-plate machine developed by ORION at the ball velocity $V = 0.04$ m/s and specific pressure of 1000 MPa. The tests were carried out at +23, +150, +350 °C. Test results are shown in Figs. 3 and 4.

Based on the analysis of data, provided in Figs. 3 and 4, one may conclude that the developed multilayer coating has the following tribological properties: high wear resistance and relatively low friction coefficient. These results are confirmed by tests conducted at ORION enterprise and at a number of industrial enterprises of Rostov region. Positive result was obtained when the coatings were used in friction assemblies of the sleeve-type bearings.

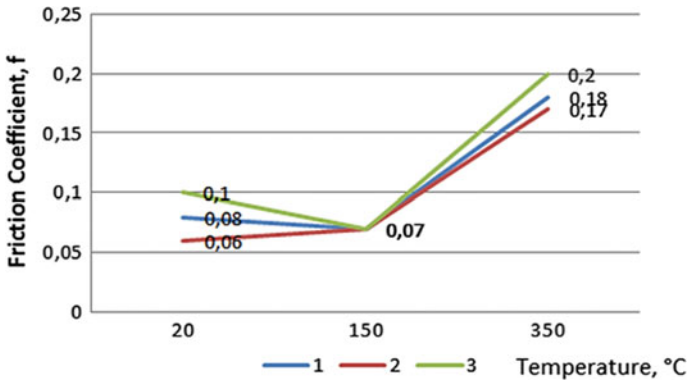


Fig. 3 Test results for composite solid lubricant coatings (friction coefficient against coated part temperature)

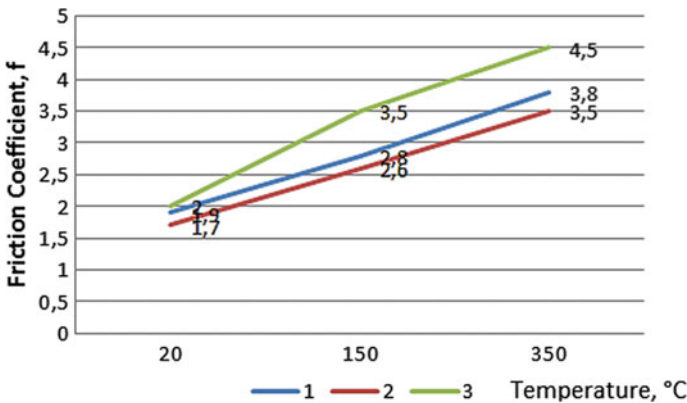


Fig. 4 Test results for composite solid lubricant coatings (wear rate against coated part temperature)

3 Summary

1. The technology for formation of multilayer composite solid lubricant coating properly functioning in ambient conditions under high specific loads and elevated temperatures has been developed.
2. The components for each layer of the multilayer composite solid lubricant coating have been selected.
3. Technical tests of the multilayer composite solid lubricant coating have been conducted: friction coefficient and wear rate depending on the composition, temperature of samples have been determined. The obtained results prove the performance capability of the coating.



References

1. Mayorova LA (1971) Solid Non-organic substances as high-temperature lubricants. New About Solid Lubricants, Nauka, Moscow, p 96
2. Mashkov YK (1996) Tribology of construction materials: study guide. OmGTU, Omsk, p 304
3. Matveevsky RM (1971) temperature stability of boundary lubricating layers and solid lubricant coatings at friction of metals and alloys. Nauka, Moscow, p 215
4. Shcherbakov IN, Trofimov GE, Loginov VT, Derlugyan PD, Gerken NV (2015) Method of formation of composite antifriction coating. RU Patent 2556155:15
5. Trofimov GE, Shcherbakov IN, Shevchenko MY, Loginov VT, Derlugyan PD, Ivanov VV, Derlugyan FP (2013) Composition of solid lubricant antifriction coating. RU Patent 2473711:27
6. Shcherbakov IN, Trofimov GE, Loginov VT, Derlugyan PD, Ivanov VV (2013) Composition of antifriction solid lubricant coating. ru patent 2493241:20
7. Braithwaite ER (1967) Solid lubricants and antifriction coatings. Chemistry, Moscow, p 396
8. All-Russia Oil Refining Research and Development Institute. <http://www.vniinp.ru/content/view/118/88/>. Accessed 28 Feb 2016
9. Vishenkov SA (1975) Chemical and electrochemical methods of metal coating deposition. Machine Engineering, Moscow, p 312
10. Trofimov GE, Shcherbakov IN, Shevchenko MY, Loginov VT, Derlugyan PD, Derlugyan FP, Ivanov VV (2012) Solution for chemical deposition of composite coating. RU Patent 2451113:20
11. Ivanov VV, Shcherbakov IN (2008) Modeling of the composite nickel-phosphorus coatings with anti-friction properties (monograph). Izd-vo zhurn. Izv. Vuzov. Sev.-Kavk. Region, Rostov na Donu, 112 p
12. Shcherbakov IN, Ivanov VV (2015) Analysis of synergic effect in compositional Ni-P-coatings. Euro J Nat History 3:48
13. Shcherbakov IN, Ivanov VV, Loginov VT et al (2011) Chemical nano-construct of the composite materials and coatings with anti-friction properties (monograph). Izd-vo zhurn. "Izv. Vuzov. Sev.-Kavk. Region. Technicheskie Nauki", Rostov na Donu, 132 p
14. Ivanov VV, Shcherbakov IN (2006) On Structuring of Chemically Deposited Nickel Phosphor Coating Modified by Polytetrafluorethylene. Izvestia Vuzov. Severo-Kavkazsky Region J Eng Sci 2:117–119
15. Shcherbakov IN (2003) Development of composite nickel phosphor coating modified by boron nitride and polytetrafluorethylene. Dissertation, South-Russian State Polytechnic University (NPI)
16. Ivanov VV, Shcherbakov IN, Ivanov AV, Bashkirov OM (2005) Analysis of synergic effect in compositional Ni-P-coatings. Izvestia Vuzov. Severo-Kavkazsky Region. Ser Eng Sci 4:62–64
17. Ivanov VV, Shcherbakov IN (2010) Modelling antifriction properties of heterogeneous gradient composite coatings on the surface of steel parts of friction assemblies. Izvestia Vuzov. Severo-Kavkazsky Region. Ser Eng Sci 5:72–75
18. Shcherbakov IN, Ivanov VV (2008) Synergism of components in composite nickel phosphor coatings used to improve performance of automobile parts. Izvestia Vuzov. Severo-Kavkazsky Region. Ser Eng Sci 4:116–118
19. Shcherbakov IN, Ivanov VV, Derlugyan PD, Balakay VI (2015) Composite nickel phosphor coatings modified by potassium polytitanate. Modern High-End Technol 8:62–64
20. Shcherbakov IN (2013) On system approach to development of composite antifriction coatings. Inzherny Vestnik Dona 1. <http://www.ivdon.ru/ru/magazine/archive/n1y2013/1567>. Accessed 28 Feb 2016

21. Shcherbakov IN (2003) Theoretical studies of structural conditions on the surface of antifriction materials preconditioning their self-organization in tribological contact. fundamental and applied problems of current technology, Printing House SKNTs, VSh, Rostov n/D, pp 102–110
22. Shcherbakov IN, Derlugyan PD, Loginov VT (2013) Phase disorder and synergism of properties of components of composite Ni-P Coatings. *Izvestia Vuzov. Severo-Kavkazsky Region. Ser Eng Sci* 1(170):97–99
23. Shcherbakov IN, Ivanov VV, Korotkiy AA (2018) Elaboration and investigation of metallic coating with inclusion of potassium polytitanate. *Solid State Phenom* 284:1140–1143
24. Shcherbakov IN, Ivanov VV (2011) Analysis of possible modifiers for obtaining composite Ni-P coatings with anti-friction properties. *Izv. Vuzov. Sev.-Kavk. Region. Technicheskie Nauki* 5:47–50
25. Shcherbakov IN, Ivanov VV, Bashkirov OM, Marchenko SI (2003) Structural-phase disordering onto surface of chemically precipitated nickel-phosphorus coating. *Izv. Vuzov. Sev.-Kavk. Region. Technicheskie Nauki* 3:54–55
26. Murzenko KV, Balakai VI (2014) Dependence of physic-mechanical properties of a nickel-cobalt-aluminum oxide composite electrolytic coating on the dispersity of the alloying component. *Rus J Appl Chem* 87(6):730–733
27. Murzenko KV, Kudryavtsev YuD, Balakai VI (2013) Properties of composite nickel-cobalt-aluminum oxide coating deposited from chloride electrolyte. *Rus J Appl Chem* 6(8):1235–1242

Modeling Wear of Tool's Front Surface During Turning



S. A. Kurguzov and M. V. Nalimova

Abstract In metal cutting, tool wear and restoration of its cutting properties are a significant problem for engineering production. Therefore, the development of a theoretical description of tool wear and its dependence on processing modes is a pressing issue for machine builders. The article offers a version of the mathematical model of wear of cutting tools made of composite hard alloy materials. The model of fatigue wear of carbide cutting tools for steel turning based on the cutting theory is developed in this article. The model takes into account cutting modes, the mechanical properties and the heterogeneity of the material being processed, the geometric parameters of the cutter, the instability of the cutting process, the periodic change in shavings thickness, the width of the cutting layer, the cutting speed and a number of other factors. The proposed approach allows predicting the fatigue wear of cutting tools made of hard alloy, as well as determining the ways to improve the structure of the hard alloy, the shape and geometry of the cutting plates.

Keywords Turning · Fatigue wear · Solid alloy · Cutting modes

1 Introduction

In metal cutting, tool wear is a significant problem for engineering production [1–6]. Therefore, the development of a theoretical description of tool wear is an actual task [7–23]. The article proposes a version of the mathematical model of wear of cutting tools made of composite materials, which include solid alloys.

S. A. Kurguzov · M. V. Nalimova (✉)

Nosov Magnitogorsk State Technical University, 38, Lenin Ave, Magnitogorsk 455000, Russia

e-mail: lite59@mail.ru

© Springer Nature Switzerland AG 2020

A. A. Radionov et al. (eds.), *Proceedings of the 5th International Conference on Industrial Engineering (ICIE 2019)*, Lecture Notes in Mechanical Engineering,

https://doi.org/10.1007/978-3-030-22041-9_134

1287

2 Model Development

In the case of a stationary machining process with a large depth of cut and a feed, the wear of the turning tool is mainly carried out on the front surface of the tool in the form of a “hole.” Moreover, this phenomenon is most intense during plastic contact of the cutting tool and shavings. Features of the contact interaction of the counterbody during metal cutting are associated with high specific pressures and significant movements of material particles. Tool wear depends on a large number of factors, such as feed, cutting speed, depth of cut and corners of the cutting part of the tool such as front corner, rear angle, plan angle and other factors.

Hard metal alloy is a composite material consisting of small particles of metal carbides bonded to each other by a metal bond such as cobalt. Suppose that the carbide particles in the cross section of a carbide plate located parallel to the speed of movement of the shavings are a circle or a polyhedron with an inscribed circle and with the same diameter D_d for all the considered particles. The cobalt bond between them is a layer of thickness B_d depending on the percentage of cobalt in the solid alloy (Fig. 1).

Each (i -th) particle protrudes above the averaged front surface of the cutting tool, by the value of h_{di} and accordingly lies on the depth h'_{di} . Consequently, the particles will be covered by a ligament with the central angle β_i . The area of the ligament layer is determined by the formula [mm]:

$$S_{\cup} = \pi \cdot A_d \cdot (D_d + 0,5B_d) \cdot \frac{\beta}{360}. \quad (1)$$

The shavings which move along the front surface of the cutting tool touch the tops of the particles with the force P'_z causing the formation of the force F'_{tr} (Fig. 2).

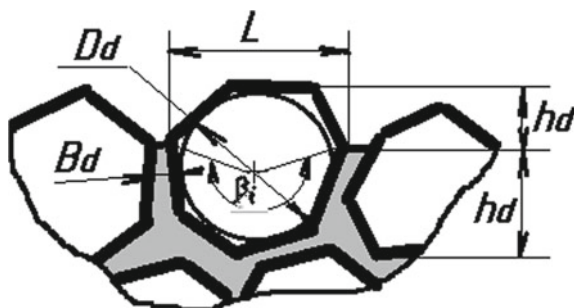
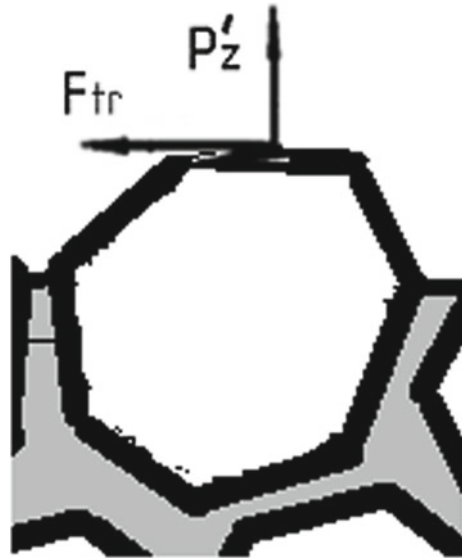


Fig. 1 Cross section of the carbide plate. D_d —particle diameter; h_d —the elevation of the particle above the plane of the cobalt bundle; h'_d —the depth of the particles; B_d —ligament layer thickness; β —angle of coverage of the particle by ligament; P'_z , F'_{tr} —part of the cutting force and frictional force attributable to this piece

Fig. 2 Diagram of the impact of forces on a particle of hard alloy



When cutting in particular when turning steel, the cutting force P_z acting on the front surface of the cutting tool is determined by the formula [24]:

$$P_z = 10 \cdot C_p \cdot t^x \cdot S^y \cdot V_\partial^n \cdot K_p, \tag{2}$$

where C_p , x , y , n —the coefficient and exponents,

- t depth of cut (mm)
- S feed (mm rev⁻¹)
- V_∂ actual cutting speed (m min⁻¹)
- K_p general correction factor [24]

The magnitude of the force P'_z acting on a single particle is determined from the condition that the particles protrude above the plane of the cobalt bond h'_{di} , and this height varies according to the law of the normal Gaussian distribution. Taking into account the fact that the particle sizes are at the level of 1 micron, therefore only 30–40% of the particles will be in contact with the shavings.

In view of the foregoing, we obtain that the cutting force acting on i -th part will be equal to [H]:

$$P'_z = \frac{P_z}{0,35 \cdot N_d}, \tag{3}$$

where

N_d the number of particles in contact with the shavings.



We can determinate N_d considering the area of shaving's contact with the front surface of the cutter, as:

$$N_d = \frac{S \cdot t \cdot \sin^2 \phi}{D_d + 2B_d}, \quad (4)$$

where

S feed (mm rev⁻¹)
 t depth of cut (mm)

Also note that

$$a = S \cdot \sin \phi, \quad (5)$$

where

ϕ the main angle in terms of the cutter (°); a —slice thickness

It should be noted that the process of cutting metals is not a stationary process. This is a process with periodically varying shavings speed and thickness. It consists of regularly increasing the cutting force and subsequent unloading by a certain amount. The shape of the free surface of the shavings which are not in contact with the front surface of the cutter confirms that. This, in turn, leads to a periodic change in the main component of the cutting force P_z with a period T . The value of this period T is conveniently expressed in relative units, in the form of the coefficient K_t or in the form of the ratio of some parameter of the shavings, for example, its thickness to the pitch of the individual shear elements.

The value of “ a ” (Eq. 5) corresponds to the greatest thickness of the shavings and the “highest” feed rate, taking into account the coefficient of shrinkage K of the shavings as follows:

$$K = \frac{a_c}{a}, \quad (6)$$

where a_c —shavings thickness, mm (measured experimentally); a —slice thickness.

The minimum shavings thickness is, as shown by measurements, 60–80% of the maximum thickness. The period of change of shavings thickness T is also expressed through its thickness:

$$T = K_t \cdot a_c, \quad (7)$$

where K_t —the ratio of the period to the thickness of the shavings.

Measurements of the shavings showed that the period T is 0.4–0.8 of the cut shavings thickness. Moreover, large values correspond to high cutting speeds.

This reasoning shows that when cutting a tool's surface, the periodically varying force P_z acts on the front of the tool which will lead to a corresponding change in the friction force on the contact surface of the shavings and tool. The frictional force

arising from the contact of the shavings and the tops of a single particle of hard alloy can be determined by the formula:

$$F'_{tr} = \mu \cdot P'_c, \quad (8)$$

where μ —friction coefficient.

Considering that with such a contact scheme, there is plastic deformation in the cutting center, and the friction coefficient will be about 0.6–0.9.

Let us determine the stresses arising in the layer of the ligament under the friction force action. Assume that the carbide particles are cylindrical and their length A_d is equal to their diameter. This is necessary for further calculations so that the area of the bond material layer of the particle contact surface in the hard alloy does not become zero.

The forces in the cobalt bond depend on the friction force, the pressure force on the particle, the total number of particles on the contact surface, the thickness of the bond layer, the angle of coverage of the particle bond, the shape of the particle and a number of other parameters. To determine the stresses in the bundle layer, we consider the equations of equilibrium of forces and moments of forces acting on a particle.

From the condition of equality of the force moments acting on a single particle, we obtain shear stresses due to the rotation of the particle by friction force acting on it as follows:

$$\tau_c = \frac{2 \cdot F_{tr}}{\pi \cdot D_d^2}. \quad (9)$$

The greatest separation stress which is formed due to the attempt to pull a piece out of an array depends on the friction force which is defined as

$$\tau_b = \frac{4 \cdot F_{tr}}{\pi \cdot D_d^2}. \quad (10)$$

The equivalent stress in the bundle layer according to the third theory of strength will be

$$\tau_{eqv} = \sqrt{\tau_c^2 + 4\tau_b^2}. \quad (11)$$

Considering Eqs. (9) and (10), we get the value of the equivalent stress in the layer of the bundle as follows:

$$\tau_{eqv} = 4\sqrt{2} \frac{\mu \cdot P_z \cdot K(D_d + 2B_d)}{a_c \cdot t \cdot \sin \phi \cdot \pi \cdot D_d^2}. \quad (12)$$

Taking into account the accepted assumptions, this equation allows to determine the magnitude and periodic variation of stresses in the layer of the ligament surrounding a single particle.

Further it is possible to determining the time or cutting path; after passing the path, a layer of carbide particles will separate from the front surface of the tool. The calculation will depend on the change in force and cutting speed, as well as the fatigue fracture curves of the bond material.

3 Conclusions

Thus, in this work, the statement of the problem of fatigue wear of solid alloy cutters is proposed. The model takes into account cutting modes, the mechanical properties of the material being processed, the geometric parameters of the cutter, the instability of the cutting process and a number of other factors. The results of the work will allow to predict the wear process of the cutting tool, to determine ways to improve the structure of the solid alloy, as well as the shape and geometry of the cutting plates.

References

1. Tabakov VP, Prudnikov YuP, Rodionovsky AYu (1998) Research of the effect of wear resistant material coatings on the wear of a cutting tool in modeling of small modular dental cutting. *Mathe Modeling Phys Econo Social Syst Process* pp 81–82
2. Pohekuev EN, Shenberger PN (2018) The study of the wear process of the working tool stamps in the environment of numerical simulation. *Soldering—2018*. In: *Digest of materials of the international scientific and technical conference*, pp 287–290
3. Platov SI, Zhelezkov OS, Yurchenko GN, Terentyev DV, Pozhidaev Y (2006) Calculation of rolling elements of bearings for contact fatigue strength using the finite element method. *Vestnik of Nosov Magnitogorsk State Technical University* 4:73–78
4. Lekhov OS, Tuv M (2015) Study of stresses in deformation areas and evaluation of wear of rolls of universal stands when rolling wide-flange beams. *Vestnik of Nosov Magnitogorsk State Technical University* 2:37–45
5. Sultanov NL, Zhirkin Y, Shlenkina MA (2014) Research of reliability of rolling bearings on tandem cold rolling mill 2000 at OJSC MMK. *Vestnik of Nosov Magnitogorsk State Technical University* 3:53–57
6. Dementieva NG (2005) Creation of methods for mathematical modeling and control of processes of tribo oxidation and diffusion tool wear during machining of metals. *Dissertation, Volgograd*
7. Simonova LA (2004) Processing of experimental data in modeling the process of tool wear. *Vestnik of KGTU im. A.N. Tupoleva* 3:19–22
8. Artemchuk VV (2011) Modeling wear of multi-layer coating. *Tribology problems* 2(60): 59–65
9. Turomsha VI, Mishchenko SN (2011) Simulation of wear and tool life when machining parts with variable depth of cut. *Vestnik of Gomel State Technical University named by P.O Sukhoy: Scientific and practical edition* 2(45):10–22

10. Filonenko S, Kosmach A (2013) Simulation of acoustic emission signals at friction and wearing the surfaces from composite materials. *Vestnik of Chernigov State Technological University, Ser Tech Sci* 3(67):22–31
11. Nikolashina A (2015) Tool blade wear modeling. *Actual Areas Res XXI Century Theory Practice* 3,5–4(16–4):128–130
12. Pimenov D (2015) Mathematical modeling of power, spent on face milling, taking into account tool wear. *Friction Wear* 36(1):56–61
13. Gubareva EA, Mozzhorina TYu, Schetinin AN (2014) Simulation of the interaction of cylindrical and spherical bodies during wear and heat generation. *Eng J Sci Innov* 3(27):5
14. Stepankin IN (2017) To the issue of contact wear of steels X12M and R6M5. *Metal Sci Heat Treatment Metals* 5(743):50–58
15. Morozov EM, Zernin MV (1999) Contact problems of fracture mechanics. Moscow, 544 p
16. Penkin NS, Penkin AN, Serbin VM (2008) The basics of tribology and tribotech. Moscow, 206 p
17. Somkina AS, Vlasov AV (2015) Wear models for predicting tool life for hot stamping. In: *The future of Russian engineering: digest of reports of the eighth all-russian conference of young scientists and specialists*, pp 192–193
18. Klopotov VD, Nesterenko VP (2005) Mathematical modeling of thermal processes in the cutting tool. *News of Tomsk Polytechnic University* 308(3):125–128
19. Markov AM, Makarova NA, Gayst SV (2017) Tool wear during milling fiberglass. *High Technol Mech Eng* 4(70):25–30
20. Kosenkov MA (2013) Investigation of disc tool wear and temperature simulation in the contact zone during milling with the displacement of the tip of the cutting edge relative to the cutting surface. *Friction Lubr Mach Mech* 10:38–40
21. Kovelonov NYu, Bolotskikh SV, Mikhailov SV, Mikhailov AS (2016) Investigation of wear resistance of carbide disc cutters with different back surface geometry. *STIN Magazine* 8: 12–16
22. Nalimova MV, Tulenkov MV (2015) Using of cubic boron nitride grinding wheels for sharpening cutting tools. In: *Modern methods of design and technology of metallurgical engineering: international digest of scientific articles*. MGТУ, Magnitogorsk, pp 44–47
23. Pozhidaev YuA, Maksimov MN, Nalimova MV, Kharchenko IV (2015) The influence of the structural elements of the turning cutters on the vibration resistance of the cutting process. In: *Modern methods of design and technology of metallurgical engineering: International digest of scientific articles*. MGТУ, Magnitogorsk, pp 63–67
24. Kosilova AG, Meshcheryakova RK (eds) (1986) Reference book of technologist—mechanical engineer. *Engineering Mechanical*, Moscow, vol 2

Evaluation of Lubricants Use with Ultrafine Copper-Containing Additives in Sliding Bearings with Reversible Friction



S. G. Dokshanim, V. S. Tynchenko and V. V. Bukhtoyarov

Abstract The paper assesses the effectiveness of the plastic lubricants use with the addition of ultrafine copper powder to increase the service life of sliding bearings operating in the swinging motion mode. When moving, when the friction force constantly changes the direction of action, the processes of the surfaces wear occur more intensively. Under the operating conditions of such a bearing assembly, the most effective method of increasing service life is the use of modified lubricants with improved anti-wear and anti-friction properties. Tribological studies have established that the introduction of ultrafine copper powder into the composition of basic industrial lubricants significantly improves performance. The use of modified lubricants resulted in a reduction of friction in the bearing assembly to 70% and a decrease in the operating temperature of the assembly to 25%. The studies carried out confirm the theoretical propositions about the positive effect of copper-containing additives on the improvement of anti-wear and anti-friction properties of grease lubricants. The presence of a lubricant that can significantly reduce friction forces reduces the amount of internal stresses and retards the development of fatigue cracks in areas of direction change. The processes of fatigue failure of the surface layers are inhibited by reducing the magnitude of shear stresses at the contact area.

Keywords Sliding bearing · Back-and-forth motion · Ultradisperse additives · Grease · Friction force · Fatigue wear · Copper-contained powder

1 Introduction

Increasing the durability of machine parts and mechanisms by reducing wear is still one of the most important problems of equipment efficient usage. Up to 90% of the failure causes are associated with the wear of the machine parts. The type of friction surfaces movement is one of the basic causes of machinery wear along with the

S. G. Dokshanim · V. S. Tynchenko (✉) · V. V. Bukhtoyarov
Siberian Federal University, 79, Svobodny pr., Krasnoyarsk 660041, Russia
e-mail: vadimond@mail.ru

loads, the speed, and the material of the machine parts. This fact is most noticeable in friction pairs operating in reciprocating or swinging movement modes. The study of the units' wear resistance operating in the reverse friction mode notes that the wear of parts in such pairs increases more than twice as compared to pairs operating unidirectional [1, 2]. During such a period of operation, the most severe friction conditions are observed in the shaft bearings due to the very small hydrodynamic effect or its complete absence. Overheating of the bearing unit caused by the increased formation of friction heat during the operation of the sliding bearing can cause jamming. The friction forces that exist have a significant influence on the stress state of the bearing material. Therefore, reducing these forces will reduce the negative effect of reverse friction [3, 4].

It is possible to reduce the wear rate and increase the durability of the bearing units with swinging movement by applying lubricants of different types and creating a strong film of such lubricants on the rubbing surfaces. Growing demands for energy efficiency of modern machines and mechanisms lead to the widespread use of nano- and ultrafine substances to create lubricants with high tribological properties. Such lubricants ensure good operation of the node in the modes of boundary and mixed friction. The lubricants should have predominantly anti-friction properties to reduce friction. The mechanism of lubricating action may be different and depends on the contact conditions. In this case, functional solid additives can be used to improve the antifriction properties of the lubricants [5–8].

The problem of creating modified lubricants with such additives as powders of soft metals, their oxides, or salts with different dispersity is in the area of high interest last decades. These are additives of fine powders of copper, tin, lead, zinc, and a number of other soft metals, as well as alloys based on them. The results of various studies have shown that lubricants with similar additives have been successfully used in bearing supports, gears, articulated joints, and other heavily loaded friction units [9–18].

The purpose of this study is to assess the possibility of the usage of grease lubricants with ultrafine copper powder additive in nodes with reversible friction such as sliding bearings. The effectiveness of lubricating compositions with ultrafine copper powder was evaluated in accordance with the methods of a rational cycle of tribological tests.

2 Experimental Study

The studies were carried out on a friction machine according to the shaft-half-sleeve scheme. A moving sample was a shaft made of steel 30 HGSA, heat-treated to hardness HRC 30–32, and shaft diameter 30 mm. The fixed sample (half-sleeve) was made of BrAZHN 10-4-4 bronze.

The tests were carried out at a specific pressure in the friction zone equal to 20 MPa without supplemental of additional lubricant during test. The shaft was to make swinging movements with a frequency of 1.8 Hz and a swinging angle equal

to 28° with the sliding friction speed equal to 2.58 cm/s. Before and after the experiments, the roughness parameters R_a were determined for the samples surfaces (the shaft and the half-sleeve). Friction torque and temperature were measured during the tests.

Industrial grease lubricants of Litol-24 and Solidol S brands were used as the base ones to create lubricating compositions with ultrafine copper powder. Litol-24 and Solidol S are widely used in bearing assemblies in different areas. Litol-24 is a lithium lubricant. It is mechanically stable and has good frost-resistant properties so it is used in a wide temperature range. Lubricant Solidol S refers to calcium lubricants and it is characterized by a narrow range of operating temperatures and low mechanical stability. However, its antifriction properties are better for lithium ones.

Ultrafine copper powder obtained by detonation synthesis in a carbon dioxide environment was used as a solid additive for basic industrial lubricant. Particle size of ultrafine copper-containing powder was from 80 to 100 nm; the concentration of copper powder in the studied lubricating compositions based on grease lubricants was in the range from 1.5 to 5 mass percent.

3 Results

The determination of the additive effectiveness and its influence on the performance properties of the lubricant compositions were investigated on the base of the following parameters: magnitude of the friction force, bearing temperature, and state of the contacting surfaces.

The graphs depicted in Figs. 1 and 2 show the dependence of friction coefficient and temperature on the friction path when using base lubricants and lubricant compositions. The lubricant was applied to the surface once, and then, the tests were carried out without replenishing the bearing assembly with lubricant throughout the friction path. For each lubricant, the tests were carried out until the friction coefficient reaches the specified threshold value of 0.2. Thereafter, friction path and value of the friction temperature increase during the passage of this path were determined.

Studies of ultrafine copper powder additive in various lubricants have shown that there is a positive effect on all lubricants used as base materials. The most effective lubricant composition is Solidol S with ultrafine copper powder additive. It was shown that such lubricating compositions made it possible to increase the friction path to achieve a given friction coefficient of 0.2 compared to base lubricants by 1.7–1.9 times and leads to 32–55% friction coefficient reduction. Also, 27–32% wear rate reduction was evaluated.

Analysis of the friction surfaces after testing allows us to judge that the effect of ultrafine copper powder additive is due the formation of high-quality micro-relief. Smoothing of irregularities on surfaces, a decrease in the number of shells, and

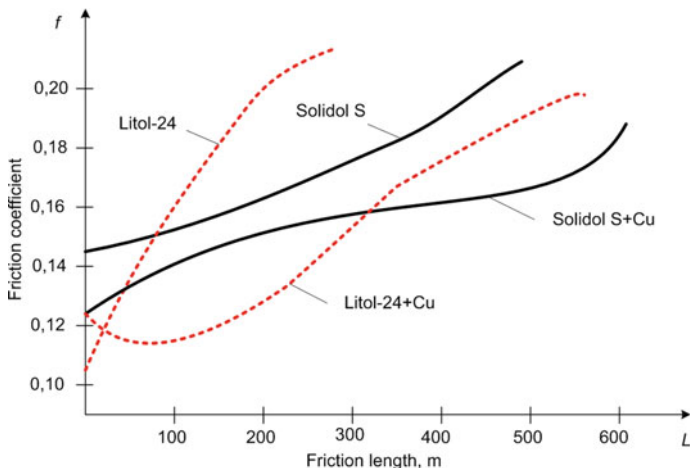


Fig. 1 Lubricants friction coefficients variation

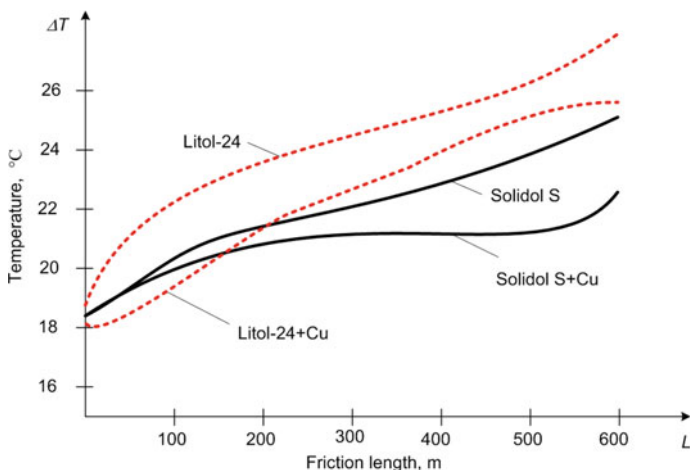


Fig. 2 Friction temperature increment variation

scratches and corrosion centers are the observed positive effects of lubricating compositions with the additive.

Such a variation in roughness increases the actual contact area, which reduces the contact pressure and more evenly distributes the load over the contour areas of contact. Figure 3 shows photographs of the sliding bearing friction surfaces obtained after testing with lubricants without additives (a) and after its addition (b).

Experimental results also make it possible to draw the conclusions about the effectiveness of adding the additive of ultrafine copper powder into a grease

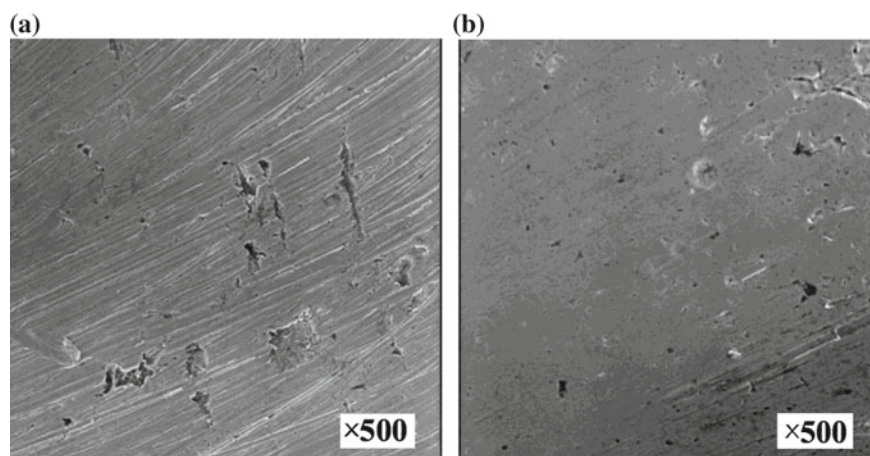


Fig. 3 Appearance of the friction tracks on the plate after experiments with lubricant Litol-24: **a** without the addition of Cu; **b** with the addition of Cu

lubricant. The damage depth, variation of the roughness value R_a/R_{a0} before and after the tests, as well as the surface quality were examined during experiments. It was found that according to these indicators, after addition of ultrafine copper powder, Litol-24 lubricant became the best. Its use allowed to get qualitative change in the friction surfaces micro-relief.

For initial lubricant Litol-24, the average ratio of R_a/R_{a0} was equal to 2.7. For Litol-24 with the addition of Cu, it decreased and was equal to $R_a/R_{a0} = 1.61$. For Solidol S, this ratio changed slightly: 1.14 and 1.06—without the addition of Cu and with the addition, respectively.

4 Discussion

The obtained results make it possible to suggest main reasons for the manifestation of good tribological characteristics of lubricants with the addition of ultrafine copper powder. It is known that the main reason for intensive wear during reverse friction is the development of fatigue cracks caused by alternating deformations. Grease deformations occur in the material when the shear stress reaches a certain value inherent for the material. From the conditions of greasiness, it is possible to establish certain relations between the friction force appearing on the surface and the yield strength for compression, tension and shear, which determine the destruction of the material [2, 3].

Friction force affects mostly shear stresses, which lead to frequent grease deformation under condition of changing the direction of motion. The tensile components of stresses and deformations caused by an increase in the friction force

lead to a decrease in the critical level of load that a part can withstand without catastrophic damage. In this case, the reduction of durability limit of the material leads to the possibility of the rapid formation of fatigue cracks in the surface layers of the material [4, 19].

The lubrication process when using a grease lubricant is somewhat different from lubrication with liquid oils. The use of oils contributes to the establishment of a friction fluid mode in the sliding bearing and the contacting surfaces of the parts will be completely separated by a lubricating layer. The anti-friction properties of the oils are related to viscosity. In the case of the grease lubricants, the boundary or mixed modes are mainly established due to the condition of the lubricant. Under working conditions, it is squeezed out of the friction path and only a thin film of lubricant remains on the contacting surfaces which perceives all contact loads. The viscosity of the lubricant thus does not affect the quality of the surfaces lubrication and the effectiveness of the lubricant and the strength of the remaining lubricant film determine only the performance properties. However, the effect of large loads and a significant increase of surface temperature can lead to its rupture and to contacting surfaces sticking consequently. In this case, the use of solid additives is required. Such additives allow to create a strong lubricant layer with good adhesion on the mechanism parts surfaces, perceiving normal and tangential loads, holding the lubricant film on rubbing surfaces, and preventing its rupture [20, 21].

The negative effect of reversible friction that occurs during swinging movement is associated with the deformation-stressed state of the material. A constant change in the direction of movement causes the deformations within a short time to change from tensile to compression and vice versa. In the contact zone, cyclically varying stresses from normal compression and alternating shear stresses from friction forces arising on the contact surface will act on the elementary volume of the material. As a result, such a combination of working conditions (slipping under friction of contacting surfaces and increasing loads) can cause an increase in stresses at the contact area, which accelerates fatigue processes [2].

A noticeable improvement in the performance properties of grease lubricants with the addition of ultrafine copper powder into them is observed especially for the friction boundary modes. Under fluid modes, the insoluble and chemically inert copper powder does not affect the composition of the lubricant. It is "lost" in its volumes weakly expressing its properties. In the boundary mode, the additive begins to show its adhesion ability to metal surfaces well due to the increased surface energy that the powder particles possess due to the production method. The rather small particle size of the ultrafine copper powder allows them to penetrate into the structural frame of a grease lubricant. It leads to a hardening of the boundary film and an increase in the resistance to fracture. The presence of its own charge forms oriented layers and firmly holds the lubricating film on the contacting surfaces. This enforces the ability of lubricant films to withstand significant loads without breaking and prevents the formation of local metal bonds.

The positive effect of the ultrafine solid additives use in lubricants can be attributed to the running-in processes of rubbing surfaces. A new roughness is formed when smoothing the most prominent irregularities. This increases the

intensity of running-in wear at the initial moment of friction unit operation, which can explain the rapid heating and the increase in the friction coefficient during this period of work. The running-in process will occur until the irregularities become large, providing an increase in the actual contact area and result in a redistribution of the load and a decrease of contact stresses—it was confirmed in previous studies. At the same time, the period of rubbing surfaces running-in before the start of the operation mode is shortened allowing stabilizing the values of the surface temperature and excluding the possible seizure of rubbing surfaces during this period.

Thus, the presence of a lubricant that significantly lower friction forces reduces the amount of internal stresses and retards the development of fatigue cracks in areas of movement direction change. At the same time, the processes of surface layers grease deformation decrease due to a decline in the magnitude of shear stresses at the contact area. The zone of fatigue cracks formation is moved deep into the material and it leads to an increase in the time before material catastrophic fatigue wear on the contacting surfaces.

5 Conclusions

Obtained results allow to conclude that the addition of ultrafine copper powder into a grease lubricant for machinery parts and assemblies with reversible friction leads to 65–70% friction force reduction and 24–28% depth of friction surface damage reduction. Based on the results of a comparative analysis of the contact stress values determined using computer simulation, it is evaluated that the addition of copper powder into the grease lubricant leads to 18–20% contact pressure reduction and make it possible to extend the service life of the bearing assembly up to 1.5–2 times compared with base lubricants.

References

1. Garkunov DN (2001) Tribotekhnika: iznos i bezysnosnost' (Tribotechnic: wear and hopelessness). Publishing house of the Moscow Agricultural Academy, Moscow
2. Evdokimov VD (1977) Reversivnost' treniya i kachestvo mashin (Friction reversibility and machine quality). Technique, Kiev
3. Kogaev VP, Drozdov YN (1991) Prochnost' i iznosostoykost' detaley mashin (Durability and wear resistance of machine parts). Higher School, Moscow
4. Sosnovsky LA, Makhutov NA (2000) Tribofatika: iznosoustalostnyye povrezhdeniya v problemakh resursa i bezopasnosti mashin (Tribo-fatigue: wear fatigue damage in problems of resource and safety of machines). NPO Tribo-fatika, Moscow-Gomel
5. Shenderova OA, Gruen DM (2007) Ultrananocrystalline diamond, synthesis, properties, and applications. William Andrew Publishing Norwich, New York

6. Terentyev VF, Erkaev NV, Dokshanin SG (2003) Tribonadezhnost' podshipnikovyykh uzlov v prisutstvii modifitsirovannykh smazochnykh kompozitsiy (Tribune reliability of bearing units in the presence of modified lubricant compositions). Publishing House "Science" SB RAS, Novosibirsk
7. Kuzmin VN, Pogodaev LI, Dudko PP (1999) Vliyaniye smazochnykh kompozitsiy s razlichnymi prisadkami na iznos tribosopryazheniy (Effect of lubricating compositions with various additives on the wear of friction units). Friction Wear Grease 1(3):24
8. Pogodaev LI, Kuzmin VN (2004) Vliyaniye smazochnykh kompozitsiy s dobavkami na rabotosposobnost' tribosopryazheniy (Influence of lubricating compositions with additives on the performance of friction units). Problems Mech Eng Mach Reliab 1:51–62
9. Dudan AV, Gushcha AA (2015) Metody i sredstva tribomodifitsirovaniya poverkhnostey treniya (Methods and means of tribomodification of friction surfaces). Bulletin of Polotsk State University. Ser B Industry Appl Sci 11:49–52
10. Kustov OY (2015) Polucheniye kompozitsiy iz smazochnogo masla, nanoporoshka oksida alyuminiya i PAV dlya snizheniya treniya v podshipnikakh kacheniya (Getting compositions from lubricating oil, nanopowder of aluminum oxide and surfactants to reduce friction in rolling bearings). Bull Perm Scientific Center 2:43–48
11. Muravyev IB, Korneev AA (2014) Problemy ispol'zovaniya i perspektivy primeneniya metalloplakiruyushchikh smazochnykh materialov (Problems of use and prospects for the use of metal cladding lubricants). Service Russia Abroad 1(48):12–20
12. Padgurskas J, Rukuiza R, Prosycevas I et al (2013) Tribological properties of lubricant additives of Fe, Cu and Co nanoparticles. Tribol Int 60:224–232
13. Kuzmin VN, Pogodaev LI, Usachev VV (2009) Lubricating materials with additives (problems and perspectives). J Mach Manuf Reliab 4(38):364–368
14. Rudnick LR (2009) Lubricant additives: chemistry and applications. CRC Press, New York
15. Tesakova MV, Parfenyuk VI, Godlevsky VA (2008) Vliyaniye dobavok ul'tradispersnykh (nanorazmernykh) med'soderzhashchikh poroshkov na tribologicheskiye svoystva promyshlennykh smazok (Influence of additives of ultrafine (nano-sized) copper-containing powders on the tribological properties of industrial lubricants). Electro Process Mater 6:56–62
16. Frishberg IV, Landau MB (2006) Grease grease. Russian Federation Patent 2267520, 10 Jan 2006
17. Kolesnikov VI, Sychev AP, Lapitsky AV et al (2014) Grease grease. Russian Federation Patent 2514919, 10 May 2014
18. Balabanov VI, Bolgov VY, Ishchenko SA et al (2011) Metal-plating reducing additive to grease lubricants. Russian Federation Patent 2432386, 10 July 2011
19. Makhutov NA (2005) Konstruktsionnaya prochnost', resurs i tekhnogennaya bezopasnost' (Structural strength, resource and man-made safety). Publishing House "Science" SB RAS, Novosibirsk
20. Kuzharov AS, Kuzharov AA (2011) Yeshcho raz i neskol'ko inache o metalloplakirovani, FABO i bezysnosnosti (Once again and somewhat differently about metal plating, FABO and hopelessness). Proc Samara Scientific Center of the Russian Acad Sci 4(3):772–775
21. Pogodaev LI, Kuzmin VN, Tretyakov DV (2003) Vliyaniye metalloplakiruyushchikh dobavok k greasemym smazkam na rabotosposobnost' tribosopryazheniy (The influence of metal-cladding additives to greases on the performance of tribo-conjugations). Problems Mech Eng Reliabf Mach 1:54–65

Numerical Modelling of Fluid-Film Bearing Lubricated with Magnetorheological Fluid



A. Babin, A. Fetisov and V. Tyurin

Abstract The present research considers the application of magnetorheological fluids as lubricants for journal fluid-film bearings. In order to solve an ever occurring problem of enhancing the performance of rotor machines to meet industrial requirements, a tribomechatronic system is proposed with a journal fluid-film bearing lubricated with a magnetorheological fluid. This type of fluids could be used as a direct actuator for a mechatronic rotor positioning system for rotor machines. As a part of a complex research on tribomechatronic bearings, the present research features a conceptual and a mathematical model of a journal fluid-film bearing that is lubricated with a magnetorheological fluid. The mathematical model is based on the Reynolds equation, and additional expressions take variable viscosity and presence of magnetic field into account. The paper features a two-step verification of the model based on comparison with experimental results by other researchers. It outlines certain peculiarities of the operation of fluid-film bearings lubricated with MRFs and sets directions for further research.

Keywords Tribomechatronics · Journal bearing · Hydrodynamic lubrication · Numerical simulation · Magnetorheological fluid · Mathematical model

1 Introduction

Enhancement of operational characteristics of bearings, namely increase of load capacity, dynamic characteristics, energy efficiency and life time, corrosion resistance, etc., is conventionally provided by means of development of functioning principles of tribo-pairs, application of new designs and modification of lubricants. Ferromagnetic and magnetorheological fluids (MRF) are one of the basic examples of modification of lubricants.

A. Babin (✉) · A. Fetisov · V. Tyurin
Research Lab “Modelling of Hydro and Mechanical Systems”, Orel State University,
29, Naugorskoe Sh., Orel 302020, Russia
e-mail: alex.mech.osu@gmail.com

Application of ferrofluids as lubricants for bearings proved to be connected with various obstacles as experimental studies showed that they require high current and strong electromagnetic field in order to control the properties of the fluid. Research in this field, however, shows promising results [1–4]. On the other hand, the properties of MRFs are significantly easier to control as they do not require a strong magnetic field. Perhaps, this is the main reason why the number of papers on MRFs and their properties is so high [5–8]. Research on MRFs as lubricants for fluid-film bearings shows that their application is reasonable in most of cases as magnetic forces are comparable in magnitude with hydrodynamic forces that occur in the fluid film [9–11]. Such effect could manifest itself under certain conditions, e.g. low rotational speed, high eccentricity and heavy loads.

Scientific idea of the fundamental research in the field of active bearings with magnetorheological fluids is to introduce ‘smart’ materials as actuators for rotor-bearing systems, where rotor’s position could be adjusted by means of controlling the rheological properties of the fluid. So, the aim of the present research is to contribute to the idea and solution of the problem in question.

2 Numerical Modelling of Active Bearings with MRF

2.1 Conceptual Model

Journal fluid-film bearing with active viscosity control is essentially a non-magnetic sleeve in which a shaft made out of a magnetically soft material rotates (Fig. 1). The radial gap between the sleeve and the rotor is filled with magnetorheological lubricant. With nonzero rotational frequency of the shaft ω , the fluid is dragged into the converging gap between the sleeve and the bearing and thus hydrodynamic pressure in the fluid film is generated which under certain conditions could provide total separation between the sleeve and the shaft. Solenoids are located around the sleeve and, as current circulates and affects magnetic particles, the magnetic particles in the fluid form chain-like structures and thus provide a certain increase of viscosity by means of increasing the yield stress of the fluid. Change of viscosity of a lubricant significantly affects pressure distribution and, consequently, load capacity of a fluid-film bearing. Current through the solenoids is set with a power supply manually or automatically. If automatic mode is switched on, the current is controlled according to a control program based on a specific control algorithm. The aim of control is to keep the shaft in the desired position, which is chosen based on some criterion, for example, energy efficiency or stability. Current position of the shaft is determined using two displacement sensors; signal is then acquired and processed by means of a data acquisition device. This way, the whole system ‘bearing—sensors—control system—actuator’ becomes a closed loop mechatronic system.

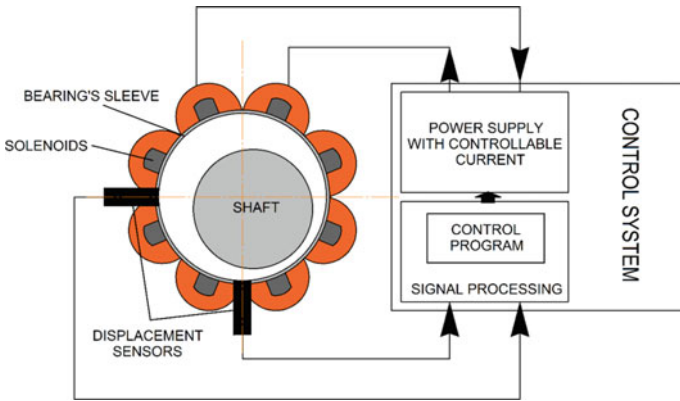


Fig. 1 Conceptual model of a bearing with MRF

2.2 Mathematical Model

Mathematical model of a journal fluid-film bearing lubricated with magnetorheological fluid is based on the calculation diagram in Fig. 2. In order to determine the influence of current through the solenoids on the characteristics of the bearing, a mathematical model has been developed based on the Reynolds equation that governs pressure distribution in the fluid film and additional expressions to take into account presence of a homogeneous magnetic field.

Generalised Reynolds equation for a case of a laminar flow of a non-Newtonian fluid, viscosity of which depends on the current through the solenoids and shear rate, takes the following form in Cartesian coordinates:

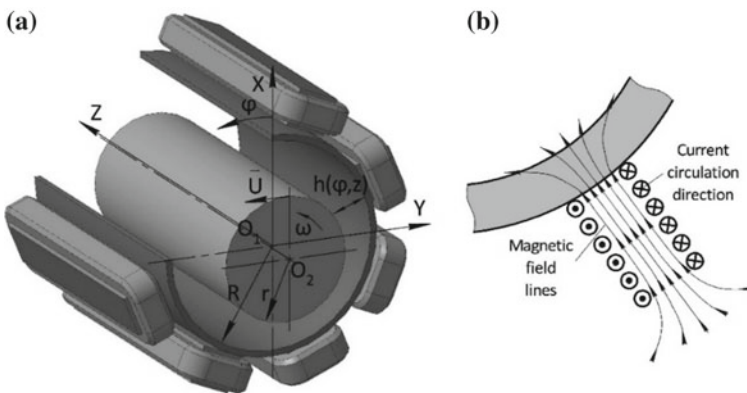


Fig. 2 Calculation diagram of the bearing (a) and magnetic field lines across the fluid film (b)

$$\frac{\partial}{\partial x} \left[\frac{h^3}{\mu} \frac{\partial p}{\partial x} \right] + \frac{\partial}{\partial z} \left[\frac{h^3}{\mu} \frac{\partial p}{\partial z} \right] = 6U \frac{\partial h}{\partial x}, \tag{1}$$

where x and z —‘circumferential’ and axial coordinates accordingly, h —local film thickness, μ —dynamic viscosity, p —local pressure and U —linear velocity of the shaft’s surface.

In order to verify the model of the fluid film at this point, comparison of numerical results obtained using the presented model and experimental results in [12] has been carried out. The following parameters were used during modelling: viscosity of the base oil— 11×10^{-3} Pa s, length of the bearing—0.08 m, diameter of the shaft—0.09984 m, radial clearance—86 μm and shaft’s rotation speed—500 rpm. Results are presented in Table 1. Here, viscosity was considered as an approximation function using the data from [12] in the following form:

$$\mu = 2^{1-z} kH^{z-1} \tag{2}$$

where z and k —constants for pseudoplastic fluids, determined using experimental data on viscosity measurements of the base oil in [12], H —intensity of shear rate, [1/s].

It could be seen that the results obtained using the model based on (1) and (2) matches experimental results very well, and so to this model a new element shall be introduced, namely magnetic field generated by solenoids. Unlike the base oil, viscosity of which changes only slightly with the change of shear rate, viscosity of an MRF depends significantly on both shear rate and magnetic induction. Manufacturers of MRFs usually include experimental data on shear stress versus shear rate and yield shear stress versus magnetic field strength, and so, based on approximation of experimental data, it is possible to model behaviour of an MRF with various parameters. As it has been shown in [13], yield shear stress of an MRF could be approximated with sufficient accuracy using the following power law:

$$\tau_0(B) = k_0 B^n, \tag{3}$$

where τ_0 —yield shear stress, B —magnetic induction and k_0 and n —power function’s constants.

Table 1 Verification of the model of the fluid film

Coordinates of the shaft’s centre $X, Y, \mu\text{m}$	Load capacity, kN [12]	Load capacity, kN (Present study)	Mean error, %
−45.82, −61.94	9	8.66	6
−49.51, −56.70	7.2	7.48	
−56.87, −34.99	3.6	4.4	
−47.31, −5.491	1.72	1.91	
−25.8, 0	0.8	0.81	

Considering the sleeve of the bearing and the shaft as a divided core of an electromagnet with the gap filled with an MRF, magnetic induction at any circumferential location of the fluid film could be expressed as follows:

$$B = k_b \mu_0 \mu_r \frac{I}{h}, \tag{4}$$

where μ_0 —vacuum permeability, μ_r —relative permeability of an MRF, I —current and k_b —design parameter.

Equations (1), (3) and (4) make up a mathematical model of a fluid-film bearing lubricated with an MRF. In order to verify the model at this point, numerical and experimental results presented in [9] are used for comparison. In [9], a quite comprehensive study of a ferrofluid APG s10n by FERROTEC and an MRF122-2ED by LORD Corp. is presented, and authors have done a great job showing the influence of shaft material and presence of magnetic field on the properties of the bearing. Experimental and numerical results presented in [9] have been digitised and used for comparison with the numerical results of the present study using the same modelling parameters: bearing’s diameter—0.05 m, bearing’s length—0.05 m, radial clearance—100 μm and dynamic viscosity of the base oil—0.042 Pa s. The maximum current intensity is 3 A, and at this current, the magnetic field into the bearing is 40 kA/m, which results in magnetic induction being 0.213 T. Verification results are shown in Fig. 3. Despite the fact that authors of [9] omit explanation of considerable deviation of numerical and experimental results in the area of high eccentricity (0.08–0.1 mm), the fact that numerical results of the present study show the same deviation, the following conclusion could be made: there are processes that affect MRF’s rheological properties that occur with high hydrodynamic pressures, e.g. temperature increase and dependency of viscosity on pressure unaccounted for. Other than that, numerical results obtained using the mathematical model presented in this paper match experimental results in [9] in the range of normal operational eccentricities, so it could be considered fully verified.

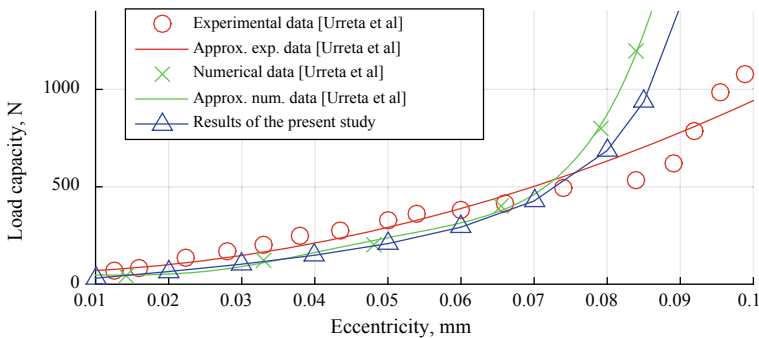


Fig. 3 To verification of the mathematical model



3 Numerical Simulations of a Bearing with MRF

As it has been determined that the presented mathematical model is accurate enough on a wide range of eccentricities, further research could be continued. As a part of a complex research of tribomechanic bearings with MRFs as active components, the present study is going to focus on determination of influence various parameters have on bearing's characteristics. The present paper covers numerical studies that are going to be followed by experimental studies using an original test rig with a developed active journal fluid-film bearing. The designed active bearing has the following parameters: length of the bearing—0.04 m, shaft's diameter—0.04 m, radial clearance—200 μm and lubricant—MRF-140CG by LORD Corp., $\mu = 0.280 \text{ Pa s}$, $n = 3000 \text{ rpm}$. All the necessary values for Eqs. (3) and (4) have been taken from the MRF's datasheet.

The most important characteristic of a fluid-film bearing is its load capacity—the value that ensures that the necessary load could be supported by the bearing. This value is crucial and used to design a bearing suitable for a specific machine. Load capacity of a fluid-film bearing is a value obtained by means of integration of the Reynolds equation:

$$R_X = - \int_0^L \int_0^{\pi D} p \sin \phi dx dz; \quad R_Y = - \int_0^L \int_0^{\pi D} p \cos \phi dx dz; \quad (5)$$

$$W = \sqrt{R_X^2 + R_Y^2} \quad (6)$$

where R_X and R_Y —components of the reaction force of the fluid film, L and D —length and diameter of the bearing accordingly, ϕ —circumferential coordinate and W —total load capacity of the bearing.

Figure 4 shows the influence of current through solenoids on the pressure distribution in mid-cross section of the bearing.

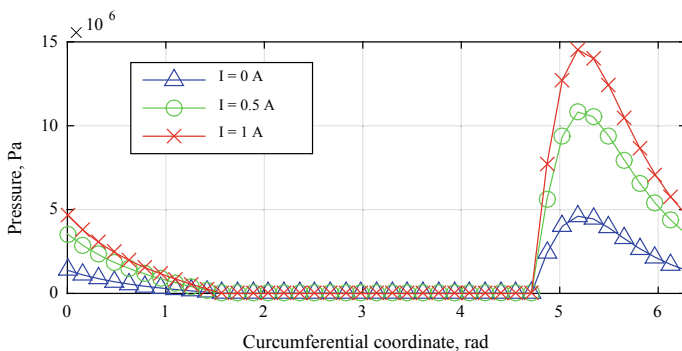


Fig. 4 Pressure versus current in solenoids

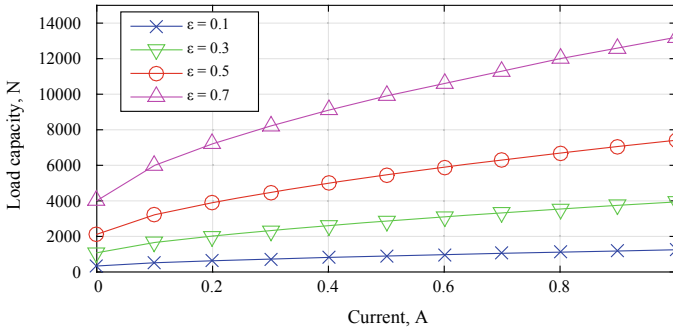


Fig. 5 Load capacity versus current in solenoids

Using Eq. (6), load capacity at different eccentricities was determined with various values of current in solenoids (Fig. 5).

From the results in Figs. 4 and 5, one could see that both pressure and consequently load capacity depend significantly on the current in solenoids. The dependency is also obviously nonlinear, which suggests, that in order to control rotor’s position by means of adjustment of rheological properties of the MRF, a nonlinear control would be needed.

4 Conclusions

The present paper features a mathematical model that has been developed as a part of a research of tribomechatronic bearings. The conceptual model of the bearing as a tribomechatronic system consists of three basic parts: tribo-pair (fluid-film bearing lubricated with an MRF), electrical part—sensors and actuators (direct—MRF and indirect—a power supply with controllable current) and a control program based on a nonlinear controller. Present research is a first step in research of a complicated tribomechatronic system, and some very important results have been obtained: (1) a mathematical model has been developed and verified using experimental data from other researchers and (2) nonlinearity of load capacity versus current in solenoids relation has been determined. Using the developed mathematical model, it has also been determined, that it is possible to increase load capacity of the designed fluid-film bearing by means of increasing the current in solenoids by almost 10 times with the given in the para. 3 parameters.

Given the promising results obtained in this paper, the following is set to be done for further research: study of dynamic characteristics of a rotor on a bearing lubricated with an MRF—development of a model of a dynamic system; introduction of a controller to the dynamic system—development of a model of an actuator and controller. Further experimental research is based on the original test rig designed to study active fluid-film bearings lubricated with MRFs.



Acknowledgements The present research has been carried out as a part of the RFBR project No. 18-38-00465.

References

1. Montazeri H (2007) Numerical analysis of hydrodynamic journal bearings lubricated with ferrofluids. *Eng Tri Proc. IMechE Part J* 222:51–60
2. Osman TA, Nada GS, Safar ZS (2001) Static and dynamic characteristics of magnetized journal bearings lubricated with ferrofluid. *Tribol Int Elsevier* 34:369–380
3. Jaw-Ren L, Po-Jui L, Tzu-Chen H (2013) Lubrication performances of short journal bearings operating with non-newtonian ferrofluids. *Z Naturforsch* 68a:249–254
4. Tipei N (1982) Theory of lubrication with ferrofluids: application to short bearings. *J Lubr* 104(4):510–515
5. Spaggiari A, Castagnetti D, Golinelli N et al (2016) Smart materials: properties, design and mechatronic applications. *J Mater Design Appl Proc IMechE Part L* 1–29
6. Ghaffari A, Hashemabadi SH, Ashtiani M (2015) A review on the simulation and modeling of magnetorheological fluids. *J Intell Mater Syst Struct* 26(8):881–904
7. Jonsdottir F, Gudmundsson KH, Dukman TB et al (2010) Rheology of perfluorinated polyether-based MR fluids with nanoparticles. *J Intell Mater Syst Struct* 21:1051–1060
8. Ashtiani M, Hashemabadi SH (2015) The effect of nanosilica and nano-magnetite on the magnetorheological fluid stabilization and magnetorheological effect. *J Intell Mater Syst Struct* 26(14):1887–1892
9. Urreta H, Leicht Z, Sanchez A et al (2010) Hydrodynamic bearing lubricated with magnetic fluids. *J Intell Mater Syst Struct* 21:1491–1499
10. Laukiavich CA, Braun MJ, Chandy AJ (2014) A comparison between the performance of ferro- and magnetorheological fluids in a hydrodynamic bearing. *Journal Eng Tribol Proc IMechE* 228(6):649–666
11. Omidbeygi F, Hashemabadi SH (2012) Experimental study and CFD simulation of rotational eccentric cylinder in a magnetorheological fluid. *J Magn Magn Mater* 324:2062–2069
12. Kasai M, Fillon M, Bouyer J et al (2012) Influence of lubricants on plain bearing performance: analysis of bearing performance with polymer-containing oils. In: 2012 STLE Annual Meeting & Exhibition, St. Louis, Missouri, USA, 5 p
13. Zapomel J, Ferfecki P, Forte P (2017) A new mathematical model of a short magnetorheological squeeze film damper for rotordynamic applications based on a bilinear oil representation—derivation of the governing equations. *Appl Math Model* 52:558–575